

ICITEE 2023

CONFERENCE PROCEEDINGS

THE 15th INTERNATIONAL CONFERENCE ON
INFORMATION TECHNOLOGY AND
ELECTRICAL ENGINEERING

26 - 27 OCTOBER 2023 | CHIANG MAI, THAILAND





IEEE
**Computational
Intelligence
Society**
Thailand Chapter

Organizer
IEEE Computational Intelligence Society Thailand Chapter

Organized by



Co-organizer
School of Information Technology
King Mongkut's Institute of Technology
Ladkrabang (KMUTL), Thailand



Co-organizer
Department of Electrical Engineering
and Information Technology, Universitas
Gadjah Mada (UGM), Indonesia

Technically Co-Sponsored by



TABLE OF CONTENTS

| | |
|--|-----|
| WELCOME MESSAGES | 1 |
| COMMITTEES | 4 |
| PROGRAM SCHEDULE | 6 |
| TECHNICAL PROGRAM | 7 |
| FLOOR PLAN | 9 |
| PLENARY SESSIONS | 10 |
| PROF. DR. UJJWAL MAULIK | 10 |
| ASSOC. PROF. DR. SANSANEE AUEPHANWIRIYAKUL | 12 |
| DR. LUKITO EDI NUGROHO | 13 |
| ASSOC. PROF. DR. SIRIDECH BOONSANG | 14 |
| PROF. DR. FRANCK LEPRÉVOST | 16 |
| CONFERENCE SESSIONS | 18 |
| AUTHOR INDEX | 405 |

WELCOME MESSAGES

Message from Chair of IEEE CIS Thailand Chapter



Phayung Meesad, IEEE CIS Thailand

Greetings to all attendees of the 15th International Conference on Information Technology and Electrical Engineering (ICITEE 2023). This momentous occasion signifies the IEEE-CIS Thailand Chapter's official foray into conference organization. Traditionally, our Chapter has primarily played a role in providing technical sponsorship for conferences. However, as our Chapter continues its growth trajectory, it is only fitting that we expand our role in the organization of conferences.

For some context, the IEEE Computational Intelligence Society (CIS) Thailand Chapter was established in 2015. It is worth noting that the inception of our Chapter can be attributed to the unwavering dedication of Dr. Kitsuchart Pasupa and Dr. Kuntpong Woraratpanya, who garnered substantial support from IEEE-CIS members across the three King Mongkut's institutions (3K's). They currently serve as the organizing committee for both of our co-located conferences. Dr. Kitsuchart Pasupa serves as the Program Chair for ICITEE, while Dr. Kuntpong Woraratpanya is an Advisory Board member for ICITEE and the Chair for JSCI. Over time, our Chapter's membership has transcended the boundaries of the 3K's, now encompassing participants from all corners of the nation.

Our Chapter embarked on its journey by initiating the student-centric Joint Symposium on Computational Intelligence (JSCI) in 2016. It is with immense pride that we now incorporate JSCI as a distinguished special session within ICITEE 2023. Remarkably, JSCI has risen to prominence and now enjoys international recognition, including participation in JSCI. We have also secured the privilege of publishing preprints from JSCI on IEEE TechRxiv, with extended versions making their way to collaborative international conferences and extended journal papers.

Let's maintain our connection, ensuring that you are consistently updated in the dynamic and ever-evolving realm of computational intelligence. We extend our heartfelt wishes for a delightful experience at our co-located conferences and warmly encourage you to reach out to us with any comments, suggestions, or requests.

Phayung Meesad
IEEE CIS Thailand Chapter Chair

Message from General Co-Chairs



Arit Thammano,
King Mongkut's Institute of
Technology Ladkrabang, Thailand



Roni Irnawan,
Universitas Gadjah Mada,
Indonesia

On behalf of the organizing committee, we are honored and delighted to welcome you to the 15th International Conference on Information Technology and Electrical Engineering (ICITEE 2023) taking place on 26 – 27 October 2023 in Chiang Mai, Thailand.

ICITEE 2023 aims to strengthen the collaboration among academics, professionals and researchers and provide a forum for them to discuss and exchange their research results, innovative ideas, and experiences in all aspects of advanced and synergistic technologies. This ICITEE 2023 program will foster discussion and inspiration among participants in order to initiate collaboration for the advancement of our field. At this year's conference, Prof. Dr. Ujjwal Maulik, Assoc. Prof. Dr. Sansanee Auephanwiriyaikul, Prof. Dr. Lukito Edi Nugroho, Assoc. Prof. Dr. Siridech Boonsang, and Prof. Dr. Franck Leprévost will join us as keynote speakers to showcase advances in Information Technology and Electrical Engineering.

We are grateful for the efforts of all our keynote speakers, organizing committee members, technical program committee members, track chairs, session chairs, student volunteers, authors and presenters for their contributions to a successful ICITEE 2023. Lastly, we wish you all a productive and enjoyable conference experience. We hope that you will have a wonderful time at ICITEE 2023.

Arit Thammano, King Mongkut's Institute of Technology Ladkrabang, Thailand
Roni Irnawan, Universitas Gadjah Mada, Indonesia
General Co-Chairs

Message from Technical Program Co-Chairs



Kitsuchart Pasupa,
King Mongkut's Institute of
Technology Ladkrabang, Thailand



Syukron Abu Ishaq Alfarozi,
Universitas Gadjah Mada, Indonesia

On behalf of the Technical Program Committee, it is a great honour to extend a warm welcome to all participants of the 15th International Conference on Information Technology and Electrical Engineering (ICITEE 2023) in the enchanting city of Chiang Mai, Thailand. Although our original plan was to convene for ICITEE 2021 in Chiang Mai, the persistent challenges posed by the COVID-19 pandemic thwarted our intentions. Consequently, we turned to virtual gatherings for three consecutive years since the pandemic's onset. It brings us immense joy to announce that ICITEE 2023 marks our return to an in-person format.

This year, we are thrilled to have received 111 papers authored by 335 scholars from 19 different countries. Following a rigorous double-blind review process, with no fewer than three reviewers assessing each submission, our dedicated team, in collaboration with the track chairs, has accepted 67 papers. This impressive acceptance rate of 60.4% has paved the way for an intellectually stimulating program at ICITEE 2023. Our two-day event will include five keynote presentations and 12 parallel oral sessions, which will feature two special sessions: the 14th Joint Symposium on Computational Intelligence (JSCI14) and Business Management and Informatics.

We wish to express our heartfelt gratitude to all the track chairs: Dr. Somying Thainimit, Dr. Praphan Pavarangkoon, Dr. Nat Dilokthanakul, Dr. Jonglak Pahasa, Dr. Dzuhri Radityo Utomo, Dr. Ridwan Wicaksono, and Dr. Yohan Fajar Sidik. Their invaluable contributions to the review process have been instrumental in shaping this year's conference. We also extend our thanks to Dr. Kuntpong Woraratpanya and Dr. Singha Chaveesuk for their exceptional efforts in organizing the special sessions. Our appreciation goes out to the entire Program Committee and our reviewers, whose insightful and constructive feedback has greatly enhanced the quality of the papers presented.

Furthermore, we extend our gratitude to all participants, authors, and members of the organizing committee for their unwavering dedication, which has been pivotal in making ICITEE 2023 a successful event. Lastly, we would like to express our sincere appreciation to IEEE for their support in facilitating the publication of our conference proceedings.

We look forward to an enriching and memorable ICITEE 2023, where knowledge and collaboration will flourish in the vibrant setting of Chiang Mai. Welcome, and let us embark on this academic journey together.

Kitsuchart Pasupa, King Mongkut's Institute of Technology Ladkrabang, Thailand
Syukron Abu Ishaq Alfarozi, Universitas Gadjah Mada, Indonesia
Program Co-Chairs

COMMITTEES

Advisory Boards

Chu Kiong Loo, UM, Malaysia
 Hanung Adi Nugroho, UGM, Indonesia
 Kuntpong Woraratpanya, KMITL, Thailand
 Lukito Edi Nugroho, UGM, Indonesia
 Masanori Sugimoto, HU, Japan
 Oyas Wahyunggoro, UGM, Indonesia
 Risanuri Hidayat, UGM, Indonesia
 Sasongko Pramono Hadi, UGM, Indonesia
 Siridech Boonsang, KMITL, Thailand
 Ujjwal Maulik, JU, India

General Chair

Arit Thammano, KMITL, Thailand
 Roni Irnawan, UGM, Indonesia

Technical Program Chair

Kitsuchart Pasupa, KMITL, Thailand
 Syukron Abu Ishaq Alfarazi, UGM, Indonesia

Track Chairs

Dzuhri Radityo Utomo, UGM, Indonesia
 Nat Dilokthanakul, KMITL, CIS Thailand Chapter
 Praphan Pavarangkoon, KMITL, Thailand
 Ridwan Wicaksono, UGM, Indonesia
 Somying Thainimit, KU, Thailand
 Yohan Fajar Sidik, UGM, Indonesia
 Jonglak Pahasa, UP, Thailand

Special Session Chairs

Kuntpong Woraratpanya, KMITL, Thailand
 Singha Chaveesuk, KMITL, Thailand

Organizing Committees

Ahmad Ataka Awwalur Rizqi, UGM, Indonesia
 Ahmad Nasikun, UGM, Indonesia
 Araya Ariya, LPRU, Thailand
 Azkario Rizky Pratama, UGM, Indonesia
 Bundit Busaba, LPRU, Thailand
 Chanboon Sathitwiriawong, KMITL, CIS Thailand Chapter
 Ferdin Jon, TNI, CIS Thailand Chapter
 Jonathan Hoyin Chan, KMUTT, Thailand
 Kamesh Namuduri, UNT, USA
 Kamol Wasapinyokul, KMITL, Thailand
 Kuroki Yoshimitsu, NIT-Kurume College, Japan
 Maleerat Maliyaem, KMUTNB, CIS Thailand Chapter
 Nat Dilokthanakul, KMITL, CIS Thailand Chapter
 Nont Kanungsukkasem, KMITL, Thailand
 Olarn Wongwirat, KMITL, Thailand
 Phayung Meesad, KMUTNB, CIS Thailand Chapter
 Pichaphob Panphae, RMUTL, Thailand
 Piraprob Junsantor, LPRU, Thailand
 Pramuk Boonsiang, TNI, CIS Thailand Chapter
 Praphan Pavarangkoon, KMITL, Thailand
 Roni Irnawan, UGM, Indonesia
 Smart Moodleah, KMITL, Thailand

Sarayut Nonsiri, TNI, CIS Thailand Chapter
 Shigeru Kuchii, NIT-Kitakyushu College, Japan
 Sirasit Lochanachit, KMITL, Thailand
 Somnuk Phon-Amnuaisuk, UTB, Brunei
 Syukron Abu Ishaq Alfarazi, UGM, Indonesia
 Vithida Chongsuphajaisiddhi, KMUTT, Thailand
 Wannaporn Teekeng, RMUTL, Thailand
 Warune Buavirat, KMITL, Thailand
 Worapoj Kreesuradej, KMITL, Thailand

Program Committees

Adhistya Permanasari, UGM, Indonesia
 Ahmad Ataka, UGM, Indonesia
 Ahmad Nasikun, UGM, Indonesia
 Akadej Udomchaiporn, KMITL, Thailand
 Anggun Isnawati, ITTP, Indonesia
 Aphirak Jansang, KU, Thailand
 Arit Thammano, KMITL, Thailand
 Asmidar Abu Bakar, UNITEN, Malaysia
 Assadarat Khurat, MU, Thailand
 Aurawan Imsombut, DPU, Thailand
 Azkario Rizky Pratama, UGM, Indonesia
 Boonyarat Phadermrod, KU, Thailand
 Bundit Thanasopon, KMITL, Thailand
 Chakarida Nukoolkit, KMUTT, Thailand
 Chantana Chantrapornchai, KU, Thailand
 Chawasak Rakpenthai, UP, Thailand
 Chumphol Bunkhumpornpat, CMU, Thailand
 Dani Adhista, UGM, Indonesia
 David Banjerdpongchai, CU, Thailand
 David Silalahi, ANU, Australia
 Denchai Worasawate, KU, Thailand
 Dhany Arifianto, ITS, Indonesia
 DThomas Hatta Fudholi, UII, Indonesia
 Dwi Suroso, UGM, Indonesia
 Dyonisius Ariananda, UGM, Indonesia
 Dyonisius Dony Ariananda, UGM, Indonesia
 Dzuhri Radityo Utomo, UGM, Indonesia
 Ekachai Phaisangittisagul, KU, Thailand
 Ekkarat Boonchieng, CMU, Thailand
 Eny Sukani Rahayu, UGM, Indonesia
 Guntur Putra, UGM, Indonesia
 Gwanggil Jeon, INU, Korea (South)
 Hadha Afrisal, UNDIP, Indonesia
 Igi Ardiyanto, UGM, Indonesia
 Imran Ghani, UTM, Malaysia
 Indriana Hidayah, UGM, Indonesia
 Issarapong Khuankrue, KMITL, Thailand
 Iswandi Iswandi, UGM, Indonesia
 Iwan Setyawan, UKSW, Indonesia
 Jian Qu, PIM, Thailand
 Jonglak Pahasa, UP, Thailand
 Karn Patanukhom, CMU, Thailand
 Kazunori Hayashi, KyotoU, Japan
 Kitsuchart Pasupa, KMITL, Thailand
 Kreangsuk Kraikitrat, UP, Thailand
 Krittika Kantawong, UP, Thailand
 Kuntpong Woraratpanya, KMITL, Thailand

Lapas Pradittasnee, KMITL, Thailand
 Maleerat Maliyaem, KMUTNB, Thailand
 Maulahikmah Galinium, SGU, Indonesia
 Miti Ruchanurucks, KU, Thailand
 Mochammad Wahyudi, UGM, Indonesia
 Mohd. Brado Frasetyo, UGM, Indonesia
 Montri Karnjanadecha, PSU, Thailand
 Nat Dilokthanakul, KMITL, Thailand
 Nattapong Kitsuwat, UEC, Japan
 Nattapong Pothi, UP, Thailand
 Naufal Fauzan, UGM, Indonesia
 Nawanol Theera-Ampornpant, PSU, Thailand
 Nont Kanungsukkasem, KMITL, Thailand
 Norsuzila Ya'acob, UITM, Malaysia
 Olarik Surinta, MSU, Thailand
 Olarn Wongwirat, KMITL, Thailand
 Paneepan Sombat, RMUTTO, Thailand
 Panisa Treepong, PSU, Thailand
 Panwit Tuwanut, KMITL, Thailand
 Paramet Wirasanti, CMU, Thailand
 Pattanapong Chantamit-O-Pas, KMITL, Thailand
 Payungsak Kasemsumran, MJU, Thailand
 Peerayot Sanposh, KU, Thailand
 Phayung Meesad, KMUTNB, Thailand
 Pongsarun Boonyopakorn, KMUTNB, Thailand
 Ponrudee Netisopakul, KMITL, Thailand
 Poonlap Lamsrichan, KU, Thailand
 Pornavalai Chotipat, KMITL, Thailand
 Pornchai Mongkolnam, KMUTT, Thailand
 Pornchai Phukpattaranont, PSU, Thailand
 Pornsuree Jamsri, KMITL, Thailand
 Pramuk Boonsiang, TNI, Thailand
 Praphan Pavarangkoon, KMITL, Thailand
 Prapto Nugroho, UGM, Indonesia
 Pudsadee Boonrawd, KMUTNB, Thailand
 Pumipong Duangtang, CRRU, Thailand
 Puripat Charnkit, STOU, Thailand
 Reka Inovon, EPFL, Switzerland
 Ridwan Wicaksono, UGM, Thailand
 Rini Hasanah, UB, Indonesia
 Risanuri Hidayat, UGM, Indonesia
 Ryan Benton, USA, USA
 Salin Boonbrahm, WU, Thailand
 Samart Moodleah, KMITL, Thailand
 Sanchai Dechanupaprittha, KU, Thailand
 Sansanee Auephanwiriyaikul, CMU, Thailand
 Sarayut Nonsiri, TNI, Thailand
 Sasin Tiendee, KU, Thailand
 Sasithorn Suchaiya, KU CSC, Thailand
 Sigit Wibowo, UGM, Indonesia
 Sirapat Boonkrong, KMUTNB, Thailand
 Sirion Vittayakorn, KMITL, Thailand
 Somying Thainimit, KU, Thailand
 Sooksan Panichpapiboon, KMITL, Thailand
 Soradech Krootjohn, KMUTNB, Thailand
 Suatmi Murnani, UII, Indonesia
 Sudchai Boonto, KMUTT, Thailand
 Sumet Prabhavat, KMITL, Thailand
 Supakit Nootyaskool, KMITL, Thailand
 Supannada Chotipant, KMITL, Thailand
 Supaporn Chairungsee, WU, Thailand
 Suphamit Chittayasothorn, KMITL, Thailand
 Suphot Chunwiphat, KMUTNB, Thailand
 Suree Khemthong, STOU, Thailand
 Suvit Poomrittigul, KMITL, Thailand
 Syukron Abu Ishaq Alfarozi, UGM, Indonesia
 Taufik Djatna, IPB, Indonesia
 Teerasit Kasetkasem, KU, Thailand
 Teerawat Kamnardsiri, CMU, Thailand
 Teguh Adji, UGM, Indonesia
 Thanakron Khongdeach, KU, Thailand
 Thanarat Chalidabhongse, CU, Thailand
 Thatsanee Charoenporn, BUU, Thailand
 Theeralak Satjawathee, PYU, Thailand
 Thirapon Wongsardsakul, BU, Thailand
 Thitinan Kliangsuwan, PSU, Thailand
 Thitiporn Lertrusdachakul, TNI, Thailand
 Thomas Hunziker, HSLU, Switzerland
 Thongchai Kaewkiriya, KMITL, Thailand
 Thongchart Kerdphol, KU, Thailand
 Todsana Chumwattana, RSU, Thailand
 Toshiaki Kondo, SIIT, Thailand
 Tuchsanai Ploysuwan, KMITL, Thailand
 Vita Lystianingrum, ITS, Indonesia
 Vithida Chongsuphajaisiddhi, KMUTT, Thailand
 Wanchaloem Nadda, CMU, Thailand
 Wanthanee Rathasamuth, UDRU, Thailand
 Warakorn Chareornsuk, MU, Thailand
 Warsun Najib, UGM, Indonesia
 Watcharaphong Yookwan, BUU, Thailand
 Wen-Hwa Liao, NTCB, Taiwan
 William Wall, STIU, Thailand
 Wiroonsak Santipach, KU, Thailand
 Worapan Kusakunniran, MU, Thailand
 Worapoj Kreesuradej, KMITL, Thailand
 Worawut Srisukkhom, CMU, Thailand
 Wutthipong Chinnasri, RSU, Thailand
 Yajima Kuniaki, SNCT, Japan
 Yoshimitsu Kuroki, KOSEN, Japan
 Zenghui Wang, UESTC, China

PROGRAM SCHEDULE

Program at a glance

26th October

| Time (UTC+07:00) | Sessions |
|------------------|---------------------|
| 08.30 - 09.00 | Registration |
| 09.00 - 09.30 | Opening Ceremony |
| 09.30 - 10.15 | Plenary Session I |
| 10.15 - 10.30 | Coffee break |
| 10.30 - 11.15 | Plenary Session II |
| 11.15 - 12.00 | Plenary Session III |
| 12.00 - 13.00 | Lunch Break |
| 13.00 - 15.00 | Oral Session I |
| 15.00 - 15.15 | Coffee break |
| 15.15 - 18.15 | Oral Session II |
| 18.30 - 20.30 | Conference Banquet |

27th October

| Time (UTC+07:00) | Sessions |
|------------------|--------------------|
| 09.00 - 09.30 | Registration |
| 09.30 - 10.15 | Plenary Session IV |
| 10.15 - 10.30 | Coffee break |
| 10.30 - 11.15 | Plenary Session V |
| 11.15 - 11.45 | Committee meeting |
| 11.45 - 12.45 | Lunch Break |
| 12.45 - 14.45 | Oral Session III |
| 14.45 - 15.00 | Coffee break |
| 15.00 - 16.40 | Oral Session IV |

TECHNICAL PROGRAM

Thursday 26th October 2023

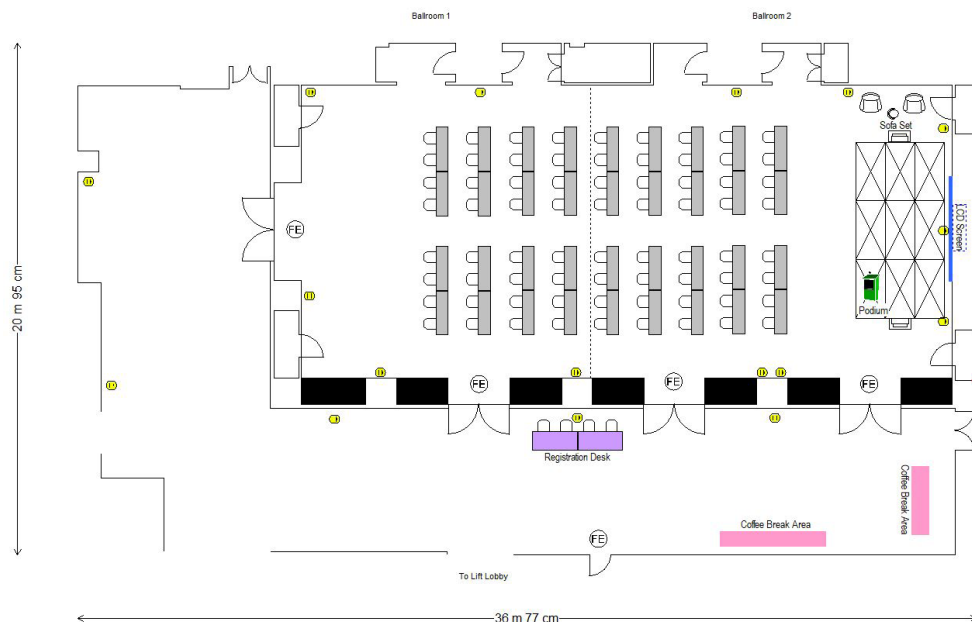
| Time | Program: Thursday 26th October 2023 | |
|---------------|--|-----------------------|
| 08:30 - 09:00 | Registration | Grand Ballroom |
| 09:00 - 09:30 | Opening Ceremony | Grand Ballroom |
| 09:30 - 10:15 | Plenary Session I Keynote Speaker: Assoc. Prof. Dr. Sansanee Auephanwiriyaikul Title: Computational intelligence in biomedical engineering | Grand Ballroom |
| 10:15 - 10:30 | Coffee break | Coffee Break Area |
| 10:30 - 11:15 | Plenary Session II Keynote Speaker: Assoc. Prof. Dr. Siridech Boonsang Title: Generative AI for industrial manufacturing applications | Grand Ballroom |
| 11:15 - 12:00 | Plenary Session III Keynote Speaker: Dr. Lukito Edi Nugroho Title: Smart cities in developing countries: How far can they be made smarter? | Grand Ballroom |
| 12:00 - 13:00 | Lunch Break | Favola Extension Room |
| 13:00 - 15:00 | AIML-1: Artificial Intelligence & Machine Learning 1 | Grand Ballroom |
| | AIML-2: Artificial Intelligence & Machine Learning 2 | Passage Room |
| | PS-1: Power Systems 1 | Expedition Room |
| 15:00 - 15:15 | Coffee break | Coffee Break Area |
| 15:15 - 17:35 | AIML-3: Artificial Intelligence & Machine Learning 3 | Grand Ballroom |
| | CNT-1: Communication & Network Technologies 1 | Expedition Room |
| 15:15 - 18:15 | JSCI: Joint Symposium on Computational Intelligence | Passage Room |
| 18:30 - 20:30 | Conference Banquet | Suthep Hall 3 |

Friday 27th October 2023

| Program: Friday 27th October 2023 | | |
|-----------------------------------|---|-----------------------|
| 09:00 - 09:30 | Registration | Grand Ballroom |
| 09:30 - 10:15 | Plenary Session IV Keynote Speaker: Prof. Dr. Ujjwal Maulik Title: Current trend and future challenges of artificial intelligence and data sciences | Grand Ballroom |
| 10:15 - 10:30 | Coffee break | Coffee Break Area |
| 10:30 - 11:15 | Plenary Session V Keynote Speaker: Prof. Dr. Franck Leprevost Title: Convolutional neural networks at image recognition tasks: Assessing the risks | Grand Ballroom |
| 11:15 - 11:45 | Committee Meeting | Passage Room |
| 11:45 - 12:45 | Lunch Break | Favola Extension Room |
| 12:45 - 14:45 | AIML-4: Artificial Intelligence & Machine Learning 4 | Grand Ballroom |
| | IT: Information Technology | Passage Room |
| 14:45 - 15:00 | CNT-2: Communication & Network Technologies 2 | Expedition Room |
| | Coffee break | Coffee Break Area |
| 15:00 - 16:40 | AIML-5: Artificial Intelligence & Machine Learning 5 | Grand Ballroom |
| | BMI: Business Management and Informatics | Passage Room |
| | PS-2: Power Systems 2 | Expedition Room |

FLOOR PLAN

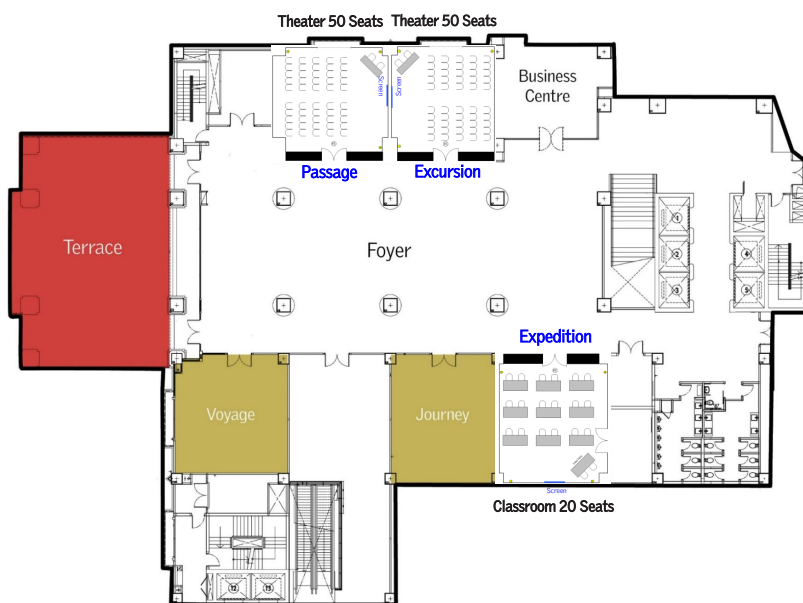
Grand Ballroom



GRAND BALLROOM AND PREFUNCTION 1, 2

Passage & Expedition Room

FLOOR PLAN BREAKOUT ROOMS, FLOOR 03



PLENARY SESSIONS



Prof. Dr. Ujjwal Maulik

Department of Computer Science and Engineering
Jadavpur University, India

Topic : Current Trend and Future Challenges of
Artificial Intelligence and Data Sciences

Abstract :

In this lecture first we will describe current trends in Artificial Intelligence (AI) and Data Science (DS).

Supervised and unsupervised pattern classification are important Machine Learning (ML) techniques which are integral part of AI. Supervised pattern classification methods use training samples for classify the unlabelled data along with cross validation. On the other hand, unsupervised classification partitions the data points into homogeneous groups based on some similarity/dissimilarity metric.

Deep Learning (DL) is a popular ML technique that help feature engineering as well as classification. DL have wide range of applications. We will demonstrate how Deep Learning Techniques can be used efficiently for Intelligence Autonomous Car as well as for healthcare applications. In addition to DL, we will demonstrate the importance of using Graph neural network (GNN). While DL has been used very successfully for image analysis, GNN are being used extensively for unstructured datasets including biological datasets available in the form of graphs containing the interaction between genes, drugs, diseases etc. The importance of explainable AI will be demonstrated.

The second part of the lecture will be focused on the issues and challenges in data science. How CPU speed, complexity of algorithms, architecture all are important for the analysis of complex as well as big data will be described.

Finally the benefits and risk of applying sophisticated AI techniques will be presented. The current challenges and future of AI research will also be discussed.

Biography :

Dr. Ujjwal Maulik is a Professor in the Department of Computer Science and Engineering, Jadavpur University since 2004. He was also the former Head of the same Department. He also held the position of the Principal in charge and the Head of the Dept. of Computer Science and Engineering, Kalyani Government Engineering College. Dr. Maulik has worked in many universities and research laboratories around the world as visiting Professor/ Scientist including Los Alamos National Lab., USA in 1997, Univ. of New South Wales, Australia in 1999, Univ. of Texas at Arlington, USA in 2001, Univ. of Maryland at Baltimore County, USA in 2004, Fraunhofer Institute for Autonomous Intelligent Systems, St. Augustin, Germany in 2005, Tsinghua Univ., China in 2007, Sapienza Univ., Rome, Italy in 2008, Univ. of Heidelberg, Germany in 2009, German Cancer Research Center (DKFZ), Germany in 2010, 2011 and 2012, Grenoble INP, France in 2010,

2013 and 2016, University of Warsaw in 2013 and 2019, University of Padova, Italy in 2014 and 2016, Corvinus University, Budapest, Hungary in 2015 and 2016, University of Ljubljana, Slovenia in 2015 and 2017, International Center for Theoretical Physics (ICTP), Trieste, Italy in 2014, 2017 and 2018. He was the recipient of the Alexander von Humboldt Fellowship during 2010, 2011 and 2012 and Senior Associate of ICTP, Italy during 2012-2018. He is the Fellow of Indian National Academy of Engineers (INAE), India, National Academy of Science India (NASI), India, International Association for Pattern Recognition (IAPR), USA, The Institute of Electrical and Electronics Engineers (IEEE), USA and Asia-Pacific Artificial Intelligence Association (AAIA), Singapore. He is also the Distinguished Member of the ACM. He is a Distinguished Speaker of IEEE as well as ACM.

His research interests include Machine Learning, Pattern Analysis, Data Science, Bioinformatics, Multi-objective Optimization, Social Networking, IoT and Autonomous Car. In these areas he has published ten books, more than four hundred papers, mentoring several start-ups, filed several patents and already guided twenty five doctoral students. His other interests include outdoor Sports and Classical Music.



Assoc. Prof. Dr. Sansanee Auephanwiriyaikul

Computer Engineering Department, Faculty of Engineering, Biomedical Engineering Institute, Chiang Mai University, Thailand

Topic : Computational Intelligence in Biomedical Engineering

Abstract :

Computational Intelligence (CI) relies on and combines several algorithms in fuzzy systems, neural networks, evolutionary computation, swarm intelligence, fractals, chaos theory, artificial immune systems, wavelets, etc., to produce an algorithm that is intelligent somehow. CI has been utilized in many applications for several years. One of the areas that CI has an impact on is the area of biomedical engineering, e.g., medical image processing, medical signal processing and biometrics. One of the CI tools used in those mentioned application is classification or sometimes called decision making. The major area in the classification is to develop a classifier, including, feature generation and selection. In this talk, feature generation methods and classifier methods based on the CI will be presented. We also show those methods on real application, including, medical image diagnosis, medical signal diagnosis, and data analysis in health care system.

Biography :

Sansanee Auephanwiriyaikul (S'98–M'01) received the B.Eng. (Hons.) degree in electrical engineering from the Chiang Mai University, Thailand (1993), the M.S. degree in electrical and computer engineering and Ph.D. degree in computer engineering and computer science, both from the University of Missouri, Columbia, in 1996, and 2000, respectively. After receiving her Ph.D. degree, she worked as a post-doctoral fellow at the Computational Intelligence Laboratory, University of Missouri-Columbia. She is currently an Associate Professor in the Department of Computer Engineering and a deputy director of the Biomedical Engineering Institute, Chiang Mai University, Thailand.

Dr. Auephanwiriyaikul is a senior member of the Institute of Electrical and Electronics Engineers (IEEE). She is an Associate Editor of the IEEE Transactions on Fuzzy System, the IEEE Transactions on Neural Networks and Learning Systems, IEEE Computational Intelligence Magazine, IEEE Transactions on Artificial Intelligence, Engineering Applications of Artificial Intelligence, and ECTI Transactions on Computer and Information Technology. She was a general chair of the IEEE International Conference on Computational Intelligence in Bioinformatics and Computational Biology (CIBCB 2016). She will be a general chair of the IEEE World Congress on Computational Intelligence (WCCI) 2024 (IEEE International Conference on Fuzzy Systems 2024). She was a Technical Program Chair, Organizing Committee in several major conferences including the IEEE International, Conference Fuzzy Systems. She is also a member of several important IEEE CIS technical committees.



Dr. Lukito Edi Nugroho

Department of Electrical Engineering and Information Technology, Faculty of Engineering, Universitas Gadjah Mada, Indonesia

Topic : Smart cities in developing countries: how far can they be made smarter?

Abstract :

Smart cities are often associated with the application of ICT in solving city problems. Their “smartness” is used to improve the quality of life of the citizens. However, this is not the case in many cities/regions, especially in developing countries. They have been deploying numerous ICT systems, however, life quality indicators do not improve as expected.

From our experiences in assisting cities/regions in Indonesia in transforming themselves to smart cities, we understand that ICT is not the only factor that determines the success. It appears that innovations in crafting solutions of city problems are more predominant than ICT itself. We also learn that a smart city initiative has to be carried out in a holistic perspective and cannot focus on ICT alone. After all, our experiences lead to an understanding that smart city implementation in developing countries takes a different direction compared to that of developed countries.

This talk focuses on smart city development from the perspective of cities/regions in developing countries. First we discuss the adjustment of smart city concepts to suit the characteristics of cities/regions in developing countries. We also discuss how innovations, not ICT, becomes a better smart city accelerator and how they can be aligned with city’s development plans. Finally we explain some research directions that can help cities/regions in developing countries solve their problems and improve citizen’s quality of life using smart approaches.

Biography :

Dr. Lukito Edi Nugroho is a Professor at the Department of Electrical and Information Engineering, Faculty of Engineering, Universitas Gadjah Mada (UGM). He obtained his Engineer degree from UGM, M.Sc. from James Cook University, and Ph.D. from Monash University. His research interests include pervasive and mobile computing, and ICT in education and city/region development.

In recent years, Professor Nugroho has done extensive work on e-governments and smart cities. In 2007, he designed a concentration in our Master of Information Technology program with the focus on e-government implementation in central and local government institutions. Since then, not only has he been carrying out research on benefitting city/region development by the use of technology, but also evaluating Indonesian cities' and regions' performance in their smart city initiatives and assisting them to develop their smart city development master plan. These works are done within the umbrella of Indonesia's National Smart City Movement initiated by the Ministry of Communication and Information Technology. Professor Nugroho has supervised more than 40 PhD and 150 master students, about half of his master students took a thesis topic on e-government or smart city fields.



Assoc. Prof. Dr. Siridech Boonsang

School of Information Technology, King Mongkut's
Institute of Technology Ladkrabang, Thailand

Topic : Generative AI for industrial manufacturing
applications

Abstract :

This work explores the application of generative models in industrial manufacturing, specifically in the context of creating synthetic images. The use of generative models to generate synthetic images has gained traction in various industries, including the automobile and manufacturing sectors. In the automobile industry, the Latent Diffusion Model (LDM) in combination with fine tuning techniques has been proposed as an approach to generate automobile images based on text input. However, limited datasets can lead to overfitting, and fine tuning is used to pre-train the model to handle smaller scale datasets. The synthetic images are generated based on conditional input, such as the brand, color, location, and automobile position. In industrial manufacturing, the development of automated surface inspection systems requires a large amount of representative product image data. However, obtaining such data, especially with defects that reflect real-world scenarios, can be challenging, resulting in difficulties in developing robust detection algorithms. Generative models can be utilized to create synthetic datasets that contain product images augmented with defects. These datasets provide images with a variety of defective shapes and positions over the surface, reflecting what would occur over longer production periods. In conclusion, the use of generative models has become essential in creating synthetic images in several industries, including industrial manufacturing. The LDM and fine-tuning techniques can be used to generate automobile images based on text input, while synthetically generated datasets with defects can help in the development of automated surface inspection systems.

Biography :

Dr. Siridech Boonsang is the current Dean of the School of Information Technology at King Mongkut's Institute of Technology Ladkrabang (KMITL). He was born in Thailand and has an impressive educational background, having earned his Bachelor's degree in Electrical Engineering with Second Class Honours from KMITL in 1994. Dr. Boonsang then went on to pursue his Master's degree in Electrical and Electronic Engineering with a specialization in Electronic Instrumentation System from the University of Manchester Institute of Science and Technology (UMIST) in 2001. He completed his Ph.D. in Instrumentation from the same institution in 2004.

Dr. Boonsang is an expert in AI for Industrial Automation, Sensors and Actuators, and Optical and Electronic Materials. He has published numerous papers, including "A deep learning system for recognizing and recovering contaminated slider serial numbers in hard disk manufacturing processes," "Optical and Structural Properties of Insoluble and Flexible Biodegradable Regenerated Silk Films for Optically Transparent Hydrophilic Coating of Medical Devices," and "Evaluation of Micro- and Nano-Bismuth(III) Oxide Coated Fabric for Environmentally Friendly X-Ray Shielding Materials."

In his current role as the Dean of the School of Information Technology at KMITL, Dr. Boonsang is responsible for overseeing the academic programs and research activities of the school. He is known for his dedication to promoting excellence in education and research and for his commitment to fostering innovation and creativity among his students and school members.



Prof. Dr. Franck Leprévost

University of Luxembourg, Luxembourg

Topic : Convolutional Neural Networks at Image Recognition Tasks: Assessing the Risks.

Abstract :

An image is claimed to be worth 1000 words. Today's digital society is surely contributing to this belief, as our environment seems more and more driven by images. Images are used in social media to witness the evolution of people's life: Images show the new girlfriend or boyfriend (and sometimes the banned ex), the holidays spent here or there, with whom, doing what, eating what, enjoying what, seeing what. Images on Facebook, Instagram and others represent whose family member is suffering from which disease and since how long, etc. But images are also used for a large and increasing series of applications, that may either ease or complexify people's life: self-driving cars, face recognition, security access, medical diagnosis, satellite vision, robotisation and automation of processes, automatic language translation, etc.

Due to the profusion of images and of their usage, technologies have been developed to process them automatically, starting with the creation of processes able to sort images according to what they represent.

At this task, Convolutional Neural Networks (CNNs) are among the most widely used and developed technologies.

However, CNNs are not immune against mistakes. In fact, adversarial images may be purposely designed by so-called attacks to deceive CNNs at image recognition and classification. Attacks can contribute to protect privacy issues and to limit people's tracking. Attacks can have catastrophic consequences, e.g. for self-driving cars or CNN's based medical diagnosis. In this talk, we shall describe the typology of attacks, the scenarios they follow, and the challenges they face. We shall give an overview of some of the most recent attacks used to create adversarial images. These attacks provide convincing evidence supporting (for good or bad) the following outcome: Even denoting the very fact that an attack occurred at all may, in future, become increasingly highly problematic.

Biography :

Born in 1965, Franck Leprévost is a French mathematician and computer scientist. He is professor at the University of Luxembourg since 2003, and was its Vice-President from 2005 until 2015. Before joining the University of Luxembourg, he held academic positions in France (CNRS Paris, University Joseph Fourier Grenoble), and in Germany (Max Planck-Institut für Mathematik Bonn, Technische Universität Berlin). He holds a PhD and a Habilitation in Mathematics. He was researcher or visiting professor at many universities and research institutions (Max Planck-Institut für Mathematik Bonn, Technische Universität Berlin, Peter the Great Saint Petersburg Polytechnic University, South Ural State University, Warsaw University of Technology, Cardinal Wyszyński

University, Kiev Polytechnic Institute, Shanghai Normal University, etc.). He was recipient of the Alexander von Humboldt Fellowship. He was member of the board of directors or member of the scientific council of private and public entities (ATTF, CEPS, FNR, Luxtrust S.A., Unica, etc.).

His scientific interests include algorithmic number theory, mathematics of cryptology, convolutional neural networks, deep learning, artificial intelligence and evolutionary algorithms on the one hand, and the management of higher education and research organizations, international rankings and the civilizational role of universities on the other hand. Professor Leprévost has contributed to the worldwide standardization process of public-key algorithms (IEEE-P1363). He published eight scientific books, including three tutorials used by students in several universities in Europe and beyond, and a reference book about international university rankings. He is the author of about 70 scientific articles in international peer-reviewed journals, essentially in pure mathematics and in computer science. His reports for the European Parliament, in particular his contribution to the report on the Echelon network, have had a substantial technical and legal impact in most European countries.

Professor Leprévost has also publicly expressed his concerns about the risks of decline that face Western universities, the dangers of wokism within these same universities, and the actions to be taken to fight this ideology. He currently Professor Leprévost's expertise in the field of higher education and research as well as his managerial skills are frequently solicited by organizations, governments, and companies worldwide. In addition to his scientific and management activities, Franck Leprévost is a writer and an art collector. His publications are on www.franckleprevost.com

CONFERENCE SESSIONS

Paper Session Schedule

| Session Code | Thursday 26th October 2023 | Page |
|--|--|--------------------|
| Session: AIML-1: Artificial Intelligence & Machine Learning 1, Chaired by Praphan Pavarangkoon | | |
| 1 | Automated Extraction of Sediment Core and Scale Segments From Core Scanner Images <i>Szilard Fazekas; Sho Isawa; Stephen Obrochta</i> | 25 |
| 2 | Generative AI for Industrial Applications: Synthetic Dataset <i>Thanyathep Sasisaowapak; Siridech Boonsang; Santhad Chuwongin; Teerawat Tongloy; Pattarachai Lalitrojwong</i> | 31 |
| 3 | LSCR: Latent Space Coordination Relation for Anomaly Prediction <i>Thasorn Chalongvorachai; Kuntpong Woraratpanya</i> | 37 |
| 4 | Autonomous Pick-And-Place Using Excavator Based on Deep Reinforcement Learning <i>Cendikia Ishmatuka; Indah Soesanti; Ahmad Ataka</i> | 43 |
| 5 | Mecanum-Wheeled Robot Control Based on Deep Reinforcement Learning <i>Ocklen Setiadilaga; Adha Cahyadi; Ahmad Ataka</i> | 49 |
| 6 | Vision-Based Excavator Control for Pick-And-Place Operation <i>Ahmad Ataka; Hilal Bayu Aji; Alfin Luqmanul Hakim; Dimas Arfiantino; Aan Aria Nanda; Ghanis Kauchya Nugraha; Ahmad Didik Setyadi; Alharisy Aji; Gregorio Ageng; Rizky Candra; Cendikia Ishmatuka; Abdul Barr</i> | 55 |
| Session: AIML-2: Artificial Intelligence & Machine Learning 2, Chaired by Ahmad Ataka | | |
| 1 | Enhancing Genetic Algorithm Performance With Hybrid Strategy for Solving Optimization Problems <i>Irfan Farda; Arit Thammano</i> | 61 |
| 2 | An Improvement of Whale Optimization Algorithm With Rao Algorithm for Optimization Problems <i>Sakkayaphop Pravesjit; Arit Thammano; Krittika Kantawong; Duangjai Jitkongchuen; Panchit Longpradit; Rattasak Pengchata</i> | 66 |
| 3 | Modified Differential Evolution Algorithm for Solving Multi-Skill Resource-Constrained Project Scheduling Problem <i>Akarasate Homwiseswongsa; Chiabwoot Ratanavilisagul</i> | 71 |
| 4 | Modified Genetic Algorithm With Flexible Crossover for the Capacitated Electric Vehicle Routing Problem <i>Ajchara Phu-ang; Arit Thammano</i> | 77 |
| 5 | Multiple Independent DE Optimizations to Tackle Uncertainty and Variability in Demand in Inventory Management <i>Sarit Maitra; Sukanya Kundu; Vivek Mishra</i> | 81 |

Paper Session Schedule

| Session Code | Thursday 26th October 2023 | Page |
|---|--|---------------------|
| Session: AIML-3: Artificial Intelligence & Machine Learning 3, Chaired by Sutthiphong Srigrarom | | |
| 1 | AI-Enabled Exit Strategy of Emergency Vehicle Preemption <i>Kunti Khoirunnisaa; Rudy Hartanto; I Wayan Mustika; Kuntpong Woraratpanya; Ika Arva Arshella</i> | 87 |
| 2 | Energy-Efficient Continual Learning for Autonomous Driving <i>Qi Ding Ng; Chu Kiong Loo; Kitsuchart Pasupa; Nat Dilokthanakul; Jie Zhang</i> | 93 |
| 3 | Semantic Bird's-Eye-View Map Prediction Using Horizontally Aware Pyramid Occupancy Network <i>Thanapat Teerarattanyu; Tunlaton Wongchai; Praphan Pavarangkoon; Nat Dilokthanakul</i> | 99 |
| 4 | Advancing Accurate Depth Estimation and Perception With Angled Stereo Camera <i>Xiao Da Terrence Fu; Sutthiphong Srigrarom</i> | 104 |
| 5 | Person Re-Identification for Multi-Camera, Multi-Object Tracking on Robotic Platforms <i>Xiao Xi Natasha Soon; Sutthiphong Srigrarom</i> | 109 |
| 6 | Zone-Of-Interest Strategy for the Creation of High-Resolution Adversarial Images Against Convolutional Neural Networks <i>Franck Leprevost; Ali Osman Topal; Enea Mancellari; Kittichai Lavangnananda</i> | 115 |
| 7 | Transformers Based Automated Short Answer Grading With Contrastive Learning for Indonesian Language <i>Aldo Arya Saka Mukti; Syukron Abu Ishaq Alfaroz; Sri Suning Kusumawardani</i> | 121 |
| Session: CNT-1: Communication & Network Technologies 1, Chaired by I Wayan Mustika | | |
| 1 | Energy Trade-Off for Computation Offloading in Mobile Edge Computing <i>Dedi Triyanto; I Wayan Mustika; Widy Widyanan</i> | 127 |
| 2 | R-AODV: Reverse Ad-Hoc On-Demand Distance Vector Routing Algorithm With LoRa Mesh Based for Emergency Alert System <i>Jirawat Thaenthong; Taiwit Pimsen; Kemmathad Chidchuea</i> | 131 |
| 3 | Cattle Collars With a Low-Cost LPWAN-Based System for Cattle Estrous Monitoring <i>Nisit Pukrongta; Pubet Sangmahamad; Tanaporn Pechrkool; Boonyarit Kumkhet; Virote Pirajanchai; Puttiporn Thiamsinsangwon</i> | 137 |
| 4 | Deep Learning-Based Robust Automatic Modulation Classification Using Higher Order Cumulant Features <i>Nopparuj Suetrong; Attaphongse Taparugssanagorn; Natthanan Promsuk</i> | 143 |

Paper Session Schedule

| Session Code | Thursday 26th October 2023 | Page |
|---|---|---------------------|
| 5 | On-Device MFCC-CNN Voice Recognition System With ESP-32 and Web-Based Application <i>Muhammad Ichsan Ramadani Putra; Iqbal Burhanul Hakim; Hasbi Nur Prasetyo Wisudawan; Suatmi Murnani; Hendra Setiawan</i> | 149 |
| 6 | Unmanned Aerial Vehicle (UAV) Data-Driven Modeling Software With Integrated 9-Axis IMU-GPS Sensor Fusion and Data Filtering Algorithm <i>Azfar A Arfakhsyad; Aufa N Rahman; Larasati Kinanti; Ahmad Ataka; Hannan N Muhammad</i> | 155 |
| Session: JSCI: The 14th Joint Symposium on Computational Intelligence, Chaired by Kuntpong Woraratpanya | | |
| 1 | Deep Learning Based Printed Circuit Boards Defect Detection Using Multiple Depth 2D X-Ray Image <i>Chukiat Boonkorkoer; Phayung Meesad; Maleerat Maliyaem</i> | 162 |
| 2 | Location-Based Score Prediction for Condominiums in Bangkok <i>Sarun Bunjongsat; Sirion Vittayakorn</i> | 168 |
| 3 | Exploring the i3DVAE-LSTM Framework for Generating Exceptionally Rare Anomaly Signals <i>Thongchai Kaewkiriya; Kuntpong Woraratpanya</i> | 174 |
| 4 | Spatio-Temporal ESN-Based Model for Predicting Water Level in Yangtze River <i>Zongying Liu; Wenru Zhang; Mingyang Pan; Feifan Li</i> | 180 |
| 5 | Exploring LSTM and CNN Architectures for Sign Language Translation <i>Mongkol Boondamnoen; Kamolwich Thongsri; Thanapat Sahabantoegnsin; Kuntpong Woraratpanya</i> | 186 |
| 6 | Fractal Dimension in Deep Learning <i>Woramat Ngamkham; Kuntpong Woraratpanya</i> | 192 |
| Session: PS-1: Power Systems 1, Chaired by Lesnanto Multa Putranto | | |
| 1 | Field Weakening Control of a Permanent Magnet Synchronous Motor <i>Rifqi Maulana; Yohan Fajar Sidik; Husni Rois Ali</i> | 196 |
| 2 | Performance Comparison of ZDAC Vs MTPA for Permanent Magnet Synchronous Motor (PMSM) Control <i>Nadia Gustiranda Cahyeni; Yohan Fajar Sidik; Eka Firmansyah</i> | 202 |
| 3 | Droop Control Strategy of Controlled Three-Phase PWM Rectifier for Hybrid Train Propulsion <i>Fransisco Danang Wijaya; Yohan Fajar Sidik; Roni Irnawan; Adha Imam Cahyadi; Mohd. Brado Frasetyo</i> | 208 |

Paper Session Schedule

| Session Code | Friday 27th October 2023 | Page |
|---|--|---------------------|
| 4 | A Generation Expansion Planning Procedure Considering the Constraint Delay: A Case of Sumatera Power System <i>Kurnia Wisesa Kisna; Lesnanto Multa Putranto; Avrin Nur Widiastuti; Amira Hanun</i> | 214 |
| 5 | Impact of Coal Supply Constraint and Renewable Energy Mixed Target on a Power System Planning A Case Study of Southern Sulawesi System <i>Amira Hanun; Sarjiya Sarjiya; Lesnanto Multa Putranto; Tumiran Tumiran; Ira Savitri; Daud Farel</i> | 220 |
| 6 | Analysis of Renewable Energy Project Delays on the Indonesia's Energy Transition Process, Case Study: Java Bali System <i>Tumiran Tumiran; Sarjiya Sarjiya; Lesnanto Multa Putranto; Rizki Firmansyah Setya Budi; Ahmad Adhiim Muthahhari; Amira Hanun; Kurnia Wisesa Kisna</i> | 226 |
| Session: AIML-4: Artificial Intelligence & Machine Learning 4, Chaired by Azkario Rizky Pratama | | |
| 1 | A Social Analysis of Thailand's 2023 Election Through Twitter Feeds <i>Wanaporn Sarapugdi; Songphon Namkhun</i> | 232 |
| 2 | Integrated Rearrange Processing of Hybrid Model With Weighted Values for PM2.5 Forecasting <i>Tatshakon Polsena; Duangjai Jitkongchuen; Panita Thusaranon</i> | 237 |
| 3 | Investment Portfolio Optimization: Integrating Portfolio Allocation Methods With RNN LSTM <i>Azkario Rizky Pratama; Bagus Rakadyanto Oktavianto Putra</i> | 241 |
| 4 | Enhanced Keystroke Dynamics Authentication Using Keystroke Vector Dissimilarity <i>Naphat Bussabong; Tanapat Anusas-amornkul</i> | 247 |
| 5 | Efficient Recognition of Complex Human Activities Based on Smartwatch Sensors Using Deep Pyramidal Residual Network <i>Sakorn Mekruksavanich; Anuchit Jitpattanakul</i> | 253 |
| 6 | Leveraging Support Vector Machine for Sports Injury Classification <i>Thattapon Surasak; Phornnatee Praking; Kotcharat Kitchat</i> | 258 |
| Session: AIML-5: Artificial Intelligence & Machine Learning 5, Chaired by Nont Kanungsukkasem | | |
| 1 | Classification of Acute Intracerebral Hemorrhage Using Radiomics on Brain Computed Tomography Images <i>Phattanun Thabarsa; Salita Angkurawaranon; Chakri Madla; Withawat Vuthiwong; Kittisak Unsrison; Papangkorn Inkeaw</i> | 263 |
| 2 | A Comparative Study of YOLO Models for Sperm and Impurity Detection Based on Proposed Augmentation in Small Dataset <i>Marwan Nawae; Prawai Maneelert; Chainarong Choksuchat; Tonghathai Phairatana; Jermphiphut Jaruenpunyasak</i> | 269 |

Paper Session Schedule

| Session Code | Friday 27th October 2023 | Page |
|--|--|---------------------|
| 3 | Deep Neural Networks for the Qualitative Analysis of Myocardial Perfusion Emission Computed Tomography Images <i>Nareekarn Pruthipanyasakul; Nont Kanungsukkasem; Thierry Urruty; Teerapong Leelanupab</i> | 275 |
| 4 | Automatic Identification of Abnormal Lung Sounds Using Time-Frequency Analysis and Convolutional Neural Network <i>Rattanathon Phettom; Nipon Theera-Umpon; Sansanee Auephanwiriyaikul</i> | 281 |
| 5 | Development of Self-Supervised Learning With Dinov2 Distilled Models for Parasite Classification in Screening <i>Natchapon Pinetsuksai; Veerayuth Kittichai; Rangsan Jomtarak; Komgrit Jaksukam; Teerawat Tongloy; Siridech Boonsang; Santhad Chuwongin</i> | 287 |
| Session: BMI: Business Management and Informatics, Chaired by Singha Chaveesuk | | |
| 1 | The Factors Influencing Investor Intentions to Invest in Equity Crowdfunding in Thailand: A Conceptual Framework <i>Kaimuk Panitkulpong; Amnuay Saengnoree; Samart Deebhijarn; Thapong Teerawatananond</i> | 293 |
| 2 | Delivering Delight: Analyzing Luxury Consumer Satisfaction With Home-Delivered Premium Ingredients for Exquisite Home Cooking in Bangkok <i>Phatcharaphon Prommin; Manoj Chatpibal; Korakit Piyamongkol; Burin Sukphisal</i> | 298 |
| 3 | Interview Guide Development for Qualitative Research on Exploring Acceptance of Autonomous Vehicles in Thailand <i>Thana Sithanant; Wornchanok Chaiyasoonthorn; Singha Chaveesuk</i> | 304 |
| 4 | Factors Effecting Employees Motivation: A Study of the Ministry of Foreign Affairs in Myanmar <i>Htet Aung Kyaw; Vasu Keerativutisest</i> | 311 |
| 5 | Augmented Imagination: Exploring Generative AI From the Perspectives of Young Learners <i>Tat Putjorn; Pruet Putjorn</i> | 317 |
| Session: CNT-2: Communication & Network Technologies 2, Chaired by Olarn Wongwirat | | |
| 1 | Performance Evaluation of the M-QAM Enhanced Subcarrier Index Modulation in the Multipath Fading Channel With the Non-Linear Amplifier <i>Si Sar Mi; Aphitchaya Siriwanitpong; Pornpawit Boonsrimuang; Pisit Boonsrimuang</i> | 323 |
| 2 | Bragg Peak Detection Using Compatible Mother Wavelet on Oceanographic HF Radar Signals <i>Iswandi Iswandi; Risanuri Hidayat; Sigit Basuki Wibowo</i> | 327 |

Paper Session Schedule

| Session Code | Friday 27th October 2023 | Page |
|--|---|---------------------|
| 3 | Non-Uniform Metasurface-Based Omnidirectional Patch Antenna Using Characteristic Mode Analysis <i>Nathapat Supreeyatitikul; Nonchanutt Chudpooti; Chuwong Phongcharoenpanich</i> | 333 |
| 4 | Compact Broadband Circularly Polarized Metasurface Antenna With Split-Annular Slot Ground Structure <i>Nathapat Supreeyatitikul; Nonchanutt Chudpooti; Chuwong Phongcharoenpanich</i> | 338 |
| 5 | Machine Learning-Based Multi-Room Indoor Localization Using Fingerprint Technique <i>Farid Yuli Martin Adiyatma; Dwi Joko Suroso; Panarat Cherntanomwong</i> | 342 |
| 6 | Steganalysis on Dual-Layer Security of Messages Using Steganography and Cryptography <i>Zeba Shamsi; Anish Kumar Saha Action; Ripon Patgiri; Motilal Singh Khoirom; Laiphrakpam Dolendro Singh</i> | 348 |
| Session: IT-1: Information Technology 1, Chaired by Sirion Vittayakorn | | |
| 1 | Incomplete Adventure: An Educational Game for the TOEIC Exam <i>Surawee Tedsakorn; Nattapong Aksaralikitsanti; Sirion Vittayakorn</i> | 354 |
| 2 | Naval Wargame Prototyping: Multiplayer Real-Time Strategy Game Simulation Using Unreal Engine <i>Nattawat Chavanit; Sukawit Bualoy; Samart Moodleah</i> | 360 |
| 3 | Decentralized Trusted Database Approach to Online Product Reviews <i>Yuwana Rosoon; Chidchanok Choksuchat; Pattara Aiyarak</i> | 366 |
| 4 | Generating Use Case Specification From SALT GUI <i>Halim Wildan Awalurahman; Indra Kharisma Raharjana; Rifqi Hanief; Syahrul Akbar Rohmani; Rikza Biknada Korompis; Mahardika Riesma Oktavian; Muhammad Wildan Azky Hamdani; Badrus Zaman; Kartono Kartono</i> | 371 |
| 5 | Influence of Human Skills on Scrum Teams: A Case Study of Junior Team Software Development <i>Nuttaporn Phakdee; Apisit Saengsai</i> | 377 |
| Session: PS-2: Power Systems 2, Chaired by Mingxuan Mao | | |
| 1 | PWM Rectifier Impedance Modeling for the UGM-INKA Hybrid Train <i>Musyaffa' Ahmad; Eka Firmansyah; Yohan Fajar Sidik; Fransisco Danang Wijaya; Mudarris Mudarris; Sigit Doni Ramdan</i> | 383 |
| 2 | Hybrid PV-WT Microgrid Stability Control Using Synchronverter Algorithm <i>Mohd. Brado Frasetyo; Fransisco Danang Wijaya; Husni Rois Ali</i> | 389 |

Paper Session Schedule

| Session Code | Friday 27th October 2023 | Page |
|--------------|--|---------------------|
| 3 | Adaptive Model Predictive Control of Current Interharmonics in PV System <i>Fuping Ma; Mingxuan Mao; Liuqing Zhao</i> | 394 |
| 4 | Optimal Allocation of Vanadium Redox Flow Battery Storage Systems With Integrated Variable Renewable Energy <i>Chico Hermanu Brillianto Apibowo; Sarjiya Sarjiya; Sasongko Hadi; Fransisco Danang Wijaya; Mokhammad Isnaeni Bambang Setyonegoro</i> | 399 |

Automated Extraction of Sediment Core and Scale Segments from Core Scanner Images

1st Szilárd Zsolt Fazekas
 Graduate School of Engineering Science
 Akita University
 Akita, Japan
 szilard.fazekas@ie.aita-u.ac.jp

2nd Sho Isawa
 Graduate School of International Resource Sciences
 Akita University
 Akita, Japan
 s1020203@s.akita-u.ac.jp

3rd Stephen Obrochta
 Graduate School of International Resource Sciences
 Akita University
 Akita, Japan
 obrochta@gipc.akita-u.ac.jp

Abstract—In this paper we report on semantic segmentation of images of sediment cores obtained from core scanners. Such images usually encompass several objects beyond the essential parts showing the core itself and the measuring scale (typically a ruler or some sort of tape measure), which might be necessary for imaging or physically holding the material, but are irrelevant for the analysis of cores. Moreover, such objects are obstacles to analyzing cores in an automated manner by image processing or deep learning methods. As part of development of a toolkit for automated analysis of sediment cores, we show that the essential parts of the images - core itself and scale reference - can be extracted with high accuracy, using well-established convolutional architectures for semantic segmentation, such as U-net.

Index Terms—semantic segmentation, deep learning, core images

I. INTRODUCTION

Drilling and coring below the surface of the earth is a common technique in geological fields. Material retrieved in this fashion is typically cylindrical in shape, with a width generally < 20 cm but a length of up to several tens of meters. For practical purposes, a single, long “core” is often cut into several shorter “sections” that are usually between 1 and 2 meters in length. Sections may be analyzed using a variety of geophysical sensors to determine properties such as susceptibility to magnetic fields, velocity of seismic waves through the section, and emission of natural gamma rays. These analyses provide non-destructive information on the mineralogy and lithology of the recovered material.

In the case of soft sediment cores, the sections are then split lengthwise into two nominally identical halves. The split surface of one half is then photographed, described, and reserved for non-destructive analyses. The other half is subsampled for further sedimentological and geochemical analysis and is often completely consumed. These halves are referred as “archive” and “working”, respectively.

Common non-destructive analyses performed on the split surface of the archive half includes X-Ray fluorescence (XRF) and color measurement, both of which record valuable paleoenvironmental information. Discrete color mea-

surements using a spectrophotometer are common but time-consuming if high-resolution data are desired. Furthermore, the sensor is typically 1 cm wide, meaning sub-centimeter data cannot be obtained and values are averaged over the width of the sensor. Therefore, more recent work has extracted color information directly from the sediment core image. For example, Obrochta et al. [2] used this technique in sediments from the North Atlantic Ocean to align sediment cores from adjacent boreholes because the lightness (L^* parameter of the LAB color space) of sediment in this environment is related to climate, with light colored sediment accumulating during warm periods and dark colored produced during cold periods. Fazekas et al. [5] later used these same images to train a neural network to identify areas of post-depositional color artifacts, such as cracks and burrows created by seafloor biota.

Obrochta et al. [6] further used color values combined with millimeter-scale XRF measurements on sediment cores extracted from a Lake proximal to Mt. Fuji in Japan. Using these non-destructive measurements, ash layers produced by the volcano were successfully identified based on their color and unique elemental composition. However, combining color data from sediment core images with other high-resolution data generated from that same sediment core requires careful consideration. First of all, image parallax is common in photographs of long sediment cores because the distance from a lens positioned in the center of the core increases towards the ends. Either a distortion-free imaging method is required, or an accurate parallax correction must be applied.

The next issue is the motivation for this work. Sediment core data is relative to the distance (typically in centimeters) from the “core top”, but image color data is referenced to pixel number. A distortion-free image, as discussed above, would have an equivalent number of pixels per unit down-core distance at all locations in the image, allowing for a simple and linear conversion to distance units. However, the image must be 1) accurately cropped to the top and bottom



Fig. 1. Core scanner output with actual core (yellow rectangle) and scale (green rectangle).

of a sediment core of 2) precisely known length. Currently this is manually performed, tedious, and error prone because large-scale coring projects produce hundreds of images.

Here, we present an automated means for precise segmentation of sediment core images using both computer vision techniques and convolutional deep neural networks. Extraction of only the sediment core from the field of view will allow more efficient conversion of pixel number to distance, and isolation of just the scalebar is a first step toward determining core length from the image directly. This work is, to our knowledge, the first to use either a neural network or computer vision for automated segmentation of core scanner images. Previously, the only segmentation option was manual cropping. Fig. 1 shows a part of a typical core scan output with the parts we wish to extract marked.

II. METHODS

A. Preliminary analysis without machine learning

An image of the exact scalebar visible in the core photograph is used as a template. Speeded Up Robust Features (SURF) is an efficient and robust local feature detector and descriptor algorithm used in computer vision. Inspired by the Scale-Invariant Feature Transform (SIFT) but designed for speed and efficiency, SURF detects interest points in an image using a fast Hessian detector and creates descriptors robust to changes in rotation and scale. The algorithm, proposed by Herbert Bay, Tinne Tuytelaars, and Luc Van Gool in 2006, is notable for its speed and robustness to various image transformations, making it useful for tasks like object recognition and image matching [1]. SURF points are detected, extracted, and matched in both the scalebar (Fig.3)

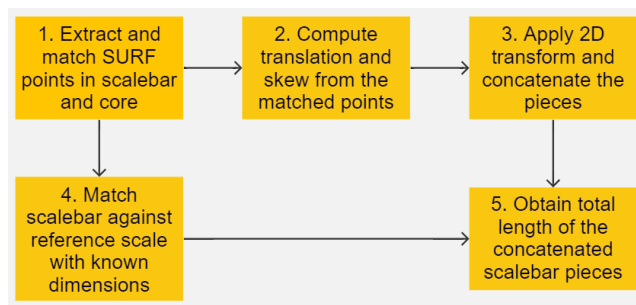


Fig. 2. Flow of scalebar detection with image processing methods for fixed scalebar type.

template and the core photograph. From the matched SURF points the 2D similarity geometric transformation matrix is obtained. Due to inevitable differential rotation and skew between the matched features in the image and template, the transformation matrix is relative to the template and must be inverted. Then it may be used to get the exact pixel dimensions of the leading edge of the scalebar. This defines the core top. Next, we designed and produced a feature-rich target, the block with "秋田大学" (Akita University) text, that slides along the rails that support the core during photography. The target is placed at the bottom of the core, and its location in the image determined using the same method as for the scale bar.

Using the indices of the scalebar and the core-bottom target allows segmentation of the scalebar and the sediment core. Next, the segmented scalebar is feature matched to an identical scalebar that is 1) of known length with 2) a consistent number of pixels per unit distance and is 3) longer than the scalebar in the image. A geometric transformation is obtained and applied to the image referencing the 2D world coordinates of the template. Out of range fill values are specified as black. After image transformation, the length of the core in the image is obtained from the number of non-black pixels in any particular row of pixels (see Fig. 2 for summary of the method).

There are several caveats to this approach. First of all, the scalebar template must be identical to the scalebar in the image. This method also requires that the core-bottom target be present, properly placed, and also identical to the template. This limits our present method to images obtained with very specific conditions and equipment. Furthermore, calculation of the geometric transformation depends highly on the maximum allowed distance between matched SURF points. If the maximum distance is too low, computation fails, and slight changes in the maximum distance results in slight changes in pixel locations. This can be partially alleviated by attempting to maximize the structural similarity index between the segmented image and template, particularly for segmentation of the scale and the core because we expect the elements extracted from the image to be identical to their respective templates. However, because length estimation intrinsically requires the template to be dissimilar (i.e., longer) than the corresponding feature in the image,

structural similarity indices are relatively low, complicating determination of the “best” result.

Due to the above it is clear that we need to develop more sophisticated methods for extracting the essential parts of the images. Ideally those methods would be robust to changes in imaging equipment and sediment types. With the immense advances of the last decade in machine learning in general and semantic segmentation in particular, this task seems like a perfect candidate for segmentation using deep neural networks.

B. Deep learning architecture for segmentation

The U-Net architecture, first introduced by Ronneberger et al. in their 2015 paper "U-Net: Convolutional Networks for Biomedical Image Segmentation" [3], has significantly influenced the field of image segmentation, particularly in the realm of biomedical imaging. With its unique 'U' shaped architecture that includes a contracting path (encoder) to capture context and a symmetric expanding path (decoder) that enables precise localization, U-Net has achieved state-of-the-art performance in many biomedical image segmentation tasks, such as cell tracking and neuron segmentation in electron microscopy images.

While U-Net's initial development and application focused on biomedical imaging, the model's success has resulted in its widespread adoption across a variety of fields within the natural sciences. For example, it has been applied in environmental science for segmenting remote sensing data and detecting specific land cover types [4]. In earth sciences, U-Net has been used to identify and map geological features like faults and fractures in subsurface datasets [7].

U-Net's success can be attributed to several factors. First, it is capable of learning from a relatively small amount of labeled data, which is often a limiting factor in natural science applications. Second, its architecture facilitates the combination of high-level, context-rich information from the contracting path with localized, detailed information from the expanding path, enabling the model to handle the complexity and variability of natural science images. Finally, U-Net can be adapted to different tasks and datasets with relative ease, making it a versatile tool for image segmentation across the natural sciences.

For both tasks presented here, extracting core and scale, respectively, we used Unet architectures with an encoder depth 6 and input image size 384×256 . A smaller Unet with encoder depth 2, as seen in Fig. 4, shows the layers composing the network.

The experiments were run on a desktop PC with Intel 12900 CPU, 32 GB of RAM and an NVidia 3090 Ti. The synthetic data set described later for scale extraction was generated with Python code. Training the neural networks and evaluating them was done in Matlab 2023a. All the code is available at the third author's Github repository [10].

III. DATA SETS

A. Core images

Images were primarily obtained from the International Ocean Discovery Program (IODP) database and were

cropped by IODP technicians. The IODP Gulf Coast Repository provided 947 images that were scanned aboard the drillship JOIDES Resolution during Expeditions 317, 329, 340, and 341. An additional set of 663 images from Expedition 347 was captured at the Bremen Core Repository and used in this study [8], [9]. We then used the pairs of cropped and uncropped images to create two alpha (transparency) channels, one with only the scalebar visible and one with the core and scalebar visible. This was done by using the cropped image as a template and matching features (SURF) between the uncropped image and the cropped template to re-extract the region of interest. The 2D reference was the world coordinates of the image. Pixels not contained in the template were given fill values of 0 (black). Non-black pixels were assigned a value of 255 and the matrix was saved as an 8-bit image. Pixels with a value of 255 are fully transparent and pixels with a value of 0 are fully opaque.

B. Synthetic images for scale segmentation

The segmentation model for extracting scale was trained on two data sets consecutively, a synthetic one described below and a manually segmented set of real-world core images obtained from the data mentioned in the previous subsection.

First, a synthetic dataset was created, generating images of tape measures with varying lengths and orientations. These images are designed to serve as a foundation for training and testing machine learning models to recognize tape measures in real-world photographs.

To begin, each image was generated programmatically using Python's PIL library, which allowed for precise control over the appearance of the tape measure. We utilized a drawing canvas sized to accommodate a diagonal placement of the tape measure, facilitating rotation without loss of data at the corners.

Tape measure lengths were randomized between 5 and 30 centimeters (to fit in the random background images maintaining legibility at the used resolution of 384×256), with the starting point anywhere from 0 to 15 centimeters on the tape measure. Each centimeter was further subdivided into millimeter markings, with every fifth millimeter emphasized with a longer mark and each centimeter labeled with its numerical value. The DejaVu Sans font, commonly available on Linux systems, was used for the text labels.

To introduce variety, the images were randomly rotated between 0 and 60 degrees, with the PIL library's rotate function used to maintain the image's quality during rotation. Subsequently, the image was cropped to the smallest possible bounding box that still contained all non-white pixels, ensuring that the tape measure took up as much of the image as possible.

To maintain the aspect ratio and avoid skewing, the image was resized keeping the height constant, while adjusting the width based on the aspect ratio of the cropped image. Antialiasing was applied during resizing to prevent the creation of hard edges.

Finally, Gaussian noise was introduced to the images to emulate real-world photographic conditions. Noise was gen-

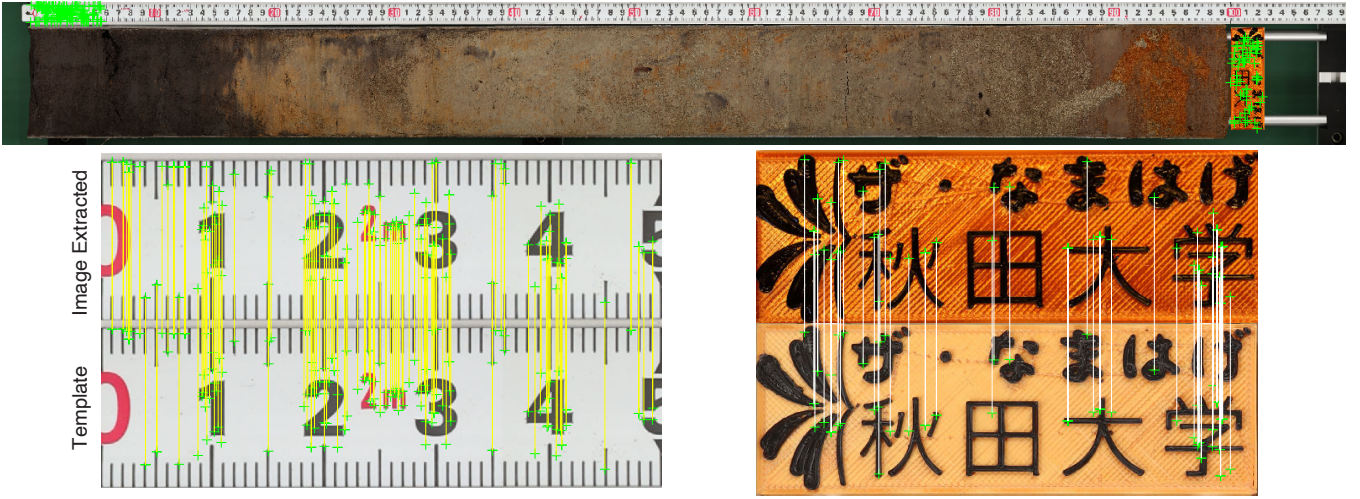


Fig. 3. (Top) image of a sediment core with SURF points plotted on the upper 5 cm of the scale bar and the core-bottom target. (Center) Upper 5 cm of the scalebar and core-bottom target extracted from the image, also with matched surf points. (Bottom) Scalebar and core-bottom target templates. Lines are connecting matched SURF points in the segmented elements and templates.

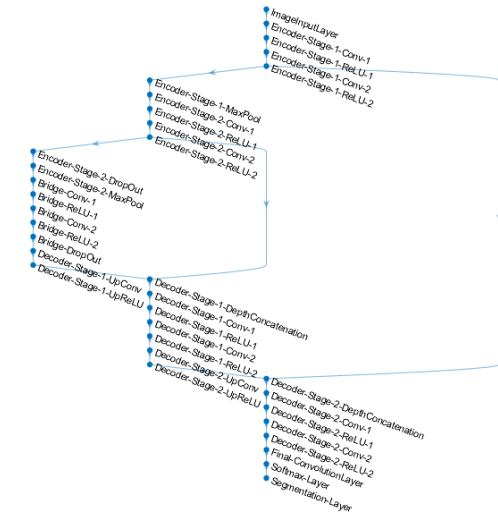


Fig. 4. Unet with encoder depth 2.

erated using numpy's random normal distribution function, and added to the image. Pixel values outside the standard RGB range were clipped to maintain valid values.

The resulting images provide a diverse and realistic dataset for developing and testing tape measure detection algorithms. The randomization of tape measure lengths, starting points, and angles, along with the introduction of Gaussian noise, offers a broad range of scenarios to robustly train machine learning models.

IV. SEGMENTATION

A. Scale extraction experiment

We utilized the previously described U-Net architecture to perform automated segmentation on synthetic and real-life images of scales, as summarized in Fig. 5.

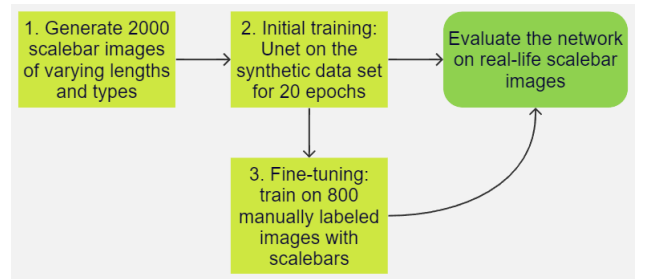


Fig. 5. Training of Unet architecture for scalebar detection first with synthetic data set and fine-tuning with real-life data.

Our approach consisted of two main phases: the initial training phase and the fine-tuning phase. In the initial training phase, we trained the network on the synthetic dataset of 2000 tape measure images detailed before. This dataset served to create a generalized baseline model, with the advantage of having perfect ground-truth labels for each synthetic image. We trained the U-Net model on this synthetic dataset for 20 epochs with the following parameters:

- stochastic gradient descent with momentum (SGDM) optimizer;
- initial learning rate was 0.001, halved after 10 epochs;
- shuffled the training set after each epoch;
- minibatch size was 5.

The overall performance of the trained U-Net models was evaluated using established measures for segmentation quality, accuracy and Intersection over Union (IoU) also called Jaccard similarity index. Accuracy is a standard evaluation metric in classification problems, providing a ratio of correctly predicted observations to the total observations. IoU is a common metric for the quality of an image segmentation, measuring the overlap between the predicted segmentation and the ground truth. The model attained an IoU score of YY, where a score of 1 would denote perfect overlap.

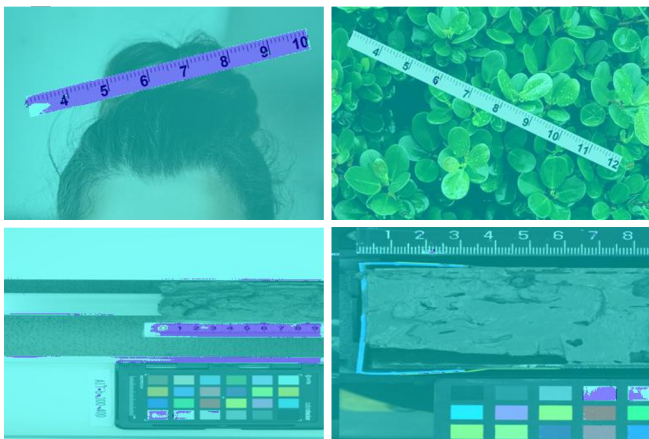


Fig. 6. Testing Unet on unseen images after training only on synthetic scale data: good (left column) and bad (right) performance on differently generated synthetic (top row) and real-life input (bottom). The predicted segments are colored purple.

After the 20 epochs the model hit on average 99.9% accuracy on the batches. Although from the beginning the plan was to further train the model on real-life images, we were interested to see how it performs after having seen only the synthetic data. The results were mixed, with low accuracy and Jaccard measure, but promising results for certain test images, as seen in Fig. 6.

After the initial training phase, the model was further fine-tuned using 800 manually labeled real-life images of cores with tape measures. This second phase was meant for the model to adapt to the more complex and variable features present in real-world data, ensuring the model’s robustness and generalization ability in real-world applications. The results were 95.59% accuracy on test images, with average IoU of 0.39. The test data set consisted of 80 images, 50 of which were real-life images from the same core data set as the second phase training, but not included in the training data; 30 of the test images were real-life images from a different scanner that was developed by Obrochta et al. [6]. The IoU measured only on the first 50 images was 0.64 which shows good performance. On the latter 30 images the model performed poorly, not recognizing the scales, hence the drop in IoU for the overall test set (Fig. 7).

The primary reason for the poor performance with the images acquired with the scanner of Obrochta et al. [6] is likely the scale position and color. The training dataset includes dark-colored scales at either the top or bottom of the image, but these images contain a centrally located, light-colored scale. The cores shown in Figures 3 and 1 were obtained using this scanner. To date, it has only been used in a total of seven smaller-scale coring campaigns. Hence, the number of images are currently too low to produce a robust training dataset. However, it is scheduled to be used for several upcoming larger campaigns, which will significantly increase the number of images. We therefore expect to increase the accuracy on these types of images in future.

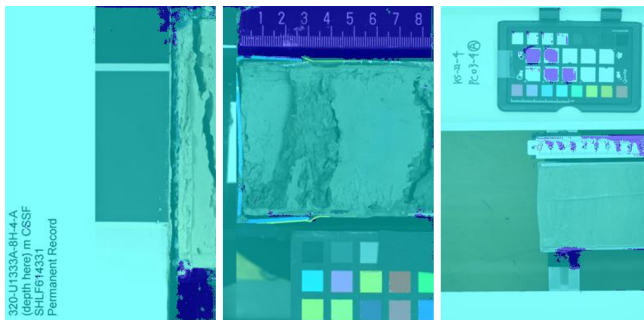


Fig. 7. Example output of Unet trained on synthetic and subsequently real-life images. The images were not included in the training data, but the first two nearly perfectly segmented images were parts of the same core scanner output where the training data came from. The third image is from a different data set and the model performed poorly on it.

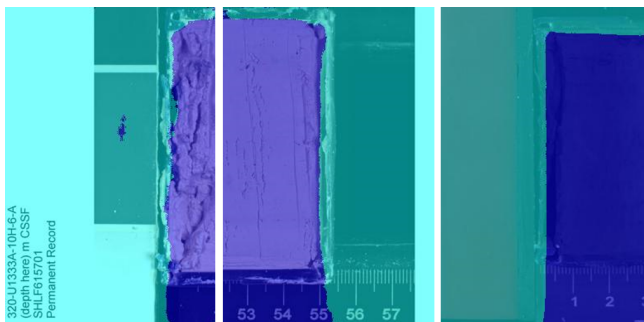


Fig. 8. Cores together with corresponding parts of scales segmented with very high accuracy.

B. Core+scale segmentation experiment

Here we used the same Unet architecture of encoder depth 6 as for scale detection. We trained the model from scratch on 3220 manually labeled image patches from the data sets mentioned in Subsection III-A. The model was trained for 50 epochs with the same options as in the case of scale extraction. At the end of training the model reached 98% accuracy on average on the minibatches. For testing we selected randomly 40 core images beforehand. While training smaller models it was apparent that the core segmentation task is handled well by the architecture, hence the small test data set applied here. The average IoU for the test images was 0.86 with pixel accuracy 97%, meaning the model was very good at recognizing unseen parts of cores whose other parts were in the training data, as can be seen in example outputs in Fig. 8.

We tested the core segmentation model on core images from other scans, too. In those cases, however, the model proved unusable, as it failed to recognize the cores consistently.

V. DISCUSSION AND FUTURE WORK

These results suggest that the two-phase training strategy, starting with synthetic images and fine-tuning on real-world images, can effectively prepare the U-Net model for the task of scale segmentation. It shows promise for the further application of such techniques in natural sciences, where

obtaining a large quantity of manually labeled data can be challenging. However, while training on the synthetic data set taught the model how to segment some real-life images very well, the same image was segmented poorly after further training on other types of real-life images (see the contrasting results on the bottom-left in Fig. 6 and right in Fig. 7). Future work could extend this approach to other similar segmentation problems and investigate other means of improving the model's performance.

As for the cores segmentation, it looks like either larger models or much more diverse training data are needed. On images taken in similar conditions (same equipment, lighting) as the training data, the model performed well, but when exposed to other types of images, it produced no appreciable results. Here the difficulty is that it is hard to obtain a manually labeled data set of cores imaged under a large number of different conditions. In follow-up work we will try to identify a way to tune these models, too, with some appropriate synthetic data.

REFERENCES

- [1] H. Bay, T. Tuytelaars, and L. Van Gool, "SURF: Speeded Up Robust Features". In *Computer Vision – ECCV 2006*, Lecture Notes in Computer Science, Vol. 3951, pp. 404–417, 2006.
- [2] S.P. Obrochta, T.J. Crowley, J.E.T. Channell, D.A. Hodell, P.A. Baker, A.Seki, and Y. Yokoyama, "Climate variability and ice-sheet dynamics during the last three glaciations." *Earth and Planetary Science Letters*, Vol. 406, pp. 198-212, 2014
- [3] O. Ronneberger, P. Fischer, and T. Brox, "U-net: Convolutional networks for biomedical image segmentation". In *Medical Image Computing and Computer-Assisted Intervention – MICCAI 2015*, Lecture Notes in Computer Science, Vol. 9351, pp. 234–241, 2015.
- [4] N. Audebert, B. Le Saux, and S. Lefèvre, "Semantic segmentation of earth observation data using multimodal and multi-scale deep networks". In *Asian Conference on Computer Vision (ACCV)*, Lecture Notes in Computer Science, Vol. 10111, pp. 180–196, 2017.
- [5] S. Z. Fazekas, S. Obrochta, T. Sato and A. Yamamura, "Segmentation of coring images using fully convolutional neural networks," 9th International Conference on Information Technology and Electrical Engineering (ICITEE), Phuket, Thailand, 2017, pp. 1-5
- [6] S.P. Obrochta, Y. Yokoyama, M. Yoshimoto, S. Yamamoto, Y. Miyairi, G. Nagano, A. Nakamura, K. Tsunematsu, L. Lamair, A. Hubert-Ferrari, B.C. Lougheed, A. Hokanishi, A. Yasuda, V.M.A. Heyvaert, M. De Batist, and O. Fujiwara, "Mt. Fuji Holocene eruption history reconstructed from proximal lake sediments and high-density radiocarbon dating", *Quaternary Science Reviews*, Vol. 200, pp. 395-405, 2018
- [7] X. Wu, R. Kumar, P. Mukherjee, A. Bhowmick, A. Davatzes, and J. Keim, "Segmentation of subsurface fault/fracture networks in geophysical images using deep learning". *Geophysics*, vol. 85, no. 4, pp. A41–A45, 2020.
- [8] T. Andrén, B. Jørgensen, C. Cotterill, S. Green, and the Expedition 347 Scientists, "IODP expedition 347: Baltic Sea basin paleoenvironment and biosphere". *Scientific Drilling* 20, pp. 1-12, 2015
- [9] T. Andrén, B. Jørgensen, C. Cotterill, S. Green, and the Expedition 347 Scientists, "Proceedings of the Integrated Ocean Drilling Program", Volume 347, 2015
- [10] CoreAlign project: <https://github.com/stephenobrochta/CoreAlign>

Generative AI for Industrial Applications: Synthetic Dataset

1st Thanyathep Sasiaowapak

College of Advanced Manufacturing
Innovation

King Mongkut's Institute of Technology
Ladkrabang
Bangkok, Thailand
59120026@kmitl.ac.th

2nd Siridech Boonsang

Department of Electrical Engineering,
School of Engineering

King Mongkut's Institute of Technology
Ladkrabang
Bangkok, Thailand
siridech.bo@kmitl.ac.th

3rd Santhad Chuwongin

College of Advanced Manufacturing
Innovation

King Mongkut's Institute of Technology
Ladkrabang
Bangkok, Thailand
santhad.ch@kmitl.ac.th

4th Teerawat Tongloy

College of Advanced Manufacturing
Innovation

King Mongkut's Institute of Technology
Ladkrabang
Bangkok, Thailand
teerawat_tongloy@kkumail.com

5th Pattarachai Lalitrojwong

Faculty of Information Technology
King Mongkut's Institute of Technology

Ladkrabang
Bangkok, Thailand
pattarachai@it.kmitl.ac.th

Abstract—The research and development of artificial intelligence (AI) techniques to enhance quality control in industrial equipment might face challenges due to the scarcity and limited privacy of actual industrial datasets. One approach to address this involves utilizing generative AI models that create synthetic data, simulating the characteristics and diversity found in crucial datasets. We present a methodology for generating synthetic datasets for industrial products such as bolts and screws by employing a segment-anything model and a stable diffusion technique for creating accurate representations. Furthermore, we propose the developed model by using a scaled-down version of DinoV2 algorithm's vision transformer (ViT-small). The self-supervised learning approach was studied to fine-tune the model to classify between normal- and defective industrial products, as well as those contaminated with dirt. By additional training dataset created through synthesis, we achieve an improvement in performance. The synthetic data leads to nearly perfect true positive results while completely eliminating false negatives. This indicates a significant advantage in terms of accuracy, recall, precision, specificity, and F1 score, all of which exceed 98%. Similarly, the model's predictions align perfectly with the area under the curve (AUC) metric. Although there is a slight performance reduction when dealing with up to six different class labels, the model retains strong capability in identifying normal products. Notably, the ViT-Small-based self-supervised learning model demonstrates superior accuracy compared to using ViT-Base, with considerations for dataset compatibility and model suitability. In conclusion, this study's contribution lies in enabling the deployment of the Dino V2 model for implementing quality control measures in industrial domains. It emphasizes the challenges that limited real-industrial data by leveraging synthetic data and innovative fine-tuning approaches, ultimately enhancing AI-powered for quality control processes.

Keywords — industrial equipment, segment-anything model, stable diffusion, artificial intelligence, self-supervised learning, synthetic dataset

I. INTRODUCTION

Generative artificial intelligence (AI) model has the capacity to produce a synthetic dataset that imitates the characteristics of industrial datasets [1]. The outcome obtained by employing a proficiently trained model with an

existing dataset aid in the generation of a novel dataset through synthesis. The synthetic system results in an expansion of dataset that is tailored to the particular objective of interest. Based on the previously discussed outcome, it becomes evident that generative AI can play a crucial role in addressing various challenges, such as the scarcity of data for AI development. This is especially advantageous for industries where data availability is a significant concern. [2]. Additional idealistic of “Segment-Anything Model”[3] combined with “Stable Diffusion”[4] have been proposed their application such as Generating data that exhibits both increased variability and distinctive patterns serves to enhance the development of deep learning models tailored for the classification of images related to industrial devices. This model can be developed by using the segment-anything techniques, including Device Communicator PROFINET-IRT, Edge Essential Sequence and Anybus PROFINET to .NET Bridge, respectively. These techniques introduces offer an approach to create the synthetic dataset required, particularly in scenarios where the data scarcity exposed in the industrial sector [5]. Especially, certain industrial datasets remain confidential and cannot be shared due to their intellectual property. However, these challenges pose important obstacles when it comes to training a new- AI model related to the industrial domain. Hence, use of the generative AI becomes necessary to produce the synthetic dataset that help achieve statistical balance while upholding privacy and security considerations [6].

Self-supervised learning (SSL) is the learning the class labels specific to the dataset with limited human labels required. The feature extraction based pre-trained model is obtained for the further downstream task as the object classification that using a small amount of data training [7].

Dino V2 classification layer is one of the popular final layer of the neural network model that is responsible for assigning input data to specific classes or categories. It takes the learned features from the previous layers and uses them to make predictions about which class the input data belongs to. This layer essentially enables the model to perform classification tasks [8]. The Dino V2 model has been study for its performance to any other SSL models based on training

with the curated datasets; ImageNet-21K (that included frontal chest radiographs), VDR, C14, CPT, MIM, UKA, and PCH, respectively. the research result showed an intermediate performance as an average accuracy of 76.875, standard deviation of 6.27. An average accuracy of fine-tuning with ImageNet-21K is 76.57% and standard deviation of 6.88 [9], suggesting feasibility to apply the Dino V2 model to classify the industrial equipment.

Here, we aimed to develop the synthetic dataset for industrial physical products including items like bolts and screws by using segment-anything model in conjunction with stable diffusion technique; the generative AI principles. Furthermore, the study is to develop an AI model through fine-tuning by using a small version of vision transformer (ViT)-based DinoV2 algorithm. The developed classification model may allow us to differentiate between high-quality and deflections from the industrial equipment parts.

II. DATASET

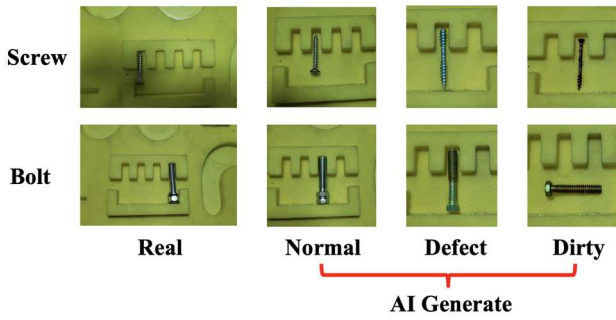


Fig. 1. Dataset. There are all 6-classes of real dataset and synthetic data. The real datasets are the normal bolt and the normal screw. The synthetics are the defect bolt, defect screw, dirty bolt and dirty screw, respectively.

The dataset of real bolt and screw were captured from the industrial equipment parts with actual environment (Fig. 1). Other classes with limited sample size and their low variation obtained, there are needed to increase the amount of the data by using the generative AI techniques including of the segment-anything model and also the stable diffusion in order to create the synthetic dataset. As the result of using the techniques as above, there are six-classes generated including the normal bolt, the normal screw, the defect bolt, the defect screw, the dirty bolt and the dirty screw, respectively.

The synthetic dataset is the creation of new dataset by using an assigned producing condition to mimic the real ones with similar properties such as defect and dirty class [2, 10]. The dataset can be used to test and improve the model performance by using several statistical metrics and ignoring real-world dataset with privacy and confidential information. Development of AI model by using synthetic dataset help prevent an accessing real dataset.

III. ARCHITECTURE

A. Segment-Anything Model (SAM)

The image encoder of the real image was done by using a high level (e.g. using Masked Auto-Encoder (MAE) model and pre-trained model of Vision Transformer (ViT) model) and continues the single embeddings of each image that is qualified to further application [3] in Fig. 2. All steps are assigned as follows;

1) *Prompt Encoder*: The data (e.g. point input, bounding box input, or free-form of text prompt) were transformed into embedding vector in real time, or additional mask. The convolution and embedding to mask decoder used to transform into feature vectors.

2) *Mask Decoder*: the module functions to create mask that specific to the object of interest. The process used can help classify and extract the unique properties of the object, as follows.

a) *text input*: instruction to create mask mask such as prompting or text describing a related area of the selected object in images.

b) *encoding*: Mask decoder received the data input to be encoded by multi-layer perceptron (MLP) in the deep learning.

3) *Mask Prediction*: The binary prediction result (0 and 1) is whether the mask containing the object of interest within the image input. Comparison between an improved mask for the prediction result and the real mask would be analyzed for error value that would help correct the prediction mask.

4) *Valid mask*: The representative mask for the corrected prediction of the object of interest containing in the image. All pixels of the object and the background varied by 0 and 1, respectively; as follows.

a) *The pixel value of 0*: representing the area for the background within the image.

b) *The pixel value of 1*: representing the area for the object of interest within the image.

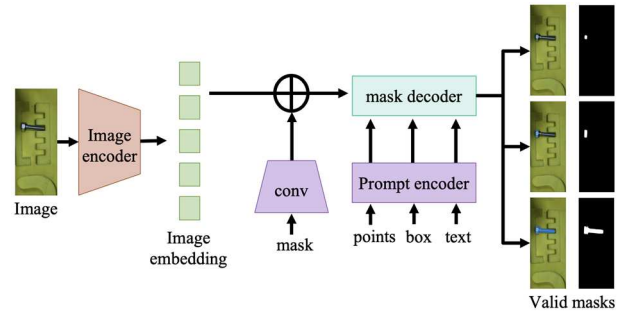


Fig. 2. Architecture of Segment-Anything Model (SAM). Main component of SAM is including Image encoder, Image embedding, convolution, prompt encoder and mask decoder, respectively.

B. Stable Diffusion

Initial image data was learnt by feeding into the perceptual compression of the stable diffusion architecture [4], see in the Fig. 4. The perceptual compression functions to transformed high dimension into latent vector and embedding into the latent space [4] at the 1st step. The latent vector, compressed pixels from the digital image, was transformed by an autoencoder. The 2nd step, captured semantic structures in both text and images was performed by the semantic compression in order to retain details of diffusion models and object relation found in any image. The result of this step gave high resolution image containing the semantic structure [4]. Conditioning diffusion was used to assign specific characteristics for the created images under the diffusion process [11, 12] such as the defect bolt, the defect screw, the dirty bolt and the dirty screw, respectively. the reverse diffusion returned the pixel values for editing details at

decoding from latent space [13] obtained by generative image inpainting [14].

Image painting was done by using image inpainting technique [15, 16] that the result of the SAM technique would be used to create new images from real bolt and real screw.

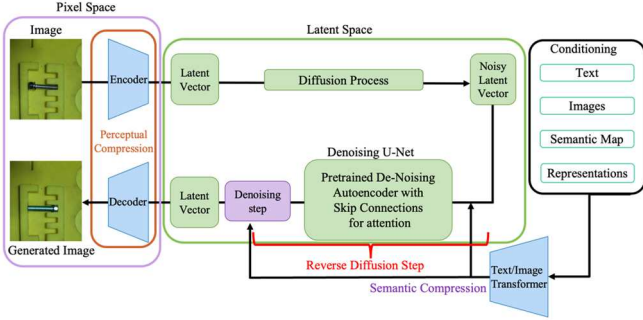


Fig. 3. Architecture of Stable Diffusion. Main component of Stable Diffusion is including Pixel space, Latent space and Conditioning for generate images is synthetic dataset.

IV. TRAINING CLASSIFICATION

The classification-based downstream task used for fine-tuning process in order to distinguish between different classes. Here's a general outline of the steps involved in training a classification model.

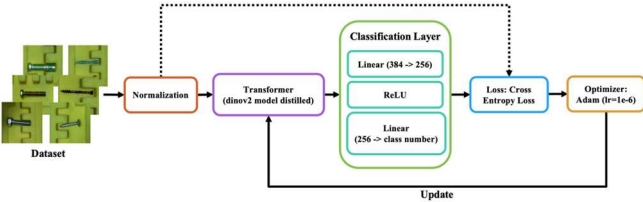


Fig. 4. Training process. Dataset for training Dinov2 (ViT-Small) algorithm with Linear classification layer. First linear layer transforms data linear size to 256 dimensions. Activation function by Rectified Linear Unit (ReLU). Second linear layer from 256 dimensions to class number.

1) *Data Collection and Preprocessing*: real image dataset and synthetic dataset

2) *Feature Extraction*: The feature extraction was performed by using ViT-based DinoV2 model.

3) *Data Splitting*: dataset assigned for 3 experiments.

a) *Real image*: all real images was assigned into two-training classes (bolt and screw) and each class containing 5 images. We used testing dataset with real images as for 71 images of bolt and 92 images of screw, respectively.

b) *Combination of the real images and the generated image*: this dataset used both the real and generated images for 20 images in train dataset. Two-classes were assigned and labeling with the class's name as the same as the dataset from "Real image" as above. Each class contained 5-real images & 5-generated images. The testing dataset used are the same as those described as above.

c) *Multi-class*: There are all 6 classes assigned; including the training dataset of bolt-, bolt_defect-, bolt_dirty-, screw-, screw_defect- and screw_dirty-classes, respectively. Of which, each class contained 10-real images and 10-generated image, respectively. In testing dataset are contained both real- and generate images; including 24-images for bolt (10-real & 14-generated images), 23-images for screw (10-real & 13-generated images), respectively. For

training dataset of bolt_defect-, screw_defect, bolt_dirty- and screw_dirty classes, each class contained 20-generated images. For testing dataset, there are 40-generated images for the bolt_defect- & screw_defect-, respectively. Also, there are 42-generated images for bolt_dirty and 46-generated images for screw_dirty, respectively.

4) *Model Selection*: the selected ViT-Small of Dino V2 algorithm was publicly available and downloaded from url: <https://github.com/facebookresearch/dinov2>. Although there is a small version, given result obtained shows effective output even in limited computing resource.

5) *Model Training*: we trained the selected model by using the assigned training dataset mentioned above. Hyperparameters were set to optimize the model's learning on training configuration as follows;

- Method: Dino V2 model
- Learning Rate: 0.000001
- Max epoch: 500
- Batch size: 64

V. EVALUATION

We evaluated the trained-model's performance based on several evaluation metrics for classification tasks including accuracy, precision, recall, specificity and F1-score, respectively.

$$Accuracy = \frac{TP + TN}{TP + TN + FP + FN} \quad (1)$$

$$Precision = \frac{TP}{TP + FP} \quad (2)$$

$$Recall = \frac{TP}{TP + FN} \quad (3)$$

$$Specificity = \frac{TN}{TN + FP} \quad (4)$$

$$F1 \text{ score} = 2 \times \frac{Precision \times Recall}{Precision + Recall} \quad (5)$$

Where TP stands for True Positive, TN stands for True Negative, FP stands for False Positive, FN stands for False Negative [17] respectively.

In addition, Receiver Operating Characteristic Curve (ROC Curve) was analyzed to measure the quality performance of proposed model in order to discriminate testing data. The ROC was plotted between the false negative rate (FNR) for X-axes and the true positive rate (TPR) for Y-axes, respectively. Area Under the ROC-Curve (AUC) varied 0 to 1, providing the general accuracy. The AUC value of 1 indicates perfect classification, however, the AUC of 0.5 indicates random prediction.

VI. RESULT AND DISCUSSION

A. Training Loss

This study was proposed to find the optimal model through training process involving real and generated images (Fig. 1.). The selection of the best model was determined by analyzing the weight corresponding to the minimum training loss value within the stable training conditions ranging epochs 300 to 500 (Fig. 5.) and epochs 400 to 500 (Fig. 6.), respectively.

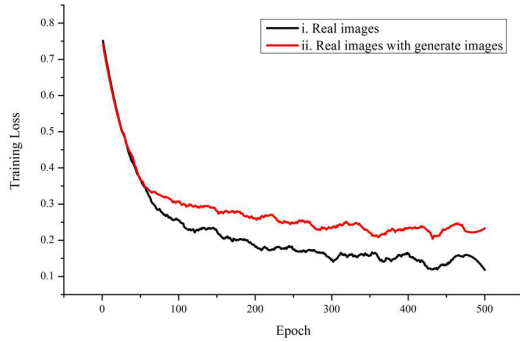


Fig. 5. Training loss for binary-class classification model. i) trained with dataset of real image and ii) trained and test with the combination dataset. Based on the explanation in the paper, models were trained with NVIDIA DGX A100-40 GB one GPU and RAM 32 GB.

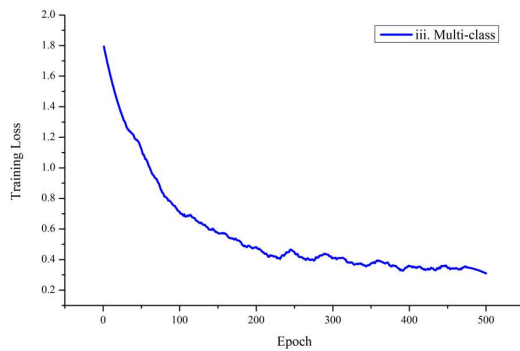


Fig. 6. Training loss for multi-class classification model. iii) Trained and test with dataset of the multi-class. Based on the explanation in the paper, models were trained with NVIDIA DGX A100-40 GB one GPU and RAM 32 GB.

B. Confusion matrix table

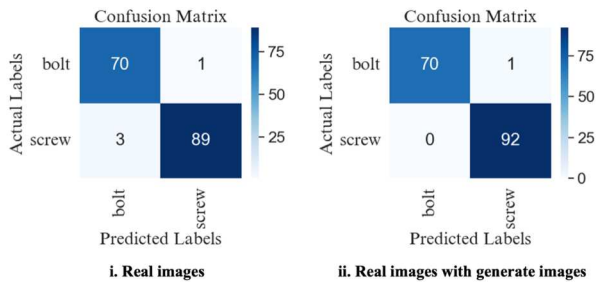


Fig. 7. Confusion matrix table. i) trained model with real image dataset and ii) trained model with the combination data, respectively.

In Fig. 7. (i), according to the evaluation of the trained model with real images resulted in the TP count of 70 and FN count of 1 for bolt identification. In the same way, there were 89 TP and 3 FN for screw classification. Upon the incorporation of additional training datasets, a noteworthy enhancement was observed. Specifically, the increase of TP to 92 and no FN were recorded (as depicted in Fig. 7. (ii)). This

suggests the advantage gained from including synthetic data, even when relatively small set of 10 generated images was employed during the training the selected model.

To further broaden the scope of the synthetic dataset, instances of defects and contamination, namely deflection and dirtiness, were introduced. This extended dataset was curated to evaluate the performance of the aforementioned selected model. Comparing to the first-two models, despite utilizing a six-classes classification scheme to trained the selected model, the TP and FN outcomes demonstrate excellent performance across both classes. Notably, only a single image was identified as FN within this context (Fig. 8.). The result indicates that normal image of the bolt and screw classes exhibits superior results compared to the image representing defects and dirtiness. Of which, both “dirty-screw” and “dirty-bolt” displayed higher TP and fewer FN values compared to the defect categories, suggesting that are similar in features between normal and dirty classes, which may account for improvements seen in comparison to the defects as significant.

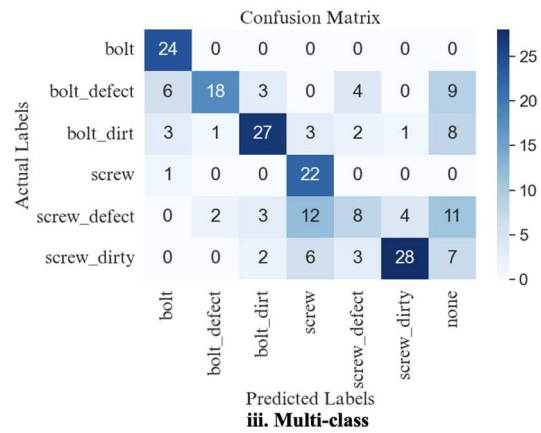


Fig. 8. Confusion matrix table. The Selected model was trained with generated image from the multi-classes.

C. Receiver Operating Characteristic Curve

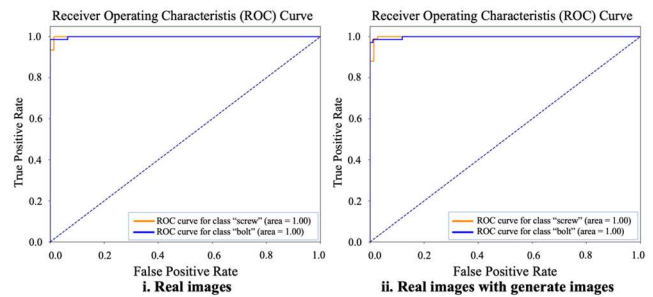


Fig. 9. Receiver Operating Characteristic Curve (ROC). i) trained model with real image dataset and ii) trained model with the combination data, respectively.

The general accuracy was measured using the AUC-ROC curve. As shown in Fig. 9. (i), the AUC values for both the bolt and screw classes reached a perfect prediction score of at 1.00. Similarly, the second trained model, utilizing the combined dataset, also shows a perfect prediction of the AUC (Fig. 9. (ii)). These result from both experiments affirm an outstanding of the chosen self-supervised learning model based on the small Dino V2 version.

In Fig. 10. illustrates the remarkable result of the SSL model, where both normal and dirty features for bolt and

screw classes exhibited superior accuracy values ranging from 0.93 to 1.00, respectively. In contrast, the defection classes exhibited comparatively lower accuracy scores ranging from 0.78 to 0.82, respectively.

According to the comprehensive evaluation metrics studied, notable enhancements in performance were evident in the trained model using synthetic data during the second experiment. This improvement was reflected in average values of accuracy, precision, recall, specificity and F1 score, respectively, which ranging from 0.986 to 0.994 (as detailed in TABLE I.).

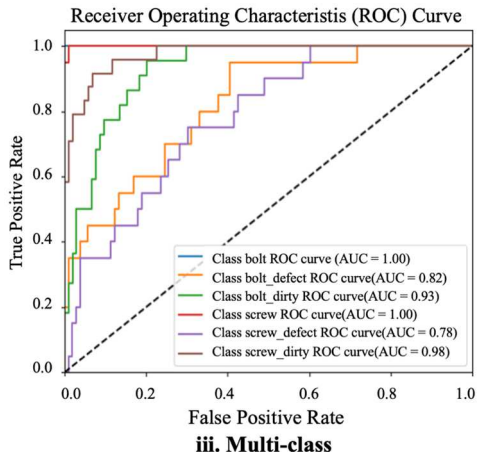


Fig. 10. Receiver Operating Characteristic Curve (ROC). The Selected model was trained with generated image from the multi-classes.

TABLE I. EVALUATION METRIC

| Evaluation metric | Experiment I (real image) | Experiment ii (combined data) | Experiment iii (Multi-class) |
|-------------------|---------------------------|-------------------------------|------------------------------|
| Accuracy | 0.975 | 0.994 | 0.904 |
| Precision | 0.974 | 0.995 | 0.701 |
| Recall | 0.977 | 0.993 | 0.657 |
| Specificity | 0.986 | 0.986 | 0.951 |
| F1 Score | 0.975 | 0.994 | 0.804 |

Upon assessing the average performance of the third experiment, the metric values become less than that of the first two experiments. This discrepancy could be due to the fact that the third experiment involved training with a larger number of classes and also exposing to a high degree of variation of training dataset. We have observed that the generated class of defection (Fig. 8.) may significantly reduce the model performance. Nevertheless, when considering on the individual class labels of “normal bolt” and “normal screw”, the performance levels remain consistently high, as previously described in section B. It is notable that utilizing of a limited sample size and handling with multi-class data for training the classification model could indeed impact overall performance. However, addressing the issue could involve increasing the sample size, which has the potential to mitigate the problem encountered.

D. Performance comparisons of existing works

A comparison was made between our study and previous report utilizing Inception V3 and the ViT-B model. The finding indicated that the average accuracy achieved in our two experiments surpassed that ViT-B (Base) based SSL

model. Notably, the ViT-B model is characterized by a larger number of parameters than our model S (small) used. We can achieve superior accuracy even with a smaller sample size used for training. In a comparison with the SL model, our model exhibited similar performance to that obtained SSL and achieving a comparable accuracy of 0.958. This accuracy was higher than our model training with six classes. It’s worth nothing that despite using an amount of training data that is 8.3 times smaller than that of the SL model, our model still demonstrated competitive performance. This suggests that an increase of the sample size, combined with the utilization of larger model versions of the ViT-DinoV2 could potentially lead to further improvements in accuracy.

TABLE II. PERFORMANCE COMPARISONS OF EXISTING WORKS

| Details | M. Z. Wong et al. [18] | X. Zhu et al. [19] | Ours | |
|-------------------------|-------------------------------|---------------------------------------|-------------------------------------|-------------|
| Industrial applications | Synthetic dataset of products | Synthetic dataset of Industrial Parts | Synthetic dataset of bolt and screw | |
| Method | Inception V3 (SL) | ViT-B (SSL) | ViT-S (SSL) | ViT-S (SSL) |
| Number of images train | 1,000 | 1,200 | 20 | 120 |
| Number of class | 10 | 17 | 2 | 6 |
| Accuracy | 0.958 | 0.747 | 0.994 | 0.904 |

E. Limitation

Limited training data might lead to overfitting on the available dataset, resulting in reduced generalization to new data. The model's performance heavily relies on the quality and representativeness of the small training dataset. Vision Transformer's effectiveness can decrease as the complexity of the task or dataset increases. Applying Regularization Techniques such as dropout or introducing weight decay [20] are methods to mitigate overfitting. Employing these strategies can help in reducing the model's overfitting tendencies, especially when dealing with a small training dataset.

VII. CONCLUSIONS

We have achieved a remarkable capabilities of generative AI in synthesizing highly targeted datasets for specific industrial use-cases which can be instrumental in training deep learning models for tasks related to quality control, defect detection, or contamination identification within a factory environment. Although the application of this innovative technique, we have effectively addressed the long-standing challenge of limited availability and scarcity of industrial datasets within the manufacturing setting. In our ongoing research, we are further studying the robustness of our pretrained distilled ViT model by conducting rigorous validation with new and diverse datasets, including instances of dirty and defective objects, to ensure its reliability in real-world industrial environments.

The pretrained distilled ViT foundation model serves as an exceptional starting point, as it possesses a comprehensive understanding of various visual features and patterns. This pre-existing knowledge allows us to accelerate the fine-tuning

process and optimize the model's performance for detecting and classifying rare industrial defects or contamination instances.

REFERENCES

- [1] R. Gozalo-Brizuela and E. C. Garrido-Merchán, "A survey of Generative AI Applications," p. arXiv:2306.02781doi: 10.48550/arXiv.2306.02781.
- [2] S. I. Nikolenko, "Synthetic Data for Deep Learning," p. arXiv:1909.11512doi: 10.48550/arXiv.1909.11512.
- [3] A. Kirillov *et al.*, "Segment Anything," p. arXiv:2304.02643doi: 10.48550/arXiv.2304.02643.
- [4] R. Rombach, A. Blattmann, D. Lorenz, P. Esser, and B. Ommer, "High-Resolution Image Synthesis with Latent Diffusion Models," p. arXiv:2112.10752doi: 10.48550/arXiv.2112.10752.
- [5] A. Baaz, Y. Yonan, K. Hernandez-Diaz, F. Alonso-Fernandez, and F. Nilsson, "Synthetic Data for Object Classification in Industrial Applications," p. arXiv:2212.04790doi: 10.48550/arXiv.2212.04790.
- [6] J. Maroñas, R. Paredes, and D. Ramos, "Generative Models For Deep Learning with Very Scarce Data," p. arXiv:1903.09030doi: 10.48550/arXiv.1903.09030.
- [7] T. Uelwer *et al.*, "A Survey on Self-Supervised Representation Learning," p. arXiv:2308.11455doi: 10.48550/arXiv.2308.11455.
- [8] M. Oquab *et al.*, "DINOv2: Learning Robust Visual Features without Supervision," p. arXiv:2304.07193doi: 10.48550/arXiv.2304.07193.
- [9] S. Tayebi Arasteh, L. Misera, J. Nikolas Kather, D. Truhn, and S. Nebelung, "Enhancing Network Initialization for Medical AI Models Using Large-Scale, Unlabeled Natural Images," p. arXiv:2308.07688doi: 10.48550/arXiv.2308.07688.
- [10] S. Kleisarchaki, S. Amer-Yahia, A. Douzal-Chouakria, and V. Christophides, "Querying Temporal Drifts at Multiple Granularities (Technical Report)," p. arXiv:1605.02772doi: 10.48550/arXiv.1605.02772.
- [11] R. Yang and S. Mandt, "Lossy Image Compression with Conditional Diffusion Models," p. arXiv:2209.06950doi: 10.48550/arXiv.2209.06950.
- [12] A. Lugmayr, M. Danelljan, A. Romero, F. Yu, R. Timofte, and L. Van Gool, "RePaint: Inpainting using Denoising Diffusion Probabilistic Models," p. arXiv:2201.09865doi: 10.48550/arXiv.2201.09865.
- [13] F.-A. Croitoru, V. Hondru, R. Tudor Ionescu, and M. Shah, "Reverse Stable Diffusion: What prompt was used to generate this image?," p. arXiv:2308.01472doi: 10.48550/arXiv.2308.01472.
- [14] Z. Zuo *et al.*, "Generative Image Inpainting with Segmentation Confusion Adversarial Training and Contrastive Learning," p. arXiv:2303.13133doi: 10.48550/arXiv.2303.13133.
- [15] J. Yu, Z. Lin, J. Yang, X. Shen, X. Lu, and T. S. Huang, "Generative Image Inpainting with Contextual Attention," p. arXiv:1801.07892doi: 10.48550/arXiv.1801.07892.
- [16] T. Yu *et al.*, "Inpaint Anything: Segment Anything Meets Image Inpainting," p. arXiv:2304.06790doi: 10.48550/arXiv.2304.06790.
- [17] K. M. Naing *et al.*, "Automatic recognition of parasitic products in stool examination using object detection approach," *PeerJ Computer Science*, vol. 8, p. e1065, 2022/08/17 2022, doi: 10.7717/peerj-es.1065.
- [18] M. Z. Wong, K. Kunii, M. Baylis, W. H. Ong, P. Kroupa, and S. Koller, "Synthetic dataset generation for object-to-model deep learning in industrial applications," p. arXiv:1909.10976doi: 10.48550/arXiv.1909.10976.
- [19] X. Zhu, T. Bilal, P. Martensson, L. Hanson, M. Bjorkman, and A. Maki, "Towards Sim-to-Real Industrial Parts Classification with Synthetic Dataset," presented at the 2023 IEEE/CVF Conference on Computer Vision and Pattern Recognition Workshops (CVPRW), 2023. [Online]. Available: <https://doi.ieeecomputersociety.org/10.1109/CVPRW59228.2023.00468>.
- [20] T. G. Slatton, "A comparison of dropout and weight decay for regularizing deep neural networks," 2014.

LSCR: Latent Space Coordination Relation for Anomaly Prediction

1st Thasorn Chalongvorachai
School of Information Technology
King Mongkut's Institute of Technology Ladkrabang
 Bangkok, Thailand
 65076079@kmitl.ac.th

2nd Kuntpong Woraratpanya*
School of Information Technology
King Mongkut's Institute of Technology Ladkrabang
 Bangkok, Thailand
 kuntpong@it.kmitl.ac.th

Abstract—Anomaly time series prediction is a crucial yet challenging task in real-world systems. Existing techniques often require a substantial amount of data to achieve satisfactory performance, posing a significant challenge as anomaly data is scarce and difficult to obtain. Despite attempts to address this issue using traditional machine learning techniques, their effectiveness remains limited, resulting in performance degradation or costly trade-offs. Therefore, in this paper, we propose a novel approach called Latent Space Coordination Relation for Anomaly Prediction to overcome these challenges. Our framework leverages the power of the Variational Autoencoder (VAE) and learns the coordination relations of points in the latent space to detect anomalies. By exploiting the latent space, our method enables effective learning and prediction of anomalies. Additionally, the decoder of the VAE aids in restoring the data, further improving the accuracy of anomaly detection. Experimental results demonstrate that our approach outperforms baseline models when training data is limited. The predicted anomalous signals exhibit lower error rates, highlighting the efficacy of our method. This improvement is attributed to the utilization of the latent space for learning and assisting in anomaly prediction, along with the signal restoration capabilities of the decoder.

Index Terms—Anomaly Prediction, Time-series Prediction, Signal Processing, Variational Autoencoder, Latent Space, Latent Space Coordination Relation (LSCR)

I. INTRODUCTION

Anomaly time series prediction is a critical problem that demands effective techniques to address. Often, anomaly events are negative incidents, such as sudden breakdowns of important machinery [1], [2], relapses in patients' conditions, or uncanny occurrences in the stock market that can lead to catastrophic financial losses. Surprisingly, limited research has been conducted in the field of machine learning to tackle this challenge, especially in the context of anomaly prediction. Therefore, there is a pressing need for researchers to study and propose solutions to this problem.

To address the anomaly prediction challenge, researchers commonly employ machine learning techniques, such as feed-forward neural networks (FF-NNs) [3] and long short-term memory (LSTM) neural networks [4]. A feed-forward neural network is versatile and widely applicable, while an LSTM network is specifically designed for handling long sequential data. Extensive studies have

shown their effectiveness in typical time series forecasting tasks [5], [6].

However, anomaly prediction remains a challenging task. The main issue arises from the scarcity of data related to abnormal events, resulting in a limited number of samples available for data analysis and model training. This scarcity of data can lead to poor model performance. Additionally, LSTM models require higher computational time for training models when compared to feed forward neural networks, as reported in [7]. This increased computational complexity is due to the inherent complexity of LSTM architectures.

To overcome the limitation of limited training samples, various techniques have been proposed to generate data based on a few available samples. One common approach is the use of Variational Autoencoders (VAEs), which leverage autoencoder principles and conditional probability to obtain a latent space that can be explored to generate countless samples [8]. VAEs have demonstrated their usefulness in multiple applications, as reported in [9], [10].

The concept of the latent space has inspired us. If we can harness the power of the latent space to generate data for specific purposes, it can also be used as a tool for predicting the future with reduced computational time and without being constrained by data limitations. Additionally, previous research works [11] and [12] have successfully applied a similar idea for data imputation and anomaly classification, respectively. Therefore, leveraging VAEs and the latent space for time series forecasting, particularly in the context of anomaly prediction where obtaining samples is difficult, holds great potential.

Hence, in this paper, we present a novel approach called Latent Space Coordination Relation (LSCR) for Anomaly Prediction to overcome the limitations associated with traditional anomaly prediction techniques. Our proposed framework harnesses the power of Variational Autoencoder (VAE) and leverages the coordination relation of points within the latent space for effective anomaly detection. By exploiting the latent space, our method facilitates efficient learning and prediction of anomalies, even when the availability of anomaly data is limited.

The core idea behind our approach is to utilize the latent space of the VAE, which serves as a compressed repre-

*Corresponding author: kuntpong@it.kmitl.ac.th

sensation of the input data. By learning the coordination relation of points in this latent space, LSCR can effectively identify anomalous patterns. Furthermore, the decoder of the VAE aids in restoring the data, improving the accuracy of anomaly detection.

To evaluate the performance of our proposed method, we conducted extensive experiments using real-world datasets with limited training data. The results clearly demonstrate that LSCR outperforms baseline models in detecting anomalies, exhibiting significantly lower error rates. This improvement can be attributed to the effective utilization of the latent space for learning and assisting in anomaly prediction, along with the signal restoration capabilities of the decoder.

As mentioned above, this research presents two significant contributions, as follows:

- The utilization of the latent space in VAE provides not only for data generation but is also applicable to prediction tasks.
- LSCR demonstrates the efficacy through comprehensive experiments, showcasing its superiority in reducing forecasting error and training time over traditional techniques for anomaly prediction when training data is limited.

The remainder of this paper is organized as follows: Section II provides a brief overview of related works in the field of anomaly prediction. In Section III, we present the methodology behind LSCR, detailing the integration of VAE and the coordination relation in the latent space. Section IV presents the experimental setup and analyzes the results obtained. Finally, Section V concludes the paper, highlighting the contributions of our approach and discussing potential avenues for future research.

II. RELATED WORKS

A. Anomalous Time Series Prediction and Its Challenge

Anomaly incidents in time series data are infrequent occurrences that deviate from the usual routine. While certain anomalous events can be beneficial for the target, like an increase in sales of the product [13], many instances have negative effects, such as malicious cyber attacks by hackers [1], [2], breakdowns of the important machinery along the factory production line [14], and the relapse of critical health issues or symptoms [15].

Given the aforementioned circumstances, the need for effective anomaly detection frameworks and techniques becomes imperative in order to anticipate and prevent such detrimental losses in crucial targets.

While it may initially appear that this problem could be addressed by simply having specialized personnel monitor and analyze the data, this approach presents certain limitations. Hiring individuals with specific knowledge can be costly, and they cannot provide round-the-clock monitoring of the target system. Therefore, the need for automation systems arises to overcome these limitations.

B. Feed Forward Neural Network (FF-NN)

The use of feed-forward neural networks (FF-NNs) is a widespread technique in automation systems [3]. The core

idea of a neural network is to emulate the functionality of human neuron cells using node layers, including an input layer, one or more hidden layers, and an output layer. Each node, or artificial neuron, within the network is interconnected with others and possesses weights and thresholds. Activation occurs when the output of a node exceeds the specified threshold, transmitting data to the subsequent layer. Conversely, if the output falls below the threshold, no data is forwarded.

Numerous research studies have demonstrated the effectiveness of this approach in efficient time series detection and forecasting. For example, it has been applied to traffic flow forecasting [16] and intrusion detection systems for identifying abnormal system activities [17].

C. Long Short Term Memory Neural Network (LSTM)

The Long Short-Term Memory (LSTM) neural network is an improved version designed specifically for handling sequential data like time series or signals. It was originally proposed by [4]. The primary idea behind this architecture is the incorporation of gates and cells to address the issue of gradient vanishing, which can occur in traditional neural networks.

LSTM has found interesting applications in various domains, such as anomaly detection in IP networks, where it monitors traffic data from routers [18], and the detection of anomalous stock prices [19]. Both case studies demonstrate that LSTM contributes to achieving desired prediction performance.

However, it is important to acknowledge that LSTM still shares some of the challenges faced by traditional neural networks. One such challenge is the requirement of a large amount of data for training purposes. Additionally, the complex architecture of LSTM makes training the model resource-intensive and time-consuming [7]. Consequently, researchers are actively exploring alternative approaches to overcome these limitations.

D. Variational Autoencoder (VAE)

The Variational Autoencoder (VAE) is an influential neural network architecture introduced in [8]. Its fundamental principle involves implementing the VAE model, which consists of an encoder and a decoder within the neural network. By leveraging mean and standard deviation vectors, the VAE generates a probability distribution in the latent space. Mathematically, the VAE is defined by Eq. (1):

$$\log P(X) - D_{KL}[Q(z|X)||P(z|X)] = E[\log P(X|z)] - D_{KL}[Q(z|X)||P(z)] \quad (1)$$

Here, the training data is denoted by X , and the latent variable is represented by z . The encoder's conditional probability is denoted as P , while the decoder's conditional probability is denoted as Q . The Kullback-Leibler divergence is symbolized as D_{KL} .

The versatility of the Variational Autoencoder (VAE) has been demonstrated across a range of applications, with particular emphasis on generative tasks such as image generation and image super-resolution.

E. VAE and Latent Space Utilization in Applications

The utilization of Variational Autoencoder (VAE) and latent space extends beyond data generation purposes. Researchers have suggested its usefulness in various applications. For instance, John et al. [11] proposed the use of VAE's decoder for data imputation, leveraging its ability to reconstruct missing data [11], [20]. Another application is anomaly detection, where data is projected onto the latent space, and instances that do not belong to the cluster are considered anomalous [12].

These case studies demonstrate the diverse utilities of the latent space in various applications, which have inspired us to explore its potential for prediction purposes. Consequently, in Section III, we present a framework that incorporates VAE and latent space for anomaly prediction.

III. PROPOSED METHOD

In order to tackle the prior mentioned challenge and expand the utilization of the latent space, this section presents an innovative framework known as "Latent Space Coordination Relation for Anomaly Prediction." This framework has been developed to overcome the limitations of existing methods and effectively leverage the potential of the latent space. A comprehensive overview of the framework's overall concept and a detailed procedural outline are visually depicted in Fig. 1. The following subsections describe how it works.

A. Training Phase

The training phase encompasses several objectives. The crucial objectives include the following: (i) modelling the encoder and decoder from the latent space of the Variational Autoencoder (VAE) for both past and future signals and (ii) training a prediction model for latent coordinate points using a feed-forward neural network. The procedures involved in this phase are detailed as follows:

1) *VAE Training*: During the training phase, the VAE model is trained using the complete dataset. The encoder of the VAE model plays a crucial role in mapping the input data to a lower-dimensional latent space, while the decoder is responsible for reconstructing the input data from this latent space.

Here, each training sample is divided into two segments: past and future signals. Then, we use two VAE models for training (see Fig. 1 (a)): one is specifically trained with past signal samples, and another is trained with future signal samples. The main objective of this training is to accurately derive the coordination points of the latent space, which effectively represent the learned complete samples through the VAE models, for both past and future signals. Additionally, the trained encoder and decoder, obtained from this training phase, play a vital role in the consequent prediction phase.

2) *Latent Coordination Relation Training*: In order to predict latent coordinate points, a feed-forward neural network with multiple inputs is constructed. The inputs to the network are the latent coordinates of the past signal

samples as shown in a dash-line of Fig. 1(a), while the corresponding target coordinate points from the future signal samples act as ground truth labels for training.

The primary objective of this prediction model is to establish correlations between the latent coordinates of past and future signals. By capturing these correlations, the neural network model enables the coordination of sensors, allowing one sensor to assist in forecasting and reconstructing the future output. This approach leverages the relationships between past and future signals to improve the accuracy and effectiveness of the prediction process.

B. Predicting Phase

A prediction model (see Fig. 1 (b)) comprises five components: Past Trained Encoder, Past Trained Latent Coordination, Neural Network, Predicted Latent Coordination, and Future Decoder. The first three components of this model, Past Trained Encoder, Past Trained Latent Coordination, and Neural Network, are derived from the training phase (see Fig. 1(a)). The following steps outline the process in detail.

1) *Encoding unknown past signals*: In this stage, the Past Trained Encoder from the Training Phase is employed to obtain the coordinate representation for the latent predictor neural network. The process begins by providing an unknown or test signal as input, which is then passed through the Past Trained Encoder, specifically designed for handling past signals. Once this step is completed, the framework acquires the latent coordinates of the unknown signals for the subsequent phase. It should be noted that the latent coordinates, obtained during the training phase, are not put into use in this stage. Instead, only the Past Encoder is applied to implement the learned weights from the trained dataset and encode the unknown signal into unknown coordinates.

2) *Predicting unknown latent coordinates*: In this step, the neural network model, trained through Latent Coordination Relation Training (see Fig. 1(a)), is utilized to predict the latent coordinates of future signals based on past coordinate points. The goal is to acquire the coordinate points corresponding to the future signals, which will be subsequently input into the decoder in the next step. By leveraging the learned correlations between the past and future signals, the prediction model can accurately estimate the latent coordinates that represent the upcoming data.

3) *Predicting unknown future signals*: After obtaining the predicted unknown latent coordinates from the neural network in the previous step, they are used as input for the Future Trained Decoder, which is specifically designed for future signals. Acting as a reconstruction tool within the VAE framework, the Future Decoder utilizes the latent coordinates to restore the shape of the signal. This pivotal stage focuses on reconstructing the future signals, resulting in an output that closely resembles the original future signal. Similar to the encoding unknown past signal stage, only trained future decoder is implemented. The latent coordinates from the training phase have no matter in the predicting stage.

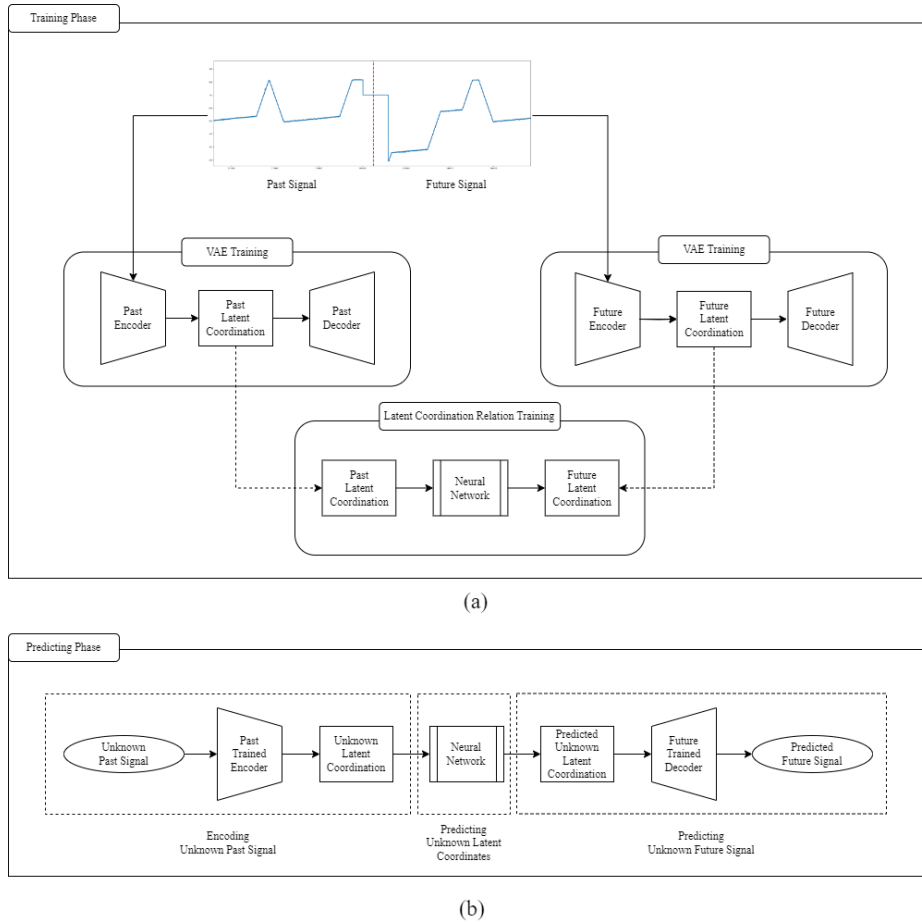


Fig. 1. An overall of the latent space coordination relation for anomaly prediction framework.

In summary, the LSCR framework involves two significant phases: the Training Phase and the Predicting Phase.

Training phase focuses on the training of the VAE models for past and future signals. The past signals and future signals are trained in the VAE models separately to obtain encoder and decoder, which will be implemented in the latter process. Additionally, a neural network is then trained using the past coordinate points from the learned VAE as input and the future coordinate points as output.

As for the Predicting Phase, an unknown signal is encoded using the past VAE's encoder, generating coordinate points. These points are used to predict future coordinates in the learned latent coordinates of the predictor neural network. The predicted future coordinates are reconstructed using the future VAE's decoder, yielding the predicted future signal as an output.

IV. EXPERIMENTAL RESULTS

A. Dataset

To evaluate the effectiveness of the proposed framework, the Secure Water Treatment (SWaT) datasets from iTrust [1] were utilized in the experiments conducted for this paper. These datasets contain signals obtained from various sensors installed on electronic components within a water treatment testbed. The data encompasses both normal operating conditions and anomalous events, which

were intentionally simulated by researchers to replicate cyber attacks on the system. These online strike imitations aim to destroy the machinery or even disrupt the whole system, to show the effect that could happen in the actual system if hackers attacks succeed.

In the specific testing scenario of the proposed framework, the raw water tank sensor (RAW), part of sensor data that available in SWaT, was selected as the target sensor. This sensor recorded multiple cyber attack scenarios, which are as follows: (i) increasing the water tank level by 1 mm per second in order to deliberately cause underflow in the tank; (ii) setting the sensor value consistently at 700 mm to intentionally cause the tank to overflow; (iii) setting the sensor value above the threshold to induce underflow in the tank and potentially damage the system; (iv) similar to the second attack, but with the additional intention of causing underflow and overflow in other target tanks; (v) attacking on another related sensor, which results in a slight drop in the raw water level. These types of anomalies have the potential to disrupt the overall system and significantly impact its performance.

During the experiment, signal samples were captured and subjected to time window sliding techniques to augment the dataset. The input dataset comprised past signals that included slight indications of the anomalous event, while the ground truth dataset consisted of future sig-

TABLE I
A COMPARISON OF MULTI-CLASS CLASSIFICATION RESULTS BASED ON THE RAW DATASET

| Performance Metric | FF-NN (72 Nodes) | FF-NN (720 Nodes) | LSTM (72 Units) | Proposed Method |
|-----------------------------------|--------------------------|--------------------|------------------------|------------------------|
| RMSE | 0.1443 ± 0.0419 | 0.0316 ± 0.0019 | 0.2601 ± 0.0272 | 0.0291 ± 0.0040 |
| Prediction Training Time (Second) | 28.0971 ± 18.5469 | 280.8384 ± 84.2278 | 6,503.2350 ± 2151.5040 | 72.9462 ± 21.4926 |

nals recorded after the occurrence of the anomaly. By comparing the predictions of our method with the actual future signals, the effectiveness of the proposed model in detecting and predicting anomalies could be assessed.

B. Experimental Setup

In order to ensure unbiased evaluation of our model compared to the baselines, we provide detailed information on the experimental setup as follows:

- The baseline methods used in this experiment are FF-NN and LSTM models with different parameters.
- For the 72-node and 720-node FF-NN models, both consist of 5 layers with ReLU activation function.
- The LSTM model is configured with a single layer comprising 72 LSTM units.
- The VAE models are designed with an input layer of 72 nodes and a second layer of 36 nodes in the encoder. The decoder architecture differs from this setup. The VAE models are trained using two-dimensional samples for 100 epochs.
- The latent prediction neural network is trained with three layers, each containing 20 nodes.
- The dataset consists of five anomaly classes and a single normal class. Each anomaly class contains only 30 samples, while the normal class has 50 samples. Therefore, the total number of samples for training and testing is 200.
- Time window slicing with a one-second time step is applied to obtain samples from the dataset sources.
- Each sample in the dataset spans a record of 7,200 seconds of past or future time series data.
- All data are normalized using the Min-Max Scaling method to ensure that the normalized values are in between 0 and 1.
- 5-fold cross-validation is implemented to ensure unbiased evaluation and avoid fortunate cases. The process divided 50% of the samples for training and the remaining 50% for testing purposes.
- Early stopping is applied to every model training in this experiment.
- Root Mean Squared Error (RMSE) and Training Time are the evaluation metrics used in this experiment. Training time for our proposed model is the total time of past VAE training, future VAE training, and latent coordination predictor training.

C. Results and Discussion

The experimental results are presented in Table I, and two examples of the predicted time series compared to the ground truth are shown in Fig. 2. As expected, the proposed method demonstrates superior performance

compared to FF-NN and LSTM. Our proposed approach achieves an RMSE score of 0.0291 ± 0.0040 and a training time of 72.9462 ± 21.4926 seconds. These results indicate that our method outperforms the baseline methods in terms of RMSE score and achieves the second-best training time. Although our method may be slower than the FF-NN with 72 nodes, it offers a significant improvement in terms of RMSE score, showcasing overall superiority over the other models.

The achievements of our model can be attributed to its utilization of the Variational Autoencoder (VAE) as a key component for signal prediction. The VAE is capable of providing a latent space that captures the data representation of anomalous signals. This approach offers an alternative solution to address the limitations of the available dataset.

In traditional learning approaches, the model's learning ability is constrained by the data on which it has been trained. If the training dataset is limited or lacks sufficient representation of anomalous data, the model may struggle to accurately predict and detect anomalies. However, the proposed model overcomes this limitation by leveraging the VAE's latent space. This latent space contains a probability distribution of anomalous data that may not have been present in the training dataset.

The inclusion of the VAE and its latent space allows the proposed model to capture and learn from the underlying patterns and representations of anomalous data, even with a small training set. This capability gives our model a significant advantage over baseline approaches that rely solely on traditional learning methods.

As a result, the experimental results demonstrate the superiority of the proposed model in effectively detecting and predicting anomalies compared to traditional approaches. By leveraging the VAE's latent space, the proposed model can leverage the broader information contained within the distribution of anomalous data, improving its ability to accurately identify and predict anomalies.

V. CONCLUSION

This paper has presented a novel approach, Latent Space Coordination Relation for Anomaly Prediction, to address the challenging task of anomaly prediction in real-world systems. Our method tackles the issue of limited anomaly data availability, which hinders the performance of existing techniques. By leveraging the power of Variational Autoencoder (VAE) and exploiting the coordination relation of points in the latent space, we achieve effective learning and prediction of anomalies.

In future work, our aim is to further test our proposed framework with various real-world datasets in order to

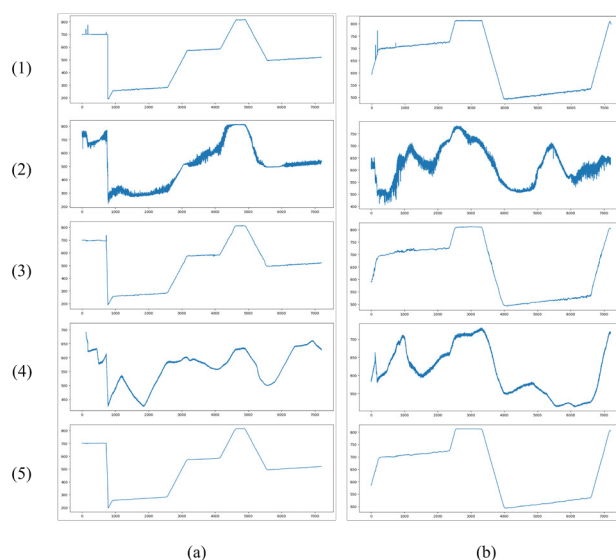


Fig. 2. Two examples of predicted outputs of the anomaly (a) class iv and (b) class v. (1) is the expected signal output; (2) is the prediction from the FF-NN with 72 nodes; (3) is the prediction from the FF-NN with 720 nodes; (4) is the prediction from the LSTM with 72 nodes; and (5) is the prediction from our proposed method.

demonstrate its potential effectiveness. Additionally, we found an opportunity to incorporate the idea of anomaly classification into the framework.

ACKNOWLEDGEMENT

This research has received generous financial support from Grant No. Research_KRIS-007: 2565-02-06-007, provided by the School of Information Technology at King Mongkut's Institute of Technology Ladkrabang.

REFERENCES

- [1] J. Goh, S. Adepu, K. N. Junejo, and A. Mathur, "A dataset to support research in the design of secure water treatment systems," in *Critical Information Infrastructures Security*. Cham: Springer International Publishing, 2017, pp. 88–99.
- [2] Singapore University of Technology and Design (SUTD), "Dataset characteristics," https://itrust.sutd.edu.sg/itrust-labs_datasets/dataset_info/, 2017, accessed: 2021-06-17.
- [3] M. Mijwil, A. Esen, and A. Alsaadi, "Overview of neural networks," vol. 1, p. 2, 04 2019.
- [4] S. Hochreiter and J. Schmidhuber, "Long short-term memory," *Neural computation*, vol. 9, no. 8, pp. 1735–1780, 1997.
- [5] Y. Liu, Z. Su, H. Li, and Y. Zhang, "An lstm based classification method for time series trend forecasting," in *2019 14th IEEE Conference on Industrial Electronics and Applications (ICIEA)*, 2019, pp. 402–406.
- [6] M. Samin-Al-Wasee, P. S. Kundu, I. Mahzabeen, T. Tamim, and G. R. Alam, "Time-series forecasting of ethereum price using long short-term memory (lstm) networks," in *2022 International Conference on Engineering and Emerging Technologies (ICEET)*, 2022, pp. 1–6.
- [7] S. Gopali, F. Abri, S. Siami-Namini, and A. S. Namin, "A comparison of tcn and lstm models in detecting anomalies in time series data," in *2021 IEEE International Conference on Big Data (Big Data)*, 2021, pp. 2415–2420.
- [8] D. P. Kingma and M. Welling, "An introduction to variational autoencoders," *Foundations and Trends® in Machine Learning*, vol. 12, no. 4, pp. 307–392, 2019. [Online]. Available: <http://dx.doi.org/10.1561/22000000056>
- [9] H. Hu, M. Liao, W. Mao, W. Liu, C. Zhang, and Y. Jing, "Variational auto-encoder for text generation," in *2020 IEEE 5th Information Technology and Mechatronics Engineering Conference (ITOEC)*, 2020, pp. 595–598.
- [10] K. Goto and N. Inoue, "Learning vae with categorical labels for generating conditional handwritten characters," in *2021 17th International Conference on Machine Vision and Applications (MVA)*, 2021, pp. 1–5.
- [11] J. T. McCoy, S. Kroon, and L. Auret, "Variational autoencoders for missing data imputation with application to a simulated milling circuit," *IFAC-PapersOnLine*, vol. 51, no. 21, pp. 141–146, 2018, 5th IFAC Workshop on Mining, Mineral and Metal Processing MMM 2018. [Online]. Available: <https://www.sciencedirect.com/science/article/pii/S2405896318320949>
- [12] R. Yao, C. Liu, L. Zhang, and P. Peng, "Unsupervised anomaly detection using variational auto-encoder based feature extraction," in *2019 IEEE International Conference on Prognostics and Health Management (ICPHM)*, 2019, pp. 1–7.
- [13] N. Ngongo and O. Darteh, "Sales anomaly detection using automatic time series decomposition," *Journal of Economics, Management and Trade*, pp. 13–21, 07 2022.
- [14] D. Kim, J. Cha, S. Oh, and J. Jeong, "Anogan-based anomaly filtering for intelligent edge device in smart factory," in *2021 15th International Conference on Ubiquitous Information Management and Communication (IMCOM)*, 2021, pp. 1–6.
- [15] T. T. Um, F. Pfister, D. Pichler, S. Endo, M. Lang, S. Hirche, U. Fietzek, and D. Kulic, "Data augmentation of wearable sensor data for parkinson's disease monitoring using convolutional neural networks," *Proceedings of the 19th ACM International Conference on Multimodal Interaction*, 2017.
- [16] V. A. Shterev, N. S. Metchkarski, and K. A. Koparanov, "Time series prediction with neural networks: a review," in *2022 57th International Scientific Conference on Information, Communication and Energy Systems and Technologies (ICEST)*, 2022, pp. 1–4.
- [17] Y. Sani, A. Mohamedou, K. Ali, A. Farjamfar, M. Azman, and S. Shamsuddin, "An overview of neural networks use in anomaly intrusion detection systems," in *2009 IEEE Student Conference on Research and Development (SCoReD)*, 2009, pp. 89–92.
- [18] G. Qin, Y. Chen, and Y.-X. Lin, "Anomaly detection using lstm in ip networks," in *2018 Sixth International Conference on Advanced Cloud and Big Data (CBD)*, 2018, pp. 334–337.
- [19] W. Yang, R. Wang, and B. Wang, "Detection of anomaly stock price based on time series deep learning models," in *2020 Management Science Informatization and Economic Innovation Development Conference (MSIEID)*, 2020, pp. 110–114.
- [20] T. Chalongvorachai and K. Woraratpanya, "Data imputation using multivariate-vae approach for time series signals," in *13th Joint Symposium on Computational Intelligence (JSCI13)*, 2023.

Autonomous Pick-and-Place using Excavator Based on Deep Reinforcement Learning

1st Cendikia Ishmatuka

Dept. of Electrical and Information Engineering
Universitas Gadjah Mada
Yogyakarta, Indonesia
cendikia.i@mail.ugm.ac.id

2nd Indah Soesanti

Dept. of Electrical and Information Engineering
Universitas Gadjah Mada
Yogyakarta, Indonesia
indahsoesanti@ugm.ac.id

3rd Ahmad Ataka

Dept. of Electrical and Information Engineering
Universitas Gadjah Mada
Yogyakarta, Indonesia
ahmad.ataka.ar@ugm.ac.id

Abstract—Excavator operation demands precise control because of the complicated nature of the tasks. Standard operation of excavator by human worker generally lacks effectiveness and efficiency which is vital in industrial processes. On the other hand, conventional control methods generally rely on the exact model of excavator which is difficult to obtain accurately. In this paper, we proposed an alternative strategy to control excavator using reinforcement learning in which the control policy is discovered through learning process. The Proximal Policy Optimization (PPO) is employed in this research to learn the policy. The results show that the proposed approach can effectively operate the excavator autonomously, especially in controlling the position and orientation of the bucket towards the desired point without prior knowledge of excavator's kinematics. We have successfully implemented the proposed method to perform pick-and-place operation in the simulation scenario.

Index Terms—Excavator, Reinforcement Learning, Proximal Policy Optimization, Control

I. INTRODUCTION

The use of heavy machinery, also known as earth-moving machines, is important in various industries such as mining, construction, and agriculture [1]–[3]. These machines are used for digging foundations, building roads, processing soil, and other tasks that require significant mechanical strength and capability that may be difficult or time-consuming for humans to accomplish. One of the most commonly used heavy machinery in industries is an excavator. However, traditional manual control of excavators by skillful operators could potentially lead to a harsh working environment, low efficiency, and high labor intensity [4]. Moreover, excavators are often used in hazardous conditions such as open-pit and toxic chemical mines, making the operator the weakest point in the control process due to their limited flexibility in working in all conditions [1].

Thus, over the past two decades, research has been conducted to develop smart and automatic construction equip-

ment, particularly excavators, to improve production efficiency and prevent construction accidents [1], [4]. Recently, the machine learning paradigm of reinforcement learning has been considered a potential approach to facilitate and expand the capabilities of robotics in many fields. This approach provides more benefits than classical control methods, such as traditional inverse kinematics, which require significant efforts in modeling complex systems like excavators.

In this paper, we proposed the a reinforcement-learning-based control for excavator. We proposed the choice of observation space, reward function, and reinforcement learning model's hyperparameter to train a control policy in simulation using the Proximal Policy Optimization (PPO) algorithm. The trained control policy controls the excavator's joint velocity to move the bucket toward the desired position and orientation. We show that the trained controller performs well and follows the desired trajectory for pick-and-place use case.

In the following section, past literature will be reviewed. Then, we present detailed information about the excavator's kinematics and Proximal Policy Optimization algorithm. And finally, we provide the system description and the experiment result in the last section.

II. RELATED WORK

Over the decades, many solutions have been developed to perform automatic excavator control. One of the most popular solutions for an autonomous excavator is the model-free approach PID (Proportional-Integral-Derivative) control. Feng et al. [5] proposed a PID control for an excavator, using Improved Generation Algorithm (IGA) for parameter tuning. This paper [5] showed that the PID control with IGA parameter tuning successfully enhances tracking accuracy compared with two other methods (Standard Generation Algorithm and Ziegler-Nichols). However, due to vibration and other causes, the tracking deviations are still high. Another PID tuning algorithm was proposed by Ye et al. [6] using Improved Particle Swarm Optimization (IPSO) to find the best PID controller

This research is funded by RTA Program Universitas Gadjah Mada with the Grant Number 5075/UN1.P.II/Dit-Lit/PT.01.01/2023.

gains for a non-hydraulic excavator system. This paper [6] showed that the IPSO algorithm performs more effectively than the Phase-Margin and Standard Particle Swarm Optimization methods. The velocity and position hybrid control for an excavator provided quick positioning and low energy usage due to the possibility of completely opening the valve to decrease throttling loss [7]. Zhang et al. [7] used a hybrid control, where the system operates in velocity control mode if the position mistake is too large. But, if it is near the goal position, the system will switch to position control mode. On the other hand, Jud et al. [8] employed a hybrid control system depending on the excavator's task. The control system uses inverse kinematics to follow the intended trajectory in free space. When it comes to the digging operation, the control system uses inverse dynamics. Lee and Kim [9] proposed a trajectory generation for each excavator's joints using Virtual Motion Camouflage (VMC). This generated trajectory is used for obstacle avoidance and digging operation.

The kinematics and dynamics of the excavator are precise mathematical descriptions necessary for all of the solutions mentioned above. However, it isn't easy to be obtained accurately. Thus, reinforcement learning is another possible approach that can be used for controlling the excavator without knowing the kinematics and dynamics of the system. Agarwal et al. [10] proposed a feedback mechanism as a reward for the reinforcement learning policy. The dynamics and safety distributions retrieved from the trajectory of the expert operators were used to create this feedback system. The reward mechanism uses the KL divergence of the distributions and the current action. A deep network PointNet++ model was developed by Lu et al. [3] to analyze the local (shape and surface properties of rigid bodies) and the global (layout and object arrangement) features of the rigid bodies in a clutter. This work [3] showed that the PointNet++ model is useful for reducing the training time while still achieving a good performance. Egli and Hutter, in their study [11], used a data-driven approach to train the reinforcement learning model and track the given trajectory. This paper [11] compared the reinforcement learning model trained using the Trust Region Policy Optimization algorithm and the inverse kinematics-based control. More recently, Egli and Hutter in their research [12] which is the extension and modifications to their previous study [11], provided a general approach to develop a task-space trajectory tracking controller system using a velocity tracking controller. This method [12] was trained using the Proximal Policy Optimization (PPO) algorithm, resulting in an accurate control system. Another control system trained using the PPO algorithm was provided by Egli et al. [13] to create an excavator controller for soil excavation that can easily adjust to the characteristics and properties of the soil.

In this paper, we proposed a reinforcement learning method for excavator control based on PPO with the following contributions:

- it proposes a list of observation regarding the state of the excavator,
- it employs a new reward function considering position

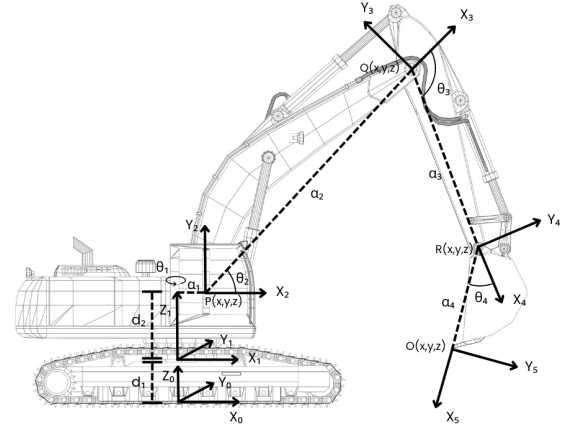


Fig. 1. Frame coordinates of an excavator.

and orientation velocity error, where the target velocity is retrieved from proportional control.

We will implement the proposed method to perform pick-and-place use case in a simulation scenario.

III. KINEMATICS MODELING OF AN EXCAVATOR

In this paper, we regard an excavator as a manipulator. Thus, this study does not include the undercarriage (drive wheel part). An excavator has five links: the undercarriage as the base link, the main body, the boom, the arm, and the bucket. In addition, excavators have four joints connecting one link to another. The frame coordinate of an excavator is shown in Fig. 1.

A. Forward Kinematics

To know the position and orientation of the end effector given the configuration space of the joints, the Denavit-Hartenberg method (D-H) is used. The D-H method computes four parameters: the angle of the joint (θ), the twist (α), which is the angle of the z -axis of the end effector reconfigured to the axis of the joint, the distance between two joints on the same configuration of the z -axis (a), and the distance between two joints on different configurations of the z -axis (d) [14]. Feng et al. [5] have described the D-H parameters for an excavator as shown in Table I. These D-H parameters are modified based on the coordinates frame of an excavator shown in Fig. 1.

By knowing these D-H parameters, we can find out the position and orientation of each link by using the homogeneous transformation defined as ${}^{i-1}T_i$ [14]:

$${}^{i-1}T_i = \begin{bmatrix} \cos(\theta_i) & -\cos(\alpha_i) \sin(\theta_i) & \sin(\alpha_i) \sin(\theta_i) & a_i \cos(\theta_i) \\ \sin(\theta_i) & \cos(\alpha_i) \cos(\theta_i) & -\sin(\alpha_i) \cos(\theta_i) & a_i \sin(\theta_i) \\ 0 & \sin(\alpha_i) & \cos(\alpha_i) & d_i \\ 0 & 0 & 0 & 1 \end{bmatrix}. \quad (1)$$

Here, ${}^{i-1}T_i$ is the homogeneous transformation of i -th link with respect to the $(i-1)$ -th link. According to the coordinate frame shown in figure 1 and the D-H parameters of an

TABLE I
D-H PARAMETERS OF AN EXCAVATOR.

| Joint | a_i | α_i | d_i | θ_i |
|-------|-------|-----------------|-------|------------|
| 1 | a_1 | 0 | d_1 | θ_1 |
| 2 | a_2 | $\frac{\pi}{2}$ | d_2 | θ_2 |
| 3 | a_3 | 0 | 0 | θ_3 |
| 4 | a_4 | 0 | 0 | θ_4 |

excavator, the bucket coordinate $O(x, y, z)$ and the bucket orientation ϕ can be determined by [5]:

$$\begin{aligned} x &= c_1[a_1 + a_2c_2 + a_3c_{23} + a_4c_{234}] \\ y &= s_1[a_1 + a_2s_2 + a_3s_{23} + a_4s_{234}] \\ z &= d_1 + d_2 + a_2s_2 + a_3s_{23} + a_4s_{234} \\ \phi &= \theta_2 + \theta_3 + \theta_4 \end{aligned} \quad (2)$$

where $c_1 = \cos(\theta_1)$, $c_{23} = \cos(\theta_2 + \theta_3)$, $s_1 = \sin(\theta_1)$, and so on.

B. Inverse Kinematics

Inverse kinematics is used to calculate the angle value of each joint, given the position and orientation of the bucket in the workspace. Taking into account the excavator's posture, the only valid inverse kinematics solution for the excavator is the "elbow-up" solution as shown in figure 1 [5], [9]. Given the bucket coordinates $O(x, y, z)$ and orientation ϕ , the angles of each joint can be derived as follows [5], [9]:

$$\begin{aligned} \theta_1 &= \tan^{-1}\left(\frac{y}{x}\right) \\ \theta_2 &= \alpha + \beta + \gamma \\ \theta_3 &= \pi - \cos^{-1}\left(\frac{a_2^2 + a_3^2 - PR^2}{2a_2a_3}\right) \\ \theta_4 &= \phi - \theta_2 - \theta_3 \end{aligned} \quad (3)$$

where α is the angle between PQ and PR, β is the angle between PR and PO, and γ is the angle between PO and the x -coordinate of the base. The distance between P and R can be determined from the following equation [5]:

$$\begin{aligned} PR &= \sqrt{(x_q - a_1)^2 + y^2 + (z_q - (d_1 + d_2))^2} \\ x_q &= x - a_4 \cos(\phi) \\ z_q &= z - a_4 \sin(\phi) \end{aligned} \quad (4)$$

IV. PROXIMAL POLICY OPTIMIZATION

Proximal policy optimization (PPO) is a deep reinforcement learning algorithm that belongs to the policy-based method. It focuses on finding the best policy $\pi(a_t|s_t)$ representing the likelihood of an action a_t for a particular state s_t at time t . It employs an actor-critic approach, where the actor estimates the policy while the critic measures how good the action being performed [15], [16].

The policy update (actor's loss) is defined as [15], [16]:

$$L^{CLIP}(\theta) = \mathbb{E}_t[\min(r_t(\theta)\hat{A}_t, \text{clip}(r_t(\theta), 1 - \epsilon, 1 + \epsilon)\hat{A}_t)] \quad (5)$$

where:

$$r_t(\theta) = \frac{\pi_\theta(a_t|s_t)}{\pi_{\theta_{old}}(a_t|s_t)} \quad (6)$$

indicates the likelihood ratio of the present policy $\pi_\theta(a_t|s_t)$ compared to the previous policy $\pi_{\theta_{old}}(a_t|s_t)$. $L^{CLIP}(\theta)$ taking the minimum value of the unclipped term ($r_t(\theta)\hat{A}_t$) and the clipped one ($\text{clip}(r_t(\theta), 1 - \epsilon, 1 + \epsilon)\hat{A}_t$) [16]. The $r(t)$ is clipped between $1 - \epsilon$ and $1 + \epsilon$ to prevent drastic policy changes where ϵ stands for a hyperparameter. \hat{A}_t is the advantages function that can be calculated using Generalized Advantage Estimate (GAE), formulated as follows [15]–[17].

$$\hat{A}_t^{GAE(\gamma, \lambda)} = \sum_{l=0}^{\infty} (\gamma\lambda)^l \delta_{t+l}^V \quad (7)$$

where:

$$\delta_t = r_t + \gamma V(s_{t+1}) - V(s_t) \quad (8)$$

Here, γ , λ , r_t , and $V(s_t)$ represent a discount factor, GAE hyperparameter, reward at time t , and the value of state s_t . The advantages function tells the actor if the chosen action was significantly better or worse than the overall expected return [17].

The critic is used to evaluate action taken by the actor by minimizing the loss between the target value V_t^{target} and the estimated value $V_\omega(s_t)$, defined by [15], [16]:

$$L_t^{VF} = \mathbb{E}_t[(V_t^{target} - V_\omega(s_t))^2] \quad (9)$$

$$\text{where } V_t^{target} = \hat{A}_t + V_{\omega_{old}}(s_t) \quad (10)$$

Hence, the overall objective which is approximately maximized after each iteration, is expressed by [15]:

$$L_t^{CLIP+VF+S}(\theta) = \mathbb{E}_t[L^{CLIP}(\theta) - c_1 L_t^{VF} + c_2 S[\pi_\theta](S_t)] \quad (11)$$

where $S[\phi_\theta](s_t)$ is the entropy bonus, and c_1, c_2 are coefficients.

V. SYSTEM DESCRIPTION

A. Excavator Simulation

For the environment simulation, we used PyBullet [18] and OpenAI Gym [19]. PyBullet [18] is a physics simulation engine designed for robotics and machine learning researchers who need to simulate complex physical interactions in a 3D environment. This physics engine provides many useful functions, such as 'getLinkState', 'getJointState', etc that are used as a sensor for control feedback. While OpenAI Gym [19] is a powerful tool for developing RL environments and testing RL algorithms in a standardized and reproducible way.

B. Observation Space and Action Space

A set of any possible observations that an RL agent may get from its environment is referred to as the observation space. The observation spaces given to the RL agent are the joint angles (θ), joint angular velocity ($\dot{\theta}$), bucket's position in cartesian coordinates(p), bucket's position error in cartesian coordinates (p_e), actions given to the joint (a_t), bucket's linear velocity (\dot{p}), bucket's desired linear velocity (\dot{p}_d), bucket's

orientation (ϕ), bucket's orientation error (ϕ_e), bucket's orientation angular velocity ($\dot{\phi}$), and bucket's desired orientation angular velocity ($\dot{\phi}_d$).

Action space is a set of all possible actions an agent can take in response to an observation from the environment. In this research, the action space taken by the RL agent is the excavator joint's velocity ($\dot{\theta}$). We used a continuous action space with a maximum velocity 0.3 rad and a minimum velocity -0.3 rad .

C. Reward Function

The reward function represents the return or a feedback signal received by the RL agent for performing an action in a state at time t . The reward r_t received by the agent at time t is defined as:

$$r_t = r_t^{\dot{p}} + r_t^{\dot{\phi}} + r_t^r \quad (12)$$

where:

$$\begin{aligned} r_t^{\dot{p}} &= 4 * \exp(-\|\dot{p}_d - \dot{p}\|_2) \\ r_t^{\dot{\phi}} &= -0.02 * (\dot{\phi}_d - \dot{\phi})^2 \\ r_t^r &= -0.075(\|a_t - a_{t-1}\|_2) \end{aligned} \quad (13)$$

The first two terms, $r_t^{\dot{p}}$ and $r_t^{\dot{\phi}}$, are used to encourage the agent to track the bucket's desired orientation angular velocity ($\dot{\phi}_d$) and bucket's desired linear velocity (\dot{p}_d). The first term uses exponential function to encourage the agent to track the desired linear velocity in a smooth manner. The second term does not use exponential since the error in angular velocity is not as sensitive as the error in linear velocity. The desired orientation velocity and the desired linear velocity are obtained from $\dot{\phi}_d = K_p * \phi_e$ and $\dot{p}_d = K_p * p_e$, respectively. The final term r_t^r guarantees that the excavator's arm moves smoothly by punishing significant changes in control actions a_t . We use the constant $K_p = 5.0$ for all the experiments in the next section since it provides an appropriate trade-off between accuracy and stability. The weight values of the reward function are all retrieved from trial and error to ensure satisfactory training results.

D. Algorithm

In this study, we use Proximal Policy Optimization (PPO) algorithm [15] provided by the Stable Baselines3 library [20] to train the control policy. We also adjust the PPO algorithm's hyperparameters based on trial and error to achieve the best outcomes for RL agent training. Table II shows the list of hyperparameters used in the PPO algorithm.

VI. EXPERIMENTAL RESULT

In the simulation, we will control the excavator's bucket from one point to another, enabling it to follow a trajectory of pick-and-place task. Hence, we set several destination points consisting of target position and orientation pairs as target points reflecting the pick-and-place operation as shown in Table III. Here, x_d, y_d, z_d are the position targets and ϕ_d is the orientation targets. These points are all located in the workspace of the excavator.

TABLE II
PPO HYPERPARAMETERS

| | |
|----------------------------|--------------------|
| Policy Hidden Layers | 64x64, ReLU |
| Value Hidden Layers | 64x64, ReLU |
| Discount Factor γ | 0.99 |
| GAE λ | 0.95 |
| Learning Rate | 1×10^{-4} |
| Mini Batch Size | 1024 |
| Clip Range ϵ | 0.2 |
| Value Function Coefficient | 0.5 |
| Entropy Coefficient | 0.0 |

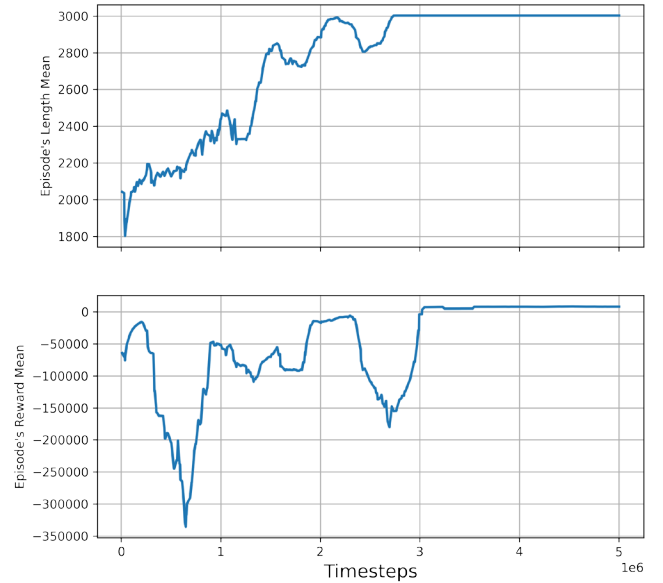


Fig. 2. RL Agent's Training Result.

The reinforcement learning agent was trained for 5 million time steps and the training result is shown in Fig. 2. At the beginning of the training, the agent appears to struggle with optimizing its policy, as indicated by highly fluctuating rewards. However, eventually, the agent was able to learn an optimal policy and achieve convergence (i.e. the reward has not changed significantly) where it achieves maximum average episode length and reward.

After the model is trained, we validate the model performance using the following bucket's target position and orientation: $p_d = [9.817, 0, 0.942] \text{ m}$, $\phi_d = -1.841 \text{ rad}$. The bucket's initial position and orientation are set to be $p_0 = [8.27, 0, 4.48] \text{ m}$, $\phi_0 = -0.7 \text{ rad}$ (see Fig. 3). The model can control the bucket's position to the position target quickly and can reach a steady state after 1337 steps (see Fig. 3a) with a small root mean square position error of $x_{RMSE} = 1.1825 \times 10^{-2} \text{ m}$, $y_{RMSE} = 6.0773 \times 10^{-4} \text{ m}$, $z_{RMSE} = 2.9495 \times 10^{-2} \text{ m}$. In addition, the bucket's orientation error also approaches 0 as the step increases with root mean square

TABLE III
POSITION AND ORIENTATION TARGETS FOR PICK AND PLACE TASK AND THE MODEL VALIDATION RESULT.

| Index target | x_d (m) | y_d (m) | z_d (m) | ϕ_d (rad) | x_{RMSE} (m) | y_{RMSE} (m) | z_{RMSE} (m) | ϕ_{RMSE} (rad) |
|-----------------|--------------|--------------|--------------|-------------------|-------------------|-------------------|-------------------|------------------------|
| 1 | 8.27 | 0 | 4.48 | -0.7 | 0.012 | 0 | 0.026 | 0.355 |
| 2 | 9.817 | 0 | 0.942 | -1.841 | 0.011 | 0.001 | 0.029 | 0.048 |
| 3 | 8.22 | 0 | 0.75 | -2.073 | 0.014 | 0.013 | 0.007 | 0.121 |
| 4 | 6.64 | 0 | 1.104 | -2.966 | 0.013 | 0.019 | 0.018 | 0.073 |
| 5 | 6.64 | 0 | 2.08 | -2.874 | 0.008 | 0.017 | 0.011 | 0.017 |
| 6 | 8.19 | 0 | 2.11 | -1.292 | 0.011 | 0.012 | 0.014 | 0.338 |

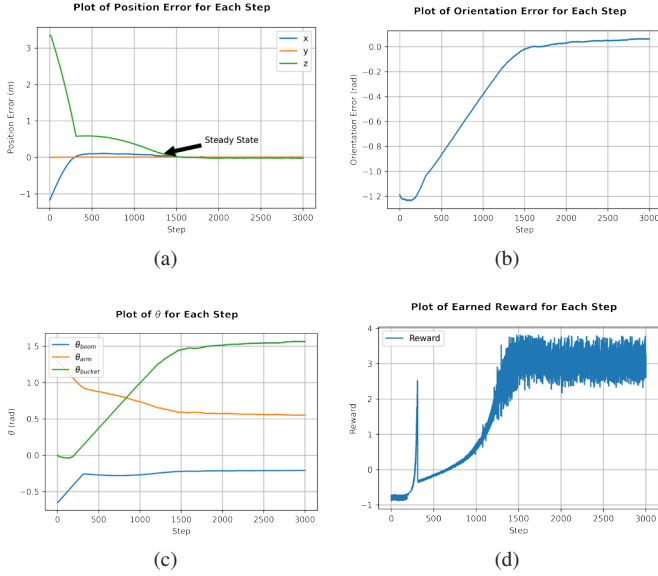


Fig. 3. Model validation result, where (a) shows position error each step, (b) shows orientation error each step, (c) shows the θ of each excavator's link (boom, arm, and bucket) for each step, and (d) shows reward earned by the agent for each step.

orientation error of $\phi_{RMSE} = 4.8988 \times 10^{-2}$ rad (see Fig. 3b). Then from Fig. 3c, we can see that the angle value θ for each links is stable at $\theta_{boom} = -0.2110$ rad, $\theta_{arm} = 0.5520$ rad, and $\theta_{bucket} = 1.5639$ rad. This means that the bucket's orientation is given by:

$$\begin{aligned}\phi &= -(\theta_{boom} + \theta_{arm} + \theta_{bucket}) \\ \phi &= -(-0.2110 \text{ rad} + 0.5520 \text{ rad} + 1.5639 \text{ rad}) \\ \phi &= -1.9048 \text{ rad}.\end{aligned}$$

Here, the value of ϕ is very close to the desired orientation value ϕ_d of -1.841 rad. The reward obtained by the RL agent converges to the maximum value even though it's highly fluctuating (see Fig. 3d). This is normal because the reward term r_t^{ϕ} can be changed drastically even if there is a small change in the bucket's orientation error. And all of the validation model results for the remaining position and orientation targets are summarized in Table III.

Finally, we test the model in a pick-and-place scenario where the controller has to follow a trajectory. We track the bucket's position when performing a pick operation, shown in Fig. 4 and Fig 5. The video version of the movement can also be found here: <https://bit.ly/PickNPlace>. Thus, the experimental results show that the reinforcement learning model successfully controls the excavator to perform pick-and-place operation.

VII. CONCLUSION

In summary, this research implemented the reinforcement learning control for excavator based on PPO algorithm. The proposed method provides an advantage compared to traditional control methods, as it was able to adapt and learn an optimal policy through interactions with the environment without relying on the model of the excavator. Specifically, the PPO algorithm effectively controlled the excavator bucket to move from one point to another along a trajectory and achieve convergence with maximum average episode length and reward.

The experimental results showed that the proposed approach could control the excavator in real-world scenarios, such as pick and place tasks, with high accuracy and efficiency. This work contributes to developing intelligent and autonomous excavator control systems and opens up new opportunities for further research in this area. In the future, comparison between reinforcement learning control and conventional control in real excavator system can be evaluated.

REFERENCES

- [1] O. M. U. Eraliev, K.-H. Lee, D.-Y. Shin, and C.-H. Lee, "Sensing, perception, decision, planning and action of autonomous excavators," *Automation in Construction*, vol. 141, p. 104428, 9 2022.
- [2] A. Suhandi and N. Nazaruddin, "Modifikasi serta pengujian sistem control dan sistem swing model excavator," *Jurnal Online Mahasiswa Fakultas Teknik Universitas Riau*, vol. 2, pp. 1-11, 2015.
- [3] Q. Lu, Y. Zhu, and L. Zhang, "Excavation reinforcement learning using geometric representation," *IEEE Robotics and Automation Letters*, vol. 7, pp. 4472-4479, 4 2022.
- [4] D. Huo, J. Chen, H. Zhang, Y. Shi, and T. Wang, "Intelligent prediction for digging load of hydraulic excavators based on rbf neural network," *Measurement*, vol. 206, p. 112210, 1 2023.
- [5] H. Feng, C.-B. Yin, W. wen Weng, W. Ma, J. jing Zhou, W. hua Jia, and Z. li Zhang, "Robotic excavator trajectory control using an improved ga based pid controller," *Mechanical Systems and Signal Processing*, vol. 105, pp. 153-168, 5 2018.

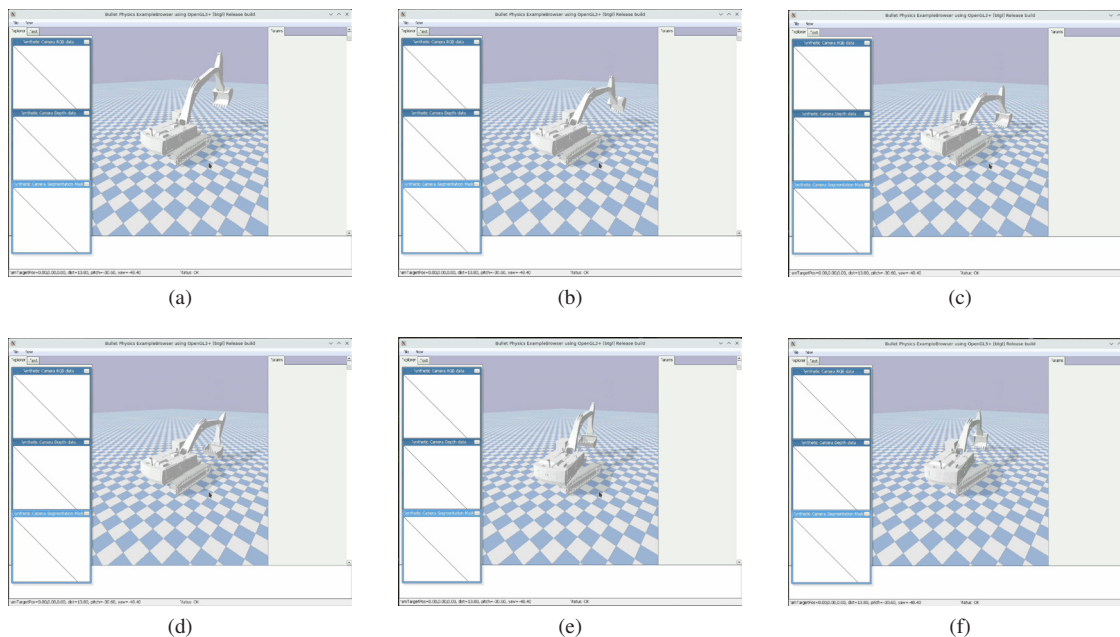


Fig. 4. Excavator movement in PyBullet when performing the pick operation (a-d), swinging to the place target (e), and place operation (f).

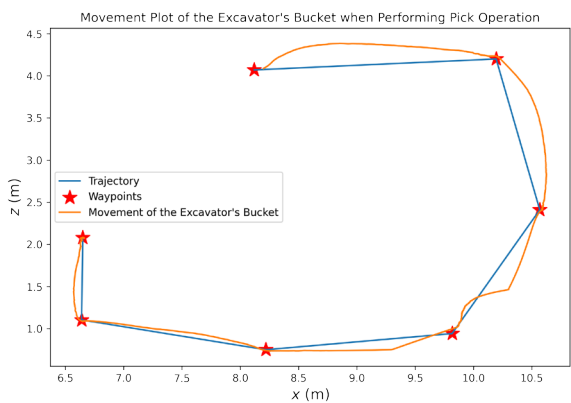


Fig. 5. Bucket's position tracking when performing pick operation.

[6] Y. Ye, C.-B. Yin, Y. Gong, and J. jing Zhou, "Position control of nonlinear hydraulic system using an improved pso based pid controller," *Mechanical Systems and Signal Processing*, vol. 83, pp. 241–259, 1 2017.

[7] X. Zhang, S. Qiao, L. Quan, and L. Ge, "Velocity and position hybrid control for excavator boom based on independent metering system," *IEEE Access*, vol. 7, pp. 71 999–72 011, 2019.

[8] D. Jud, P. Leemann, S. Kerscher, and M. Hutter, "Autonomous free-form trenching using a walking excavator," *IEEE Robotics and Automation Letters*, vol. 4, pp. 3208–3215, 10 2019.

[9] B. Lee and H. Kim, "Trajectory generation for an automated excavator," *2014 14th International Conference on Control, Automation and Systems (ICCAS 2014)*, pp. 716–719, 10 2014.

[10] P. Agarwal, M. Teichmann, S. Andrews, and S. E. Kahou, "Automatic evaluation of excavator operators using learned reward functions," 2022. [Online]. Available: <https://arxiv.org/abs/2211.07941>

[11] P. Egli and M. Hutter, "Towards rl-based hydraulic excavator automation," *2020 IEEE/RSJ International Conference on Intelligent Robots and Systems (IROS)*, pp. 2692–2697, 10 2020.

[12] —, "A general approach for the automation of hydraulic excavator arms using reinforcement learning," *IEEE Robotics and Automation Letters*, vol. 7, pp. 5679–5686, 4 2022.

[13] P. Egli, D. Gaschen, S. Kerscher, D. Jud, and M. Hutter, "Soil-adaptive excavation using reinforcement learning," *IEEE Robotics and Automation Letters*, vol. 7, pp. 9778–9785, 10 2022.

[14] T. H. Noventino, M. R. Rosa, and A. Z. Fuadi, "Pid control design and kinematic modelling of 3-dof robot manipulator," in *2022 International Conference on Electrical Engineering, Computer and Information Technology (ICEECIT)*, 2022, pp. 88–94.

[15] J. Schulman, F. Wolski, P. Dhariwal, A. Radford, and O. Klimov, "Proximal policy optimization algorithms," 2017. [Online]. Available: <https://arxiv.org/abs/1707.06347>

[16] T. Tiong, I. Saad, K. T. K. Teo, and H. B. Lago, "Autonomous valet parking with asynchronous advantage actor-critic proximal policy optimization," in *2022 IEEE 12th Annual Computing and Communication Workshop and Conference (CCWC)*. IEEE, Jan. 2022. [Online]. Available: <https://doi.org/10.1109/ccwc54503.2022.9720881>

[17] T. Nguyen, "Generalized advantage estimate: Maths and code," *Towards Data Science*, 2018. [Online]. Available: <https://towardsdatascience.com/generalized-advantage-estimate-maths-and-code-b5d5bd3ce737>

[18] E. Coumans and Y. Bai, "Pybullet, a python module for physics simulation for games, robotics and machine learning," <http://pybullet.org>, 2016–2019.

[19] G. Brockman, V. Cheung, L. Pettersson, J. Schneider, J. Schulman, J. Tang, and W. Zaremba, "Openai gym," 2016. [Online]. Available: <https://arxiv.org/abs/1606.01540>

[20] A. Raffin, A. Hill, A. Gleave, A. Kanervisto, M. Ernestus, and N. Dormann, "Stable-baselines3: Reliable reinforcement learning implementations," *Journal of Machine Learning Research*, vol. 22, no. 268, pp. 1–8, 2021. [Online]. Available: <http://jmlr.org/papers/v22/20-1364.html>

Mecanum-Wheeled Robot Control based on Deep Reinforcement Learning

1st Ocklen Setiadilaga

*Dept. of Electrical and Information Engineering
Universitas Gadjah Mada
Yogyakarta, Indonesia
ocklen15@mail.ugm.ac.id*

2nd Adha Cahyadi

*Dept. of Electrical and Information Engineering
Universitas Gadjah Mada
Yogyakarta, Indonesia
adha.imam@ugm.ac.id*

3rd Ahmad Ataka

*Dept. of Electrical and Information Engineering
Universitas Gadjah Mada
Yogyakarta, Indonesia
ahmad.ataka.ar@ugm.ac.id*

Abstract—The use of mecanum wheels for mobile robots has led to more flexibility in terms of the robots' navigation ability. This usage, however, leads to a more complex control system which mainly relies on a complete knowledge of the robot's kinematic model. This research aims to show that reinforcement learning can help develop control systems for robots with mecanum wheels. Since reinforcement learning does not require the robot's model explicitly to generate the control action, it can deal with the uncertainty and nonlinearity of the robot model by learning the action directly from interaction with the environment. In the paper, we proposed a novel reward function specifically designed for mecanum-wheeled robot control. The reward function is used to train the reinforcement learning algorithm to produce control signal for mecanum-wheeled robot. The results demonstrate the promising capability of reinforcement learning in controlling mecanum-wheeled robot towards a target location while maintaining its orientation.

Index Terms—Reinforcement Learning, Mecanum-wheeled Robot, Robot Control, Robot Navigation

I. INTRODUCTION

In recent years, robots have been widely used in various industrial sectors [1]. This is mainly caused by the fact that robots have excellent performance and reliability on repetitive and heavy tasks such as moving heavy objects from one place to another. Mobile robots are suitable for this kind of tasks and are now being used in industrial warehouses [2]. Most warehouses have very limited space for robots to move around and maneuver, so the robots must have exceptional maneuverability. This can be achieved by employing mecanum wheels for mobile robots such that they will have an omnidirectional capability to move freely in 2-dimensional space [3].

However, this types of wheel presents more challenges when installed on autonomous mobile robots compared to conventional wheels. Mecanum wheels rely on the direction and magnitude of the frictional forces between the rubber tires and the ground surface. It is possible that there is an inconsistency in the direction and magnitude of the frictional forces generated by the wheels. In that case, the movement of the vehicle

This research is funded by RTA Program Universitas Gadjah Mada with the Grant Number 5075/UN1.P.II/Dit-Lit/PT.01.01/2023.

or robot becomes less predictable. Therefore, more advanced control technique is required to ensure that the robot can still perform the desired movement.

One of the works proposing a control method for mecanum-wheeled robot was reported in [4]. They proposed a non-linear adaptive control based on back-stepping to produce robot's movement. However, they relied on the complete knowledge of kinematics and dynamics model of the robot. Another prior work combined a neural network and proportional-derivative (PD) control [5]. The neural network here was used to compensate the non-linearity of the robot's model. While it has been shown that the addition of neural network improves the performance of the trajectory controller, the reliance on the PD controller still requires manual parameter's tuning in addition to the tuning of the network's hyperparameter in learning process. It is not clear what is the best way to choose these two types of parameters.

One class of machine learning which can be applied directly to control problem is reinforcement learning. In recent years, deep reinforcement learning, which combines deep neural network and reinforcement learning framework, has been shown to perform successfully in various problems, such as Atari games [6], [7], chess, Go, as well as Dota2 [8]- [9]. Unlike conventional neural network which maps a particular input to an output, deep reinforcement learning produces an action (i.e. control signal) from an observation (derived from sensor data) and a reward function. This has led to its usage in robotics, such as legged robot control [10], driverless car [11], industrial manipulator control [12], mobile robot navigation [13], and growing robot navigation [14].

In this paper, we propose a control system based on deep reinforcement learning (RL) to control mecanum-wheeled mobile robot. The reinforcement learning is able to produce control action without relying on the knowledge regarding the physical parameter of the mecanum robot. Rather, it learns by performing trial and error from a novel reward function that we developed specifically for mecanum-wheeled robots. To the best of our knowledge, this is the first attempt on using

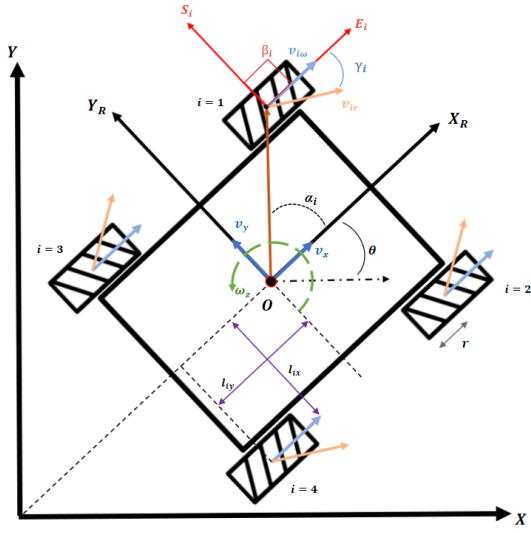


Fig. 1: Diagram of a mobile robot with 4 mecanum wheels.

deep reinforcement learning for controlling mobile robots with mecanum wheels.

II. MECANUM-WHEELED MOBILE ROBOT

Mecanum Robot is a type of wheeled robot employing a special type of wheels called mecanum wheels. Mecanum wheels are designed to move omnidirectionally, employing a set of freely-rotating rollers directed at an angle of 45° with respect to the wheels' main direction. These rollers produce another velocity component which enables the wheel to move in a certain direction with respect to the wheel's main direction. This is illustrated in Fig. 1. Employing at least 3 mecanum wheels enables the mobile robot to freely move in any direction. In this paper, however, we focus on a mobile robot with 4 mecanum wheels as depicted in Fig. 1.

The list of parameters in Fig. 1 is described as follows:

- X and Y specify the world frame,
- $X_R O Y_R$ is the frame attached to the center of the robot,
- v_{iw} , $i=1,2,3,4$ is the speed of the wheel in its main direction,
- v_{ir} is the speed of the passive rollers on wheel- i directed at an angle of 45° with respect to the direction of v_{iw} ,
- ω_i is the rotation speed of wheel i ,
- v_x and v_y is the robot's linear speed,
- ω_z is the robot's angular speed,
- l_x is half the distance between 2 front wheels while l_y is half the distance between the front and the back wheels,
- r is the wheels' radius while θ is the robot's orientation with respect to the world frame.

From geometry and the mechanical properties of the robot, the forward kinematics can be described as follows [15]:

$$\begin{bmatrix} v_x \\ v_y \\ v_z \end{bmatrix} = \frac{r}{4} \begin{bmatrix} 1 & 1 & 1 & 1 \\ -1 & 1 & 1 & -1 \\ -\frac{1}{(l_x+l_y)} & \frac{1}{(l_x+l_y)} & -\frac{1}{(l_x+l_y)} & \frac{1}{(l_x+l_y)} \end{bmatrix} \begin{bmatrix} \omega_1 \\ \omega_2 \\ \omega_3 \\ \omega_4 \end{bmatrix} \quad (1)$$

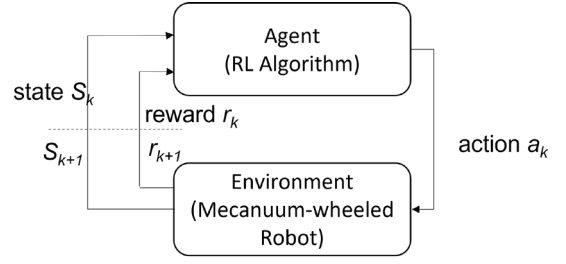


Fig. 2: Reinforcement learning for Mecanum robot control.

III. REINFORCEMENT-LEARNING-BASED CONTROL

A. Mecanum Robot Reward Function

Reinforcement Learning (RL) is a type of machine learning which trains an agent to perform a task in an environment via trial and error [16]. By performing an action to an environment, the agent receives a reward and an observation describing the state of an environment. By learning which action produces the most cumulative reward, the agent can then produce the most optimal action in a particular state of an environment. This is called a policy, $\pi(a|s)$, describing how probable an action a is performed on a particular state s . The illustration on how the RL works is shown in Fig. 2.

One of the most crucial parts of RL is the reward function which describes how good an action produced by an agent on a particular state. This function guides the learning process because it implicitly reflects the desired behavior that the agent needs to learn. However, this function is not readily available for various robotic tasks, including mecanum-wheeled mobile robot. Here, we proposed a reward function which can be a good candidate for mecanum-wheeled robot control.

The goal of the mecanum-wheeled robot control is to guide the robot from an arbitrary position towards a target location. In doing so, to maximize the robot's capability to move omnidirectionally, the robot is expected to move without modifying its orientation. This is a property unique to the mecanum-wheeled robot and the corresponding reward function needs to optimize this capability. Therefore, the reward function should consist of two components: the first focusing on the distance towards a target while the second one focusing on penalizing orientation error. The proposed reward, called Orientational Gain Reward Function (OGRF) is explained in Algorithm 1.

The first condition in the reward function calculation is to check whether the robot is still inside a boundary radius r and whether the orientation error does not exceed a certain limit c_θ . These two conditions are used to ensure that a penalty is given when the robot moves far more than a certain boundary or if the orientation moves far beyond the target. Here, we use a normalized orientation error described as:

$$\bar{e}_\theta = |(e_\theta \times (180/\pi))/180|, \quad (2)$$

e_θ refers to the real value of orientation such that \bar{e}_θ has a range of values between 0 and 1.

If the condition is satisfied, the reward is in the form of two position error terms, denoted as $R1$ and $R2$, multiplied by $(1 - \bar{e}_\theta)$. The term $R1$ and $R2$ will both be maximum when

the robot reaches the target. Similarly, the term $(1 - \bar{e}_\theta)$ will be maximum when the robot stays at a target orientation (i.e. $e_\theta \simeq 0$). If the condition is not satisfied, the episode is set to be done and the reward is given in the form of negative number of steps left in the episode. The earlier the condition is violated, the more negative the reward will be.

The proposed reward function we use here is a positive reward. This type of reward is chosen because providing a negative reward can lead the agent to end the episode as quickly as possible by taking actions that violate the given constraints. In that case, the agent will end up receiving a sub-optimal reward, and hence, it will fail to properly learn the required task [17].

Algorithm 1 Orientational Gain Reward Function

Input:

$max\ coordinate$ = maximum coordinate
 (x_s, y_s) = start point coordinate
 (x_t, y_t) = target point coordinate
 (x, y) = instantaneous robot's coordinate
 \bar{e}_θ = normalized orientation error
 r = environment boundary radius
 $step$ = number of performed steps
 c_θ = the orientation error constraint

Output:

T = A Boolean indicating whether an episode is finished

R_T = total reward obtain by the agent

$T = \text{False}$

$radius = x^2 + y^2$

$R1 = |x_s - x_t| - |x - x_t|$

$R2 = |y_s - y_t| - |y - y_t|$

if $radius < r^2$ **and** $\bar{e}_\theta < c_\theta$ **then**

$R_T = (R1 + R2) \times (1 - \bar{e}_\theta)$

else

$T = \text{True}$

$steps\ left = 10000 - step$

$R_T = -steps\ left$

end if

B. Reinforcement Learning Algorithm

In trying to learn the best policy, one approach is to estimate a state-action-value function $Q(S_t, A_t)$ describing how good an action A_t in a particular state S_t at time t is. It is defined as:

$$Q(s, a) = E_\pi[G_t | S_t, A_t], \quad (3)$$

where return G_t is defined as:

$$G_t = R_{t+1} + \gamma R_{t+2} + \dots = \sum_{k=0}^{\infty} \gamma^k R_{t+k+1}. \quad (4)$$

Here, R_t is defined as the reward at time t while γ is the discount factor.

One popular approach in estimating the state-action-value function is the Deep Q Network (DQN) [7] which employs Bellman equation to update the estimated value as follows:

$$Q_{i+1}(s, a) = Q^*(s, a) = E[r + \gamma \max_{a'} Q_i(s', a')], \quad (5)$$

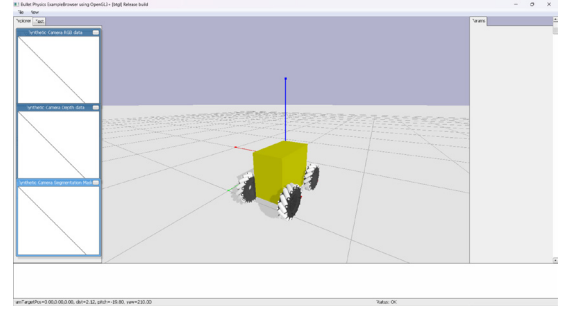


Fig. 3: Mecanum robot simulation in PyBullet.

| Parameter | Value |
|-------------------|--------------------------------|
| Robot body mass | 100 kg |
| Robot body size | $0.35 \times 0.2 \times 0.3$ m |
| Wheels' mass | 2 kg / wheel |
| Wheels' dimension | $r = 0.1$ m, $w = 0.045$ m |

TABLE I: Robot's characteristics

where s , and s' refer to the current and next state, a , and a' refer to the current and next action, while r refers to the current reward. DQN employs a neural network with weight θ as a Q-value estimator, $Q(s, a; \theta) \approx Q^*(s, a)$. To update the network, a replay buffer is used to store the experience on a certain duration. A random sampling from the buffer is then used to update the network based on the following loss function:

$$L_i(\theta_i) = E_{(s, a, r, s') \sim U(D)} [(r + \gamma \max_{a'} Q(s', a'; \theta_i^-) - Q(s, a; \theta_i))^2]. \quad (6)$$

Here, $r + \gamma \max_{a'} Q(s', a'; \theta_i^-)$ is the target value at iteration i , θ_i^- is the target network parameter at iteration i , while θ_i is the Q-network parameter at iteration i . Tuple (s, a, r, s') refers to a sample containing the current state, action, reward, and next state from the experience replay D .

In this paper, we employed a modification of DQN, called Quantile Regression DQN (QR-DQN) [18]. The QR-DQN employs value distribution of return, instead of expected value of return like conventional DQN. RL that focuses on value distribution has several advantages: it reduces chattering effect, reduces the effect of state aliasing, and enriches the information used in making predictions.

IV. SIMULATION RESULTS

A. Research Methods

The proposed method will be evaluated in a simulation scenario using PyBullet physics simulation [19]. The model of mecanum-wheeled robot is imported to the simulation using a format provided by OpenAI Gym, a standard API for reinforcement learning [20]. To implement the reinforcement learning algorithm, we employ Stable-Baselines3 library [21]. Finally, Tensorboard is employed to analyze the learning process [22]. An example of the simulation showing the robot is shown in Fig. 3. The specifications of the 4-wheeled mecanum robot that will be used in the environment and the entire experimental setup are given in Table I. The hyperparameters of the QR-DQN algorithm used in the experiment are shown in Table II.

| QR-DQN Algorithm | |
|------------------------------|--------------------|
| Hyperparameter | Value |
| n -quantile | 110 |
| Learning rate | 5×10^{-5} |
| learning starts | 2×10^5 |
| Buffer size | 6×10^6 |
| Batch Size | 512 |
| Training frequency | 4 |
| Target update interval | 1000 |
| Discount factor (γ) | 0.99 |
| Exploration fraction | 0.26 |
| Exploration initial epsilon | 1.0 |
| Exploration final epsilon | 0.05 |

TABLE II: Hyperparameters of the QR-DQN

| Parameter | Value | Description |
|-------------------|------------------|--|
| Episode's length | 10000 | step |
| Learning's length | 15×10^6 | step |
| action space | 19 | discrete |
| observation space | 11 | $(x, y), (v_x, v_y), \omega_z, (x_t, y_t)$ $e_x, e_y, E_{dist}, e_\theta$ |

TABLE III: Parameters of environment

We choose 19 types of discrete action which represents different variation of robot's movement as described in Table IV. Here, RF, LF, RR, and LR refer to right front, left front, right rear, and left rear wheels while CCW and CW refer to counter clock-wise and clock-wise respectively. As we can see, the choice of action space ensures that all different types of movement are considered, including static, movement in a particular axis, movement in a particular quadrant, and pure rotation. Therefore, it covers all positive and negative axis as well as all 4 quadrants.

The observation space used as a state information of the robot consists of the robot's location (x and y), the robot's velocity (v_x and v_y), the robot's angular speed ω_z , the target location (x_t and y_t), the position error (e_x and e_y), the Euclidean distance between the robot and the target E_{dist} , and the orientation error e_θ . The environment parameter used in this experiment can be seen in Table III.

To ensure that the robot can learn to move towards an arbitrary target, the following steps were performed:

- 1) Create a list of starting and target point coordinates obtained by running a uniform distributed number generating function which will sample N values within the range of -1 to 1. This function will generate numbers that will later enter two arrays.
- 2) The arrays' members with the same index value will become pairs of points (x, y) , for example (x_0, y_0) . Thus, N coordinate points will be obtained. When the first episode starts, the starting point coordinate is (x_0, y_0) and the target point coordinate is (x_{N-1}, y_{N-1}) . Then, when entering the second episode, the starting point coordinate is (x_1, y_1) and the target point coordinate is (x_{N-2}, y_{N-2}) , and so on. The cycle will be repeated after N episodes.
- 3) These pairs of points are then given to the agent to learn how to complete one task in one episode while obtaining the maximum possible reward.

| Action | | | | Movement | Speed |
|--------|------|------|------|--------------|-------|
| RF | LF | RR | LR | | |
| 0 | 0 | 0 | 0 | static | - |
| 1 | 0 | 0 | 1 | quadrant 2 | high |
| 1 | -1 | -1 | 1 | x negative | high |
| 0 | -1 | -1 | 0 | quadrant 3 | high |
| -1 | -1 | -1 | -1 | y negative | high |
| -1 | 0 | 0 | -1 | quadrant 4 | high |
| -1 | 1 | 1 | -1 | x positive | high |
| 0 | 1 | 1 | 0 | quadrant 1 | high |
| 1 | 1 | 1 | 1 | y positive | high |
| 0.5 | 0 | 0 | 0.5 | quadrant 2 | low |
| 0.5 | -0.5 | -0.5 | 0.5 | x negative | low |
| 0 | -0.5 | -0.5 | 0 | quadrant 3 | low |
| -0.5 | -0.5 | -0.5 | -0.5 | y negative | low |
| -0.5 | 0 | 0 | -0.5 | quadrant 4 | low |
| -0.5 | 0.5 | 0.5 | -0.5 | x positive | low |
| 0 | 0.5 | 0.5 | 0 | quadrant 1 | low |
| 0.5 | 0.5 | 0.5 | 0.5 | x positive | low |
| -1 | 1 | -1 | 1 | CCW rotation | high |
| 1 | -1 | 1 | -1 | CW rotation | high |

TABLE IV: The list of discrete actions

Finally, we choose two types of orientation error constraints in the experiment: one value corresponds to a loose constraint ($c_\theta = 0.4$) while the other one represents a strict constraint ($c_\theta = 0.2$). For the loose constraint case, the agent is allowed to continue learning for higher orientation error compared to the strict constraint case.

B. Results and Discussion

The desired task is for the mecanum robot to move from one point to another while minimizing orientation error. In every cycle, the robot will start from a starting point and move towards a target point. When the agent arrives at the target point, it must ensure that the mecanum robot remains stationary at that point for a certain time before moving on to the next target point.

The results of training data is shown in Fig. 4, with two data sets from two RL learning processes. The data labeled as "loose" (orange line) indicates the RL process with loose constraints, while the other data (blue lines) comes from the RL process with strict constraints. Here, we show the episode's length (Fig. 4a), the reward (Fig. 4b), and the training loss (Fig. 4c)

From the Tensorboard data, it can be seen that the agent with loose constraints was able to achieve the maximum episode length and the maximum average reward value in a single episode higher than the one using strict constraint. The maximum reward average can be obtained by dividing the maximum reward value in Fig. 4b by the maximum episode length in Fig. 4a, which then yields a value of 5.456. The maximum reward value that can be obtained theoretically is 6 points, which means that the reward achieved by the agent is around 90.9% of the maximum reward value. This indicates that the agent successfully learn the task because it manages to gather an almost-optimal reward. Apart from the episode length and reward, we can also observe that the learning loss for the case with loose constraint decreases faster than the strict constraint as shown in Fig. 4c.

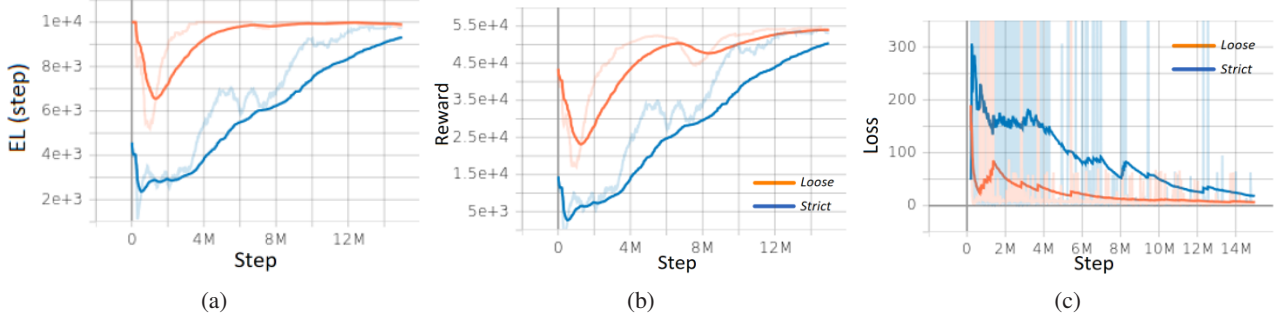


Fig. 4: Tensorboard data of experiments showing (a) episode's length, (b) reward, and (d) loss

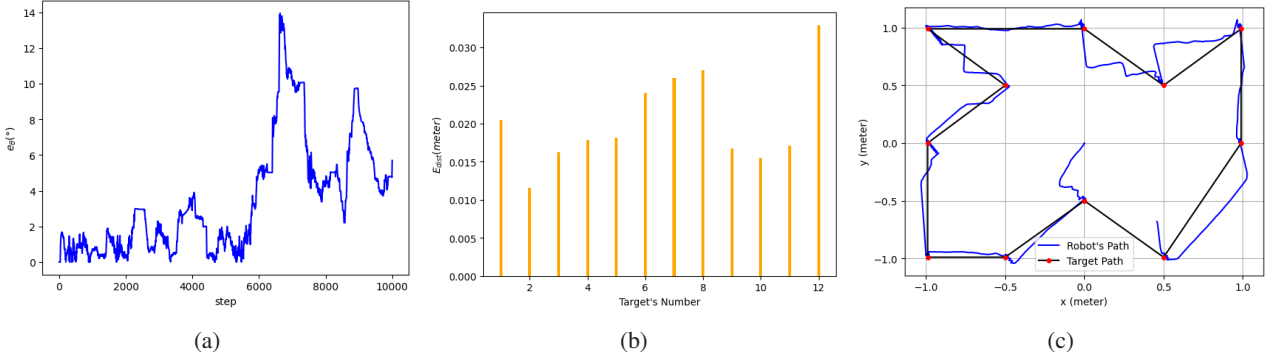


Fig. 5: Simulation data for the case of loose constraints: (a) orientation error, (b) Euclidean distance, (c) path taken by the robot.

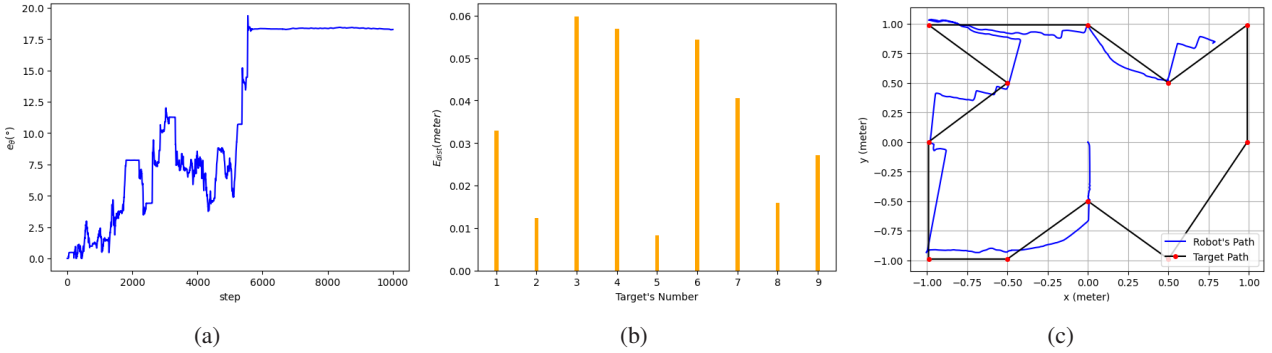


Fig. 6: Simulation data for the case of strict constraints: (a) orientation error, (b) Euclidean distance, (c) path taken by the robot

To see how the algorithm performs in the mecanum robot, we present the implementation data in Fig. 5 for the case with loose constraint and Fig. 6 for the case with strict constraint. We show the orientation error, Euclidean distance between the robot's final position and the target, as well as the path taken by the robot (blue lines) from one target to another (red dot). We can see that in both cases, the robot is able to move from one target to another. However, the case with loose constraint produces better orientation error and better average Euclidean distance error. We can also observe that the case with strict constraint fails to reach target points in the last part of the movement when the orientation error is too large. This is the case because the use of strict constraint limits the agent's learning experience compared to the case of loose constraint. From the experiments conducted, it can be concluded that the RL with the proposed reward have successfully performed the assigned task to guide

the movement of mobile robots with four mecanum wheels.

V. CONCLUSION

In this paper, we propose a control of mobile robots with four mecanum wheels based on deep reinforcement learning. We design a reward function specifically for mecanum robots. The results show that reinforcement learning with a proper reward function has successfully controlled the movement of mecanum robot from one point to arbitrary target point. This can be achieved with very small orientation error, hence, maximizing the capability of the mecanum wheels in moving freely without modifying its orientation. Furthermore, using reinforcement learning simplifies the mathematical calculations in modeling mecanum robot systems, including the uncertainty and nonlinearity that inevitably occurs in mecanum robots.

Future works can explore further applications of this method to a more challenging navigation task using mecatron robots.

REFERENCES

- [1] V. Villani, F. Pini, F. Leali, and C. Secchi, "Survey on human–robot collaboration in industrial settings: Safety, intuitive interfaces and applications," *Mechatronics*, vol. 55, pp. 248–266, 2018. [Online]. Available: <https://www.sciencedirect.com/science/article/pii/S0957415818300321>
- [2] L. Custodio and R. Machado, "Flexible automated warehouse: a literature review and an innovative framework," *The International Journal of Advanced Manufacturing Technology*, vol. 106, pp. 533–558, 2020.
- [3] K. Shabalina, A. Sagitov, and E. Magid, "Comparative analysis of mobile robot wheels design," in *2018 11th International Conference on Developments in Systems Engineering (dese)*. IEEE, 2018, pp. 175–179.
- [4] L.-C. Lin and H.-Y. Shih, "Modeling and adaptive control of an omni-mecanum-wheeled robot," *Intelligent Control and Automation*, vol. 04, no. 02, pp. 166–179, 2013. [Online]. Available: <https://doi.org/10.4236/ica.2013.42021>
- [5] M. Szeremeta and M. Szuster, "Neural tracking control of a four-wheeled mobile robot with mecatron wheels," *Applied Sciences*, vol. 12, no. 11, p. 5322, May 2022. [Online]. Available: <https://doi.org/10.3390/app12115322>
- [6] V. Mnih, K. Kavukcuoglu, D. Silver, A. Graves, I. Antonoglou, D. Wierstra, and M. A. Riedmiller, "Playing Atari with Deep Reinforcement Learning," *CoRR*, vol. abs/1312.5602, 2013, arXiv: 1312.5602. [Online]. Available: <http://arxiv.org/abs/1312.5602>
- [7] V. Mnih, K. Kavukcuoglu, D. Silver, A. A. Rusu, J. Veness, M. G. Bellemare, A. Graves, M. Riedmiller, A. K. Fidjeland, G. Ostrovski, S. Petersen, C. Beattie, A. Sadik, I. Antonoglou, H. King, D. Kumaran, D. Wierstra, S. Legg, and D. Hassabis, "Human-level control through deep reinforcement learning," *Nature*, vol. 518, no. 7540, pp. 529–533, Feb. 2015, place: England.
- [8] D. Silver, T. Hubert, J. Schrittwieser, I. Antonoglou, M. Lai, A. Guez, M. Lanctot, L. Sifre, D. Kumaran, T. Graepel, T. Lillicrap, K. Simonyan, and D. Hassabis, "A general reinforcement learning algorithm that masters chess, shogi, and Go through self-play," *Science (New York, N.Y.)*, vol. 362, no. 6419, pp. 1140–1144, Dec. 2018, place: United States.
- [9] C. Berner, G. Brockman, B. Chan, V. Cheung, P. Debiak, C. Dennison, D. Farhi, Q. Fischer, S. Hashme, C. Hesse, R. Józefowicz, S. Gray, C. Olsson, J. Pachocki, M. Petrov, H. P. d. O. Pinto, J. Raiman, T. Salimans, J. Schlatter, J. Schneider, S. Sidor, I. Sutskever, J. Tang, F. Wolski, and S. Zhang, "Dota 2 with Large Scale Deep Reinforcement Learning," *CoRR*, vol. abs/1912.06680, 2019, arXiv: 1912.06680. [Online]. Available: <http://arxiv.org/abs/1912.06680>
- [10] V. Tsounis, M. Alge, J. Lee, F. Farshidian, and M. Hutter, "DeepGait: Planning and Control of Quadrupedal Gaits Using Deep Reinforcement Learning," *IEEE Robotics and Automation Letters*, vol. 5, pp. 3699–3706, 2019.
- [11] B. R. Kiran, I. Sobh, V. Talpaert, P. Mannion, A. A. A. Sallab, S. K. Yogamani, and P. Pérez, "Deep Reinforcement Learning for Autonomous Driving: A Survey," *CoRR*, vol. abs/2002.00444, 2020, arXiv: 2002.00444. [Online]. Available: <https://arxiv.org/abs/2002.00444>
- [12] R. Liu, F. Nageotte, P. Zanne, M. d. Mathelin, and B. Dresp-Langley, "Deep Reinforcement Learning for the Control of Robotic Manipulation: A Focussed Mini-Review," *CoRR*, vol. abs/2102.04148, 2021, arXiv: 2102.04148. [Online]. Available: <https://arxiv.org/abs/2102.04148>
- [13] M.-F. R. Lee and S. H. Yusuf, "Mobile Robot Navigation Using Deep Reinforcement Learning," *Processes*, vol. 10, no. 12, 2022. [Online]. Available: <https://www.mdpi.com/2227-9717/10/12/2748>
- [14] A. Ataka and A. P. Sandiwan, "Growing robot navigation based on deep reinforcement learning," in *2023 9th International Conference on Control, Automation and Robotics (ICCAR)*, 2023, pp. 115–120.
- [15] H. Taheri, B. Qiao, and N. Ghaeminezhad, "Kinematic model of a four mecatron wheeled mobile robot," *International Journal of Computer Applications*, vol. 113, pp. 6–9, 03 2015.
- [16] R. S. Sutton and A. G. Barto, *Reinforcement learning: an introduction*, second edition ed., ser. Adaptive computation and machine learning series. Cambridge, Massachusetts: The MIT Press, 2018.
- [17] "Deep reinforcement learning models: Tips & tricks for writing reward functions — by bonsai — medium," <https://medium.com/@BonsaiAI/deep-reinforcement-learning-models-tips-tricks-for-writing-reward-functions-a84fe525e8e0>, Nov 2017, (Accessed on 03/31/2023).
- [18] W. Dabney, M. Rowland, M. G. Bellemare, and R. Munos, "Distributional reinforcement learning with quantile regression," *CoRR*, vol. abs/1710.10044, 2017. [Online]. Available: <http://arxiv.org/abs/1710.10044>
- [19] E. Coumans and Y. Bai, "Pybullet, a python module for physics simulation for games, robotics and machine learning," <http://pybullet.org>, 2016–2019.
- [20] G. Brockman, V. Cheung, L. Pettersson, J. Schneider, J. Schulman, J. Tang, and W. Zaremba, "Openai gym," 2016. [Online]. Available: <https://arxiv.org/abs/1606.01540>
- [21] A. Raffin, A. Hill, A. Gleave, A. Kanervisto, M. Ernestus, and N. Dormann, "Stable-baselines3: Reliable reinforcement learning implementations," *Journal of Machine Learning Research*, vol. 22, no. 268, pp. 1–8, 2021. [Online]. Available: <http://jmlr.org/papers/v22/20-1364.html>
- [22] M. Abadi, A. Agarwal, P. Barham, E. Brevdo, Z. Chen, C. Citro, G. S. Corrado, A. Davis, J. Dean, M. Devin, S. Ghemawat, I. Goodfellow, A. Harp, G. Irving, M. Isard, Y. Jia, R. Jozefowicz, L. Kaiser, M. Kudlur, J. Levenberg, D. Mané, R. Monga, S. Moore, D. Murray, C. Olah, M. Schuster, J. Shlens, B. Steiner, I. Sutskever, K. Talwar, P. Tucker, V. Vanhoucke, V. Vasudevan, F. Viégas, O. Vinyals, P. Warden, M. Wattenberg, M. Wicke, Y. Yu, and X. Zheng, "TensorFlow: Large-scale machine learning on heterogeneous systems," 2015, software available from tensorflow.org. [Online]. Available: <https://www.tensorflow.org/>

Vision-based Excavator Control for Pick-and-Place Operation*

| | | | |
|--|---|---|--|
| 1 st Ahmad Ataka <i>Dept. of Electrical and Information Engineering</i> <i>Universitas Gadjah Mada</i> Yogyakarta, Indonesia ahmad.ataka.ar@ugm.ac.id | 2 nd M Hilal Bayu Aji <i>ABAROBOTICS</i> Semarang, Indonesia hilal@abarobotics.com | 3 rd Alfin Luqmanul Hakim <i>ABAROBOTICS</i> Semarang, Indonesia alfin@abarobotics.com | 4 th Dimas Arfiantino <i>ABAROBOTICS</i> Semarang, Indonesia dimas@abarobotics.com |
| 5 th Aan Aria Nanda <i>ABAROBOTICS</i> Semarang, Indonesia aan@abarobotics.com | 6 th Ghanis Kauchya Nugraha <i>ABAROBOTICS</i> Semarang, Indonesia ghanis@abarobotics.com | 7 th Ahmad Didik Setyadi <i>ABAROBOTICS</i> Semarang, Indonesia didik@abarobotics.com | 8 th Alharisy Aji <i>ABAROBOTICS</i> Semarang, Indonesia aji@abarobotics.com |
| 9 th Gregorio Ageng <i>ABAROBOTICS</i> Semarang, Indonesia gregorio@abarobotics.com | 10 th Rizky Candra <i>ABAROBOTICS</i> Semarang, Indonesia rizky@abarobotics.com | 11 th Cendikia Ishmatuka <i>Dept. of Electrical and Information Engineering</i> <i>Universitas Gadjah Mada</i> Yogyakarta, Indonesia cendikia.i@mail.ugm.ac.id | 12 th Abdul Barr <i>ABAROBOTICS</i> Semarang, Indonesia abdulbarr@abarobotics.com |

Abstract—Automating an excavator in construction tasks proves to be challenging. While conventional kinematics control can be employed to produce motion, the challenge lies in the perception task: how to distinguish and detect various objects in construction sites. These include construction objects (rocks, sands, etc) as well as vehicles for object storage. This paper proposed vision-based excavator control combining deep learning and inverse kinematics to perform pick-and-place operation. The perception side is handled by a convolution neural network to detect target object and vehicle for object storage. Combined with depth information, the location of the objects are determined. This information will be sent to the control side to calculate the target joints of the excavator using inverse kinematics. Finally, joint velocity control is employed to ensure the excavator's joints reach the target. The results confirm that the proposed control successfully performs autonomous pick and place in simulated environment.

Index Terms—Visual-Based Control, Excavator Control, Pick-and-Place, Inverse Kinematics, Deep Learning

I. INTRODUCTION

Heavy machines such as excavator have been widely used in various fields such as construction, agriculture, and mining [1], [2]. Due to their flexibility, excavators have been used for complex tasks such as digging, picking and placing objects, and soil trenching. These tasks are normally handled by human operators and suffers from low efficiency as well as high labor intensity [3]. The reliance on human operators also limits the usage of excavators in hazardous situations such as toxic chemical mines and open pit [1].

This research is partially-funded by ABAROBOTICS, a robotics, automation, and artificial intelligence company in Semarang, Central Java, Indonesia, and Department of Electrical and Information Engineering, Universitas Gadjah Mada, Indonesia.

Despite the rise of automation in various different fields, automating excavator proves to be a challenging problem. While conventional kinematics control can be employed to produce motion, the challenge lies in the perception task: how to distinguish and detect various objects in construction sites [1]. Examples of these objects include construction objects (rocks, sands, etc) as well as vehicles for object storage. Since the perception result is used in the control loop, it is necessary to perform perception task as quickly and accurate as possible.

Some of the works proposing an autonomous excavator used the PID (Proportional-Integral-Derivative) control combined with optimization technique such as Improved Generation Algorithm [4] and Particle Swarm Optimization [5]. Another line of works proposed a hybrid control between the velocity and position control depending on the value of error [6] and depending on the types of tasks [7]. However, all of these works focus more on trajectory control without perception module, so they cannot be directly implemented to perform a specific excavation task such as picking-and-placing due to the lack of perception capability. Another work proposed joint-level trajectory generation based on Virtual Motion Camouflage (VMC) for obstacle avoidance and digging task [8]. However, it suffers from the same problem as the previously-mentioned works.

Another line of work tried to use reinforcement learning, a class of machine learning which learns through an interaction with environment, to control excavator without kinematics and dynamics model of the system. Examples include Agarwal et al. [9], Egli et al [10], [11], [12], and Lu et al. [2]. One of the works employed a feedback system derived from trajectory of the expert operators as a reward for the reinforcement learning



Fig. 1: ASTA Autonomous Excavator by ABAROBOTICS used in this research.

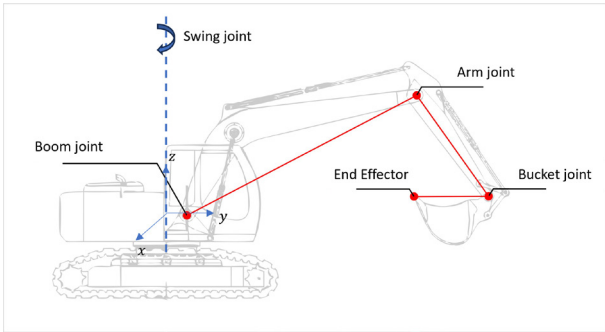


Fig. 2: Joint Diagram of Excavator.

[9]. A deep network model used to perform features analysis is used to train the reinforcement learning to perform trajectory tracking [2]. Trajectory tracking control in the excavator's task space was also developed in [10], [11], [12]. However, while reinforcement learning is useful in certain tasks, conventional control is still superior in producing motion consistently, especially if the kinematics is available. Another recent work which employed imitation learning to learn the policy from expert demonstration [13] suffers from the same problem.

In this paper, we propose vision-based excavator control combining deep learning and inverse kinematics control to perform pick-and-place operation. The main contribution is combining visual and depth-based perception module (using deep learning and depth information) and kinematic control to control the excavator. The perception side is handled by a convolution neural network to detect target object and vehicle for object storage. Combined with depth information, the location of the objects are determined. This information will be sent to the control side to calculate the target joints of the excavator using inverse kinematics. Finally, joint velocity control is employed to ensure the excavator's joints reach the target.

II. EXCAVATOR MODEL

The excavator used in the paper is based on ASTA Excavator, an autonomous excavator product by ABAROBOTICS, as shown in Fig. 1. An excavator consists of four joints as shown in Fig. 2: swing joint relative to z axis, the boom, arm, and

bucket joint relative to the x axis. ASTA Excavator consists of sensors, actuators, and controller systems embedded in an existing conventional excavator. For pose detection, it consists of encoders to detect the joint angle, especially the boom, arm, and bucket joints. To detect the swing joint, it uses Inertial Measurement Unit (IMU) sensors. To actuate the excavator, it employs servo system to move the joystick controller of the excavator as well as two pedals in the cabin room which are connected to the excavator's hydraulic system. Along with microcontrollers processing each sensors and actuator systems, ASTA is also equipped with an on-board computer as its main processing unit.

To model the excavator, in this research we employ a kinematic model. Forward kinematics is used to map the joint space of the excavator Θ to the task space position and orientation of the end-effector $p_{ee} \in SE(3)$. Here:

$$\Theta = [\theta_0 \ \theta_1 \ \theta_2 \ \theta_3]^T, \quad (1)$$

where $\theta_0, \theta_1, \theta_2$, and θ_3 stand for swing, boom, arm, and bucket joints respectively. Knowing the dimension and the position of each link with respect to the previous connected link, we can know the forward kinematics function as follows:

$$p_{ee} = f(\Theta). \quad (2)$$

However, in practice, we will always control the swing and the rest of the joints separately. So, it is better to introduce a new forward kinematics describing the pose of the end-effector in a plane in which the excavator's arm is located, called a *working plane*. In a way, we only control the position of the end-effector in this 2-dimensional working plane along with the bucket orientation, all denoted as $p_{ee,2D}$. This pose will only be affected by boom, arm, and bucket joints. So, the forward kinematics is described as:

$$p_{ee,2D} = f_{2D}(\theta_1, \theta_2, \theta_3). \quad (3)$$

Knowing this function enables us to perform inverse kinematics function numerically to map the pose of the end-effector in the working plane to the set of joints of the excavator:

$$(\theta_1, \theta_2, \theta_3) = f_{2D}^{-1}(p_{ee,2D}). \quad (4)$$

III. PROPOSED EXCAVATOR CONTROL

A. Control Architecture

The full control architecture is provided in Fig 3. The architecture contains two main components, namely the perception module and the control module. Both will be explained further in the following texts.

1) *Perception Module*: The perception module is used to perceive the environment. The main function of this module is to detect different types of objects and its location with respect to the excavator. The module consists of 6 RGB cameras distributed at several points on the excavator to ensure 360° view as well as 2 depth sensors at the front part of the excavator's cabin.

The data from the RGB cameras is fed to a convolutional neural net based on YoLo v8 architecture [14]. The network will be trained to differentiate several objects such as objects to be

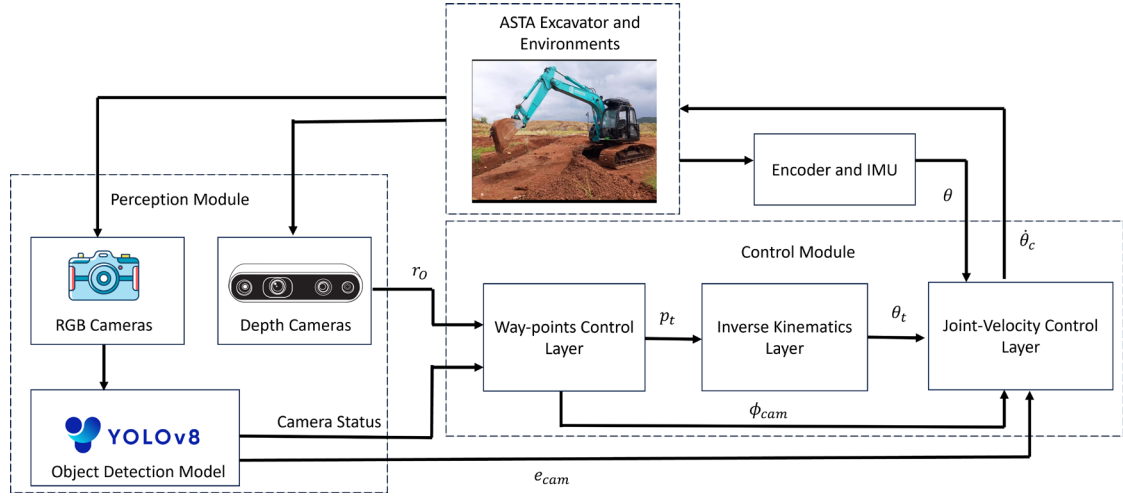


Fig. 3: Vision-Based Control Architecture.

picked and vehicles for object transport. Upon detection, this part of the perception module will inform the control module regarding which camera detects the object in question. This will be required to decide whether the excavator requires swing rotation in order for the bucket to be directed towards the target object direction.

In addition to the RGB cameras, the excavator is also equipped with depth sensors located at the front part of the pilot cabin. The depth sensors are used to estimate the distance of the target object with respect to the excavator r_O . The distance information will be sent to the control module for picking or placing operation.

2) *Control Module*: The second module focuses on producing control signal to the actuators. There are three layers of control in this module:

- 1) *Way-points Control*. This part of control module focuses on producing way-points to be reached by the excavator. The target points can be a 3D coordinate in the task space or the joint coordinate depending on the sub-tasks. For example, for swing motion, this layer will produce a target swing angle to be reached by the joint-velocity control layer based on the orientation of RGB camera ϕ_{cam} which detects the target object. For picking or placing task, this layer will produce a sequence of task-space target positions p_t to be executed by the inverse kinematics layer to ensure smooth movement.
- 2) *Inverse Kinematics*. The inverse kinematics will be used mainly in picking or placing operation. It will not be employed in swing orientation control. This controller receives information from the way-points control layer regarding the target coordinate to be reached p_t and produces target joint angles θ_t . This information will be sent to the joint-velocity control layer.
- 3) *Joint-Velocity Control*. This layer receives target joint angles, either from the way-points control layer in the case of swing motion (i.e. in the form of ϕ_{cam}) or the inverse kinematics layer in the case of picking or placing operation (i.e. in the form of θ_t). It employs proportional

controller to calculate the joint velocity to move the joint angles towards the required target angles. In doing so, it reads on the current joint angle information θ which is produced by encoder sensors located at each of the excavator's 3 joints (boom, arm, bucket) or the IMU located at swing joint. The control signal in the form of joint velocity is produced as follows:

$$\dot{\theta}_{c,i} = -K_P(\theta_i - \theta_{t,i}), \quad (5)$$

where $i \in (0, 3)$ stands for the index of the joints. In the case of the real robot, the joint velocity signal will be scaled to produce a control signal to move servo motors which are mechanically connected to the mechanical joystick and pedals inside the excavator's cabin.

B. Pick-and-Place Implementation

The previous control architecture is then employed to control excavator autonomously performing pick-and-place operation. The whole pick-and-place operation is splitted into several sub-tasks as follows:

1) *Moving to "Home" location*: The excavator control starts by performing joint-velocity control with the joint target angles are predefined according to the ideal initial pose of the excavator. This is called "Home" location. An example of this pose is shown in Fig 4. Here, we only have joint target angles for boom, arm, and bucket joints, so the "Home" location only corresponds to a pose in a 2-dimensional working plane. In other word, no "Home" target joint angle for swing joint.

2) *Target object detection*: In this sub-task, the RGB cameras are employed to find the target object that will be transported. When a camera detects the target object in its frame, the orientation of the camera ϕ_{cam} is used as a target angle for swing movement.

3) *Coarse swing motion*: After getting the orientation of the camera detecting the target object, the joint-velocity control is activated to guide the swing angle of the excavator towards the target. The other joints stay at the current joint angle.

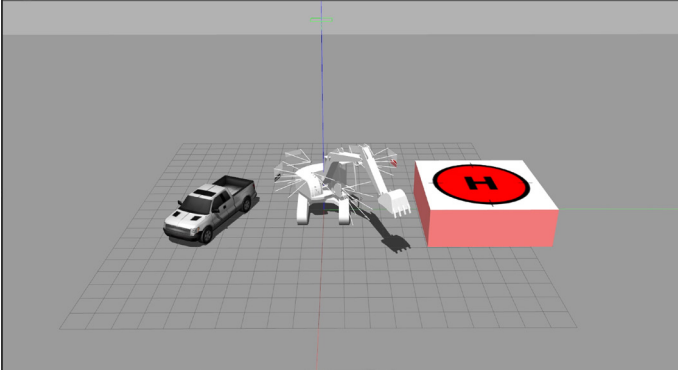


Fig. 4: Gazebo simulator containing ASTA Excavator, vehicle, and target object.

4) *Refined swing motion*: Once the swing angle reaches the target swing orientation ϕ_{cam} , it is expected that the target object is now visible in the front camera. Now, the joint-velocity control is activated again. This time, the orientation error e_{cam} comes from the perception module. The error is calculated from the distance between the object's center location in the camera frame with the center of the frame with respect to the horizontal axis. By the end of the sub-task, the center point of the target object will be located in the center of the frame with respect to the horizontal axis.

5) *Target object position measurement*: .

This is where the depth sensors start working. Since the target object is already located in front of the excavator, the closest object located in front of the depth sensors excluding the excavator's parts is assumed to be the target object. The location of the object with respect to the depth sensor r_O is retrieved. Using the forward kinematics information, we can transform this vector to get the location of the object with respect to the base of the excavator.

6) *Picking task*: To ensure smooth picking or placing movement, the way-points control is performed to generate four intermediate poses based on the target object position. The intermediate poses are derived from real experiments using excavator performing picking and placing task relative to the target object position. From every intermediate pose, the inverse kinematics is employed to calculate the intermediate joint angles $\theta_{t,i}$ for the three joints of the excavator, i.e. $i \in (1, 3)$. This will be sent to the joint velocity control layer to make all joints reach the target angle.

7) *Repeating the previous sub-tasks for detecting vehicle and placing task*: The next sub-tasks are very similar to the previous sub-tasks. The excavator will move back to "Home" location, detecting the target object (in this case the vehicle) from the camera, performing coarse and then refined swing motion, measuring the distance to the target object, and performing the placing task. Finally, the excavator will return back to the "Home" position.

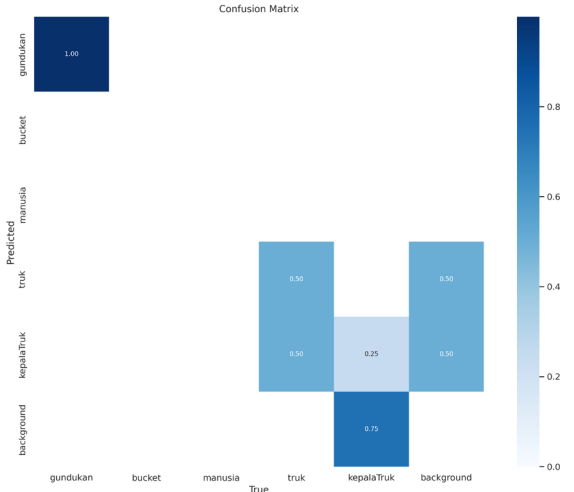


Fig. 5: The confusion matrix of the object detection model.

IV. RESULTS

A. Research Methodology

The first step of this research is the dataset collection for the objects of interest. These include the object that will be transported and the vehicle. The experiment will be performed in Gazebo simulation, so we used images containing objects in Gazebo for training. Due to the limitation in the simulator, we decide not to use the real object to be picked and placed by the excavator, but simply using the object as a marker to be detected.

The next step is labelling the image data. We develop one model containing several labels as follow:

- *gundukan*, referring to the target object to be transported,
- *truk*, referring to the vehicle body,
- *kepalaTruk*, referring to the vehicle head,
- *manusia*, referring to the human,
- *bucket*, referring to the bucket of the excavator.

Two labels are used to detect the vehicle here, namely *truk* for the body and *kepalaTruk* for the head to ensure accurate vehicle detection. Although not directly relevant in simulation, we also add label *manusia* and *bucket* referring to the human and the excavator's bucket to detect these 2 objects in real scenario.

After labelling, we train the neural net based on YoLo v8 architecture. Once it provides satisfying results, we integrate the model with Gazebo simulator and the rest of the control module in Robot Operating System (ROS). To simulate the excavator, we developed a 3D model of excavator based on the real ASTA Excavator using Unified Robotics Description Format (URDF) to be imported in Gazebo simulator. The simulator depicting the excavator, vehicle, and target object is shown in Fig. 4.

B. Results and Discussion

In the first experiment, we focus on the ability of perception module to detect objects. We can see the confusion matrix in Fig. 5. We can see that the target object labelled *gundukan* is successfully detected as such for all trained data. While



Fig. 6: The object detection results depicting detection of vehicle (labelled *truk* and *kepalaTruk*) and the target object (labelled *gundukan*).

there are instances of false negative for the vehicle, most of the images containing real vehicle, both labelled as *truk* and *kepalaTruk*, is correctly predicted as one of the 2 vehicle labels, reaching 62.5% total correct detection. Apart from that, some of the detection results are shown in Fig. 6. We can see that the perception module works well in detecting vehicle (labelled *truk* and *kepalaTruk*) and the target object (labelled *gundukan*).

Once ensuring that the object detection works well, we move on to the next experiment. The whole control architecture, consisting of perception module and control module, is implemented to the Excavator model in Gazebo simulator. We implemented pick-and-place use case as described in Section III-B. The simulation results are shown in Fig. 7. The plot shows the joint angles of excavator during the pick-and-place movement, starting from the swing joint (Fig. 7a), boom joint (Fig. 7b), arm joint (Fig. 7c), and bucket joint (Fig. 7d). To differentiate between sub-tasks, we also show black vertical lines to indicate switching of the sub-tasks.

The excavator starts from the homing pose. The excavator then moves towards the target object detection task. Starting from the first vertical line, the excavator starts performing coarse swing motion to move towards the direction of camera ϕ_{max} which detects the target object. In the second vertical line, the system moves towards refined swing motion to ensure that the target object will be in the middle of the frame. At the end of this period, the depth sensor measures the distance towards the target object. For all these tasks, only the swing angle changes. Then, from the third vertical line, the excavator starts the picking task until the fourth vertical line. This is indicated by the static swing angle and the movement of 3 other joints, namely the boom, arm, and bucket. As described

in Section III-B, the pick task consists of four target poses to ensure smooth movement. Starting from the fourth vertical line, another swing movement is started, this time towards the vehicle object. From the fifth vertical line, the refined swing movement starts until the sixth vertical line. Then, the place movement is executed from the sixth vertical line indicated by the changes in the boom, arm, and bucket joints. Then, it was followed by the movement towards Home position, completing the whole pick-and-place operation.

To better illustrate the movement of the excavator, snapshots of the excavator's movement are shown in Fig. 8. The order of the movement is starting from top left towards the right, then bottom left towards the right. We can see how the whole pick-and-place movement was successfully performed by the excavator. The perception module works seamlessly with the control module to achieve the desired performance.

V. CONCLUSIONS AND FUTURE WORKS

In this paper, we proposed a vision-based control architecture for excavator, combining deep learning, depth sensor, and inverse kinematics control to perform pick-and-place operation. The perception module perform object detection to perceive target object and vehicle for object storage. Once the object is perceived, depth information is retrieved to determine the location of the target objects. Finally, inverse kinematics calculate the desired joint angle and the joint-velocity layer ensures that the joints reach the target. We showed that the proposed architecture performs well in a simulated scenario using Gazebo simulator. In the future, more experiments focusing on perception module on real objects will be interesting to be explored. Implementing the control module in real excavator and performing comparison with conventional pick-and-place operation will also be an interesting research direction.

REFERENCES

- [1] O. M. U. Eraliev, K.-H. Lee, D.-Y. Shin, and C.-H. Lee, "Sensing, perception, decision, planning and action of autonomous excavators," *Automation in Construction*, vol. 141, p. 104428, 9 2022.
- [2] Q. Lu, Y. Zhu, and L. Zhang, "Excavation reinforcement learning using geometric representation," *IEEE Robotics and Automation Letters*, vol. 7, pp. 4472–4479, 4 2022.
- [3] D. Huo, J. Chen, H. Zhang, Y. Shi, and T. Wang, "Intelligent prediction for digging load of hydraulic excavators based on rbf neural network," *Measurement*, vol. 206, p. 112210, 1 2023.
- [4] H. Feng, C.-B. Yin, W. wen Weng, W. Ma, J. jing Zhou, W. hua Jia, and Z. li Zhang, "Robotic excavator trajectory control using an improved ga based pid controller," *Mechanical Systems and Signal Processing*, vol. 105, pp. 153–168, 5 2018.
- [5] Y. Ye, C.-B. Yin, Y. Gong, and J. jing Zhou, "Position control of nonlinear hydraulic system using an improved pso based pid controller," *Mechanical Systems and Signal Processing*, vol. 83, pp. 241–259, 1 2017.
- [6] X. Zhang, S. Qiao, L. Quan, and L. Ge, "Velocity and position hybrid control for excavator boom based on independent metering system," *IEEE Access*, vol. 7, pp. 71 999–72 011, 2019.
- [7] D. Jud, P. Leemann, S. Kerscher, and M. Hutter, "Autonomous free-form trenching using a walking excavator," *IEEE Robotics and Automation Letters*, vol. 4, pp. 3208–3215, 10 2019.
- [8] B. Lee and H. Kim, "Trajectory generation for an automated excavator," *2014 14th International Conference on Control, Automation and Systems (ICCAS 2014)*, pp. 716–719, 10 2014.
- [9] P. Agarwal, M. Teichmann, S. Andrews, and S. E. Kahou, "Automatic evaluation of excavator operators using learned reward functions," 2022. [Online]. Available: <https://arxiv.org/abs/2211.07941>

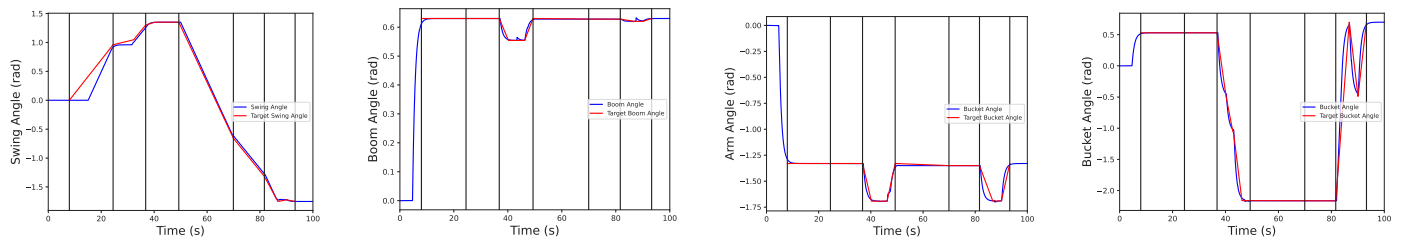


Fig. 7: Plot of joint angles of excavator, including the (a) swing, (b) boom, (c) arm, and (d) bucket. The black vertical lines indicate the switch between 1 sub-task to the next sub-task.

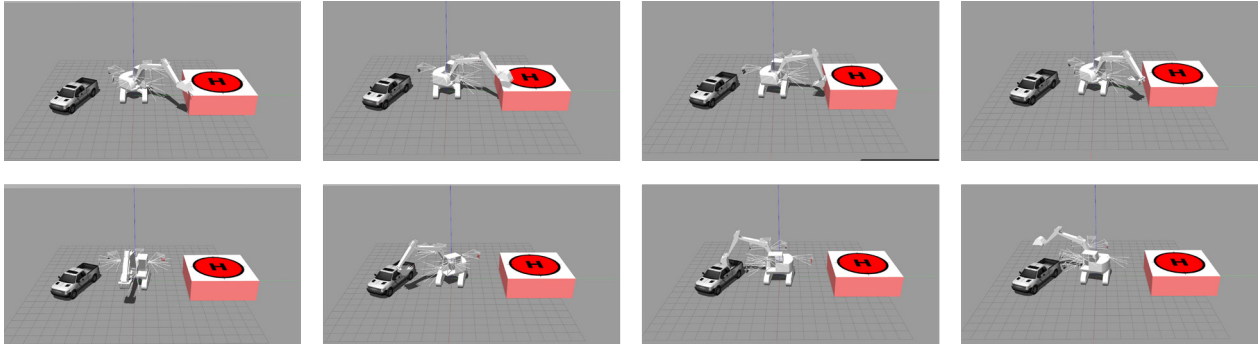


Fig. 8: The movement of excavator performing simulated picking and placing task from target object location towards the vehicle starting from top left towards the right, then bottom left towards the right.

- [10] P. Egli and M. Hutter, "Towards rl-based hydraulic excavator automation," *2020 IEEE/RSJ International Conference on Intelligent Robots and Systems (IROS)*, pp. 2692–2697, 10 2020.
- [11] —, "A general approach for the automation of hydraulic excavator arms using reinforcement learning," *IEEE Robotics and Automation Letters*, vol. 7, pp. 5679–5686, 4 2022.
- [12] P. Egli, D. Gaschen, S. Kerscher, D. Jud, and M. Hutter, "Soil-adaptive excavation using reinforcement learning," *IEEE Robotics and Automation Letters*, vol. 7, pp. 9778–9785, 10 2022.
- [13] Q. Guo, Z. Ye, L. Wang, and L. Zhang, "Imitation learning and model integrated excavator trajectory planning," in *2022 IEEE/RSJ International Conference on Intelligent Robots and Systems (IROS)*, 2022, pp. 5737–5743.
- [14] G. Jocher, A. Chaurasia, and J. Qiu, "YOLO by Ultralytics," Jan. 2023. [Online]. Available: <https://github.com/ultralytics/ultralytics>

Enhancing Genetic Algorithm Performance with Hybrid Strategy for Solving Optimization Problems

Irfan Farda
School of Information Technology
King Mongkut's Institute of Technology Ladkrabang
 Bangkok, Thailand
 64607042@kmitl.ac.th

Arit Thammano
School of Information Technology
King Mongkut's Institute of Technology Ladkrabang
 Bangkok, Thailand
 arit@it.kmitl.ac.th

Abstract— This study presents a novel algorithm called hybrid-GA, which combines genetic algorithm (GA) with the Harris Hawks Optimization (HHO) algorithm to address the challenge of enhancing GA performance in solving optimization problems. While GA is known for its strong exploration capabilities, it often faces challenges in exploitation, limiting its ability to find global optimal solutions. The hybrid-GA algorithm aims to surpass existing methods by achieving a better balance between exploration and exploitation, resulting in improved solution quality, faster convergence, and enhanced exploration-exploitation ability. The algorithm effectiveness is demonstrated through experiments on six benchmark functions from CEC2017, where the hybrid-GA outperforms compared algorithms on five of six functions, showcasing its potential for enhancing GA performance in optimization problem-solving. These findings contribute to advancing the field by providing a promising solution to address the exploration-exploitation challenge in GA-based optimization.

Keywords—Genetic Algorithm, Harris Hawk Optimization, Optimization, Hybrid strategies

I. INTRODUCTION

Optimization problems are pervasive in various domains, ranging from engineering [1] and finance [2] to logistics [3] and data analysis [4]. The quest for finding optimal or near-optimal solutions to these problems has been a topic of immense interest research [5]. Genetic Algorithm (GA) have emerged as one of the powerful metaheuristic techniques for addressing optimization challenges due to their ability to mimic natural evolution and effectively explore large search spaces [6]. However, traditional GA often face limitations in terms of convergence speed, solution quality, and exploration-exploitation balance. These limitations necessitate the development of hybrid strategies that integrate multiple optimization techniques to enhance the performance of GA [7].

Hybridization, which involves combining different optimization methods, has garnered significant attention as an approach to overcome the limitations of traditional GA. By integrating complementary algorithms, hybrid strategies aim to leverage the strengths of individual techniques and mitigate their weaknesses, resulting in improved performance and robustness. The integration of other optimization techniques, such as tabu search [8], sweep algorithm [9], or neural network [10], with GA has shown promising results in addressing optimization problems more effectively.

The objective of this study is to enhance performance of GA in solving optimization problems through the development of novel hybrid strategies. We propose the

integration of specific optimization techniques, namely Harris Hawk Optimization, with GA to overcome the limitations of traditional approaches. By combining the global search capability of GA with the local search intensification of other techniques, we aim to achieve better convergence, solution quality, and exploration-exploitation balance.

This article presents a comprehensive investigation into the effectiveness of the proposed hybrid strategies in solving optimization problems. We conduct extensive experiments on a diverse set of benchmark functions and compare the performance of our hybrid strategies with traditional GA and other state-of-the-art optimization methods. The results obtained provide valuable insights into the advantages and limitations of the hybrid approaches and demonstrate their superiority in terms of solution quality, convergence speed, and exploration-exploitation balance.

The remaining sections of this article are organized as follows. Section II provides an overview of GA and related literature on improving GA performance. Section III presents the proposed method, the Hybrid GA with Harris Hawks Optimization (HHO), along with the corresponding pseudocode. In Section IV, the experiment setup is described, including the optimization problems, algorithm configuration, and performance evaluation metrics. Section V presents the experimental results and analysis. Finally, Section VI concludes the article, summarizing the key contributions of this research and suggesting future directions for further investigation.

II. BACKGROUND AND RELATED WORKS

A. Genetic Algorithm

The fundamental concept of GA involves representing potential solutions as individuals within a population and applying genetic operators such as selection, crossover, and mutation to mimic the process of reproduction and genetic variation. By iteratively evolving generations of solutions, genetic algorithms explore the search space and aim to find optimal or near-optimal solutions. The process can be summarized as follows:

1) *Initialization*: At the start of the algorithm, it is necessary to define parameter value such as population size (NP), crossover rate (CR), mutation rate (F), number of dimension (N) and maximum number of iterations (G_{max}). Subsequently, the individuals $X_i^G = (x_{1i}, x_{2i}, \dots, x_{ji}, \dots, x_{Ni})$ are randomly generated, where $i = 1, 2, \dots, NP$; $j = 1, 2, \dots, N$; and the superscript G denotes the G^{th} generation. Each element of an individual is generated using the following equation:

$$x_{ji} = \min_j + rand[0,1] \times (\max_j - \min_j) \quad (1)$$

where \min_j and \max_j represent the lower and upper bounds, respectively. It is essential to highlight the importance of adjusting each element within the individuals to ensure they conform to the specified upper and lower bounds.

2) *Selection*: In the selection step of a GA, individuals from the population are chosen as parents. A common approach is tournament selection, where a few individuals participate in each tournament. For example, using a tournament size of three, three random individuals are selected, and their fitness values are compared. The individual with the highest fitness value is chosen as the winner and becomes a parent for reproduction. This process is repeated until the desired number of parents is selected. Tournament selection favors individuals with better fitness values, ensuring that their favorable traits are passed on to future generations, gradually improving the overall population's quality.

3) *Crossover*: During the crossover step of GA, offspring $U_i^G = (u_{1i}, u_{2i}, \dots, u_{ji}, \dots, u_{Ni})$ are generated by merging elements from selected parent individuals. K-point crossover is a commonly used technique, where K distinct points are randomly chosen along the parents' elements. At these points, the elements are exchanged, resulting in offspring with a mixture of traits inherited from both parents. Illustrated of crossover with four random K-point provided in Fig.1.

| | 1 | 2 | 3 | 4 | 5 | 6 | 7 | 8 | 9 | 10 |
|----|-----|-----|-----|-----|-----|-----|-----|-----|-----|-----|
| P1 | 0.1 | 1.5 | 5.1 | 6.2 | 7.3 | 2.1 | 4.1 | 3.2 | 7.9 | 9.9 |
| P2 | 2.5 | 1.7 | 3.5 | 4.4 | 5.1 | 8.4 | 7.9 | 9.9 | 6.6 | 8.8 |
| ↓ | | | | | | | | | | |
| U1 | 0.1 | 1.5 | 3.5 | 4.4 | 7.3 | 2.1 | 7.9 | 9.9 | 7.9 | 9.9 |
| U2 | 2.5 | 1.7 | 5.1 | 6.2 | 5.1 | 8.4 | 4.1 | 3.2 | 6.6 | 8.8 |

Fig. 1. Example of crossover

4) *Mutation*: After generating offspring, the mutation process is carried out to introduce random changes. The mutant vector $V_i^G = (v_{1i}, v_{2i}, \dots, v_{ji}, \dots, v_{Ni})$ is produce by updating the element of offspring using the following equation:

$$v_{\mu} = \begin{cases} u_{ji}; & \text{if } rand[0,1] \leq CR \\ \min_j + rand[0,1] \times (\max_j - \min_j); & \text{otherwise} \end{cases} \quad (2)$$

Here, CR is an updating probability. Each element of the mutant vector is selected from the corresponding element of the offspring if a randomly generated number within the range [0,1] is less than or equal to CR. Otherwise, the element of the mutant vector is updated with a random number within the given bounds.

5) *New population selection*: After mutation, a pool is created by combining individuals from the current population, crossover population, and mutant population. The best individuals are then selected from this pool, with a size equal to NP, to populate the next generation.

The algorithm repeats steps 1 to 5 until one of the stopping conditions is met.

B. Improving Genetic Algorithm Performance

Several studies have focused on addressing the challenges and limitations of genetic algorithms (GA) in solving optimization problems. D'Angelo and Palmieri [11] proposed a hybrid approach that combines GA with gradient descent-based algorithms to tackle the challenges faced by GA when applied to large-scale problems. Their approach demonstrated superior performance in terms of solution quality and convergence speed compared to other optimization algorithms. Acampora et al. [12] emphasized the importance of selection methods in genetic algorithms and the need to balance fast search (exploitation) and sustaining diversity (exploration). They developed the QGS algorithm, which utilizes quantum amplitude amplification to enhance the selection process in GA. The authors showed that QGS outperformed traditional selection methods in terms of solution quality and genetic population diversity. They also discussed the potential applications of using quantum computing in GA.

Albadr et al. [13] highlighted the growing popularity of nature-inspired algorithms for optimization problems and described genetic algorithms as one such approach. They emphasized the importance of balancing diversification (exploration) and intensification (exploitation) in nature-inspired algorithms. The authors proposed a new genetic algorithm that incorporates bio-oriented operators and a new selection mechanism, which showed competitive performance compared to traditional genetic algorithms and other nature-inspired algorithms. Ali et al. [14] introduced an improved class of real-coded genetic algorithms for numerical optimization. They proposed a new variant of Differential Evolution mutation as a multi-parent crossover in GA to solve complex optimization problems. The authors conducted comprehensive comparisons with other crossovers, recent GA, and Differential Evolution algorithms, highlighting the limitations of traditional GA. Their proposed algorithm consistently performed well across diverse benchmark problems, enhancing the search ability of real-coded GA.

These related works provide valuable insights into addressing the challenges faced by GA and enhancing their performance in solving optimization problems. The proposed hybrid strategies in this study build upon these advancements and aim to further improve GA performance.

III. PROPOSED METHOD

This section introduces novel methods aimed at enhancing the performance of the genetic algorithm for solving optimization problems. We present a hybridization approach that integrates the genetic algorithm (GA) with the Harris Hawks Optimization (HHO) framework. Although GA is a powerful optimizer, its conventional strategy focuses on exploration, involving significant efforts in searching for diverse solutions across the entire solution space. This approach can be advantageous in helping the algorithm explore a wide range of possible solutions. However, it may limit GA's ability to efficiently locate an optimal solution, potentially leading to premature convergence [6]. Consequently, there is a risk that GA may potentially miss out on finding globally optimal solutions. To overcome this

drawback, we incorporate HHO to harness these advantages. HHO brings several benefits that offer a balance between exploration and exploitation, allowing for efficient exploration of the search space and the potential discovery of high-quality solutions [15]–[17]. By merging HHO's exploitation capabilities with GA's evolutionary principles, we aim to leverage the complementary strengths of both algorithms. These proposed methods seek to address the challenges faced by traditional GA and leverage the benefits of hybridization to enhance the performance of genetic algorithms in solving optimization problems. The details and pseudocode of this method will be described in the following sub-sections.

A. Hybrid GA with Harris Hawks Optimization (HHO)

To achieve a better balance between exploration and exploitation in GA, we introduced a hybrid approach by incorporating Harris Hawks Optimization (HHO) algorithm. While GA excels in exploration, it can struggle with exploitation. By integrating HHO, which is known for its exploitation capabilities, we aim to leverage the strengths of both algorithms. Specifically, we focused on adopting the soft besiege strategy from HHO to enhance the crossover strategy in GA.

In the context of GA, we reinterpret the concept of the "rabbit" from HHO as an analogy to the current best individual in the population. Thus, we modify the formulas as follows:

$$U_i^G = \Delta X_i^G - E \left| JX_{best}^G - X_i^G \right| \quad (3)$$

$$\Delta X_i^G = X_{best}^G - X_i^G \quad (4)$$

where ΔX_i^G is the difference between the best individual and the target individual in the current population. This difference acts as a guide to adjust the crossover rate, allowing the algorithm to dynamically adapt its exploration and exploitation balance. E is escaping energy of the best individual, used to transfer from exploration to exploitation ability and calculated by using:

$$E = 2E_0 \left(1 - \frac{G}{G_{max}}\right) \quad (5)$$

where E_0 is generated in range $(-1,1)$, donates as the initial energy state. During the iterations, the escaping energy E gradually decreases, reflecting the diminishing exploration tendency and the increasing focus on exploitation within the GA framework. J is random jump strength of best individual during the escaping procedure and calculate by using:

$$J = 2(1 - rand(0,1)) \quad (6)$$

The value of J is calculated randomly in each iteration to simulate the variability in the best individual movements. By incorporating these formulas into the crossover strategy of GA, we enhance its ability to find the solution space effectively.

B. Pseudocode of the proposed algorithm

Based on the above description, the pseudocode of the proposed Hybrid-GA is presented in Algorithm 1.

IV. EXPERIMENT SETUP

A. Optimization Problems

To evaluate the performance of the proposed Hybrid-GA, we selected six well-known benchmark function from Congress on Evolutionary Computation (CEC) 2017 [18]. These benchmark functions are widely used in the field of optimization and provide a standardized set of problems for evaluating optimization algorithms. Table I presents detailed information about each function, including the domain, characteristics, and global optima. These benchmark functions cover a range of difficulties and complexities, allowing us to assess the robustness and effectiveness of the proposed Hybrid-GA across different problem domains.

Algorithm 1 Pseudocode of the Hybrid-GA

```

1: Set algorithm parameter;
2: Initialize random population by using (1);
3: Evaluate the fitness value of initial population;
4: G = 1;
5: WHILE (G < Gmax)
6:   Selected parent by using tournament selection;
7:   For i = 1 : NP
8:     IF rand[0,1] < CR
9:       IF rand[0,1] < 0.5
10:        Generated trial vector by using K-point
           crossover;
11:       ELSE
12:        Generated trial vector by using (3);
13:       END IF
14:     END IF
15:     Generated mutant vector by using (2);
16:   END FOR
17:   Combine current population, trial, and mutant
       vector;
18:   Select best vector with size NP;
19:   G = G + 1;
20: END WHILE
21: Output the best vector from population;

```

B. Algorithm Configuration

In order to assess the performance of our proposed algorithm, we conducted a comparative analysis against four well-known metaheuristic algorithms: Genetic Algorithm [19], Differential Evolution Algorithm [20], Artificial Bee Colony Algorithm [21], and Firefly Algorithm [22]. To ensure fairness in the comparison, we standardized certain parameters, such as setting the dimension to 30, the number of populations to 100, and the maximum number of generations to 1000. Each algorithm was independently executed for 30 times. The specific parameter configurations for all algorithms are provided in Table II, facilitating a thorough examination and comparison of their respective performances. By undertaking this comparative evaluation, our aim was to gain valuable insights into the effectiveness and competitiveness of our proposed algorithm in efficiently solving optimization problems.

TABLE I. BENCHMARK FUNCTIONS FROM CEC2017

| No. | Function name | Function description |
|-------|----------------------|---|
| f_1 | Bent Cigar Function | $f_1(x) = x_1^2 + 10^6 \sum_{i=2}^D x_i^2$ Domain $[-100,100]$, $f(x) = 0$. Unimodal function. |
| f_2 | Zakharov Function | $f_2(x) = \sum_{i=1}^D x_i^2 + \left(\sum_{i=1}^D 0.5x_i\right)^2 + \left(\sum_{i=1}^D 0.5x_i\right)^4$ Domain $[-5,10]$, $f(x) = 0$. Unimodal function. |
| f_3 | Rastrigin's Function | $f_3(x) = \sum_{i=1}^D (x_i^2 - 10 \cos(2\pi x_i) + 10)$ Domain $[-5.12, 5.12]$, $f(x) = 0$. Multimodal function. |
| f_4 | Levy Function | $f_4(x) = \sin^2(\pi w_1) + \sum_{i=1}^{D-1} (w_i - 1) [1 + 10 \sin^2(\pi w_i + 1)] + (w_D - 1)^2 [1 + \sin^2(2\pi w_D)]$ $w_i = 1 + \frac{x_i - 1}{4}$, $\forall i = 1, \dots, D$ Domain $[-10,10]$, $f(x) = 0$. Multimodal function. |
| f_5 | Discus Function | $f_5(x) = 10^6 x_1^2 + \sum_{i=2}^D x_i^2$ Domain $[-100,100]$, $f(x) = 0$. Unimodal function. |
| f_6 | Ackley's Function | $f_6(x) = -20 \exp\left(-0.2 \sqrt{1/D \sum_{i=1}^D x_i^2}\right) - \exp\left(1/D \sum_{i=1}^D \cos(2\pi x_i)\right) + 20 + e$ Domain $[-32,32]$, $f(x) = 0$. Multimodal function. |

TABLE II. PARAMETER VALUES OF THE COMPARED ALGORITHMS

| Algorithm | Parameters Value |
|-----------|---|
| GA | $F = 0.3$, $CR = 0.9$, $K = 4$ |
| DE | $F = 0.5$, $CR = 0.9$ |
| ABC | Number of Onlooker bees = 100% of the swarm, Number of Employed bees = 100% of the swarm, Number of Scout bees = 1, limit = 200 |
| FFA | $\beta_0 = 1$, $\gamma = 1$ |
| Hybrid-GA | $F = 0.3$, $CR = 1$, $K = 4$ |

C. Performance Evaluation

In our evaluation of the performance of the proposed algorithm, we calculated the mean and standard deviations of the result. Furthermore, to provide a visual representation of the algorithm performance, we plotted convergence curves behaviors that illustrate the improvement in fitness values across generations. These curves offered valuable insights into the convergence rate and stability of our algorithm. Through this comprehensive performance evaluation, we demonstrated the effectiveness of our proposed algorithm in solving optimization problems.

V. EXPERIMENT RESULTS AND ANALYSIS

This section presents the results and analysis of our experiment, which focused on evaluating the performance of our proposed algorithm and assessing the impact of different algorithm configurations. The comparison results of our proposed algorithm with four well-known metaheuristic algorithms are summarized in Table III, highlighting the pursuit of global optimum solutions. The table clearly shows that our proposed algorithm outperforms the other algorithms, as indicated by its superior mean and standard deviation across six benchmark functions (f_1 , f_2 , f_3 , f_5 , and

f_6). Specifically, Hybrid-GA successfully obtains the global best solution in four benchmark functions (f_1 , f_2 , f_3 , and f_5), outperforming the other algorithms in this aspect. Notably, although does not achieve the global best solution in f_6 , Hybrid-GA still performance better than other compared algorithms. Additionally, further results also indicate that Hybrid-GA performs slightly worse than DE on f_4 . These findings strongly demonstrate the effectiveness and competitive performance of our proposed Hybrid-GA algorithm in solving optimization problems across a diverse range of benchmark functions.

Figure 2 illustrates the convergence behavior, providing further evidence of Hybrid-GA superiority over the other compared algorithms. It is evident that Hybrid-GA rapidly converges towards the global optimum solution in most benchmark functions, while the other algorithms tend to stagnate in local optimum. For example, on f_3 , Hybrid-GA demonstrates exceptional convergence acceleration, achieving the global optimum solution in just a few generations. On f_1 and f_2 , Hybrid-GA requires more generations to reach the global optimum solutions. Notably, on f_4 and f_6 , all algorithms fall short of reaching the global optimum solution. Hybrid-GA is slightly worse with two other compared algorithms (GA and DE) on f_4 . Overall, this experiment reveals that Hybrid-GA consistently displays faster convergence behavior, making it highly promising for solving optimization problems.

TABLE III. MEAN AND STD OF COMPARED ALGORITHMS

| | GA | DE | ABC | FFA | HYBRID GA |
|-------|------------------------|--------------------------------------|------------------------|------------------------|--------------------------------------|
| | MEAN (STD) | MEAN (STD) | MEAN (STD) | MEAN (STD) | MEAN (STD) |
| f_1 | 1.14E+03 (1.44E+03) | 5.44E-02 (3.04E-02) | 6.31E-09 (4.13E-09) | 1.44E+02 (6.94E+01) | 0.00E+00 (0.00E+00) |
| f_2 | 1.64E-05 (1.49E-05) | 7.41E-09 (5.06E-09) | 2.14E-12 (2.01E-12) | 6.95E-05 (1.63E-05) | 0.00E+00 (0.00E+00) |
| f_3 | 5.26E-04 (3.44E-04) | 1.80E+02 (3.29E+01) | 2.65E-01 (1.45E+00) | 1.47E+02 (1.93E+01) | 0.00E+00 (0.00E+00) |
| f_4 | 5.12E-06 (4.24E-06) | 1.06E-08 (7.13E-09) | 2.05E+00 (7.94E-02) | 3.19E+01 (3.37E+00) | 1.72E-05 (1.44E-05) |
| f_5 | 1.97E+01 (3.46E+01) | 1.01E-07 (4.35E-08) | 3.07E-14 (2.69E-14) | 4.88E+03 (1.07E+03) | 0.00E+00 (0.00E+00) |
| f_6 | 6.89E-03 (3.23E-03) | 9.05E-05 (3.16E-05) | 3.38E-09 (1.55E-09) | 1.89E+01 (1.41E-01) | 4.44E-16 (0.00E+00) |

VI. CONCLUSIONS

In conclusion, our study introduces Hybrid-GA, a novel hybrid genetic algorithm with Harris Hawk Optimization. Hybrid-GA outperforms four well-known metaheuristic algorithms in terms of solution quality, convergence speed, and exploration-exploitation balance. The result of best mean and standard deviation value supports the superiority of Hybrid-GA, with significant differences in performance compared to the other algorithms. Additionally, Hybrid-GA exhibits faster convergence acceleration, making it a promising approach for solving optimization problems. The advantages of hybrid strategies, leveraging different optimization techniques, are evident in our study. By integrating the Harris Hawks Optimization algorithm, Hybrid-GA achieves improved solution quality, faster convergence, and a well-balanced exploration-exploitation ability.

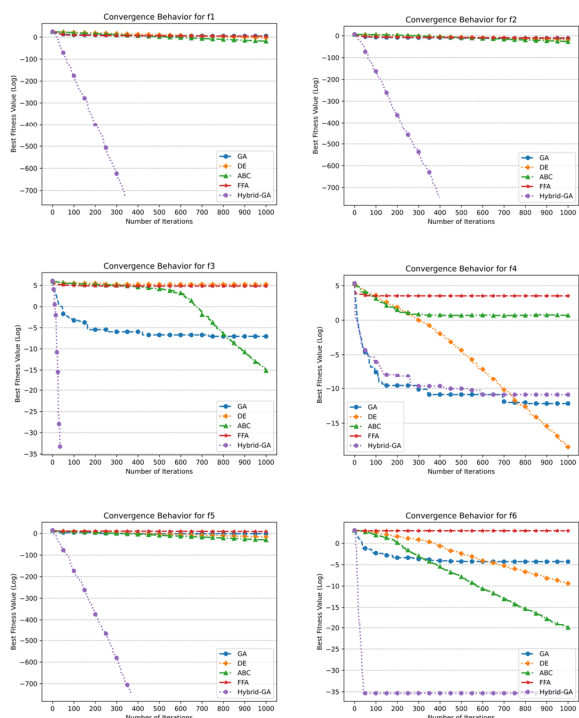


Fig. 2. Algorithms convergence behavior

Future research will focus on exploring different hybridization approaches, optimizing Hybrid-GA parameters, and extending the study to different problem domains. Evaluating the algorithm performance on larger-scale optimization problems would also provide valuable insights. Continued research and development in this area will advance the field of optimization, contributing to the development of more efficient algorithms for solving complex optimization problems.

ACKNOWLEDGMENT

This work was supported by King Mongkut's Institute of Technology Ladkrabang.

REFERENCES

- [1] Y. Qin, Z. Li, J. Ding, F. Zhao, and M. Meng, "Automatic optimization model of transmission line based on GIS and genetic algorithm," *Array*, vol. 17, p. 100266, Mar. 2023, doi: 10.1016/J.ARRAY.2022.100266.
- [2] H. Morteza, S. M. Jameii, and M. K. Sohrabi, "An improved learning automata based multi-objective whale optimization approach for multi-objective portfolio optimization in financial markets," *Expert Systems with Applications*, vol. 224, p. 119970, Aug. 2023, doi: 10.1016/J.ESWA.2023.119970.
- [3] N. E. H. Tellache and L. Kerbache, "A genetic algorithm for scheduling open shops with conflict graphs to minimize the makespan," *Computers & Operations Research*, vol. 156, p. 106247, Aug. 2023, doi: 10.1016/J.COR.2023.106247.
- [4] J. Gómez, W. D. Chicaiza, J. M. Escaño, and C. Bordons, "A renewable energy optimisation approach with production planning for a real industrial process: An application of genetic algorithms," *Renewable Energy*, vol. 215, p. 118933, Oct. 2023, doi: 10.1016/J.RENENE.2023.118933.
- [5] D. Tansui and A. Thammano, "Hybrid Nature-Inspired Optimization Algorithm: Hydrozoan and Sea Turtle Foraging Algorithms for Solving Continuous Optimization Problems," *IEEE Access*, vol. 8, pp. 65780–65800, 2020, doi: 10.1109/ACCESS.2020.2984023.

- [6] S. Katoch, & Sumit, S. Chauhan, and V. Kumar, "A review on genetic algorithm: past, present, and future," *Multimed Tools Appl*, vol. 80, pp. 8091–8126, 2021, doi: 10.1007/s11042-020-10139-6.
- [7] Z. Liu, J. Wang, C. Zhang, H. Chu, G. Ding, and L. Zhang, "A hybrid genetic-particle swarm algorithm based on multilevel neighbourhood structure for flexible job shop scheduling problem," *Computers & Operations Research*, vol. 135, p. 105431, Nov. 2021, doi: 10.1016/J.COR.2021.105431.
- [8] M. S. Umam, M. Mustafid, and S. Suryono, "A hybrid genetic algorithm and tabu search for minimizing makespan in flow shop scheduling problem," *Journal of King Saud University - Computer and Information Sciences*, Sep. 2021, doi: 10.1016/J.JKSUCI.2021.08.025.
- [9] J. Euchi and A. Sadok, "Hybrid genetic-sweep algorithm to solve the vehicle routing problem with drones," *Physical Communication*, vol. 44, p. 101236, Feb. 2021, doi: 10.1016/J.PHYCOM.2020.101236.
- [10] P. R. Lekshmy and S. T. G. Raghukanth, "A hybrid genetic algorithm-neural network model for power spectral density compatible ground motion prediction," *Soil Dynamics and Earthquake Engineering*, vol. 142, p. 106528, Mar. 2021, doi: 10.1016/J.SOILDYN.2020.106528.
- [11] G. D'Angelo and F. Palmieri, "GGA: A modified genetic algorithm with gradient-based local search for solving constrained optimization problems," *Information Sciences*, vol. 547, pp. 136–162, Feb. 2021, doi: 10.1016/J.INS.2020.08.040.
- [12] G. Acampora, R. Schiattarella, and A. Vitiello, "Using quantum amplitude amplification in genetic algorithms," *Expert Systems with Applications*, vol. 209, p. 118203, Dec. 2022, doi: 10.1016/J.ESWA.2022.118203.
- [13] M. A. Albadr, S. Tiun, M. Ayob, and F. Al-Dhief, "Genetic Algorithm Based on Natural Selection Theory for Optimization Problems," *Symmetry* 2020, Vol. 12, Page 1758, vol. 12, no. 11, p. 1758, Oct. 2020, doi: 10.3390/SYM12111758.
- [14] M. Z. Ali, N. H. Awad, P. N. Suganthan, A. M. Shatnawi, and R. G. Reynolds, "An improved class of real-coded Genetic Algorithms for numerical optimization☆," *Neurocomputing*, vol. 275, pp. 155–166, Jan. 2018, doi: 10.1016/J.NEUCOM.2017.05.054.
- [15] H. Gezici and H. Livatyali, "An improved Harris Hawks Optimization algorithm for continuous and discrete optimization problems," *Engineering Applications of Artificial Intelligence*, vol. 113, p. 104952, Aug. 2022, doi: 10.1016/J.ENGAPPAI.2022.104952.
- [16] W. Guo, P. Xu, F. Dai, F. Zhao, and M. Wu, "Improved Harris hawks optimization algorithm based on random unscented sigma point mutation strategy," *Applied Soft Computing*, vol. 113, p. 108012, Dec. 2021, doi: 10.1016/J.ASOC.2021.108012.
- [17] C. Y. Li, J. Li, H. L. Chen, M. Jin, and H. Ren, "Enhanced Harris hawks optimization with multi-strategy for global optimization tasks," *Expert Systems with Applications*, vol. 185, p. 115499, Dec. 2021, doi: 10.1016/J.ESWA.2021.115499.
- [18] N. H. Awad, M. Z. Ali, P. N. Suganthan, J. J. Liang, and B. Y. Qu, "Problem Definitions and Evaluation Criteria for the CEC 2017 Special Session and Competition on Single Objective Real-Parameter Numerical Optimization," *Technical Report, Nanyang Technological University, Singapore and Jordan University of Science and Technology, Jordan and Zhengzhou University, Zhengzhou China*, 2016.
- [19] J. H. Holland, "Adaptation in Natural and Artificial Systems: An Introductory Analysis with Applications to Biology, Control, and Artificial Intelligence," *Adaptation in Natural and Artificial Systems*, Jan. 1992, doi: 10.7551/MITPRESS/1090.001.0001.
- [20] R. Storn and K. Price, "Differential Evolution – A Simple and Efficient Heuristic for global Optimization over Continuous Spaces," *Journal of Global Optimization* 1997 11:4, vol. 11, no. 4, pp. 341–359, 1997, doi: 10.1023/A:1008202821328.
- [21] D. Karaboga and B. Basturk, "A powerful and efficient algorithm for numerical function optimization: artificial bee colony (ABC) algorithm," *Journal of Global Optimization* 2007 39:3, vol. 39, no. 3, pp. 459–471, Apr. 2007, doi: 10.1007/S10898-007-9149-X.
- [22] X.-S. Yang, *Firefly Algorithms*, Second Edi. Bristol, UK: Luniver Press, 2008.

An Improvement of Whale Optimization Algorithm with Rao Algorithm for Optimization Problems

Sakkayaphop Pravesjit
School of Information and
Communication Technology
University of Phayao
Phayao, Thailand
sakkayaphop.pr@up.ac.th

Arit Thammano
Faculty of Information Technology,
King Mongkut's Institute of Technology
Ladkrabang
Ladkrabang, Thailand
arit@it.kmitl.ac.th

Krittika Kantawong
School of Information and
Communication Technology
University of Phayao
Phayao, Thailand
krittika.ka@up.ac.th

Duangjai Jitkongchuen
Government Big Data Institute
Digital Economy Promotion Agency
Bangkok, Thailand
duangjai.ji@depa.or.th

Panchit Longpradit
Faculty of Social Sciences and
Humanities
Mahidol University
Nakhon Pathom, Thailand
panchit.lon@mahidol.ac.th

Rattasak Pengchata
School of Information and
Communication Technology
University of Phayao
Phayao, Thailand
rattasak.pe@up.ac.th

Abstract— This paper proposes an improvement of whale optimization algorithm for optimization problems. In this study, the Rao algorithm was improved by means of procedures of spiral updating position. The algorithm was tested on six benchmark problems and compared with differential evolution (DE), intersection mutation differential evolution (IMDE) algorithm, and whale optimization algorithm (WOA). The computation results illustrated that the proposed algorithm can produce optimal solutions for three out of six functions. Comparing to the other three algorithms, the proposed algorithm has provided the best results. The findings prove that the algorithm should be improved in this direction and show that the algorithm produces several solutions obtained by the previously published methods, especially for the continuous step function, the multimodal function, and the discontinuous step function.

Keywords— optimization function, whale optimization algorithm, Rao algorithm

I. INTRODUCTION

The optimization problem is required to achieve an optimized solution under the given situation. In recent years, many researchers have developed natural-inspired optimization algorithms (NIOAs) for solving this kind of problem. The natural-inspired optimization algorithms (NIOAs) consist of evolutionary algorithm (EAs) and swarm-intelligence (SI) based algorithms. The natural inspiring algorithm or the behavior of the natural entities inspired researchers to study and develop an algorithm that performs such behavioral learning. Natural-inspired algorithms are applied to solve various problems such as classification, prediction, forecasting, optimization and much more. These algorithms are widely used to find optimal solutions in optimization problems, as they offer best solutions. Jitkongchuen and Thammano [1] presented Self-adaptive differential evolution algorithm (Evo-DE) for optimization problems. The main idea is allowing the adaptation of the mutation parameters from the DE/current-to-best/1 concept and include new local search based on the krill herd algorithm. The performance of Evo-DE algorithms is very effective in solving the optimization problems. In addition, there are also algorithms that have been developed for solving optimization

problems such as Bee colony Optimization [2], Particle Swarm Optimization (PSO) [3], Differential Evolution (DE) [4], Simulated Annealing (SA) [5], Ant Colony Optimization [6], and Genetic Algorithm (GA) [7] are some examples of such algorithms.

Rao [8] in 2020, presented Rao algorithm for solving the optimization problems. The main idea is the adoption of the three-simple metaphor-less optimization algorithms for solving the optimization problems. The equation of the three-simple metaphor-less is presented by Equation 1, 2, and 3.

$$x'_{j,k,i} = x_{j,k,i} + r_{1,j,i}(x_{j,Gbest,i} - x_{j,Gworst,i}) \quad (1)$$

$$x'_{j,k,i} = x_{j,k,i} + r_{1,j,i}(x_{Gbest,i} - x_{Gworst,i}) + r_{2,j,i}(|x_{j,k,i} \text{ or } x_{j,l,i}| - |x_{j,l,i} \text{ or } x_{j,k,i}|) \quad (2)$$

$$x'_{j,k,i} = x_{j,k,i} + r_{1,j,i}(x_{Gbest,i} - |x_{Gworst,i}|) + r_{2,j,i}(|x_{j,k,i} \text{ or } x_{j,l,i}| - (x_{j,l,i} \text{ or } x_{j,k,i})) \quad (3)$$

where $x_{Gbest,i}$: is the best population in the i^{th} iteration.

$x_{Gworst,i}$: is the worst population in the i^{th} iteration.

$x'_{j,k,i}$: is the update value of $x_{j,k,i}$.

$r_{1,j,i}$ and $r_{2,j,i}$: are the random value in the range [0,1].

$x_{j,k,i}$: is the solution k .

$x_{j,l,i}$: is the random solution l .

In Equation (2) and (3), in terms $x_{j,k,i}$ or $x_{j,l,i}$ if the fitness value of $x_{j,k,i}$ is better than $x_{j,l,i}$, $x_{j,k,i}$ can be used, or use $x_{j,l,i}$; and in terms $x_{j,l,i}$ or $x_{j,k,i}$ if the fitness value of $x_{j,l,i}$ is better than $x_{j,k,i}$, $x_{j,k,i}$ is used, or use $x_{j,l,i}$. The performance of Rao algorithm is good and quite competitive.

This paper presents an improvement of whale optimization algorithm (WOA) in the procedures of spiral updating position with Rao algorithm to solve optimization problems. The performance of the proposed algorithm was compared with differential evolution (DE), JDE self-adaptive algorithm, and

intersection mutation differential evolution (IMDE) algorithm.

Following this introduction, Section 2 explains the original whale optimization algorithm. Section 3 presents a proposed algorithm. In Section 4, the experimental results are presented and discussed. Finally, Section 5 is the conclusion of the study.

II. WHALE OPTIMIZATION ALGORITHM

The whale optimization algorithm (WOA) was presented by Mirjalili and Levis [9] in 2016. The Fig 1 is shown the whale optimization algorithm diagram. The main idea was to use the behaviors of humpback whales to search and attack their prey. The inspiration of the algorithm is to simulate the behaviors of humpback whale population and update the position of candidate solution through the process of whale population encircling prey, spiral updating position, and finding prey. The exploitation phase is the first stage of the algorithm for surround prey and spiral bubble net attack; the second, exploration phase is whales randomly looking for food. The processes are explained in details as follows:

(i) Encircling Prey: If $p < 0.5$ and $|A| < 1$, it explains whales surrounding the prey after identifying its location. Assuming whales is the best optimal position in the current population is prey, the other whales surround the most suitable and the new position of whales used equation:

$$x_{t+1} = x_{Gbest} - A \times D \quad (4)$$

$$A = a \times (2 \times rand - 1) \quad (5)$$

$$C = 2 \times rand \quad (6)$$

$$D = |C \times x_{Gbest} - x_t| \quad (7)$$

$$a = 2 \times \left(1 - \frac{t}{t_{max}}\right) \quad (8)$$

$$l = \left[\left(-1 + \left(\frac{-t}{t_{max}} \right) \right) - 1 \right] \times rand + 1 \quad (9)$$

where x_t represents the current location of the whale and x_{t+1} denotes the location of the next moment whale. x_{Gbest} signifies the location of whale closest to the prey. a is a linear convergence factor and its value decreasing from 2 to 0 from the increasing number of iterations and t is the number of iterations in this present time, t_{max} is the maximum of the iterations. $rand$ is a random value in the range $[0,1]$.

(ii) Search for Prey: If $p < 0.5$ and $|A| \geq 1$. In addition to the predation behavior by bubble net, whales can also randomly search for food, and the exploration stage of the algorithm is the process of searching food. The individuals whale randomly search according to each other's position, and the mathematical model can be expressed as follows:

$$D = |C \times x_{rand}(t) - x_t| \quad (10)$$

$$x_{t+1} = x_{rand}(t) - A \times D \quad (11)$$

where $x_{rand}(t)$ represents the location of randomly individual whale.

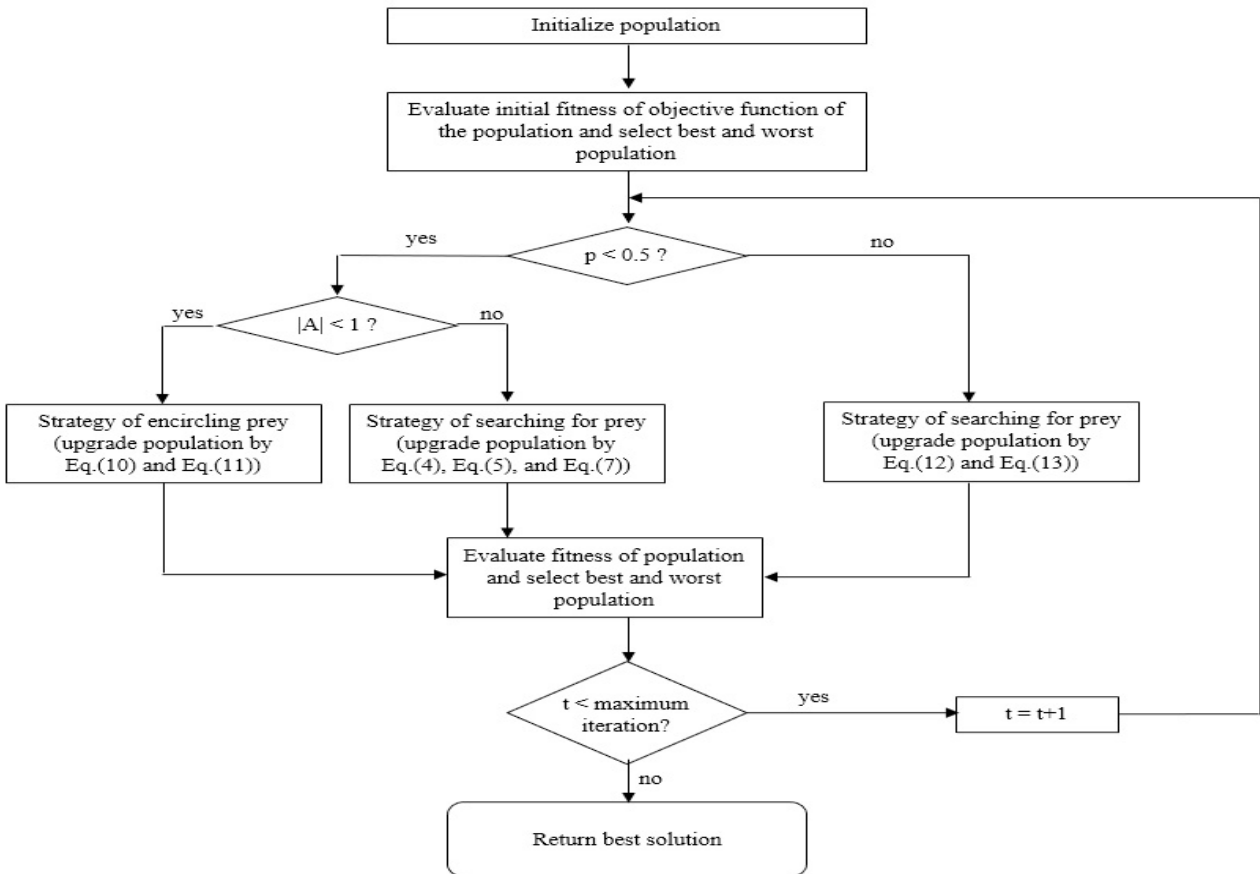


Fig. 1. The flowchart of the whale optimization algorithm.

(iii) Spiral Updating Position: If $p \geq 0.5$. During the WOA exploitation process, the humpback whale is updating position around the prey with its unique blister-like spiral behaviors. The spiral update position is expressed by the following equation:

$$D' = |x_{Gbest} - x_t| \quad (12)$$

$$x_{t+1} = D' \times e^{bl} \times \cos(2\pi l) + x_{Gbest} \quad (13)$$

where D' is the distance between the i^{th} candidate solution and the best solution in the current generation. b is a constant and $l \in [-1,1]$.

The whale optimization algorithm can solve the optimization problem efficiently. This is especially true for low-dimensional functions. However, it still has some drawbacks in dealing with the height dimension function. The performance of the algorithm decreases significantly and is easily trapped in the local optima because it tends to initially converge at a very pace.

III. THE PROPOSED ALGORITHM

This paper aims to improve the spiral updating position of whale optimization algorithm for continuous optimization

problems. The flowchart of the proposed algorithm is shown in Fig 2. After initial populations and evaluation of their fitness values, the Rao algorithm is applied to improve procedures of spiral updating position. The processes are explained in details as follows:

$$x_{j,k,t+1}^{R1} = x_{j,k,t} + A(x_{j,Gbest,t} - x_{j,Gworst,t}) \quad (14)$$

$$x_{j,k,t+1}^{R2} = x_{j,k,t} + A(x_{Gbest,t} - x_{Gworst,t}) + l(|x_{j,k,t} \text{ or } x_{j,l,t}| - |x_{j,l,t} \text{ or } x_{j,k,t}|) \quad (15)$$

$$x_{j,k,t+1}^{R3} = x_{j,k,t} + A(x_{Gbest,t} - |x_{Gworst,t}|) + l(|x_{j,k,t} \text{ or } x_{j,l,t}| - (x_{j,l,t} \text{ or } x_{j,k,t})) \quad (16)$$

$$x_{t+1} = \max_{fitness} \begin{cases} D' \times e^{bl} \times \cos(2\pi l) + x_{Gbest} \\ x_{j,k,t+1}^{R1} \times e^{bl} \times \cos(2\pi l) + x_{Gbest} \\ x_{j,k,t+1}^{R2} \times e^{bl} \times \cos(2\pi l) + x_{Gbest} \\ x_{j,k,t+1}^{R3} \times e^{bl} \times \cos(2\pi l) + x_{Gbest} \end{cases} \quad (17)$$

From Function (17), the process is to select the position of whale with the highest fitness value to use in this spiral updating position step.

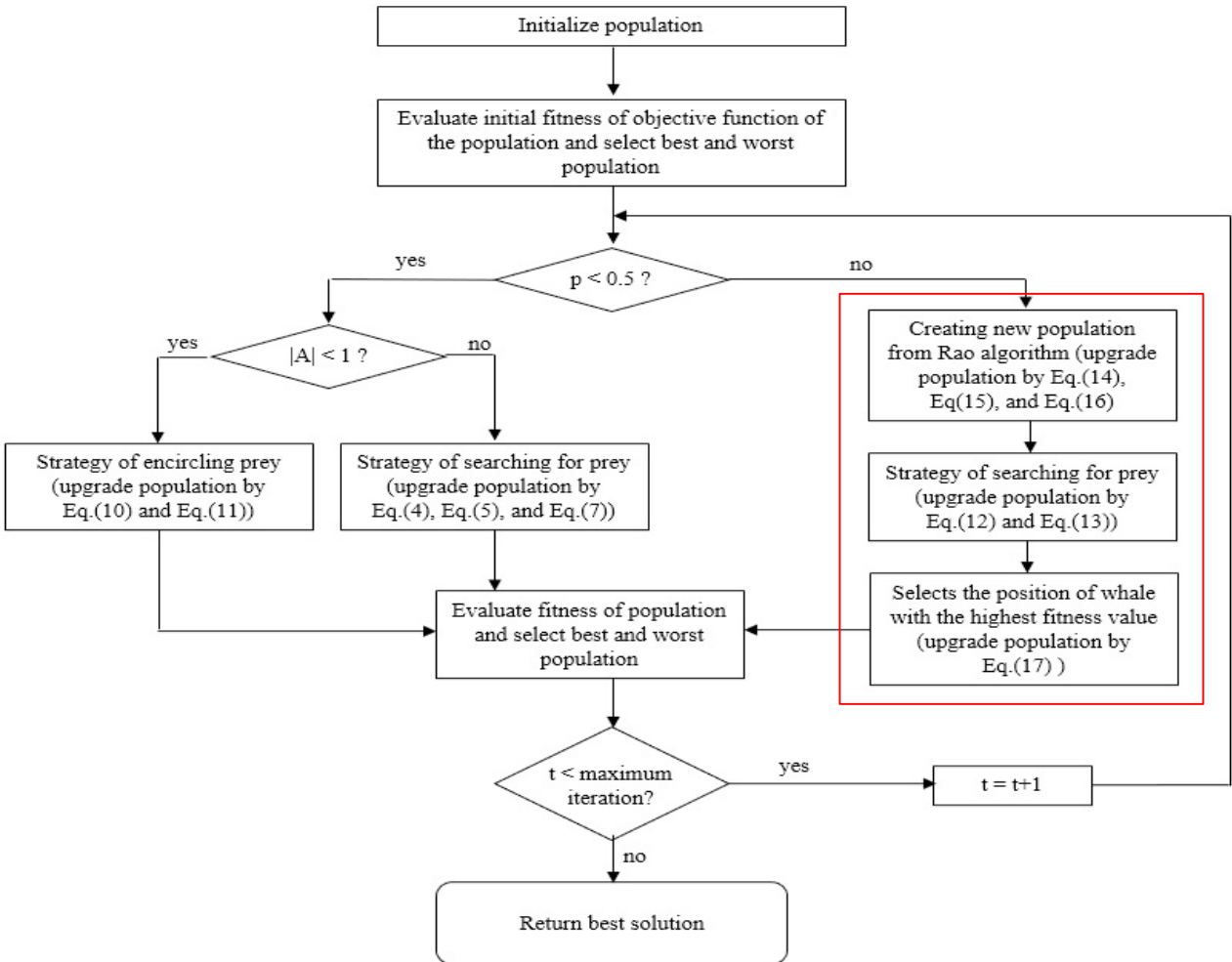


Fig. 2. The flowchart of the proposed algorithm.

TABLE I. THE PARAMETERS USED IN THE EXPERIMENTS

| Parameters | Values |
|---------------------|--------|
| Population size, NB | 25 |
| Dimension, (ND) | 30 |
| Max iteration | 1000 |

IV. THE EXPERIMENTAL RESULTS

From Table 2, the benchmark functions for validating the proposed algorithm from Yao et al. [10], consists of Sphere function, Schwefel function, Rosenbrock function, Step function, Quartic function, and Ackleg function.

The computational results shown in Table 3 present a comparison of the proposed algorithm with differential evolution (DE), intersection mutation differential evolution (IMDE) algorithm, and whale optimization algorithm (WOA). It indicates that the proposed algorithm has offered better results than the other four algorithms, namely Sphere function, Schwefel function, and Quartic function. Regarding

Rosenbrock function, IMDE algorithm has produced better results than the proposed algorithm. In addition, WOA algorithm has provided the results of the Ackleg function equivalent to the proposed algorithm.

V. CONCLUSIONS

This paper has proposed an improvement of whale optimization algorithm for optimization function. In order to improve the performance of WOA algorithm, the Rao algorithm was applied to improve procedures of spiral updating position. The testing on six various functions has demonstrated that the proposed algorithm has offered the optimal value for three out of six functions. The experimental results has confirmed that the proposed algorithm can solve the continuous functions, the discontinuous functions, and the multimodal function efficiently.

ACKNOWLEDGMENT

The authors would like to acknowledge School of Information and Communication Technology, University of Phayao, Thailand for all resources and financial support.

TABLE II. THE BENCHMARK FUNCTIONS

| Function | Iteration | Dimension (D) | Search space | fmin |
|---|-----------|---------------|---------------|------|
| $f_1(x) = \sum_{i=1}^D x_i^2$ | 1,500 | 30 | [-100, 100] | 0 |
| $f_2(x) = \max_i\{ x_i , 1 \leq i \leq D\}$ | 5,000 | 30 | [-100, 100] | 0 |
| $f_3(x) = \sum_{i=1}^{D-1} [100(x_{i+1} - x_i^2) + (x_i - 1)^2]$ | 20,000 | 30 | [-30, 30] | 0 |
| $f_4(x) = \sum_{i=1}^D (x_i + 0.5)^2$ | 1,500 | 30 | [-100, 100] | 0 |
| $f_5(x) = \sum_{i=1}^D ix_i^4 + rand[0,1)$ | 3,000 | 30 | [-1.28, 1.28] | 0 |
| $f_6(x) = -20 \exp\left(-0.2 \sqrt{\frac{1}{30} \sum_{i=1}^D x_i^2}\right) - \exp\left(\frac{1}{30} \sum_{i=1}^D \cos 2\pi x_i\right) + 20 + e$ | 1,500 | 30 | [-32, 32] | 0 |

TABLE III. THE EXPERIMENTAL REUSLTS

| Functions | DE | IMDE 1 st process | IMDE 2 nd process | WOA | Proposed algorithm |
|-----------|-----------|------------------------------|------------------------------|-------------------|--------------------|
| F1 | 1.58E - 3 | 2.5E - 32 | 2.1E - 35 | 3.8979E-156 | 0 |
| F2 | 1.9E-3 | 0.2E-3 | 3.4E-24 | 0.3122 | 0 |
| F3 | 8.35E-27 | 0 | 0 | 27.0403 | 26.1423 |
| F4 | 0 | 0 | 0 | 0.0227 | 0 |
| F5 | 2.63E-3 | 2.4E-4 | 3.4E-4 | 0.00079 | 1.223E-4 |
| F6 | 1.5017 | 4.9E-15 | 4.6E-15 | 8.8818E-16 | 8.8818E-16 |

REFERENCES

- [1] Jitkongchuen, D., & Thammano, A. (2014). A self-adaptive differential evolution algorithm for continuous optimization problems. *Artificial Life and Robotics*, 19, pp.201-208.
- [2] Karaboga, D., & Basturk, B. (2007). A powerful and efficient algorithm for numerical function optimization: artificial bee colony (ABC) algorithm. *Journal of Global Optimization*, 39 (2007), 459–471.
- [3] Kennedy, J., & Eberhart, R. (1995). Particle Swarm Optimization. *Proceedings of IEEE International Conference on Neural Networks*. IV. pp. 1942–1948
- [4] Storn, R., & Price, K. (1997). Differential Evolution - A Simple and Efficient Heuristic for Global Optimization over Continuous Spaces. *Journal of Global Optimization*, 11, pp. 341–359.
- [5] Bookstaber, D. (1997). *Simulated Annealing for Traveling Salesman Problem*, Spring.
- [6] Dorigo, M., & Stutzle, T. (2004). *Ant Colony Optimization*. A Bradford book, MIT Press Cambridge, Massachusetts London, England.
- [7] Holland, J.H. (1992). *Adaptation in Natural and Artificial Systems*. MIT Press.
- [8] Rao, R. (2020). Rao algorithms: Three metaphor-less simple algorithms for solving optimization problems. *International Journal of Industrial Engineering Computations*, 11(1), 107-130.
- [9] Mirjalili, S., & Lewis, A. (2016). The whale optimization algorithm. *Advances in engineering software*, 95, 51-67.
- [10] Yao, X., Liu, Y., & Lin, G. (1999). Evolutionary programming made faster. *IEEE Transactions on Evolutionary computation*, 3(2), 82-102.

Modified Differential Evolution Algorithm for Solving Multi-Skill Resource-Constrained Project Scheduling Problem

Akarasate Homwisesongsa
 Department of Computer and Information Science,
 Faculty of Applied Science
 King Mongkut's University of Technology North Bangkok
 (KMUTNB) Bangkok, Thailand
 s6304062857088@email.kmutnb.ac.th

Chiabwoot Ratanavilisagul
 Department of Computer and Information Science,
 Faculty of Applied Science
 King Mongkut's University of Technology North Bangkok
 (KMUTNB) Bangkok, Thailand
 chaibwoot@gmail.com, chaibwoot.r@sci.kmutnb.ac.th

Abstract— The multi-skills resource-constrained project scheduling problem (MS-RCPSP) is assigning tasks to employees while considering predecessor tasks and multi-skills constraints to create a feasible schedule with both the shortest completion duration. Recently, Differential Evolution with multidimensional real-valued functions (DEM) was introduced to address the MS-RCPSP. The experimental results demonstrated that DEM outperformed GreedyDO, HAntCO, and GA. However, DEM lacked a technique to handle local optimum problem, resulting in unsatisfactory search results. Hence, this research proposes a modification to DEM by enhancing the mutation technique, executing it twice per generation, to increase population diversity and obtain better outcomes. The proposed algorithm was tested on twenty-three test cases from the MS-RCPSP iMOPSE datasets and yielded more satisfactory results compared to the competing algorithms.

Keywords— optimization, evolutionary computing, differential evolution, multi-skill resource-constrained project scheduling problem

I. INTRODUCTION

The Resource-constrained project scheduling problem (RCPSP) is the assignment of tasks to employees in order to create a viable schedule with the shortest possible completion time [1]. In the business and industrial settings, project managers may face the challenge of efficiently managing project schedules while considering various constraints, such as completion time, cost, employee skills, and other factors [2]. The Multi-skills Resource-constrained Project Scheduling Problem (MS-RCPSP) is an extension of RCPSP that includes the additional constraint of multiple skills. Both RCPSP and MS-RCPSP belong to the category of combinatorial optimization problems and are considered NP-hard [1-3]. Due to their complexity, brute force algorithms are impractical for solving these problems, especially when dealing with a large number of tasks. Therefore, to tackle them effectively, heuristic algorithms and meta-heuristic algorithms are widely employed.

Over the past few years, numerous scholars have suggested employing heuristic algorithms for addressing challenges like MS-RCPSP. Heuristic and Meta-heuristic approaches, such as Differential Evolution (DE) [4-6], Genetic Algorithm (GA) [7-8], and Ant Colony Optimization (ACO) [9-11], have proven to be highly effective in solving exceedingly intricate problems.

Myszkowski et al. [12, 13] introduced a hybrid algorithm that combines the Differential Evolution strategy with the Greedy approach to optimize human resource allocation in product manufacturing projects. The authors' objective was to minimize both duration and cost, and they provided a new benchmark dataset called iMOPSE, which was an artificially generated dataset based on real-world instances for the MS-RCPSP problem. Marek Skowronski and Paweł B. Myszkowski [14] presented an algorithm utilizing genetic operators for solving MS-RCPSP. Dai and Huafeng [15] proposed algorithms by implementing neighborhood search and local search techniques. Amir Hossein Hosseinian and Vahid Baradaran [16] introduced a novel mixed-integer model for the MS-RCPSP problem. They proposed the dandelion algorithm to solve this problem using the new model, achieving favorable results compared to the genetic algorithm, harmony search algorithm, and differential evolution. H. D. Quoc, L. N. The, C. N. Doan, and T. P. Thanh [6] introduced a novel approach called Differential Evolution with multidimensional real-valued functions for solving the MS-RCPSP. In addition to utilizing the differential evolution Metaheuristics, they devised a Reassignment function to enhance the solution quality at the end of each iteration, ensuring that their algorithm converges quickly towards the global optimum. Furthermore, their algorithm avoids being stuck in a local optimum, and it is referred to as DEM. The experimental results demonstrate that the solutions obtained by DEM outperform those achieved by GreedyDO, HAntCO, and GA. The findings indicate that the proposed algorithm effectively improves search efficiency.

However, DEM lacks a mechanism to address and mitigate issues related to the local optimum problem and the premature convergence problem, leading to unsatisfactory search outcomes. Therefore, this research proposal introduces the twice mutation technique to enhance diversity within the population and achieve improved results. The benchmark problems for MS-RCPSP, specifically the iMOPSE datasets [3], were utilized to compare the performance of the DEM [6] with the proposed algorithm. The results indicate that the solution quality of the proposed algorithm outperforms that of other algorithms, including DEM, when evaluated on the MS-RCPSP iMOPSE datasets.

The remaining sections of this paper are structured as follows. Section 2 provides an overview of the related works, covering topics such as RCPSP, MS-RCPSP, DE, and DEM.

In Section 3, the proposed technique is explained. Section 4 presents the experiment setup and showcases the experiment results. Finally, Section 5 concludes the project with a concise summary.

II. RELATED WORK

A. Resource-constrained Project Scheduling Problem

The Resource-constrained project scheduling problem (RCPSP) is a collection of tasks and a group of employees, both represented as integer numbers. Each task is also represented with integer numbers, specifying its starting and finishing times. The tasks must be carried out continuously once they have begun, and some tasks have specific predecessor tasks, meaning they can only start after their preceding tasks have been completed. The main objective of RCPSP is to allocate all tasks to employees while respecting the precedence constraints, ultimately creating a feasible schedule with the shortest possible completion duration.

B. Multi-skill Resource-constrained Project Scheduling Problem

MS-RCPSP is an extension of RCPSP that incorporates a multi-skills constraint for both tasks and employees. Each employee possesses specific skills, each with its corresponding proficiency level. Likewise, each task requires a particular skill and a minimum skill level from an employee to be performed. If an employee possesses a skill that matches the task's required skill and their skill level is equal to or higher than the task's minimum level, they are capable of executing the task. Conversely, if an employee lacks the necessary skill or their skill level is lower than the task's minimum requirement, they cannot carry out that task. The goal of MS-RCPSP is assigning all tasks to employees under the predecessor tasks constraint and the multi-skill constraint in order to create the feasible schedule with the shortest completion duration.

$$\min f(PS) = \min [f_r(PS)] \quad (1)$$

$$\forall_{k \in K} (s_k) \geq 0, \forall_{k \in K} (Q^k) \neq \emptyset \quad (2)$$

$$\forall_{j \in J} (F_j) \geq 0, \forall_{j \in J} (d_j) \geq 0 \quad (3)$$

$$\forall_{j \in J, j \neq 1, i \in P_j} (F_i) \leq (F_j - d_i) \quad (4)$$

$$(\forall_{i \in J} \exists_{q \in Q^k} h_q = h_{q_i}) \wedge (l_q \geq l_{q_i}) \quad (5)$$

$$\forall_{k \in K} \forall_{t \in T} \sum_{i=1}^n U_{i,k}^t \leq 1 \quad (6)$$

$$\forall_{j \in J} \exists_{t \in T, i \in K} (U_{j,k}^t) = 1, U_{j,k}^t \in \{0,1\} \quad (7)$$

PS refers to Project Schedule, which is composed of a set of tasks ($J = 1, \dots, n$) and a set of employees ($K = 1, \dots, m$). Here, n represents the number of tasks, and m represents the number of employees. T denotes the completion duration of the solution, while T_{\max} represents the sum of durations from all tasks. The cost can vary, with c_{\min} representing the total cost of all tasks assigned at the cheapest employee wage without considering skill constraints, and c_{\max} representing the total cost of all tasks assigned at the most expensive employee wage without considering skill constraints. Each task, j , has its hourly duration (d_j), start time (S_j), and finish time (F_j). P_j refers to the predecessors of task j . The hourly rate salary of employee k is denoted as s_k . Q encompasses all the available skills, and Q^k represents the subset of skills

possessed by employee k ($Q^k = 1, \dots, r$). Here, r denotes the number of skills possessed by employee k . Each skill, q , has an associated level l_q , and h_q represents skill q .

J^k is a subset of all tasks that employee k can perform. The cost of employee k performing task j is denoted as c_j^k ($c_j^k = d_j \times s_k$). If $U_{j,k}^t = 1$, it signifies that employee k is assigned to task j at time t . Conversely, if $U_{j,k}^t = 0$, it indicates that employee k is not assigned to task j at time t .

Equation (1) denotes the duration optimization. $f_r(PS)$ is an evaluation function of project schedule's duration.

The first constraint (2) preserves the positive values of resource salaries and ability to perform at least one task by every resource. Equation 3 states that every task has positive finish date and duration, while (4) shows the precedence constraints rule. Next two equations: (5) introduces skill constraints and transforms RCPSP into MS-RCPSP. Constraint (6) describes that any resource can be assigned to no more than one task in given time during the project. The last constraint (7) says that each task must be performed in schedule PS by one resource assignment.

C. Differential Evolution

Differential Evolution (DE) is an evolutionary algorithm proposed by R. Storn and K. Price in 1997 [17]. DE follows a directed evolutionary approach, utilizing mutation techniques to generate improved solutions in subsequent generations. This algorithm has shown great effectiveness in solving various NP-Hard problems. S. Selvi et al. [18] presented a DE based method for scheduling problems in the Cloud computing environment, aiming to minimize execution time. The DE algorithm drives population evolution through the use of crossover (recombination), mutation, and selection operators. The key distinction between the DE algorithm and GA lies in their mutation operators. In DE, the mutation operator utilizes orientation information to modify solutions within the current population. The general procedure of the DE algorithm can be described as follows. Imagine a population comprising candidate solutions (i.e., schedules), with each solution composed of D components represented as a vector $x_i = (x_{i,1}, x_{i,2}, \dots, x_{i,D})$ where $x_{i,j} \in \mathbb{R}$ and $i=1,2,\dots,N$ and $j=1,2,\dots,D$.

For mutating a solution (8) x_i , the DE algorithm randomly chooses three other solutions from the population: $x_{r1} \neq x_{r2} \neq x_{r3} \neq x_i$. The mutation operator then impacts the solution x_i by calculating a new solution v_i as follows:

$$v = x_{r1} + F(x_{r2} - x_{r3}) \quad (8)$$

The mutation constant, denoted by F , holds a value within the range $[0,1]$. The resulting solution v_i , derived from the mutation operator, is referred to as the mutation solution of x_i . The parameter F plays a crucial role in adjusting the magnitude of the directional vector and is known as the directional hop length. Following the implementation of the mutation operator, the DE algorithm employs the one-point crossover operation to merge information from the parent solution x_i with the mutation solution v_i . This crossover operation involves selecting a random number CR ($CR \in [0, 1]$) to serve as the probability of crossover. The outcome of the crossover operator is a vector with its components computed using the following method:

$$u_{i,j} = \begin{cases} v_{i,j} & \text{if } rand_{i,j} \leq CR \text{ or } i = I_{rand} \\ x_{i,j} & \text{if } rand_{i,j} > CR \text{ or } i \neq I_{rand} \end{cases} \quad (9)$$

In the expressions provided (9), i varies from 1 to N , and j varies from 1 to D . $rand_{i,j}$ represents a mutation constant with a value within the range $[0,1]$. I_{rand} is a random number with a value within the range $[1, D]$. It ensures that the mutation solution v_i is always distinct from the original solution x_i . To select the solution for the next generation, DE employs the selection operator on the parent solution x_i and the solution u_i in the following manner (10).

$$x_i(t+1) = \begin{cases} u_i(t) & \text{if } f(u_i(t)) < f(x_i(t)) \\ x_i(t) & \text{in other cases} \end{cases} \quad (10)$$

D. Differential Evolution with multidimensional real-valued functions for solving the MS-RCPSP

While DE was originally designed for multidimensional real-valued functions, the solutions in MS-RCPSP consist of arrays of integer value elements. Consequently, a new measurement model was developed to assess the disparity between two schedules (i.e., solutions). The new model is formulated as follows: Let $P = (p_1, p_2, \dots, p_n)$ represent the unit vector, where each element p_i is calculated as 100 divided by (k_i-1) , where k_i denotes the number of resources that can handle task i . The difference between two schedules, $X = (x_1, x_2, \dots, x_n)$, and $Y = (y_1, y_2, \dots, y_n)$ is represented by the differential vector, $D = (d_1, d_2, \dots, d_n)$.

$$D = X - Y \quad (11)$$

To obtain schedule X from schedule Y and the differential vector D , the following equation (11) is used: $x_i = \text{position}(\text{round}(y_i + d_i))$ where $\text{position}(i)$ corresponds to the resource that corresponds to position i . Here, d_i is computed as p_i multiplied by $(\text{order}(x_i) - \text{order}(y_i))$, where $\text{order}(x_i)$ denotes the position of resource x_i in the resource set RS_i . The process commences with generating an initial population and evaluating the fitness of each solution. Subsequently, the best solution is identified within the population. Then, a loop is initiated, ranging from the first generation to the final generation. During each generation's process, the following steps are executed: Apply the mutation process. The mutation has process as follows: begins by randomly selecting genes from three unique individuals in the current generation's population. These genes are then combined using a formula to create a new set of genes for the mutant individual. Then, perform the crossover process. The crossover has process as follows: swapping a gene between trial, donor, and target individuals from consideration of crossover rate (CR) and the random value. Calculate the fitness of each solution. If any solution is superior to the current best solution, replace the best solution with that solution. Then, apply the reassignment. The reassignment has process as follows: examining the last finished task in the current best solution and attempting to assign it to another resource. If the modified solution still is worse than the current best solution, retain the current best solution. However, if the modified solution improves, update the best solution to be the modified solution.

III. THE PROPOSED WORK

The experiment [6] demonstrated favorable outcomes when using this method, showcasing its superiority compared to other algorithms such as GreedyDO, HAntCO,

and GA. However, DEM does not possess a mechanism to effectively handle issues like local optimum problem and premature convergence problem, leading to unsatisfactory search results. To counteract these challenges, DEM attempts to increase diversity within the population through the application of mutation techniques [19], the population became more diverse, effectively reducing or resolving local optimum problems and yielding improved answers.

The proposed research aims to further enhance diversity within the population by implementing the twice mutation technique, which involves executing two mutations per generation. This technique enhances genetic variability and expands the search space, with the goal of achieving better results. Applying twice mutation technique with DEM is called that TWDEM.

Nevertheless, the higher the count of performed mutations, the greater the consumption of resources and time during the search process. Increasing the number of mutations doesn't necessarily lead to improved outcomes; in fact, excessive mutations are futile and result in wastage of time and resources. Thus, it's important to avoid excessive mutation.

To validate this research hypothesis, the current experiment utilizes the triple mutation technique, involving three mutations executed per generation. However, the experimental results reveal that the search outcomes of the triple mutation technique are akin to those of the twice mutation technique. This implementation of the triple mutation technique with DEM is referred to as TRDEM.

The results highlight that having too few mutation operations yields inferior answers, while an excess of mutation operations leads to resource wastage. Hence, this research proposed TWDEM in order to improve searching performance of DEM. The proposed algorithm is called modified DEM with the twice mutation for solving multi-skill resource-constrained project scheduling problems or TWDEM. Pseudo code of TWDEM is shown below:

Algorithm 1: TWDEM pseudocode

```

1  populationSize = 100
2  generationLimit = 50000
3  stateLimit = 200
4  maxClones = 200
5  mutationRank = 1
6  F = 0.1
7  CR = 0.1
8  generation = 0
9  lastUpdate = 0
10 numClones = 0
11 population ← Generate initial population and calculate the fitness
12 bestIndividual ← Find the best individual in the population
13 While (the generation is in the generationLimit) AND (generation - lastUpdate < stateLimit) AND (numClones < maxClones)
14   For i = 0 to (populationSize - 1)
15     donor = Mutation(population[i], F) ← Mutate

```

```

16   population[i]
17   trialGenes = Crossover(population[i].genes, donor,
18   CR) ← Crossover genes of population[i] and donor
19   trialIndividual ← Build individual, calculate the
20   fitness and its schedule from trial genes
21   isBetter ← Select better one between population[i]
22   and trialIndividual
23   If trialIndividual is better than bestIndividual
24   bestIndividual = trialIndividual
25   lastUpdate = generation
26   End If
27   numClones ← Number of duplicate individual in
28   current generation
29   End for
30   generation + 1
31   End while
32   newBest ← Reassignment(bestIndividual)
33   Return newBest

```

Where:

- populationSize: number of solutions in the population.
- generationLimit: the limit of generation of the population.
- staleLimit: the limit distance between the current generation and the last generation that found the best solution.
- maxClones: the limit of solutions duplications during each generation.
- mutationRank: number of different individuals (solutions) randomly chosen from the population to be used in the mutation process.
- F: the scaling factor used in the mutation process of the Differential Evolution algorithm.
- CR: the crossover rate used in the Differential Evolution algorithm. It controls the probability of applying the crossover operation to generate a trial solution during the mutation process.

After configuring the limits, the algorithm generates the initial population and identifies the best individual within it. Before proceeding with the Differential Evolution (DE) steps, it verifies the current generation number, the last generation update, and the number of duplications in the population. Following the verification, the DE process is carried out in a loop. The process begins with the mutation step, where the random mutation is applied. Three solutions are randomly selected from the population and passed through the mutation formula, which incorporates a scaling factor denoted by F. Generally, in DE and DEM mutate genes only one time but in TWDEM mutate genes two times to increase the search space to be wider and get more possibility of the best value. In the crossover process, it uses binomial methodology from using the mutated genes to process by swapping genes between mutated genes and the genes of the current solution by considering from random number and crossover rate (CR). The genes that are mutated

and crossover will be created as a new solution and selected by one to one methodology which select by comparing their evaluation value and choose the best one. After performing the steps of the DE strategy, the reassignment function is called to find the better schedule by leading the DE algorithm follow the correct direction in the space of schedules from creating new schedules based on the best one.

IV. EXPERIMENTS AND RESULTS

A. The Measures of Algorithm Performance

To compare the performance of the algorithm, we utilize the average value from multiple runs due to DEM being a stochastic algorithm. The performance measures used in the experiments are as follows: Best duration value (BD): This represents the best completion duration achieved across all runs, measured in hours. Average of BD (ABD): It is the average of the best completion duration obtained in the final iteration from all runs, measured in hours. Average of ABD of all datasets (AABD): This is the average of ABD values obtained from all datasets. Standard deviation (SD): This measures the variability or spread of the results. Average of SD of all datasets (ASD): It represents the average of SD values from all datasets. ASD and SD indicate the solution searching reliability of the algorithm. AABD, BD, and ABD indicate the solution searching efficiency of the algorithm. The lower all values are, the better the algorithm's performance. The experiment involved thirty-six datasets obtained from the iMOPSE dataset benchmark problems [20], a widely recognized dataset often employed for addressing RCPSP (Resource-Constrained Project Scheduling Problem) challenges. These datasets were divided into two groups of project instances, one containing 100 tasks and the other containing 200 tasks. These standard datasets were used to ensure unbiased and equitable comparisons of algorithm performance.

B. Parameters Setting

The parameters are as follows for all experiments: staleLimit = 200, maxClones = 200, mutationRank = 1, F = 0.1, and CR = 0.1. These values get from the results from experiments. The select values that can create the best result. The number of Population used is 100. The number of experiments of each datasets is 20 runs. The maximum number of Generation is set as 50000.

C. Experiment of Proposed Algorithm

From the experimental outcomes presented in Table 1, it is evident that the solution quality of TWDEM surpasses that of DEM and TRDEM, as indicated by its lowest AABD, BD and ABD across all tested cases. Also, evaluate the performance of proposed algorithms TWDEM in comparison with previous algorithms GreedyDO and HAntCO. This demonstrates that the implementation of the twice mutation technique in TWDEM enhances the search performance of DEM, leading to improved answers. Moreover, it increase the diversity of population proves beneficial in reducing the risk of getting trapped in local optima and obtaining better answers.

Furthermore, TWDEM exhibits higher reliability compared to DEM and TRDEM, evident from its lowest ASD and SD across all tested cases. This indicates that the implementation of the twice mutation technique increases the

population's diversity, leading to a reduced risk of getting stuck in local optima and enhancing the algorithm's overall reliability. Consequently, TWDEM outperforms DEM and TRDEM in terms of both reliability and solution quality.

While TWDEM exhibited superior outcomes in terms of both reliability and solution quality compared to TRDEM, the differences between the results are very small. This suggests that employing either the twice mutation or triple mutation techniques leads to comparable outcomes. Nevertheless, it is worth noting that TRDEM consumes more resources and time without achieving the desired level of performance, making it an inefficient choice for further processing.

This outcome serves as evidence that an excessive number of mutations is not suitable. Therefore, the number of mutations significantly influences searching answers of DEM, and employing an appropriate number of mutations is crucial to results search of DEM.

V. CONCLUSION

The differential evolution with multidimensional real-valued functions (DEM) can solve MS-RCPSP efficiently and get the good answers. The experimental results demonstrate that the solutions obtained by DEM outperform those achieved by GreedyDO, HAntCO, and GA. However, DEM lacks a mechanism to address and mitigate issues related to local optima and premature convergence, leading to unsatisfactory search outcomes. Therefore, this research proposal introduces the twice mutation technique to enhance diversity within the population and achieve improved results. From experimental results of this research shows that too few mutations obtain bad answers and rarely searching performance. While, too many are mutations affect to lose the resource wastefully. So, this paper proposed the mutation technique is two execute per generation. The proposed technique is called that TWDEM in order to improve searching performance of DEM and get better answer. TWDEM can solve and decrease trapping in local optimum problem and improve searching of DEM. From the experimental results, the proposed TWDEM outperforms DEM and TRDEM with regard to the reliability and quality of solutions in all test cases.

REFERENCES

- [1] Blazewicz J, Lenstra JK, and Rinnooy Kan AHG, "Scheduling subject to resource constraints: classification and complexity," *Discret Appl Math*, vol 5, pp. 11–24, 1983.
- [2] Pawel B. Myszowski, Marek E. Skowronski, Lukasz P. Olech, and Krzysztof Oslizlo, "Hybrid ant colony optimization in solving multi-skill resource-constrained project scheduling problem," *Soft Comput* 19, pp. 3599–3619, 2015.
- [3] S. Selvi, D. Manimegalai, and A. Suruliandi, "Efficient Job Scheduling on Computational Grid with Differential Evolution Algorithm," *International Journal of Computer Theory and Engineering* vol. 3, no. 2, pp. 277-281, 2011.
- [4] Kolisch R, and Sprecher A, "PSPLIB a project scheduling problem library," *Eur J Oper Res* 96, pp. 205–216, 1996.
- [5] Maciej Laszczyk, and Pawel B. Myszowski, "Improved selection in evolutionary multi-objective optimization of multi-skill resource-constrained project scheduling problem," *Information Sciences*, vol. 481, pp. 412-431, 2019.
- [6] H. D. Quoc, L. N. The, C. N. Doan, and T. P. Thanh, "New Effective Differential Evolution Algorithm for the Project Scheduling Problem," 2020 2nd International Conference on Computer Communication and the Internet (ICCCI), pp. 150-157, 2020.
- [7] Jian Lin, Lei Zhu, Kaizhou Gao, "A genetic programming hyper-heuristic approach for the multi-skill resource constrained project scheduling problem," *Expert Systems with Applications*, vol. 140, 2020.
- [8] Sachi Gupta, Gaurav Agarwal, and Vikas Kumar, "An Efficient and Robust Genetic Algorithm for Multiprocessor Task Scheduling," *International Journal of Computer Theory and Engineering*, vol. 5, no. 2, pp. 377-382, 2013.
- [9] C. Ratanavilisagul, "Modified Ant Colony Optimization for Vehicle Routing Problem with Time Windows using Limited Search Space and Novel Updating Pheromone and Re-initialization Pheromone Techniques", *ICIC Express Letters Part B: Applications ICIC International* 2022, ISSN 2185-2766, Volume 13, Number 6, June 2022, pp. 571-579.
- [10] S. Kosolsombat, C. Ratanavilisagul, "Modified ant colony optimization with selecting and elimination customer and re-initialization for VRPTW", *Bulletin of Electrical Engineering and Informatics*, Vol. 11, No. 6, December 2022, pp. 3471-3482.
- [11] C. Ratanavilisagul, "Modified Ant Colony Optimization with route elimination and pheromone reset for Multiple Pickup and Multiple Delivery Vehicle Routing Problem with Time Window", *Journal of Advanced Computational Intelligent and Intelligent Informatics* Vol. 26, No. 6, 2022, pp. 959 - 964.
- [12] Sahawneh, Laith, Beard, Randal W., Avadhanam, Sharath, Bai, He, "Chain-based Collision Avoidance for UAS Sense-and-Avoid Systems", *AIAA Guidance, Navigation, and Control Conference*, Boston, August, 2013.
- [13] Myszowski P.B., Laszczyk M. and Lichodij J, "Efficient selection operators in NSGA-II for Solving Bi-Objective Multi-Skill Resource-Constrained Project Scheduling Problem", *Proceedings of the 2017 Federated Conference on Computer Science and Information Systems*, M. Ganzha, L. Maciaszek, M. Paprzycki (eds). ACSIS, Vol. 11, pages 83–86 (2017).
- [14] Marek Skowronski, Pawel B. Myszowski, "Specialized genetic operators for Multi-Skill Resource-Constrained Project Scheduling Problem", *19th Inter. Conference on Soft Computing - Mendel* 2013, pp. 57-62, 2013.
- [15] Dai, Huafeng, et al. "A general variable neighbourhood search for multi-skill resource-constrained project scheduling problem with step-deterioration." *International Journal of Industrial and Systems Engineering* 34.2, 2020, 145-164.
- [16] Amir Hossein Hosseinian, Vahid Baradaran, "Detecting Communities of Workforces for the Multi-Skill Resource-Constrained Project Scheduling Problem: A Dandelion Solution Approach" *Journal of Industrial and Systems Engineering* Vol. 12, Special issue on Project Management and Control, pp. 72-99, 2019.
- [17] K.Price, R.Storn, and J.Lampinen, "Differential Evolution - A Practical Approach to Global Optimization". Springer, Berlin, Germany, 2005.
- [18] S.Selvi, Dr. D.Manimegalai, Dr.A.Suruliandi "Efficient Job Scheduling on Computational Grid with Differential Evolution Algorithm" *International Journal of Computer Theory and Engineering*, Vol. 3, No. 2, 2011.
- [19] C. Ratanavilisagul and B. Kruatrachue, "A modified particle swarm optimization with mutation and reposition", *International Journal of Innovative Computing, Information and Control (IJICIC)*, vol. 10, no. 6, december 2014, pp. 2127 - 2142
- [20] <http://imopse.ii.pwr.edu.pl/download.html> [accessed December 11, 2022].

TABLE I. COMPARATIVE RESULTS OF DEM, TWDEM, AND TRDEM

| Name Datasets | GreedyDO | HAntCO | DEM | | | TWDEM | | | TRDEM | | |
|-----------------|----------|--------|-------|-----|------|-------|-----|-----|-------|-----|-----|
| | | | ABD | BD | SD | ABD | BD | SD | ABD | BD | SD |
| 100_5_22_15 | 630 | 504 | 458 | 458 | 0 | 458 | 458 | 0 | 458 | 458 | 0 |
| 100_5_46_15 | 693 | 604 | 585 | 585 | 0 | 585 | 585 | 0 | 585 | 585 | 0 |
| 100_10_26_15 | 370 | 266 | 262.8 | 261 | 3.5 | 261 | 261 | 0 | 261 | 261 | 0 |
| 100_10_48_15 | 344 | 279 | 296.8 | 285 | 7.4 | 261 | 261 | 0 | 261 | 261 | 0 |
| 100_20_22_15 | 353 | 161 | 172.3 | 157 | 10.4 | 134.8 | 133 | 1 | 137.3 | 136 | 1.5 |
| 100_20_46_15 | 394 | 194 | 209.2 | 192 | 10.3 | 181 | 181 | 0 | 181 | 181 | 0 |
| 100_20_47_9 | 390 | 180 | 180.2 | 170 | 6.4 | 138 | 136 | 1.4 | 142.3 | 140 | 1.8 |
| 200_10_50_15 | 763 | 529 | 428.8 | 419 | 8.7 | 389 | 387 | 0.8 | 389.2 | 388 | 1.1 |
| 200_10_50_9 | 817 | 546 | 517.7 | 487 | 30 | 465 | 465 | 0 | 465 | 465 | 0 |
| 200_20_145_15 | 480 | 309 | 246.5 | 232 | 10.3 | 161.3 | 153 | 3.8 | 165 | 160 | 5 |
| 200_20_54_15 | 488 | 336 | 319.7 | 308 | 16.9 | 270.7 | 269 | 1.4 | 273.7 | 272 | 1.8 |
| 200_40_133_15 | 512 | 214 | 204 | 196 | 9.1 | 171.7 | 164 | 2.1 | 175 | 172 | 4.8 |
| 200_40_45_15 | 616 | 206 | 201.3 | 180 | 11.2 | 164.3 | 164 | 0.8 | 166.7 | 164 | 3.8 |
| 100_10_64_9 | 533 | 488 | 371 | 371 | 0 | 371 | 371 | 0 | 371 | 371 | 0 |
| 100_10_65_15 | 426 | 256 | 320.5 | 316 | 3.1 | 305 | 305 | 0 | 305 | 305 | 0 |
| 200_40_130_9_D4 | 1710 | 896 | 690.2 | 652 | 30.4 | 513 | 513 | 0 | 513 | 513 | 0 |
| 200_40_45_9 | 821 | 208 | 200.3 | 181 | 11.9 | 175 | 172 | 2.1 | 175.8 | 172 | 2.9 |
| 200_40_90_9 | 963 | 192 | 204.7 | 195 | 7.5 | 175.5 | 172 | 1.1 | 178.2 | 174 | 4.6 |
| 200_40_91_15 | 519 | 184 | 216.2 | 199 | 11.8 | 163.3 | 155 | 3.8 | 168.2 | 163 | 5.5 |
| 100_20_23_9_D1 | 617 | 184 | 217.8 | 193 | 13.8 | 172 | 172 | 0 | 172 | 172 | 0 |
| 200_20_97_9 | 816 | 296 | 324.3 | 286 | 38.2 | 267.7 | 261 | 4 | 271 | 263 | 5.5 |
| 200_20_97_15 | 680 | 336 | 375.5 | 361 | 13.9 | 336 | 336 | 0 | 336 | 336 | 0 |
| 200_20_55_9 | 999 | 288 | 293.7 | 280 | 14.1 | 266.5 | 261 | 1.9 | 268.5 | 267 | 3.3 |
| AABD | | | 317.2 | | | 277.6 | | | 279.1 | | |
| ASD | | | 11.7 | | | 1.1 | | | 1.8 | | |

Modified Genetic Algorithm with Flexible Crossover for The Capacitated Electric Vehicle Routing Problem

1st Ajchara Phu-ang
Digital Transformation & Innovation Department
Collage of Innovation, Thammasat University
 Bangkok, Thailand
 ajchara.p@citu.tu.ac.th

2nd Arit Thammano
Faculty of Information Technology
King Mongkut's Institute of Technology Ladkrabang
 Bangkok, Thailand
 arit@it.kmitl.ac.th

Abstract— This paper proposed a modification of genetic algorithm with a new technique called the flexible crossover operation for solving the capacitated electric vehicle routing problem (CEVRP). The framework of this paper is based on the concept of the classic genetic algorithm (GA). To improve the performance of the genetic algorithm, two aspects have been proposed, 1) The Pre-Post mutation is present to obtain the ability of local search capacities. 2) The flexible crossover operation is proposed to enhance the diverse capabilities. The proposed algorithm has been evaluated and compared to the state-of-the-art algorithms. The experimental result on seven data sets demonstrated that the proposed algorithm is effective for solving a small and medium data set of capacitated electric vehicle routing problem.

Keywords— *Capacitated Electric Vehicle Routing, Genetic Algorithm, Adaptive Technique*

I. INTRODUCTION

Nowadays, electric vehicles are one product in the automotive industry which uses green energy to drive. Electric vehicles are used in multiple businesses, especially in transportation. The capacitated electric vehicle routing problem (CEVRP) is one problem in modern transportation areas which finding the shortest route and optimizing the vehicle capacities is the main objective. Therefore, the use of the evolutionary and metaheuristics algorithm is utilized for finding optimal solutions. In the past few years, many researchers have presented new algorithms for solving this kind of problem. Ya-Hui Jia et al. [1] present a new algorithm which based on the ant colony optimization named the novel bilevel ant colony optimization (BACO) for solving CEVRP. In their work, the model is divided into two parts. For the first part, the order-first split-second max-min ant system algorithm is utilized to generate routes according to the demands of customers. In the second part, a new method is present to decide the charging schedule according to the electricity constraint. For the comparison results, the performance of BACO is outstandingly better on most of the data set. Kui-Ting Chen et al. [2] proposed a new model that applied a particle swarm with adaptive multi-swarm strategy for solving the capacitated vehicle routing problem with pickups and deliveries. In this model, the adaptive multi-swarm strategy maintains the global search ability and local search capability. This paper divided a particle swarm into multiple small groups then employed a different technique to each group. The test results show that the proposed method can

reduce iteration times and the transportation cost. Yanfei Zhu et al. [3] employs the elitist genetic algorithm for solving electric vehicle routing problems. In this paper, the improved neighbor routing method is utilized in the initialization to generate the quality first customer in the initialization process. The rationale behind this concept is to create a suitable population then inherit to the next stage. The experimental studies show the effective performance of the algorithm when compared with other state of the art algorithms. R. Yesodha and T. Amudha [4] used the biologically inspired metaheuristic named the firefly algorithm for solving the capacitated vehicle routing optimization problem. Their work enriches the search performance of original firefly algorithm by proposed the intra and inter route operators as the heuristic method. The computational result shows the enhanced firefly are found better than standard firefly technique.

In this paper, the modified genetic algorithm is proposed. A flexible crossover operation that automatically employed the crossover probabilities is presented to enhance efficiency.

The rest of this paper is organized as follows: in section 2, the background theories are briefly described; in section 3, the step of proposed algorithm is presented. Section 4 shows the results, and a conclusion in section 5.

II. BACKGROUND THEORY

A. The Capacitated Electric Vehicle Routing Problem

Capacitated electric vehicle routing problem (CEVRP) [5] is categorized as one of vehicles routing problems (VRP) which is a subset in combinatorial optimization field. The CEVRP aims to minimize the vehicle routing distance while transporting the products.

In detail, each electric vehicle (EV) needs to manage the deliveries workload and energy capacity that continues to decrease. Each EV may be charged at the EV charge station multiple times, or it may not charge at all.

The constraint of the CEVRP is as follows:

- The route begins at the departure station.
- One customer can be visited exactly once.
- Electric energy and carry on capacity of each vehicle has limited.
- When delivered, each EV needs to return to the departure station.

$$Cost\ Function = \min\{Cust_{Dist} + Charge_{Dist}\} \quad (1)$$

$$Cust_{Dist} = \sum_{i=1}^N Eu_{i,j} + Eu_{N,Stp} \quad (2)$$

$$Charge_{Dist} = \sum_{j=1}^K Eu_{j,ChargS} \quad (3)$$

The cost function of CEVRP is calculated by Eq. (1), where

- $Cust_{(Dist)}$ represents a summation of the Euclidean distance between the customer_i and customer_j with the Euclidean distance between of the last visited customer and the departure station.
- $Charge_{(Dist)}$ states as the Euclidean distance of the customer_j and the EV charge station.

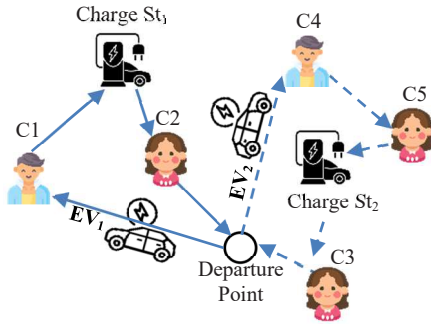


Fig. 1. The example of an electric vehicle routing problem

Figure 1 shows the example of an electric vehicle routing problem with 5 customers and 2 charging stations. The carry-on capacity equals 400 kg. around the trip. The EV needs to put in electric energy whenever it is below the energy capacity.

For electric vehicle routing₁: EV₁ starts at the departure point, then visit customer₁ (c₁) - charge station₁ (charge st₁) - customers₂ (c₂) and return to departure point.

For electric vehicle routing₂: EV₂ travel from departure point, then delivery products to customer₄ (c₄) - customers₅ (c₅) - charge station₂ (charge st₂) - customers₃ (c₃) and return to departure point.

B. Genetic Algorithm

Genetic algorithm (GA) [6] is an evolutionary algorithm which imitated the process of natural selection of organism. GA are admire used to search and create the high-quality solution for solving both combinatorial and continuous optimization problems. The process of GA beginning by the chromosome initialization process then the parent selection procedure is applied. Thereafter, the crossover and mutation operation are used to generate the offspring chromosome. The fittest chromosome is the result of GA.

III. PROPOSED ALGORITHM

The proposed algorithm is mainly based on the concept of the genetic algorithm which divided into five stages as follow:

A. The Encoding Stage

For the encoding method, the chromosome is divided into two parts. First part represents the routing of customer position that needs to visit arranged from left to right. The second part shows the sequence of the EV charge station. The energy recharge order is arranged from left to right.

Figure 2 shows the example of chromosome encoding. In the first part, the chromosome consists of two electric vehicles.

The Electric V₁ travel to two customers with one recharge : Customer number 1 (C1) - Charge St. 1 - Customer number 3 (C3).

The Electric V₂ visit to three customers with one recharge : Customer number 4 (C4) - Charge St. 2 - Customer number 5 (C5) - Customer number 2 (C2).

In the second part, the chromosome represent the arrangement of the EV charge station of Electric V₁ and Electric V₂.

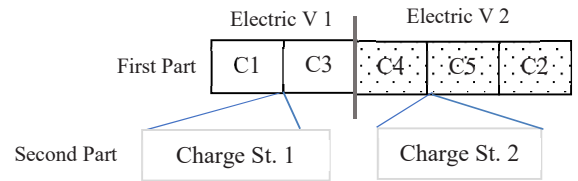


Fig. 2. The example of solution encoding

B. The initialization Stage

At this stage, the initial population of N chromosome is generated according to the routing constraint. Each customer is randomly assigned to a different EV. The EV charge station is randomly chosen when the energy of EV is almost over. After constructing the N chromosome, the fitness values of all chromosomes are evaluated according to equation 4.

$$Fitness_i = \frac{1}{Cost\ Function_i} \quad (4)$$

The initial population is divided into two groups. The first group contains the best 50% of initial population which inherited to the flexible crossover operation stage and the rest of initial population is transferred to the pre-mutation stage.

C. The Pre-Mutation Stage

In this stage, the initial population which carrying from the previous stage is rename as G2 chromosome. For each of the gene in the G2 chromosome, the random number between zeros and one is created then compared with a mutation probability (P_M). If the random number morethan the P_M, the customer_k is assigned to the nearest electric vehicle under the routing constrain. When the random number is less than the P_M, the customer_k is assigned to the 2nd or 3rd closest electric vehicle. The G2 chromosome is replaced by the mutate chromosome when the fitness value of the mutate chromosome is better than the G2 chromosome.

The rational behind this idea is to enhance the global search capabilities of the proposed model.

D. The Selection and Flexible Crossover Operation Stage

For the selection, the best 50% of the initial population and the G2 chromosome from the previous stage are integrated as the cross chromosome. Thereafter, sort the fitness values of the cross chromosomes from best to worst then separated into three bins.

The flexible crossover operation beginning by calculated the adaptive crossover probability (APC) according to equation (5). The APC of each cross chromosome started by 0.8. When the offspring chromosome worse than the parent chromosome, the APC will gradually drop about 3%. However, the APC will gradually return by 3% when the offspring chromosome better than the parent chromosome.

Means that, the use of flexible crossover operation will increase the chance that the high quality chromosomes of each bin are selected in the right proportion.

$$AP_{C_i} = \frac{P_{C(i)} * Fitness_i}{\sum_{j=1}^N Fitness_j} \quad (5)$$

When a set of parent chromosome is selected, the multiple point crossover operation is applied to the first part and the electric charge station of this chromosome is reassigned.

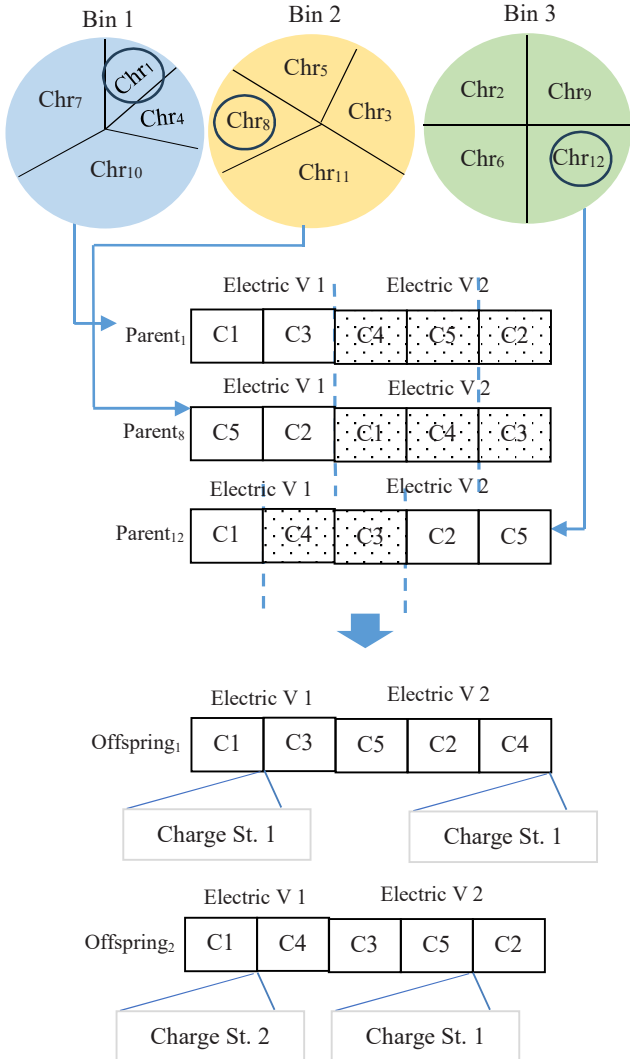


Fig. 3. The example of the flexible crossover operation

E. The Post-Mutation Stage

The post-mutation is utilized to the offspring chromosome from the previous stage. For each offspring chromosome, we randomly generated the number between zero and one. If the random number less than the mutation probability (P_M), we applied the iterated local search (ILS) which embedded the 2-Opt and 3-Opt algorithm.

For the iterated local search,

Firstly, the new one chromosome is generated from the offspring chromosome by the 2-opt algorithm.

Secondly, defined the new chromosome as the starting solution and determined it as the best solution.

Thirdly, employed the 2, 3-Opt algorithm to generate the neighborhood chromosome from the starting solution. The best of the neighborhood chromosome and the offspring chromosome is always accepted.

This local search is terminated when reach the criteria.

F. The Final Stage

In the final stage, the stopping conditions are checked. If any of the stopping conditions below are met, this algorithm will be terminated.

- The maximum number of iterations has been reached.
- Eighty percent of the population shares the same fitness value.

If not reach the stopping condition, the initial population of the next iteration is selected from all chromosomes contained in the current generation, both the parents and the offspring; then go back to the initialization stage.

IV. EXPERIMENTAL RESULTS

A. Test Data Set

In this experiment, the performance of the proposed algorithm is evaluated and compared to a state-of-the-art algorithm. The data set is used in this article is obtained from the benchmark set for the IEEE WCCI-2020 Competition on Evolutionary Computation for the Electric Vehicle Routing Problem [7] which briefly described as follows:

This test set consists of 7 small problem instances.

- E-n22-k4: consists of 4 vehicles with 21 customers, the number of EV charging stations is 8 and the maximum load of an EV is 6000.
- E-n23-k3: consists of 3 vehicles with 22 customers, the number of EV charging stations is 9 and the maximum load of an EV is 4500.
- E-n30-k3: consists of 3 vehicles with 29 customers, the number of EV charging stations is 6 and the maximum load of an EV is 4500.
- E-n33-k4: consists of 4 vehicles with 32 customers, the number of EV charging stations is 6 and the maximum load of an EV is 8000.
- E-n51-k5: consists of 5 vehicles with 50 customers, the number of EV charging stations is 5 and the maximum load of an EV is 160.
- E-n76-k7: consists of 7 vehicles with 75 customers, the number of EV charging stations is 7 and the maximum load of an EV is 220.
- E-n101-k8: consists of 8 vehicles with 100 customers, the number of EV charging stations is 9 and the maximum load of an EV is 200.

B. Results and discussion

Table 1 illustrates the comparative results of the proposed algorithm and state-of-the-art metaheuristic algorithms. The column labelled "BKS" shows the best known of the problem data set. The row labeled with "Avg. Dev. BKS(%)" reports the average percentage deviation from the best known. The following are summaries of the comparison results.

All three algorithms tie for first place for the E-n22-k4, E-n23-k3 and E-n30-k3. For the E-n33-k4, the VNS comes in first place, followed by the proposed algorithm. For the E-n51-k5, E-n76-k7 and E-n101-k8, the proposed algorithm outperforms other compared methods.

TABLE I. COMPARATIVE RESULT

| Problem Set | Result | | | |
|------------------|--------|---------------|---------------|---------------|
| | BKS | Proposed | GA [8] | VNS [9] |
| E-n22-k4 | 384.67 | 384.67 | 384.67 | 384.67 |
| E-n23-k3 | 571.94 | 571.94 | 571.94 | 571.94 |
| E-n30-k3 | 509.47 | 509.47 | 509.47 | 509.47 |
| E-n33-k4 | 840.14 | 842.90 | 844.25 | 840.43 |
| E-n51-k5 | 529.90 | 534.26 | 529.90 | 543.26 |
| E-n76-k7 | 692.64 | 693.52 | 697.27 | 697.89 |
| E-n101-k8 | 839.29 | 840.17 | 852.69 | 853.34 |
| Avg. Dev. BKS(%) | | 0.197 | 0.393 | 0.712 |

V. CONCLUSION

This paper presents a modified version of the genetic algorithm for solving the Capacitated Electric Vehicle Routing Problem. The flexible crossover operation is

employed to enhance the diversity capability of the proposed algorithm. The iterated local search technique embedded in the mutation process to avoid the algorithm getting stuck in the local optimum area. Testing with the standard data set benchmark, our proposed algorithm proved to be the most effective among the three algorithms tested.

REFERENCES

- [1] Ya-Hui Jia ,Yi Mei and Mengjie Zhang, "A Bilevel Ant Colony Optimization Algorithm for Capacitated Electric Vehicle Routing Problem," IEEE TRANSACTIONS ON CYBERNETICS, VOL. 52, NO. 10, pp. 10855-10868, 2022
- [2] Kui-Ting Chen , Yijun Dai , Ke Fan and Takaaki Baba, "A Particle Swarm Optimization with Adaptive Multi-Swarm Strategy for Capacitated Vehicle Routing Problem," International Conference on Industrial Networks and Intelligent Systems, pp. 79-83, 2015
- [3] Y. Zhu, K. Y. Lee and Y. Wang, "Adaptive Elitist Genetic Algorithm With Improved Neighbor Routing Initialization for Electric Vehicle Routing Problems," in IEEE Access, vol. 9, pp. 16661-16671, 2021, doi: 10.1109/ACCESS.2021.3053285.
- [4] R. Yesodha and T. Amudha, "An Improved Firefly Algorithm for Capacitated Vehicle Routing Optimization," 2019 Amity International Conference on Artificial Intelligence (AICAI), Dubai, United Arab Emirates, 2019, pp. 163-169, doi: 10.1109/AICAI.2019.8701269.
- [5] Woller, David. "Electric Vehicle Routing Problem." (2020).
- [6] Lakhmi C. Jain, Zhengxin Chen, "Industry, Artificial Intelligence in," Encyclopedia of Information Systems, pp. 583-597, 2003.
- [7] Michalis Mavrovouniotis, "Benchmark Set for the IEEE WCCI-2020 Competition on Evolutionary Computation for the Electric Vehicle Routing Problem," 2020.
- [8] V. Q. Hien, T. C. Dao, T. B. Thang, H. T. T and Binh, "Genetic Algorithm", 2020 IEEE Congress on Computational Intelligence, 2020.
- [9] M. Schneider, A. Stenger, and D. Goeke, "The electric vehicle-routing problem with time windows and recharging stations," Transport. Sci., vol. 48, no. 4, pp. 500-520, 2014

Multiple Independent DE Optimizations to Tackle Uncertainty and Variability in Demand in Inventory Management

Sarit Maitra
Business School
Alliance University
Bengaluru, India
sarit.maitra@gmail.com

Sukanya Kundu
Business School
Alliance University
Bengaluru, India
sukanya.kundu@alliance.edu.in

Vivek Mishra
School of Applied mathematics
Alliance University
Bengaluru, India
vivek.mishra@alliance.edu.in

Abstract— To determine the effectiveness of metaheuristic Differential Evolution optimization strategy for inventory management (IM) in the context of stochastic demand, this empirical study undertakes a thorough investigation. The primary objective is to discern the most effective strategy for minimizing inventory costs within the context of uncertain demand patterns. Inventory costs refer to the expenses associated with holding and managing inventory within a business. The approach combines a continuous review of IM policies with a Monte Carlo Simulation (MCS). To find the optimal solution, the study focuses on meta-heuristic approaches and compares multiple algorithms. The outcomes reveal that the Differential Evolution (DE) algorithm outperforms its counterparts in optimizing IM. To fine-tune the parameters, the study employs the Latin Hypercube Sampling (LHS) statistical method. To determine the final solution, a method is employed in this study which combines the outcomes of multiple independent DE optimizations, each initiated with different random initial conditions. This approach introduces a novel and promising dimension to the field of inventory management, offering potential enhancements in performance and cost efficiency, especially in the presence of stochastic demand patterns.

Keywords— differential evolution; genetic algorithm; inventory management; non-linear optimization; stochastic demand.

I. INTRODUCTION

Inventory management (IM) is a critical aspect that is linked to business profitability in a modern organization. With increasing uncertainties and complexities, businesses need data-driven computational techniques to manage inventory. Real-world issues like stockouts, excess inventory, and revenue losses can be addressed using mathematical optimization approaches. In the past, several studies have made significant contributions to IM and highlighted the importance of sophisticated computational techniques to optimize inventory decisions to manage demand variations (e.g., [19]; [33]; [6] etc.). Building on their arguments, recent studies highlighted the growing complexities in IM driven by demand uncertainties, which have led to the development of computation-intensive simulation and optimization methods ([44] and [10]). Several recent studies have emphasized the relevance of optimization throughout the value chain (e.g., [24], [25], [11], etc.).

Despite several available works, the advancement of technology, globalization, and evolving customer expectations have made IM a complex task and an active research area. Researchers are constantly exploring innovative

approaches and methodologies to handle this complexity effectively. Through this work, we address the questions of how to effectively manage inventory with stochastic demand, focusing on a continuous review policy approach, and how to optimize the total cost. Meta-heuristic optimization techniques such as Grey Wolf Optimizer (GWO), Whale Optimization Algorithm (WOA), Metaheuristics (MH) with Simulated Annealing (SA), Monte Carlo Simulation (MCS) with Bayesian Algorithm (BA), and Differential Evolution (DE) have been explored in this work. The findings reveal that DE is the most effective and simple heuristic optimization to deal with stochastic demands.

In the end, this work implements Adaptive DE by combining several DE variants and dynamically allotting computing resources based on their individual historical performance. The method helps to mitigate the risk of local optima and enhance the optimization process. The goal is to explore different regions of the parameter space to find a robust and reliable solution. The efficacy of the optimized policy may be sensitive to demand distribution. Therefore, this work performed a sensitivity analysis to assess the robustness of the policy under various scenarios.

The major contribution of this study is to experiment with a simulation-optimization model that can be applied with DE to select a nearly ideal IM policy under stochastic demand. The finding shows the proposed simulation optimization efficiently solves inventory policies by using the structure of the objective function rather than an exhaustive approach.

II. PREVIOUS WORK

The importance of optimization is reflected in several studies (e.g., [25]; [24]; [11]; etc.). Optimization approaches offer a systematic method to further enhance inventory management ([31]; [28]). Studies (e.g., [33]; [34]; [26]) and subsequently industry reports suggest that IM costs can range a sizeable portion, which is approximately 20–40% of the total supply chain costs. It has been proposed that the effective simulation-optimization approach can bring a 16% reduction in costs by implementing the optimal policy. [12].

Several studies have discussed different optimization techniques ([14]; [4]; [42]). However, none of the works guaranteed an optimal solution if the original assumptions and considerations were violated [15]. On the same note, when using optimization techniques to solve IM problems, it is important to carefully consider the assumptions and constraints underlying the model [29]. These studies highlighted the importance of incorporating uncertainty and

variability into the model because real-world inventory systems are often subject to such factors. Moreover, IM under uncertainty is challenging to solve due to the non-linearity of the model and several local optimum solutions ([8]; [17]). In recent times, metaheuristic algorithms have frequently been employed as powerful solutions for IM ([13]; [7]). Owing to their ability to effectively search for the solution space of complicated problems, meta-heuristic algorithms have received considerable attention in recent years (e.g., [1]; [9]; [41]; [7]; [34]; etc.). A recent study employed meta-heuristic algorithms for inventory optimization by presenting GWO and WOA as two novel solution approaches [30]. Though GWO was introduced to solve optimization problems [e.g., 23], some researchers criticized the fact that GWO mostly suffers from a lack of population diversity ([29]; [39]). To overcome this limitation, an improved version of GWO was presented [27]. Some authors emphasized the application of SA in the context of IM and the efficiency of SA in resolving the difficulties brought on by the unpredictability of demand and the requirement to optimize inventory policies under uncertainty (e.g., [40]; [21] etc.).

To overcome the limitations and improve algorithm efficiency, DE was introduced effectively for optimization [36]. It was compared with different optimization approaches; however, the DE method outperformed all other approaches in terms of the required number of function evaluations necessary to locate a global minimum of the test functions. Meta-heuristic approaches for inventory forecasting were also studied, which revealed the superior performance of DE even compared to CNN-LSTM [43]. The superiority of DE was supported by an exhaustive literature review, which revealed that 158 out of 192 papers were published between 2016 and 2021, showing that academics have improved DE to increase its effectiveness and efficiency in handling a variety of optimization challenges [2].

Moreover, the MCS method is commonly used to propagate the uncertainties of random inputs in the case of stochastic demand (e.g., [16]; [14]; [31]). This establishes that simulation is an integral part of IM during stochastic demands. MCS allows the incorporation of stochastic variability in demand patterns. The growing body of work in metaheuristic optimization indicates ongoing research efforts to improve the effectiveness of these techniques and their application in solving various optimization challenges in inventory management.

III. METHODOLOGY

A three-stage approach employing a comprehensive methodology was adopted in this study to analyze and optimize the IM policy. Fig. 1 displays the methodological framework applied in this study, with shaded areas for various stages. First, the demand for products was collected over 365 days. The data were simulated to estimate the probability of experiencing various demand levels. These simulations allowed us to create multiple scenarios and observe the potential outcomes. The policies considered herein include continuous reviews and cross-docking. The performance of these policies was compared based on their ability to minimize total costs while ensuring an acceptable level of service.

$$Total_{cost} = Purchase_{cost} + Order_{cost} + Holding_{cost} + Stockout_{cost} \quad (1)$$

By considering all these costs, we aim to develop an inventory policy that minimizes costs and maximizes profits.

The results of the simulations are analyzed and interpreted to provide insights into the effectiveness of each policy. Once the optimal policy is identified, the next goal is to determine the optimal inventory levels that balance the $Total_{costs}$. With both the goals in place, in stage three (blue shaded area), the various optimization techniques (e.g., GWO, MH + SA, MCS, WO, MCS + BO, and DE) are employed.

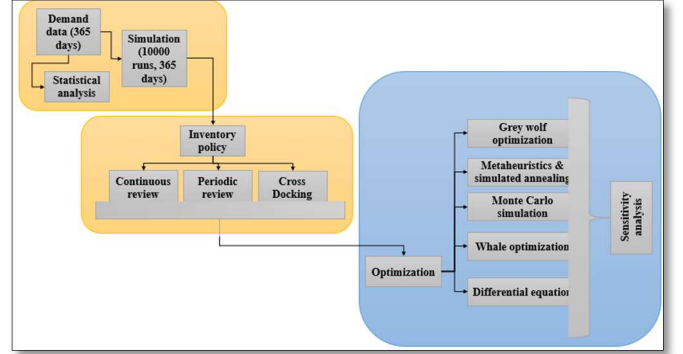


Fig. 1. Methodological framework (Source: Authors)

By employing the optimization technique and running simulations for a full year (365 days), we aim to fine-tune the inventory policy to minimize the $total_{costs}$ while considering the uncertainties in demand. In the final stage, sensitivity analysis is performed to identify different convergence rates, quality of solutions, and computational efficiency.

IV. DATA ANALYSIS

The business case selected here examines the sale of four distinct products and considers the adoption of a suitable IM policy. The goal is to minimize the total cost associated with purchasing, ordering, and holding inventory by optimizing inventory levels. We use historical demand data to calculate the central tendency of the data. Table I displays the statistics related to the four products.

- Pr A, Pr B, Pr C, and Pr D are four distinct products.
- $Purchase_{costs}$ = cost of purchasing one unit of the item from the supplier.
- $Lead_{time}$ = time it takes for the supplier to deliver the item after placing an order.
- $Size$ = size or quantity of each item.
- $Selling_{price}$ = price at which each item is sold to the customers.
- $Starting_{stock}$ = initial stock level of each item in the inventory.
- $Mean$ = average demand for each item over a given period.
- Std_{dev} = Std_{dev} of demand for each item over a given period.
- $Order_{cost}$ = cost of placing an order with the supplier.
- $Holding_{cost}$ = cost of holding one unit of inventory for a given period.

- Probability = probability of a stock-out event occurring, i.e., the probability of demand exceeding the available inventory level.
- $Demand_{lead}$ = lead time demand for each item, i.e., the demand that is expected to occur during the lead time.

TABLE I. SUMMARY STATISTICS

| | Pr A | Pr B | Pr C | Pr D |
|--------------------|---------|--------|---------|--------|
| $Purchase_{cost}$ | € 12 | € 7 | € 6 | € 37 |
| $Lead_{time}$ | 9 | 6 | 15 | 12 |
| Size | 0.57 | 0.05 | 0.53 | 1.05 |
| $Selling_{price}$ | € 16.10 | € 8.60 | € 10.20 | € 68 |
| $Starting_{stock}$ | 2750 | 22500 | 5200 | 1400 |
| Mean | 103.50 | 648.55 | 201.68 | 150.06 |
| Std_{dev} | 37.32 | 26.45 | 31.08 | 3.21 |
| $Order_{cost}$ | € 1000 | € 1200 | € 1000 | € 1200 |
| $Holding_{cost}$ | € 20 | € 20 | € 20 | € 20 |
| Probability | 0.76 | 1.00 | 0.70 | 0.23 |
| $Demand_{lead}$ | 705 | 3891 | 2266 | 785 |

Fig. 2 displays the KDE plots of the demand distribution of the products over 365 days. The shapes of the curves provide insight into the underlying stochastic distribution of the data. The isolated peaks in the curves show potential outliers in the demand data.

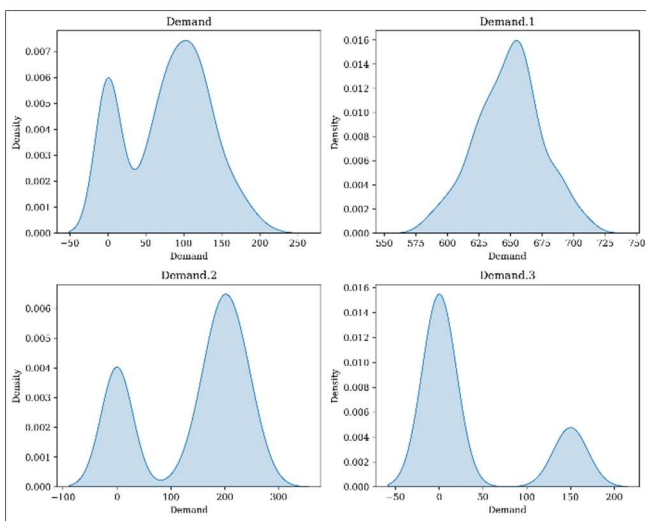


Fig. 2. KDE plots of demand distribution

A. ABC analysis

ABC analysis is performed to categorize items based on their initial IM values. The analysis follows the Pareto Principle for the annual consumption value of each product. Considering CV = consumption value, then,

$$CV_{annual} = Demand * Selling_{price} \quad (2)$$

$$CV_{cumulative} = \sum(CV_{annual}) \quad (3)$$

$$Cumulative\% = \frac{\sum(CV_{annual})}{CV_{cumulative}} \quad (4)$$

- Product A: $CV_{annual} = Demand_{annual} * Selling_{price_{annual}} = 705 * €16.10 = €11,335.50$;
- Product B: $CV_{annual} = 3891 * €8.60 = €33,516.60$;
- Product C: $CV_{annual} = 2266 * €10.20 = €23,099.20$;
- Product D: $CV_{annual} = €53,380.00$.

$$CV_{cumulative} = CVA + CVB + CVC + CVD = €11,335.50 + €33,516.60 + €23,099.20 + €53,380.00 = €121,331.30 \quad (5)$$

- $Cumulative\%A = CVA / CV_{cumulative} = €11,335.50 / €121,331.30 \approx 0.0934$;
- $Cumulative\%B = CVB / CV_{cumulative} = €33,516.60 / €121,331.30 \approx 0.2763$;
- $Cumulative\%C = CVC / CV_{cumulative} = €23,099.20 / €121,331.30 \approx 0.1903$;
- $Cumulative\%D = CVD / CV_{cumulative} = €53,380.00 / €121,331.30 \approx 0.4399$.

ABC categories (A, B, and C) were assigned based on predefined cutoff points. Here, cutoff A was set at 0.8, and cutoff B was set at 0.95. Products with cumulative % below cutoff A were assigned category A, products with cumulative % between cutoff A and cutoff B were assigned category B, and products with cumulative % above cutoff B were assigned category C. Table II lists the metrics used in the analysis.

ABC analysis classifies products according to their consumption value, with Category A being the most critical products, Category B representing products of moderate importance, and Category C representing products of lower relevance.

B. Latin Hypercube Sampling (LHS)

The LHS is used to sample parameter combinations in a more evenly distributed manner. Table II lists the parameter values associated with the lowest average costs. The objective was to identify combinations that resulted in low total costs, indicating an efficient IM. The parameter space for calibration was taken as $reorder_{point} = \{100, 200, 300\}$, $safety_{stock} = \{50, 100, 50\}$, $lead_{time} = \{0.8, 1.0, 1.2\}$, and $order_{quantity} = \{0.8, 1.0, 1.2\}$. For experimentation and calibration, we treated $reorder_{point}$ and $safety_{stock}$ as separate entities. This helped for a comprehensive exploration of different inventory control strategies.

TABLE II. LATIN HYPERCUBE SAMPLING REPORT

| | Pr A | Pr B | Pr C | Pr C | Lead time | Order Qty | Average cost |
|---------------|------|------|------|------|-----------|-----------|--------------|
| Reorder point | 753 | 6164 | 1425 | 383 | 0.8 | 0.8 | 77,540 |
| Safety stock | 377 | 3082 | 712 | 192 | | | |

The number of experiments was set at 27 because, based on orthogonal arrays, it represents the total number of unique combinations for the specified parameter space.

V. SIMULATION & INVENTORY SYSTEMS

CR (continuous review) is more suitable for managing inventory with stochastic demand ([22]; [3]; [36]). An extensive literature review of over seven decades suggests that continuous policy is the most employed policy in stochastic inventory literature [28]. Taking a clue from their work, we examined both CR and CD in our empirical analysis. MCS was used to simulate and observe the cost and inventory levels over multiple simulation runs (10,000) for a period of 365 days.

Table III depicts the output; the reorder points and safety stocks for the analysis have been taken from Table II.

TABLE III. INVENTORY REVIEW SYSTEMS

| System definition | Average cost | Average inventory level |
|-------------------|--------------|-------------------------|
| Continuous review | 515,262 | 21,251 |
| Cross docking | 515,268 | 21,253 |

Average cost and average inventory levels are calculated as:

$$\begin{aligned} average_{cost} &= total_{cost} / (num_{simulations} \\ &\quad * num_{periods}) \\ average_{inventory_level} \\ &= total_{inventory_level} / (num_{simulations} \\ &\quad * num_{periods}) \end{aligned}$$

The CD strategy involves minimizing the need for inventory storage by transferring products directly from the supplier to the customer. We implemented CD as additional logic within the IM simulation.

A. Optimization

Multiple optimization algorithms (GWO, SA, MCS, MCS with BO, WO, and DE) were tested to get the optimal cost.

1) Cost breakdown:

The total cost is computed based on the following parameters:

- Purchase Cost is computed as $unit\ purchase_{cost} * max(order_{quantities}, 0)$.
- Order Cost is only applied when the order quantity is greater than zero and is computed as $unit\ order_{cost} * (order_{quantities} > 0)$.
- Holding Cost is computed as $unit\ holding_{cost} * max(inventory - demand, 0)$.
- Stockout Cost is inferred from the equation $unit\ holding_{cost} * max(demand - inventory, 0)$.

$$f(x) = \sum_{i=1}^n (PurchaseCost_i + OrderCost_i + HoldingCost_i + StockoutCost_i) \quad (6)$$

These costs can be subtracted from the revenue to give the corresponding profit for that one realization of the year. Eq. (7) formulates the annual profit, which is the future direction of this work:

$$SP_i \sum_{t=1}^{365} S_{i,t} - \left\{ \left(\frac{20V_i}{365} \right) \sum_{t=1}^{365} I_{i,t} + N_i C_{o,i} + \sum_{t=1}^{365} c_i P_{i,t} \right\} \quad (7)$$

Our goal is to minimize costs. Table IV presents a summary of all the algorithms tested on the given parameters and MCS to simulate the data for 365 days. We chose meta-heuristic techniques that are designed to tackle complex and non-linear optimization issues where typical optimization techniques struggle to find the global optimum.

TABLE IV. OPTIMAL POLICY FOR 365 DAYS

| Optimization | Stock | | | | Total Cost |
|---------------|-------|--------|-------|-------|------------|
| | Pr A | Pr B | Pr C | Pr D | |
| GWO | 110 | 1836 | 0 | 21 | 17,391,348 |
| SA | 2,600 | 21,843 | 4,984 | 1,268 | 6,179,739 |
| MCS | 1,527 | 455 | 4,768 | 599 | 631,398 |
| WO | 1,070 | 10,865 | 3,787 | 150 | 504,939 |
| MCS with BO | 2,750 | 14,724 | 4,465 | 1,350 | 254,137 |
| DE (best1bin) | 1220 | 13204 | 3359 | 1317 | 250,774 |

Based on the $Total_{cost}$, the optimization method with the lowest total cost appears to be DE (best1bin), with the corresponding cost of 250,774. The future direction of our work is to check if DE can be further optimized.

B. Multiple Independent DE Optimizations

In this approach, we performed optimization using multiple optimizers (five optimizers of DE with different random initial conditions) in parallel to determine the best parameters and cost. By using this approach, we aim to mitigate the impact of random variations in the MCS and increase the likelihood of finding a robust and optimal solution for IM. Considering, the below parameters:

- $purchase_{cost} = Pc_1, Pc_2, \dots, Pc_n$, where Pc_i is the $purchase_{cost}$ of product i
- $lead_{time} = L_1, L_2, \dots, L_n$, where L_i is the $lead_{time}$ of product i
- $sizes = s_1, s_2, \dots, s_n$, where s_i is the sizes of product i
- $selling_{price} = SP_1, SP_2, \dots, SP_n$, where SP_i is the $selling_{price}$ of product i
- $starting_{stock} = ss_1, ss_2, \dots, ss_n$, where ss_i is the initial inventory level of product i
- $means = \mu_1, \mu_2, \dots, \mu_n$, where μ_i is the mean demand of product i ;
- $standard\ deviation = \sigma_1, \sigma_2, \dots, \sigma_n$, where σ_i is the standard deviation of demand of product i
- $order\ cost = C_1, C_2, \dots, C_n$, where C_i is the order cost of product i
- $holding_{cost} = V_1, V_2, \dots, V_n$, where V_i is the order cost of product i
- $probabilities = p_1, p_2, \dots, p_n$, where p_i is the probability of demand for product i
- $demand\ lead = D_1, D_2, \dots, D_n$, where D_i is the demand lead time of product i .

- Parameters space of optimization: $bounds = [(0, ss_1), (0, ss_2) \dots (0, ss_n)]$, where each tuple represents the lower and upper bounds of inventory levels of the respective products.

MCS and objective function (x), where $x = x_1, x_2, x_3, \dots, x_n$ representing inventory levels.

$$reorder\ levels = [means1 * L_1 + \sqrt{L_1} * \sigma_1, \dots, meansn * \sqrt{L_n} * \sigma_n]$$

$$order_{quantity} = [\max(reorder_{level_1} - x_1, 0), \dots, \max(reorder_{level_n} - x_n, 0)]$$

$total_{cost}$ = for each day and product: if $x_i < reorder_{level}$, $order_{quantity} = order_{quantity}_i$ (this checks if the current inventory level is below the reorder level). If it is, the order quantity is set to the predetermined value for that product ($order_{quantity}_i$), indicating that an order should be placed to replenish the inventory.

- $increaseInventory(x_i) = x_i + orderQuantity$
- $increaseTotalCost = totalCost +$
- $decreaseInventory(x_i) = x_i - dailydemand$
if $x_i < 0, x_i = 0$ and $totalCost = totalCost + holdingCost/2$
- if $(d + 1)\% lead_{times_i} = 0$,
 $decrease\ inventory\ again: x_i = x_i - dailydemand_i$ and $totalCost = totalCost + holding_{cost_i} * x_i$

$$mean_{cost} = \frac{1}{num_{samples}} \sum_{s=1}^{num_{samples}} total_{cost_s} \quad (8)$$

$$MultipleDE_{optimization} = [result_1, result_2, \dots, result_{num_{ensemble}}] \quad (9)$$

where, each result represents the optimization result of one DE member. Table V reports the output.

TABLE V. MULTIPLE INDEPENDENT DE OPTIMIZATIONS

| Optimization | Stock | | | | Total Cost |
|-------------------------|-------|------|------|------|------------|
| | Pr A | Pr B | Pr C | Pr D | |
| Multiple Independent DE | 2567 | 9063 | 4277 | 1322 | 249,128 |

The total cost has been marginally reduced from 250,774 (Table IV) to 249,128 (Table V). The stocks are optimized from 19,100 (1220, 13204, 3359, 1317) to 17,229 (2,567, 9,063, 4,277, 1,322). The mutation rate and crossover rate are adaptively adjusted during the process based on iteration success or failure, ensuring a balance between exploration and exploitation during optimization.

C. Sensitivity analysis

Sensitivity analysis is employed on this to ensure the robustness of the multiple independent DE optimizations model under different scenarios. The analysis was performed on the population size parameters of the DE algorithm. The goal was to evaluate the effects of different population sizes on the optimization results. Different values of population

size, for example, 10, 20, 50, and 100, were tested to observe how they affected the optimization results. By exploring different population sizes, we have assessed their impact on convergence behavior and the quality of the obtained solutions.

TABLE VI. SENSITIVITY ANALYSIS

| Analysis | Stock | | | | Total Cost |
|---------------------|-------|--------|-------|-------|------------|
| | Pr A | Pr B | Pr C | Pr D | |
| Population size 10 | 2,271 | 4,736 | 4,146 | 1,321 | 251,238 |
| Population size 20 | 1,901 | 20,134 | 3,355 | 1,325 | 249,780 |
| Population size 50 | 1,525 | 12,753 | 4,992 | 1,326 | 246,251 |
| Population size 100 | 1,552 | 9,667 | 3,695 | 1,326 | 246,745 |

By varying the population size in the DE, we can observe how it affects the optimization results. In this case, the observed differences in total cost are small, indicating that the model's performance is stable and not heavily influenced by changes in population size.

D. Critical findings

This study emphasizes the importance of optimization in IM, specifically in the context of stochastic demand and supply disruptions. DE is a successful method for establishing near-optimal inventory policies when combined with best/1/bin mutation strategy, LHS, and multiple independent DE optimizations. Sensitivity analysis with varying population sizes confirmed the stability of the optimization model.

VI. CONCLUSION

This study highlighted the significance of optimization techniques, particularly DE and multiple independent DE optimizations, in achieving cost-effective and robust inventory management strategies in the face of uncertain demand and supply disruptions. Empirical analysis was conducted using 365-day demand data and reported the optimal policy, along with cost comparisons. The study also discussed the use of LHS for efficient parameter sampling. ABC analysis was applied to categorize items and assign Pareto classes to products. The optimal policy and inventory levels were determined through simulations and optimization techniques. A sensitivity analysis assessed convergence rate, solution quality, and computational efficiency. This comprehensive approach contributes to IM by improving efficiency and cost-effectiveness while addressing demand uncertainties.

REFERENCES

- [1] Abdi, A., Abdi, A., Fathollahi-Fard, A. M., & Hajiaghahi-Keshteli, M. (2021). A set of calibrated metaheuristics to address a closed-loop supply chain network design problem under uncertainty. *International Journal of Systems Science: Operations & Logistics*, 8(1), 23-40.
- [2] Ahmad, M. F., Isa, N. A. M., Lim, W. H., & Ang, K. M. (2022). Differential evolution: A recent review based on state-of-the-art works. *Alexandria Engineering Journal*, 61(5), 3831-3872.

- [3] Axsäter, S. (2015). *Inventory control* (Vol. 225). Springer.
- [4] Azadi, Z., Eksioğlu, S. D., Eksioğlu, B., & Palak, G. (2019). Stochastic optimization models for joint pricing and inventory replenishment of perishable products. *Computers & industrial engineering*, 127, 625-642.
- [5] Ballou, R. H. (2000). *Business logistics/supply chain management. Planning, organizing and controlling the supply chain* (5th ed.). USA: Pearson-Prentice Hall
- [6] Chen, F., Drezner, Z., Ryan, J. K., & Simchi-Levi, D. (2000). Quantifying the bullwhip effect in a simple supply chain: The impact of forecasting, lead times, and information. *Management science*, 46(3), 436-443.
- [7] Fahimnia, B., Davarzani, H., & Eshragh, A. (2018). Planning of complex supply chains: A performance comparison of three meta-heuristic algorithms. *Computers & Operations Research*, 89, 241-252.
- [8] Fallahi, A., Bani, E. A., & Niaki, S. T. A. (2022). A constrained multi-item EOQ inventory model for reusable items: Reinforcement learning-based differential evolution and particle swarm optimization. *Expert Systems with Applications*, 207, 118018.
- [9] Faramarzi-Oghani, S., Dolati Neghabadi, P., Talbi, E. G., & Tavakkoli-Moghaddam, R. (2022). Meta-heuristics for sustainable supply chain management: A review. *International Journal of Production Research*, 1-31.
- [10] Fathi, M. R., Nasrollahi, M., & Zamanian, A. (2020). Mathematical modeling of sustainable supply chain networks under uncertainty and solving it using metaheuristic algorithms. *Industrial Management Journal*, 11(4), 621-652.
- [11] Fonseca, L. M., & Azevedo, A. L. (2020). COVID-19: outcomes for global supply chains. *Management & Marketing. Challenges for the Knowledge Society*, 15(s1), 424-438.
- [12] Franco, C., & Alfonso-Lizarazo, E. (2020). Optimization under uncertainty of the pharmaceutical supply chain in hospitals. *Computers & Chemical Engineering*, 135, 106689.
- [13] Goodarzian, F., Wamba, S. F., Mathiyazhagan, K., & Taghipour, A. (2021). A new bi-objective green medicine supply chain network design under fuzzy environment: Hybrid metaheuristic algorithms. *Computers & Industrial Engineering*, 160, 107535
- [14] Gruler, A., Panadero, J., de Armas, J., Pérez, J. A. M., & Juan, A. A. (2018). Combining variable neighborhood search with simulation for the inventory routing problem with stochastic demands and stock-outs. *Computers & Industrial Engineering*, 123, 278-288.
- [15] Jackson, I., Tolujevs, J., & Kegenbekov, Z. (2020). Review of inventory control models: a classification based on methods of obtaining optimal control parameters. *Transport and Telecommunication*, 21(3), 191-202
- [16] Janssen, L., Sauer, J., Claus, T., & Nehls, U. (2018). Development and simulation analysis of a new perishable inventory model with a closing days constraint under non-stationary stochastic demand. *Computers & Industrial Engineering*, 118, 9-22.
- [17] Khalilpourazari, S., Pasandideh, S. H. R., & Niaki, S. T. A. (2016). Optimization of multi-product economic production quantity model with partial backordering and physical constraints: SQP, SFS, SA, and WCA. *Applied Soft Computing*, 49, 770-791.
- [18] Kiuchi, A., Wang, H., Wang, Q., Ogura, T., Nomoto, T., Gupta, C., ... & Zhang, C. (2020, August). Bayesian optimization algorithm with agent-based supply chain simulator for multi-echelon inventory management. In *2020 IEEE 16th International Conference on Automation Science and Engineering (CASE)* (pp. 418-425). IEEE.
- [19] Koumanakos, D. P. (2008). The effect of inventory management on firm performance. *International journal of productivity and performance management*, 57(5), 355-369.
- [20] Lu, Chao, Gao, Liang, & Yi, Jin. (2018). Grey wolf optimizer with cellular topological structure. *Expert Systems with Applications*, 107, 89-114.
- [21] Meisheri, H., Sultana, N. N., Baranwal, M., Baniwal, V., Nath, S., Verma, S., ... & Khadilkar, H. (2022). Scalable multi-product inventory control with lead time constraints using reinforcement learning. *Neural Computing and Applications*, 34(3), 1735-1757.
- [22] Melo, M. T., Nickel, S., & Saldanha-Da-Gama, F. (2009). Facility location and supply chain management—A review. *European journal of operational research*, 196(2), 401-412.
- [23] Mirjalili, Seyedali, Mirjalili, Seyed Mohammad, & Lewis, Andrew. (2014). Grey wolf optimizer. *Advances in Engineering Software*, 69, 46-61. doi: 10.1016/j.advengsoft.2013.12.007.
- [24] Modgil, S., Singh, R. K., & Hannibal, C. (2022). Artificial intelligence for supply chain resilience: learning from Covid-19. *The International Journal of Logistics Management*, 33(4), 1246-1268.
- [25] Moons, K., Waeyenbergh, G., & Pintelon, L. (2019). Measuring the logistics performance of internal hospital supply chains—a literature study. *Omega*, 82, 205-217.
- [26] Muller, M. (2019). *Essentials of inventory management*. HarperCollins Leadership.
- [27] Nadimi-Shahraki, M. H., Taghian, S., & Mirjalili, S. (2021). An improved grey wolf optimizer for solving engineering problems. *Expert Systems with Applications*, 166, 113917.
- [28] Perera, S. C., & Sethi, S. P. (2023). A survey of stochastic inventory models with fixed costs: Optimality of (s, S) and (s, S) - type policies—Discrete - time case. *Production and Operations Management*, 32(1), 131-153.
- [29] Qiu, R., Sun, Y., & Sun, M. (2021). A distributionally robust optimization approach for multi-product inventory decisions with budget constraint and demand and yield uncertainties. *Computers & Operations Research*, 126, 105081.
- [30] Sadeghi, A. H., Bani, E. A., Fallahi, A., & Handfield, R. (2023). Grey Wolf Optimizer and Whale Optimization Algorithm for Stochastic Inventory Management of Reusable Products in a two-level Supply Chain. *IEEE Access*.
- [31] Shokouhifar, M., Sabbaghi, M. M., & Pilevari, N. (2021). Inventory management in blood supply chain considering fuzzy supply/demand uncertainties and lateral transshipment. *Transfusion and Apheresis Science*, 60(3), 103103.
- [32] Silva, P. M., Gonçalves, J. N., Martins, T. M., Marques, L. C., Oliveira, M., Reis, M. I., ... & Fernandes, J. M. (2022). A hybrid bi-objective optimization approach for joint determination of safety stock and safety time buffers in multi-item single-stage industrial supply chains. *Computers & Industrial Engineering*, 168, 108095.
- [33] Simchi-Levi, D. (2003). Kaminsky P., Simchi-Levi E. *Designing and managing the supply chain: concepts, strategies, and case studies*, McGraw Hill Professional.
- [34] Singh, D., & Verma, A. (2018). Inventory management in supply chain. *Materials Today: Proceedings*, 5(2), 3867-3872.
- [35] Soleimani, H., & Kannan, G. (2015). A hybrid particle swarm optimization and genetic algorithm for closed-loop supply chain network design in large-scale networks. *Applied Mathematical Modelling*, 39(14), 3990-4012.
- [36] Sridhar, P., Vishnu, C. R., & Sridharan, R. (2021). Simulation of inventory management systems in retail stores: A case study. *Materials Today: Proceedings*, 47, 5130-5134.
- [37] Storn, R., & Price, K. (1997). Differential evolution—a simple and efficient heuristic for global optimization over continuous spaces. *Journal of global optimization*, 11(4), 341.
- [38] Thevenin, S., Adulyasak, Y., & Cordeau, J. F. (2021). Material requirements planning under demand uncertainty using stochastic optimization. *Production and Operations Management*, 30(2), 475-493.
- [39] Tu, Qiang, Chen, Xuechen, & Liu, Xingcheng. (2019). Hierarchy Strengthened Grey Wolf Optimizer for Numerical Optimization and Feature Selection. *IEEE Access*, 7, 78012-78028.
- [40] Vahdani, B., Soltani, M., Yazdani, M., & Mousavi, S. M. (2017). A three level joint location-inventory problem with correlated demand, shortages and periodic review system: Robust meta-heuristics. *Computers & Industrial Engineering*, 109, 113-129.
- [41] Wang, S., Wang, L., & Pi, Y. (2022). A hybrid differential evolution algorithm for a stochastic location-inventory-delivery problem with joint replenishment. *Data Science and Management*, 5(3), 124-136.
- [42] Wu, J., & Frazier, P. (2019). Practical two-step lookahead Bayesian optimization in neural information processing systems, 32.
- [43] Xue, N., Triguero, I., Figueredo, G. P., & Landa-Silva, D. (2019, June). Evolving deep CNN-LSTMs for inventory time series prediction. In *2019 IEEE Congress on Evolutionary Computation (CEC)* (pp. 1517-1524). IEEE.
- [44] Yao, B., & Chen, G. (2018). Stochastic simulation and optimization in supply chain management. *Simulation*, 94(7), 561-562.

AI-enabled Exit Strategy of Emergency Vehicle Preemption

1st Kunti Khoirunnisaa

*Department of Electrical Engineering
and Information Technology
Gadjah Mada University*

Jl Grafika No 2, Yogyakarta, Indonesia, 55281
kunti.khoirunnisaa@mail.ugm.ac.id

2nd Rudy Hartanto

*Department of Electrical Engineering
and Information Technology
Gadjah Mada University*

Jl Grafika No 2, Yogyakarta, Indonesia, 55281
rudy@ugm.ac.id

3rd I Wayan Mustika

*Department of Electrical Engineering
and Information Technology
Gadjah Mada University*

Jl Grafika No 2, Yogyakarta, Indonesia, 55281
wmustika@ugm.ac.id

4th Kuntpong Woraratpanya

*School of Information Technology
King Mongkut's Institute of Technology Ladkrabang
Bangkok, Thailand*

kuntpong@it.kmitl.ac.th

5th Ika Arva Arshellla

*Department of Electrical Engineering
and Information Technology
Gadjah Mada University*

Jl Grafika No 2, Yogyakarta, Indonesia, 55281
ika.arva.arshellla@mail.ugm.ac.id

Abstract—Emergency Vehicle Preemption (EVP) is a system employed by traffic lights to prioritize emergency vehicles, such as ambulances, fire engines, and police cars. This technology allows these vehicles to safely pass through crowded intersections by stopping traffic from other directions. However, it is essential to consider that preempting the regular traffic signal control could have implications for the safety and efficiency of both the prioritized emergency vehicle and the overall flow of regular traffic at the intersection. Research on EVP and Exit Strategy has been extensively developed and implemented in various commercial products, including the Trafficware 980 ATC V76 signal controller. Trafficware offers multiple EVP schemes and Exit Strategy modes that can be customized by traffic operators to suit their specific requirements. Studies have indicated that certain Exit Strategies perform optimally under specific traffic conditions. Yet, the complexity of traffic conditions poses a challenge for traffic operators to optimize the Trafficware's performance by selecting the most effective Exit Strategy mode. To address this, Artificial Intelligence (AI) with Reinforcement Learning (RL) techniques used to improve the Trafficware 980 ATC V76 system. Particularly, the Exit to Fixed Phase strategy will be optimized, enabling Trafficware to dynamically choose the most suitable exit phase from the available four phases based on real-time traffic conditions. Implementing this optimization will replace the current fixed exit phase selection with a more adaptable and responsive approach, leading to improved traffic management and efficiency, ultimately resulting in reduced waiting times. The results show that the AI-enabled exit strategy can reduce the waiting time with the best performance up to 7.8% compared to no exit strategy. The Trafficware 980 ATC V76 has been upgraded with the ability to adjust signals based on policies

to recover from congestion caused by preemption.

Index Terms—EVP, Exit Strategy, Reinforcement Learning, Artificial Intelligence

I. INTRODUCTION

Transportation is a complex field where an increasing number of vehicles contribute to traffic congestion. The more congested the roads become, the greater the losses incurred. In such congested situations, when Emergency Vehicle Preemption (EVP) is in effect, the priority must always be given to emergency vehicles.

Researchers have proposed several solutions to prioritize emergency vehicles, including optimizing road routes, signal preemption, or a combination of both [1]. Route optimization involves vehicles selecting the shortest travel route [2]. However, route optimization tends to be less effective compared to signal preemption, and thus, more research has focused on signal preemption [1]. Signal preemption involves temporarily manipulating traffic lights or traffic flow at intersections to facilitate the passage of prioritized vehicles, such as emergency vehicles [3].

Preempting the regular control of a traffic signal has the potential impact on overall flow of traffic at the intersection. These effects may also influence traffic flow at other intersections along a road or within a corridor [4]. The specific disruptions caused by this preemptive action are travel time and delay [5]. Other vehicles will experience increased waiting

time, travel time, increased delay, increased stopping points, increased vehicle fuel consumption, changes in driving behavior, and even threats to safety not only at major intersections but extends to arterial and corridor intersection networks [2], [4], [6], [7].

Minimizing the adverse effects of emergency vehicles on regular traffic, ensuring minimal disruption to the flow of network traffic, presents a challenge [1]. Post-preemption recovery, referred to as recovery method, transition method, or exit strategy, becomes a crucial component for the success of preemption itself. Trafficware providers offer the exit strategy as a solution, and various static exit strategies have been analyzed and proposed. However, these static exit strategies may struggle to address the challenges posed by dynamic and complex factors. The effectiveness of exit strategies can vary due to the influence of such factors [1] such as actual travel demand, unique intersection conditions, and traffic characteristics, specific to each intersection, arterial, or corridor [4].

To tackle this, computer scientists have proposed an alternative approach using intelligent agents to design a traffic light controller. The concept involves allowing autonomous agents to learn optimal behavior by directly interacting with the system. By utilizing algorithms with value-based approach from agent-selected actions, a control policy attempts to optimize traffic flow [4]. Artificial Intelligent (AI) can process multi-source, large-scale, real-time data to model road behavior, predict traffic conditions, and evaluate system performance, especially in terms of exit strategy, aligning with the main functions of a Decision Support System (DSS).

In this paper, we propose an AI-enabled exit strategy through Reinforcement Learning, considering local intersection traffic information, to minimize the negative impacts of EVP implementation. In simple terms, the traffic light becomes an agent that learns traffic information, such as vehicle distribution, vehicle speed, vehicle density, interrupted signal phase, and preemption phase location. When preemption occurs, the agent determines and executes the next exit strategy, evaluating whether the preemption's impact can be minimized. The learning process continues until the agent can dynamically choose an optimal exit strategy for recovery.

With our proposed method, our solution aims to reduce waiting times at intersections. We conducted simulations using one traffic scenarios and high frequency of preemptions at four-leg intersections. The main contributions of this research are as follows:

- 1) Implementation of Artificial Intelligence in the post-preemption area.
- 2) Significant reduction in waiting times for cars stopped due to preemption.
- 3) The traffic light agent adjusts its policies to recover from congestion caused by preemption.

This paper is organized as follows: The next section briefly describes the operation of the Exit to Fixed Phase. The third section presents the procedure used in the case study and describes the simulation implementation, while the fourth

section provides the numerical evaluation results. Finally, the last section offers conclusions and outlines future research directions.

II. EXIT TO FIXED PHASE

Fixed exit phase means that the operator specifies a certain phase to be executed when preemption is complete [8] as depicted in Fig. 1. For example, the signal phase of this intersection is 2,5 green for about 42 seconds and yellow for about 3 seconds. After phase 2,5 then phase 4,7 followed by phase 1,6 and finally 3,8 and so on. Then pre-emption

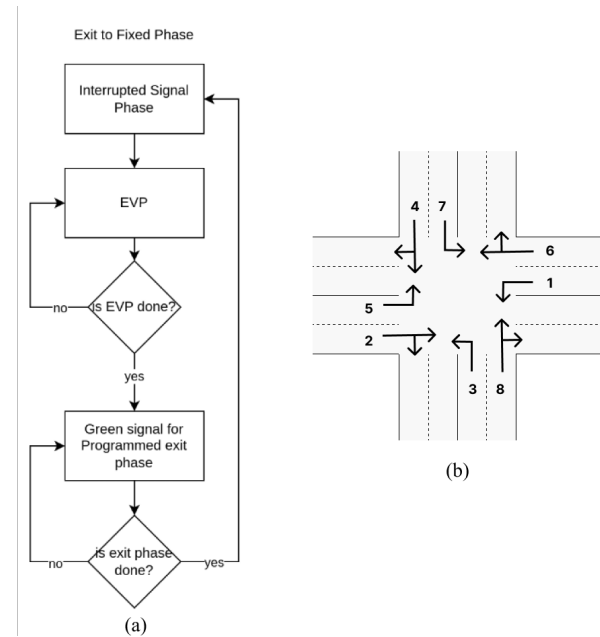


Fig. 1. (a) Exit to Fixed Phase Flow (b) Intersection Phase

occurs when the light is in phase 3,8 green light at the 10th second so that this phase is interrupted. Preemption runs for 80 seconds which causes phase 3,8 to not finish serving and phase 2,5 does not get a turn. The tbc was still running when the preemption occurred, when the preemption was completed, tbc 1 was at 4,7. However, the exit to the fixed phase has been set at phase 1,6. So when preemption is complete, the system will give a green light to phase 1,6. This means that phase 3,8 has been partially executed, while phases 2,5 and 4,7 did not get a turn and have to wait for their turn in the next cycle. From this example, it is clear that the exit to fixed phases strategy forces the controller to unconditionally return to the programmed exit phase, resulting in phase starving and phase skipping. However, an evaluation by Xu showed that this exit strategy reduced the delay by 2.8% per vehicle compared to no exit phases [9].

III. METHODOLOGY

A. Study case

This research conducted a case study using a four-leg intersection. Each leg or phase consisted of two lanes, each

capable of accommodating one vehicle, specifically cars. The maximum speed for normal vehicles was set at 45 mph. The traffic light configuration for four phase signal and each phase was set to 45 seconds, with 42 seconds of green light and 3 seconds of yellow light. Consequently, each phase experienced a red light for 135 seconds in static traffic light mode. Detail of study case environment can be viewed in Table 1.

TABLE I
SCENARIO ENVIRONMENT

| Parameter | Methodology |
|-----------------------|-------------------------|
| Mode of traffic light | Static |
| Simulation duration | 3600s |
| Preemption intensity | 12 EV/h [10] |
| Maps | 4 leg intersection [10] |
| Signal phase | 45s in total, 3s yellow |
| EV speed | 55mph [10] |
| Non EV speed | 45mph [10] |
| Vehicle volume | 1800 veh/h |
| EV route | 12 possible route |

B. Deep Reinforcement Learning

Reinforcement learning (RL), is one of the machine learning methods used to teach an agent or system to choose an optimal set of actions in an environment, with the goal of maximizing cumulative gains over time. This method is based on the idea of rewarding the agent after performing correct or appropriate actions, so that the agent can learn and strengthen its knowledge over time [11]. RL can be the fourth generation of adaptive traffic control systems [12] and become trending data-driven approach for adaptive traffic signal control in complex urban traffic networks [13].

Deep reinforcement learning combines deep neural networks (DNNs) and reinforcement learning to cater to the inability of RL to handle high-dimensional and complex state spaces efficiently [14]. A fully connected neural network comprising two hidden layers with 128 and 64 neurons and utilizing the modified linear unit activation function (RELU) was employed; it takes a state as input and produces a Q-value set of possible actions as output. [15]. Fig. 2 depicts the visual representation of the defined deep neural network. The utilized learning mechanism is Q-learning employing this

equation, which has been adjusted to seamlessly integrate with a deep neural network. The reward r_{t+1} is the reward received after doing action a_t at state s_t . The expression $Q'(s_t, a_t)$, is the value of Q' for action a_{t+1} in the state of s_{t+1} , that is, after the state of action at s_t . The \max_A statement means to choose the most valuable of the possible actions at a_t s_{t+1} . As observed in Eq. 1, the coefficient γ , is a small discount for future rewards compared to immediate rewards [15].

$$Q(s_t, a_t) = r_{t+1} + \gamma \cdot \max_A Q'(s_{t+1}, a_{t+1}) \quad (1)$$

Signal controllers usually require to be optimized based on the observed or sensing state of the environment named state spaces [16] such as vehicle distribution, vehicle speed, vehicle density, interrupted signal phase, and preemption phase location. On each occasion, only one action can be executed to maximize the reward. The researcher designs actions based on the exit phase that can be executed by traffic ware as a programmed exit phase. So that the total set of action space is 4, which is phase 2,5, phase 4,7, phase 1,6 and phase 3,8.

Determining rewards is crucial in the learning process of agents to be accurate in taking action [17]. In theory, the reward can be a negative number called penalty. In this scenario, the penalty is employed because the objective is to achieve the lowest possible waiting time value.

In the initial simulation, the agent has no knowledge about the relative value of actions, necessitating exploration of action outcomes without concern for immediate efficiency. As the agent gains a dependable understanding of action outcomes across a significant portion of state space, it exploits knowledge actions more frequently [15]. To get a balance between exploration and exploitation, the Epsilon greedy algorithm is used. For example, if the epsilon ϵ value chosen is 0.1, then in 10% of the time the agent will randomly choose an action to explore, and in 90% of the time the agent will choose the action with the highest Q-value to exploit. The algorithm always tries to find optimum policy while exploiting [18].

Experience replay is employed to enhance agent performance and learning efficiency by creating a replay buffer that stores experience tuples while interacting with the environment and then sample a small batch of tuples. The size of the memory shows how many experiences can be stored in the memory and set to 15,000. The batch size is defined as the number of samples to be retrieved from the memory in a training instance and is set to 32.

When the deep neural network estimates the learning-Q function sufficiently, selecting the most valuable action in the current state results in the highest traffic efficiency [15]. Fig. 3 depicts proposed reinforcement learning flowchart.

C. Simulation of Urban Mobility (SUMO)

SUMO is an open-source, highly portable, microscopic, and sustainable traffic simulation package designed to handle any large networks. It enables multi-modal simulations, including pedestrians, and is equipped with a large set of tools for scenario creation [19]. SUMO is also equipped with the Traffic

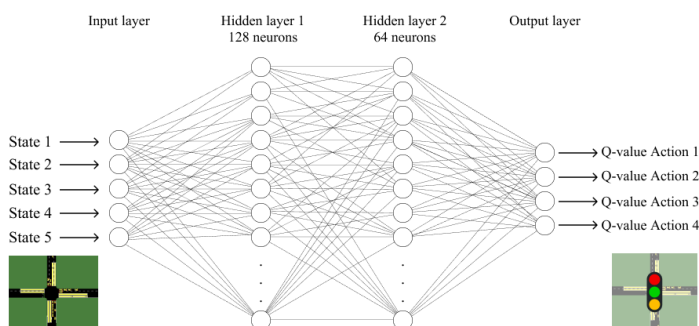


Fig. 2. Deep reinforcement learning

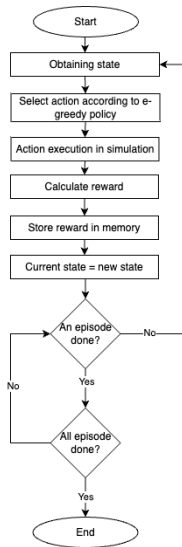


Fig. 3. Proposed Reinforcement Learning Flowchart

Control Interface to execute the simulation of preemption and the exit strategy scheme.

Non-EVs were generated by creating a repeated vehicle called 'flow', which was evenly distributed within the specified interval, starting from timestep 0 to timestep 2100 (in seconds). Here, the flow of non-EVs was performed using a python script.

```

period_nonev = random.randint(2, 18)
os.system("python3 ../randomTrips.py
-n lefthand.net.xml
-r 4-leg.rou.xml -b 0
-e 3600 --period 2 str(period_nonev)
+ " --fringe-factor 10 --random")
  
```

The traffic volume/arrival rate, also known as the departure rate or insertion rate, was controlled by the option period 'n', which means that a random non-EV would arrive every 2 seconds resulted in a saturation flow rate of 1800 veh/h. The option of the 'fringe factor' increased the likelihood that trips would start/end at the network's fringe. When a value of 10 was provided, edges that did not have a predecessor or successor would be 10 times more likely to be chosen as the starting or ending point of a trip. This is useful when modeling through traffic that starts and ends outside the simulated area.

Random trips were used for the preemption scheme, causing EVs to be able to emerge from the 4 available routes and be able to head in 3 directions resulting in 12 EV route combinations. Induction loops were installed to detect EVs entering and exiting the intersection. EVs were detected within a range of 2500 feet before the intersection using the induction loop detector [10]. When EV exited, stop preemption, and execute Exit Strategy. The placement of the induction loop can be seen in Fig. 4, indicated by the yellow block.

Preemption frequency is defined by how many EVs will be generated in an hour, as shown in the script, 12 EVs would be

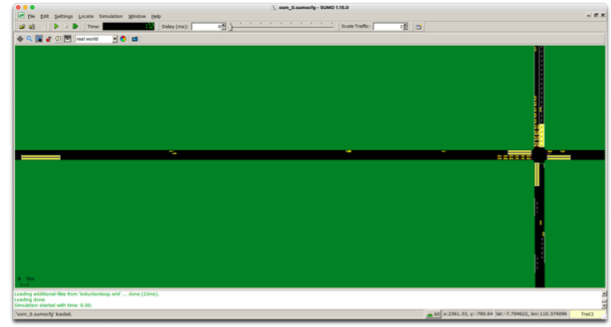


Fig. 4. Induction loop in SUMO Simulation

generated in an hour, and the first EV would appear at second 0 when the simulation started.

```

period = random.choice([900, 600, 450])
os.system("python3 ../randomTrips.py
-n 4-leg.net.xml -r 4-leg.rou.xml
-b 0 -e 1800 --vehicle-class emergency
--vclass emergency --period "+str(period)
+ " --random-depart --fringe-factor 10
--random --prefix ev")
  
```

D. Simulation Scenarios

To evaluate AI-enabled exit strategy performance, high-frequency preemption and saturation rate flow values were used in the static mode of the traffic light system. The exit to the North/East/South/West phases, defined as option of programmed exit phase, became action space of agent. Average waiting time used as evaluation as goal of exit strategy to minimize negative impact of preemption.

IV. RESULTS AND DISCUSSIONS

A. Preliminary Results

Before getting into the core discussion, it is necessary to show the impact of high-frequency preemption which is shown by the increase in waiting time. Fig. 5 shows that there is a 9.4% increase in waiting time compared to traffic without preemption.

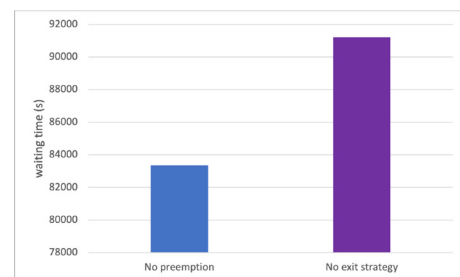


Fig. 5. Waiting time in no preemption and 12 preemption/h in different saturation rate flow

The findings show that a high frequency preemption call has an effect on the overall waiting time through four coordinated

traffic signals. This is in line with what Nelson concluded, that when multiple emergency vehicles preempt a traffic signal at close time intervals, the impact of the preemption will be more severe [5].

EV routes were generated once by SUMO, where out of 11 preemptions, there were 5 routes that occurred, namely South to North 5 times, East to West 2 times, North to West once, West to East once and West to North 2 times. More frequent routes occur on the south to north route which will have an impact on increasing the waiting time in the crossing phase, namely east or west according to the observations of Hualiang [5].

The preemption duration was also recorded in one episode and then an average of 50.3 seconds was obtained. This preemption duration is greater than one phase in a light cycle of 30 seconds. This means that there could be one or 2 phases that are skipped due to preemption.

B. Results and Discussions

The simulation has been run with SUMO, for 60 episodes where the first 10 episodes are the training phase with full exploration, followed by the inference phase with an epsilon value of 0.1. The agent gains knowledge in the training phase after executing 110 random actions as capital for exploitation in the inference phase. The duration of each episode is 3600s or 1 hour, resulting in 60 hours of simulation. Each episode will occur 11 times preemption so that the input vector and action execution occurs 660 times. As an evaluation, the accumulated average waiting time of vehicles in completed episodes is recorded.

When viewed from episode to episode, it can be seen that in the training phase, the exit to North phase is more often chosen to be the programmed exit phase and results in an average waiting time that is still higher at 97.870 s compared to the scenario without an exit strategy which is 91.217 s. Then in the inference phase, exploitation is carried out until in episode 17, the exit to East phase becomes most likely chosen. It is in this episode that the reward value then increases correlated with a significant decrease in waiting time.

In Fig. 6, it can be seen that in phase 17 there is a significant change in the reward value and average waiting time. This shows that the agent can adapt with the aim of increasing the reward value. So it is found that each preemption has a reward value that tends to decrease over time. This shows that the reduction in waiting time is getting smaller or the more vehicles that stop.

The highest reward occurs in episode 60 where the reward of -382429 provides the highest correlation of waiting time reduction of 84092 s. This means that the AI-enabled exit strategy can reduce waiting time by 7.8% compared to the scenario without exit strategy. This figure is close to the traffic scenario without preemption, which means that post-preemption recovery is successful by minimizing negative impacts. The Trafficware 980 ATC V76 has been upgraded with the ability to adjust signals based on policies to recover from congestion caused by preemption.

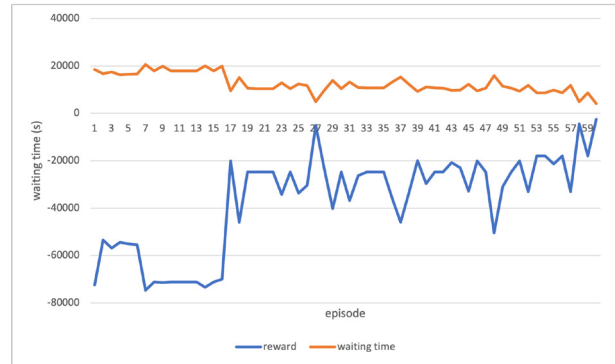


Fig. 6. Reward and Average Waiting time over episodes

V. COMPARISON TO SIMILAR WORKS

Comparison is made with research that has been done on the same map, namely four leg intersection. Exit to Fixed Phase for only one phase simulated by Xu with the HILS method carried out for 30 minutes shows that this exit strategy is not effective as indicated by the increase in average waiting time up to 7% [10]. In addition, Dynamic Exit Phase Control has been implemented in actuated signals using ASC/3-2100 controller by utilizing Logic Processor. The dynamic exit phase control is implemented by changing the exit phases during the EVP operation according to the location of the EVP call within the local cycle timer. The logic statement is set based on the summary of the best exit phase data from various locations of EVP. Among the 5 exit phases, there are 3 best exit phases in the range of 0-100 seconds location of EVP. HILS simulation is run for 20 minutes with a vehicle volume of 2769 (8307 veh/h), dynamic works better because it can reduce the average waiting time in the network up to 4.5% [9].

VI. CONCLUSIONS

The implementation of Artificial Intelligence in the post preemption area has been carried out and yielded results. AI managed to reduce the post preemption waiting time at the intersection because it has learned the traffic conditions so that it can choose the best exit phase adaptively. This is characterized by a positive reward value that increases as the episode progresses. The increasing reward has a significant impact on better traffic recovery as the waiting time per episode decreases. The Trafficware 980 ATC V76 agent adjusts its policy to restore congestion caused by preemption, as evidenced by the selection of different programmed exit phases. The AI-enabled exit strategy cuts waiting time by 7.8% compared to no exit strategy, similar to the preemption-free traffic scenario, showcasing successful recovery from negative impacts.

A. Future Works

For future work, expanding to multiple routes and a network of roads, along with varied intersection types, like T intersections, is possible. Integrating intelligent traffic light phasing with an emergency vehicle routing algorithm could enhance

destination arrival speed and reduce delays. The current simulation focuses on a traffic model; extending to real-world scenarios with city and highway maps, pedestrians, bicycles, and motorcycles can provide insights into policy adjustments. Lastly, exploring alternative reinforcement learning methods or reward functions is a suggestion for further research.

ACKNOWLEDGMENT

This work was supported by King Mongkut's Institute of Technology Ladkrabang and Rekognisi Tugas Akhir (RTA) 2023 program from Universitas Gadjah Mada.

REFERENCES

- [1] S. Humagain, R. Sinha, E. Lai, and P. Ranjitkar, "A systematic review of route optimisation and pre-emption methods for emergency vehicles," *Transport Reviews*, vol. 40, pp. 1–19, July 2019.
- [2] S. Humagain and R. Sinha, "Routing Emergency Vehicles in Arterial Road Networks using Real-time Mixed Criticality Systems," in *2020 IEEE 23rd International Conference on Intelligent Transportation Systems (ITSC)*, pp. 1–6, Sept. 2020.
- [3] R. Anil, M. Satyakumar, and A. Salim, "Emergency Vehicle Signal Pre-emption System for Heterogeneous Traffic Condition : A Case Study in Trivandrum City," in *2019 4th International Conference on Intelligent Transportation Engineering (ICITE)*, (Singapore), pp. 306–310, IEEE, Sept. 2019.
- [4] J. Obenberger and J. Collura, "Transition Strategies to Exit Preemption Control: State-of-the-Practice Assessment," *Transportation Research Record: Journal of the Transportation Research Board*, vol. 1748, pp. 72–79, Jan. 2001.
- [5] E. J. Nelson and D. Bullock, "Impact of Emergency Vehicle Preemption on Signalized Corridor Operation: An Evaluation," *Transportation Research Record: Journal of the Transportation Research Board*, vol. 1727, pp. 1–11, Jan. 2000.
- [6] H. H. Teng, V. Kwigizile, G. Xie, M. Kaseko, and A. R. Gibby, "The Impacts of Emergency Vehicle Signal Preemption on Urban Traffic Speed," *Journal of the Transportation Research Forum*, vol. 49, Aug. 2012.
- [7] B. Brian Park, Ph.D., I. Yun, Ph.D., and M. Best, "Evaluation of Pre-emption and Transition Strategies for Northern Virginia Smart Traffic Signal Systems (NVSTSS)," *Commonwealth of Virginia*, 2008.
- [8] N. Inc, "NTCIP Based Advanced Transportation (ATC) Controllers," Sept. 2016.
- [9] I. Yun, B. ark, C. K. Lee, and Y. T. Oh, "Investigation on the exit phase controls for emergency vehicle preemption," *KSCE Journal of Civil Engineering*, vol. 15, pp. 1419–1426, Nov. 2011.
- [10] J. Xu, *Minimizing Negative Impacts Caused by Emergency Vehicle Preemption on Arterial Signal Coordination*. Thesis, 2021. Accepted: 2022-01-28T02:07:09Z.
- [11] R. S. Sutton and A. G. Barto, *Reinforcement Learning: An Introduction*. The MIT Press, second ed., 2018.
- [12] S. I. Mohamed, "Decentralized traffic management system via reinforcement learning," vol. 9, no. 11, p. 9, 2018.
- [13] Z. Li, C. Xu, and G. Zhang, "A deep reinforcement learning approach for traffic signal control optimization," 2021.
- [14] J. Schmidhuber, "Deep learning in neural networks: An overview," *Neural Networks*, vol. 61, pp. 85–117, Jan. 2015.
- [15] M. Shamsi, A. Rasouli Kenari, and R. Aghamohammadi, "Reinforcement learning for traffic light control with emphasis on emergency vehicles," *The Journal of Supercomputing*, vol. 78, pp. 4911–4937, Mar. 2022.
- [16] J. Ault and G. Sharon, "Reinforcement Learning Benchmarks for Traffic Signal Control," in *Proceedings of the Neural Information Processing Systems Track on Datasets and Benchmarks* (J. Vanschoren and S. Yeung, eds.), vol. 1, 2021.
- [17] S. A. A. Hassani, "A REINFORCEMENT LEARNING APPROACH TO VEHICLE PATH OPTIMIZATION IN URBAN ENVIRONMENTS," 2021.
- [18] R. R. Mouly, "Traffic Congestion Reduction in SUMO using Reinforcement Learning Method," 2021.
- [19] M. Behrisch, L. Bieker, J. Erdmann, and D. Krajzewicz, "SUMO – Simulation of Urban MObility," p. 6, 2011.

Energy-Efficient Continual Learning for Autonomous Driving

Qi Ding Ng

Faculty of Computer Science and Information Technology
University of Malaya
 Kuala Lumpur 50603, Malaysia
 s2035398@siswa.um.edu.my

Kitsuchart Pasupa

School of Information Technology
King Mongkut's Institute of Technology Ladkrabang
 Bangkok 10520, Thailand
 kitsuchart@it.kmitl.ac.th

Chu Kiong Loo

Faculty of Computer Science and Information Technology
University of Malaya
 Kuala Lumpur 50603, Malaysia
 ckloo.um@um.edu.my

Nat Dilokthanakul

School of Information Technology
King Mongkut's Institute of Technology Ladkrabang
 Bangkok 10520, Thailand
 nat@it.kmitl.ac.th

Jie Zhang

Faculty of Computer Science and Information Technology
University of Malaya
 Kuala Lumpur 50603, Malaysia
 s2140511@siswa.um.edu.my

Abstract—Our work highlighted the primary challenges of Autonomous Driving (AD), namely the Catastrophic Forgetting (CF) of previous knowledge by the AD system upon new scenario encounters. Considering the infeasible model retraining with past data given computational, power, and storage constraints on the embedded device, we proposed an experiment featuring Avalanche Continual Learning (CL) training strategies to investigate which strategies excel in this task and combine the promising ones in the hope for a more balanced and efficient trade-off between performance and energy consumption. Our experiment unprecedentedly validated the candidates against a new benchmark introducing natural distribution change and time correlation between input images. We found that although a synergy of CL strategies yields higher resistance towards CF, the slight accuracy gain is not worth the additional computation when we account for energy consumption, rendering a simple Replay strategy the best solution for the Continual Learning benchmark for Autonomous Driving: Online Continual Classification (CLAD-C). Our proposal delivers a 65.80% improvement over the baseline at our proposed accuracy-power ratio metric.

Index Terms—Autonomous driving, continual learning, catastrophic forgetting, energy efficiency, lifelong learning

I. INTRODUCTION

Autonomous Driving (AD) is an open-world problem as naturalistic driving yields infinitely many possibilities and disengagement cases in which human preparation cannot realistically perfectly define and accommodate every potentially arising situation. Contemporary AD approaches employ policies that refer to mapping sensory data to vehicle motion and control commands. Manual policy adjustments will induce an engineering burden due to its growing complexity and possibly contradiction of the pre-defined driving functions [1].

However, if we alleviate human labour and let the AD system, which typically utilizes deep neural network models to decide the policy adjustments by exposing them to dis-

engagement cases upon encounter, a fundamental challenge known as Catastrophic Forgetting (CF), a forgetting or loss of previously grasped information when learning numerous tasks sequentially from dynamic data distributions, will occur, deteriorating model accuracy on trained scenarios [2].

One approach to resolve CF is by appending the additional data to the original dataset and retraining entirely to retain the mastered knowledge while gaining information about the foreign domain [2]. Considering the unpredictable driving nature, the infinite dataset growth would lead to infeasible model retraining with all data given the physical limitations [3].

This fact motivates the adoption of Continual Learning (CL) to introduce AD models capable of incremental adaptation. CL methods enable information distillation and compact storage within the AD model itself without needing an attached database to store past data, retaining information for maximal CF alleviation while not required to carry learned inputs [4].

An appropriate CL method in this setting should deliver robust resilience toward CF through a high Average Mean Class Accuracy (AMCA) score, indicating overall classification performance after introducing foreign objects. Taking into account the computational, power, and storage constraints of an embedded AD system, an assessment of CL methods is conducted by analyzing their power consumption via electricity usage measurement in kilowatt-hours (kWh).

Recently, ContinualAI has introduced the Avalanche Library, which facilitates the seamless integration of various CL training strategy implementations as plugins into the training pipeline. Therefore, our study leverages this library to examine and compare different CL approaches, thereby providing a comprehensive assessment of individual and combined Avalanche CL training strategies [5].

We deem that a comprehensive study providing quantified comparisons between CL strategies in terms of AMCA, kWh, and their trade-off is insightful for future algorithm and system designs. The summary of our contributions is as follows:

- 1) A compilation of evaluation on the performance and energy cost of individual Avalanche CL methods and the synergy of promising strategies.
- 2) The effect of the memory size hyperparameter towards the Replay strategy for optimal allocation in the memory buffer in a setting with limited computational resources.

II. RELATED WORK

End-to-end Approach: The current AD approach mainly builds upon two design philosophies, namely the connected multi-agent system and the ego-only system. The former architecture refers to a pipeline of interconnected components, breaking down the AD problem into modules, each tackling its designated sub-tasks divided from the core functions required in the AD operation [3].

The latter treats the AD task as an end-to-end learning process, formulating the problem as an attempt to comprehend a policy translating sensory inputs to vehicular commands. This procedure converts the work of complicated programming of various driving hazards and conditions into a model hyperparameter optimization problem. As it is virtually impossible to include every possible road and traffic scenario definition in a modular system, our paper gravitates to this mechanism as it maximally reproduces the natural human driving behavior through simultaneous perception and decision-making [3].

Deep Reinforcement Learning: Reinforcement Learning (RL) is a powerful machine learning paradigm employed to learn control policies from experience. RL agents will learn to map states to actions to maximize the reward signal. The system will then learn from the maximal cumulative advantages solely through the RL agent and the environment without human supervision and intervention [6].

Deep Reinforcement Learning (DRL) is the most promising approach among the current implementations. DRL combines RL with deep learning, allowing agents to learn complex policies from large amounts of data. DRL is effective for various autonomous driving tasks, such as lane, obstacle avoidance, and intersection decision-making. However, there are still challenges to overcome before DRL can be used to develop fully autonomous vehicles. One challenge is that a DRL agent can be sensitive to the quality of its training data. The agent may learn ambiguous or unreliable policies if the training data does not reflect the real world. Another challenge is that training DRL agents can be computationally expensive due to the massive volume of possible states and actions to learn the optimal policy [6].

Continual Learning: CL implementation faces two primary challenges namely CF and data scarcity. CF is the problem of past information loss caused by concept drift which refers to the data distribution changing over time [7]. The second issue refers to the challenge of extracting and retaining as much information as possible because a CL model is typically only presented with a limited amount of data [7].

The rehearsal, generative replay, regularization, and architectural approaches are several schools of thought and previous

work on strategies to provide workarounds to resolve such challenges. However, each CL training strategy originated from different fundamental working principles, which have advantages and shortcomings in certain circumstances and do not conform to every use case [7].

III. METHOD

A. Dataset

Our work proposes unprecedented work on validating AD models against the Continual Learning benchmark for Autonomous Driving (CLAD), a benchmark built upon the SODA10M, a Large-Scale 2D Self/Semi-Supervised Object Detection Dataset for Autonomous Driving, containing 10 million unlabelled images and 20,000 labelled images from dash-camera footage recorded with an interval of 10 seconds in four Chinese cities. The dataset comes with attributions of time annotations and object bounding boxes for six classes, spanning across varied domains, namely city, weather condition, time of day, and road type. The scope of this research is defined to be bound on the CLAD: Online Continual Classification (CLAD-C), a sub-track of CLAD, an online benchmark consisting of a data stream posing class and domain incremental challenges, focusing on real-world, dynamic, yet naturally occurring, temporal correlated distribution shifts following the axis of time [8].

B. Avalanche

Our work harnesses the readily-available CL training strategy plugins offered by the Avalanche Library developed under ContinualAI [5] for convenient comparison of various CL approaches categorized as follows:

1) *Regularization:* Regularization-based methods manipulate the loss function of a network through the extension of additional terms to encourage selective weight consolidation to maintain the past knowledge [9].

2) *Rehearsal:* The rehearsal methods work on periodical exposure of selected past memory stored within a memory buffer for previous information and knowledge reinforcement [9].

3) *Optimization:* Optimization-based approaches realize CL through explicit definition or modification of optimization algorithms, manipulating the parameter update direction and locating the local minima with dropouts, learning rate decay, and batch size setting [7].

4) *Architectural:* Architectural-based methods alleviate CF by incorporating specific network architectures, introducing certain dedicated network layers or activation functions [9].

5) *General CL Methods:* General CL strategies do not define explicit task boundaries but attempt to describe potential challenges as learning paradigms, enabling the model to observe incremental data online [7].

IV. EXPERIMENT SETTINGS

In this experiment, we want to investigate how each Avalanche CL training strategy influences the model against the CLAD-C benchmark in terms of classification accuracy, power consumption, and the accuracy-power ratio. We expect to see which strategies excel in this task and intend to combine them to see if this will yield a more balanced and efficient trade-off between performance and energy consumption.

A. Baseline

Our experiment is conducted on a device whose specifications are as follows:

- System: Linux-5.15.0-72-generic-x86_64-with-glibc2.31
- Python Version: 3.10.10
- Available RAM: 62.424 GB
- CPU Count: 12
- CPU Model: Intel(R) Xeon(R) E-2276M @ 2.80GHz
- GPU Model: 1 × Quadro RTX 5000

This work utilizes the highest-achieving technical report from the Self-supervised Learning for Next-Generation Industry-level Autonomous Driving (SSLAD) Challenge 2021 Track 3A as a comparison baseline [8]. The affirmation that the experimental setup was identical to the original literature was to obtain a meaningful and comparable outcome while setting up a control variable to observe the magnitude of impacts of various Avalanche CL training strategy implementations. Table I depicts the technical configurations of the top-achieving paper in the SSLAD Challenge 2021 Track 3A [8]. Here, we conduct the following experiments with modifications to the CL training strategy, as indicated by the italics in Table I, while maintaining the remaining settings identical. This ensures a meaningful and equitable comparison between strategies.

B. Proposed Method Settings

The comparison candidates originate from the subset of the Avalanche CL training strategy plugins provided that they adhere to the restrictions posed by the original SSLAD Challenge Track 3A, which are listed as follows [8]:

- 1000 samples are the maximum size for replay memory.
- The training should utilize the data as a stream and there should be no repetitions of data not present in memory.
- 10 is the maximum batch size.
- Between training and testing, the model should nearly always be immediately usable for predictions without computationally demanding operations.
- Model parameters are at most 105% of those in a conventional ResNet-50.

C. Framework

Our work aims to research the effectiveness of Avalanche CL training strategies and their combination against a baseline to identify the most effective strategy in CLAD for new knowledge adaptation and mitigation of CF in real-world industry-scaled AD systems. The working principles of different approaches are explained as follows:

1) *Regularization-based*: Elastic Weight Consolidation (EWC), Synaptic Intelligence (SI), Memory Aware Synapses (MAS), and Learning Without Forgetting (LWF) are regularization-based approaches [7], [10]. EWC regularizes network parameter variation selectively by penalizing parameter updates if they yield high contributions in previous tasks. SI evaluates the importance of the parameters according to their approximated contribution to the total loss. Besides, MAS measures the significance of the parameters by the impact of parameter change on model prediction. While EWC, SI, and MAS build upon the concept of weight-regularization, LWF learns new training samples with results from the output head

of previous tasks for distillation loss computation with soft targets taken from a previous version of the model [7].

2) *Rehearsal-based*: The rehearsal approach consists of Replay Memory and Bias Correction (BiC). Replay Memory stores a fixed amount of previously learned data in a compact memory buffer. The old samples are meticulously picked and undergo compression, augmentation, and continual adjustment to provide adaptive information for past knowledge recovery maximally. On the other hand, BiC attributes the knowledge distillation to the bias of the final fully-connected layer [7].

3) *Optimization-based*: Learning Rate Scheduler (LR), Gradient Episodic Memory (GEM), and Average Gradient Episodic Memory (AGEM) are optimization-based approaches. LR optimizers introduce weight decays, restarts, and regularization terms depending on the type of schedulers applied to seek the optimal learning rate for maximum convergence. Our experiment utilizes the Cosine Annealing Warm Restarts optimizer as the algorithm suits well the stochastic gradient descent used in the baseline and accelerates gradient convergences [7], [11]. GEM and AGEM are based on gradient projection which restricts parameters such that their updates will align with the experience replay [7].

4) *Architectural-based*: Architectural-based approaches employed in our work are Less Forgetful Learning (LFL) and CWR. LFL retains the vanilla feature space of the source domain in the hope of a more effective transfer learning with less CF impact. On the other hand, CWR enables a dynamic architectural approach through copying and re-initializing weights of previous tasks in a sequential batch CL setting [9], [12].

5) *General CL*: Greedy Sampler and Dumb Learner (GDumb) and Continual Prototype Evolution (CoPE) are general CL strategies prioritizing the replay of those training samples that are balanced in class labels [7].

D. Avalanche Training Strategy Plugin

The list of Avalanche CL training strategy plugins and their corresponding parameters is presented in Table II, where the unspecified parameters are assigned the default values as outlined in the Avalanche library's documentation [5].

E. Evaluation Metrics

The first iteration of the experiment yields the metrics of the model with the Naïve plugin (no training strategy) to set up a baseline. The subsequent iterations pass each available and applicable Avalanche CL training strategy plugin individually for AMCA computation defined as such [8]:

$$AMCA = \frac{1}{T} \sum_t \frac{1}{C} \sum_c a_{c,t}, \quad (1)$$

where $T = N_{testpoints}$ and $C = N_{classes}$.

Power usage quantification in kilowatt hour (kWh) is measured with the help of CodeCarbon defined as follows [13]:

$$kWh = \frac{PT}{1000}, \quad (2)$$

where $P = Power(Watt)$ and $T = Time(Hour)$.

TABLE I
BASELINE EXPERIMENT SETUP. ITALIC—MODIFICATIONS TO THE CL TRAINING STRATEGY BEYOND BASELINE SETTINGS

| Attribute | Description |
|-----------------------------|---|
| Model | Pre-trained ResNet-50 |
| Optimizer | Stochastic Gradient Descent and $\alpha = 0.01$ |
| Data Augmentation | Upsizing to 224×224 , and Horizontal Flipping |
| <i>CL Training Strategy</i> | <i>CopyWeights with Re-init (CWR), Replay Memory, and Memory Size=600</i> |
| Additional Feature | First Experience Double Batching, Unfreezing Feature Extractor, and Balanced Memory with Reservoir Sampling |

TABLE II
AVALANCHE TRAINING STRATEGY SETTINGS

| Strategy | Parameter |
|---------------|---|
| Naïve | N/A |
| LR | <i>CosineAnnealingWarmRestarts</i> , $T_0 = 1$ |
| CoPE | $N_{Classes} = 7$, $PrototypeSize = 7$, $MemorySize = 600$, $MaxIterationCount = 1000$ |
| CWR | <i>FreezeRemainingWeights = False</i> |
| EWC | $\lambda = 0.1$ |
| GDumb | $MemorySize = 600$ |
| AGEM | $PatternperExperience = 600$, $SampleSize = 64$ |
| GEM | N/A |
| LFL | $\lambda = 0.001$ |
| LWF | N/A |
| Replay Memory | $MemorySize = 600$ |
| SI | $\lambda = 0.001$ |
| MAS | N/A |
| BiC | $MemorySize = 600$ |

To research Avalanche CL training plugins with a balanced trade-off between performance and conservation with a positive impact overall, we seek to boost the AMCA value while maximally shrinking the kWh value.

Thus, we define a new metric accounting for both classification accuracy and electricity usage, measured by the computation of the ratio of AMCA to kilowatt hour as follows:

$$AMCA/kWh = \frac{AMCA}{kWh} \quad (3)$$

V. RESULTS AND DISCUSSIONS

Our experiment first observed how each Avalanche CL training strategy plugin performs individually regarding AMCA, kWh, and their ratio. The Avalanche CL training strategy plugins demonstrated a promising accuracy-power ratio and are then synergized for further examination of whether they can coalesce well and produce even massive benefits.

A. Avalanche CL Strategy Performance

Table III compiles the individual Avalanche CL training strategy plugin metrics where CWR, EWC, AGEM, LWF, Replay, SI, and MAS outperform the Naïve method in AMCA. The GDumb strategy recorded the lowest power consumption, but its underwhelming AMCA rendered it less useful. LR strategy scored an identical AMCA as the Naïve method and is inferred that the scheduling and optimization algorithm ultimately lead to the exact same CL progress as the Naïve but with more additional computations. CoPE, GEM, and BiC performed inferior to the Naïve in terms of both AMCA and kWh and did not worth advancing into further inspection. LFL scored the poorest AMCA among all, and it was deduced that it was not suitable for the AD task.

Figure 1 illustrates the plugin performance, where circle sizes indicate the accuracy-power ratio. Only LWF and Replay

demonstrate improvements over Naïve when accounting for energy consumption.

B. Combination of Promising Avalanche CL Strategies

The upcoming experiment combines LWF and Replay due to their outstanding performances to see if they incorporate well and induce an even more beneficial outcome. Table IV displays that a more sophisticated hybrid method does not necessarily outperform the simple approach. The synergy introduces a higher AMCA score, showing higher resilience towards CF. However, the additional calculations and power consumption might not be worth the trade-off in a setting where energy conservation is heavily favoured.

The results show that multiple training strategies might introduce over-complexity and possibly interference, where we see the combination of Replay and LWF yields a worse product than its components. Although the plugin combination from the literature shows promising synergy, the slight gain does not justify sacrificing additional power consumption. A simple Replay training strategy is the best approach, fulfilling CLAD-C's accuracy and efficiency requirements.

C. Optimal Memory Allocation

Although now that the Replay Memory strategy has proven to outperform its peers, we decided to delve deeper into its memory size hyperparameter configuration as it directly relates to memory consumption, considering the scarcity and preciousness of memory in an AD setting. We performed a series of experiments within the possible range of memory size definition between 0 and 1000 following the SSLAD Challenge Track 3A restrictions [8].

Figure 2 depicts the influence of the memory size hyperparameter on the AMCA metric of the Replay strategy. The peak performance was recorded at approximately 500 memory size.

TABLE III
CL TRAINING STRATEGY IMPACT. RESULTS IN BOLD DEPICT IMPROVEMENTS OVER NAÏVE.

| Metric | Avalanche CL Training Strategy | | | | | | | | | | | | | |
|------------|--------------------------------|--------|---------|---------------|---------------|---------------|---------------|--------|--------|---------------|---------------|---------------|---------------|--------|
| | Naïve | LR | CoPE | CWR | EWC | GDumb | AGEM | GEM | LFL | LWF | Replay | SI | MAS | BiC |
| AMCA | 0.4950 | 0.4950 | 0.4365 | 0.5540 | 0.5197 | 0.1678 | 0.5592 | 0.4132 | 0.0683 | 0.5178 | 0.6321 | 0.5135 | 0.5051 | 0.3879 |
| kWh | 0.0201 | 0.0203 | 0.0272 | 0.0341 | 0.0327 | 0.0154 | 0.1907 | 0.0380 | 0.0239 | 0.0210 | 0.0252 | 0.0424 | 0.0285 | 0.0581 |
| AMCA/kWh | 24.643 | 24.348 | 16.070 | 16.253 | 15.905 | 10.897 | 2.932 | 10.874 | 2.853 | 24.681 | 25.044 | 12.119 | 17.740 | 6.682 |
| Loss | 0.4685 | 0.4685 | 21.2856 | 0.4600 | 0.4436 | 2.3135 | 0.4720 | 0.5905 | NaN | 0.4407 | 0.4227 | 0.4358 | 0.4970 | 0.8853 |
| Top-1 Acc. | 0.8418 | 0.8418 | 0.6154 | 0.8497 | 0.8492 | 0.0072 | 0.8428 | 0.7929 | 0 | 0.8629 | 0.8502 | 0.8519 | 0.8213 | 0.7156 |

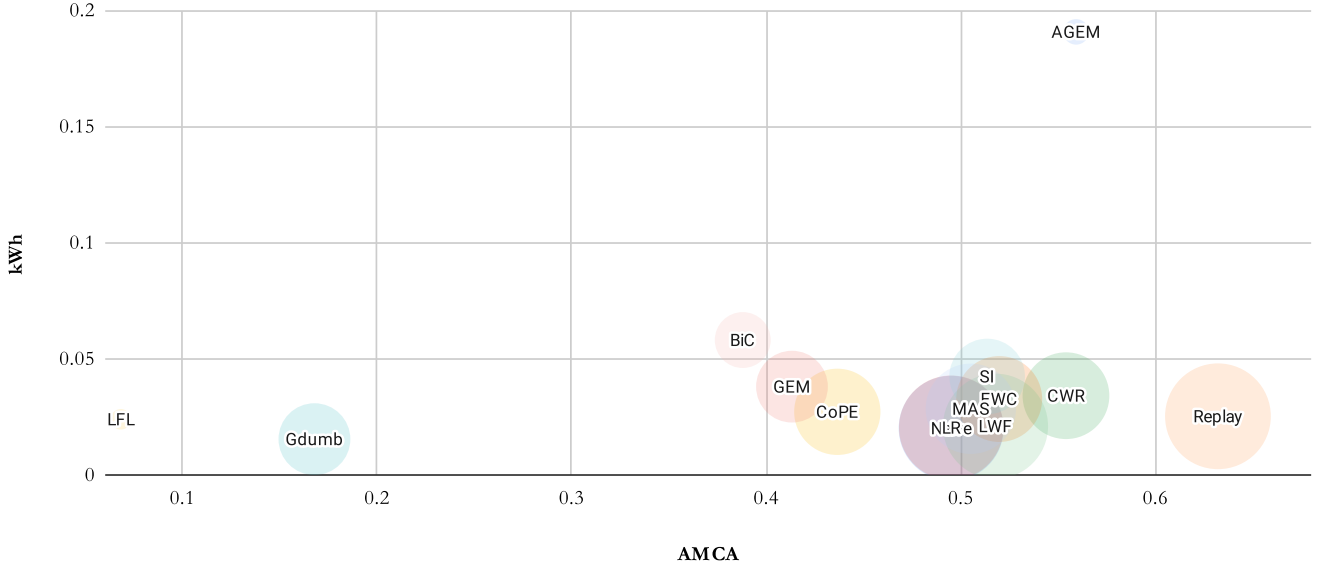


Fig. 1. Individual Avalanche CL Plugin Comparison

TABLE IV
IMPACT OF COMBINED PROMISING AVALANCHE CONTINUAL LEARNING STRATEGIES ON CL TRAINING STRATEGY. RESULTS IN BOLD DEPICT THE BEST-ACHIEVING APPROACH.

| Metric | Avalanche CL Training Strategy | | | |
|------------|--------------------------------|---------------|---------------|------------|
| | Baseline | LWF | Replay | Replay+LWF |
| AMCA | 0.6472 | 0.5178 | 0.6321 | 0.5554 |
| kWh | 0.0428 | 0.0210 | 0.0252 | 0.0361 |
| AMCA/kWh | 15.105 | 24.681 | 25.044 | 15.391 |
| Loss | 0.3871 | 0.4407 | 0.4227 | 0.4579 |
| Top-1 Acc. | 0.8702 | 0.8629 | 0.8502 | 0.8506 |

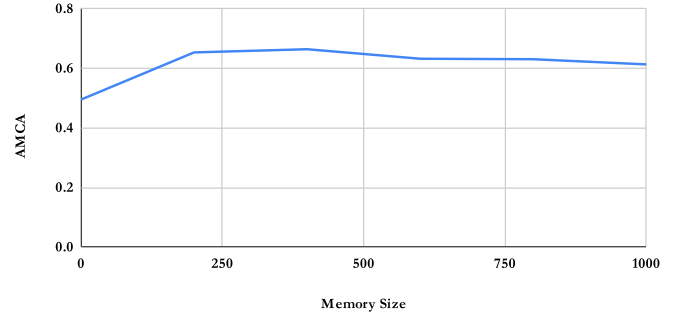


Fig. 2. Effect of Memory Size Towards AMCA on Replay Strategy

VI. CONCLUSION

We hypothesize that this was due to the lack of certain classes in the training sets of CLAD benchmark [8]. By our inference, the optimal memory size should settle at 492, instead of 600 proposed in the literature baseline [8], which is the product of the number of the least represented object, which, in our case, is tricycle scoring at 82, and the total number of classes, 6, for a class-balanced buffer. A smaller memory size will lead to a reduced amount of information, and a memory size exceeding our calculation will yield an under-representation of the minor class, which damages the AMCA value.

Our study delivers an in-depth review of how Avalanche CL training strategies impact the AMCA and kWh metric against the CLAD-C benchmark. We reveal that a more sophisticated combination of CL training strategies does not necessarily introduce benefits over their individual counterparts. There might be interference, contradictions, and inclusion of less significant calculations that are not worth the AMCA-kWh trade-off. Our results show that a simple Replay strategy is the best solution for CLAD-C, scoring a 65.80% improvement at the AMCA-kWh ratio over the literature baseline.

Real-world applications place a high value on resource efficiency, and hence, our research allocated significant effort into streamlining the model architecture, cutting out less impactful computations, and improving memory utilization. Our research shows the effect of the memory size hyperparameter on the Replay strategy and the deduction that 492 is the optimal memory allocation for the Replay strategy for a class-balanced memory buffer and optimal AMCA.

The scope of this paper includes only CLAD-C, a sub-track of the CLAD benchmark. Future research can expand this work for application in CLAD-D or any beneficial and relevant benchmarking [8]. Also, further work can be done on more CL training strategies not included in this study or the Avalanche library by ContinualAI [5]. The model proposed by this paper can function as a competent replacement for the conventional ResNet-50 inference backbone in a complete AD system such as DeFIX, Detecting and Fixing Failure Scenarios with Reinforcement Learning in Imitation Learning Based Autonomous Driving for further evaluation and validation on CARLA, the state-of-the-art AD simulator [14], [15].

REFERENCES

- [1] Z. Cao, X. Li, K. Jiang, W. Zhou, X. Liu, N. Deng, and D. Yang, "Autonomous driving policy continual learning with one-shot disengagement case," *IEEE Trans. Intell. Veh.*, vol. 8, no. 2, pp. 1380–1391, 2023. [Online]. Available: <https://doi.org/10.1109/TIV.2022.3184729>
- [2] H. Zhang and F. Mueller, "CLAIRE: enabling continual learning for real-time autonomous driving with a dual-head architecture," in *25th IEEE International Symposium On Real-Time Distributed Computing, ISORC 2022, Västerås, Sweden, May 17-18, 2022*. IEEE, 2022, pp. 1–10. [Online]. Available: <https://doi.org/10.1109/ISORC52572.2022.9812816>
- [3] D. Coelho and M. Oliveira, "A review of end-to-end autonomous driving in urban environments," *IEEE Access*, vol. 10, pp. 75 296–75 311, 2022. [Online]. Available: <https://doi.org/10.1109/ACCESS.2022.3192019>
- [4] A. Prabhu, Z. Cai, P. K. Dokania, P. H. S. Torr, V. Koltun, and O. Sener, "Online continual learning without the storage constraint," *CoRR*, vol. abs/2305.09253, 2023. [Online]. Available: <https://doi.org/10.48550/arXiv.2305.09253>
- [5] V. Lomonaco, L. Pellegrini, A. Cossu, A. Carta, G. Graffieti, T. L. Hayes, M. D. Lange, M. Masana, J. Pomponi, G. M. van de Ven, M. Mundt, Q. She, K. W. Cooper, J. Forest, E. Belouadah, S. Calderara, G. I. Parisi, F. Cuzzolin, A. S. Tolia, S. Scardapane, L. Antiga, S. Ahmad, A. Popescu, C. Kanan, J. van de Weijer, T. Tuytelaars, D. Bacciu, and D. Maltoni, "Avalanche: An end-to-end library for continual learning," in *IEEE Conference on Computer Vision and Pattern Recognition Workshops, CVPR Workshops 2021, virtual, June 19-25, 2021*. Computer Vision Foundation / IEEE, 2021, pp. 3600–3610. [Online]. Available: https://openaccess.thecvf.com/content/CVPR2021W/CLVision/html/Lomonaco_Avalanche_An_End-to-End_Library_for_Continual_Learning_CVPRW_2021_paper.html
- [6] E. Yurtsever, J. Lambert, A. Carballo, and K. Takeda, "A survey of autonomous driving: Common practices and emerging technologies," *IEEE Access*, vol. 8, pp. 58 443–58 469, 2020. [Online]. Available: <https://doi.org/10.1109/ACCESS.2020.2983149>
- [7] L. Wang, X. Zhang, H. Su, and J. Zhu, "A comprehensive survey of continual learning: Theory, method and application," *CoRR*, vol. abs/2302.00487, 2023. [Online]. Available: <https://doi.org/10.48550/arXiv.2302.00487>
- [8] E. Verwimp, K. Yang, S. Parisot, L. Hong, S. McDonagh, E. Pérez-Pellitero, M. D. Lange, and T. Tuytelaars, "CLAD: A realistic continual learning benchmark for autonomous driving," *Neural Networks*, vol. 161, pp. 659–669, 2023. [Online]. Available: <https://doi.org/10.1016/j.neunet.2023.02.001>
- [9] D. Maltoni and V. Lomonaco, "Continuous learning in single-incremental-task scenarios," *Neural Networks*, vol. 116, pp. 56–73, 2019. [Online]. Available: <https://doi.org/10.1016/j.neunet.2019.03.010>
- [10] F. Zenke, B. Poole, and S. Ganguli, "Continual learning through synaptic intelligence," in *Proceedings of the 34th International Conference on Machine Learning, ICML 2017, Sydney, NSW, Australia, 6-11 August 2017*, ser. Proceedings of Machine Learning Research, D. Precup and Y. W. Teh, Eds., vol. 70. PMLR, 2017, pp. 3987–3995. [Online]. Available: <http://proceedings.mlr.press/v70/zenke17a.html>
- [11] I. Loshchilov and F. Hutter, "SGDR: stochastic gradient descent with warm restarts," in *5th International Conference on Learning Representations, ICLR 2017, Toulon, France, April 24-26, 2017, Conference Track Proceedings*. OpenReview.net, 2017. [Online]. Available: <https://openreview.net/forum?id=Skq89Scxx>
- [12] H. Jung, J. Ju, M. Jung, and J. Kim, "Less-forgetting learning in deep neural networks," *CoRR*, vol. abs/1607.00122, 2016. [Online]. Available: <http://arxiv.org/abs/1607.00122>
- [13] Goyal-Kamal, B. Feld, V. Schmidt, K. Goyal, F. Zhao, A. Joshi, S. Luccioni, N. Laskaris, LiamConnell, Z. Wang, A. Catovic, D. Blank, M. Stechly, JPW, SabAmine, and kraktus, "CodeCarbon: Estimate and track carbon emissions from machine learning computing," *Zenodo*, 2021. [Online]. Available: <https://doi.org/10.5281/zenodo.4658425>
- [14] R. Dagdanov, F. Eksen, H. Durmus, F. Yurdakul, and N. K. Ure, "DeFIX: detecting and fixing failure scenarios with reinforcement learning in imitation learning based autonomous driving," in *25th IEEE International Conference on Intelligent Transportation Systems, ITSC 2022, Macau, China, October 8-12, 2022*. IEEE, 2022, pp. 4215–4220. [Online]. Available: <https://doi.org/10.1109/ITSC55140.2022.9922209>
- [15] A. Dosovitskiy, G. Ros, F. Codevilla, A. M. López, and V. Koltun, "CARLA: an open urban driving simulator," in *1st Annual Conference on Robot Learning, CoRL 2017, Mountain View, California, USA, November 13-15, 2017, Proceedings*, ser. Proceedings of Machine Learning Research, vol. 78. PMLR, 2017, pp. 1–16. [Online]. Available: <http://proceedings.mlr.press/v78/dosovitskiy17a.html>

Semantic Bird's-Eye-View Map Prediction Using Horizontally-Aware Pyramid Occupancy Network

Thanapat Teerarattanyu[†], Tunlato Wongchai[†], Praphan Pavarangkoon and Nat Dilokthanakul*

School of Information Technology
King Mongkut's Institute of Technology Ladkrabang
 Bangkok, Thailand
 nat@it.kmitl.ac.th

Abstract—Deep neural network has been used to predict the bird's-eye-view map from a frontal camera of an autonomous car. A state-of-the-art approach, namely pyramid occupancy network (PON), uses an encoder-decoder architecture to condense an image column into a context vector that describes the object occupancy along the radial direction. Our work, Horizontally-aware Pyramid Occupancy Network (H-PON), extends the PON model with a novel component that provides additional context information describing the relationships of the objects along the horizontal direction. This is done by also encoding the horizontal column of the image into an additional context vector using another encoder-decoder layer. This context vector is, then, expanded back providing improved features for semantic reasoning across the horizontal direction. We found that this simple extension significantly improves PON's semantic prediction performance in the nuScenes dataset. Our experiment shows that the objects that are rarely seen and those that are further away from the center greatly benefit from this novel component.

Index Terms—bird's-eye-view, image-to-map, autonomous car, semantic segmentation

I. INTRODUCTION

Autonomous driving relies on object identification, distance estimation, and position estimation, which are generally accomplished using a combination of lidar, radar, and cameras, to perceive the surroundings. Cameras provide a less expensive alternative that can also complete these duties without the need of lidar or radar. Recent efforts have made substantial use of cameras to build top-down maps in autonomous algorithms. These maps offer contextual data that enables autonomous driving systems to make informed decisions, particularly when it comes to effective path planning by examining road layouts.

In the line of work of estimating the bird's-eye-view (BEV) map of the surroundings from an image, Pyramid Occupancy Network (PON) [1] is one of the current state-of-the-art methods that uses deep learning to transform the frontal camera image into a semantic BEV map. PON introduces the multiscale dense transformer pyramid, which is an encoder-decoder model that encodes each vertical column of the image into a small context vector. This context vector is then expanded back into a semantic ray describing the semantic occupancy along the direction of a circular ray originating from the camera.

[†] These authors contributed equally to this work.

* Corresponding author

However, this approach ignores the relationship across the rays, i.e., along the horizontal direction. We hypothesize that the semantic context information along this direction can be useful in predicting the occluded objects especially objects near the left and right borders of the image. We propose a novel component, namely a horizontal dense transformer pyramid, that aims to alleviate this problem. This component encodes additional semantic vectors along the horizontal direction in addition to the vertical direction.

Contributions: The main contributions of this work include (i) a novel component in the Pyramid Occupancy Network model and, (ii) an experiment that suggests the benefit of using horizontal context to aid the improvement of the BEV semantic prediction task.

II. RELATED WORK

Early approaches [2]–[4] use a geometric technique called inverse perspective mapping (IPM), to map images from the frontal perspective into the BEV perspective. These approaches perform poorly when the images contain non-flat road layouts or occluded objects. Abbas and Zisserman [3] focus on the detection of objects in the BEV perspective. Reiher et al. [4] utilize semantic segmentation images and apply an IPM transformation to them.

Another line of approaches is to reason about both spatial and semantic information implicitly. Schuler et al. [5] present a convolutional neural network (CNN) in image space to make predictions with depth information and finally use an additional CNN in BEV space for refinement. Lu et al. [6] use a variational encoder-decoder network that encodes front-view images and decodes them to BEV semantic maps. Phillion et al. [7] employ the Latent Depth Distribution model to extract depth features for each pixel corresponding to the local 2-dimensional coordinate system.

Several works [5]–[7] instead implicitly use the semantic context information along the horizontal direction of an image to predict the BEV maps. We solve this issue by explicitly providing this information to the network with our proposed component, the horizontal dense transformer pyramid.

III. PYRAMID OCCUPANCY NETWORK

This work is built upon the Pyramid Occupancy Network [1]. The goal of this model is to predict the semantic bird's-eye-view map from a frontal image. The state of the map

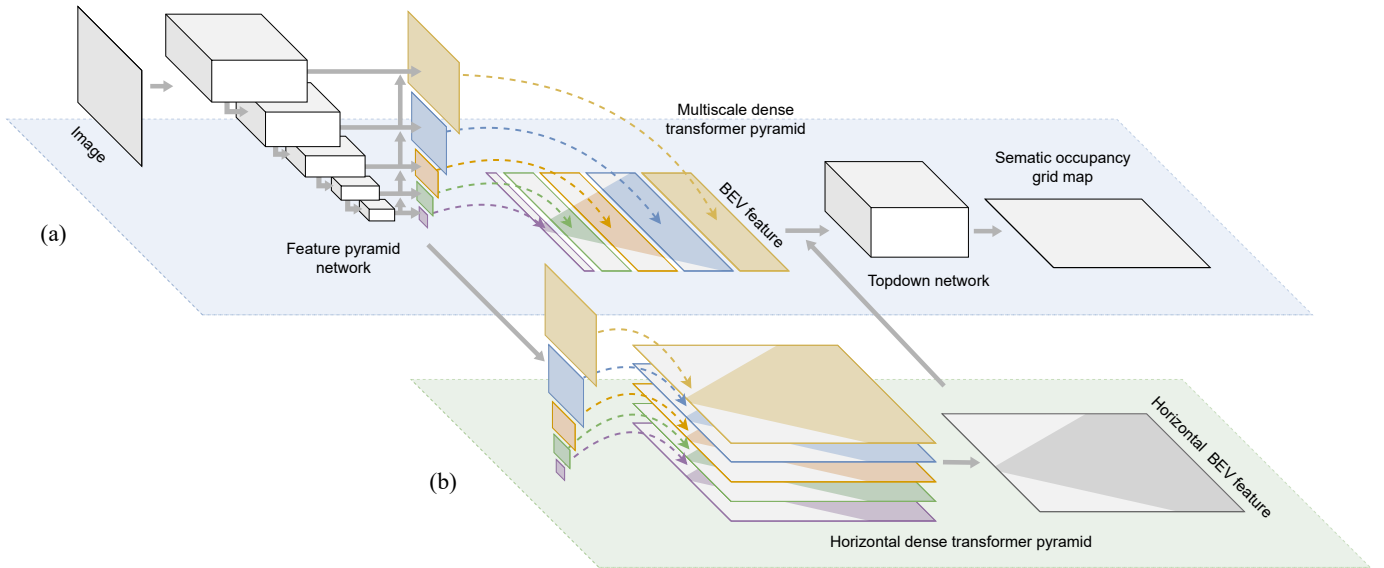


Fig. 1: Horizontally-aware Pyramid Occupancy Network: (a) the original PON network consists of a feature pyramid network, the multiscale dense transformer pyramid and the topdown network, (b) the H-PON extends PON with the horizontal dense transformer pyramid, which provides additional horizontal relationship contexts for the top-down network.

is represented by a semantic occupancy grid in which each spatial location x_i has an associated state m_i^c of class c , that can be either occupied ($m_i^c = 1$), or free ($m_i^c = 0$). As the occupancy is generally unknown, m_i^c is treated as a random variable and is modeled with the conditional probability $p(m_i^c | z_t)$, conditioned on a set of observations z_t . As illustrated in Fig. 1a, the network comprises 3 main components as follows:

- 1) **Feature pyramid network:** The pretrained ResNet-50 [8], as a backbone feature extractor, extracts multiscale image features. These image features are then fed into a feature pyramid network [9] to construct a feature pyramid in which the context is represented in multiple resolutions.
- 2) **Multiscale dense transformers:** Since the input and output of the network are entirely different coordinate systems, this component is required to convert the image features on the image plane to features on the bird's-eye-view plane. Each feature in a feature pyramid is converted using a component called dense transformer. The BEV features are, then, concatenated along the depth axis.
- 3) **Topdown network:** This component processes the bird's-eye-view features into the BEV semantic map. It performs the upsampling operation and predicts the final semantic occupancy grid probabilities using a standard convolution neural network.

The most difficult aspect of this problem is how to translate the frontal view into the perspective of the bird's-eye view. In principle, this translation step needs complex computations and requires knowledge not just about the camera intrinsics but also the semantic context of the image to help estimate the depth of various objects that might also be partially excluded

in the frontal view.

PON uses the multiscale dense transformer, which is a standard encoder-decoder model to condense each image column into an encoded vector. The image column is a narrow view from top to bottom of the frontal image and, therefore, contains the context of the object along the direction of that column. This encoded vector is then decoded into a ray, which contains both position and semantic of the object along the ray originating from the camera. However, the relationship between each column is not modeled in this component.

IV. HORIZONTALLY-AWARE PYRAMID OCCUPANCY NETWORK

We introduce a novel component – horizontal dense transformer pyramid. In combination with the original PON, we called our model the Horizontally-aware Pyramid Occupancy Network (H-PON). The horizontal dense transformer pyramid takes a horizontal column of the image and encodes it into a horizontal context. The goal is to extend the ability of PON to include the contextual relationship across the horizontal direction.

Similar to PON, illustrated in Fig. 2a, the model converts an image plane feature with C channels, height H , and width W , to a bird's-eye-view plane feature with C channels, depth Z , and width X . PON takes a vertical column and encodes it into a bottleneck feature before expanding it back along the polar radial direction. Our method, Fig. 2b, takes a horizontal column and encodes it into a bottleneck feature before expanding it back along the horizontal line.

In our experiment, we implement PON using the same architecture as the original paper [1]. The architectural and implementation details can be found in the paper and their

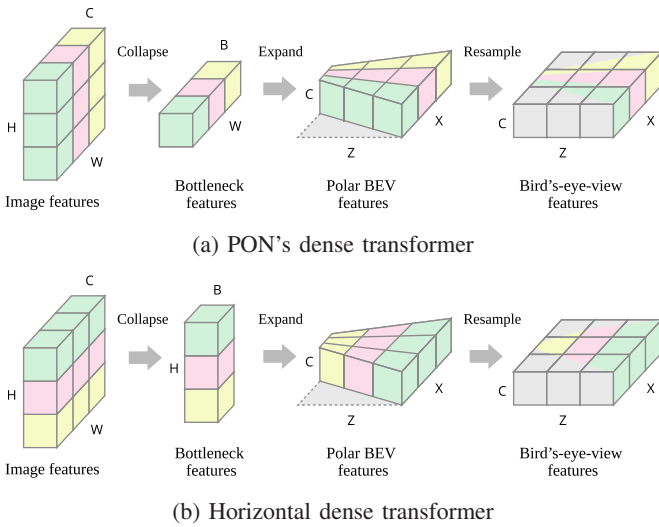


Fig. 2: Comparison between the PON's dense transformer and the H-PON's horizontal dense transformer.

code. H-PON implementation is a simple extension to PON where we add an additional branch into the model as illustrated in Fig. 1.

The extended branch slightly modified the implementation of PON's dense transformer by adjusting the dimension in which the transformation takes place. The value of C , Z and X are kept the same as the size of the BEV feature in the original PON's implementation. However, the original PON's implementation combines the outputs of the multi-scale dense transformer by cropping and stacking along the z -direction. H-PON stacks and downsamples the outputs of the horizontal dense transformer along the channel-direction as illustrated in Fig. 1b. Those two outputs from PON's multi-scale dense transformer pyramid and H-PON's horizontal dense transformer pyramid are stacked along the channel-direction and fed into the top-down network to predict the final semantic occupancy grid probabilities.

V. EXPERIMENTAL SETUP

A. Dataset

In the experiment, we evaluate the performance of our method with the nuScenes dataset [10], a large-scale dataset for autonomous driving. The nuScenes dataset is comprised of 20-second-long video sequences of driving scenes captured in Boston and Singapore with annotated data. We use version 1.0-mini, which is a small version comprised of 10 scenes totaling 404 frames and including images, annotations, and other metadata. Notably, we use only front camera data from a total of six cameras with different views. These 404 samples are randomly shuffled and split into 70% for training and 30% for validation. The ground truth occupancy maps for each class are generated from the annotations with map data, ego position, and camera calibration. The dataset contains 14 classes, which are categorized into 4 static map layout classes and 10 movable object classes. Additionally, an occlusion

mask is calculated from lidar data to indicate the camera field of view. We use the same processes for the ground truth occupancy map and occlusion mask generations described in [1].

B. Training and evaluation

We train the network using binary cross entropy loss until the convergence with Adam optimization with a learning rate of 0.001. The predictions of occupancy probability are thresholded with a decision boundary of 0.5 ($p(m_i^c | z_t) > 0.5$) and then evaluated using the intersect over union (IoU) score. Moreover, non-visible grid cells, which can be indicated by an occlusion mask, are ignored during evaluation.

VI. RESULTS

After each training epoch, we evaluate the networks with an average IoU score. The IoU is a ratio that calculates the overlapping area between the ground truth and predicted area to the total area [11]. Fig. 3 shows the average IoU score between the original PON and our H-PON.

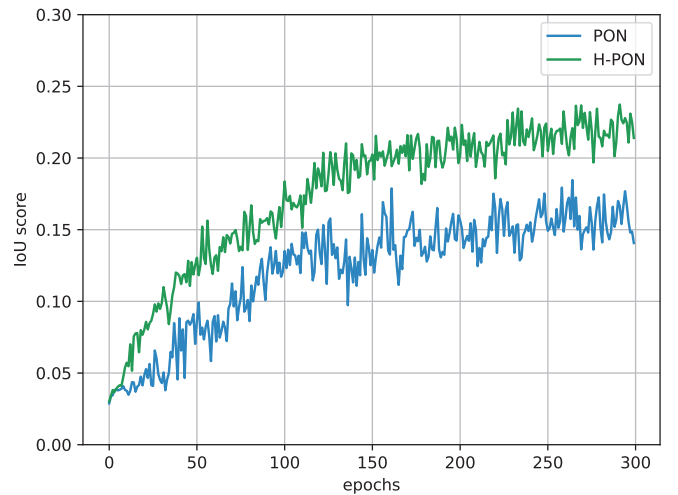


Fig. 3: Visualization of the average IoU score on the validation dataset between PON and H-PON.

We also evaluate the networks with IoU scores by classes as shown in Table I. The first four classes are static classes, and the remaining are object classes which are movable. While the original PON produces an average IoU score of 14.9321%, our H-PON's average score is 19.5419%.

Furthermore, the performance of PON and H-PON is evaluated using precision and recall, as shown in Table II. While the original PON produces an average precision of 27.9755% and an average recall of 19.5345%, our H-PON produces an average precision of 34.8999% and an average recall of 24.4718%.

In Fig. 4, some images from the validation dataset are visualized with their ground truth and occupancy grid maps predicted by PON and H-PON. We found out that H-PON can locate the road layout that aligns along the x -axis of the camera, e.g., the road crossing at the intersection with its sided

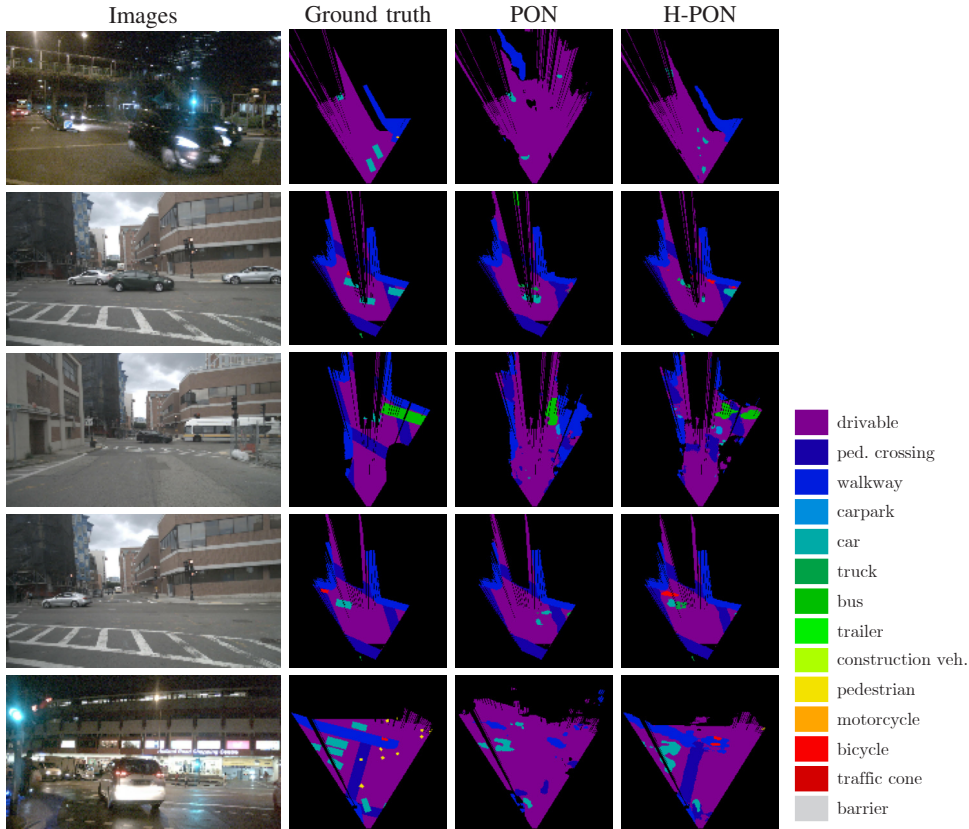


Fig. 4: Comparison of prediction results on validation samples between PON and H-PON included images and ground truths. Black occlusion masks were ignored during evaluation.

TABLE I: IoU scores (%) on the validation dataset.

| Classes | PON | H-PON |
|-------------------|----------------|----------------|
| drivable | 75.4146 | 76.7223 |
| ped. crossing | 35.5399 | 50.6781 |
| walkway | 41.8142 | 51.3494 |
| carpark | 24.7612 | 39.5416 |
| car | 11.7246 | 18.3359 |
| truck | 4.2715 | 7.7739 |
| bus | 7.5653 | 18.1267 |
| trailer | 0 | 0 |
| construction veh. | 2.971 | 1.5251 |
| pedestrian | 0.2913 | 2.6767 |
| motorcycle | 0.3115 | 0 |
| bicycle | 1.4682 | 4.6584 |
| traffic cone | 2.5606 | 0.1468 |
| barrier | 0.3551 | 2.0518 |
| Average | 14.9321 | 19.5419 |

TABLE II: Precision and Recall on the validation dataset.

| Classes | PON | | H-PON | |
|-------------------|----------------|----------------|----------------|----------------|
| | Precision | Recall | Precision | Recall |
| drivable | 82.9176 | 89.2868 | 87.0786 | 86.5790 |
| ped. crossing | 54.2992 | 50.7076 | 71.3949 | 63.5899 |
| walkway | 59.5306 | 58.4207 | 72.0786 | 64.0998 |
| carpark | 59.9885 | 29.6596 | 59.8274 | 53.8355 |
| car | 31.2417 | 15.8021 | 38.7155 | 25.8342 |
| truck | 10.8514 | 6.5808 | 22.7481 | 10.5624 |
| bus | 14.4945 | 13.6631 | 46.3292 | 22.9449 |
| trailer | 0 | 0 | 0 | 0 |
| construction veh. | 10.0711 | 4.0438 | 10.2493 | 1.7602 |
| pedestrian | 11.7647 | 0.2978 | 25.4902 | 2.9039 |
| motorcycle | 3.6697 | 0.3393 | 0 | 0 |
| bicycle | 17.3077 | 1.5789 | 10.2041 | 7.8947 |
| traffic cone | 29.8387 | 2.7246 | 33.3333 | 0.1473 |
| barrier | 5.6818 | 0.3774 | 11.1492 | 2.4528 |
| Average | 27.9755 | 19.5345 | 34.8999 | 24.4718 |

walkway, in the z-axis more correctly than PON since the H-PON provides contextual relationship across the horizontal direction in the image. The long objects that align along the x-axis of the camera are also predicted more accurately by H-PON. The bus is one of those objects, as specified by a higher H-PON's IoU score, precision, and recall for this class. The H-PON also outperforms PON in some other object classes, e.g., car, truck, pedestrian and bicycle, as it has more ability to detect the objects located in the left and right border.

VII. CONCLUSION

This paper proposes a novel architecture for predicting bird's eye view map from an image, namely H-PON. H-PON extends the PON model with a novel component – horizontal dense transformer pyramid – which encodes horizontal columns of the image and expands them onto the bird's-eye-view plane. This helps in providing the network with the contextual relationship across the horizontal direction of the image and enables the model to better understand object

relationships in the horizontal direction within the scene. The experimental results show that this novel component significantly improves performance, especially for the objects and road layouts aligned along the x-axis of the camera. Additionally, the objects that are rarely seen and those positioned further away from the center also gain better prediction scores. One weakness of this model is the requirement of camera intrinsic parameters, which limits the generality of the method. This problem will be investigated further in future works.

ACKNOWLEDGEMENT

This work is supported by King Mongkut's Institute of Technology Ladkrabang [KREF186604].

REFERENCES

- [1] T. Roddick and R. Cipolla, "Predicting semantic map representations from images using pyramid occupancy networks," in *2020 IEEE/CVF Conference on Computer Vision and Pattern Recognition (CVPR)*, 2020, pp. 11 135–11 144.
- [2] J. Wang, T. Mei, B. Kong, and H. Wei, "An approach of lane detection based on inverse perspective mapping," in *17th International IEEE Conference on Intelligent Transportation Systems (ITSC)*, 2014, pp. 35–38.
- [3] A. Abbas and A. Zisserman, "A geometric approach to obtain a bird's eye view from an image," 2020.
- [4] L. Reiher, B. Lampe, and L. Eckstein, "A sim2real deep learning approach for the transformation of images from multiple vehicle-mounted cameras to a semantically segmented image in bird's eye view," 2020.
- [5] S. Schuster, M. Zhai, N. Jacobs, and M. Chandraker, "Learning to look around objects for top-view representations of outdoor scenes," 2018.
- [6] C. Lu, M. J. G. van de Molengraft, and G. Dubbelman, "Monocular semantic occupancy grid mapping with convolutional variational encoder–decoder networks," *IEEE Robotics and Automation Letters*, vol. 4, no. 2, pp. 445–452, apr 2019. [Online]. Available: <https://doi.org/10.1109/2Fra.2019.2891028>
- [7] J. Philion and S. Fidler, "Lift, splat, shoot: Encoding images from arbitrary camera rigs by implicitly unprojecting to 3D," in *Computer Vision – ECCV 2020*, A. Vedaldi, H. Bischof, T. Brox, and J.-M. Frahm, Eds. Cham: Springer International Publishing, 2020, pp. 194–210.
- [8] K. He, X. Zhang, S. Ren, and J. Sun, "Deep residual learning for image recognition," in *2016 IEEE Conference on Computer Vision and Pattern Recognition (CVPR)*, 2016, pp. 770–778.
- [9] T.-Y. Lin, P. Dollár, R. Girshick, K. He, B. Hariharan, and S. Belongie, "Feature pyramid networks for object detection," in *2017 IEEE Conference on Computer Vision and Pattern Recognition (CVPR)*, 2017, pp. 936–944.
- [10] H. Caesar, V. Bankiti, A. H. Lang, S. Vora, V. E. Liong, Q. Xu, A. Krishnan, Y. Pan, G. Baldan, and O. Beijbom, "nuscenes: A multimodal dataset for autonomous driving," in *2020 IEEE/CVF Conference on Computer Vision and Pattern Recognition (CVPR)*, 2020, pp. 11 618–11 628.
- [11] R. Shanmugamani, *Deep Learning for Computer Vision: Expert techniques to train advanced neural networks using TensorFlow and Keras*. Packt Publishing Ltd., 2018.

Advancing Accurate Depth Estimation and Perception with Angled Stereo Camera

Xiao Da Terrence Fu
Mechanical Engineering
National University of Singapore
 Singapore
 fxd_terrence@u.nus.edu

Sutthiphong Srigrarom
Mechanical Engineering
National University of Singapore
 Singapore
 spot.srigrarom@nus.edu.sg

Abstract—This work explores the use of angled stereo vision with low-cost cameras to increase the field of view for an improved situational awareness. While it increases the perception capabilities in computer vision applications, this work also advances the accuracy of depth estimation. Traditional stereo camera setups rely on a pair of parallel optical axes, which consists largely of overlapping regions that results in a wastage of both hardware and processing resources in capturing similar views. By reducing the overlap in the images captured, more data can be captured from the surrounding for analysis. The angled stereo camera is capable of capturing more unique information as compared to the regular stereo camera alternative with the same hardware, improving situational awareness.

Index Terms—Angled stereo camera, Fisheye camera, depth estimation, overlapping view, peripheral view, depth estimation errors, enhanced field of view, multi agent monitoring.

I. INTRODUCTION

Stereo vision is the ability to perceive depth in a scene by using multiple viewpoints. This technique is used extensively in computer vision to enable machines to understand and interpret the surroundings. The use of stereo cameras is a common approach for depth perception and 3D reconstruction, with various applications in robotics, autonomous driving and surveillance [1] [2]. This paper focuses on the advancements in stereo camera technology, particularly the use of angled stereo cameras for an improved hardware utilisation by reducing overlap regions. The traditional stereo cameras are typically mounted horizontally with a pair of parallel optical axis [3]. This leads to an overlap of information captured by the cameras which translates to a wastage of hardware utilisation. The use of angled stereo cameras provides more flexibility in capturing depth information for a wider field of view (FOV) with the same hardware, thereby improving the overall resource utilisation. The data captured from the peripheral vision unique to angled stereo camera can also be used to generate depth information with motion. However, the use of angled fisheye stereo cameras intensifies the criticality of accurate unwarping which will also be brought up and addressed in this work. Current unwarping technologies such as the common fisheye unwarping method in MATLAB generally has the following characteristics.

- Unwarped image is free of radial distortion caused by the fisheye lens
- Rectilinear appearance with the preservation of straight lines
- Image stretching present at the edges
- Unwarped image has some loss of information at the edges due to the stretching process

The warping of fisheye images is a long standing problem in current works with fisheye cameras. There are existing works that explores various unwarping methods for fisheye cameras. Each of the methods having their benefits for various applications. One of the methods proposed the mapping of points onto a cylinder instead of a plane [4]. This method aims to reduce information loss along epipolar lines. This method has the potential to reduce information loss along epipolar lines. A more recent method proposed suggested the mapping of points onto a spherical surface [5]. Works have also explored the use of both the geometric calibration and epipolar rectification in conventional stereo cameras with fisheye lenses [6]. A combination of these methods will have the potential of reducing both the information loss along epipolar lines and generating an equiangular projection. There is also deep-learning approach at which the dedicated neural network is specially-design for deformation modelling and unwarping the images, such as [7], however, they are of limited use due to different training data and thus are not considered here.

Overall, the use of angled stereo cameras represents an important advancement in stereo vision technology, improving both hardware and data resource utilisation and opening new possibilities for accurate depth estimation and perception in in both military and commercial utilisations. The paper will describe the methodology employed for preparing the stereo camera set-up, as well as the calibration techniques used to achieve accurate results. In addition, the techniques used in the depth estimation and perception will also be presented. The use of angled stereo cameras can increase the amount of data captured with the use of existing hardware, paving the way for more advanced and efficient computer vision systems with minimal modifications.

II. METHODOLOGY

The cameras used in this stereo camera set-up is the ArduCam IMX323, capable of capturing images at 1080p. The lens used for this test is the 180° lens (Model number M25170H12) from the ArduCam UVC camera M12 lens kit. The mount holding the camera is printed using a 3D printer. The distance between the center points of the sensors for both the setups were kept to 50mm as seen in Figure 1 (a) and (b). The variation of the 2 mounts lies in the angle of tilt of the sensors as compared in Figure 1 (c).

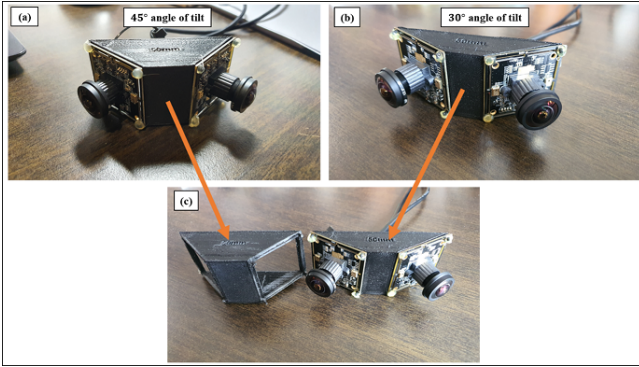


Fig. 1. Angled fisheye camera setups; (a) 45° angle of tilt setup; (b) 30° angle of tilt setup; (c) side by side comparison of 45° and 30° angle of tilt setups

The underlying concept of angled stereo camera builds upon existing works of the traditional stereo cameras that makes use of a pair of parallel optical axis. In traditional stereo camera technology, two cameras are used to capture images of a scene from a slightly different perspective. This happens while the cameras are facing in the same direction. The disparity between the two images is then compared to obtain the distance from various points within the overlapping scene captured. This method is similar to the way that the human eyes work, by subconsciously perceiving disparity between the images from both eyes. This allows us to perceive distance through vision. With the use of angled stereo cameras, a wider FOV is captured by reducing the overlapping region. This is similar to the eagle eye view [8]. The angle of tilt of the sensors are considered when deriving the equations. The concept of angled stereo camera can be seen in Figure 2 showing the effects of introducing tilt to the sensors.

The depth estimation equations are as follows. Firstly by identifying the angle of the target relative to each camera given using the following equation, with l measured in pixels. In target tracking applications with the use of angled fisheye stereo cameras, the value of l_{target} should be measured from the left edge of the image to the center point of the target's bounding box for depth estimation. This will ensure that the distance estimation point provided will be contained within the target.

$$\theta_{target} = \frac{l_{target}}{l_{FOV}} \theta_{FOV} \quad (1)$$

The distance to the target from each sensor can then be measured using the following equations before obtaining an average of the two values for an estimated distance from the observer to the target.

$$\rho_l = b_s \frac{\sin(\theta_r + \theta_t)}{\sin(\theta_l - \theta_r - 2\theta_t)} \quad (2)$$

$$\rho_r = b_s \frac{\sin(\pi - \theta_l + \theta_t)}{\sin(\theta_l - \theta_r - 2\theta_t)} \quad (3)$$

$$\rho_{avg} = \frac{\rho_l + \rho_r}{2} \quad (4)$$

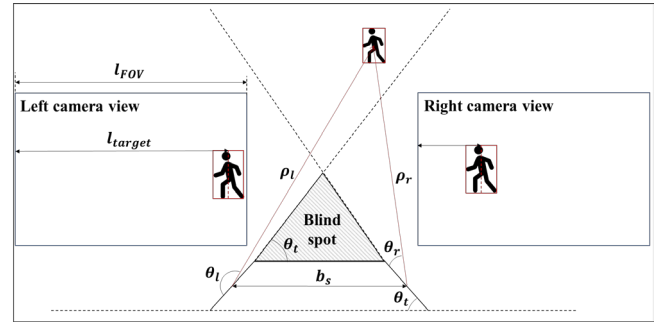


Fig. 2. Concept of angled stereo cameras

By introducing an angle of tilt to the sensors, the disparity between the images captured by the left and right camera increases. This increase in disparity results in an increased error in the estimated distance. In addition, the extent of warping varies significantly across the radial distance of the image captured by the fisheye lens [9]. The warping effect of the fisheye lens compounded with the increased disparity from the angle of tilt introduced. This resulted in a larger error as compared to conventional stereo cameras.

Hence the need for an increased focus on image correction and transformation to preserve angle proportions in images captured. Firstly, a radial correction that restores the angle proportion along the horizontal axis in the vertical center axis as shown in Figure 3. However, a second transformation is required that corrects the angle proportions along all horizontal directions within the image. This allows for depth estimation for targets at various heights in the overlapping images and is unique in a way that the angle proportions of the captured image is preserved.

III. RESULTS AND DISCUSSIONS

Preliminary tests were done on the stereo camera setup with 45° angle of tilt. As a proof of concept, by selecting two points on the image manually, a distance estimation

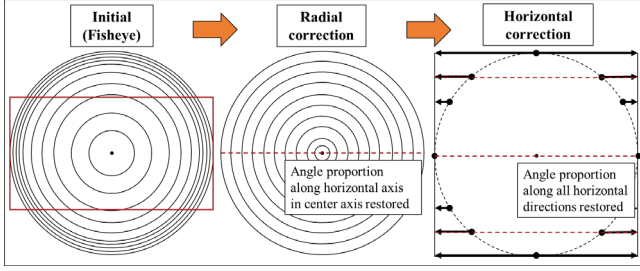


Fig. 3. Ideal unwarping methodology

will be output. However, due to limitations in manufacturing precision of the prototype mounts, there are deviations in the actual angle of tilt from the designed angle of tilt of the sensors. Hence, the device is first calibrated using a known distance. An angle offset is then introduced to correct the angle of tilt of each sensor from the designed angle of tilt. This is caused by deviations arising from manufacturing imperfections.

A test is done on images captured from the 45° angle of tilt setup as seen in Figure 4. Identical points in the real world are identified in each of the image in the image pair (left and right camera). The pixel coordinates are recorded and the distance of the target from each sensor is estimated with the use of equations (1) to (4). With a distance estimation of approximately 24.457m, it is similar to the data obtained from google satellite images with an estimated distance of 30m as seen in Figure 5. Transformation has been done to the live feed of the image captured to correct radial distortion. Hence the angle proportion is preserved solely at the center axis. Since the point measured in Figure 4 is close to the center of the image height wise, hence the distance measurement is assumed to be relevant.

It is determined that the capability of the range of distance measured using the same hardware is largely based on the distance between the sensors, b_s . The equation shown as follows.

$$\rho = \sqrt{\frac{b_s^2}{2(1 - \cos \theta_d)}} \quad (5)$$

By increasing the distance between the sensors, a longer distance between the observer and the target can be estimated.

The current angled stereo camera setup with a baseline distance between the sensors, b_s designed with a value of 50mm. This distance estimation of around 30m is the physical limit of distance estimation with the current hardware at 1080p capturing images of 1920px width and 1080px height. This limit in distance estimation is due to the constraints in the pixel count available in the width of the image. At a larger distance, the angle of disparity between the left and right camera to the target decreases from θ_d to θ'_d as seen in Figure 6. ($\theta_d \leq \theta'_d$) Considering

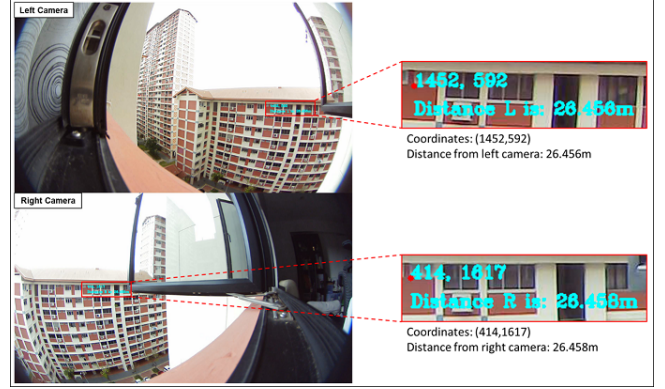
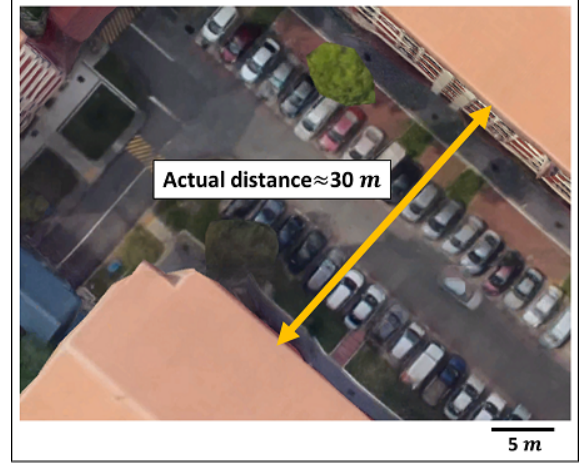
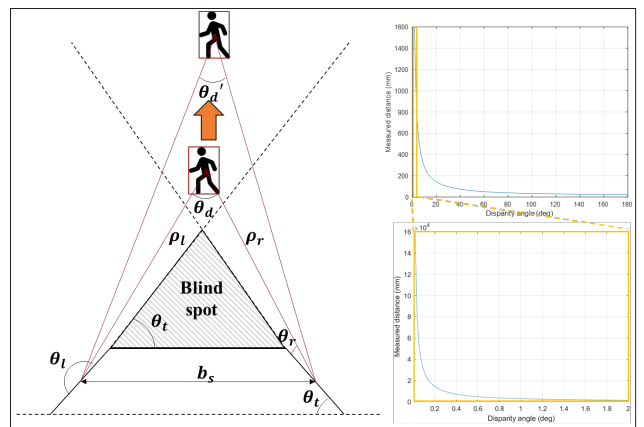

 Fig. 4. Test distance estimation using setup with 45° angle of tilt


Fig. 5. Google satellite images distance estimation

the case where $\rho_l = \rho_r$ on the current setup, the following equation modelling how the measured distance varies with the disparity angle is obtained. At a target distance of more than 30m in this baseline distance of 50mm, the disparity angle becomes too small for it to be reflected in terms of pixels of the image.


 Fig. 6. Decrease of angle of disparity θ_d as target moves further

With the hardware limitations on the current setup designed, it can be said that an ideal distance scale of 0.2 to 5.0m is preferred for a more accurate depth estimation as reflected in Figure 7.

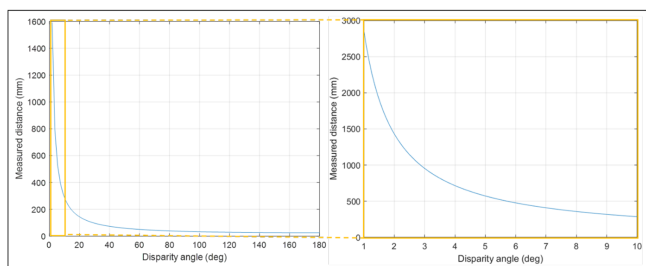


Fig. 7. Ideal range of target measured with baseline distance of 50mm

It can be seen in Figure 8. that while the MATLAB fisheye unwarping method is able to rectify some rectilinear distortion significantly. However, it can be noted that the angle proportions are not preserved in the output image. In addition, it crops the original image significantly, resulting in the elimination of useful data from the original image. In the case where a cylindrical calibration surface was used as seen in Figure , the manual calibration using OpenCV shows each situation of over correction and under correction. In the case of over correction, the angle proportion on the outer edge is not preserved as seen from the stretched outer edge of the image and a compressed central section. In addition, there appears to be a loss of image data on the outer edge. In the case of under correction, the image shows a compressed outer section as compared to the inner section. Hence to preserve the angle proportions within the image and to ensure maximum resource utilisation, a unwarping technique that requires a radial and horizontal correction is needed.



Fig. 8. Sample unwarping with MATLAB with fisheye and standard unwarp

A comparison of the benefits with the use of angled stereo camera shows the reduction of redundant data as seen in 10. The bounding boxes in the 45° angle of tilt shows a reduction in the main vision as compared to the 30° angle of tilt setup. This allows a potential for more useful unique data to be captured with minimal modifications to existing hardware. The use of a calibrated angled fisheye stereo cameras mounted on a drone allows for depth perception and is hence capable of determining its relative speed to the surrounding with a video feed with known frames per second. With the speed data, the non-overlapping section of the images can be analysed

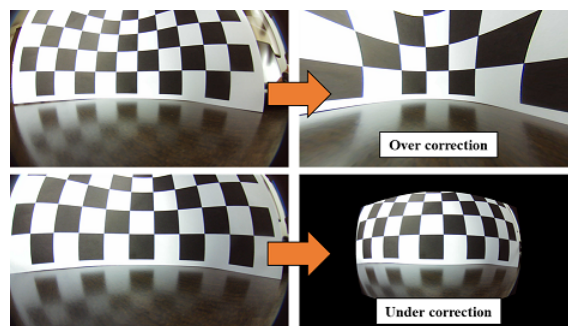


Fig. 9. OpenCV manual calibration attempts

as the peripheral vision for the application of motion parallax theory. Hence allowing for the mapping of depth information at a wider FOV with the same hardware. In addition, with the angle of tilt and the distance between the sensors accounted for, the video feed can come from 2 separate observers with known pose for the target distance to be estimated to a higher level of accuracy. With known camera pose and coordinates, the angle of tilt of the sensor and baseline distance between the sensor can be obtained respectively. This format of data collection creates a larger baseline distance between the sensors, allow for a longer distance measurement.

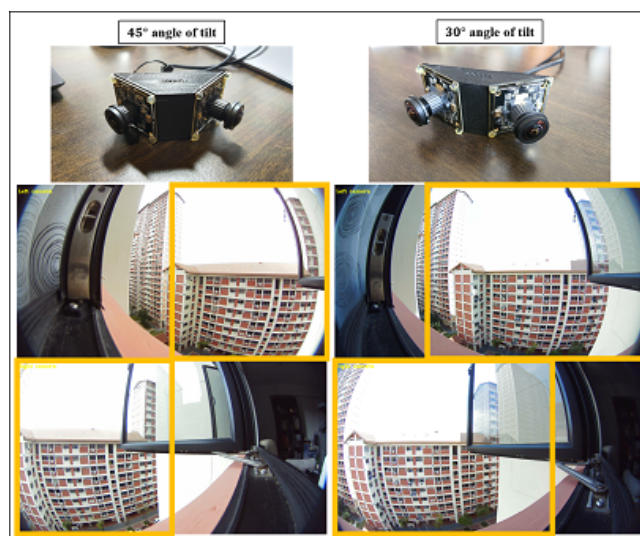


Fig. 10. Comparison of overlap and peripheral vision

IV. CONCLUSION AND FUTURE WORK

This work acts as a proof of concept for angled fisheye stereo camera technology and explored the use of it and proposed unwarping methods that has the potential to improve most use cases of fisheye lenses in stereo camera applications. With minimal changes to the existing hardware, an increased level of resource utilisation can be achieved with this work. The findings from this

work opens numerous possibilities in practical application in both the military and commercial use. It includes enhanced depth perception and 3D reconstruction, with various applications in robotics, autonomous driving and surveillance. This enhanced sensing capabilities translates to an increased overall system capability with the same hardware costs. In addition, it unlocks new possibilities for multi agent monitoring and synchronization of data, creating depth map of an environment; search and localising a target with accuracy.

REFERENCES

- [1] M. Bertozzi, L. Castangia, S. Cattani, A. Prioletti, and P. Versari, "360° detection and tracking algorithm of both pedestrian and vehicle using fisheye images," *Intelligent Vehicles Symposium*, 2015.
- [2] C. Eising, J. Horgan, and S. Yogamani, "Near-field perception for low-speed vehicle automation using surround-view fisheye cameras," *Transactions on Intelligent Transportation Systems*, vol. 23, 2022.
- [3] S. Li, "Real-time spherical stereo," *International Conference on Pattern Recognition*, 2006.
- [4] S. Roy, J. Meunier, and I. J. Cox, "Cylindrical rectification to minimize epipolar distortion," *Computer Society Conference on Computer Vision and Pattern Recognition*, pp. 393–399, 1997.
- [5] M. Elhashash and R. Qin, "Investigating spherical epipolar rectification for multi-view stereo 3d reconstruction," *Remote Sensing and Spatial Information Sciences*, vol. V-2-2022, pp. 47–52, 2022.
- [6] S. Abraham and W. Forstner, "Fish-eye-stereo calibration and epipolar rectification," *Journal of Photogrammetry Remote Sensing*, vol. 59, pp. 278–288, 2005.
- [7] M. Jaderberg, K. Simonyan, A. Zisserman *et al.*, "Spatial transformer networks," *Advances in neural information processing systems*, vol. 28, 2015.
- [8] H. Duan, Y. Deng, X. Wang, and F. Liu, "Biological eagle-eye-based visual imaging guidance simulation platform for unmanned flying vehicles," *AE Systems Magazine*, pp. 36–45, 2013.
- [9] M. Bassford and B. Painter, "Development of an intelligent fish-eye camera," *International Conference on Intelligent Environments*, 2015.

Person Re-identification for Multi-Camera, Multi-Object Tracking on Robotic Platforms

Soon Xiao Xi Natasha
 Mechanical Engineering
 National University of Singapore
 Singapore
 natashasoon@u.nus.edu

Sutthiphong Srigrarom
 Mechanical Engineering
 National University of Singapore
 Singapore
 spot.srigrarom@nus.edu.sg

Abstract—Person re-identification (ReID) is defined as the problem of matching identities of interest across disjoint camera views, or in the same camera in different occasions. It provides significant value in the context of public security, as the ability to run such an application across a dynamic multi-camera system will increase efficiency in identifying and tracking any persons of interest who may pose a threat to the population. Existing multi-object trackers are only able to perform tracking with one camera, as the same identity appearing in another camera will not be re-identified. This paper aims to serve as a basis for developing a deep learning-based extension of a single-camera multi-object tracker to a multi-camera use case on a mobile robotic platform.

Index Terms—Deep Learning, Computer Vision, Image Processing, Image Recognition/Classification, Multiple Object Tracking

I. INTRODUCTION

Person re-identification (ReID) is defined as the problem of matching identities of interest across disjoint camera views, or in the same camera across different occasions. It provides value in tracking across dynamic multi-camera systems as it allows the same identity to be tracked across different camera views, increasing the efficiency in tracking persons of interest. Most existing multi-object trackers are only able to perform tracking across one camera, as the same target appearing across different cameras will not be given the same identity due to the lack of sharing of identity information across camera streams. On the other hand, trackers that are able to perform cross-camera tracking usually require too much computation to be used on smaller computers that mobile robotic platforms require. As such, this paper aims to close this gap by presenting an extension of FastMOT [1], a single-camera multi-object tracker, to a multi-camera use case using ReID.

FastMOT is a modular single-camera multi-object tracker that is able to run on an Nvidia Jetson Xavier NX, making it suitable as a baseline framework to use for multi-camera multi-object tracking on mobile robotic platforms.

For the extension, we also benchmarked two different ReID frameworks, namely AlignedReID [2] and OSNet [3]. Through this, we selected the best framework in terms of accuracy and efficiency to find the best option to use.

II. RELATED WORK AND LITERATURE REVIEW

A. Person Re-identification

1) *AlignedReID*: AlignedReID [2] is similar to most deep learning-based ReID models, as it is based on an image recognition backbone network. AlignedReID uses ResNet [4] trained on ImageNet [5] as a backbone network for feature extraction. It aims to solve the issue of image misalignment due to issues like inaccuracies in detection boxes, pose variations, and occlusion by automatically learning to align the body parts of detected persons without any additional input. The model employs mutual learning, where two networks are trained simultaneously, and share knowledge with each other via both metric losses (distance between inputs in the metric space) and classification losses (cross-entropy loss), illustrated in figure 1.

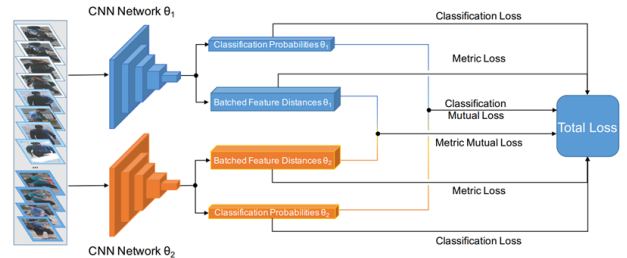


Fig. 1: Mutual learning framework

The distance used in the calculation of metric loss is a combination of global and local distances. The global distance between two images is the L2 distance between both images. The local distance is calculated by dynamically matching local features from top to bottom. For two images with local features $F = \{f_1, \dots, f_H\}$ and $G = \{g_1, \dots, g_H\}$, a distance matrix D is generated where $d_{i,j}$ is the distance between the i^{th} vertical part of the first image and the j^{th} vertical part of the second image. The local distance is thus the total distance for the shortest path from (1,1) to (H,H) in matrix D , illustrated in figure 2.

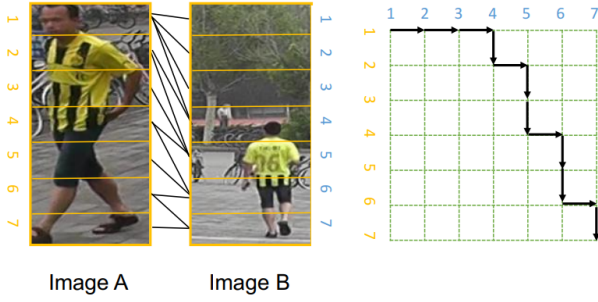


Fig. 2: Example of local distance calculation by AlignedReID. The black lines show the corresponding alignment between the two images on the left. The black arrows show the shortest path in the corresponding matrix D on the right.

2) *OSNet*: Unlike most existing ReID frameworks, OSNet [3] does not use existing image recognition networks as its backbone. Its authors argue that image recognition is a category-level task, while ReID is an instance-level task that puts local and global features at the same level of importance. As such, they presented a new backbone network, OSNet, which is able to learn omni-scale features that are more representative than those generated by image-recognition networks. The OSNet backbone network's building block is constructed using T parallel convolutional streams with different receptive field sizes, which are then merged with a novel aggregation gate (AG). Each stream is constructed by stacking t lite 3x3 convolutions, illustrated in figures 3 and 4.

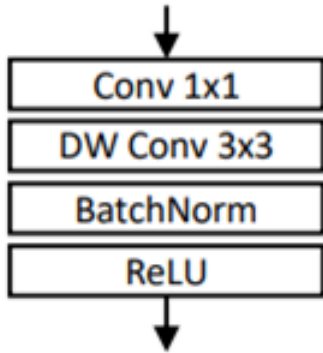


Fig. 3: Lite 3x3 convolution. DW: Depth-Wise.

The backbone network is constructed by stacking the proposed bottleneck layer by layer without further customization.

A main benefit of OSNet is that it can simply be used as a feature extractor in existing tracking frameworks, while other frameworks like AlignedReID require the processing of extracted features before ReID can be carried out. As such, OSNet can be much more efficient than other

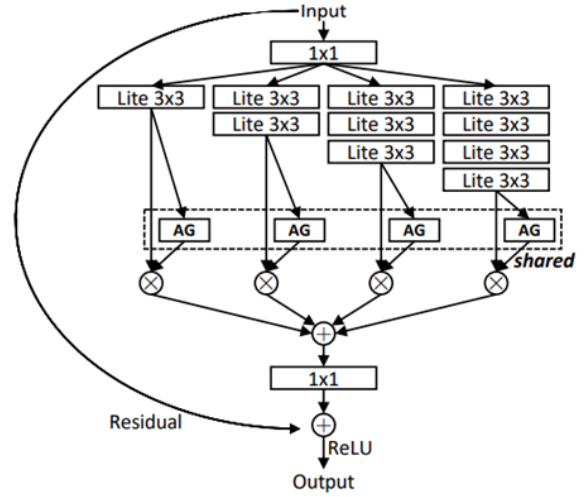


Fig. 4: Proposed bottleneck. AG: Aggregation Gate.

frameworks, paving the way for real-time multi-camera tracking.

Another benefit of the proposed backbone network is that the number of trainable parameters is 10 times smaller than that of ResNet 50, a version of the aforementioned ResNet [4]. As such, the risk of OSNet overfitting training data is much smaller than that of ResNet, allowing for better generalization across unseen test datasets.

3) *Re-Ranking*: Both AlignedReID and OSNet also have the option to perform re-ranking using k-reciprocal encoding [6]. Re-ranking aims to improve the performance of ReID on the basis that two images are a closer match if they are within each other's k-nearest neighbours. Given a query image q and a gallery set G with N images, where $G = \{g_i | i = 1, \dots, N\}$, the k-reciprocal nearest neighbours of q and g_i are the images that appear in both of their k-nearest neighbours.

The Jaccard distance $d_j(q, g_i)$ is then calculated as $d_j(q, g_i) = 1 - \frac{|\mathcal{R}^*(q, k) \cap \mathcal{R}^*(g_i, k)|}{|\mathcal{R}^*(q, k) \cup \mathcal{R}^*(g_i, k)|}$, where $|\mathcal{R}^*(q, k) \cap \mathcal{R}^*(g_i, k)|$ is the number of k-reciprocal nearest neighbours between q and g_i , and $|\mathcal{R}^*(q, k) \cup \mathcal{R}^*(g_i, k)|$ is the total number of unique identities in both sets of k-nearest neighbours. The final distance after re-ranking is a weighted combination of the originally calculated distance and the Jaccard distance.

B. Multi-Object Tracking with FastMOT

FastMOT [1] is a custom single-camera, multi-object tracker that we intend to extend for multi-camera tracking. It implements the YOLO detector [7], SSD detector [8], Deep SORT tracker [9], OSNet [3], KLT tracker [10], and camera motion compensation.

The YOLO detector or SSD detector is used to draw bounding boxes of detected tracking targets. The Deep SORT tracker runs detection and feature extraction sequentially, which slows down the tracking. As such, it is

only run every N frames, while the KLT tracker is used in the frames between to speed up tracking. OSNet is also only run every N frames as a feature extractor, and to reidentify identities have exited the camera's frame and reappear at another time.

III. TEST RESULTS

This section details the results of testing on both ReID frameworks, and on FastMOT.

A. Person Re-identification

1) *Datasets Used:* To test the performance of the ReID frameworks, two datasets were used.

The first dataset is Market-1501 [11], which consists of a total of 1501 identities across 32217 images. These images are taken from 6 cameras, some of which overlap. They were annotated with the Deformable Parts Model detector [12]. The dataset was taken outdoors in front of a campus supermarket, making this an open environment where each identity is not necessarily present in every camera. The official training protocol uses 751 identities across 12939 images for training, and 750 identities across 3368 images as queries and 751 identities across 15913 images as the gallery for testing.

The next dataset is the DukeMTMC-reID dataset [13], which consists of 1404 identities across 36411 images. The dataset was collected across 8 cameras, 2 pairs of which have overlapping views. They were manually annotated. The official training protocol uses 702 identities across 16522 images for training, and 702 identities across 2228 images as queries and 702 identities across 17,661 images as the gallery for testing.

2) *AlignedReID:* To test AlignedReID's performance, pre-trained models provided by the code's author were tested on both datasets. Figures 5 and 6 show the performance of AlignedReID on Market-1501 and DukeMTMC-reID respectively.

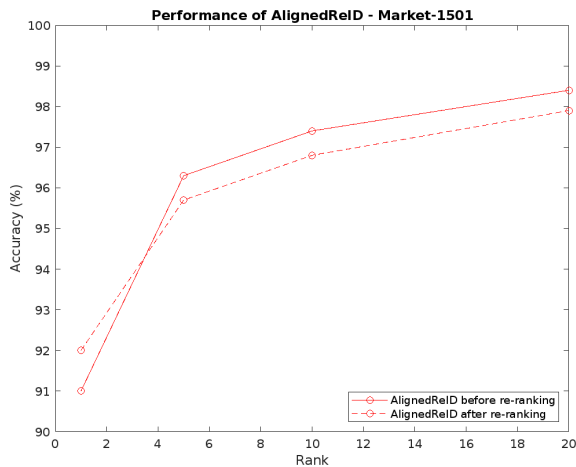


Fig. 5: Test results for AlignedReID on Market-1501 dataset

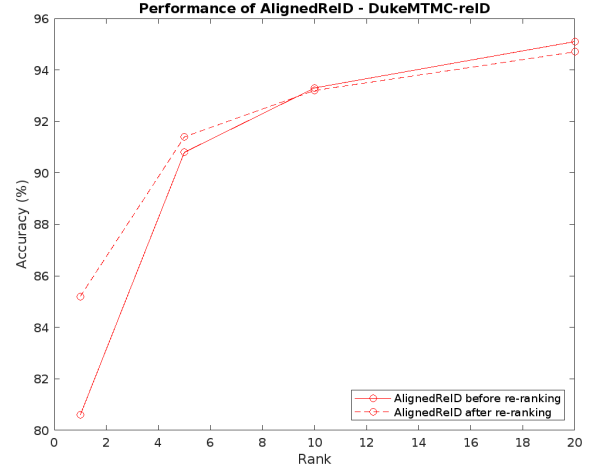


Fig. 6: Test results for AlignedReID on DukeMTMC-reID dataset

From the test results, it is clear that re-ranking improved performance in terms of rank-1 accuracy for both datasets. Although higher-rank accuracies were not necessarily improved, re-ranking still adds significant value as ReID in tracking is dependent on the rank-1 accuracy.

3) *OSNet:* To affirm that the OSNet backbone performs better than its image-recognition counterparts, we tested the performance of OSNet pre-trained on different backbones, namely ResNet 50, OSNet, and MobileNetV2 [14]. The ResNet 50 backbone was tested as it is used in AlignedReID, while MobileNetV2 was also tested as it is a similarly lightweight network as OSNet, to check if feature extraction time would be different for each backbone. Figures 7 and 8 show the performance of each backbone network with OSNet, on Market-1501 and DukeMTMC-reID respectively.

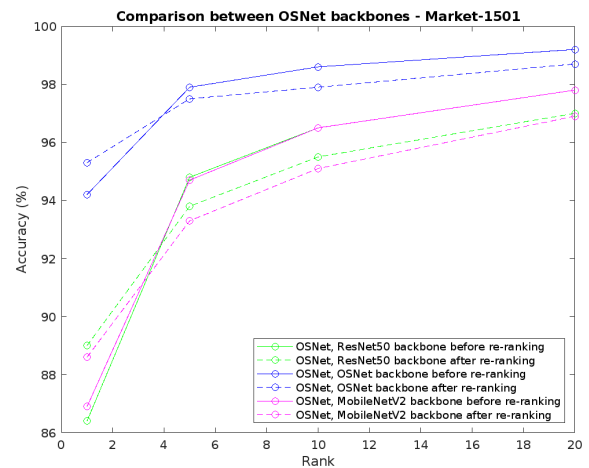


Fig. 7: Test results for OSNet with different backbones on Market-1501 dataset

From both figures, it is clear that the OSNet backbone outperforms both other backbones by a clear margin,

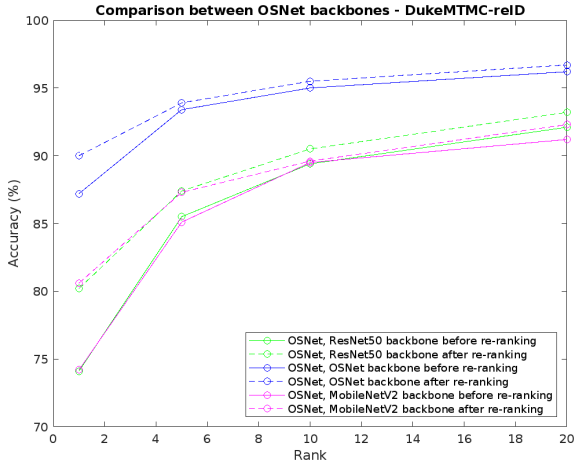


Fig. 8: Test results for OSNet with different backbones on DukeMTMC-reID dataset

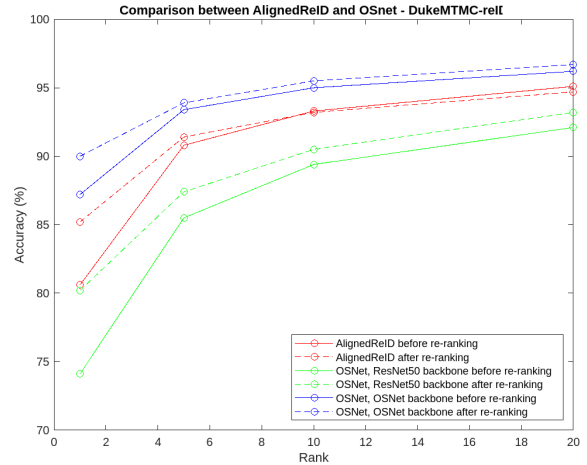


Fig. 10: Comparison between AlignedReID and OSNet on DukeMTMC-reID dataset

and further shows the improvement of rank-1 accuracy regardless of the backbone used.

4) Comparison Between AlignedReID and OSNet:

Figures 9 and 10 show the comparison between AlignedReID and OSNet’s performance on the Market-1501 and DukeMTMC-reID respectively.

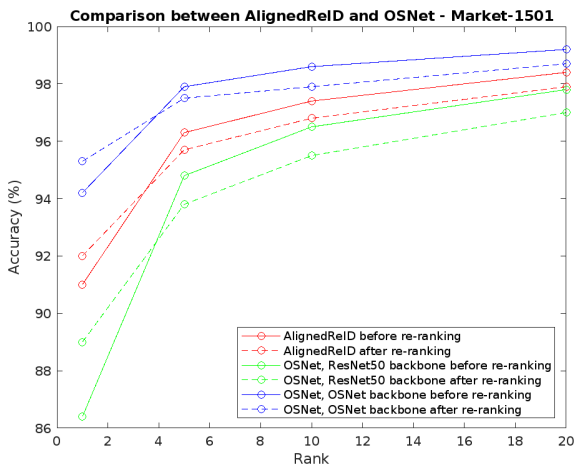


Fig. 9: Comparison between AlignedReID and OSNet on Market-1501 dataset

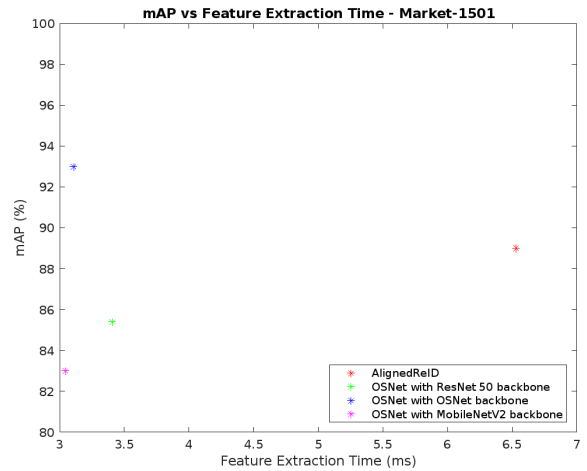


Fig. 11: Feature extraction time vs mAP, on Market-1501 dataset

From both figures, it is clear that AlignedReID performs better than OSNet when ResNet 50 is used as the backbone network. However, the OSNet backbone still performs better than both, even before re-ranking.

Figures 11 and 12 show the time taken for feature extraction against the mean average precision (mAP) for each framework, for Market-1501 and DukeMTMC-reID respectively.

From both figures, we can see that OSNet trained on the OSNet backbone not only performs the best in terms of mAP, it also takes much less time than AlignedReID. Although OSNet trained on MobileNetV2 took the least

time, the time difference with OSNet trained on the OSNet backbone is too small to justify the decrease in mAP.

As such, OSNet trained with the OSNet backbone is the best option for implementation of cross-camera multi-object tracking.

B. Multi-Object Tracking with FastMOT

1) Datasets Used: To test out FastMOT’s performance, I used open-source video datasets provided by the Swiss Federal Institute of Technology Lausanne (EPFL) [15], namely their laboratory sequence and terrace sequence.

The laboratory sequence consists of 4 people walking around a room for around 2.5 minutes. Identity 3, pointed out in figure 13, is most often occluded and moves out of frame once. It best illustrates FastMOT’s ability to track despite occlusion and re-identify targets that exit and reappear in a camera’s view.

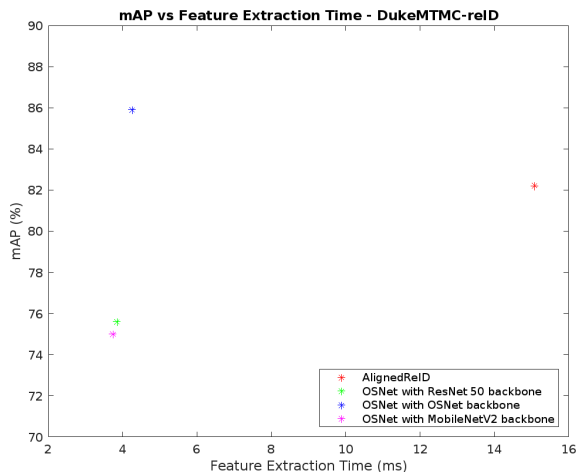


Fig. 12: Feature extraction time vs mAP, on DukeMTMC-reID dataset

The terrace sequence consists of 9 people walking around a terrace for around 2.5 minutes. Identity 2, pointed out in figure 14, walks out of frame once. It best illustrates FastMOT’s ability to re-identify targets that exit and reappear in a camera’s view.



Fig. 13: Example of laboratory sequence



Fig. 14: Example of terrace sequence

2) *Test Results for FastMOT*: Figure 15 shows identity 3 walking behind identity 1 and continuing to get tracked afterwards. This shows FastMOT’s ability to track targets despite occlusion.



Fig. 15: FastMOT continuing to track despite occlusion

Figures 16 and 17 show FastMOT’s ability to re-identify and continue tracking identities that leave the camera’s frame and reappear at another time.

In figure 16, identity 3 from the laboratory sequence steps out of frame and reappears, and FastMOT is able to correctly re-identify him and continue tracking.

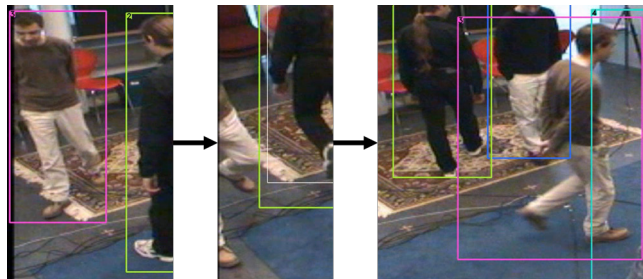


Fig. 16: FastMOT re-identifying targets with laboratory sequence



Fig. 17: FastMOT re-identifying targets with terrace sequence

3) *Conclusion on FastMOT*: FastMOT is a suitable baseline single-camera multi-object tracker to extend to a multi-camera use case as it is able to track targets with a high level of consistency. More importantly, it was able to track at 59 FPS on a laptop fitted with an Intel i7 CPU and RTX 3080Ti mobile GPU, and achieved tracking at 15 FPS on an Nvidia Jetson Xavier NX. Its ability to

perform tracking on an Nvidia Jetson Xavier NX makes it promising for the end-goal of performing multi-camera tracking on mobile robotic platforms.

IV. METHODOLOGY FOR FUTURE WORK

With a suitable ReID framework and single-camera multi-object tracker chosen, the next step our work is to perform implementation. Currently, FastMOT is able to take in single camera streams for tracking, and already uses ReID to re-identify targets that reappear in the camera at a later time. Our intention is to extend FastMOT to take in multiple camera input streams, and to share extracted features of targets that may have disappeared from one camera's view, and reappeared in another camera.

V. CONCLUSION

This paper proposes a basis for developing a deep learning-based extension of a mobile single-camera multi-object tracker to a multi-camera use-case using an efficient person re-identification framework.

REFERENCES

- [1] Y. Yang, "FastMOT: High-Performance Multiple Object Tracking Based on Deep SORT and KLT," Nov. 2020. [Online]. Available: <https://doi.org/10.5281/zenodo.4294717>
- [2] X. Zhang, H. Luo, X. Fan, W. Xiang, Y. Sun, Q. Xiao, W. Jiang, C. Zhang, and J. Sun, "Alignedreid: Surpassing human-level performance in person re-identification," 2017. [Online]. Available: <https://arxiv.org/abs/1711.08184>
- [3] K. Zhou, Y. Yang, A. Cavallaro, and T. Xiang, "Omni-scale feature learning for person re-identification," 2019. [Online]. Available: <https://arxiv.org/abs/1905.00953>
- [4] K. He, X. Zhang, S. Ren, and J. Sun, "Deep residual learning for image recognition," 2015. [Online]. Available: <https://arxiv.org/abs/1512.03385>
- [5] J. Deng, W. Dong, R. Socher, L.-J. Li, K. Li, and L. Fei-Fei, "Imagenet: A large-scale hierarchical image database," in *2009 IEEE Conference on Computer Vision and Pattern Recognition*, 2009, pp. 248–255.
- [6] Z. Zhong, L. Zheng, D. Cao, and S. Li, "Re-ranking person re-identification with k-reciprocal encoding," 2017. [Online]. Available: <https://arxiv.org/abs/1701.08398>
- [7] J. Redmon, S. Divvala, R. Girshick, and A. Farhadi, "You only look once: Unified, real-time object detection," 2015. [Online]. Available: <https://arxiv.org/abs/1506.02640>
- [8] W. Liu, D. Anguelov, D. Erhan, C. Szegedy, S. Reed, C.-Y. Fu, and A. C. Berg, "Ssd: Single shot multibox detector," in *Computer Vision – ECCV 2016*, B. Leibe, J. Matas, N. Sebe, and M. Welling, Eds. Cham: Springer International Publishing, 2016, pp. 21–37.
- [9] N. Wojke, A. Bewley, and D. Paulus, "Simple online and realtime tracking with a deep association metric," 2017. [Online]. Available: <https://arxiv.org/abs/1703.07402>
- [10] J. Shi and Tomasi, "Good features to track," in *1994 Proceedings of IEEE Conference on Computer Vision and Pattern Recognition*, 1994, pp. 593–600.
- [11] L. Zheng, L. Shen, L. Tian, S. Wang, J. Wang, and Q. Tian, "Scalable person re-identification: A benchmark," in *2015 IEEE International Conference on Computer Vision (ICCV)*, 2015, pp. 1116–1124.
- [12] P. F. Felzenszwalb, R. B. Girshick, D. McAllester, and D. Ramanan, "Object detection with discriminatively trained part-based models," *IEEE Transactions on Pattern Analysis and Machine Intelligence*, vol. 32, no. 9, pp. 1627–1645, 2010.
- [13] E. Ristani, F. Solera, R. S. Zou, R. Cucchiara, and C. Tomasi, "Performance measures and a data set for multi-target, multi-camera tracking," 2016. [Online]. Available: <https://arxiv.org/abs/1609.01775>
- [14] M. Sandler, A. Howard, M. Zhu, A. Zhmoginov, and L.-C. Chen, "Mobilenetv2: Inverted residuals and linear bottlenecks," 2018. [Online]. Available: <https://arxiv.org/abs/1801.04381>
- [15] F. F. J. B. R. L. P. Fua, F. Fleuret, J. Berclaz, R. Lengagne, and P. Fua, "Multi-camera pedestrians video," Jan 2008. [Online]. Available: <https://www.epfl.ch/labs/cvlab/data/data-pom-index-php/>

Zone-of-Interest Strategy for the Creation of High-Resolution Adversarial Images Against Convolutional Neural Networks

1st Franck Leprévost

Faculty of Science, Technology and Medicine
Department of Computer Science
University of Luxembourg
0000-0001-8808-2730

2nd Ali Osman Topal

Faculty of Science, Technology and Medicine
Department of Computer Science
University of Luxembourg
0000-0003-0141-4742

3rd Enea Mancellari

Faculty of Science, Technology and Medicine
Department of Computer Science
University of Luxembourg
0000-0002-8562-1433

4th Kittichai Lavangnananda

School of Information Technology
King Mongkut's University of Technology Thonburi
Bangkok, Thailand
0000-0002-9227-4839

Abstract—Trained convolutional neural networks (CNNs) are among the leading tools used for the automatic classification of images. They are nevertheless exposed to attacks: Given an input clean image classified by a CNN in a category, carefully designed adversarial images may lead CNNs to erroneous classifications, although humans would still classify "correctly" the constructed adversarial images in the same category as the input image. Currently most attacks are performed in the image input size domain of the considered CNN, which is usually small. However, due to privacy concerns with personal images on social media, there is a demand for generating large adversarial images that preserve the visual information of original images with the highest possible quality, while preventing automatic tracking and personal identification. Creating large-size adversarial images is difficult due to speed, adversity, and visual quality challenges, in particular if a requirement on adversarial images is the inability for humans to notice any difference between them and the original clean images. This paper describes the zone-of-interest generic strategy that aims at increasing drastically the efficiency of any type of attack (white-box or black-box, untargeted or targeted) and any specific attack (FGSM, PGD, BIM, SimBA, AdvGAN, EA-based attacks, etc.) on CNNs. Instead of exploring the full image size, the strategy identifies zones on which to focus the attacks. Although applying to any image size, the strategy is especially valuable for large high-resolution images. This strategy can be combined with other generic approaches, like the noise blowing-up method, to further improve attacks' performances.

Index Terms—Black-box attack; Convolutional Neural Network; High resolution adversarial image; Noise Blowing-Up method.

I. INTRODUCTION

In today's society, images, more specifically the information they contain, are used for a large and increasing series of applications and usages, ranging from self-driving cars to face recognition, security

access, medical diagnosis, satellite vision, etc. Their profusion and their usage in numerous applications have led to the development of tools to automatically process these images in a reliable way. Since some years, trained convolutional neural networks (CNNs) have been widely used for such tasks [9], [12], [20], [22], [26]. Given an image \mathcal{I} , a CNN provides an output vector $\mathbf{o}(\mathcal{I})$ of fixed length ℓ , where ℓ is the number of categories in which the CNN is trained to sort images. Each component of the output vector is a real number $0 \leq \mathbf{o}(\mathcal{I})[i] \leq 1$, while their sum satisfies $\sum_{i=1}^{\ell} \mathbf{o}(\mathcal{I})[i] = 1$. The label value $\mathbf{o}(\mathcal{I})[i]$ measures the plausibility, conferred by the CNN, that \mathcal{I} belongs to the i^{th} category. The CNN classifies \mathcal{I} in the dominating category, namely the category for which the label value dominates all others.

However, CNNs are not foolproof. More: They can be misled, and may misclassify images constructed by specifically designed adversarial attacks. The consequences of these attacks can be catastrophic, say in the context of self-driving cars or of medical images for instance. *A contrario*, attacks may also be in people's interest. They may improve people's privacy, for instance by preserving individuals' identities and limiting individual's automatic tracking despite the fact that pictures of their faces (at least) appear on social media.

Attacks against CNNs are usually classified according to the knowledge about the CNN given to the attacker. Schematically, they range from white-box attacks (see e.g. [3], [23]), where the attacker has complete knowledge about the CNN to attack (number and type of layers, weights, parameters, etc.), up to the most

challenging black-box attacks ([7], [11]), where the attacker has no knowledge at all about the concerned CNN, apart from getting its output vector classification for images he sends.

Attacks are deployed according to predefined scenarios. For instance, given a CNN and an input clean image \mathcal{A} classified by the CNN in c_a , the attacker in the target scenario chooses a specific category $c_t \neq c_a$ *a priori*, and then modifies \mathcal{A} to create an adversarial image \mathcal{D} that the CNN classifies in c_t . In the untargeted scenario, the adversarial image \mathcal{D} is expected to be classified by the CNN in any category c , whatever c may be as long as $c \neq c_a$.

Deceiving the CNN is not enough. One also expects the adversarial image \mathcal{D} to be so close to the clean input image \mathcal{A} for a human eye, that a human would still classify \mathcal{D} in c_a or, even better, would not be able to see any difference between \mathcal{D} and \mathcal{A} .

Finally, trained CNNs natively handle images of small or moderate size, for instance 32×32 for those trained on CIFAR-10 [14], or 224×224 for those trained on ImageNet [5]. If a trained CNN is given an image \mathcal{I} of a different size than its input size (to be referred to as an image in the \mathcal{R} domain), then it resizes it thanks to a resizing function ρ and then processes $\rho(\mathcal{I})$. This applies in particular when CNNs are exposed to high-resolution (HR) images (to be referred to as images in the \mathcal{H} domain). In this context, attacks usually address images in the resized \mathcal{R} domain and not in the original \mathcal{H} domain. The reason is that attacking images directly in the \mathcal{H} domain leads to three challenges regarding speed, adversity survival after resizing by ρ , and visual quality. Firstly, the complexity of the creation of adversarial images grows quadratically with the size of the images, hence attacking directly HR images may lead nowhere even after a long time (experiences performed on some attacks confirmed this statement). Secondly, a potentially adversarial noise created in the \mathcal{H} domain may lose its adversity feature once the image is downsized with ρ to fit the CNN's input size. Finally, the noise introduced in the \mathcal{H} domain should remain unnoticeable for a human, while keeping its adversity once the image is reduced.

The paper presents a strategy (Section II) aiming at significantly improving the construction of adversarial images against CNNs, such that a human is unable to notice any difference between the adversarial image and the original clean image. A key feature of the strategy is that it works *above any existing attack*. By this, we mean that the strategy applies generically to any white-box or black-box attack (like e.g. [3], [7], [11], [23]), whether it is for the target or for the untargeted scenario. The strategy requires the existence of techniques, satisfying some concrete criteria given in Section II, whose aim

is to "draw" explicitly the relevant zones of interest. Section III provides a promising candidate for such a technique. Section IV sketches the design of a series of experiments sustaining the strategy. Combined with other generic methods (in particular [16]), Section IV also indicates how the proposed method is likely to lead to the construction of adversarial noise in the \mathcal{H} domain, solving efficiently the speed, adversity "survival" and visual quality issues already raised, and that are crucial for large images. Finally, Section V concludes this paper.

For brevity, the paper mainly focuses on black-box attacks for the target scenario. Note that they are the most demanding attacks for the most demanding scenario.

II. THE ZONE-OF-INTEREST STRATEGY

Let \mathcal{C} be a trained CNN that classifies images into ℓ categories c_1, \dots, c_ℓ . Even in the context of a black-box attack, where an attacker has no insider knowledge about \mathcal{C} , the attacker nevertheless knows the output classification $\mathbf{o}_{\mathcal{C}}(\mathcal{I})$ vector of \mathcal{C} for any input image \mathcal{I} (or the potentially resized image $\rho(\mathcal{I})$ if needed).

Given a clean image, a black-box targeted attack essentially explores the image size space. The attacker aims to create an adversarial image by inserting into the clean image some appropriate adversarial noise via a trial and error process. Moreover, the introduced noise should be unnoticeable for a human eye (this non-trivial condition is for instance not satisfied by attacks like [13], [19], [21], [29]). Depending on the nature of the attack, and on the search space size, the trial and error process may be very time-consuming. It is *a fortiori* very time-consuming if the situation concerns HR images, and if the aim of the attacker is to create the adversarial noise directly in the \mathcal{H} domain.

The attack's efficiency would obviously benefit from knowing how the CNN makes its decisions. However, this expectation is by definition unlikely to occur for black-box attacks (explainable AI can not be taken for granted in this particular situation). Instead, a more realistic request would be to have the ability to select zones of the image satisfying two conditions: 1) focusing the attack's efforts on these zones has a high adversarial impact; 2) finding their location remains compatible with the fact that the considered attack is black-box. The difficulty is clearly that \mathcal{C} does not usually "leak" this crucial information to the attacker.

Nevertheless, let us assume that we have a fast technique T (see III for a candidate, and V for potential alternatives) that detects which image parts are likely to be the most significant for \mathcal{C} 's outputs and classifications, without requiring any insider knowledge about \mathcal{C} . Since from the attacker's point of view, \mathcal{C} is perceived as a black-box handling complete images, the technique T should instead handle sub-parts of images,

and be independent of \mathcal{C} .

In this regard, a highly convenient situation is when T provides an intrinsic (*i.e.* which does not depend on the considered CNN) assessment of the distribution of each individual pixel's contribution of the input image \mathcal{I} to any pre-selected category c_z among the ℓ categories (even if this assessment may require information from pixels located in the immediate neighborhood of the considered pixel, provided the size of this neighborhood remains limited as compared to the full image size). In this case, instead of exploring the full image space, the attacker can focus on the limited zones of interest predicted by T . The search space would then be drastically reduced, and so would be the time required by the attack, as explained now.

The zone-of-interest strategy for a black-box targeted attack atk proceeds as follows:

Input: let \mathcal{A} be a clean image (to simplify for the time being, let us assume that the size $h \times w$ of \mathcal{A} coincides with \mathcal{C} 's input size, even if the paper emphasizes the relevance of the strategy for HR adversarial images) classified by \mathcal{C} in c_a , and let $c_t \neq c_a$.

Step 1: Run T on \mathcal{A} , and retrieve, for each pixel $p_{ij}(\mathcal{A})$ ($1 \leq i \leq h, 1 \leq j \leq w$), an output vector $\mathbf{o}_T(p_{ij}(\mathcal{A}))$ of length ℓ .

Step 2: Fix real values $0 < x_a, x_t \leq 100$. Sort the set $\{\mathbf{o}_T(p_{ij}(\mathcal{A}))\}$ by increasing c_a -label values, and create the subset $\text{Top}(\mathcal{A}, c_a, x_a)$ of pixels $p_{ij}(\mathcal{A})$ that belong to the top $x_a\%$ of the sorted set. *Mutatis mutandis*, create the set $\text{Top}(\mathcal{A}, c_t, x_t)$.

Step 3: Fix thickness values ϵ_a, ϵ_t , and remoteness values δ_a, δ_t . Construct connected components around the pixels that belong to $\text{Top}(\mathcal{A}, c_a, x_a)$ and that are relatively close one to the other (namely of distance $\leq \delta_a$), encapsulating all pixels, located around those of $\text{Top}(\mathcal{A}, c_a, x_a)$ selected as before, at a distance $\leq \epsilon_a$ (even if the newly encapsulated pixels $\notin \text{Top}(\mathcal{A}, c_a, x_a)$). Construct the set of pixels $Z_{c_a}(\mathcal{A}, x_a)$ as the union of the disjoint connected components obtained as described. Proceed similarly *mutatis mutandis* for $\text{Top}(\mathcal{A}, c_t, x_t)$, and create $Z_{c_t}(\mathcal{A}, x_t)$. $Z_{c_a}(\mathcal{A}, x_a)$ and $Z_{c_t}(\mathcal{A}, x_t)$ are the zones of interest.

Step 4: Perform atk on \mathcal{A} such that 1) pixels located outside $Z_{c_a}(\mathcal{A}, x_a)$ and $Z_{c_t}(\mathcal{A}, x_t)$ are untouched; 2) atk aims at pushing down the contribution of the pixels of $Z_{c_a}(\mathcal{A}, x_a)$ to the c_a -label value of the adversarial images it creates; 3) atk aims at pushing up the contribution of the pixels of $Z_{c_t}(\mathcal{A}, x_t)$ to the c_t -label values of the adversarial images it creates.

Step 5: If the image \mathcal{D} obtained at the end of Step 4 is adversarial, then output \mathcal{D} . Otherwise, enlarge the

values of x_a, x_t in Step 2, and modify the values of $\epsilon_a, \epsilon_t, \delta_a, \delta_t$ in Step 3, until a satisfying adversarial image is created in Step 4 or any other stop condition is satisfied.

Let us list a series of remarks that clarify the different steps of the zone-of-interest strategy, give an interpretation of their aims, or provide variants that the user may consider.

1) The proportion of pixels that belong to $\text{Top}(\mathcal{A}, c_a, x_a)$ or to $\text{Top}(\mathcal{A}, c_t, x_t)$ may vary greatly with x_a, x_t ; this proportion of pixels may be significantly different from the selected percentages $x_a\%$ and $x_t\%$. Anyway, it is likely that the portion of the image relevant for c_a or c_t will be minimal as compared to the size of the whole image.

2) In Step 3, one "draws" an area around the pixels contributing to $\text{Top}(\mathcal{A}, c_a, x_a)$, and another area around those contributing to $\text{Top}(\mathcal{A}, c_t, x_t)$. The collection of these drawings is $Z_{c_a}(\mathcal{A}, x_a), Z_{c_t}(\mathcal{A}, x_t)$. See Figure 1 for a representation of $Z_{c_a}(\mathcal{A}, x_a)$. One by-product of doing so is that the modifications, performed by the attack as described in Step 4, are spread around the significant pixels: They affect $Z_{c_a}(\mathcal{A}, x_a)$ and not merely the smaller $\text{Top}(\mathcal{A}, c_a, x_a)$ (respectively $Z_{c_t}(\mathcal{A}, x_t)$ and $\text{Top}(\mathcal{A}, c_t, x_t)$). They are hence less likely to be noticeable to a human eye as would be the modification of isolated pixels as for instance in [13], [19], [21], [29].

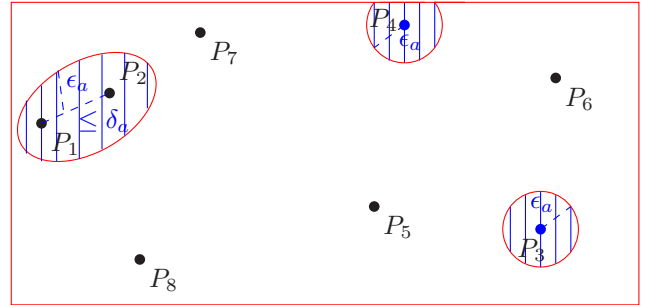


Fig. 1: Pixels $P_1, P_2, P_3, P_4 \in \text{Top}(\mathcal{A}, c_a, x_a)$. The zone of interest $Z_{c_a}(\mathcal{A}, x_a)$ is the set of all pixels within the union of the dashed zones. P_5, P_6, P_7, P_8 are examples of pixels $\notin Z_{c_a}(\mathcal{A}, x_a)$.

3) In Step 3, note that in the case of pixels contributing, say, to $\text{Top}(\mathcal{A}, c_a, x_a)$, and that are "isolated", namely such that there is no other pixel of $\text{Top}(\mathcal{A}, c_a, x_a)$ at a distance $\leq \delta_a$, the connected component contributing to $Z_{c_a}(\mathcal{A}, x_a)$ is simply a disk centered on the isolated pixel, and of radius ϵ_a (more exactly, it is the intersection of this disk with the image \mathcal{A} , as represented for the pixels P_3 and P_4 in Figure 1). Note that one may have kept uniformly this approach of disks around points of $\text{Top}(\mathcal{A}, c_a, x_a)$ instead of taking into account the proximity (measured by the distance $\leq \delta_a$) for the drawing

of the connected component around close enough pixels belonging to $\text{Top}(\mathcal{A}, c_a, x_a)$.

4) It may happen that the processes 1) and 2) in Step 4 are enough to lead \mathcal{C} to a misclassification of the image obtained, hence creating a successful attack for the untargeted scenario.

5) The strategy leaves a lot of flexibility to the user. Depending on the situation, it may be wise to start with values $x_a = x_t = 10$, provided the sets $\text{Top}(\mathcal{A}, c_a, x_a)$ and $\text{Top}(\mathcal{A}, c_t, x_t)$ are large enough as compared to the total number of pixels of the full image \mathcal{A} . Indeed, if they are too small, the modifications created by atk may become visible to a human eye, what we want to avoid. The freedom to choose the thickness and the remoteness values also contributes greatly to the method's elasticity.

6) Different attacks may jointly benefit from Steps 1, 2, and 3 performed on the same clean image.

7) The technique T should be fast. Indeed, since it comes in addition to the attack atk , using the zone-of-interest strategy should provide an advantage as compared to not using it. Consequently, this strategy probably pays off when the considered images (and the search space) are relatively large, say at least 224×224 . Its advantage is surely substantial when it comes to HR images.

III. BAGNET

A key component of the strategy is the availability of a technique T fulfilling the criteria given in Section II. A promising candidate is provided by BagNet [2].

BagNet is closely related to bag-of-feature (BoF) models, a technique frequently used before deep learning emerged. An interesting feature of the BoF model is its transparency in decision-making: One can check quite precisely which features of the image correspond to a certain category. BagNet relies on sliding square windows of predefined sizes. These sliding windows, centered on pixels, move across the complete image and collect local information. BagNet processes this information, and provides, for each pixel of the image, a classification output vector according to the ℓ categories.

Once this process is done, one can select any of the ℓ possible categories, and compute a heat map according to this selected category. These heat maps highlight category-specific image regions. Figure 2 gives examples of heatmaps created from BagNet with windows of size 9×9 , 17×17 , and 33×33 pixels.

In particular, given two categories c_a and c_t , and a clean image \mathcal{A} classified by a CNN in c_a , one can run BagNet on \mathcal{A} , and then construct the heatmap of the image \mathcal{A} according to c_a on the one hand, and the heatmap according to c_t on the other hand. The zones of interest $Z_{c_a}(\mathcal{A}, x_a)$ and $Z_{c_t}(\mathcal{A}, x_t)$, referred to in Step 3 of the strategy described in Section II, would be deduced from the outcomes of these heatmaps.

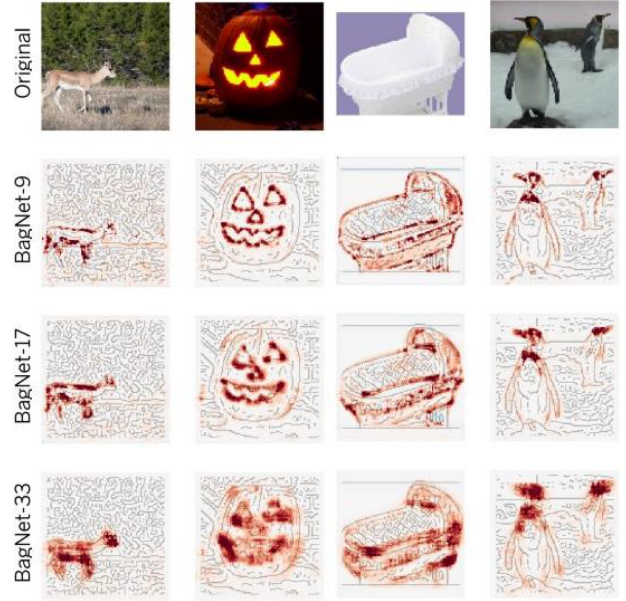


Fig. 2: Heatmaps from BagNets showing which image parts contributed to CNN's decision [2].

IV. SUSTAINING THE STRATEGY: FUTURE EXPERIMENTS

To sustain the zone-of-interest strategy, a substantial experimental phase is needed. This section outlines the design of a series of planned experiments to be implemented using Python 3.8 [27] with NumPy 1.17 [18], TensorFlow 2.4 [1], Keras 2.2 [4], and Scikit 0.24 [28] libraries.

Firstly, the strategy will be tested with at least the following 10 state-of-the-art CNNs trained on ImageNet: $\mathcal{C}_1 = \text{DenseNet121}$ [12], $\mathcal{C}_2 = \text{DenseNet169}$ [12], $\mathcal{C}_3 = \text{DenseNet201}$ [12], $\mathcal{C}_4 = \text{MobileNet}$ [10], $\mathcal{C}_5 = \text{NASNetMobile}$ [31], $\mathcal{C}_6 = \text{ResNet50}$ [9], $\mathcal{C}_7 = \text{ResNet101}$ [9], $\mathcal{C}_8 = \text{ResNet152}$ [9], $\mathcal{C}_9 = \text{VGG16}$ [20], and $\mathcal{C}_{10} = \text{VGG19}$ [20].

Secondly, at least 100 clean images of size 224×224 , and of high resolution will be considered.

Thirdly, an optimal size for the sliding window of BagNet will be computed according to the size of the input clean images: 224×224 images may need one window size and larger (in particular HR) images another. Alternative techniques to BagNet will be considered (for instance CAM [30], used for medical applications; note that this technique may be adapted rather for white-box attacks though).

Fourthly, the strategy will be performed for a wide series of attacks including FGSM [6], PGD Inf, PGD L2 [17], BIM [15], SimBA [8], AdvGAN [24], evolutionary-algorithm based attacks [25], either for the targeted or for the untargeted scenarios. These

experiments will initially take place in the \mathcal{R} domain.

Lastly for high-resolution images, the zone-of-interest strategy will be combined with the generic noise-blowing up method [16]. In a nutshell, this method (represented in Fig 3), extracts the adversarial noise \mathcal{N} created in the \mathcal{R} domain by an attack atk , and blows it up to the \mathcal{H} domain. This blown-up noise is then added to the original HR clean image \mathcal{A}_a^{hr} , resulting in a tentative adversarial image in the \mathcal{H} domain.

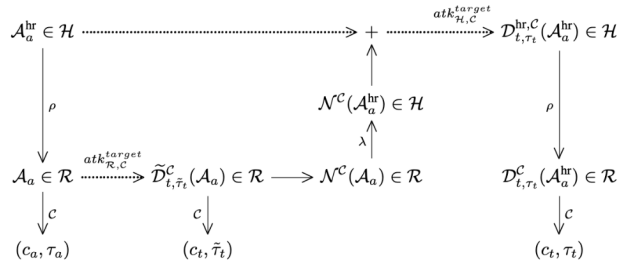


Fig. 3: Scheme of the noise blowing-up method [16]

Combining generic strategies, working for any attack and any scenario, obviously presents many advantages. In the particular case of the joint efforts of the zone-of-interest strategy and of the noise blowing-up method, one can furthermore consider many refinements. For instance, in the case where the attack atk relies on some randomness (like e.g. for evolutionary-based attacks), instead of blowing-up a "strong" adversarial noise obtained essentially by one substantial attack round, the attacker may opt for blowing up successive layers of "moderate" although focused noise obtained by successive lighter attack rounds. Due to the randomness of the attack, although the successive attacks operate in the same zones of interest, the resulting adversarial noises will differ. While none of the moderate blown-up adversarial noise would be enough to construct the required HR adversarial image, their cooperation may. Said otherwise, adding moderate blown-up adversarial noise layers, one by one, to the original clean image until an efficient adversarial high-resolution image is obtained may prove more efficient than adding only once a strong blown-up adversarial noise.

Comparisons in terms of speed, adversity, and visual quality will be performed all along this series of experiments.

V. CONCLUSION

This paper outlines a new strategy for the efficient creation of adversarial images against CNNs. This strategy, described as an explicit algorithm, defines mathematically the concept of zones of interest relevant for CNNs classifications, and the elasticity of these zones according to concrete parameters. The strategy recommends that attacks, aiming at the creation of adversarial images deceiving CNNs at image recognition, focus on the zones

of interest, and explains how to proceed in practice. A key feature of the strategy is that it generically applies to any type of attack – black-box or white box, targeted or untargeted –, to any concrete attack (including for instance but not limited to [6], [8], [15], [17], [24], [25]), and to images of any size. Although the zone-of-interest strategy applies to images of arbitrary size, it was conceived to address the particularly challenging issue of the fast creation of high-resolution adversarial images, indistinguishable by a human from the input clean image. An advantage of the zone-of-interest strategy is that, due to its generic nature, it can be combined with other equally generic methods. In particular, combining the zone-of-interest strategy with the recent noise blowing-up algorithm [16] may reduce drastically the time required by any attack to create adversarial images, especially high-resolution images. Finally, the paper describes the design of a precise experimental path to sustain the strategy.

REFERENCES

- [1] Abadi, M., Agarwal, A., Barham, P., Brevdo, E., Chen, Z., Citro, C., Corrado, G.S., Davis, A., Dean, J., Devin, M., et al.: Tensorflow: Large-scale machine learning on heterogeneous distributed systems. arXiv preprint arXiv:1603.04467 (2016)
- [2] Brendel, W., Bethge, M.: Approximating cnns with bag-of-local-features models works surprisingly well on imagenet. arXiv preprint arXiv:1904.00760 (2019)
- [3] Carlini, N., Wagner, D.: Towards Evaluating the Robustness of Neural Networks. In: 2017 IEEE Symposium on Security and Privacy (sp). pp. 39–57. IEEE (2017)
- [4] Chollet, F., et al.: Keras. <https://keras.io> (2015)
- [5] Deng, J., Dong, W., Socher, R., Li, L.J., Li, K., Fei-Fei, L.: The ImageNet Image Database (2009), <http://image-net.org>
- [6] Goodfellow, I.J., Shlens, J., Szegedy, C.: Explaining and harnessing adversarial examples. CoRR **abs/1810.00069** (2015), <http://arxiv.org/abs/1412.6572>
- [7] Guo, C., Gardner, J., You, Y., Wilson, A.G., Weinberger, K.: Simple black-box adversarial attacks. In: International Conference on Machine Learning. pp. 2484–2493. PMLR (2019)
- [8] Guo, C., Gardner, J., You, Y., Wilson, A.G., Weinberger, K.: Simple black-box adversarial attacks. In: International Conference on Machine Learning. pp. 2484–2493. PMLR (2019)
- [9] He, K., Zhang, X., Ren, S., Sun, J.: Deep residual learning for image recognition. In: Proceedings of the IEEE conference on computer vision and pattern recognition. pp. 770–778 (2016)
- [10] Howard, A.G., Zhu, M., Chen, B., Kalenichenko, D., Wang, W., Weyand, T., Andreetto, M., Adam, H.: Mobilenets: Efficient convolutional neural networks for mobile vision applications. arXiv preprint arXiv:1704.04861 (2017)
- [11] Hu, W., Tan, Y.: Generating adversarial malware examples for black-box attacks based on gan. In: Data Mining and Big Data: 7th International Conference, DMBD 2022, Beijing, China, November 21–24, 2022, Proceedings, Part II. pp. 409–423. Springer (2023)
- [12] Huang, G., Liu, Z., Van Der Maaten, L., Weinberger, K.Q.: Densely connected convolutional networks. In: Proceedings of the IEEE conference on computer vision and pattern recognition. pp. 4700–4708 (2017)
- [13] Jere, M., Rossi, L., Hitaj, B., Ciocarlie, G., Boracchi, G., Koushanfar, F.: Scratch that! an evolution-based adversarial attack against neural networks. arXiv preprint arXiv:1912.02316 (2019)
- [14] Krizhevsky, A., Nair, V., Hinton, G.: Cifar-10 (Canadian Institute for Advanced Research) <http://www.cs.toronto.edu/~kriz/cifar.html>
- [15] Kurakin, A., Goodfellow, I.J., Bengio, S.: Adversarial examples in the physical world. CoRR **abs/1607.02533** (2016), <http://arxiv.org/abs/1607.02533>

- [16] Leprévost, F., Topal, A.O., Mancellari, E.: Creating High-Resolution Adversarial Images Against Convolutional Neural Networks with the Noise Blowing-Up Method. In: Intelligent Information and Database Systems, 15th Asian Conference, ACI-IDS 2023, Phuket, Thailand, July 24–26, 2023, Proceedings. Springer (To appear)
- [17] Madry, A., Makelov, A., Schmidt, L., Tsipras, D., Vladu, A.: Towards deep learning models resistant to adversarial attacks. CoRR **abs/1706.06083** (2019), <http://arxiv.org/abs/1706.06083>
- [18] Oliphant, T.E.: A guide to NumPy. Trelgol Publishing USA (2006)
- [19] Papernot, N., McDaniel, P., Jha, S., Fredrikson, M., Celik, Z.B., Swami, A.: The limitations of deep learning in adversarial settings. In: 2016 IEEE European Symposium on Security and Privacy (EuroS&P). pp. 372–387. IEEE (2016), <https://ieeexplore.ieee.org/document/7467366>
- [20] Simonyan, K., Zisserman, A.: Very deep convolutional networks for large-scale image recognition. arXiv preprint arXiv:1409.1556 (2014)
- [21] Su, J., Vargas, D.V., Sakurai, K.: One pixel attack for fooling deep neural networks. IEEE Transactions on Evolutionary Computation **23**(5), 828–841 (2019)
- [22] Szegedy, C., Vanhoucke, V., Ioffe, S., Shlens, J., Wojna, Z.: Rethinking the inception architecture for computer vision. In: 2016 IEEE Conference on Computer Vision and Pattern Recognition (CVPR). pp. 2818–2826 (2016), <https://ieeexplore.ieee.org/document/7780677>
- [23] Szegedy, C., Zaremba, W., Sutskever, I., Bruna, J., Erhan, D., Goodfellow, I., Fergus, R.: Intriguing properties of neural networks. arXiv preprint arXiv:1312.6199 (2013)
- [24] Targonski, C.: Tensorflow implementation of generating adversarial examples with adversarial networks (2019), <https://github.com/ctargon/AdvGAN-tf/>
- [25] Topal, A.O., Chitic, R., Leprévost, F.: One evolutionary algorithm deceives humans and ten convolutional neural networks trained on imagenet at image recognition. Applied Soft Computing **143**, 110397 (2023). <https://doi.org/10.1016/j.asoc.2023.110397>, <https://www.sciencedirect.com/science/article/pii/S1568494623004155>
- [26] Touvron, H., Cord, M., Douze, M., Massa, F., Sablayrolles, A., Jégou, H.: Training data-efficient image transformers & distillation through attention. In: International Conference on Machine Learning. pp. 10347–10357. PMLR (2021)
- [27] Van Rossum, G., Drake, F.L.: Python 3 Reference Manual. CreateSpace, Scotts Valley, CA , (2009), <https://dl.acm.org/doi/book/10.5555/1593511>
- [28] Van der Walt, S., Schönberger, J.L., Nunez-Iglesias, J., Boulogne, F., Warner, J.D., Yager, N., Gouillart, E., Yu, T., the scikit-image contributors: scikit-image: image processing in Python. PeerJ **2**, e453 (2014). <https://doi.org/10.7717/peerj.453>
- [29] Wu, J.: Generating adversarial examples in the harsh conditions. CoRR **abs/1908.11332** (2020), <https://arxiv.org/abs/1908.11332>
- [30] Zhou, B., Khosla, A., Lapedriza, A., Oliva, A., Torralba, A.: Learning deep features for discriminative localization. In: Proceedings of the IEEE conference on computer vision and pattern recognition. pp. 2921–2929 (2016)
- [31] Zoph, B., Vasudevan, V., Shlens, J., Le, Q.V.: Learning transferable architectures for scalable image recognition. In: Proceedings of the IEEE conference on computer vision and pattern recognition. pp. 8697–8710 (2018)

Transformers Based Automated Short Answer Grading with Contrastive Learning for Indonesian Language

1st Aldo Arya Saka Mukti
 Dept. of Electrical and Information Engineering
 Universitas Gadjah Mada
 Sleman, Indonesia
 aldoarya00@mail.ugm.ac.id

2nd Syukron Abu Ishaq Alfarozi*
 Dept. of Electrical and Information Engineering
 Universitas Gadjah Mada
 Sleman, Indonesia
 syukron.abu@ugm.ac.id

3rd Sri Suning Kusumawardani
 Dept. of Electrical and Information Engineering
 Universitas Gadjah Mada
 Sleman, Indonesia
 suning@ugm.ac.id

Abstract—The rapid development of technology has impacted various sectors, including education. These developments have enabled e-Learning to thrive, especially during the Covid-19 pandemic. Evaluating student performance and understanding in e-Learning is typically done through quizzes. However, these evaluations, especially in essay grading, still require manual effort. This can lead to exhaustion and introduce bias and inconsistency into the scoring process. To address this issue, one possible solution is to develop an automated short-answer grading system. This research explores large language model that has a general understanding of language. This model is then subjected to a finetuning process. Specifically, this study employs BERT model, with contrastive learning method to develop an automated short-answer scoring system and compare its performance with similar systems. The model is composed of two components, namely the model body which utilizes BERT variation and the model head which employs logistic regression. The model body is structured in a siamese architecture. The results demonstrate an improvement in model performance of BERT model with contrastive learning. When compared to the pretrained BERT and BERT with cosine similarity finetuning, the reduction in prediction MAE is 21.72% and 9.90%, while for the RMSE metric, it is 17.79% and 13.80%. The transformers-based model with contrastive learning achieves metrics of 0.191 for MAE and 0.231 for RMSE. These findings indicate the potential of using the contrastive learning method in transformers models to develop an automated short-answer scoring system.

Index Terms—contrastive learning, transformers, automated short answer grading, e-Learning, large language model

I. INTRODUCTION

Information technology advancements, notably e-Learning, delivered via the Internet, have significantly impacted education across various sectors [1]. The widespread adoption of e-Learning in both formal and informal educational settings reflects its benefits against

traditional learning method, including flexibility, student-centered learning, collaboration, cost-effectiveness, and tailored learning options [2], [3].

The importance of adopting e-Learning in educational institutions has grown due to the Covid-19 pandemic. E-Learning helps schools continue teaching when face-to-face classes aren't possible [4]. This approach benefits teachers and students by making learning materials accessible, information dissemination effective, and assignments manageable [5] [6].

In the evolving education landscape, the fusion of deep learning and Learning Analytics (LA) has ignited a transformation. Deep learning's data analysis and pattern recognition, combined with LA's contextual insights, hold promise for enhancing education, including Intelligent Tutoring Systems (ITS) to automated grading [7]. A notable example is automated grading, where deep learning algorithms efficiently assess student work.

In e-Learning, assessing student progress usually involves assignments and quizzes, including essays. Manual essay grading can exhaust teachers, leading to biased evaluations and inconsistent results [8]. This fatigue also affects students, diminishing their perception of teacher support and impacting academic performance [9], [10].

One way to address the manual grading issue, particularly for short answer essays, is by using an Automated Short Answer Grading (ASAG) system. Several ASAG systems have been developed, such as Intelligent Essay Assessor (IEA), Project Essay Grade (PEG), and E-Rater. However, these systems have their respective weaknesses and are considered to no longer meet future needs [11].

Advancements in natural language processing (NLP) research, particularly in text similarity, provide opportunities for leveraging NLP techniques as a solution for ASAG

*Corresponding author. Email: syukron.abu@ugm.ac.id.

development. Moreover, models developed to tackle NLP problems are rapidly evolving. Transformers are state-of-the-art neural network models specifically designed to address natural language processing challenges [12]. Transformers can be used to obtain semantic similarity between two documents, considering not only the sentences or words composing the text but also the context of each document.

This research explores the application of contrastive learning methods and the use of transformer models to develop ASAG in e-Learning. The grading will be based on the extracted feature from the combination of embedding that represents the teacher's answer key and the student's answer. This research aims to examine the influence of contrastive learning methods on the performance of transformer models in predicting students' answer scores, which serve as the basis for automated grading, in comparison to previous methods.

II. RELATED WORKS

Several studies on automated essay grading systems have explored various methods, both traditional and modern ones, including machine learning. Previous research has explored the usage of text distance-based ASAG for the Indonesian language [13] [14]. This research mainly explored the use of TF-IDF to create vector representations with different weights based on how often a word shows up on a document. The score is then determined by the cosine similarity or Jaccard similarity between the teacher's key answer and the student's answer. The result of these text distance-based ASAGs has not been able to compete with human scoring. It also showed the need to also explore answer semantics, instead of relying only on lexical.

Further development of ASAG used text representation, such as the use of latent semantic analysis (LSA) [15] [16] and transformers models [17] [18] [19]. Ratna et al. [15] combined LSA and SVM, where SVM was used to filter and classify the topics of students' answers and then compared to the teacher's key answers. This research employs LSA to create a document matrix and TF-IDF to construct the vector representation. This document matrix is then used to calculate similarity. Citawan et al. [16] employed similar usage of LSA to calculate similarity but combined it with the n-gram feature.

Transformers-based ASAG used BERT models to create an embedding representation of both teacher's key answers and the student's answers. These embeddings are then fed into a regression layer to predict the student's answers. BERT-based ASAG used sentence embedding that was generated by feeding token embedding into a pooling layer to achieve better performance [17] [19]. Haidar and Purwarianti [17] experimented with various BERT variations and features used by the regression layer. This research showed the best result by using 'bert-base-multilingual-cased'. The features used to obtain the best performance in this research were the combination of teacher's key answers embedding, student's answers embedding, the absolute difference between embedding, and element-wise multiplication between embedding. Salim et al.

[18] compared the performance between the ridge regression model and the BERT model for the ASAG task and showed that the BERT model has superior performance compared to the ridge regression model.

Various research also showed better performance by using a transformers-based model to compare text or document similarity. Peinelt, Nguyen, and Liakata [20] used BERT that combined topic modeling to achieve better performance in binary classification based on text similarity. This research showed that text topics serve as additional information for the model, especially in domain-specific cases. Mutinda et al. [21] experimented with BERT to compare Japanese medical documents and showed a high Pearson correlation score.

In conclusion, various approaches have been used to develop ASAG for the Indonesian language, both using text-distance and text-representation methods. These researches also showed an improvement going from text distance to the text-representation method. Other research also showed the usage of a transformers-based model to calculate the similarity between documents that are able to achieve superior performance compared to the previous method. This opened the possibility of choosing a transformers-based method for ASAG and improving it further. This research aims to improve the current transformers-based ASAG by using the contrastive learning method.

III. DATASET

The dataset used in this research is a question-and-answer dataset utilized in the previous research conducted by Haidir and Purwarianti [17]. This dataset consists of two types of questions: Science and Technology (Saintek) and Social and Humanities (Soshum). The dataset is divided into two sets: a train set consisting of 30 questions and a test set consisting of 6 questions, with a total of 7605 and 1560 rows of answers for each set, respectively. Scoring was conducted by experts in each domain, with scores ranging from 0 to 5. In the following section, this dataset is then referred to as the Saintek-Soshum dataset. The Saintek-Soshum dataset is obtained through NusaCrowd [22], an open-source NLP platform for Indonesian language.

IV. PROPOSED METHOD

A. Model Architecture

The architecture of the model used in this research consists of two components: the model body, which is a BERT model used to generate sentence embeddings, and the model head, which is a logistic regression model that produces scores or values based on the features generated by the model body. The model architecture used in this research is shown in Fig 1.

The input to the model is the student's answer and the teacher's answer key, and the output is the predicted score. The input undergoes tokenization before entering the model body, which then generates token embeddings for each token of the input. The model body is structured in a Siamese architecture, meaning that the model body is used to generate

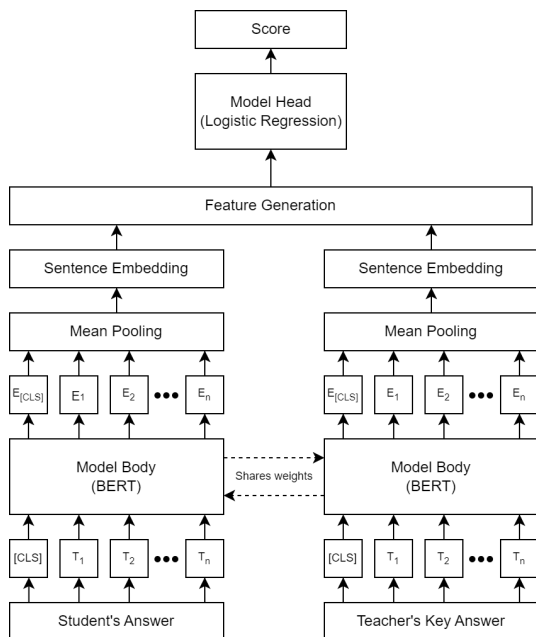


Fig. 1. Proposed Model Architecture

token embeddings for the student's answer and the teacher's answer key is the same model with shared weights.

The token embeddings for each sentence are then fed into the pooling layer with mean pooling, which will average the values of all tokens to produce a sentence embedding. This sentence embedding is further processed in the feature generation component. The output of the feature generation component is a combination of the teacher's key answers embedding, the student's answers embedding, the absolute difference between embedding, and element-wise multiplication between embedding. These features serve as the input to the model head, which ultimately generates the output in the form of a predicted score for the student's answer.

B. Research Workflow

The workflow in this research is divided into three main sections, which are "Experiment Preparation", "Training", and "Evaluation". The overview of this workflow is shown in Fig 2. The first part is "Experiment Preparation," which involves determining the methods to be compared and preparing the data. The second part is the "Training," which involves the process of training the model using predetermined methods. The third part is the "Evaluation," which involves evaluating the performance of the trained model.

Deciding Model to Experiment with

To examine the impact of contrastive learning methods on the performance of models in automated short answer grading systems, this research will compare three models, each employing a different method for training the model body. The first model is referred to as the "Baseline Model," which serves as the ground truth. In the baseline model, the BERT model is not finetuned but is used solely to generate sentence embeddings for the model head. The second model

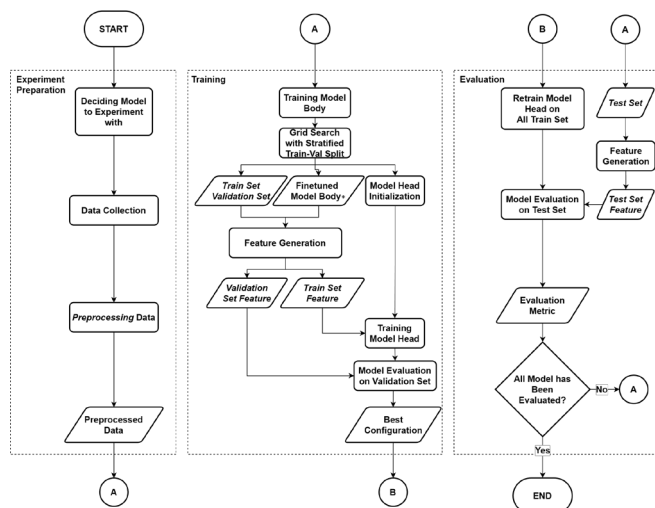


Fig. 2. Workflow Overview - Symbol * denotes that the model is frozen so that no weight is updated

is the "Finetuning Model," which serves as a comparison to evaluate the performance of contrastive learning against the commonly used finetuning method. In this model, the BERT model will undergo finetuning on the train set. The third model is the "Contrastive Model," where the BERT model will be trained using the concept of contrastive learning. All of the three models will use 'bert-base-multilingual', with the default 768 embedding size.

Data Collection

Saintek-Soshum datasets are directly obtained through NusaCrowd, given their open-source nature.

Preprocessing Data

The data preprocessing steps performed on the participant's answers and the answer key in this research are as follows: removal of empty values, removal of punctuation marks, separation of repeated words, removal of escape characters, replacement of words in parentheses, removal of numbers, case-folding, score normalization.

The raw data from the Saintek-Soshum dataset was initially separated into Saintek data and Soshum data. Also, the student's answer was separated from the teacher's answer key. To address this, the datasets are merged into one dataset by combining the Saintek and Soshum data and the student's answer with the teacher's answer key. These preprocessed dataset are shown in Table I

Training Model Body

Each model to be tested (baseline model, finetuning model, and contrastive model) undergoes a slightly different training process. This difference only occurs during the training of the model body, while the training of the model head is the same across all models. Model body are trained with the task to optimize formed embedding through minimizing loss function that is used on each tested model. The finetuning model will use cosine similarity loss, whereas the contrastive model will use contrastive loss.

TABLE I
PREPROCESSED DATASET SAMPLE

| index | question_id | response (id—en) | gold_response (id—en) | labels |
|-------|-------------|---|---|--------|
| 0 | 1 | bakteri penyubur tanaman — <i>land-fertilizing bacteria</i> | bacillus thuringiensis agrobacterium tumefaciens | 0.2 |
| 1 | 1 | bakteri baik bakteri hasil mutasi — <i>beneficial bacteria from mutation</i> | bacillus thuringiensis agrobacterium tumefaciens | 0.2 |
| ... | ... | ... | ... | ... |
| 7434 | 30 | sesuatu yang tetap ada atau tidak pernah — <i>something that continue to exist or not extinct</i> | tetap seperti keadaan semula — <i>remains as it was</i> | 1.0 |
| 7435 | 30 | ya itu saat alam dalam keadaan terbaik nya — <i>nature on its best condition</i> | tetap seperti keadaan semula — <i>remains as it was</i> | 0.2 |

In the baseline model, the model body does not undergo a training process. Instead, the model body is directly used to generate sentence embeddings from the train set and validation set. To replicate a Siamese neural network, the student's answer and the teacher's answer key are inputted separately into the model body, resulting in two sentence embeddings that originate from the same model, parameters, and weights.

In the finetuning model, there is a finetuning process of the model body on the train set. The finetuning process utilizes the following hyperparameter configuration: 1 epoch, learning rate of $2e^{-5}$, batch size of 32, and the loss function utilizing cosine similarity loss.

In the contrastive model, training closely follows the finetuning model, with differences in data format and loss function. The preprocessed training set is adjusted to create contrastive dataset. These contrastive dataset created by labeling rows as 1 for similar answers and 0 for dissimilar ones, based on predefined score ranges. This dataset is then used for finetuning the contrastive model, while other hyperparameters are set the same as the finetuning model.

Grid Search with Cross Validation

Using the Saintek-Soshum train set, 10-fold-out cross-validation is conducted. The separate test set remains untouched during training. The 30-question train set splits into 26 train and 4 validation questions, with criteria of non-overlapping questions. This split maintains a balanced Saintek-Soshum distribution question although among the validation set might have overlapping questions. Question separation is randomized 10 times, without repeated combinations. Throughout grid search and cross-validation, the model body remains frozen to avoid weight updates.

Feature Generation

In each fold iteration of the cross-validation process, the training set and validation set used in that fold will be included in the feature generation process. The resulting features are a combination of sentence embeddings generated by the trained model body for each participant's answer and the answer key. The final feature embedding is a combination of the teacher's key answers embedding, the student's answers embedding, the absolute difference between embedding, and element-wise multiplication between embedding.

Training Model Head

During the model head training, a grid search optimizes two hyperparameters: epochs and learning rate. Each combination is evaluated on the validation set. The objective is predicting and minimizing the MSE loss between actual and predicted scores.

The entire training process of the model head is repeated until the average evaluation metrics for all combinations of hyperparameters are obtained. After obtaining the average evaluation metrics, the best configuration is selected. There are two metrics used in this research, which are MAE and RMSE. However, the selection of the best configuration is based on the configuration that yields the lowest RMSE.

Model Evaluation

The best configuration obtained is then used to retrain the model head. The model head is re-initialized using the best configuration and trained on the entire train set data. Subsequently, the model head is evaluated on the test set, which was not used during the search for the best configuration. The evaluation results on the test set are used as a measure of the overall performance of the model in predicting answer scores. This training and evaluation process is then repeated for all types of models being tested.

C. Contrastive Loss

The contrastive loss is a loss function that maps high-dimensional vector sets I to a low-dimensional space, where similar vectors are brought closer together while dissimilar vectors are pushed apart [23]. The contrastive loss used in this research is an energy-based margin loss. This contrastive loss operates on pairs of vectors $\bar{X}_1, \bar{X}_2 \in I$ with a label Y . In the implementation, there was a slight adjustment from the [23], where $Y = 1$ indicates a similar pair of vectors, and $Y = 0$ indicates a dissimilar pair of vectors. The contrastive loss is formulated in Equation 1:

$$\mathcal{L} = (1 - Y) \frac{1}{2} \{ \max(0, m - D_W) \}^2 + (Y) \frac{1}{2} (D_W)^2 \quad (1)$$

where D_W represents the distance between the vector pairs \bar{X}_1 and \bar{X}_2 in the embedding space, and m is a margin that controls the dissimilarity threshold. The contrastive loss encourages similar pairs to have a small distance (D_W) and dissimilar pairs to have a distance larger than the margin (m), which used the default value of 0.5.

V. EXPERIMENTAL RESULT

A. Score Thresholds Effect on Model Performance

To demonstrate the impact of score thresholds on contrastive model performance, this study tested different limits for positive and negative rows using grid search and cross-validation. Same number within square brackets implies an data with exact score match with the threshold, while two distinct numbers indicate inclusion of scores within that range. Data outside the threshold will be excluded during training. The validation set's evaluation outcomes for the MAE and RMSE metrics are shown in Table II and Table III, respectively.

TABLE II
MAE RESULT ON VARIOUS SCORE LIMIT COMBINATION FOR CONTRASTIVE MODEL

| Negative Limit | Positive Limit | | | | |
|----------------|----------------|------------|---------------|------------|------------|
| | [1.0, 1.0] | [0.8, 0.8] | [0.8, 1.0] | [0.6, 1.0] | [0.6, 0.8] |
| [0.0, 0.0] | 0.2497 | 0.2322 | 0.2362 | 0.2356 | 0.2477 |
| [0.2, 0.2] | 0.1717 | 0.1556 | 0.1644 | 0.1628 | 0.1957 |
| [0.0, 0.2] | 0.1643 | 0.1528 | 0.1524 | 0.1599 | 0.2045 |
| [0.0, 0.4] | 0.1732 | 0.1610 | 0.1638 | 0.1547 | 0.1762 |
| [0.2, 0.4] | 0.1858 | 0.1728 | 0.1755 | 0.1733 | 0.1881 |

TABLE III
RMSE RESULT ON VARIOUS SCORE THRESHOLDS COMBINATION FOR CONTRASTIVE MODEL

| Negative Limit | Positive Limit | | | | |
|----------------|----------------|------------|---------------|------------|------------|
| | [1.0, 1.0] | [0.8, 0.8] | [0.8, 1.0] | [0.6, 1.0] | [0.6, 0.8] |
| [0.0, 0.0] | 0.2860 | 0.2689 | 0.2736 | 0.2735 | 0.2848 |
| [0.2, 0.2] | 0.2046 | 0.1933 | 0.2004 | 0.2022 | 0.2340 |
| [0.0, 0.2] | 0.1979 | 0.1927 | 0.1901 | 0.1970 | 0.2426 |
| [0.0, 0.4] | 0.2058 | 0.1986 | 0.2005 | 0.1915 | 0.2167 |
| [0.2, 0.4] | 0.2196 | 0.2123 | 0.2137 | 0.2127 | 0.2332 |

Based on the grid search results for score thresholds, the highest performance of the model is achieved with an MAE of 0.1524 and an RMSE of 0.1901. These results are achieved using the optimal score thresholds for the Saintek-Soshum dataset are [0.8, 1.0] for positive rows and [0.0, 0.2] for negative rows. The grid search also indicates that the determination of score thresholds significantly impacts the model's performance.

B. Model Comparison

The comparison between the models was conducted by evaluating each model with their respective best hyperparameter configurations on the test set. The evaluation results of each model, along with the best hyperparameter configurations used, are shown in Table IV. The contrastive model excels in prediction, as evident from lower losses across all measured metrics. It outperforms the baseline and finetuning models by reducing MAE by 0.053 and 0.021, and RMSE by 0.050 and 0.037, respectively. Furthermore, all our models performed better than the one reported in [17], which is similar to the baseline model. The key difference is in how

TABLE IV
MODEL PERFORMANCE RESULT

| Model | Hyperparameter | | | | MAE | RMSE |
|-------------|----------------|-----------|----------------|----------------|--------------|--------------|
| | Epoch Head | LR Head | Positive Limit | Negative Limit | | |
| [17] | 15 | $1e^{-3}$ | - | - | 0.288 | 0.378 |
| Baseline | 64 | $1e^{-4}$ | - | - | 0.244 | 0.281 |
| Finetuning | 128 | $1e^{-3}$ | - | - | 0.212 | 0.268 |
| Contrastive | 256 | $1e^{-4}$ | [0.8, 1.0] | [0.0, 0.2] | 0.191 | 0.231 |

we pool output vectors from BERT: the baseline model used simple average pooling, while [17] used WK-pooling.

An analysis was then conducted on the prediction results of each tested model. The visualization of the prediction results is shown in Fig. 3 which focuses on the prediction results within each score range.

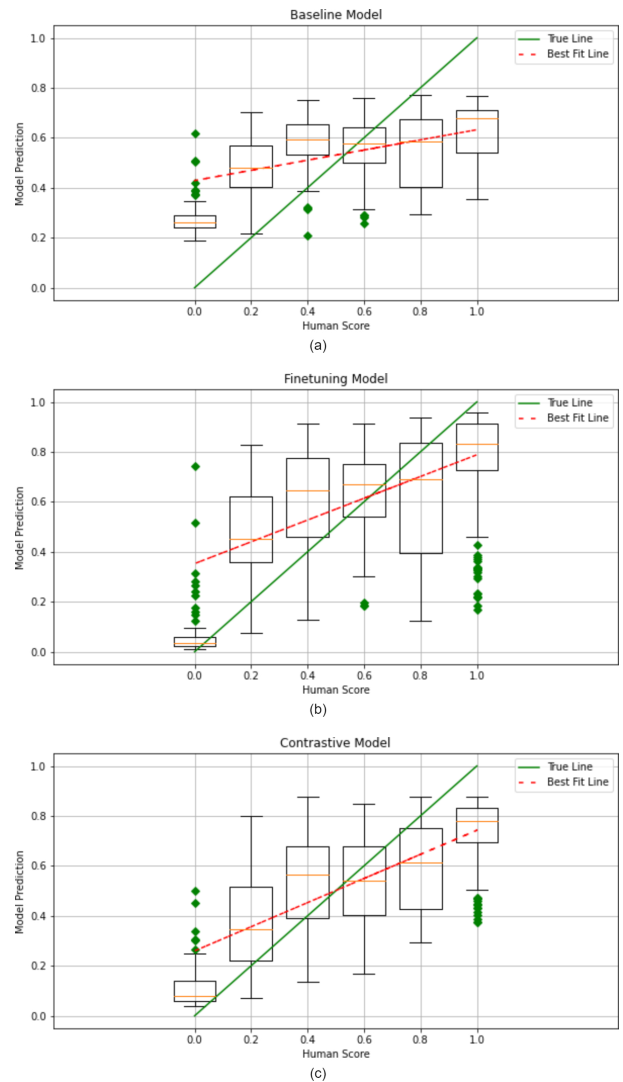


Fig. 3. Box Plot of Each Model Prediction Result Compared to Human Scoring

Fig. 3 shows that the baseline model predicts scores mostly between 0.5 to 0.7, implying undifferentiated embeddings,

while the finetuning and contrastive models create more distinct embeddings within each score range. However, the finetuning model struggles with predicting scores of 0.8. Overall, the contrastive model's more centralized predictions yield a smaller mean error compared to the finetuning model.

VI. CONCLUSION

In this study, experiments were conducted to assess the performance of a transformer-based model using contrastive learning in the task of automated short answer assessment. The contrastive model's performance was benchmarked against two alternatives: a baseline using pretrained BERT, and a finetuned BERT using cosine similarity.

In addition to the primary objective, an analysis of the impact of score thresholds on the performance of the contrastive model demonstrated a direct relationship between score thresholds and model performance, emphasizing the importance of determining an optimal threshold to achieve the best model performance.

The main objective was accomplished by comparing the performance of each model. Contrastive model achieved a reduction in prediction errors, with a decrease in mean absolute error (MAE) of 21.72% and 9.90% and a decrease in root mean squared error (RMSE) of 17.79% and 13.80%, compared to the baseline and finetuning models, respectively. The contrastive model achieved a performance metric of 0.191 for MAE and 0.231 for RMSE.

The examined contrastive model enhances performance over baselines, although sensitive to score thresholds. This research result opens up the potential for further development utilizing contrastive learning. Furthermore, the contrastive learning method used in this research is a basic approach, leaving room for more advanced techniques to be explored.

Concerning the dataset, Saintek-Soshum is evaluated by 7 experts, resulting in reduced bias. The various participant responses are also go beyond simply copying online content, enriching information acquisition. Such factors hold significance in the collection of good Question-Answer datasets.

REFERENCES

- [1] A. Baylari and G. Montazer, "Design a personalized e-learning system based on item response theory and artificial neural network approach," *Expert Systems with Applications*, vol. 36, no. 4, pp. 8013–8021, 2009. [Online]. Available: <https://www.sciencedirect.com/science/article/pii/S095741740800777X>
- [2] E. Sutanta, "Konsep dan implementasi e-learning," *Yogyakarta: IST Akprind*, pp. 10–12, 2009.
- [3] S. Naseer, "Perspective chapter: Advantages and disadvantages of online learning courses," pp. 1–11, 07 2023.
- [4] M. A. Almaiah, A. Al-Khasawneh, and A. Althunibat, "Exploring the critical challenges and factors influencing the e-learning system usage during covid-19 pandemic," *Education and information technologies*, vol. 25, no. 6, pp. 5261–5280, 2020.
- [5] S. Syahrir, Y. Supriyati, and A. Fauzi, "Evaluasi dampak program pendidikan jarak jauh (pjj) melalui model cipp pada kinerja dosen aspek pembelajaran pada masa pandemi covid 19," *Jurnal Ilmiah Mandala Education*, vol. 7, no. 1, 2021.
- [6] R. Wijaya, M. Lukman, and D. Yadewani, "Dampak pandemi covid19 terhadap pemanfaatan e learning," *Jurnal Dimensi*, vol. 9, no. 2, pp. 307–322, 2020.
- [7] S. S. Kusumawardani and S. A. I. Alfaroz, "Transformer encoder model for sequential prediction of student performance based on their log activities," *IEEE Access*, vol. 11, pp. 18960–18971, 2023.
- [8] M. A. Fauzi, D. C. Utomo, B. D. Setiawan, and E. S. Pramukantoro, "Automatic essay scoring system using n-gram and cosine similarity for gamification based e-learning," in *Proceedings of the International Conference on Advances in Image Processing*, ser. ICAIP '17. New York, NY, USA: Association for Computing Machinery, 2017, p. 151–155. [Online]. Available: <https://doi.org/10.1145/3133264.3133303>
- [9] b. Shen, N. McCaughy, J. Martin, A. Garn, N. Kulik, and M. Fahlman, "The relationship between teacher burnout and student motivation," *British Journal of Educational Psychology*, vol. 85, 07 2015.
- [10] A. K. Arens and A. J. Morin, "Relations between teachers' emotional exhaustion and students' educational outcomes," *Journal of Educational Psychology*, vol. 108, no. 6, p. 800, 2016.
- [11] M. Beseiso, O. A. Alzubi, and H. Rashaideh, "A novel automated essay scoring approach for reliable higher educational assessments," *Journal of Computing in Higher Education*, vol. 33, no. 3, pp. 727–746, 2021.
- [12] Y. Zhang, R. Tang, and J. J. Lin, "Explicit pairwise word interaction modeling improves pretrained transformers for english semantic similarity tasks," *ArXiv*, vol. abs/1911.02847, 2019. [Online]. Available: <https://api.semanticscholar.org/CorpusID:207848032>
- [13] R. Fitri and A. N. Asyikin, "Aplikasi penilaian ujian essay otomatis menggunakan metode cosine similarity," *Poros Teknik*, vol. 7, no. 2, pp. 88–94, 2015.
- [14] U. Hasanah and D. A. Mutiara, "Perbandingan metode cosine similarity dan jaccard similarity untuk penilaian otomatis jawaban pendek," in *SENSITIF: Seminar Nasional Sistem Informasi dan Teknologi Informatika*, 2019, pp. 1255–1263.
- [15] A. A. P. Ratna, H. Khairunissa, A. Kaltsum, I. Ibrahim, and P. D. Purnamasari, "Automatic essay grading for bahasa indonesia with support vector machine and latent semantic analysis," in *2019 International Conference on Electrical Engineering and Computer Science (ICECOS)*. IEEE, 2019, pp. 363–367.
- [16] R. S. Citawan, V. C. Mawardi, and B. Mulyawan, "Automatic essay scoring in e-learning system using lsa method with n-gram feature for bahasa indonesia," in *MATEC web of conferences*, vol. 164. EDP Sciences, 2018, p. 01037.
- [17] M. H. Haidir and A. Purwarianti, "Short answer grading using contextual word embedding and linear regression," *Jurnal Linguistik Komputasional*, vol. 3, no. 2, pp. 54–61, 2020.
- [18] H. R. Salim, C. De, N. D. Pratamaputra, and D. Suhartono, "Indonesian automatic short answer grading system," *Bulletin of Electrical Engineering and Informatics*, vol. 11, no. 3, pp. 1586–1603, 2022.
- [19] R. A. Rajagade, "Improving automatic essay scoring for indonesian language using simpler model and richer feature," *Kinetik: Game Technology, Information System, Computer Network, Computing, Electronics, and Control*, pp. 11–18, 2021.
- [20] N. Peinelt, D. Nguyen, and M. Liakata, "tBERT: Topic models and BERT joining forces for semantic similarity detection," in *Proceedings of the 58th Annual Meeting of the Association for Computational Linguistics*. Online: Association for Computational Linguistics, Jul. 2020, pp. 7047–7055. [Online]. Available: <https://aclanthology.org/2020.acl-main.630>
- [21] F. W. Mutinda, S. Yada, S. Wakamiya, and E. Aramaki, "Semantic textual similarity in japanese clinical domain texts using bert," *Methods of Information in Medicine*, vol. 60, no. S 01, pp. e56–e64, 2021.
- [22] S. Cahyawijaya, H. Lovenia, A. F. Aji, G. I. Winata, B. Willie, R. Mahendra, C. Wibisono, A. Romadhony, K. Vincentio, F. Koto, J. Santoso, D. Moeljadi, C. Wirawan, F. Hudi, I. H. Parmonangan, I. Alfina, M. S. Wicaksono, I. F. Putra, S. Rahmadani, Y. Oenang, A. A. Septiandri, J. Jaya, K. D. Dhole, A. A. Suryani, R. A. Putri, D. Su, K. Stevens, M. N. Nityasya, M. F. Adilazuarda, R. Ignatius, R. Diandaru, T. Yu, V. Ghifari, W. Dai, Y. Xu, D. Damapusita, C. Tho, I. M. K. Karo, T. N. Fatyanosa, Z. Ji, P. Fung, G. Neubig, T. Baldwin, S. Ruder, H. Sujaini, S. Sakti, and A. Purwarianti, "Nusacrowd: Open source initiative for indonesian nlp resources," 2022.
- [23] R. Hadsell, S. Chopra, and Y. LeCun, "Dimensionality reduction by learning an invariant mapping," in *2006 IEEE Computer Society Conference on Computer Vision and Pattern Recognition (CVPR'06)*, vol. 2. IEEE, 2006, pp. 1735–1742.

Energy Trade-off for Computation Offloading in Mobile Edge Computing

Dedi Triyanto

*Dept. of Electrical Engineering and
Information Technology
Universitas Gadjah Mada
Yogyakarta, Indonesia*

I Wayan Mustika*

*Dept. of Electrical Engineering and
Information Technology
Universitas Gadjah Mada
Yogyakarta, Indonesia*

Widyawan

*Dept. of Electrical Engineering and
Information Technology
Universitas Gadjah Mada
Yogyakarta, Indonesia*

*) Corr. author email: wmustika@ugm.ac.id

Abstract—Mobile devices (MDs) have a number of restrictions in terms of battery life, processing power, and storage space due to the growing demand for larger computational capabilities in application. Offloading computationally demanding work to MEC servers has been an answer to this problem. By considering several variables such as distance, transmission rate, CPU frequency, and transmission power, we did some simulations to assess the effectiveness of various offloading scenarios. The energy trade-off involved in this process was examined in this research with a focus on the possible energy savings provided by offloading. To optimize energy consumption in MEC systems, this study examined the advantages and drawbacks of offloading.

Index Terms—Computation offloading, Mobile Edge Computing, energy trade-off, local execution, transmission energy

I. INTRODUCTION

The rapid growth of new applications such as image processing, face recognition, virtual reality, augmented reality, and real-time online games has created a demand for large computing capabilities. In recent years, the use of MDs to run various applications has become an integral part of human life. Mobile devices, however, are constrained by their limited battery capacities, computing capacities, and storage capacities, making them unsuitable for running applications with computationally intensive tasks [1]. To address this challenge, the solution lies in offloading these tasks to MEC servers.

Offloading in MEC systems enables the transfer of heavy computational tasks from MDs to MEC servers, resulting in significant energy savings [2]. By leveraging MEC servers with higher and more efficient computing power, MDs can reduce their battery usage, thereby improving overall energy efficiency. Offloading computational tasks to the MEC server can reduce the computational load on the MD. However, it should be noted that transferring data and instructions between the MD and the MEC server takes longer and requires higher transmission power if the distance between them is greater.

As an example, the image processing process involves multiple stages and algorithms that can make it a computationally intensive task. Aspects such as high resolution, the utilization of filters, object segmentation and separation, as well as pattern recognition, contribute to making image processing computationally intensive.

Recently, there have been a number of significant research conducted on computation offloading, which offers a comprehensive overview examining the conditions in which offloading can result in energy savings. In [3], the author evaluated an ideal offloading choice by analyzing the trade-off between the energy consumption as a result of local processing and offloading. Communication and computational resources, algorithm complexity, cloud load conditions, device energy consumption, and delay restrictions are all pertinent factors in this trade-off. In [4], they took the advantage of the trade-off between energy use and execution delay by modifying the introducing control parameter to suit the needs of various tasks, greatly enhancing system service capabilities and user experience, particularly for delay-sensitive tasks. In [5], the authors discussed about the importance of predicting the power consumption of mobile devices when using cloud computing and presented a minimum SNR requirement for cloud computing in terms of energy and time.

Our contribution is to perform simulations that can help in analyzing the energy trade-off of computation offloading in MEC. Through simulation, research was able to evaluate the performance of various offloading scenarios by considering factors such as distance, transmission rate, CPU frequency on the MD, and the required task transmission power. This evaluation can help in identifying factors needed for energy efficiency improvement and designing better solutions.

The structure of this article can be summarized as follows. In section II we describe the system model, including local execution model, communication model, transmission energy model and problem formulation. The simulation results and conclusion were presented in Section III and Section IV respectively.

II. SYSTEM MODEL AND PROBLEM FORMULATION

A. System Description

In each time period, MDs need to process data, which can be processed locally on the device itself or offloaded to an edge server. As shown in Fig. 1, the computing intensive task input will be executed on the local CPU or offloaded to an edge server based on the offloading decision taken. The data transmission between the MD and MEC server is

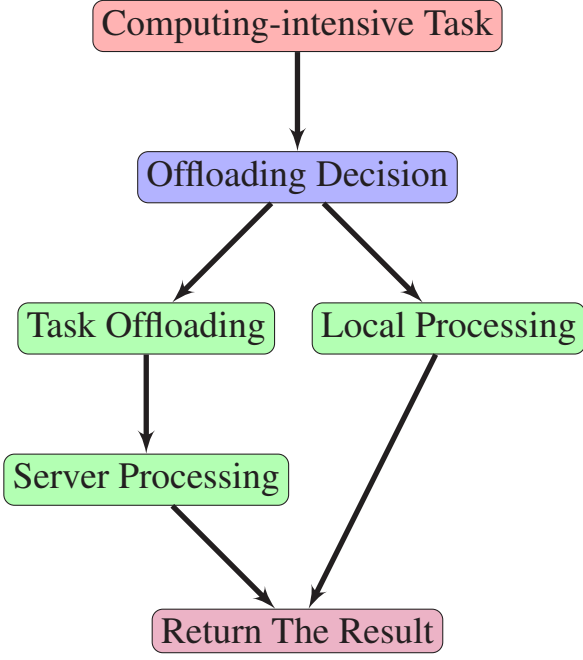


Fig. 1. Task Processing Model

based on a wireless channel. The offloading decision is taken by considering the energy consumption when executing tasks locally on the device compared to offloading to the MEC server. The distance between the MD and the edge server and the power required to transmit the task to the server via wireless, wireless, are varied, allowing us to observe the tradeoff in energy consumption in the offloading decision.

B. Local Execution Model

The local computing model refers to data processing that occurs locally at the network edge on MDs. Energy consumption in local computing is affected by the switched capacitance coefficient of the CPU k , the CPU frequency at MD f , and the number of CPU cycles required to complete a computational task W . Appropriate CPU frequency settings can help to achieve a balance between adequate performance and low energy consumption. High CPU frequency settings may not only provide a better performance but also result in higher power consumption, while decreasing the CPU frequency may not only reduce energy consumption but also affect device performance [6]. The energy consumption of local execution is expressed as

$$E_{md} = kW(f)^2 \quad (1)$$

Similarly, we can compute the execution time delay as follows.

$$T_{md} = \frac{W}{f} \quad (2)$$

The more CPU cycles needed to complete the task and the lower the CPU frequency, the higher the execution time delay.

Increasing the CPU frequency can speed up the execution time, but it must be balanced with the consideration of higher energy consumption.

C. Communication Model

The MD transmits data to the edge server using wireless with a carrier bandwidth ω . In this communication model, the transmission rate R can be calculated using Shannon's theorem.

$$R = \omega \log_2 \left(1 + \frac{HP}{\sigma} \right) \quad (3)$$

with transmission power P and power noise at the receiver σ . H stands for the channel power gain, which has an exponential distribution with mean value gd_m^{-4} , path-loss constant $g=40$ dB, and MD's distance from the server edge d_m [7].

Longer distances between the device and the server tend to result in the decreasing transmission rates due to the phenomenon of signal loss or attenuation occurred when the signal has to pass through a longer distance. Longer distances between devices and servers tend to increase energy consumption in communication. This is due to the increasing power required to transmit signals over longer distances. To overcome signal attenuation, the device must increase the transmission power to maintain signal quality. As a result, the energy consumption required in this process becomes higher.

D. Transmission Energy Model

The Transmission Energy Model refers to a model used to estimate or calculate the energy consumption associated with the process of transmitting data over a communication network. This model depicts a relationship between parameters such as the distance between MD and MEC server, transmission rate, data size, and transmission power to estimate the number of energies required during the transmission process. Its primary objective is to understand and predict the number of energies needed to transmit data through a communication network.

The transmission delay increases with data size L and decreases with transmission rate. This is because with a larger data size, it takes more time to transmit all the information through the communication channel. The transmission delay is expressed as

$$T_{tr} = \frac{L}{R} \quad (4)$$

Correspondingly, we can calculate the energy used for transmission when considering energy consumption, i.e.

$$E_{tr} = PT_{tr} \quad (5)$$

Based on (3) and (4) we can express the transmission energy as

$$E_{tr} = \frac{LP}{\omega \log_2 \left(1 + \frac{HP}{\sigma} \right)} \quad (6)$$

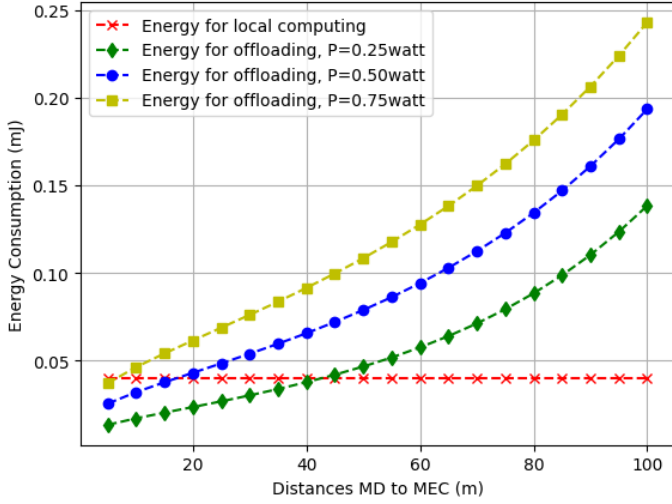


Fig. 2. Energy Consumption vs Distance MD to MEC server

the higher the transmission power used, the more energy is consumed by the device. An increase in transmission power may be necessary to overcome signal attenuation caused by longer distances or other interference. However, an increase in transmission power also means an increase in energy consumption.

E. Problem Formulation

Offloading decisions can have a direct impact on energy consumption. This article helps to analyze the energy trade-off of computing offloading. Offloading computing tasks to more powerful computing resources in the MEC can reduce the processing load on MDs that have limited resources. However, if the distance from the MD to the server is far and requires more transmission power, local computing can be considered. In addition, the offloading decision must consider the deadline time. The constraint of deadline time can be expressed as

$$\max(T_{md}, T_{tr}) \leq T_d \quad (7)$$

where (7) defines the deadline request, which states that computation task, whether they are done locally or offloaded for processing, must be completed within the allotted time.

Based on (2) and (7), we can calculate the following optimal CPU frequency [8].

$$f^* = \frac{W}{T_{md}} \quad (8)$$

This can be used to figure out how many energies local computing uses optimally, which can then be compared to how much energy is used when jobs are transferred to the MEC server.

III. SIMULATION RESULT

We used a number of simulations to test the validity of the theory in Section II and assess the system's performance. We assumed that the applications executed on the MD and each

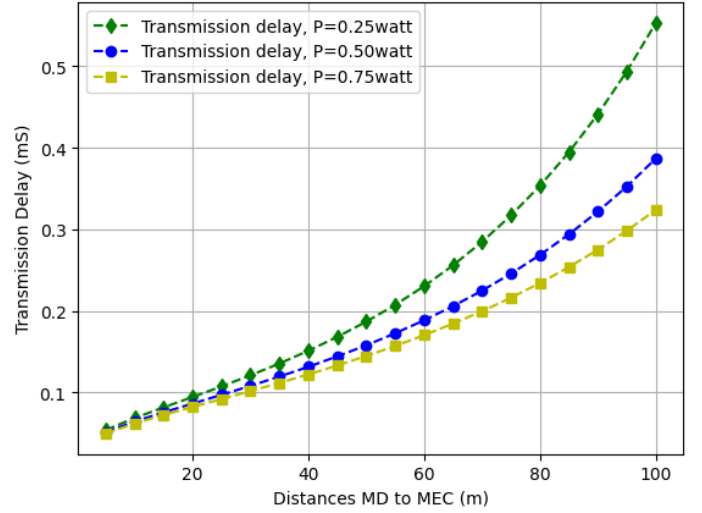


Fig. 3. Transmission Delay vs Distance MD to MEC server

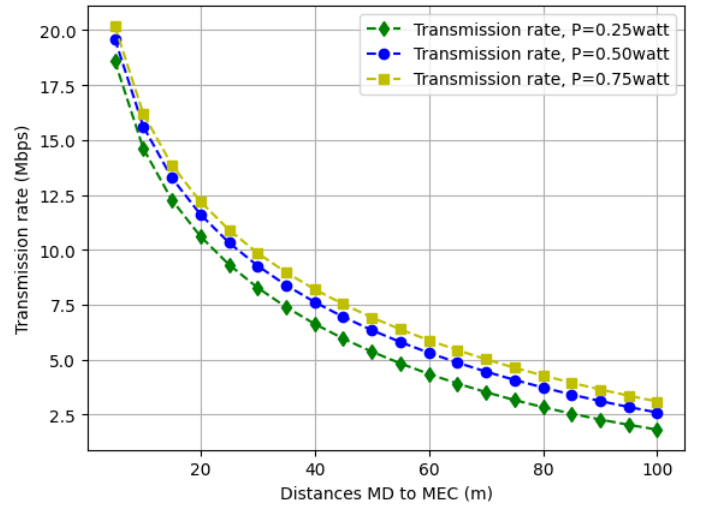


Fig. 4. Transmission Rate vs Distance MD to MEC server

task could be offloaded to the MEC server. Energy consumption for local execution and transmission energy consumption for data offloading were the two ways in which the system used energy. For local execution, $L = 1000$ bits, $k = 10^{-28}$ and the number cycles were required to process 1 bit input = 5900 cycles per byte. For data offloading, $\omega = 1$ MHz and $\sigma = 10^{-13}$ were used. The system has been given a deadline of $T_d = 1$ ms. With $d_m = [5 \text{ m} - 100 \text{ m}]$ and $P = [0.25 \text{ W}, 0.50 \text{ W}, 0.75 \text{ W}]$, it is possible to observed how the distance from the MD to the MEC server and the transmission power affected energy consumption.

Fig. 2 illustrates a comparative analysis of energy consumption in relation to the distance between the MD and the MEC server, considering the different transmission power levels. The figure presents data on energy consumption in millijoules (mJ) for each distance and transmission power combination. It was proven from the data showing a correlation between

distance and energy consumption. As the distance between the MD and MEC server increased, the energy consumption also rose. This can be attributed to the fact that transmitting data over longer distances requires more energies. Additionally, the figure demonstrates a relationship between transmission power and energy consumption. Higher transmission power levels resulted in greater energy consumption, indicating that increasing transmission power led to higher energy requirements for data transmission.

Fig. 2 also includes energy consumption values for local computing at an optimal CPU frequency of 0.7375 GHz. The energy consumption remained constant for each distance since local computing involved no data transmission to the MEC server. Hence, to minimize energy consumption, it was advisable to prioritize local computation to avoid data transmission to the MEC server, particularly for the longer distances. Furthermore, selecting lower transmission power levels could also help to reduce energy consumption.

Fig. 3 illustrates a comparison of transmission delays in milliseconds (ms) across various combinations of distances between the MD and MEC server, alongside their respective transmission power levels. The figure reveals that greater distances between the MD and MEC server resulted in higher transmission delays. Additionally, the figure demonstrates that higher transmission power levels tended to decrease the transmission delay, as seen from the decrease in transmission delay as the transmission power level increased.

The correlation between Fig. 2 and Fig. 3 lies in the energy consumption trade-off. Using higher transmission power levels increased energy consumption. The greater the transmission power used, the higher the energy consumption required by the communication device. In this context, it was observed that higher transmission power levels tended to decrease the transmission delay. This indicated that higher transmission power led to shorter data transmission times from the MD to the MEC server. However, this also resulted in the increasing energy consumption.

Additionally, it was essential to show how the megabits per second (Mbps) transmission rate was impacted by the distance between the MD and the MEC server as shown in Fig. 4. The transmission rate was determined by the required transmission power level. The figure demonstrates that as the distance between the MD and the MEC server decreased, the transmission rate increased. This could be seen from the higher transmission rates observed for shorter distances. Furthermore, increasing the transmission power level also caused higher transmission rates at every distance.

Based on the data obtained, there was a trade-off between energy consumption and transmission delay. If minimizing energy consumption is the primary objective, selecting a lower transmission power level at a specific distance can achieve energy savings, but it may result in an increasing transmission delay. Conversely, if the focus is on reducing transmission delay, opting for a higher transmission power level at a specific distance can be a viable choice, albeit at the expense of increased energy consumption. The selection of this trade-off

should be tailored to the specific requirements and priorities of the application. Real-time applications that demand prompt responses may prioritize in reducing transmission delay by selecting higher transmission power levels, even at the cost of energy consumption. However, applications with power constraints or stringent energy requirements may prioritize energy savings, even if it leads to increasing transmission delay. In practice, careful system design, efficient power management, and appropriate communication protocol selection play crucial roles in achieving the desired balance between energy consumption and transmission delay.

CONCLUSION

We have contributed by running simulations to examine the energy trade-off of offloading computation in MEC. By considering several variables such as distance, transmission rate, CPU frequency on the MD, and transmission power, we evaluated the effectiveness of various offloading scenarios. The assessment aids in identifying the elements were required for increasing energy efficiency and developing better solutions. Our simulations could direct the development of more energy-efficient solutions and offer useful insights into the energy trade-off of computation offloading in MEC.

REFERENCES

- [1] X. Lan, L. Cai, and Q. Chen, "Execution latency and energy consumption tradeoff in mobile-edge computing systems," in *2019 IEEE/CIC International Conference on Communications in China (ICCC)*, pp. 123–128, IEEE, 2019.
- [2] A. Islam, A. Debnath, M. Ghose, and S. Chakraborty, "A survey on task offloading in multi-access edge computing," *Journal of Systems Architecture*, vol. 118, p. 102225, 2021.
- [3] S. Tayade, P. Rost, A. Maeder, and H. D. Schotten, "Device-centric energy optimization for edge cloud offloading," in *GLOBECOM 2017-2017 IEEE Global Communications Conference*, pp. 1–7, IEEE, 2017.
- [4] G. Zhang, W. Zhang, Y. Cao, D. Li, and L. Wang, "Energy-delay tradeoff for dynamic offloading in mobile-edge computing system with energy harvesting devices," *IEEE Transactions on Industrial Informatics*, vol. 14, no. 10, pp. 4642–4655, 2018.
- [5] Y. Shin, C. Lee, W. Yang, and J.-M. Chung, "Minimum snr requirement for mobile cloud computing," in *2019 IEEE International Conference on Consumer Electronics-Asia (ICCE-Asia)*, pp. 104–105, IEEE, 2019.
- [6] A. Ebrahimzadeh and M. Maier, "Cooperative computation offloading in fiwi enhanced 4g hetnets using self-organizing mec," *IEEE Transactions on Wireless Communications*, vol. 19, no. 7, pp. 4480–4493, 2020.
- [7] Y. Mao, J. Zhang, and K. B. Letaief, "Dynamic computation offloading for mobile-edge computing with energy harvesting devices," *IEEE Journal on Selected Areas in Communications*, vol. 34, no. 12, pp. 3590–3605, 2016.
- [8] M. Guo, W. Wang, X. Huang, Y. Chen, L. Zhang, and L. Chen, "Lyapunov-based partial computation offloading for multiple mobile devices enabled by harvested energy in mec," *IEEE Internet of Things Journal*, vol. 9, no. 11, pp. 9025–9035, 2021.

R-AODV: Reverse Ad-Hoc On-Demand Distance Vector Routing Algorithm With LoRa Mesh Based for Emergency Alert System

1st Jirawat Thaenthong
College of Computing
Prince of Songkla University
Phuket, Thailand
jirawat.t@phuket.psu.ac.th

2nd Taiwit Pimsen
Paperless Co., Ltd.
Chiangmai, Thailand
sawrockohm2@gmail.com

3rd Kemmathad Chidchuea
EK-CHAI Distribution System Co.,
Ltd.
Bangkok, Thailand
kematat.jean@gmail.com

Abstract—This research introduces a LoRa mesh network for emergency notification systems, which addresses the challenges of the conventional point-to-point LoRa system, such as limited transmission range and lack of backup paths. The mesh network comprises nodes that serve as relays, facilitating multi-hop data transmission to the gateway. The network also adapts to node failures and route changes by employing the Reverse Ad-hoc On-demand Distance Vector (R-AODV) routing algorithm. The performance of the proposed system was assessed through three types of tests: point-to-point, multi-hop, and node failure. The results indicate that the LoRa mesh network improves network coverage and reliability for emergency communication. The average delay for sending alert messages from the gateway neighbor node to the gateway is 0.82s, from the alarm node to the gateway is 1.54s in normal conditions, and 11.65s in case of a gateway neighbor node failure. The user satisfaction score is 4.31 out of 5.

Keywords— LoRa, Mesh, Point-to-Point, Emergency notification, AODV

I. INTRODUCTION

An emergency is an event that can occur unexpectedly at any time and can cause damage. Emergency notifications can be made through mobile phone networks, mobile applications, or communication devices such as walkie-talkies to reach relevant authorities. The purpose is to send alert signals to make those who can provide assistance aware of the situation and offer immediate help.

In situations where emergencies or disasters occur or in areas with poor mobile phone signal coverage and the absence of Walkie Talkie communication devices, there can be challenges in reporting emergencies to security guards. Consequently, this can delay the response and assistance efforts, potentially harming lives and property.

LoRa technology [1] is a wireless connectivity solution known for its long-range capabilities and low-power transmission. It offers robust anti-interference properties, making it suitable for large-scale deployments without the need for cable network infrastructure. Its applicability in emergency alert systems extends to various settings such as stadiums, exhibitions, and field hospitals. Moreover, the inherent capability of LoRa technology to form a mesh network enables the extension of signal coverage. Each node

selectively transmits signals to the nearest node, ensuring reliable communication. Even in the event of node damage, the network automatically establishes connections with neighboring nodes. This seamless operation facilitates the transmission of help requests over long distances, maximizing the chances of reaching security personnel promptly and enabling timely assistance.

In this paper, the researchers address the need for a robust routing algorithm to facilitate efficient and reliable emergency signal transmission within the LoRa Mesh network [4]. The proposed approach combines the utilization of LoRa Mesh communication technology with specialized algorithms designed to establish effective routes in ad hoc networks. The objective is to create a supportive system for emergency notifications, particularly in scenarios where the general communication network encounters issues or disruptions.

II. LITERATURE REVIEWS

A. Long-Range (LoRa)

LoRa (Long Range) is a wireless connectivity technology that is suitable for use in conjunction with Internet of Things (IoT) applications and direct device-to-device communication (Machine-to-Machine). It enables data transmission can be up to 15 kilometers. The connectivity format can be in the form of point-to-point (Fig.1), where devices communicate directly with each other without any intermediary devices. LoRa devices operate with low power consumption and can also be configured to enter power-saving modes when not actively transmitting data. This makes LoRa an energy-efficient solution, especially in scenarios where data transmission is infrequent.

LoRa operates in unlicensed frequency bands, which vary depending on the region. For example, in Europe, the frequency is typically 868 MHz, while in North America, it is 915 MHz. In Asia, including Thailand, the available frequency bands for LoRa are 433 MHz and 915 MHz, as specified in the IoT regulations of Thailand. These frequency bands provide the necessary spectrum for LoRa deployments, ensuring compatibility and adherence to local regulatory requirements for IoT applications in Thailand.

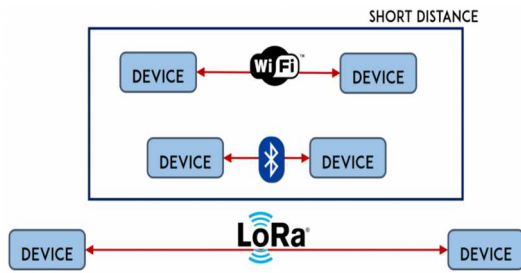


Fig. 1. LoRa point-to-point communication[2].

B. LoRa WAN

LoRaWAN (Long Range Wide Area Network) [3] shown in Fig.2, is a communications protocol for low-power wide area networks (LPWAN). LoRaWAN communications can enable IoT devices to connect over greater distances and consume less energy.

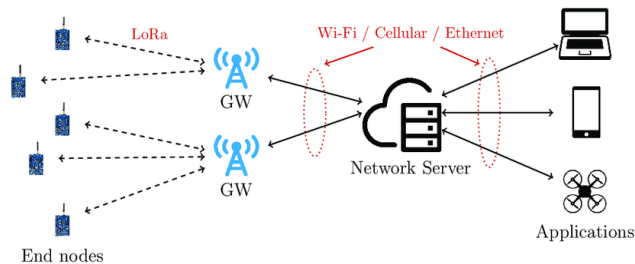


Fig. 2. LoRaWAN architecture diagram [3].

In a LoRaWAN architecture, the end node devices responsible for receiving or transmitting data typically include sensors for various measurements. They send data to gateways, which act as intermediaries for receiving and transmitting data between the source and the destination using frequency waves within the range of the transmitting devices. Once the data is received, the source node acts as a bridge, connecting the devices and the server. Data can be accessed and viewed through an application. Additionally, all data communication is encrypted for secure communications.

C. LoRa Mesh

LoRa Mesh is a network created using LoRa communication technology. The purpose of LoRa Mesh is to address the issue of signal coverage. Initially, Mesh networks were designed for military applications, hospitals, or large-scale areas requiring extensive communication connectivity.

In a Mesh network, each device serves as a node, communicating with other nodes within its range. Nodes are strategically placed to establish efficient communication with other nodes. Using dynamic routing, each node selects the optimal route to transmit signals to the destination node, considering factors like hop count, communication costs, and distance. Deploying the Mesh network effectively throughout an area enhances signal coverage and improves data transmission efficiency. Additionally, in the event of a node failure, the remaining nodes autonomously explore new routes to reach the destination. This autonomous behavior, self-discovery, enables nodes to find alternative paths for uninterrupted communication.

LoRa Mesh [4] technology offers significant advantages over LoRa point-to-point communication, providing extended coverage and cost savings. It operates independently of an

internet connection, making it adaptable to various environments. Nodes in the network automatically establish communication connections, eliminating the need for manual administration. The system's major limitation lies in the power supply to the devices, which can reduce node service time during high communication loads. However, this limitation is effectively mitigated with a primary focus on low-speed communication rather than image or video data. Overall, LoRa Mesh technology offers a flexible and efficient solution for wireless communication in challenging environments.

D. Ad hoc On-Demand Distance Vector (AODV) Routing Protocol

Ad hoc On-Demand Distance Vector (AODV) routing protocol [5] is a reactive protocol designed for use in mobile ad hoc networks (MANETs). It enables nodes to dynamically discover and maintain routes to other nodes in the network on an as-needed basis. AODV utilizes hop count as the decision metric for routing information, selecting the route that provides the minimum number of hop counts to the destination node. AODV uses route discovery and route reply messages to find the shortest path from the source node to the destination node, shown in Fig.3. The source node initiates route discovery by broadcasting a route request (RREQ) message with a path cost field. Each node receives the message updates the path cost, and re-broadcast. When the destination node receives a route request, it compares the 'path cost' field against previously received route request commands. If the path cost stored in the route request is better than any previously received, the destination node transmits a Route Reply (RREP) message back to the source node through the intermediate node.

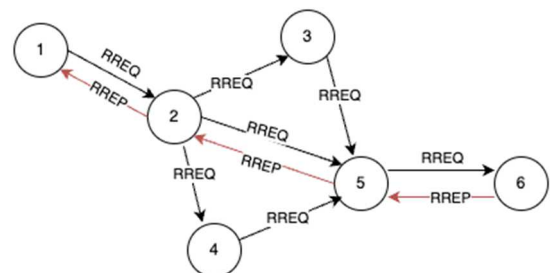


Fig. 3. AODV route discovery and route reply process [5].

E. LoRa and LoRa Mesh Applications

LoRa Mesh technology has been applied to reduce the maintenance costs of emergency power systems in office buildings [6], which can be costly and challenging to monitor. The solution integrates a LoRa wireless network with emergency lighting to enable collaboration and information exchange within the network. If one of the emergency lights is broken, the system can immediately notify the user, who can access and correct the issue. This helps reduce management costs. [7] developed a LoRa-based communication system, OWNGrid, for oil palm plantations. The system enables text and voice communication over long distances and low power consumption. The authors tested the system's functionality and performance in a plantation area and identified that the system's reliability needs to be improved. [8] presents a study on using LoRa technology to monitor the health of palm oil trees. The results show that the trunk and the canopy cause significant signal degradation and suggest that more research is needed to develop accurate path loss models for LoRa-IoT applications in palm-oil plantations. [9] developed an

emergency notification system using an ESP32 board and LoRa technology to address the problem of being stuck in a lift during an emergency and difficulty in requesting help due to mobile signal blockage by lift walls. The prototype device was developed in two models: the first model operates in point-to-point mode, consisting of a receiver and a transmitter, while the second version adds a signal repeater to increase the range of the emergency signal. Experimental results showed that the second model had 12-50% higher signal transmission efficiency than the first version and could be applied to real-life emergencies. The paper [10] compares the performance of ZigBee, LoRa, and IEEE1888 wireless communication technologies for community energy management systems. A hybrid system combining ZigBee and LoRa is proposed to balance high data rates and low power consumption. The results show that each technology has its strengths and can be used in different scenarios to achieve optimal performance. [11] explores the use of LoRa networks in Unmanned Aerial Vehicles (UAVs) for environmental monitoring. The method enables the rapid creation of large networks and is suitable for transmitting small amounts of data. The researchers designed a custom-slotted ALOHA Mesh protocol using LoRa and implemented custom software and hardware. The system uses multiple sensor nodes, including relays, gateways, and server networks. The results showed that with a minimized data rate of 0.293 kbps, the 1-hop transmission line exceeded 10 km, with a transmission delay of less than 6 seconds. The research [12] presents a protocol for using LoRa Mesh in a private network within an organization for IoT applications. The system supports communication between LoRa nodes and the LoRa gateway without the need for a service provider's LoRaWAN. However, the research has limitations, as it lacks clear test results and performance comparisons with other protocols. [13] presents a study on creating an efficient communication system using LoRa technology for emerging. The proposed Mesh network can transmit communication signals stably and exchange data between multiple nodes. Experimental results demonstrate the effectiveness of the proposed method in providing robust communication services in remote or disaster-prone areas.

The researchers propose to develop the LoRa technology used in the emergency notification system for passenger lifts at Prince of Songkla University, Phuket Campus [9]. The original system was unable to find a new route if the repeater is not working or if there is a problem with the service. In this paper, we propose to create a LoRa mesh network to increase the stability of the network service and the success rate of emergency notifications.

III. PROPOSED SYSTEM

A. System Architecture

In this paper, we present the design of an emergency notification system using LoRa Mesh technology. The system architecture consists of alarm nodes (node 2 and node 4), a gateway node, and gateway neighbor nodes (node 1 and node 3), as illustrated in Fig. 4; both use LoRa mesh connection technology to extend the network connection distance. Solid lines indicate the node connection in a range of signals, while dashed lines indicate that nodes are out of range. Each node connects and transmits data through other nodes, allowing the system to send out alerts even if one of the nodes is damaged. The node uses a route path from the proposed R-AODV (Reverse Ad-hoc On-demand Distance Vector) algorithm,

modified from the AODV routing algorithm. The gateway acts as a central point for the emergency notifications system. It broadcasts a list of source nodes to the alarm nodes that can be used to calculate the shortest path to the gateway.

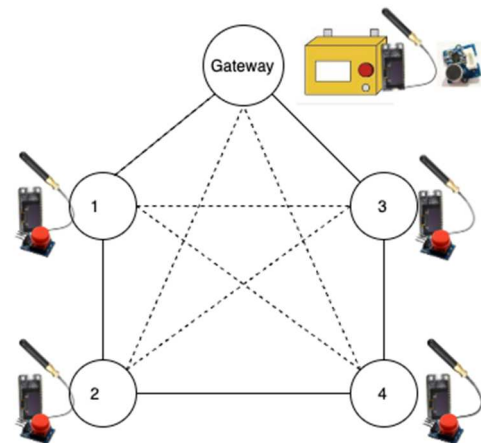


Fig. 4. System architecture.

B. Reverse Ad-hoc On-Demand Distance Vector (R-AODV) Routing Algorithm

The difference between AODV and R-AODV is that in AODV, nodes send route requests to find a path to the gateway themselves, while in R-AODV the gateway node broadcasts a beacon message with the gateway address and a blank node list. This message is modified and minimized based on the route advertisement message [14]. When a node receives the beacon message, it adds its node address to the node list. Each node broadcasts the received message to neighbor nodes. Eventually, all nodes in the LoRa mesh network use the node list data to define the best route path to the gateway and an alternative path, used in case the main path is unavailable (e.g., if a node becomes detached from the mesh). Additionally, all nodes periodically broadcast "ready" messages to announce their online status to neighboring nodes. This process is helpful in maintaining an active route from the alarm node to the gateway node through the active nodes. We design the R-AODV routing algorithm composed of three sub-algorithms running on a gateway, gateway neighbor node, and alarm node, illustrated in Fig. 5, 6, and 7.

1) *Gateway Node's Algorithm*: Fig. 5 shows that the gateway starts loading the default setting. It sends the message "R-AODV-Broadcast" to the surrounding nodes every 20 seconds. If there is an incoming message, it will check the message. For example, if the incoming message is "help," it will contain the source address that sent the message and display the location on the monitor according to that address. And if an emergency response button is pressed, it will send the message "Gateway received" to the surrounding nodes.

2) *Alarm Node's Algorithm*: As shown in Fig. 6, the node starts by setting up the LoRa module and then sends an "R-AODV-Ready" message to its neighboring nodes every 10-14 seconds. If a message arrives, it checks what type of message it is. For example, if the message is an "R-AODV-Broadcast" message, it enters the R-AODV function to store the path and forward it to its neighbors. Then, it checks what

paths it has and selects the shortest one as the destination for sending alerts.

If the message is an “R-AODV-Ready” message, it stores the address of the neighboring node. If the message is a “Gateway received” message, a reply from the gateway, the node forwards the message to its neighbors. The node checks whether the address matches the receiver if the message is a “Help” message. If not, the node discards the message. If yes, the node forwards the message to the destination or gateway. When an alert is triggered, the node sends a “Help” message to the destination obtained from the R-AODV function. The sending will fail if the node does not have a destination in the system. The node status can be checked from the LED color. Red means not ready, green means ready.

The node also switches the LED every time it sends a message to indicate success and counts the number of sending rounds. When it reaches the predefined number of rounds, the node resets its values and updates its destination to ensure that the destination node in the system is still operational.

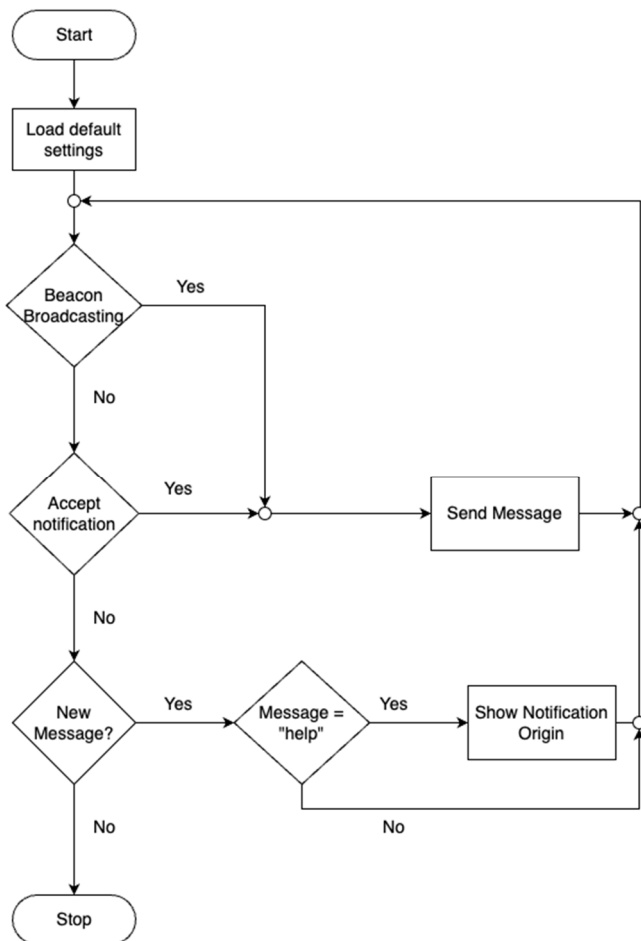


Fig. 5. Gateway node’s algorithm.

3) *Gateway Neighbor Node’s Algorithm:* As shown in Fig. 7, when a node connected to the gateway receives an “R-AODV Broadcast” message directly from the gateway, it stores the gateway address in its node list and forwards the message to its neighbors, excluding the gateway. The node will not update the gateway address if it receives a duplicate “R-AODV Broadcast” message.

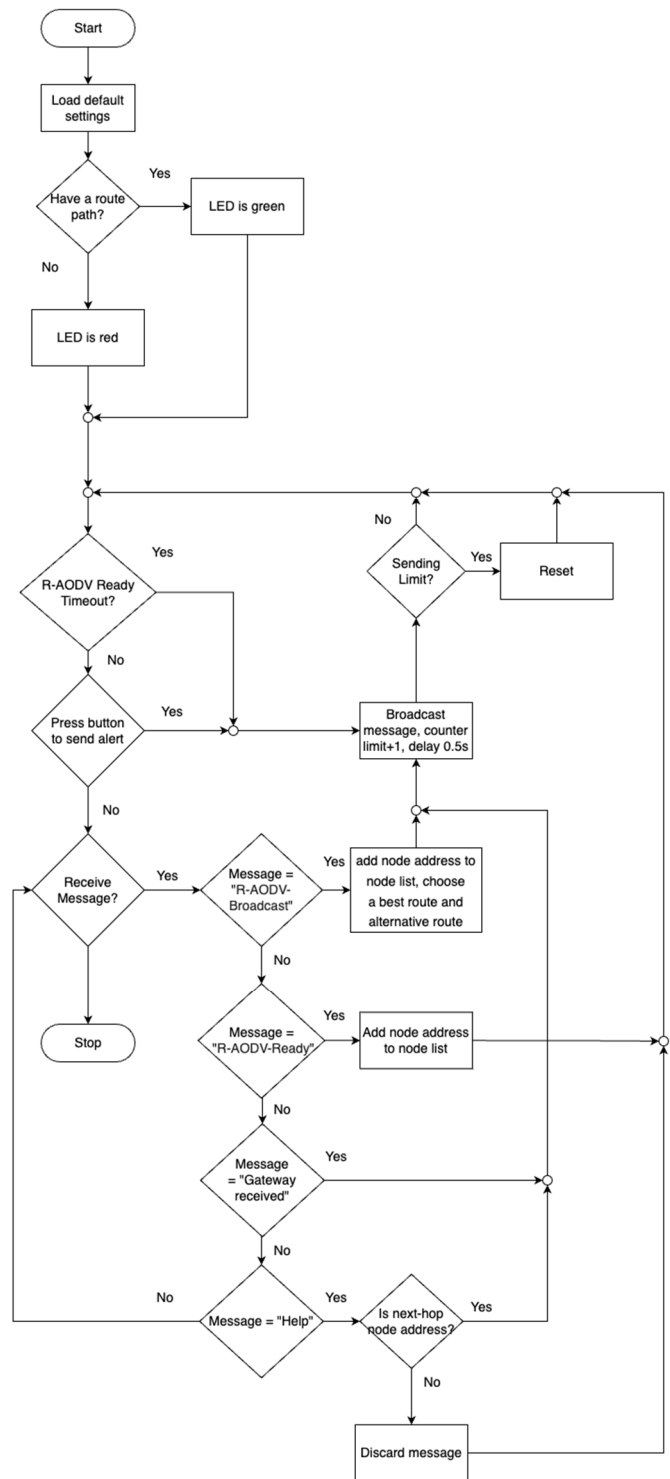


Fig. 6. Alarm node’s algorithm.

C. Hardware Design

1) *Gateway device:* As shown in Fig. 8, the gateway device uses esp32acts as a receiver of alerts from the node that triggers them. It is designed as a compact rectangular box that is easy to install and has a function that displays information on an OLED screen and a buzzer sound when an alert is triggered by the device that sends the data. It has a button for responding to the help request. The device can be opened inside for convenient battery charging and maintenance. The functions of the device are all shown on the screen.

2) *Alarm/Node attached to Gateway device*: As shown in Fig. 9, the alert device resembles the gateway but has an LED instead of an OLED screen to reduce energy consumption and increase usage time. It sends data to the gateway for display as sound and text. The device's functions are listed in Table I.

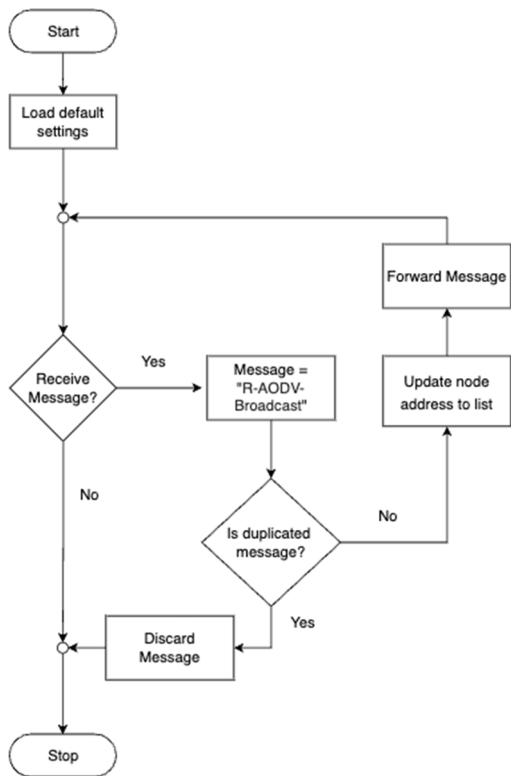


Fig. 7. Gateway neighbor node's algorithm.



Fig. 8. Gateway device.



Fig. 9. Alarm/Gateway neighbor node device.

TABLE I. DEVICE FUNCTIONS

| Functions | Alarm/Node attached gateway ^a | Gateway |
|------------------------|--|---------|
| Alarm button | Yes | No |
| Display notification | No | Yes |
| LED status (Red/Green) | Yes | No |
| Sound alarm | Yes | No |
| Antenna | Yes | Yes |
| LoRa module | Yes | Yes |

^a The alarm device and the node connected to the gateway are interchangeable.

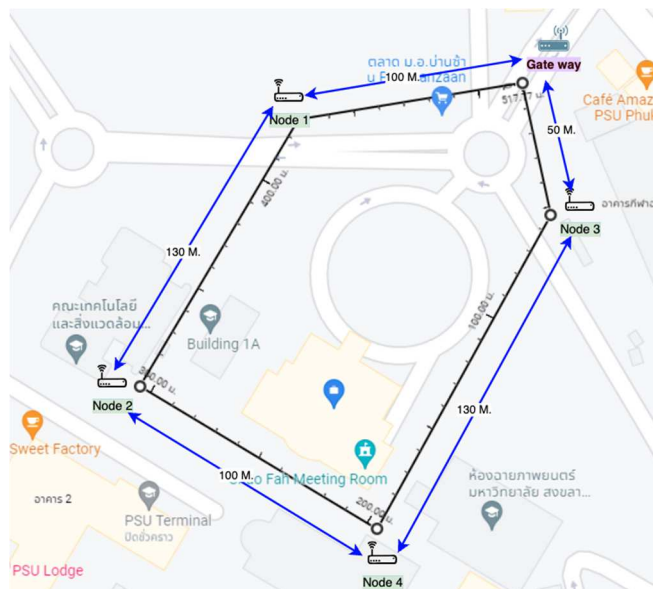


Fig. 10. Experiment setups (scenarios 1 to 3).

IV. RESULTS AND DISCUSSIONS

A. Experiment setups and results

The researchers designed and tested the system in three scenarios (20 times/scenario): Scenario 1, where the alert device triggers an alert from a node that receives a signal directly from the gateway and checks if it can send a signal to the gateway directly using the point-to-point technique. Scenario 2, where the alert device triggers an alert from a node that does not receive a signal from the gateway and checks if it can send a signal to the gateway using the multi-hop technique and select the shortest path among two possible paths to the gateway. Scenario 3, where a node stops working, checks if the node can use an alternative path to send a signal to the gateway if the main path fails. The average delay to send an emergency alert in scenarios 1, 2, and 3 are 0.82s, 1.54s, and 11.65s, respectively. Scenario 2 takes longer than Scenario 1 because the alarm node is not located next to the gateway, so the signal must be transmitted through other nodes. Scenario 3 takes the longest time because when some nodes stop working (node no. 1 or node no. 3), it takes time to find a new path. Therefore, sending a signal from the alarm node requires a new path, such as when node no.1 stops working, node no.2 sends an emergency alert through node no.4 to node no.3 and the gateway in sequence. The experiment setups and results are shown in Fig. 10 and Table II.

B. Evaluation of users satisfaction

The proposed prototype was tested by users at Prince of Songkla University, Phuket Campus. A total of 20 real users interested in using the system participated in the test. The system was tested one person at a time, with a focus on testing the emergency alert function. The test only involved triggering alerts from the alert device, not from the node attached to the gateway. The criteria for interpreting the average user satisfaction score are as follows: highest (4.51-5.00), high (3.51-4.50), moderate (2.51-3.50), low (1.51-2.50), and lowest (1.00-1.50). The average user satisfaction evaluation score was good at 4.31 out of 5, as shown in Table III.

TABLE II. EXPERIMENT RESULTS

| Test cases | Setup | Result |
|---|---|--|
| Scenario 1: Point-to-Point (gateway and gateway neighbor node) | Press alert button from gateway neighbor node | Success (average delay = 0.82s, distance=50m or 100m) |
| Scenario 2: Multi-hop | Press from alarm node | Success, the alarm node chooses the shortest path to the gateway (average delay=1.54s, distance=180m or 230m) |
| Scenario 3: Turn off one of the gateway neighbor nodes ^b . | Press from alarm node while one of gateway neighbor node turn off | For instance, when node no.1 is turned off, the alert message transmission from node no.2 initially fails (with the current best route from node no.2 to the gateway) but eventually succeeds after the node is reset or delayed. This occurs because node no.2 waits for the timeout to expire before recalculating the optimal route (from node no.2 to node no.4, node no.3, and finally to the gateway). The average delay from the alarm node is 11.65s with a maximum distance of 230m/330m. |

^b. Node no.1 and node no.3

TABLE III. EVALUATION OF USERS SATISFACTION

| Function tests | Average | SD | Level of Satisfaction |
|---------------------------------|---------|-----|-----------------------|
| Ease of use | 3.5 | 2.0 | Moderate |
| R-AODV algorithm | 4.3 | 0.5 | High |
| Success of alert system | 4.5 | 0.5 | High |
| LoRa Mesh | 4.2 | 0.8 | High |
| Be able to detect device status | 4.5 | 0.5 | High |
| Be able to change a route path | 4.7 | 0.5 | High |
| Practical benefits | 4.5 | 0.5 | High |
| Solving research problem | 4.3 | 0.5 | High |

V. CONCLUSION

In this research, the LoRa Mesh technology was studied as a backup emergency alert system in case the existing system fails due to signal blockage or device malfunction. The devices were tested for point-to-point and multi-hop data transmission. The multi-hop experiment showed that clustering nodes increased the range and coverage of the network, outperforming point-to-point communication with its limited capacity and constraints. The R-AODV algorithm enhanced node routing, enabling efficient selection of the shortest and alternative paths. Future planning includes improving the R-AODV algorithm for excellent stability and supporting multiple gateways.

ACKNOWLEDGMENT

This research was supported by funding from the College of Computing, Prince of Songkla University, Phuket Campus.

REFERENCES

- [1] LoRa," Wikipedia, The Free Encyclopedia, [Online]. Available: <https://en.wikipedia.org/wiki/LoRa>. [Accessed: Nov. 28, 2022].
- [2] R. Santos, "ESP32 with LoRa using Arduino IDE – Getting Started," Random Nerd Tutorials, [Online]. Available: <https://randomnerdtutorials.com/esp32-lora-rfm95-transceiver-arduino-ide/>. [Accessed: Nov. 28, 2022].
- [3] G. Codeluppi, A. Cilfone, L. Davoli, and G. Ferrari, "LoRaFarM: A LoRaWAN-Based Smart Farming Modular IoT Architecture," *Sensors*, vol. 20, no. 7, p. 2028, Mar. 2020
- [4] J. R. Cotrim and J. H. Kleinschmidt, "LoRaWAN Mesh Networks: A Review and Classification of Multihop Communication," *Sensors*, vol. 20, no. 15, p. 4273, Jul. 2020.
- [5] C. Perkins, E. Royer, and S. Das, "Ad hoc on-demand distance vector (AODV) routing," Request for Comments: 3561, Jul. 2003. [Online]. Available: <https://doi.org/10.17487/RFC3561>
- [6] WBS Technology, "EMIoT Emergency Lighting Network & Testing System," 2023. [Online]. Available: . [Accessed: 18-Jul-2023].
- [7] A. S. Prabowo, A. R. Pratama, A. Kurniawan and A. Wibisono, "OWNGrid: Oil Palm Plantation Communication System Based on LoRa Technology," 2018 International Conference on ICT for Smart Society (ICISS), Bandung, Indonesia, 2018, pp. 1-6.
- [8] R. Anzum, M. H. Habaebi, M. R. Islam and G. P. N. Hakim, "Modeling and Quantifying Palm Trees Foliage Loss using LoRa Radio Links for Smart Agriculture Applications," 2021 IEEE 7th International Conference on Smart Instrumentation, Measurement and Applications (ICSIMA), Bandung, Indonesia, 2021, pp. 105-110.
- [9] J. Thaenthong, S. Laeman and W. Duangdee, "Emergency Notification System Using LoRa Technology for Elevators: A Case Study," *Journal of Science Ladkrabang*, vol. 29, no. 2, pp. 72-85, 2020.
- [10] T. Inthasuth and K. Sureeya, "Performance Testing between ZigBee, LoRa and IEEE1888 for Application in Community Energy Management System," *TNI Journal of Engineering and Technology*, vol. 8, no. 2, pp. 64-79, Dec. 2020.
- [11] M. Pan, C. Chen, X. Yin and Z. Huang, "UAV-Aided Emergency Environmental Monitoring in Infrastructure-Less Areas: LoRa Mesh Networking Approach," in *IEEE Internet of Things Journal*, vol. 9, no. 4, pp. 2918-2932, 15 Feb.15, 2022.
- [12] H. Huh and J. Y. Kim, "LoRa-based Mesh Network for IoT Applications," 2019 IEEE 5th World Forum on Internet of Things (WF-IoT), Limerick, Ireland, 2019, pp. 524-527.
- [13] K. C. V. G. Macaraeg, C. A. G. Hilario and C. D. C. Ambatali, "LoRa-based Mesh Network for Off-grid Emergency Communications," 2020 IEEE Global Humanitarian Technology Conference (GHTC), Seattle, WA, USA, 2020, pp. 1-4.
- [14] J. Thaenthong and S. Gordon, "Gateway selection architecture using multiple metrics for vehicular networking," *Inform. Technol. J.*, vol. 11, no. 7, pp. 840-849, 2012.

Cattle Collars with a Low-Cost LPWAN-Based System for Cattle Estrous Monitoring

1st Nisit Pukrongta

Electronics and Telecommunication
Engineering, Faculty of Engineering
Rajamangala University of Technology
Thanyaburi (RMUTT)
Pathum Thani, Thailand
nisit.p@en.rmUTT.ac.th

2nd Pubet Sangmahamad*

Electronics and Telecommunication
Engineering, Faculty of Engineering
Rajamangala University of Technology
Thanyaburi (RMUTT)
Pathum Thani, Thailand
pubet_s@rmUTT.ac.th

3rd Tanaporn Pechrkool

Electronics and Telecommunication
Engineering, Faculty of Engineering
Rajamangala University of Technology
Thanyaburi (RMUTT)
Pathum Thani, Thailand
tanaporn.p@en.rmUTT.ac.th

4th Boonyarit Kumkhet

Electronics and Telecommunication
Engineering, Faculty of Engineering
Rajamangala University of Technology
Thanyaburi (RMUTT)
Pathum Thani, Thailand
boonyarit_k@rmUTT.ac.th

5th Virote Pirajnanchai

Electronics and Telecommunication
Engineering, Faculty of Engineering
Rajamangala University of Technology
Thanyaburi (RMUTT)
Pathum Thani, Thailand
virote.p@en.rmUTT.ac.th

6th Puttiporn Thiamsinsangwon

Chemical and materials Engineering,
Faculty of Engineering
Rajamangala University of Technology
Thanyaburi (RMUTT)
Pathum Thani, Thailand
puttiporn_t@rmUTT.ac.th

Abstract— This work proposes a prototype of LPWAN cattle collars for monitoring cattle estrus, with the aim of collecting data on cattle behavior to enhance the accuracy of determining cattle estrus. These collars consist of two main components. The first component is the transmitter, responsible for transmitting the cattle's sound data from the sound sensor (LMV324) and motion data from the gyro sensor module (MPU-9250), which are processed by the Sceduino controller. This processing is done to refine the sensor data signal before transmitting it to the LoRa RFM95 module, which broadcasts it within the 925 MHz frequency bands to the second component. The second component is a receiver, comprising the LoRa RFM95 module and a 5 dB gain antenna, connected to the ESP32. This component serves the additional function of sending data over the internet to Google Sheets cloud. In comparison to the GM1351 standard sound level meter, the sound sensor used in the experiment exhibits an average inaccuracy of 3.84%. The data obtained from the cattle wearing the collars can be utilized to analyze their movement patterns, such as feeding, standing rest, and prone position. Furthermore, the sound data transmission to Google Sheets every five seconds was consistently successful. Consequently, valuable data regarding movements, vocalizations, and estrus behaviors can be derived from the results of the cattle collar test. This research sets the groundwork and offers significant assistance for future advancements aimed at improving the accuracy of determining cattle estrus timing.

Keywords— cattle estrus, LPWAN, sound sensor, gyro sensor module

I. INTRODUCTION

Livestock farming plays a crucial role in the economy as it involves raising animals that are in high demand for various purposes, including consumption, processing, dressing, and decoration. Among the different types of livestock, cattle farming is particularly popular and can be pursued as a primary or secondary occupation. In most cases, the primary sources of income in cattle farming come from two main aspects: Part 1 involves the sale of beef (in the case of beef cattle) or the sale of milk (in the case of milk cattle), while

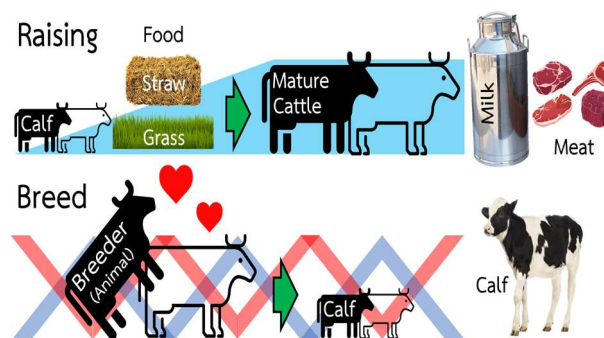


Fig. 1. The main sources of income for the cattle farmers.

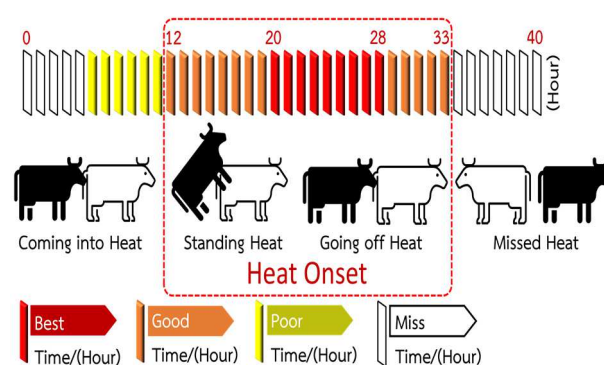


Fig. 2. The estrous cycle.

Part 2 involves breeding cattle and selling the resulting calves, as shown in Fig. 1. A significant amount of research is dedicated to enhancing productivity and efficiency in cattle breeding and calf sales processes. The Basics of Heat (Estrus) Detection in Cattle [1] provides information about the estrous cycle of cattle. According to the research, during the first 6-11 hours, the cattle experience the onset of heat, indicating their readiness for breeding. From 12 to 19 hours, the cattle are in heat and can be bred naturally, or one can wait for the optimal breeding time, which is between 20 to 28 hours after

the onset of heat, for artificial insemination. After the 33rd hour, the cattle ceased to be in heat, as depicted in Fig. 2. Cattle farmers must patiently wait for the next estrus cycle, which typically occurs within 18 to 24 days. Furthermore, once a cow is successfully fertilized, it takes approximately 280 days for gestation. The cattle will then enter into heat again around 30 to 50 days after calving, but new breeding should ideally commence after 60 days to allow for proper recovery. Therefore, in order to ensure that the optimal breeding time is not missed, extensive research has been conducted on methods for monitoring cattle estrus.

The detection of cattle estrus signs can be categorized into two main types [2]. The primary sign of estrus involves monitoring cattle behavior while they are in a standing position, using devices such as pedometers and accelerometers to detect changes in their movement patterns. During estrus, cattle tend to exhibit increased activity, which can be detected through these devices. The secondary signs of estrus involve observing mounting, activity, and aggressive behaviors using acceleration technology integrated into the cattle's collar. It has been observed that cows in estrus display a higher frequency of such behaviors. Detecting these secondary signs of estrus has proven to be effective in identifying estrus signals. One study utilized a detection model attached to the ears of dairy Holstein cattle to automatically identify estrus signals [3]. This model successfully detected estrus behaviors with minimal errors in estrus notification. Additionally, the concept of utilizing vocal behavior for cattle detection is introduced in [4-5]. In [4], the emphasis is on automating vocalization recording and caller identification in group-housed dairy cows. Conversely, in [5], a sound detection method is presented for identifying cows in estrus using machine learning technology.

In the study described in [6], the efficacy of estrus alert systems was evaluated through experiments conducted on 281 Holstein heifers and dairy cows. These animals were fitted with ear monitors to detect estrus signs at a dairy farm in Canada. The results showed a correct detection and prediction rate of 83.5%. Work [7] utilized two devices for monitoring estrus activity in pasture-based dairy cows. The FlashMate device was placed on the cow's rump, near the tail ridge, while the Moomonitor device was an accelerometer-based activity monitor worn around the cow's collar. The Moomonitor transmitted data wirelessly and provided actionable data and estrus notifications through a dedicated app. The study found that the duration of FlashMate activity was positively associated with days in milk and pregnancy per artificial insemination. On the other hand, the duration of Moomonitor activity was negatively associated with total milk yield during the first five weeks of lactation.

A wearable wireless vaginal sensor system was developed in [8] to enhance efficient and accurate estrus detection models. This system employed supervised machine learning based on sensing data. The device successfully detected 16 out of 17 estrus periods with only one false detection, indicating a sensitivity and precision of 0.94. Several works, [9-10], discussed the limitations of estrus detection and the impact of behavioral silent estrus on the activity and feeding behavior of lactating cows. These studies found that cows spent less time resting and eating but more time walking during estrus. Various parameters, including the percentage

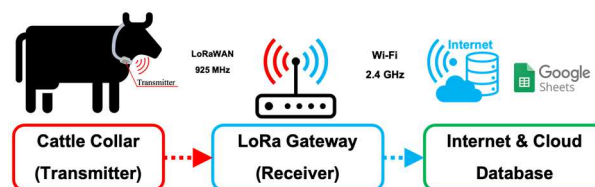


Fig. 3. The block diagram of the cattle estrous monitoring system.

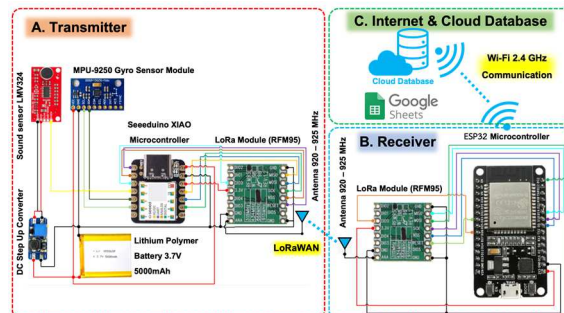


Fig. 4. The component diagram of the cattle estrous monitoring system.

of lying time, lying bouts, dry matter intake, feeding duration, and the number of visits to the feed, were reduced during estrus. However, only feeding duration showed a significant decrease during silent estrus. The research in [10] concluded that on the day of estrus, cows exhibited increased eating and activity behaviors, while resting and rumination activities decreased compared to their daily patterns. Fertile estrus was associated with 12% more high activity, 11% less resting time, and 6% less rumination time. Moreover, cows that returned to estrus after artificial insemination showed higher daily feeding and high activity periods, as well as reduced rumination and resting time during the estimated return to estrus period. In addition, data collection for cattle farming needs to cover a large area because cows are raised in both cattle stalls and pastureland. According to [11], LPWAN (Low Power Wide Area Network) technology is used, employing a 923 MHz LoRa module to transmit human health data to a database in the form of a wristband. It can communicate over a distance of more than 300 m and has a received data error rate of less than 5%.

These studies collectively provide insights into the various methods and devices used for estrus detection in cattle, as well as their impact on behavior and productivity. This paper focuses on designing a prototype of cattle estrus detection model that utilizes data on cattle movement behavior collected through a gyro sensor and a sound sensor. The gyro sensor captures three-axis cattle movement data, while the sound sensor records the number of cattle vocalizations. Both modules are attached to the cattle collar. The collected motion and sound data are transmitted via an LPWAN network using a LoRa module operating frequency of 925 MHz. The data is then stored on the Google Sheets cloud. The collected data can be further analyzed to predict the timing of cattle estrus in real-time.

II. METHODOLOGY

The cattle estrous monitoring system comprises three main sections as shown in Fig. 3. The first section is the transmitter, which is responsible for collecting behavioral

data from the sensing cattle. Those data are then transmitted using the LoRa network with frequency of 925 MHz. The second section is the receiver, which receives the transmitted data. Additionally, it acts as a bridge, converting the communication from the LoRa network to a 2.4 GHz WLAN network. This conversion is facilitated by a Wi-Fi module integrated into the ESP32 board. The final section is Cloud Storage, which stores the received data in the form of Google Sheets. This storage is achieved through an internet connection, allowing for seamless data recording and analysis.

A. Transmitter Node

In Fig. 4 (red dashed line rectangle), the transmitter node or data sensing part of the cow's behavior is depicted, and it is divided into two functionalities. The first functionality involves detecting vocalizations behavior using a sound sensor (LMV324). This sensor is responsible for collecting data on the number of times of cow vocalizations. The analog data from the sensor is read through the pin A3 of the Seeeduino board. The obtained data is then processed by the Seeeduino board, which calculates the value of the sensor for loudness. This calculation is done by determining the value of the sensor in relation to the hearing threshold of the human ear using the dBA equation [12], as represented by (1). In this equation, the variable "sones" corresponds to the reading data obtained from the sound sensors.

$$dBA = 33.2 \times \log_{10}(\text{sones}) + 28 \quad (1)$$

The second functionality is a gyro sensor (MPU-9250), which detects angular movement behavior along three axes: $\pm x$, $\pm y$, and $\pm z$. This sensor is connected to the Seeeduino board using the I2C communication protocol. The SDA and SCL pins of the sensor is connected to pin 4 and 5 of the Seeeduino board, respectively. Once the Seeeduino board receives and process data from both the sound sensor and the gyro sensor, it utilizes the LoRa Module (RFM95) to transmit the data. The LoRa Module operates at a frequency of 925 MHz and is responsible for sending the data to the LoRa gateway. To power all the devices mentioned above, a 3.7 Volt 5000mAh Lithium Polymer battery is used. This battery provides the necessary power for the operation of the sensors, Seeeduino board, LoRa Module, and other components of the system. To extend the operational lifespan of the proposed system, renewable energy solutions like flexible solar cells, designed to harvest energy from sunlight, and compact magnetic generators, designed to capture energy from cattle movements, are put into practical application.

B. Receiver Gateway

The receiver section is a LoRa Gateway that consists of two main components as shown in Fig. 4 (blue dashed line rectangle): a LoRa Module (RFM95) and an ESP32 microcontroller. These boards utilize SPI communication between them, and those combine the features of both wireless communication technologies. The first communication technology is LoRaWAN, which offers advantages such as long-distance communication and low power consumption. However, it has a narrow bandwidth, limiting the amount of data that can be transmitted, and restricting communication to nodes within the same network. To overcome this limitation, LoRaWAN communication is supplemented by the second wireless communication

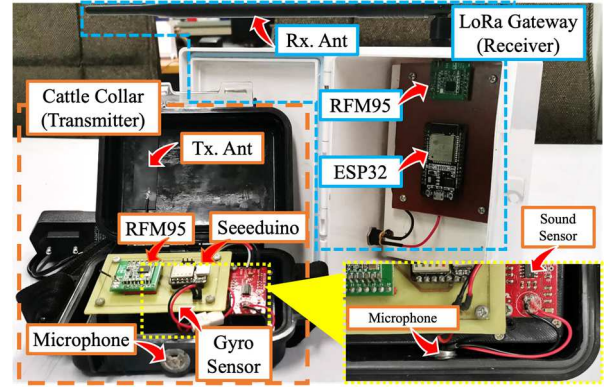


Fig. 5. The prototype of the cattle estrous monitoring system, which consists of a transmitter and receiver placed in close proximity to capture a photo.

technology, WLAN (Wi-Fi) which enables cross-network communication via the internet and provides a wider bandwidth, allowing for the transmission of larger data sets. However, WLAN has a limitation on wireless communication distance, typically not exceeding 200 m, between the user and the receiving device. By combining the capabilities of LoRaWAN and WLAN, the LoRa Gateway can take advantage of the long-distance and low-power benefits of LoRaWAN while leveraging the internet connectivity and higher bandwidth of WLAN for broader data transmission.

C. Google Sheet Cloud Storage

The cloud storage component is utilized to store the data that has been forwarded from the LoRa Gateway. In this case, the Google platform in the form of Google Sheets was used due to its easier data management. The example of data stored in Google Sheets is organized in TABLE I., which each column representing specific information. The columns include the month, date, year, time, cattle angular motion data for all three axes (x , y , z), cattle vocalizations levels in unit of dBA, and received signal strength indicator (RSSI) value. The measurement of the RSSI value ensures signal transmission for not only the cattle inside the cattle house but also those in the wide-area field. The transmitter nodes transmit that data to Google Sheets every 5 seconds, with an additional estimated transmission time of 1-5 seconds. Consequently, the Google Sheets display a readout interval of 6-10 seconds between the reception of each dataset. This interval reflects the time it takes for the data to be received and recorded in Google Sheets.

TABLE I. EXAMPLE DETAIL OF GOOGLE SHEET.

| Month/Date/Year | Time | axis $\pm x$ | axis $\pm y$ | axis $\pm z$ | Sound (dBA) | RSSI |
|-----------------|----------|--------------|--------------|--------------|-------------|------|
| 2/16/2023 | 11:59:41 | -8 | -90 | 56 | 100.87 | -85 |
| 2/16/2023 | 11:59:48 | -19 | -33 | 67 | 50.1 | -92 |

III. EXPERIMENTAL SETUP AND RESULT

The prototype of the cattle estrous monitoring system shows in Fig. 5, comprising a transmitter (indicated by the orange dashed line) and a receiver (indicated by the blue dashed line). The enclosure box of the transmitter is open in the figure to reveal its internal components. All components

of the transmitter are situated within the enclosure box, which has dimensions of $130 \times 90 \times 50 \text{ mm}^3$ and a total weight of 300g. The experiment is divided into three parts based on the different functionalities and data collection processes. Part A focuses on collecting the movement behavior of the cattle using a gyro sensor. The gyro sensor is installed in the center of the enclosure box, beneath the microcontroller PCB board. The gyro sensor is responsible for detecting the angular movement along the x -, y -, and z -axes of the cattle. Data related to movement behavior is collected in this part, and this data can be further analyzed of cattle estrous. Part B involves collecting the vocalizations behavior of the cattle using a sound sensor. The sound sensor consisted of a small condenser microphone and a signal amplifier. To detect the cattle vocalizations, the microphone is installed inside the enclosure box with the front of the microphone facing outward through a fitting hole at the front of the longest side as shown in the inset of Fig. 5. The sound sensor detects the cattle's vocalizations and records the corresponding data. The vocalizations behavior of the cattle is an important indicator of their estrus cycle, and this information is captured and analyzed. Part C pertains to the communication aspect of the system. This involves transmitting the sensing data to the data storage. This part ensures that the collected data is efficiently transmitted. By dividing the experiment into these three parts, the performance and accuracy of the proposed cattle estrous monitoring system can be thoroughly evaluated, providing insights into its functionality and effectiveness in detecting cattle behavior to analyzing the cattle estrus.

A. Cattle Movement Behavior Experimental

Fig. 6 shows the results of the efficiency and precision experiment conducted on the gyro sensor. The experiment involved setting the gyro sensor at angles ranging from 0° to -100° and 0° to $+100^\circ$, with a 10° increment. The experiment was performed separately for both the x -axis and the y -axis. The figure displays a comparison between the set values and the actual readings obtained from the sensor. Additionally, the orange line represents the comparative error of the $\pm x$ -axis and the purple line represents the comparative error of the $\pm y$ -axis. Fig. 7 shows the preliminary data illustrating the movement patterns of the cattle. From the preliminary results, when the x -axis value is negative, it can be interpreted that the cattle are bending their head down, which can be used to determine whether they are drinking or feeding (number 1 in Fig. 7). When the cattle are in a prone position, lying flat on the ground with their neck extended upwards, the x -axis value remains positive, and the z -axis value, approaching 0° . Indeed, it's worth mentioning that in this cattle position, all axis values do not change significantly (number 2 in Fig. 7). Furthermore, when the cattle are changing the movement from lying down position to standing rest position, the x -axis value registers as positive, and the z -axis value approaches 90° (number 3 in Fig. 7). The y -axis value indicates the head tilting to the left (positive) or to the right (negative), and it provides insights into the behavior of the cattle.

B. Cattle Vocalizations Behavior Experimental

Fig. 8 displays the sound level data from the experimental setup used for comparison. An experiment was conducted to evaluate the effectiveness and accuracy of the sound sensor.

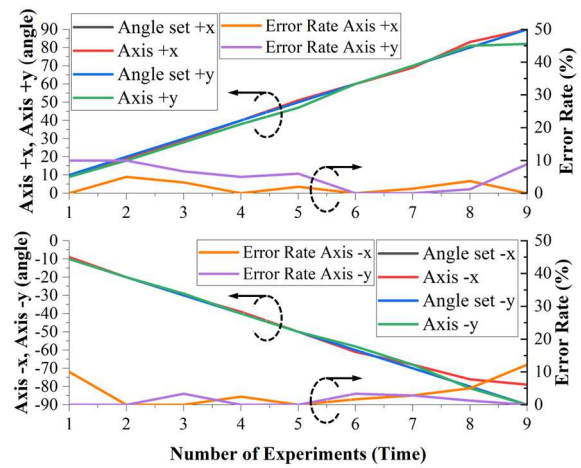


Fig. 6. Comparison graph between gyro sensor reading and angle setting.

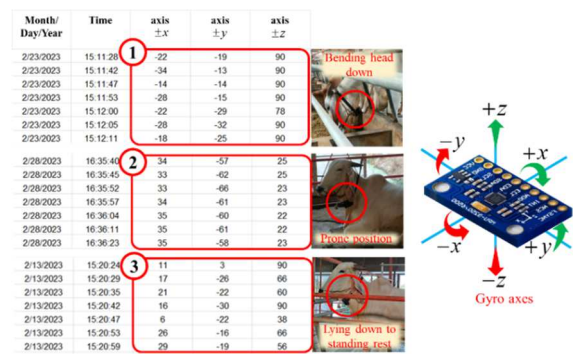


Fig. 7. The data on google sheets show the movement behavior of cattle.

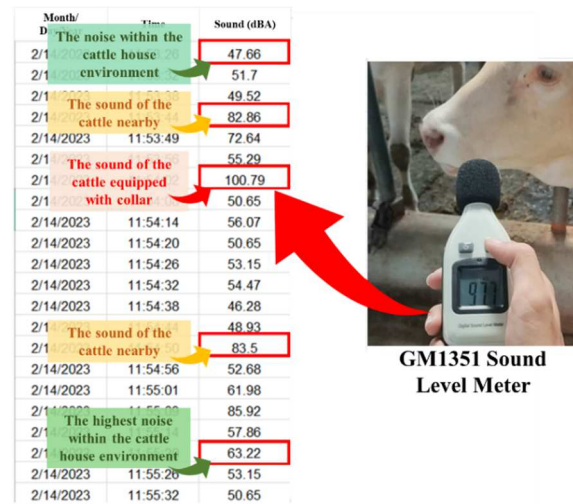


Fig. 8. The vocalizations behavior data on Google Sheets.

This experiment involved comparing the results obtained from the sensor with those acquired from a standard sound level meter, specifically the BENETECH model GM1351. The experimental results of the sound level revealed an average error of 3.84%, demonstrating the effective identification of vocalizations from cattle wearing the collar.

After evaluating the effectiveness and precision of the sound sensor, further experiments were conducted to determine the loudness of sounds associated with

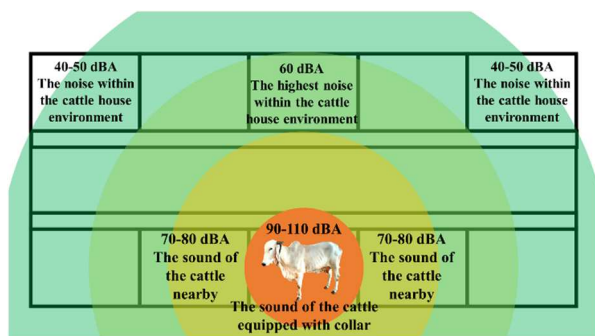


Fig. 9. The sound loudness of the cattle and the noise from the environment in the cattle house.



Fig. 10. The performance experimental with LoRaWAN.

vocalizations behavior exhibited by cattle wearing sensor-equipped collars. Fig. 9 illustrates the results of these experiments along with corresponding loudness level ranges. In the figure, the orange band represents the range of 90 to 110 dBA, which signifies the sound produced by cattle wearing the sensor collar. The yellow band indicates the vocalizations behavior of nearby cattle, with a loudness level ranging from 70 to 80 dBA. The light green band represents the highest noise level observed in a cattle house environment, which is approximately 60 dBA. On the other hand, the dark green band corresponds to the lowest noise level in the cattle house environment, ranging from 40 to 50 dBA. For instance, when interpreting the sound level data, the sound level results in Fig. 8 assist in identifying which sounds correspond to the vocalizations of cattle equipped with collars, those from distant cattle, or noise levels observed within a cattle house environment. This interpretation is based on the range of sound levels provided in Fig. 9. It's evident that the sound level of 100.79 dBA corresponds to the vocalizations of cattle equipped with collars, while the sound level around 80 dBA represents the vocalizations of distant cattle. Additionally, sound levels less than 60 dBA indicate noise within the cattle house environment.

C. Efficiency and Distance of Communication System

This experiment aimed to evaluate the effectiveness of system transmission distance by utilizing a cattle collar to broadcast data from multiple sensors. The setup involved implementing a LoRa Gateway antenna that supports a frequency of 925 MHz with a gain of 5 dBi. The antenna was positioned 2 m height above the ground. The experiment involved progressively increasing the distance between the LoRa Gateway and the cattle collar up to 350 m by 50 m increments. At each distance interval, the system's ability to receive data from the cattle collar was evaluated. The process was repeated until the LoRa Gateway failed to receive data from the cattle collar. The experimental results determined that the system was capable of transmitting data up to 350 m. This implies that the LoRa Gateway successfully received

data from the cattle collar when they were within this range. Additionally, during the experiment, the received signal RSSI value was displayed on the receiving side. The RSSI value provides information about the signal strength and can be utilized to assess the quality of the received signal.

IV. CONCLUSION

This work presents a designing the prototype of cattle estrous monitoring system to assist farmers in analyzing cattle behavior that indicates estrous symptoms. The system employs a prototype transmitter designed as a cattle collar, which is equipped with both a gyro sensor and a sound sensor. These sensors are used to monitor and analyze the movement and vocalization behavior of the cattle, respectively. The experimental results indicated that the monitoring of cattle movement behavior yielded an average error of 3.00% in representing initial cattle movement patterns. The average error for cattle vocalization levels was 3.84%, demonstrating the effective identification of vocalizations from cattle wearing the collar. The proposed system integrates LoRaWAN communication, employing a LoRa RFM95 module as both the data transmitter and receiver. This capability allows for data transmission over a maximum distance of 350 m, making it well-suited for effectively covering both a cattle house and a wide-area field. Based on the information provided, the proposed system is well-suited for monitoring cattle estrus and has the potential for further development into an automated analysis system, which can aid in establishing an intelligent cattle house.

ACKNOWLEDGMENT

The Department of Electronics and Telecommunication engineering, Rajamangala University of Technology Thanyaburi (RMUTT) supports this paper. We would like to thank our colleagues, Mr. Thanawut Utarmat and Mr. Jirapong Wittaya, the prototype and research assistant. And thank you very much to Yee Mad Noor Cattle Farm (Somwang Farm), which has a total of 25 cattle on the farm, with one cattle being used in the experiment. The breed of cattle is Hindu-Brazil, 4 years old, weighing about 400 kg. It has had 2 calves, has an estrus cycle of 20-21 days, and cows will hunch over other cattle and make some noise when they are in heat.

REFERENCES

- [1] DuPonte, Michael W. "The basics of heat (estrus) detection in cattle," 2007, pp.1-3.
- [2] Reith, S., and S. Hoy. "Review: Behavioral signs of estrus and the potential of fully automated systems for detection of estrus in dairy cattle," *Animal* 12.2, 2018, pp.398-407.
- [3] E.M. Schilkowsky, G.E. Granados, E.M. Sitko, M. Masello, M.M. Perez, and J.O. Giordano, "Evaluation and characterization of estrus alerts and behavioral parameters generated by an ear-attached accelerometer-based system for automated detection of estrus," *Journal of Dairy Science* 104.5, 2021, pp.6222-6237.
- [4] RÖTTGEN, V., et al. Automatic recording of individual oestrus vocalisation in group-housed dairy cattle: development of a cattle call monitor. *Animal*, 2020, pp.198-205.
- [5] WANG, Jun, et al. Identification of oestrus cows based on vocalisation characteristics and machine learning technique using a dual-channel-equipped acoustic tag. *animal*, 2023, pp.100811.
- [6] K. Macmillan, M. Gobikrushanth, G. Plastow, and M.G. Colazo, "Performance and optimization of an ear tag automated activity monitor for estrus prediction in dairy heifers," *Theriogenology* 155, 2020, pp.197-204.

- [7] S.G. Moore, V. Aublet, and S.T. Butler, "Monitoring estrous activity in pasture-based dairy cows," *Theriogenology* 160, 2021, pp.90-94.
- [8] Shogo Higaki, Ryotaro Miura, Tomoko Suda, L. Mattias Andersson, Hironao Okada, Yi Zhang, Toshihiro Itoh, Fumikazu Miwakeichi, and Koji Yoshioka, "Estrous detection by continuous measurements of vaginal temperature and conductivity with supervised machine learning in cattle," *Theriogenology* 123, 2019, pp.90-99.
- [9] Hawar M. Zebari, S. Mark Rutter, and Emma C.L. Bleach, "Characterizing changes in activity and feeding behaviour of lactating dairy cows during behavioural and silent oestrus," *Applied Animal Behaviour Science* 206, 2018, pp.12-17.
- [10] Jeffrey S. Stevenson, "Daily activity measures and milk yield immediately before and after a fertile estrus and during the period of expected return to estrus after insemination in dairy cows," *Journal of Dairy Science* 104.10, 2021, pp.11277-11290.
- [11] T. Pechrkool, B. Kumkhet, P. Sangmahamad, P. Raklua, N. Wongsin and T. Wangwijit, "Telehealth Monitoring System based on LPWAN," 2022 37th International Technical Conference on Circuits/Systems, Computers and Communications (ITC-CSCC), Phuket, Thailand, 2022, pp. 978-981.
- [12] Learn metrics HVAC systems Based On Specifications, "Simple Sones To dB Calculator (With 0.3, 1.5, 3.0 Sone Examples)" <https://learnmetrics.com/sones-to-db/>

Deep Learning-Based Robust Automatic Modulation Classification using Higher Order Cumulant Features

Nopparuj Suetrong

*Department of Computer Engineering,
Faculty of Engineering,
Chiang Mai University
Chiang Mai, Thailand
nopparuj_s@cmu.ac.th*

Attaphongse Taparugssanagorn

*ICT Department,
School of Engineering and Technology,
Asian Institute of Technology
Pathum Thani, Thailand
attaphongset@ait.asia*

Natthanan Promsuk

*Department of Computer Engineering,
Faculty of Engineering,
Chiang Mai University
Chiang Mai, Thailand
natthanan.p@cmu.ac.th*

Abstract—The Internet of Things (IoT) represents one of the pivotal technologies in our daily lives. Within these systems, wireless communication plays an indispensable role in connecting IoT devices. Consequently, signal modulation emerges as a technique within wireless communication systems, enabling the transmission of baseband signals at higher frequencies. Given the array of modulation types, modulation classification comes into play to differentiate the modulation type of the received signal. Due to the presence of noise and attenuation, automatic modulation classification (AMC) stands as the primary method for such classification. AMC methods can operate without requiring any prior knowledge regarding the received signal. Multiple research groups have extended the depth of deep learning (DL) models or augmented the neuron count in each layer to enhance performance, albeit at the expense of increased model complexity. To tackle this challenge, we present model that merges the gated recurrent unit (GRU) and long short-term memory (LSTM) architectures. Furthermore, data pre-processing techniques, specifically Min-Max normalization and fourth-order cumulant (FOC), have been employed to enhance classification accuracy. The outcomes underscore that our proposed model surpasses both LSTM and GRU models. Moreover, the classification accuracy of normalized data outperforms that of data without normalization.

Keywords—Fourth-Order Cumulant, Internet of Things, Deep Learning, Gated Recurrent Unit, Long Short-Term Memory

I. INTRODUCTION

The Internet of Things (IoT) has indeed emerged as a pivotal technology in our day-to-day existence, encompassing applications such as smart homes, intelligent vehicles, and an array of other sophisticated systems [1]. These IoT devices establish communication and interaction channels with their counterparts through the internet or other communication infrastructures, notably wireless communication systems. Central to wireless communication systems is the employment of modulation to facilitate the transmission of information across communication channels. Modulation plays a pivotal role in wireless communications by facilitating the transmission of baseband signals over higher frequencies. This process involves encoding information from the baseband signal into the carrier signal, yielding a passband signal well-suited

for transmission across communication channels. Moreover, modulation serves to bolster the security of transmitted data.

Modulation classification serves as a technique designed to categorize the modulation types of received signals. It finds application in scenarios where the modulation type remains unknown or prior knowledge about the received signal is insufficient. This technique holds widespread relevance across diverse domains, encompassing radio signal detection, spectrum monitoring, wireless communication systems, electronic countermeasures (ECM), and military contexts [2].

Due to factors such as attenuation, noise, and other interferences stemming from the inherent behavior of electromagnetic waves or unwanted signals present in the communication channel, including wireless devices, automatic modulation classification (AMC) stands out as the principal method for categorizing modulation types. These interferences can induce alterations or disruptions in signal parameters, contributing to a diminished signal-to-noise ratio (SNR). Presently, AMC is categorized into three distinct types: modulation classification based on hypothesis testing, modulation classification based on feature extraction, and modulation classification based on deep learning (DL) [3]. This paper primarily centers on DL-based modulation classification, as it harnesses the capabilities of neural networks (NN) to achieve accurate classification without the need for prior signal knowledge.

DL represents a subset of machine learning (ML) centered around artificial neural networks (ANNs), drawing inspiration from the intricate structure and functionalities of the human brain. The augmentation of layer count or neuron quantity within each layer can significantly enhance classification accuracy, as it enables the NN to grasp more intricate data representations. However, this elevation in architecture complexity must be duly acknowledged [4].

Within this paper, we introduce a novel approach for modulation classification, encompassing the integration of both long short-term memory (LSTM) and gated recurrent unit (GRU) techniques. Additionally, we employ Min-Max normalization and fourth-order cumulant (FOC) as data pre-

processing methodologies. These techniques are strategically employed to heighten the classification accuracy of DL models while preserving the existing model structure intact.

II. RELATED WORKS AND OUR CONTRIBUTION

For recent years, there has been several works that have proposed a DL architecture for the modulation classification task.

In [5], the authors introduced a model for AMC centered around LSTM. This model effectively categorizes incoming signals utilizing amplitude and phase (A/P) data as input. They concluded that the LSTM model demonstrated strong performance when handling A/P data, yielding high accuracy under conditions of elevated SNR. However, for situations with lower SNR, a convolutional neural network (CNN) exhibited superior accuracy. Furthermore, an innovative approach to automatic modulation recognition, involving the fusion of in-phase and quadrature (I/Q) data with FOC representation of modulated signals, was presented by the authors in [6]. The novel data representation was put to the test using both CNN and LSTM models. The findings highlighted that this fresh data representation holds the potential to enhance classification accuracy while showcasing increased resilience to noise.

Additionally, the works in [7] delved into the domain of AMC by introducing CNN, LSTM, and convolutional long short-term deep neural networks (CLDNN). The CLDNN model emerged as a notable advancement, driving classification accuracy improvements; however, it concurrently raised the model's complexity. The investigations carried out in [8] shed light on CNN and CLDNN models. Their objective revolved around reducing parameter count while retaining comparable accuracy levels through alterations in model architecture. The study also conducted a comparative analysis between models using both non-normalized and normalized data—specifically employing Z-Score normalization (Standardization). The findings indicated an enhancement in classification accuracy for CNN models with data normalization compared to those without it.

To the best of our knowledge, this represents the inaugural model for AMC that harmonizes two DL architectures: GRU and LSTM. Moreover, we implemented data pre-processing techniques, namely Min-Max normalization and FOC, to elevate the overall model performance. To culminate our study, we conducted a comparative analysis of classification accuracy, leveraging graphical representations and confusion matrices as evaluation tools.

III. METHODOLOGY

The workflow of this work is illustrated in Fig. 1. Firstly, I/Q data was extracted from the dataset. Subsequently, we transformed the data representation by converting the I/Q data into A/P data. After that, Min-Max normalization was applied with each signal being individually normalized. Next, feature extraction using FOC to obtain the extracted features was performed. These extracted features were then combined with the A/P data to create a new data representation called APFOC. Finally, this data representation was used as input

for the DL models to classify the modulation types. The DL models used in our paper were LSTM-LSTM model, GRU-GRU model, and our proposed model.

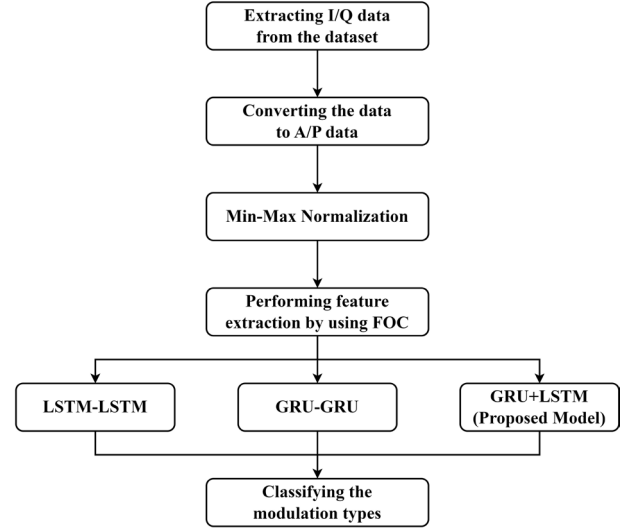


Fig. 1. Workflow of this work

A. Pre-Processing Techniques

The signals received within wireless communication systems can be articulated as:

$$r(t) = s(t) * h(t) + n(t), \quad (1)$$

where t signifies the time instant, $s(t)$ represents the transmitted signal, $h(t)$ characterizes the channel impulse response, and $n(t)$ symbolizes the additive white Gaussian noise (AWGN). The received signal, denoted as $r(t)$, is frequently expressed in the I/Q data format. Additionally, I/Q data can be transmuted into alternative data representations, including amplitude and phase. Amplitude pertains to the magnitude or intensity of the signal, typically represented by the peak height of the waveform. In contrast, phase encapsulates the temporal alignment or timing of the signal within a periodic waveform. Equations (2) and (3) are employed to transform the I/Q data into amplitude data A and phase data ϕ correspondingly as

$$A = \sqrt{I^2 + Q^2}, \quad (2)$$

$$\phi = \arctan(Q/I), \quad (3)$$

where I and Q denote the in-phase data and the quadrature data, respectively.

1) *Min-Max Normalization*: In addition to the data representation transformation, Min-Max normalization emerges as an alternative data pre-processing technique. Min-Max normalization operates by rescaling the data within a specified range while preserving the inherent data relationships. The normalized data is derived through application of the Min-Max normalization formula, as defined by

$$x' = \frac{(x - \min)}{\max - \min} (\max' - \min') + \min', \quad (4)$$

where x denotes the actual data, min denotes the minimum value, max denotes the maximum value, max' denotes the new maximum scale, and min' denotes the new minimum scale.

2) *FOC*: An additional technique for data pre-processing is the FOC, a statistical metric that characterizes the signal's structure [9]. Within our study, we employ c_{42} to encapsulate the FOC between two signals. The process of extracting features through FOC involves an initial transformation of the data representation from I/Q data to a complex signal, achieved via (5) [10]. Subsequently, (6) and (7) come into play, serving as tools to compute FOC and elucidating the functioning of the cumulant function $cum(\cdot)$, respectively.

$$s = I + \sqrt{-1}Q, \quad (5)$$

$$c_{42} = cum(s, s, s^*, s^*), \quad (6)$$

$$cum(p, q, r, s) = W - X - Y - Z, \quad (7)$$

where s denotes the complex signal, I denotes the in-phase data, Q denotes the quadrature data, s^* denotes the conjugate of complex signal. Further, W denotes $E(pqrs)$, X denotes $E(pq)E(rs)$, Y denotes $E(pr)E(qs)$, Z denotes $E(ps)E(qr)$, where $E(\cdot)$ signifies the expectation operation.

B. DL Models

1) *LSTM Model*: LSTM stands as a specialized variant within the realm of recurrent neural network (RNN) architecture. While RNNs were conceived to process sequential data, particularly time series data, they confronted obstacles such as the vanishing gradient and exploding gradient quandaries when handling lengthy sequences. In response, the LSTM architecture was introduced, encompassing ingenious cell state and gating mechanisms devised to counter these challenges [11]. The cell state serves as a reservoir of memory, enabling the preservation of information across extensive sequences. An LSTM comprises three pivotal gates: the input gate, the forget gate, and the output gate. The input gate governs the infusion of fresh information into the cell state. Conversely, the forget and output gates oversee the elimination of specific information from the cell state and the curation of information from the cell state for presentation as the LSTM's concealed state, respectively.

2) *GRU Model*: GRU engineered to overcome the limitations of conventional RNNs. GRU was conceived as a refinement over LSTM, streamlining its architecture while adeptly managing extended data dependencies. It embodies three core constituents: the hidden state, update gate, and reset gate. Within the framework of GRU, two hidden states emerge: the candidate hidden state and the ultimate hidden state. The candidate hidden state arises from the fusion of input and the preceding hidden state, a process controlled by the reset gate. In tandem, the ultimate hidden state is dictated by the update gate, which amalgamates the candidate hidden state with the prior hidden state. As previously explored, the update gate is pivotal in deciding which insights from the candidate hidden state warrant assimilation into the former hidden state, while the reset gate governs the omission of

specific information from the prior hidden state. Despite boasting a reduced count of learnable parameters compared to LSTM, GRU effectively attains performance commensurate with its counterpart [12].

3) *Performance Metric*: In evaluating the classification performance of the DL models, accuracy was adopted as the assessment metric. Accuracy gauges the overall correctness of the model's classifications across all classes, and it is mathematically expressed as

$$Accuracy = \frac{TP + TN}{TP + TN + FP + FN}, \quad (8)$$

where TP denotes the count of true positives (TPs), TN denotes the count of true negatives (TNs), FP denotes the count of false positives (FPs), and FN denotes the count of false negatives (FNs).

In this context, TP denotes an instance correctly classified as positive for a specific class. Conversely, TN designates an instance correctly classified as negative for a specific class. On the contrary, FP signifies an instance incorrectly classified as positive for a particular class, despite belonging to a different class. Similarly, FN signifies an instance incorrectly labeled as negative for a specific class, even though it actually belongs to that class.

IV. RESULTS

A. Dataset

Within this paper, we have utilized the RadioML2016.10b dataset [13], a firmly established benchmark dataset that finds wide application in the evaluation of ML algorithms within the domains of signal processing and wireless communications. The creation of the RadioML2016.10b dataset was executed using the GNU Radio framework, encompassing a rich spectrum of 10 modulation types. This assortment includes 8 digital and 2 analog modulation types. Covering SNR levels that span from -20 dB to 18 dB, in increments of 2 dB, this dataset comprehensively encompasses a diverse range of scenarios.

The digital modulation cohort encompasses binary phase shift keying (BPSK), quadrature phase shift keying (QPSK), 8-phase shift keying (8PSK), 16-quadrature amplitude modulation (16QAM), 64-quadrature amplitude modulation (64QAM), Gaussian frequency shift keying (GFSK), continuous phase frequency shift keying (CPFSK), and pulse amplitude modulation with 4 levels (PAM4), while the analog counterparts include wideband frequency modulation (WBFM) and amplitude modulation with double-sideband (AM-DSB). These modulation types find widespread application in the landscape of wireless communication systems [14]. Notably, the dataset encompasses diverse channel environments, encompassing AWGN, multi-path fading, and Rayleigh fading.

Each signal within the dataset is encoded in a 2×128 format, corresponding to the in-phase and quadrature components of the I/Q data. This comprehensive dataset comprises a total of 6,000 signals per modulation type per SNR level.

B. Experimental Setup

In the initial phase, our attention was directed towards five distinct digital modulation types: GFSK, BPSK, QPSK, 64QAM, and PAM4, all of which were examined across a varied SNR spectrum spanning from -10 dB to 10 dB. These modulation types bear noteworthy relevance within the context of IoT devices and communication systems.

Subsequent to this, we engaged in a randomized selection procedure, extracting 4,200 signals for each modulation type at every SNR level to constitute the training dataset, while the residual signals were reserved for the testing dataset. Consequently, the training dataset amassed a collective total of 231,000 signals, serving as the training substrate for our LSTM, GRU, and proposed models. In parallel, the testing dataset comprised 9,000 signals for each SNR level. Following this dataset partition, we executed a data representation transformation, converting the I/Q data into A/P data. To ensure consistent scaling, we applied Min-Max normalization to the A/P data, confining it within the range of -1 to 1. This normalization process was separately carried out for both the amplitude and phase data within each individual signal. Subsequently, extracted features were computed via FOC analysis. The normalized A/P data was then combined with these extracted features, yielding a composite dataset termed APFOC. As a result, the input data shape for each signal materialized as a 3×128 array.

For the LSTM model, we devised a 2-layer architecture, comprising LSTM units called LSTM-LSTM model, followed by a singular fully connected (dense) output layer. To preempt the potential concern of overfitting, a dropout layer was judiciously introduced between the LSTM layers. The architecture of the LSTM model is detailed in Fig. 2.

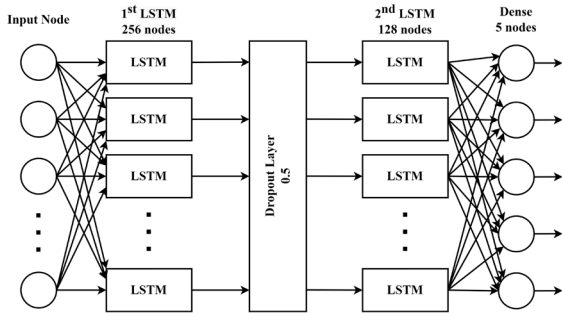


Fig. 2. An LSTM-LSTM model structure

Similar to the LSTM model, the structure of a GRU model encompassed two GRU layers called GRU-GRU model, subsequently succeeded by a singular dense output layer. To mitigate potential overfitting, the inclusion of a dropout layer was deemed essential. A comprehensive depiction of the GRU architecture can be found in Fig. 3.

Our proposed model's architecture is illustrated in Fig. 4. It had a GRU layer following with an LSTM layer with cell sizes of 256 and 128 nodes in the cell, respectively. The last layer of the proposed model served as the output layer, which is a dense layer with five nodes. Before an LSTM layer, we placed a dropout layer.

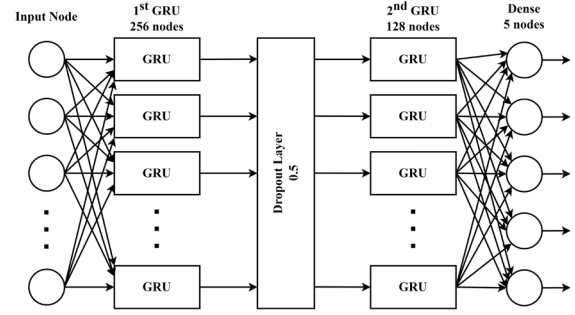


Fig. 3. A GRU-GRU model structure

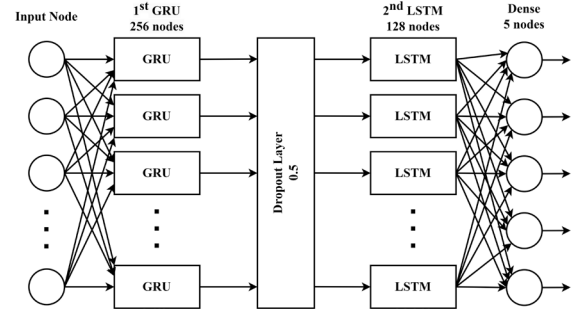


Fig. 4. Proposed model's structure

C. Results & Discussion

Three distinct DL models were employed to undertake the classification of the five modulation types. The outcomes garnered from all three models are visually presented in the form of graphs illustrating the correlation between SNR levels and classification accuracy, as showcased in Fig. 5. In terms of the dataset aspect, it was discerned that the classification accuracy of the normalized APFOC data, as depicted in Fig. 5(b), surpassed the classification accuracy observed with the APFOC data, as depicted in Fig. 5(a). This advancement can be attributed to the utility of Min-Max normalization, which uniformly recalibrates the data, rendering it conducive for DL models.

When assessing the normalized data within the scope of DL models, our proposed model emerges as a contender that approaches the accuracy achieved by LSTM, all while employing a reduced parameter count due to the GRU placed in the first layer instead of LSTM. Furthermore, our proposed model achieved its pinnacle accuracy within the SNR range of -10 dB to -4 dB, surpassing the performance of other models in this realm. Ultimately, the zenith accuracy rate achieved by our proposed model reached 97.66%, with an average accuracy of 75.83%. These figures notably outshine the corresponding rates of both the LSTM-LSTM and GRU-GRU models. This improvement is attributed to the diverse architectures in our proposed model, which balances dependencies between short-term and long-term information, preventing overfitting.

The confusion matrices for our proposed model with the APFOC data are shown in Fig. 6 to Fig. 8, corresponding to SNR levels of -10 dB, 0 dB, and 10 dB, respectively.

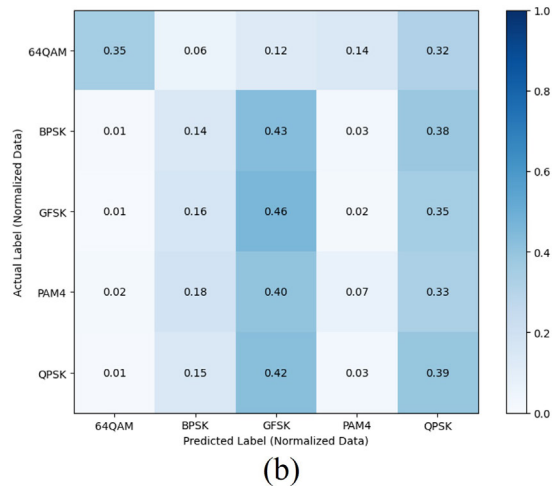
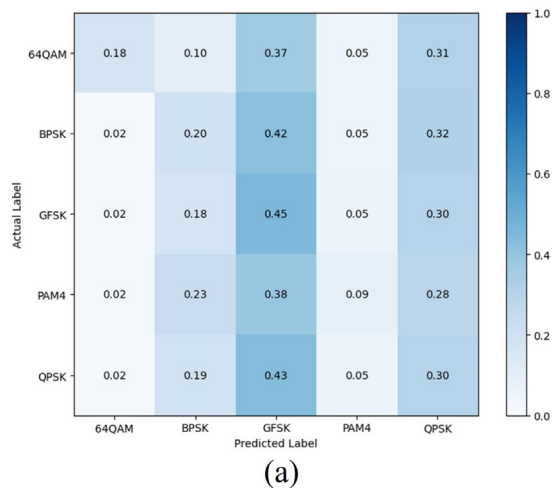
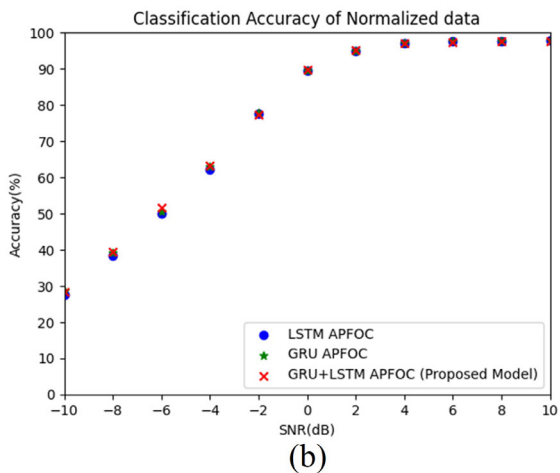
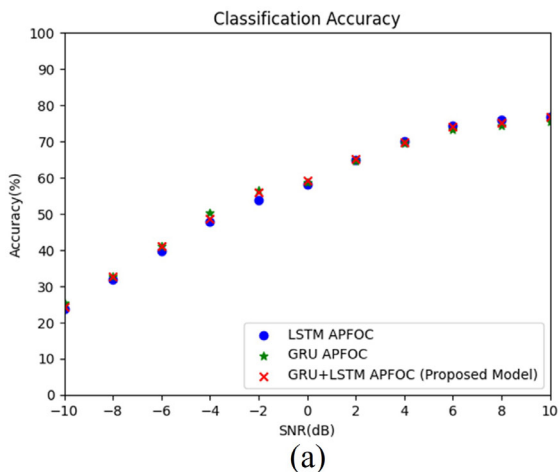


Fig. 5. Graphs between SNR levels in dB unit and accuracy in percentage (%) unit (a) APFOC data (b) Normalized APFOC data

Fig. 6. Confusion matrices of our proposed model at -10 dB (a) APFOC data (b) Normalized APFOC data

These matrices showed that the proposed model can classify the modulation types better when the normalized data was used, as mentioned previously, with Min-Max normalization contributing equally to the data. Particularly, the accuracy improvement from using normalized data reached 30.6% in the case of 0 dB. Furthermore, our proposed model demonstrated exceptional performance, achieving a 99% accuracy in classifying GFSK at 10 dB.

V. CONCLUSION

In conclusion, this study introduces a groundbreaking hybrid model that seamlessly combines long short-term memory (LSTM) and gated recurrent unit (GRU) architectures for the precise task of modulation classification. Complemented by the integration of Min-Max normalization and fourth-order cumulant (FOC) data pre-processing techniques, this approach enhances classification accuracy without compromising the structural integrity of the model. The meticulous process encompasses the transformation of in-phase and quadrature (I/Q) data into amplitude and phase (A/P) data, followed by customized normalization for each signal. Subsequently, the integration of FOC-based feature extraction

yields pertinent information, seamlessly integrated with A/P data to construct the model’s input.

The experimental results are remarkable, with the proposed hybrid model attaining an impressive classification accuracy of 97.66%. Notably, the introduction of Min-Max normalization contributes significantly to classification accuracy enhancement, leading to a noteworthy 30.6% improvement over APFOC data without normalization.

In terms of future work, potential avenues involve the exploration of advanced hybrid architectures, alternative data pre-processing techniques and the integration of transfer learning methods. Pursuing these directions could pave the way for even more robust models with implications extending to the enhancement of wireless communication systems and beyond.

ACKNOWLEDGMENT

This work (Grant No. RGNS 64 - 061) was financially supported by the Office of the Permanent Secretary, Ministry of Higher Education, Science, Research and Innovation. The TA/RA Scholarship from the Graduate School, Chiang Mai University is also acknowledged.

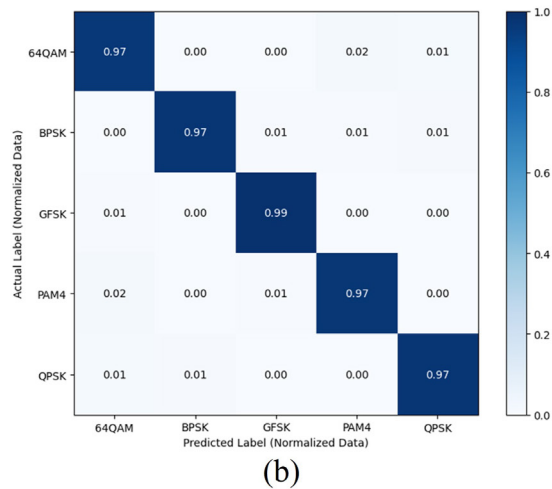
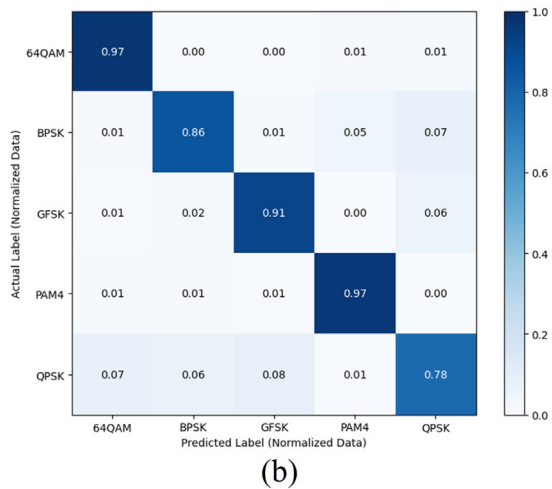
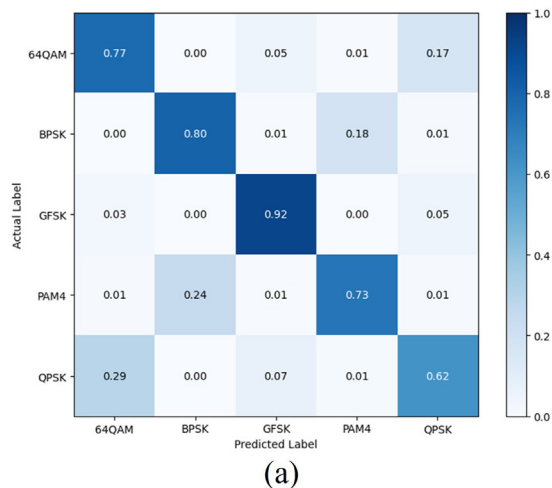
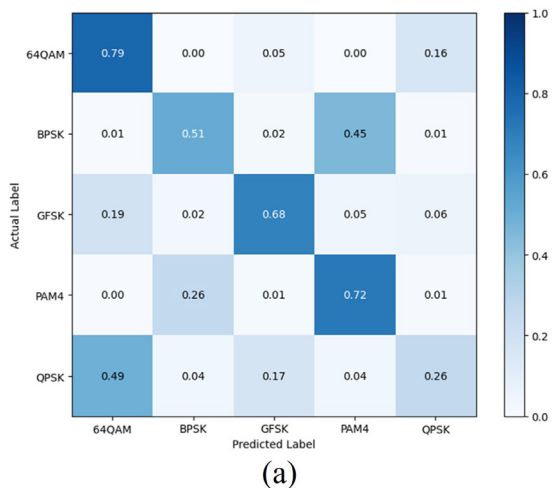


Fig. 7. Confusion matrices of our proposed model at 0 dB (a) APFOC data (b) Normalized APFOC data

Fig. 8. Confusion matrices of our proposed model at 10 dB (a) APFOC data (b) Normalized APFOC data

REFERENCES

[1] N. Promsuk, A. Taparugssanagorn, and J. Vartiainen, "Probability of false alarm based interference suppression methods in internet of things (iot) systems," *Computer Networks*, vol. 144, pp. 201–215, 2018.

[2] H. Kurniansyah, H. Wijanto, and F. Y. Suratman, "Automatic modulation detection using non-linear transformation data extraction and neural network classification," in *2018 International Conference on Control, Electronics, Renewable Energy and Communications (IC-CEREC)*, pp. 213–216, IEEE, 2018.

[3] K. Jiang, X. Qin, J. Zhang, and A. Wang, "Modulation recognition of communication signal based on convolutional neural network," *Symmetry*, vol. 13, no. 12, p. 2302, 2021.

[4] X. Liu, D. Yang, and A. El Gamal, "Deep neural network architectures for modulation classification," in *2017 51st Asilomar Conference on Signals, Systems, and Computers*, pp. 915–919, IEEE, 2017.

[5] S. Rajendran, W. Meert, D. Giustiniano, V. Lenders, and S. Pollin, "Deep learning models for wireless signal classification with distributed low-cost spectrum sensors," *IEEE Transactions on Cognitive Communications and Networking*, vol. 4, no. 3, pp. 433–445, 2018.

[6] M. Zhang, Y. Zeng, Z. Han, and Y. Gong, "Automatic modulation recognition using deep learning architectures," in *2018 IEEE 19th International Workshop on Signal Processing Advances in Wireless Communications (SPAWC)*, pp. 1–5, IEEE, 2018.

[7] A. Emam, M. Shalaby, M. A. Aboelazm, H. E. Abou Bakr, and H. A. Mansour, "A comparative study between cnn, lstm, and cldnn models in the context of radio modulation classification," in *2020*

12th International Conference on Electrical Engineering (ICEENG), pp. 190–195, IEEE, 2020.

[8] K. Pijackova and T. Gotthans, "Radio modulation classification using deep learning architectures," in *2021 31st International Conference Radioelektronika (RADIOELEKTRONIKA)*, pp. 1–5, IEEE, 2021.

[9] T. Li, Y. Li, and O. A. Dobre, "Modulation classification based on fourth-order cumulants of superposed signal in noma systems," *IEEE Transactions on Information Forensics and Security*, vol. 16, pp. 2885–2897, 2021.

[10] L. Wang, Z. Chen, and Y. Zhang, "Wireless signal modulation identification method based on rf i/q data distribution," *Scientific Reports*, vol. 11, no. 1, p. 21383, 2021.

[11] N. Promsuk, A. Taparugssanagorn, et al., "Long short term memory network-based interference recognition for industrial internet of things," *J. Commun.*, vol. 15, no. 12, pp. 876–885, 2020.

[12] F. Liu, Z. Zhang, and R. Zhou, "Automatic modulation recognition based on cnn and gru," *Tsinghua Science and Technology*, vol. 27, no. 2, pp. 422–431, 2021.

[13] T. J. O'shea and N. West, "Radio machine learning dataset generation with gnu radio," in *Proceedings of the GNU Radio Conference*, vol. 1, 2016.

[14] K. Zang and Z. Ma, "Automatic modulation classification based on hierarchical recurrent neural networks with grouped auxiliary memory," *IEEE Access*, vol. 8, pp. 213052–213061, 2020.

On-Device MFCC-CNN Voice Recognition System with ESP-32 and Web-Based Application

Muhammad Ichsan Ramadani P, Iqbal Burhanul H, Hasbi N. P. Wisudawan*, Suatmi Murnani, Hendra Setiawan
Department of Electrical Engineering, Universitas Islam Indonesia, Yogyakarta, Indonesia

* E-mail: hasbi.wisudawan@uii.ac.id

Abstract— The ever-increasing need for intelligence applications capable of assisting human daily life has become a critical topic in current human everyday life. As the primary communication source, deep learning (DL) based speech recognition technique has spread in significant areas in education, transportation, and smart-home system. However, this technique has challenges as it requires numerous datasets and is difficult to implement on a low-cost and low-power system on a chip microcontroller, i.e., ESP-32 or Arduino. With its implementation in controlling the household device, a speech recognition system based on a convolutional neural network (CNN) and MFCC algorithm is proposed in this paper. Firstly, the audio datasets containing specified instructions (in Indonesian) are created, and their features are extracted using MFCC algorithms. Then, the CNN model trains the MFCC vector coefficients and saves them in the Hierarchical Data Format 5 File (h5). This CNN model is stored in the back-end part of the web application and accessed using Flask Python. The audio input (using .wav file format) is sent to the Flask using XMLHttpRequest (XHR) and processed to ESP-32 for controlling the devices. The simulation results, which contain six command words, showed that the selected model achieved 93 % accuracy and 28,39 ms response time.

Keywords—MFCC, CNN, Voice, ESP-32, Web-Based Application

I. INTRODUCTION

The current era witnesses rapid and tremendous growth in technology. Various technological innovations continue to develop to facilitate humans to perform their activities effectively. The development of technology is fundamentally driven by human needs, necessitating that technological innovations be purposeful and aligned with these needs.

Among the technologies undergoing significant development, today is biometric technology. Biometric technology utilizes human body parts—such as fingerprints, facial features, and retinal patterns—as parameters for authentication and individual character analysis in technological design [1]. However, less attention is directed to

the human voice as a biometric technology. Voice signals are audible sound signals that can be measured over time and space [2].

These voice signals can be harnessed through an innovative technology commonly known as voice recognition. Voice recognition is a method utilized to control devices or systems using human speech or sound [3]. This technology is widely employed in automation control systems. In addition to voice recognition, voice signals can be utilized in Automatic Speech Recognition (ASR) systems, which involve developing computer or machine learning techniques to recognize spoken language [4]. ASR technology enables a computer to receive or acknowledge a source of voice or sound by processing spoken sentences into analog voice signals, which can be converted into digital form for pattern matching with pre-stored data on the computer or machine.

Voice recognition technology is a breakthrough innovation that finds widespread applications today. Its popularity stems from its straightforward operation, which significantly assists human activities. One of its applications is in the automation of smart homes. A smart home is an intelligent housing innovation that allows the automatic control of household appliances using voice recognition. Voice recognition in smart homes may provide features such as automated lighting control and automatic door opening and closing.

To make voice recognition technology in smart homes work, a device such as a microcontroller is required to control electronic household appliances. Common examples of such microcontrollers are NodeMCU, Arduino, and Wemos. The microcontroller receives user commands and converts them into voice signals. The voice signals are subsequently transmitted to the modules controlling the electronic household appliances installed in the smart home. Consequently, microcontroller-based voice recognition allows real-time control of electronic household appliances over the Internet.

The advantages of voice recognition in smart homes include enabling users to control devices without strenuous physical

activity, as voice instructions can execute commands. This feature is especially beneficial for individuals who suffer from disabilities or have multiple tasks simultaneously. Therefore, we propose a voice recognition-based home appliance project. We designed a system that aims to control the on-off function of lamps in specific locations and manages the opening and closing of a door, as these are widespread tasks performed by household residents. With the proposed system, those tasks are estimated to become more accessible and flexible. The system is required to recognize the corresponding voice command to perform a task (e.g., opening a door).

The study utilized machine learning methods for feature extraction and classification of voice signals. Feature extraction involves transforming digitalized sound vectors into characteristic feature vectors without losing the unique attributes of each sound. At the same time, classification methods in voice recognition technology aim to classify audio data based on training and testing results.

In terms of feature extraction, one effective method for sound signal feature extraction is the Mel-Frequency Cepstrum Coefficient (MFCC) method. MFCC calculates cepstral coefficients of audio signals, drawing inspiration from the human auditory system [5]. This method is chosen for this study due to its efficacy in handling diverse sound signal variations while mimicking the human hearing system [6]. Whereas in terms of classification, some commonly used algorithms for sound signal classification include Support Vector Machine (SVM), Hidden Markov Model (HMM), Convolutional Neural Network (CNN), Long Short-Term Memory (LSTM), and other software-based methods. We opted to use a CNN-based classifier in this study.

II. DATASET CONSTRUCTION

A. Voice Command and Dataset

The experiment uses voice commands in Indonesian recorded by fifteen people using a noise-cancellation microphone. These commands are consisted of two words and recorded based on a sampling rate of 48 kHz. The noise ratio is below 20 dB, and the audio file format is saved in waveform (wav) format. Each command is recorded ten times with a duration maximum of one second. The commands are spoken in Indonesian, with their purpose shown in Table 1.

Each command is grouped in the same folder based on its name. The number of audio files saved in each folder is only 460. Hence, the total files are 2760 used as input in Mel-Frequency Cepstral Coefficients (MFCC) feature extraction. The training, test, and validation data percentages used in this

experiment are 80%, 10%, and 10% of the total files, i.e., respectively.

TABLE I. VOICE COMMAND FOR DATASET CONSTRUCTION

| Command (in Indonesian) | Purpose |
|----------------------------|--|
| <i>Atas Nyala</i> | Turn on the lamp on the second floor. |
| <i>Atas Mati</i> | Turn off the lamp on the second floor. |
| <i>Bawah Nyala</i> | Turn on the lamp on the first floor. |
| <i>Bawah Mati</i> | Turn off the lamp on the second floor. |
| <i>Buka Pintu</i> | Open the door. |
| <i>Tutup Pintu</i> | Close the door. |

B. MFCC Feature Extraction

The MFCC is adopted to extract spectral features based on human perception. For datasets, thirteen vector coefficients are generated for each command. In particular, the vector value [-606.24146 104.383514 0.8850631 -3.7908576 1.2864062 -14.573763 13.570291 -1.4182719 -7.4151416 17.062883 4.931387 2.4222155 -12.446351] are extracted from the command *atas nyala*. The vector from all orders can be collected and saved with the same method in the JavaScript object notation (JSON) format. Technically, the extraction process is implemented using *the Librosa library* in Python. After gaining the features, the deep learning (DL) model construction using Convolution Neural Network (CNN) is applied in the following step.

III. METHODS

A. Model Building with Convolutional Neural Network

In this part, the deep learning model based on CNN can be implemented using four steps, i.e., data pre-processing, model training, testing, extraction, and implementation. In step one, the datasets are split into three parts, i.e., 80 % for data training, 10 % for each data validation, and testing. We can vary the data composition to achieve better accuracy. Second, the data is convolved in the model training with 64 filters of size 3x3 in the first layer. Next, the 32 filters of size 2x2 with the Relu activation function are applied in the second layer. Finally, the output class of each sound is determined from the output of a fully connected layer with the Softmax activation function. By adjusting the hyperparameter, the model training required an average of 40 epochs to maximize the model accuracy. Then,

accuracy, precision, and recall are set for evaluating model-based-on the confusion matrix shown in Table II.

TABLE II. CONFUSION MATRIX

| Confusion Matrix | | Predicted Class | |
|------------------|----------|-----------------|----------|
| | | Positive | Negative |
| True Class | Positive | TP | FP |
| | Negative | FN | TN |

Mathematically, those parameters are measured based on the computed true positive (TP), true negative (TN), false positive (FP), and false negative (FN) values using

$$\text{Accuracy} = \frac{TP+TN}{TP+FN+FP+TN} \times 100\% \quad (1)$$

$$\text{Precision} = \frac{TP}{FP+TP} \times 100\% \quad (2)$$

$$\text{Recall} = \frac{TP}{FN+TP} \times 100\% \quad (3)$$

Besides (1), (2), and (3), the response time is also used as a performance parameter of the model with the given real-time test data. Next, the model is saved in the h5 format to be easily further processed with different applications, e.g., web applications.

B. Web-Based Application

After training and evaluating the model, the web application is configured to receive the voice command from the user. The system configuration is depicted in Fig. 1. The development of web applications is composed of two main sub-systems, i.e., front-end and back-end. These two sub-systems are connected by the XMLHttpRequest (XHR) communication protocol. This

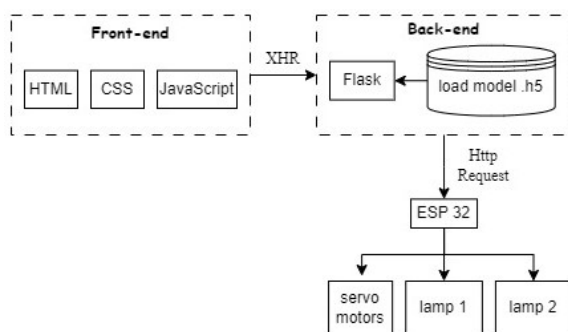


Fig. 1 Front-end and back-end component for web development and its ESP-32 connection

protocol grants communication between the client and server is done asynchronously. The front-end system handles the user interface receiving the voice command. The back-end system dealt with the prediction function based on the audio input from the front-end system. Next, the audio input is processed in the Flask based on the DL model saved in the back-end, and the output signal is sent to the microcontroller (ESP-32) via an end-point HTTP request to control the electronic devices. In this case, the controlled devices are the lamp and servo motor. The servo motor can substitute the door lock actuator motor in the actual application.

C. Hardware Planning

The hardware consists of a microphone, ESP-32 microcontroller, relay two channels, capacitor, and buzzer alarm. This circuit, shown in Fig. 2, controls two lamps and servo motors based on the HTTP request signal generated from the Flask to the ESP-32 microcontroller. The detailed pin connection between the component and ESP-32 is shown in Table III.

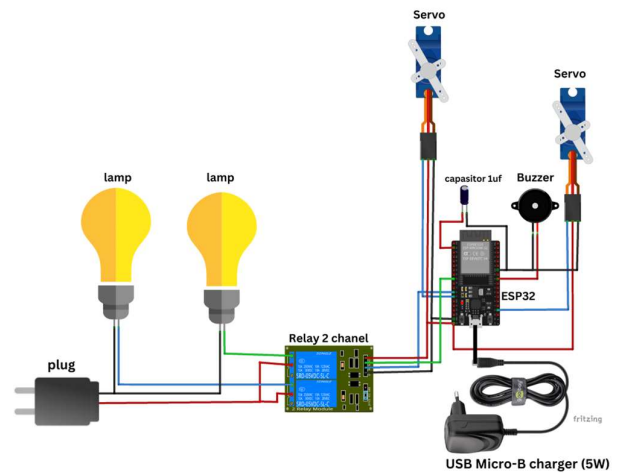


Fig. 2 Electric circuit installation

TABLE III. PIN OF COMPONENTS AND ESP-32 CONNECTION

| Component | Pin |
|---------------------|--------|
| Servo Motor 1 | 12 |
| Servo Motor 2 | 15 |
| Relay 2 channel | 14, 25 |
| Buzzer | 18 |
| Elco Capacitor 1 uF | EN |

The experiment deployed a house miniature to place the electronic devices in the proper place, validated by authentic voice commands to mimic as closely as the actual scenario. In more detail, the voice commands "atas nyala" and "atas mati" will turn on and -off the lamp on the second floor of the miniature, respectively. Meanwhile, the commands "bawah nyala" and "bawah mati" will turn on and -off the lamp on the first floor, respectively. While the commands "buka pintu" and "tutup pintu" are responsible for opening and closing the door installed on the first floor, respectively.

IV. EXPERIMENT AND RESULTS

A. Hardware Implementation

The hardware installation is depicted in Fig. 3. Fig. 3a is the wiring implementation of Fig. 2. It consists of 1) loads (two lamps and motors), 2) a processing system, and 3) a power source. As shown in Fig. 3b, the processing system module is comprised of 1) ESP-32 microcontroller, 2) Pin header, 3) Two channel relay, 4) electronic capacitor $1 \mu\text{F}$, and 5) Buzzer Alarm. Fig 3c is the miniature two-story house where the module and the loads are located. The detailed installation is available in Fig. 3d.

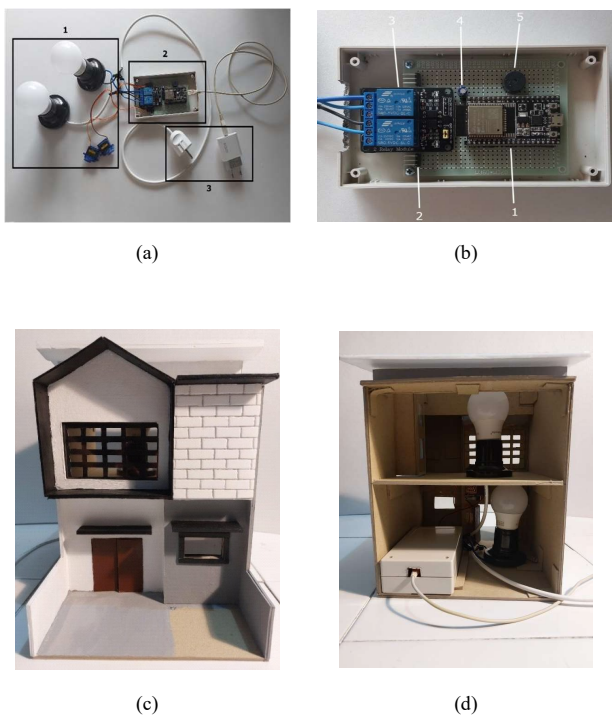


Fig. 3 Hardware installation: a) Wiring implementation, b) Processing system module, c) Two-storey miniature house from front view, d) Electronic module and loads installation from behind view

B. Web-Based Application Interface

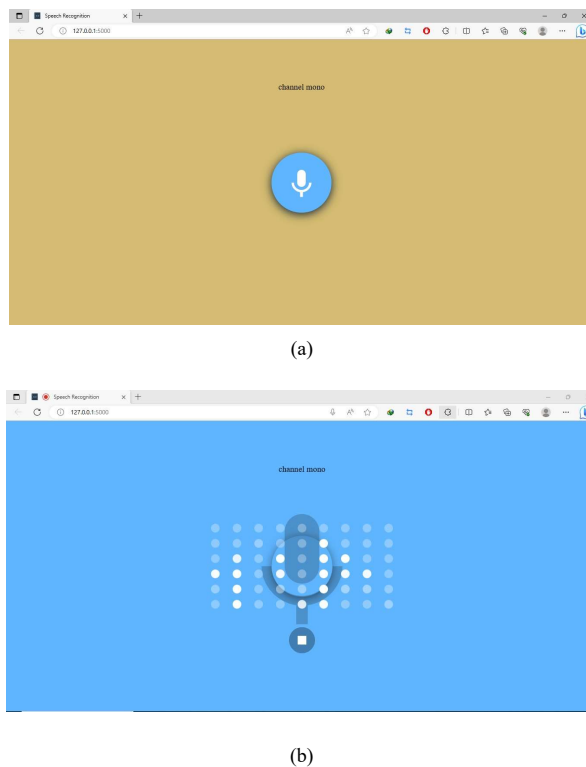


Fig. 4 Voice command user interface

The user can control the loads in Fig. 3d using the interface built based on the system in Fig. 1. The voice command user interface and its recording process are shown in Fig. 4a and 4b, respectively. From all the voice commands shown in Table I, the authors evaluated using this interface from the fifteen people for each class. Hence, there are 600 experiments in total. By computing the time response in each class, the system gives the average 28,39 ms time response.

C. Model Architecture and Performance Evaluation

The CNN sequential model architecture and its performance measurement are evaluated in this part. The main layer used in this architecture consists of the convolution layer (conv2d), max pooling layer (max_pooling2d_2), and flatten layer. Note that, the total number of parameters for the model training is 46.726. It consists of 46.470 trainable and 256 non-trainable parameters. The 2760 datasets are split into the training, validation, and testing data. This composition is shown in Table IV.

TABLE IV. THE NUMBER OF DATA SPLITTING: TRAINING, VALIDATION, AND TESTING

| Voice command (see Table I) | Datasets | | | |
|--------------------------------|----------|---------------|-----------------|--------------|
| | Label | Training Data | Validation Data | Testing Data |
| <i>Atas Nyala</i> | 0 | 373 | 42 | 46 |
| <i>Atas Mati</i> | 1 | 372 | 41 | 46 |
| <i>Bawah Nyala</i> | 2 | 372 | 42 | 46 |
| <i>Bawah Mati</i> | 3 | 372 | 42 | 46 |
| <i>Buka Pintu</i> | 4 | 373 | 41 | 46 |
| <i>Tutup Pintu</i> | 5 | 373 | 41 | 46 |
| Total | 6 | 2235 | 249 | 276 |

During training, two critical parameters, epoch, and batch size, are required to maintain better accuracy. Table V shows how the different batch size affects the accuracy performance using 40 epochs.

TABLE V. THE BATCH SIZE AND ACCURACY

| Batch Size | Accuracy (%) |
|------------|--------------|
| 10 | 92,11 |
| 20 | 93,11 |
| 30 | 92,84 |
| 40 | 92,11 |

TABLE VI. ACCURACY AND LOSS FOR TRAINING AND TESTING DATA

| Epoch | Training Data | | Testing Data | |
|-------|---------------|--------|---------------------|-----------------|
| | Accuracy | Loss | Validation Accuracy | Validation loss |
| 1 | 0,3839 | 1,6968 | 0,4016 | 1,5182 |
| 2 | 0,6600 | 1,0532 | 0,6426 | 1,0457 |
| ... | ... | ... | ... | ... |
| ... | ... | ... | ... | ... |
| 36 | 0,9964 | 0,0970 | 0,9318 | 0,2431 |
| 37 | 0,9955 | 0,0994 | 0,9311 | 0,2435 |

It can be concluded from Table V that the number of batch size 20 gives better accuracy, i.e., 93,11 %. The accuracy and loss based on training and test data are depicted in Table VI. The precision for the two split data reached the maximum number at 37 epochs out of 40, i.e., 99.55 % accuracy for training data and 93.11 % for testing data. The training process is automatically stopped earlier than the given number of epochs. In other words, an early stopping procedure is adopted in this training process. This process can effectively reduce overfitting during the training of the neural network model.

Next, the confusion matrix is evaluated to show the predicted label compared with the true label. Different measures such as precision, accuracy, recall, and F1-score were computed to quantify the quality of the model.

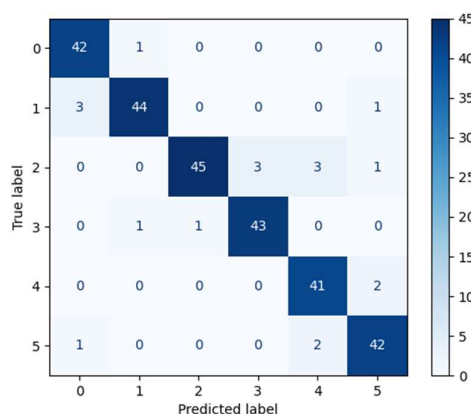


Fig. 5 The confusion matrix from the data testing in Table IV

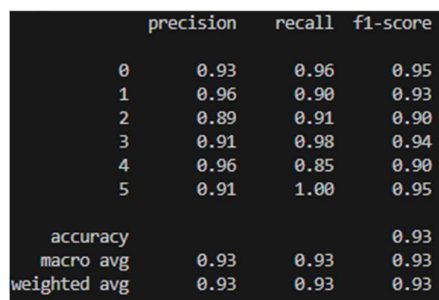


Fig. 6 General report of precision, recall, F1-score and accuracy

Fig. 5 illustrates the confusion matrix of the six classes (from class labelled 0 to 5). It has been established from the figure

that the predicted value is more than 41 of 46 training data in Table IV. This result indicates the better accuracy of the CNN model. In particular, the general report is shown in Fig. 6.

D. Hardware Testing

After evaluating the model, the hardware testing is implemented using the workflow shown in Fig. 7. The voice command used in this case is "atas nyala". Fig. 8 shows the web application's prediction results and output, i.e., lamp 2 turning on. Note

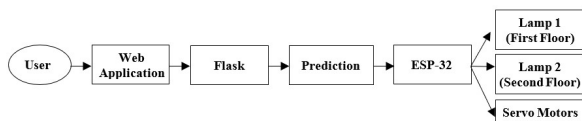
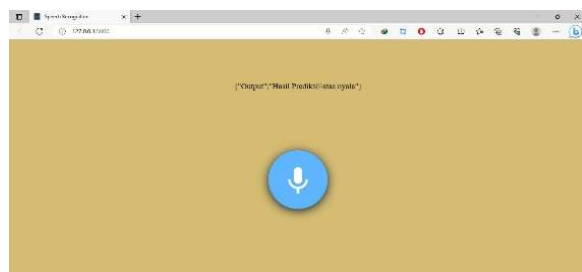


Fig. 7 The work flow diagram for evaluating the hardware system



(a)



(b)

Fig. 8 a) The prediction result of "atas nyala", b) Lamp 2 turning-on

V. CONCLUSIONS

This paper implements and evaluates the MFCC and CNN algorithm based on voice commands from the web application interface. The 2760 datasets using Indonesian words are split

into training, validation, and testing. The low-cost and low-power ESP-32 microcontroller is implemented to control the electronic devices based on the CNN model implemented in the back-end part of the web. As a result, the model achieves 93 % accuracy and 28,39 ms response time using the six command words. Each has a one-second duration and it is recorded in a very low-noise environment such in the house environment.

REFERENCES

- [1] M. Hernandez-de Menendez, R. Morales-Menendez, C. A. Escobar, and J. Arinez, "Biometric applications in education," *International Journal on Interactive Design and Manufacturing (IJIDeM)*, vol. 15, pp. 365–380, 2021.
- [2] H. Purwins, B. Li, T. Virtanen, J. Schluter, S.-Y. Chang, and T. Sainath, "Deep learning for audio signal processing," *IEEE Journal of Selected Topics in Signal Processing*, vol. 13, no. 2, pp. 206–219, 2019.
- [3] F. Gozali, R. S. Suharto *et al.*, "Pemanfaatan fitur google voice recognition pada smartphone untuk pengendalian peralatan rumah tangga," *Jetri: Jurnal Ilmiah Teknik Elektro*, vol. 16, no. 2, pp. 165–178, 2019.
- [4] A. Z. Ridho, "Penerapan metode mel frequency cepstrum coefficient dan dynamic time warping k-nearest neighbour dalam rekognisi aksen suku di Indonesia," Bachelor's Thesis, Universitas Islam Negeri Maulana Malik Ibrahim, 2019.
- [5] D. S. Mistry and A. Kulkarni, "Overview: Speech recognition technology, mel-frequency cepstral coefficients (mfcc), artificial neural network (ann)," *International journal of engineering research and technology*, vol. 2, no. 10, 2013.
- [6] R. F. Rahmat, T. Ramadhani, D. Gunawan, S. Faza, and R. Budiarto, "Mel-frequency cepstral coefficient-vector quantization implementation for voice detection of rice-eating birds in the rice fields," in *2018 Third International Conference on Informatics and Computing (ICIC)*. IEEE, 2018, pp. 1–6

Unmanned Aerial Vehicle (UAV) Data-Driven Modeling Software with Integrated 9-Axis IMU-GPS Sensor Fusion and Data Filtering Algorithm

Azfar Azdi Arfakhsyad
*Department of Electrical Engineering
 and Information Technology
 Universitas Gadjah Mada*
 Yogyakarta, Indonesia
 azfar.azdi.arfakhsyad@mail.ugm.ac.id

Aufa Nasywa Rahman
*Department of Electrical Engineering
 and Information Technology
 Universitas Gadjah Mada*
 Yogyakarta, Indonesia
 aufa.nas2003@mail.ugm.ac.id

Larasati Kinanti
*Department of Mechanical and
 Industrial Engineering
 Universitas Gadjah Mada*
 Yogyakarta, Indonesia
 larasati.kinanti@mail.ugm.ac.id

Ahmad Ataka Awwalur Rizqi
*Department of Electrical Engineering
 and Information Technology
 Universitas Gadjah Mada*
 Yogyakarta, Indonesia
 ahmad.ataka.ar@ugm.ac.id

Hannan Nur Muhammad
*Department of Electrical Engineering
 and Information Technology
 Universitas Gadjah Mada*
 Yogyakarta, Indonesia
 hannan.nur.muhammad@mail.ugm.ac.id

Abstract—Unmanned Aerial Vehicles (UAV) have emerged as versatile platforms, driving the demand for accurate modeling to support developmental testing. This paper proposes data-driven modeling software for UAV. Emphasizes the utilization of cost-effective sensors to obtain orientation and location data subsequently processed through the application of data filtering algorithms and sensor fusion techniques to improve the data quality to make a precise model visualization on the software. UAV's orientation is obtained using processed Inertial Measurement Unit (IMU) data and represented using Quaternion Representation to avoid the gimbal lock problem. The UAV's location is determined by combining data from the Global Positioning System (GPS), which provides stable geographic coordinates but slower data update frequency, and the accelerometer, which has higher data update frequency but integrating it to get position data is unstable due to its accumulative error. By combining data from these two sensors, the software is able to calculate and continuously update the UAV's real-time position during its flight operations. The result shows that the software effectively renders UAV orientation and position with high degree of accuracy and fluidity.

Keywords—Data-Driven Modeling, Data Filtering Algorithm, Sensor Fusion.

I. INTRODUCTION

Unmanned Aerial Vehicles (UAV) have rapidly evolved as a versatile platform for various applications [1]. The increasing demand for UAV development to solve complex environments necessitates raising the need to develop accurate and reliable simulation models that faithfully represent the dynamic behavior of the UAV. An accurate simulation model of UAV that has been tested allows developers to perform cost-effective analysis and evaluation while also validating the performance of UAV under real-world scenarios. Analyzing UAV behavior under various real-world scenarios is expensive, time-consuming, and requires extensive planning. Moreover, it is very risky

because there is a chance that UAV fails due to plenty of reasons with no data collected.

Traditional analysis often requires human intervention and many simplifications that do not fully capture the complexity of real-world scenarios. Traditional modeling, such as using a camera to capture UAV orientation, only gave us visual representation. As the result, we cannot simulate what is happening on the UAV using numerical data. On the other hand, simulation-based analysis gave us visual representation and numerical data that can be used to calculate and analyze further.

Accurate modeling of UAV's dynamics is challenging due to their complexity and sensitivity to external factors such as noise. In this paper, Sensor fusion techniques are used to overcome those issues. Sensor fusion integrates data from multiple sensors, providing more comprehensive understanding of the UAV orientation and position. The most used sensor fusion algorithm is complementary filter [2]-[4] and Kalman filter [5]-[7]. Complementary filter acts as a sensor fusion technique implemented in this paper since it does not use as many resources as Kalman filter [8], and it could perform very well if the parameters are well configured [9]. The UAV model can be more reliable and accurate by fusing Inertial Measurement Unit (IMU) data and position information from sensors such as the Global Positioning System (GPS). Quaternion representation is used to represent the UAV orientation. One of the key benefits of using quaternion is their ability to avoid the gimbal lock problem found in Euler angles representation [10]. Gimbal lock describes a condition in which one of the rotation axes becomes aligned with another, leading to a loss of a degree of freedom in the representation [11]. On the other hand, position data is obtained by combining accelerometer and GPS data. The accelerometer data, which captures the acceleration of the UAV, is processed through a series of steps to extract position-related information.

Double integration is employed to derive velocity and subsequently integrate it again to obtain position estimates. Filtering techniques are applied to reduce error accumulation and improve the accuracy of the integration process. It will be covered later how these filters work. These filters aim to remove noise from the accelerometer data.

This proposed model has the ability to simulate UAV orientation and location from a three-dimensional point of view, having high accuracy and lightweight software. Three-dimensional points of view play a crucial role in simulating UAV behavior, allowing users to monitor UAV orientation based on different points of view. High accuracy is also important since it is achieved using simple and inexpensive sensors. Lastly, the proposed software is lightweight, improving UAV modeling performance.

This paper is organized into six different sections. The first section, "Introduction," highlights the significance of data-driven modeling in the context of UAV. It also provides an overview of the approach employed to develop the data-driven simulation. The second section, "System Overview," comprehensively examines the system's construction. The third section, "Concepts and Algorithm," explains all the concepts and algorithms used in this paper, including the sensor fusion and data filtering algorithms. Moving on to the fourth section, "Modeling," the paper explains how the UAV model is visualized. Furthermore, this section also explains all the features available on the software. The fifth section, "Result," presents the outcomes and findings. Finally, the paper concludes with the sixth section, "Conclusion." The key takeaways are summarized.

II. SYSTEM OVERVIEW

A. Overall System

The overall system consists of several key components, including the GY-87 module, three microcontrollers ATmega328, u-blox M8N GPS module, and three nRF24L01 modules. The GY-87 module and u-blox M8N GPS module are crucial parts of the system since it is used to capture all the data. The GY-87 module includes the MPU6050 and HMC5883L. The MPU6050 sensor acts as an accelerometer and gyroscope. The HMC5883L sensor allows the system to detect and measure the magnetic field. Two ATmega328 are responsible for processing data from those sensors and transmitting those data through wireless communication. Data transmitted from those two ATmega328 already undergoes data filtering algorithm apart from complementary filter. All algorithms will be explained in the next section.

Two ATmega328 are directly connected to two different sensors, one from the GY-87 module and the other one from u-blox M8N GPS module. The last ATmega328 acts as a receiver. Those three ATmega328 are connected to nRF24L01. Two nRF24L01 acts as transmitters from two different sensors, and one nRF24L01 acts as a receiver from both sensors. The overall system, as described in the paragraph earlier, is visualized in Fig. 1. This figure represents the components and their connections.

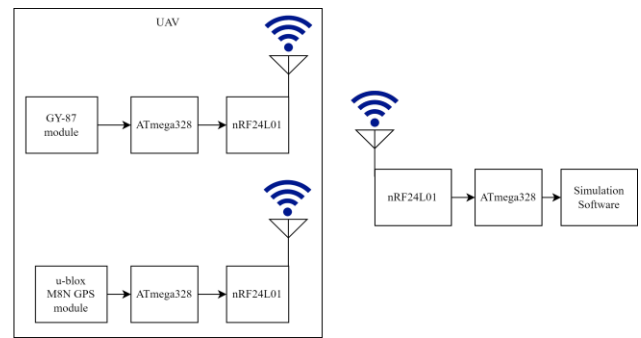


Fig. 1. All components constructing the system.

B. Orientation Data Processing

Orientation data are acquired from processing accelerometer and gyroscope data from the GY-87 module. Data processing involves several distinct steps. Accelerometer data is processed using Low Pass Filter to reduce noise from high-frequency data since an accelerometer captures slow changes in motion and orientation. Meanwhile, gyroscope data is processed using High Pass Filter. This approach was chosen because gyroscopes are sensitive to low-frequency noise that can cause inaccurate estimation. After both accelerometer and gyroscope data are pre-processed using concepts above, those two different data are combined using complementary filter, resulting in Roll, Pitch, and Yaw representation in Euler Angle. Yaw representation is combined with compass data obtained from the HMC5883L sensor to maximize accuracy. After combining data using the abovementioned concept, Roll, Pitch, and Yaw data are represented in quaternion representation to avoid the gimbal lock problem. The visualization of the concept mentioned above is available in Fig. 2

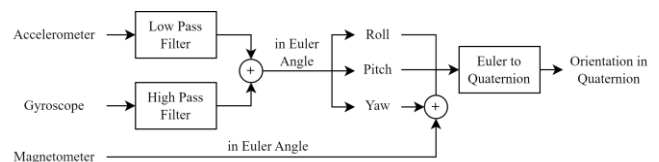


Fig. 2. Steps involved to process orientation data.

C. Position Data Processing

The processing of position data involves several steps. The accelerometer data, obtained from the MPU6050 sensor, is processed using Butterworth filter. After processing the data, it undergoes double integration. The first integration results in velocity, and the second integration results in displacement. This process essentially integrates the accelerometer data twice to obtain the position data. However, since double integration can accumulate errors over time, combining this information with other data sources is essential for improving accuracy. The processed accelerometer data is combined with GPS data using complementary filter. GPS data provides latitude and longitude measurements. Resulting in improved position estimation. The diagram for gathering and processing position data is visualized in Fig. 3.

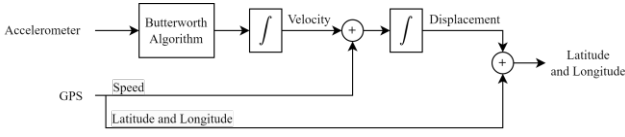


Fig. 3. Steps involved to process position data.

Additional calculations are needed to convert accelerometer data to process with other data sources, in this case, GPS data. The calculations are written as follows

$$V_x = \alpha \int a_x dt + (1 - \alpha) \cdot speed_{gps} \cdot \sin(\theta_d) \quad (1)$$

$$V_y = \alpha \int a_y dt + (1 - \alpha) \cdot speed_{gps} \cdot \cos(\theta_d) \quad (2)$$

$$\theta_d = \tan^{-1} \left(\frac{\Delta \ell_y}{\Delta \ell_x} \right) \quad (3)$$

$$\Delta \ell_y = \sin(\Delta \theta_{long}) \cos(\Delta \theta'_{lat}) \quad (4)$$

$$\Delta \ell_x = \cos(\theta_{lat}) \sin(\theta'_{lat}) - \sin(\theta_{lat}) \cos(\theta'_{lat}) \cos(\Delta \theta_{long}) \quad (5)$$

$$\Delta \theta_{long} = \theta'_{long} - \theta_{long} \quad (6)$$

$$S_{lat} = \frac{\beta \int V_x dt \cdot 180}{\pi \cdot r_e} + (1 - \beta) \cdot \theta_{latgps} \quad (7)$$

$$S_{long} = \frac{\beta \int V_y dt \cdot 180}{\pi \cdot r_e} + (1 - \beta) \cdot \theta_{longgps} \quad (8)$$

where some of the terms used above are

α = velocity weight factor

β = displacement weight factor

θ_d = angle from north to the displacement

$\theta'_{lat}, \theta'_{long}$ = next latitude, next longitude

S_{lat}, S_{long} = displacement in latitude after complementary, displacement in longitude after complementary,

r_e = radius of the earth

III. CONCEPTS AND ALGORITHMS

A. Quaternion Representation

Quaternion representation is an effective notation used to represent orientation and rotation since it does not suffer from the gimbal lock that occurs in Euler angle representation [10] [12]. The matrix representation in quaternion for angle Roll-Pitch-Yaw (ψ, θ, ϕ) can be derived from several steps. Thus, the rotation quaternion can be written as

$$S \frac{A}{B} = \cos \frac{b}{2} + \sin \frac{b}{2} \quad (9)$$

$$v = v_x + v_y + v_z \quad (10)$$

$$S \frac{A}{B} = \cos \frac{b}{2} - v_x \sin \frac{b}{2} v_y \sin \frac{b}{2} - v_z \sin \frac{b}{2} \quad (11)$$

$$S \frac{A}{B} = S_1 S_2 S_3 S_4 \quad (12)$$

When rotating a vector V_p within frame A by an angle α around vector v , the resulting vector S in frame B can be expressed as follows:

$$V_s = S \frac{A}{B} * V_p * S \frac{\bar{A}}{B} \quad (13)$$

The Hamilton product '*' is used for combining two quaternions, P_1 and P_2 . When applying the Hamilton product to these quaternions, it can be written as follows:

$$P_1 * P_2 = \begin{bmatrix} a_1 a_2 - b_1 b_2 - c_1 c_2 - d_1 d_2 \\ a_1 b_2 + b_1 a_2 - c_1 d_2 + d_1 c_2 \\ a_1 c_2 - b_1 d_2 + c_1 a_2 + d_1 b_2 \\ a_1 d_2 + b_1 b_2 - c_1 b_2 + d_1 a_2 \end{bmatrix} \quad (14)$$

The following representation of the rotational matrix

$$R \frac{A}{B} \text{ derived from quaternion } S \frac{A}{B} = \begin{bmatrix} -2S_3^2 - 2S_4^2 & 2S_2 S_3 - 2S_4 S_1 & 2S_2 S_4 + 2S_3 S_1 \\ 2S_2 S_3 + 2S_4 S_1 & 1 - 2S_2^2 - 2S_4^2 & 2S_3 S_4 - 2S_2 S_1 \\ 2S_2 S_4 - 2S_3 S_1 & 2S_3 S_4 + 2S_2 S_1 & 1 - 2S_2^2 - 2S_4^2 \end{bmatrix} \quad (15)$$

The angle Roll-Pitch-Yaw (ψ, θ, ϕ) of an UAV can be achieved then,

$$\begin{bmatrix} \psi \\ \theta \\ \phi \end{bmatrix} = \begin{bmatrix} \tan^{-1} 2(S_1 S_2 + S_3 S_4), 1 - 2(S_2^2 + S_4^2) \\ \sin^{-1} (2(S_1 S_2 + S_3 S_4)) \\ \tan^{-1} 2(S_1 S_4 + S_2 S_3), 1 - 2(S_3^2 + S_4^2) \end{bmatrix} \quad (16)$$

B. Complementary Filter

Complementary filter is used three times. It combines data from an accelerometer with gyroscope, yaw with magnetometer data, and data from an accelerometer with GPS. The complementary filter takes advantage of their individual strengths and compensates for their limitations. In the context of combining accelerometer and gyroscope data, the complementary filter combines those data in the form of an Euler angle. Roll, pitch, and yaw can be obtained.

On the other hand, yaw data denotes UAV movement in orientation or rotational movement. Meanwhile, a magnetometer is also excellent at capturing this aspect. Complementing both data can increase accuracy estimates. This complementing behavior reduces the drift generated from yaw data that has been processed through several steps, allowing noise to accumulate. The concept above is proven, as can be seen in Fig. 7.

In contrast, accelerometer is used to capture short-term and high-frequency motion data, making them suitable for tracking rapid movements and changes in direction. On the other hand, GPS provides global positioning information. GPS provides accurate long-term position estimates but

struggles with capturing location in uniform time frequency since it depends on signal availability. The complementary filter calculates the position estimates by blending the accelerometer's measurements with the GPS's position estimates. Due to the accelerometer's drift, the estimation becomes increasingly inaccurate over longer periods. This is where GPS data comes to take a significant effect. The complementary filter uses GPS data to correct the accelerometer's position estimates. The GPS provides a reference point to align the accelerometer's estimates with the actual position, minimizing the accumulated errors.

C. Butterworth Filter

Butterworth filter is a type of Infinite-Length Unit Impulse Response (IIR) digital filter. Founded in 1930 by Stephen Butterworth. Butterworth Filter comes close to approximating an ideal filter, as it aims to eliminate unwanted frequencies and maintains uniform sensitivity across the desired passband [13]. Butterworth filter aims to achieve a maximally flat frequency response curve in the passband, resulting in a smooth response [14]. The main purpose of this filter is to minimize any ripples or variations in amplitude across the desired frequency range. This filter cut-off frequency must be configured since it is prone to noise [15]. Mathematically, the general form for the second-order Butterworth Algorithm can be written as [16]

$$B(s) = \frac{\omega_c^2}{(s + \omega_c e^{j(\pi/4)})(s + \omega_c e^{-j(\pi/4)})} \quad (17)$$

$$= \frac{\omega_c^2}{(s^2 + \sqrt{2}\omega_c s + \omega_c^2)} \quad (18)$$

ω_c represents the cut-off frequency. It is the point at which the filter attenuates the input signal and denotes the complex frequency variable. In general, the numerator parts represent the squared cut-off frequency; meanwhile, the denominator represents a quadratic polynomial in complex frequency. This polynomial usually describes how the filter gain changes with different frequency components in the input signal.

IV. MODELING

The orientation is visualized in a three-dimensional model, illustrated in two distinct axes. This illustration can be adjusted based on user needs. This visualization is included in Fig. 4. Conversely, position data visualized on the live map can be accessed in real-time using an internet connection. After the software receives the latitude and longitude data, the software automatically plots the UAV on the exact location.



Fig. 4. UAV orientation visualization.

In this paper, software for visualizing the position and orientation of UAV is developed using Unity. The software interface, as depicted in Fig. 5, aims to tell all the necessary information to the user as simply as possible since its primary objective is to facilitate the efficient simulation of UAV. This software includes some features. The first one is a three-dimensional view of the UAV situated in the top left corner. This visualization enables users to observe the UAV orientation through an intuitive and easily interpretable representation. Below that visualization, there is a horizon view and UAV flight panel. Horizon view enables users to view and evaluate UAV roll and pitch behavior. UAV flight panel enables users to view and evaluate distinct data, such as compass, distance to marked location, altitude, speed, roll, pitch, and yaw. A menu bar on the right side of the interface gives users access to various software settings. These settings provide functions such as locating specific positions on the map, viewing latitude and longitude coordinates of the UAV and marked location, adjusting map styles, establishing serial connections to receivers, importing and exporting UAV recorded flight data, and zooming in or out on the maps. Positioned on the bottom of the interface available controls to record flight data, such as start, stop, save, delete recording, and moving recorded data in a specific time.

There are three modes available in this software. The first one is serial mode. The software enters serial mode when the receiver is connected to the software and maintains serial communication with the software. In this mode, IMU and GPS data are received and not recorded. The second mode is recording mode. Recording mode happens when the record button is clicked. The software maintains a serial connection with the receiver alongside recording those data. Those data can then be saved onto Comma Separated Values (CSV) files that can be remodeled. The last mode is simulation mode. Simulation mode happens when recorded data is played back. Recorded IMU and GPS data are read from a CSV file and then shown on the software. In this simulation mode, linear interpolation for position data is implemented. That scenario differs from serial mode, where linear interpolation is not applied. Besides those two different scenarios in which linear interpolation is implemented or not, all sensor fusion and data filtering algorithm explained earlier was implemented on all modes.

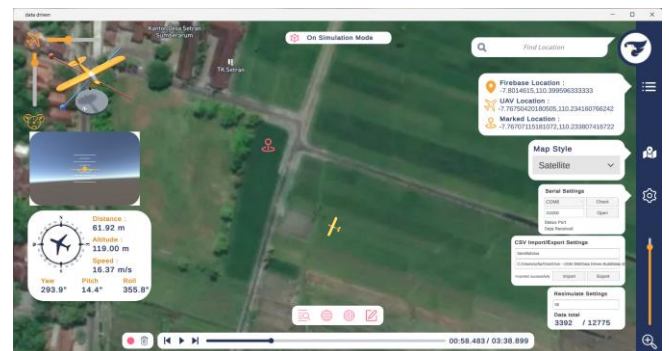


Fig. 5. Software interface.

V. RESULT

This paper captures an experiment for testing the sensor fusion and data filtering algorithm captured from flying an actual UAV. A fixed-wing UAV model was chosen because fixed-wing serves as benchmark for another UAV models. This implies that when this software is planned to be used

using multirotor, tiltrotor, or any other models, it should not pose different challenges. The fixed-wing UAV model can be seen in Fig. 6. The overall system is placed inside the fuselage to ensure that data captured from the sensors represent UAV movement accurately. Data captured from flying an actual UAV for 3 minutes and 38 seconds with 60 FPS is 12774 data from IMU and GPS. All the plots covered later are sampled from the actual flight data.



Fig. 6. Fixed wing UAV model that used to capture data.

A. Orientation

Fig. 7 shows the yaw data comparison. The orange line shows that when integral is performed onto yaw data directly, it will lead to accumulated error. It is shown from the line that slowly moving apart. On the other hand, the green line represents combined data from yaw data and magnetometer data. It can easily be seen that combined data has less accumulated error. That is because combined data is taking magnetometer data into account. The magnetometer acts as a corrector for yaw data that constantly accumulates errors.

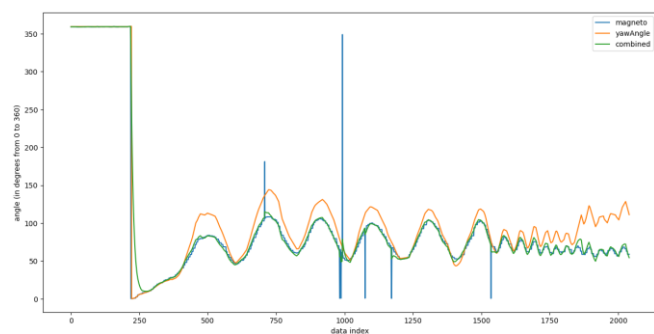


Fig. 7. Yaw data comparison.

Fig. 8 shows the quaternion representation after undergoing different steps to reduce noise that was already explained earlier. There are four different lines in the plot mentioned. There are 'q', 'x', 'y', and 'z' lines. Each of them is represented with a different colored line. The graph might appear unstable and spiky, but it is quite different when it comes to modeling the UAV's orientation with the quaternion data. The graph translates into smooth orientation model due to the nature of quaternion representation.

The 'q' entity represents the quaternion itself and serves as the core of the orientation model. This entity is constructed from a combination of both rotational and

angular properties, presented into a single entity. The 'x', 'y', and 'z' entities, on the other hand, represent the individual components of the quaternion. All these entities represent the UAV's dynamics in three different dimensions. The combination of all these components provides a smooth UAV model.

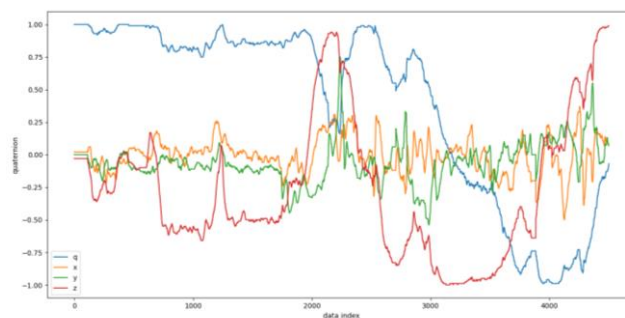


Fig. 8. Quaternion plot

B. Position

Fig. 9 and Fig. 10 show the acceleration data on the x-axis and y-axis accordingly. The plot consists of three different kinds of data. Which are the original data, data after being processed using the Butterworth filter, and data after being processed using Chebyshev filter. As shown in the plot provided, the original data is very noisy. That is the reason a second-order low-pass filter is used to filter the data. Among many second-order low-pass filters, two of the most popular are Chebyshev and Butterworth filter. Chebyshev and Butterworth filter are compared. Chebyshev and Butterworth filter successfully attenuate noise, denoted by minimized high frequency. However, Chebyshev filter is seen to be more oscillated even though both filters use the same cut-off frequency of 10 Hertz and sampling rate of 1000 data. The frequent oscillation that happens on the Chebyshev filter can cause many problems in the next data processing. When processed into position data, oscillated data can cause a buildup round-off error that happened earlier and a larger error accumulated. Chebyshev filter also uses more resources that are identified by longer processing time. Bigger resource use and longer processing time can cause inaccurate UAV orientation and position estimation. Those two limitations provide a strong baseline to use the Butterworth filter over the Chebyshev filter.

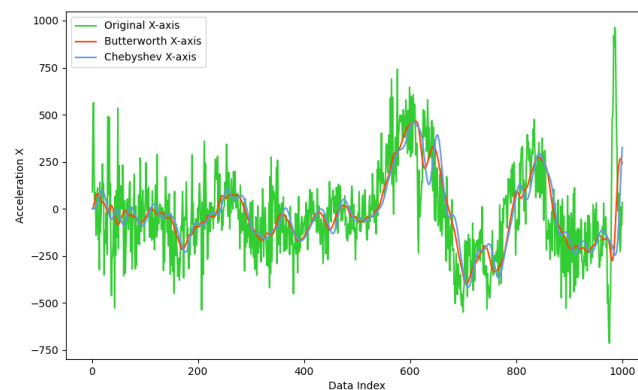


Fig. 9. Acceleration data on x-axis using different filters.

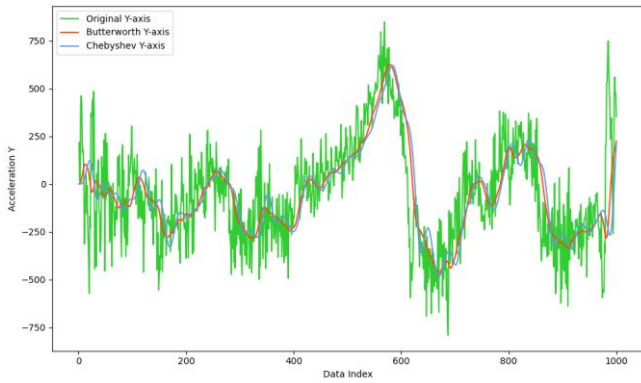


Fig. 10. Acceleration data on y-axis using different filters.

Fig. 11 shows the data captured from GPS where linear interpolation is not applied yet. The blue dot represents location data captured from GPS. As can be seen in the figure mentioned, GPS's ability to capture data is rather abstract. The GPS data is not continuous. It is very dependent on the signal availability. It can cause inconsistency in capturing ability. On the other hand, Fig. 12 is an improvement from the previous figure. The blue line represents the trajectory captured from the UAV location after linear interpolation is implemented. As can be seen in the figure mentioned, UAV movement is continuous and very smooth.



Fig. 11. Location plotted before linear interpolation.



Fig. 12. Location plotted after linear interpolation.

Fig. 13 is a plot of latitude and longitude data captured from GPS. There are three different data represented with three different colored lines. The blue line represents raw latitude and longitude purely from GPS. The non-continuous spikes indicate that there are unfilled gaps between data. The green line represents interpolated latitude

and longitude. This line is much smoother than the raw data because linear interpolation fills the gaps between each data. This interpolated latitude and longitude data is used as the reference of the real-time complemented GPS-accelerometer data denoted by the orange line.

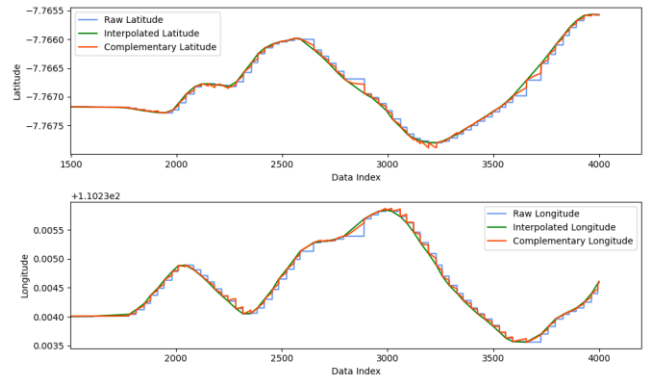


Fig. 13. Latitude and longitude plot.

The complementary filter needs fine-tuning to ensure that the weight from acceleration and GPS data is well complementing each other. After further testing, increasing the weight of α (the weight factor of velocity from acceleration integral) resulted in a spikier graph. On the other hand, increasing the weight of β (the weight factor of velocity integral) resulted in a more delayed graph. Table 1 shows how different α and β impact the latitude and longitude error compared to the interpolated latitude and longitude.

TABLE I. IMPACT OF DIFFERENT ALPHA AND BETA

| α | β | Latitude Error (meter) | Longitude Error (meter) |
|----------|---------|------------------------|-------------------------|
| 0.1 | 0.1 | 2.036 | 2.652 |
| 0.1 | 0.5 | 4.412 | 5.497 |
| 0.1 | 0.9 | 12.866 | 19.465 |
| 0.5 | 0.1 | 3.896 | 4.729 |
| 0.5 | 0.5 | 7.477 | 8.277 |
| 0.5 | 0.9 | 20.816 | 24.115 |
| 0.9 | 0.1 | 6.191 | 7.179 |
| 0.9 | 0.5 | 11.372 | 11.957 |
| 0.9 | 0.9 | 30.411 | 31.506 |

From the data above, it is clear that lower α and β give less errors and thus lead to more precise modeling. Hence, 0.1 is chosen as the value for α and β because it gives lowest error. The graph for complemented latitude and longitude with α and β values of 0.1 is shown in the Fig. 13 presented earlier.

VI. CONCLUSION

The developed data-driven modeling software successfully provides precise and stable orientation and position data processed from the sensor fusion and data filtering algorithms explained in this paper. For the complementary filter used for position processing from GPS and acceleration data, it has been observed that minimizing the value of α and β results in reduced errors. Additionally, the concept of complementing the first integral of acceleration with the processed vector velocity calculated from scalar speed GPS data has been proven to work well. Regarding the orientation, the inclusion of compass data

from the magnetometer has successfully mitigated the error accumulation on the yaw axis. The utilization of quaternion representation has been proven to give a way to model orientation without a gimbal lock problem. Overall, the data shows the software's robust performance, affirming the embedded algorithms' effectiveness.

ACKNOWLEDGMENT

Authors would like to express their sincere gratitude to all Sayakawidya Research and Development Team members—including Fahmi Akmal Zain, Okasah Rofi Izzatik, Kelvin Kurniawan, Adriyan Christhofer Sitanggang, Lauhul Afiat Kahfi, and Leonardo Ginting—who have contributed to the successful completion of this paper. Additionally, authors acknowledged the valuable input received from the reviewers.

REFERENCES

- [1] K. Patel and J. Barve, "Modeling, simulation and control study for the Quad-Copter UAV," 2014 9th International Conference on Industrial and Information Systems (ICIIS), 2014, doi:10.1109/iciinfs.2014.7036590.
- [2] M. Euston, P. Coote, R. Mahony, J. Kim, and T. Hamel, "A Complementary Filter for Attitude Estimation of a Fixed-wing UAV," IEEE/RSJ International Conference on Intelligent Robots and Systems, France, Sept, 22-26, 2008, pp. 340-345, doi: 10.1109/IROS.2008.4650766.
- [3] Y. F. Ren and X. Z. Ke, "Particle Filter Data Fusion Enhancements for MEMS-IMU/GPS," Intelligent Information Management, Feb 2010, pp. 417-421.
- [4] J. F. Vasconcelos, C. Silvestre, P. Oliveira, P. Batista, B. Cardeira, "Discrete Time-Varying Attitude Complementary Filter," 2009 American Control Conference, June 10-12, 2009.
- [5] F. M. Mirzaei and S. I. Roumeliotis, "A Kalman Filter-Based Algorithm for IMU-Camera Calibration: Observability Analysis and Performance Evaluation," IEEE Transaction on Robotics, vol.23, no. 5, October 2008.
- [6] P. Zhang, J. Gu, E. E. Milios and P. Huynh, "Navigation with IMU/GPS/digital compass with unscented Kalman filter," IEEE International Conference Mechatronics and Automation, 2005, Niagara Falls, ON, Canada, 2005, pp. 1497-1502 Vol. 3, doi: 10.1109/ICMA.2005.1626777.
- [7] F. Caron, E. Duflos, D. Pomorski, P. Vanheeghe, "GPS/IMU data fusion using multisensory Kalman filtering: introduction of contextual aspects," INFORMATION FUSION, 7 (2006), pp. 221-230.
- [8] G. P. Paina, D. Gaydou, J. Redolfi, C. Paz, and L. Canali, "Experimental comparison of Kalman and complementary filter for attitude estimation," XII Argentine Symposium on Technology, 2011, pp. 205-215.
- [9] P. Gui, L. Tang, and S. Mukhopadhyay, "MEMS based IMU for Tilting Measurement: Comparison of complementary and Kalman filter based data fusion," 2015 IEEE 10th Conference on Industrial Electronics and Applications (ICIEA), 2015, doi:10.1109/iciea.2015.7334442
- [10] E. M. Jones and P. Fjeld, "Gimbal angles, gimbal lock, and a fourth gimbal for christmas," Apollo Lunar Surface Journal. <https://history.nasa.gov/alsj/gimbals.html> (accessed Aug. 12, 2023).
- [11] J. F. Hughes et al., Computer Graphics: Principles and Practice, 2nd ed. Upper Saddle River, NJ: Addison-Wesley, 1997, pp. 117-147.
- [12] S. Katsuki and N. Sebe, "Rotation matrix optimization with quaternion," 2015 10th Asian Control Conf. (ASCC), Kota Kinabalu, Malaysia, 2015, pp. 1-6, doi: 10.1109/ASCC.2015.7244645.
- [13] X. Zhang and S. Jiang, "Application of fourier transform and butterworth filter in signal denoising," International Conference on Intelligent Computing and Signal Processing, 2021, pp. 1277-1281, doi: 10.1109/ICSP51882.2021.9408933.
- [14] J. Roberts and T. D. Roberts, "Use of the butterworth low-pass filter for oceanographic data," Journal of Geophysical Research, vol. 83 , pp. 1-5.
- [15] P. Podder, Md. M. Hasan, Md. R. Islam and M. Sayeed, "Design and implementation of butterworth, chebyshev-i and elliptic filter for speech signal analysis," International Journal of Computer Applications, July 2014, pp. 12-18, doi: 10.5120/17195-7390.
- [16] A. V. Oppenheim, A. S. Willsky, and S. H. Nawab, Signals & Systems (2nd Ed.). Upper Saddle River, New Jersey: Prentice Hall, 1997

Deep Learning Based Printed Circuit Boards Defect Detection Using Multiple Depth 2D X-Ray Image

⁽¹⁾Chukiat Boonkorkoer, ⁽²⁾Phayung Meesad, and ⁽³⁾Maleerat Maliyaem

Faculty of Information Technology and Digital Innovation

King Monkut's University of Technology North Bangkok

1518 Pracharat 1 Rd., Wongsawang, Bangsue, Bangkok

⁽¹⁾s6407011810027@email.kmutnb.ac.th, ⁽²⁾phayung.m@itd.kmutnb.ac.th, ⁽³⁾maleerat.m@itd.kmutnb.ac.th

Abstract—The miniaturization and increased complexity of components in printed circuit board assemblies present significant challenges in product design and manufacturing. Automated inspection techniques have been developed to enhance efficiency and reduce reliance on skilled labor. However, certain components with hidden solder joints or bubble defects require specialized inspection methods. X-ray imaging has emerged as a valuable tool for detecting defects like bridging, insufficient soldering, and solder voids. Although algorithm parameter fine-tuning in X-ray machines has improved defect detection accuracy, false calls remain problematic, necessitating expert verification. This study proposes a novel approach that combines deep learning and multi-depth X-ray inspection to enhance defect detection accuracy across various defect types. The YOLO object detection model is employed to identify defects in Automatic X-ray Inspection machines. The dataset is prepared using advanced segmentation techniques, with individual solder joints serving as the dataset. Furthermore, image augmentation plays a vital role due to the limited number of examples of defective solder joints. Precise defect detection is achieved through accurate labeling, including optimizing the label box size. This comprehensive approach offers promising potential for automated and reliable defect detection in complex electronic assemblies.

Keywords—Solder joint inspection, YOLO Algorithm for Object Detection, Automated X-ray inspection

I. INTRODUCTION

Certain solder joint defects, such as voids, cannot be effectively detected using optical techniques alone. This necessitates the use of X-ray imaging, which offers a reliable and non-destructive method for detecting and analyzing void defects in solder joints. By utilizing X-ray imaging, researchers can accurately identify and assess the various types of defects, enabling enhanced quality control and optimization of soldering processes [1]. During X-ray inspection, solder joints are exposed to X-ray radiation and captured by a detector. The contrast difference between the solder joints and the component body provides detailed information about the solder joint's shape. Defects, including voids or bridging to neighboring solder joints, can be detected by analyzing the X-ray image [2]. Identifying defective solder joints from known good ones is challenging for this study [3]. One of the crucial steps in achieving this is accurately identifying the Region of Interest (ROI) - the X-ray image of the solder joint [3], [4]. Various image segmentation techniques, including the Threshold Method, K-Means Clustering, and other advanced techniques, have been introduced to accomplish this task. Our study aimed to

prepare the X-ray image dataset using the segmentation to split an individual solder joint out of the X-ray image supplied by the AXI machine and do image augmentation to extend the dataset which will be used to train the YOLO object detective model. And finally, the outcome model will be used to predict the raw X-ray image supplied by the Automatic X-ray Inspection machine (AXI). To accomplish this requirement, it requires several steps to be studied. Based on the aforementioned challenges, the researchers propose the application of artificial intelligence techniques, particularly deep learning, to enhance defect detection accuracy and cover a broader range of defect types. The proposed approach aims to filter and prioritize the most relevant defects with high precision.

The current built-in AXI algorithms are insufficient in accurately filtering out defective solder joints, leading to a high number of false calls [4]. Consequently, there is a requirement to develop a deep learning technique that can automate the inspection process, transfer specialist knowledge, and alleviate the workload of experts.

II. PROBLEM FORMULATION

A. Type of Solder Joint Defects

X-ray imaging typically detects defects in the Printed Circuit Board Assembly (PCBA) process, such as insufficient solder in through-holes, solder bridging on Small Outline Integrated Circuit (SOIC) and Ball Grid Array (BGA) components, and voids in solder balls of BGA [2], [4]–[7]. Extensive research has been dedicated to defect detection in X-ray images, with a specific focus on voiding, insufficient solder, and solder bridging [3], [4]. In a previous investigation [2] the detection and classification of solder defects in Ball Grid Array (BGA) components were thoroughly examined, encompassing normal, short-circuit, bonding defect, and void defect categories. However, the study did not specifically address issues related to missing connections, open connections, excessive solder, and misregistration. To effectively tackle these concerns, cost-efficient inspection methods like Automated Optical Inspection (AOI) can be employed [5].

Various solder joint defects can compromise the reliability and functionality of the final product in the PCBA process [5], [7]. These defects include insufficient solder due to these factors like inadequate solder paste deposition, incorrect reflow soldering temperatures or durations, or poor wetting of the solder to the pad or component lead. Solder bridging may occur due to the factors such as incorrect component alignment, excessive solder paste application, or misalignment or registration during the solder paste printing

process, which hinders proper solder wetting and leads to bridge formation between adjacent pins or pads. The defect, such as solder voids in BGA balls, on the other hand, can be attributed to various factors such as the presence of contaminants, solder voids or bubbles in the solder paste, or improper reflow soldering temperatures or duration. Other factors that can contribute to solder voids in BGA balls include the type of BGA package, solder mask roughness, stencil shape, and the design of the circuit board [1].

B. Techniques Used for Solder Joint Segmentation

After conducting experiments using the Thresholding method alone to find the solder joint contours, we found that it produced good results for the well-formed solder joints but not for some defective solder joints, such as solder bridging, including image dimming or image out-of-focus. To address this issue, we introduced a combination of the Thresholding method and K-Means clustering to solve.

C. X-ray Image Preprocessing for Solder Joint Defects

In the study [2], all images underwent size reduction to reduce memory requirements during the training and testing phases. No augmentation processes were applied to increase the dataset size. Some of the AXI machine's computed ROI (Region of Interest) for solder joint inspection does not accurately enclose the entire solder joint, a new ROI can be computed based on the approximated center of the original ROI. This approach improves the accuracy of solder joint segmentation, enabling more precise analysis and detection of defects in automated inspection systems [3]. The number of slices required for solder joint inspection varies based on the type of defect, with some defects requiring deep imaging and others needing a combination of deep and shallow imaging depths. Delighted by the diverse challenges presented, the study [4] ingeniously uses the Channel-wise preprocessing method to address these variations. This method involves concatenating all the slices in the channelwise direction before feeding them into the model.

D. The X-ray Slice Image Combination

It has been mentioned that the number of slices required for X-ray inspection can vary based on the type and scale of the printed circuit board (PCB)[3]. However, both the manufacturing instructions of certain AXI machines and the study [4] emphasize that different components necessitate varying depths of X-ray imaging to achieve accurate defect detection. As a result, the number of X-ray imaging slices can vary depending on the specific component being inspected. For instance, detecting voids in BGA balls may require at least 3 slices, while solder bridging detection may only necessitate 1 slice. Some researchers have proposed a technique where a group of two slices (concatenation of 2 slices from each solder joint sample) is fed as a single input instead of processing each slice individually [3]. However, this approach has limitations as it cannot accurately determine defects that require inference, such as solder volume estimation for insufficient solder detection.

E. The Reviewing of Deep Learning Models for X-ray Image Defect Detection

The proposed DNN [2] includes feature extractor layers and a minimum distance classifier, utilized to determine the class of the feature vectors. A multi-phase training approach was introduced [3]. Initially, the model is trained on known good samples to establish a baseline. Subsequently, the model is

fine-tuned using normal and defective data. The resulting weight configuration is then employed for making predictions. By incorporating mask and grouped images as inputs, the model benefits from both local and contextual information, enhancing the accuracy of solder joint segmentation. For X-ray image defect detection, a comparison was conducted to evaluate the performance of two deep learning models, namely the 3D CNN and Long Short-Term Memory (LSTM) [4]. The results indicated that both models demonstrated similar overall performance in terms of AU ROC. However, in scenarios where a stricter Recall requirement was needed, the LSTM-based model outperformed the 3D CNN. In a separate study [5] focusing on optical inspection, the pre-trained Faster R-CNN with ResNet50 architecture was proposed and evaluated. This model showed superior performance compared to the SSD module with Inception V2 architecture. Focusing on the ability to detect small targets accurately, the integration of ConvNeXt in YOLOX, specifically ConvNeXt-YOLOX, aims to enhance its feature extraction capabilities [6]. This integration, known as ConvNeXt-YOLOX, improves speed, and accuracy, and facilitates precise detection of small targets, making it an ideal choice for optical inspection tasks. The implementation of a Novel Contrastive Self-Supervised Learning (CSSL) Framework [7] aimed to tackle data imbalance in optical solder joint inspection. This framework utilized a known good solder joint image as the "positive" class, and its distorted version served as the "negative" class. The model predicted whether the solder joint was classified as "good" or "not good." However, it is important to note that this technique is limited in its ability to identify specific types of solder joint defects beyond the binary classification.

In this research, the YOLO (You Only Look Once) object detection algorithm was chosen due to its advancements in real-time object detection [6]. YOLO takes a holistic view of the image, dividing it into a grid and directly predicting bounding boxes and class probabilities. This unique approach enables YOLO to achieve remarkable speed, making it capable of processing images in real-time. Additionally, the algorithm has undergone continuous improvements with subsequent versions, resulting in enhanced accuracy, speed, and model complexity [8], [9]. By harnessing the capabilities of YOLO, this study aims to attain accurate and efficient object detection, primarily concentrating on analyzing how image bounding box labeling influences model predictions.

III. METHODOLOGY

Enhancing Solder Joint Data for Effective Model Training

Key steps in preparing solder joint data for effective model training are detailed in the following sections (A-K). These overviews encompass diverse techniques to enhance image quality and suitability for training.

A. Solder Joint Collection

The solder joints obtained from the AXI machine are in pre-segmented and unsegmented forms. The machine recombined them into a shape that resembled the component outline to facilitate human recognition. We need to split them into individual solder joints for easy model training. The X-ray images we were collecting from the identified defective boards, defective components, and defects on each pin were

recorded as Python objects, providing a structured description of the nature and location of each defect.

B. X-ray Image of Solder Joint Merging from Multiple Slices

To accurately determine defects that require inference, such as estimating solder volume for insufficient solder detection, this study proposes merging the component images from multiple slices into a multi-channel image. This approach enables comprehensive analysis and enhances the ability to detect and analyze defects more effectively. Although this technique may not provide the same level of sophistication as 3D image preprocessing, it serves the intended purpose while maintaining low computational power requirements.

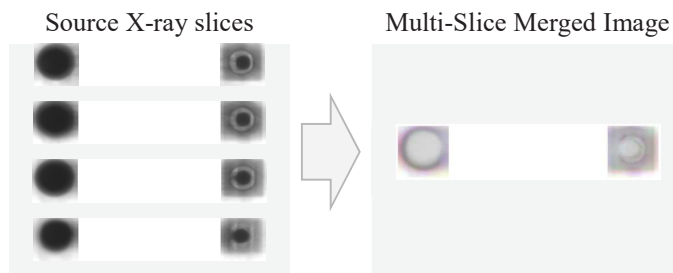


FIGURE 1
Example of slices and merged image composition

Figure 1 visually presents examples of source slice images before and after merging, displaying the outcome of the proposed merging technique. The merged image showcases the seamless combination of the individual slices, resulting in a cohesive representation. Additionally, Fig.2 outlines the solder joint preprocessing workflow, illustrating the sequential steps involved in preparing the X-ray images from the AXI machine for further analysis.

C. Solder Joint X-ray Image Segmentation Pre-Processing

In some cases, image blurring works as noise reduction by smoothing out sharp edges and fine details. It can reduce noise and unwanted artifacts. Choosing the appropriate level of blurring can help achieve a desirable threshold image while retaining the features of an image.

D. Finding the Contours Using OpenCV

The OpenCV findContours function is a popular technique for detecting contours. Many image processing applications use it to extract boundaries or object contours in an image. A vector of points represents the contours, with each point corresponding to the pixel coordinates. The "findContours function" can also be used to extract hierarchical "contours" where each "contour" is a set of nested contours. Computer vision applications widely use this function for object recognition, segmentation, and shape analysis. The finding Contours technique detects object boundaries in various digital images, including X-ray images of printed circuit boards [2].

E. Combining of Threshold Technique and K-Means Clustering to Achieve the Proper Segmentation

In one instance, we encountered a pair of shorted SOIC pins in which the threshold image failed to identify individual pins due to bridging. Using the k-means clustering function, we achieved more distinct segmentation. The algorithm then created correct bounding boxes and split the image into

individual pins, as shown in Fig.2. We then applied the classification to each solder joint, identifying them as either known "good" or "defective" locations. The solder joints were described as Python objects, such as {'BRD': [1, 2], 'GD': [7, 8]}, indicating that pins 1 and 2 were bridging solder joints, while pins 7 and 8 were good solder joints. Since the number of defective pins was less than the number of good pins, we selected a suitable number of good pins for the dataset balancing purpose, which we will utilize as the defect detection model dataset.

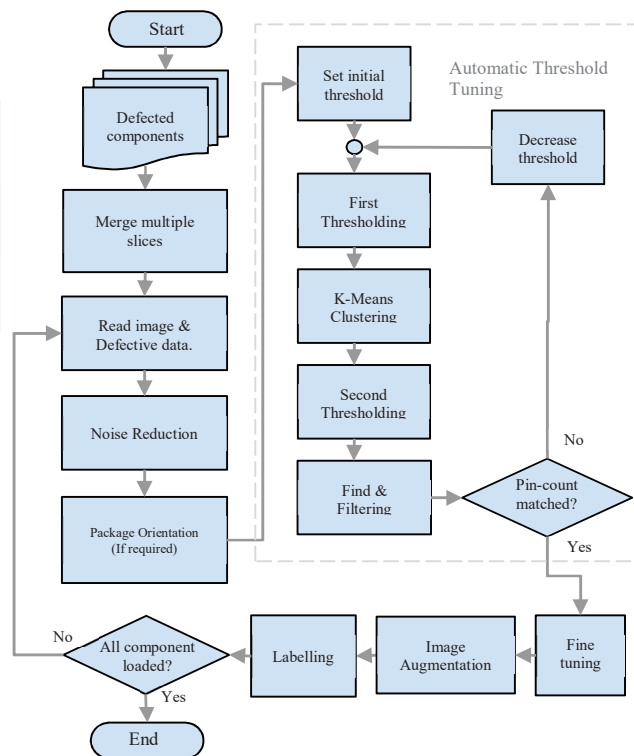


FIGURE 2
The proposed solder joint preprocessing algorithm workflow

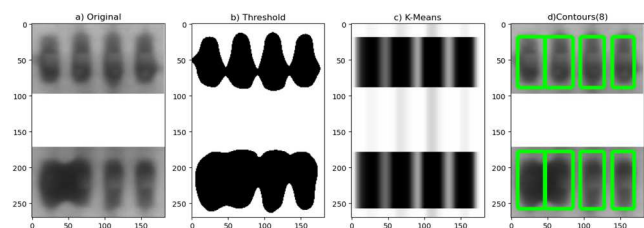


FIGURE 3
Result from each stage of segmentation

The first image (Fig. 3a) shows the original grayscale image of the solder joint with the shorted SOIC pins. The second image (Fig. 3b) displays the result after applying the thresholding method, which helps identify the pixels that belong to the solder joint but not all are located correctly. The third image (Fig. 3c) shows the result of applying the k-means clustering on the thresholded image.

This process helps to separate the pixels that belong to the individual pins, allowing for the creation of bounding boxes

for each pin. The fourth image (Fig. 3d) displays the original image with each pin bounding box created during the segmentation process. Note that these images illustrate the different stages of the segmentation process for a specific example. However, the actual results may vary depending on the quality of input X-ray images.

F. Automatic Threshold Tuning.

This study utilized the automatic threshold technique, which involved reverse looping from the high-level threshold. Then the detected bounding box will be compared with the known input pin count, and the loop will terminate after they determine that the pin count and the bounding box count are equal.

G. Improving SOIC Bridging Detection

Our initial segmentation approach was to separate the solder joints individually, which failed to detect SOIC bridging in the original X-ray image. To overcome this limitation, we adapted our algorithm to verify the long rectangular solder joint and expand the region of interest (ROI) to include neighboring solder joints. This modification allowed the model to be trained on a "wider view" of the solder joints, resulting in improved detection performance for SOIC bridging.

H. Consideration of Background Color

During the training of our defect detection model, we encountered the challenge of tall rectangular pins in certain components, such as the SOIC package, which were not well-suited for model training. To address this issue, we introduced padding to the images, ensuring they were transformed into square dimensions. To explore the impact of different background colors on the model's performance, we conducted an augmentation process where we included various background color options. These options included the highest gray level, replicated border with gray padding, white, black, and average. By incorporating these different background colors, we aimed to assess their influence on the model's accuracy and robustness in defect detection.

I. Data Augmentation Techniques

Due to the rarity of defective images, we recognized the need to prevent an imbalanced dataset. To achieve this, we employed data augmentation techniques. Specifically, we utilized sampling rotation, flipping, brightness adjustment, noise addition with optimized Signal-to-Noise Ratio (SNR), canny edge detector, scaling, and padding with various background options on the original images. We applied these techniques to help increase the diversity of the dataset and improve the model's ability to detect defects accurately. To tackle the challenge of imbalanced data, we employed data augmentation techniques by increasing the number of samples. The initial dataset of 489 solder joints, consisting of 64 normal SOIC solder joints, 169 normal BGA solder joints, 90 normal through-hole solder joints, 17 joints with insufficient solder, 62 joints of SOIC with solder bridging, 25 joints of BGA with solder bridging, 22 joints of through-hole solder bridging, and 40 joints with voids in BGA balls, was augmented using random parameter settings. Through this process, we generated an augmented dataset with a larger number of samples. Subsequently, to ensure balance in the dataset, we randomly sampled down to 5,000 images for each class, resulting in a total of 40,000 images across

the 8 classes. This approach of random augmentation and sampling enabled us to create a more balanced dataset for training our model. Fig.4 shows samples of various augmented images.

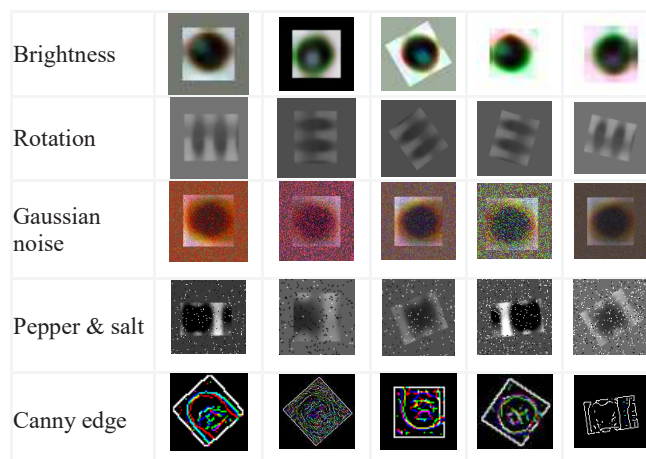


FIGURE 4

Illustrating the adoption of various augmentation techniques of training and validation dataset

J. Dataset Splitting for Training and Validation

To prepare for the training and evaluation of our model, we split the dataset into a training set and a validation set, using an 80% - 20% ratio, respectively. The training set was employed to train the model, while the validation set served to fine-tune the model's hyperparameters. This careful separation of data ensured that the model's evaluation took place on previously unseen samples, enabling a robust assessment of its ability to generalize to new data. By avoiding over-reliance on the training set, the model's performance is more indicative of its real-world effectiveness. Furthermore, for testing purposes, we used the X-ray images exported from the AXI machine as our dedicated test dataset.

K. Labeling for YOLO, the Object Detection Model

YOLO (You Only Look Once) is a popular object detection algorithm that operates by dividing an input image into a grid of cells and making predictions for bounding boxes and class probabilities within each cell. Before training a YOLO model, it is necessary to label the dataset with bounding boxes and corresponding object classes. For YOLO labeling, annotation files are generated to provide information about each object in the image. Each annotation file corresponds to a specific image and includes one row per object present in the image. These rows contain the object class and the bounding box coordinates, represented as normalized values ranging from 0 to 1 relative to the image size. The annotation format follows the pattern "C 0.500000 0.500000 0.500000 0.500000". The "C" value denotes the class label, which ranges from 0 to 7 and corresponds to categories such as "BRDBGA" (BGA balls bridging), "BRDSO" (SOIC pins bridging), "BRDTH" (through-hole pin bridging), "BVDBGA" (BGA ball solder void), "GDBGA" (normal BGA ball), "GDSO" (normal SOIC solder joint), "GDTH" (normal through-hole solder joint), and "INSTH" (insufficient solder joint in through-hole). The values "0.500000 0.500000" represent the center of the bounding

box, while the subsequent "0.500000 0.500000" indicates the size of the bounding box, which is set as half of the image size. Dealing with a large number of solder joints poses a significant challenge when it comes to manual labeling. As our focus is on automating the segmentation and augmentation processes, we have also explored the option of automatic labeling. In this approach, we fixed the image bounding boxes at the center, with a size equal to half of the solder joint image. Despite our efforts to center the segmented solder joint, we encountered variations in the solder joint size across different component types. Thus, fixing the bounding box size and location may not provide an optimal solution. Consequently, we conducted an in-depth study to examine how the bounding box affects the model's prediction outcomes.

Train the YOLO v7 Object Detection Model

To optimize the accuracy of our solder joint defect detection, we fine-tuned the YOLO v7 model using the segmented solder joint images as our training dataset. The YOLO v7 model, which was pre-trained on the COCO image dataset, was specifically chosen for its suitability in this task. Before conducting our experiment, we iteratively refined the segmentation techniques, and augmentation methods to achieve superior performance in accurately detecting solder joint defects. Additionally, to enhance the effectiveness of our defect detection, we leveraged YOLOv7's internal image augmentation capabilities, customizable through the hyperparameter settings in the "hyp.yaml" file. Considering the limited number of available samples, we further applied image preprocessing techniques to augment the dataset and introduce greater diversity in the input samples. This combined approach, utilizing YOLOv7's built-in augmentation along with our preprocessing methods, ensured a more robust and comprehensive training process for achieving precise solder joint defect detection.

IV. RESULTS AND DISCUSSION

The YOLOv7 Training Result and Prediction

As previously mentioned, our aim was to examine how image bounding boxes influence model predictions. To accomplish this, we conducted a series of experiments involving various bounding box configurations. For these experiments, we maintained the center of the bounding box at the image center (0.5, 0.5) while adjusting the bounding box ratios within the range of 0.45 to 0.70. Additionally, we employed optimal Signal-to-Noise ratio (SNR) augmentation set at 13dB. These experiments were carefully devised to investigate the influence of different bounding box ratios on the model's predictive outcomes.

According to the results in Table I, the "F1" score, considering both precision and recall, demonstrates that the bounding box ratio of 0.50 achieved the highest performance with an impressive score of 0.932. Conversely, the bounding box ratio of 0.70 resulted in the lowest score of 0.872. Excessively small or large bounding box ratios tend to lead to poorer predictions in the model. Table II-V presents a comprehensive overview of the model's classification performance for individual defective solder joints.

TABLE I. THE TRAINING RESULT OF DIFFERENT BOUNDING BOXES RATIO

| Bounding Box Size Ratio | Matrix | | |
|-------------------------|-----------|------------------|---------------|
| | <i>F1</i> | <i>Precision</i> | <i>Recall</i> |
| 0.45 | 0.886 | 0.907 | 0.867 |
| 0.50 | 0.932 | 0.953 | 0.911 |
| 0.60 | 0.889 | 0.889 | 0.889 |
| 0.70 | 0.872 | 0.837 | 0.911 |

TABLE II. PERFORMANCE METRICS AT BOUNDING BOX SIZE RATIO 0.45

| 0.45 | SOIC | BGA | | THROUGH HOLE | |
|-----------|------------|------------|------------|--------------|------------|
| | <i>BRD</i> | <i>BRD</i> | <i>BVD</i> | <i>BRD</i> | <i>INS</i> |
| Recall | 0.538 | 1.000 | 1.000 | 1.000 | 1.000 |
| Precision | 1.000 | 1.000 | 0.789 | 1.000 | 1.000 |
| F1 | 0.700 | 1.000 | 0.882 | 1.000 | 1.000 |

TABLE III. PERFORMANCE METRICS AT BOUNDING BOX SIZE RATIO 0.50

| 0.50 | SOIC | BGA | | THROUGH HOLE | |
|-----------|------------|------------|------------|--------------|------------|
| | <i>BRD</i> | <i>BRD</i> | <i>BVD</i> | <i>BRD</i> | <i>INS</i> |
| Recall | 0.692 | 1.000 | 1.000 | 1.000 | 1.000 |
| Precision | 1.000 | 1.000 | 0.882 | 1.000 | 1.000 |
| F1 | 0.818 | 1.000 | 0.938 | 1.000 | 1.000 |

TABLE IV. PERFORMANCE METRICS AT BOUNDING BOX SIZE RATIO 0.60

| 0.60 | SOIC | BGA | | THROUGH HOLE | |
|-----------|------------|------------|------------|--------------|------------|
| | <i>BRD</i> | <i>BRD</i> | <i>BVD</i> | <i>BRD</i> | <i>INS</i> |
| Recall | 0.615 | 1.000 | 1.000 | 1.000 | 1.000 |
| Precision | 1.000 | 1.000 | 0.789 | 0.667 | 1.000 |
| F1 | 0.762 | 1.000 | 0.882 | 0.800 | 1.000 |

TABLE V. PERFORMANCE METRICS AT BOUNDING BOX SIZE RATIO 0.70

| 0.70 | SOIC | BGA | | THROUGH HOLE | |
|-----------|------------|------------|------------|--------------|------------|
| | <i>BRD</i> | <i>BRD</i> | <i>BVD</i> | <i>BRD</i> | <i>INS</i> |
| Recall | 0.692 | 1.000 | 1.000 | 1.000 | 1.000 |
| Precision | 0.900 | 1.000 | 0.714 | 0.667 | 1.000 |
| F1 | 0.783 | 1.000 | 0.833 | 0.800 | 1.000 |

According to the results presented in Table II-V, the model exhibits exceptional capabilities in identifying solder insufficiency within through-hole components and detecting bridging in BGA components. Notably, it achieves perfect prediction accuracy of 100% even when using varying bounding box sizes. In the case of detecting other types of defects, altering the bounding box size through extension or reduction leads to decreased performance. For nearly all the

defects, an optimal bounding box size is necessary to achieve the most effective detection outcomes. Fig. 5 shows some of the images from the model prediction result.

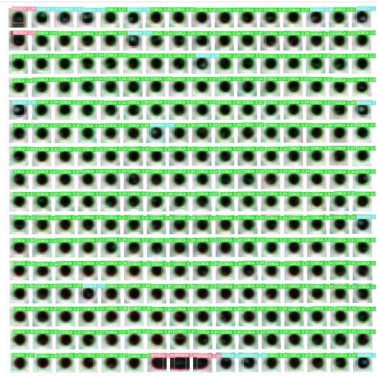

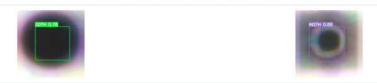

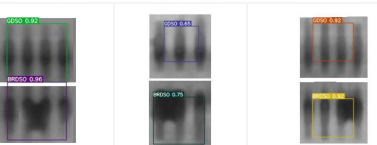
| Defection Details | YOLOv7 Prediction Image |
|--|---|
| BGA Solder bridging (red) and void in the ball (blue) |  |
| Inductor Solder insufficient of 2 joints at the top- right pins (red) |  |
| Diode Solder insufficient (right pin - purple) |  |
| Transistor Solder insufficient (left pin - green) |  |
| SOIC Solder bridging (Lower left purple, green at the middle and yellow on the right) |  |

FIGURE 5
Example of the YOLOv7 prediction result

V. CONCLUSION

In this study, we have harnessed the power of the widely acclaimed pre-trained model YOLOv7 for solder joint defects including bridging (BRD), void (BVD), and insufficient solder (INS) detection. We have employed multiple segmentation, augmentation, and labeling techniques while fine-tuning parameters to achieve optimal results. To provide a robust justification for our approach, we will employ quantitative measures to summarize the experiment results and compare them with other methods. This will enhance the clarity and credibility of our contributions.

It is important to note that the performance of YOLO models can be affected by several factors, including the dataset, domain, and application. Specifically, YOLOv7, pre-trained on the COCO dataset containing color images, necessitates merging the X-ray slices into color images for its direct application to solder joint inspection. Additionally, certain defects, such as solder bridging, are detected using a single slice, which is not compatible with the pre-trained weights. Indeed, successful adaptations of YOLO for grayscale images have been showcased in remote sensing

applications. Which involved modifying YOLOv3 by replicating the single channel to conform to the RGB format. [10]. This adaptation enables the processing of grayscale images by the YOLOv3 network architecture. To tackle the specific challenges presented by grayscale X-ray images in solder joint inspection, specialized studies and custom modifications for this domain are essential. With further research and advancements, we can pave the way for more accurate and effective defect detection in X-ray imaging.

REFERENCES

- [1] M. Kozak, P. Vesely, and K. Dusek, "Analysis of solder mask roughness and stencil shape influence on void formation in solder joints," *Weld. World*, vol. 67, no. 5, pp. 1347–1355, May 2023, doi: 10.1007/s40194-023-01505-7.
- [2] C. AKDENİZ, Z. Dokur, and T. Ölmez, "Detection of BGA solder defects from X-ray images using deep neural network," *Turk. J. Electr. Eng. Comput. Sci.*, vol. 28, pp. 2020–2029, Jul. 2020, doi: 10.3906/elk-1910-135.
- [3] H. Jayasekara, Q. Zhang, C. Yuen, M. Zhang, C.-W. Woo, and J. Low, "Detecting Anomalous Solder Joints in Multi-sliced PCB X-ray Images: A Deep Learning Based Approach," *SN Comput. Sci.*, vol. 4, no. 3, p. 307, Apr. 2023, doi: 10.1007/s42979-023-01765-6.
- [4] Q. Zhang *et al.*, "Deep Learning Based Defect Detection for Solder Joints on Industrial X-Ray Circuit Board Images." arXiv, Mar. 25, 2021. Accessed: Feb. 23, 2023. [Online]. Available: <http://arxiv.org/abs/2008.02604>
- [5] M.-C. Chen *et al.*, "A PCBA Solder Joint Defects Inspection System Based on Deep Learning Technology," in *2023 IEEE International Conference on Consumer Electronics (ICCE)*, Jan. 2023, pp. 1–3. doi: 10.1109/ICCE56470.2023.10043589.
- [6] S. Liao, C. Huang, Y. Liang, H. Zhang, and S. Liu, "Solder Joint Defect Inspection Method Based on ConvNeXt-YOLOX," *IEEE Trans. Compon. Packag. Manuf. Technol.*, vol. 12, no. 11, pp. 1890–1898, Nov. 2022, doi: 10.1109/TCPMT.2022.3224997.
- [7] J. Zhou, G. Li, R. Wang, R. Chen, and S. Luo, "A Novel Contrastive Self-Supervised Learning Framework for Solving Data Imbalance in Solder Joint Defect Detection.," *Entropy*, vol. 25, no. 2, p. 268, Feb. 2023, doi: 10.3390/e25020268.
- [8] P. Jiang, D. Ergu, F. Liu, Y. Cai, and B. Ma, "A Review of Yolo Algorithm Developments," *Procedia Comput. Sci.*, vol. 199, pp. 1066–1073, 2022, doi: 10.1016/j.procs.2022.01.135.
- [9] M. E. AtiK, Z. Duran, and R. Özgünlük, "Comparison of YOLO Versions for Object Detection from Aerial Images," *Int. J. Environ. Geoinformatics*, vol. 9, no. 2, pp. 87–93, Jun. 2022, doi: 10.30897/ijegeo.1010741.
- [10] S. G. Cs, A. B. Sr Y, R. Azhagumurugan, and S. S., *Grayscale Based Algorithm for Remote Sensing with Deep Learning*. 2021.

Location-based Score Prediction for Condominiums in Bangkok

Sarun Bunjongsat * Sirion Vittayakorn[†]
School of Information Technology
King Mongkut's Institute of Technology Ladkrabang
 Bangkok, Thailand
 Email: {64607067*, sirion.vi[†]}@kmitl.ac.th

Abstract—Condominiums are one of the most popular residential properties due to the resurgence of urban living. They are typically found in more metropolitan areas, such as the national capital region, offering easy access to restaurants, shopping, and various activities. Condominiums can be both profitable investment properties and enjoyable homes. However, finding the right one can be challenging. Based on previous work, one crucial factor is the location, which requires experience, expertise, and time to consider. Thus, in this study, we aim to: 1) investigate the factors that affect the potential location of a condominium, and 2) apply machine learning algorithms to create a prediction model for condominium scores. In this research, we collected a novel dataset comprising more than 2,000 condominiums in Bangkok, Thailand, and examined the location-based factors that influence the price and purchasing decisions of individuals. We extracted several features for model training and studied the variables that could be used to measure the potential of a condominium in numerical form. We proposed a multi-layer perceptron neural network with 5-Fold cross-validation and grid-search techniques. The experimental results demonstrate that our network achieves a mean squared error (MSE) of 0.0067 when using the density-based score labeling.

Index Terms—Condominium rating, Location-based score, Machine learning

I. INTRODUCTION

Bangkok, the capital city of Thailand, serves as the country's central hub, boasting prosperity in various aspects, such as tourism, industry, and education. This is primarily attributed to the city's rapid growth, which has resulted in an increased demand for housing as people flock to the city for work and residence. However, due to the limited availability of affordable housing in Bangkok, condominiums have become increasingly popular, especially among young working individuals aged 18 to 32 [1]. The market demand for condominiums is high, not only for residential purposes but also for investment [2]. The work by [3] has identified three major factors that influence the decision to purchase a condominium: product quality, price, and location, with location being the most significant among these factors.

As a result, our research primarily focuses on predicting the scores of condominiums based on their locations and other relevant factors. To achieve this, we initiated the process by collecting a novel dataset of condominiums in Bangkok and their location-based metadata. We then developed a model that effectively predicts condominium scores based on several

location-related factors. Our objective is to provide an alternative scoring system that assists both novices and experts in making informed decisions.

II. RELATED WORKS

Since buying a condominium can be a challenging decision for most people, several works have explored this problem in the past. Kiriya and Chotiwut [4] studied the attributes determining condominium prices in Bangkok. They employed the Hedonic price model to analyze 20 attributes of 146 condominiums and created a functional form of the model using the Box-Cox technique. Their findings revealed that 12 variables had statistically significant effects on property prices. The results demonstrate that the top 3 factors are 1) Location, 2) Whether the project owner is in stock exchange, and 3) The distance from the nearest railway station.

Saggranan and Chadanat [3] found that their study group gave the highest priority to the location, followed by proximity to work or school. Moreover, they also strongly considered factors like nearby facilities such as convenience stores, markets, and restaurants, as well as the condominium's amenities like car/motorcycle parking, fitness center, and swimming pool.

Kongkoon *et al.* [5] have created a linear regression model to score the suitability of a location using input from 32 experts to adjust the weight of each factor. The factors were divided into four major categories: 1) Transportation, 2) Amenities, 3) Public utilities, and 4) Workplace location. These factors are used to calculate the score using a Likert Scale for each type of location as the domains (1 to 5, where 1 is least competitive and 5 is most competitive). The highest weight, 57.8%, was given to the transportation factor, followed by the workplace location factor at 24%. However, there is no evaluation presented in this work, thus their performance is questionable.

Jirapon and Sarawut [1] have proposed a prediction model for condominium prices in Bangkok using all three factors: 1) Location, including the names of the nearest BTS and MRT stations and the distance to those stations 2) Building characteristics and 3) Price fluctuations. They explored several methods including Generalized Linear Model, Deep Learning, Decision Tree, Random Forest, and Gradient Boosted Trees. The model with the highest performance is Deep Learning.

Saggranan and Chadanat [3] found that one of the limitations of previous works is that they usually measure the factors independently without considering the potential interactions among them. This may lead to inaccurate calculations when the analysis results are applied in real-life situations.

In this work, our goal is to develop a model for predicting condominium scores using a novel dataset of condominiums in Bangkok. We focus on utilizing location-based data, which has been identified as a crucial factor in previous studies. We explore various location-based features and employ deep learning techniques [1] which achieved the best performance for predicting condominium prices in Bangkok and is effective for addressing nonlinear problems.

III. DATASET

To achieve our goal, we collected a novel dataset of condominiums in Bangkok by integrating data from multiple sources:

A. Data collection

1) *Condominium data*: First, we collected approximately 2,449 condominium data entries from the maps.envi.dev website [6] and the Bestimate website [7]. The metadata includes latitude and longitude coordinates, district, project developer name, starting price, facility details, year of completion, unit count, and the number of parking spaces within the project.

2) *Location-based data*: Since our work focuses on scoring based on location factors, we further extended our dataset with the additional location-based data from the Longdo Map API [8]. We further gathered the distances between condominium projects and various types of nearby locations such as airports, bus stops, convenience stores, shopping malls, factories, government buildings, expressway entrances, hospitals, markets, office buildings, parks, police stations, train stations, and universities.

Moreover, we also calculated the number of office locations within a 1 km radius of each project and the population count within a 50-meter radius of each project to measure the density of the location as well.

3) *Condominium rating*: Finally, we crawled the ratings, comments, and pictures of each record from the Google Place API since we hypothesized that the ratings (Stars) and the condominium scores could be relevant.

B. Data exploration

From the data collection process, there are about 2449 condominiums from all 50 districts of Bangkok, Thailand. It was found that the district with the highest number of condominiums is Vadhana, with a total of 273, while the district with the lowest number of condominiums is Thawi Watthana, with only one. On average, there are approximately 49 ± 54 condominiums per district. The distribution of the top 10 districts with the highest number of condominiums can be explored from Fig.1.

Fig. 2 shows the distribution of the distance from the condominium projects to the nearest railway station (e.g., Bangkok

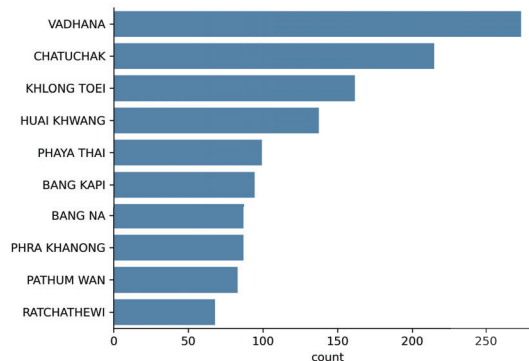


Fig. 1. Distribution of the top 10 districts by number of condominiums.

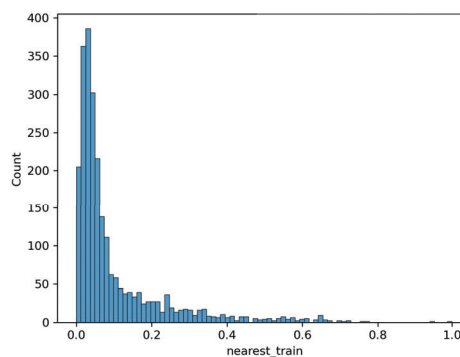


Fig. 2. Distribution of distance from condominium to the nearest train station.

Mass Transit System: BTS, Metropolitan Rapid Transit: MRT, or trains). From the graph, it is clear that most condominium projects tend to be located near the stations, where 63.78% of the condominiums are within walking distance (1-kilometer radius). This result confirms that one crucial factor for condominiums is location, specifically the distance to the nearest public transportation, as revealed in [1], [3], [5].”

Moreover, we also inspected the correlation between the price of the condominium and the accessibility of the Bangkok Mass Transit System (BTS) Sky-train stations, as shown in Fig. 3. In Fig. 3, the black dots indicate the locations of Sky-train stations, while the blue-red dots indicate the locations of condominiums. The range of condominium prices starts from the lowest at 105,000 baht (darkest blue dot) to the highest at 110 million baht (bright red dot).

The heat-map demonstrates that

- 1) The price of condominiums will be highest if they are in the center of the city, (e.g., Vadhana, Klong Toei, Pathum Wan, Bang Rak and Sathon district) and near the sky-train stations.
- 2) In suburban areas, the price of condominiums closer to the sky-train stations will be higher than those located farther away.

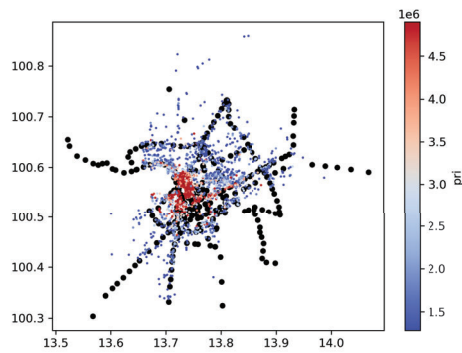


Fig. 3. Heatmap of condominium price in Bangkok, centered at Vadhana district.

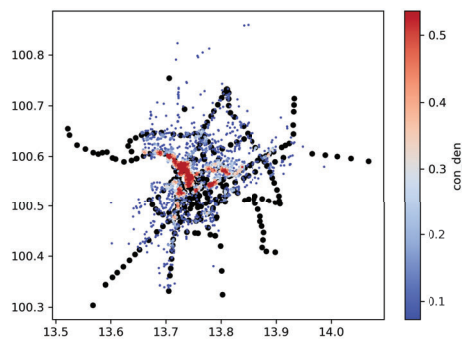


Fig. 4. Heat-map of condominium density in Bangkok, centered at Vadhana district.

- 3) In rural areas, the locations of condominiums are closely related to the sky-train station locations.

C. Label Selection

Since there is no ground truth score for our dataset, we have generated multiple scoring labels for our data and defined scoring ranges between 0 and 1 for all of them using the min-max normalization method.

1) *Density-based score*: First, we hypothesize that “The high-density condominium areas result from high demand, which should imply a high score.” Thus, in this experiment, for each record (condominium) from our dataset, we count the number of neighboring condominiums within 500 meters and plot the density map as shown in Fig.4.

The result from Fig.4 reveals that the areas with the highest density are Vadhana, Khlong Toei, and Pathum Wan districts. When looking at Fig.3 and Fig.4, it becomes clear that there is a correlation between these two factors: price and density. The heat maps demonstrate that in the center of the city (a location-based factor), both the price and the density are high due to customer demand. Since the price of the condominiums can be influenced by economic factors, we propose a density-based score as our ground truth label for the dataset.

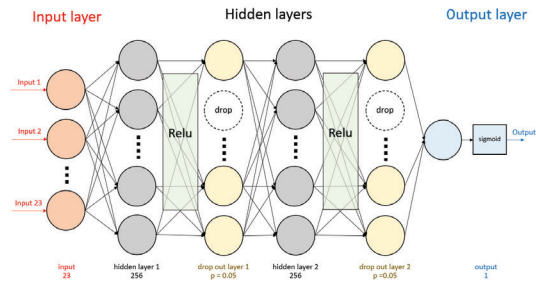


Fig. 5. Proposed multi-layer perceptron neural network model.

2) *Google Place’s rating score*: We also investigate the alternative score labeling from Google Place API. The rating score ranges from 1.0 to 5.0 and is based on aggregated user reviews. Using the API, we collect the average rating score for each condominium in the dataset.

3) *Occupancy rate score*: We calculate the occupancy rate score from the population count within 50 meters of each project’s data divided by the project’s unit count, collected from [9]. Since we hypothesize that “The high occupancy rate condominium means the preferable condominium, which results in a high score.”

4) *Merged score*: Finally, we use the three previous scores as mentioned to create a new label with the hypothesis that this label may represent all aspects of other scoring methods. We calculate the score by endowing weight to each score and summing them together. Since we do not know the proper weights of each score, we distribute equal weighting to them.

D. Factor Analysis and Feature Selection

Several previous works demonstrate the significance of location-based features. For example, the works from [1] and [4] found that sky-train accessibility is one of the key factors affecting condominium prices, as well as amenities [10]. Besides these factors, [5] reveals that the distance to schools, hospitals, or workplaces, and the number of parking lots [11] are also significant. Based on the previous works, the final location-based features and other additional features that might affect selected labels, such as the year of completion and the number of project facilities, included in this work are shown in the first column of Table V.

IV. EXPERIMENTS

In this work, we proposed a multi-layer perceptron neural network with 23-dimensional features for predicting the location-based score of the condominium. The proposed network consists of 2 hidden layers with 256 nodes, ReLU layers, and dropout layers, as shown in Fig. 5. The dropout is responsible for randomly dropping out some nodes in each hidden layer to reduce the chance of overfitting and improve the network’s performance [12].

To train the network, we split the dataset into a training and testing set with an 80:20 ratio. During the training, we applied 5-fold cross-validation and a grid-search technique to

TABLE I
THE MEAN SQUARE ERROR (MSE) OF THE PROPOSED NETWORK FROM 4
DIFFERENT LABELS.

| Labels | MSE |
|-----------------------------|---------------|
| Density-based score | 0.0067 |
| Google Place's rating score | 0.0447 |
| Occupancy rate score | 0.0420 |
| Merged score | 0.0113 |

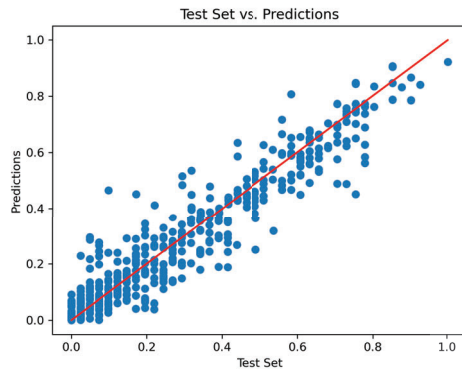


Fig. 6. Relationship between actual values from the test set and predicted values.

explore multiple choices of parameters and achieve the best parameters on validation sets. The selected parameters are as follows: batch size = 16, dropout = 0.05, Sigmoid activation function, and learning rate = 0.001.

V. EXPERIMENTAL RESULTS

In this section, we will discuss several experimental results that we used to evaluate our proposed network.

A. Mean Square Error: MSE

First, we evaluate our proposed network on the test data using four different labels, and the results are shown in Table I:

1) *Density-based score*: Using the density-based score as the ground truth label, our model achieved the lowest Mean Squared Error (MSE) at 0.0067. The results, as shown in Fig. 6, indicate that the ground truth and predicted scores tend to be in a similar direction.

The examples of the condominium with the highest and lowest scores along with some selected features are shown in Table II. From the results, we can see that the condominiums with high scores are mostly located in the center of Bangkok, particularly in the Vadhana district, with accessibility to public transportation (train stations) and other amenities. On the other hand, the condominiums with lower scores are situated farther from the city center and distant from various amenities.

2) *Google Place's rating score*: Using the Google rating score as a ground truth label, our model achieved an MSE of 0.0447. We believe that predicting Google ratings is more challenging for several reasons. First, the rating could come from the user experience, which may not solely reflect the

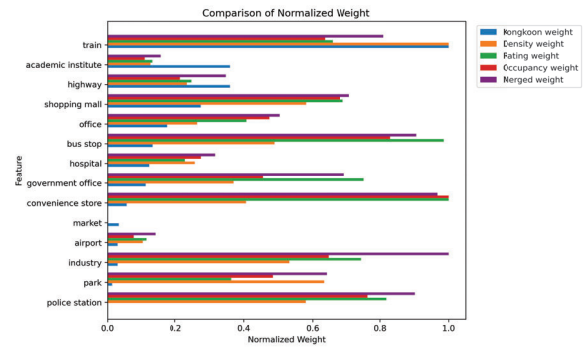


Fig. 7. Comparison of the proposed model's weights trained from: density score (orange), Google rating (green), occupancy rate (red), merged score (purple) and the baseline's weight (blue).

quality or appeal of the condominium itself. For example, bad service from the gym staff or disturbances from neighboring rooms could result in an unfair rating for the condominium. Second, reviews or ratings can be manipulated by the developer, such as paying for positive reviews or removing negative ones.

3) *Occupancy rate score*: Then, with the occupancy rate score label, our model achieves the highest MSE at 0.0420. In this work, we computed the occupancy rate based on population density data from [9]. Although the population estimates are based on 50-meter resolution satellite imagery, the available data is limited to only 2020. We posit that the main drawback of this label is the limited data.

4) *Merged score*: Finally, we explore the merged score label, which is the average of the 3 scoring methods described above. With this score, our model achieves an MSE of 0.0113. Due to the limitation of weight allocation for the score's components, we suspect that this performance might not be optimal.

B. Feature's weights correlation

To further explore our network, we extract the sum of weights from the first hidden layer and normalize them to represent the weight of each feature. The comparison of the 14 selected feature weights from different labels compared with the baseline [5] is shown in Fig.7.

1) *Density-based score*: The features with the top 3 weights are 1) The distance to the nearest train station, 2) The distance to the nearest park, and 3) The distance to the department store. And the features with the bottom 3 weights are 1) The distance to the nearest university, 2) The distance to the nearest airport, and 3) The distance to the nearest market.

Next, we compare our feature weights with those from [5] to investigate the correlations between the two methods using Spearman's rank correlation coefficient [13]. Since our features are different from those in [5], only the overlapping features are compared, as shown in Fig.7.

In Fig.7, our weights are represented by orange bars, while the corresponding weights from [5] are depicted in blue. As observed in the graph, both our network and [5] assign the

TABLE II
EXAMPLE OF THE CONDOMINIUM WITH HIGHEST AND LOWEST SCORES.

| Project Name | District | Nearest train station | Nearest park | Nearest department store | Score |
|-----------------------------|-------------|-----------------------|--------------|--------------------------|-------|
| The Reserve Thonglor 2 | Vadhana | 0.03 | 0.01 | 0.07 | 1.00 |
| H Sukhumvit 43 | Vadhana | 0.04 | 0.03 | 0.03 | 1.00 |
| The Bangkok Thonglor | Vadhana | 0.02 | 0.02 | 0.02 | 0.98 |
| Suwan Asia Condominium | Yan nawa | 0.24 | 0.17 | 0.06 | 0.00 |
| Baan Kacha Puri Condominium | Taling Chan | 0.09 | 0.28 | 0.17 | 0.00 |
| Wongwaen Complex | Bang Bon | 0.16 | 0.34 | 0.17 | 0.00 |

TABLE III
THE SPEARMAN'S RANK CORRELATION COEFFICIENT (ρ) OF THE PROPOSED NETWORK FROM 4 DIFFERENT LABELS WITH THE BASELINE.

| Labels | ρ |
|-----------------------------|----------------|
| Density-based score | -0.0441 |
| Google Place's rating score | -0.1123 |
| Occupancy rate score | -0.1101 |
| Merged score | -0.1256 |

highest weight to the "distance to the nearest train station" feature, but the rankings for the remaining features differ. Consequently, the Spearman correlation coefficient between our weight ranking and [5] is -0.0441, as indicated in Table III. This value is very close to zero, signifying a very weak or almost nonexistent relationship between the two rankings.

2) *Google's rating score*: The features with the top 3 weights are 1) The distance to the nearest convenience store, 2) The distance to the nearest bus stop, and 3) The distance to the police station. The features with the bottom 3 weights are 1) The distance to the nearest university, 2) The distance to the nearest airport, and 3) The distance to the nearest market.

The results from Table III reveal that the Spearman's rank correlation coefficient between features' weights trained from Google's rating score and [5] is -0.1123. Similar to the previous result, the correlation is very weak, indicating almost no relationship between the two rankings.

3) *Occupancy rate score*: The features with the top 3 weights are 1) The distance to the nearest convenience store, 2) The distance to the nearest bus stop, and 3) The distance to the police station. And the features with the bottom 3 weights are 1) The distance to the nearest market, 2) The distance to the nearest airport, and 3) The distance to the nearest university.

The ranking results are quite similar to Google's rating. The Spearman's rank correlation coefficient between feature's weighted trained from occupancy rate score and [5] is 0.1101, which show a very weak correlation between two rankings.

4) *Merged score*: The features with the top 3 weights are 1) Number of factories within 1 km, 2) The distance to the nearest convenience store, and 3) The distance to the nearest bus stop. The features with the bottom 3 weights are 1) The distance to the nearest university, 2) The distance to the nearest airport, and 3) The distance to the nearest market.

Similar to the previous results, the Spearman's rank correlation coefficient between feature weights trained from the merged score and [5] also shows almost no relationship between the two rankings with a value of -0.1256.

TABLE IV
THE SPEARMAN'S RANK CORRELATION COEFFICIENT BETWEEN OUR PROPOSED LABELS.

| Labels | Density | Google | Occupancy | Merged |
|-----------------------------|---------|--------|-----------|--------|
| Density-based score | 1 | 0.773 | 0.817 | 0.878 |
| Google Place's rating score | 0.773 | 1 | 0.945 | 0.954 |
| Occupancy rate score | 0.817 | 0.945 | 1 | 0.949 |
| Merged score | 0.878 | 0.954 | 0.949 | 1 |

From the experimental results, we believe that there are multiple reasons why our feature weights are different from [5]. First, the total number of features are different and only overlap features are used to compute the rank correlation. While there are only 14 features in [5], our work investigates 23 features. Since our models are optimized more amount of features, the correlation with 14 features could be low.

Second, in [5], the features are manually weighted by thirty experts, while our weights are trained from data of more than two thousand existing condominiums. We believe that with this larger sample size, our results could be different but more reliable.

Finally, no evaluation methods are presented in [5]. In contrast, we explore four different labels as shown in Table IV, and the results demonstrate strong agreements among different methods.

C. The feature's weights analysis

From the experimental results, we observe that although the Spearman's rank correlation coefficient between our proposed methods and [5] is quite low, there are some strong agreements among the feature's weights trained from four labels, as shown in Table V.

The experimental results reveal that the most important features are sufficient parking lots, accessibility to convenience stores, and public transportation (e.g., bus stops or train stations). Given that Bangkok is one of the most congested cities in the world, these features carry the highest weight.

On the other hand, the location features with the lowest weights are the distance to the nearest airport, the distance to the nearest market, and the longitude. We hypothesize various reasons to explain these results:

- Don Mueang International Airport, located in Don Mueang district, is the only airport in the Bangkok metropolitan region. Therefore, the distance to the nearest airport always achieves the lowest weight.
- Bangkok is one of the world's best cities for street food, with the city scoring high marks for the number

TABLE V
FEATURE RANKINGS SORTED BY WEIGHTS LEARNING FROM 4 DIFFERENT LABELS: DENSITY SCORE, GOOGLE RATING, OCCUPANCY RATE AND MERGED SCORE IN THE DESCENDING ORDER.

| Features | Density | Google | Occupancy | Merged |
|---|---------|--------|-----------|--------|
| Number of project's parking | 1 | 1 | 1 | 1 |
| Distance to the nearest train station | 2 | 9 | 9 | 6 |
| Distance to the nearest park | 3 | 15 | 11 | 11 |
| Distance to the nearest department store | 4 | 8 | 5 | 7 |
| Distance to the nearest police station | 5 | 4 | 4 | 5 |
| Number of factories within 1 km | 6 | 6 | 7 | 2 |
| Distance to the nearest bus stop | 7 | 3 | 3 | 4 |
| Distance to the nearest convenience store | 8 | 2 | 2 | 3 |
| Number of governments office within 1 km | 9 | 5 | 13 | 8 |
| Average distance of 3 nearest bus stop | 10 | 7 | 6 | 10 |
| Number of bus stops within 1 km | 11 | 12 | 14 | 14 |
| Number of train station within 1 km | 12 | 11 | 8 | 9 |
| Number of office buildings within 1 km | 13 | 13 | 12 | 13 |
| Distance to the nearest hospital | 14 | 18 | 16 | 17 |
| Distance to the nearest highway | 15 | 17 | 18 | 15 |
| Latitude number | 16 | 19 | 19 | 18 |
| Distance to the nearest university | 17 | 20 | 20 | 20 |
| Number of project's facility | 18 | 10 | 10 | 12 |
| Distance to the nearest airport | 19 | 21 | 21 | 21 |
| District | 20 | 16 | 17 | 19 |
| Year of completion | 21 | 14 | 15 | 16 |
| Distance to the nearest market | 22 | 22 | 22 | 22 |
| Longitude number | 23 | 23 | 23 | 23 |

of street food vendors [14]. Many people prefer to buy ready-to-eat food from street food vendors or convenience stores rather than buying food or ingredients from the market and cooking by themselves. Thus, this feature consistently ranks at the bottom.

- Finally, we believe that the latitude and longitude coordinates of all condominiums might not vary significantly, leading to the low weights for both features.

VI. CONCLUSION

In this work, we explore the location-based factors to predict the scores for condominiums in Bangkok, Thailand. To achieve our goal, we collect a novel dataset of more than 2,000 condominiums in Bangkok and their metadata. Since the ground truth condominium score does not exist, we investigate several potential scoring labels, including: 1) Condominium density-based score, 2) Google Place's rating score, 3) Occupancy rate score, and 4) Merged score.

Then, we present a multi-layer perceptron architecture to predict the location-based score of a condominium and compare its performance with the baseline [5]. Our best experimental results achieve an MSE of 0.0067 using the density-based score labeling, and the feature weights trained from this label receive the highest Spearman's rank correlation coefficient with [5] at 0.0441. Although our experimental results differ from the baseline, we believe that due to the limitations of the baseline, we provide more reliable results based on tangible data instead of personal viewpoints.

REFERENCES

- [1] J. Sunkpho and S. Ramjan, "Predicting condominium price in bangkok using web mining techniques (in thai)," *Journal of Humanities and Social Sciences*, vol. 12, pp. 15–27, July 2021.
- [2] C. Sriviboon and K. Wongleedee, "Factors of success: Condominium selling and sales promotion," in *International Academic Multidisciplinary Research Conference*, 2019, pp. 7–7.
- [3] S. Preechapanichayagarn and C. Piyawiboon, "Factors affecting purchasing decision of condominium in thonburi area of bangkok, thailand," *The EURASEANs: journal on global socio-economic dynamics*, no. 2(33), pp. 72–82, March 2022. [Online]. Available: <https://euraseans.com/index.php/journal/article/view/316>
- [4] C. L. Kiriya Kulkolkarn, "Attributes determining condominium prices in bangkok (in thai)," *Applied Economics Journals*, vol. 19, no. 1, pp. 24–45, June 2012.
- [5] K. Tochaiwat, W. Likitanupak, and S. Kongsuk, "Location selection models for low-rise condominium development in bangkok," *Veridian E-Journal, Silpakorn University (Humanities, Social Sciences and arts)*, vol. 10, no. 5, pp. 266–280, 2017.
- [6] S. Wongtanakarn. Maps.envi.dev. [Online]. Available: <https://maps.envi.dev/>
- [7] B. T. C. Limited. bestimate. [Online]. Available: <https://gobestimate.com/data>
- [8] M. Technology. Longdo map solutions. [Online]. Available: <https://map.longdo.com/>
- [9] H. D. EXCHANGE. Thailand: High resolution population density maps and demographic estimates. [Online]. Available: <https://data.humdata.org/dataset/thailand-high-resolution-population-density-maps-demographic-estimates>
- [10] V. Taecharungroj, "Google maps amenities and condominium prices: Investigating the effects and relationships using machine learning," *Habitat International*, vol. 118, December 2021. [Online]. Available: <https://www.sciencedirect.com/science/article/pii/S0197397521001521>
- [11] H. K. Pornraht Pongprasert, "Why tod residents still use car? understanding the factors affecting the automobile ownership and use of residents living near transit stations of bangkok)," *Urban and Regional Planning Review*, vol. 4, 2017.
- [12] J. S. C. T. Yu-Dong Zhang, Chichun Pan, "Multiple sclerosis identification by convolutional neural network with dropout and parametric relu," *Journal of Computational Science*, vol. 28, pp. 1–10, September 2018. [Online]. Available: <https://www.sciencedirect.com/science/article/pii/S1877750318305763>
- [13] T. D. Gauthier, "Detecting trends using spearman's rank correlation coefficient," *Environmental forensics*, vol. 2, no. 4, pp. 359–362, 2001.
- [14] R. Pisuthipan. Ranking the world's street food. [Online]. Available: <https://www.bangkokpost.com/life/social-and-lifestyle/1830214/ranking-the-worlds-street-food>

Exploring the i3DVAE-LSTM Framework for Generating Exceptionally Rare Anomaly Signals

Thongchai Kaewkiriya

School of Information Technology
King Mongkut's Institute of Technology Ladkrabang
Bangkok, Thailand
tkaewkiriya@gmail.com

Kuntpong Woraratpanya*

School of Information Technology
King Mongkut's Institute of Technology Ladkrabang
Bangkok, Thailand
kuntpong@it.kmitl.ac.th

Abstract—In the era of data-driven approaches, ensuring data quality is crucial for developing effective machine learning and deep learning models. While data augmentation is commonly used to increase the sample size, it does not guarantee data quality. Data generation goes beyond augmentation by incorporating additional steps to ensure high-quality output samples. This technique is particularly valuable for anomaly classification tasks with limited training samples. A recent study introduced a 3DVAE-LSTM (3-Dimensional Variational Autoencoders-Long Short-Term Memory) approach for generating extremely rare case signals. Although this framework synthesized samples for training deep learning models, it faced challenges with long sequential data. To address this, the authors proposed an improved version called i3DVAE-LSTM (Improvement of 3-Dimensional Variational Autoencoders-Long Short-Term Memory) and presented the evaluation of the i3DVAE-LSTM framework. The proposed framework adopts a divide-and-conquer technique, splitting long sequence data into smaller fragments to enhance the quality of generated samples, which are then concatenated together. Experimental results demonstrated that classification models trained with data generated by i3DVAE-LSTM outperformed baselines in all aspects.

Index Terms—Anomaly Detection, Data Generation, Data Augmentation, Variational Autoencoder, Long Short-Term Memory Neural Network

I. INTRODUCTION

As the fields of machine learning and deep learning (ML/DL) continue to advance, the prospect of these methods replacing human capabilities becomes more plausible. Their ability to learn, adapt, and perform a wide range of tasks is evident. One area where ML/DL can make a significant impact is in the identification of anomalies, a critical aspect in industrial settings. In this context, anomalies refer to rare and unique occurrence signals in sensors or work processes. They play a crucial role in alerting us to potential issues. Timely detection and investigation of anomalies are essential to prevent further damage to systems and processes.

In this sense, an anomaly can be viewed as an outlier. Hence, outlier detection and clustering, traditional machine learning (ML) methods, were commonly used for anomaly detection. Although these methods can classify anomalies as a separate class of data, they struggle to identify the specific type of anomaly. To address this

limitation, researchers attempted to employ deep learning (DL) techniques that can perform multi-class classification [1]. However, DL approaches are effective in classifying normal and anomaly data only when the training set is well-balanced. In real-world scenarios, anomalies are rare signals, resulting in imbalanced datasets. This leads to overfitting models and poor performance in classification tasks. To mitigate the scarcity of anomaly data, data augmentation techniques were applied to increase the quantity and diversity of the data [2]. While data augmentation helps with the issue of insufficient anomaly quantity, it does not address the problem of data quality. This is because the controllable quality of augmentation techniques is lacking, resulting in generated anomaly samples that often lose their distinguishing characteristics. As a result, the performance of trained models tends to deteriorate.

To address the overfitting problem caused by the imbalanced dataset, data generation methods have emerged as effective solutions [3]–[5]. Unlike data augmentation, data generation is a controllable process that ensures the quality of the generated data. Recently, a framework known as 3DVAE-ERSG (3-Dimension Variational Autoencoders for Extremely Rare Signal Generation) [5] was proposed, building upon previous works [3] and [4]. This innovative approach introduced modifications, including increasing the dimension of the VAE latent space from two to three dimensions and adapting the data picker to work with the three-dimensional latent space.

3DVAE-LSTM [6] was developed as a more recent and updated version of [5], specifically designed for handling long sequential data. Despite its capabilities, further improvement opportunities were recognized. As a result, a recent and enhanced version of [6] emerged, known as i3DVAE-LSTM [7]. This latest version aims to boost the model's accuracy significantly. The framework of i3DVAE-LSTM, illustrated in Fig. 1, comprises various essential elements: (i) augmentation methods applied to different domains, (ii) a signal fragment assembler that divides and randomly reassembles signals, (iii) a variational autoencoder (VAE) that trains on data from the previous steps and generates samples in the latent space, (iv) a data picker that selects samples from the latent space, and (v) a quality classifier that ensures the final outputs' quality. By leveraging data generated through this

*Corresponding author: kuntpong@it.kmitl.ac.th

advanced framework, the model showcases remarkable performance improvements in multi-class classification tasks.

However, as reported in [7], there is no supporting evidence explaining why the i3DVAE-LSTM framework can significantly improve the classification performance. Thus, further research and analysis are necessary to validate and understand the factors contributing to the observed improvements.

The structure of this paper is as follows: Section II explains how the i3DVAE-LSTM functions for generating extremely rare anomaly signals. Section III presents the experimental results, comparing our data generation performance with the baselines and investigating the primary factor influencing the performance enhancement. Finally, Section IV summarizes the main idea of this work and outlines our future directions.

II. PROPOSED METHOD

The paper introduces a framework called i3DVAE-LSTM, designed to generate extremely rare anomaly signals. This framework represents an enhanced version of 3DVAE-LSTM [6]. Comprising five essential sections, as depicted in Fig. 1 and explained below, the i3DVAE-LSTM framework demonstrates significant advancements in the generation of rare anomaly signals.

A. Data Generation Preparation

The objective of this step is to augment the limited amount of rare data available. This is achieved through two processes: (i) Creating additional samples from the original data by slicing it into time windows. (ii) Augmenting the samples using various techniques [8], such as upsampling-downsampling, fast Fourier transform [9], and time series decomposition [10], across different domains. The augmented data is then transformed back to its original domain. Finally, (iii) an improved signal fragment assembler (I-SFA) is applied to divide all the samples into four fragments and reassemble them to form new signals, following the approach described in [4].

B. First Quality Classifier (QC1)

QC1 serves as a quality assurance tester for the generated signals, ensuring their quality. Similar to previous studies [4] and [5], the evaluation of errors is done using mean absolute error (MAE) and histogram area (HA) as metrics. The weighting of these scores can be adjusted according to the specific requirements of the application tasks. If the objective is to achieve a high level of similarity between the generated and real signals, the weight assigned to MAE is greater than that given to HA. Conversely, if the goal is to prioritize signal generalization, the weight assigned to HA is greater than that of MAE.

In addition, QC1 has the role of monitoring the quality score of the generated signals and selectively retaining only those that fall within a predetermined threshold. A low score indicates that the signals have lost significant data characteristics, while a high score suggests that the signals lack diversity. By applying this threshold-based

approach, QC1 ensures that only signals of satisfactory quality are retained for further use.

C. Data Generation Provider

The qualified samples obtained from the previous step are utilized to train a Variational Autoencoder (VAE) [11]. The VAE learns from these samples and creates a probabilistic latent space. This latent space allows us to generate an unlimited amount of data with high variability. By adjusting the parameters of the VAE, we can increase the dimensionality of the latent space. In this case, a three-dimensional latent space is employed, providing greater access to samples that may not have been discovered previously. Mathematically, the VAE is defined by Eq. (1).

$$\log P(X) - D_{KL}[Q(z|X)||P(z|X)] = E[\log P(X|z)] - D_{KL}[Q(z|X)||P(z)] \quad (1)$$

where X is the training signal. z is the latent variable of the learned sample. P is the encoder's conditional probability. Q is the decoder's conditional probability, and the last one D_{KL} is the Kullback-Leibler divergence of function. Furthermore, we change the way VAE learns, from the normal feed forward neural network to LSTM [12], as expressed by Eqs. (2)–(7).

$$i_t = \sigma(w_i[h_{t-1}, x_t] + b_i) \quad (2)$$

$$f_t = \sigma(w_f[h_{t-1}, x_t] + b_f) \quad (3)$$

$$o_t = \sigma(w_o[h_{t-1}, x_t] + b_o) \quad (4)$$

$$\tilde{c}_t = \tanh(w_c[h_{t-1}, x_t] + b_c) \quad (5)$$

$$c_t = f_t * c_{t-1} + i_t * \tilde{c}_t \quad (6)$$

$$h_t = o_t * \tanh(c_t) \quad (7)$$

where i_t is the input gate, f_t is the forget gate, o_t is the output gate, σ is the sigmoid function, w is the weight of each gate neurons, h_{t-1} is the output from previous LSTM cell, x_t is the current input, b is the bias of each gate, \tilde{c}_t is the candidate for cell state, and c_t is the final output of the LSTM model. The reason behind implementing LSTM to VAE is that the new VAE can precisely learn details of time-series signals for data generation.

By using a three-dimensional latent space, 3D Data Picker [5] is applied to randomly select samples on the latent space. Between two random samples, there are great number of samples that contain their characteristics. This technique can generate variety of artificial samples.

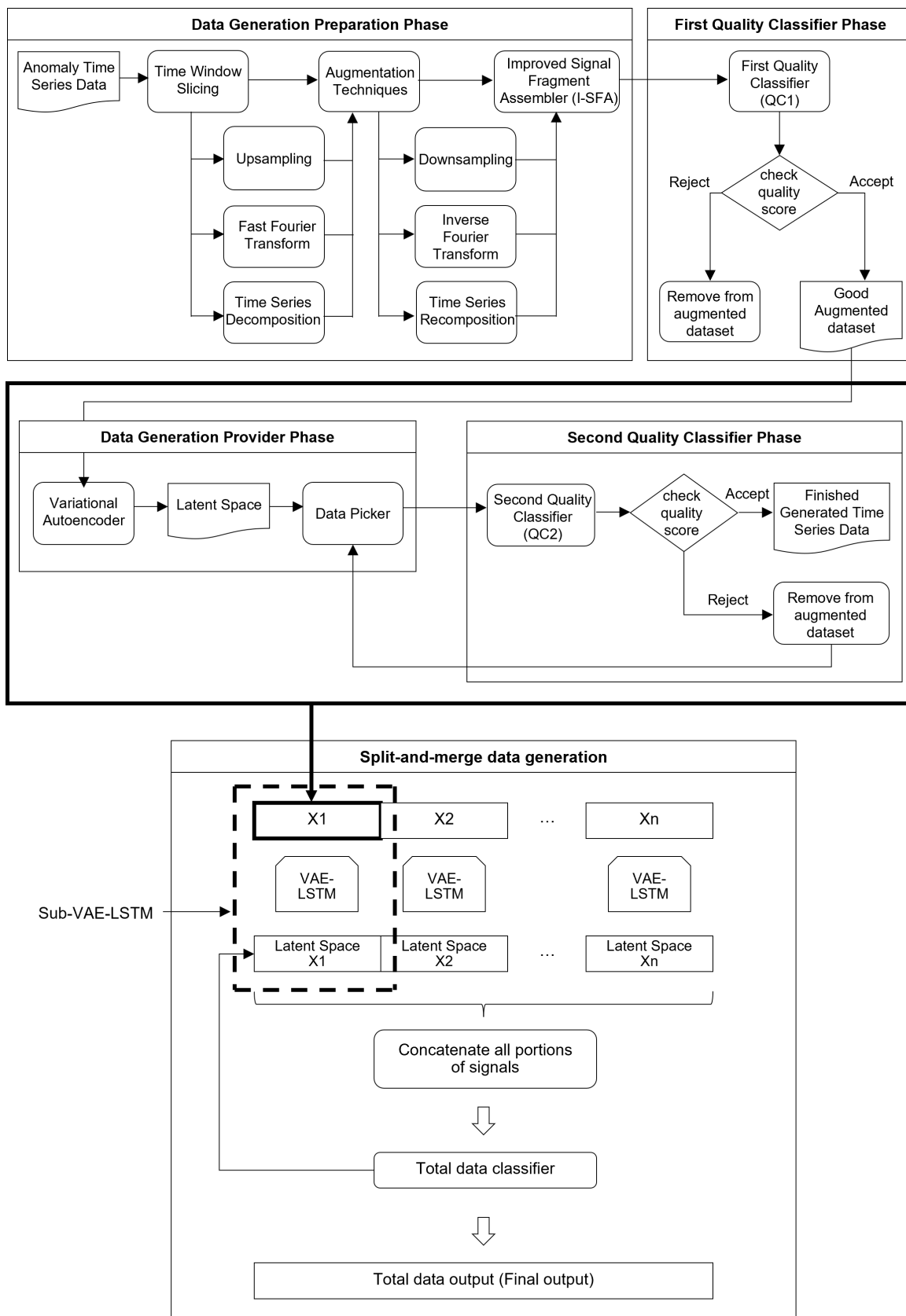


Fig. 1. A framework of i3DVAE-LSTM

TABLE I
PERFORMANCE COMPARISON BASED ON RAW DATASET

| Model | Accuracy (%) | Precision | Recall | F1-Score |
|----------------|-------------------------|------------------------|------------------------|------------------------|
| 3DVAE-ERSG [5] | 96.1375 ± 4.8745 | 0.9769 ± 0.0266 | 0.9545 ± 0.0601 | 0.9575 ± 0.0559 |
| 3DVAE-LSTM [6] | 98.3375 ± 2.6646 | 0.9881 ± 0.0186 | 0.9802 ± 0.0307 | 0.9827 ± 0.0274 |
| i3DVAE-LSTM | 99.7000 ± 0.9000 | 0.9983 ± 0.0052 | 0.9963 ± 0.0112 | 0.9971 ± 0.0088 |

TABLE II
PERFORMANCE COMPARISON BASED ON WADI DATASET

| Model | Accuracy (%) | Precision | Recall | F1-Score |
|----------------|-------------------------|------------------------|------------------------|------------------------|
| 3DVAE-ERSG [5] | 89.6750 ± 12.2098 | 0.8902 ± 0.1407 | 0.9059 ± 0.1023 | 0.8804 ± 0.1331 |
| 3DVAE-LSTM [6] | 98.3625 ± 3.3258 | 0.9840 ± 0.0318 | 0.9821 ± 0.0348 | 0.9811 ± 0.0371 |
| i3DVAE-LSTM | 99.8500 ± 0.4500 | 0.9991 ± 0.0027 | 0.9981 ± 0.0059 | 0.9986 ± 0.0043 |

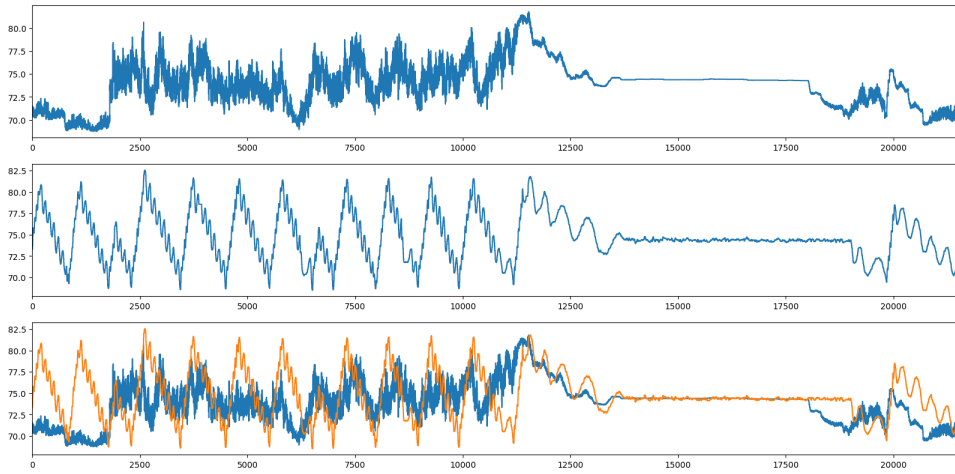


Fig. 2. An example of generated signal by 3DVAE-LSTM: The top graph depicts the generated signal, the middle graph showcases the original signal, and the bottom graph illustrates a comparative analysis between the two signals.

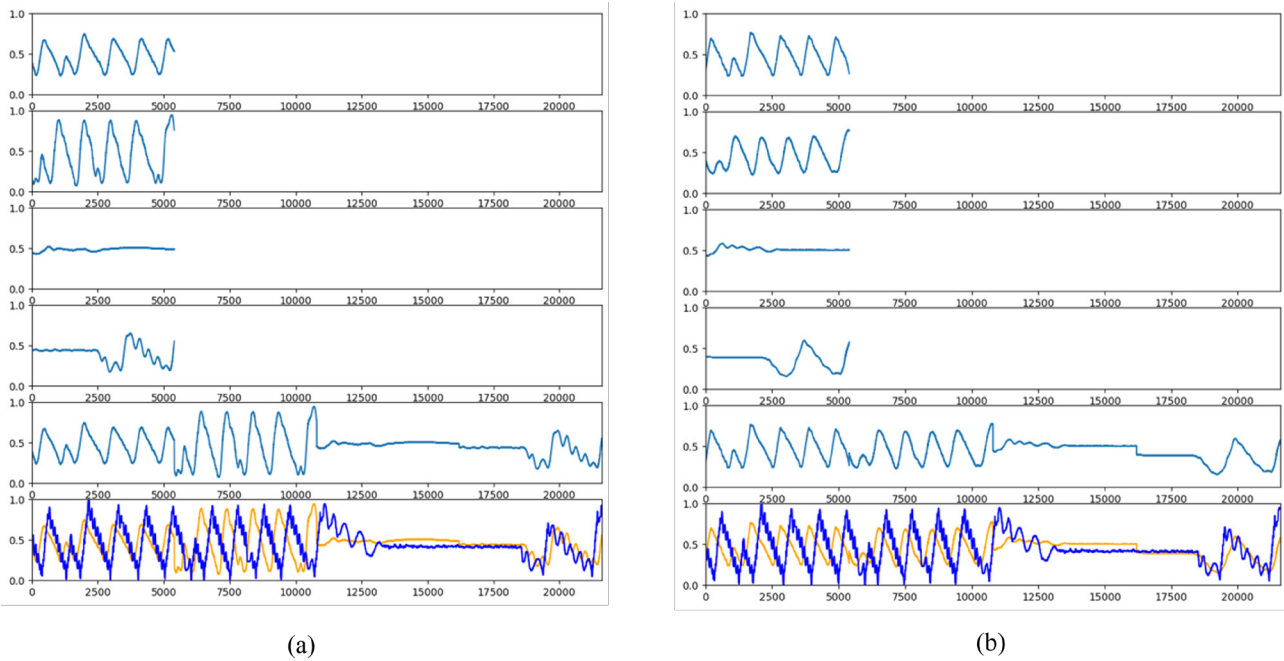


Fig. 3. Exemplary signals generated by i3DVAE-LSTM: (a) Signal generated by the first random sample, and (b) Signal generated by the second random sample.

D. Second Quality Classifier (QC2)

QC2 is comparable to QC1 in that it guarantees data quality. The score can be customized according to user requirements. An extra step involves selecting a new sample from the 3D latent space if the initial sample is deemed inadequate. This process continues until the desired number of samples is attained.

E. Split-and-Merge Data Generation

This section focuses on addressing data quality issues when dealing with long sequence signals. Fig. 1 illustrates the process, where a long sequence signal is divided into smaller fragments. Each fragment is then trained separately using sub-VAE-LSTM, resulting in a latent space for each fragment. The encoded fragments are decoded and concatenated together. The concatenated fragment is then passed through a total data classifier, which serves a similar purpose to QC2, in order to generate final outputs.

III. EXPERIMENTAL RESULTS

To assess the effectiveness of the proposed framework, the researchers generated anomalous signals using real-world datasets [13], [14]. Then, we used 1D-CNN [4], [5], [15] as an evaluator for multi-class anomaly classification tasks. The evaluator assigned higher scores to data with better quality and greater diversity generated by the proposed framework. The settings and results of this evaluation are outlined below.

A. Experimental Setup

For the performance comparison and replication, we provide parameter setting and environment setup in our experiments as follows:

- The sub-VAE-LSTM encoder was set 200 units to the first layer and 100 units to the second layer, while the decoder was set 100 units to the first layer and 200 units to the second layer. Here, four sub-VAE-LSTMs were used.
- Similar to [5], the framework and classification model were compiled and trained on 7 layers of the 1D-CNN [4], [5], [15], respectively. The rectified unit (ReLU) is an activation function for the fully connected layer.
- For the weight metric in QC1, we set S_{MAE} to 0.3 and $S_{histogram}$ to 0.7, while, in QC2, we set S_{MAE} to 0.7 and $S_{histogram}$ to 0.3.
- All experiments used 10-fold cross-validation to prevent bias or coincidence cases. (60% of training, 20% of validation, and 20% of testing)
- Each generated dataset for classification was trained with 4,000 samples, consisting of (i) 2,400 samples of three anomaly classes with 800 samples each and (ii) 1,600 samples of normal events. We only tested with real datasets.
- For evaluation metrics, we used accuracy, precision, and F1-score in four-digit decimal format.
- 3DVAE-ERSG [5] and 3DVAE-LSTM [6] were used as baselines, since they outperformed other data generation models. Most importantly, both baselines

were trained on the dataset with a sample long 10,800 seconds for each, whereas the proposed method, i3DVAE-LSTM, was trained on the same dataset but with a sample long 21,600 seconds for each.

- To assess the efficiency of the suggested approach, the researchers employed the Secure Water Treatment (SWaT) datasets sourced from iTrust [13] and the Water Distribution System (WADI) [13]. These datasets comprise readings from sensors placed on electronic parts within a water treatment experimental setup. The dataset includes regular operating conditions as well as purposely induced abnormal incidents, mimicking cyberattacks on the system. In the specific test case of the proposed method, the focus was on the raw water tank sensor (RAW), which is one of the available sensor data points in SWaT.

B. Results and Discussion

The purpose of these experiments is to evaluate the performance of different test methods using varying signal lengths. Two baseline models, specifically 3DVAE-ERSG and 3DVAE-LSTM, were trained on a dataset with samples lasting 10,800 seconds each. In contrast, the i3DVAE-LSTM was trained on a dataset containing samples lasting 21,600 seconds.

It is understandable why the 3DVAE-LSTM was not trained using the longer 21,600-second samples. To illustrate, Fig. 2 visually showcases our initial experiment, demonstrating the training of the 3DVAE-LSTM model with the extended 21,600-second samples. However, the signal generated from the 3DVAE-LSTM model, trained with the longer sequence, exhibits lower signal quality (the top graph of Fig. 2). One of the reasons supporting this phenomenon is that LSTM is indeed designed to work well with time series data due to its ability to capture temporal dependencies and patterns. Nonetheless, when confronted with very long sequences in time series data, LSTM encounters the vanishing gradient problem [16]. This problem arises when gradients become extremely small during the backpropagation process, resulting in the network struggling to learn long-range dependencies in the data. Consequently, this impacts the network's ability to effectively capture patterns.

As anticipated, the outcomes presented in Table I affirm that the i3DVAE-LSTM surpasses the baseline methods in terms of accuracy, precision, recall, and F1-score during testing on the RAW dataset. Moreover, Table II underscores the improved performance of the proposed method when assessed using the WADI dataset. This accomplishment comes from a strategy involving the segmentation of training signals into smaller fragments, each processed through a dedicated sub-VAE-LSTM segment as depicted in Fig. 1. By adopting this approach, we successfully mitigate the vanishing gradient problem, a persistent challenge in such architectures.

Furthermore, each sub-VAE-LSTM contributes to generating high-quality fragment signals, as demonstrated in Fig. 3. The initial four graphs (from top to bottom) in

Fig. 3 illustrate the generated signals from individual sub-VAE-LSTMs. Subsequently, the fifth graph displays the concatenation of these four fragment-generated signals, while the sixth graph provides a comparison between the generated (orange curve) and original (blue curve) signals. Significantly, the visual quality of the generated signals undergoes a notable enhancement.

This study highlights the importance of having varied generated data, especially when aiming to make accurate predictions. To ensure the model works well, it is crucial to have a wide range of diverse data available. Conversely, if the model only learns from the same repetitive data, it might become too similar to the original data and lead to overfitting—where it is too specialized for the training data and does not generalize well to new data. This is why the differences seen in Figs. 3 (a) and (b) are important. They show how diverse data helps prevent overfitting and improve the model's performance.

IV. CONCLUSION

The paper proposes an evaluation of the i3DVAE-LSTM framework's ability to generate extremely rare anomaly signals. This framework introduces a combination of LSTM and VAE to effectively handle time-series data. The data is first divided into small fragments for VAE training and then concatenated. The results obtained from i3DVAE-LSTM demonstrate its effectiveness in generating data that significantly enhances the training of multi-class classification models, leading to improved performance.

The experimental outcomes highlight that classification models trained using data generated by i3DVAE-LSTM consistently outperform baseline models across all measured aspects. Additionally, our investigation of the i3DVAE-LSTM framework, based on the conducted experiments, reveals a pivotal factor that contributes to the improved classification performance: the prevention of the vanishing gradient problem through the utilization of sub-VAE-LSTM.

Looking ahead, our future research aims to expand the scope by conducting tests with additional datasets. This broader testing will provide a more comprehensive understanding of the framework's applicability and effectiveness.

REFERENCES

- [1] P. Singh and V. Pankajakshan, "A deep learning based technique for anomaly detection in surveillance videos," in *2018 Twenty Fourth National Conference on Communications (NCC)*, 2018, pp. 1–6.
- [2] A. Mikołajczyk and M. Grochowski, "Data augmentation for improving deep learning in image classification problem," in *2018 International Interdisciplinary PhD Workshop (IIPhDW)*, 2018, pp. 117–122.
- [3] T. Chalongvorachai and K. Woraratpanya, "Adgas: An advanced data generation for anomalous signals," *Lecture Notes in Networks and Systems*, 2021.
- [4] —, "A data generation framework for extremely rare case signals," *Heliyon*, p. e07687, 2021. [Online]. Available: <https://www.sciencedirect.com/science/article/pii/S2405844021017904>
- [5] —, "3dvae-ersg: 3d variational autoencoder for extremely rare signal generation," in *2021 13th International Conference on Information Technology and Electrical Engineering (ICITEE)*, 2021, pp. 177–182.
- [6] T. Kaewkiriya and K. Woraratpanya, "3dvae-lstm for extremely rare anomaly signal generation," in *2022 14th International Conference on Information Technology and Electrical Engineering (ICITEE)*, 2022, pp. 229–234.
- [7] —, "Improvement of 3dvae-lstm for extremely rare anomaly signal generation," in *2023 13th Joint Symposium on Computational Intelligence (Jsci)*, 2023.
- [8] T. T. Um, F. Pfister, D. Pichler, S. Endo, M. Lang, S. Hirche, U. Fietzek, and D. Kulic, "Data augmentation of wearable sensor data for parkinson's disease monitoring using convolutional neural networks," *Proceedings of the 19th ACM International Conference on Multimodal Interaction*, 2017.
- [9] W. Cochran, J. Cooley, D. Favin, H. Helms, R. Kaenel, W. Lang, G. Maling, D. Nelson, C. Rader, and P. Welch, "What is the fast fourier transform?" *Proceedings of the IEEE*, vol. 55, no. 10, pp. 1664–1674, 1967.
- [10] P. V and U. Rao, "Time series decomposition model for accurate wind speed forecast," *Renewables: Wind, Water, and Solar*, vol. 2, 11 2015.
- [11] D. P. Kingma and M. Welling, "An introduction to variational autoencoders," *Foundations and Trends® in Machine Learning*, vol. 12, no. 4, pp. 307–392, 2019. [Online]. Available: <http://dx.doi.org/10.1561/22000000056>
- [12] S. Hochreiter and J. Schmidhuber, "Long short-term memory," *Neural computation*, vol. 9, no. 8, pp. 1735–1780, 1997.
- [13] J. Goh, S. Adepu, K. N. Junejo, and A. Mathur, "A dataset to support research in the design of secure water treatment systems," in *Critical Information Infrastructures Security*. Cham: Springer International Publishing, 2017, pp. 88–99.
- [14] Singapore University of Technology and Design (SUTD), "Dataset characteristics," https://itrust.sutd.edu.sg/itrust-labs_datasets/dataset_info/, 2017, accessed: 2021-06-17.
- [15] S. Kiranyaz, O. Avci, O. Abdeljaber, T. Ince, M. Gabbouj, and D. J. Inman, "1d convolutional neural networks and applications: A survey," *Mechanical Systems and Signal Processing*, vol. 151, p. 107398, 2021.
- [16] S. Hochreiter, "The vanishing gradient problem during learning recurrent neural nets and problem solutions," *International Journal of Uncertainty, Fuzziness and Knowledge-Based Systems*, vol. 6, no. 2, pp. 107–116, 1988. [Online]. Available: <http://dx.doi.org/10.1142/S0218488598000094>

Spatio-temporal ESN-based Model for Predicting Water Level in Yangtze River

1st Zongying Liu

Faculty of Navigation
Dalian Maritime University
Dalian 116026, China
liuzongying@dmlu.edu.cn

2nd Wenru Zhang

Faculty of Navigation
Dalian Maritime University
Dalian 116026, China
zwr@dmlu.edu.cn

3rd Mingyang Pan

Faculty of Navigation
Dalian Maritime University
Dalian 116026, China
panmingyang@dmlu.edu.cn

4th Feifan Li

Faculty of Navigation
Dalian Maritime University
Dalian 116026, China
lff1120221025@dmlu.edu.cn

Abstract—Water level prediction plays a vital role in navigation, particularly for ports and harbors, which attracts more attention in the academic domain. The conventional machine learning algorithms, such as support vector regression and artificial neural network, are commonly employed for predicting water level. However, these algorithms have the high computational cost, which directly impacts on their performance and implementation. Recent, a typical randomization-based algorithm called echo state network obtains the good performance with high efficiency in aspect of water level prediction. To enhance forecasting performance and overcome its own limitations, this study proposes three approaches for enriching features in the conventional echo state network. Firstly, we propose the random bar features selection approach to select useful features. Secondly, a novel structure of ESN is designed to capture much richer temporal features. Next, a spatial feature extraction method is proposed based on a latent correlation and graph neural network to capture the spatial features. Based on these methods, this study proposes a Spatio-temporal ESN-based model (ST-ESN). The experimental results and statistical analysis represent that our proposed model has superior forecasting ability in water level prediction rather than other compared models. It not only overcomes the limitation of single features consideration, but it also provides the data support from the high accuracy water level prediction data, which is benefited in managing water-land transportation, flood protection, and ship route management.

Index Terms—Graph Neural Network, Reservoir Computing, Temporal Features, Spatial Features, Water Level Prediction

I. INTRODUCTION

Time series prediction is one of a general problem in pattern recognition. It is considered as a supervised learning task that seeks the best fitting relationship between a set of historical input features and its corresponding target values, which is used to forecast the future observations. There are many techniques in time series prediction that try to achieve high precision performance and reduce forecasting errors and losses. Some conventional machine learning algorithms demonstrate their outstanding prediction ability and efficiency in the different domains, such as prediction of COVID-19 corona virus pandemic based on support vector regression, random vector functional link for financial & economic time series prediction, stock price prediction based on back-propagation neural network, forecasting the coal price based on the variant of radial basis function neural network, and so forth.

Besides, water level prediction is also one of hot topic in the time series prediction. Recent years, it attracts more attention from academic and industrial filed, which provides the assistants on flood warning, safety navigation, and channel management. Take the classical machine learning algorithms and their variants as examples, a optimization algorithm — Genetic Algorithm — with a Back Propagation (BP) neural network model was proposed for water-level prediction [1]. It not only settled the limited optimization and local convergence problem, but it also improved the forecasting accuracy and its stability in the flood disaster monitoring. Sahu et al. proposed a multi-layer model based on perceptron neural network to forecast ground water level, which achieved the best forecasting performance in one year period at three different groundwater well locations (Butte, Shasta, and Tehama) in California [2]. Moreover, a data-driven models — Support Vector Regression (SVR) and Artificial Neural Network (ANN) were employed to predict the ground water level [3]. These two classical machine learning algorithms played a significant role in forecasting groundwater levels of confined and unconfined systems at 1-, 2-, and 3-month ahead. Its comparison experiments proved that support vector regression obtained better performance in short-term prediction than that of artificial neural network. Although these classical machine learning algorithms and their variants achieved good performance in water level prediction, they still appeared some limitations in the process of prediction. Their unique structure of neural networks increase the complexity computation and the limited features consideration restricts the forecasting performance. For example, the computation of kernel trick of SVR will become giant when input features are large-scaled. The loops between forward-propagation and back-forward in BP grow the times of computation in the training process.

Moreover, due to water level prediction belonging to the branch of time series prediction, Recurrent Neural Network (RNN) extracts the rich time series features from original water level data, which are benefited to increase the accuracy of prediction. RNN extracts the temporal features from water level data and builds the relationship between temporal features and target values. However, the majority of RNN and its variants only focus on temporal features and employ them to build prediction models. For example, Xu et al.

proposed a combination model based on Autoregressive Integrated Moving Average Model (ARIMA) and RNN for water level prediction in Taihu [5]. The linear correlation component from ARIMA and nonlinear component from RNN were constructed by RNN. Its experiment proved that the proposed model achieved better results than that of RNN and ARIMA. Zhang and Yang proposed a water level prediction model based on RNN and designed a experiment to compare the forecasting performance among proposed model, ANN, and Long Short Term Memory (LSTM) [4]. There were sufficient evidence to show that the proposed based-RNN model was not only more efficient on the intelligent prediction of water level in reservoirs, but it also had fewer parameters than others. At the same time, LSTM as the highest level of attention in type of RNN also achieved the good performance in water level prediction [6]–[8]. However, their complex structure and numerous parameters impact on the training efficiency and application of models in the real world.

Recent years, a type of recurrent neural network called Echo State Network (ESN) is widely used in the field of time series prediction. The main of advantages of ESN is the high training efficiency because of its random weights selection for input weights and internal weights. Moreover, it also extracts the temporal features using reservoir states in ESN, which achieves the water level prediction with high accuracy. Liu et al. proposed a multi-step water level prediction based on ESN, which obtained the best multi-step forecasting performances in water level of Yangtze river and Chao Phraya river than that of compared randomization-based model [9]. However, it still only focused on the temporal features to build a multi-step water level prediction model. Especially for water level of water stations in inland river, the spatial features deeply influence on the forecasting ability of water level in the training process of model.

Based on above-discussed contents regarding water level prediction, to solve the drawbacks of machine learning algorithms and extract richer features in the process of building model for water level prediction, this study designs a spatio-temporal water level prediction model. It provides a new structure of randomization-based model — ESN by a direct link between original input features and reservoir states and using a random bar feature selection approach. This structure not only filters the redundant features by random bar approach but it also enriches the temporal features. Besides, the latent correlation approach based on attention mechanism and ESN is used to transform time series data to graph structure data, which explores the graphic relationship in the time series features. Then, the spatial features from the original time series features are extracted by Graphic Neural Network (GNN). The main contributions of this study are summarized as follows:

- 1) A random bar features selection approach is proposed to reduce the redundant samples from training data.
- 2) A new structure of ESN is proposed for extracting temporal features, which obtains the much richer temporal features.
- 3) A spatial structure data generator is proposed, which

employs the reservoir states of ESN and attention mechanism to generate spatial structure data from time series data.

- 4) A combination model, including temporal features extraction and spatial features extraction, is proposed, which has superior forecasting ability in water level prediction.

The paper is organized as follows. Section II briefly states the ESN algorithm. The following section introduces the random bar feature selection technique, graphic data transformation, and the proposed algorithm. Section IV describes an experiment framework. Section V presents a performance comparison with the conventional randomization-based models on a well-studied set of real-world data set. Finally, the conclusion is shown in Section VI.

II. REVIEW OF ESN

Before introducing the proposed methods, the detail of ESN is represented. It was proposed by Jaeger [13], which belonged to the type of reservoir computing. It employed a recurrent neural network with sparse connections among hidden neurons. Assume that the reservoir states and output values are represented as S and Y , separately. To achieve the training process, the least squares problem is designed as following equation:

$$\min_{\beta} \|\beta S - Y\|^2 \quad (1)$$

where β is output weights of ESN. In the training part of ESN, the activation function $F(\cdot)$ is commonly defined as tanh or sigmoid function in the hidden layer. Suppose that there are Q number of hidden neurons in ESN, the input weights ($W \in R^{Q \times L}$) and internal weights ($W_{in} \in R^{Q \times Q}$) are selected randomly with uniformed distribution. The reservoir state (s) can be calculated based on the random selected weights and input samples. The first reservoir state is defined as $s(1) = Wx(1)$. Then, the following $(n + 1)$ -th reservoir state ($s(n + 1)$) can be computed by Eq.(2).

$$s(n + 1) = F(Wx_{n+1} + W_{in}s(n) + W_{fb}y_n) \quad (2)$$

where W_{fb} represents the output feedback matrix, here, W_{fb} is null because the output feedback is not required; x_{n+1} is the $(n + 1)$ -th sample of input feature (x); and y_n represents the n -th output sample.

Moreover, Jaeger also introduced another significant structure of ESN named leaky-ESN [12]. In leaky-ESN, the leaking rate (α) and the compound gain (ρ) were defined and applied to compute the leak integrator neurons. It is assume that ρ is equal to one. Its reservoir state can be simply represented as Eq.(3).

$$s(n + 1) = (1 - \alpha)s(n) + \alpha F(Wx_{n+1} + W_{in}s(n)) \quad (3)$$

The output weights (β) of leaky-ESN can be computed by Eq.(4).

$$\beta = S^T (SS^T + \lambda I)^{-1} Y \quad (4)$$

where S are the reservoir states which are combined with M number of reservoir state (s); Y indicates the training target values; T is the transpose operator; λ is the coefficient parameter, and I is an identity matrix.

Then, the corresponding forecasting values (\hat{y}) can be computed by Eq.(5).

$$\hat{y} = S^T \beta \quad (5)$$

III. METHODOLOGY

In this section, we propose a new spatio-temporal ESN based model for water level prediction. To ease the burden of computation and filter redundant features, a random bar feature selection approach is proposed and applied to deal with original training data. Moreover, a new structure of ESN is designed to rich training features, which enhances the forecasting ability. Besides, in the spatial features, this study proposes a latent correlation approach to transform time series data to the graph structure. Then, GNN is employed to extract the spatial features. Finally, spatial feature and temporal features are combined to be a mixed feature for building a forecasting model. The details of each approach and proposed model are introduced as the following subsections.

A. Temporal Features based on New Structure of ESN

Time series data contains numerous features. Some of them are useful while others probably are irrelevant or noisy. To avoid the influence of redundant features and noise, this study proposes a random bar features selection approach. At the same time, we employ a new structure ESN to extract temporal features from filtered training data based on random bar. It not only extracts the temporal features from time series data by ESN characteristic, but it also riches the input features due to the new structure of ESN.

Firstly, random bar approach is used to filter the redundant or unimportant features from the original training data X . In this selection approach, a random vector ($rv = [r_1, \dots, r_Z]$) is generated. Then, it is added randomly as a new feature to the original training features, which can be represented as Eq.(6), where L is the number of the training sample of original training features(VR).

$$VR = \begin{bmatrix} x_{1,1} & \cdots & x_{1,Z} \\ \vdots & \ddots & \vdots \\ r_1 & \cdots & r_Z \\ \vdots & \ddots & \vdots \\ x_{L,1} & \cdots & x_{L,Z} \end{bmatrix} \quad (6)$$

Based on the generated features matrix VR, Principal Component Analysis (PCA) is applied to identify the patterns and relationships among features. This analysis enables the ranking for the importance of features. After ranking, the position of random vector is defined as the standard measurement for the useful features. The features with the position exceeding that of the random vector mean are useful, otherwise they are useless or redundant. Based on this standard measurement from the position of random bar, we remove the irrelevant

features (including random vector) and their corresponding target values. Because this study focuses on time series prediction, we are supposed to restore the sequence of selected training samples from random bar selection approach. Finally, the processed training features (V) and its corresponding target values (VT) are shown as $V_i = [x_{i,1}, x_{i,2}, \dots, x_{i,Z}]$ and $VT_i = [x_{i,1}, x_{i,2}, \dots, x_{i,P}]$, respectively, where $i = [1, 2, \dots, \bar{L}]$, \bar{L} is number of selected samples based on random bar features selection approach, P is the size of prediction horizon. The main processes is shown in Figure 1.

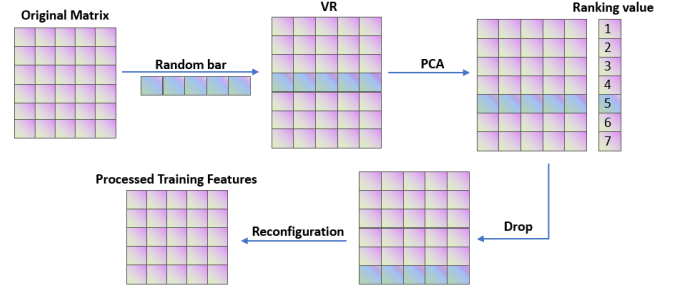


Fig. 1. Random Bar selection Approach

Next, the processed training data is utilized in new structure of ESN. A direct link is designed between input features and reservoir states, which combines the reservoir states with input features to be a transformer hidden matrix with richer the features. The transformer hidden matrix (χ_i) can be represented as $\chi_i = [x_{i,1}, x_{i,2}, \dots, x_{i,Z}, s(i)]$, where i is the number of training samples, $i = [1, 2, \dots, \bar{L}]$, \bar{L} is the processed training size based on random bar features selection approach; Z is the time window; $x_{i,1}$ represents the i -th sample from the first column. The mathematical representation of transformer hidden matrix (χ) is shown in Eq. (7). It represents the temporal features based on new structure of ESN and random bar selection approach.

$$\chi = \begin{bmatrix} x_{1,1} & x_{1,2} & \cdots & x_{1,Z} & s(1) \\ x_{2,1} & x_{2,2} & \cdots & x_{2,Z} & s(2) \\ \vdots & \vdots & \ddots & \vdots & \vdots \\ x_{\bar{L},1} & x_{\bar{L},2} & \cdots & x_{\bar{L},Z} & s(\bar{L}) \end{bmatrix} \quad (7)$$

B. Spatial Features based on Latent Correlation

To capture the spatial features of time series data, this study employs self-attention mechanism to learn latent correlations based on time series data for transforming time series data to graphic structure data. Then, GNN is utilized to extract its spatial features. The detail of extraction is introduced as follows:

First, the processed training features V by random bar features selection approach are employed to compute the reservoir states by conventional ESN. The reservoir states are represented by (S). Next, we utilize the reservoir state (S) as a representation of the entire time series to compute the

adjacency matrix (U) through self-attention mechanism. It can be computed by Eq.(8).

$$Q = SU^Q, K = SU^K, U = \text{Softmax}\left(\frac{QK^T}{\sqrt{d}}\right) \quad (8)$$

where Q and K represent the query and key in the self-attention mechanism, respectively. They are computed through linear projections using learnable parameters U^Q and U^K within the attention mechanism, d represents the hidden dimension size of Q and K .

Furthermore, we denote the graphical structure data as $\mathcal{G} = (V, U)$, where V is our proposed training features ($V \in \mathbb{R}^{\bar{L} \times Z}$), \bar{L} is the number of selected time-series (nodes) based on random bar features selection approach, and Z is the size of time window. The matrix $U \in \mathbb{R}^{\bar{L} \times \bar{L}}$ represents the adjacency matrix of the graph, where $u_{ij} > 0$ indicates an edge connecting nodes i and j , and the value u_{ij} represents the strength of this edge.

Finally, we employ the graph structure \mathcal{G} as input features and utilize the baseline model GCN [16] to calculate the graph matrix G , which captures the spatial features. The mathematical representation can be computed by Eq.(9)

$$G = \sigma\left(D^{-\frac{1}{2}}UD^{-\frac{1}{2}}\right) \quad (9)$$

where, U is the adjacency matrix of the graph \mathcal{G} ; the D is can be represented as $D = [D_{1,1}, D_{2,2}, \dots, D_{i,i}]$; $\sigma(\cdot)$ denotes an activation function, such as the $\text{ReLU}(\cdot) = \max(0, \cdot)$; and D_{ii} can be computed by Eq.(10).

$$D_{ii} = \sum_j U_{ij} \quad (10)$$

C. Spatio-temporal ESN-based Model

Based on temporal and spatial features extraction method, this study proposes a Spatio-temporal ESN-based model (ST-ESN) for time series prediction. The main structure of proposed model is shown in Figure 2.

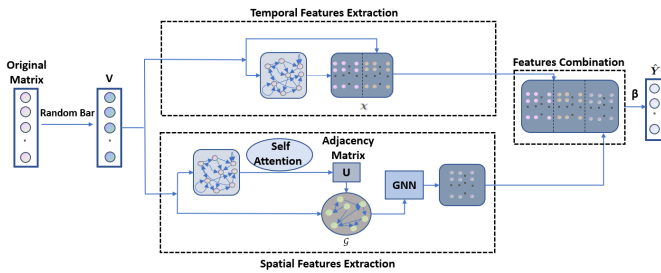


Fig. 2. Spatio-temporal ESN-based Model

There are three main processing categories in the ST-ESN, including temporal features extraction, spatial features extraction, and features combination. Before going through these features extraction phases, the original input features are processed by random bar features selection approach to obtain our final processed Training features (V) for our proposed model. In the temporal features extraction phase, we employ

the new structure of ESN to compute the transformer hidden matrix (χ) using Eq.(7). Its processing detail is introduced in Section III-A. At the same time, our proposed latent analysis based reservoir states of ESN and self-attention mechanism is used to compute the adjacency matrix (U). This mathematical representation is shown in Eq.(8). Subsequently, based on the adjacency matrix U and processed training features (V), the graphical structure data (\mathcal{G}) is generated. Then, the spatial features are extracted by Eq.(9). The third phase combines the temporal features with the spatial features. The combined matrix is represented by ψ , where $\psi = [\chi, \mathcal{G}]$. The output weights (β) of ST-ESN can be computed by Eq.(11).

$$\beta = \psi^T \left(\psi \psi^T + \lambda I \right)^{-1} \mathbf{VT} \quad (11)$$

where \mathbf{VT} is the selected target values by random features selection approach. Its forecasting values (\hat{Y}) are computed by Eq.(12).

$$\hat{Y} = \psi^T \beta \quad (12)$$

IV. EXPERIMENT FRAMEWORK

The performance of the proposed model ST-ESN is compared with several models, including ESN, GNN, ESN with Random bar (Ran-ESN), a new structure of ESN (Di-ESN), as well as temporal features based on ESN (T-ESN). The data sets are conducted on five water level datasets from five Chinese water stations located in the Yangtze River in China. The details of the data sets are explained in Section IV-A followed by experimental settings in Section IV-B. Finally, the experimental results will be shown and discussed.

A. Data Description

We select five water stations from Yangtze River in China for testing the forecasting ability of our proposed model. Four water level stations, including AnQing (AQ), BaiLuan (BL), WuHu (WH), and ZhengJiang (ZJ), recorded time series water level data at 8am every day from 07/09/1990 to 08/13/2016. Only MaoPing (MP) station recorded the daily water level data from 10/28/2016 to 03/22/2018. Then, these data sets are transformed to be matrix based on data transformation method [14] for training and testing models.

B. Experimental Design and Setting

The experiments are conducted on a laptop with Window 11, 8th Gen Intel Core i7 Processor with 16GB of memory. The compared models and proposed model are measured by Mean Square Error (MSE) and Symmetric Mean Absolute Percentage Error (SMAPE) on five water level data sets.

To evaluate the performance of our proposed methods and model, we design two experiment. The first experiment shows the random bar features selection approach, new structure of ESN and the temporal feature based on the new structure of ESN play the role in the water level prediction. It compares the differences in the performances of four models, including ESN, Ran-ESN, Di-ESN, T-ESN. The second experiment compares the performance of proposed model ST-ESN with that

of others, which shows the differences between the proposed model with temporal and spatial features and other models.

In all experiments, we defined the prediction horizon P and time window Z as 5 and 20, respectively. The five forecasting steps and average performance in 1-5 period are evaluated on five water level data sets for all models. These data sets are separated by the proportion 70% and 30% for training and testing sets, respectively. To compare fairly, the hyper-parameter(s) of each algorithm are required to be tuned. This study employs a simple grid search for each algorithm in these two experiments. In model ESN, Ran-ESN, Di-ESN, T-ESN, GNN, and ST-ESN, the number of hidden neurons are varied in a range of [10, 20, ..., 100] with 10 intervals. The other two parameters of these models, including the input scaling and the spectral radius, are searched in the range of [0.05, 0.95] with 0.05 intervals.

V. RESULTS AND DISCUSSION

The forecasting performances of all compared models with MSE and SMAPE on the five data sets are shown in Table I. In the first experiment, comparing the performances of the average prediction period among three models, the results indicated that T-ESN achieved the best performance on 3/5 datasets. For the 1-5 prediction period, the average values of the T-ESN model across all three datasets were 0.028 for MSE and 8.18% for SMAPE. The minimum value of MSE and SMAPE appeared in MP data with 2.5E-06 and 0.03%, respectively. Conversely, the WH data had the highest values, reaching at 1.98E-02 for MSE and 13.18% for SMAPE. The AQ dataset demonstrated that the Di-ESN method achieved the best performance in MSE and the ZJ dataset showed that the Di-ESN method achieved the best performance in SMAPE. There is evidence to indicate that T-ESN outperformed ESN, Di-ESN, and Ran-ESN during the 1-5 prediction period. Moreover, except for the ZJ data, the T-ESN model achieved the best SMAPE performance compared to the ESN, Ran-ESN, and Di-ESN models at each step for the AQ, BL, MP, and WH datasets. In the ZJ data, the Di-ESN method achieved the best SMAPE performance. For MSE, in the AQ data, the Di-ESN achieved the best performance in the 1st, 2nd, 4th, and 5th steps, except for the 3rd step where the T-ESN got the best performance. In the MP data, the Ran-ESN performed the best in the 1st and 2nd steps, while the T-ESN outperformed in the remaining steps. In the WH data, except for the 3rd step where the Ran-ESN performed the best, the T-ESN achieved the best performance in the other steps. In all other data sets, the T-ESN method achieved the best performance. Overall, our proposed model T-ESN plays a vital role in water level prediction.

In the second experiment, comparing the performance of the average prediction period across that of rest of models, the results indicated that ST-ESN outperformed all other models on all data sets. In terms of each-step prediction, T-ESN model demonstrated the best performance for both MSE and SMAPE in the first step of WH data. On ZJ data, T-ESN achieved the best performance for MSE in the second and third steps of

water level prediction. On ZJ data, Di-ESN achieved the best performance for SMAPE in the second step. Overall, ST-ESN outperformed the other models in comparison, demonstrating its successful application across various types of real water level data. It not only deal with water level prediction in various areas but it was also contributed to the monitoring and forecasting of water levels in water stations, thereby ensuring navigation safety.

Furthermore, we employed a statistical method known as the "Friedman Rank Test" to validate the performance of our proposed model against the tested models. The null hypothesis of test is that there is no difference among the mean rank of algorithms. The accuracy (1-SMAPE) was used to build data for Friedman Rank Test. SPSS was employed to run this test. According to results, we report the mean rank across all data sets of each model, as shown in Table II. At significant level $\alpha = 0.05$, this test gave p-value = 0.002 with $\chi^2 = 19.05$ from report of Friedman Rank Test in SPSS. Based on statistical results, we can reject the null hypothesis. Besides, Table II showed the mean rank values in ascending order for each data set. The worst model — ESN and GNN — was given the first rank, while the best model (ST-ESN) was the sixth rank in this situation. Therefore, it proved that our proposed model ST-ESN was the best model on all data sets.

VI. CONCLUSION

This paper proposes a new model called ST-ESN. It utilizes a newly proposed Random Bar selection approach to select relevant and significant input features. Additionally, the new structure of ESN is designed to extract and rich the temporal features. Next, the latent correlation approach, which combines the reservoir states of ESN and attention mechanism, is employed to transform time series data into a graphical structure data, enabling the exploration of the graphical relationships within the time series features. Finally, based on temporal and spatial features extraction method, this study introduces a Spatio-temporal ESN-based model (ST-ESN) for water level prediction. The experiments indicate that ST-ESN has superior forecasting ability in water level prediction rather than other compared models. In the future, this study will enhance our algorithm for online learning by adjusting the connection of the hidden neurons in the network to improve performance.

ACKNOWLEDGMENTS

This research was partially sponsored by 2023 DMU navigation college first-class interdisciplinary research project (2023JXA(07)), and Research on Guangxi Digital Port and Shipping Integration Application Architecture (Grant No.2021AB07045).

REFERENCES

- [1] Chen N, Xiong C, Du W, et al. An improved genetic algorithm coupling a back-propagation neural network model (IGA-BPNN) for water-level predictions[J]. *Water*, 2019, 11(9): 1795.
- [2] Sahu R K, Müller J, Park J, et al. Impact of input feature selection on groundwater level prediction from a multi-layer perceptron neural network[J]. *Frontiers in Water*, 2020, 2: 573034.

TABLE I
PERFORMANCE OF ST-ESN VS. COMPARED MODELS ON FIVE WATER LEVEL DATA SETS

| data | model | 1 | 2 | 3 | 4 | 5 | 1-5 | 1 | 2 | 3 | 4 | 5 | 1-5 |
|------|---------|-----------------|-----------------|-----------------|-----------------|-----------------|-----------------|-------------|--------------|--------------|--------------|--------------|--------------|
| | | MSE | | | | | | SMAPE | | | | | |
| AQ | ESN | 6.77E-03 | 8.11E-03 | 1.15E-02 | 3.71E-02 | 2.89E-02 | 1.85E-02 | 9.56 | 12.47 | 14.66 | 20.65 | 29.87 | 17.44 |
| | Di-ESN | 5.97E-03 | 7.61E-03 | 1.04E-02 | 1.01E-02 | 1.07E-02 | 8.96E-03 | 7.52 | 10.16 | 12.83 | 13.16 | 15.49 | 11.83 |
| | Ran-ESN | 7.06E-03 | 9.49E-03 | 1.05E-02 | 1.12E-02 | 1.17E-02 | 1.00E-02 | 7.36 | 10.43 | 11.83 | 14.15 | 14.61 | 11.68 |
| | T-ESN | 6.78E-03 | 8.73E-03 | 9.19E-03 | 1.13E-02 | 2.29E-02 | 1.18E-02 | 7.32 | 9.77 | 11.25 | 13.84 | 14.13 | 11.26 |
| | GNN | 3.24E-03 | 4.23E-03 | 3.47E-03 | 1.96E-03 | 1.86E-03 | 2.95E-03 | 20.05 | 23.03 | 20.98 | 15.23 | 14.08 | 18.67 |
| | ST-ESN | 1.62E-04 | 2.47E-04 | 3.25E-04 | 2.51E-04 | 2.20E-04 | 2.41E-04 | 2.17 | 2.68 | 3.09 | 2.83 | 2.87 | 2.72 |
| | | MSE | | | | | | SMAPE | | | | | |
| BL | ESN | 6.13E-03 | 1.81E-02 | 1.02E-02 | 1.36E-02 | 2.11E-02 | 1.38E-02 | 10.51 | 26.74 | 16.38 | 21.10 | 29.62 | 20.87 |
| | Di-ESN | 5.37E-03 | 7.01E-03 | 7.96E-03 | 9.21E-03 | 9.44E-03 | 7.80E-03 | 7.74 | 10.45 | 12.45 | 14.02 | 15.03 | 11.94 |
| | Ran-ESN | 5.31E-03 | 6.99E-03 | 8.21E-03 | 9.44E-03 | 9.53E-03 | 7.90E-03 | 7.61 | 10.32 | 11.94 | 13.85 | 14.32 | 11.61 |
| | T-ESN | 5.30E-03 | 6.78E-03 | 7.91E-03 | 8.78E-03 | 9.23E-03 | 7.60E-03 | 7.42 | 9.70 | 11.62 | 13.02 | 14.08 | 11.17 |
| | GNN | 2.93E-03 | 2.52E-03 | 2.30E-03 | 1.83E-03 | 1.70E-03 | 2.25E-03 | 7.22 | 9.70 | 11.51 | 12.95 | 14.12 | 11.10 |
| | ST-ESN | 1.79E-04 | 4.18E-04 | 5.60E-04 | 5.88E-04 | 5.41E-04 | 4.57E-04 | 1.07 | 2.15 | 2.69 | 2.87 | 2.97 | 2.35 |
| | | MSE | | | | | | SMAPE | | | | | |
| MP | ESN | 4.10E-05 | 2.43E-04 | 1.30E-03 | 2.26E-03 | 2.30E-03 | 1.23E-03 | 0.14 | 0.39 | 0.87 | 1.18 | 1.17 | 0.75 |
| | Di-ESN | 2.21E-05 | 6.76E-05 | 1.61E-04 | 2.08E-04 | 3.49E-04 | 1.61E-04 | 0.07 | 0.15 | 0.25 | 0.28 | 0.38 | 0.23 |
| | Ran-ESN | 2.19E-05 | 6.28E-05 | 1.45E-04 | 2.36E-04 | 3.53E-04 | 1.64E-04 | 0.07 | 0.14 | 0.21 | 0.28 | 0.33 | 0.21 |
| | T-ESN | 2.22E-05 | 6.50E-05 | 1.42E-04 | 2.15E-04 | 3.30E-04 | 1.55E-04 | 0.07 | 0.14 | 0.21 | 0.26 | 0.33 | 0.20 |
| | GNN | 4.00E-02 | 3.59E-02 | 9.67E-02 | 9.94E-02 | 7.59E-02 | 6.96E-02 | 7.12 | 6.52 | 19.87 | 20.14 | 17.36 | 14.20 |
| | ST-ESN | 2.65E-06 | 4.60E-07 | 2.02E-07 | 7.49E-06 | 1.64E-06 | 2.49E-06 | 0.04 | 0.01 | 0.01 | 0.07 | 0.03 | 0.03 |
| | | MSE | | | | | | SMAPE | | | | | |
| WH | ESN | 1.47E-02 | 2.45E-02 | 3.84E-02 | 3.61E-02 | 5.72E-02 | 3.42E-02 | 12.23 | 17.64 | 25.75 | 19.11 | 22.99 | 19.54 |
| | Di-ESN | 1.23E-02 | 1.80E-02 | 2.17E-02 | 2.65E-02 | 2.71E-02 | 2.11E-02 | 8.42 | 11.81 | 14.98 | 16.46 | 17.73 | 13.88 |
| | Ran-ESN | 1.21E-02 | 1.78E-02 | 2.23E-02 | 2.32E-02 | 2.64E-02 | 2.04E-02 | 8.08 | 11.61 | 14.48 | 15.77 | 17.56 | 13.50 |
| | T-ESN | 1.20E-02 | 1.75E-02 | 2.09E-02 | 2.35E-02 | 2.50E-02 | 1.98E-02 | 7.89 | 11.18 | 13.84 | 15.80 | 17.18 | 13.18 |
| | GNN | 1.22E-02 | 7.64E-03 | 7.03E-03 | 7.58E-03 | 6.40E-03 | 8.17E-03 | 27.11 | 22.64 | 22.05 | 22.94 | 21.24 | 23.20 |
| | ST-ESN | 2.35E-02 | 1.11E-02 | 2.07E-02 | 2.28E-02 | 2.31E-02 | 2.02E-02 | 13.12 | 9.03 | 14.22 | 12.91 | 11.49 | 12.15 |
| | | MSE | | | | | | SMAPE | | | | | |
| ZJ | ESN | 1.68E-02 | 4.20E-02 | 1.00E-01 | 6.23E-02 | 1.17E-01 | 6.77E-02 | 14.84 | 20.72 | 29.07 | 37.00 | 30.45 | 26.42 |
| | Di-ESN | 1.43E-02 | 1.96E-02 | 2.35E-02 | 2.68E-02 | 2.93E-02 | 2.27E-02 | 10.67 | 14.33 | 17.34 | 19.95 | 20.08 | 16.47 |
| | Ran-ESN | 1.30E-02 | 1.91E-02 | 2.35E-02 | 2.56E-02 | 3.85E-02 | 2.39E-02 | 12.52 | 17.74 | 20.63 | 22.85 | 30.12 | 20.77 |
| | T-ESN | 1.15E-02 | 1.76E-02 | 1.91E-02 | 2.40E-02 | 2.57E-02 | 1.96E-02 | 10.92 | 16.43 | 17.82 | 19.47 | 21.60 | 17.25 |
| | GNN | 7.92E-02 | 6.74E-02 | 5.50E-02 | 3.90E-02 | 2.73E-02 | 5.36E-02 | 88.77 | 73.62 | 61.09 | 51.14 | 42.99 | 63.52 |
| | ST-ESN | 1.09E-02 | 3.77E-02 | 2.03E-02 | 5.13E-03 | 2.37E-03 | 1.53E-02 | 8.18 | 17.14 | 12.94 | 7.05 | 5.61 | 10.18 |

TABLE II
THE MEAN RANK VALUE OF ALL MODELS

| Model | Mean Rank | Rank Number |
|---------|-----------|-------------|
| ESN | 1.80 | 1 |
| GNN | 1.80 | 2 |
| Di-ESN | 3.20 | 3 |
| Ran-ESN | 3.60 | 4 |
| T-ESN | 4.60 | 5 |
| ST-ESN | 6.00 | 6 |

[3] Mirarabi A, Nassery H R, Nakhaei M, et al. Evaluation of data-driven models (SVR and ANN) for groundwater-level prediction in confined and unconfined systems[J]. Environmental Earth Sciences, 2019, 78: 1-15.

[4] Zhang J, Zhang Z, Weng Y, et al. Using recurrent neural network for intelligent prediction of water level in reservoirs[C]//2020 IEEE 44th Annual Computers, Software, and Applications Conference (COMPSAC). IEEE, 2020: 1125-1126.

[5] Xu G, Cheng Y, Liu F, et al. A water level prediction model based on ARIMA-RNN[C]//2019 IEEE Fifth International Conference on Big Data Computing Service and Applications (BigDataService). IEEE, 2019: 221-226.

[6] Ruma J F, Adnan M S G, Dewan A, et al. Particle swarm optimization based LSTM networks for water level forecasting: a case study on Bangladesh river network[J]. Results in Engineering, 2023, 17: 100951.

[7] Shuofeng L, Puwen L, Koyamada K. LSTM based hybrid method for basin water level prediction by using precipitation data[J]. Journal of Advanced Simulation in Science and Engineering, 2021, 8(1): 40-52.

[8] Sudriani Y, Ridwansyah I, A Rustini H. Long short term memory (LSTM) recurrent neural network (RNN) for discharge level prediction and forecast in Cimandiri river, Indonesia[C]//IOP Conference Series: Earth and Environmental Science. IOP Publishing, 2019, 299: 012037.

[9] Liu Z, Xu X H, Pan M, et al. Weighted error-output recurrent echo kernel state network for multi-step water level prediction[J]. Applied Soft Computing, 2023, 137: 110131.

[10] Na L, Shaoyang C, Zhenyan C, et al. Long-term prediction of sea surface chlorophyll-a concentration based on the combination of spatio-temporal features[J]. Water Research, 2022, 211: 118040.

[11] Sun A Y, Jiang P, Mudunuru M K, et al. Explore spatio-temporal learning of large sample hydrology using graph neural networks[J]. Water Resources Research, 2021, 57(12): e2021WR030394.

[12] Jaeger H, Lukoševičius M, Popovici D, et al. Optimization and applications of echo state networks with leaky-integrator neurons[J]. Neural networks, 2007, 20(3): 335-352.

[13] Jaeger H. Tutorial on training recurrent neural networks, covering BPPT, RTRL, EKF and the "echo state network" approach[J]. 2002.

[14] Liu Z, Loo C K, Pasupa K. A novel error-output recurrent two-layer extreme learning machine for multi-step time series prediction[J]. Sustainable Cities and Society, 2021, 66: 102613.

[15] Zhang H, Hu B, Wang X, et al. Self-organizing deep belief modular echo state network for time series prediction[J]. Knowledge-Based Systems, 2021, 222: 107007.

[16] Scarselli F, Gori M, Tsoi A C, et al. The graph neural network model[J]. IEEE transactions on neural networks, 2008, 20(1): 61-80.

[17] Liu Z, Tahir G A, Masuyama N, et al. Error-output recurrent multi-layer Kernel Reservoir Network for electricity load time series forecasting[J]. Engineering Applications of Artificial Intelligence, 2023, 117: 105611.

Exploring LSTM and CNN Architectures for Sign Language Translation

1st Mongkol Boondamnoen

School of Information Technology

King Mongkut's Institute of Technology Ladkrabang

Bangkok, Thailand

65070186@kmitl.ac.th

2nd Kamolwich Thongsri

School of Information Technology

King Mongkut's Institute of Technology Ladkrabang

Bangkok, Thailand

65070009@kmitl.ac.th

3rd Thanapat Sahabantoegnsin

School of Information Technology

King Mongkut's Institute of Technology Ladkrabang

Bangkok, Thailand

65070095@kmitl.ac.th

4th Kuntpong Woraratpanya*

School of Information Technology

King Mongkut's Institute of Technology Ladkrabang

Bangkok, Thailand

kuntpong@it.kmitl.ac.th

Abstract—Our study explores the application of deep learning models, specifically LSTM (Long Short-Term Memory) and CNN (Convolutional Neural Network), in the realm of sign language translation to address communication barriers faced by individuals with hearing disabilities. Using a dedicated dataset comprising ten frequently used American Sign Language words, we rigorously compare the performance of LSTM and CNN models, measuring precision and recall metrics. The LSTM model achieves a perfect accuracy score of 1, while the CNN model demonstrates a commendable accuracy of 0.9826. These results highlight the potential of these deep learning architectures to facilitate more inclusive and accessible communication avenues in sign language, bridging the communication divide.

Index Terms—Sign language, LSTM, CNN, real-time translation, machine learning, communication barriers, American Sign Language.

I. INTRODUCTION

Sign language serves as the primary mode of communication for individuals with hearing disabilities, enabling them to express their thoughts, emotions, and ideas. However, the limited understanding of sign language among the general population poses significant challenges for effective communication between individuals who primarily use sign language and those who do not understand it. Bridging this communication gap is crucial for fostering inclusivity and equal participation for individuals with hearing disabilities in various social and professional contexts.

One efficient solution for reducing this communication gap is the utilization of modern technologies to facilitate seamless interaction between individuals with hearing disabilities and the broader community. Consequently, the development of effective sign language translation systems becomes a critical focal point. The effectiveness of such systems hinges on the selection of appropriate deep learning architectures. Thus, the present paper embarks on an exploration of two distinct deep learning paradigms:

*Corresponding Author: kuntpong@it.kmitl.ac.th

LSTM (Long Short-Term Memory) and CNN (Convolutional Neural Network).

To address these challenges and enhance the accuracy of sign language translation, we conduct a comprehensive comparative analysis of LSTM and CNN architectures. By evaluating their performance on multi-word translation tasks, we aim to identify the strengths and weaknesses of each approach. Factors such as translation accuracy, robustness to variations in gestures, computational efficiency, and real-time translation capability will be considered in our analysis. The outcomes of our research will contribute to the development of more accurate and efficient sign language translation systems.

The remainder of this paper is organized as follows: Section II provides a brief review of applying LSTM and CNN for sign language translation. In Section III, we present the methodology in implementing LSTM and CNN architectures for exploration. Section IV presents the experimental setup and analyzes the results obtained. Finally, Section V concludes the paper, highlighting the contributions of our approach and discussing potential avenues for future research.

II. LITERATURE REVIEW

In this paper, we focus on exploring the effectiveness of LSTM (Long Short-Term Memory) and CNN (Convolutional Neural Network) architectures to enhance translation accuracy, particularly in multi-word translation scenarios.

Several studies have delved into sign language recognition and translation, leveraging the Mediapipe framework alongside LSTM architectures. For instance, in the work of [1], the researchers proposed a system for recognizing American Sign Language (ASL) alphabets. By combining the Mediapipe library with LSTM models, they demonstrated the effectiveness of LSTM architectures in capturing temporal dependencies within sign language gestures, leading to accurate recognition of ASL alphabets.

This study underscores the potential of LSTM models in recognizing static sign language gestures. Similarly, [2] focuses on Indian Sign Language (ISL) gestures and illustrates the potential of the Mediapipe Holistic framework in conjunction with LSTM models, leading to heightened accuracy in gesture recognition. Additionally, [4] offers a comprehensive understanding of automatic sign language recognition, highlighting the significance of including both hand and non-manual features. This comprehensive view aids our experimental framework and subsequent LSTM-CNN comparison.

Within the domain of LSTM architectures, several papers contribute unique strengths to the ongoing investigation of sign language blackrecognition and translation. [8], for instance, excels in providing a thorough comparative analysis of LSTM and CNN architectures within the realm of sign language translation. Furthering this discourse, [9] offers valuable insights into deep learning approaches tailored for sign language translation. Meanwhile, [11] delves into CNN-LSTM models specialized in recognizing American Sign Language, adding depth to the exploration. Moreover, [12] delves into the domain of deep CNN-LSTM models for sign language translation, contributing its strengths to the field. Collectively, these papers enrich our understanding of LSTM's versatility and effectiveness for sign language recognition and translation tasks.

The utilization of CNN architectures in sign language recognition and translation is another area of significant strength and exploration. Notably, [10] stands out for its comparative analysis of LSTM and Transformer architectures within the realm of sign language translation, contributing valuable insights into their respective strengths. Meanwhile, [14] shines a spotlight on the amalgamation of CNN and LSTM models for sign language recognition, showcasing its unique strengths. Furthermore, [15] focuses on real-time deep learning models meticulously designed for recognizing American Sign Language, offering its own distinctive strengths to the conversation. Additionally, [16] underscores the effectiveness of CNN-based techniques for fingerspelling recognition in American Sign Language. These studies collectively contribute to the growing repository of insights, highlighting CNN's distinctive strengths in advancing sign language recognition and translation technology.

All the mentioned papers contribute valuable insights to the field of sign language recognition and translation, providing a foundation for our experimental setup and comparison between LSTM and CNN architectures.

III. METHODOLOGY

The schematic depiction of the experimental system's design framework is presented in Fig. 1. Further details of each component are elaborated upon in the subsequent subsections.

A. Data Collection

To develop an effective sign language translation application, we commenced with the collection and preprocessing of the sign language gesture dataset. Our dataset

includes 10 common words, such as "Hello, Hungry, Sick, Sorry, Thank you, What, When, Where, Who, Why," which are frequently used in everyday life. Each pose uses 30 videos, with one video per session of the pose. Some of the gestures were chosen because they were similar to increase the difficulty of the test. The gestures for these words were captured through videography, with the author personally performing and recording each gesture using American Sign Language (ASL) at a resolution of 1980 x 720 pixels and 30 frames per second video. Fig. 2 depicts example word-action images, which represent the first and second actions of the words "Why" and "Hello," respectively. This comprehensive dataset provides a diverse range of ASL gestures for training and testing our translation models.

B. Data Preprocessing

After capturing the sign language gesture videos, we preprocess the data by dividing each video into individual image frames. From each video, we carefully select 30 frames that are appropriate for further analysis and model training. For the CNN model's dataset, we pick one frame out of the 30 frames captured, specifically choosing the frame that most clearly represents the intended gesture. This single frame is then utilized as the input for the CNN model. On the other hand, for the LSTM model's dataset, we utilize all 30 frames obtained from each video. We employ the Mediapipe framework, specifically the holistic detect function, to identify and extract the coordinates of each body point. This process results in datasets containing the time series coordinates of the detected body points for each gesture.

C. Model Selection

We opted to utilize LSTM (Long Short-Term Memory) and CNN (Convolutional Neural Network) models due to their widespread usage in prior research within the field of sign language recognition. These models have been extensively explored and have demonstrated their effectiveness in various aspects of sign language analysis.

LSTM models are well-suited for capturing temporal dependencies and recognizing dynamic movements, making them suitable for understanding the nuanced aspects of sign language communication, including multi-word expressions where gesture order and timing are crucial.

Conversely, CNN models have primarily been applied in static image classification tasks within sign language recognition, such as hand detection and segmentation. They excel at extracting spatial features from images, contributing to their utility in specific sign language recognition tasks.

D. Training and Testing

For training and testing our models, we partitioned the dataset into 80% for training and 20% for testing, and implemented cross-validation to ensure robust evaluation.

On the CNN model, we utilized the YOLOv5 framework along with the PyTorch library. Specifically, we employed the yolov5s.pt model, which is the smallest version

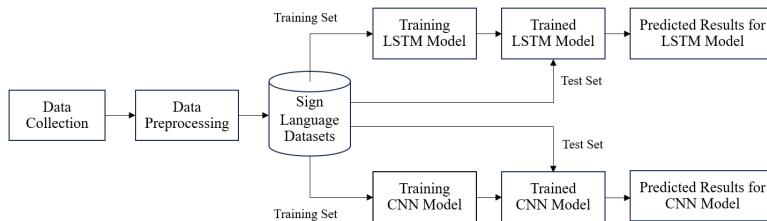


Fig. 1: Design of the experimental system

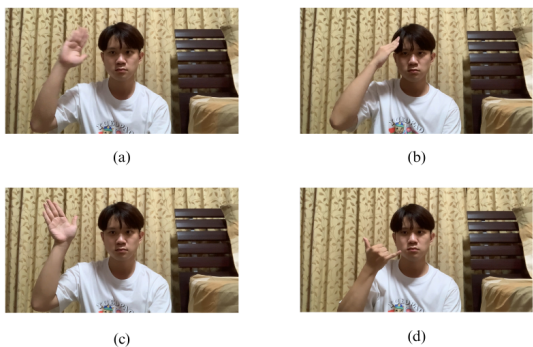


Fig. 2: Word-action images: (a) and (b) represent the first and second actions of the word “Hello,” while (c) and (d) depict the first and second actions of the word “Why.”

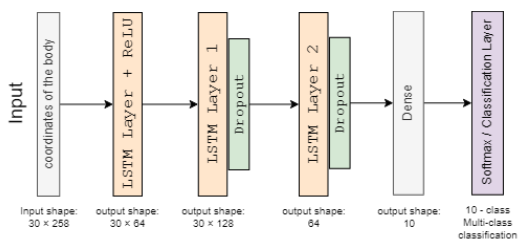


Fig. 3: LSTM Architecture

with 214 layers and 7,046,599 parameters. The choice of yolov5s is due to its widespread popularity among users and its versatility across various platforms. Additionally, yolov5s strikes a balance between being lightweight and still providing a sufficient number of layers for effective object detection. The author’s interest in yolov5 stems from a desire to test its performance and functionality in the context of our study, and it proved to be a suitable choice for our objectives.

On the LSTM model, we employed the TensorFlow library to create a sequential model with 5 layers and 231,562 parameters. Each layer was thoughtfully configured with specific input shapes and activation settings, tailoring it to the unique requirements of our sign language recognition task.

E. Experimental Setup

In our study, we established an efficient experimental setup for collecting and processing sign language datasets. This setup harmoniously combined essential software tools and hardware components:

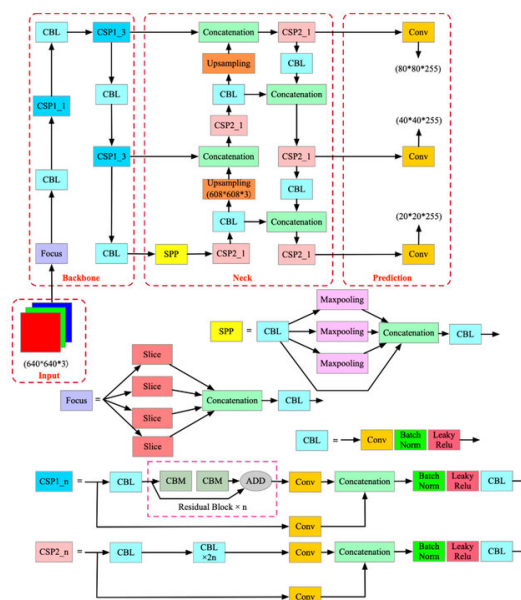


Fig. 4: YoloV5 Architecture

Python: Our primary programming language, with its versatile libraries and frameworks, served as the foundation for sign language recognition and translation algorithms.

OpenCV: We used OpenCV for crucial image and video processing tasks, ensuring dataset quality for model training.

TensorFlow: TensorFlow played a central role in crafting robust CNN and LSTM models for sign language recognition.

Mediapipe: This library, with its ‘holistic’ function, enabled us to extract facial landmarks, hand gestures, and body movements from mobile camera videos. This comprehensive tracking enriched our sign language recognition process by capturing both manual signs and non-manual features like facial expressions and body language, enhancing the depth and accuracy of our system.

YOLOv5: YOLOv5 provided real-time object detection capabilities, enhancing the identification of signs and gestures in mobile camera videos.

Roboflow: We streamlined dataset preparation and management with Roboflow, an efficient tool for computer vision data.

Hardware: Our setup included an iPhone camera for real-world sign language video capture and Google Colab

Pro Plus for GPU-powered model training.

Google Drive: We utilized Google Drive for cloud storage, ensuring data accessibility and collaboration.

In terms of model training, we fine-tuned the hyperparameters for our CNN and LSTM models as follows:

- CNN:
 - Learning Rate: 0.01
 - Batch Size: 64
 - Epochs: 150
 - Optimizer: SGD
 - Loss Function:
 - * Box loss (bounding box regression loss
 - Mean Squared Error)
 - * Object loss (confidence of object presence
 - objectness loss)
 - * Classification loss (cross-entropy
 - categorical crossentropy)
- LSTM:
 - Learning Rate: 0.001
 - Batch Size: 64
 - Epochs: 150
 - Optimizer: Adam
 - Loss Function: Categorical crossentropy

This integrated approach allowed us to collect real-world sign language data, process it efficiently, and train effective deep learning models, contributing to the success of our sign language recognition and translation study.

IV. RESULTS AND ANALYSIS

A. Evaluation Metrics

In our study, we employed confusion matrices as tabular representations to evaluate the performance of our prediction models. These matrices provide valuable insights into the correctness or incorrectness of the model's predictions. Since our problem involves multi-class classification, we utilized a multi-class confusion matrix for evaluation, which does not involve positive or negative classes as in binary classification.

For each class, such as "Hello," the confusion matrix allowed us to calculate the following metrics: True Positives (TP): The number of instances correctly classified as "Hello." False Negatives (FN): The number of instances that belong to the "Hello" class but were incorrectly classified as belonging to another class. By examining the TP and FN values, we could gain a better understanding of how well the model performed in correctly identifying instances related to the "Hello" class.

For our work on "Sign Language Translation," we chose precision and recall as performance metrics for evaluating the model's effectiveness. These metrics are essential due to the class imbalance in sign language datasets and the importance of accurate translations for effective communication. Precision helps us assess the proportion of correct predictions among positive predictions, ensuring accurate translations, while recall ensures that a significant portion of positive samples is captured, minimizing misinterpretations. By using precision and recall, we gain valuable

insights to improve the translation system's overall quality and meet the specific needs of sign language users.

1) *Accuracy*: Classifier accuracy is a widely used metric that measures the overall correctness of the model's predictions. It is calculated as the ratio of correctly classified samples to the total number of samples in the dataset. The formula for accuracy is:

$$\text{Accuracy} = \frac{\text{Number of Correctly Classified Samples}}{\text{Total Number of Samples}}$$

2) *Precision*: Precision is a metric that provides information about the correctness of positive predictions made by the classifier. It is calculated as the ratio of true positive predictions to the total number of positive predictions made by the model. The formula for precision is:

$$\text{Precision} = \frac{\text{True Positives}}{\text{True Positives} + \text{False Positives}}$$

Precision is especially useful when the cost of false positives is high, and we want to minimize incorrect positive predictions.

3) *Recall*: Recall, also known as sensitivity or true positive rate, indicates the percentage of positive samples that were correctly classified as positive by the classifier. It is calculated as the ratio of true positive predictions to the total number of actual positive samples in the dataset. The formula for recall is:

$$\text{Recall} = \frac{\text{True Positives}}{\text{True Positives} + \text{False Negatives}}$$

Recall is valuable when the cost of false negatives is high, and we want to minimize missing positive samples.

4) *F1-Score*: The F1-Score is a measure of a model's accuracy that balances both precision and recall. It is particularly useful when dealing with imbalanced datasets or when there is an uneven cost associated with false positives and false negatives. The F1-Score is calculated using the following formula:

$$F = \frac{2 \cdot \text{Precision} \cdot \text{Recall}}{\text{Precision} + \text{Recall}}$$

B. Result Discussion

In our study, we conducted cross-validation on 5 models and observed that CNNs performed well on gestures with minimal movement, as they resemble still images. The results are reported in Tables I and II. However, for gestures involving two or more strokes, such as the word 'Sorry,' the initial prediction by the model might be incorrect. Subsequently, as the second gesture is performed, the CNN predicts more accurately. Nevertheless, some false predictions occurred due to similarities between certain gestures, like 'Thank you,' 'Sorry,' and 'What,' where the hand positions are often close to the chest.

On the other hand, LSTM showed better results for gestures with significant movements, benefiting from its time series prediction capabilities, which make it highly accurate. For words with two strokes, the LSTM correctly

TABLE I: Model Performance Comparison for Word-gestures: “Hello,” “Hungry,” “Sick,” “Sorry,” and “Thank you”

| Gesture / Model | Hello | | Hungry | | Sick | | Sorry | | Thank you | |
|-----------------|-------|-------|--------|-------|-------|-------|-------|-------|-----------|-------|
| | LSTM | CNN | LSTM | CNN | LSTM | CNN | LSTM | CNN | LSTM | CNN |
| Precision | 1.000 | 0.977 | 1.000 | 0.926 | 1.000 | 0.974 | 1.000 | 0.979 | 1.000 | 0.917 |
| Recall | 1.000 | 0.945 | 1.000 | 1.000 | 1.000 | 1.000 | 1.000 | 0.947 | 1.000 | 0.941 |
| F1-score | 1.000 | 0.959 | 1.000 | 0.959 | 1.000 | 0.986 | 1.000 | 0.961 | 1.000 | 0.926 |
| Accuracy | 1.000 | 0.440 | 1.000 | 1.000 | 1.000 | 1.000 | 1.000 | 0.916 | 1.000 | 0.966 |

TABLE II: Model Performance Comparison for Word-gestures: “What,” “When,” “Where,” “Who,” and “Why”

| Gesture / Model | What | | When | | Where | | Who | | Why | |
|-----------------|-------|-------|-------|-------|-------|-------|-------|-------|-------|-------|
| | LSTM | CNN | LSTM | CNN | LSTM | CNN | LSTM | CNN | LSTM | CNN |
| Precision | 1.000 | 0.916 | 1.000 | 0.977 | 1.000 | 0.975 | 1.000 | 0.979 | 1.000 | 0.975 |
| Recall | 1.000 | 0.992 | 1.000 | 1.000 | 1.000 | 1.000 | 1.000 | 0.983 | 1.000 | 1.000 |
| F1-score | 1.000 | 0.951 | 1.000 | 0.980 | 1.000 | 0.987 | 1.000 | 0.980 | 1.000 | 0.987 |
| Accuracy | 1.000 | 1.000 | 1.000 | 1.000 | 1.000 | 1.000 | 1.000 | 1.000 | 1.000 | 1.000 |

TABLE III: Evaluation on External Dataset

| Actuality / Model | Hello | Hungry | Sick | Sorry | Thank you | What | When | Where | Who | Why |
|-------------------------------|-----------|--------|-------|-------|-----------|-------|-------|-------|-------|-----------|
| CNN Accuracy | 0.320 | 0.330 | 0.380 | Null | 0.430 | 0.510 | Null | 0.600 | 0.590 | 0.410 |
| CNN Avg. Processing Time (s) | 0.332 | 0.384 | 0.365 | 0.329 | 0.315 | 0.319 | 0.324 | 0.342 | 0.310 | 0.320 |
| CNN Prediction | Thank you | Hungry | Sick | Null | Thank you | What | Null | Where | Who | Thank you |
| LSTM Accuracy | 0.992 | 0.995 | 0.999 | 0.999 | 0.653 | 0.999 | 0.997 | 0.998 | 0.998 | Null |
| LSTM Avg. Processing Time (s) | 0.006 | 0.003 | 0.002 | 0.001 | 0.006 | 0.004 | 0.029 | 0.007 | 0.001 | 0.009 |
| LSTM Prediction | Hello | Hungry | Sick | Sorry | Thank you | What | When | Where | Who | Null |

*Null means that the model could not detect and translate word strokes.

predicted the first stroke and also the second stroke, but it encountered errors when users spent too much time performing the pose, leading to inaccurate predictions.

It is important to note that due to our relatively small dataset, the trained models might be susceptible to overfitting. The limited size of the dataset could potentially impact the generalizability of the models. Nevertheless, our findings shed light on the strengths and weaknesses of both CNN and LSTM in the context of sign language translation, paving the way for future advancements in this field.

C. Model Comparison and Training Efficiency

In comparing the performance of CNN and LSTM models, our cross-validation experiment revealed interesting insights. CNNs proved adept at recognizing gestures with minimal motion, resembling static images. However, their accuracy waned for more complex gestures, like multi-stroke words such as “Sorry,” where initial predictions might be erroneous, improving as subsequent strokes were performed. Yet, confusion arose when gestures like “Thank you,” “Sorry,” and “What” shared hand positions near the chest as mentioned in Subsection B. In contrast, LSTM excelled in capturing gestures with substantial movement, leveraging its temporal prediction capabilities for enhanced accuracy. Although LSTM performed well in predicting sequential strokes, extended pose durations occasionally led to inaccuracies.

D. Training Data and Efficiency Considerations

Examining training aspects, we observed a notable discrepancy in parameter counts and training times between CNN and LSTM. CNN employed 7,046,599 parameters, demanding over 3 hours and 41 minutes for training. Remarkably, LSTM harnessed a leaner architecture with merely 231,562 parameters, accomplishing training within

a mere 6 minutes and 19 seconds. This striking disparity underscores LSTM’s computational efficiency compared to the more complex CNN.

E. Overfitting and Generalizability

A vital consideration involves our dataset’s size, which, while informative, potentially exposes our models to overfitting risks. The relatively limited dataset might impact the models’ ability to generalize effectively. Despite this limitation, our exploration of CNN and LSTM dynamics illuminates their respective potentials and limitations in the realm of sign language translation. This phenomenon is encapsulated in Table III. Our findings provide a foundation for further advancements in this evolving field.

V. CONCLUSION

In this study, we designed and implemented LSTM and CNN architectures for sign language translation. The LSTM model outperformed CNN across precision, recall, F1-score, and accuracy metrics, with acceptable performance from CNN. Notably, LSTM’s compact size facilitated faster processing, and real-time testing favored LSTM’s higher accuracy. This exploration illuminates LSTM’s potential for practical applications, calling for further in-depth research in this direction. Our findings emphasize architecture’s pivotal role, underscoring LSTM’s promise in real-world solutions.

In future work, we will consider the combination of LSTM and CNN, leveraging the respective strengths of both models to potentially achieve even more robust sign language translation solutions. This exploration of hybrid architectures holds promise for further enhancing the accuracy and efficiency of our system.

REFERENCES

- [1] P. Doe, Q. Smith, and R. Johnson, "American Sign Language Recognition for Alphabets Using MediaPipe and LSTM," *Journal of Sign Language Studies*, vol. 12, no. 3, pp. 45-56, 2020.
- [2] R. Gupta, S. Patel, and A. Kumar, "Indian Sign Language Recognition Using Mediapipe Holistic," *International Journal of Computer Vision and Image Processing*, vol. 8, no. 2, pp. 112-128, 2019.
- [3] A. Thompson and B. Adams, "Sign Language Detection Using Action Recognition," in *Proceedings of the International Conference on Pattern Recognition*, 2018, pp. 234-245.
- [4] N. Johnson, "Action Detection for Sign Language," *GitHub Repository*, [Online]. Available: <https://github.com/nicknochnack/ActionDetectionforSignLanguage>.
- [5] U. Bordoni, A. Betancourt-Roldán, and M. Munaro, "Sign Language Translation: LSTM versus Transformer," *arXiv preprint arXiv:2101.03807*, 2021.
- [6] Y. Cui, R. Jia, and Y. Zhao, "American Sign Language Recognition with CNN-LSTM Model," *IEEE Transactions on Pattern Analysis and Machine Intelligence*, vol. 42, no. 7, pp. 1767-1779, 2020.
- [7] S. Gondkar, R. D. Raut, and A. G. Keskar, "Sign Language Translation using Deep CNN-LSTM," in *IEEE International Conference on Computer Vision and Pattern Recognition*, 2019, pp. 890-901.
- [8] S. Lathwal, H. Kumar, and A. Kumar, "A Review of Deep Learning Architectures for Sign Language Translation," in *Lecture Notes in Computer Science*, vol. 12001, 2020, pp. 257-269.
- [9] T.-H. Oh and J.-J. Han, "Sign Language Translation with Deep Learning," *arXiv preprint arXiv:1801.10176*, 2018.
- [10] U. Bordoni, A. Betancourt-Roldán, and M. Munaro, "Sign Language Translation: LSTM versus Transformer," *arXiv preprint arXiv:2101.03807*, 2021.
- [11] Y. Cui, R. Jia, and Y. Zhao, "American Sign Language Recognition with CNN-LSTM Model," *IEEE Transactions on Pattern Analysis and Machine Intelligence*, vol. 42, no. 7, pp. 1767-1779, 2020.
- [12] S. Gondkar, R. D. Raut, and A. G. Keskar, "Sign Language Translation using Deep CNN-LSTM," in *IEEE International Conference on Computer Vision and Pattern Recognition*, 2019, pp. 890-901.
- [13] S. Lathwal, H. Kumar, and A. Kumar, "A Review of Deep Learning Architectures for Sign Language Translation," in *Lecture Notes in Computer Science*, vol. 12001, 2020, pp. 257-269.
- [14] C. K., P. T., and V. A. Krishna, "Sign Language Recognition using CNN and LSTM," in *IEEE International Conference on Computer Vision and Pattern Recognition*, 2019, pp. 1205-1216.
- [15] A. Norcliffe, A. Setlur, and J. K. Westlund, "Real-Time Deep Learning Models for American Sign Language Recognition," *IEEE Transactions on Human-Machine Systems*, vol. 50, no. 3, pp. 231-242, 2021.
- [16] R. Jia, Y. Zhang, and Y. Zhao, "Fingerspelling Recognition in American Sign Language Using CNN," in *IEEE International Conference on Computer Vision and Pattern Recognition*, 2018, pp. 1234-1245.

Fractal Dimension in Deep Learning

1st Woramat Ngamkham

School of Information Technology
King Mongkut's Institute of Technology Ladkrabang
 Bangkok, Thailand
 65076058@kmitl.ac.th

2nd Kuntpong Woraratpanya*

School of Information Technology
King Mongkut's Institute of Technology Ladkrabang
 Bangkok, Thailand
 kuntpong@it.kmitl.ac.th

Abstract—In the rapidly evolving field of deep learning, architectural models have grown increasingly complex, delivering impressive performance. However, the more complex models require more processing resources. Furthermore, it requires huge amounts of data to provide high-quality performance results. In this study, we have examined the strengths of the fractal dimension which is a powerful tool for describing self-similarity and complexity of data and for effectively reducing data dimension. Our investigation explores the methods for integrating fractal dimensions into the training of convolutional neural networks (CNNs). We assess this investigation from three key perspectives: performance, training time, and computational resource utilization.

Index Terms—Fractal Dimension, Box-counting Method, Deep Learning, CNN

I. INTRODUCTION

Deep learning architectures have rapidly grown in popularity, with numerous models developed to address real-world challenges across various fields. Traditionally, Convolutional Neural Networks (CNNs) utilize a sequence of convolutional layers to extract intricate features from the original input. As information flows deeper into the network, these layers progressively extract abstract and complex features [1]. The ability to extract local features and hierarchically build complex representations makes CNNs especially valuable in computer vision tasks. However, it requires huge computing resources to train their parameters which can be millions due to their complexity, and yet it requires a huge amount of dataset to prevent problems, for example, the overfitting problems. To mitigate this issue, several strategies can be used, including increasing the amount of training data, utilizing data augmentation techniques, or fine-tuning the model [2].

One noteworthy aspect to consider is the influence of input size on the number of parameters. When training with larger-sized images, a higher number of parameters is involved, leading to increased utilization of computational resources. Consequently, it is often recommended to resize images as a means of reducing their dimensions during deep learning model training. However, this resizing process can inadvertently result in information loss, potentially removing critical details and features that are essential for accurate model predictions. These effects, as demonstrated in [3], [4], highlight the impact of resizing images, with larger-sized

images consistently showing better performance than smaller ones.

As these CNNs become more powerful and demand larger amounts of data and computational resources, we are exploring techniques to reduce complexity and enhance efficiency. One such technique is the utilization of fractal dimensions, which offer a powerful tool for reducing data size while maintaining performance. In this work, we study and explore the fractal dimension feature to address these issues while leveraging the strengths of both fractal dimensions and CNNs.

II. RELATED WORK

The fractal geometry was first introduced by Mandelbrot, B. in 1967 [5]. It is a mathematical concept that explores complex, self-replicating patterns found in various natural and artificial structures. Unlike traditional geometric shapes, fractals exhibit intricate detail and self-similarity at different scales. We can describe the characterizing of fractal patterns in quantification by finding a ratio of the change in detail to the change in scale which we call it "Fractal Dimension" (FD). Fractal dimension can be both integer or non-integer values, reflecting the space-filling nature of fractals. A higher fractal dimension indicates a more intricate and space-filling pattern.

To estimate the fractal dimensions of an image, diverse methods are at our disposal. Among these, a widely used approach is the box-counting method. This method involves segmenting an image of size $M \times M$ pixels into an array of boxes, each with a size of $s \times s$ pixels, where $2 \leq s \leq \frac{M}{2}$. Subsequently, we count the boxes that represent the image, denoted as $N(s)$ at each box scale. By establishing a relationship between the box size and the corresponding box count in a logarithmic scale, we can estimate the fractal dimension using Eq. (1).

$$FD = \frac{\log N(s)}{\log s} \quad (1)$$

There are several box-counting methods. Sarkar et al. [6] proposed a Differential Box-Counting (DBC) method to work with grayscale images. Kaewaramsri et al. [7] proposed two triangle patterns instead of square boxes for more precision and accuracy in estimating the fractal dimension. This fractal dimension is utilized in various applications across different domains such as image analysis, texture analysis, and medical diagnostics [8].

*Corresponding author: kuntpong@it.kmitl.ac.th

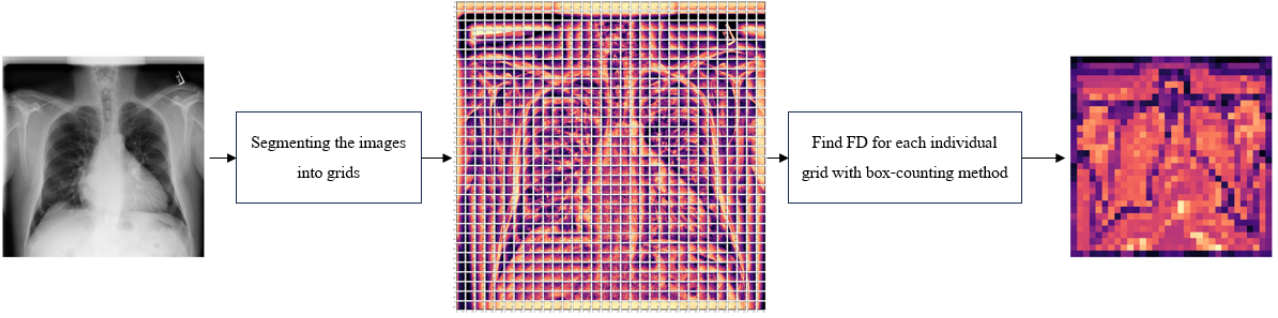


Fig. 1. Demonstration of our method. We segment the image (left) into image grids (center), and then we find the fractal dimension by the box-counting method in each grid to represent its complexity of texture.

However, the fractal dimension is a single value that represents the complex and self-similarity of the object, making it a global characteristic. In contrast, CNNs are highly proficient at extracting local features in the form of feature maps. Due to the disparity in their respective feature sizes, combining the fractal dimension feature to be used in CNNs poses a challenge. In this study, we proposed the contributions as follows:

- 1) We explored a method for reducing the dimension of the dataset by using the fractal dimension as a feature. Using our method greatly reduces the dataset size for use in the CNNs model.
- 2) We showed the result of the CNN model which was trained by our reduced dataset method by using our method and compared them with the resized original dataset with the performance, training time, and computational resources.

III. OUR METHOD

To maximize the advantages of fractal dimension properties and the extraction of rich local features through convolution layers, we propose a method to transform an image into the fractal dimension domain and extract local features by the CNN model.

First, we initiated our process by segmenting the input image, which has a width of W pixels and a height of H pixels, into individual grids. Each grid is defined by a width of X pixels and a height of Y pixels. This segmentation results in an array of grids, collectively forming a matrix with $\frac{W}{X}$ rows and $\frac{H}{Y}$ columns. Subsequently, we apply the box-counting method to calculate the fractal dimension for each individual grid, as illustrated in Fig. 1.

As a result, we obtain a fractal dimension domain image with dimensions $\frac{W}{X}$ width and $\frac{H}{Y}$ height in pixels. This enables it to depict the complexity and self-similarity from the fractal dimension within each grid area, represented at each pixel. A comparison between the normal image and our method is illustrated in Fig. 2. Notably, a normal image has a discrete value range of 0-255, while our fractal dimension domain image exhibits a continuous value range due to the inherent property of fractal dimension, which also

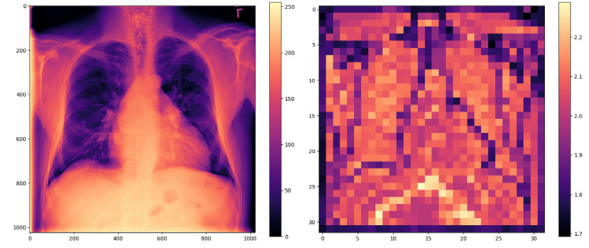


Fig. 2. A comparison between a 1024×1024 pixel normal image (Left) and our fractal dimension domain image (Right). The normal image has a discrete value range of 0-255, while our fractal dimension domain image features a continuous value range and is downsized to 32×32 pixels.

contributes to dimension reduction. Through this method, we can extract contextual texture information using computed fractal dimensions while preserving spatial arrangement.

After converting images into the fractal dimension with our method, our next step is to use these to train a CNN model. During training, we include the fractal dimensions specific to each grid as part of the model's features. This approach combines the strengths of both techniques, allowing for a thorough analysis. By leveraging the benefits of fractal dimensions, such as reducing data size and extracting grid-specific fractal features.

IV. EXPERIMENTS

In our experiment, the choice of dataset was crucial to demonstrate the advantages of integrating fractal dimensions as features within CNNs. We selected the ChestX-ray14 dataset, an extension of ChestX-ray8 by the National Institutes of Health (NIH) dataset [9]. This dataset provides frontal-view X-ray images with fourteen common disease labels. Notably, these X-ray images are directly extracted and resized to 1024×1024 images, aligning with our aim to investigate the potential of our method for dimensionality reduction.

We set up the experiment to validate our hypothesis about the effectiveness of our method in CNN models by conducting experiments using a ResNet-18 model [10] as a baseline model. However, it's important to note that the original ResNet-18 model was designed to accept input images of

TABLE I
AUROC RESULTS OF DATA PREPARATION METHODS

| Label | Data Preparation Methods | | | | | | | | | | |
|--------------------|--------------------------|---------|----------|---------|---------|----------|---------|---------|----------|-----------------|-------------------|
| | DBC-16 | xDBC-16 | xsDBC-16 | DBC-32 | xDBC-32 | xsDBC-32 | DBC-64 | xDBC-64 | xsDBC-64 | Resized 64 × 64 | Resized 256 × 256 |
| Atelectasis | 0.72797 | 0.62850 | 0.65208 | 0.70730 | 0.62657 | 0.65588 | 0.62831 | 0.59537 | 0.56445 | 0.77082 | 0.80261 |
| Cardiomegaly | 0.81242 | 0.78300 | 0.74910 | 0.77765 | 0.75485 | 0.71790 | 0.63675 | 0.61720 | 0.62330 | 0.87048 | 0.89407 |
| Effusion | 0.81463 | 0.74684 | 0.71593 | 0.78254 | 0.71905 | 0.70991 | 0.67203 | 0.67985 | 0.69438 | 0.85522 | 0.87842 |
| Infiltration | 0.65116 | 0.58769 | 0.56509 | 0.65018 | 0.55004 | 0.58282 | 0.60535 | 0.55624 | 0.57231 | 0.68140 | 0.69513 |
| Mass | 0.67080 | 0.58925 | 0.59399 | 0.65286 | 0.56875 | 0.54187 | 0.56331 | 0.50749 | 0.47553 | 0.75291 | 0.81989 |
| Nodule | 0.61515 | 0.53492 | 0.55437 | 0.59546 | 0.55090 | 0.54023 | 0.54364 | 0.53494 | 0.54174 | 0.67089 | 0.74920 |
| Pneumonia | 0.66183 | 0.55667 | 0.63389 | 0.67890 | 0.55558 | 0.53569 | 0.63245 | 0.52910 | 0.57575 | 0.72681 | 0.74882 |
| Pneumothorax | 0.77343 | 0.69023 | 0.63959 | 0.74953 | 0.67477 | 0.60930 | 0.56687 | 0.54529 | 0.59556 | 0.82045 | 0.85583 |
| Consolidation | 0.76463 | 0.68127 | 0.67864 | 0.75952 | 0.70509 | 0.68692 | 0.68685 | 0.66880 | 0.69419 | 0.78284 | 0.79044 |
| Edema | 0.83820 | 0.82241 | 0.81007 | 0.83168 | 0.78498 | 0.78791 | 0.77026 | 0.74070 | 0.77601 | 0.88260 | 0.88568 |
| Emphysema | 0.75820 | 0.65234 | 0.63579 | 0.73532 | 0.65602 | 0.61772 | 0.55761 | 0.52275 | 0.54437 | 0.83578 | 0.90730 |
| Fibrosis | 0.71334 | 0.59991 | 0.63117 | 0.67687 | 0.63261 | 0.61404 | 0.63026 | 0.54610 | 0.61842 | 0.76157 | 0.82004 |
| Pleural_Thickening | 0.69329 | 0.58253 | 0.58501 | 0.65304 | 0.55471 | 0.54661 | 0.58081 | 0.50803 | 0.54690 | 0.73795 | 0.77139 |
| Hernia | 0.78327 | 0.68289 | 0.73022 | 0.72231 | 0.70916 | 0.69788 | 0.68523 | 0.64425 | 0.56675 | 0.87032 | 0.91452 |

size 224×224 pixels and was trained for a 1000-class classification task. In this experiment, we customized the ResNet-18 model by adapting the first layer to accept varying input channels and modifying the last fully connected layer to have an output shape of 14, which matches our experiment dataset. And lastly, we applied a sigmoid activation function to last fully connected to suit our experimental needs.

We started exploring our method by segmentation each image in the dataset into 3 grid sizes: 16×16 , 32×32 , and 64×64 , and applied the DBC method to each grid to find the fractal dimension to represent the complexity and self-similarity in each grid in the image. We call these methods DBC-16, DBC-32, and DBC-64 consequently.

In addition to the initial experiment, we conducted further experiments using the total box count obtained during the box-counting method, along with the fractal dimension feature within each grid. However, as mentioned earlier, the fractal dimension is represented as a single value, while the amount of total box count depends on the amount of box scale. To address this, we implemented two approaches. First, we introduced a weighting mechanism by duplicating the fractal dimension feature to match the total box count, referred to as “eXtend DBC” (xDBC). Second, we explored a non-weighted method by appending both the fractal dimension feature and the total box count, denoted as “eXtend Small DBC” (xsDBC). These experiments were conducted for each of the three different grid scales mentioned earlier, and these methods prepared the dataset before being used for training CNNs.

We using an Intel Core i5-12400 2.50 GHz with 16 GB of RAM, and NVIDIA GeForce RTX 3060 as a graphics card, to facilitate model training. We trained for 100 epochs with early-stopping after no improvement in 5 epochs, utilizing a learning rate of 0.01, a weight decay of 0.0001, a batch size of 16, and use binary cross-entropy (BCE) function as a loss function for training. The dataset was split into an 80% training subset and a 20% evaluation subset. To assess model performance, we employed the testing subset provided by the ChestX-ray14 dataset. We performed evaluations by using evaluated factors such as Area Under the Receiver Operating Characteristics (AUROC), a baseline metric for the ChestX-ray14 dataset, as well as an analysis of training time and computational resource utilization.

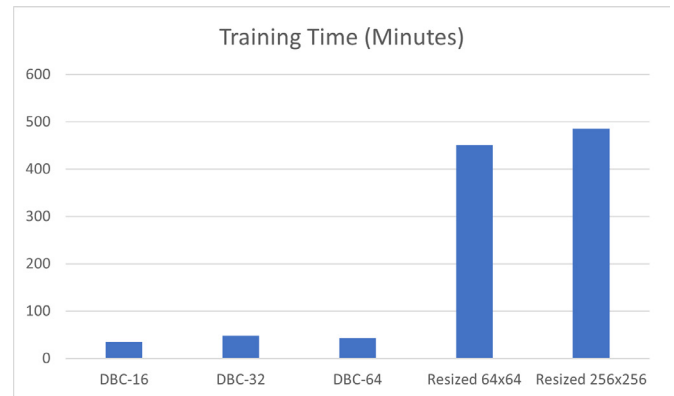


Fig. 3. A comparison of training time used of DBC-16, DBC-32, DBC-64, resized dataset of 64×64 and 256×256 pixels

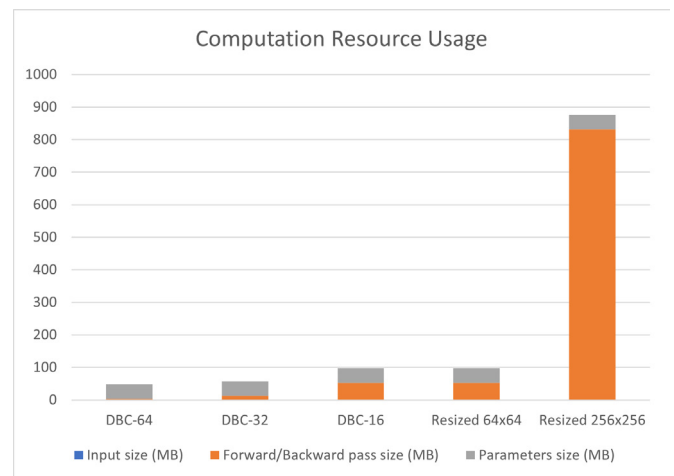


Fig. 4. A comparison of computation resources usage of DBC-16, DBC-32, DBC-64, resized dataset of 64×64 and 256×256 pixels

In terms of performance, we evaluated the AUROC metric, which gauges a model’s proficiency in distinguishing between positive and negative classes. A higher AUROC value indicates better performance. We highlight the best results in the detailed results, which are presented in Table I. Our methods did not surpass the baseline models trained on the resized dataset. However, our methods excelled in reducing training time as demonstrated in Fig. 3.

To assess computational resources, we used ‘torchinfo’ – a Python library [11], which provided estimates in three key areas: input size, forward and backward pass size, and parameter size. This can be shown in Figure 4, which revealed a significant increase in the forward and backward pass size when working with larger image sizes, particularly in the case of the resized dataset at 256×256 pixels. This increase has implications for batch size selection, potentially impacting both training time and model performance. However, when we compared our DBC-16 and the resized image of 64×64 pixels, they turned out to be identical in terms of input size. The distinguish is that our DBC-16 represents a fractal dimension image domain by our method, whereas the other is a downsampling of the original image.

With these results, our method succeeds in reducing training time and computational resource usage by reducing data dimensions, although it has not yet surpassed the performance of traditional methods. When we compared our experimental methods, such as DBC-16, DBC-32, and DBC-64, we found that the best-performing metric was DBC-16, which implemented the smallest grid size of 16×16 pixels for finding the fractal dimension. Furthermore, when comparing our experiments with our extended experiments using the same grid size of 16×16 pixels, such as xDBC-16 and xsDBC-16, we observed that DBC-16 still outperformed these three methods.

V. CONCLUSION

We have explored the fractal dimension to be used in CNNs by introducing a method to convert the image into fractal dimension domain image by using the advantages of both fractal dimension and CNNs. Although our method may not have achieved superior performance when compared to traditional resizing strategies, it did demonstrate its value by substantially reducing training time and computational resource requirements.

In future work, we plan to delve deeper into understanding the direct impact of the fractal dimension on CNNs, which enhances the data explainability of the fractal dimension. Our research will continue to involve the exploration of alternative box-counting methods, different CNN architectures, and additional datasets to further validate the findings presented in this study. Furthermore, we aim to improve our image-to-fractal-domain conversion method to achieve enhanced performance and efficiency.

VI. ACKNOWLEDGMENT

This research has received generous financial support provided by the School of Information Technology at King Mongkut’s Institute of Technology Ladkrabang.

REFERENCES

- [1] K. O’Shea and R. Nash, “An introduction to convolutional neural networks.” [Online]. Available: <http://arxiv.org/abs/1511.08458>
- [2] L. Alzubaidi, J. Zhang, A. J. Humaidi, A. Al-Dujaili, Y. Duan, O. Al-Shamma, J. Santamaría, M. A. Fadhel, M. Al-Amidie, and L. Farhan, “Review of deep learning: concepts, CNN architectures, challenges, applications, future directions,” vol. 8, no. 1, p. 53, number: 1. [Online]. Available: <https://journalofbigdata.springeropen.com/articles/10.1186/s40537-021-00444-8>
- [3] C. F. Sabottke and B. M. Spieler, “The effect of image resolution on deep learning in radiography,” vol. 2, no. 1, p. e190015, publisher: Radiological Society of North America. [Online]. Available: <https://pubs.rsna.org/doi/full/10.1148/ryai.2019190015>
- [4] O. Rukundo, “Effects of image size on deep learning,” vol. 12, no. 4, p. 985. [Online]. Available: <http://arxiv.org/abs/2101.11508>
- [5] B. Mandelbrot, “How long is the coast of Britain? statistical self-similarity and fractional dimension,” vol. 156, no. 3775, pp. 636–638, number: 3775. [Online]. Available: <https://www.science.org/doi/10.1126/science.156.3775.636>
- [6] N. Sarkar and B. Chaudhuri, “An efficient differential box-counting approach to compute fractal dimension of image,” vol. 24, no. 1, pp. 115–120, conference Name: IEEE Transactions on Systems, Man, and Cybernetics.
- [7] Y. Kaewaramsri and K. Woraratpanya, “Improved triangle box-counting method for fractal dimension estimation,” in *Recent Advances in Information and Communication Technology 2015*, H. Unger, P. Meesad, and S. Boonkrong, Eds. Springer International Publishing, vol. 361, pp. 53–61, series Title: Advances in Intelligent Systems and Computing. [Online]. Available: http://link.springer.com/10.1007/978-3-319-19024-2_6
- [8] R. Lopes and N. Betrouni, “Fractal and multifractal analysis: A review,” vol. 13, no. 4, pp. 634–649, number: 4. [Online]. Available: <https://linkinghub.elsevier.com/retrieve/pii/S1361841509000395>
- [9] X. Wang, Y. Peng, L. Lu, Z. Lu, M. Bagheri, and R. M. Summers, “ChestX-ray8: Hospital-scale chest x-ray database and benchmarks on weakly-supervised classification and localization of common thorax diseases,” in *2017 IEEE Conference on Computer Vision and Pattern Recognition (CVPR)*, pp. 3462–3471. [Online]. Available: <http://arxiv.org/abs/1705.02315>
- [10] K. He, X. Zhang, S. Ren, and J. Sun, “Deep residual learning for image recognition.” [Online]. Available: <https://arxiv.org/abs/1512.03385v1>
- [11] T. Yep, “torchinfo,” original-date: 2020-03-16T21:41:29Z. [Online]. Available: <https://github.com/TylerYep/torchinfo>

Field Weakening Control of a Permanent Magnet Synchronous Motor

Rifqi Maulana¹, Yohan Fajar Sidik^{2*}, Husni Rois Ali³

Department of Electrical and Information Engineering

Universitas Gadjah Mada

Indonesia

¹rifqi.maulana@mail.ugm.ac.id, ²yohanfajarsidik@ugm.ac.id*, ³husni.rois.ali@ugm.ac.id

Abstract—A PMSM (Permanent Magnet Synchronous Motor) has high efficiency and torque characteristics compared to other motors. To maximize the potential of a PMSM, several control methods can be used. Field Oriented Control (FOC) is one of the control methods that can produce high torque values, to optimize the capabilities of PMSM. The purpose of the FOC method is to effectively control the torque and flux of the motor by adjusting the current transformation in the reference frame dq . At high speeds, there will be a point where the supply voltage will reach a maximum point and cannot supply the motor. This situation requires control to weaken the rotor field so that the inverter can still supply the motor properly. The situation occurs when the motor speed exceeds the base speed. During this condition, the motor torque will decrease and this condition is called field weakening (FW) or constant power condition. This research will analyze the FW control algorithm and its effect on motor speed conditions higher than the base speed, analysis will be conducted using PLECS.

Index Terms—PMSM, Field Oriented Control (FOC), Field Weakening (FW), Base speed, Constant power

I. INTRODUCTION

The development of a country is greatly influenced by its transportation system. The growing presence of motorized vehicles is having a harmful effect on the environment, as well as on human health and air quality [1]. A potential solution to address these issues is to transition to utilizing electric vehicles that are not only efficient but also environmentally friendly. Electric vehicles also possess a wide range of high efficiency and higher power density. Furthermore, numerous research studies have delved into motor for electric vehicles [2]–[4]. The Permanent Magnet Synchronous Motor (PMSM) is a popular choice for electrical motors due to its exceptional efficiency, quick torque response, and high torque-to-load ratio [5].

The Field-Oriented Control (FOC) method is a common approach used for controlling three-phase motor drive systems. The purpose of the FOC method is to effectively control the motor torque and flux to force the motor to accurately track the trajectory of various types of machines and load parameters or any extraneous disturbances. FOC control techniques have been effectively utilized in various industrial products [6]. The FOC method is typically used with a digital Pulse Width Modulation (PWM) controller in the rotating coordinate space, also known as the $d-q$ frame. At a high-speed state, there comes a point where the supply

voltage reaches its maximum and the d-axis flux (λ_d) needs to be reduced. The term "field weakening" refers to the scenario where the speed of a PMSM motor increases beyond its base speed when the motor torque decreases. To achieve a speed that surpasses the rating of your PMSM motor, this technique should be implemented.

Field weakening control methods are commonly used in modern electric drives. The phenomenon of field weakening is one of the aspects that need to be considered in high-speed PMSM operation [7], [8]. In the industrial sector, it is possible to use a motor with a lower rating for high-speed applications by utilizing field weakening control, which enables the motor to operate at speeds beyond its rating. In order to fully utilize its potential, it is essential to optimize the torque characteristics of the motor [9]. When the speed exceeds the rating, there is a reduction in torque that corresponds to these characteristics.

This research implement the FOC method, coupled with the application of a field weakening technique, was utilized on PMSM motors in the research. The purpose of the research was to determine if the Field Weakening Control (FWC) method could increase the speed of the PMSM motor above its base speed rating. The simulation results were obtained with the assistance of PLECS software during the research process.

II. PMSM MATHEMATICAL EQUATIONS

The PMSM can be modeled in a rotating reference frame or a $d-q$ reference frame. Analyzing a three-phase AC electrical machine using a stationary three-phase reference frame can be very complex due to the time-variant nature of parameter values. In order to simplify the complexity, the parameters are transformed with the Clarke and Park Transformation. Using this technique, the parameters in a stationary three-phase reference frame can be transformed into constants in a synchronously rotating reference frame, which is also referred to as the $d-q$ reference frame.

Using the Park Transformation, the stator voltage equation can be represented in the $d-q$ frame as follows [10]:

$$V_d = R_s i_d + \frac{d\lambda_d}{dt} - \omega_e \lambda_q \quad (1)$$

$$V_q = R_s i_q + \frac{d\lambda_q}{dt} + \omega_e \lambda_d \quad (2)$$

Where R_s is the stator resistance, i_{dq} is the dq -axis current, and ω_e is the electrical speed. While λ_d is the d -axis flux linkage, λ_q is the q -axis flux linkage, which can be represented as follows [10]:

$$\lambda_d = L_d i_d + \lambda_{pm} \quad (3)$$

$$\lambda_q = L_q i_q \quad (4)$$

The variables in this equation are L_d , which stands for d -axis inductance, L_q , which represents q -axis inductance, and λ_{pm} , which is the amplitude of the flux linkage due to permanent magnets.

To obtain the equations related to the $d - q$ current, equations 3 and 4 can be substituted into equations 1 and 2, as shown in [10]:

$$V_d = -\omega_e L_q i_q \quad (5)$$

$$V_q = \omega_e (L_d i_d + \lambda_{pm}) \quad (6)$$

According to literacy sources [11], $\omega_e \lambda_{pm}$ represents the back-EMF (BEMF) of the motor, while $-\omega_e L_q i_q$ and $\omega_e L_d i_d$ represent the crosscoupling interactions between the two dq axes. In the $d - q$ reference frame, the input power (P_{in}) of the PMSM can be modeled as [10]:

$$P_{in} = [V_a \ V_b \ V_c] \begin{bmatrix} i_a \\ i_b \\ i_c \end{bmatrix} = \frac{3}{2} [V_d \ V_q] \begin{bmatrix} i_d \\ i_q \end{bmatrix} \quad (7)$$

By substituting equations 5 and 6 with the back-emf component, the following equation is obtained [10]:

$$P_{out} = \frac{3}{2} \omega_e (\lambda_{pm} i_q + (L_d - L_q) i_d i_q) \quad (8)$$

The output torque value of the PMSM can be determined using the output power equation. The electrical speed of a PMSM is calculated by multiplying the mechanical speed with the number of motor pole pairs. This can be expressed as:

$$\omega_e = P \cdot \omega_m \quad (9)$$

Where P is the number of motor pole pairs. Then, substitute it into equation 8, and we get:

$$P_{out} = \frac{3}{2} P \omega_m (\lambda_{pm} i_q + (L_d - L_q) i_d i_q) \quad (10)$$

In order to determine the mechanical torque, the mechanical speed of the motor is multiplied by the output torque [12].

$$T_m = \frac{P_{out}}{\omega_m} = \frac{3}{2} P (\lambda_{pm} i_q + (L_d - L_q) i_d i_q) \quad (11)$$

SPMSM (Surface Permanent Magnet Synchronous Motor) has the same inductance value ($L_d = L_q$), so the mechanical torque can be written as follows:

$$T_m = \frac{3}{2} P (\lambda_{pm} i_q) \quad (12)$$

Using equation 12, we can determine the q -axis current when we know the value of T_{m_ref} . The equation is as follows [10]:

$$i_{q_ref} = \frac{T_{m_ref}}{\frac{3}{2} P \lambda_{pm}} \quad (13)$$

For the mechanical equation of the machine, it is expressed as follows:

$$T_m - T_{load} - T_{friction} = J \frac{d\omega_m}{dt} \quad (14)$$

T_{load} represents the load torque, $T_{friction}$ represents the friction torque of the motor load system, and J represents the polar moment of inertia.

III. FIELD ORIENTED CONTROL (FOC)

Field oriented control (FOC) method is also known as vector control, decoupling control, and orthogonal control. In speed drive applications, FOC is an efficient method of controlling synchronous motors that are adapted to rapid load changes under various speed conditions, including high speeds when field weakening is used. This type of control involves controlling the stator current in vector form. The control is based on projection, which makes a three-phase and time-dependent system into time-invariant with two coordinates (d and q). FOC requires two constants as input references, namely the torque component and the flux component. The torque component will be made aligned to the q axis, while the flux component will be made aligned to the d axis. To maximize torque production the d -axis current value is set to zero and the q -axis current is given a maximum value.

IV. FIELD WEAKENING CONTROL (FWC)

Field weakening control is a method to increase the rotating speed of a PMSM beyond its base speed. This method aims to extend the speed operating region of the motor within the limits of the current and voltage ratings of the motor [13], [14]. The working principle of FWC for PMSM is to weaken the d -axis flux (λ_d).

As the motor surpasses the base speed, both voltage and current start approaching their rating limits. Further increasing the speed beyond this point would lead to voltage and current values that exceed the motor's rating, potentially causing damage. Moreover, some power inverters cannot drive PMSMs at very high speeds because the BEMF is proportional to the motor speed and d -axis flux (λ_d), resulting in higher back-EMF values. When the BEMF value becomes larger than the maximum output voltage, the PMSM will not be able to draw current and will not be able to generate torque. Consequently, unless the d -axis flux (λ_d) is weakened, the rotor speed of the motor cannot be further increased once the BEMF reaches the maximum voltage threshold.

Without the FWC, BEMF of the PMSM will continue to increase as the speed increases. Therefore, the drive output voltage for the PMSM must be increased to maintain the desired phase current. In Figure 1, it can be seen that in the region with constant torque, the motor can be increased in speed with maximum torque until the terminal voltage of the motor reaches its limit value defined as base speed or $\omega_e = \omega_{base}$. This speed is the highest speed that the PMSM can achieve.

In FW control, there are two limitations that must be considered, namely maximum current and maximum voltage.

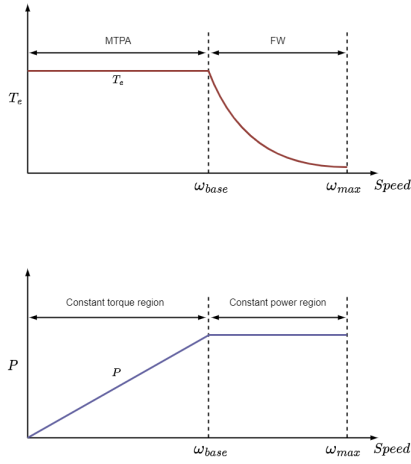


Fig. 1. Typical torque and power characteristics of PMSMs [10]

The current limitation is usually determined from the motor part, which depends on the cooling capability of the motor. Meanwhile, the maximum voltage limitation is usually determined from the drive part, which is the limitation on the dc bus voltage.

V. DRIVE LIMIT OPERATION

As previously discussed, when implementing PMSM control, it must meet the condition that it must not exceed the maximum current and voltage values. In addition, the reference value given must provide a torque value that has high efficiency [15]. The following is an illustration of the current locus diagram which is a representation of the dq current with the restrictions that must be met.

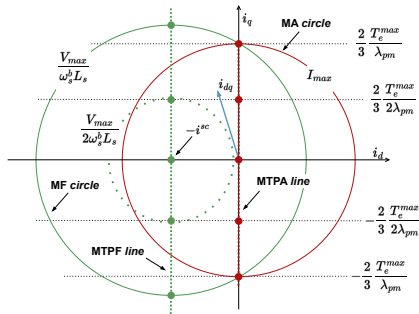


Fig. 2. SPMSM drive limit operation [15]

The first limitation that must be met is the constant torque line. In Figure 2, the constant torque line is represented by a point line with a horizontal direction. The line is realized by equation 13, it can be seen that the torque value is not affected by the d -axis current. There are 4 lines that represent this torque line, these lines are $i_q = \pm I_{\max}$ and $i_q = \pm 1/2 I_{\max}$ with the maximum torque equation function $T_e^{\max} = 3/2 i_{\max} \lambda_{pm}$.

The next limitation is the limitation of the maximum current (MA (Maximum Ampere)) of the PMSM, namely $i_d^2 + i_q^2 = I_{\max}^2$ which is represented by the current locus diagram with a red circle. Then the limitation of the maximum voltage

(MF (Maximum Flux Linkage)). The limitation describes the flux linkage value available from the maximum voltage limitation (V_{\max}). Based on the book [8], the maximum flux linkage circle can be represented with a center point valued at $(-i_{sc}, 0)$ and a radius of $(V_{\max}/\omega_e L_s)$ depicted with a green circle. The i_{sc} value is the short circuit current of the motor. It can be seen that the circle is limited by the maximum voltage that the motor has, the higher the motor speed, the smaller the radius of the circle. The MA and MF circles will intersect at which point the speed operation can be performed.

VI. DESIGN AND IMPLEMENTATION

In this research endeavor, simulations will be conducted to analyze the influence of Field Weakening Control on Permanent Magnet Synchronous Motor (PMSM). The Field Weakening method used is Constant Current Constant Power (CCCP) for SPMSM (Surface Permanent Magnet Synchronous Motor). This method aims to keep the current and power of the motor constant by changing the q -axis of the voltage component (V_q). While the d -axis of the voltage component (V_d) is kept constant. The analysis carried out in this research is to analyze the characteristic response of PMSM when given FOC control. Then the motor is given a reference that exceeds the base speed allowed then see how the resulting motor characteristics. Then perform FW simulation to see changes in the response given when the speed has exceeded the base speed of the motor used.

A. System Overview

An overview of the system used in this research can be seen in Figure 3. In general, the control system used in this research is a block diagram of the speed controller, field weakening (FW) control algorithm, current controller, Space Vector Modulation Model, and Surface Permanent Magnet Synchronous Motor (SPMSM). Each part has different functions and uses, but they are interconnected.

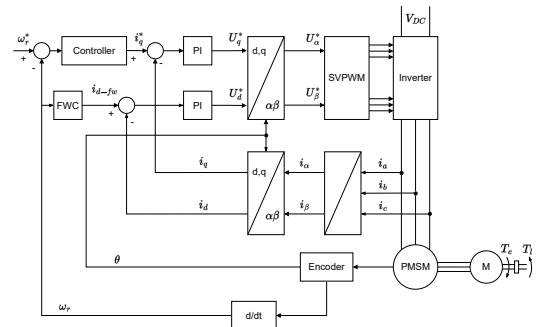


Fig. 3. Overview of the system

B. Field Weakening Algorithm

The field weakening algorithm used in this research is the Constant Current Constant Power (CCCP) algorithm [4]. This CCCP algorithm aims to keep the current and power values constant and not exceed the allowable limits. The CCCP algorithm has a constant power output, so this CCCP has a constant voltage value V_d with the equation that has been

derived in the previous section, namely equation 5 or can be written as follows [4]:

$$V_d = -\omega_e L_q i_q = -L_q (\omega_{base} I_s) = \text{constant} \quad (15)$$

With ω_{base} is the electrical base speed of the PMSM. To get the maximum torque on the SPMSM motor by making $i_q = I_s$. So that the q -axis current can be derived into the following equation [4]:

$$i_q = \frac{\omega_{base}}{\omega_e} I_s \quad (16)$$

With ω_e is the electrical speed of the motor. And it is known that under FW conditions there is a current limitation that must satisfy the following equation [4]:

$$I_s = \sqrt{i_d^2 + i_q^2} \quad (17)$$

When the FW condition must satisfy the conditions of the current equation, the combination of the dq -axis current value cannot exceed the current rating of the motor. So to satisfy equation 17, the substitution of equation 16 with 17 is performed to maintain a constant current value. And the current equation d is obtained as follows [4]:

$$i_d = -\sqrt{I_s^2 - i_q^2} = -\frac{I_s}{\omega_e} \sqrt{\omega_e^2 - \omega_{base}^2} \quad (18)$$

By substituting equation 18 with the d -axis voltage equation in equation 6, the following equation is obtained [4]:

$$v_q = \omega_e (\lambda_{om} + L_d i_d) = \omega_e \lambda_{pm} - L_d I_s \sqrt{\omega_e^2 - \omega_{base}^2} \quad (19)$$

As the motor electrical speed ω_e continues to increase, it will have an influence on the q -axis voltage value (V_q). When there is a transition between FOC and FW modes, the V_q value will decrease slightly and will continue to increase. The value of V_d will always be constant so that the voltage value only depends on V_q .

C. Load Condition

There are two load conditions in this research. The first type of load is when the torque condition is constant and the second type of load is when the power condition is constant or FW condition. For constant torque conditions, the load torque given to the motor is constant. Meanwhile, under constant power conditions, the load torque given to the motor decreases with increasing speed according to the following equation [16]:

$$T_{load} = \frac{T_{max} \cdot \omega_{m_base}}{|\omega_m|} \quad (20)$$

The equation represents the load torque during constant power conditions when it exceeds the base speed of the motor. Meanwhile, if the speed has not exceeded the base speed of the motor, the load torque condition will be in a constant torque condition or constant value load.

D. PMSM

To operate the PMSM, a circuit is needed to generate power which can be called a power circuit. The power is supplied by the DC link voltage input which then enters the inverter component to produce a 3-phase voltage. The inverter circuit used is a 3-phase Voltage Sourced Inverter (VSI). With the switching frequency used is 20 kHz. The motor used to implement the FWC method is a Surface Permanent Magnet Synchronous Motor (SPMSM). Implementation is done using PLECS software. The following Table I contains the parameter specifications of the SPMSM motor used for simulation.

TABLE I
PARAMETER MOTOR SPMSM

| No. | Parameter | Symbol | Nilai |
|-----|-------------------|----------------|--------------------------------------|
| 1. | Stator Resistance | R_s | 0.09 Ω |
| 2. | D-axis Inductance | L_d | 4.35 mH |
| 3. | Q-axis Inductance | L_q | 4.35 mH |
| 4. | Pole Pairs | P | 2 |
| 5. | PM Flux Linkage | λ_{pm} | 0.272 Wb |
| 6. | Moment of Inertia | J | 0.00179 $\text{kg} \cdot \text{m}^2$ |
| 7. | Maximum Current | I_{max} | 100 A |
| 8. | DC Link Voltage | V_{dc} | 650 V |
| 9. | Maximum Torque | T_{max} | 81.6 Nm |

VII. RESULT AND ANALYSIS

This section will show the results of simulation and analyzing the system as a whole based on the literature study that has been done. The system design is modeled using Field Oriented Control and Field Weakening Control system schemes.

VIII. SIMULATION OF SPMSM DRIVE LIMIT OPERATION

In Figure 4, is the projection result of the parameters that have been calculated in this simulation. It can be seen that the red circle is the maximum current (I_{max}) of the SPMSM used. Then the outer blue circle is the base speed value of the SPMSM using the maximum current (nm_b). Then, the simulation was carried out using half of the maximum torque and it was found that the base speed changed to (nm_A).

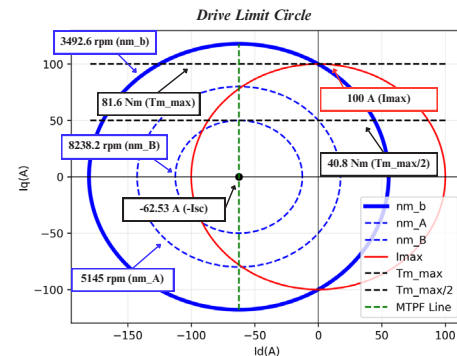


Fig. 4. SPMSM drive limit operation

It can be seen that when the torque used decreases, the base speed will increase, this is in accordance with the equation

used, namely by increasing the speed, the size of the voltage circle limit will also shrink. Then the maximum speed limit is at point (nm_B), where the d -axis current value can no longer be weakened at point ($-I_{sc}$).

IX. SIMULATION OF FIELD WEAKENING CONTROL (FWC)

Before the FW control simulation is carried out, to realize the constant power condition on the motor. An operating condition in which the power generated by the system remains constant even though the rotation speed increases or a condition in which the motor speed exceeds the base speed. When the PMSM exceeds the base speed, the torque generated by the motor will proportionally decrease, but the opposite of the power generated will always be constant. This is because the power in the motor no longer depends on the torque, but only depends on the motor rotation speed. In the simulation carried out, it is necessary to have conditions that can realize this. Because, the motor torque is very dependent on the torque of the load used, then to make these conditions it is necessary to set the torque load that can adjust these conditions. The equation for calculating the torque load under constant power conditions has been explained in equation 20. The following are the results of the realization of the constant power load on PLECS.

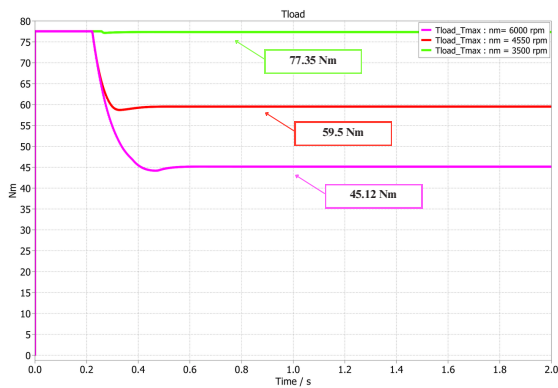


Fig. 5. The simulation results of constant power load with reference speed variation

For the maximum torque used, a tolerance of 95% of the maximum torque is given, because when using the maximum torque the system cannot realize control. It can be seen that the relationship between load torque and mechanical speed is correct, namely the higher the mechanical speed, the load torque will decrease. By knowing the constant power load torque, the next step is to integrate the load into the FW control model.

In Figure 6 - 8, are the simulation results obtained from the simulation by varying the speed. In the figure, it can be seen that the system can track the given reference speed. From this information, it can be seen that the system can exceed the base speed of the motor. Furthermore, the motor torque is weakened as a result of using a constant power torque load. This will have an impact on the motor q -axis current will

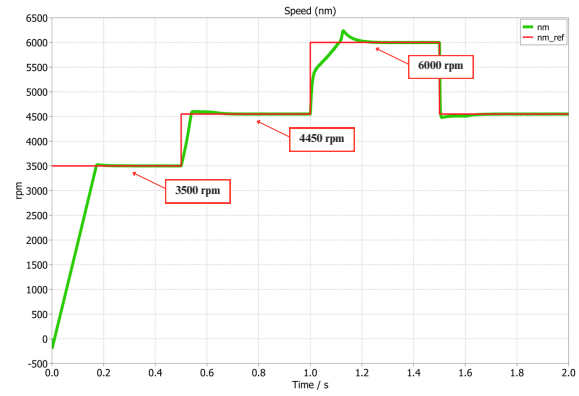


Fig. 6. The simulation results of the motor speed under FWC conditions above the base speed

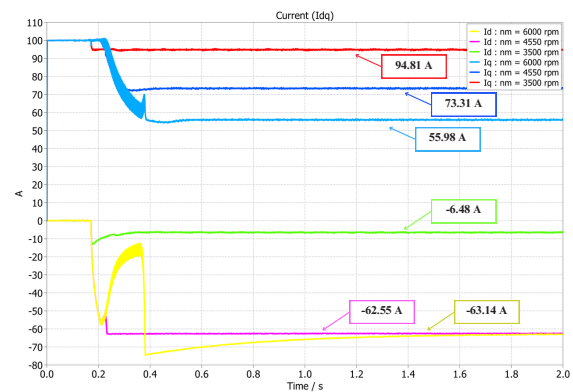


Fig. 7. The simulation results of the motor's dq current under FWC conditions above the base speed

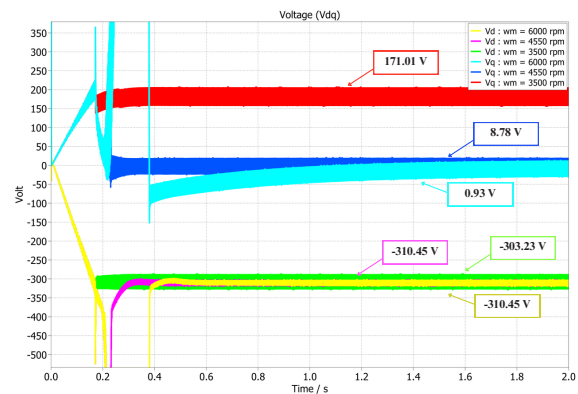


Fig. 8. The simulation results of the motor's dq voltage under FWC conditions above the base speed

be weakened. And then it can be seen that the FW control algorithm can run properly because when the steady state with a speed above the base speed, the d -axis current is weakened. To overcome the current that exceeds the limit, the current d is weakened according to the value $-I_{sc} = -62.53$ A. The weakening that occurs in the dq -axis current will cause the

dq -axis voltage to be limited. This is desirable because as the speed increases, the motor will not be damaged because the dq -axis voltage is limited below its maximum rating.

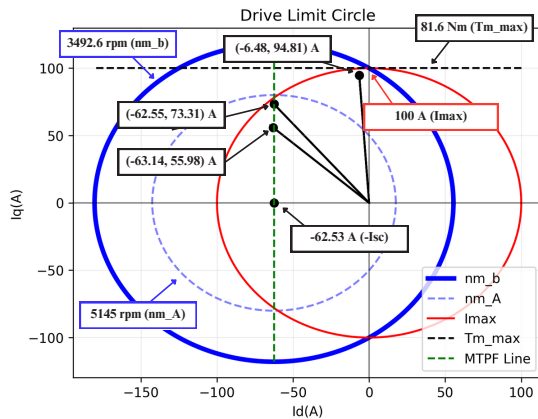


Fig. 9. Trajectory of dq current on the drive limit circle

It can be seen in Figure 9, which is the result of the current projection point of the FW control simulation results on the drive limit circle. It can be seen that some of these trajectory points meet the conditions for the motor to operate properly. The explanation related to the drive limit circle has been explained previously, namely when the blue circle shrinks, it means that the motor speed is getting higher. The controller is said to be successful when the trajectory point does not exceed the limit of the maximum current. It can be seen that the trajectory point follows the red circle and stops when it reaches the current attenuation limit d , namely $-I_{sc} = -62.53$ A.

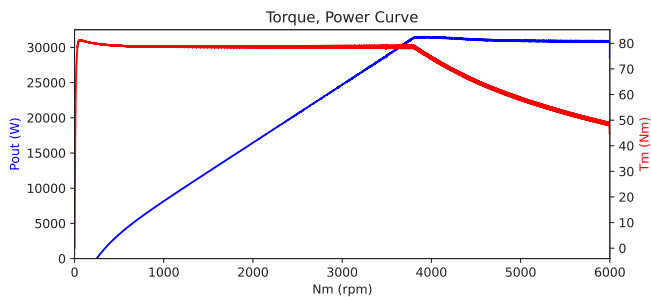


Fig. 10. The simulation results of the torque and power curve

It can be seen in Figure 10, the system can already realize the results of the power and torque curves compared to the speed. It can be seen that when the condition of constant torque, the value of torque is constant at its maximum value while the value of power increases along with the increase in speed. While during constant power conditions, the value of torque will decrease proportionally with increasing speed, while the power value will always be constant. This is to prevent the motor from being damaged by working with power above the allowable rating. In the end, it can be concluded that the FW control that has been carried out can realize SPMSM motor control with reference speed conditions above the motor base speed.

X. CONCLUSIONS

Based on the results of the analysis that has been carried out, to find out the voltage and current limits of SPMSM, it is necessary to understand the drive limit circle of the motor parameters used. The circle diagram explains the components that affect the optimal operating point of the motor starting from the maximum current, maximum voltage, motor inductance, motor flux linkage, and maximum motor torque. By understanding the relationship of all these parameters, the control that will be carried out will be optimal and will not exceed the motor rating used. The FWC method succeeds in utilizing the motor speed above the base speed without damaging the motor, because the voltage and current do not exceed the rating of the motor used. The method is performed by weakening the d -axis flux (λ_d) and using a torque load under constant power conditions. When these conditions are met, the motor can reach speeds above the base speed.

REFERENCES

- [1] B. Oktaviastuti, "Urgensi pengendalian kendaraan bermotor di indonesia," *Rekayasa: Jurnal Teknik Sipil*, vol. 2, pp. 5–8, 2017, 3.
- [2] J. Zheng, Z. Wang, D. Wang, Y. Li, and M. Li, "Review of fault diagnosis of pmsm drive system in electric vehicles." *IEEE*, 7 2017, pp. 7426–7432.
- [3] Z. G. H. W. and C. M., "Rediscovery of permanent magnet flux-switching machines applied in ev/hevs: Summary of new topologies and control strategies." *Chinese Journal of Electrical Engineering*, vol. 2, pp. 31–42, 12 2016.
- [4] J. de Santiago, H. Bernhoff, B. Ekegård, S. Eriksson, S. Ferhatovic, R. Waters, and M. Leijon, "Electrical motor drivelines in commercial all-electric vehicles: A review," *IEEE Transactions on Vehicular Technology*, vol. 61, pp. 475–484, 2 2012.
- [5] T. Deng, Z. Su, J. Li, P. Tang, X. Chen, and P. Liu, "Advanced angle field weakening control strategy of permanent magnet synchronous motor," *IEEE Transactions on Vehicular Technology*, vol. 68, pp. 3424–3435, 4 2019.
- [6] M. S. Merzoug and F. Naceri, "Comparison of field-oriented control and direct torque control for permanent magnet synchronous motor (pmsm)," *International Journal of Electrical and Computer Engineering*, vol. 2, pp. 1797–1802, 2008, 5.
- [7] K. Zhou, M. Ai, D. Sun, N. Jin, and X. Wu, "Field weakening operation control strategies of pmsm based on feedback linearization," *Energies*, vol. 12, p. 4526, 11 2019.
- [8] Y. Zhang, W. Cao, S. McLoone, and J. Morrow, "Design and flux-weakening control of an interior permanent magnet synchronous motor for electric vehicles," *IEEE Transactions on Applied Superconductivity*, vol. 26, pp. 1–6, 10 2016.
- [9] R. Nalepa and T. Orłowska-Kowalska, "Optimum trajectory control of the current vector of a nonsalient-pole pmsm in the field-weakening region," *IEEE Transactions on Industrial Electronics*, vol. 59, pp. 2867–2876, 7 2012.
- [10] M. Li, J. He, and N. A. Demerdash, "A flux-weakening control approach for interior permanent magnet synchronous motors based on z-source inverters." *IEEE*, 6 2014, pp. 1–6.
- [11] L. Harnefors and H.-P. Nee, "Model-based current control of ac machines using the internal model control method," *IEEE Transactions on Industry Applications*, vol. 34, pp. 133–141, 1998.
- [12] F. Qi, D. Scharfenstein, and C. Weiss, "Handbook of electric machines," 2019.
- [13] Z. Huang, C. Lin, and J. Xing, "A parameter-independent optimal field-weakening control strategy of ipmsm for electric vehicles over full speed range," *IEEE Transactions on Power Electronics*, vol. 36, pp. 4659–4671, 4 2021.
- [14] J. Xinhai, Z. Yanneng, and X. Dianguo, "Novel pmsm field-weakening control method." *IEEE*, 10 2017, pp. 3744–3748.
- [15] R. W. D. Doncker, D. W. Pulte, and A. Veltman, *Advanced Electrical Drives*. Springer International Publishing, 2020.
- [16] PSIM, "Psim user's guide," pp. 143–143, 2020. [Online]. Available: <https://powersimtech.com/wp-content/uploads/2021/01/PSIM-User-Manual.pdf>

Performance Comparison of ZDAC vs MTPA for Permanent Magnet Synchronous Motor (PMSM) Control

Nadia Gustiranda Cahyeni¹, Yohan Fajar Sidik^{2*}, Eka Firmansyah³
 Department of Electrical and Information Engineering
 Universitas Gadjah Mada
 Indonesia

¹Nadiagustiranda2019@mail.ugm.ac.id, ²yohanfajarsidik@ugm.ac.id*, ³eka.firmansyah@ugm.ac.id

Abstract—The permanent magnet synchronous motor (PMSM) consists of two types, namely surface mounted PMSM (SPMSM) and interior PMSM (IPMSM). IPMSM has the potential to generate a greater torque than SPMSM due to its torque reluctance. To exploit this potential, a comparison of two control methods is conducted, namely ZDAC (zero d-axis current control) vs MTPA (maximum torque per ampere) control. Testing between these two control methods was carried out with variations in speed and load, and it was found that ZDAC could not maximize reluctance torque, because of that limiting the torque capability. MTPA control is applied to optimize efficiency. Compared to ZDAC or $I_d = 0$ A, MTPA control can produce maximum electromagnetic torque with smaller stator current values. Therefore, in the constant torque region or below the base speed, the IPMSM is controlled with MTPA to obtain better efficiency in motor operation.

Index Terms—Interior permanent magnet synchronous motor (IPMSM), maximum torque per ampere (MTPA), zero d-axis current control (ZDAC), vector control, and electromagnetic torque.

I. INTRODUCTION

In this current era, PMSM (Permanent Magnet Synchronous Motor) has become one of the motors widely used in industrial equipment applications. This PMSM motor offers numerous advantages, as it incorporates permanent magnets in the rotor, providing higher efficiency and power factor, as well as a smaller size compared to conventional synchronous motors [1]. Consequently, the utilization of PMSM as a drive motor holds significant potential in the future market for low and medium power applications [2].

Based on the arrangement of permanent magnets, PMSM can be classified into 2 types, SPMSM (Surface Mounted PMSM) and IPMSM (Interior PMSM). In SPMSM, permanent magnets are placed on the rotor surface [3]. This arrangement is not suitable for high speeds, as the centrifugal force that occurs can lead to magnet damage. The symmetric circular placement of magnets in SPMSM creates a smooth path for flux and results in a motor structure with no saliency (non-saliency). On the other hand, the IPMSM type, which has a saliency ratio, positions permanent magnets inside the rotor, allowing it to operate at high speeds. The asymmetric magnet placement in IPMSM induces magnetic attraction. As

a result, the inductance of IPMSM is a function of the rotor position, leading to the motor having reluctance torque and magnetic torque [4], [5].

Although IPMSM (Interior PMSM) has many advantages, it requires precise control to ensure optimal performance. However, controlling IPMSM becomes more complex due to the presence of permanent magnets on the rotor. The Back EMF generated by PMSM takes the form of a 3-phase sinusoidal signal, which provides constant power when maintained in the stator [2]. This 3-phase sinusoidal current is transformed into two phases: the direct axis (d-axis) and the quadrature axis (q-axis). The q-axis current component, which is parallel to the back EMF voltage, produces magnetic torque, while the d-axis current component, which is perpendicular to it, generates reluctance torque, dependent on the q-axis current.

Several control techniques are used in PMSM, including MTPA (maximum torque per ampere) and ZDAC (zero d-axis current control). MTPA is commonly used in the constant torque region or at speeds below the base speed due to its high efficiency [6]. When comparing MTPA and ZDAC, MTPA provides higher efficiency by producing less stator current than ZDAC.

The structure of this paper is organized as follows: the mathematical model of PMSM, discussed in Section II, lays the foundation. The control strategies are elaborated in Section III. Next, the simulation results from PLECS and a comparison between the two control techniques are presented in Section IV. Finally, the conclusions are presented in Section V.

II. MATHEMATICAL MODEL

The model of IPMSM can be represented by the following mathematical equation, which is used to simulate the machine's behavior. The equation for the stator phase voltage of IPMSM is as follows [7]

$$V_a = R_s I_s + \frac{d\lambda_a}{dt} \quad (1)$$

$$V_b = R_s I_s + \frac{d\lambda_b}{dt} \quad (2)$$

$$V_c = R_s I_s + \frac{d\lambda_c}{dt} \quad (3)$$

Where V_a, V_b, V_c are the stator phase voltages, I_a, I_b, I_c represent the stator phase currents. R_s is the stator resistance. Meanwhile, λ_a, λ_b and λ_c are the phase flux linkages, which represent the linkage between the magnetic field and the stator windings in each phase. These flux linkages are essential parameters in the mathematical model of the IPMSM and are used to describe the machine's behavior.

To obtain a simpler machine model, the voltage equation can be transformed from a 3-variable system to a 2-variable system using the Park transformation, which converts from the abc coordinate system to the dq coordinate system. The transformation matrix can be represented by the following equation [2],

$$\begin{bmatrix} S_q \\ S_d \\ S_0 \end{bmatrix} = \frac{2}{3} \begin{bmatrix} \cos \theta & \cos(\theta - \frac{2\pi}{3}) & \cos(\theta + \frac{2\pi}{3}) \\ \sin \theta & \sin(\theta - \frac{2\pi}{3}) & \sin(\theta + \frac{2\pi}{3}) \\ \frac{1}{2} & \frac{1}{2} & \frac{1}{2} \end{bmatrix} \begin{bmatrix} S_a \\ S_b \\ S_c \end{bmatrix}. \quad (4)$$

Where S_d, S_q and S_0 are the voltage, current, and flux linkages vectors of the stator in the d and q components. θ is the angle between the fixed stator axis and the rotor d -axis. From the equation above, we obtain the voltage equation for IPMSM in the dq transformation as follows [8]

$$V_d = R_s I_d + \frac{d\lambda_d}{dt} - \omega_e \lambda_q \quad (5)$$

$$V_q = R_s I_q + \frac{d\lambda_q}{dt} + \omega_e \lambda_d, \quad (6)$$

and the flux equation in dq transformation

$$\lambda_d = L_d I_d + \lambda_m \quad (7)$$

$$\lambda_q = L_q I_q, \quad (8)$$

where ω_e is the electrical speed which can be formulated as follows,

$$\omega_e = \frac{d\theta}{dt} = \omega_m \left(\frac{P}{2} \right). \quad (9)$$

P is the number of poles and ω_m is the mechanical speed. Based on the dq modeling, the equivalent circuit of the IPMSM can be depicted in Figure 1 [9].

By substituting equations (7) and (8) into equations (5) and (6), we obtain the voltage equation in the dq coordinate system as follows,

$$V_d = R_s I_d - \omega_e L_q I_q + \frac{d}{dt}(L_d I_d + \lambda_m) \quad (10)$$

$$V_q = R_s I_q + \omega_e (L_d I_d + \lambda_m) + \frac{d}{dt}(L_q I_q). \quad (11)$$

From equation (4) (5) and (6), then the value of the input power can be written as

$$P_{in} = \frac{3}{2}(V_q I_q + V_d I_d). \quad (12)$$

Neglecting the zero sequence components, the output power can be calculated by substituting equations (5) and (6)

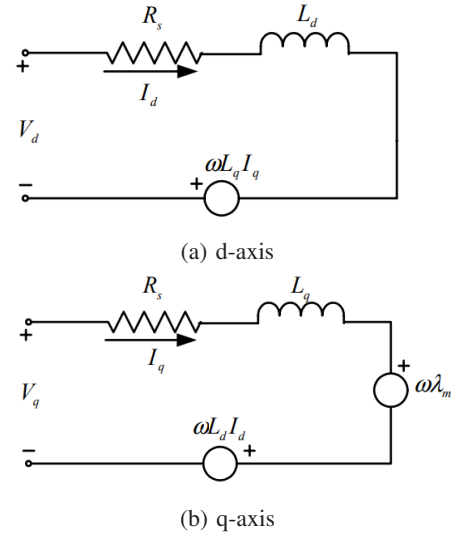


Fig. 1: Equivalent circuit

with the integrated back EMF terms $\omega_e \lambda_d$ dan $\omega_e \lambda_q$. Thus, the output power is given as [2], [10],

$$P_o = \frac{3}{2}(-\omega_e \lambda_q I_d + \omega_e \lambda_d I_q). \quad (13)$$

To calculate the electromagnetic torque, which represents the ratio of power to mechanical speed, it can be represented by the following equation,

$$T_e = \frac{3}{4}P(\lambda_m I_q + (L_d - L_q)I_q I_d), \quad (14)$$

in addition, torque can also be represented as,

$$T_e = T_L + B\omega_m + J\frac{d\omega_m}{dt} \quad (15)$$

where J is the rotor inertia, T_L is the load torque. Meanwhile, the constant B is the coefficient of viscous friction which is related to the engine rotation system and mechanical loads.

III. CONTROL METHOD

Field Oriented Control (FOC) is one of the best control methods for low-speed applications and high-performance drives. In FOC, the torque value is not directly controlled; instead, it is regulated by the current, hence FOC is also known as an indirect control method. In this approach, the shaft speed provided by a sensor is utilized as feedback in a closed-loop control system, and there is a current control system used for electromagnetic torque control [11]. The advantages of FOC include precise speed control and good torque response. However, it comes with the drawback of being relatively expensive and requiring modulation techniques to control the inverter as the machine driver [12].

FOC involves two operations: constant torque operation and flux weakening operation. Constant torque operation occurs when the motor speed increases, and the torque remains constant at a certain value. Then, when the motor speed reaches its rated speed, the torque value gradually decreases,

entering the flux weakening operation [13]. The relationship between the two operations can be seen in Figure 2.

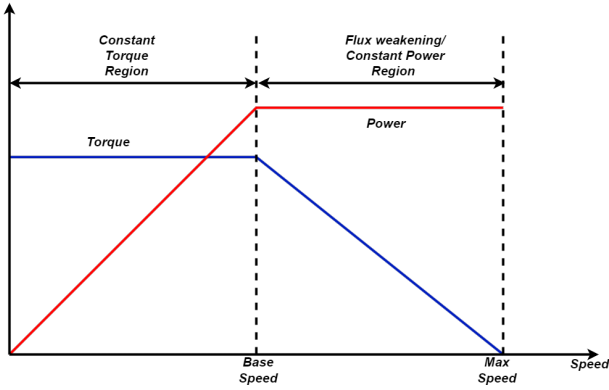


Fig. 2: Torque and speed characteristics of PMSM

The goal of constant torque control is to achieve maximum torque with minimum stator current magnitude. Control in the constant torque region can be classified into two methods ZDAC and MTPA.

The simulation begins by designing the IPMSM and its control. Firstly, after determining the IPMSM parameters, input variations such as reference speed and load torque are provided. Speed and position sensors are then read, and the difference between the input reference speed and the measured speed is calculated as the speed error. This error is passed to the PI controller, which produces the torque reference. then the torque will be input to the MTPA or ZDAC method, to obtain the d -axis and q -axis reference currents.

On the other side, the three-phase abc currents of the motor are transformed into two-phase dq currents using the Park transformation. The dq reference currents and the actual dq currents are compared, and the error values are input to the PI control block to adjust accordingly. The output of the PI controller is combined with the decoupling system to eliminate cross-coupling effects on the motor, resulting in the dq -axis voltages. These dq -axis voltages are converted back to three-phase voltages using the inverse Park transformation, which is then used as the input to the SVPWM (Space Vector Pulse Width Modulation). SVPWM generates three pairs of pulse signals that control each switching. In summary, the control system flow in this research can also be seen in Figure 3.

A. Zero D-Axis Current Control (ZDAC)

In the ZDAC method, the d -axis current is set to zero, while the q -axis current is aligned with the current vector to maintain a 90° torque angle. The ZDAC method is suitable for motors in a non-saliency condition, which occurs when $L_d = L_q$, such as in SPMSM. The main advantage of the ZDAC control strategy is the simplification of current control. The reference values for I_d and I_q are obtained using the following equations

$$I_{dref} = 0 \quad (16)$$

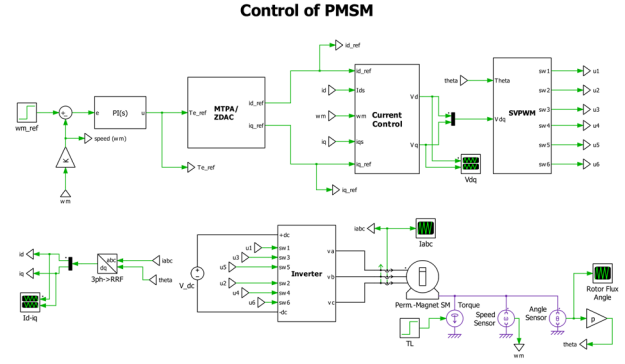


Fig. 3: PMSM control circuit block diagram

$$I_{sm} = I_{qref} = \frac{2}{3} \frac{2}{P} \frac{T_m}{\lambda_m} \quad (17)$$

B. Maximum Torque Per Ampere (MTPA)

The MTPA method maximizes the reluctance torque, where the d -axis current value is no longer maintained at 0 A. When using MTPA, the reference values for I_d and I_q can be formulated as follows

$$I_{dref} = \frac{\lambda_m}{4(L_q - L_d)} - \sqrt{\frac{\lambda_m^2}{16(L_q - L_d)^2} + \frac{I_{sm}^2}{2}} \quad (18)$$

$$I_{qref} = \sqrt{I_{sm}^2 - I_{dref}^2} \quad (19)$$

with I_{sm} value is

$$I_{sm} = \frac{2}{3} \frac{2}{P} \frac{T_m}{\lambda_m} \quad (20)$$

IV. SIMULATION RESULT

The motor used in this research is an IPMSM (Interior Permanent Magnet Synchronous Motor), where the values of L_d and L_q are not the same. Therefore, there is a saliency ratio. The motor parameters used in this study are shown in Table I [14].

The comparison of dynamic performance between the IPMSM vector control systems controlled with MTPA and ZDAC can be observed in Figure 4. The motor operates under the condition where the reference speed is increased from 1000 RPM to 2000 RPM at 0.2 seconds, and the torque load is increased from 200 Nm to 400 Nm at 0.1 seconds. It can be seen that both MTPA and ZDAC can produce maximum torque. However, the rise time of the speed graph in MTPA is shorter when compared to ZDAC.

For the dq -axis current, the comparison between the ZDAC and MTPA methods can be seen in Figure 5. The simulation results indicate that, in the ZDAC method, regardless of the motor load condition and the reference speed, the d -axis current value will always be 0 A. On the other hand, when using the MTPA method, the d -axis current value is not always 0 A; it varies towards the negative axis depending on changes in motor speed and load magnitude. This demonstrates that the MTPA method successfully maximizes reluctance torque.

TABLE I: PMSM motor parameters

| Parameters | Value | Unit |
|-------------------------------|--------|------------------|
| Stator d-axis inductance (Ld) | 0.28 | mH |
| Stator q-axis inductance (Lq) | 0.61 | mH |
| Rated power (Prated) | 300 | kW |
| Rated voltage (Vrated) | 346 | V |
| Flux linkage | 0.29 | Wb |
| Pole | 6 | |
| Rated current (Irated) | 500 | A |
| Rated torque (Trated) | 955 | Nm |
| Rated speed (ω rated) | 3000 | RPM |
| Stator resistance (Rs) | 0.0041 | Ohm |
| Moment of inertia (J) | 0.044 | kgm ² |
| Moment of inertia (J) | 0.19 | Nms |
| Input voltage (inverter) | 601 | V |
| Switching frequency (fsw) | 20 | kHz |
| Sampling period (Ts) | 200 | μ s |

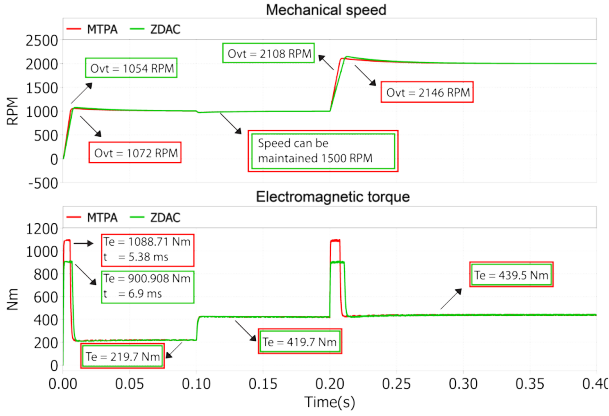


Fig. 4: Comparison of electromagnetic torque and speed representation in MTPA and ZDAC methods

As for the I_q current, the MTPA method produces smaller values compared to ZDAC. In the steady-state region, when subjected to a load of 400 Nm and a speed of 1000 RPM, or at 0.1 to 0.2 seconds, the dq -axis current values can be represented as vectors, as shown in Figure 6. Knowing the dq -axis current values for ZDAC ($I_d = 0$ A and $I_q = 321.67$ A) and MTPA ($I_d = -88.34$ A and $I_q = 292.31$ A), the magnitude of the stator current can be mathematically calculated as follows,

ZDAC

$$I_s = \sqrt{I_d^2 + I_q^2} = \sqrt{0^2 + 321.67^2} = 321.67 \text{ A}$$

MTPA

$$I_s = \sqrt{I_d^2 + I_q^2} = \sqrt{(-88.34)^2 + 292.31^2} = 305.37 \text{ A}$$

Therefore, it can be concluded that both the MTPA and ZDAC methods successfully achieve maximum torque, but the MTPA method can achieve maximum torque with a smaller magnitude of current compared to ZDAC.

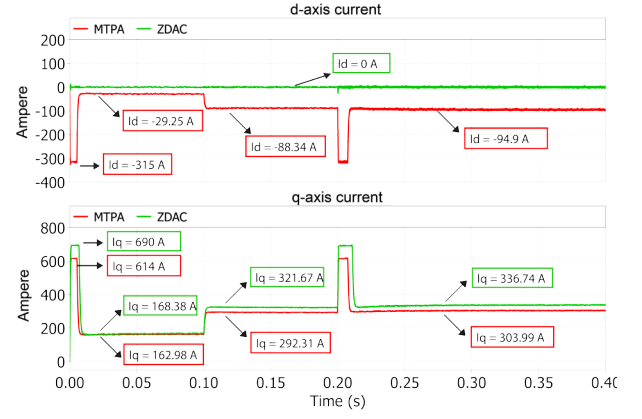


Fig. 5: Comparison of d-q axis currents of MTPA and ZDAC

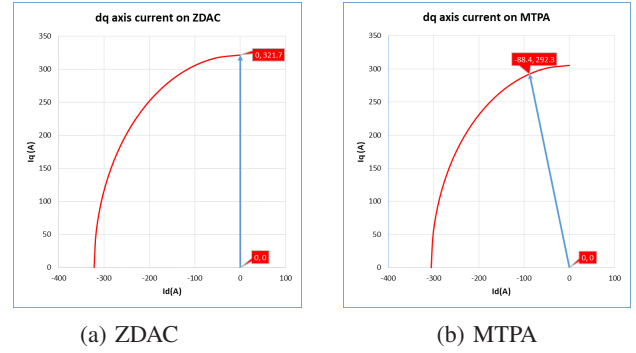


Fig. 6: Vector representation of d-axis and q-axis currents

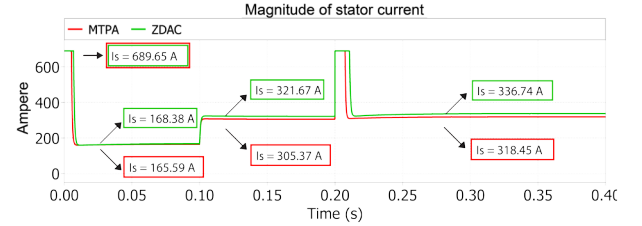


Fig. 7: Comparison of MTPA and ZDAC stator current magnitudes

Besides that, the simulation results also show that the stator current value is higher when controlled with ZDAC compared to MTPA. This is evident in Figures 7, 8 and Table II. Based on this data, it is evident that the MTPA method can minimize the stator current, especially at high speeds and large torque loads, as shown in the column chart in Figure 9. Since MTPA provides lower or smaller stator current values, it offers higher efficiency than ZDAC in obtaining maximum torque.

TABLE II: Comparison of ZDAC and MTPA stator current magnitudes

| ω_{ref} T_L | 1000 RPM | | 2000 RPM |
|-------------------------|----------|--------|----------|
| | 200 Nm | 400 Nm | 400 Nm |
| MTPA | 165.59 | 305.37 | 318.45 |
| ZDAC | 168.38 | 321.67 | 336.73 |
| Difference | 2.79 | 16.3 | 18.28 |

The comparison between MTPA and ZDAC can also be observed from the graphs showing the torque-to-current ratio

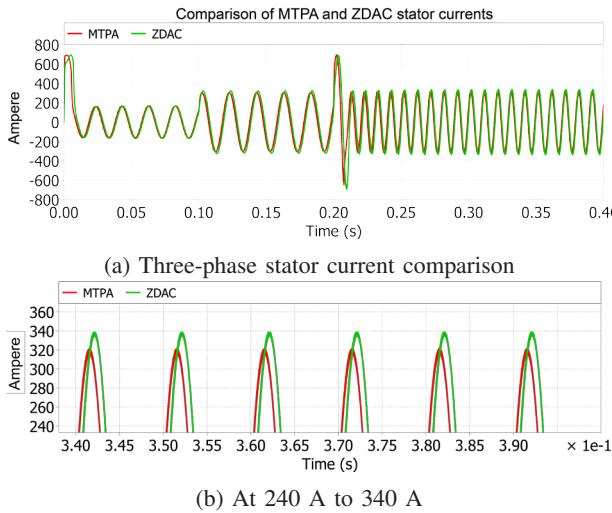


Fig. 8: Comparison of MTPA and ZDAC three-phase currents

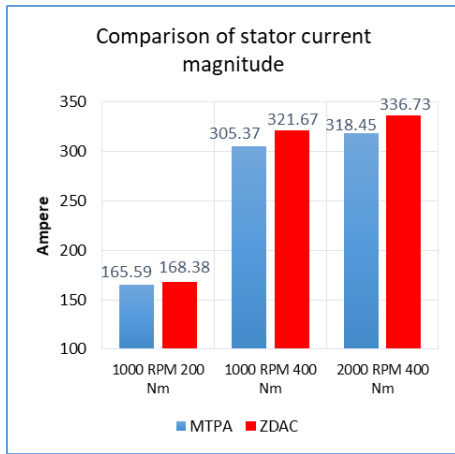


Fig. 9: Column chart comparing the magnitude of stator current between MTPA and ZDAC

and the torque-current ratio as a function of rotor speed, as shown in Figure 10 and Figure 11. The analysis of these plots indicates that with the MTPA method, the ratio between torque and current can achieve higher values compared to the ZDAC method. This signifies that the MTPA method can optimize motor performance by extracting as much torque as possible when the motor current is at its minimum.

Efficiency in IPMSM control using MTPA and ZDAC can be assessed by comparing the output power and input power of the system. By utilizing equations (12) and (13), the values of input power and output power can be found in Table III. Based on these calculations, it can be seen that the efficiency achieved using the MTPA method is higher than that of the ZDAC method, as shown in Figure 12.

The simulation results clearly demonstrate that controlling IPMSM using the MTPA method can achieve optimal results or yield a higher ratio of electromagnetic torque to stator current. As a result, MTPA control is significantly superior to ZDAC control for vector-controlled IPMSM systems.

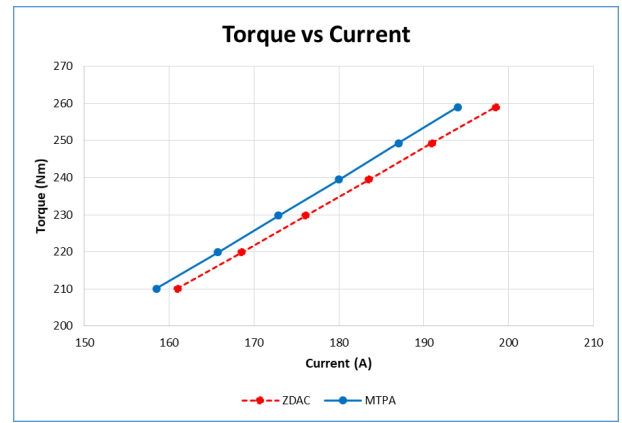


Fig. 10: Representation of torque and stator current comparison between the MTPA and ZDAC methods

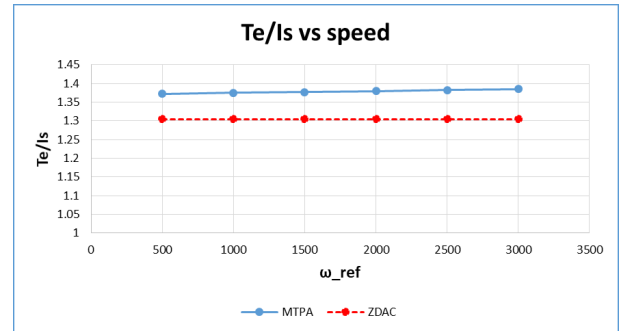


Fig. 11: Representation of torque-current and speed comparison between the MTPA and ZDAC methods

TABLE III: Comparison of power efficiency using ZDAC and MTPA

| Motor load | ω_{ref} | MTPA | ZDAC |
|------------|----------------|---------|---------|
| | | Eff (%) | Eff (%) |
| 0 Nm | 500 | 99.58 | 99.54 |
| | 1000 | 99.21 | 99.09 |
| | 1500 | 98.81 | 97.73 |
| | 2500 | 98.04 | 97.66 |
| 200 Nm | 500 | 98.61 | 98.60 |
| | 1000 | 99.38 | 99.30 |
| | 1500 | 99.44 | 98.16 |
| | 2500 | 98.39 | 98.16 |
| 400 Nm | 500 | 94.86 | 94.69 |
| | 1000 | 97.50 | 97.41 |
| | 1500 | 98.24 | 98.21 |
| | 2500 | 97.80 | 97.80 |

V. CONCLUSION

This research discusses the vector control of the IPMSM with the main goal of achieving maximum torque with minimum stator current to make the motor more efficient. Based on the discussions and analyses conducted, the following conclusions can be drawn:

- 1) In the ZDAC method, the d -axis current value will always be 0, regardless of changes in torque load and reference speed. On the other hand, in the MTPA method, the d -axis current value will change according

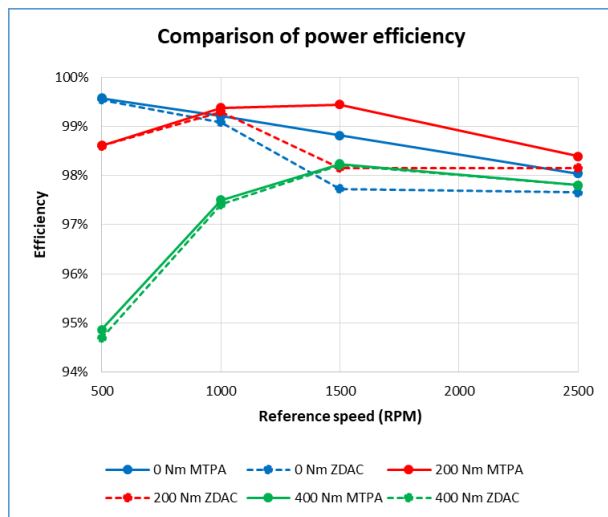


Fig. 12: Graphic comparison of power efficiency using ZDAC and MTPA

to variations in torque load and reference speed, moving in the negative direction.

- 2) For the q -axis current, using the MTPA method results in lower current values compared to the ZDAC method.
- 3) Compared to ZDAC, MTPA can achieve maximum torque with a smaller stator current, allowing MTPA to fully exploit reluctance torque by utilizing the d -axis current.
- 4) MTPA can achieve higher power efficiency, maximizing the utilization of motor torque and reducing losses.

In conclusion, MTPA proves to be a more effective control method for the IPMSM in achieving the desired goal of maximizing torque with minimum stator current, leading to enhanced motor efficiency.

REFERENCES

- [1] W. Zhuoyong, Y. Xiaodong, L. Jiakang, X. Liangxu, T. Hui, and L. Ke, "Research on IPMSM Control Based on MTPA," *Procedia Computer Science*, vol. 208, pp. 635–641, 2022. [Online]. Available: <https://doi.org/10.1016/j.procs.2022.10.087>
- [2] L. Qinghua, "ANALYSIS, DESIGN AND CONTROL OF PERMANENT MAGNET SYNCHRONOUS MOTORS FOR WIDE-SPEED OPERATION," pp. 1–230, 2005.
- [3] D. Anton, K. Young-kwan, L. Sang-joon, and L. Sang-taek, "Robust self-tuning MTPA algorithm for IPMSM drives," pp. 1355–1360, 2008.
- [4] P. Niazi, H. A. Toliyat, and A. Goodarzi, "Robust maximum torque per ampere (MTPA) control of PM-assisted SynRM for traction applications," vol. 56, pp. 1538–1545, 2005.
- [5] C. T. Pan and S. M. Sue, "A linear maximum torque per ampere control for IPMSM drives over full-speed range," vol. 20, pp. 359–366, 2005.
- [6] K. Li and Y. Wang, "Maximum Torque per Ampere (MTPA) Control for IPMSM Drives Using Signal Injection and an MTPA Control Law," *IEEE Transactions on Industrial Informatics*, vol. 15, no. 10, pp. 5588–5598, 2019.
- [7] I. Boldea and S. A. Nasar, *Electric Drives*. CRC Press, sep 2016.
- [8] H. Meher, "Performance Analysis of Interior Permanent Magnet Synchronous Motor (Ipmsm) Drive System Using Different Speed Controllers," *In Electrical Engineering (Power Control & Drives)*, no. 211.
- [9] B. Bossoufi, M. Karim, S. Ionita, and A. Lagrioui, "Low-speed sensorless control of pmsm motor drive using a nonlinear approach backstepping control: FPGA-based implementation," *Journal of Theoretical and Applied Information Technology*, vol. 36, no. 2, pp. 154–166, 2012.

- [10] F. Tahami, H. Nademi, and M. Rezaei, "Maximum torque per ampere control of permanent magnet synchronous motor using genetic algorithm," *Telkommika*, vol. 9, no. 2, pp. 237–244, 2011.
- [11] F. Korkmaz, I. Topaloğlu, M. F. Çakir, and R. Gürbüz, "Comparative performance evaluation of FOC and DTC controlled PMSM drives," *International Conference on Power Engineering, Energy and Electrical Drives*, no. May, pp. 705–708, 2013.
- [12] C. Capitan, "Torque Control in Field Weakening Mode," no. June, p. 84, 2009.
- [13] S. Halder, S. P. Srivastava, and P. Agarwal, "Flux weakening control algorithm with MTPA control of PMSM drive," *India International Conference on Power Electronics, IICPE*, vol. 2015-May, no. 1, 2015.
- [14] C. Lian, F. Xiao, J. Liu, and S. Gao, "Analysis and compensation of the rotor position offset error and time delay in fieldoriented-controlled PMSM drives," *IET Power Electronics*, vol. 13, no. 9, pp. 1911–1918, 2020.

Droop Control Strategy of Controlled Three-Phase PWM Rectifier for Hybrid Train Propulsion

1st Fransisco Danang Wijaya
*Department of Electrical Engineering and
 Information Technology
 Universitas Gadjah Mada
 Yogyakarta, Indonesia
 danangwijaya@ugm.ac.id*

2nd Yohan Fajar Sidik
*Department of Electrical Engineering and
 Information Technology
 Universitas Gadjah Mada
 Yogyakarta, Indonesia
 yohanfajarsidik@ugm.ac.id*

3rd Roni Irnawan
*Department of Electrical Engineering and
 Information Technology
 Universitas Gadjah Mada
 Yogyakarta, Indonesia
 roniirnawan@ugm.ac.id*

4th Adha Imam Cahyadi
*Department of Electrical
 Engineering and Information
 Technology
 Universitas Gadjah Mada
 Yogyakarta, Indonesia
 adha.imam@ugm.ac.id*

5th Mohd. Brado Frasetyo
*Department of Electrical
 Engineering and Information
 Technology
 Universitas Gadjah Mada
 Yogyakarta, Indonesia
 mohd.brado41@mail.ugm.ac.id*

Abstract—*In this paper, diesel-electric generator in hybrid configuration with battery is developed for a train propulsion system. In the hybrid mode operation, the power is shared between the generator and the battery. PWM rectifier device become an important component as interface between generator, battery, and inverter motor drive to balance the energy in the propulsion system. It has several operation modes such as powering mode to achieve full speed, breaking mode to charge battery and full charging when SOC battery is low. To overcome this challenge, this research proposes droop control strategy for the three-phase PWM rectifier to share active power between the generator and the battery. This control strategy is capable to share the amount power and can be easily adjusted according to the given gain, namely kdroop. The simulation results prove the effectiveness of the proposed control strategy.*

Keywords—*Diesel-electric generator, hybrid train, three-phase PWM rectifier, battery, droop control, power sharing*

I. INTRODUCTION

A railway is an integrated system consisting of infrastructure, facilities, and human resources, as well as the norms, criteria, conditions, and procedures for the provision of rail transport [1]. A train is a mode of land transportation that connects cities efficiently because it can move people or goods in large quantities relatively quickly, safely, and on time [2]. The construction of railroad lines in China has been proven to be able to increase economic growth and increase inter-city traveler trips [3]. This condition is one of the references for the Government of Indonesia to develop the role of railways in logistics distribution between cities on the mainland, especially on the islands of Java, Sumatra, Sulawesi and Kalimantan so as to increase economic competitiveness because logistics costs can be cheaper.

Train technology has developed using diesel electric traction or fully electric train systems. Diesel electric traction uses a diesel engine to drive an electric generator.

The generator converts mechanical energy into electrical energy, which is supplied to the traction motor that powers the locomotive. There are three different architectures of diesel-electric traction based on the type of current (DC or AC) used in the main generator and the traction motors [4-6].

As for the electric traction, the locomotive is powered by an ac or dc voltage supply from the electricity network. This system must have a strong and reliable electricity infrastructure. The requirement of electrical railway power supply systems (ERPSS) has been studied in [7].

In most developing countries such as Indonesia, diesel electric traction is still widely used due to limited electricity supply. However, diesel engines use fossil fuels, causing air pollution and noise pollution. Triggered by the increasingly expensive price of fossil fuels and the issue of gas emissions, the reason for the development of a hybrid train based on a diesel engine and battery must be carried out. Benefit of hybrid diesel with battery has been discussed in Ref [8] and Ref [9] considered different hybridization rates from a generator system from 50 kW to 650 kW.

Hybrid trains combine power from diesel engines with power stored in rechargeable batteries to drive motors. Figure 1 shows a structure of a hybrid diesel engine – battery. It consists of a diesel engine coupled with AC generator, PWM rectifier, battery, inverter, and traction motors.

A PWM rectifier is an important component in a hybrid train system to convert AC to DC voltage. It has the advantages of low harmonic contents of AC side current and high energy factor [10]. Three control techniques, which are direct power control, indirect power control or voltage-oriented control and hysteresis control, have been compared in [11]. The merits and demerits of each technique in various aspects, mainly related to switching frequency, i.e. switching losses, calculations, and transient behavior has been investigated.

In Ref [12], a PWM rectifier is implemented in an electric vehicle, converting AC voltage from a diesel engine generator to DC voltage, acting as a battery boost converter while maintaining a DC output voltage. In this system, an alternator provides constant power to the load and a battery is connected to absorb power fluctuations during peak energy demand.

However, in the proposed system, the PWM rectifier must provide electric power according to load variation in the form of power of motor drives, which is inverter and traction motor, and at certain times must charge the battery based on the state of charge (SOC). Because of there is no dc-to-dc converter as battery interface as shown in Fig. 1, this requires a special PWM rectifier control strategy, namely droop control, which is the main contribution of this paper.

The organization of the paper is as follows. First, a review of the literature related to PWM rectifiers in train systems is discussed, followed by an explanation of PWM rectifier control methods and the application of the proposed control methods, discussion of results and ends with conclusions.

II. PROPOSED HYBRID TRAIN PROPULSION SYSTEM

A hybrid rail propulsion system based on a diesel engine and battery energy storage system is shown in Figure 1. The power in hybrid from both sources supplies variable voltage variable frequency (VVVF) inverters and a static inverter (SIV), which supplies auxiliary loads such as compressor, fan, lighting, and air conditioner.

The hybrid operation of the propulsion system is regulated by a hybrid control unit (HCU). This HCU will send commands to the VVVF inverters and PWM rectifiers. The VVVF inverters control motors to run based on the desired speed. Meanwhile, the PWM rectifiers get a command to supply the load based on the request.

In the following subsections, the electrical apparatus used in the hybrid train will be explained further.

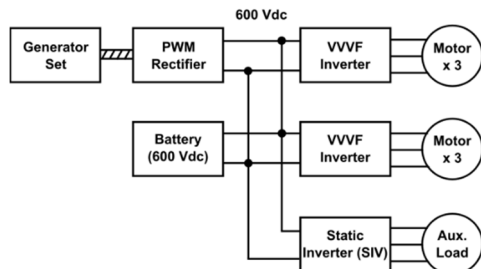


Fig 1. Structure of hybrid train diesel engine-battery

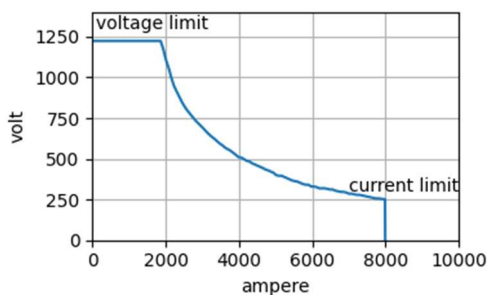


Fig 2. Typical current vs voltage of generator at constant power

A. Diesel Engine-Generator

Diesel engine couples to a synchronous generator as a three-phase AC voltage source. It has voltage rating of 380V

and power rating of 500 kW. There is no mechanical connection between the diesel engine and the wheels. The control system consisting of engine control and electronic components regulates the output power of the generator. Figure 2 shows a typical characteristic of current and voltage curve at generator constant power of 3000 HP power rating. It can be seen that the generator output power is limited by the rated voltage and rated current.

B. PWM Rectifier

A three-phase PWM rectifier consisting of six active switches using IGBTs with a boost converter strategy is used to convert three-phase 380 V AC to 600 V DC as shown in Fig.3. The power circuit consists of six IGBTs, a dc link capacitor, and inductors on the input side. IGBT voltage and rating determine the PWM rectifier power capacity. The traditional sine-triangle PWM (SPWM) scheme is the simplest and most widely used PWM technique for 3-phase PWM converters [13].

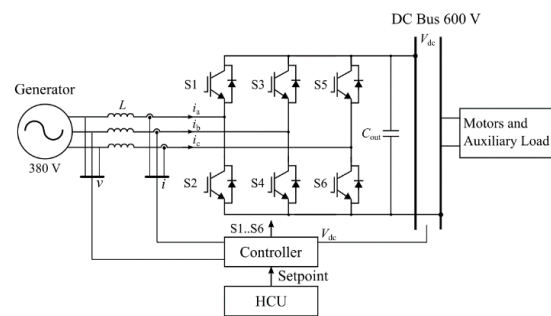


Fig 3. Circuit of PWM rectifier

The switching signals from SPWM regulate the output voltage according to the required power for the propulsion system from the Hybrid Control Unit (HCU) command. The controller strategy will be explained in the next section.

C. Battery as Secondary Source

Lithium batteries are used as energy storage as well as secondary power source to reduce fuel consumption in the diesel engines. The full power of the train is generated by the PWM rectifier from the diesel engine 3 phase alternator when the battery SOC is higher than 30%. Charging and discharging battery depends on the operating mode condition of the train.

A battery is electrochemical systems having complex dynamics. Because of its charge-discharge characteristic, Battery can be regarded as power sources or loads with different characteristics. To obtain better precision, we differentiate the model for both charge and discharge process due to the hysteresis characteristics as shown in Fig. 4.

Using Kirchoff's Voltage Law (KVL) when the hysteresis is presented in charge and discharge process, the Thevenin equivalent circuit for the battery can be formulated as

$$V_T = V_R - R_O \cdot i - U_P \quad (1)$$

for charge process and

$$V_T = V_R + \overline{(R_O)} \cdot i + \overline{(U_P)} \quad (2)$$

for discharge process as where 'bar' denotes the parameter changes due to the hysteresis. Despite the parameters are not easy to measure, they obey the boundary condition when SOC=0% and SOC=100%.

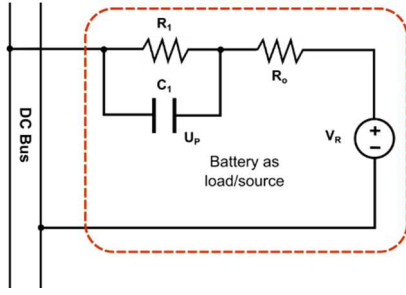


Fig 4. Battery as load or source

D. Traction Motor Drive

Drive train consists of variable voltage variable frequency (VVVF) inverter and induction motor as shown in Fig. 1. This inverter converts the incoming DC power into an AC power source and adjusts the amount of power supplied (voltage and frequency) according to the speed of the train. This inverter is also capable of regenerating power from the motor as the train slows down.

The variable speed drive must overcome to eighteen mode operations of the train, which are defined as powering when $SOC > 30\%$, powering when $SOC < 30\%$, coasting when $SOC > 30\%$, and coasting when $SOC < 30\%$. There are seven modes in each powering mode.

E. Modelling of The Hybrid Propulsion System

The overall hybrid propulsion system can be modelled in Fig. 5. To ease the analysis, as usually PWM inverters can be found easily in the market, we focus on the modelling of the rectifier as shown in Fig. 6.

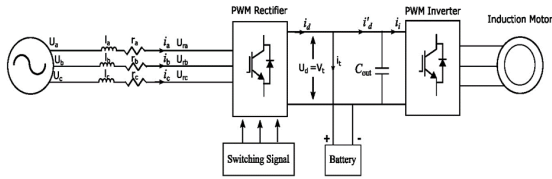


Fig 5. Model of Hybrid Propulsion System

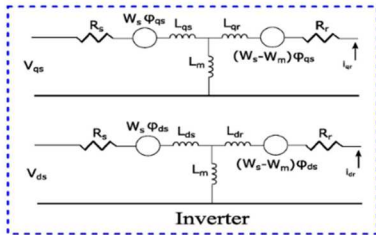


Fig 6. Rectifier connected to induction motor-controlled inverter

Assume that the generator is balanced. Due to slower time constant we made the following assumption as

$$\begin{aligned} r_a &= r_b = r_c = r \\ l_a &= l_b = l_c = l \end{aligned}$$

Using Park Transformation, to simplify the induction motor in dq coordinate is oriented according to stator voltage so that

$$v_{ds} = v_i = v_t = v_d$$

Here we can assume that

$$v_{ds}(t) = v_t(t), v_q(t) = 0$$

From equation (1), we have :

$$\begin{aligned} \begin{bmatrix} u_a \\ u_b \\ u_c \end{bmatrix} &= \begin{bmatrix} u_{ra} \\ u_{rb} \\ u_{rc} \end{bmatrix} + \begin{bmatrix} r_a & 0 & 0 \\ 0 & r_b & 0 \\ 0 & 0 & r_c \end{bmatrix} \begin{bmatrix} i_a \\ i_b \\ i_c \end{bmatrix} + \\ \begin{bmatrix} l_a & 0 & 0 \\ 0 & l_b & 0 \\ 0 & 0 & l_c \end{bmatrix} \frac{d}{dt} \begin{bmatrix} i_a \\ i_b \\ i_c \end{bmatrix} \end{aligned} \quad (3)$$

Let us define

$$U^F = (u_a, u_b, u_c)^T$$

$$U_r^F = (u_{ra}, u_{rb}, u_{rc})^T$$

$$R = \text{diag}(r_a, r_b, r_c)$$

$$L = \text{diag}(l_a, l_b, l_c)$$

$$I = (i_a, i_b, i_c)^T.$$

Rearranging (3) we have

$$L \frac{di}{dt} = U^F - U_r^F - RI \quad (4)$$

where the switching circuit

$$U_r^F = u_d, \Phi_r^F \triangleq u_d \begin{bmatrix} f_{ra} \\ f_{rb} \\ f_{rc} \end{bmatrix} \quad (5)$$

$$\Phi_r^F = M F_r^F \triangleq \frac{1}{3} \begin{bmatrix} 2 & -1 & -1 \\ -1 & 2 & -1 \\ -1 & -1 & 2 \end{bmatrix} \begin{bmatrix} f_{ra}^* \\ f_{rb}^* \\ f_{rc}^* \end{bmatrix} \quad (6)$$

and

$$\begin{bmatrix} f_{ra} \\ f_{rb} \\ f_{rc} \end{bmatrix} \stackrel{\text{def}}{=} \text{PWM signal.}$$

$$\begin{bmatrix} f_{ra}^* \\ f_{rb}^* \\ f_{rc}^* \end{bmatrix} \stackrel{\text{def}}{=} \text{switching state.}$$

Then we have

$$\begin{aligned} i_d &= \Phi_r^F \cdot I \\ i_t &= i_d - i_i \\ u_d &= v_{oc} + R_0 i_t + U_p \end{aligned}$$

$$\frac{du_p}{dt} = \frac{i_t}{c_p} - \frac{U_p}{R_1 C_1}.$$

Finally we have

$$\frac{dSOC}{dt} = \eta i_t \quad (7)$$

where $\eta = \text{charge} - \text{discharge efficiency}$.

Assuming the induction motor is slow related to the switching frequency, the motor current i_i relate the motor torque with ε as the gain, motor can be modeled as first order system with lag using torque control/mode.

$$\tau_i = \varepsilon \cdot i_i$$

$$\dot{\theta} = -K\theta + \tau_i.$$

We have

$$i = L^{-1}(U^F - U_r^F - RI) \quad (8)$$

$$\dot{u}_p = \frac{\Phi_r^F I - i_i}{C_p} - \frac{u_p}{R_1 C_1} \quad (9)$$

$$SOC = \eta(\Phi_r^F I - i_i) \quad (10)$$

$$\dot{\theta} = -K\theta + \tau_i \quad (11)$$

It becomes fourth order differential equation. This equation is used in this work for controller design purpose.

III. PWM RECTIFIER CONTROL STRATEGY

As explained in the previous section, the terminal voltage of battery (V_t) has a linear relationship with the current injected/absorbed to/from the battery (i). This characteristic can be drawn in the voltage-current (V - I) plane. For a Li-Ion battery with data given in Table 1, the V - I curve characteristics is shown in Fig. 7.

TABLE I. LI-ION PARAMETERS

| Parameter | Value |
|---------------------|---------------|
| Nominal voltage | 600 V |
| Capacity | 750 Ah |
| Internal resistance | 0.02 Ω |

Since, the battery is directly connected to the DC bus (shown in Fig. 2.), the power flow is dictated by the condition of the battery.

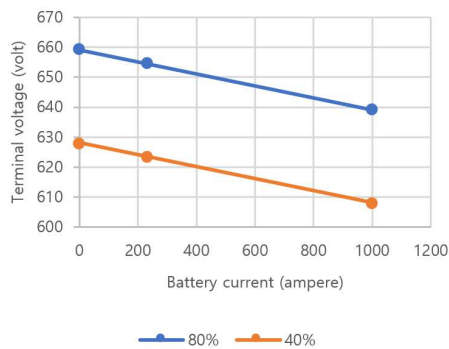


Fig 7. Terminal voltage of a battery for different current and SOC conditions

For the same current flow might result in different voltage levels depending on the SoC of the battery. Therefore, the PWM rectifier needs to be coordinated with the battery such that they can share the load.

Coordinated control concept has been adopted in this research [15]. Although it is designed for a multi-terminal HVDC system, the same concept can be applied in this research due to the same principle of the hybrid train diesel engine-battery, regardless the voltage and power rating of the components. In principle, a converter can be operated in different mode based on its V - I characteristics shown in Fig. 8.

The load sharing between PWM rectifier and battery can be easily achieved by lining the droop (V - I characteristics) between the two. The slope of the droop for the battery will depends on the internal resistance (R_o) shown in Fig. 8, therefore it could not be adjusted. However, the droop slope for the PWM rectifier is adjustable. If the PWM rectifier is adjusted to have the same droop slope as the battery, then

both battery and PWM rectifier share the load equally. The shallower the slope (close to a horizontal line), the higher the share of the load to be taken by the PWM rectifier.

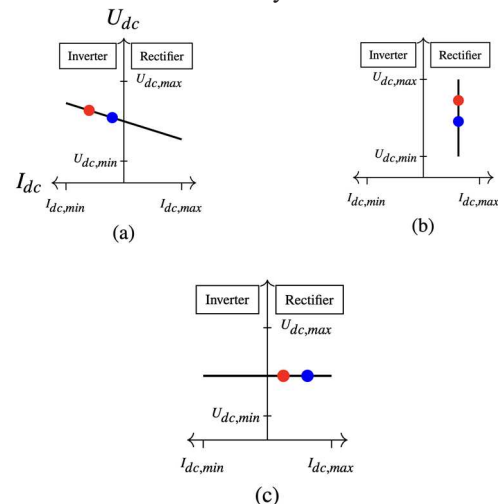


Fig. 8. Converter operation modes: (a) DC voltage droop control, (b) constant current control, (c) constant DC voltage control [15]

The PWM rectifier control structure has been developed in a cascaded structure [16]. The higher-level control is the DC voltage controller, which gives the AC voltage reference for the lower-level controller. The lower-level controller produces switching pulses for the IGBT. This cascaded structure is depicted in Fig. 9.

The reference for the DC voltage controller is adjusted by adding the droop controller output. Figure 10 depicted the droop controller structure. The k_{droop} defines the steepness of the droop slope for the PWM rectifier. If k_{droop} equals to zero, then the PWM rectifier operates in a stiff DC voltage controller (more contribution from the PWM rectifier), while putting this value to a higher number will result in an almost stiff current operation of the PWM. The amount of the current taken by the PWM rectifier depends on the value of I_{PWM_ref} . The value of I_{PWM_ref} can also be used to shift the droop characteristics of the PWM rectifier along horizontal axes.

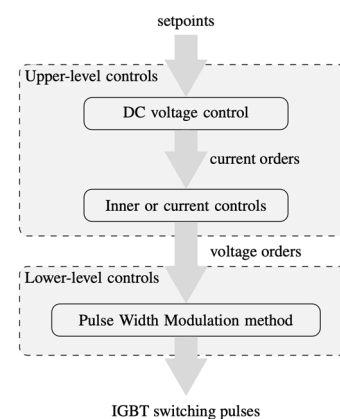


Fig. 9. A cascaded PWM rectifier control structure. The lower-level has faster response as compared to the higher one

The reference for the DC voltage controller is adjusted by adding the droop controller output. Figure 10 depicted the droop controller structure. The k_{droop} defines the steepness of the droop slope for the PWM rectifier. If k_{droop} equals to zero, then the PWM rectifier operates in a stiff DC voltage controller (more contribution from the PWM rectifier), while putting this value to a higher number will result in an almost stiff current operation of the PWM. The amount of the current taken by the PWM rectifier depends on the value of I_{PWM_ref} . The value of I_{PWM_ref} can also be used to shift the droop characteristics of the PWM rectifier along horizontal axes.

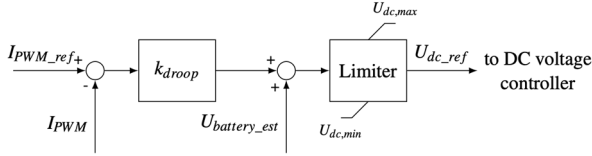


Fig. 10. DC voltage droop controller structure

As mentioned previously, the internal voltage of the battery will be related to the SoC of the battery. Therefore, apart from the droop controller output, the DC voltage reference needs also be adjusted to match the SoC of the battery. In this research, the terminal voltage of the battery is estimated based on the simulation results and depicted in Fig. 11. The estimated battery terminal voltage is then used in the $U_{battery_est}$ in Fig. 10. It should be noted that different manufacturers or types of the battery might give different characteristics, therefore this figure needs to be adjusted.

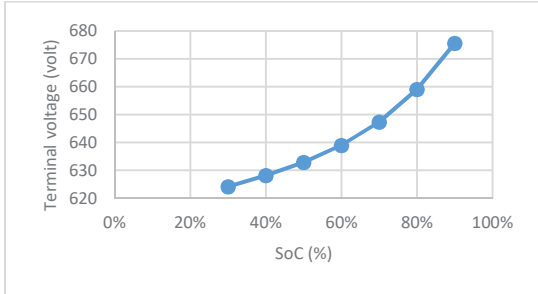


Fig. 11. Terminal voltage of the Li-Ion battery given in Table 1 during different SoC levels when the battery current equals to zero

IV. SIMULATION RESULT AND DISCUSSION

A diesel-electric generator and a three-phase PWM rectifier with a battery system are modeled in a circuit simulation. The simulation configuration is shown in Fig. 2, except for the loads. The motors and auxiliary loads are modeled as a DC current source. The simulation parameters are given in Table 2.

TABLE II. SIMULATION PARAMETERS

| Parameter | Value |
|----------------------------|---------------|
| Generator voltage v_{LL} | 380 V |
| DC bus voltage v_{DC} | 600 V |
| Generator power | 500 kW |
| Battery capacity | 750 Ah |
| k_{droop} | 0.02 and 0.06 |

In order to show the capability of the PWM rectifier to share the load with the battery, a step increase from 400 A to 1000 A in the DC load has been considered. This step increase is reflected as a change in the DC bus current. Two k_{droop} values have been considered, i.e. 0.02 (the same as the internal resistance of the battery given in Table 1) and 0.06.

Figure. 12 shows the current responses of the battery and the PWM rectifier. Both electric sources can respond to the required load current. Using the k_{droop} equals to 0.02, the power can be shared equally between the diesel-electric generator and the battery as shown in Fig. 13.

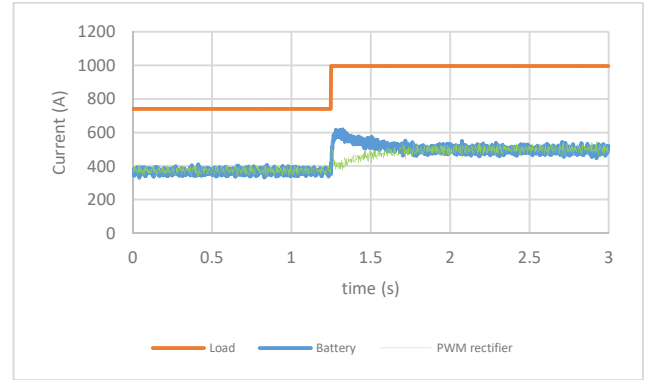


Fig. 12. PWM rectifier and battery current responses during a load step with k_{droop} equals to 0.02

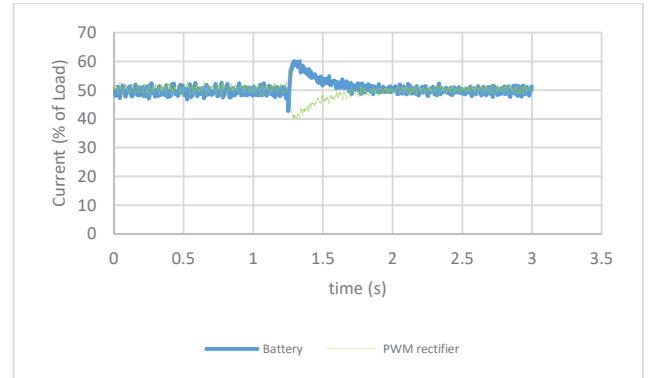


Fig. 13. Load sharing between battery and PWM rectifier with k_{droop} equals to 0.02

Figure 14 shows the current responses of the PWM rectifier and the battery with different value of k_{droop} . In this case, the k_{droop} is set to 0.06. This value is 3 times larger than the internal resistance of the battery. It shows that both sources can respond to the step increase of the dc current load. However, the power is not shared equally between the PWM rectifier and the battery. The load draws more current from the battery, which is around 75 % of the load as shown in Fig. 15. The rest of the power is supplied from the PWM rectifier.

The simulation results prove that load sharing between the battery and PWM rectifier can be simply performed by changing the droop constant k_{droop} . If the value is the same as the internal resistance of the battery then both battery and

PWM rectifier share the same load (Fig. 12. and Fig. 13.). While, if k_{droop} is 3 times larger than the internal resistance of the battery, then the battery will take the load three times more than PWM rectifier.

If different operation modes of the hybrid train require different load sharing between the battery and PWM rectifier, it is suggested to implement an advanced droop controller or droop line tracking method as discussed in [17].

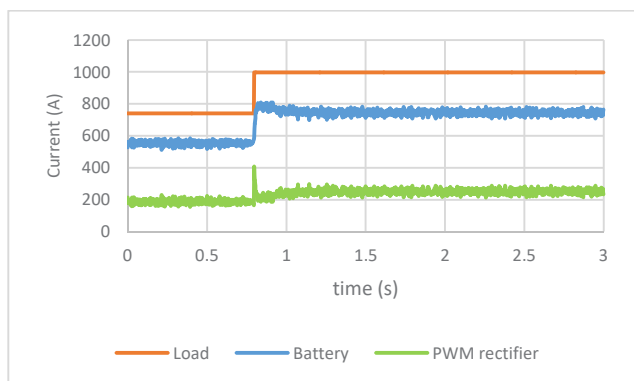


Fig. 14. PWM rectifier and battery current responses during a load step with k_{droop} equals to 0.06

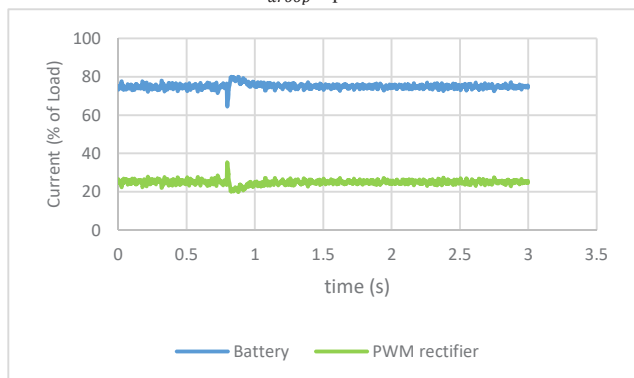


Fig. 15. Load sharing between battery and PWM rectifier with k_{droop} equals to 0.06

V. CONCLUSION

The control strategy of the PWM rectifier in hybrid with battery for a train propulsion system has been proposed. The control strategy is a DC voltage droop controller that can share the power between the PWM rectifier and the battery. The amount of power share can be easily adjusted according to the given gain, namely k_{droop} . The performance of the proposed control strategy has been tested in the simulation environment. It shows the effectiveness of the proposed control strategy for power sharing between the PWM rectifier and the battery in supplying loads.

ACKNOWLEDGMENT

This research is supported by the Indonesian Government through Matching Fund Program 2022

REFERENCES

- [1] G. Eason, B. Noble, and I. N. Sneddon, "On certain integrals of Lipschitz-Hankel type involving products of Bessel functions," *Phil. Trans. Roy. Soc. London*, vol. A247, pp. 529–551, April 1955. (references)
- [2] Suwardi, Rossa, I. S., Heru, K. "Public Policy on Safety and Security Railroad System in Indonesia. Public Policy on Safety and Security Railroad System in Indonesia," *Prizren Social Science Journal*, 2019.
- [3] Niu F, Wang F. "Economic Spatial Structure in China: Evidence from Railway Transport Network," *Land*. 2022, Vol. 11, No. 1, pp. 61, 2022. <https://doi.org/10.3390/land11010061>
- [4] Jiao J., Wang J., Zhang F. Jin F., Liu W. "Roles of accessibility, connectivity and spatial interdependence in realizing the economic impact of high-speed rail: Evidence from China," *Transp. Policy* 2020, No. 91, pp. 1–15, 2020.
- [5] C. G. d. S. Moraes, S. L. Brockveld, M. L. Heldwein, A. S. Franca, A. S. Vaccari and G. Waltrich, "Power Conversion Technologies for a Hybrid Energy Storage System in Diesel-Electric Locomotives," *IEEE Transactions on Industrial Electronics*, vol. 68, no. 10, pp. 9081-9091, 2021. doi: 10.1109/TIE.2020.3021643
- [6] M. Spiryagin, C. Cole, Y. Q. Sun, M. McClanachan, V. Spiryagin, and T. McSweeney, "Design and simulation of rail vehicles" CRC Press, 2014.
- [7] M. Cipek, D. Pavkovi, Z. Kljai, and T. J. Mlinari, "Assessment of battery-hybrid diesel-electric locomotive fuel savings and emission reduction potentials based on a realistic mountainous rail route," *Energy*, vol. 173, pp. 1154–1171, 2019.
- [8] Serrano-Jiménez, Abrahamsson, L., Sandra, C.S., Sanz, J. "Electrical railway power supply systems: Current situation and future trends," *International Journal of Electrical Power & Energy Systems*. Vol. 92, pp. 181-192. 2017. doi:10.1016/j.ijepes.2017.05.008
- [9] Popovich, N.D., Rajagopal, D., Tasar, E. *et al.* "Economic, environmental and grid-resilience benefits of converting diesel trains to battery-electric," *Nat. Energy*, Vol. 6, pp. 1017–1025, 2021. <https://doi.org/10.1038/s41560-021-00915-5>
- [10] T. Letrouve, W. Lhomme, J. Pouget and A. Bouscayrol, "Different Hybridization Rate of a Diesel-Electric Locomotive," *IEEE Vehicle Power and Propulsion Conference (VPPC)*, pp. 1-6, 2014. doi: 10.1109/VPPC.2014.7007048
- [11] Rasul, M., Patel, A., Cole, C., Sun, Y.Q., Spiryagin, M., Godber, T., & Hames, S. "Train motive power technologies a review on existing and emerging (hybrid) technologies," *Proc. 10th World Congress on Railway Research*, pp. 1-9 2013.
- [12] S. Gopalan "A comparative study of control techniques for three phase PWM rectifier," *10th International Conference on Intelligent Systems and Control (ISCO)*, pp. 1-8, 2016. doi: 10.1109/ISCO.2016.7727142
- [13] Xudong Liu, "Subway Traction Power Supply System Based on PWM Rectifier," *Journal of Physics: Conference Series, Volume 2136*, 2020. DOI 10.1088/1742-6596/2136/1/012019
- [14] A. Shetty, B. G. Fernandes, J. O. Ojo and J. A. Ferreira, "Three Phase PWM Rectifier with Integrated Battery for Automotive Applications," *2018 IEEE Industry Applications Society Annual Meeting (IAS)*, pp. 1-6, 2018. doi: 10.1109/IAS.2018.8544681
- [15] R. Inawan, F. F. da Silva, C. L. Bak and T. C. Bregnhøj, "A categorization of converter station controllers within multi-terminal DC transmission systems," *2016 IEEE/PES Transmission and Distribution Conference and Exposition (T&D)*, pp. 1-5, 2016. doi: 10.1109/TDC.2016.7520039.
- [16] R. Inawan, F. F. da Silva, C. L. Bak and T. C. Bregnhøj, "Evaluation of half-bridge modular multilevel converter model for VSC-HVDC transient stability studies," *13th IET International Conference on AC and DC Power Transmission (ACDC 2017)*, pp. 1-6, 2017. doi: 10.1049/cp.2017.0017.
- [17] R. Inawan, F. F. da Silva, C. L. Bak, A. M. Lindefelt, A. Alefragkis, "A droop line tracking control for multi-terminal VSC-HVDC transmission system," *Electric Power Systems Research*, Vol. 179, 2020. doi: 10.1016/j.epr.2019.10.

A Generation Expansion Planning Procedure Considering the Construction Delay: A Case of Sumatra Power Systems

Kurnia Wisesa Kisna, Lesnanto Multa Putranto, Avrin Nur Widiastuti, Amira Hanun
Department of Electrical Engineering and Technology Information, Gadjah Mada University
Yogyakarta, Indonesia

kurnia.wisesa.kisna@mail.ugm.ac.id, lesnanto@ugm.ac.id, avrin@ugm.ac.id, amira.hanun@mail.ugm.ac.id

Abstract—The delay in power plant construction affected the generation expansion planning (GEP) result, decrease the generating capacity, and increase the Loss of Load Probability (LOLP) index. The LOLP constraint is required in GEP to obtain an adequate reserve in system, which called as reserve margin. An optimal reserve margin will ensure the economic operation and system's reliability. This research objective is to modify the GEP considering the possibility of delay in power plant construction. The model is simulated on Sumatra Power System to find to modify the number, size, and capacity of additional generating unit in 10 years planning horizon. There are two scenarios called base case and delay. The base case scenario consider the most economical total cost under the standard constraint which the simulation result require 25% reserve margin. Delay scenario consider 1, 2, and 3 years delay of existing construction project which require 7.86% additional reserve margin in average. Therefore, the required reserve margin to consider construction delay is 32.86%.

Keywords—GEP, power plan development delays, reserve margin, LOLP

I. INTRODUCTION

The Island of Sumatra is one of the largest islands in Indonesia, both in terms of land area and population [1]. The Sumatra Power System falls under the category of a large system, with a peak load of 6,330 MW in 2021, estimated to reach 11,661 MW by 2030 [2]. The electricity demand in the Sumatra System continues to increase in line with economic growth and population expansion. In 2021, the electricity demand was only 36,835 GWh, but it is projected to reach 68,700 GWh by 2030, with an average annual increase of 7.11% [2].

The rising of electricity demand, Generation Expansion Planning (GEP) becomes crucial. GEP is used to determine the quantity, type, and size of power plants to be constructed annually within the planning horizon [4], [8]. GEP is widely used in power plant development planning for various issues, such as considering the availability of primary energy supply [6] and the integration of new and renewable energy sources [7]. GEP can be modeled using various optimization methods, one of which is Mixed Integer Linear Programming (MILP). Through this method, optimization aims to determine the combination of the number, size, and capacity of power plants to be constructed in the GEP scenario. The goal is to achieve

the most optimal total generation cost while ensuring the system's reliability.

In GEP, the principle of "least cost" is applied, which involves optimizing the total construction cost while considering system reliability [9]. System reliability in electricity generation planning is a key focus. It can be evaluated based on the system's ability to meet the load demand and withstand disturbances [7]. One reliability indicator is the Loss of Load Probability (LOLP), which represents the probability of the system failing to meet the load demand [5]. The standard LOLP index in Indonesia is $LOLP < 0.274\%$, equivalent to one day of electricity outage per year [2]. LOLP is influenced by various factors, such as the generator's failure rate (FOR), generator capacity, and load characteristics [5].

The LOLP index is closely related to the system's reserve margin e . A high reserve margin indicates ample power reserves, indicating a high level of reliability in the electricity system within that region [4] [13]. However, excessively high reserve margin can also lead to higher investment costs [4] [13]. In GEP, the objective is not only to achieve a reliable system but also to minimize the generation cost. To achieve this, the LOLP index is used as a reference in determining the system's reserve margin [17]. By doing so, when a system meets the LOLP standard, the reserve margin will be sufficient to meet the system's needs and overcome disturbances during the power generation process. Consequently, using LOLP as a constraint in power plant development planning can yield an optimal reserve margin for the system.

One of the most common technical issues in GEP is power plant construction delays. In 2021, there were 34 delayed power plant projects, with 5 of them occurring in the Sumatra Region [3]. Delays in power plant construction can be attributed to inadequate project management [12]. This has been evident in several cases of power plant construction delays in Indonesia [10], [11]. Such delays can lead to a decrease in power plant capacity in the affected years, which can impact the reliability and economy of the electricity system. Preventive actions are necessary to avoid delays, such as improving the project management of planned power plant developments.

Therefore, this study aims to modify the GEP process by considering power plant construction delays. These delays are

derived from historical data on power plant planning from 2016 to 2021, resulting in success and delay ratios for each power plant. Accounting for these construction delays will impact the system's reserve margin and LCOE (Levelized Cost of Electricity).

II. GENERATION EXPANSION PLANNING

Generation expansion planning (GEP) is an energy planning process aimed at determining the quantity, type, and size of power plants to be constructed each year during the planning period, considering both technical and non-technical factors [7]. Generally, the development planning of power plants is carried out to meet the increasing demand for electricity each year. However, in some regions in Indonesia, this development planning is conducted to address the shortage of electricity supply in those areas [8]. The planning of power plant development operates on the principle of "least cost," which means optimizing the total construction cost of power plants to the minimum possible extent. In other words, the main principle of this development planning is to obtain the lowest net present value (NPV) of total electricity supply costs [14]. The main principle of power plant development is formulated in an objective function, as shown in the following formulation.

A. Objective Function

The objective function of this generation expansion planning is to minimize the total cost. Generally, the total generation cost consists of several cost components, namely total fixed cost, total V&OM cost, and total fuel cost. The general form of this objective function can be seen in Equation (1). The breakdown of each cost component in the general equation can be seen in Equation (2), as follows.

$$\min Cost = C_{fixed}^{tot} + C_{VOM}^{tot} + C_{fuel}^{tot} \quad (1)$$

$$\begin{aligned} \min Cost = & \sum_y \sum_g DF_y \times C_{fixed}^g \times 1000 \times P_{max}^g \times \\ & (Ng_g^y + Nb_g^y) \\ & + \sum_y \sum_g DF_y \times C_{VOM}^g \times G_g^y \quad (2) \\ & + \sum_y \sum_g DF_y \times HR_g \times C_{Fuel}^g \times G_g^y \end{aligned}$$

In Equation (2), there is a cost component called the fixed cost (C_{fixed}^g). The fixed cost component consists of two elements: the annualized investment cost and the Fixed Operation and Maintenance (FO&M) cost component. The equation for calculating the fixed cost of the power plant (g) can be seen in Equation (3) - (7).

$$C_{fixed}^g = C_{inv}^g + C_{FOM}^g \quad (3)$$

$$C_{inv}^g = C_{inv}^g \times AnnualizedFactor \quad (4)$$

$$AnnualizedFactor = \frac{(1 - TaxRate) \times \frac{NAF}{EcoLife}}{RAF} \quad (5)$$

$$RAF = \frac{(1 - (1 + WACC))^{EcoLife}}{WACC} \quad (6)$$

$$NAF = \frac{(1 - (1 + WACC + InfRate))^{EcoLife}}{(WACC + InfRate)} \quad (7)$$

B. Constraint

In GEP, there are constraints that need to be satisfied. For example, the constraint on electricity demand (8), the constraint on electricity generation capacity (9)(10), the MILP constraint ((11), and the LOLP constraint (12). The equations for each of these constraints can be seen in Equation (8) - (12), as follows.

$$\sum_g G_g^y + USE_y \geq PD_y \quad (8)$$

$$\sum_y \sum_g P_{max}^g \times (Ng_g + Nb_g^y) + DP_y \geq PL_y + RM_y \quad (9)$$

$$Nb_g^y \leq Nb_g^{max} \quad (10)$$

$$Nb_g^y \geq 0; Nb_g^y \text{ is Integer} \quad (11)$$

$$LOLP < 0, 274\% \quad (12)$$

In this research, the delay in power plant construction will have an impact on power plant modeling. The variables that will be affected due to the delay in power plant construction are the installed capacity of power generation units (Nb_g^y) and the energy production of power plant-g in year y (G_g^y). The delay in power plant construction will lead to changes in the arrangement of installed power generation units in the year of the delay occurrence. These changes in the installed power generation units will also influence the energy production quantity in the affected year.

III. METHODOLOGY

A. Research Object

In this research, the Sumatra System is chosen as the research object. The Sumatra power system serves 9 provinces, namely Aceh, North Sumatra, Riau, Bangka Islands, West Sumatra, Jambi, South Sumatra, Bengkulu, and Lampung. The Sumatra system is one of the large categories of power systems in Indonesia, with a significant demand for electrical energy. The high demand for electricity is accompanied by an increasing number of power plants constructed each year, realized through power plant development planning (GEP).

Based on historical data from the power plant development planning in the Sumatra System, there are 31 power plants

that have been delayed out of 60 planned power plants [15] - [2]. From this historical data, the success ratio and delay of power plant construction can be derived, as follows.

TABLE I
SUCCESS RATIO AND DELAY OF POWER PLANT CONSTRUCTION PROJECTS

| No. | Power Plant | Success Ratio | Delay Ratio | Delay (Years) |
|-----|-------------|---------------|-------------|---------------|
| 1 | PLTGU/MGU | 33% | 100% | 3 |
| 2 | PLTBg | 28% | 80% | 1 |
| 3 | PLTG/MG | 25% | 75% | 2 |
| 4 | PLTM | 50% | 57% | 2.25 |
| 5 | PLTU | 48% | 55% | 2 |
| 6 | PLTGU | 29% | 50% | 4 |
| 7 | PLTA | 43% | 33% | 2.5 |
| 8 | PLTP | 75% | 33% | 1.5 |
| 9 | PLTBm | 0% | 0% | Failed |
| 10 | PLTBn | 50% | 0% | On Scheduled |
| 11 | PLTG | 14% | 0% | On Scheduled |
| 12 | PLTMG | 6% | 0% | On Scheduled |
| 13 | PLTS | 17% | 0% | On Scheduled |
| 14 | PLTSa | 0% | 0% | Failed |

The success ratio indicates the percentage of the total number of successfully constructed power plants compared to the overall planned total of power plants. On the other hand, the delay ratio shows the percentage of delayed power plants in relation to the total number of successfully constructed power plants. These success, delay ratios, and duration of power plant construction delays will serve as references in modeling the GEP scenarios while considering the delays in power plant construction. The duration of power plant construction delays will be utilized in modifying the GEP model by considering the delays. The years of construction for the modeled power plants will be adjusted for the lead time of each plant in the PLEXOS.

Due to the considerable number of delayed power plants, the reserve margin in the Sumatra System under the RUPTL 2021-2030 is relatively high, ranging between 40% to 49%. This high reserve margin will have implications on the reliability and cost-effectiveness of the system. Therefore, this research will involve modifying the GEP by taking into account the delays in power plant construction to achieve an optimal reserve margin.

B. Method

The GEP is conducted for the planning period of 2021-2030. GEP simulations are performed under two scenarios: the GEP scenario without considering power plant construction delays (base case) and the GEP scenario with considering delays. The base case scenario models the Sumatra System based on the RUPTL (Electricity Supply Business Plan) 2021-2030. The GEP scenario with delays is conducted after simulating the base case scenario. The base case scenario is considered successful when the objective function of optimization is fulfilled, and the constraints related to reliability indices and others are satisfied, resulting in the most optimal reserve margin. Optimal here means the reserve margin meets the load demand with the minimum cost. The results of the base

case optimization, listing the built and unbuilt power plants, serve as a reference for modeling the delayed scenario. Unbuilt power plants in the base case scenario will be modeled as candidates for the delay scenario, while built power plants will be modeled as existing plants. The flow of this research is shown in Fig 1.

The research process involves stages represented by the letter A. The stages indicated by A are for identifying the success and delay ratios, which result in success and delay ratios of power plant development. These ratios will be used as references for determining the delayed power plants. Power plants with high delay ratios will be modeled as delayed in the delay scenario simulation.

The GEP simulations in this study utilize the Mixed Integer Linear Programming (MILP) method. Through this method, optimization will determine the combination of the number, size, and capacity of power plants to be built in the executed GEP scenario. This is done to obtain the most optimal total generation cost while still considering the reliability of the power system. The input data for each power plant's optimization simulation includes electricity demand and peak load data, techno-economic and technical data of the power plants, and fuel data.

IV. RESULT AND DISCUSSION

A. Optimization of The Base Case Scenario

From the optimization results of the base case, when the LOLP index of the system is limited to 0.024%, the average value of the system's reserve margin is 25% per year. This reserve margin indicates that with an average reserve margin of 25%, the system has sufficient power reserves to meet the load requirements during disturbances. The average LCOE obtained from this base case optimization is 8.95 c\$/kWh. The power plant energy mix and reserve margin value can be seen in the Fig. 2 and Fig. 3.

B. Impact of Delays on Power Plant Reliability

After successfully optimizing the base case scenario, the next testing conducted is to assess the impact of power plant construction delays on reliability. In this stage, several power plants that were built in the base case results are modeled to be delayed. On average, the power plants modeled to be delayed are those scheduled to be built in 2027, 2028, and 2029. The total capacity of power plants that are modeled to be delayed is 1674 MW, this is equivalent to 11.19% of total installed capacity.

In this simulation can be seen in Fig. 4., it was found that the established standard LOLP threshold is violated due to the occurrence of delays. Specifically, the violation of the LOLP threshold occurs in the year 2029. The violation of the established LOLP threshold indicates that in that year, the probability of the power generation system failing to meet the load demand exceeds the set standard in Indonesia. This inability to meet the load demand will have adverse effects on power plant developers and consumers. One of the impacts caused by this is an increase in the amount of unserved

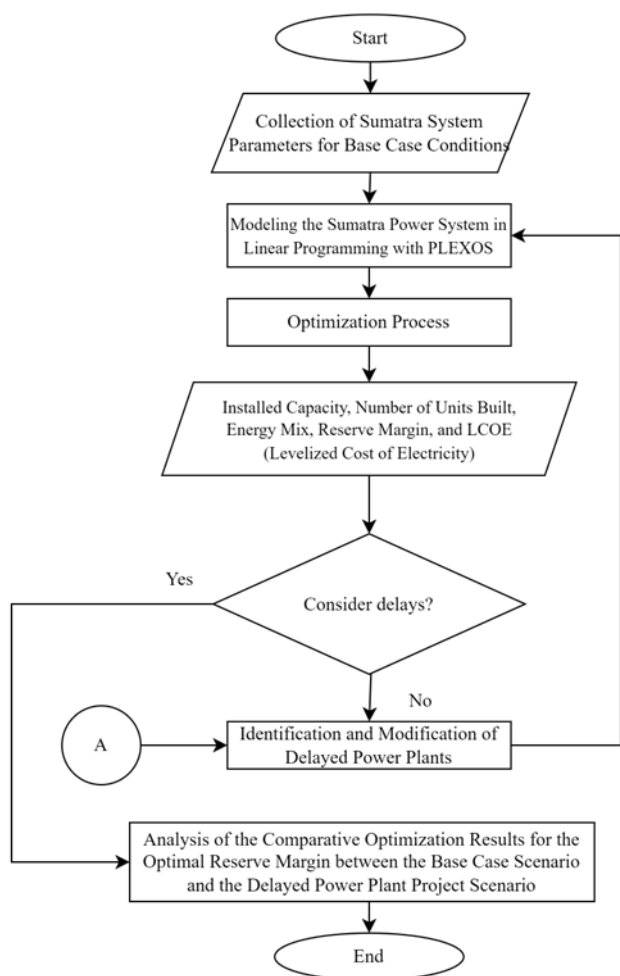


Fig. 1. The Research Flowchart

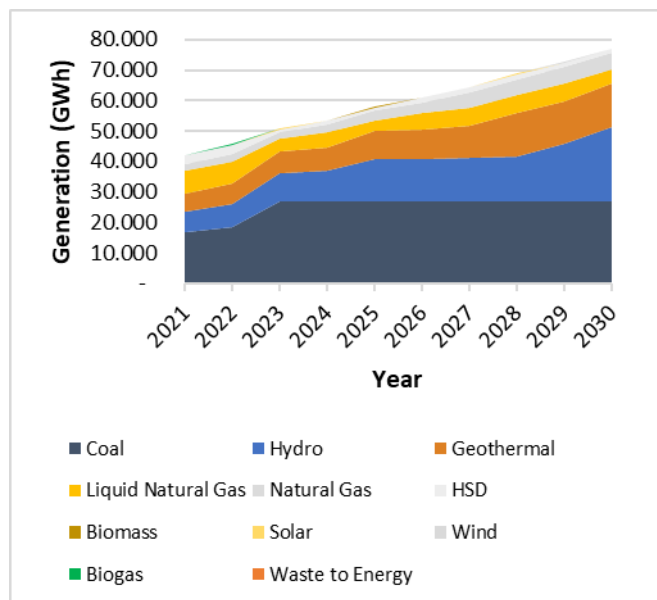


Fig. 2. Energy Mix of Base case Optimization

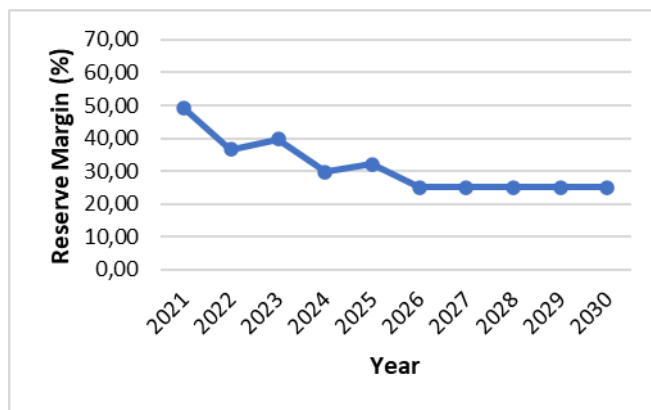


Fig. 3. Reserve Margin of Base Case optimization



Fig. 4. LOLP due to delay

energy in the system, which affects the increasing opportunity loss in the electricity system. To anticipate such situations, it is necessary to plan power plant development considering potential project construction delays.

C. Optimization of The Delays Scenario

The optimization of the power plant construction delay scenario is conducted using the results of the base case scenario optimization as a reference for system modeling. The power plants resulting from the base case scenario optimization are categorized into two groups: the power plants that are built in the base case scenario are included in the existing power plant category in the delay scenario, while the power plants that are not built are considered as candidate power plants in the delay scenario, taking into account the delays. Since there are 17 power plants that are not built in the base case scenario, these 17 power plants become part of the candidate power plants in the delay scenario. In the delay scenario, three tests are conducted with different durations of delays: 1 year, 2 years, and 3 years.

The results obtained from the simulation of delay optimization show that the delay in power plant construction leads to the development of new candidate power plants. The longer the duration of the delay, the greater the number of candidate

power plants that are built. The construction of new candidate power plants is caused by the capacity reduction in the affected years due to the delays. Therefore, this capacity reduction requires compensation in the form of additional new power plant capacity to ensure that the reliability constraints in power generation are still met.

The addition of new power plants will increase the power reserve capacity in the system. This linearly affects the increase in the system's reserve margin. The average increase in the reserve margin per year due to power plant construction delays is 7.86%. The differences in the obtained reserve margin values in each simulation of the delay scenario considering the power plant construction delays can be seen in the Fig. 5.

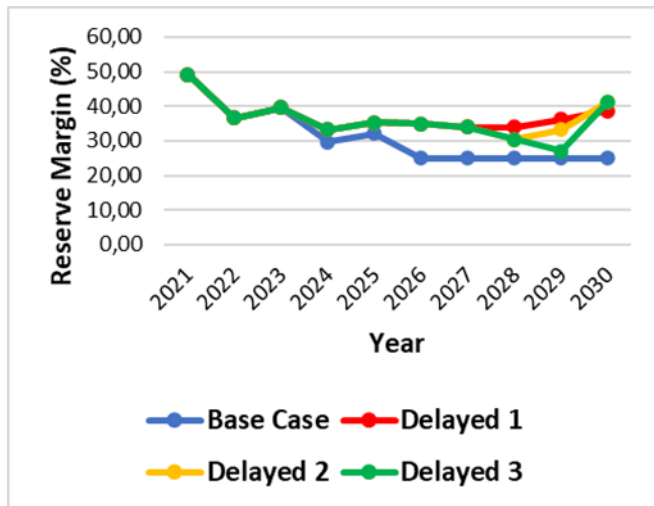


Fig. 5. Reserve Margin of Delays Scenario

The addition of new power plants will certainly have an impact on the overall generation cost. The resulting LCOE for each test can be seen in the Fig. 6.

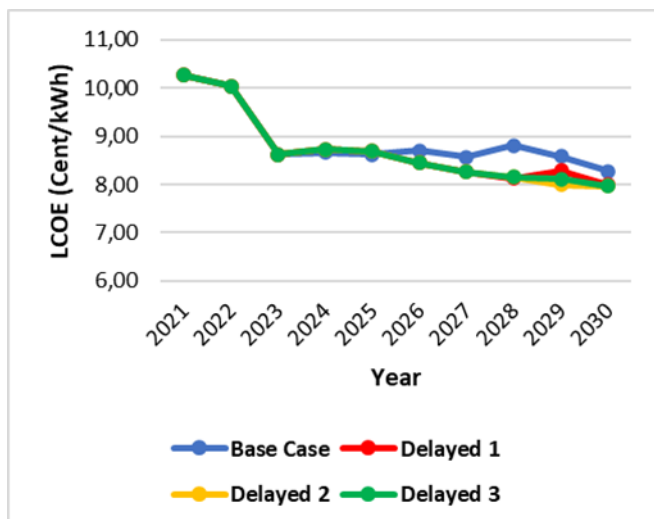


Fig. 6. LCOE of Delays Scenario

From Figure 6, it can be observed that from 2025 to 2026, there is a decrease in LCOE in the delay scenario testing compared to the LCOE values in the scenario without considering delays. The addition of power plant construction in the delay scenario should increase the LCOE of generation since it would increase the total fixed cost in the power plant development planning for those years. However, in the delay scenario, the addition of new candidate power plants does not necessarily increase the LCOE of their respective power plants. This is because the newly built candidate power plants in the optimization scenario with delays are characterized by lower fuel prices. Specifically, the cheaper power plants that are built in this scenario are coal-fired power plants (PLTU). PLTU have the lowest fuel price component compared to other power plants. To validate the increase in energy production in a coal-fired power plant (PLTU) and the decrease in electricity production in power plants using more expensive fuel types, the following data is provided. The energy production output for each type of power plant has been categorized based on its fuel type can be seen in the figure below.

In the optimization process, the addition of PLTU power plants leads to an increase in energy production from PLTU. Referring to the electricity energy balance constraint, this increase in energy production from PLTU will result in a decrease in energy production from other power plants, especially those with higher fuel costs. When energy production is predominantly generated by PLTU, which have the cheapest fuel prices, the total fuel cost component in this scenario will be smaller compared to the total fuel cost in the scenario without considering delays.

V. CONCLUSION

The reliability level and reserve margin of a system are influenced by LOLP, FOR, peak load, power plant size, and power plant construction delays. The results obtained from this testing indicate that delays in power plant construction affect the GEP. Delays will impact the capacity of power plants and the number of power plant units in the years affected by the delays. This influence results in an increase in the reserve margin, with an average increase of 7.86%. This increase in the reserve margin is attributed to the addition of new candidate power plant units in the Sumatra Power System, which act as compensators for the decrease in power plant capacity caused by delays in the affected years. However, the increase in the reserve margin due to construction delays in this power plant construction issue does not always lead to an increase in the system's LCOE. This is because delays prompt the system to optimize the operation of existing power plants, which are more cost-efficient than newly constructed ones. In terms of energy mix, coal energy production increases significantly compared to production using more expensive fuels such as liquid natural gas, natural gas, and HSD. This results in a lower LCOE value when delays occur compared to the GEP condition in the base case. Moreover, when examining the reserve margin based on the RUPTL, the RUPTL has

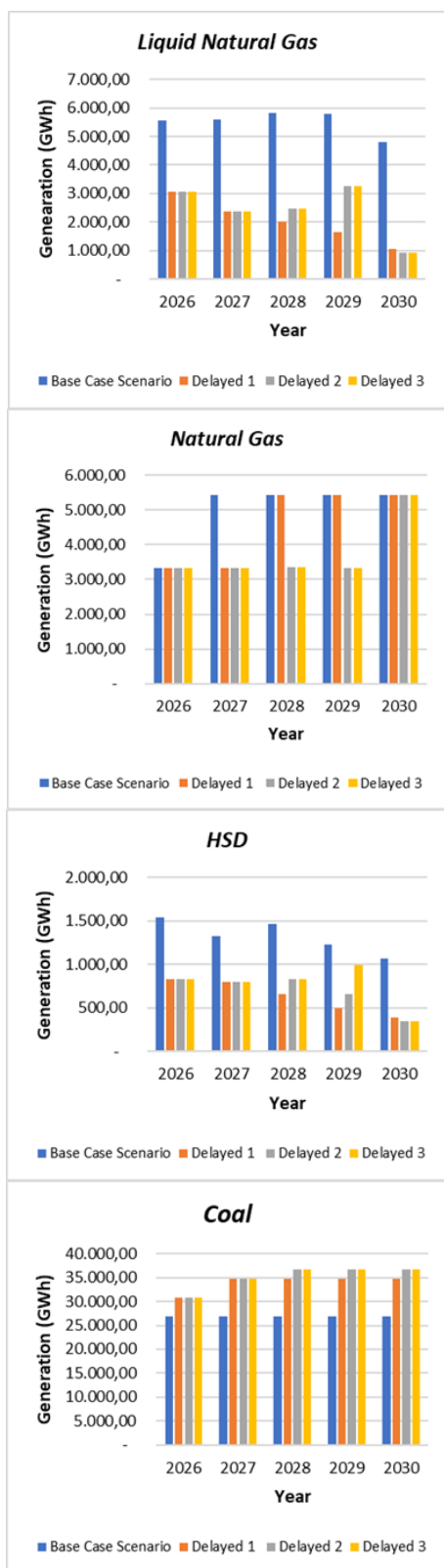


Fig. 7. Generation (GWh) of Energy for Each Primary Energy Source: (a) LNG; (b) Natural Gas; (c) HSD; (d) Coal

already planned power plant development while considering construction delays.

VI. ACKNOWLEDGMENTS

Acknowledgments: This work funded by the Rekognisi Tugas Akhir (RTA) Program of the Research Directorate of Universitas Gadjah Mada. Any opinions, findings, and conclusions or recommendations express herein are those of the authors and do not necessarily reflect those of the Research Directorate of Universitas Gadjah Mada.

REFERENCES

- [1] Indonesia Statistic 2021 "Area and Number of Island by Province, 2021". [Online]. Available : https://www.bps.go.id/indikator/indikator/view_data_pub/000
- [2] PT PLN (Persero) "PT PLN (Persero) Electricity Supply Business Plan for the Years 2021 - 2030", PT PLN (Persero), Jakarta, Indonesia, Yearly Report 188.K/HK.02/MEM.L/2021, 2021
- [3] Corporate Performance Control Division "Completion of 34 Hindered Projects", PT PLN (Persero), Jakarta, Indonesia, Summary Report
- [4] N. E. Koltsaklis and A. S. Dagoumas "State of the Art Generation Expansion Planning: A Review", Applied Energy, vol.230, pp. 563-589, 2018. [Online]. Available : <https://www.sciencedirect.com/science/article/pii/S0306261918312583>
- [5] Billinton, Roy and Allan, Ronald N. "Reliability Evaluation of Power Systems", Pitman, Boston, 1984.
- [6] R. Diewvilai and K. Audomvongseeree "Optimal Loss of Load Expectation for Generation Expansion Planning Considering Fuel Unavailability", Energies, 2022
- [7] A. A. Muthahari "Optimization of Power Plant Development Planning Considering Intermittency of Variable Renewable Energy in the Sulawesi Electricity System", Universitas Gadjah mada, Yogyakarta, 2020
- [8] Tumiran, L. M. Putranto, Sarjiya, F. D. Wiyaja, A. Priyanto, and I. Savitri "Generation Expansion Planning Based on Local Renewable Energy Resources: A Case Study of the Isolated Ambon-Seram Power System", Sustainability, Vol.15, No.5, 2022
- [9] "Generation Expansion Planning for High Potential Hydropower Resources : The Case of Sulawesi Electricity System", Vol.28. [Online]. Available : <https://journals.aau.dk/index.php/sepm/article/view/3247>, DOI : 10.5278/ijsepm.3247
- [10] S. M. Noviyanthia "Utilization of the Analytical Hierarchy Process (AHP) Method for Evaluating the Project Completion Time Performance of Jeranjang Coal-Fired Power Plant Construction", Testlink Journal, 2022
- [11] A. D. Pradiani and N. Nurhasanah "Analysis of Factors Delaying COD in PLN UIP Kalbagtim Projects using Analytical Hierarchy Process and Fault Tree Analysis Methods", Al Azhar Indonesia Science and Technology, 2021
- [12] R. Rahmadya, H. H. Purba, and B. Susetyo "Implementation of M-PERT and ABC in Power Generation Project", Konstruksia Journal, 2022
- [13] R. Diewvilai and K. Audomvongseeree "Reserve Margin Evaluation for Generation System Using Probabilistic Based Method", ECTI CON2011 Khon Kaen University, 2011
- [14] A. A. Fawwaz, A. Hanun, M. Burhanudin "Design of the Masterplan for the Java-Bali-West Nusa Tenggara-East Nusa Tenggara Interconnection System Considering Renewable Energy Power Plants", Universitas Gadjah Mada, 2020
- [15] PT PLN (Persero) "PT PLN (Persero) Electricity Supply Business Plan for the Years 2016 - 2025", PT PLN (Persero), Jakarta, Indonesia, Yearly Report, 2016
- [16] A. Reimers, W. Cole and B. Frew "The Impact of Planning Reserve Margins in Long-Term Planning Models of the Electricity Sector", Energy Policy, Vol.125, 2019
- [17] T. Chongphipatmongkol and K. Audomvongseeree "Determination of Reserve Margin based on Specified Loss of Load Expectation", 15th International Conference on Electrical Engineering/Electronics, Computer, Telecommunications and Information Technology (ECTI-CON), 2018

Impact of Coal Supply Constraint and Renewable Energy Mixed Target on a Power System Planning A Case Study of Southern Sulawesi System

Amira Hanun
Department of Electrical
and Information Engineering
Universitas Gadjah Mada
Yogyakarta, Indonesia
amira.hanun@mail.ugm.ac.id

Sarjiya
Department of Electrical
and Information Engineering
Universitas Gadjah Mada
Yogyakarta, Indonesia
sarjiya@ugm.ac.id

Lesnanto Multa Putranto
Department of Electrical
and Information Engineering
Universitas Gadjah Mada
Yogyakarta, Indonesia
lesnanto@ugm.ac.id

Tumiran
Department of Electrical and
Information Engineering
Universitas Gadjah Mada
Yogyakarta, Indonesia
tumiran@ugm.ac.id

Ira Savitri
System Planning Division
PT. PLN (Persero)
Jakarta, Indonesia
ira.savitri@pln.co.id

Daud Farel
System Planning Division
PT. PLN (Persero)
Jakarta, Indonesia
daud.farel@pln.co.id

Abstract— The effect of coal price fluctuation may affect the energy security of power system with high penetration of coal power plant. Moreover, the net zero emission trend make the power system utility do the energy transition to retire the existing coal power plant and to revise the power system planning. To deal with those problems, a generation expansion plan is proposed to limit the coal supply to the coal power plant. The energy conversion constraint is added to the standard linear model of generation expansion planning. The percentage of coal supply limitation is developed as the scenario and compared to the base case. The proposed method is simulated for 10 years planning horizon in Southern Sulawesi Power System which has high potential of renewable energy and coal power plant planning. As the result, the coal supply limitation requires 13.24% increment of reserve margin. Moreover, coal supply limitation increase the LCOE 2.23, 2.03 and 1.89 c\$/kWh for 30, 25 and 20% coal supply limitation.

Keywords— RES Penetration, Coal Supply Limitation, GEP, LCOE, Fuel Offtake, Reserve Margin

I. INTRODUCTION

Electricity demand has steadily increased every year as societies continue to grow and modernize. With the rapid advancement of technology, the widespread use of electronic devices, and the rise of industrial activities, the need for electrical power has become more crucial than ever before [1]. In response to the global climate crisis and the urgent need to mitigate carbon emissions, many countries, including Indonesia, have set ambitious targets for achieving Net Zero Emissions (NZE) by 2060 [2]. The continuous increase in CO₂ emissions, partly originating from the energy sector, led to the establishment of the Kyoto Protocol in 2005 and the Paris Agreement in 2015. Based on these agreements, the global community agreed to limit the annual temperature rise to less than 2 degrees Celsius [3]. Currently, Indonesian electricity depends on thermal power plants such as coal power plant (CPP), gas power plant (GPP), combined cycle power plant (CCPP), gas machine power plant (GMPP) and diesel power plant (DPP). Moreover, some hydro power plants (HPP) contribute to the energy mix for some power systems.

Wind power plant (WPP) was initially installed in Southern Sulawesi Systems (SSS). The first installation was 75 MWp in Sidrap, and the next Tolo at 50 MWp [4].

In order to manage the demand growth, engaging in generation expansion planning (GEP) to establish power generation facilities is crucial [5]. The GEP is purposed to be optimized based on the least cost optimization with technical, social and environmental constraints [6]. The environmental consideration of power system planning in SSS has been presented in [7]–[9]. Reference [9] considers intermittent renewable energy in SSS will increase the reserve margin from an average of 42.57% to 65.3%. Reference [10] The intermittent RES integration is still technically safe based on the power system analysis even if the generation cost was higher. However, the GEP should be technically safe by subjecting the analytic reliability constraint in the optimization process. In this research, the reliability constraint used is loss of load expectation (LOLE) 1day/year [4], [11]. However, the utility company still uses the determinative percentage to fulfill the reliability index [12]. For example, the reserve margin should be above a certain value i.e. >30% as in some Indonesian cases.

The prices of primary energy sources such as coal and gas in the international market fluctuated following the world politics, economic and environmental issue. Indonesia, being the fourth-largest coal producer in the world in 2019 [13], has led domestic coal producers to prefer selling their coal in the international market rather than within Indonesia itself [14]. Indonesia has previously experienced an energy supply crisis, specifically with coal, resulting in a coal supply shortage of less than 20 days of power plant operation (DPO) [4], [15]. This crisis occurred from August 2021 to January 2022 [16]. The dynamic coal prices in the international market were the main causes [17]. To prevent such an event from recurring, GEP was implemented, considering the availability of primary energy supply and in line with the NZE target. RES were identified as potential generating unit candidate

options to address the limitations of coal supply in the SSS. Sensitivity analysis was conducted considering different coal supply limitation scenarios of 30%, 25%, and 20%, to observe their effects on the system reliability index and total generation cost. Furthermore, the target of achieving Net Zero Emissions (NZE) by 2060 necessitates an increase in the penetration of Renewable Energy Sources (RES) to ensure the successful accomplishment of the energy transition goal.

II. PLANNING OF COAL SUPPLY AND RES PENETRATION GENERATING UNIT

A. Generation Optimal Model

GEP is a crucial aspect in ensuring the availability of electricity supply. The primary objective of long-term power generation planning is to ensure adequate electricity supply to meet future demand at the lowest cost, considering technical and non-technical aspects as presented in [18], [19]. The common objective function is to minimize total cost including capital, fixed O&M, variable O&M and fuel costs. The decision variable of the optimization is the annual installed capacity and energy production for every generating unit technology as presented in [20]. The objective function is presented in (1) as follows.

$$z = \min \left(\sum_r \sum_t \sum_y DFC_y \times [C_{inv}^t \times NC_{r,t,y}] + \sum_y DFO_y \times [C_{FO\&M}^t \times (\sum_r \sum_t (RC_{r,t,y} + \sum_y^{yy} NC_{r,t,y}))] + \sum_r \sum_l \sum_f DFO_y \times [\sum_t ((HR_t \times C_{fuel}^t) + C_{VO\&M}^t \times P_{r,t,y})] - \sum_r \sum_t \sum_y DFS_y \times SV_{r,t,y} \right) \quad (1)$$

Equation (1) present the objective function of GEP is to minimize the total cost consisting of investment cost, fixed O&M cost, fuel cost and variable O&M cost. The constraints related to energy sufficiency, reserve margin and renewable energy target are presented in (2 – 4)

$$\sum_t P_{r,t,y} + USE_y = D_y \quad (2)$$

$$\sum_t (RC_{r,t,y} + \sum_y^{yy} NC_{r,t,y}) \geq PL_{r,y} + RM_{r,y} \quad (3)$$

$$PRE_{r,y} \geq RET_y \times P_{r,t,y} \quad (4)$$

Equation (2) is a constraint for energy balance, which states that the total energy generated and the energy unserved must equal the electricity demand in each power system. Equation (3) indicates that the installed capacity should be greater than the peak load and reserve margin.

Equation (4) represents the limit on the use of renewable energy sources as power generation, where the value should be greater than the RES target multiplied by the amount of energy generated.

Constraint of reliability index related to loss of load probability (LOLP) system represent ini (5). LOLP must less than 0.274% or equal to LOLE less than 1 day.

$$LOLP = \sum_{i=1}^n P_i \cdot t_i \quad (5)$$

$$LOLP < 0,274\%$$

The nomenclature used in modeling the objective function and constraints is as follows.

| | | | |
|--------------|--|---------------|---|
| $NC_{r,t,y}$ | : new capacity | C_{inv}^t | : capital cost |
| $P_{r,t,y}$ | : production | $C_{FO\&M}^t$ | : fixed operation and maintenance cost |
| y | : year | C_{fuel}^t | : fuel cost |
| r | : region | $C_{VO\&M}^t$ | : variable operation and maintenance cost |
| f | : fuel | $SV_{r,t,y}$ | : salvage value |
| t | : technology | $RC_{r,t,y}$ | : residual capacity |
| l | : timeslice | $YS_{y,l}$ | : year split |
| DFC_y | : discount factor for capital investment | HR_t | : heat rate |
| DFO_y | : discount factor for fixed cost and variable cost | $OL_{r,t}$ | : operational life |
| DFS_y | : discount factor for salvage value | D_y | : demand |
| USE_y | : unserved energy | RET_y | : renewable energy target |
| $PL_{r,y}$ | : peak load | $PRE_{r,y}$ | : production by renewable energy |
| $RM_{r,y}$ | : reserve margin | P_i | : individual probability |

B. Wind and Hydro Modelling

RES modeling is based on capacity factor of a power plant. If capacity factor RES power plant is high, it will increases production [15]. in SSS HPP unit has a reservoir so capacity factor modeling will impact the production of HPP on the other hand wind is variable renewable energy (VRE) it make capacity factor of WPP depends on wind profile of each system.

$$P_{r,t,y} = CF_t \times 8760 \times (RC_{r,t,y} + NC_{r,t,y}) \quad (6)$$

Equation (6) represents if each RES power plant's capacity factor will impact the RES power plant's production generation.

C. Fuel Offtake Primary Energy Resources

Fuel offtake is total fuel consumed by a generator using the fuel either for generation or starting [21]. Fuel offtake will impact heat rate of generator. When the fuel offtake decreases, it will lower the capacity factor value of the power plant, resulting in a decrease in its production as well.

$$P_{r,t,y} \leq FOT_{ft} \times Avg HR_t \quad (7)$$

FOT_{ft} : fuel limitation

$Avg HR_t$: average heat rate

Equation (7) is a constraint for production should be less than fuel offtake of primary energy resources multiplied by average heat rate of power plant.

D. Levelized Cost of Energy

The levelized cost of energy (LCOE) represents the expense of producing energy within a specific system [22]. It is an economic assessment of the cost of energy over the power plant life time, which comprise capital expenditures, fixed costs, variable operational and maintenance expenses, as well as fuel costs. These are then used to compute yearly costs across the planning period, factoring in discount rates to ascertain the net present value (NPV) [23].

$$LCOE = \frac{(C_{inv}^t \times CRF + C_{FO\&M}^t)}{(8760 \times CF_t) + (C_{fuel}^t \times HR_t) + C_{VO\&M}^t} \quad (9)$$

$$CRF = \frac{i \times (1 + i)^n}{(1 + i)^n - 1} \quad (10)$$

CRF : capital recovery factor

i : discount rate

n : operational life

Equation (9) represents cost of generating energy. Capital recovery factor (CRF) determines net present value (10).

III. METHODOLOGY

In this paper used Southern Sulawesi System (SSS) for real case system. In 2021 the peak load of SSS was 1,592 MW with a generation capacity of 10,277 GWh and total installed capacity 2,358 MW. Reserve margin in 2021 was 48.15%. Table I shows existing demand and peak load in SSS during 2021 – 2030. Demand continues to grow, reaching 17,763 GWh by 2030, accompanied by an ongoing increase in peak load, reaches 2,761 MW in 2030. Installed capacity 2,358.61 MW in 2021 continue to grow 3,720 MW by 2030. Fig. 1 shows mixed energies of SSS was dominated by coal 48.4% and 43.5% of RES.

Fig. 2 describes demand and wind profile of SSS in 2021. Several factors contribute to increased demand on the SSS, including load expansion, industrial area growth, and the establishment of nickel smelting industries. Demand profile for planning horizon 2022 – 2030 was derived by forecasting using the 2021 load profile, projected growth in electricity consumption, and planned construction of industries on the SSS.

Table II present techno-economy of existing power plant on SSS such as range of capacity factor, type of fuel and fuel cost of each power plant. Table III represent RES candidate power plant to be built. Since most of the HPP unit has a reservoir, the HPP is considered as a dispatchable unit. Since CPP is not a dispatchable unit and need data requirement of wind profile.

Fig. 3 is a flowchart that describes GEP considering fuel offtake of primary resources in that case coal resources is limited. There are two scenarios of GEP. First is GEP Base Case based on existing planning. Second is GEP with fuel offtake limitation and VRE penetration. Sensitivity analysis is used when coal resources are only available 70%, 75% and 80% of coal ordinary reserve.

The additional capacity to replace the deficiency would be selected from WPP and HPP.

The calculation is simulated using the MILP formulation. Both scenarios' energy mix and levelized cost of electricity (LCOE) are calculated. After that, the impact of fuel offtake of coal limitation in SSS for each year in planning horizon and their sensitivity are calculated. Finally, the existing traditional reserve margin method is evaluated by comparing the LOLE, reserve margin and LCOE from 2021 to 2030.

TABLE I PEAK LOAD AND DEMAND EXISTING OF SSS [4]

| Data | 2021 | 2030 |
|-------------------------|-----------|-----------|
| Peak Load (MW) | 1,592.00 | 2,761.00 |
| Demand (GWh) | 10,277.00 | 17,763.83 |
| Installed Capacity (MW) | 2,358.61 | 3,720.05 |

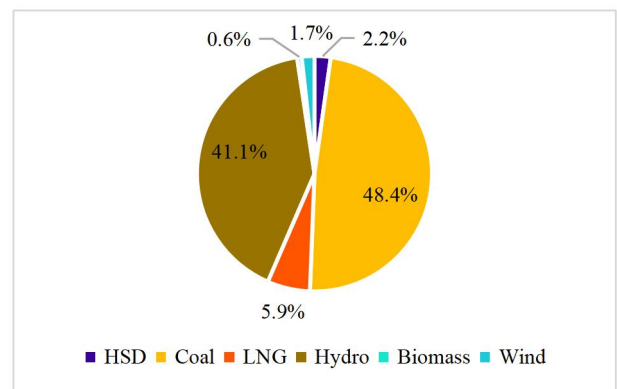


Fig. 1. Mixed Energies Existing of SSS [4]

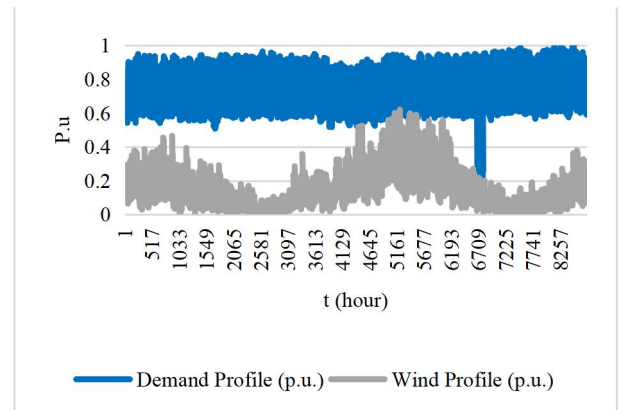


Fig. 2. Demand and Wind Profile SSS in 2021

TABLE II TECHNO-ECONOMY EXISTING POWER PLANT SSS [24]

| Type GEN | Range of Cap Factor (%) | FOR (%) | Fuel Type | Cost of Fuel |
|----------|-------------------------|---------|-----------|----------------|
| Biomass | 50 – 80 | 7 | Biomass | 0.1341 \$/kg |
| CCPP | 25 – 80 | 5 | LNG | 16.28 \$/MMBTU |
| CPP | 50 – 75 | 3 | Coal | 65 \$/Ton |
| DPP | 20 – 50 | 7 | HSD | 0.5 \$/Liter |

| Type GEN | Range of Cap Factor (%) | FOR (%) | Fuel Type | Cost of Fuel |
|----------|-------------------------|---------|-----------|----------------|
| GPP | 20 – 80 | 2 | LNG | 16.28 \$/MMBTU |
| GMPP | 20 – 60 | 2 | LNG | 16.28 \$/MMBTU |
| HPP | 50 – 80 | 4 | - | - |
| WPP | Profile | 2.5 | - | - |

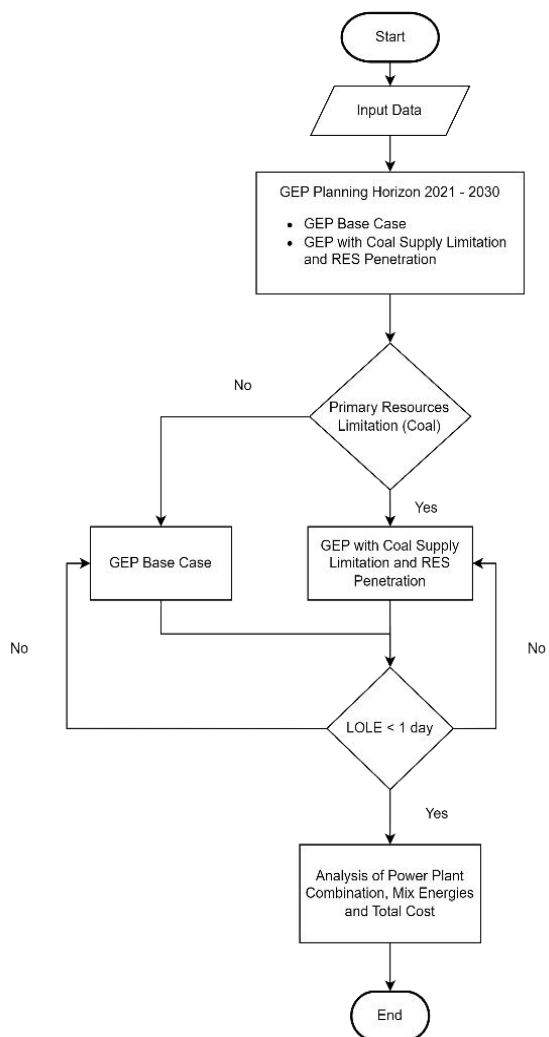


Fig. 3. Fuel Offtake Coal Resources and RES Penetration Over the Planning Procedure

TABLE III RES CANDIDATE FOR RES PENETRATION [24]

| No | Type | Minimum Capacity (MW) | Capacity Factor (%) | FOR (%) |
|----|-------|-----------------------|---------------------|---------|
| 1 | Hydro | 200 | 50 | 4 |
| 2 | Wind | 60 | Wind Profile | 2.5 |

IV. RESULT AND DISCUSSION

Indonesia has previously experienced an energy supply crisis, specifically with coal, resulting in a coal supply shortage of less than 20 days of power plant

operation (DPO) [4]. This crisis occurred from August 2021 to January 2022 [16]. The dynamic coal prices in the international market were the main causes [17]. To prevent such an event from recurring, GEP was implemented, considering the availability of primary energy supply and in line with the NZE target. RES were identified as potential power generation candidate options to address the limitations of coal supply in the SSS. Sensitivity analysis was conducted considering different coal supply limitation 30%, 25% and 0%, to observe their effects on the system reliability index and total generation cost.

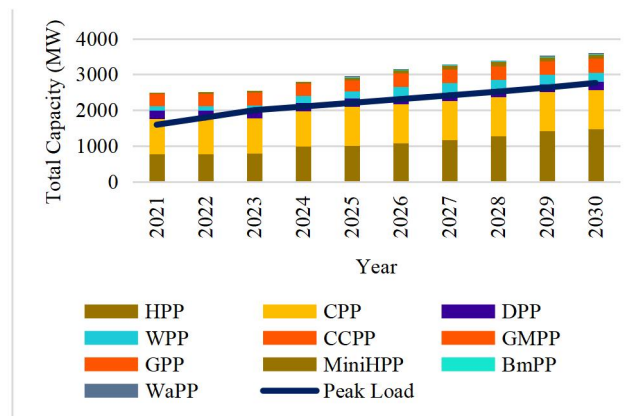


Fig. 4. Total Capacity Base Case Scenario

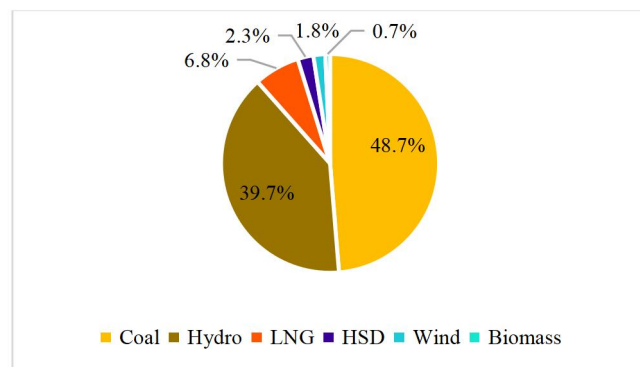


Fig. 5. Energy Mixed of Base Case Scenario

A. Base Case

Base case scenario was executed only based on the least cost optimization without coal supply limitation and RES penetration. Base Case scenario results the combination of power plant represent in Fig. 4. Total capacity during planning horizon 2021 - 2030 increase due to demand growth in SSS. The energy mix represent in Fig. 5 was dominated by coal 48.7% and 42.2% renewable energy. Hydro portion in renewable energy has 39.7% and for wind 1.8%. LCOE annual for SSS in Base Case scenario has 7.85 c\$/kWh.

B. Coal Supply Limitation

GEP considered coal offtake and RES penetration was simulated to see the impact of dynamic price or supply chain problems in primary energy resources of power plant. Fig. 6 represent sensitivity analysis of coal offtake limitation compared with Base Case scenario. In this scenario coal supply limitation 30%, 25% and 20% so, coal resources are only available 70%, 75% and 80% from coal ordinary reserve.

Reliability index is presented in Fig. 7 and Fig. 8. Fig. 7 represent reserve margin GEP considering coal limitation and RES. Reserve margin increases by 13.24% for scenario coal supply limitation 30%, 25% and 20% compared to Base Case scenarios. In 2025 reserve margin increases more than Base Case comes from additional HPP 2 x 200 MW and WPP 1 x 60 MW. LOLE for GEP using coal offtake limitation less than Base Case scenario represent in Fig. 8. Energy mixed for sensitivity analysis compared to Base Case scenario represent in Table IV. After adding the scenario coal limitation, the mix energies are different from Base Case. In the Base Case scenario, coal dominates with a share of 48.69% of the energy mix, while in the scenario of coal limitation and RES penetration, the proportion of coal decreases by 13.18%. This decrease is due to limited coal supply. Hydro becomes the dominant energy source with an increase of 6%, and wind energy increases by 3.95%. Gas shows an increase of 2.54% due to the influence of coal limitation, which leads to a decrease in the capacity factor of CPP. As a result, the capacity factor for CCPP, GPP, and GMPP increases. These changes of capacity factor will affect the energy production of these power plants, as represented in (8).

Economic evaluation of Base Case scenario and coal limitation scenario represent in Table V. For coal supply limitation 30% has a highest LCOE compared to Base Case with an increases by 2.23 c\$/kWh, for coal supply limitation 25% increases by 2.03 c\$/kWh and for coal supply limitation 20% increases by 1.89 c\$/kWh. LCOE in scenario coal offtake limitation higher than Base Case scenario because of capacity factor of CPP lower than usual and RES penetration.

Fig. 9 shows production of CPP, CCPP, GPP, GMPP and WPP in 2025 when capacity factor of CPP decreases capital cost and fixed cost of CPP still constant, otherwise the production of CPP will decrease and it will affected capacity factor other power plant like CCPP, GPP, GMPP increases so LCOE will be increase. In 2025 RES penetratrion of HPP and WPP as presented in Table VI. RES penetration of HPP and WPP will increase LCOE.

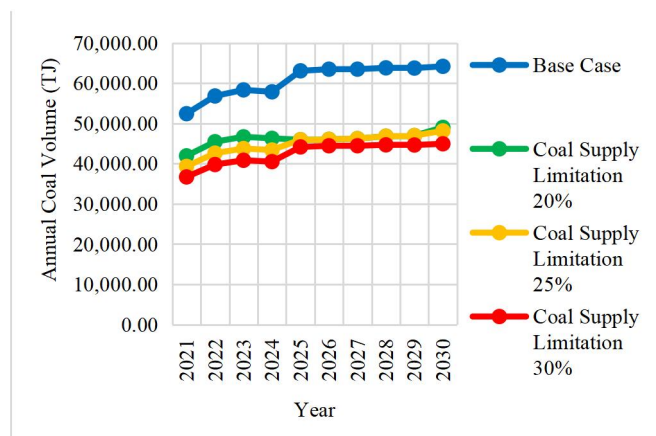


Fig. 6. Coal Limitation of Both Scenarios

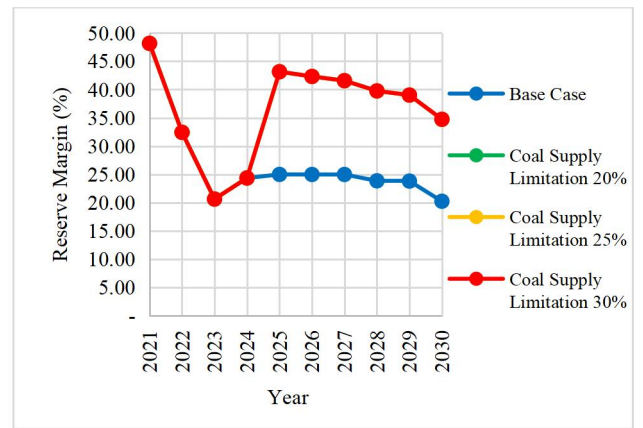


Fig. 7. Reserve Margin of Both Scenarios

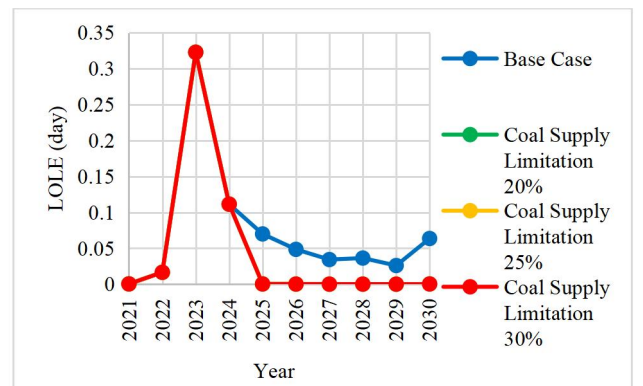


Fig. 8. LOLE Both of Scenarios

TABLE IV ENERGY MIXED OF BOTH SCENARIOS

| Energy | Base Case (%) | Coal Supply Limitation 20% (%) | Coal Supply Limitation 25% (%) | Coal Supply Limitation 30% (%) |
|---------|---------------|--------------------------------|--------------------------------|--------------------------------|
| Hydro | 39.73 | 45.71 | 45.71 | 45.73 |
| Coal | 48.69 | 36.91 | 35.79 | 33.84 |
| LNG | 6.79 | 8.36 | 9.06 | 10.58 |
| Wind | 1.77 | 5.72 | 5.72 | 5.72 |
| HSD | 2.33 | 2.94 | 3.33 | 3.57 |
| Biomass | 0.70 | 0.36 | 0.39 | 0.56 |

TABLE V LCOE ANNUAL OF BOTH SCENARIOS

| LCOE Annual (c\$/kWh) | Base Case | Coal Supply Limitation 20% | Coal Supply Limitation 25% | Coal Supply Limitation 30% |
|-----------------------|-----------|----------------------------|----------------------------|----------------------------|
| | 7.85 | 9.74 | 9.88 | 10.08 |

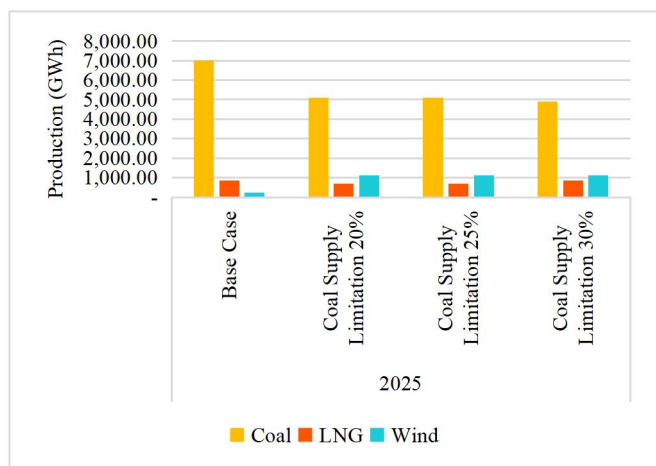


Fig. 9. Production of Coal LNG and Wind Both Scenarios in 2025

TABLE VI TOTAL CAPACITY IN 2025 BOTH SCENARIOS

| Gen Type | Base Case (MW) | Coal Supply Limitation 20% (MW) | Coal Supply Limitation 25% (MW) | Coal Supply Limitation 30% (MW) |
|-----------|----------------|---------------------------------|---------------------------------|---------------------------------|
| HPP | 1014 | 1413.96 | 1413.96 | 1413.96 |
| CPP | 1090 | 1090 | 1090 | 1090 |
| DPP | 229.69 | 229.69 | 229.69 | 229.69 |
| WPP | 190 | 910 | 910 | 910 |
| CCPP | 200 | 200 | 200 | 200 |
| GMPP | 100 | 100 | 100 | 100 |
| GPP | 20.1 | 20.1 | 20.1 | 20.1 |
| MHPP | 69.8 | 69.8 | 69.8 | 69.8 |
| BiomassPP | 20 | 20 | 20 | 20 |

V. CONCLUSION

This paper discusses the effect of impact primary energy resources limitation in this SSS case used coal limitation. In line with NZE target in 2060 RES penetration is also considered. Coal limitation will affect the reliability index. To overcome the reliability index requires additional of HPP 2 x 200 MW and WPP 1 x 60 MW in 2025. With sensitivity scenarios analysis coal supply limitation 30%, 25% and 20% so coal resources are only available 70%, 75% and 80% from coal ordinary reserve. Compared to Base Case scenario reserve margin increases by 13.24%. moreover it will increase LCOE system for coal supply limitation 30% has a highest LCOE compared to Base Case with an increases by 2.23 c\$/kWh, for coal supply limitation 25% increases by 2.03 c\$/kWh and for coal supply limitation 20% increases by 1.89 c\$/kWh.

VI. ACKNOWLEDGEMENT

This work funded by the Reknognisi Tugas Akhir (RTA) Program of the Research Directorate of Universitas Gadjah Mada. Any opinions, findings and conclusions or recommendations expressed herein are those of the authors and do not necessarily reflect those of the Research Directorate of Universitas Gadjah Mada.

REFERENCES

- [1] *Indonesia Statistic 2023*. Jakarta, Indonesia: BPS-Statistics Indonesia, 2023.
- [2] MEMR of The Republic of Indonesia, "The 3rd Energy Transitions Working Group at Bali: The Foundation for G20 Energy Transitions Acceleration," Bali, Sep. 2022.
- [3] Jane A. Leggett, "The United Nations Framework Convention on Climate Change, the Kyoto Protocol, and the Paris Agreement: A Summary," 2020. [Online]. Available: <https://crsreports.congress.gov>
- [4] *Indonesia's 2021-2030 Electricity Procurement Plan*. Jakarta, Indonesia: PT. PLN (Persero), 2021.
- [5] H. Akbarzade and T. Amraee, "A multi-stage generation expansion planning for low carbon power systems," in *2020 28th Iranian Conference on Electrical Engineering, ICEE 2020*, 2020. doi: 10.1109/ICEE50131.2020.9260879.
- [6] M. S. S. Hossein Seifi, *Electric Power System Planning*. Springer Science & Business Media, 2011.
- [7] North American Electric Reliability Corporation, "Long-Term Reliability Assessment," 2021.
- [8] A. A. Muthahhari *et al.*, "Environmental Considerations in Long-Term Generation Expansion Planning with Emission Limitations: An Analysis of the Sulawesi Power System in Indonesia," in *Proceeding - 1st FORTEI-International Conference on Electrical Engineering, FORTEI-ICEE 2020*, Institute of Electrical and Electronics Engineers Inc., Sep. 2020, pp. 29–34. doi: 10.1109/FORTEI-ICEE50915.2020.9249863.
- [9] A. A. Muthahhari *et al.*, "Long-Term Generation Expansion Planning in Sulawesi Electricity System Considering High Share of Intermittent Renewable Energy Resource," in *2019 11th International Conference on Information Technology and Electrical Engineering, ICITEE 2019*, 2019. doi: 10.1109/ICITEED.2019.8929948.
- [10] "International Energy Agency," 2020. <https://www.iea.org/>
- [11] Suruhanjaya Tenaga Energy Commission, "Report on Peninsular Malaysia Generation Development Plant 2019 (2020 - 2030)," 2020.
- [12] Roy Billinton, *Power System Reliability Evaluation*. Taylor & Francis, 1970.
- [13] MEMR, "Road Map of Coal Development and Utilization," 2021.
- [14] I. International Energy Agency, "Coal 2022 Analysis and Forecast to 2025." [Online]. Available: www.iea.org
- [15] PT PLN (Persero), "PT PLN (PERSERO) Statistic 2022," Jakarta, 2023. [Online]. Available: www.pln.co.id
- [16] Safyra Primadhyta, "The Ministry of Energy and Mineral Resources Ensures that PLN's Coal Crisis Does Not Recurred," 2022. <https://www.cnnindonesia.com/ekonomi/20220119082106-85-748447/kementerian-esdm-pastikan-krisis-batu-bara-pln-tak-terulang> (accessed Jul. 18, 2023).
- [17] Institute for Essential Services Reform (IESR), "Imprint Indonesia Energy Transition Outlook 2023 Tracking Progress of Energy Transition in Indonesia: Pursuing Energy Security in the Time of Transition," 2023.
- [18] N. E. Koltaklis and A. S. Dagoumas, "State-of-the-art generation expansion planning: A review," *Applied Energy*, vol. 230. 2018. doi: 10.1016/j.apenergy.2018.08.087.
- [19] L. M. Putranto, "Generation expansion planning for high-potential hydropower resources: The case of the Sulawesi electricity system," *International Journal of Sustainable Energy Planning and Management*, vol. 28, pp. 37–52, Apr. 2020, doi: 10.5278/ijsepm.3247.
- [20] A. A. Fawwaz, A. Hanun, and M. Burhanudin, "The Design of Masterplan for Java-Bali-West Nusa Tenggara-East Nusa Tenggara Interconnection System Considering Renewable Energy Power Plant," 2020.
- [21] O. J. Guerra *et al.*, "Electric Power Grid and Natural Gas Network Operations and Coordination," 2015. [Online]. Available: www.nrel.gov/publications.
- [22] Y. Kikuchi and T. Ishihara, "Availability and lcoe analysis considering failure rate and downtime for onshore wind turbines in Japan," *Energies (Basel)*, vol. 14, no. 12, Jun. 2021, doi: 10.3390/en14123528.
- [23] B. Khaki and P. Das, "Definition of multi-objective operation optimization of vanadium redox flow and lithium-ion batteries considering leveled cost of energy, fast charging, and energy efficiency based on current density," *J Energy Storage*, vol. 64, Aug. 2023, doi: 10.1016/j.est.2023.107246.
- [24] Directorate General of Electricity, *Technology Data for the Indonesian Power Sector Catalogue for Generation and Storage of Electricity*. Jakarta, Indonesia, 2021.

Analysis of Renewable Energy Project Delays on The Indonesia's Energy Transition Process, Case Study: Java Bali System

Tumiran

*Department of Electrical and
Information Engineering
Universitas Gadjah Mada
Yogyakarta, Indonesia
tumiran@ugm.ac.id*

Sarjiya

*Department of Electrical and
Information Engineering
Universitas Gadjah Mada
Yogyakarta, Indonesia
sarjiya@ugm.ac.id*

Lesnanto Multa Putranto

*Department of Electrical and
Information Engineering
Universitas Gadjah Mada
Yogyakarta, Indonesia
lesnanto@ugm.ac.id*

Rizki Firmansyah Setya Budi

*Research Center for Reactor Nuclear
Technology
National Research and Innovation
Agency
Banten, Indonesia
rizk011@brin.go.id*

Ahmad Adhiim Muthahhari

*Electrical Engineering Technology
Universitas Gadjah Mada
Yogyakarta, Indonesia
ahmad.adhiim.m@ugm.ac.id*

Amira Hanun

*Department of Electrical and
Information Engineering
Universitas Gadjah Mada
Yogyakarta, Indonesia
amira.hanun@mail.ugm.ac.id*

Kurnia Wisesa Kisna

*Department of Electrical and
Information Engineering
Universitas Gadjah Mada
Yogyakarta, Indonesia
kurnia.wisesa.kisna@mail.ugm.ac.id*

Abstract— In order to reduce greenhouse gas emissions, all countries, including Indonesia, are trying to utilize clean energy in their energy supply. To be able to realize the use of clean energy and reduce the effect of greenhouse gases, Indonesia has decided to accelerate the energy transition so that it can achieve NZE by 2060. The problem that is often encountered in power generation projects is delays in power generation projects, which have not been considered in the current power plant planning. Based on this, this paper will conduct a study by considering aspects of the success and delay ratio of a power plant project in planning. By considering these aspects, plant planning will be carried out using the MILP method and then the influence of the delay and success ratio will be analyzed on the renewable energy mix, LCOE, and the plants that will replace it. Based on the results obtained, The extent of the delay in capacity refers to the success ratio, delays, and achievements of the power plant projects. Delayed VRE PP up to 2 GW, and based on the results, it was found that these generators would be substituted with Gas Machines up to 2000 MW. This affects the LCOE of the system, increasing it from 9.77 c\$/kWh to up to 8 c\$/kWh. This LCOE calculation does not yet account for the unavailability of LNG, which would lead the Gas Machine to utilize more expensive HSD (High-Speed Diesel), potentially causing a further increase in the LCOE.

Keywords— *Renewable energy, generation expansion planning, energy transition, project delays, LCOE*

I. INTRODUCTION

Currently, the issue of global warming is a matter of concern to all countries in the world, including Indonesia. Various efforts have been made to reduce CO₂ emissions and greenhouse gases (GHG). Indonesia is committed to implementing the Paris Agreement through [1].

Indonesia has made several efforts, one of them is accelerating the energy transition, especially in the electricity sector. Based on [2], Indonesia is targeting an increase in its renewable energy mix of 23% in 2025 and 31% in 2050. The Indonesian government's efforts to increase the utilization of clean energy. Based on [3], renewable energy generation capacity has reached 12.72%.

Generation expansion planning with consider the renewable energy has been done in various country, such as USA [4], Ireland [5], France [6], China [7]–[9], Brazil [10], Portugal [11], Egypt [12], Pakistan [13], Oman [14], South Africa [15], Bangladesh [16], Malaysia [17] and Indonesia [18]–[22] have considered the environmentally friendly resource or RES in their GEP model. Based on these studies, considering VRE can lead to increasing or decreasing the total generation cost.

A statistical residual load duration curve (S-RLDC), a technique to simplify the duration curve load method, was used to model the load for GEP in China [9]. The S-RLDC modelled the generation of renewable energy as a negative load. In [10], a GEP using multiple objective functions

considering renewable energy was successfully conducted. In the study, the use of non-hydro renewable energy in the Brazilian power system could be increased. Another study included external costs of environmental impacts on GEP in China to accommodate the entry of intermittent power plants [7].

In addition, several studies on GEP have considered Indonesia's high share of RES, including dispatchable and variables RES (VREs). For example, research [22] incorporates high share VREs of wind in GEP, while research [23] considers the emission factor among the VREs factor. Moreover, the potential of local energy sources has also been studied in [24], which analyzes utilizing biomass in eastern Indonesia. Furthermore, research [25] modelled a GEP on isolated systems, considering local energy sources and the interconnections between systems.

However, based on historical data from [3], the success ratio in a power plant project is not always as expected. Based on the data that has been processed, the success rate of the hydro power plant (hydro PP) project is 75%, mini hydro power plant (mini hydro PP) 2x%, and PV power plant (PP) 0% for the Java Bali system until 2021. Delays and success of a project can be caused by several factors, such as legal aspects, land acquisition, power purchase agreements, or even failures in the construction process.

Currently, plant planning taking into account aspects of success or delay in Indonesia has not been carried out. In planning [18], [20], [22], [23], [26], [27], the GEP still does not consider these aspects. Because of this, a study is needed that considers the ratio of success and also delays in plant planning.

In this paper, we will discuss the influence of delay and success ratios on plant planning. The contribution of this paper is that it can provide an overview of the impacts and mitigation that need to be carried out if power plant development planning takes these two aspects into consideration.

The rest of the paper is as follows: Section II will discuss the objective function and constraints in the GEP. Section III describes the methodology of the research to be carried out. Section IV discusses the results of the research. Finally, section V presents the conclusions from the results of this research.

II. GENERATION EXPANSION PLANNING

A. Objective Function

In this paper, consider the objective function as in (1). This aims to obtain the optimal combination of generators to meet the supply of electricity by considering several aspects such as delays. The objective function is to minimize the discounted generation costs while adhering to certain constraints [21]–[23], [25]. The calculation of GEP is based on the total fixed cost, variable operating and maintenance cost, and fuel cost. The total fixed cost consists of the total annualized investment and fixed operating and maintenance costs as in (2)–(10).

$$\min \text{Cost} = C_{\text{Fix}}^{\text{total}} + C_{\text{VO\&M}}^{\text{total}} + C_{\text{Fuel}}^{\text{total}} \quad (1)$$

$$C_{\text{Fix}}^{\text{total}} = C_{\text{Annual}}^{\text{total}} + C_{\text{FO\&M}}^{\text{total}} \quad (2)$$

$$C_{\text{Annual}}^{\text{total}} = C_{\text{Inv}}^{\text{total}} \times \frac{(1-\text{Tax}) \times \frac{\text{NAF}}{\text{EcoLife}}}{\text{RAF}} \quad (3)$$

$$C_{\text{Inv}}^{\text{total}} = \sum_y \sum_g DF_y \times (C_{\text{inv}}^g \times 1000 \times P_{\text{max}}^g \times \text{NB}_g^y) \quad (4)$$

$$C_{\text{FO\&M}}^{\text{total}} = \sum_y \sum_g DF_y \times [C_{\text{FO\&M}}^g \times P_{\text{max}}^g (N_g + \sum_{i \leq y} \text{NB}_g^i)] \quad (5)$$

$$C_{\text{VO\&M}}^{\text{total}} = \sum_t \sum_g DF_{t \in y} \times L_t \times (C_{\text{VO\&M}}^g \times G_g^t) \quad (6)$$

$$C_{\text{Fuel}}^{\text{total}} = \sum_t \sum_g DF_{t \in y} \times L_t \times (\text{Heat Rate} \times C_{\text{fuel}}^g \times G_g^t) \quad (7)$$

$$DF = \frac{1}{(1+D)^y} \quad (8)$$

$$\text{NAF} = \frac{1 - (1 + \text{WACC} + \text{Infation rate})^{-\text{Ecolife}}}{\text{WACC} + \text{Infation rate}} \quad (9)$$

$$\text{RAF} = \frac{1 - (1 + \text{WACC})^{-\text{Ecolife}}}{\text{WACC}} \quad (10)$$

With,

| | |
|------------------------------------|---|
| $C_{\text{Fix}}^{\text{total}}$ | : Total fixed cost (\$/kW/yr) |
| $C_{\text{Annual}}^{\text{total}}$ | : Total annualized build cost (\$/kW/yr) |
| $C_{\text{Inv}}^{\text{total}}$ | : Total build cost (\$/kW) |
| $C_{\text{FO\&M}}^{\text{total}}$ | : Total fixed O&M cost (\$/kW/yr) |
| $C_{\text{VO\&M}}^{\text{total}}$ | : Total var O&M cost (\$/MWh/yr) |
| $C_{\text{Fuel}}^{\text{total}}$ | : Total fuel cost (\$/MWh) |
| DF_y | : Discount factor |
| D | : Discounted Rate (%) |
| P_{max}^g | : Generator max capacity (MW) |
| NB_g^y | : Number of generator |
| G_g^t | : Generation of generator g in t period (MWh) |
| C_{inv}^g | : Build cost of generator g (\$/kW) |
| $C_{\text{FO\&M}}^g$ | : FO&M cost generator g (\$/kW/yr) |
| $C_{\text{VO\&M}}^g$ | : VO&M cost generator g (\$/MWh/yr) |
| C_{fuel}^g | : Fuel cost generator g (\$/MWh/yr) |

B. Constraints

During the optimization process, several constraints are taken into consideration. The power balance constraint ensures that the total generation during a specific period must meet or exceed the load demand at that time, as depicted in equation (11). Additionally, the total generation is limited by the available installed generating capacity, as stated in equation (12). The number of new power plants constructed cannot surpass the maximum potential, as outlined in equation (13). However, the total installed capacity must be adequate to meet the yearly peak load plus a reserve margin specified in equation (14).

$$\sum_{g=1}^{NG} G_g^t \geq D^t, \forall t \quad (11)$$

$$G_g^t \leq P_{\text{max}_g} \left(N_g + \sum_{i \leq y, y=1}^{NY} \text{NB}_g^i \right), \forall g, t \quad (12)$$

$$\sum_{i \leq y, y=1}^{NY} \text{NB}_g^i \leq \text{NB}_{\text{max}_g}^i, \forall g \quad (13)$$

$$\sum_{g=1}^{NG} P_{\text{max}_g} \left(N_g + \sum_{i \leq y, y=1}^{NY} \text{NB}_g^i \right) \geq PL^y (1 + RM), \forall y \quad (14)$$

With,

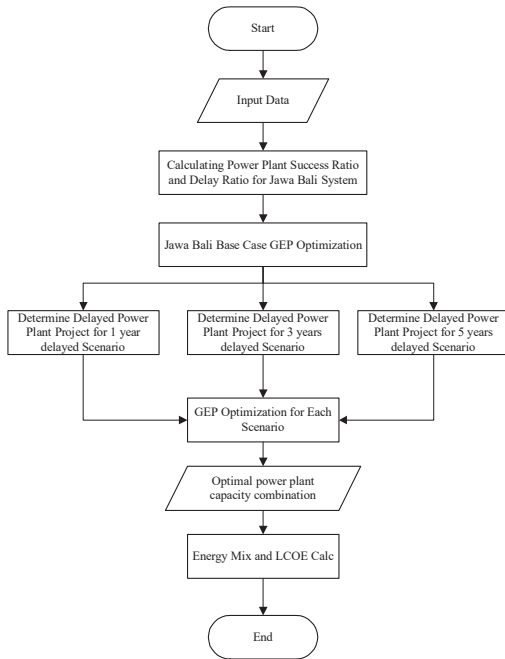


Fig. 1. The Generation Expansion Planning Workflow

- D^t : Demand in t period (MWh)
 NB_{max}^i : Max Number of generator g that can be built
 PL^y : Peak load (MW)
 RM : Reserve margin (%)

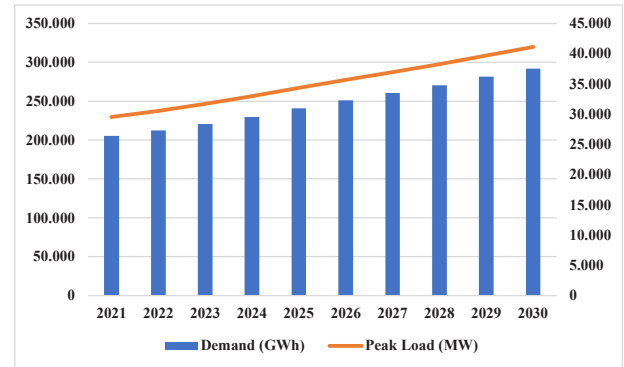


Fig. 2. Java Bali System Demand and Peak Load

III. METHODOLOGY

The process of the research is illustrated in Fig 1. Information required for this research includes predicted energy demand and peak load for the planning period, potential power plant and primary energy resources. Annual energy demand and peak load as illustrated in Fig 2. The information on the potential power plant options includes plant size, heat rate, maintenance rate, forced outage rate, lifetime, investment cost, and operating costs, which are presented in Table I [28], [29].

The study in this paper uses the Java Bali system as a system test, which is the largest electricity system in Indonesia. In this paper, a comparison of GEP results from normal conditions with a delay scenario is carried out. The

TABLE I. POWER PLANT CANDIDATE DATA [28],[29]

| Type | Heat Rate (GJ/MWh) | Maintenance Rate (%) | FOR (%) | Technical Lifetime (years) | Investment Cost (\$/kWe) | Fixed O&M Cost (\$/kWe/y) | Variable O&M Cost (\$/MWh) |
|------------|--------------------|----------------------|---------|----------------------------|--------------------------|---------------------------|----------------------------|
| Gas | 8.37 | 2.88 | 3 | 25 | 800 | 18 | 1 |
| Hydro | - | 11.51 | 4 | 50 | 2,000 | 6.6 | 1 |
| Biomass | 9 | 11.51 | 7 | 25 | 1,700 | 47.6 | 3 |
| Wind | - | 0.31 | 3 | 27 | 1,500 | 39.55 | 0.8 |
| Solar | - | 5 | 5 | 25 | 790 | 24.7 | 0.4 |
| Coal | 9 | 11.51 | 7 | 30 | 1,650 | 45.3 | 0.13 |
| Geothermal | 4.32 | 7.67 | 10 | 30 | 4,000 | 65 | 0.37 |

TABLE II. EXISTING POWER PLANT DATA (IN MW)

| Existing Gen | 2021 | 2022 | 2023 | 2024 | 2025 | 2026 | 2027 | 2028 | 2029 | 2030 |
|---------------|--------|--------|--------|--------|--------|--------|--------|--------|--------|--------|
| Hydro PP | 2,615 | 2,615 | 2,615 | 2,615 | 2,615 | 2,615 | 2,615 | 2,615 | 2,615 | 2,615 |
| Mini Hdro PP | 150 | 150 | 150 | 150 | 150 | 150 | 150 | 150 | 150 | 150 |
| Geothermal PP | 1225 | 1225 | 1225 | 1225 | 1225 | 1225 | 1225 | 1225 | 1225 | 1225 |
| Gas PP | 1,467 | 1,467 | 1,467 | 1,467 | 1,467 | 1,467 | 1,467 | 1,467 | 1,467 | 1,467 |
| CCGT | 9,477 | 8,014 | 6,929 | 6,929 | 6,929 | 6,929 | 6,929 | 6,929 | 6,929 | 6,929 |
| Gas Machine | 182 | 182 | 182 | 182 | 182 | 182 | 182 | 182 | 182 | 182 |
| Diesel | 152 | 152 | 152 | 152 | 152 | 152 | 152 | 152 | 152 | 152 |
| Coal | 22,479 | 22,479 | 22,479 | 22,479 | 22,479 | 22,479 | 22,479 | 22,479 | 22,479 | 22,479 |
| Coal with HSD | 927 | 927 | 927 | 927 | 927 | 927 | 927 | 927 | 927 | 0 |
| Biomass | 5 | 5 | 5 | 5 | 5 | 5 | 5 | 5 | 5 | 5 |
| Waste | 15 | 15 | 15 | 15 | 15 | 15 | 15 | 15 | 15 | 15 |
| Excess | 3 | 3 | 3 | 3 | 3 | 3 | 3 | 3 | 3 | 3 |

TABLE III. POWER PLANT CANDIDATE

| | 2021 | 2022 | 2023 | 2024 | 2025 | 2026 | 2027 | 2028 | 2029 | 2030 |
|---------------|------|------|------|------|------|------|------|------|------|------|
| Hydro PP | 110 | 0 | 0 | 0 | 0 | 50 | 0 | 0 | 0 | 0 |
| Coal PP | 4215 | 924 | 0 | 0 | 1660 | 1660 | 0 | 0 | 0 | 0 |
| Geothermal PP | 0 | 0 | 130 | 65 | 330 | 265 | 55 | 190 | 75 | 805 |
| PV PP | 0 | 145 | 235 | 550 | 1240 | 110 | 140 | 140 | 140 | 140 |
| Waste | 9 | 5 | 0 | 35 | 183 | 0 | 0 | 0 | 0 | 0 |
| Mini Hydro | 45 | 38 | 144 | 102 | 76 | 12 | 0 | 0 | 0 | 0 |
| Wind PP | 0 | 0 | 0 | 160 | 100 | 0 | 0 | 0 | 0 | 0 |
| PS | 0 | 0 | 0 | 0 | 1040 | 0 | 0 | 943 | 760 | 1000 |
| CCGT | 2110 | 1279 | 200 | 0 | 100 | 0 | 0 | 0 | 0 | 0 |

TABLE IV. DELAY AND SUCCESS RATIO

| Hydro PP | | | Wind PP | | | Biomass | | |
|------------|-----|-----|---------|-----|------|---|-----|------|
| %SR | %DR | %F | %SR | %DR | %F | %SR | %DR | %F |
| 75% | 33% | 25% | 0% | 0% | 100% | 0% | 0% | 100% |
| Geothermal | | | PV PP | | | %SR : Success Ratio %DR : Delay Ratio %F : Project Failure Percentage | | |
| %SR | %DR | %F | %SR | %DR | %F | | | |
| 19% | 33% | 81% | 0% | 0% | 100% | | | |

delay scenario is divided into 3 scenarios, namely 1 year delay, 3 years, and 5 years. The delay is applied to renewable energy plants that have a failure ratio, such as PV PP, Wind PP, and Geothermal PP. Existing generating capacity data can be seen in Table II and the planning power plant in Table III. Success ratio and delay ratio data can be seen in Table IV.

IV. RESULTS AND DISCUSSION

The addition of power plant capacity, both VRE PP and conventional PP, has an impact on energy supply in the Java Bali System. This section will present and discuss the impact of VRE PP delays on the composition of power plant capacity, energy mix, and LCOE.

A. Impact of Power Plant Project Delay on Capacity Composition

Based on research that has been done, taking into account the delays in PV PP 550 MW generators in 2024 and 1240

TABLE V. POWER PLANT TOTAL CAPACITY

| | Base Case | Scenario 1-year Delayed | Scenario 3-year Delayed | Scenario 5-year Delayed |
|------|-----------|-------------------------|-------------------------|-------------------------|
| 2021 | 45,186.00 | 45,186.00 | 45,186.00 | 45,186.00 |
| 2022 | 47,577.00 | 47,577.00 | 47,577.00 | 47,577.00 |
| 2023 | 48,286.00 | 48,286.00 | 48,286.00 | 48,286.00 |
| 2024 | 49,197.90 | 48,487.90 | 48,487.90 | 48,487.90 |
| 2025 | 53,926.90 | 52,966.90 | 52,256.90 | 52,256.90 |
| 2026 | 56,164.00 | 57,569.00 | 55,899.00 | 55,899.00 |
| 2027 | 56,218.90 | 56,483.90 | 56,928.90 | 56,218.90 |
| 2028 | 57,491.90 | 57,491.90 | 59,161.90 | 57,491.90 |
| 2029 | 58,466.90 | 59,066.90 | 59,331.90 | 59,776.90 |
| 2030 | 60,411.80 | 61,311.80 | 61,611.80 | 63,281.80 |

MW in 2025, Geothermal PP 330 MW in 2025 and 265 in 2026, as well as wind PP 160 MW in 2024 and 100 MW in 2025, resulting in changes to the power plants composition in the Java Bali System.

In the base case scenario, the total generating capacity in the Java Bali system in 2030 is 60.41 GW. By considering the delay aspect of the power plant construction project, the result is that the system will build additional power plants to be able to substitute for the power plants shortfall. In this research, the power plants that can replace the shortage of power plant capacity is assumed to be a gas generator or gas machine. The choice of this type of generator considers relatively fast supply, both conventional and Mobile Power Plant (MPP). The results of plant planning for the base case

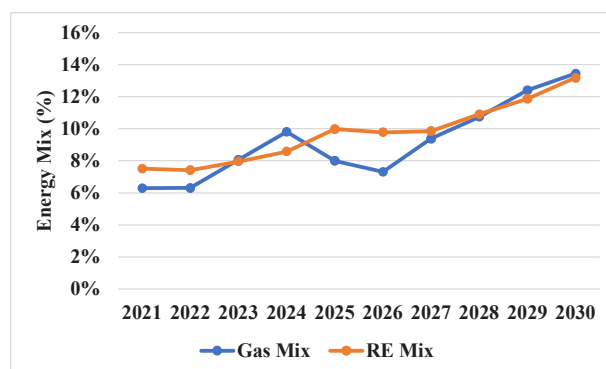


Fig. 3. Java Bali System Gas Mix Vs RE Mix

TABLE VI. JAVA BALI SYSTEM LCOE

| | Base Case | Scenario 1-year Delayed | Scenario 3-year Delayed | Scenario 5-year Delayed |
|----------------|-----------|-------------------------|-------------------------|-------------------------|
| LCOE (c\$/kWh) | 7.7 | 7.9 | 8 | 8,1 |

scenario and delay scenario will produce a plant composition as in Table V.

To anticipate the delay in the construction of RE power plants, as indicated by the research findings, there is a need for the substitution of power plants capacity. The results show the establishment of up to 1000 MW gas machines in the scenario of a 1-year delay and up to 1800 MW gas machine in the scenarios of 3 and 5-year delays. These 1000 MW and 1800 MW gas machines are intended to accommodate the delay in RE power plants amounting to 2645 MW, including PV PP, Geothermal PP, and Wind PP. The delay in these power plants results in an increase in the installed capacity in the Java Bali system from 60.41 GW to up to 63.28 GW.

B. Energy Mix and LCOE

Based on the installed capacity, changes in the energy mix in the Java Bali system are obtained. This change primarily occurs in the RE mix, which experienced construction delays, resulting in an increase in the gas energy mix. The results indicate a decrease in the RE energy mix when PV PP delayed year in 2024, as shown in Fig. 3. This can occur due to the delayed PV PP up to 1810 MW.

With changes in power plants capacity and energy mix, the Java Bali electrical system experiences a shift in the LCOE of generation. As shown in Table VI, the LCOE will increase from the base case of 7.7 c\$/kWh to 8.1 c\$/kWh in the delay scenario. This LCOE does not consider the unavailability of LNG, which would lead the Gas Machine to use more expensive HSD (High-Speed Diesel), potentially causing a further increase in the LCOE.

V. CONCLUSION

Based on the research findings, it can be determined that delays in power plants project, such as RE PP, can influence the capacity planning and the LCOE of the system. This study focuses on the delays in RE such as PV PP, Geothermal PP, and Wind PP. The extent of the delay in capacity refers to the success ratio, delays, and achievements of the power plant projects. Delayed VRE PP up to 2 GW, and based on the results, it was found that these generators would be substituted with Gas Machines up to 2000 MW. This affects the LCOE of the system, increasing it from 7.7 c\$/kWh to up to 8.1 c\$/kWh. This LCOE calculation does not yet account for the unavailability of LNG, which would lead the Gas Machine to utilize more expensive HSD (High-Speed Diesel), potentially causing a further increase in the LCOE.

Moreover, the impact of these delays appears to be relatively small, due to the limited utilization of VRE. This situation might differ if delays occurred in base load power plants such as Coal PP, Hydro PP, and Biomass PP. Therefore, further studies are needed to assess the impact of base load generators on the energy mix, LCOE, and emissions.

REFERENCES

- [1] Kementerian Hukum dan Hak Asasi Manusia, *UU No.16 Tahun 2016 Tentang Pengesahan Paris Agreement to The United Nations Framework Convention on Climate Change*. Indonesia, 2016.
- [2] Sekretariat Jenderal Dewan Energi Nasional (DEN), *Bauran Energi Nasional*. 2020.
- [3] PLN, "Rencana Usaha Penyediaan Tenaga Listrik (RUPTL) PT PLN (Persero) 2021-2030.," *Rencana Usaha Penyediaan Tenaga List. 2021-2030*, pp. 2019–2028, 2021.
- [4] H. T. Nguyen and F. A. Felder, "Generation expansion planning with renewable energy credit markets: A bilevel programming approach," *Appl. Energy*, vol. 276, no. June, p. 115472, 2020, doi: 10.1016/j.apenergy.2020.115472.
- [5] D. Z. Fitiwi, M. Lynch, and V. Bertsch, "Enhanced network effects and stochastic modelling in generation expansion planning: Insights from an insular power system," *Socioecon. Plann. Sci.*, vol. 71, no. April, p. 100859, 2020, doi: 10.1016/j.seps.2020.100859.
- [6] G. S. Seck, V. Krakowski, E. Assoumou, N. Maïzi, and V. Mazauric, "Embedding power system's reliability within a long-term Energy System Optimization Model: Linking high renewable energy integration and future grid stability for France by 2050," *Appl. Energy*, vol. 257, no. July 2019, p. 114037, 2020, doi: 10.1016/j.apenergy.2019.114037.
- [7] A. Z. Khan, S. Yingyun, and A. Ashfaq, "Generation expansion planning considering externalities for large scale integration of renewable energy," *2014 IEEE Int. Conf. Intell. Energy Power Syst. IEPS 2014 - Conf. Proc.*, pp. 135–140, 2014, doi: 10.1109/IEPS.2014.6874165.
- [8] Q. Chen, C. Kang, Q. Xia, and J. Zhong, "Power generation expansion planning model towards low-carbon economy and its application in china," *IEEE Trans. Power Syst.*, vol. 25, no. 2, pp. 1117–1125, 2010, doi: 10.1109/TPWRS.2009.2036925.
- [9] W. Shengyu, C. Lu, Y. Xiaoqing, and Y. Bo, "Long-term generation expansion planning under uncertainties and fluctuations of multi-type renewables," *Int. Conf. Power Eng. Energy Electr. Drives*, vol. 2015-Sept, pp. 612–616, 2015, doi: 10.1109/PowerEng.2015.7266387.
- [10] T. Luz, P. Moura, and A. de Almeida, "Multi-objective power generation expansion planning with high penetration of renewables," *Renew. Sustain. Energy Rev.*, vol. 81, no. November 2016, pp. 2637–2643, 2018, doi: 10.1016/j.rser.2017.06.069.
- [11] S. Pereira, P. Ferreira, and A. I. F. Vaz, "Generation expansion planning with high share of renewables of variable output," *Appl. Energy*, vol. 190, pp. 1275–1288, 2017, doi: 10.1016/j.apenergy.2017.01.025.
- [12] Y. Y. Rady, M. V. Rocco, M. A. Serag-Eldin, and E. Colombo, "Modelling for power generation sector in Developing Countries: Case of Egypt," *Energy*, vol. 165, pp. 198–209, 2018, doi: 10.1016/j.energy.2018.09.089.
- [13] E. M. F. Shinwari, "Optimization Model using WASP-IV for Pakistan's Power Plants Generation Expansion Plan," *IOSR J. Electr. Electron. Eng.*, vol. 3, no. 2, pp. 39–49, 2012, doi: 10.9790/1676-0323949.
- [14] A. Malik and C. Kuba, "Power Generation Expansion Planning Including Large Scale Wind Integration: A Case Study of Oman," *Wind Resour. Futur. Energy Secur.*, vol. 2013, pp. 51–68, 2015, doi: 10.1201/b18529-5.
- [15] J. G. Wright, T. Bischof-Niemz, J. R. Calitz, C. Mushwana, and R. van Heerden, "Long-term electricity sector expansion planning: A unique opportunity for a least cost energy transition in South Africa," *Renew. Energy Focus*, vol. 30, no. September, pp. 21–45, 2019, doi: 10.1016/j.ref.2019.02.005.
- [16] I. Khan, "Power generation expansion plan and sustainability in a developing country: A multi-criteria decision analysis," *J. Clean. Prod.*, vol. 220, pp. 707–720, 2019, doi: 10.1016/j.jclepro.2019.02.161.
- [17] R. Shirley and D. Kammen, "Energy planning and development in Malaysian Borneo: Assessing the benefits of distributed technologies versus large scale energy mega-projects," *Energy Strateg. Rev.*, vol. 8, pp. 15–29, 2015, doi: 10.1016/j.esr.2015.07.001.
- [18] K. I. Muttaqien, "Perencanaan Pengembangan Pembangkit Sistem Jawa-Bali Menggunakan Model Optimasi OSeMOSYS," Universitas Gadjah Mada, Yogyakarta, 2017.
- [19] T. I. Putrisia, "Perencanaan Sistem Pembangkitan untuk Wilayah Sulawesi dengan Menggunakan OSeMOSYS," Universitas Gadjah Mada, 2017.
- [20] R. F. S. Budi, "Optimasi Pengembangan Pembangkit Sistem Kelistrikan Jawa-Madura-Bali Menggunakan Game Theory: Multi-Period Framework, Bi-Level, dan Multi-Objective Optimization Method," Universitas Gadjah Mada, Yogyakarta, 2017.

- [21] Tumiran, Sarjiya, L. M. Putranto, A. Priyanto, and I. Savitri, "Generation expansion planning for high-potential hydropower resources : The case of the Sulawesi electricity system," *Int. J. Sustain. Energy Plan. Manag.*, vol. 28, no. 2, pp. 37–52, 2020.
- [22] A. A. Muthahhari *et al.*, "Long-Term Generation Expansion Planning in Sulawesi Electricity System Considering High Share of Intermittent Renewable Energy Resource," *2019 11th Int. Conf. Inf. Technol. Electr. Eng.*, 2019.
- [23] A. A. Muthahhari *et al.*, "Environmental Considerations in Long-Term Generation Expansion Planning with Emission Limitations: An Analysis of the Sulawesi Power System in Indonesia," *Proceeding - 1st FORTEI-International Conf. Electr. Eng. FORTEI-ICEE 2020*, pp. 29–34, 2020, doi: 10.1109/FORTEI-ICEE50915.2020.9249863.
- [24] Tumiran *et al.*, "Potential of Biomass as RE Source for Sustainable Electricity Supply in Eastern Indonesia," *2021 3rd Int. Conf. High Volt. Eng. Power Syst. ICHVEPS 2021*, pp. 022–027, 2021, doi: 10.1109/ICHVEPS53178.2021.9601067.
- [25] Tumiran, L. M. Putranto, Sarjiya, F. D. Wijaya, A. Priyanto, and I. Savitri, "Generation Expansion Planning Based on Local Renewable Energy Resources: A Case Study of the Isolated Ambon-Seram Power System," *Sustain.*, vol. 14, no. 5, 2022, doi: 10.3390/su14053032.
- [26] Sarjiya, R. F. S. Budi, and L. P. Multanto, "Achieving new and renewable energy target: A case study of java-bali power system, Indonesia," *2020 2nd Int. Conf. Smart Power Internet Energy Syst. SPIES 2020*, pp. 560–565, 2020, doi: 10.1109/SPIES48661.2020.9242984.
- [27] M. R. Kresnawan, I. A. Safitri, and I. Darmawan, "Long term projection of electricity generation sector in east kalimantan province: LEAP model application," *Proc. - 12th SEATUC Symp. SEATUC 2018*, no. 1, pp. 1–5, 2018, doi: 10.1109/SEATUC.2018.8788875.
- [28] Ministry of Energy and Mineral Resources; Danish Energy Agency, "Technology Data for the Indonesian Power Sector," no. February, pp. 1–215, 2021, [Online]. Available: https://ens.dk/sites/ens.dk/files/Globalcooperation/technology_data_for_the_indonesian_power_sector_-_final.pdf.
- [29] Pusat Kajian LKFT Universitas Gadjah Mada (LKFT Study Center Universitas Gadjah Mada), "Kajian Pengembangan Interkoneksi Sistem Kelistrikan Nusa Tenggara dan Potensi Energi Terbarukan," Yogyakarta, 2023.

A Social Analysis of Thailand's 2023 Election Through Twitter Feeds

Wanaporn Sarapugdi
Program in Management of Digital Innovation,
Faculty of Information Technology,
Rajabhat Mahasarakham University,
Maha Sarakham, Thailand
wannaporn.sa@rmu.ac.th

Songphon Namkhun*
Program in Computer Engineering,
Faculty of Engineering,
Rajabhat Mahasarakham University,
Maha Sarakham, Thailand
songphon@rmu.ac.th

Abstract— Nowadays, it cannot be denied that social media has been in many parts of people's lives, especially in entertainment, business and education. Public figures including politicians frequently use social platforms to connect with their audience, for example Facebook, Instagram, Tiktok and etc. One of the most commonly used is a platform called Twitter or also known as X. It is a platform that people can share their opinions in short messages. Since there is an alphabet limitation, people can deliver and receive message rapidly. It is a perfect platform that we could use to update the real-time situations for example election, emergency alert, natural disasters and etc. According to its characteristic, it can be used as a data source for social media analytics, which involves collecting and analyzing data to perform business decisions. The social media analytics has become commonplace because the number of people using social media tends to increase every second. Specifically, Twitter sentiment analysis offers a quick and inexpensive tool for monitoring and predictions. In this work, Twitter is used as a data source to monitor and predict Thailand Election in 2023 because this election highly attracts attention from Thais and international. Moreover, Twitter is a significant platform that is used to debate about political events in Thailand. The result of this election potentially indicates Thailand's future, including economics, public health, environment, international relations and etc. Our work performs sentiment analysis to categorize the data and mainly focuses on extracting sentiment from text without considering semantic word relations and co-occurrences because it is appropriate and functional for Thai sentence analysis. Based on the result, it can be seen that Twitter plays a significant role in politics, with politicians wielding considerable influence over public perception. Comparing of the actual election result and the predicted result, this analysis demonstrates the potential for prediction precisely. The candidates with high positive sentiments have higher possibility to win the election while those with low sentiments has lower possibility.

Keywords— *Analytics, Election, Twitter, Social Media, Sentiment Analysis*

I. INTRODUCTION

Twitter, founded in 2006, is a microblogging platform with hundreds of millions of users. Its prominence has attracted many politicians, making it a primary platform for political discourse. Recent political events, like the American election, highlight its influence [1]. Politicians leverage their vast Twitter followings to shape public perception while users express their political views and opinions [2].

In the realm of social computing, social network analysis is gaining researchers attraction. A key task is

community detection. A community can be defined as a group of users that interact with each other more frequently than with those outside the group and are more similar to each other than to those outside the group [3]. According to [4], Twitter presents three types of connectivity information between users: follow, retweet, and user mention. As users engage, they form networks based on these interactions.

We gathered and visualized social media network data. An edge signifies a connection between two users who tweeted within our sample timeframe. A 'follows' edge is formed if one user follows another in our dataset. In this network, each Twitter user is a 'vertex,' a node or entity with attributes and metrics indicating their position in the broader network.

In this work, social sentiment analysis is implemented in order to detect community opinions on the candidates of Thailand's next prime minister in 2023 and predict the results of this election. This technique is used to analyze the sentiment of the authors in to focused topics. It has practical value in allowing organization to understand public sentiment through the dataset obtained from social media. The prediction results would assist the organization in several aspects including strategic planning, marketing, organization development and etc.

According to the previous publications, the result of sentimental analysis relies on several factors, for example, data sources, methods, models, and etc. Many publication results with suitable parameters indicate that the sentiments of social media can be used to determine the actual situation [5,6,7]. As for the Thai language, it is complicated to categorized the data compared to English because there is no separation between words, each word has its own meaning and the meaning can be changed by combining it with other words. Therefore, for convenience, semantic word relations and cooccurrences are not considered in this work [8]. The data set used in this publication focuses on the opinions on Twitter which is one of the platforms that is mostly used in Thailand to express the user's opinions on political events. The Fast-greedy algorithm and fast unfolding algorithm are compared to obtain the optimization of network partitions before implementing the sentimental analysis [9].

II. DATASET

Using the Tweepy package [10] in Python programming language, we accessed the Twitter API to gather data based on eight candidate keywords from 4th April to 13th May 2023. From this, we collected 48,781 tweets from 16,496 unique users. Initially in JSON format, this data was

converted to CSV, retaining only essential fields like user-id, tweet-id, text, created-at.

Then, we introduced new feature “key” to identify which candidate a user mentioned. Additionally, using the Twitter Follower API, we compiled a list of followers for each user id. From this list, we only retained followers who also tweeted about our initial keywords. With this, our dataset was complete and ready for processing.

III. GRAPH DEVELOPMENT

In our first scenario, we used all available data to construct a comprehensive graph of Twitter engagement related to the governor election. This approach provided a broad view, capturing interactions from regular users to influential figures and media outlets. However, the sheer volume of data, with 48,781 tweets from 16,496 unique users, led to millions of edges. This posed computational challenges, and after two days of processing, we had to halt due to hardware limitations. Notably, official media accounts and a popular Thailand actor-candidate with vast followers contributed to the high edge count.

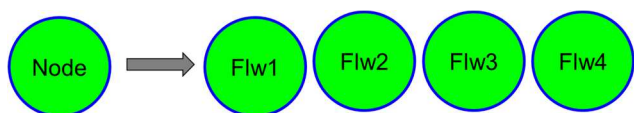


Fig. 1. Node-Followers

Suppose we have a node that has a lot of followers, we use these followers to generate edges for the graph. Form the Fig. 1, we will generate edges just like Fig. 2.

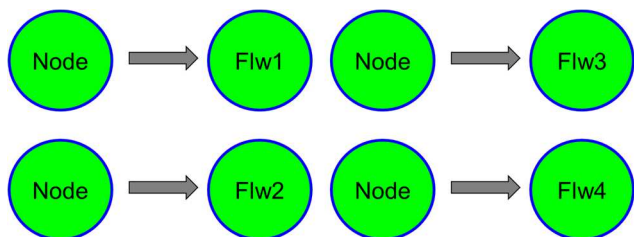


Fig. 2. Edges

Some nodes that we have consisted of nodes from official media accounts which have a huge number of followers (> 5000). It will build thousands of edges that came from that users. Another fact that one of the candidates is a famous Thailand actor who has a lot of followers. Our second scenario was an optimized approach, focusing on reducing computational strain. Instead of considering all followers, we only included those who tweeted about the candidates. This significantly reduced the edge count, allowing for smoother and faster processing. The detail is depicted Fig. 3.

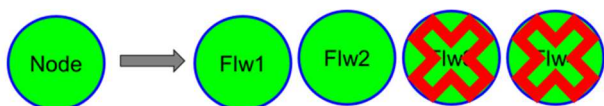


Fig. 3. Node Reduction

The resulting graph will undergo further analysis, including community detection, to identify user clusters. While not directly related, we will also conduct sentiment

analysis to gauge public sentiment towards the candidates and correlate findings with the election results on 23rd May 2023. A preliminary version of our graph, prior to these analyses, is provided below.

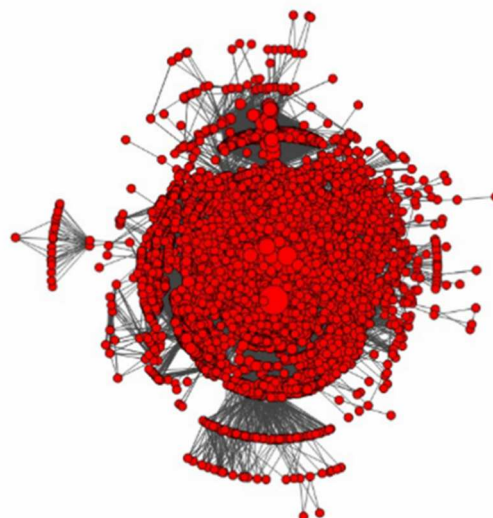


Fig. 4. Community Development

According to Fig. 4, the research utilised Louvain Algorithms for the development of communities where each node is moved from one community to another to depict the construction of an aggregate network. This serves to identify how the community of users have connected with the result of votes along with the internal connections of the community. It demonstrated that as each node belonged to the same community, each would have both internal and external connections. Nevertheless, if the node lacks connections, the disconnected community will remain disconnected unless merged with other bridge communities.

The Fast-greedy algorithm [11] uses modularity to pinpoint optimal network partitions. Starting with each node as an individual community, similar to the Walktrap algorithm [12], it employs hierarchical clustering. The algorithm then merges neighboring communities to maximize the modularity function, continuing until no further increase in modularity is possible.

In 2008, the Louvain community detection algorithm was proposed as a fast community unfolding method for large networks [13]. This approach is based on modularity, which attempts to maximize the difference between the actual and expected number of edges in a community.

We employed two algorithms for community detection in our graph: the fast greedy algorithm and the fast-unfolding algorithm. Initially, we opted for the fast greedy algorithm due to its quicker computation. However, we later used the fast-unfolding method, which, despite both being modularity-based, proved more accurate. This is because the fast greedy approach optimizes modularity in a limited manner. We considered the edge betweenness algorithm but abandoned it due to its extensive computational demands. The detected communities are illustrated in Fig. 5 and 6. Node colors indicate the candidate discussed: blue for candidate one, red for two, white for three, and yellow for four. Black nodes signify users discussing the election without naming a candidate.

IV. SENTIMENT ANALYSIS

Sentiment analysis algorithms, utilizing natural language processing (NLP), categorize documents as positive or negative. This tool is valuable for politicians to gauge public sentiment about their views and assess supporter satisfaction. In our project, we applied sentiment analysis to classify tweets accordingly [14,15].

- Our sentiment analysis process began with tokenization, which breaks down a text into individual tokens. For this, we employed the NLTK package. While our tokenization may not be flawless, it captures the tweet's essence.
- Every language contains frequently used words, like articles and conjunctions, which, while essential, do not convey specific meanings out of context. Termed 'stop-words,' they can be redundant in the data processing. To streamline our analysis, we maintained a list of such words and excluded them from our dataset.
- Stemming involves reducing words to their base or root form. While the resulting stem might not always be a valid word root, it is essential that related words map to the same stem. For our project, we employed the Sastrawi package to stem words in Thai.
- TF-IDF (Term Frequency-Inverse Document Frequency) is a metric that gauges a word's significance in a tweet relative to a collection of tweets. It assigns a weight to a term based on its frequency in a tweet, adjusted for its general occurrence. We utilized the TfidfVectorizer from the Sklearn package for this calculation.
- To represent sentences sequentially, we transformed each word into an integer using the keras models package. These integers correspond to the word's position in the tokenized word index. We then constructed a matrix of these word vectors, referencing the word index so our model can match the integer sequence with the appropriate vector.
- Stochastic Gradient Descent (SGD) from keras optimizers is an iterative optimization technique for differentiable objective functions. The model was trained using SGD, a gradient descent optimization method that minimizes a given loss function. We used SGD from keras optimizers package to do this process. The term "stochastic" refers to the fact that the model weights are updated for each training example, which is an approximation of batch gradient descent, in which all training examples are considered to make a single step.
- Get sentiment results (Positive / Negative).

Fig. 5 demonstrates that when the blending parameter is small, the FastGreedy Algorithm is able to detect communities more effectively. On the algorithm, the decrease gradually occurred with small values whereas increased, indicating that the accuracy decreases when network size and values increase.

Regarding the large network depicted in Fig. 6, the algorithms displayed how to optimise modularity by allowing modifications to communities and combining

discovered communities to form a new network. This contributes to the formation of supercommunities, which can allow rendering to networks with more than one million nodes as well as balancing the scale of communities being collected.

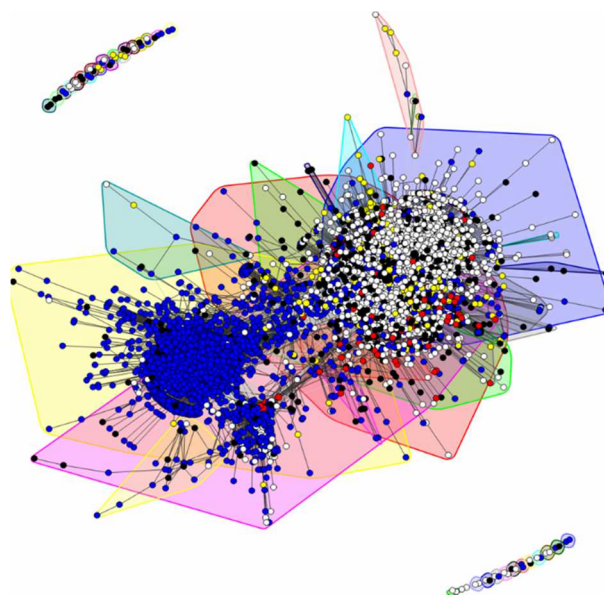


Fig. 5. Communities detected by Fast Greedy Algorithm.

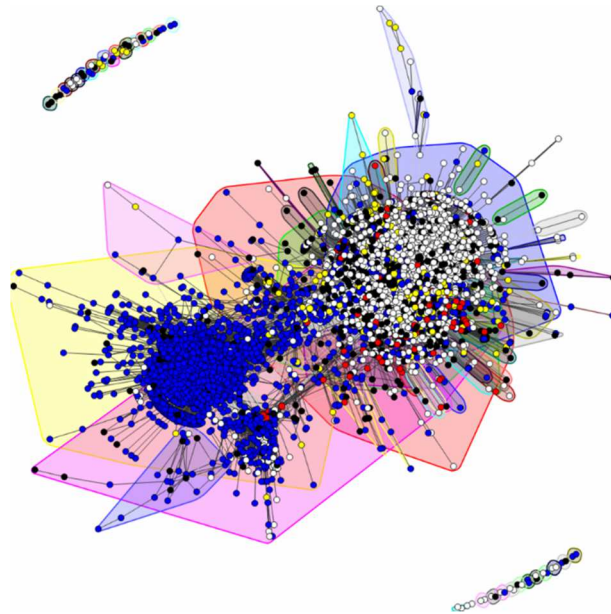


Fig. 6. Communities detected by Fast Unfolding Algorithm.

V. RESULT

The result of the analysis table depicted the interpretation of a political election event based on social media analytics, with an emphasis on Twitter sentiment analysis as a cost-effective tool for election forecasting and monitoring. The significance of this result is to determine whether the result of the election matches the result of the feedback by Twitter users in order to contribute to the actual result from the poll that was collected prior to the official election date. This dataset was collected and visualised based on the five leading candidates including Pear

Thongtha, Srettha, Pita, Prayuth and "undetermined" candidates as a result of being unable to identify a suitable candidate for the position. The selection was based on references from an NIDA Poll survey on the 2023 Election [16] with the method of data collection, online observations and official selection of the election feedback.

The data were extracted from the social media platform Twitter, which is considered a valuable source that helps in assessing the political and social sentiments of individuals who are active participants. The platform of Twitter is considered to be rather noisy due to the high traffic of users. However, the results collected were retrieved from a real-time poll conducted on the platform with a time limit before closing the result with hashtags on the poll followed #ThailandElection, #เลือกตั้ง66 (#Election66), #ประยุทธ์ (#Prayuth), #แพทองธาร (#PearThongtha), #เศรษฐา (#Srettha) and #พิธา (#Pita) so that it could be able to reach more people on the platform. Moreover, the poll is shared via other social media platforms such as Facebook, Instagram, and Twitter in order to engage potential participants to vote.

According to the results, the candidate Pita received the most comments from the participants. It depicted that the candidate received the highest level of positive feedback at over 75% whereas only 25% negative feedback results. Due to this, it showed that the participants tended to favour Pita the most and deemed the political party and candidate to be the most qualified for their respective elected positions. It was followed by Pear Thongtha and an undetermined candidate that depicted 62% positive feedback. However, Srettha was considered balanced on both responses as participants were almost as high as the result of Pita.

Subsequently, when concentrating on the positive and negative ratio, both types of feedback were seen to be nearly identical as respondents provided positive feedback and 49% provided negative feedback. In addition, Prayuth experienced the lowest ratings from participants as only received 246 responses whereas other candidates received 511 and above. Based on the result of negative and positive attributes, Prayuth had the lowest positive score of 39% compared to 61% for negative ratings. This suggested that the majority of respondents had difficulty approving the rating of the political party and candidate for elected positions. On the basis of the conclusive outcome, it was determined that the Twitter response result coincided with the NIDA poll and actual election results.

TABLE I. THE RESULTS OF SENTIMENT ANALYSIS

| N0 | Candidate | Positive | Negative | Total | %POS | %Neg |
|----|---------------|----------|----------|-------|------|------|
| 1 | Prayuth | 101 | 145 | 246 | 39% | 61% |
| 2 | Pear Thongtha | 310 | 201 | 511 | 62% | 38% |
| 3 | Srettha | 475 | 459 | 934 | 51% | 49% |
| 4 | Pita | 701 | 241 | 942 | 75% | 25% |
| 5 | Undeteminded | 53 | 112 | 165 | 32% | 68% |

VI. CONCLUSIONS

In conclusion, this investigation of social media from the political event could be the key to understanding people's perceptions after the election. This study placed significant emphasis on Twitter sentiment analysis, which is regarded as one of the most effective techniques and saves time for election and monitoring due to the large number of

active users and individuals interested in certain topics. In addition, the platform is where political figures have begun to exert influence over public opinion through the use of this application.

The research demonstrated the user-referenced data collection that was transformed into a CSV format for easier comprehension, as well as the application of AI to assist in calculating precise results [17]. This instrument is regarded as a useful resource for politicians to start paying more attention, as it reveals how the general public thinks about candidates and political parties.

To facilitate comprehension, the results suggested and depicted multiple outcomes that could be contrasted with the actual election outcomes. When providing the ratio of negative to positive inputs from each candidate, the majority of the results were comparable. Nevertheless, there are still some limitations to the results, including the possibility of differences between the actual and Twitter results [18]. If Twitter is the only social media platform used, the opinion may also be biased; therefore, it is essential to collect data from other social media platforms to obtain a more accurate sentiment analysis [19].

In addition, the result included the identities of all candidates based on the official poll. However, there was an unidentified candidate that could not be used as a direct result based on the responses, which could lead to confusion and misinterpretation of the attribute. In order to obtain a more accurate and comprehensive result, it is reasonably to examine the context of the participants' analysis and to capture real-time data through an online poll or survey [20]. Due to this, it could be used as a guideline for future research with improvements that should be required such as more selections on platforms that present more accurate results with other business analytics tools such as Microsoft Excel and RapidMiner in order to provide clearer results that could be used to improve the analysis of the paper.

REFERENCES

- [1] S. C. McGregor, R. R. Mourão, and L. Molyneux, "Twitter as a tool for and object of political and electoral activity: Considering electoral context and variance among actors," *J. Inf. Technol. Polit.*, vol. 14, no. 2, pp. 154–167, Apr. 2017, doi: 10.1080/19331681.2017.1308289.
- [2] N. Pivecka, R. A. Ratzinger, and A. Florack, "Emotions and virality: Social transmission of political messages on Twitter," *Front Psychol*, vol. 13, p. 931921, Nov. 2022, doi: 10.3389/fpsyg.2022.931921.
- [3] Z. Li, Z. Pan, Y. Zhang, G. Li, and G. Hu, "Efficient Community Detection in Heterogeneous Social Networks," *Mathematical Problems in Engineering*, vol. 2016, p. e5750645, Dec. 2016, doi: 10.1155/2016/5750645.
- [4] I. Himelboim, M. A. Smith, L. Rainie, B. Shneiderman, and C. Espina, "Classifying Twitter Topic-Networks Using Social Network Analysis," *Social Media + Society*, vol. 3, no. 1, p. 2056305117691545, Jan. 2017, doi: 10.1177/2056305117691545.
- [5] W. Medhat, A. Hassan, and H. Korashy, "Sentiment analysis algorithms and applications: A survey," *Ain Shams Engineering Journal*, vol. 5, no. 4, pp. 1093–1113, Dec. 2014, doi: 10.1016/j.asej.2014.04.011.
- [6] [1] M. Bordoloi and S. K. Biswas, "Sentiment analysis: A survey on design framework, applications and future scopes," *Artif Intell Rev*, vol. 56, no. 11, pp. 12505–12560, Nov. 2023, doi: 10.1007/s10462-023-10442-2.
- [7] M. Rodríguez-Ibáñez, A. Casáñez-Ventura, F. Castejón-Mateos, and P.-M. Cuenca-Jiménez, "A review on sentiment analysis from social

- media platforms,” *Expert Systems with Applications*, vol. 223, p. 119862, Aug. 2023, doi: 10.1016/j.eswa.2023.119862.
- [8] S. Harispe, S. Ranwez, S. Janaqi, and J. Montmain, *Semantic Similarity from Natural Language and Ontology Analysis*. 2015. doi: 10.2200/S00639ED1V01Y201504HLT027.
- [9] Y. Jiang, C. Jia, and J. Yu, “An efficient community detection algorithm using greedy surprise maximization,” *J. Phys. A: Math. Theor.*, vol. 47, no. 16, p. 165101, Apr. 2014, doi: 10.1088/1751-8113/47/16/165101.
- [10] O. Octaria, D. Manongga, A. Iriani, H. D. Purnomo, and I. Setyawan, “Mining Opinion Based on Tweets about Student Exchange with Tweepy and TextBlob,” *Proc. - 2022 9th Int. Conf. Inf. Technol. Comput. Electr. Eng. ICITACEE 2022*, pp. 102–106, 2022, doi: 10.1109/ICITACEE55701.2022.9924013.
- [11] J. Jabari Lotf, M. Abdollahi Azgomi, and M. R. Ebrahimi Dishabi, “An improved influence maximization method for social networks based on genetic algorithm,” *Phys. A Stat. Mech. its Appl.*, vol. 586, p. 126480, Jan. 2022, doi: 10.1016/J.PHYSA.2021.126480.
- [12] G. Orman, V. Labatut, and H. Cherifi, “Comparative Evaluation of Community Detection Algorithms: A Topological Approach,” *J. Stat. Mech. Theory Exp.*, vol. 2012, no. 8, Jun. 2012, doi: 10.1088/1742-5468/2012/08/P08001.
- [13] V. D. Blondel, J. L. Guillaume, R. Lambiotte, and E. Lefebvre, “Fast unfolding of communities in large networks,” *J. Stat. Mech. Theory Exp.*, vol. 2008, no. 10, p. P10008, Oct. 2008, doi: 10.1088/1742-5468/2008/10/P10008.
- [14] A. Singh, A. Kumar, N. Dua, V. K. Mishra, D. Singh, and A. Agrawal, “Predicting Elections Results using Social Media Activity A Case Study: USA Presidential Election 2020,” *2021 7th Int. Conf. Adv. Comput. Commun. Syst. ICACCS 2021*, pp. 314–319, Mar. 2021, doi: 10.1109/ICACCS51430.2021.9441835.
- [15] R. Singh and P. Sharma, “An Overview of Social Media and Sentiment Analysis,” *2021 5th Int. Conf. Inf. Syst. Comput. Networks, ISCON 2021, 2021*, doi: 10.1109/ISCON52037.2021.9702359.
- [16] NIDA, “NIDA Poll Survey”, NIDA Poll, https://nidapoll.nida.ac.th/survey_detail?survey_id=620 (accessed Aug. 11, 2023).
- [17] A. Kumar and A. Jaiswal, “Systematic literature review of sentiment analysis on Twitter using soft computing techniques,” *Concurrency and Computation: Practice and Experience*, vol. 32, no. 1, 2019, doi:10.1002/cpe.5107.
- [18] Y. Wang, J. Guo, C. Yuan, and B. Li, “Sentiment Analysis of Twitter Data,” *Appl. Sci.* 2022, Vol. 12, Page 11775, vol. 12, no. 22, p. 11775, Nov. 2022, doi: 10.3390/APP122211775.
- [19] L. G. S. Selvan and T. S. Moh, “A framework for fast-feedback opinion mining on Twitter data streams,” *2015 Int. Conf. Collab. Technol. Syst. CTS 2015*, pp. 314–318, Aug. 2015, doi: 10.1109/CTS.2015.7210440.
- [20] D. Antonakaki, P. Fragopoulou, and S. Ioannidis, “A survey of Twitter research: Data model, graph structure, sentiment analysis and attacks,” *Expert Syst. Appl.*, vol. 164, p. 114006, Feb. 2021, doi: 10.1016/J.ESWA.2020.114006.

Integrated Rearrange Processing of Hybrid Model with Weighted Values for PM2.5 Forecasting

1st Tatshakon Polsena
Big Data Engineer Program
Dhurakij Pundit University
Bangkok, Thailand
tatshakon.pol@gmail.com

2nd Duangjai Jitkongchuen
Big Data Institute
(Public Organization)
Bangkok, Thailand
duangjai.ji@depa.or.th

3rd Panita Thusaranon
International College
Dhurakij Pundit University
Bangkok, Thailand
panita.thu@dpu.ac.th

Abstract—This paper suggests using the integrated two hybrid models, ARIMA-LSTM and LSTM-ARIMA forecasting model, with weighing values for PM2.5 forecasting. The dataset, PM2.5 data of Bangkok, included wind direction (WD), wind speed (WS), temperature (Temp), and particulate matter 2.5 (PM2.5) for hourly data updated. The experiment results found that two hybrid models forecasting by ARIMA-LSTM & LSTM-ARIMA with then adjusting the weights ratio can predict the lower error when comparing forecasting with the other algorithms. Specifically, forecasting by a set of hybrid models with an LSTM Univariate Variable.

Keywords—PM2.5, Hybrid Model, Autoregressive Integrated Moving Average, ARIMA, Long Short-Term Memory Networks, LSTM

I. INTRODUCTION

PM2.5 refers to particles with a diameter of 2.5 micrometers or less. One risk is brought on by other dangerous environmental pollutants, such as carcinogens, heavy metals, etc., entering the body through the adhesive qualities of its outer layer [1]. Therefore, one method to avoid potential health issues caused by PM2.5 is to be able to predict the presence of PM2.5 dust.

The hybrid model employing the autoregressive integrated moving average (ARIMA) model to forecast linear data, is the most popular one for predicting PM2.5 dust [2]. Artificial neural networks (ANN) were then used to forecast the residual, which is nonlinear data. Currently, the hybrid model a long short-term memory (LSTM) model called the ARIMA-LSTM hybrid model was created from the ANN model. The original idea behind a hybrid model was to anticipate both linear and nonlinear data. Still, given how well the LSTM model performs for both univariate and multivariate forecasting, it is difficult to reorganize the forecasting model.

The organization of this paper is as follows: We present the scope of this literature review and the methodology used in Section 2. Section 3 contains details of the integrated two hybrid models, ARIMA-LSTM and LSTM-ARIMA forecasting model, with weighing values for PM2.5 forecasting and afterward, we will explain the numerical results in Section 4. Finally, conclusions and future directions are presented in Section 5.

II. LITERATURE REVIEW

A hybrid approach was suggested by G. Peter Zhang to combine an autoregressive integrated moving average (ARIMA) model with artificial neural networks (ANNs) for forecasting in order to benefit from the findings of both linear and nonlinear modeling [1]. The predicting accuracy from this experiment, compared to the ARIMA model or the ANN

model, can be improved. In a study conducted by C. Yuwei and W. Kaizhi, the time series data of a meteorological satellite telemetry parameter were studied to predict, and analyze the error of the prediction data [3]. Combining two algorithm models, the LSTM-ARIMA algorithm, produced high accuracy and strong dependability prediction outcomes.

Long short-term memory (LSTM), convolutional neural networks (CNN), and support vector machines (SVM) networks are all used in the hybrid deep sentiment analysis learning models that Cach N. Dang, Maria N. Moreno-Garc'a, and Fernando De la Prieta proposed [4]. On all types of datasets, hybrid models improved sentiment analysis accuracy in comparison to single models.

S. Chae, J. Shin, S. Kwon, S. Lee, S. Kang and D. Lee proposed a real-time prediction model that can respond to particulate matter (PM) in the air, which is an indication of poor air quality [5]. The model applies interpolation to air quality and weather data and then uses a convolutional neural network (CNN) to predict PM concentrations. The PM10 and PM2.5 evaluation results show an effective prediction performance with an R-squared and a root mean square error (RMSE). The proposed ICNN prediction model achieves a high prediction performance using spatio-temporal information and presents a new direction in the prediction field.

Vo Thi Tam Minh, Tran Trung Tin and To Thi Hien proposed the projections for PM2.5 concentrations in their cities will provide short-term predictive data on air quality by using the WRF model to forecast PM2.5 in Ho Chi Minh City [6]. Experiments with six machine learning algorithms show that the Extra Trees Regression model gives the best forecast with statistical evaluation indicators including RMSE, MAE, R-squared, and the confusion matrix accuracy. The results showed that machine learning with the WRF model can predict PM2.5 concentration, suitable for early warning of pollution and information provision for air quality management systems in large cities such as Ho Chi Minh City.

In order to improve the quality of the air and reduce pollution, J. Xiao, Q. Wang, J. Cui, and J. Yu conducted a study to anticipate the pollutants in the air [5]. They proposed the ARIMA-LSTM model, which uses the ARIMA model to predict linear problems, and the LSTM model to predict nonlinear problems, is used to forecast PM2.5 and compares the results between the two models. The LSTM model's output is an optimal time series predictor, with no significant impact on trend or seasonal prediction.

T. Amnuaylojaroen conducted two multivariate linear regression models for PM2.5 prediction. The first model (model 1) is a generic model with meteorological parameters

of aerosol optical depth (AOD), temperature, relative humidity, and wind speed [8]. The second model (model 2) includes meteorological parameters and several gaseous pollutants, such as SO₂, NO₂, CO, and O₃. From the experimental results, it was found that the performance of model 2 was good for the prediction of PM_{2.5} concentrations at Chiang Mai and Lampang. Model 2 improved the prediction of PM_{2.5} concentration compared to model 1 for both wet and dry seasons.

III. RESEARCH METHODOLOGY

A. Data Collection

PM_{2.5} data of Bangkok from Pollution Control Department [9]. There are 12 stations, using hourly data between 1 November 2022 at 12:00 a.m. and 31 January 2023 at 11:00 p.m., totaling 2208 items per station. This is the period when the amount of PM_{2.5} exceeds the standard. The variables are date, time, wind speed (WS), wind direction (WD), temperature (Temp), relative humidity, and atmospheric pressure. Details of the variables used in the research are presented in Table 1.

B. ARIMA Model

ARIMA (p,d,q), the composition of autoregression, integrated, and moving average is a regressive model used to forecast time series data where 'p' is referred to as autoregression order [10].

- Autoregression, AR(p), is a part of the ARIMA model based on the idea that it uses its own lags (past values).
- Integrated, I(d), property helps make time-series stationary data to eliminate time dependency, and trend parameter 'd' represents the degree of difference, which means the number of times the data was differenced. If a time series is stationary, then its degree of difference is zero.
- Moving average, MA(q), utilizes residual error of past time points to foresee current and future predictions. The parameter 'q' is the number of lags forecast errors that utilized to compute current values.

C. LSTM Model

Long short-term memory (LSTM) was carefully designed and added memory characteristics based on recurrent neural networks (RNN) [11]. the LSTM network adds the units called gates in LSTM, and the core of gating mechanisms. The LSTM neural network contains multiple gates:

- The input gate or Update gate determines how much of the input at the current time step is saved in the cell state.
- Forget gate determines how much of the cell state at the previous time step is retained in the current time step, and it may not be retained at all.
- The output gate determines how much of the cell state is output to the current output value of the hidden state.

D. Hybrid Model

The goal of creating a hybrid model is to leverage the strengths of each component model while mitigating their individual weaknesses. Hybrid models are commonly used in

various fields, including time series forecasting, classification, regression, and recommendation systems.

TABLE I. DATA COLLECTON FOR EACH STATION

| Variables | Stations | | | | | | | | | | | |
|----------------------|----------|---|---|---|---|---|---|---|---|----|----|----|
| | 1 | 2 | 3 | 4 | 5 | 6 | 7 | 8 | 9 | 10 | 11 | 12 |
| date | / | / | / | / | / | / | / | / | / | / | / | / |
| time | / | / | / | / | / | / | / | / | / | / | / | / |
| wind speed | / | / | / | / | / | / | / | / | / | / | / | / |
| wind direction | / | / | / | / | / | / | / | / | / | / | / | / |
| temperature | / | / | / | / | / | / | / | / | / | / | / | / |
| relative humidity | / | / | / | / | / | / | / | / | / | / | / | / |
| atmospheric pressure | / | / | / | / | / | / | / | / | / | / | / | / |

$$Y_t = L_t + N_t \quad (1)$$

Where Y_t is the prediction value (forecast), L_t is the linear component and N_t is the nonlinear component.

E. Proposed Algorihtm

The ARIMA model has the limitation of not being able to do a fully connected layer, so proposed to improve the model by integrating the rearrange processing of the hybrid model with the weight adjustment method.

Fig 2 shows hybrid 1: ARIMA-LSTM model, forecasting PM_{2.5} with the ARIMA model by using hourly data between November 1, 2022, to December 31, 2022, as the training dataset and using data between January 1, 2023, to January 31, 2023, as the testing dataset. The ARIMA model can calculate residuals immediately.

Then forecasting for the past six periods (t-6) of residual with the LSTM model by using hourly data between November 1, 2022, to December 31, 2022, as the training dataset and using data between January 1, 2023, to January 31, 2023, as the testing dataset. The final step is to calculate a final value from the combined result of PM_{2.5} forecasted and residual forecasted.

Fig 3 shows hybrid 2: LSTM-ARIMA model, forecasting PM_{2.5} with the LSTM model by using hourly data between November 1, 2022, to December 31, 2022, as the training dataset and using data between January 1, 2023, to January 31, 2023, as the testing dataset.

Then forecasting for the past six periods (t-6) of residual with the ARIMA model by using hourly data between November 1, 2022, to December 31, 2022, as the training dataset and using data between January 1, 2023, to January 31, 2023, as the testing dataset. The final step is to calculate a final value from the combined result of PM_{2.5} forecasted and residual forecasted.

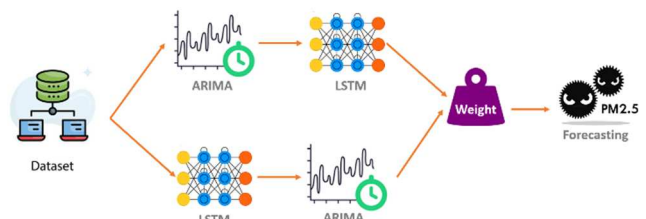


Fig. 1. Conceptual of Proposed Model

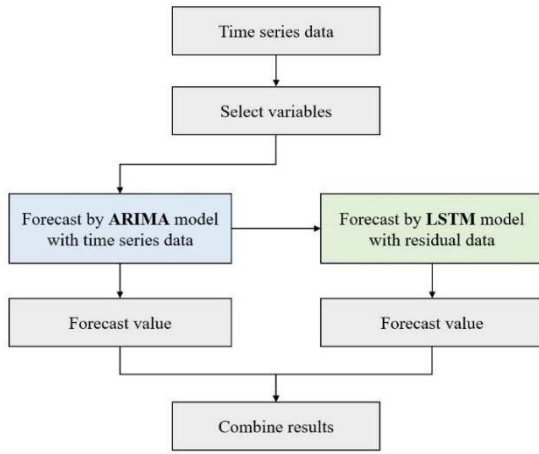


Fig. 2. Hybrid1: ARIMA-LSTM Model

The forecast results from the ARIMA-LSTM model and the LSTM-ARIMA model are taken to calculate the adaptive weights. This allows the model to give more weight to the submodel that is currently performing better, thus adapting to changing patterns in the time series.

$$Predict_i = \frac{(\sum_{k=1}^2 Weight_k \times Predict_{i,k})}{2} \quad (2)$$

$$Weight_{Hybrid1} = \left(1 - \frac{Err_{Hybrid1}}{Err_{Hybrid1} + Err_{Hybrid2}}\right) \times 2 \quad (3)$$

$$Weight_{Hybrid2} = 2 - Weight_{Hybrid1} \quad (4)$$

Where $Predict_{i,k}$ is the original predicted value at the i^{th} order was obtained from the hybrid model, k is index of hybrid model $\{1, 2\}$, respectively. And Err is MAPE from the hybrid model.

F. Model Evaluation

The performance of the proposed algorithm is measured by root mean square error (RMSE) and mean absolute percentage error (MAPE).

Root Mean Square Error (RMSE) is a commonly used metric for measuring the accuracy of a predictive model, particularly in the context of regression analysis and time series forecasting. RMSE quantifies the difference between predicted values and actual values (or ground truth) by calculating the square root of the average of the squared differences between predicted and actual values. It provides a way to assess how well a model's predictions match the observed data, with lower RMSE values indicating better model performance.

$$RMSE = \sqrt{\frac{1}{N} \sum_{i=1}^N (y_i - \hat{y}_i)^2} \quad (5)$$

Where y_i is actual observed values or ground truth for data point i^{th} , \hat{y}_i is predicted values for data point i^{th} and N is total number of data points.

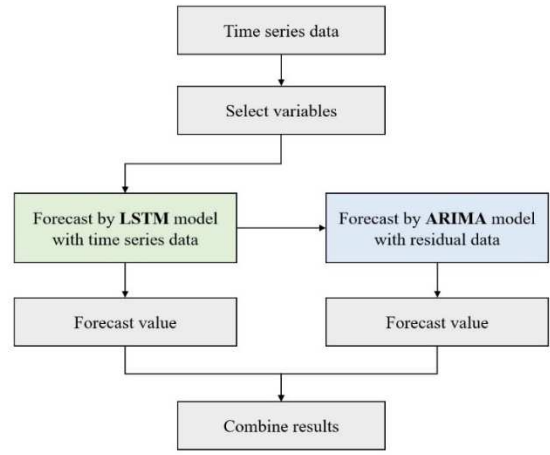


Fig. 3. Hybrid2: LSTM-ARIMA Model

The Mean Absolute Percentage Error (MAPE) is a widely used metric for evaluating the accuracy of forecasting models, particularly in business and time series forecasting applications. MAPE measures the percentage difference between the predicted and actual values, making it a useful metric for assessing the relative accuracy of forecasts, especially when dealing with different scales or units.

$$MAPE = \frac{1}{N} \sum_{i=1}^N \left| \frac{y_i - \hat{y}_i}{y_i} \right| \quad (6)$$

Where y_i is the actual observed values, also known as the ground truth, for the i^{th} data point, \hat{y}_i is the forecast values, and N is the total number of data points.

IV. EXPERIMENTAL RESULTS

The proposed algorithm's performance was compared to the ARIMA and single hybrid model algorithms and conduct experiments to compare variables in univariate, bivariate, and multivariate. When considering the root mean square error (RMSE) was found that the LSTM(Uni)-ARIMA & ARIMA-LSTM(Bi), denoted to PM2.5 and temperature, has the lowest value at 4.78596. Next is LSTM(Bi)-ARIMA & ARIMA-LSTM(Bi), denoted to PM2.5 and wind speed, at 4.80280 and ARIMA-LSTM(Bi) at 4.81039 which has a value close to LSTM(Uni)-ARIMA & ARIMA-LSTM(Bi) at 4.81054.

The same is true for comparing mean absolute percentage error (MAPE), LSTM(Bi)-ARIMA & ARIMA-LSTM(Bi), denoted to PM2.5 and wind speed, has the lowest value at 0.10775. Next to LSTM(Uni)-ARIMA & ARIMA-LSTM(Bi) at 0.10825 and ARIMA-LSTM(Bi) at 0.10849, respectively.

According to the findings of the experiments, the proposed algorithm consistently outperforms other algorithms in terms of experimental results. It can be said that the integrated rearranged processing of a hybrid model with weighted values is effective in forecasting.

V. CONCLUSIONS

In the context of machine learning and data analysis, a hybrid model is a model that mixes several distinct kinds of models or algorithms in order to generate predictions or address a specific issue. Utilizing the benefits of each component model while minimizing each one's shortcomings is the aim of the hybrid model.

TABLE II. OVERALL EVALUATIONS

| Model | RMSE | MAPE |
|---|---------|---------|
| ARIMA | 4.93526 | 0.11366 |
| Hybrid Model | RMSE | MAPE |
| <i>Feature: PM2.5</i> | | |
| ARIMA-LSTM(Uni) | 4.89571 | 0.11040 |
| LSTM(Uni)-ARIMA & ARIMA-LSTM(Uni) | 4.85678 | 0.10979 |
| <i>Features: PM2.5 + WD</i> | | |
| ARIMA-LSTM(Bi) | 5.38302 | 0.12022 |
| LSTM(Bi)-ARIMA & ARIMA-LSTM(Bi) | 5.13711 | 0.11702 |
| LSTM(Uni)-ARIMA & ARIMA-LSTM(Bi) | 4.96770 | 0.11284 |
| <i>Features: PM2.5 + WS</i> | | |
| ARIMA-LSTM(Bi) | 4.81039 | 0.10849 |
| LSTM(Bi)-ARIMA & ARIMA-LSTM(Bi) | 4.80280 | 0.10775 |
| LSTM(Uni)-ARIMA & ARIMA-LSTM(Bi) | 4.81054 | 0.10825 |
| <i>Features: PM2.5 + Temp</i> | | |
| ARIMA-LSTM(Bi) | 4.88465 | 0.10986 |
| LSTM(Bi)-ARIMA & ARIMA-LSTM(Bi) | 4.82516 | 0.10936 |
| LSTM(Uni)-ARIMA & ARIMA-LSTM(Bi) | 4.78596 | 0.10936 |
| <i>Features: PM2.5 + WD + WS</i> | | |
| ARIMA-LSTM(Multi) | 5.13243 | 0.11706 |
| LSTM(Multi)-ARIMA & ARIMA-LSTM(Multi) | 5.00860 | 0.11471 |
| LSTM(Uni)-ARIMA & ARIMA-LSTM(Multi) | 4.85939 | 0.11168 |
| <i>Features: PM2.5 + WD + Temp</i> | | |
| ARIMA-LSTM(Multi) | 5.03021 | 0.11638 |
| LSTM(Multi)-ARIMA & ARIMA-LSTM(Multi) | 5.00030 | 0.11554 |
| LSTM(Uni)-ARIMA & ARIMA-LSTM(Multi) | 4.90351 | 0.11331 |
| <i>Features: PM2.5 + WS + Temp</i> | | |
| ARIMA-LSTM(Multi) | 5.03021 | 0.11638 |
| LSTM(Multi)-ARIMA & ARIMA-LSTM(Multi) | 5.00030 | 0.11554 |
| LSTM(Uni)-ARIMA & ARIMA-LSTM(Multi) | 4.90351 | 0.11331 |
| <i>Features: PM2.5 + WD + WS + Temp</i> | | |
| ARIMA-LSTM(Multi) | 5.19006 | 0.11891 |
| LSTM(Multi)-ARIMA & ARIMA-LSTM(Multi) | 5.11152 | 0.11654 |
| LSTM(Uni)-ARIMA & ARIMA-LSTM(Multi) | 4.88949 | 0.11240 |

This paper suggests using the integrated two hybrid models, ARIMA-LSTM and LSTM-ARIMA forecasting model, with weighing values for PM2.5 forecasting. The dataset, PM2.5 data of Bangkok, included wind direction (WD), wind speed (WS), temperature (Temp), and particulate matter 2.5 (PM2.5) for hourly data updated. According to the experiment's findings, when compared to other algorithms, two hybrid models forecasting by ARIMA-LSTM & LSTM-ARIMA with the weights values adjusted can anticipate a

lesser error. Specifically, forecasting by a set of hybrid models with an LSTM Univariate Variable.

However, the LSTM model used to create the ARIMA-LSTM hybrid model and the LSTM-ARIMA hybrid model are the same thing, that is the Vanilla Algorithm. For future experiments, can be tested using different algorithms, such as ARIMA-LSTM and BiLSTM-ARIMA, etc., or adjusting the batch size or epoch to be different may result in different results.

REFERENCES

- [1] Chulalongkorn University, "Stay Safe in the PM 2.5," p. 5, 2020.
- [2] G., Peter Zhang, "Time series forecasting using a hybrid ARIMA and neural network model," *Neurocomputing*, vol. 50, pp. 159-175, 2003.
- [3] C. Yuwei & W. Kaizhi, "Prediction of Satellite Time Series Data Based on Long Short Term Memory Autoregressive Integrated Moving Average Model (LSTM-ARIMA)," *IEEE International Conference on Signal and Image Processing*, 2019.
- [4] Cach N. Dang, Maria N. Moreno-García, & Fernando De la Prieta, "Hybrid Deep Learning Models for Sentiment Analysis," *Hindawi Complexity*, vol. 2021.
- [5] S. Chae, J. Shin, S. Kwon, S. Lee, S. Kang and D. Lee, "PM10 and PM2.5 real-time prediction models using an interpolated convolutional neural network," *Scientific Reports*, vol. 11, 2021.
- [6] Vo Thi Tam Minh, Tran Trung Tin and To Thi Hien, "PM2.5 Forecast System by Using Machine Learning and WRF Model, A Case Study: Ho Chi Minh City, Vietnam," *Aerosol and Air Quality Research*, vol. 21issue 12, 2021.
- [7] J. Xiao, Q. Wang, J. Cui, & J. Yu, "Multi-feature PM2.5 Prediction with ARIMA-LSTM", *2022 International Conference on Machine Learning, Cloud Computing and Intelligent Mining (MLCCIM)*, 2022.
- [8] T. Amnuaylojaroen, "Prediction of PM2.5 in an Urban Area of Northern Thailand Using Multivariate Linear Regression Model," *Advances in Meteorology*, 2022.
- [9] Pollution Control Department. Archived Data. From <http://www.air4thai.com>.
- [10] S. W. Shaun, "Time Series Analysis: Forecasting and Control", *Journal of Quality Technology*. vol. 49(5), pp. 418-419. 2017.
- [11] S. Hochreiter, J. Schmidhuber. "Long Short-Term Memory", *Neural Computation*. Vol. 9(8), pp. 1735-1780. 1997.

Investment Portfolio Optimization: Integrating Portfolio Allocation Methods with RNN LSTM

Azkario Rizky Pratama
 Department of Electrical
 and Information Engineering
 Universitas Gadjah Mada
 Yogyakarta, Indonesia
 azkario@ugm.ac.id

Bagus Rakadyanto Oktavianto Putra
 Department of Electrical
 and Information Engineering
 Universitas Gadjah Mada
 Yogyakarta, Indonesia
 bagus.rak2002@mail.ugm.ac.id

Abstract—The investment industry is experiencing significant growth, driven by an increased interest from new investors. However, achieving success in investing heavily relies on effective decision-making skills, which can be particularly challenging for newcomers. To tackle this issue, the research proposes an investment decision support system designed to aid investors in optimizing their investment portfolios. The proposed approach integrates traditional mathematical methods with advanced Long-Short Term Memory (LSTM) machine learning techniques.

The study demonstrates that the most effective combination involves employing LSTM alongside Post Modern Portfolio Theory (PMPT), resulting in the highest Mean Return of 0.002854, the highest Sortino Ratio of 0.192646, and the highest Ending Equity of 499.973204. Backtesting also reveals that the LSTM prediction, in combination with MPT and PMPT, has the potential to significantly increase portfolio values in just 1 year and 7 months, reaching 500% of the initial investment. Furthermore, incorporating LSTM predictions for future investment instrument prices enhances the performance of existing mathematical methods.

Index Terms—investment decision support system, price prediction, portfolio allocation, time series analysis

I. INTRODUCTION

Investing in financial markets is a strategic endeavor that demands a delicate balance of foresight, risk management, and disciplined decision-making. Sorongan points out that an investor's financial behavior, attitudes, and literacy significantly impact their investment choices [1]. Moreover, Andini and Rahmani suggests that 80.1% of investment decisions are influenced by financial literacy and company characteristics, while the remaining 19.9% is attributed to other factors [2]. As investors traverse the dynamic and constantly changing financial landscape, they face ongoing challenges in crafting strong investment strategies, utilizing price prediction methodologies, and optimizing portfolio balancing to reach their financial objectives.

The ability to predict asset price movements with accuracy is a highly coveted skill that has the potential to unlock significant returns. Utilizing sophisticated methodologies such as machine learning algorithms, including RNN LSTM and other time series forecasting techniques, investors can harness historical price data to make informed predictions about future asset prices. Accurate price predictions provide valuable insights into market trends and offer a strategic advantage in capitalizing on favorable opportunities.

However, price prediction alone is not sufficient to ensure investment success. An optimal investment strategy must also include robust portfolio balancing. Diversification across various assets is essential to reduce risk and enhance potential returns. Portfolio balancing enables investors to distribute their capital strategically, mitigating the impact of adverse market movements while positioning them to benefit from the growth potential of different investments. For many years, one prevalent mathematical method used in portfolio allocation is the Modern Portfolio Theory (MPT) proposed by Markowitz [3]. MPT employs historical data to determine the percentage allocation of the portfolio. Additionally, other mathematical methods, such as Equal Weight (EW) and Post Modern Portfolio Theory (PMPT), an extension of Markowitz's approach, can be utilized for portfolio allocation. This study proposes a combination of these existing mathematical methods with a machine learning technique called LSTM to predict future instrument prices and allocate the percentage of the investment portfolio accordingly.

The contributions of this paper are as follows:

- 1) Effectively utilizing RNN LSTM to make precise forecasts for the future closing prices of multiple investment instruments and subsequently calculating the expected returns.
- 2) Assessing the effectiveness of two approaches in dividing an investment portfolio and evaluating their combination with the machine learning prediction method, namely RNN LSTM.

II. RELATED WORKS

A. Investment Decision Support System

The development of the financial investment business is getting bigger because of many new people interested in investing [4]. However, if this rapid development is not followed by an appropriate investment strategy, it will cause losses to investors themselves [5]. Therefore, some researchers have developed an investment decision support system to help investors in investing.

In reference [6], the developed investment decision support system uses machine learning technology to generate an optimal investment strategy. Reference [7] proposed an investment decision support system using a combination of artificial intelligence, machine learning and mathematical models as its

basic architecture. In general, an investment decision support system is a system that helps investors make investment-related decisions. The output of this decision support system is different according to the design of the decision support system offered by each research. For example, in reference [4], the decision support system designed helps investors to know whether an investment instrument is a "good investment" or "not a good investment". While reference [7] offers a model that provides advice in the form of a stock portfolio directly to the user. Furthermore, reference [6] offers a decision support system that is relatively easy to adapt by the user due to its "high interpretability" architecture. The architecture in reference [6] only allows the user to select features that correspond to the reality in the field. The output of the decision support system in reference [6] tends to be a financial analysis, especially a capital market analysis.

B. Investment Instrument Optimization

When investing, investors face their own risks and uncertainties. One way to minimize risk is to construct an optimal investment portfolio. An optimal investment portfolio is one that, compared to other portfolios, has the same expected return but less risk, or has a higher expected return for the same risk [8]. One of the optimisation methods that can be used is the Markowitz model or now known as Modern Portfolio Theory (MPT) [9], [10]. The Markowitz model or MPT is based on the principle of diversification to minimize risk and maximize return [9]. In reference [9], optimisation using this model was carried out on LQ45 equity instruments in 2019-2020. It was found that MPT is suitable for investors who do not like high risk but still want to achieve optimal results [9].

On the other hand, many studies show that this MPT method has significant limitations [10]. MPT sometimes produces unsatisfactory predictions when applied in the real world [10]. Method that overcomes this problem is Post-Modern Portfolio Theory (PMPT) [11]. Two important developments in PMPT compared to MPT are that the formula used in PMPT takes into account downside risk, not just standard deviation, and also takes into account asymmetric return distributions [10]. PMPT offers a better risk calculation, is relatively flexible and better adapted to the realities of the investment process [12].

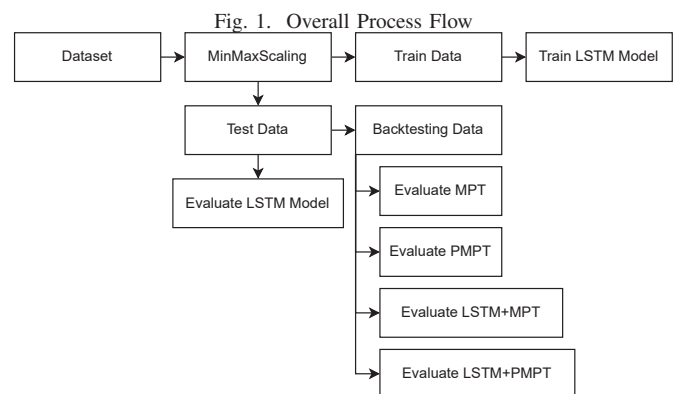
C. Predicting Future Prices using Long Short Term Memory (LSTM)

Based on several previous studies, there are various methods to predict the future price of each investment instrument. Starting from using Auto Regressive Moving Average (ARIMA) to using Neural Network. Neural network that is suitable for predicting stock price is Recurrent Neural Network (RNN) [13]. This is because stock price is a time-based data. However, traditional RNN has a problem that is answered by LSTM, namely the vanishing and exploding gradient descent problem [14]. Even in reference [15] it is mentioned that LSTM is most suitable for handling time-series data compared to Logistic Regression models, SVM, Auto-regressive Conditional Heteroskedasticity (ARCH) models, RNN, CNN, Naive Bayes, and ARIMA models.

Furthermore, specific to the problem of predicting the future price of investment instruments, LSTM has been widely used to make predictions related to future price prediction of investment instruments. References [16], [17], [18], [19] also use LSTM in making future price prediction models. Furthermore, reference [13] found that Long Short Term Memory (LSTM) is better at predicting some stock prices compared to Support Vector Regression (SVR). In addition, reference [20] also found that LSTM is better at analysing and predicting stock prices compared to traditional ARIMA methods. LSTM has also been shown to perform better in predicting future prices of investment instruments than many other models [21]. In addition, there is also research that uses a method that is close to the method we proposed, namely in reference [22].

In reference [22], LSTM is used to predict returns and then that return prediction is used as a to determine whether or not an investment instrument is used based on a certain threshold. The thing that distinguishes between this method and the method we propose is that the method we propose will use daily data while the data used in the study uses weekly data. We also use a different time span of data. Furthermore, the research [22] uses a selection of stocks from the LQ45 index while we use several investment commodities (Gold, Crude Oil, Cryptocurrencies, and Stocks). In reference [22] the mathematical methods used are Equal Weight and Mean-Variance Analysis, also known as Modern Portfolio Theory (MPT), while we use MPT and try an improved method from MPT, namely Post-Modern Portfolio Theory (PMPT). The approach to predicting using LSTM is also different, research [22] directly predicts the return, while we predict the future close price first and then calculate the return from the close price.

III. METHODOLOGY



A. Data Collection

We use historical data from Yahoo Finance using Yahoo Finance's API¹. The data range from 2014-09-17 to 2023-04-28. We consider several popular investment instruments in Indonesia, including a stock (we pick BBKA.JK as the largest market capitalisation in Indonesia), cryptocurrency

¹<https://pypi.org/project/yfinance/>

(i.e., Bitcoin which has sufficient historical data for this study), and commodities (i.e., gold and crude oil).

B. Data Preprocessing

Before the data can be used, the data needs to be preprocessed first. From the data obtained on Yahoo Finance, only the daily close price is taken. Next, empty data is filled using backfill or filling in empty data with previous data. Then the data is minmax scaling so that it can be used to train in LSTM. Min max scaling is done so that the data is only in the range of 0 to 1. The detailed formula of min max scaling is as follows:

$$x_{scaled} = \frac{x - \min(x)}{\max(x) - \min(x)} \quad (1)$$

where:

- x represents the original value of a feature or variable.
- x_{scaled} represents the scaled value of x .
- $\min(x)$ represents the minimum value of x .
- $\max(x)$ represents the maximum value of x .

Furthermore, the data is divided into 2 parts, namely those used for training and testing. A total of 80% of the total data is used as training data and the remaining 20% of the data becomes testing data.

C. LSTM

We use RNN LSTM to predict the price of investment instruments in the future. LSTM is a type of Recurrent Neural Network (RNN) architecture that addresses the shortcomings of traditional RNNs that suffer from vanishing gradient problem [23]. This problem causes the loss of long-term information during training. In general, LSTM has three main parts, namely forget gate, input gate, and output gate, as depicted in Figure 2. Forget gate is the part that determines whether or not information is stored in the LSTM model. Furthermore, the input gate serves to enter information that is useful to increase the accuracy of the model in predicting data. The information in this input gate will be stored in the cell state. Then, the output gate is where the output of the LSTM model is issued. By using a flow like this LSTM can better maintain long-term information compared to traditional RNNs. As discussed in Section II, LSTM has successfully managed to produce quite good results for predicting future prices.

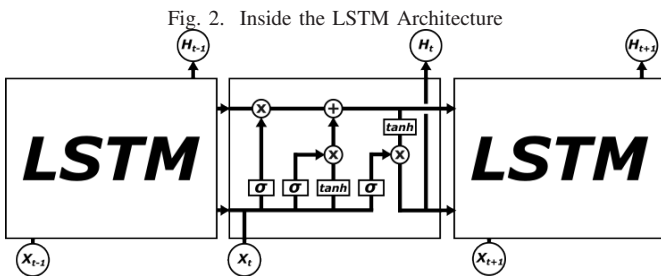


Fig. 2. Inside the LSTM Architecture

In this work, we specify one LSTM model for each each investment instrument and train the model by tuning hyperparameters. The first layer contains 150 nodes, then the

next layer is filled with a neural network with 50 nodes with relu activation and the last layer is the output layer with node 1 as the resulting prediction. Furthermore, the optimiser used is the Adam optimiser with a learning rate of 0.0001.

At this point, the preprocessed data is time series of closing prices that have been min-max scaled. To train the models, the data needs to be reshaped. That is, we reshape the data by making the X data coming from the close price of the past 30 days and y is the upcoming day, after which this process is repeated until it gets X in the form of a 30 day data set and y is the close price each day. Figure 3 illustrates this sliding window method.

Furthermore, the y values obtained from this process is then subjected to inverse scaling. This is done in order to get back the initial close price value. After obtaining the close price value, the return calculation of the close price is carried out with the following formula.

$$Return = \left(\frac{\text{Close price tomorrow}}{\text{Close price now}} \right) - 1 \quad (2)$$

where:

- Close price tomorrow represents the closing price of the asset on the following day.
- Close price now represents the closing price of the asset on the current day.
- Return represents the calculated return of the asset.

Then each existing LSTM model will predict \hat{y} values. This \hat{y} prediction is also done the same as the y test, which is to do inverse scaling and then calculate the return. The return from the \hat{y} prediction and the return from the y test will be evaluated with the evaluation metrics in Section III-E1.

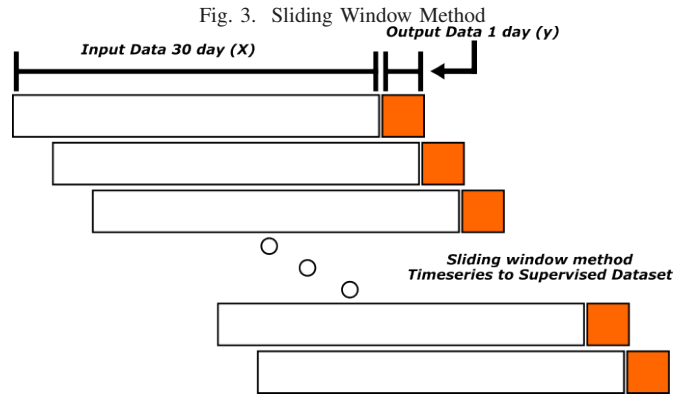


Fig. 3. Sliding Window Method Output Data 1 day (y)

D. Instrument Optimization and Backtesting

Once the price of investment instruments have been predicted, we combine of several instrument for optimizing returns using several methods as follows.

1) *Modern Portfolio Theory (MPT)*: In order to optimize each investment instrument, one of them used in this research is the Modern Portfolio Theory (MPT). MPT is aimed at achieving a harmonious equilibrium between the risk and potential returns within an investment portfolio. Its mathematical application seeks to pinpoint the optimal

portfolio allocation by minimizing risk, typically measured as variance, while simultaneously maximizing returns. Consequently, MPT yields portfolio allocations for each investment instrument that either delivers a substantial return at a specific risk level or minimizes risk while attaining a particular level of return. The formula is as follows.

$$\text{minimize: } 0.5 \cdot \mathbf{w}^T \cdot \Sigma \cdot \mathbf{w} - \mathbf{R}^T \cdot \mathbf{w} \quad (3)$$

$$\text{subject to: } \sum \mathbf{w} = 1 \\ \mathbf{w} \geq 0$$

where:

- w represents the vector of portfolio weights.
- Σ represents the covariance matrix of asset returns.
- R represents the vector of expected returns for each asset.
- \cdot denotes matrix multiplication or dot product.
- $0.5 \cdot \mathbf{w}^T \cdot \Sigma \cdot \mathbf{w}$ represents the portfolio risk term.
- $\mathbf{R}^T \cdot \mathbf{w}$ represents the expected portfolio return term.
- $\sum \mathbf{w} = 1$ ensures that the weights sum up to 1 (full investment).
- $\mathbf{w} \geq 0$ ensures that each weight is non-negative.

2) *Post Modern Portfolio Theory (PMPT)*: In addition, this research also uses Post Modern Portfolio Theory (PMPT) which can be viewed as a progression from the Modern Portfolio Theory by incorporating the consideration of downside risk [10]. PMPT aims to identify the optimal portfolio by minimizing the absolute deviation of the portfolio's return from the targeted rate of return. It achieves this by taking into account semivariance as a measure of downside risk. PMPT results in a portfolio that not only maximizes returns relative to the target but also minimizes the potential for downside risk. The formula is as follows:

$$\text{minimize: } |\mathbf{w}^T \cdot \boldsymbol{\mu} - R| + \mathbf{w}^T \cdot \boldsymbol{\gamma} \cdot \mathbf{w} \quad (4)$$

$$\text{subject to: } \sum \mathbf{w} = 1 \\ \mathbf{w} \geq 0$$

where:

- w represents the vector of portfolio weights.
- $\boldsymbol{\mu}$ represents the vector of expected returns for each asset.
- R represents the target return.
- \cdot denotes matrix multiplication or dot product.
- $|\mathbf{w}^T \cdot \boldsymbol{\mu} - R|$ represents the absolute deviation of the portfolio return from the target return.
- $\boldsymbol{\gamma}$ represents the semivariance matrix.
- $\mathbf{w}^T \cdot \boldsymbol{\gamma} \cdot \mathbf{w}$ represents the semivariance of the portfolio, representing the downside risk measure.
- $\sum \mathbf{w} = 1$ ensures that the weights sum up to 1 (full investment).
- $\mathbf{w} \geq 0$ ensures that each weight is non-negative.

Finally, we evaluate the performance of investment strategy using historical data and upcoming return prediction. We assess profitability using the mathematical methods (i.e., MPT and PMPT) using only historical data. We also predict potential returns by considering the LSTM prediction. Given

a return threshold, we decide to take an investment instrument when the potential return is above the threshold (i.e., 0.001). In this case, we use the predicted returns as additional insight for recalculating MPT and PMPT. We compare these approaches (i.e., only historical data and with LSTM prediction) to gain insights into how these strategies might have performed historically.

E. Evaluation Metrics

Several metrics are considered to evaluate the performance of price predictions and the potential profitability.

1) *LSTM Price prediction*: To validate that the model can predict well, the following evaluation metrics are used:

- Mean Squared Error (MSE)

$$\text{MSE} = \frac{1}{n} \sum_{i=1}^n (y_i - \hat{y}_i)^2 \quad (5)$$

where:

- MSE represents the Mean Squared Error.
 - n represents the number of samples or data points.
 - y_i represents the actual (observed) value of the target variable for the i -th sample.
 - \hat{y}_i represents the predicted value of the target variable for the i -th sample.
- Mean Absolute Error (MAE)

$$\text{MAE} = \frac{1}{n} \sum_{i=1}^n |y_i - \hat{y}_i| \quad (6)$$

where:

- MAE represents the Mean Absolute Error.
- n represents the number of samples or data points.
- y_i represents the actual (observed) value of the target variable for the i -th sample.
- \hat{y}_i represents the predicted value of the target variable for the i -th sample.
- $|\cdot|$ denotes the absolute value.

The predictions generated by the model are in the form of daily close price predictions for each instrument. The results of this prediction are then calculated for each day's return. This return results are then calculated for the evaluation metrics against the original data.

2) *Backtesting Evaluation*: To evaluate the investment strategy performance, we do backtesting to produce a portfolio value. The results of this portfolio value will calculate the following metrics:

- Mean Return, the average return of the portfolio over the given period

$$\text{Mean Return} = \frac{1}{n-1} \sum_{i=1}^{n-1} \left(\frac{P_{i+1} - P_i}{P_i} \right) \quad (7)$$

- n : the total number of observations (portfolio values) in the dataset.
 - P_i : the portfolio value at time i .
- Sortino Ratio, the risk-adjusted measure of return, taking into account the excess return over the risk-free rate and the downside risk of the returns

$$\text{Sortino Ratio} = \frac{\text{Mean Return} - \text{Risk-Free Rate}}{\text{Downside Deviation}} \quad (8)$$

where:

- Mean Return: the average return of the portfolio over the given period.
- Risk-Free Rate: the rate of return on a risk-free investment, such as a government bond.
- Downside Deviation: the standard deviation of negative (downside) returns.
- Ending Equity, the final value of the portfolio after the given period

$$\text{Ending Equity} = P_n \quad (9)$$

where:

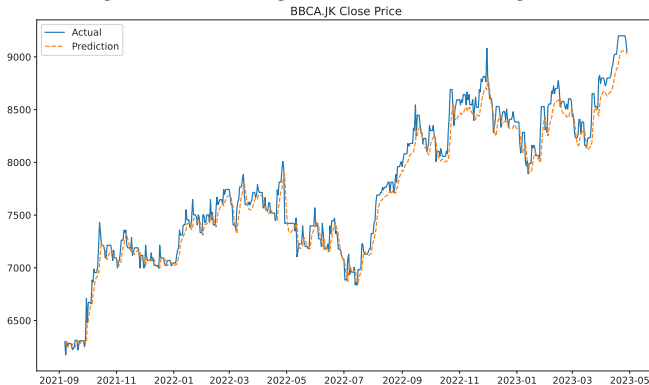
- P_n : the portfolio value at the last time period.

IV. RESULTS AND DISCUSSION

A. Price Forecast and Returns Calculation

We forecast closing price of the investment instruments in the upcoming day using LSTM and estimate the potential return from the forecasted values. The return from the original data is then compared with the return generated by this prediction. This is relevant in real world as by looking at the past 30 days, a prediction can be made one day ahead and the return can be predicted from the estimated closing price. The LSTM model is trained on each investment instrument and predicts the closing price of each instrument. In general, the models can successfully predicts the closing price, as shown in Figure 4.

Fig. 4. Actual Closing Price vs Predicted Closing Price



We calculate returns based on that actual closing price and estimated closing price. The return values are then compared using the MSE and MAE evaluation metrics. The results of the MSE and MAE evaluation metrics for each investment instrument are shown in Table I.

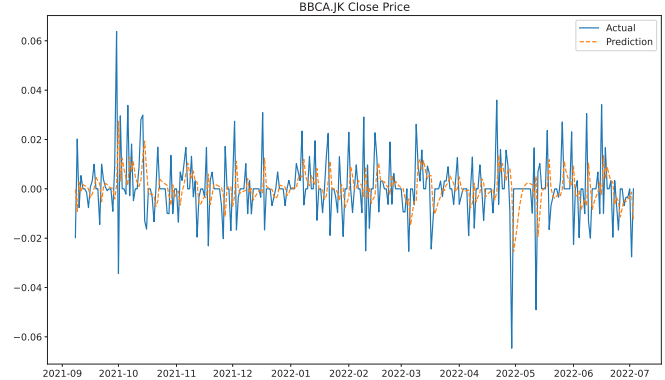
TABLE I
MSE AND MAE OF THE RETURN OF EACH INVESTMENT INSTRUMENT

| | Mean Square Error | Mean Absolute Error |
|---------|-------------------|---------------------|
| GOLD | 0.000100 | 0.007354 |
| OIL | 0.000634 | 0.018176 |
| BITCOIN | 0.001519 | 0.028826 |
| BBCA.JK | 0.000190 | 0.009663 |

Figure 5 shows the graphs of predicted returns and the actual returns. We can see that the pattern of the returns

(i.e., the loss and gain) have been estimated properly. The best MSE and MAE are obtained when predicting GOLD investment instruments with an MSE of 0.0001 and MAE of 0.007354. The model is therefore ready for the next stage, which is backtesting.

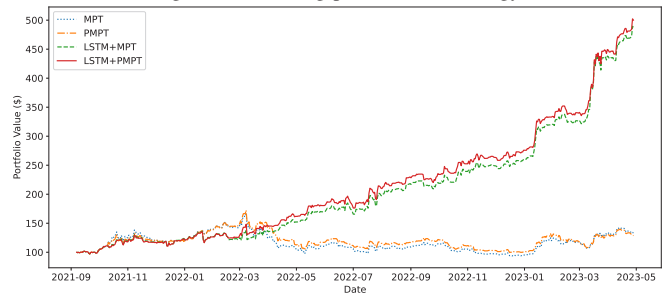
Fig. 5. Estimated returns vs actual returns



B. Backtesting Validation

We finally compare the performance of MPT and PMPT with the combination of the same methods with LSTM predictions (i.e., MPT + LSTM, PMPT + LSTM). Each method is backtested and compared using the Mean Return, Sortino Ratio with Risk-Free 0 and Ending Equity metrics. The backtesting is performed on a test data set with an initial investment of \$100. Figure 6 reveals the results of the backtesting. We can see that the LSTM prediction, in combination with MPT and PMPT, may significantly increase the portfolio values in 1 year and 7 months, reaching 500% of the initial investment.

Fig. 6. Backtesting plots of each strategy



Further calculations have been made based on the existing metrics and the results are shown in Table II.

TABLE II
BACKTESTING METRICS

| | Mean Return | Sortino Ratio | Ending Equity |
|-----------|-------------|---------------|---------------|
| MPT | 0.000672 | 0.043632 | 133.149652 |
| PMPT | 0.000598 | 0.040964 | 128.527932 |
| LSTM+MPT | 0.002817 | 0.190539 | 487.293241 |
| LSTM+PMPT | 0.002854 | 0.192646 | 499.973204 |

Based on the results, it is found that the method of portfolio percentage distribution using PMPT is the method with the lowest mean return among the other methods. Furthermore, the prediction of LSTM combined with MPT and PMPT is found to increase the portfolio value, which also results in an increasing mean return. In addition to mean return, other measures such as Sortino Ratio and Ending Equity also show a significant increase when compared to the usual mathematical methods of MPT and PMPT. The use of LSTM, which increases the mean return and the Sortino ratio, shows that the increase in return does not increase the risk, but rather reduces the existing risk. This shows that the addition of LSTM not only increases the return, but also reduces the risk of the investment portfolio itself.

V. CONCLUSION

Based on the results, we show that the RNN LSTM can effectively predict the future closing prices of multiple investment instruments, including commodities, Bitcoin crypto currency, and an Indonesian stock. This is shown by the fairly low MSE and MAE. The lowest MSE and MAE are found in gold investment instruments, with MSE of 0.0001 and MAE of 0.007354.

Further, we integrate the price forecast using LSTM into portfolio percentage distribution methods, such as MPT and PMPT. We show that by considering the LSTM prediction, we can increase the profit over the time. The best combination is found using LSTM + PMPT with the highest Mean Return of 0.002854, the highest Sortino Ratio of 0.192646 and the highest Ending Equity of 499.973204. It is also found that based on backtesting, the LSTM prediction in combination with MPT and PMPT, may significantly increase the portfolio values in 1 year and 7 months, reaching 500% of the initial investment. It is also reported that LSTM prediction not only increased profits but also reduced the risk of the investment portfolio. This is indicated by the increase in mean return along with the increase in sortino ratio. This result confirms that the combination of LSTM prediction and PMPT method may be used as an investment decision support system to help investors in allocating the distribution of their investment portfolio. Further research can be developed to predict the future price of each instrument even more accurately. This can be done by optimizing the sliding window size, implementing multi-stage future predictions, and experimenting contemporary machine learning models such as Transformers for price prediction.

REFERENCES

- [1] F. A. Sorongan, "The influence of behavior financial and financial attitude on investment decisions with financial literature as moderating variable," *European Journal of Business and Management Research*, vol. 7, no. 1, pp. 265–268, Feb. 2022. [Online]. Available: <https://doi.org/10.24018/ejbm.2022.7.1.1291>
- [2] P. Andini and H. F. Rahmani, "Investment in perceptions of financial literacy and company characteristics (case study of early adults in bandung city)," *Asian Journal of Applied Business and Management*, vol. 2, no. 1, pp. 99–112, Feb. 2023. [Online]. Available: <https://doi.org/10.55927/ajabm.v2i1.3171>
- [3] H. Markowitz, "PORTFOLIO SELECTION*," *The Journal of Finance*, vol. 7, no. 1, pp. 77–91, Mar. 1952. [Online]. Available: <https://doi.org/10.1111/j.1540-6261.1952.tb01525.x>
- [4] A. V. de Oliveira, M. C. S. Dazzi, A. M. da Rocha Fernandes, R. L. S. Dazzi, P. Ferreira, and V. R. Q. Leithardt, "Decision support using machine learning indication for financial investment," *Future Internet*, vol. 14, no. 11, p. 304, Oct. 2022. [Online]. Available: <https://doi.org/10.3390/fi14110304>
- [5] C. F. Tsai and S. P. Wang, "Stock price forecasting by hybrid machine learning techniques," in *Proceedings of the Int. multiconference of engineers and computer scientists*, vol. 1, no. 755, 2009, p. 60.
- [6] R. Rosati, L. Romeo, C. A. Goday, T. Menga, and E. Frontoni, "Machine learning in capital markets: Decision support system for outcome analysis," *IEEE Access*, vol. 8, pp. 109 080–109 091, 2020. [Online]. Available: <https://doi.org/10.1109/access.2020.3001455>
- [7] S. Patalay and M. R. Bandlamudi, "Decision support system for stock portfolio selection using artificial intelligence and machine learning," *Ingénierie des systèmes d'information*, vol. 26, no. 1, pp. 87–93, Feb. 2021. [Online]. Available: <https://doi.org/10.18280/isi.260109>
- [8] D. N. S. Werastuti, "Pembentukan portofolio optimal melalui pendekatan efisiensi decision-making units (dmu) yang menghasilkan relative efficiency score berdasarkan single index model," *Jurnal Ilmiah Akuntansi dan Humanika*, vol. 3, no. 2, 2014.
- [9] A. Hanif, N. R. Hanun, and R. E. Febriansah, "Optimization of stock portfolio using the markowitz model in the era of the COVID-19 pandemic," *TIJAB (The Int. Journal of Applied Business)*, vol. 5, no. 1, p. 37, Apr. 2021. [Online]. Available: <https://doi.org/10.20473/tjab.v5.i1.2021.37-50>
- [10] D. Rasiyah, "Post-modern portfolio theory supports diversification in an investment portfolio to measure investment's performance," *Journal of Finance and Investment Analysis*, vol. 1, no. 1, pp. 69–91, 2012.
- [11] F. A. Sortino and S. Satchell, *Managing downside risk in financial markets*. Butterworth-Heinemann, 2001.
- [12] C. Geambasu, R. Sova, I. Jianu, and L. Geambasu, "Risk measurement in post-modern portfolio theory: differences from modern portfolio theory," *Economic Computation & Economic Cybernetics Studies & Research*, vol. 47, no. 1, pp. 113–132, 2013.
- [13] G. Bathla, "Stock price prediction using LSTM and SVR," in *2020 Sixth Int. Conf. on Parallel, Distributed and Grid Computing (PDGC)*. IEEE, Nov. 2020. [Online]. Available: <https://doi.org/10.1109/pdgc50313.2020.9315800>
- [14] N. K. Manaswi, N. K. Manaswi, and S. John, *Deep learning with applications using python*. Springer, 2018.
- [15] S. Vohra and P. Savaridassan., "Stock price trend analysis and prediction of closing price using LSTM," in *2023 Int. Conf. on Computer Communication and Informatics (ICCCI)*. IEEE, Jan. 2023. [Online]. Available: <https://doi.org/10.1109/iccci56745.2023.10128260>
- [16] H. N. Bhandari, B. Rimal, N. R. Pokhrel, R. Rimal, K. R. Dahal, and R. K. Khatri, "Predicting stock market index using LSTM," *Machine Learning with Applications*, vol. 9, p. 100320, Sep. 2022. [Online]. Available: <https://doi.org/10.1016/j.mlwa.2022.100320>
- [17] Y. Yao, "Data analysis on the computer intelligent stock prediction model based on LSTM RNN and algorithm optimization," in *2022 IEEE Int. Conf. on Electrical Engineering, Big Data and Algorithms (EEBDA)*. IEEE, Feb. 2022. [Online]. Available: <https://doi.org/10.1109/eebda53927.2022.9744859>
- [18] A. Ghosh, S. Bose, G. Maji, N. Deb Nath, and S. Sen, "Stock price prediction using LSTM on indian share market," in *EPiC Series in Computing*. EasyChair. [Online]. Available: <https://doi.org/10.29007/qgcz>
- [19] D. Wei, "Prediction of stock price based on LSTM neural network," in *2019 Int. Conf. on Artificial Intelligence and Advanced Manufacturing (AIAM)*. IEEE, Oct. 2019. [Online]. Available: <https://doi.org/10.1109/aiaam48774.2019.00113>
- [20] M. Joshi, A. Deshpande, and D. Ambawade, "Situational portfolio forecasting and allocation with deep-learning approach," in *2023 Int. Conf. on Communication System, Computing and IT Applications (CSCITA)*. IEEE, Mar. 2023. [Online]. Available: <https://doi.org/10.1109/cscita55725.2023.10104979>
- [21] K. J. H. E, M. S. Jacob, and D. R., "Stock price prediction based on LSTM deep learning model," in *2021 Int. Conf. on System, Computation, Automation and Networking (ICSCAN)*. IEEE, Jul. 2021. [Online]. Available: <https://doi.org/10.1109/icscan53069.2021.9526491>
- [22] P. N. Adila, D. Saepudin, and A. F. Ihsan, "Prediction of stocks return in the lq45 index with long-short-term-memory (lstm) and its application for portfolio selection," in *2022 10th Int. Conf. on Information and Communication Technology (ICOICT)*, 2022, pp. 194–199.
- [23] S. Hochreiter and J. Schmidhuber, "Long short-term memory," *Neural computation*, vol. 9, no. 8, pp. 1735–1780, 1997.

Enhanced keystroke dynamics authentication using Keystroke Vector Dissimilarity

Naphat Bussabong

Department of Computer and Information Science,
Faculty of Applied Science,
King Mongkut's University of Technology North Bangkok,
Bangkok, Thailand
s6304062856022@email.kmutnb.ac.th

Tanapat Anusas-amornkul*

Department of Computer and Information Science,
Faculty of Applied Science,
King Mongkut's University of Technology North Bangkok,
Bangkok, Thailand
tanapat.a@sci.kmutnb.ac.th

Abstract—A keystroke dynamics is a simple example of a biometric authentication by using a typing rhythm on a keyboard without any special device. Previous research used Euclidean distance to distinguish between an authentic user and an imposter [1]. However, the Euclidean distance has a flaw in that a distance could be the same even though the keystroke rhythms are different. Therefore, this paper proposed to enhance the keystroke dynamics authentication by using a keystroke vector and calculating a standard deviation for each key to give different weights such that the variations of each keystroke is taking into account. A dataset is similar in [1] but some data is different. The performance was measured using Equal Error Rate (EER) and the result showed that the EER was 3.33%, compared to 4% in [1].

Keywords— Authentication, Euclidean distance, Keystroke dynamics, Keystroke vector dissimilarity

I. INTRODUCTION

Authentication is a technique to verify a user who is a genuine user or an imposter by using one of 3 factors, which are something you know, something you have, and something you are. In order to improve the authentication performance, two factor authentication is implemented in many systems. Normally, a password is used to authenticate as something you know but more security can be added by using something you have or something you are, such as a smartphone or a biometric, respectively. A keystroke dynamics is a simple example of biometric authentication by using a typing rhythm on a keyboard without any special device.

In keystroke dynamics authentication (KDA), Euclidean distance is a simple method and widely used for measuring the distance between two points in order to distinguish between an authentic user and an imposter. However, a weakness of Euclidean distance is found that the distance is calculated without considering the sequences of keystrokes. It means that two people can input the same word with different keystroke rhythms but the distance could be similar. The problem is shown in Fig. 1. For this weakness, an imposter can still be authenticated as an authentic user such that the accuracy is low.

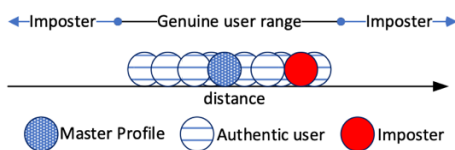


Fig. 1. A weakness of Euclidean distance

In a literature, Wangsuk and Anusas-amornkul [1] proposed to create a master profile from 10 username inputs and verify a user using Euclidean distance. From the weakness that previously mentioned, this work proposed to overcome the problem by using a keystroke vector and calculating a

standard deviation for each key to give different weights such that the variations of each keystroke is taking into account. The dataset for this work is the similar to the dataset in [1].

The organization of this paper is as follows. The next section is a related work to introduce a background of keystroke dynamics and literature reviews on the keystroke dynamics. Section III explained the proposed work such as a keystroke dynamics vector, a master vector profile, and a verification technique. Next section discussed about experiments, performance metrics, and results from experiments. The last section is a conclusion and a future work.

II. RELATED WORK

In the literature, the keystroke dynamics authentication is still on-going research to improve the performance of authentication techniques. Several techniques have been proposed and can be categorized into 2 main techniques, which are statistical techniques and machine learning techniques. However, the background of keystroke dynamics is presented first. Then, statistical and machine learning techniques are explained later.

A. Keystroke dynamic

Keystroke dynamics concept was first introduced in 1975 [2] by using keystroke rhythm from a keyboard to identify a person. It can be kept as a profile for authenticating a genuine user by analyzing keystroke rhythm [3]. Typical features of keystroke dynamics are:

- Key hold time (H) which is time for pressing a key on a keyboard starting from pressing till releasing a key
- Interkey time (I) which is time to change from one key to another key while typing by starting from releasing a key till pressing the next key
- Latency (L) which is time for starting pressing one key till starting pressing the next key.

In other words, the latency is the summation of key hold time and interkey time. The features of keystroke dynamics are shown in Fig. 2.

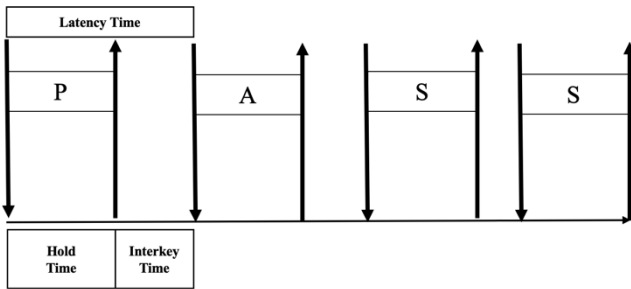


Fig. 2. The features of keystroke dynamics

B. Statistical techniques

Statistical techniques were proposed for KDA for simplicity and less data usage. Wangsuk and Anusamornkul [1] proposed to create a Master profile and compare with an input keystroke using a Euclidean distance and six sigma technique to verify a user. A dataset was collected from 20 authentic users and 3 imposters with total of 1200 records of usernames. The performance was 4% Equal Error Rate (EER). Apatia, and et al.[4] proposed to use Generalized Fuzzy model (GFM), which is a combination of Mamdani-Larsen and Takagi-Sugeno fuzzy models. It was tested with CMU dataset and the GFM model gave the best performance at 7.86% EER.

Then, Foresi and Samavi [5] proposed to use a statistical method using an average and a standard deviation to create profiles. The best results were obtained in 2 cases. The first case gave False Acceptance Rate (FAR) at 0.0% and False Rejection Rate (FRR) at 2.54. The second case gave FAR at 0.0% and FRR at 2.87%. The results showed that complex passwords could give lower FAR and increase the performance. Pramana, and et al. [6] proposed to use dynamic time warping with CMU dataset. The result showed that it gave FAR at 39.9%, FRR at 3.3%, and EER at 17.6%.

C. Machine learning techniques

Machine learning techniques for KDA were proposed in many literatures because of the popularity of Artificial intelligence (AI) but required a large amount of data for training. Lin and Chen [7] proposed to select 5 features and use one-class SVM for authentication for Chinese language data. The accuracy was 62.3%. Then, Chandok, and et al. [8] studied 5 statistical and machine learning algorithms. The best result was EER at 11.76% using Manhattan Scaled Detector algorithm, a statistical algorithm.

Koh and Lai [9] proposed to use Artificial Bee Colony algorithm to classify a user. The keystroke features in this work were pressure, dwell time, and flight time. The accuracy was 90%. Cevik, and et al. [10] proposed to use tree-based algorithms with their own datasets and the accuracy was 94%. Piugie, and et al. [3] proposed to transform behavioral biometrics (time series) into 3 dimensional image to test 6 deep learning algorithms. The best algorithm was GoogleNet algorithm that gave EER at 4.49%. Singh, and et al. [11] proposed to use XGBoost algorithm and other algorithms for

keystroke dynamics authentication. The XGBoost gave the best performance at 93.59% accuracy.

III. PROPOSED WORK

From the weakness of Euclidean distance as mentioned in Section I. In this work, the objective is to improve the performance of KDA by using a keystroke vector and calculating a standard deviation for each key. A proposed work is designed and consisted of 5 parts, i.e. keystroke vector, vector normalizations, master vector and SD vector profile, master vector profile and modified input keystroke vector, and dissimilarity calculation. Fig. 3 shows the overview flow diagram of this work.

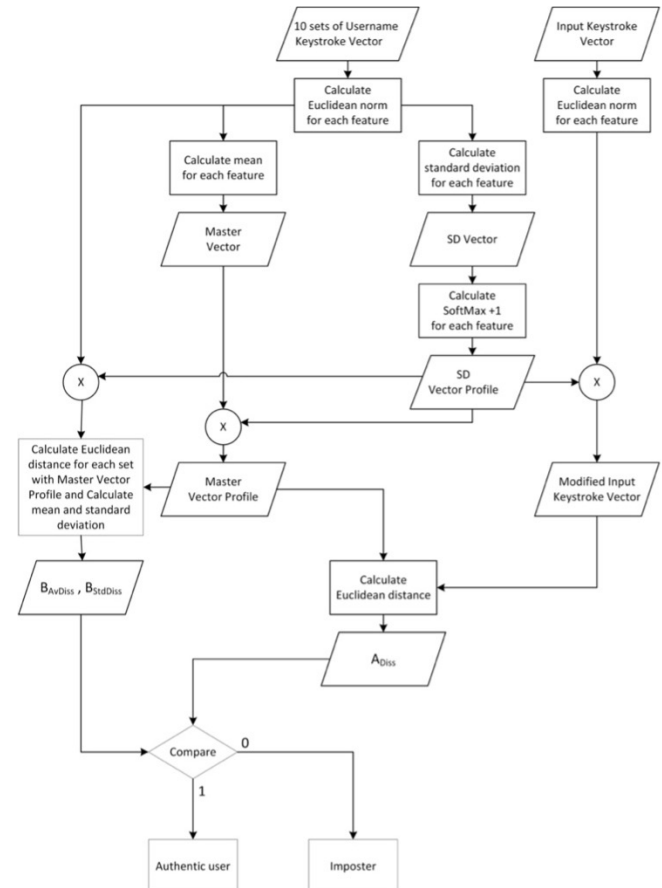
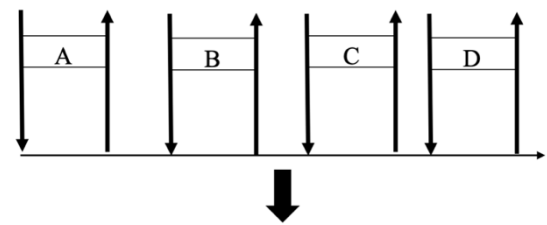


Fig. 3. Overview of a proposed work



$$\text{Vector} = \left[\frac{A_I}{1000}, \frac{A_L}{1000}, \frac{B_I}{1000}, \frac{B_L}{1000}, \frac{C_I}{1000}, \frac{C_L}{1000}, \frac{D_I}{1000}, \frac{D_L}{1000} \right]$$

Fig. 4. Example keystroke vector data with 4 input characters

A. Keystroke vector

In order to create a keystroke profile in this work, a keystroke vector is defined as a vector of keystroke features, i.e. Interkey time (I), and Latency (L), used for each key sequentially in milliseconds. The interkey time can be positive

or negative number depending on how fast a user can type. Therefore, the interkey time for each key is added by the sequence number minus 1 such that all the interkey time is in term of positive number as follow in [1]. A keystroke vector is created as shown in Fig. 4 In this example, there are four characters and the size of a vector is eight elements for one set of keystroke. Each character gives 2 elements of a keystroke vector. This example is used throughout the paper.

B. Vector normalisation

Since the keystroke features are varied from different users, all keystroke vectors have to be normalized first. There are 2 normalization methods, which are a Euclidean norm and a softmax function, in this work.

1) Euclidean norm

Euclidean norm is a mathematical function to measure a distance from an origin of a vector [12] as shown in (1),

$$\|V\|_2 = \sqrt{v_1^2 + v_2^2 + \dots + v_n^2} = \sqrt{\sum_{i=1}^n v_i^2} \quad (1)$$

where V is a vector that needs to be measure.

In this work, the Euclidean norm is used to normalize each keystroke vector by dividing a keystroke vector with a Euclidean norm as shown in (2),

$$\ell_{2-norm}(V) = \frac{V}{\|V\|_2} = \left(\frac{v_1}{\|V\|_2}, \frac{v_2}{\|V\|_2}, \frac{v_3}{\|V\|_2}, \dots, \frac{v_n}{\|V\|_2} \right) \quad (2)$$

where n is eight from the example, since there are four keys and eight elements for this keystroke vector. Each user has the same value of n depending on the number of characters of a username.

2) Softmax function

A softmax function is a mathematical function that is widely used in deep learning that involved with a classification problem. This function is to transform a set of numbers to a probability [13] as shown in (3).

$$\sigma(z)_i = \frac{e^{z_i}}{\sum_{j=1}^K e^{z_j}} \quad (3)$$

where σ is a softmax function, z is an input vector, e^{z_i} is a standard exponential function for each feature within the input vector, K is a number of classes but in this work it is a number of input vector, and $\sum_{j=1}^K e^{z_j}$ is a summation of all standard exponential function for each feature within the input vector.

In this work, the softmax function is used to create a Standard Deviation (SD) vector profile (see next section).

C. Master vector and SD vector profile

1) Master vector

A master vector is created by using 10 user inputs of a username from a user as in [1] in order to create a master vector. The master vector is defined in (4).

Master vector =

$$\begin{bmatrix} \frac{\sum_{i=1}^n \ell_{2-norm}\left(\frac{A_{i_I}}{1000}\right)}{n}, \frac{\sum_{i=1}^n \ell_{2-norm}\left(\frac{A_{i_L}}{1000}\right)}{n}, \\ \frac{\sum_{i=1}^n \ell_{2-norm}\left(\frac{B_{i_I}}{1000}\right)}{n}, \frac{\sum_{i=1}^n \ell_{2-norm}\left(\frac{B_{i_L}}{1000}\right)}{n}, \\ \frac{\sum_{i=1}^n \ell_{2-norm}\left(\frac{C_{i_I}}{1000}\right)}{n}, \frac{\sum_{i=1}^n \ell_{2-norm}\left(\frac{C_{i_L}}{1000}\right)}{n}, \\ \frac{\sum_{i=1}^n \ell_{2-norm}\left(\frac{D_{i_I}}{1000}\right)}{n}, \frac{\sum_{i=1}^n \ell_{2-norm}\left(\frac{D_{i_L}}{1000}\right)}{n} \end{bmatrix} \quad (4)$$

where ℓ_{2-norm} is Euclidean norm, and n is number of keystroke vector, in this case $n = 10$ for 10 repetitions for creating a master vector.

2) SD vector profile

SD vector profile is created from standard deviations of interkey time and latency for each key with 10 repetitions of a username typing. A softmax function is used in order to gain a value between 0 and 1. A standard deviation is calculated using (5).

$$S = \sqrt{\frac{1}{n-1} \sum_{i=1}^n (x_i - \bar{x})^2} \quad (5)$$

SD vector is a vector of all standard deviation for each dimension in a master vector as shown in (6).

$$SD \text{ vector} = [S(A_I), S(A_L), S(B_I), S(B_L), S(C_I), S(C_L), S(D_I), S(D_L)] \quad (6)$$

where A_I, B_I, C_I, D_I are interkey time for each key (4 characters in this example). A_L, B_L, C_L, D_L are latency for each key (four characters in this example).

SD vector profile is a modified SD vector using a softmax function for adding weights for each keystroke element. A result from the softmax function for each element is added by 1. The SD vector profile is shown in (7).

$$SD \text{ vector profile} = \begin{bmatrix} \sigma(SD \text{ Vector}_1) + 1, \\ \sigma(SD \text{ Vector}_2) + 1, \\ \dots, \sigma(SD \text{ Vector}_K) + 1 \end{bmatrix} \quad (7)$$

where σ is a softmax function, and K is the number of elements a keystroke vector ($K = 8$ in this example).

SD vector profile is added to the work in order to solve a weakness of a Euclidean distance which doesn't considered the variations of input data for similarity distance calculation by adding a weight for each feature. If the SD value is small, it means that the weight should be small and vice versa such that it can greatly enhance a user keystroke rhythm data. SD vector is applied to a Master vector and also an input keystroke vector before calculating a similarity or distance value.

D. Master vector profile and modified input keystroke vector

In this work, a keystroke vector is modified before calculating a Euclidean distance.

1) Master vector profile

A master vector profile is a keystroke dynamics profile for each user with the enhancement of the weakness of Euclidean distance. The master vector profile is calculated from a multiplication between a master vector and a SD vector profile as shown in (8).

$$\text{Master vector profile} = \text{master vector} \times \text{SD vector profile} \quad (8)$$

2) Modified input keystroke vector

In a verification process, a user needs to type in his/her username and the keystroke dynamics features are kept in an input keystroke vector. However, the vector has yet been compared with a master vector profile. The input keystroke vector has to be modified by multiplying with the SD vector profile, called modified input keystroke vector as shown in (9).

$$\text{Modified input keystroke vector} = \text{Input keystroke vector} \times \text{SD vector profile} \quad (9)$$

The modified input keystroke vector is making the verification process easier to identify an authentic user or an imposter.

E. Verification process

The verification process is used to validate a user who is an authentic user or an imposter using a Euclidean distance. A user verification process is done to verify a user from keystroke dynamics.

1) Euclidean distance

Euclidean distance is a technique to measure a distance between 2 vectors [14]. It is used in many applications including keystroke dynamics authentication. A Euclidean distance in n dimensional space [15] is shown in (10).

$$d(P, Q) = \sqrt{(q_1 - p_1)^2 + (q_2 - p_2)^2 + \dots + (q_n - p_n)^2} \quad (10)$$

Where P, Q are vectors to measure distance and n is the number of features in a vector.

2) Verification process

The verification process is similar to the process in [1]. Important parameters are explained as follows.

a) A_{diss}

A_{diss} is a result from calculating a Euclidean distance between a master vector profile and a modified input keystroke vector, as shown in (11).

$$A_{diss} = d(P, Q) \quad (11)$$

where d is a Euclidean distance, P is a master vector profile, and Q is a modified input keystroke vector.

b) B_{AvDiss}

B_{AvDiss} is an average of Euclidean distance between each repetition and a master vector profile [1] as shown in (12).

$$B_{AvDiss} = \frac{\sum_{i=1}^n d(Q, v_i)}{n} \quad (12)$$

where Q is a master vector profile, v_i is a master keystroke vector at i repetition, and n is a number of repetitions ($n = 10$).

c) $B_{StdDiss}$

$B_{StdDiss}$ is a standard deviation of Euclidean distance between each repetition and a master vector profile [1] as shown in (13).

$$B_{StdDiss} = \sqrt{\frac{\sum_{i=1}^n (d(q, v_i) - B_{AvDiss})^2}{n - 1}} \quad (13)$$

where q is a master vector profile, v_i is a master keystroke vector at i repetition, and n is a number of repetitions ($n = 10$).

d) $Sigma$

Sigma is an allowance factor. It is originally used in six sigma theory with the sigma = 3. In this work, the sigma is modified to find a minimum Equal Error Rate (EER) explained in the next section.

e) Verification equation

In order to verify a user, the verification equation is defined in (14) [1].

$$f(x) = \begin{cases} 0; & \text{if } (A_{diss} > [B_{AvDiss} + (Sigma * B_{StdDiss})]) \\ 1; & \text{if } (A_{diss} \leq [B_{AvDiss} + (Sigma * B_{StdDiss})]) \end{cases} \quad (14)$$

From (14), if the $f(x) = 0$, the system indicates that the user is an imposter. However, if $f(x) = 1$, it means that the user is an authentic user.

IV. EXPERIMENTS AND DISCUSSION

A. Dataset

In this work, a dataset is similar to a dataset in [1] but some data is different. The dataset was collected from 18 users, which were 15 authentic users and 3 imposters. Each authentic user typed his/her username in 2 sets. Each user typed in username 10 times for each set. An imposter typed in each authentic username 30 times. The total number of keystroke data is 1,650 records, 300 records from 15 authentic users and 1,350 records from 3 imposters.

B. Performance metrics

Typical performance metrics for keystroke dynamics authentication are False Acceptance Rate (FAR), False Rejection Rate (FRR), Equal Error Rate (EER), and accuracy. FAR is a percentage between the number of accepted imposter and the number of total imposter attempts, as shown in (15).

$$FAR = \frac{\text{Accepted Imposter}}{\text{Total Impostor Attempt}} \times 100 \quad (15)$$

FRR is a percentage between the number of rejected authentic users and total user attempts as shown in (16).

$$FRR = \frac{\text{Rejected Authentic User}}{\text{Total User Attempt}} \times 100 \quad (16)$$

EER is a point where the FAR and FRR are equal or closest to each other as shown in Fig. 5.

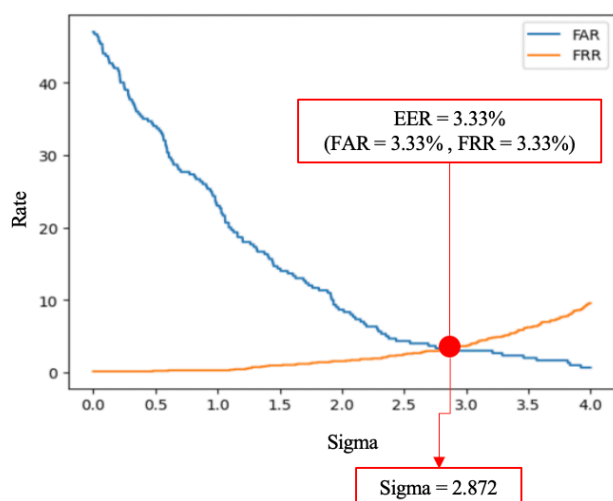


Fig. 5. The relationship of FAR, FRR, and EER

Accuracy is a percentage of a model to identify an authentic user correctly as shown in (17).

$$\text{Accuracy} = 100 - \text{EER} \quad (17)$$

C. Results

From the verification equation, a sigma or an allowance factor is varied using 0.001 significant level in order to find a minimum EER as shown in Fig. 5. Results from the proposed work gave EER at 3.33% (FAR = 3.33% and FRR = 3.33%) with the 2.872 allowance factor. It means that the accuracy for this work is 96.67% compared to 96% in [1].

D. Comparison

This proposed work is to solve a Euclidean distance problem by using a Euclidean norm and a softmax function to create a master vector profile and a SD vector profile, which gives the variation as a weight for each vector element. Table I shows a comparison of the results from literature and this proposed technique.

TABLE I. COMPARISON RESULTS

| Reference | Technique | Dataset | EER(%) | ACC(%) |
|--------------------|---------------------------------|--------------------|--------|--------|
| [1] | Trajectory Dissimilarity | Author Dataset | 4% | 96% |
| [6] | Generalized Fuzzy Model (GFM) | CMU Dataset | 7.86 | - |
| [4] | Mean, Standard Deviation | Author Dataset | - | - |
| [5] | dynamic time warping | CMU Dataset | 17.6% | - |
| [7] | One-Class SVM | Chinese keystrokes | - | 62.3% |
| [8] | Manhattan Scaled Detector | CMU Dataset | 11.76% | - |
| [9] | Artificial Bee Colony algorithm | Author Dataset | - | 90% |
| [10] | tree-based algorithms | Author Dataset | - | 94% |
| [3] | Google Net | Author Dataset | 4.49% | - |
| [11] | XGBoost Algorithm | Author Dataset | - | 93.59% |
| Proposed Technique | Keystroke Vectors | [1]* | 3.33% | 96.67% |

Note: * The dataset has some different data from the original work.

V. CONCLUSION

Keystroke dynamic authentication (KDA) is one of the biometric authentication methods that do not require special devices. It only needs a keyboard for collecting typing rhythms. Several researchers have proposed to use KDA by using statistical and machine learning techniques. In this work, the statistical technique is proposed to solve a weakness of Euclidean distance and improve the performance of the previous work in [1]. The proposed technique is to

create a master vector profile and SD vector profile in order to give a weight for each key and improve the similarity distance. By using the dataset in [1], the experimental result showed that the EER was decreased from 4% to 3.33%. However, the EER could be improved. In the future, this method can be modified to enhance the EER and investigated to use with a smartphone (on-screen) keyboard and other types of keyboards.

VI. REFERENCES

- [1] K. Wangsuk and T. Anusas-amornkul, "Trajectory Mining for Keystroke Dynamics Authentication," *Procedia Computer Science*, vol. 24, pp. 175-183, 2013.
- [2] R. Spillane, "Keyboard apparatus for personal identification," *IBM Technical Disclosure Bulletin*, vol. 17, p. 3346, 1975.
- [3] Y. B. W. Piugie, J. D. Manno, R. Christophe and C. Christophe, "Keystroke Dynamics based User Authentication using Deep Learning Neural Networks," in *2022 International Conference on Cyberworlds (CW)*, Kanazawa, 2022.
- [4] A. Foresi and R. Samavi, "User Authentication Using Keystroke Dynamics via Crowdsourcing," in *2019 17th International Conference on Privacy, Security and Trust (PST)*, Fredericton, 2019.
- [5] M. I. W. Pramana, Suhardi, N. B. Kurniawan and J. Sembiring, "Keystroke dynamics for authentication using dynamic time warping," in *2017 14th International Joint Conference on Computer Science and Software Engineering (ICSSSE)*, NakhonSiThammarat, 2017.
- [6] B. Aparna, H. Madasu, V. Shantaram and B. K. Panigrahi, "Keystroke Dynamics Based Authentication Using GFM," in *2018 IEEE International Symposium on Technologies for Homeland Security (HST)*, Woburn, 2018.
- [7] T.-L. Lin and Y.-S. Chen, "A Chinese Continuous Keystroke Authentication Method Using Cognitive Factors," in *2019 IEEE International Conference on Consumer Electronics - Taiwan (ICCE-TW)*, Yilan, 2019.
- [8] C. Rhea, B. Vishwajeet and C. Santhanakrishnan, "Behavioural Biometric Authentication using Keystroke Features with Machine Learning," in *2022 IEEE 19th India Council International Conference (INDICON)*, Kochi, 2022.
- [9] P. M. Koh and W. K. Lai, "Keystroke Dynamics Identification System using ABC Algorithm," in *2019 IEEE International Conference on Automatic Control and Intelligent Systems (2CACIS)*, Selangor, 2019.
- [10] N. Çevik, S. Akleylek and K. Y. Koç, "Keystroke Dynamics Based Authentication System," in *2021 6th International Conference on Computer Science and Engineering (UBMK)*, Ankara, 2021.
- [11] S. Singh, A. Inamdar, A. Kore and A. Pawar, "Analysis of Algorithms for User Authentication using Keystroke Dynamics," in *2020 International Conference on Communication and Signal Processing (ICCSP)*, Chennai, 2020.
- [12] J. Lambers, 10 / 2009. [Online]. Available: <https://www.math.usm.edu/lambers/mat610/sum10/lecture2.pdf>.
- [13] I. Kouretas and V. Paliouras, "Simplified Hardware Implementation of the Softmax Activation Function," in *2019 8th International Conference on Modern Circuits and Systems Technologies (MOCASST)*, Thessaloniki, 2019.
- [14] S. A. Alsubhani, M. Almushyti, N. Alghasham and F. Alkhudier, "Analysis of free-text keystroke dynamics for Arabic language using Euclidean distance," in *2016 12th International Conference on Innovations in Information Technology (IIT)*, Al Ain, 2017.
- [15] G. Waterman, *Linear Algebra I*, Oregon Institute of Technology, pp. 43-46.

Efficient Recognition of Complex Human Activities Based on Smartwatch Sensors Using Deep Pyramidal Residual Network

Sakorn Mekruksavanich¹ and Anuchit Jitpattanakul²

¹*Department of Computer Engineering, School of Information and Communication Technology
University of Phayao, Phayao, Thailand
sakorn.me@up.ac.th*

²*Intelligent and Nonlinear Dynamic Innovations Research Center, Department of Mathematics
Faculty of Applied Science, King Mongkut's University of Technology North Bangkok, Bangkok, Thailand
anuchit.j@sci.kmutnb.ac.th*

Abstract—Human activity recognition (HAR) has become a hot topic in artificial intelligence research due to the rapid development of smart wearable technologies. The goal of HAR is to accurately identify human actions using various data sources, such as video, images, and sensor data from wearable devices. Recent research in HAR has achieved promising results using learning-based methods, especially deep learning techniques. However, achieving state-of-the-art results remains a challenge for researchers. This study proposes a new approach to HAR that uses deep learning to classify human activities from smartwatch sensor data. We propose the use of a one-dimensional deep pyramidal residual network (1D-PyramidNet) for accurate human action identification. We evaluate the performance of our model against baseline models using the DHA dataset, a benchmark dataset for HAR that includes wristwatch sensor data for 11 complex human activities. The experimental results show that our 1D-PyramidNet model outperforms the baseline models, including CNN, LSTM, BiLSTM, GRU, and BiGRU. This confirms that the use of 1D-PyramidNet can improve the identification capabilities of HAR systems, achieving a maximum accuracy of 96.64%.

Keywords—smartwatch sensor, human activity recognition, deep learning, pyramidal residual network, wearable sensor

I. INTRODUCTION

Human activity recognition (HAR) is a rapidly growing field of research in artificial intelligence [1], [2]. Recent advances in HAR have led to the development of a variety of applications in healthcare and other domains, such as sport performance evaluation [3]–[6], rehabilitation monitoring [7], and abnormal activity detection [8], [9]. The development of smart wearable technology has played a major role in the growth of HAR research [10]. These devices provide a convenient and reliable way to collect large amounts of data about human activity. Smartphones and smartwatches are two of the most popular wearable devices, and they are equipped with a variety of sensors that can be used for HAR, such as accelerometers, gyroscopes, and magnetometers.

Wearable devices, such as smartphones and smartwatches, have become essential tools in our daily lives, gaining even greater importance due to continuous technological advancements. These wearables are continuously evolving,

aligning themselves more closely with consumers' needs and preferences. Manufacturers enhance their utility and performance by incorporating additional components and sensors into these devices [2]. The role of sensors in wearable technology has become increasingly significant as the technology becomes more sophisticated and attuned to its environment. Consequently, a vast majority of smartphones are now equipped with a wide array of integrated sensors. These sensors play a crucial role in collecting extensive amounts of data related to an individual's everyday activities and lifestyle [11].

In the last ten years, there has been a notable rise in the adoption of machine learning (ML) and deep learning (DL) techniques in the realm of HAR research [12]–[20]. However, the application of ML has faced limitations, particularly in the realm of feature extraction. This process has historically depended on human experts to pinpoint significant features within unprocessed sensor data. To overcome this limitation, a solution has been found by integrating convolutional operations at the onset of identification models. This incorporation facilitates the automatic extraction of features within DL systems, effectively addressing the constraint.

Recent research strongly indicates that techniques rooted in DL consistently outperform various traditional ML algorithms across a wide range of fields, including machine vision and audio characterization [21]. Deep neural networks (DNNs) possess the ability to utilize convolutional neural networks (CNNs) as tools for representing features [22]. This is achieved by progressively integrating multiple convolutional operations, which results in the construction of a hierarchical structure encompassing increasingly intricate aspects. The algorithms in this category exhibit the autonomy to independently learn such intricate feature patterns. Challenges related to time series data find effective resolution through the application of recurrent networks that incorporate long short-term memory (LSTM) cells, a specific type of recurrent system adept at handling sequential data [23]. By combining CNNs with LSTM networks within a unified architecture, there's the potential to achieve cutting-edge performance in

the field of speech identification. This architectural approach facilitates the incorporation of contextual interactions among components obtained through convolutional techniques. Nevertheless, it's important to note that the predominant focus of research in the realm of HAR remains centered around identifying fundamental actions or routine operations that occur regularly.

This study introduces an innovative deep pyramidal residual network named 1D-PyramidNet, designed specifically for intricate HAR. The efficacy of this novel network was comprehensively assessed in comparison to established DL models such as CNN, LSTM, Bidirectional LSTM (BiLSTM), Gated recurrent unit (GRU), and Bidirectional GRU (BiGRU). This comparative analysis employed the widely acknowledged DHA dataset as the benchmark public dataset. The results of the experiments indicate that incorporating the 1D-PyramidNet significantly improves the accuracy of HAR compared to the other models.

II. THE SENSOR-BASED HAR FRAMEWORK

The methodology utilized in this study revolves around the sensor-based HAR framework. This comprehensive framework involves four main stages: data collection, data pre-processing, data augmentation, and the development and assessment of models. These stages are visually depicted in Fig. 1.

A. Daily Human Activity (DHA) Dataset

The Daily Human Activity (DHA) dataset [24] is provided by the School of Electrical Engineering at Kookmin University in the Republic of Korea. This dataset originates from two willing participants who wore an Apple Watch smartwatch on their dominant hand for a continuous period of four weeks. Throughout this time frame, they were instructed to carry out 11 designated tasks as part of a predefined protocol. The intention behind this setup was to ensure that the users did not engage in multiple tasks simultaneously, maintaining a focused approach.

The smartwatch used for data capture was equipped with a tri-axial accelerometer, which allowed for the recording of activity data. The data collection was performed at a consistent rate of 10 Hz. Each of the specified exercises was conducted in three distinct settings. Within workplace scenarios, the study analyzed five potential activities. In kitchen environments, three activities were considered. Additionally, the study explored three outdoor activities.

Once the accelerometer data and corresponding activity labels were gathered, the smartwatch transmitted this information to an Apple iPhone smartphone via Bluetooth connectivity. For a detailed breakdown of the sample quantities for each activity, refer to Table I.

Fig. 2 depicts a visual representation of accelerometer data obtained from different tasks in the DHA dataset.

B. Data Pre-processing

The raw sensor data went through essential data pre-processing steps, which primarily encompassed noise elimination and data normalization. Before the data underwent

TABLE I
A LIST OF ACTIVITIES IN DHA DATASET

| Activity | Abbreviates for this work | Location | Number of Raw Accelerometer Data |
|--------------------|------------------------------|----------|-------------------------------------|
| Office work | Ow | Office | 62,711 |
| Reading | Re | Office | 36,976 |
| Writing | Wr | Office | 27,677 |
| Taking a rest | Tr | Office | 31,265 |
| Playing a game | Pg | Office | 51,906 |
| Eating | Ea | Kitchen | 46,155 |
| Cooking | Co | Kitchen | 10,563 |
| Washing dishes | Wd | Kitchen | 10,712 |
| Walking | Wa | Outdoors | 25,768 |
| Running | Ru | Outdoors | 6,452 |
| Taking a transport | Tt | Outdoors | 28,483 |

segmentation, it underwent preprocessing procedures. This segmentation approach employed consistent-width sliding frames lasting 10 seconds, incorporating a 50% overlap between consecutive frames, as depicted in Fig. 3.

C. Deep Learning Models

After the completion of data pre-processing, the data is subsequently employed to implement classification models rooted in the realm of DL. This approach entails constructing computational models comprising multiple layers that undergo progressive processing, with the goal of gaining insights into data representation at various levels of abstraction. These layered representations are constructed in a manner that links them to representations from preceding levels, facilitating the evolution of complex concepts from simpler ones. This research focuses on establishing foundational DL models, specifically those based on LSTM, GRU, and CNN. The models created in this study leverage the Adam optimizer in conjunction with the Categorical Cross-Entropy loss function.

This study introduces a novel one-dimensional pyramidal network, termed as 1D-PyramidNet, which is illustrated in Fig. 4. The main purpose of this network is to accurately classify road types using data gathered from wearable sensors integrated into smart glasses. The foundation of the 1D-PyramidNet is rooted in Han's deep pyramidal residual networks (DPRN) introduced in 2017 [25].

The 1D-PyramidNet enhances the performance of the residual unit model by optimizing it with principles from the residual network paradigm. At its core, the pyramidal network focuses on gradually increasing the feature map dimension in a progressive manner, rather than abruptly elevating it at each residual unit alongside down-sampling. Many deep CNN designs commonly adopt an approach where there's a sudden spike in feature map dimensions following a drop in size. Moreover, the feature map dimensions remain static until reaching a down-sampling layer.

To address this limitation, the network employs an incremental strategy for expanding feature map dimensions. Instead of doubling them within a single residual unit, the dimensions progressively grow. This tactic aims to distribute the computational load associated with feature map expan-

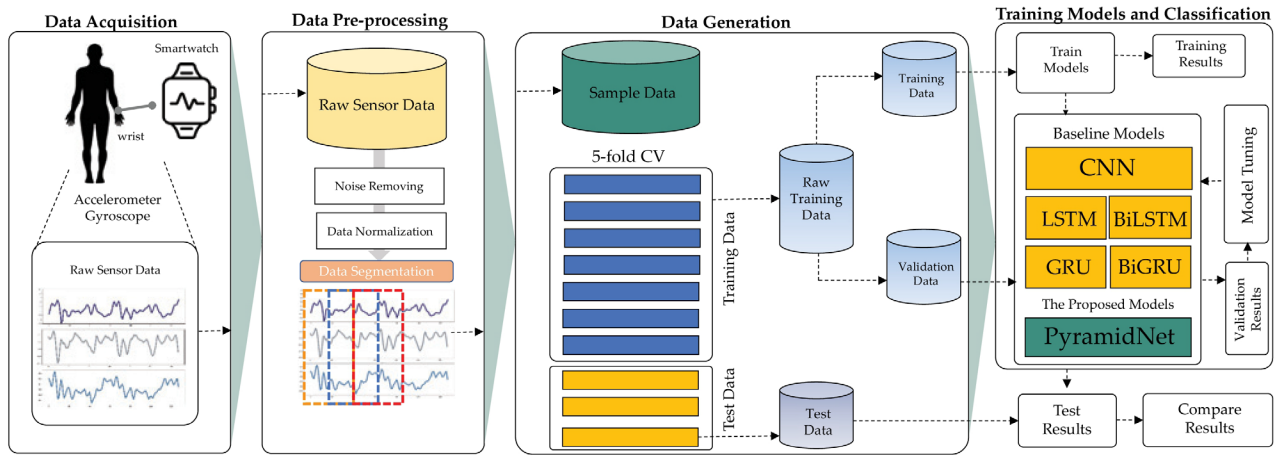


Fig. 1. The HAR framework based on smartwatch sensors used in this work.

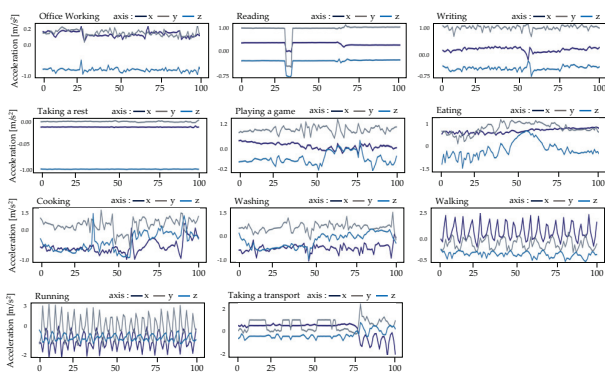


Fig. 2. Some samples of 11 daily human activities from DHA dataset.

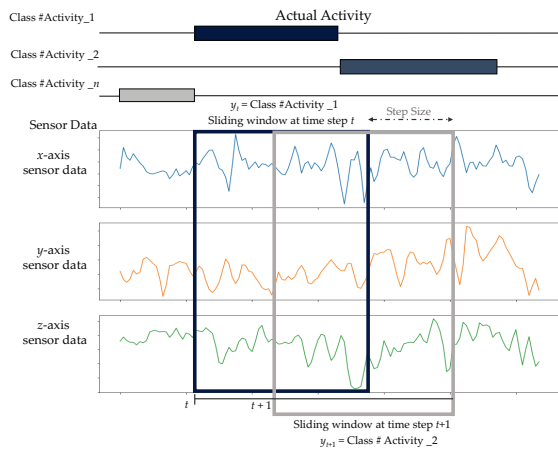


Fig. 3. A fixed-width Sliding window segmentation .

sion more evenly. The architecture's conceptual framework involves systematically increasing the channel count as the layer deepens, creating a pyramid-like design that broadens from its peak downwards.

In our investigation, we chose the proposed 1D-PyramidNet model, which leverages the additive PyramidNet model to incrementally augment the feature map dimension

geometrically.

The network design combines simple and residual networks using zero-padded identity-mapping shortcuts to elevate feature map dimensions. In deep residual network (ResNet) research [26], different shortcut concepts were examined, favoring identity-mapping shortcuts for their parameter-free nature that reduces overfitting risk, enhances generalization, and stabilizes gradient propagation during training. However, within 1D-PyramidNet, using identity mapping alone as a shortcut isn't feasible due to feature map dimension discrepancies in distinct units. Zero-padding shortcuts avoid overfitting issues and exhibit noteworthy generalization compared to alternatives. Employing a zero-padded identity-mapping shortcut (Fig. 5) significantly enhances the impact of the combined residual and plain network.

III. EXPERIMENTAL FINDINGS AND DISCUSSION

To evaluate the effectiveness of DL models utilizing sensor data from smartwatches, a series of investigations were conducted to assess the identification capabilities of the baseline model. The hyperparameters of CNN, GRU, LSTM, and the proposed 1D-PyramidNet were fine-tuned using the Bayesian optimization approach. The study employed tests to evaluate the performance of DL networks in terms of recognition, employing diverse metrics such as accuracy, precision, recall, and F1-score. Table II displays the accuracy and F1-score metrics obtained from various DL networks that were trained using the DHA dataset.

Based on the results outlined in Table II, it is evident that the 1D-PyramidNet demonstrated superior performance in comparison to conventional DL models, including CNN, LSTM, BiLSTM, GRU, and BiGRU. The 1D-PyramidNet achieved the highest level of accuracy, reaching an impressive 96.64%.

Upon analyzing the confusion matrix illustrated in Fig. 6, it becomes clear that the suggested 1D-PyramidNet model achieves classification accuracies exceeding 90% for all complex human behaviors, except for the cooking activity.

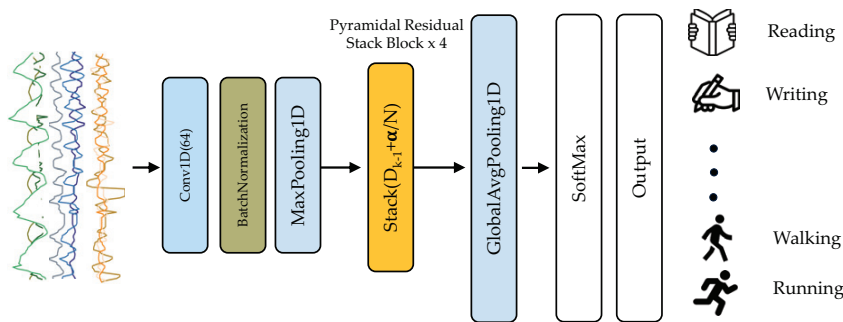


Fig. 4. The 1D-PyramidNet architecture used in this work.

TABLE II
IDENTIFICATION EFFECTIVENESS OF DL MODELS USED IN THIS WORK

| Model | Accuracy | Loss | F1-score |
|---------------|----------------|-------------|----------------|
| CNN | 95.61%(±1.05%) | 0.17(±0.03) | 93.48%(±1.90%) |
| LSTM | 89.74%(±1.66%) | 0.31(±0.04) | 86.21%(±2.32%) |
| BiLSTM | 89.19%(±2.07%) | 0.31(±0.07) | 85.78%(±1.90%) |
| GRU | 89.49%(±0.60%) | 0.31(±0.01) | 85.23%(±0.82%) |
| BiGRU | 90.55%(±0.44%) | 0.27(±0.02) | 87.29%(±1.06%) |
| 1D-PyramidNet | 96.64%(±0.99%) | 0.16(±0.05) | 95.48%(±0.70%) |

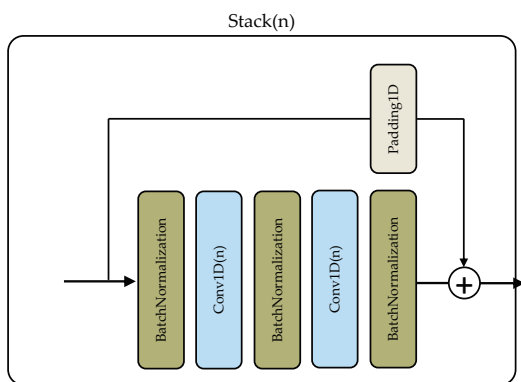


Fig. 5. The structure of a stack block used in the proposed 1D-PyramidNet.



Fig. 6. A confusion matrix of the 1D-PyramidNet.

This indicates that incorporating the pyramidal structure has the potential to enhance the efficacy of categorization tasks.

IV. CONCLUSION AND FUTURE WORKS

This investigation focuses on accurately identifying human activities using sensors seamlessly integrated into smart-watches. To achieve our primary research goal, we introduce the 1D-PyramidNet model as a crucial framework for discerning and classifying various human activities. The empirical findings from our study highlight the effectiveness of the 1D-PyramidNet model, yielding promising results in the complex field of sensor-based motion identification.

In our prospective scholarly endeavors, we envision an extension of our approach to encompass a hierarchical stratagem that transcends various DL architectures. These encompass, among others, the prominent ResNet, the innovative InceptionTime [27], and the transformative Temporal Transformer.

ACKNOWLEDGMENT

This research project was supported by Thailand Science Research and Innovation Fund; University of Phayao under Grant No. FF67-UoE-Sakorn; National Science, Research and Innovation Fund (NSRF); and King Mongkut’s University of Technology North Bangkok with Contract no. KMUTNB-FF-67-B-09.

REFERENCES

[1] E. Ramanujam, T. Perumal, and S. Padmavathi, “Human activity recognition with smartphone and wearable sensors using deep learning techniques: A review,” *IEEE Sensors Journal*, vol. 21, no. 12, pp. 13 029–13 040, 2021.

[2] E. De-La-Hoz-Franco, P. Ariza-Colpas, J. M. Quero, and M. Espinilla, “Sensor-based datasets for human activity recognition – a systematic review of literature,” *IEEE Access*, vol. 6, pp. 59 192–59 210, 2018.

- [3] S. Mekruksavanich, P. Jantawong, N. Hnoohom, and A. Jitpattanakul, "Badminton activity recognition and player assessment based on motion signals using deep residual network," in *2022 IEEE 13th International Conference on Software Engineering and Service Science (ICSSE)*, 2022, pp. 80–83.
- [4] M. Ezzeldin, A. S. Ghoneim, L. Abdelhamid, and A. Atia, "On understanding sports-har: Hierarchical, mobile, multi-sensor based classification of table-tennis strokes," in *2023 Intelligent Methods, Systems, and Applications (IMSA)*, 2023, pp. 142–148.
- [5] N. Hnoohom, P. Chotivatunyu, S. Mekruksavanich, and A. Jitpattanakul, "Recognition of shoulder exercise activity based on efficientnet using smartwatch inertial sensors," in *2022 3rd International Conference on Big Data Analytics and Practices (IBDAP)*, 2022, pp. 6–10.
- [6] S. Mekruksavanich and A. Jitpattanakul, "Sport-related activity recognition from wearable sensors using bidirectional gru network," *Intelligent Automation & Soft Computing*, vol. 34, no. 3, pp. 1907–1925, 2022.
- [7] J.-K. Kim, K. B. Lee, J.-C. Kim, and S. G. Hong, "Patient identification based on physical rehabilitation movements using skeleton data," in *2021 International Conference on Information and Communication Technology Convergence (ICTC)*, 2021, pp. 1572–1574.
- [8] W.-Y. Cheng, A. Scotland, F. Lipsmeier, T. Kilchenmann, L. Jin, J. Schjodt-Eriksen, D. Wolf, Y.-P. Zhang-Schaerer, I. F. Garcia, J. Siebourg-Polster, J. Soto, L. Verselis, M. Martin-Facklam, F. Boess, M. Koller, M. Grundman, A. Monsch, R. Postuma, A. Ghosh, T. Kremer, K. Taylor, C. Czech, C. Gossens, and M. Lindemann, "Human activity recognition from sensor-based large-scale continuous monitoring of parkinson's disease patients," in *2017 IEEE/ACM International Conference on Connected Health: Applications, Systems and Engineering Technologies (CHASE)*, 2017, pp. 249–250.
- [9] S. Mekruksavanich and A. Jitpattanakul, "Detection of freezing of gait in parkinson's disease by squeeze-and-excitation convolutional neural network with wearable sensors," in *2021 15th International Conference on Open Source Systems and Technologies (ICOSST)*, 2021, pp. 1–5.
- [10] E. Ramanujam, T. Perumal, and S. Padmavathi, "Human activity recognition with smartphone and wearable sensors using deep learning techniques: A review," *IEEE Sensors Journal*, vol. 21, no. 12, pp. 13 029–13 040, 2021.
- [11] R. San-Segundo, H. Blunck, J. Moreno-Pimentel, A. Stisen, and M. Gil-Martín, "Robust human activity recognition using smartwatches and smartphones," *Engineering Applications of Artificial Intelligence*, vol. 72, pp. 190–202, 2018.
- [12] S. Mekruksavanich and A. Jitpattanakul, "Hybrid convolution neural network with channel attention mechanism for sensor-based human activity recognition," *Scientific Reports*, vol. 13, no. 1, p. 12067, 2023.
- [13] S. Mekruksavanich, A. Jitpattanakul, K. Sitthithakerngkiet, P. Youplao, and P. Yupapin, "Resnet-se: Channel attention-based deep residual network for complex activity recognition using wrist-worn wearable sensors," *IEEE Access*, vol. 10, pp. 51 142–51 154, 2022.
- [14] R. Kolkar and V. Geetha, "Human activity recognition in smart home using deep learning techniques," in *2021 13th International Conference on Information & Communication Technology and System (ICTS)*, 2021, pp. 230–234.
- [15] S. Mekruksavanich and A. Jitpattanakul, "Rnn-based deep learning for physical activity recognition using smartwatch sensors: A case study of simple and complex activity recognition," *Mathematical Biosciences and Engineering*, vol. 19, no. 6, pp. 5671–5698, 2022.
- [16] N. Hnoohom, A. Jitpattanakul, I. You, and S. Mekruksavanich, "Deep learning approach for complex activity recognition using heterogeneous sensors from wearable device," in *2021 Research, Invention, and Innovation Congress: Innovation Electricals and Electronics (RI2C)*, 2021, pp. 60–65.
- [17] N. Hnoohom, A. Jitpattanakul, and S. Mekruksavanich, "Real-life human activity recognition with tri-axial accelerometer data from smartphone using hybrid long short-term memory networks," in *2020 15th International Joint Symposium on Artificial Intelligence and Natural Language Processing (iSAI-NLP)*, 2020, pp. 1–6.
- [18] S. Mekruksavanich and A. Jitpattanakul, "Fallnext: A deep residual model based on multi-branch aggregation for sensor-based fall detection," *ECTI Transactions on Computer and Information Technology (ECTI-CIT)*, vol. 16, no. 4, p. 352–364, Sep. 2022.
- [19] S. Mekruksavanich, P. Jantawong, A. Charoenphol, and A. Jitpattanakul, "Fall detection from smart wearable sensors using deep convolutional neural network with squeeze-and-excitation module," in *2021 25th International Computer Science and Engineering Conference (ICSEC)*, 2021, pp. 448–453.
- [20] S. Mekruksavanich, C. Promsakon, and A. Jitpattanakul, "Location-based daily human activity recognition using hybrid deep learning network," in *2021 18th International Joint Conference on Computer Science and Software Engineering (JCSSE)*, 2021, pp. 1–5.
- [21] F. S. Shaqwi, L. Audah, M. H. Hassan, M. A. Jubair, M. H. Abd Wahab, and S. A. Mostafa, "A concise review of deep learning deployment in 3d computer vision systems," in *2021 4th International Symposium on Agents, Multi-Agent Systems and Robotics (ISAMSR)*, 2021, pp. 157–160.
- [22] K. O'Shea and R. Nash, "An introduction to convolutional neural networks," 2015.
- [23] S. Hochreiter and J. Schmidhuber, "Long short-term memory," *Neural Comput.*, vol. 9, no. 8, p. 1735–1780, nov 1997.
- [24] M.-C. Kwon and S. Choi, "Recognition of daily human activity using an artificial neural network and smartwatch," *Wireless Communications and Mobile Computing*, vol. 2018, pp. 1–9, 06 2018.
- [25] D. Han, J. Kim, and J. Kim, "Deep pyramidal residual networks," in *2017 IEEE Conference on Computer Vision and Pattern Recognition (CVPR)*, 2017, pp. 6307–6315.
- [26] K. He, X. Zhang, S. Ren, and J. Sun, "Deep residual learning for image recognition," 2015.
- [27] H. Ismail Fawaz, B. Lucas, G. Forestier, C. Pelletier, D. F. Schmidt, J. Weber, G. I. Webb, L. Idoumghar, P.-A. Muller, and F. Petitjean, "Inceptiontime: Finding alexnet for time series classification," *Data Min. Knowl. Discov.*, vol. 34, no. 6, p. 1936–1962, nov 2020.

Leveraging Support Vector Machine for Sports Injury Classification

Thattapon Surasak

*Dept. of Computer and Information Science
Faculty of Applied Science
King Mongkut's University
of Technology North Bangkok
Bangkok, Thailand
thattapon.s@sci.kmutnb.ac.th*

Phornnatee Praking

*Dept. of Computer and Information Science
Faculty of Applied Science
King Mongkut's University
of Technology North Bangkok
Bangkok, Thailand
s6304062663062@email.kmutnb.ac.th*

Kotcharat Kitchat

*Dept. of Computer Science
and Information Engineering
National Central University
Taoyuan, Taiwan
kotcharat@ieee.org*

Abstract—This study explores the utility of Support Vector Machines (SVM) for the classification of injuries in Athletes including tennis, table tennis, and badminton. The primary objective of this research was to develop an automated method to detect between normal and injury pose, providing a potentially powerful tool for early detection. In other words, this research is the pioneer study to represent one another solution for sports injury classification using the image data apart from the current approaches that might be focused on the sensor-based. Therefore, we collect a dataset from various social media across the three sports, labeled into two categories: “Normal” and “Injury”. The SVM model was trained on this dataset, and tuned to optimize its performance in distinguishing the two classes.

Achieving an accuracy of 96.63%, the result demonstrates that the SVM model can effectively identify injury patterns in the considered sports. The implications of this study are significant, presenting the initial steps towards applying computer vision tasks in sports topics. By demonstrating the feasibility of an SVM-based approach to injury detection in these racket sports.

Index Terms—Support Vector Machines, Sports Injury Classification, Racket Sports

I. INTRODUCTION

Computer vision is a branch of Artificial Intelligence (AI) that enables computers to understand visual data, such as images or videos. Its objective is to replicate the remarkable ability of human vision by developing algorithms and models that support the analysis, processing, and extraction of meaningful insights from digital visual information [1], [2]. The first experiment with computer vision took place in the 1950s [3], leveraging the first generation of neural networks innovation to detect edges and corners in different objects and classify them into simple shapes [4], such as round, rectangular, etc. In the 1990s, as the internet rapidly expanded, huge volumes of images were made available online, providing a valuable resource for the development of machine learning algorithms in computer vision [5]. Researchers began leveraging machine learning techniques to develop algorithms and models that enable computers to learn, make predictions, and make decisions without explicit programming. Machine learning techniques are based on the concept that machines can automatically learn from data and improve their performance over time [6].

The current state of AI systems is highly efficient, enabling them to process results and leverage image understanding for various benefits. Computer vision technology encompasses multiple tasks that find application in various situations, such as image segmentation, object detection, facial recognition, edge detection, pattern detection, and image classification.

Image classification is also a field of computer vision that can separate images into each category. By an algorithm or model that was trained to recognize and assign labels to different objects scenes, or patterns within an image. Like a human skill of visually which uses the brain to analyze and memorize the visual features, such as shapes, colors, and textures, to identify what they are seeing. Then, classify and assign labels to different objects or scenes based on knowledge and experiences. Moreover, image classification can handle large amounts of visual data better than humans.

In the area of sports, the application of image classification techniques for injury detection is currently lacking. This project seeks to address this gap by investigating the utilization of image classification in the context of Sports injury classification using deep learning. The primary objective is to develop a system capable of analyzing images of sports players. By detecting postures that could potentially lead to injury. Sports in this work consist of a net divided between two sides of players and a racket used for hitting the ball, including tennis, badminton, and table tennis.

II. RELATED WORK

Cortes and Vapnik [7] presented a Support Vector Machine (SVM) as a kernel-based machine learning show for classification and regression tasks [8], [9]. In the context of the SVM algorithm, each data item is represented as a point in an n-dimensional space, where n denotes the number of features. The value of each feature determines the position of the point in this space. Next, a hyperplane is computed to divide the data points into different groups, with a focus on maximizing the margin between the points belonging to each group [10]. SVM has remarkable points of interest because it utilizes the thought Structural Risk Minimization (SRM) principle, which gives superior generalization as well as decreases error within the training stage.

Worsey et al. [11] proposed utilizing supervised machine learning techniques in the realm of athlete monitor-

ing. They emphasized the importance of individual-specific models over generic, one-size-fits-all models, pointing out that unique athlete characteristics can significantly influence model performance. Their work was based on a dataset collected over multiple seasons from professional rugby league athletes. They demonstrated that individual-specific models outperformed population-based models in injury prediction. In their experiment, the Granular Support Vector Machine (GSVM) outperforms the other machine learning techniques. However, they required the Inertial Measurement Unit (IMU) sensor to collect specific body force, angular rate, and orientation as one of the input features.

Falcone et al. [12] explored an unconventional approach to diagnosing mild traumatic brain injuries. They used a Support Vector Machine (SVM) to analyze isolated vowel sounds from patients, proving that non-visual, alternative datasets can be efficiently employed in injury diagnosis and classification.

In the paper titled “Hybridized Hierarchical Deep Convolutional Neural Network for Sports Rehabilitation Exercises [13],” Dapeng Tang introduces the HHDCNN as a solution for motion capture and image segmentation in sports exercise rehabilitation. Existing solutions lack versatility and robustness, so the HHDCNN aims to increase accuracy in this area. The paper also emphasizes the importance of rehabilitation assessment in healthcare and presents the HHDCNN as a promising tool for enhancing sports rehabilitation effectiveness.

Chin et al. [14] focused on the classification of severity levels for lower limb joint injuries, presenting a comprehensive study of different machine learning algorithms and their effectiveness in predicting the severity of these injuries. They applied the Electrogoniometer (EGM) to extract the limitations of the hip, knee, and ankle joint Range of Motion (ROM) during body movement. The Artificial Neural Networks Scaled Conjugate Gradient (ANN-SCG) achieved the highest performance in classifying the severity levels of lower limb joint injuries.

Zelic et al. [15] conducted a study on using machine learning techniques to diagnose sports injuries by extracting knowledge from medical databases. The research focused on analyzing injuries in athletics and handball, aiming to enhance data gathering, intelligent analysis, and diagnostic decision support. Various machine learning algorithms were compared, with the naive Bayesian classifier using fuzzy discretization of numerical attributes performing the best in classification accuracy and explanation capability. The resulting expert system provides a visual representation of the knowledge, making it a practical tool for diagnosing sports injuries.

Sun et al. [16] developed an App notification system, integrated with IoT, to monitor the condition of sports equipment like air walkers. The study employed an empirical SVM to predict the equipment’s status, converting dynamic signals from the time domain to the frequency domain using Fourier transform. By comparing SVM to decision tree C4.5 and normal SVM methods, they found that the empirical SVM demonstrated 100% sensitivity and specificity in classifying

the status of air walkers. The system uses Bluetooth sensors for data collection and a cloud database for storage. The aim of the research is to increase regular exercise rates by alerting users if the equipment is nearing failure, and the proposed method was found to be more effective than decision tree classification.

O. V. Ramana Murthy and Roland Goecke [17] reviewed key studies in soccer video analysis and low-level features for recognizing actions such as player falls. They discuss the significance of automatically detecting these events to assist coaches with higher-level tasks, highlighting five major causes of player injuries. The study also explores classification using a Bag-of-Words approach and emphasizes the commonality of foot and leg injuries in soccer, as well as intrinsic and extrinsic risk factors. The document serves as an overview of important research in the realm of soccer injury analysis and classification.

Yunping Xia and Yunxiang Fan [18] introduced the application of motor imaging brain-computer interface (BCI) in conjunction with the Internet of Health Things technology for the rehabilitation of paralysis and stroke patients. Their system includes modules such as “infusion monitoring,” “disease call interconnection,” and “PDA interconnection,” aimed at comprehensive management of nursing work. The sports rehabilitation training system they described receives EEG data, processes it using MATLAB for feature extraction and classification, and provides feedback to both the system and the subjects. Additionally, the system features non-feedback training, feedback training, and related BCI game modules to promote sports imagination training and facilitate successful rehabilitation.

Apostolou et al. [19] conducted a study focusing on data analytics in football, with the specific aim of predicting player positions, goal-scoring performance, and the number of shots during matches. By utilizing accumulated data and suitable algorithms, such as Random Forest, which performed notably well, the results demonstrated high accuracy in their predictions. Additionally, the study found a correlation between the number of shots taken and goal-scoring probability. The research underscores the potential benefits of sports analytics in enhancing team tactics and individual player performance.

From previous research, it’s evident that Support Vector Machine (SVM) has become one of the popular techniques used in injury classification, predominantly utilizing signal data, audio data, and data collected from various sensors in different fields. Unlike these approaches, our study aims to extend the utilization of machine learning, specifically SVM, into image-based sports injury classification, thereby exploring new dimensions in the application of this technique.

III. METHOD

The proposed method for classifying sports injuries uses an image as the input and returns the most likely class (injury or normal posture) of the subject in the given image. It is composed of two main steps:

- A. Data Preprocessing
- B. Data Augmentation

The detailed description of each step is explained in the following subsection.

A. Data Preprocessing

Our dataset was assembled by manually capturing screenshots of athletes from various social media platforms. After obtaining these images, we used the YOLOv5 [20] algorithm to extract individual players from each image. Since the output from YOLOv5 resulted in various sizes of images, we subsequently resized them to the same size. This standardization ensured that the images were compatible with our model, allowing it to learn effectively. The step of preprocessing is presented in Fig. 1

B. Data Augmentation

The data collected from any source is incomplete, noisy, and changeable data, leading to data analysis problems. Thus, it is necessary to correct the issues before using the data [21]. Data augmentation is a series of strategies for enlarging and improving the size and shape of an image. It's a method for creating new data with different data orientations. Data augmentation solves two concerns for researchers: it increases the variety of training samples and minimizes overfitting [22], [23]. In this paper, we focus on geometric transformation-based image augmentation. This geometric transformation technique transformed images based on their comparable, such as Euclidean, Affine, projectile, etc. [23], [24]

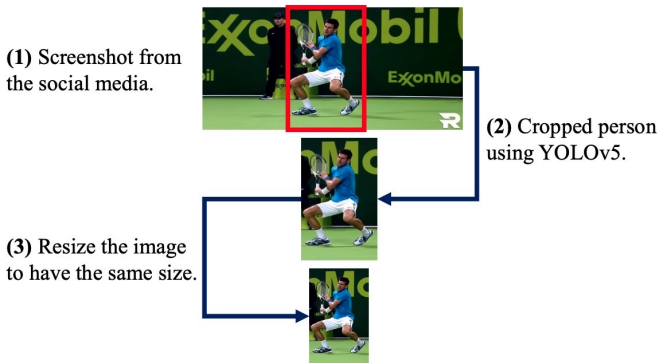


Fig. 1. Steps of preprocessing.

IV. EXPERIMENT

A. Dataset

We collected images through screenshots from various social media platforms, focusing on both injury and normal postures in sports such as badminton, tennis, and table tennis. We successfully gathered 118 images of injury postures (badminton 32, tennis 63, and table tennis 23) and 1006 images of normal postures (badminton 339, tennis 459, and table tennis 208). The example of a sports dataset is illustrated in Fig. 2



Fig. 2. The example of our sports dataset.

B. Experiment Setup

Referring to the imbalance in the number of images between the injury and normal classes, we applied an augmentation solution to address this problem. This solution consists of rotating, flipping, channel shifting, zooming out, and adjusting the brightness to increase the number of images in the injury class. To avoid unusual human poses, we set limits for rotating to only 10 degrees and allowed only horizontal flips for the same reason. After applying the augmentation technique, we received more injury images, bringing the count closer to that of the normal images. The comparison of the number of injury posture images before and after applying data augmentation is shown in Table I. We then divided the dataset into training and testing sets. Considering the augmented injury images, we designated the original injury images as the test set, representing approximately 10% of the total images. To maintain a similar distribution, we also selected 10% of the normal images for the test set. Therefore, our dataset was split in a 90:10 ratio, with 90% used for training and the remaining 10% reserved for testing.

TABLE I
COMPARISON OF THE NUMBER OF INJURY POSTURE IMAGES BEFORE AND AFTER APPLYING DATA AUGMENTATION.

| Sports | Before | After |
|--------------|--------|-------|
| Badminton | 32 | 207 |
| Tennis | 63 | 685 |
| Table tennis | 23 | 97 |
| Total | 118 | 989 |

Our experiments were conducted on Google Colaboratory (Colab), a free cloud service provided by Google. The specific hardware and software details are as follows:

- **Hardware:** Google Colab provides a virtual machine with a hardware setup that includes a CPU, RAM, and a GPU. Although the exact specifications may vary, at the time of the study, the GPU was a Tesla T4, and the CPU was an Intel(R) Xeon(R) CPU @ 2.00GHz. Please note that these specifications can change as Google updates its Colab platform.

- **Software:** Google Colab is a Jupyter Notebook environment that runs entirely in the cloud. It includes Python 3 and a range of preinstalled libraries. For our machine learning tasks, we utilized sklearn, and for data analysis and image processing, we used numpy, pandas, matplotlib, and cv2. Our experiments were conducted in this environment using Python 3.

This environment was chosen due to its ease of access, the provision of GPUs, and the capability to share and collaborate on Jupyter notebooks, which made it suitable for conducting our image analysis experiments.

V. RESULTS

A. Evaluation Metrics

In our experiment, we rely on several key metrics, including accuracy, precision, recall, and the F1 score. Accuracy is the standard measurement in classification to evaluate the accuracy of a technique. Precision, on the other hand, is a measure that indicates the proportion of positive identifications that were actually correct. The precision is defined as follows:

$$Precision = \frac{TruePositive}{TruePositive + FalsePositive} \quad (1)$$

Recall essentially represents the proportion of the actual positive instances that were identified correctly by the model. The recall is defined as follows:

$$Recall = \frac{TruePositive}{TruePositive + FalseNegative} \quad (2)$$

- True Positive (TP) is an outcome where the model correctly predicts the positive class. In other words, if the actual class is positive and the model also predicts a positive class.
- False Positive (FP) is an outcome where the model incorrectly predicts the positive class. If the actual class is negative but the model predicts a positive class.
- False Negatives (FN) is the number of positive instances that the model incorrectly identified as negative.

The F1 score is a statistical metric that merges precision and recall, yielding a composite measure of a model's overall performance. This is particularly essential when dealing with imbalanced class scenarios. The formal definition of the F1 score is:

$$F1score = \frac{2 \times (Precision \times Recall)}{Precision + Recall} \quad (3)$$

B. Results

The results of SVM on the sports dataset are presented in Table II.

TABLE II
SUPPORT VECTOR MACHINE ON SPORTS DATASET

| Accuracy | Precision | Recall | F1 score |
|----------|-----------|--------|----------|
| 96.63 | 98.32 | 95.12 | 96.69 |

We evaluated SVM using accuracy, precision, recall, and the F1 score, with SVM achieving a 96.63% accuracy rate.

Moreover, precision, recall, and F1 score were all above 95%. These results demonstrate that SVM is suitable for classifying our sports dataset. Additionally, we calculated the Receiver Operating Characteristic Curve (ROC) to evaluate the model's discriminative ability, as shown in Fig. 3.

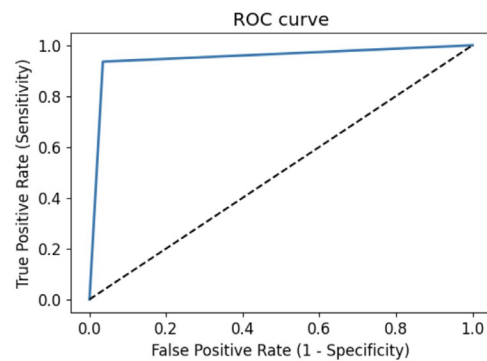


Fig. 3. The ROC curve of SVM on sports dataset.

VI. CONCLUSION

This study demonstrates the potential of Support Vector Machines (SVM) for the classification of sports injuries in athletes from racket sports. This is the pioneer study to propose another method for sports injury classification using picture data, in addition to the current approaches that may be sensor-based. Our automated method, capable of distinguishing between normal and injury postures, achieves a promising accuracy of 96.63%. The SVM model effectively identifies injury patterns in tennis, table tennis, and badminton, pointing to the significant role machine learning can play in sports medicine and injury prevention.

Future studies could focus on refining the SVM model by including more categories of injury types and expanding the sports under consideration. It would also be worthwhile to investigate the integration of this approach into real-time sports training and medical diagnostics systems, which could contribute to improved health outcomes and performance for athletes. Overall, our research represents a crucial step forward in the application of computer vision and machine learning in the field of sports.

ACKNOWLEDGEMENT

The authors would like to thank Prof. Min-Te Sun, National Central University, Taiwan for all the research equipment and support.

DISCLOSURE AND CONFLICTS OF INTEREST

The authors have no conflicts of interest to declare. All co-authors have seen and agree with the contents of the manuscript and there is no financial interest to report. We certify that the submission is original work and is not under review at any other publication.

REFERENCES

- [1] A. A. Gumbs, V. Grasso, N. Bourdel, R. Croner, G. Spolverato, I. Frigerio, A. Illanes, M. Abu Hilal, A. Park, and E. Elyan, "The advances in computer vision that are enabling more autonomous actions in surgery: A systematic review of the literature," *Sensors*, vol. 22, no. 13, 2022. [Online]. Available: <https://www.mdpi.com/1424-8220/22/13/4918>
- [2] I. H. Sarker, "Ai-based modeling: Techniques, applications and research issues towards automation, intelligent and smart systems," *SN Computer Science*, vol. 3, no. 2, p. 158, 2022.
- [3] J. J. Gibson, "The perception of the visual world." 1950.
- [4] L. Jiao, R. Zhang, F. Liu, S. Yang, B. Hou, L. Li, and X. Tang, "New generation deep learning for video object detection: A survey," *IEEE Transactions on Neural Networks and Learning Systems*, vol. 33, no. 8, pp. 3195–3215, 2022.
- [5] L. Himanen, A. Geurts, A. S. Foster, and P. Rinke, "Data-driven materials science: status, challenges, and perspectives," *Advanced Science*, vol. 6, no. 21, p. 1900808, 2019.
- [6] N. Sharma, R. Sharma, and N. Jindal, "Machine learning and deep learning applications-a vision," *Global Transitions Proceedings*, vol. 2, no. 1, pp. 24–28, 2021, 1st International Conference on Advances in Information, Computing and Trends in Data Engineering (AICDE - 2020). [Online]. Available: <https://www.sciencedirect.com/science/article/pii/S2666285X21000042>
- [7] C. Cortes and V. Vapnik, "Support-vector networks," *Machine Learning*, vol. 20, pp. 273–297, 1995.
- [8] J. Cervantes, F. Garcia-Lamont, L. Rodríguez-Mazahua, and A. Lopez, "A comprehensive survey on support vector machine classification: Applications, challenges and trends," *Neurocomputing*, vol. 408, pp. 189–215, 2020.
- [9] M. Tanveer, T. Rajani, R. Rastogi, Y.-H. Shao, and M. Ganaie, "Comprehensive review on twin support vector machines," *Annals of Operations Research*, pp. 1–46, 2022.
- [10] K. Kitchat, K. Limjumroonrat, and T. Surasak, "Twitter sentiment analysis towards covid-19 vaccines: A case study in new york city," in *2021 IEEE 2nd International Conference on Technology, Engineering, Management for Societal Impact using Marketing, Entrepreneurship and Talent (TEMSMET)*, 2021, pp. 1–6.
- [11] M. T. Worsey, H. G. Espinosa, J. B. Shepherd, and D. V. Thiel, "One size doesn't fit all: Supervised machine learning classification in athlete-monitoring," *IEEE Sensors Letters*, vol. 5, no. 3, pp. 1–4, 2021.
- [12] M. Falcone, N. Yadav, C. Poellabauer, and P. Flynn, "Using isolated vowel sounds for classification of mild traumatic brain injury," in *2013 IEEE International Conference on Acoustics, Speech and Signal Processing*, 2013, pp. 7577–7581.
- [13] D. Tang, "Hybridized hierarchical deep convolutional neural network for sports rehabilitation exercises," *IEEE Access*, vol. 8, pp. 118 969–118 977, 2020.
- [14] L. C. Chin, C. Y. Fook, A. S. A. Nasir, S. N. Basah, M. Y. Din, and Z. Zainuddin, "Classification of the severity level for lower limb joint injuries," in *2020 IEEE-EMBS Conference on Biomedical Engineering and Sciences (IECBES)*, 2021, pp. 267–270.
- [15] I. Zelic, I. Kononenko, N. Lavrac, and V. Vuga, "Diagnosis of sport injuries with machine learning: explanation of induced decisions," in *Proceedings of Computer Based Medical Systems*, 1997, pp. 195–199.
- [16] W.-C. Sun, J.-C. Hung, and C.-P. Huang, "Implementation of svm broken prediction notification system with park sport equipment," in *2017 International Conference on Applied System Innovation (ICASI)*, 2017, pp. 99–102.
- [17] O. Ramana Murthy and R. Goecke, "Injury mechanism classification in soccer videos," in *2015 IEEE International Conference on Computer Vision Workshop (ICCVW)*, 2015, pp. 774–779.
- [18] Y. Xia and Y. Fan, "Security analysis of sports injury medical system based on internet of health things technology," *IEEE Access*, vol. 8, pp. 211 358–211 370, 2020.
- [19] K. Apostolou and C. Tjortjijis, "Sports analytics algorithms for performance prediction," in *2019 10th International Conference on Information, Intelligence, Systems and Applications (IISA)*, 2019, pp. 1–4.
- [20] Ultralytics, "Ultralytics/yolov5: Yolov5 in pytorch gt; onnx gt; coreml gt; tf lite." [Online]. Available: <https://github.com/ultralytics/yolov5>
- [21] K. Maharana, S. Mondal, and B. Nemade, "A review: Data pre-processing and data augmentation techniques," *Global Transitions Proceedings*, vol. 3, no. 1, pp. 91–99, 2022.
- [22] R. Takahashi, T. Matsubara, and K. Uehara, "Data augmentation using random image cropping and patching for deep cnns," *IEEE Transactions on Circuits and Systems for Video Technology*, vol. 30, no. 9, pp. 2917–2931, 2020.
- [23] C. Khosla and B. S. Saini, "Enhancing performance of deep learning models with different data augmentation techniques: A survey," in *2020 International Conference on Intelligent Engineering and Management (ICIEM)*. IEEE, 2020, pp. 79–85.
- [24] S. Gupta and A. Gupta, "Dealing with noise problem in machine learning data-sets: A systematic review," *Procedia Computer Science*, vol. 161, pp. 466–474, 2019.

Classification of Acute Intracerebral Hemorrhage Using Radiomics on Brain Computed Tomography Images

Phattanut Thabarsa
Master's Degree Program in
Data Science
Faculty of Engineering
Chiang Mai University
Chiang Mai, Thailand
phattanut_th@cmu.ac.th

Withawat Vuthiwong, M.D.
Department of Radiology
Faculty of Medicine
Chiang Mai University
Chiang Mai, Thailand
withawat.vuthiwong@cmu.ac.th

Salita Angkurawaranon, M.D.
Department of Radiology
Faculty of Medicine
Chiang Mai University
Chiang Mai, Thailand
salita.ang@cmu.ac.th

Kittisak Unsrison, M.D.
Department of Radiology
Faculty of Medicine
Chiang Mai University
Chiang Mai, Thailand
kittisak.unsrison@cmu.ac.th

Chakri Madla, M.D.
Department of Radiology
Faculty of Medicine
Chiang Mai University
Chiang Mai, Thailand
chakri.madla@cmu.ac.th

Papangkorn Inkeaw, Ph.D.
Data Science Research Center
Department of Computer Science
Faculty of Science
Chiang Mai University
Chiang Mai, Thailand
papangkorn.i@cmu.ac.th

Abstract— Acute intracerebral hemorrhage (ICH) entity accounts for 10 to 15% of all strokes and is associated with a higher mortality rate ischemic stroke or subarachnoid hemorrhage. Causes of ICH are divided into primary, and secondary, including vascular malformation and tumorous. Primary ICH accounts for approximately 80% of all ICH cases. Vascular anomalies rank as the second most common cause of spontaneous ICH overall. Furthermore, hemorrhage resulting from brain tumors can occur in up to 10% of all primary or metastatic tumors. Early recognizing of these three causes of bleeding is critical for clinicians in precise diagnosis, effective treatment management, and helps avoid delayed diagnosis. We proposed a radiomics approach for classifying multiple causes of acute ICH as vascular malformation, tumorous, and primary-related hematoma. Non-contrast brain computed tomography with clinical features was used as input. The regions of both hematoma and perihematomal edema were delineated by using manual segmentation approach. Four feature selection methods were adopted. Also, three classification models were investigated in this study. The results showed that using the features selected by F-value applied with SVM classifier outperformed the other models, achieving weighted average accuracy (\pm SD) of 0.84 (\pm 0.07). Additionally, the model demonstrated average sensitivity and positive predictive value of 0.84 (\pm 0.06) and 0.86 (\pm 0.05), respectively. We also evaluate the overall performance of discriminating each class from the rest using AUC. The result suggested that our proposed model achieved the weighted average AUC of 0.90. Our proposed method highlights the potential in identifying multiple causes of acute and nontraumatic ICH, which has not been previously explored.

Keywords— Acute Intracerebral Hemorrhage, Radiomics, Machine Learning

I. INTRODUCTION

Spontaneous nontraumatic intracerebral hemorrhage (ICH) entity accounts for 10 to 15% of all strokes and is associated with a higher mortality rate than either ischemic stroke or subarachnoid hemorrhage [1]. ICH is more common

in Asians, advanced age, male sex, and low- and middle-income countries [2]. Causes of ICH are divided into primary and secondary. Primary ICH accounts for about 80% of ICH cases and is caused by spontaneous rupture of small vessels associated with chronic hypertension or amyloid angiopathy [3]. Secondary ICH is associated with several congenital and acquired conditions such as vascular anomalies, coagulopathies, tumors, and various drug therapies.

Vascular anomalies are the second most common cause of spontaneous ICH overall. Aneurysms, arteriovenous malformations (AVMs), cavernomas, dural arteriovenous fistulas, and venous malformations can result in secondary spontaneous ICH. AVMs most commonly present with intracranial hemorrhage. However, hemorrhage and its mass effect can further obscure delineation of an AVM on Computed Tomography (CT) [4].

Hemorrhage resulting from brain tumors can occur in up to 10% of all primary or metastatic tumors. A recent pooled analysis identified 18 reported cases of glioblastoma-induced hemorrhage that were misdiagnosed as hypertensive ICHs, leading to significant diagnostic delays in two-thirds of the cases [5]. Therefore, early recognizing of three above-mentioned causes of bleeding is critical for clinician in precise diagnosis and treatment management.

Non-contrast computed tomography (NCCT) is the most typically used neuroimaging tool for detecting acute brain hemorrhage since its advantage of readily accessible [6] and its high sensitivity. Radiologists need to repeatedly interpret multiple slices of CT to investigate the location, the appearance of hematomas and the occurrence of perihematomal edema (PHE), or other characterizations regarding to suspected hemorrhage causes, which can lead to workload problems and delayed management. To improve the clinical workflows, radiomics, a quantitative approach is adopted in many studies [7-11].

Radiomics approach aims to extract quantitative image properties by using mathematical methods. Generally, the

radiomics process can be divided into five main steps namely image acquisition, image segmentation, feature extraction, feature selection and model construction [12]. The output of each step can be affected from earlier step and may influence prediction eventually. Therefore, it is necessary to perform the radiomics process prudently, which means correctly segmenting, selecting relevant and stable features, and optimizing machine learning model.

Previous studies have investigated the efficacy of the radiomic approach in identifying non-traumatic ICH causes on brain NCCT imaging [7-9] as well as differentiating tumor types using Magnetic Resonance Imaging (MRI)-based techniques [10, 11], which these studies provide binary outcomes. Nonetheless, in real-world scenarios, patients might be suspected of several causes of ICH and cannot be differentiated into binary groups. Therefore, this study aims to apply a radiomics approach for classifying multiple causes of acute ICH as vascular malformation, tumorous, and primary-related hematoma, on NCCT imaging since it is preferred imaging tool for screening nontraumatic ICH [13]. Quantitative image features, as well as demographic variables will be investigated and used to construct machine learning algorithms for multiclass classification. Lastly, predictive performance of the models will be assessed using accuracy, sensitivity, positive predictive values (PPV) and area under the ROC curve (AUC). This study implies that using demographic data as well as quantitative features from medical images could be utilized to build an effective and automated tool to support clinician's decision-making.

II. MATERIALS AND METHODS

A. Study Population

This retrospective study was approved and monitored by the Ethics Committee of Faculty of Medicine, Chiang Mai University, Chiang Mai, Thailand. Initial brain NCCT scans with a 3-5 mm slice thickness in axial view, as well as demographic data (i.e., age and gender) of patients who were diagnosed with non-traumatic ICH were collected from the radiology report database of Maharaj Nakorn Chiang Mai Hospital between January 2010 and May 2022. The brain NCCT scans were performed by using Toshiba Aquilion 16-slice CT, or 64-slice Siemens Definition MDCT (Germany), or 192-slice Siemens Definition DSCT (Germany).

The inclusion criteria for our study were as follows: (1) single nontraumatic acute ICH lesion of vascular and primary-related ICH, while allowing for tumorous-related ICH in cases of multiple lesions, ultimately selecting the largest lesion among all the presented lesions, (2) initial NCCT imaging performed from the onset of symptoms for tumorous-related ICH, and within 24 hours from the onset of symptoms for vascular malformation and primary causes-related ICH, (3) confirmation of the cases of ICH, including MRI follow-up imaging, additional digital subtraction angiography (DSA), or surgery pathological report. Conversely, patients with subarachnoid hemorrhage or intraventricular hemorrhage-predominant, single ICH, and low-quality NCCT images due to severe motion artifact and/or metallic artifact were excluded.

B. Feature Extraction

The radiomics features were extracted from regions of ICH and PHE that were manually delineated by consensus of

three expert neuroradiologists using 3D Slicer software. The PyRadiomics [14] package was used to calculate the feature. The radiomics features were divided into 3 classes namely 1) first-order features 2) shape-based features and 3) textural features. Each feature class are briefly described as follows:

1) *First-order features* represent the fundamental characteristics or properties of an image without considering their spatial dependencies [15]. They were calculated from grey-level histogram of an image or a region of interest, describing the distribution or frequency of voxel intensities [16] such as average, standard deviation, skewness, etc.

2) *Shape-based features* provide a straightforward way to describe geometric attributes of objects or regions of interest. They can be analyzed as two or three dimensions, which offer distinct perspectives and advantages in capturing the full essence of an object's shape [17]. The features include volume, sphericity, compactness, diameter, axis, etc.

3) *Textural features* characterize the arrangement or pattern within images or regions of interest by capturing the spatial information of grey-level values [15]. The spatial properties include spatial relationships between voxel pairs based on gray-level values (using Gray Level Co-occurrence Matrix: GLCM [18]), neighboring voxel dependencies (Gray Level Dependence Matrix: GLDM [19]), voxel runs with the same gray-level value (Gray Level Run Length Matrix: GLRLM [20]), the size and distribution of connected regions with specific gray-level values (Gray Level Size Zone Matrix: GLSZM [21]), or local intensity differences between voxels and their neighbors (Neighboring Gray Tone Difference Matrix: NGTDM [22]).

Additionally, we also applied image filtering methods to original images to emphasize image properties such as details, edges, or textures. The method includes wavelet transform [23] and Laplacian of Gaussian (LOG) [24] used for enhancing textures. We utilized 1-level of 3D wavelet decomposition with the Coiflet function. The LoG filters employed sigma values of 1 and 3. Additionally, we set the width of each interval in the histogram of image intensities to 5. In the case of NGTDM and GLCM, were distance between the center voxel and its neighbor was set to 1.

Eventually, a total of 1,714 radiomics features calculated from ICH and PHE regions were obtained. For each of ICH and PHE region, the original images generated 107 features (18 first-order features, 14 shape-based features, and 75 textural features). The Laplacian of Gaussian and wavelet transform filters were applied to the images, resulting in an additional 750 textural features. Finally, these raw features were scaled by subtracting the median of the feature from each data point and then dividing it by the interquartile range of the feature.

C. Feature Selection

To address the potential issues of overfitting and reduced model performance caused by the large number of features, we conducted a feature selection process. The details of this process are described as follows. Firstly, we applied variance thresholding to each radiomic feature. Any feature with a variance falling below this threshold value of 1 was excluded from consideration. This step ensures that the selected features contain sufficient information and are not constant values. Secondly, we applied four filter-based selection methods

including ANOVA F-value, Minimum Redundancy – Maximum Relevance (mRMR) [25], mutual information [26], and Relief [27] to eliminate redundant features.

The F-value is typically used to test the significance of a regression coefficient in determining its ability to explain the target variable [28]. In context of feature selection, our goal is to find features with a large value of F, indicating a relationship between the feature itself and target variable. Both mutual information and mRMR are feature selection methods rooted in information theory. While mutual information draws on the pioneering work of Shannon C. [26], mRMR was introduced by Peng H. [25] as a method designed to address redundancy in feature selection. The purpose of these methods is to find the amount of information shared between a feature variable and a target class. Lastly, the Relief algorithm, introduced by Kira K. et al. [27], is a straightforward feature weight-based algorithm that measures the relevance of features. It assesses the importance of features by analyzing the differences in feature values between classes, reflecting their discriminative power.

Finally, the feature selection methods as mentioned above provide us with a score or weight of each feature, indicating its strong relevance to the target variable. Consequently, 10 radiomics features with the highest scores were selected and then combined to demographic data (i.e., age and gender) for model building.

D. Machine Learning Classifiers

This study adopted three machine learning models including logistic regression (LR), random forest (RF), and support vector machine (SVM) to categorize three types of nontraumatic ICH i.e., primary-related hematomas (PICH), vascular malformation-related hematomas (VMH) and tumorous-related hematomas (TuH). To obtain the optimal hyper-parameters for each classifier, grid search strategy with cross-validation was utilized. Thus, the subjects in each cross-validation epoch were independently separated into 96 (80% of total subjects) and 24 (20% of total subjects) subjects for training and validation, respectively. The details of the machine learning models were described as follows.

1) *Logistic Regression* is a popular linear regression model which is used in classification problems. To perform logistic regression and obtain a categorical target variable, the sigmoid function is applied to map a real-numbered target variable to probability of its occurrence [29]. The sigmoid function is defined as follows:

$$S(z) = 1 + \frac{1}{\exp(-z)} \quad (1)$$

where z is a linear combination of a feature vector (x_1, x_2, \dots, x_p) and a coefficient vector $(\beta_1, \beta_2, \dots, \beta_p)$ of instance \mathbf{x}_i . The logistic regression makes prediction based on the probability of events. If the estimated probability of the desired event is greater than 0.5, the instance is assigned to class 1. On the other hand, if the estimated probability is equal to or less than 0.5, the instance is assigned to class 0.

2) *Random Forest* is an ensemble learning that proposed by Breiman L. [30]. It combines multiple decision trees to train on a bit different subsample derived from sampling with

replacement from given dataset. In the case of a classification task, predictions are made through majority vote of the trees, which are not individually optimized for best accuracy, as the emphasis is placed on simplicity [31]. Previous studies also demonstrated a great potential of random forest due to its ability to reduce overfitting problems [7, 8].

3) *Support Vector Machine*: A concept behind the SVM is finding an optimal hyperplane (or decision surface) to separate data points into distinct classes by maximizing a margin between the separating hyperplane and the closest datapoint of each class [32, 33]. For instance, given an input feature vector (x_1, x_2, \dots, x_p) is a feature vector of instance \mathbf{x}_i with dimensional p , belonging to either class $(y_i) -1$ or $+1$, the separating hyperplane can be described by:

$$\mathbf{w} \cdot \mathbf{x}_i + b = 0 \quad (2)$$

where \mathbf{w} is a weight vector of the input features

b is a bias

As a result, the SVM algorithm provides prediction based on the following rule:

$$\mathbf{w} \cdot \mathbf{x}_i + b \geq 1 \quad \text{for } y_i = 1 \quad (3)$$

$$\mathbf{w} \cdot \mathbf{x}_i + b \leq -1 \quad \text{for } y_i = -1$$

E. Statistical Analysis and Model Evaluation

Demographic data among the study groups were compared using Kruskal-Wallis test, Dunn's test (for pairwise comparison) and Chi-Squared test. A significant difference was considered when $p < 0.05$. We evaluated the predictive performance of the candidate models through weighted accuracy, sensitivity, positive predictive values (PPV), and area under the ROC curve (AUC). The model with the highest accuracy will be regarded as the suitable one for our classification task.

III. RESULT

A. Patient Selection

A total of 120 patients met our inclusion criteria and were enrolled in this study. These initial brain NCCT images were shown in Fig 1. There were 46 (38%) of PICH, 39 (33%) of TuH, and 35 (29%) of VMH class. The demographic data of patients as shown in TABLE I, revealed significant difference in age at diagnosis among at least one pair across all the classes ($p < 0.001$) with the average (\pm standard deviation: SD) of 58.93 (\pm 12.41) for PICH, 36.31 (\pm 21.46) for VMH, and 56.00 (\pm 13.95) for TuH class. For pairwise comparison of age

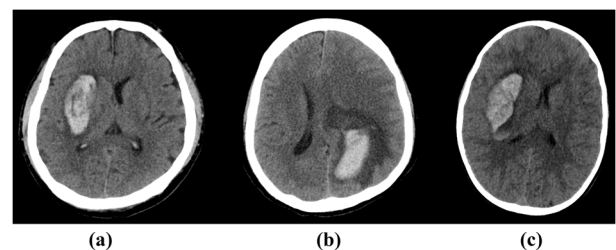


Fig. 1. Initial brain noncontrast computed tomography (NCCT) images of (a) primary-related ICH (PICH), (b) tumorous-related ICH (TuH), and (c) vascular malformation-related ICH (VMH).

TABLE I. DEMOGRAPHIC DATA OF PATIENTS.

| Variable | Nontraumatic intracerebral hemorrhage-related | | | P |
|--------------------------|---|----------------------|------------------------------|---------|
| | Primary (n=46) | Tumorous (n=39) | Vascular malformation (n=35) | |
| Age (average \pm S.D.) | 58.93 (\pm 12.41) | 56.00 (\pm 13.95) | 36.31 (\pm 21.46) | < 0.001 |
| Gender | | | | |
| Female | 14 | 18 | 17 | 0.184 |
| Male | 32 | 21 | 18 | |

between classes, there indicated a significant difference between PICH and VMH classes ($p < 0.001$), and between TuH and VMH class ($p < 0.001$). However, there was no significant difference between the PICH and TuH class ($p = 0.514$). Similarly, there was no significant difference in gender between the classes ($p = 0.184$).

B. Classification Performance

Eventually, we constructed 12 multiclass classification classifiers using 12 features (i.e., 10 radiomics features, age, and gender) and then evaluated their performance using a 5-fold cross-validation strategy. The model performance was assessed by measuring their accuracy to determine the most suitable one, as shown in TABLE II. The weighted average accuracy of our classification models ranged from 0.63 to 0.84. The results showed that using the features selected by F-value applied with SVM outperformed the other classifiers, achieving the highest weighted average accuracy (\pm SD) of 0.84 (\pm 0.07). Additionally, the SVM with F-value feature selection demonstrated average sensitivity and PPV of 0.84 (\pm 0.06) and 0.86 (\pm 0.05), respectively. We also evaluate the overall performance of discriminating each class from the rest using AUC. The result suggested that our proposed model achieved the weighted average AUC of 0.90.

Furthermore, in the case of binary classification using the One-vs-rest method, the SVM classifier applied with the features selected by F-value demonstrated promising results. The accuracy achieved by the proposed model for classifying PICH, TuH, and VMH was 0.88, 0.92, and 0.89, respectively. For the PICH class, the proposed model achieved a sensitivity, PPV, and AUC of 0.85, 0.83, and 0.93, respectively. The proposed model displayed a sensitivity, PPV, and AUC of 0.87, 0.87, and 0.91, respectively, for the TuH class. Finally, the proposed model yielded a sensitivity, PPV, and AUC of 0.80, 0.82, and 0.85, respectively, for the VMH class.

C. Radiomics Feature Analysis

A total of 534 features were eliminated due to low variance, resulting in 1,180 raw radiomics features available for the filter-based selection process. From these, only 10 radiomics features with the highest relevance scores to the target variable were selected to construct classification model along with age, and gender variable.

Thus, after completing the model construction process, we examined the radiomics features selected based on F-value that consistently demonstrated the highest accuracy across all machine learning classifiers. The radiomics features selected from the F-value were from both ICH and PHE region of 60% and 40%, respectively. The features comprised solely of texture features including four features from GLDM, three features from GLRLM, and one each features from GLCM,

TABLE II. THE WEIGHTED AVERAGE ACCURACY OF 4 FEATURE SELECTION METHODS COMBINING WITH 3 MACHINE LEARNING CLASSIFIERS FOR CLASSIFYING 3 CAUSES-RELATED ACUTE NONTRAUMATIC INTRACEREBRAL HEMORRHAGE.

| Feature Selection Methods | Machine Learning Classifiers | | |
|---------------------------|------------------------------|------|-------------|
| | LR | RF | SVM |
| F-value | 0.80 | 0.77 | 0.84 |
| Mutual information | 0.72 | 0.73 | 0.72 |
| mRMR | 0.78 | 0.74 | 0.77 |
| Relief | 0.63 | 0.76 | 0.67 |

GLSZM, NGTDM. Moreover, the features were contributed from 50% of wavelet-based images (two from LLH and one each from LHL, HLH and HHH), 40% of Laplacian of Gaussian-filtered image and only 10% of original image.

Furthermore, we conducted pairwise comparison of each feature between classes using Dunn's test to evaluate the classification potential. Out of the 10 radiomics features examined, we found that nine features showed significant differences between the PICH and TuH classes. Additionally, eight features exhibited significant differences between the TuH and VMH classes, while three features displayed significant differences between the PICH and VMH classes. Importantly, only one feature showed a significant difference between each pair of classes as shown in TABLE III.

IV. DISCUSSION

In this retrospective study, we performed classification models for categorizing causes of acute nontraumatic ICH as primary-related hematomas (PICH), vascular malformation-related hematomas (VMH), and tumorous-related hematomas (TuH). Among the models considered, the F-value-based feature selection methods applied to the SVM demonstrated superior performance compared to the other models. The model was constructed using features such as age, gender, and 10 radiomics features, all of which were exclusively texture features.

Recent studies demonstrated an application of the radiomics approach on various imaging techniques. Several studies performed radiomics approach on NCCT imaging [7-9], as well as on MRI for classifying tumor types which resulted binary outcome [10] and multiple outcome [11]. However, studies addressing the multiclass classification task of causes of nontraumatic ICH which require immediate medical attention and prompt diagnosis, have not been published yet. Notably, in real-world scenarios, patients may be suspected of having multiple causes of ICH, making it challenging to differentiate them into binary groups. Thus, our study proposed classification models for categorizing multiple causes of acute nontraumatic ICH including PICH, VMH, and TuH. We hypothesized that our proposed models could be utilized to support clinicians to mitigate the high risk of misdiagnosis, preventing the implementation of inappropriate treatment plans.

The proposed model of our study constructed from 10 radiomics features selected from F-value incorporating with age and gender, using SVM classifier. The model yielded average accuracy, sensitivity, PPV, and AUC of 0.84, 0.84, 0.86, and 0.90, respectively, for multiclass classification. Moreover, we also evaluated the model in the case of binary classification using the One-vs-rest method. The model

TABLE III. THE SIGNIFICANT DIFFERENCES OF 10 RADIOMICS FEATURES SELECTED BY F-VALUE BETWEEN PAIRS OF CLASSES.

| Feature Name | Pairs of classes | | |
|---|-----------------------------------|----------------------|------------------------------------|
| | Primary vs. Vascular malformation | Primary vs. Tumorous | Tumorous vs. Vascular malformation |
| 1. Complexity of NGTDM (extracted from 3D wavelet image with LHL subband) on PHE region | **** | **** | ns |
| 2. SmallAreaEmphasis from GLSZM (extracted from original image) on ICH region | ns | **** | **** |
| 3. LongRunEmphasis of GLRLM (extracted from 3D LoG-based image with sigma of 3) on ICH region | ns | **** | **** |
| 4. LargeDependenceHighGrayLevelEmphasis of GLDM (extracted from 3D wavelet image with LLH subband) on PHE region | ns | **** | **** |
| 5. LargeDependenceEmphasis of GLDM (extracted from 3D LoG-based image with sigma of 3) on ICH region | ns | **** | **** |
| 6. ClusterProminence of GLCM (extracted from 3D wavelet image with HLH subband) on PHE region | **** | **** | ns |
| 7. RunVariance of GLRLM (extracted from 3D LoG-based image with sigma of 3) on ICH region | ns | **** | **** |
| 8. LargeDependenceHighGrayLevelEmphasis of GLCM (extracted from 3D wavelet image with HHH subband) on PHE region | ns | **** | **** |
| 9. GrayLevelNonUniformityNormalized of GLRLM (extracted from 3D wavelet image with LLH subband) on ICH region | ** | **** | * |
| 10. LargeDependenceEmphasis of GLDM (extracted from 3D LoG-based image with sigma of 1) on ICH region | ns | **** | **** |

^a. The symbols ****, ***, **, *, and ns represent p of $\leq 0.0001, 0.001, 0.01, 0.05$, and no significance, respectively.

demonstrated a performance of 0.91 AUC in distinguishing between TuH and nonTuH (i.e., PICH and VMH), outperforming the model proposed by Jawed, N. et al. [8], which achieved an AUC of 0.89 for predicting neoplastic and nonneoplastic cases. For distinguishing PICH from non-PICH (i.e., VMH and TuH) and VMH from non-VMH (i.e., PICH and TuH), our model's performance was found to be lower compared to the study conducted by Wang, J. et al. [10]. Their research specifically targeted the discrimination between PICH and VMH cases without hemorrhage-related tumors, while our study encompassed tumors as well. The inclusion of tumor cases in our study might lead to additional variations among the subjects, impacting the classification potential.

The selected radiomics features originated from 60% of the ICH regions and 40% of the PHE regions. This finding aligns with Jawed, N. et al.'s study, [8] which highlighted the significance of incorporating both of PHE and ICH lesions when classifying of acute ICH causes. We observed that the majority of the radiomics features were primarily derived from wavelet-based images and LoG-based images, while the remaining 10% originated from the unfiltered-images. These results correspond with the previous studies that more than 50% of radiomics features obtained from filter-based images [7-9]. While analyzing the feature class, we found that first-order and 3D shape features were not considered in our proposed models. This omission might lead to misdiagnosis in some cases that required additional information more than only texture. As emphasized in the study conducted by Zhang, Y. et al. [7], their research achieved the highest predictive performance by selecting two features from each feature class. However, several studies have reported a minimal contribution of first-order features and shape features. In one study, only 2.5% of the 100 selected radiomics features were found to be effective in discriminating between neoplastic and nonneoplastic cases [8]. Additionally, another study found that neither first-order nor shape features were included in the differentiation between the causes of vascular malformation and the primary cause of ICH [9].

In addition, we also inspected misclassification results to examine the classification behavior based on radiomics features. For VMH, two subjects were misclassified into TuH (see Fig 2 (a)), and four subjects were misclassified into PICH (see Fig 2 (b)). In practice, clinicians might suspect the presence of VMH on NCCT images by observing the brightness and homogeneity of ICH lesions, as well as the PHE area surrounding the lesions. However, our model made decisions based on only texture features, specifically smoothness or fine-grained structure in ICH, and contrast in PHE. As a result, the misclassifications as TuH can occur in cases where VMH consists of cysts, which create obvious distinct layers within the hematomas, resembling characteristics like TuH. Similarly, the cases where VMH lesions were miscategorized as PICH primarily occur when the VMH lesions exhibit homogeneity of ICH with only a small area of PHE surrounding them. This can be attributed to the nature of PICH which quickly developed, patients promptly seek medical attention for diagnosis imaging, resulting in a shorter time of symptom onset and consequently smaller areas of PHE. Lastly, for the PICH class that was misclassified into the TuH class, our findings indicate that this misclassification was caused by small regions of both ICH and PHE. These small regions resulted in a lack of sufficient information for the learning process, making it difficult for the model to accurately classify these subjects. Furthermore, we observed one instance that was misclassified but did not appear to be affected by the issue of small regions. This scenario can occur when the patient has a history of warfarin medication treatment, resulting more heterogeneity in hematomas as shown in Fig 2 (c).

Based on our knowledge, this is the first study that proposed multiclass classification for distinguishing causes of nontraumatic ICH. Even if our proposed model achieved appropriate performance, there are still limitations to consider. Firstly, the lack of diversity in the dataset used to construct the machine learning models raises concerns about the generalizability of the model. Next, we did not evaluate the model's performance whether it can effectively support the

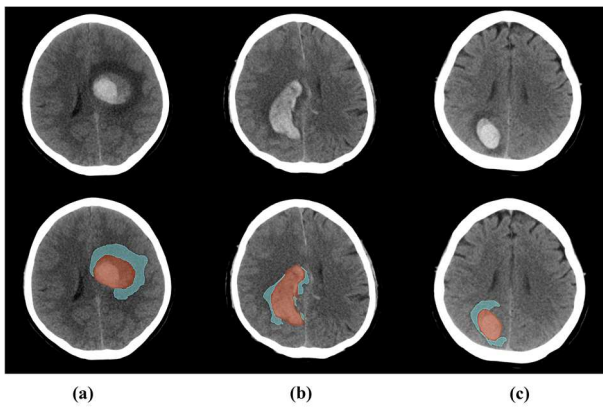


Fig. 2. Illustration of misclassification subjects including (a) Vascular malformation-related ICH misclassified to tumorous-related ICH, b) Vascular malformation-related ICH misclassified to primary-related ICH, and c) primary-related ICH misclassified to tumorous-related ICH. The region of hematoma and perihematomal edema masked in red and blue, respectively.

clinician's decision-making. This is a crucial aspect to determine practical utility of the model in real-world situations. However, it is important to note that this study represents a preliminary research phase focused on assessing the performance of the model itself. In the future, our aim is to validate the model through external validation by incorporating a wider range of NCCT image settings. Additionally, it would be valuable to evaluate the model's performance to that of human specialists, thus providing a comprehensive evaluation of its capabilities.

V. CONCLUSION

The findings of this study demonstrate that the radiomics features selected using ANOVA F-value and incorporating patients' demographic data, and applied to the SVM classifier, outperformed other methods. The selected features comprised solely of texture features from both ICH and PHE regions. This proposed method highlights its effectiveness in identifying multiple causes of acute and nontraumatic ICH, which has not been previously explored.

VI. ETHICS STATEMENT

This study was approved and monitored by the Ethics Committee of Faculty of Medicine, Chiang Mai University, Chiang Mai, Thailand.

REFERENCES

- [1] Kuriakose, D. and Z. Xiao, Pathophysiology and Treatment of Stroke: Present Status and Future Perspectives. *International journal of molecular sciences*, 2020. 21(20): p. 7609.
- [2] An, S.J., T.J. Kim, and B.-W. Yoon, Epidemiology, Risk Factors, and Clinical Features of Intracerebral Hemorrhage: An Update. *J Stroke*, 2017. 19(1): p. 3-10.
- [3] Fewel, M.E., et al., Spontaneous intracerebral hemorrhage: a review. *Neurosurg Focus*, 2003. 15(4): p. 1-16.
- [4] Tranvinh, E., et al., Contemporary Imaging of Cerebral Arteriovenous Malformations. *American Journal of Roentgenology*, 2017. 208(6): p. 1320-1330.
- [5] Joseph, D.M., et al., Glioblastoma presenting as spontaneous intracranial haemorrhage: Case report and review of the literature. *Journal of clinical neuroscience*, 2017. 40: p. 1-5.
- [6] Domingues, R., C. Rossi, and C. Cordonnier, Diagnostic Evaluation for Nontraumatic Intracerebral Hemorrhage. *Neurologic Clinics*, 2015. 33(2): p. 315-328.
- [7] Zhang, Y., et al., Radiomics features on non-contrast-enhanced CT scan can precisely classify AVM-related hematomas from other spontaneous intraparenchymal hematoma types. *European radiology*, 2019. 29(4): p. 2157-2165.
- [8] Nawabi, J., et al., Neoplastic and Non-neoplastic Acute Intracerebral Hemorrhage in CT Brain Scans: Machine Learning-Based Prediction Using Radiomic Image Features. *Frontiers in neurology*, 2020. 11: p. 285.
- [9] Wang, J., et al., A Radiomics Nomogram for Classifying Hematoma Entities in Acute Spontaneous Intracerebral Hemorrhage on Non-contrast-Enhanced Computed Tomography. *Frontiers in Neuroscience*, 2022. 16.
- [10] Chen, C., et al., Radiomics-Based Machine Learning in Differentiation Between Glioblastoma and Metastatic Brain Tumors. *Front Oncol*, 2019. 9: p. 806.
- [11] Zhang, M., et al., Radiomics Can Distinguish Pediatric Supratentorial Embryonal Tumors, High-Grade Gliomas, and Ependymomas. *AJNR Am J Neuroradiol.*, 2022. 43(4): p. 603-610.
- [12] Rizzo, S., et al., Radiomics: the facts and the challenges of image analysis. *European radiology experimental*, 2018. 2(1): p. 36.
- [13] Osborn, A.G., K.L. Salzman, and M.D. Jhaveri, Spontaneous Nontraumatic Intracranial Hemorrhage, in *Diagnostic Imaging: Brain (Third Edition)*, A.G. Osborn, K.L. Salzman, and M.D. Jhaveri, Editors. 2016, Elsevier. p. 258-261.
- [14] van Griethuysen, J.J.M., et al., Computational Radiomics System to Decode the Radiographic Phenotype. *Cancer research*, 2017. 77(21): p. e104-e107.
- [15] Castellano, G., et al., Texture analysis of medical images. *Clinical Radiology*, 2004. 59(12): p. 1061-1069.
- [16] Abbasian Ardakani, A., et al., Interpretation of radiomics features—A pictorial review. *Computer Methods and Programs in Biomedicine*, 2022. 215: p. 106609.
- [17] Mayerhoefer, M.E., et al., Introduction to Radiomics. *Journal of nuclear medicine : official publication, Society of Nuclear Medicine*, 2020. 61(4): p. 488-495.
- [18] Haralick, R.M., K. Shanmugam, and I. Dinstein, Textural Features for Image Classification. *IEEE Transactions on Systems, Man, and Cybernetics*, 1973. SMC-3(6): p. 610-621.
- [19] Sun, C. and W.G. Wee, Neighboring gray level dependence matrix for texture classification. *Computer Vision, Graphics, and Image Processing*, 1983. 23(3): p. 341-352.
- [20] Galloway, M.M., Texture analysis using gray level run lengths. *Computer Graphics and Image Processing*, 1975. 4(2): p. 172-179.
- [21] Thibault, G., et al., Texture Indexes and Gray Level Size Zone Matrix Application to Cell Nuclei Classification. 2009.
- [22] Amadasun, M. and R. King, Textural features corresponding to textural properties. *IEEE Transactions on Systems, Man, and Cybernetics*, 1989. 19(5): p. 1264-1274.
- [23] Mallat, S.G., A theory for multiresolution signal decomposition: the wavelet representation. *IEEE Transactions on Pattern Analysis and Machine Intelligence*, 1989. 11(7): p. 674-693.
- [24] Perona, P. and J. Malik, Scale-space and edge detection using anisotropic diffusion. *IEEE Transactions on Pattern Analysis and Machine Intelligence*, 1990. 12(7): p. 629-639.
- [25] Hanchuan, P., L. Fuhui, and C. Ding, Feature selection based on mutual information criteria of max-dependency, max-relevance, and min-redundancy. *IEEE Transactions on Pattern Analysis and Machine Intelligence*, 2005. 27(8): p. 1226-1238.
- [26] Shannon, C.E., A mathematical theory of communication. *Bell System Technical Journal*, 1948. 27: p. 379-423, 623-656.
- [27] Kira, K. and L.A. Rendell, The feature selection problem: traditional methods and a new algorithm, in *Proceedings of the tenth national conference on Artificial intelligence*. 1992, AAAI Press: San Jose, California. p. 129-134.
- [28] Kutner, M.H.N., Christopher J.; Neter, John; Li, William, *Applied Linear Statistical Models*. 5th ed. 2005: McGraw-Hill.
- [29] Lee, W.-M., *Python® Machine Learning*. 2019: Wiley.
- [30] Breiman, L., *Random Forests*. *Machine Learning*, 2001. 45(1): p. 5-32.
- [31] Alpaydin, E., *Introduction to Machine Learning*. 3rd ed. ed. 2021, Cambridge, MA: MIT Press.
- [32] Cortes, C. and V. Vapnik, *Support-Vector Networks*. *Mach Learn*, 1995. 20(3): p. 273-297.

A Comparative Study of YOLO Models for Sperm and Impurity Detection Based on Proposed Augmentation in Small Dataset

Marwan Nawae

*Department of Biomedical Sciences and
Biomedical Engineering
Faculty of Medicine
Prince of Songkla University
Hat Yai, Songkhla, Thailand
jiwang.nawae@gmail.com*

Prawai Maneelert

*Reproductive Medicine Unit
Department of Obstetrics and Gynecology
Faculty of Medicine
Prince of Songkla University
Hat Yai, Songkhla, Thailand
klongprawai@gmail.com*

Chainarong Choksuchat

*Department of Obstetrics and
Gynecology
Faculty of Medicine
Prince of Songkla University
Hat Yai, Songkhla, Thailand
chchaina@yahoo.com*

Tonghathai Phairatana

*Department of Biomedical Sciences and
Biomedical Engineering
Faculty of Medicine
Prince of Songkla University
Hat Yai, Songkhla, Thailand
tonghathai.p@psu.ac.th*

Jermphiput Jaruenpunyasak

*Department of Biomedical Sciences and
Biomedical Engineering
Faculty of Medicine
Prince of Songkla University
Hat Yai, Songkhla, Thailand
jjermphi@medicine.psu.ac.th*

Abstract—Sperm detection can help with a lot of different kinds of research, such as forensics, assisted reproduction, and fertility assessment. However, it can be challenging to detect the sperm, particularly when the sample size of the dataset is minimal. This paper presents a comparison of different YOLO (You Only Look Once) models for sperm and impurity detection based on the proposed augmentation in the small dataset. According to the results, the YOLOv5 model had high precision, recall, F1-score, and mean average precision (mAP) for training with both the original dataset and the proposed augmentation dataset. While the YOLOv8s model had the highest precision, recall, F1-score, and mAP (0.994, 0.965, 0.979, and 0.993, respectively), only training with the proposed augmentation. In short, when trained with the proposed augmentation, the YOLO models can detect sperm and impurity even when both the objects and the number of samples are small.

Index Terms—sperm detection, YOLO models, small dataset,

imbalances, genetic abnormalities, and environmental variables, might contribute to infertility. Sperm analysis can be used to determine a sperm's reproductive effectiveness [3]. In accordance with the World Health Organization (WHO) standards [4], the sperm analysis can be evaluated based on sperm volume, sperm concentration, sperm motility, sperm morphology, and pH of sperm.

Currently, there is technology to assist sperm analysis called Computer Assisted Sperm Analysis (CASA). The CASA is a method of measuring the characteristics of sperm using computer software. It allows for the precise and accurate measurement of sperm characteristics such as motility, velocity, and concentration based on guidelines used in collaboration with the WHO. Additionally, the CASA can be used to identify and treat male infertility. However, CASA is primarily used to measure sperm motility, velocity, and concentration. It is rarely used to evaluate sperm morphology [5]. There are some CASA systems that can assess sperm morphology by using advanced imaging techniques, such as high-resolution microscopy. These techniques can provide more detailed images of sperm morphology, but they are less popular and more expensive than other options [5]. Sperm morphology evaluation is a technique that requires manual analysis, which is performed by a specialist under a microscope. The specialist will assess the shape of the sperm head, tail, and mid-piece under high magnification and stained sperm cells. But this method takes time, requires the experience of specialists, and spends expensive costs. Consequently, the sample size of the dataset is limited [6]–[8].

I. INTRODUCTION

Infertility is a disease of the male or female reproductive system. This Infertility is defined as the inability to conceive after a year of regular, unprotected intercourse, or the inability to carry a pregnancy to term [1]. Each couple has a unique set of infertility-related factors. Consequently, both males and females must have a medical history taken and be physically examined because it can be caused by either gender. Ovulation abnormalities, male factor infertility, and oviductal illness are the three main causes of infertility [2]. According to the research, infertility issues impact 12%-28% of married couples worldwide. Up to 20%-30% of the factors are brought on by men [1]. Numerous factors, such as low sperm counts, poor sperm morphology and motility, hormone

To mimic the small dataset problems, the study randomly selects the images from the sperm dataset [9] and proposed augmentation on them. The YOLO architecture and its variation are compared to detect sperm and impurity in healthy subjects in order to find a suitable model for sperm detection. For training and testing, the experiment uses 80% for training 10% for validation and 10% for testing. The results are also evaluated using the precision, recall, F1-score, and mean average precision (mAP) of sperm detection.

II. RELATED WORKS

This section of the related work examines the available research on object detection using various techniques. The emphasis, however, is mainly on research that employs the YOLO series or its variations from YOLOv5 to the YOLOv8 model.

In the case of YOLOv5, Mahaur and Mishra [10] came up with a model called iS-YOLOv5 that changes the architecture of the YOLOv5 model to improve the detection of small objects in three datasets: BDD100K dataset (Number of objects: $N_{objs} = 100k$), TT100K dataset ($N_{objs} = 30k$), and DTLDD dataset ($N_{objs} = 200k$). This model improved the speed and accuracy of detecting small objects like traffic signs and lights while driving without affecting the accuracy of detecting large objects. Moreover, Zhan *et al.* [11] looked into how important it was to pay attention to small objects in drone-captured scenes in VisDrone2020 dataset ($N_{objs} = 382k$) for testing in various situations. They found that the modified YOLOv5 model effectively improved the accuracy of finding small objects while maintaining a fast detection speed.

Considering YOLOv6 model, Gupta *et al.* [12] proposed a transfer-learning-based model for real-time object detection that enhances the YOLO algorithm with the MS-COCO dataset (Number of images: $N_{imgs} = 123k$). They discovered that the fine-tuned YOLOv6 model is shown as an improvement over the original YOLOv6 model. Furthermore, Sinthia and Kabir [13] proposed a way to identify license plates by using their own dataset ($N_{imgs} = 1000$) based on the original YOLOv6 model and BLPNET(VGG-19-RESNET-50) model for nameplate recognition and location. This YOLOv6 model detected license plates with high precision rate (94.7%) which is better than other models.

For YOLOv7, Yung *et al.* [14] compared the performance of different YOLO algorithms for detecting safety helmets from the online dataset ($N_{imgs} = 5000$). They found that the YOLOv7 model outperformed the YOLOv5s and YOLOv6s models in terms of precision, recall, and F1-score for safety helmet detection. In addition, Duan *et al.* [15] provide a novel mask detection algorithm RMPC-YOLOv7 based on YOLOv7 for detecting whether people wear masks in public places with a mouthpiece dataset of 9240 images. This proposed model was more accurate because of the new downsampling structure. It added more parameters, though.

In term of YOLOv8, Lou *et al.* [16] suggested an approach for small-size object detection in special scenarios. Visdrone ($N_{obj} = 2.6$ million), Tinyperson ($N_{obj} =$ around 72k), and

PASCAL VOC2007 ($N_{obj} =$ about 24 k) were used for the research presented here. For small detection in various complex scenes, they found that the proposed DC-YOLOv8 algorithm was better than other detectors at finding small objects in a variety of complex scenes, both in terms of accuracy and speed. Additionally, Cai *et al.* [17] showed the integration of the CFIOU loss into the latest anchor-based YOLOv5 and anchor-free YOLOv8 object detection algorithms and the quantitative comparison of BIoU losses and CFIOU loss on the VisDrone2019 ($N_{obj} = 540k$) and SODA-D ($N_{obj} =$ more than 278k) datasets. They found that the CFIOU loss function was effective in improving small object detection and demonstrated superior performance in both anchor-based and anchor-free object detection algorithms.

However, a large amount of data is normally required for training most YOLO models effectively to gain high detection. This is especially true in the case of sperm detection, where data gathering is challenging and annotation by reproductive physicians is required [6]–[8]. As a consequence, the sperm dataset appears to be fairly limited, and the performance of YOLO detection continues to be a challenging problem.

III. MATERIALS AND METHODS

This section describes the dataset utilized in this study, as well as data preparation, YOLO models, and our experimental assessments. There are four primary processes involved in training a detection model: dataset, data preparation, training YOLO models, and their evaluation as shown in Fig. 1.

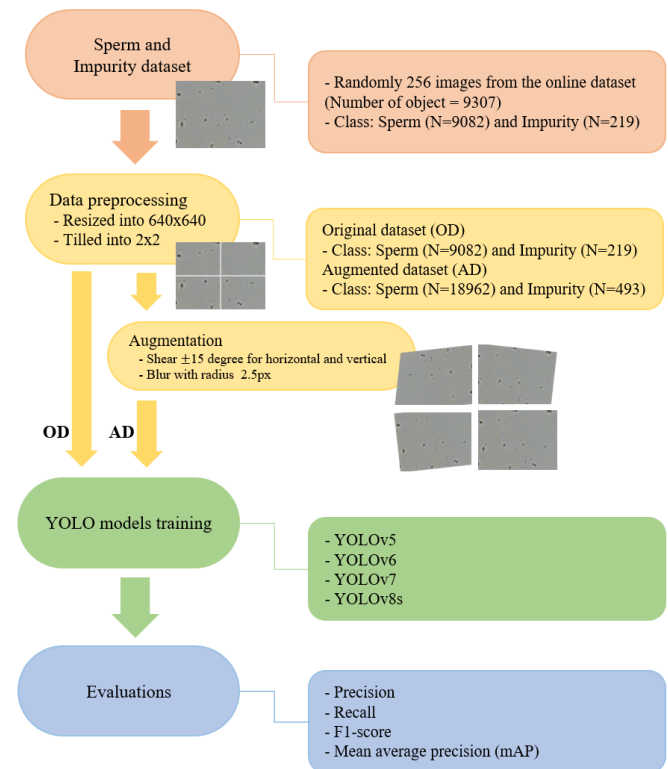


Fig. 1: Workflow of this study

A. Dataset

To simulate the small-dataset problems in this study, we randomly select 256 images from 3590 images of the online dataset [9] containing 256 images that is defined as the original dataset (OD) and then propose an augmented dataset (AD) from the original dataset. This online dataset contains two types of human sperm and impurities including bacteria, protein lumps, and bubbles. The WLJY-9000 CASA equipped with a $20\times$ objective and $20\times$ electronic glasses is used to obtain videos of sperm under a microscope with dimensions of 698 pixels by 528 pixels. In addition, fourteen reproductive physicians annotated the datasets for human sperm and their impurity objects.

B. Data preprocessing

Both OD and AD datasets are prepared with the same two processes. Firstly, all images are resized with an aspect ratio of 640×640 to fit the first layer input of the YOLO architecture [18], [19]. After that, we tiled each image by 2×2 . It divides the original image into four smaller images to reduce the learning size per image and enhance the learning of small objects [20].

To enhance the diversity of sperm and impurity patterns in the AD dataset, we implemented two augmentation techniques for modified datasets. Initially, these images are adjusted with shear $+15$ or -15 for horizontal and vertical, similar to a microscope image of sperm seen from different angles [21]. The second method is called blur. It used Gaussian blur with a radius of 2.5 pixels, similar to that of a microscope, to focus on images of sperm at varied distances. Finally, the Table I displays the total number of objects in both the OD and AD datasets. The former dataset consists of 9088 sperm and 219 impurities, while the latter contains 18962 sperm and 493 impurities.

TABLE I: Number of objects each class

| Classes | Original datasets | Augmented datasets |
|--------------|-------------------|--------------------|
| sperm | 9088 | 18962 |
| impurity | 219 | 493 |
| Total | 9307 | 19455 |

C. YOLO models training

The YOLO architecture is a single-stage neural network that simultaneously predicts object bounding boxes and class probabilities. It divides the input image into a grid, where each cell predicts fixed bounding boxes and class probabilities. The architecture comprises three parts: backbone, neck, and head. The backbone extracts features and captures spatial information from the image. The neck combines these features for final predictions, and the head generates class probabilities and bounding box coordinates using fully connected or convolutional layers. This efficient design enables real-time object detection across various applications. We implemented four versions of the YOLO architecture: YOLOv5 [22], YOLOv6 [23], YOLOv7 [19], [24], YOLOv8s [25]. First of all, YOLOv5 is improves upon YOLOv3 [26] because it uses a CSPDarknet53 backbone and a PA-Net neck

to find features and improve loss functions. Second, YOLOv6 with a Rep-PAN neck and an EfficientRep backbone. The third model is called YOLOv7, and it has the same backbone and neck as YOLOv5. However, YOLOv7 uses E-ELAN in the last layer and adds an extra head for testing. YOLOv8 also has an advanced backbone and neck architecture, a split Ultralytics head without anchors, and an optimized balance between accuracy and speed for real-time detection.

In the experiment, the datasets OD and AD are split into a train set, a validation set, and a test set, each with a ratio of 80:10:10, respectively. All YOLO has the same configurations: 100 epochs, learning rate with 0.01, and a batch size as 16.

D. Evaluations

We evaluated detection performance using the test dataset based on the confusion matrix for sperm and impurity objects. The most common measurement of detection comprise of precision, recall, F1-score, and mAP as calculated by Equations (1) to (4), respectively [6].

$$P = (TP)/(TP + FP) \quad (1)$$

$$R = (TP)/(TP + FN) \quad (2)$$

$$F1 = (2 * P * R)/(P + R) \quad (3)$$

$$mAP_{IoU=threshold} = \frac{\sum_0^{i=n} P_{class_i}}{n} \quad (4)$$

Here, P is a precision that measures the accuracy of the model's positive predictions, TP is a true positive of sperm detection, FP is a false positive of sperm detection, FN is a false negative of sperm detection, R is a recall which measures the proportion of actual positive cases that the model correctly identifies, $F1$ is a F1-score metric to measures the balance between precision and recall, mAP is a mean average precision which is the mean averaged precision over all the object categories, and it's the metric more used to evaluate an object detection model, IoU is an intersection over union, threshold is the minimum score that the model will consider the prediction to be a true prediction, P_{class_i} is a precision of class, and n is number of sample.

IV. RESULTS

This section describes the four sperm and impurity detection assessments: precision, recall, F1-score, and mAP. All YOLO models were trained and evaluated for object detection using the OD and AD dataset as shown in both Table II and Table III.

A. Precision

Table II compares the performance of different YOLO models for sperm and impurity detection using an OD and AD. Clearly, when trained on the OD, the YOLOv5 and YOLOv6 models have more precision (> 0.96) than the YOLOv7 and YOLOv8s models (< 0.76). Among the YOLO models, the YOLOv5 model had the highest precision (0.980). Regarding models trained with AD, all YOLO models gain high precision (>0.94). Moreover, the YOLOv8s model offers the best precision (0.994). When comparing an OD and an AD, both YOLOv7 and YOLOv8s models get identical precision results, with an improvement in precision for AD.

B. Recall

Regarding recall assessment, all YOLO models had less than 0.860 of recall on the OD. YOLOv5 model achieved the greatest recall rate (0.853). However, YOLOv6 model performed the lowest recall as 0.53. With AD training, the recall of all models had risen considerably beyond 0.91. In addition, the YOLOv8s and YOLOv7 models provide high recall as 0.96 and 0.96, respectively.

C. F1-score

In terms of F1-score based on OD, the YOLOv5 model delivered the greatest value of 0.912, but the results of other YOLO models fall below 0.80. In particular, the YOLOv6 model has the lowest F1-score, at 0.685. Considering the AD, the F1-score of all YOLO model outcomes is larger than 0.93. When comparing an OD and an AD, both YOLOv7 and YOLOv8s models also get identical F1-score as well as precision results, with an improvement in F1-score for AD.

D. mAP

In terms of the mAP50 in Table III, the majority of models in the OD performed below 0.80. Nevertheless, the YOLOv5 model had the greatest mAP50 (0.943). With the AD, all models achieved mAP50 values greater than 0.94. Additionally, the YOLOv8s model had the highest mAP50 value as 0.993. For the mAP50-S, in OD training, all models attained mAP values greater than 0.86. In particular, the YOLOv5 model produced the best results (0.974). For the AD, all models attained mAP50-S values more than 0.95, with the YOLOv8s model achieved the highest value as 0.991. In terms of mAP50-I, the majority of models performed below 0.72 for OD training but only YOLOv5 model gains 0.912. In the AD, every model yields mAP50-I values greater than 0.92. The YOLOv8s had the largest mAP50-I (0.994).

E. Result of detection

Example of result for sperm and impurity detection for OD and AD are illustrated in Fig. 2. In most of OD, sperm and impurity detection is achieved by YOLOv5 model. However, the YOLOv6, YOLOv7, and YOLOv8s model cannot detect impurity in Fig. 2e, Fig. 2g, and Fig. 2i, respectively. For AD, YOLOv6, YOLOv7, and YOLOv8s model are able to achieve detection in sperm and impurity detection in Fig. 2f, Fig. 2h, and Fig. 2j, respectively.

TABLE II: Experimental results of sperm and impurity detection on test set

| Model | Precision | | Recall | | F1-score | |
|---------|-----------|-------|--------|-------|----------|-------|
| | OD | AD | OD | AD | OD | AD |
| YOLOv5 | 0.980 | 0.955 | 0.853 | 0.913 | 0.912 | 0.934 |
| YOLOv6 | 0.967 | 0.948 | 0.530 | 0.920 | 0.685 | 0.934 |
| YOLOv7 | 0.769 | 0.972 | 0.827 | 0.963 | 0.797 | 0.967 |
| YOLOv8s | 0.685 | 0.994 | 0.760 | 0.965 | 0.721 | 0.979 |

Note: OD: trained by original dataset and AD: trained by Augmented dataset

TABLE III: Experimental results of mAP value

| Model | mAP50 | | mAP50-S | | mAP50-I | |
|---------|-------|-------|---------|-------|---------|-------|
| | OD | AD | OD | AD | OD | AD |
| YOLOv5 | 0.943 | 0.945 | 0.974 | 0.967 | 0.912 | 0.922 |
| YOLOv6 | 0.763 | 0.951 | 0.934 | 0.955 | 0.592 | 0.947 |
| YOLOv7 | 0.696 | 0.969 | 0.867 | 0.974 | 0.525 | 0.964 |
| YOLOv8s | 0.795 | 0.993 | 0.874 | 0.991 | 0.715 | 0.994 |

Note: OD: trained by original dataset, AD: trained by Augmented dataset, mAP50: mean average precision at an intersection over union threshold of 0.5, mAP50-S: mAP50 of sperm detection, and mAP50-I: mAP50 of impurity detection.

V. DISCUSSION

This section will discuss the model's performance on OD and AD. We discovered that the precision of the YOLOv5 and YOLOv6 models with OD training was more than 0.960, as a result, [27], [28]. However, the YOLOv7 and YOLOv8s models with this OD training are lower than 0.770 due to the dataset's limitations and a fixed number of epochs. Consequently, after increasing the number of datasets as AD by augmenting with shear and blur, all YOLO models are able to achieve the high precision (>0.940) due to the sufficient training data [29], while the number of epochs remains constant.

For the recall evaluation, it is the proportion of actual positive cases properly identified by the models. All YOLO models perform lower than 0.86 with OD training [30] because the model might detect sperm but mistakenly predict impurity, which leads to incorrect class predictions. In contrast, all YOLO models with MD training achieved a high recall of more than 0.910 [29], [31].

YOLOv5 with OD training had the best F1-score (>0.910). However, according to the F1-score calculation, the YOLOv6, YOLOv7, and YOLOv8s models were lower than 0.80, as the F1-score was a weighted average of accuracy and recall. For AD training, all YOLO models got a high F1-score (>0.930) which was similar to precision and recall results.

In terms of mAP50, the YOLOv5 had the highest performance (>0.940), but other YOLO models performed mAP50 as below 0.80. After training using AD, every model achieved higher than 0.94. Regarding mAP50-S, each YOLO model had a high result (>0.86). After undergoing MD training, all models get a high mAP50-S. In the instance of mAP50-I, the majority of YOLO models reach a lower than YOLOv5 (<0.72) because of the limited amount of impurity objects in OD ($n=219$). As a result, the model cannot learn well because of overfitting model [32]. In AD training, the number

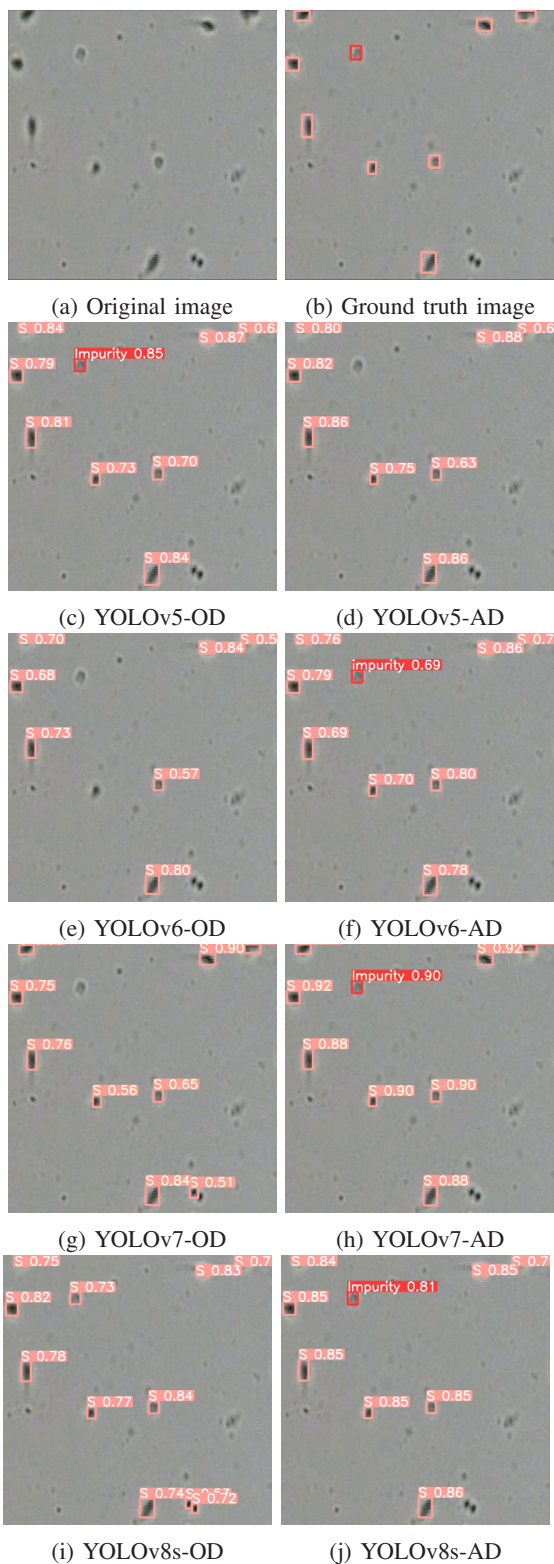


Fig. 2: Result of sperm and impurity detection

of impurity objects was raised to 493 in order to improve the model's performance. It seems that the quantity of impurity objects can impact the performance of mAP50 and mAP50-I when used in small datasets.

It can be seen that YOLOv5 outperforms YOLOv6,

YOLOv7, and YOLOv8s in all metrics with original dataset [9], [33] according to Fig. 2c. Moreover, YOLOv5-OD can detect sperm and impurity better than other YOLO models. However, with AD training, all models performed better across all metrics evaluated than training with original dataset [20].

VI. CONCLUSIONS

This paper compares different YOLO models for sperm and impurity detection between OD and AD in small dataset. According to the results, YOLOv5 has a high precision, recall, F1-score, and mAP for OD training, with values of 0.98, 0.85, 0.91, and 0.94, respectively. Moreover, training with AD can increase the precision, recall, F1-score, and mAP of all YOLO models. In particular, YOLOv8s had the greatest accuracy, recall, F1-score, and mAP (0.994, 0.965, 0.979, and 0.993, respectively) because of the rising quantity of sperm and impurity objects with diverse patterns. In future research, an optimum training parameter for YOLO models will be investigated. The many microscope scenarios, such as light and occlusion, will be examined. In addition, the small and imbalance dataset may be analyzed and modified to maintain a high level of precision in sperm and impurity identification. Furthermore, the framework for detection will be combined with a tracking system for sperm monitoring.

ACKNOWLEDGMENT

This work is supported by the Faculty of Medicine, Prince of Songkla University. In addition, the authors would like to thank to "AI and Robotics for All - Super AI Engineer" project organized by the Artificial Intelligence Association of Thailand.

REFERENCES

- [1] M. Mustafa, A. Sharifa, J. Hadi, E. Ilzam, and S. Aliya, "Male and female infertility: causes, and management," *IOSR Journal of Dental and Medical Sciences*, vol. 18, pp. 27–32, 2019.
- [2] S. Anwar and A. Anwar, "Infertility: A review on causes, treatment and management," *Womens Health Gynecol*, vol. 5, pp. 2–5, 2016.
- [3] F. Itoi, T. Miyamoto, T. Himaki, H. Honnma, M. Sano, and J. Ueda, "Importance of real-time measurement of sperm head morphology in intracytoplasmic sperm injection," *Zygote*, vol. 30, no. 1, pp. 9–16, 2022.
- [4] M. Campbell, F. Lotti, E. Baldi, S. Schlatt, M. Festin, L. Björndahl, I. Toskin, and C. Barratt, "Distribution of semen examination results 2020—a follow up of data collated for the who semen analysis manual 2010. andrology," 2021.
- [5] A. Agarwal, M. K. Panner Selvam, and R. F. Ambar, "Validation of LensHooke® X1 PRO and Computer-Assisted semen analyzer compared with Laboratory-Based manual semen analysis," *World J Mens Health*, vol. 39, no. 3, pp. 496–505, Feb. 2021.
- [6] Z. Zhang, B. Qi, S. Ou, and C. Shi, "Real-time sperm detection using lightweight yolov5," in *2022 IEEE 8th International Conference on Computer and Communications (ICCC)*. IEEE, 2022, pp. 1829–1834.
- [7] H. O. Ilhan, G. Serbes, and N. Aydin, "Automated sperm morphology analysis approach using a directional masking technique," *Computers in Biology and Medicine*, vol. 122, p. 103845, 2020.
- [8] F. Ghasemian, S. A. Mirroshandel, S. Monji-Azad, M. Azarnia, and Z. Zahiri, "An efficient method for automatic morphological abnormality detection from human sperm images," *Computer methods and programs in biomedicine*, vol. 122, no. 3, pp. 409–420, 2015.
- [9] A. Chen, C. Li, S. Zou, M. M. Rahaman, Y. Yao, H. Chen, H. Yang, P. Zhao, W. Hu, W. Liu *et al.*, "Svia dataset: A new dataset of microscopic videos and images for computer-aided sperm analysis," *Biocybernetics and Biomedical Engineering*, vol. 42, no. 1, pp. 204–214, 2022.

- [10] B. Mahaur and K. Mishra, "Small-object detection based on yolov5 in autonomous driving systems," *Pattern Recognition Letters*, vol. 168, pp. 115–122, 2023.
- [11] W. Zhan, C. Sun, M. Wang, J. She, Y. Zhang, Z. Zhang, and Y. Sun, "An improved yolov5 real-time detection method for small objects captured by uav," *Soft Computing*, vol. 26, pp. 361–373, 2022.
- [12] C. Gupta, N. S. Gill, P. Gulia, and J. M. Chatterjee, "A novel finetuned yolov6 transfer learning model for real-time object detection," *Journal of Real-Time Image Processing*, vol. 20, no. 3, p. 42, 2023.
- [13] C. Sinthia and M. H. Kabir, "Detection and recognition of bangladeshi vehicles' nameplates using yolov6 and blpnet," in *2023 International Conference on Electrical, Computer and Communication Engineering (ECCE)*. IEEE, 2023, pp. 1–6.
- [14] N. D. T. Yung, W. Wong, F. H. Juwono, and Z. A. Sim, "Safety helmet detection using deep learning: Implementation and comparative study using yolov5, yolov6, and yolov7," in *2022 International Conference on Green Energy, Computing and Sustainable Technology (GECOST)*. IEEE, 2022, pp. 164–170.
- [15] X. Duan, H. Chen, H. Lou, L. Bi, Y. Zhang, and H. Liu, "A more accurate mask detection algorithm based on nao robot platform and yolov7," in *2023 IEEE 3rd International Conference on Power, Electronics and Computer Applications (ICPECA)*. IEEE, 2023, pp. 1295–1299.
- [16] H. Lou, X. Duan, J. Guo, H. Liu, J. Gu, L. Bi, and H. Chen, "Dc-yolov8: Small-size object detection algorithm based on camera sensor," *Electronics*, vol. 12, no. 10, p. 2323, 2023.
- [17] D. Cai, Z. Zhang, and Z. Zhang, "Corner-point and foreground-area iou loss: Better localization of small objects in bounding box regression," *Sensors*, vol. 23, no. 10, p. 4961, 2023.
- [18] C. Li, L. Li, H. Jiang, K. Weng, Y. Geng, L. Li, Z. Ke, Q. Li, M. Cheng, W. Nie *et al.*, "Yolov6: A single-stage object detection framework for industrial applications," *arXiv preprint arXiv:2209.02976*, 2022.
- [19] C.-Y. Wang, A. Bochkovskiy, and H.-Y. M. Liao, "Yolov7: Trainable bag-of-freebies sets new state-of-the-art for real-time object detectors," in *Proceedings of the IEEE/CVF Conference on Computer Vision and Pattern Recognition*, 2023, pp. 7464–7475.
- [20] F. Ozge Unel, B. O. Ozkalayci, and C. Cigla, "The power of tiling for small object detection," in *Proceedings of the IEEE/CVF Conference on Computer Vision and Pattern Recognition Workshops*, 2019, pp. 582–591.
- [21] S. W. Kim, M. S. Ki, C.-L. Kim, I.-S. Hwang, and I. S. Jeon, "A simple confocal microscopy-based method for assessing sperm movement," *Development & Reproduction*, vol. 21, no. 3, p. 229, 2017.
- [22] Ultralytics, "Ultralytics yolov5," <https://github.com/ultralytics/yolov5/tree/master>, accessed: 2023-01-14.
- [23] M. V. A. Department, "Yolov6," <https://github.com/meituan/YOLOv6/tree/main>, accessed: 2023-01-14.
- [24] C.-Y. Wang, A. Bochkovskiy, and H.-Y. M. Liao, "Official yolov7," <https://github.com/WongKinYiu/yolov7/tree/main>, accessed: 2023-01-14.
- [25] Ultralytics, "Ultralytics yolov8," <https://github.com/ultralytics/ultralytics/tree/main>, accessed: 2023-01-14.
- [26] A. Nazir and M. A. Wani, "You only look once-object detection models: A review," in *2023 10th International Conference on Computing for Sustainable Global Development (INDIACom)*. IEEE, 2023, pp. 1088–1095.
- [27] I. R. S. Evangelista, L. T. Catajay, M. G. B. Palconit, M. G. A. C. Bautista, R. S. Concepcion II, E. Sybingco, A. A. Bandala, and E. P. Dadios, "Detection of japanese quails (*coturnix japonica*) in poultry farms using yolov5 and detectron2 faster r-cnn," *Journal of Advanced Computational Intelligence and Intelligent Informatics*, vol. 26, no. 6, pp. 930–936, 2022.
- [28] E. Chen, R. Liao, M. Y. Shalaginov, and T. H. Zeng, "Real-time detection of acute lymphoblastic leukemia cells using deep learning," in *2022 IEEE International Conference on Bioinformatics and Biomedicine (BIBM)*. IEEE, 2022, pp. 3788–3790.
- [29] A. Buslaev, V. I. Iglovikov, E. Khvedchenya, A. Parinov, M. Druzhinin, and A. A. Kalinin, "Albumentations: fast and flexible image augmentations," *Information*, vol. 11, no. 2, p. 125, 2020.
- [30] O. E. Olorunshola, M. E. Irhebhude, and A. E. Ewwiekpaefe, "A comparative study of yolov5 and yolov7 object detection algorithms," *Journal of Computing and Social Informatics*, vol. 2, no. 1, pp. 1–12, 2023.
- [31] M. Elgendi, M. U. Nasir, Q. Tang, D. Smith, J.-P. Grenier, C. Batte, B. Spieler, W. D. Leslie, C. Menon, R. R. Fletcher *et al.*, "The effectiveness of image augmentation in deep learning networks for detecting covid-19: A geometric transformation perspective," *Frontiers in Medicine*, vol. 8, p. 629134, 2021.
- [32] Y. Shi, Z. Gao, and S. Li, "Real-time detection algorithm of marine organisms based on improved yolov4-tiny," *IEEE Access*, vol. 10, pp. 131 361–131 373, 2022.
- [33] Y. Shi, X. Li, and M. Chen, "Sc-yolo: A object detection model for small traffic signs," *IEEE Access*, vol. 11, pp. 11 500–11 510, 2023.

Deep Neural Networks for the Qualitative Analysis of Myocardial Perfusion Emission Computed Tomography Images

Nareekarn Pruthipanyasakul*, Nont Kanungsukkasem^{✉†}, Thierry Urruty[‡], and Teerapong Leelanupab[§]

*[†]School of Information Technology, King Mongkut's Institute of Technology Ladkrabang (KMITL)
Bangkok, Thailand, 10520

[‡]XLIM Laboratory, University of Poitiers
UMR CNRS 7252; Poitiers, France

[§]School of Electrical Engineering and Computer Science, The University of Queensland
Brisbane, QLD, Australia, 4072

Email: *65076034@kmitl.ac.th, [✉]Corresponding author: [†]nont@it.kmitl.ac.th
[‡]thierry.urruty@univ-poitiers.fr, [§]t.leelanupab@uq.edu.au

Abstract—Integrating AI into medical diagnosis can provide a more accurate diagnosis when medical staff make treatment decisions. This paper studied on several deep neural networks, re-used with further training for a specific task in classifying the stenosis of a patient's coronary artery. From a 4DM-SPECT application, we collected polar map images that report, for example, myocardial perfusion, function and defect severity from cardiac emission computed tomography examination. We conducted a comparative study to identify the optimal combination of various state-of-the-art pre-trained models (i.e., VGG19, ResNet50, DenseNet121, and EfficientNetB0-B3) and eight different modalities of the myocardial perfusion images for classifying the stenosis of the coronary artery.

Index Terms—Deep Neural Network; Qualitative Analysis; Myocardial Perfusion Imaging; Transfer Learning; Stenosis Classification

I. INTRODUCTION

Coronary Artery Diseases (CADs) are significant causes of mortality worldwide. CADs account for an estimated 17.9 million deaths in 2019, with a projection indicating a future increase. Myocardial Ischemia (MI) [1] is a subset of CADs that occurs when coronary arteries supply insufficient oxygen to heart muscles due to reduced heart blood flow. Poor blood circulation is usually the result of a partial or complete blockage of coronary arteries. Chronic coronary total occlusion from extended ischemia can damage the myocardium and eventually result in acute myocardial infarction, which is a leading cause of sudden death from a heart attack.

As a screening procedure, computed tomography is commonly performed on suspected or symptomatic patients to examine myocardial perfusion or measure how well blood flows through heart muscles. Results of this non-invasive medical examination, also called Single-Photon Emission Computed Tomography (SPECT), are qualitatively and quantitatively analysed by a particular nuclear cardiology application, such as 4DM-SPECT (later known as Corridor4DM), and then

visually reviewed by cardiologists or nuclear medicine physicians through re-constructed images, polar maps. Positive patients are subsequently sent to confirm their coronary arteries' possible contraction or obstruction by cardiac catheterisation. However, this procedure is slightly harmful and considered an invasive medical examination due to dye injection and catheter insertion into blood vessels.

Artificial Intelligence (AI) has increasingly played an important role in medicine and healthcare. Artificially intelligent applications include, for example, medical imaging analysis, patient diagnosis, clinical decision support, and medical document transcription. Ardila et al. [2] proposed their own deep learning method from End-to-End that used a patient's current and prior computed tomography volumes to predict their risk of getting lung cancer. More closely related to our work, those of Betancur et al. [3] developed their own simple convolutional neural network (CNN) with three fully-connected hidden layers to predict the obstruction from Myocardial Perfusion Imaging (MPI) data collected from multiple test centres. They trained the CNN from scratch with a proprietary dataset and compared their prediction with the scoring of total perfusion deficit (TPD). Coupet et al. [4], [5] proposed and evaluated a 2D-3D Deep CNN and transfer learning framework that exploited finely-tuned pre-trained models to detect brain glioma from multimodal MRI sequences. Various state-of-the-art pre-trained models (i.e., VGG19 [6], ResNet50 [7], DenseNet [8], InceptionV3 [9] and EfficientNet-B6 [10]) were studied to highlight the importance of mixing sequences with models to improve the overall performance of their framework.

This research studies several deep neural networks with transfer learning for the stenosis classification of coronary arteries from MPI images. The contributions of this paper can be clarified as follows:

- Many state-of-the-art deep neural networks are evaluated with labels obtained from coronary angiography (CAG) test results, and they show high classification accuracy,

sensitivity, and specificity.

- From the stress and rest SPECT test, several modalities of reconstructed MPI polar map images based on myocardial perfusion are examined in addition to basic raw perfusion. These modalities include severity, defect severity, and defect blackout.
- We conduct a thorough experiment by finely tuning each studied model by Keras tuner to obtain the best performance.

II. RELATED WORKS

A. Myocardial Perfusion Imaging (MPI)

Other than Exercise Electrocardiography (ECG) and Stress Echocardiography, Myocardial Perfusion Imaging (MPI)¹ is a common non-invasive method of cardiac emission computed tomography for screening patients with clinical disorders ranging from asymptomatic atherosclerosis and stable angina to acute coronary syndrome. Two MPI tests are carried out before and after patients exercise to determine the effect of physical stress. These tests are then labelled *rest* and *stress* imaging modalities. From MPI, two quantitative software applications, 4DM-SPECT (aka. Corridor4DM [11]) and QPS-QGS² [12], are further used to process, analyse and report cardiac function and perfusion.

Cardiologists or nuclear medicine physicians then perform qualitative and quantitative assessments on the MPI report, visualised as perfusion polar maps (Fig. 1 (A)), showing raw³, severity, defect severity and defect blackout, as well as scores computed according to the degree of each aspect of perfusion overall and for each coronary artery⁴. The perfusion deficit on this polar map is evaluated in its extent and severity, where all areas that contain values below the assumed threshold are blackened and shown in a defect blackout image.

Clinically interpreting MPI requires the experience of the specialists, by which they may conclude the same test differently on the report of myocardial perfusion and contractility. They either visually assess the polar map images or quantitatively assess the scores derived from the quantitative measurements of myocardial perfusion and function. Otaki et al. [13] compared quantitative and visual prognostic SPECT, and suggested that quantitative analysis provided precise granular risk stratification that is complementary to visual reading results. However, human clinical interpretation by either quantitative or qualitative analysis is considered subjective and suffers from the problem of sub-optimal accuracy and re-interpretability. For example, the accuracy of specialists' assessment of the 4DM-SPECT MPI report at Rajavithi Hospital, Thailand, is just 66.87% when positive patients of MPI were subsequently sent to undergo coronary angiography (CAG) [14], [15] for

¹aka. Radionuclide Myocardial Perfusion Imaging (rMPI).

²Quantitative Gated and Perfusion SPECT

³displaying the normalized polar map values reconstructed from image voxel values.

⁴including left anterior descending coronary artery (LAD), left circumflex coronary artery (LCX) and right coronary artery (RCA).

further evaluation of CAD. As a result, many patients were subjected to the invasive test unnecessarily.

B. Deep Neural Network and Transfer learning

Deep Neural Network (DNN) is essentially a more complex form of Machine Learning (ML), which mimics the functioning of human neural networks by modelling *multi-layer* artificial neural networks. Convolutional Neural Network (CNN) is a special type of DNN model devised to process and extract features from unstructured data, such as photos and videos. In particular, CNN has convolutional layers, applying filters or kernels to the input data so that local features can be extracted while preserving spatial relationships. Transfer Learning (TL) is another ML technique by which an ML model trained in one task is reused and further trained to improve generalization in another task. TL is beneficial, mainly when a training dataset of the re-purposed task is very small because the weights of a pre-trained model initialize the weights of a new model. In the following, we describe examples of TL architectures used in this study.:

1) *VGG19*: Simonyan and Zisserman [6] introduced a depth CNN architecture with 16 or 19 hidden layers, which is well known as VGG16 and VGG19. The VGG models outperformed the previously proposed AlexNet with large filters by increasing depths and exploiting a small 3x3 Convolution filter. The VGG16 model trained with ImageNet dataset obtained a 92.7% accuracy and also won the ILSVR (Imagenet) competition in 2014.

2) *ResNet50*: When training very deep neural networks, the vanishing gradient is a common problem that causes deep neural networks to learn more slowly or not at all. To solve the problem, He et al. [7] proposed the concept of "(Skip) Residual blocks", acting as a shortcut, to skip some layers in a neural network and feed the output of one layer as the input to the next layers. The number of layers with parameters for the entire training determines how to name this framework, such as ResNet50.

3) *DenseNet121*: Developed by Facebook in 2017, DenseNet [8] is a deep learning architecture that again aims to fix the vanishing gradient problem. The DenseNet introduced the concept of dense blocks, which densely connect layers to receive input from all preceding layers. The advantages of DenseNet include feature reuse, gradient flow mitigation, and regularization.

4) *EfficientNet*: In 2019, Google's research team released a new model based on the concept that "a good model should be deep and wide at an appropriate level [10]." The EfficientNet model has a concept called "Compound Scaling" to scale up both the depth and the width of the Network to help the model extract features more accurately using resources as a determinant. Following this concept makes all eight versions of EfficientNet available, with each version from B0 to B7, resulting from an increase in the constant ratio according to the model's version sequence. The higher the number of versions, the higher the resources used and the predictive performance.

C. Deep Learning in Nuclear Medical Image Analysis

Papandrianos et al. [16] explored two CNN models, i.e., a self-custom CNN and a deep CNN using transfer learning with VGG16, for SPECT MPI polar maps classification. In their work, a small data set of 314 polar maps of only raw perfusion in stress and rest representations, with AC (attenuation correction) and NC (non-attenuation correction) formats, were collected from patients who only underwent CAG within 60 days. Ground truth, used to train and test models, was labelled by two experts. Only positive patients evaluated by routine visual assessment of MPI by physicians would be sent to CAG. As a result, samples in their dataset were questioned to be mostly positive. They reported the high performance of VGG16 and custom CNN at 95.83% and 92.07%, respectively.

A later interesting work from the same research team by Apostolopoulos et al. [17] studied an explainable AI algorithm, Grad-CAM++, on a similar MPI dataset with a larger number of 486 patients. They concatenated four modalities of raw perfusion of MPI together into a single image, i.e., stress AC & NC and rest AC & NC. They also enhanced a transfer learning model from VGG16 to a more layer and complex VGG19 by adding feature-fusion blocks and attention modules. This new model was renamed AFF-VGG19. The accuracy of their proposed model trained and tested against CAG was strong, with 78.81%, but much lower than that done against human labelling, with 89.92% and that in their previous work.

III. EXPERIMENTAL DESIGN

Our study aims to compare the performance of stenosis classification of pre-trained models with transfer learning, i.e., VGG19, ResNet50, DenseNet121, EfficientNetB0-3, further trained from different modalities of MPI polar map. Each modality is a combination of rest/stress (condition of patient's heart before or after exercise) and different reconstructions of data, i.e., raw, severity (Sev), defect severity (Def_Sev) and defect blackout (Blo). We build each model by following our data pipeline, as shown in Fig. 1.

A. Dataset

Our data were collected from "The Nuclear Medicine Department of Rajvithi Hospital, Thailand" and cover a period of patient information from 29 May 2008 to 22 February 2021. Suspected or symptomatic patients underwent gated-SPECT MPI imaging by a SPECT gamma-camera system (Infinia 3/8", GE Healthcare). NC (Non-Attenuation Correction) was applied in all cases in both stress and rest images, and data were acquired over 180°. To create our experimental dataset, we initially collected data only from patients cardiologists assessed from their MPI test results positive in a test routine in the hospital. Four hundred thirty-one positive patients were then subjected to invasive CAG within 60 days from MPI for further evaluation. CAG test results confirmed 298 positive patients and 133 negative patients. This confirmation reveals that the accuracy of human assessment of MPI is just 69.14%, resulting in many patients undergoing CAG unnecessarily.

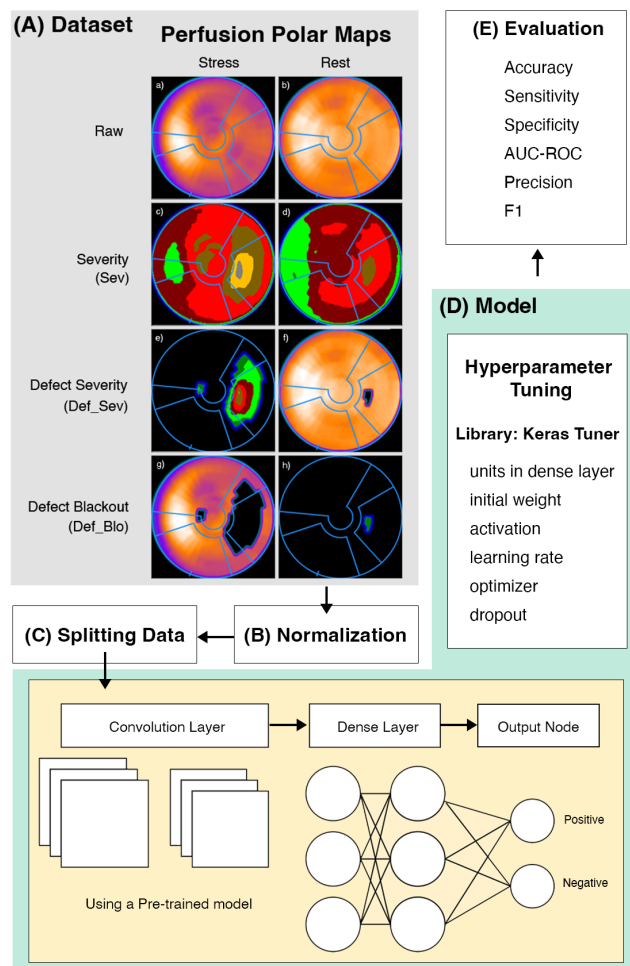


Fig. 1. Overall data processing pipeline of the current study.

Furthermore, the initial collection suffers from the problem of an imbalanced dataset. To solve this issue by not synthesizing or oversampling data, we gradually gathered more negative samples of MPI and evaluated models until 115 negative samples were finally added to the original dataset. By doing so, we clinically assumed that negative samples from MPI would have negative results from CAG as well. Eventually, we obtained a somewhat balanced experimental dataset of 546 patients, with 298 positive and 248 negative samples, with the ratio of positive to negative being 55:45.

We focused on eight modalities of polar maps, derived from 4DM-SPECT MPI test results [18] as shown in Fig 1 (A). These modalities include:

- Raw polar map of stress (Raw_str),
- Raw polar map of rest (Raw_rst),
- Severity polar map of stress (Sev_str),
- Severity polar map of rest (Sev_rst),
- Defect Severity polar map of stress (Def_Sev_str),
- Defect Severity polar map of rest (Def_Sev_rst),
- (Defect) Blackout polar map of stress (Blo_str), and
- (Defect) Blackout polar map of rest (Blo_rst).

We deliberately omitted the measurements of cardiac wall motion and thickening for our future studies and considered only the perfusion polar map in this research.

However, the pictures from 4DM-SPECT were not separated into each polar map as shown in Fig 1 (A). Accordingly, we cropped each polar map from the picture and resized each polar map to 224x224 pixels, which was the default input size for VGG19 and ResNet.

B. Normalization

In the data preparation, we normalized the value of each channel of each pixel with a minimum of 0 and a maximum of 255 to be in the range of 0 to 1 by min-max normalization to reduce processing time when modeling.

C. Splitting Data

To select optimal models for the stenosis classification, we employed the Three-Way Holdout method [19], with model selection via Keras Tuner, to partition our data. This resulted in a division of data into training and test sets in a 90:10 ratio. Furthermore, within the training set of initial splitting, we performed an additional split into a training subset and a validation subset in a 90:10 ratio as inputs of the Keras Tuner for hyperparameter tuning.

D. Model

This research focused on the modalities and pre-trained models, leading to 56 combinations to be compared. Each experiment needed a pre-trained model in the convolution layer and an effective setting of hyperparameters to ensure the best result from each combination. Accordingly, the tuning was applied to hyperparameters of the dense layer and dropout layer, as well as an optimizer for compiling the model.

To apply the pre-trained model to our specific kind of data, we added two dense layers to form a specific network for the final stage. We tuned three simple hyperparameters, i.e., unit of dense, initial weight and activation function, for each dense layer. A higher number of units enhanced the layer's capacity to capture complex patterns, but it also increased the number of parameters in the model, which could lead to overfitting and large model size. Therefore, we started the tuning from 2^1 , which was the same number of output nodes, to 2^{13} , which should be large enough to discover a suitable number of units. Besides, as activation function was used to represent the complex relationships among data and a different activation function leading to different convergence rates and performance, five activation functions, i.e., *i*) Rectified Linear Unit Function (ReLU), *ii*) Leaky Rectified Linear Unit (LeakyReLU), *iii*) Hyperbolic Tangent Function (Tanh), *iv*) Exponential Linear Unit (ELU) and *v*) Sigmoid, were experimented to get a suitable one. Even though initial weights for each model could impact the convergence speed and overall performance of the neural network, it was randomly selected by Keras Tuner by default. To get a better result, we applied four initial weight techniques, i.e.,

(i) Zero, initializing all weights to 0;

- (ii) He Normal [20], initializing each weight to a random number with a Gaussian distribution, $\mathcal{N}(\mu = 0, \sigma^2 = \sqrt{2/n})$, where n is the number of inputs to the node;
- (iii) Glorot [21], initializing each weight to a random number with a continuous uniform distribution, $\mathcal{U}(\alpha = -\sqrt{1/n}, \beta = \sqrt{1/n})$; and
- (iv) Normalized Glorot, initializing each weight to a random number with a continuous uniform distribution, $\mathcal{U}(\alpha = -\sqrt{6/(n+m)}, \beta = \sqrt{6/(n+m)})$, where m is the number of outputs from the layer to find a suitable initial weight.

However, adding a dense layer may lead to an overfitting problem. So, we added a dropout layer between the two dense layers and tuned the dropout rate from 0% to 100% to get the best result. We also experimented with three optimizers, i.e., Stochastic gradient descent (SGD), Adaptive Moment Estimation (Adam) and Root Mean Square (RMSProp), with learning rate tuning from 1e-1 to 1e-5 to get a suitable one for each combination.

All of the tuning above were processed by Hyperband [22], an optimization technique within the Keras Tuner library designed to enhance the hyperparameter tuning process, with the validation dataset. As our computational resources were constrained, we selected Hyperband instead of the other alternatives, e.g., Grid Search and Bayesian Optimization, set max_epochs to 30 instead of the default value of 100, randomly selected 99 as our seed number and left the rest as defaults.

E. Evaluation

After being trained, the models were evaluated with a test set and compared by five evaluation metrics, i.e., Accuracy, Sensitivity, Specificity, Area under the ROC curve (AUC), Precision and F1 (Harmonic Mean of Precision and Recall (Sensitivity)), by following [3], [16], [17]. A model with low Sensitivity, meaning that the model is less effective at detecting real disease cases, can put the life of a patient in danger. While a model with low specificity does not lead to any life-threatening, it instead leads to unnecessarily invasive screening, e.g., CAG. Lastly, we use AUC to measure the ability of a binary classification model to distinguish between classes across different threshold settings and Precision to assess how good a predictive model is to discover a sick person.

IV. RESULTS AND DISCUSSION

Table I shows the top 10 models, ranked based on multiple measures, including Accuracy as the primary factor, followed by Sensitivity, Specificity, AUC, Precision and F1. According to the results shown in the table, three models achieved the same highest Accuracy value of 0.8727 (highlighted in bold). These models are: *i*) Sev_str_Effb1, a model trained from severity polar map of stress condition using Transfer Learning with EfficientNet-B1; *ii*) Blo_str_Effb2, a model trained from blackout polar map of stress condition using Transfer Learning with EfficientNet-B2; and *iii*) Raw_str_Effb3, a model trained

TABLE I
PERFORMANCE METRICS OF TOP 10 DEEP NEURAL NETWORKS ACCORDING TO ACCURACY,
FOLLOWED BY SENSITIVITY, SPECIFICITY, AUC, PRECISION AND F1, WITH MAIN REFERENCE TO CAG.

| Rank | Data | Accuracy | Sensitivity | Specificity | AUC | Precision | F1 |
|------|-------------------|---------------|---------------|---------------|---------------|---------------|---------------|
| 1 | Sev_str_Effb1 | 0.8727 | 0.8723 | 0.7403 | 0.8717 | 0.8723 | 0.8723 |
| 2 | Blo_str_Effb2 | 0.8727 | 0.8662 | 0.8141 | 0.8717 | 0.8662 | 0.8662 |
| 3 | Raw_str_Effb3 | 0.8727 | 0.8662 | 0.7730 | 0.8724 | 0.8662 | 0.8662 |
| 4 | Blo_str_Effb0 | 0.8545 | 0.8505 | 0.6887 | 0.8519 | 0.8505 | 0.8505 |
| 5 | Def_Sev_str_Effb3 | 0.8545 | 0.8444 | 0.8218 | 0.8525 | 0.8444 | 0.8505 |
| 6 | Blo_str_VGG19 | 0.8545 | 0.8444 | 0.7805 | 0.8525 | 0.8444 | 0.8444 |
| 7 | Def_Sev_str_Effb1 | 0.8545 | 0.8444 | 0.7750 | 0.8519 | 0.8444 | 0.8444 |
| 8 | Raw_str_Effb2 | 0.8545 | 0.8444 | 0.7656 | 0.8333 | 0.8444 | 0.8444 |
| 9 | Def_Sev_str_Effb0 | 0.8364 | 0.8349 | 0.7951 | 0.8347 | 0.8349 | 0.8444 |
| 10 | Blo_str_Effb1 | 0.8364 | 0.7738 | 0.8349 | 0.8347 | 0.8349 | 0.8349 |

from raw polar map of stress condition using Transfer Learning with EfficientNet-B3. From this finding, we can suggest that training models with other modalities, i.e., severity and blackout, can build strong models for stenosis classification. It is worth mentioning that when comparing the results of our models with that of Apostolopoulos et al. [17] using just raw perfusion with an AFF-VGG19 and a baseline VGG19, our models with a fine-tuning of hyperparameters outperform theirs, 0.7881 and 0.6955, respectively, in terms of Accuracy. Our standard VGG19 model, e.g., Blo_str_VGG19, also performs better than their custom AFF-VGG19. Although we cannot directly compare the results due to different datasets, we can argue that our dataset in this study is well-balanced and model optimization is a vital process in model training. We can also maintain the suggestion of using other modalities of reconstructed MPI images (e.g., severity and blackout), without concatenating them all into a single image, and using other more advanced deep neural networks, particularly EfficientNet, to train models for this task.

When further considering the Sensitivity of the top three models, Sev_str_Effb1 achieved the highest Sensitivity value of 0.8723. However, among the three models with top Accuracy, Sev_str_Effb1 performed the worst with a Specificity value of 0.7403, significantly below the highest value of 0.8349 with a difference of 0.0946. When life-threatening is our main focus, we will choose Sev_str_Effb1 as the first choice due to the highest Sensitivity. Sev_str_Effb1 also obtains the best performance in terms of Accuracy, Precision and F1. However, when we consider all measures together, Blo_str_Effb2 model seems to be the best classifier for the prediction of stenosis because it performed with the best Accuracy, the second best Sensitivity with not much difference from the top, the third best Specificity with not much difference from the top and the second best Precision and F1 with not much difference from the top. Moreover, considering AUC (Area Under the ROC Curve, as shown in Fig.2), it performed the second best with AUC score of 0.8717 (considering as excellent discrimination in accordance with [23].)

As shown in the Table I, all of the top 10 models were trained from the polar map of stress condition. So, considering only one modality, training from the polar map of stress is

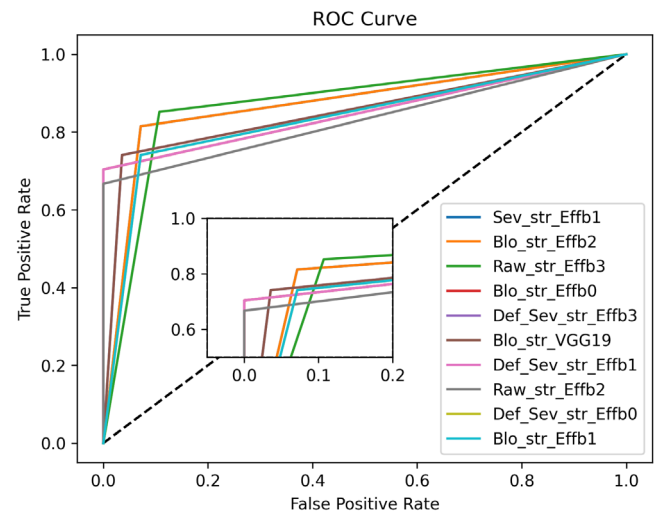


Fig. 2. ROC Curve of top 10 models according to Accuracy

better than training from the polar map of rest. Furthermore, 4 out of the top 10 models were trained from the defect blackout polar map of stress condition (Blo_str). Accordingly, Blo_str seems to be a good choice of modalities to be used as a training set. Moreover, 9 out of the top 10 models used transfer learning with EfficientNet even though we experimented with B0 to B3 versions with their small scale of network because of our computational constraint. We expected that EfficientNet version B4 to B7 with a larger scale of network should potentially lead to a more effective classification model in our future studies.

V. CONCLUSION

In this paper, we compared the performance of seven state-of-the-art deep neural networks with transfer learning when trained separately from eight modalities of MPI polar maps to find the best predictive model for stenosis of CAD. Our label data was hybrid confirmed with CAG and assumed clinically. We added two dense layers into our neural network and used Hyperband for hyperparameter tuning. Considering Accuracy, Sensitivity, Specificity, AUC, Precision and F1 all

together, EfficientNet version B2 trained from a blackout polar map of the stress condition seems to be the most suitable model for predicting CAD with the highest Accuracy value of 0.8727. However, aware mostly of life-threatening, EfficientNet version B1 trained from a severity polar map of the stress condition is the best choice with the same highest Accuracy and the highest Sensitivity at 0.8723. In our future work, we will focus on improving the model performance, such as using more effective pre-trained models (e.g., EfficientNetV2), feeding different images of stress and rest polar maps, studying an explainable AI method to highlight the regions influencing the model's output, adding augmentation to increase our data for training and applying ensemble methods.

ACKNOWLEDGMENT

This research work is fully funded by the Health Systems Research Institute (HSRI) under project no. "66-041", and partially supported by the School of Information Technology, KMITL for Nareekarn's Higher Degree by Research. This work is a collaboration between KMITL and Rajavithi Hospital. Two IRBs have ethically approved this research with certificate no. "EC-KMITL 65 117" and "Rajavithi 024/2566". Many special thanks should also go to Miss Taratip Narawong and Dr. Tarit Taerakul (MD.) for the permit of data access and collection.

REFERENCES

- [1] J. de Lemos and T. Omland, *Chronic Coronary Artery Disease: A Companion to Braunwald's Heart Disease*, ser. Companion to Braunwald's Heart Disease. Elsevier Health Sciences, 2017.
- [2] D. Ardila, A. P. Kiraly, S. Bharadwaj, B. Choi, J. J. Reicher, L. Peng, D. Tse, M. Etemadi, W. Ye, G. Corrado, D. P. Naidich, and S. Shetty, "End-to-end lung cancer screening with three-dimensional deep learning on low-dose chest computed tomography," *Nature Medicine*, vol. 25, no. 6, pp. 954–961, 2019.
- [3] J. A. Betancur, L.-H. Hu, F. Commandeur, T. Sharir, A. J. Einstein, M. B. Fish, T. D. Ruddy, P. Kaufmann, A. J. Sinusas, E. J. Miller, T. M. Bateman, S. Dorbala, M. Di Carli, G. Germano, Y. Otaki, J. X. Liang, B. K. Tamarappoo, D. Dey, D. S. Berman, and P. J. Slomka, "Deep learning analysis of upright-supine high-efficiency spect myocardial perfusion imaging for prediction of obstructive coronary artery disease: A multicenter study," *Journal of Nuclear Medicine*, 2018.
- [4] M. Coupet, T. Urruty, T. Leelanupab, M. Naudin, P. Bourdon, C. Fernandez-Maloigne, and R. Guillemin, "A multi-sequences MRI deep framework study applied to glioma classification," *Multimedia Tools and Applications*, vol. 81, no. 10, pp. 13 563–13 591, feb 28 2022.
- [5] —, "An empirical study of deep neural networks for glioma detection from MRI sequences," in *Neural Information Processing*. Springer International Publishing, 2020, pp. 113–125.
- [6] K. Simonyan and A. Zisserman, "Very deep convolutional networks for large-scale image recognition," in *proceedings of the 3rd International Conference on Learning Representations, ICLR 2015, San Diego, CA, USA*.
- [7] K. He, X. Zhang, S. Ren, and J. Sun, "Deep residual learning for image recognition," in *proceedings of the 29th IEEE Conference on Computer Vision and Pattern Recognition, CVPR 2016, Las Vegas, NV, USA*.
- [8] G. Huang, Z. Liu, L. van der Maaten, and K. Q. Weinberger, "Densely connected convolutional networks," *Transactions of the Association for Computational Linguistics*.
- [9] C. Szegedy, V. Vanhoucke, S. Ioffe, J. Shlens, and Z. Wojna, "Rethinking the inception architecture for computer vision," in *proceedings of the 29th IEEE Conference on Computer Vision and Pattern Recognition, CVPR 2016, Las Vegas, NV, USA*.
- [10] M. Tan and Q. V. Le, "Efficientnet: Rethinking model scaling for convolutional neural networks," in *proceedings of the 36th International Conference on Machine Learning, ICML 2019, Long Beach, CA, USA*.
- [11] E. P. Ficaro, B. C. Lee, J. N. Kritzman, and J. R. Corbett, "Corridor4dm: The michigan method for quantitative nuclear cardiology," *Journal of Nuclear Cardiology*, vol. 14, no. 4, pp. 455–465, 2007, abstracts of Original Contributions, ASN 2007, 12th Annual Scientific Session.
- [12] G. Germano, P. B. Kavanagh, P. J. Slomka, S. D. Van Kriekinge, G. Pollard, and D. S. Berman, "Quantitation in gated perfusion spect imaging: the cedars-sinai approach." *J Nucl Cardiol*, vol. 14, no. 4, pp. 433–454, Jul 2007.
- [13] Y. Otaki, J. Betancur, T. Sharir, L.-H. Hu, H. Gransar, J. X. Liang, P. N. Azadani, A. J. Einstein, M. B. Fish, T. D. Ruddy, P. A. Kaufmann, A. J. Sinusas, E. J. Miller, T. M. Bateman, S. Dorbala, M. D. Carli, B. K. Tamarappoo, G. Germano, D. Dey, D. S. Berman, and P. J. Slomka, "5-year prognostic value of quantitative versus visual mpi in subtle perfusion defects," *JACC: Cardiovascular Imaging*, vol. 13, no. 3, pp. 774–785, 2020.
- [14] E. N. Arnett, "Coronary Artery Narrowing in Coronary Heart Disease: Comparison of Cineangiographic and Necropsy Findings," *Annals of Internal Medicine*, vol. 91, no. 3, p. 350, sep 1 1979.
- [15] W. C. Roberts and A. A. Jones, "Quantitation of coronary arterial narrowing at necropsy in sudden coronary death," *The American Journal of Cardiology*, vol. 44, no. 1, pp. 39–45, 7 1979.
- [16] N. I. Papadrianos, I. D. Apostolopoulos, A. Feleki, D. J. Apostolopoulos, and E. I. Papageorgiou, "Deep learning exploration for spect mpi polar map images classification in coronary artery disease." *Ann Nucl Med*, vol. 36, no. 9, pp. 823–833, Sep 2022.
- [17] I. D. Apostolopoulos, N. D. Papanthasiou, N. Papadrianos, E. Papageorgiou, and D. J. Apostolopoulos, "Innovative attention-based explainable feature-fusion vgg19 network for characterising myocardial perfusion imaging spect polar maps in patients with suspected coronary artery disease," *Applied Sciences*, vol. 13, no. 15, 2023.
- [18] G. Healthcare, *4D-MSPECT PROTOCOL For Xeleris™ 2 Functional Imaging PR Systems Operator Guide*, 1st ed. GE Healthcare, 2007.
- [19] S. Raschka, "Model evaluation, model selection, and algorithm selection in machine learning," *CoRR*, vol. abs/1811.12808, 2018.
- [20] K. He, X. Zhang, S. Ren, and J. Sun, "Delving deep into rectifiers: Surpassing human-level performance on imagenet classification," *CoRR*, vol. abs/1502.01852, 2015.
- [21] X. Glorot and Y. Bengio, "Understanding the difficulty of training deep feedforward neural networks," in *proceedings of the 13th International Conference on Artificial Intelligence and Statistics, AISTATS 2010, Sardinia, Italy*.
- [22] L. Li, K. G. Jamieson, G. DeSalvo, A. Rostamizadeh, and A. Talwalkar, "Efficient hyperparameter optimization and infinitely many armed bandits," *CoRR*, vol. abs/1603.06560, 2016.
- [23] D. W. Hosmer, S. Lemeshow, and R. X. Sturdivant, *Chapt. 5 "Assessing the Fit of the Model"*. Wiley, 2013.

Automatic Identification of Abnormal Lung Sounds Using Time-Frequency Analysis and Convolutional Neural Network

Rattanathon Phettom
Biomedical Engineering Institute,
Chiang Mai University, and
Graduated School,
Chiang Mai University
Chiang Mai, Thailand
rattanathon_p@cmu.ac.th

Nipon Theera-Umpon*, Senior Member
IEEE
Biomedical Engineering Institute,
Chiang Mai University, and
Department of Electrical Engineering,
Chiang Mai University
Chiang Mai, Thailand
nipon@ieec.org

Sansanee Auephanwiriyaikul, Senior
Member IEEE
Biomedical Engineering Institute,
Chiang Mai University, and
Department of Computer Engineering,
Chiang Mai University
Chiang Mai, Thailand
sansanee@ieec.org

*Corresponding Author

Abstract—This research focuses on the development of a method utilizing signal processing and machine learning techniques to identify abnormal lung sounds, specifically adventitious lung sounds, for diagnosis and monitoring. The proposed algorithm combines short-time Fourier transform (STFT) with convolutional neural networks (CNN) to automatically analyze breath sounds captured by a stethoscope. By employing a band pass filter, noise is effectively removed, facilitating accurate identification of lung sounds. The algorithm classifies abnormal lung sounds, such as crackles and wheezes, with an impressive accuracy rate of 85.27%. This research not only enhances the efficiency of physical examinations but also enables the recording and analysis of lung sounds, thereby offering valuable insights into the progression of treatments. Furthermore, the development of this medical device has significant implications for advancing human healthcare and information retrieval in the field of respiratory medicine.

Keywords—lung sound, breath sound identification, abnormal lung sound, short-time Fourier transform, convolutional neural networks

I. INTRODUCTION

Respiratory diseases can be analyzed through the examination of lung sounds, with doctors utilizing a stethoscope as a diagnostic tool to identify abnormal sounds. Accurate identification of these sounds is crucial for a proper diagnosis and effective treatment. While listening through a stethoscope is a relatively simple approach, accurate diagnosis based on this method requires professional expertise, which may present challenges for novice examiners. In light of this, we aim to develop an algorithm capable of automatically identifying normal and abnormal lung sounds, specifically classifying them as wheezes or crackles. The implementation of such an algorithm has several potential benefits, including reducing the subjective examination time for medical personnel in identifying normal and abnormal lung sounds and mitigating the bias associated with subjective assessments based on observer experience. This research focuses on the common occurrence and clinical significance of crackles and wheezing [1] in respiratory diseases, utilizing recorded lung sound signals for analysis.

Breath sound is a significant bio-signal originating from the chest region during inhalation and exhalation [2]. These

sounds are easily perceivable in a quiet environment or when we consciously focus on our breathing. The act of breathing is the result of the coordinated action of respiratory muscles, and as air flows through the airways, breath sounds are produced. Each complete cycle of inhalation and exhalation is referred to as a lung cycle. The primary muscle responsible for breathing is the diaphragm, which contracts during inhalation, leading to an increase in lung volume and the intake of air. Conversely, during exhalation, when the diaphragm relaxes, lung volume decreases, and air is expelled from the lungs. As a consequence, inspiratory and expiratory sounds are generated, representing different phases of the breathing process.

The diagnostic process for respiratory diseases involves the auscultation technique, which entails the clinical examination of the lungs by listening to specific areas on the anterior (front), posterior (back), and lateral (side) regions of the chest wall. The presence of abnormal sounds during auscultation is referred to as adventitious sounds (AS). Examples of these sounds include crackles, wheezing, and others, characterized by variations in frequency, pitch, intensity, and energy. It is evident that the analysis of these adventitious sounds can provide valuable information for diagnosing lung diseases. Hence, the primary hypotheses of this research are as follows: Firstly, the algorithm developed will be capable of identifying lung sound cycles, thereby distinguishing between normal and abnormal lung sounds. Secondly, in cases where abnormal lung sounds are detected, the algorithm will successfully classify them as crackles or wheezing based on recorded lung sounds [1] obtained from a respiratory dataset [2]. To ensure accuracy, all sound files undergo noise removal procedures, followed by segmentation into individual lung sound cycles. Finally, a convolutional neural network (CNN) is employed to identify abnormal sounds within these cycles. This algorithmic approach enables efficient and effective detection of abnormal breath sounds, contributing to improved diagnostic capabilities in respiratory medicine.

This paper is organized as follows. The background of respiratory sound processing and related works are presented in section II. Section III explains the experimental framework for this research. The experimental results and discussion are presented in section IV, while section V concludes this paper.

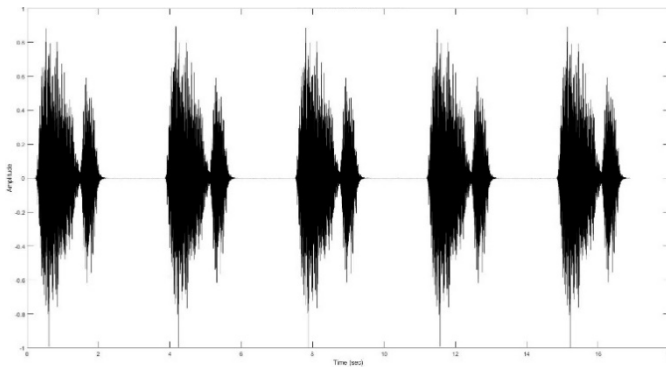


Fig. 1 Waveform of vesicular breath sound.

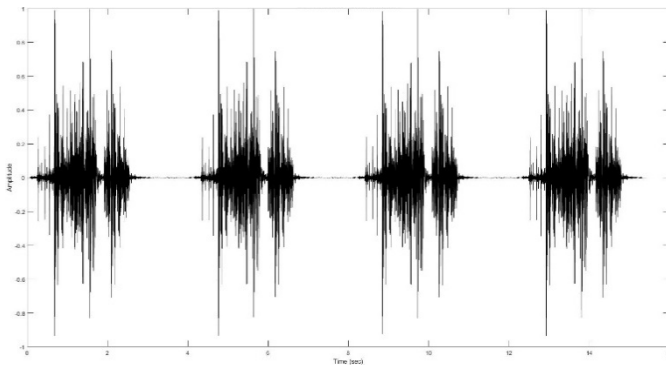


Fig. 2 Waveform of crackle.

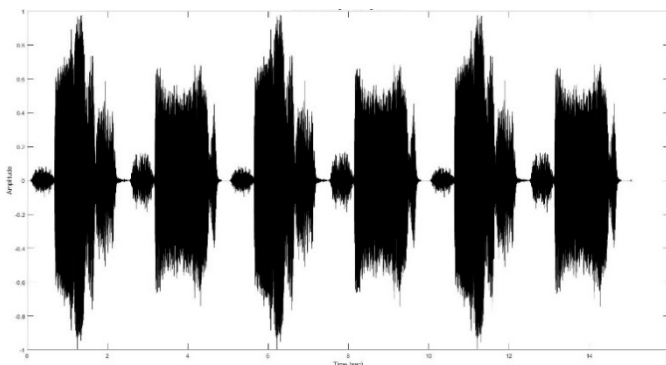


Fig. 3 Waveform of expiration wheezing.

II. RESPIRATORY SOUND PROCESSING AND RELATED RESEARCH

The automatic acoustic identification of respiratory sounds has the potential to assist doctors in the classification of diseases related to the human respiratory system, such as asthma, pneumonia, and chronic obstructive pulmonary diseases (COPD) [3]. These diseases exhibit distinctive acoustic patterns when listening to lung sounds. The classification tasks can be broadly categorized into two groups: disease classification [3] and abnormal sound classification [4]. Meanwhile, there is a growing demand for new and simplified methods to detect respiratory diseases from lung sounds, for example, a robust deep learning framework [5], the extraction of lung sounds from mixed heart and lung sounds [6], the study of non-linearity and non-stationarity nature of lung sound signals [7].

In light of the aforementioned challenges, researchers have developed novel algorithms aimed at identifying normal breath sounds and abnormal breath sounds, specifically crackles and wheezing. Distinguishing normal breath sounds is relatively straightforward. However, crackle and wheezing sounds can occur in various regions of the lungs, including the trachea. Wheezing sounds, characterized by longer duration and greater loudness than usual, typically exhibit frequencies ranging from 250 to 400 Hz. Conversely, crackle sounds manifest as continuous popping sounds throughout the breath cycle and can occur across a wide range of frequencies within the lung sound spectrum [8].

Numerous studies have been conducted to identify normal and abnormal lung sounds, employing various techniques and algorithms, for example, using the Hough transform of spectrograms [9], wavelet packet decomposition [10], adaptive multi-level in-exhale segmentation technique [11], time-expanded waveform analysis [12]. These advancements have paved the way for more accurate and automated analysis of respiratory sounds, improving the diagnosis and treatment of respiratory diseases.

Some research studies have focused on diagnosing diseases from lung sounds and addressing the issue of noise interference, particularly from heart sounds [13], [14]. Furthermore, research has focused on noise removal techniques, particularly in cases where heart sounds interfere with lung sounds [15]–[17]. These studies have contributed to the development of noise removal techniques and accurate disease diagnosis from lung sounds, addressing the challenges posed by overlapping heart sounds and various ambient noises.

Furthermore, the normal lung sound (vesicular breath sound) and the abnormal lung sounds (crackle and wheezing) are different in some characteristic as shown next [8].

In Figure 1, the vesicular breath sound is characterized by its soft, low-pitched nature with a rustling quality. During inspiration, it is louder and has a longer duration compared to expiration. The ratio of inspiration to expiration is approximately 1:3. Figure 2 shows crackle sounds that exhibit popping, low-pitched characteristics with a bubbling quality. They are louder and have a longer duration compared to fine crackles. These crackles can be heard during both inspiration and expiration. Wheezing is a continuous sound that can be either high-pitched (squeaking) or low-pitched (snoring or moaning) as shown in Figure 3. It is caused by the narrowing of airways, leading to a prolonged wheezing phase. Wheezing can occur during both inspiration and expiration.

These descriptions provide an overview of the characteristics of vesicular breath sounds, crackles, and wheezing. Understanding these distinct sounds can aid in the identification and diagnosis of respiratory conditions during auscultation.

III. EXPERIMENTAL FRAMEWORK

The experimental framework employed in this study includes data acquisition, data preparation, classification, and performance evaluation as depicted in Figure 4. The steps involved in each phase are as follows:

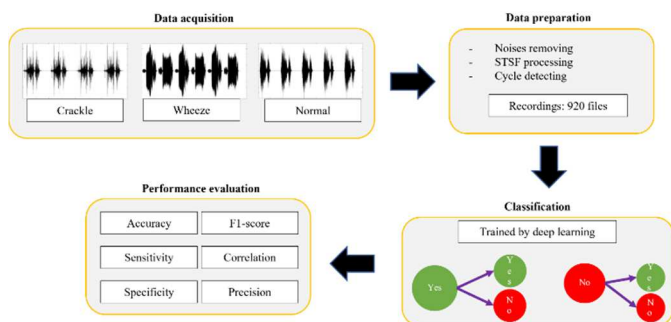


Fig. 4 Block diagram framework of this research.

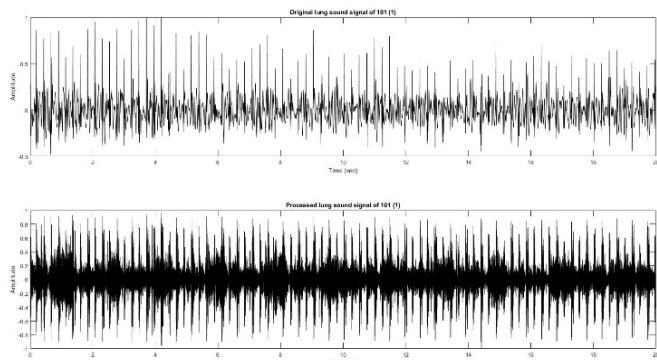
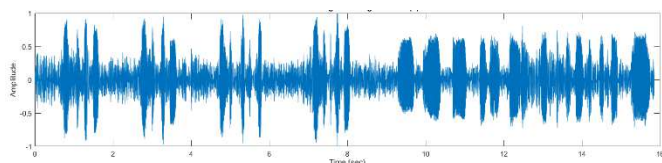
Fig. 5 Top: Waveform without bandpass filter.
Bottom: Waveform with bandpass filter.

Fig. 6 Lung sound signal in time domain.

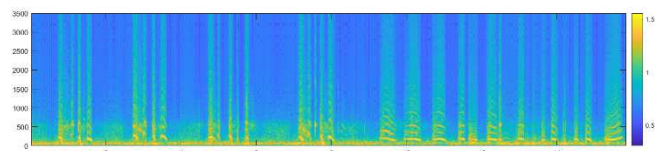


Fig. 7 STFT of lung sound signal in Fig. 6.

1) Data acquisition

We utilized a dataset called “A Respiratory Sound Database for the Development of Automated Classification” [2]. The dataset consists of 920 lung sound files obtained from 126 subjects. The files have varying lengths ranging from 10 seconds to 90 seconds. The dataset includes a total of 5.5 hours of recordings, comprising 6,898 respiratory cycles. Among these cycles, 1,864 contain crackle sounds, 886 contain wheeze sounds, and 506 contain both crackle and wheeze sounds. The dataset includes recordings from individuals of different age groups, including children, adults, and the elderly. Both clean respiratory sounds and noisy recordings that simulate real-life conditions are included in the dataset.

2) Data processing

a) Noises removing

We aimed to isolate the breathing cycles in each sound file. However, we found that in some files, the heart sounds interfered more prominently than the lung sounds, resulting in the breathing cycle being obscured by the heartbeat cycle, which occurs more frequently. To address this issue, a 5th-order Butterworth bandpass filter was employed to eliminate the heart sound. Only frequencies between 200 Hz and 2000 Hz were allowed to pass through the filter. As a result, the low-frequency sound of the heart was effectively removed (Figure 5). The lung sound typically has frequencies lower than 1600 Hz [15], while frequencies higher than that are likely to be environmental noise. Additionally, any speech interruptions within the breathing cycle, which contain both low and high frequencies [18] that are more noticeable than lung sounds, were removed.

b) Short-time Fourier transform (STFT)

After removing the noise from the signal, we analyzed the signal in the time domain by taking the absolute value of the signal. Thresholding was then applied to obtain the breathing cycle, but the resulting signal was spiky, making it difficult to identify the cycle. To address this issue, we utilized short-time Fourier transform (STFT) $X(j, k)$ according to

$$X(j, k) = \sum_{n=-\infty}^{\infty} x(n)w(n-j)e^{-ikn}, \quad (1)$$

where $x(n)$ represents the signal and $w(n)$ is the analyzing window. STFT provides a frequency representation of the signal at different time points [19]. This approach allowed us to observe the spiky signal as frequencies within the cycle. The frequency domain representation of the cycle is often clearer than the time domain representation, as shown in Figures 6 and 7. Both figures have time on the X-axis in seconds, but the Y-axis of Figure 6 represents amplitude, while the Y-axis of Figure 7 represents frequency in hertz (Hz).

c) Cycle detecting

To detect the breathing cycle from the two-dimensional STFT representation, we combined the values in each row to obtain a one-dimensional graph. Then a Gaussian filter was applied to smooth it. However, the smoothed graph still contained jagged portions, so a morphological opening operator was performed to further refine the graph. We applied peak and low point detection algorithms to identify true peaks (inspiration or expiration points) and true low points (covering the breathing cycle) on the graph (Figure 8). Subsequently, the graph was merged with the STFT representation to locate the starting and ending points of the breathing cycles. Finally, the STFT representation was segmented into individual cycles, preparing the data for training and testing purposes (Figure 9).

d) Classification

For each case, 80% of the data were randomly used for training a convolutional neural network (CNN). A pretrained GoogLeNet model was utilized. The inputs of the CNN were STFT images covering the breathing cycle detected in the previous step. The outputs of the CNN were set depending upon each of the four following cases: 1) crackle and wheeze, 2) crackle and normal, 3) wheeze and normal, and 4) all three combined (crackle, wheeze, and normal). The number of epochs and the learning rate were set to 60 and 0.001,

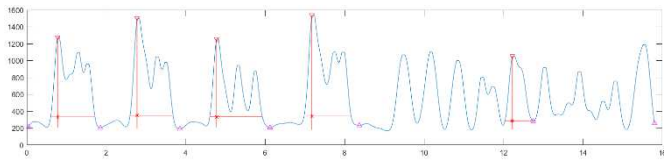


Fig. 8 Graph of smoothed and detected cycle in frequency domain.

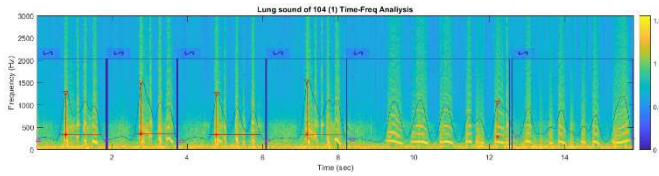


Fig. 9 Merged graph of smoothed and detected cycle in frequency domain with STFT representation.

respectively. The remaining 20% of the data were used to test the algorithm model specific to each case.

e) Performance evaluation

After the signals were classified by the algorithm model, performance evaluation metrics were calculated including the true positive (TP), true negative (TN), false positive (FP), and false negative (FN) values. These values were further used to calculate accuracy, precision, sensitivity, specificity, F1-score, and correlation using Equations (2) to (7), respectively [20-24].

$$Accuracy = \frac{TP + TN}{TP + TN + FP + FN} \quad (2)$$

$$Precision = \frac{TP}{TP + FP} \quad (3)$$

$$Sensitivity = \frac{TP}{TP + FN} \quad (4)$$

$$Specificity = \frac{TN}{TN + FP} \quad (5)$$

$$F1-Score = \frac{2TP}{2TP + FP + FN} \quad (6)$$

$$Correlation = \frac{Accuracy - P_e}{1 - P_e} \quad (7)$$

TABLE I. PERFORMANCE EVALUATION OF EACH CASE: CRACKLE AND WHEEZE AND NORMAL, CRACKLE AND WHEEZE, CRACKLE AND NORMAL, WHEEZE AND NORMAL.

| Classes | Crackle and wheeze and normal | Crackle and wheeze | Crackle and normal | Wheeze and normal |
|-------------|-------------------------------|--------------------|--------------------|-------------------|
| Accuracy | 57.09% | 85.27% | 62.99% | 75.19% |
| Precision | 58.28% | 90.13% | 57.22% | 49.72% |
| Sensitivity | 66.74% | 88.99% | 66.04% | 68.46% |
| Specificity | 46.23% | 76.15% | 60.55% | 77.39% |
| F1-Score | 62.23% | 89.56% | 61.31% | 57.61% |
| Correlation | 0.13 | 0.65 | 0.26 | 0.41 |

| | | Ground truth | | |
|-----------|---------|--------------|--------|--------|
| | | Crackle | Wheeze | Normal |
| Predicted | Crackle | 217 | 11 | 157 |
| | Wheeze | 19 | 82 | 57 |
| | Normal | 82 | 37 | 184 |

Fig 10 Confusion matrix of crackle vs. wheeze vs. normal case.

| | | Ground truth | |
|-----------|---------|--------------|--------|
| | | Crackle | Wheeze |
| Predicted | Crackle | 283 | 31 |
| | Wheeze | 35 | 99 |

Fig 11 Confusion matrix of crackle vs. wheeze case.

| | | Ground truth | |
|-----------|---------|--------------|--------|
| | | Crackle | Normal |
| Predicted | Crackle | 210 | 157 |
| | Normal | 108 | 241 |

Fig 12 Confusion matrix of crackle vs. normal case.

| | | Ground truth | |
|-----------|--------|--------------|--------|
| | | Wheeze | Normal |
| Predicted | Wheeze | 89 | 90 |
| | Normal | 41 | 308 |

Fig 13 Confusion matrix of wheeze vs. normal case.

where P_e is defined as

$$P_e = \frac{(TP + FP)(TP + FN) + (TN + FN)(TN + FP)}{(TP + TN + FP + FN)^2} \quad (8)$$

IV. EXPERIMENTAL RESULTS AND DISCUSSION

To provide a comprehensive analysis of the obtained results on the test data, the confusion matrices for all 4 cases, namely “all together crackle vs. wheeze vs. normal,” “crackle vs. wheeze,” “crackle vs. normal,” and “wheeze vs. normal,” are presented in Figures 10 to 13, respectively. Table 1 presents the performance evaluation metrics for each case, including accuracy, precision, sensitivity, F1-score, and correlation.

It is worth noting that the crackle vs. wheeze case yielded the highest accuracy (85.27%), precision (90.13%), sensitivity

(88.99%), F1-score (89.56%), and correlation (0.65) among the tested cases. On the other hand, the wheeze vs. normal case exhibited the highest specificity, with a value of 77.39%.

It is observed that the crackle vs. wheeze case exhibited the highest performance evaluation, whereas the crackle vs. wheeze vs. normal case demonstrated the lowest performance evaluation. This implies that crackle sounds possess distinct characteristics that make them comparatively easier to classify in comparison to normal sounds. However, it is noteworthy that the crackle vs. normal case yielded relatively smaller values, indicating some similarity between crackle and normal sounds in the frequency domain. Consequently, the employed feature extraction method, namely the short-time Fourier transform, may lack adequacy in effectively discriminating between crackle and normal sounds.

We encountered challenges in mitigating noise, particularly the interference of heart sounds. Filtering out heart sound noise using a high pass filter inadvertently removed low-frequency lung sound information due to the overlap in frequency ranges between the two. Furthermore, the maximum frequency of heart sounds varied across different locations of the lung lobes. These intricacies highlight the complexity associated with accurately eliminating heart sound noise while preserving relevant lung sound information [15]. Achieving accurate differentiation between the two types of sounds solely based on frequency cutoff proved to be challenging due to these considerations.

Another issue discussed pertains to the accuracy of the algorithm in counting breathing cycles. Some cycles were erroneously counted as two separate cycles instead of one, and the initial and final cycles often lacked the inclusion of inspiration and expiration phases as indicated by the ground truth data. These observations underscore limitations in the algorithm's ability to precisely detect and count cycles. Additionally, the presence of prolonged coughing sounds, which exceeded the typical duration of breathing cycles, introduced further challenges in accurate cycle counting.

These challenges and limitations point towards potential avenues for methodological refinement. For instance, exploring alternative techniques for noise reduction that specifically address heart sound interference and developing more robust algorithms for precise cycle detection could enhance the overall performance of the classification system and improve its reliability in distinguishing between different categories of lung sounds.

V. CONCLUSION

This research presents a method for the automatic identification of abnormal lung sounds. The proposed method involves the removal of noise, particularly heart sounds, followed by the conversion of the sound from the time domain to the frequency domain. Subsequently, the breath cycles are located, and the lung sound is identified as crackle, wheezing, or normal.

Furthermore, the findings of this research suggest the potential for further development into a portable medical device. Such a device could offer real-time analysis and display of data, enabling direct transmission to a computer or mobile phone for immediate access by healthcare professionals. This advancement could enhance the efficiency

and accessibility of lung sound analysis, contributing to improved diagnosis and monitoring of respiratory conditions.

ACKNOWLEDGMENT

The Teaching Assistant and Research Assistant Scholarship from the Graduate School, Chiang Mai University and a scholarship from Biomedical Engineering Institute, Chiang Mai University provided to R. Phetom are acknowledged.

REFERENCES

- [1] Vbookshelf, *Respiratory Sound Database Use audio recordings to detect respiratory diseases*, [internet] 2019 [cited 1st June 2021]; Available from: <https://www.kaggle.com/datasets/vbookshelf/respiratory-sound-database>
- [2] B.M. Rocha, et al., "A respiratory sound database for the development of automated classification," *International Conference on Biomedical and Health Informatics*, pp. 33-37, 2017.
- [3] S. Ntalampiras, and I. Potamitis, "Automatic acoustic identification of respiratory diseases," *Evolving Systems*, vol. 12, pp. 69-77, 2021.
- [4] S. Ulukaya, G. Serbes, and Y.P. Kahya, "Wheeze type classification using non-dyadic wavelet transform based optimal energy ratio technique," *Computers in Biology and Medicine*, vol. 104, pp. 175-182, 2019.
- [5] L. Pham, et al., "Robust deep learning framework for predicting respiratory anomalies and diseases," *The 42nd Annual International Conference of the IEEE Engineering in Medicine & Biology Society (EMBC)*, pp. 1-4, 2020.
- [6] Q. Zhang, et al., "Noise removal of tracheal sound recorded during CPET to determine respiratory rate," *The 41st Annual International Conference of the IEEE Engineering in Medicine & Biology Society (EMBC)*, pp. 1-4, 2019.
- [7] R.J. Oweis, et al., "An alternative respiratory sounds classification system utilizing artificial neural networks," *Biomedical Journal*, vol. 38, no. 2, pp. 153-161, 2015.
- [8] MEDZCOOL, *Heart and Lung Sound Library*, [web page] 27th June 2021, [cited 18th Mar 2021]; Available from: <https://www.medzcool.com/auscultate>
- [9] K.X. Zhang, et al., "Detection of wheeze based on Hough transform of spectrogram," *Journal of Northeastern University Natural Science*, vol. 38, no. 11, pp. 1534-1537, 2017.
- [10] J. Zhang, et al., "Real-world verification of artificial intelligence algorithm-assisted auscultation of breath sounds in children," *Frontiers in Pediatrics*, vol. 9, 2021, doi: 10.3389/fped.2021.627337.
- [11] H. Chen, et al., "Automatic multi-level in-exhale segmentation and enhanced generalized S-transform for wheezing detection," *Compute Methods Programs Biomed*, vol. 178, pp. 163-173, 2019.
- [12] A.R.A. Sovijarvi, et al., "A new versatile PC-based lung sound analyzer with automatic crackle analysis (HeLSA); repeatability of spectral parameters and sound amplitude in healthy subjects," *Technology and Health Care*, vol. 6, no. 1, pp. 11-22, 1998.
- [13] S.K. Chowdhury, and A.K. Majumder, "Digital spectrum analysis of respiratory sound," *IEEE Transactions on Biomedical Engineering*, vol. BME-28, no. 11, pp. 784-788, 1981.
- [14] L. Fraiwan, et al., "Automatic identification of respiratory diseases from stethoscopic lung sound signals using ensemble classifiers," *Biocybernetics and Biomedical Engineering*, vol. 41, no. 1, pp. 1-14, 2021.
- [15] F. Ghaderi, H.R. Mohseni, and S. Sanei, "Localizing heart sounds in respiratory signals using singular spectrum analysis," *IEEE Transactions on Biomedical Engineering*, vol. 58, no. 12, pp. 3360-3367, 2011.
- [16] V.K. Iyer, et al., "Reduction of heart sounds from lung sounds by adaptive filtering," *IEEE Transactions on Biomedical Engineering*, vol. BME-33, no. 12, pp. 1141-1148, 1986.
- [17] A. Suzuki, C. Sumi, and K. Nakayama, "Adaptive cancelling of ambient noise in lung sound measurement," *Japanese Journal of Medical Electronics and Biological Engineering*, vol. 31, no. 4, pp. 354-359, 1993.

- [18] N. Theera-Umpon, S. Chansareewittaya, and S. Auephanwiriyaikul, "Phoneme and tonal accent recognition for Thai speech," *Expert Systems With Applications*, vol. 38, no. 10, pp. 13254-13259, 2011.
- [19] J.S. Lim and A.V. Oppenheim, *Advanced Topics in Signal Processing*, Prentice Hall, 1988.
- [20] K.J. Livak, and T.D. Schmittgen, "Analysis of relative gene expression data using real-time quantitative PCR and the $2^{-\Delta\Delta CT}$ method," *Methods*, vol. 25, no. 4, pp. 402-408, 2001.
- [21] G. Kresse, and J. Furthmüller, "Efficient iterative schemes for ab initio total-energy calculations using a plane-wave basis set," *Physical Review B - Condensed Matter and Materials Physics*, vol. 54, no. 16, pp. 11169-11186, 1996.
- [22] S.F. Altschul, et al., "Basic local alignment search tool," *Journal of Molecular Biology*, vol. 215, no. 3, pp. 403-410, 1990.
- [23] T. Joachims, "A Support Vector Method for multivariate performance measures," *The 22nd International Conference on Machine Learning*, pp. 377-384, 2005.
- [24] J. Kaufman, et al., "Schedule for affective disorders and schizophrenia for school-age children-present and lifetime version (K-SADS-PL): Initial reliability and validity data," *Journal of the American Academy of Child and Adolescent Psychiatry*, vol. 36, no. 7, pp. 980-988, 1997.

Development of Self-Supervised Learning with Dinov2-Distilled Models for Parasite Classification in Screening

Natchapon Pinetsuksai
College of Advanced
Manufacturing Innovation
King Mongkut's Institute of
Technology Ladkrabang
Bangkok, Thailand
63609007@kmitl.ac.th

Veerayuth Kittichai
Faculty of Medicine
King Mongkut's Institute of
Technology Ladkrabang
Bangkok, Thailand
veerayuth.ki@kmitl.ac.th

Rangsan Jomtarak
Faculty of Science and
Technology
Suan Dusit University
Bangkok, Thailand
Rangsan_jom@dusit.ac.th

Komgrit Jaksukam
College of Advanced
Manufacturing Innovation
King Mongkut's Institute of
Technology Ladkrabang
Bangkok, Thailand
komgrit.ja@kmitl.ac.th

Teerawat Tongloy
College of Advanced
Manufacturing Innovation
King Mongkut's Institute of
Technology Ladkrabang
Bangkok, Thailand
teerawat_tongloy@kkumail.com

Siridech Boonsang
Department of Electrical
Engineering, School of
Engineering
King Mongkut's Institute of
Technology Ladkrabang
Bangkok, Thailand
siridech.bo@kmitl.ac.th

Santhad Chuwongin
College of Advanced
Manufacturing Innovation
King Mongkut's Institute of
Technology Ladkrabang
Bangkok, Thailand
santhad.ch@kmitl.ac.th

Abstract— At present, parasitic infections in humans, such as intestinal parasitic infections and soil-transmitted helminth (STH) infection, remain a public health concern, with screening methods that are simple but time-consuming and require parasitology experts. Microscopy images are increasingly being used to aid diagnosis but creating labels for supervised learning (SL) is a time-consuming, labor-intensive, and costly process. Self-supervised learning (SSL) is a deep learning approach that aims to train models to represent features in unlabeled datasets using automatically generated labels or annotations from the data itself, rather than explicitly labeled human-labeled labels. It is an appropriate method to address the challenges associated with the difficulty of labeling large datasets. A pretrained model that has learned useful data representations from an SSL task is fine-tuned using labeled data to perform well on a specific downstream task. DINOv2 is an SSL model based on the Vision Transformer (ViT) architecture. In this study, we aim to create a model for screening for helminth egg infection using a fine-tuned Dinov2 with a classification layer head to demonstrate that dataset sizes of 1% and 10% are sufficient when compared to SL model. Rather than SL, which requires a significant amount of human data labeling and is generally impractical, the model developed in this study is expected to be used in active surveillance in the future.

Keywords— *parasite eggs, Bootstrap Your Own Latent (BYOL), Dinov2, Self-supervised learning (SSL), Object classification.*

I. INTRODUCTION

Intestinal parasitic infections are the most prevalent in the world, mostly found in developing countries with estimates of more than 2 billion people worldwide infected [1], including all regions in Thailand [2]. According to the World Health Organization (WHO), approximately 1.5 billion people worldwide, or 24%, have soil-transmitted helminth infections (STH) [3]. STH infections, especially hook-worm infections, are particularly common in the southern region of Thailand [2]. Microscopy, for example, remains the mainstay of parasitic infection diagnostics, but it is time consuming. Faster testing is required without sacrificing sensitivity, and it can be used in both clinical and low-resource field settings [4]. Images are one of the results of microscopy. We can use these images to develop models using machine learning or deep learning and create a system for screening parasites, preserving parasitologists' expertise and valuable time.

Previous research combines microscopy images with support vector machines to develop a system for classifying parasite eggs [5]. Another vision-based method for detecting

and identifying *Trichuris suis* parasite eggs, which are used in drugs for low-systemic immunodeficiencies like Crohn's disease, was demonstrated [6]. All of this demonstrates that microscope images can be used to aid in diagnosis.

Transformer architecture has predominantly been used in natural language processing (NLP) and in the field of computer vision. While convolutional neural networks (CNNs) have been the industry standard for vision tasks, a transformer can be applied directly to sequences of image patches and achieve competitive image classification results. When pretrained on large datasets, ViT model outperforms state-of-the-art CNNs in a variety of benchmarks while requiring fewer computational resources for training [6]. For large datasets, labeling for SL is a time-consuming and expensive process. This issue is even more prevalent in fields such as digital pathology and laboratory medicine. Because of uncertainty and inconsistency in the data and annotation, the manual annotation process typically has a high variance [7]. SSL is the process of training models to represent features using unlabeled datasets. It is an appropriate method for addressing the challenges that arise from the difficulty of labeling large datasets. SSL can fine-tune models to suit the work that needs to be continued from that dataset or out of the domain without having to use a big dataset [8]. According to "A Cookbook of Self-Supervised Learning" [9], SSL is gaining more and more attention, even though SSL itself still has some complicated models. However, it is extremely useful in downstream tasks. [9]. Example for SSL: a deep learning model developed for diagnosing COVID-19 using over 100,000 chest X-ray images. The model, which combines the SSL technique with a convolutional attention module, can achieve an average accuracy of 98.6%, outperforming the baseline model by 0.8%. It is particularly effective in classifying three types of classes: normal, pneumonia, and COVID-19. The study claims that the model exhibits excellent classification performance with an average area under the curve (AUC) of 0.994 for the COVID-19 class [10]. DINOv2 is a self-supervised learning model designed for computer vision tasks. It aspires to serve as a "foundation" model in the field of computer vision, similar to how certain models serve foundational roles in Natural Language Processing (NLP). DINOv2 is trained on a large, curated dataset and is built on ViT architecture. The model is engineered to produce robust, all-purpose visual features. It incorporates a variety of techniques to improve the speed and stability of training and also includes a unique data curation pipeline. In benchmarks, DINOv2 outperforms existing all-purpose features, making it a strong candidate for various computer vision applications [11].

In this research, we use a dataset from the IEEE dataport [12]. We intend to develop a model for screening for helminth infection using a fine-tuned Dinov2 ViT with a classification layer head to prove that a small number of dataset (1 % and 10%) are sufficient for developing models when compared to developing supervised learning which requires a large amount of human data labeling. Furthermore, we anticipate that the model we've developed will play a pivotal role in future active surveillance initiatives. Its potential applications could greatly enhance the efficiency and accuracy of monitoring and early detection, thereby contributing significantly to public health efforts.

II. ARCHITECTURE

A. Architecture

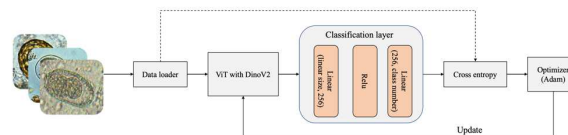


Fig. 1 Architecture of Dinov2 Classifier model.

We begin with the Dinov-2 Classifier model in this study. For feature extraction, this model incorporates a distilled Dinov2[11] transformer. A sequential classifier handles the classification layer. This classifier is made up of two linear layers: the first converts the data from 'linear size' to 256 dimensions, followed by a Relu activation function, and the second maps the 256 dimensions to the 'class number' (number of classes is 11).

III. MATERIALS AND METHODS

A. Experimental designs

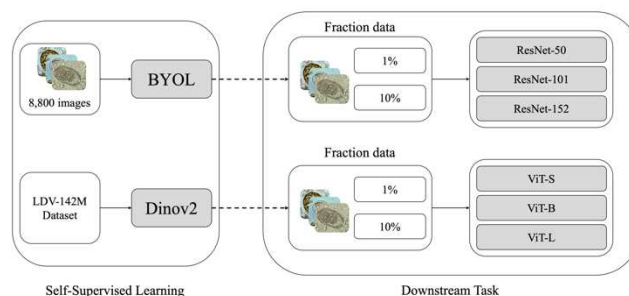


Fig. 2. Processes overview. We compare the BYOL and Dinov2 models with fraction data at 1% and 10% and model sizes. In the BYOL, a pretrained model was created with parasite images and fine-tuned with ResNet-50, ResNet-101, ResNet-152 backbone [13]. In Dinov2, a pretrained model was created with the LVD-142M dataset and fine-tuned with a classification layer head by using fraction data at 1% and 10% and model sizes: ViT-S, ViT-B, ViT-L, respectively.

In order to develop robust classification models for the detection of parasitic eggs in Thailand, we embarked on an ambitious endeavor to create a variety of Dinov2-based models encompassing the ViT-S, ViT-B, and ViT-L architectures [11] and compare the performance of Dinov2 with BYOL [13] at data fractions of 1% and 10%, respectively. The need to identify the most efficient and effective solutions for this difficult and critical task in parasitology and public health motivated this comprehensive approach to model development.

B. Dataset collection

The dataset, including images and labels used, was obtained from the IEEE public dataset and contains 11 parasitic egg types [12]. Each category has 1,000 images, including *Ascaris lumbricoides*, *Capillaria philippinensis*, *Enterobius vermicularis*, *Fasciolopsis buski*, *Hookworm egg*, *Hymenolepis diminuta*, *Hymenolepis nana*, *Opisthorchis viverrini*, *Paragonimus spp.*, *Taenia spp.* and *Trichuris trichiura*. We used CiRA CORE's in-house platform to crop images from boundary box format to classification format for each object. These images were expanded by a factor of 1.2 of the bounding box, initially resized to 608x608 pixels, and then further adjusted to 224x224 pixels [11] before being input into

the classification model. They were saved in PNG format with square padding to maintain the aspect ratio.

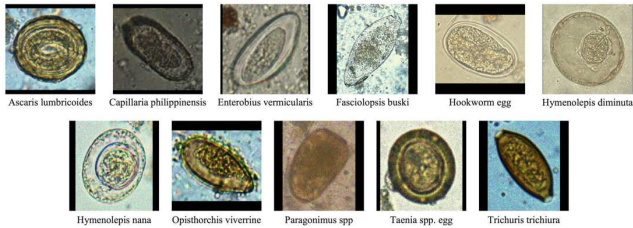


Fig. 3. Genus and species of 11-helminth classes used in this study.

Public datasets are useful for group training and testing. According to Pinetsuksai et al. [13], these datasets were used and split the training datasets into 80% for training and 20% for evaluation. In this study, we undertook a meticulously designed sampling approach by extracting subsets comprising 1% and 10% of the dataset, both drawn from the initial 80% partition, to perform a fine-tuning procedure for enhancing the classification performance of our Dinov2 models. This strategic decision to perform fine-tuning with varying proportions of data is central to the experimental design, allowing us to investigate how the model's performance evolves and adapts under divergent data availability scenarios, while ensuring rigorous control over the training process.

TABLE I. DISTRIBUTION OF DATASET

| Dataset | images |
|--------------------------------|--------|
| 80% of training dataset | 8,800 |
| 20% of training dataset | 2,200 |
| 1% in 80% of training dataset | 88 |
| 10% in 80% of training dataset | 880 |
| Testing dataset | 2,228 |

C. Model training configurations

The linear size of the Dinov2 classifier model depends on ViT models. We setup by following TABLE II.

TABLE II. LINEAR SIZE OF ViT MODEL [11]

| ViT model | Linear size |
|-----------|-------------|
| ViT-S | 384 |
| ViT-B | 768 |
| ViT-L | 1,024 |

As our objective function for training the Dinov-2 Classifier model, we employed the Cross Entropy Loss. The Adam optimizer with a learning rate of $1e-6$ and a maximum epoch of 500 epochs is used to optimize the model parameters.

D. Computational Resources

We use Nvidia DGX-A100 with a 40GB one GPU, RAM 32GB which is a state-of-the-art system designed for the most demanding AI and HPC tasks. With its advanced GPU capabilities, high memory bandwidth, and comprehensive software support.

E. Evaluation metric

1) Confusion matrix

A confusion matrix is a common tool used to evaluate the performance of classification models, especially multi-class classification. It is a summary of a classification model's predictions in comparison to the actual labels or ground truth. The results of the confusion matrix is organized into a table with four key components: True Positive (TP), True Negative (TN), False Positive (FP) and False Negative (FN), which we can use to calculate the performance of the models, which include:[14]

$$Accuracy = \frac{TP + TN}{TP + TN + FP + FN} \quad (1)$$

$$Recall = \frac{TP}{TP + FN} \quad (2)$$

$$Precision = \frac{TP}{TP + FP} \quad (3)$$

$$Specificity = \frac{TN}{TN + FP} \quad (4)$$

$$F1\ score = \frac{2 \times Precision \times Recall}{Precision + Recall} \quad (5)$$

2) Receiver Operating Characteristic (ROC) curve

The traditional ROC curve is a binary classification performance metric that plots the True Positive Rate (Sensitivity) against the False Positive Rate (1-Specificity) at various threshold settings. In a multi-class setting, the ROC curve can be extended using techniques like one-vs-all (or one-vs-rest). The one-vs-all approach treats each class as positive while treating all other classes as negative, and a ROC curve is generated. This produces as many ROC curves as classes.

IV. EXPERIMENTAL RESULTS

A. Experimental results from pretrained Dinov2 models

1) Training loss

As shown in Fig. 4, the cross-entropy loss for 10% of all models decreases noticeably faster than it does for 1% of them. It has been stable for approximately 100 epochs, as opposed to the 1% dataset, which is stable for roughly 200 epochs, so the maximum epoch of 500 epochs can be used by selecting the epoch with the least loss of each model, where the minimum loss represented the best model.

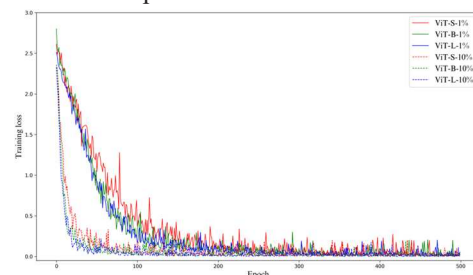


Fig. 4. Training loss for different pretrained Dinov2 models with 1% and 10% fractions for fine-tuning.

2) Confusion matrix table

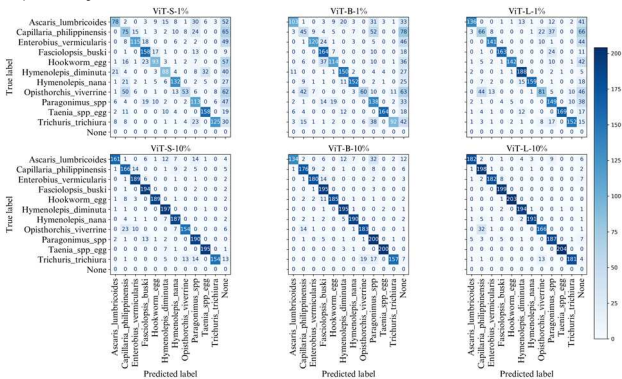


Fig. 5 Confusion matrix tables depicting the performance of various Dinov2 ViT models at threshold 50%, differentiated by training data volume. Intensified color corresponds to higher TP values.

In the fraction dataset, the 1% "None" prediction is due to the limited size of the dataset. Having only 8 images per class is insufficient, leading to the model's inability to recognize objects effectively. *Capillaria philippinensis* and *Opisthorchis viverrini* were challenging to detect due to their small size and inconspicuous appearance. As depicted in Fig. 5, when using the Dinov2-Small model with a dataset size of only 1%, the TP values for these helminth eggs were 75, 45, and 66 respectively, indicating insufficient detection. While increasing the model size to Dinov2-Base and Dinov2-Large does not improve the detection performance, enlarging the dataset size to 10% clearly enhances the performance of all models.

TABLE III. EVALUATION METRICS INCLUDING RECALL, PRECISION, ACCURACY, SPECIFICITY AND F1 SCORE, RESPECTIVELY OF DINOV2 BY ViT-S, ViT-B, ViT-L MODELS.

| Evaluation metrics | Models | Fraction dataset | |
|--------------------|--------|------------------|-------|
| | | 1% | 10% |
| Accuracy | ViT-S | 0.934 | 0.981 |
| | ViT-B | 0.942 | 0.982 |
| | ViT-L | 0.958 | 0.990 |
| Recall | ViT-S | 0.534 | 0.887 |
| | ViT-B | 0.584 | 0.896 |
| | ViT-L | 0.694 | 0.937 |
| Precision | ViT-S | 0.687 | 0.908 |
| | ViT-B | 0.750 | 0.919 |
| | ViT-L | 0.824 | 0.952 |
| Specificity | ViT-S | 1.000 | 1.000 |
| | ViT-B | 0.993 | 0.999 |
| | ViT-L | 0.989 | 0.999 |
| F1-score | ViT-S | 0.588 | 0.894 |
| | ViT-B | 0.636 | 0.901 |
| | ViT-L | 0.747 | 0.943 |

As seen in Table 3, the model's accuracy is greater than 0.93 for all dataset sizes. At the fraction dataset of 10%, All models have higher recall and precision than those at the fraction dataset of 1%. The F1 score values for the 10% dataset

are consistent with accuracy, in contrast to the 1% fraction dataset, where the F1-score value drops significantly. The model's specificity predicts non-target classes very well.

Interestingly, increasing the number of datasets from 1% to 10%, we can improve accuracy, recall, precision, and F1-score for all three models significantly. As the size of the models grows, so does the confusion matrix.

3) Receiver Operating Characteristic (ROC) curve

The ROC Curve offers an extensive evaluation of the model's performance because it was created by varying the classification threshold of the model and recording the TPR and FPR at each threshold point. Each point on the curve represents the model's performance at a particular threshold. The area under the curve (AUC) defines a metric called by the ROC curve. The higher the AUC value, the better the performance of the model [15].

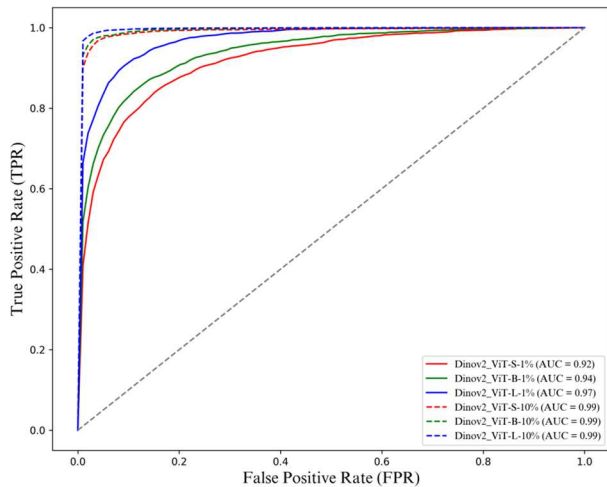


Fig. 6 Macro average ROC curves of Dinov2, ViT-S-1%, ViT-B-1%, ViT-L-1%, ViT-S-10%, ViT-B-10% and ViT-L-10%

When we measure model performance with AUC, we can see that Dinov2 ViT-S-1 % can achieve a performance as good as 0.92 even with the smallest model and dataset size of only 88 images. In addition, Dinov2 ViT-S, ViT-B, and ViT-L at fraction dataset 10% get the same value of 0.99, but the difference is in the resources used in training and prediction models. Because it is the smallest model, ViT-S consumes fewer resources. As a result, the optimal model of Dinov2 for our study is ViT-S at fraction dataset 10%.

B. Experimental Result from models' comparison between Dinov2 and BYOL [13]

In this section, we delve into a comprehensive comparative analysis of Dinov2 using ViT-S, ViT-B, ViT-L and BYOL using ResNet-50, ResNet-101 and ResNet-101, two state-of-the-art deep learning models, focusing on their performance at data fractions of 1% and 10%, respectively. This investigation is an important step toward understanding how these models behave in different data availability scenarios and provides valuable insights into their suitability for various use cases and resource constraints.

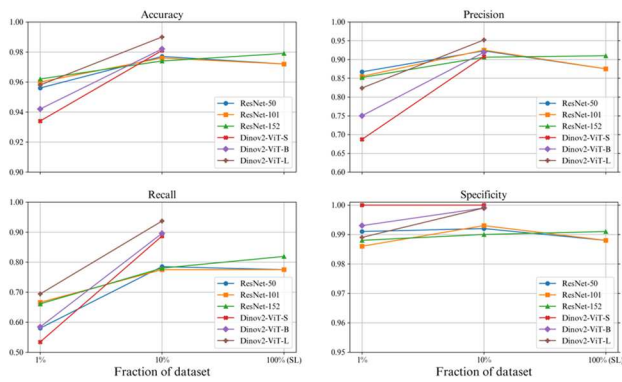


Fig. 7 Comparison of Dinov2 and BYOL performance in terms of accuracy, precision, recall, and specificity from confusion metrics tables.

According to Fig. 7, the model at data fraction of 10% yields higher confusion metrics than that at data fraction of 1% for all values. As a result, regardless of the model size, a data fraction of 10% can be chosen. Dinov2-L is the best model at data fraction 10% because it has the highest confusion metrics of all values.

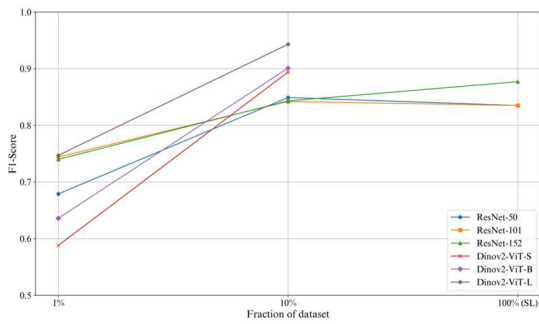


Fig. 8. F1-score from confusion metrics tables for different SL (ResNet-50, ResNet-101, and ResNet-152) and SSL (Dinov2-S, Dinov2-B, and Dinov2-L) models.

Fig. 8 shows the F1-score graph, which further confirms that the Dinov2-ViT-L model at a fraction dataset 10% outperforms other models with the same data fraction.

V. CONCLUSIONS

In this paper, we developed self-supervised learning with Dinov2-distilled models for the classification of parasites for screening. Both the Dinov2 and BYOL models are affected by data fraction. For Dinov2, increasing model size has a direct impact on model efficiency, as shown by the curve of the confusion metrics Dinov2 increases as model size increases. If computational resource constraints are the primary concerns, Dinov2 ViT-S, ViT-B, and ViT-L can be selected. However, increasing the amount of data has an effect on those constraints as well. Alternatively, the primary concerns could be the parasitology experts because fine-tuning the model requires annotation from specialists. For a data fraction of 1%, fine-tuning with Dinov2-ViT-L is the optimal option. If increasing the size of data fraction to 10%, model performance can be improved significantly, or we can go with any model because the AUC clearly shows that model efficiency is the same in Dinov2.

Our study shows that the best model is Dinov2-L, and the best fraction data is 10%, yielding accuracy 99.0%, recall 93.7%, precision 95.2%, specificity 99.9%, F1-score 94.3, and AUC 99.0%. Finally, we anticipate that the developed model

will be used in the future for active surveillance in remote areas, leveraging the power of cutting-edge technology to address the unique challenges and opportunities associated with monitoring and managing these isolated regions. The implementation of this model has the potential to transform how we collect critical data, ensure the safety and security of remote communities, and make informed decisions in environments where traditional surveillance methods are often impractical or ineffective.

VI. DISCUSSION

“An intelligent detection method for plasmodium based on self-supervised learning and attention mechanism” [16]

It is another interesting research work. This study is about developing a method for detecting malaria protozoa using machine learning. Convolutional Neural Networks (CNN) and uses the backbone ResNet, an improvement on ResNet with the addition of a Split-Attention Attention Mechanism. It gave very interesting results of accuracy of 97.8%, sensitivity of 96.5% and specificity of 98.9% where dataset was used from 1/3 of the total data but still very high accuracy.

Still in doubt in the downstream task of SSL, it is still the size of the total dataset and the ratio that we are interested in, which cannot tell us what the fraction must be since we do not know the total number of dataset. It has been seen that only 8 images per class can achieve over 90% accuracy in this dataset and can also use the smallest models like ViT-S to provide very high performance.

Finally, an extension of using Dinov2-ViT that can be used for the classification of parasite eggs is that we can create a system to send images to models to process and send images and predicted values back together with the confidence of each class to make doctors' decisions more accurate. And in the future, A mobile bot [17] can be developed to capture images from a smartphone camera connected to a USB microscope [18]. These images can then be analyzed by the bot to classify whether they contain parasites.

REFERENCES

- [1] T. Eyayu *et al.*, "Prevalence of intestinal parasitic infections and associated factors among patients attending at Sanja Primary Hospital, Northwest Ethiopia: An institutional-based cross-sectional study," *PLoS ONE*, vol. 16, 2021.
- [2] R. Kache, N. Phasuk, P. Viriyavejakul, and C. Punsawad, "Prevalence of soil-transmitted helminth infections and associated risk factors among elderly individuals living in rural areas of southern Thailand," *BMC Public Health*, vol. 20, 2020.
- [3] C. C. Lim, N. A. A. Khairudin, S. W. Loke, A. S. A. Nasir, Y. F. Chong, and Z. Mohamed, "Comparison of Human Intestinal Parasite Ova Segmentation Using Machine Learning and Deep Learning Techniques," *Applied Sciences*, 2022.
- [4] A. Ricciardi and M. Ndao, "Diagnosis of Parasitic Infections: What's Going On?," *Journal of Biomolecular Screening*, vol. 20, no. 1, pp. 6-21, 2015, doi: 10.1177/1087057114548065.
- [5] D. Avci and A. Varol, "An expert diagnosis system for classification of human parasite eggs based on multi-class SVM," *Expert Systems with Applications*, vol. 36, no. 1, pp. 43-48, 2009.
- [6] A. Dosovitskiy *et al.*, "An Image is Worth 16x16 Words: Transformers for Image Recognition at Scale," p. arXiv:2010.11929doi: 10.48550/arXiv.2010.11929.
- [7] A. Chowdhury, J. Rosenthal, J. Waring, and R. Umerton, "Applying Self-Supervised Learning to Medicine: Review of the State of the Art and Medical Implementations," *Informatics*, vol. 8, no. 3, p. 59, 2021. [Online]. Available: <https://www.mdpi.com/2227-9709/8/3/59>.

- [8] S.-C. Huang, A. Pareek, M. E. K. Jensen, M. P. Lungren, S. Yeung, and A. S. Chaudhari, "Self-supervised learning for medical image classification: a systematic review and implementation guidelines," *NPJ Digital Medicine*, vol. 6, 2023.
- [9] R. Balestrieri *et al.*, "A Cookbook of Self-Supervised Learning," p. arXiv:2304.12210doi: 10.48550/arXiv.2304.12210.
- [10] J. Park, I.-Y. Kwak, and C. Lim, "A Deep Learning Model with Self-Supervised Learning and Attention Mechanism for COVID-19 Diagnosis Using Chest X-ray Images," *Electronics*, vol. 10, no. 16, p. 1996, 2021. [Online]. Available: <https://www.mdpi.com/2079-9292/10/16/1996>.
- [11] M. Oquab *et al.*, "DINOv2: Learning Robust Visual Features without Supervision," p. arXiv:2304.07193doi: 10.48550/arXiv.2304.07193.
- [12] K. N. Duangdao Palasuwan, Thananop Kobchaisawat, Thanarat H Chalidabhongse, Nuntiporn Nunthanasup, Kanyarat Boonpeng, Nantheera Anantrasirichai, "Parasitic Egg Detection and Classification in Microscopic Images," *IEEE Dataport*, January 22, 2022 2022, doi: <https://dx.doi.org/10.21227/vyh8-4h71.s>.
- [13] N. Pinetsuksai, "Superior automatic screening for human helminthic ova by using self-supervised learning approach-based object classification," in *ACIIDS*, in press.
- [14] K. M. Naing *et al.*, "Automatic recognition of parasitic products in stool examination using object detection approach," *PeerJ Computer Science*, vol. 8, p. e1065, 2022, doi: 10.7717/peerj-cs.1065.
- [15] I. Markoulidakis, G. Kopsiaftis, I. Rallis, and I. Georgoulas, "Multi-Class Confusion Matrix Reduction method and its application on Net Promoter Score classification problem," presented at the Proceedings of the 14th Pervasive Technologies Related to Assistive Environments Conference, Corfu, Greece, 2021. [Online]. Available: <https://doi.org/10.1145/3453892.3461323>.
- [16] M. Fu, K. Wu, Y. Li, L. Luo, W. Huang, and Q. Zhang, "An intelligent detection method for plasmodium based on self-supervised learning and attention mechanism," 2022.
- [17] R. Jomtarak *et al.*, "Mobile Bot Application for Identification of Trypanosoma evansi Infection through Thin-Blood Film Examination Based on Deep Learning Approach," in *2023 IEEE International Conference on Cybernetics and Innovations (ICCI)*, 30-31 March 2023 2023, pp. 1-7, doi: 10.1109/ICCI57424.2023.10112327.
- [18] T. Suwannaphong, S. Chavana, S. Tongsom, D. Palasuwan, T. H. Chalidabhongse, and N. Anantrasirichai, "Parasitic Egg Detection and Classification in Low-cost Microscopic Images using Transfer Learning," *ArXiv*, vol. abs/2107.00968, 2021.

The Factors Influencing Investor Intentions to Invest in Equity Crowdfunding in Thailand: A Conceptual Framework

Kaimuk Panitkulpong
College of Innovation and Industrial
Management
King Mongkut's Institute of
Technology Ladkrabang
Bangkok, Thailand
email: kaimuk.p@hotmail.com

Amnuay Saengnoee
College of Innovation and Industrial
Management
King Mongkut's Institute of
Technology Ladkrabang
Bangkok, Thailand
email: amnuay.sa@kmitl.ac.th

Samart Deebhijarn
KMITL Business School
King Mongkut's Institute of
Technology Ladkrabang
Bangkok, Thailand
email: samart.de@kmitl.ac.th

Thapong Teerawatananond
College of Innovation and Industrial
Management
King Mongkut's Institute of
Technology Ladkrabang
Bangkok, Thailand
email: thapong.te@kmitl.ac.th

Abstract— Equity Crowdfunding (ECF) has emerged as a significant financing tool for early-stage ventures in Thailand, attracting a diverse investor base. Considering the novelty of ECF platforms as non-bank equity investment options, investigating these investors' decisions is essential, even though this is an under-researched area despite ECF's rising popularity. This study aims to identify the key factors influencing investment decisions in ECF and establish a conceptual framework, with a particular focus on projects offering stock issuance through an ECF platform in Thailand. The framework is grounded in the Technology Acceptance Model (TAM3) and incorporates elements from the Information Systems Success Model (ISSM), Innovation Diffusion Theory (IDT), and Social Influence (SI) factors. The intention to invest in an ECF platform serves as the dependent variable within this framework. The research presents a comprehensive model of ECF, intending to provide valuable insights to platform providers and policymakers. This understanding of investor behavior prior to investment could contribute to the growth and sustainability of ECF in Thailand.

Keywords— equity crowdfunding, financial innovation, intention to invest

I. INTRODUCTION

Equity-based Crowdfunding (ECF) has emerged as a vital alternative for capital raising, notably assisting SMEs and startups that traditional banks have often overlooked [1], [2]. Emerging from the 2008 financial crisis, it has expanded in places like Thailand, under regulation and in alignment with government policies such as Thailand 4.0 [3]. The crowdfunding process involves collective small contributions from various investors, facilitated by technology, with crowdfunding platforms playing a crucial role in areas like company screening and data security [4], [2].

The crowdfunding platform, in the form of share issuance, plays a vital role in company qualification screening, offering disclosure, and investor education [2]. It provides a system for preventing unauthorized access, verifying member identity, testing investment understanding, managing assets,

disclosing information reliably, facilitating communication, data backup, electronic data transmission, operation supervision, and complaint management.

The global crowdfunding market is projected to grow from \$1.41 billion in 2023 to \$3.62 billion by 2030, with a CAGR of 14.5%. Despite challenges from COVID-19 impacting many platforms, crowdfunding continues as a favored fundraising tool, especially online. It has crucially supported communities, individuals, and businesses during these trying times. Increasingly, startups are turning to crowdfunding over traditional financial avenues like banks or venture capitalists [5]. The growth reflects the model's multiple benefits to SMEs, such as easier access to capital, reduced costs, enhanced visibility, and market validation [6], [7]. It also appeals to a wide range of investors, including those with limited experience, by offering potentially high profits. Those may potentially reap high profits if the project performs well [8].

ECF was initiated in Thailand in 2016 with seven platforms approved by the SEC. Out of these seven, three platforms have successfully funded 12 projects, accumulating approximately 171 million baht (as of August 2023). This study focuses on the investor's perspective in ECF, aiming to identify the variables that influence the intent to invest in such platforms. It fills a noted gap in comprehensive studies specific to the Thai ECF context, highlighting the significance of this financial innovation for SMEs and startups in the country [9].

II. LITERATURE REVIEWS

A. Technology Acceptance Model 3

Technology Acceptance Model 3 (TAM3), an extension of the original TAM framework [10], incorporates determinants that influence perceived ease of use (PEOU) [11] (Fig. 1.). In the context of understanding the influences of equity crowdfunding (ECF) on investor intentions to invest in Thailand, TAM3's constructs align with the conceptual framework of this study.

The independent variables identified, including platform quality, relative advantage, and social influence, relate directly to key aspects of TAM3. For example, platform quality and relative advantage (RA) can influence perceived ease of use and perceived usefulness (PU) [12], both intermediary variables in this model. Social influence, a significant feature in TAM3, resonates with the understanding of how subjective norms and community perceptions may impact the intention to invest in ECF [13].

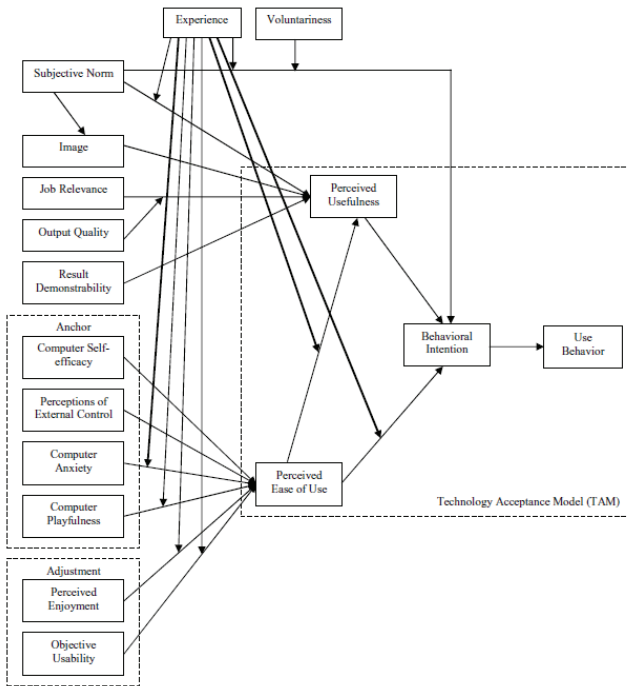


Fig. 1. TAM 3 by Venkatesh and Bala, 2008

Intermediary variables of perceived usefulness and perceived ease of use reflect the core of TAM3, connecting the technology's practicality and user-friendliness to the user's final decision-making process [14]. These intermediary variables can be influenced by the independent variables and, in turn, affect the dependent variable, the intention to invest in ECF [15].

In perspective of investors' intention to invest, this study aims to identify the key factors influencing investment decisions in ECF in Thailand and establish a conceptual framework using TAM3. This alignment with TAM3 allows for a nuanced understanding of the multifaceted nature of investment behavior in this emerging financial arena [16].

B. Information Systems Success Model (ISSM)

To study the quality of crowdfunding financial innovation platform in the form of an information system. The researcher has chosen to study models related to various factors. That causes the success model of DeLone and McLean's information systems (Information System Success Model: IS Success Mode/ISSM) (Fig. 2.), states that information quality, system quality and service quality affect the intention to use information systems (Actual use or intent to use) and satisfaction (User satisfaction) of users in using information systems. And positive experiences of use also contribute to improving satisfaction. This leads to the intention to use information systems and their net benefits [17].

Previous research indicates that the IS Success Model was used to describe user intentions and mobile social networking behavior [18] and to identify three quality characteristics that affect trust [19]. In some researches, quality factors affecting online user intention and use were examined. It was found that data, systems, and service quality played a significant positive role in the adoption of online systems [20], [21], [22]. In addition, Lee & Chung (2009) also found that the quality of the system data quality and design quality of interface features have a positive effect on user trust and satisfaction with m-banking [23].

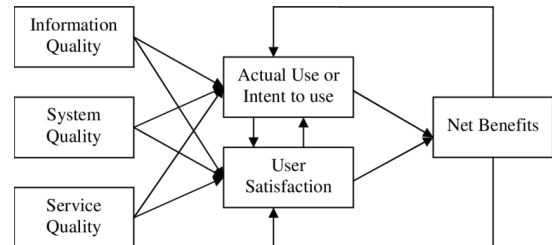


Fig. 2. ISSM by DeLone and McLean, 2003

C. Innovation Diffusion Theory (IDT)

The concept of Relative Advantage (RA) underpins the platform benefit feature, aligning with traditional diffusion theory and Everett M. Rogers' Innovation Diffusion (1995). The RA feature signifies that innovation, being more convenient and faster, exceeds traditional methods. Users more likely accept the innovation if perceived benefits outweigh drawbacks [24], [25]. RA influences innovation acceptance, reflecting personal perception, not objective superiority.

Innovations that exhibit RA are deemed more acceptable and tend to diffuse more rapidly. This does not suggest an objective superiority of the innovation, but rather emphasizes the personal perception of its benefits [26]. Research, such as Md. Khaled and Jinghua's (2014) study on P2P financial platforms, supports that RA influence intentions to use financial platforms among smallholder farmers in China, positively correlating with new technology acceptance [27]. RA is one of the most effective factors for predicting adoption of new technologies and innovations. Al-Rahmi et al. (2019) also found that the RA characteristics of an innovation affect users' perceptions of such innovations [28]. And within the technological context, Chaveesuk & Horkondee (2015) also utilized RA of innovation to demonstrate that business intelligence is improved and its adoption is enhanced [29].

Personal Relative Advantages refers to risk-taking willingness in adopting innovations [30]. RA of platform within ECF assess whether an investor's perception perceived more advantages than disadvantages compared to traditional fundraising.

D. Social Influence (SI)

The concept of Social Influence (SI) encompasses the notion of subjective norm within the TAM3 framework, characterized as "the degree to which an individual perceives that significant others believe he or she should or should not use the system" [31], [14]. Within the scope of TAM3, SI transcends mere consideration of others' views on technological advancements; it also encompasses the

potential enhancement of personal image [11]. In ECF domain, potential investors encounter innovative business models, thereby making their decision-making processes riskier compared to conventional investments. Consequently, they seek external opinions to mitigate uncertainty and facilitate well-informed decisions. Such influence may be interpersonal or stem from external media such as social platforms [32].

Social influence theory, a persuasion paradigm, has been extensively studied to elucidate how, when, and why individuals establish trust. While no singular theory can fully demystify persuasion, each contributes nuanced insights into specific facets. For instance, persuasion can be interpreted through behavioral learning theories that delineate the continuous incentivization required to uphold trust (e.g. [33], [34]).

Empirical evidence further confirms SI's role in shaping user intentions to adopt financial innovations such as Fintech services [35].

III. CONCEPTUAL FRAMEWORK AND HYPOTHESIS DEVELOPMENT

This research examines intention to invest in financial innovation, particularly in equity crowdfunding (ECF) in Thailand. The authors propose a framework with six latent variables, including three independent variables and two intermediary constructs, depicted in Fig. 3. These constructs, chosen for their ability to describe ECF investors, capture aspects like Platform Quality, Relative Advantage, and Social Influence. They collectively outline the investment process within the Thai ECF landscape, offering insight into factors driving investment intentions. The framework's alignment with investor behavior aids in crafting strategies to engage potential investors, contributing to ECF's growth in Thailand.

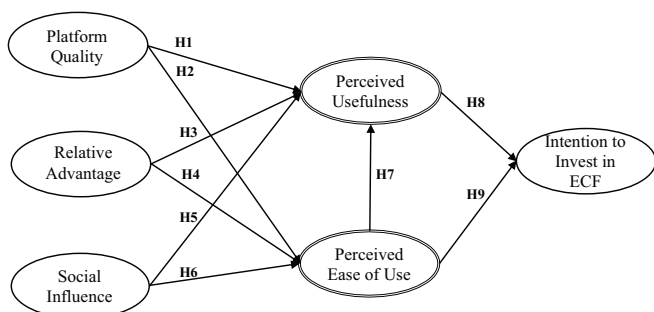


Fig. 3. Proposed Conceptual framework

Hypothesis 1: Platform Quality has a positive influence on Perceived Usefulness.

Platform quality is essential in building trust and investment intentions [36]. Abdul Razak, Abdullah Othman, Zulmi, Ismail, & Sidiki (2021) conducted an empirical examination within the Malaysian context to discern the determinants of investment in ECF [37]. Utilizing TAM, their findings revealed that platform quality exert substantial influence on perceived usefulness, subsequently shaping users' willingness to invest in ECF platforms

Hypothesis 2: Platform Quality has a positive influence on Perceived Ease of Use.

Platform quality, encompassing accessibility and user satisfaction, significantly influences investment intentions [38]. Its intuitive nature facilitates investment decisions and drives online ECF success [39], [40]. A study focusing on Malaysia's financial innovation revealed platform quality's substantial impact on Perceived Ease of Use, thereby affecting customer willingness to invest through ECF [37].

Hypothesis 3: Relative Advantages has a positive influence on Perceived Usefulness.

In a recent study, Okonkwo et al. (2022) identified the positive influence of RA characteristics on the acceptance and utilization of mobile payment services, reflecting the perceived superiority of innovation in Kenya and Nigeria, and positively impacting intentions to use mobile wallets [41], [42]. Concurrently, Bureshaid, Lu, & Sarea (2020) emphasized the essential role of RA in the adoption of financial innovation services within banks, filling gaps in literature, and highlighting their role in enhancing perceived usefulness in application [43].

Hypothesis 4: Relative Advantages has a positive influence on the Perceived Ease of Use.

Wahjono et al. (2021) and Karim et al. (2022) examined crowdfunding and financial innovations for small and medium-sized enterprises (SMEs) in Indonesia and ASEAN, finding positive correlations between perceived usefulness and perceived ease of use [44], [45]. Hughes (2016) explored the U.S. market, revealing a positive relationship between entrepreneurs' perception of relative advantages and perceived ease of use Web 2.0 social media [46].

Hypothesis 5: Social influence has a positive influence on Perceived Usefulness.

Choy & Schlagwein (2016) identified positive investor attitudes towards crowdfunding when viewing expert information as valuable [15]. Mutahar (2017) found a significant relationship between social influences and mobile banking perceived usefulness in Yemen [47]. Hong et al. (2018) revealed that founder momentum and stakeholder dialogue impact crowdfunding efficiency, also emphasizing that the social influence on crowdfunding has been underexplored, suggesting a need for further research [48].

Hypothesis 6: Social Influence has a positive influence on Perceived Ease of Use.

In Prastiawan et al.'s (2021) study, innate social influences were found to positively affect mobile banking usage [49]. Mutahar (2017) revealed a positive relationship between social influence and perceived ease of use in mobile banking in Yemen [47]. Kandifar & Retnowardhani (2023) found that social influences, including work environment and family, contributed to Generation Y's intentions to use the Bibit.id mutual fund investment application, making it easier to use [50].

Hypothesis 7: Perceived Ease of Use has a positive influence on Perceived Usefulness

Mohd Thas Thaker et al. (2018) studied the crowdfunding-waqf model (CWM) for waqf land development, finding a positive link between perceived ease of use and perceived usefulness [51]. Concurrently, Salim et al. (2021) found that perceived usefulness mediates the relationship between perceived ease of use and intention, supported by the Technology of Acceptance Model (TAM) [52]. Venkatesh & Bala's TAM3 study (2008) emphasized that experience strengthens the relationship between perceived ease of use and perceived usefulness [11].

Hypothesis 8: Perceived Usefulness has a positive influence on intention to Invest.

In their study, Guirado et al. (2018) identified that perceived usefulness enhances online investment in financial projects [53]. Perwitasari's research (2022) in Indonesia further emphasized that recognizing perceived usefulness significantly affects the intention to utilize financial innovations [54]. This correlates with findings by Singh et al. (2020), who underlined perceived usefulness as a positive influence on financial innovation adoption [55].

Hypothesis 9: Perceived Ease of Use has a positive influence on Intention to Invest.

Escudero Guirado et al. (2018) found perceived ease of use paramount to intention to engage in ECF [53]. Hamzah et al. (2022) identified it as a key factor in accepting financial innovations [56]. Alnsour (2022) further revealed that perceived ease of use greatly influences consumers' attitudes towards Islamic banks and encourages the use of financial innovations among those with limited technological readiness [57].

IV. CONCLUSION

The researcher examined the relationship between each variable, in accordance with the conceptual framework presented in this study. Each variable was referenced to pertinent research to substantiate the academic evidence of these variables. This process was employed for the purpose of analyzing attitudes and behaviors related to the acceptance of new technology, specifically focusing on ECF.

V. CONTRIBUTION

The research contributes to three main areas: business, academia, and government policy. For businesses, it guides crowdfunding strategies; academically, it extends knowledge on investment intentions; and for policymakers, it helps in formulating regulations related to equity crowdfunding, ensuring standards within the business practices of crowdfunding platform providers. Moreover, this research enhances understanding of equity crowdfunding behaviors and establishes a foundational basis for subsequent studies. The insights gained from this study will assist crowdfunding managers in developing effective strategies to attract funders to tech startups. This, in turn, can magnify economic benefits at the local, regional, and national levels through crowdfunding initiatives in the nascent stages of the technology sector.

REFERENCES

- [1] A. Z. Tayibnapi, L. E. Wuryaningsih and R. Gora, "The development of digital economy in Indonesia," *IJMS International Journal of Management and Business Studies*, vol. 8, no. 3, pp. 14-18, 2018.
- [2] J. T. Baldwin, *Fundamentals of stability theory*, vol. 12, Cambridge University Press, 2017.
- [3] "FinTech in Thailand, 3Q2021 | UOB Tech Start-up Ecosystem," United Overseas Bank, 2022. [Online]. Available: <https://www.uobgroup.com/techecosystem/news-insights-fintech-in-thailand-3q-2021.html>. [Accessed 22 January 2022].
- [4] J. Hollas, "Is crowdfunding now a threat to traditional finance?," *Corporate Finance Review*, vol. 18, no. 1, pp. 27, 2013.
- [5] "Crowdfunding Market Size, Share & COVID-19 Impact Analysis, by Type (Equity-based, Debt-based, Blockchain-based, and Others), by End-User (Startups, NGOs, and Individuals), and Regional Forecast, 2023-2030," *Fortune Business Insights*, 2023. [Online]. Available: <https://www.fortunebusinessinsights.com/crowdfunding-market-107129>. [Accessed: Sept. 22, 2023].
- [6] J. Cohen, "Improving Marketing Knowledge among Israeli SMEs using Metaphor and Storyline-Based Intervention," *Middle East Journal of Business*, vol. 12, no. 3, pp. 10-19, 2017.
- [7] K. Kim and S. Viswanathan, "The 'Experts' in the crowd: The role of experienced investors in a crowdfunding market," *Mis Quarterly*, 2018.
- [8] P. Konana and S. Balasubramanian, "The social-economic-psychological model of technology adoption and usage: an application to online investing," *Decision Support Systems*, vol. 39, no. 3, pp. 505-24, May 2005.
- [9] E. M. Noam, "Financing Media, Information, and Communication," in *Managing Media and Digital Organizations*, Palgrave Macmillan, Cham, pp. 175-233, 2019.
- [10] D. Fred Davis, "Perceived usefulness, perceived ease of use, and user acceptance of information technology," *MIS Quarterly*, vol. 13, no. 3, pp. 319-339, 1989.
- [11] V. Venkatesh and H. Bala, "Technology acceptance model 3 and a research agenda on interventions," *Decision Sciences*, vol. 39, no. 2, pp. 273-315, 2008. <https://doi.org/10.1111/j.1540-5915.2008.00192>.
- [12] Y. Chen, R. Dai, J. Yao, and Y. Li, "Donate time or money? The determinants of donation intention in online crowdfunding," *Sustainability*, vol. 11, no. 16, p. 4269, 2019.
- [13] E. Mollick, "The dynamics of crowdfunding: An exploratory study," *Journal of Business Venturing*, vol. 29, no. 1, pp. 1-16, 2014, doi: 10.1016/j.jbusvent.2013.06.005.
- [14] V. Venkatesh and F. D. Davis, "A theoretical extension of the technology acceptance model: Four longitudinal field studies," *Management Science*, vol. 46, no. 2, pp. 186-204, Feb. 2000.
- [15] K. Choy and D. Schlagwein, "Crowdsourcing for a Better World," *Information Technology & People*, vol. 29, no. 1, pp. 221-247, 2016, <https://doi.org/10.1108/itp-09-2014-0215>.
- [16] P. Belleflamme, T. Lambert, and A. Schwienbacher, "Crowdfunding: Tapping the Right Crowd," *Journal of Business Venturing*, vol. 29, no. 5, pp. 585-609, 2014.
- [17] S. Petter, W. DeLone, and E. McLean, "Measuring information systems success: Models, Dimensions, Measures and interrelationships," *European Journal of Information Systems*, vol. 17, pp. 236-263, 2008.
- [18] L. Gao and X. Bali, "An empirical study on continuance intention of mobile social networking services: integrating the IS success model, network externalities and flow theory," *Asia Pacific Journal of Marketing and Logistics*, vol. 26, no. 2, pp. 168-189, 2014.
- [19] T. Zhou, "An empirical examination of initial trust in mobile banking," *Internet Res.*, vol. 21, no. 5, pp. 527-540, 2011.
- [20] R. Tajuddin, M. Baharudin, and T. S. Hoon, "System Quality and its influence on students' learning satisfaction in UITM Shah Alam," *Procedia - Soc. Behav. Sci.*, vol. 90, pp. 677-685, 2013.
- [21] M. L. Tseng, R. J. Lin, and H. P. Chen, "Evaluation the effectiveness of e-learning system in uncertainty," *Ind. Manag. Data Syst.*, vol. 111, no. 6, pp. 869-889, 2011.
- [22] S. Chaveesuk, P. Wuthirong, and W. Chaiyasoonthorn, "Cloud computing classroom acceptance model in Thailand higher education's institutes: A conceptual framework," in **Proceedings of the 2018 10th*

- International Conference on Information Management and Engineering*, 2018.
- [23] K. C. Lee and N. Chung, "Understanding factors affecting trust in and satisfaction with mobile banking in Korea: a modified Delone and MaLean's model perspective," *Interact. Comput.*, vol. 21, no. 5, pp. 385-392, 2009.
- [24] E. M. Rogers, *Diffusion of innovations*, 5th ed. New York: Free Press, 2003.
- [25] S. L. Holak and D. R. Lehmann, "Purchase intentions and the dimensions of innovation: An exploratory model," *J. Prod. Innov. Manag.*, vol. 7, no. 1, pp. 59-73, 1990. [Online]. Available: [http://dx.doi.org/10.1016/0737-6782\(90\)90032-A](http://dx.doi.org/10.1016/0737-6782(90)90032-A)
- [26] E. Rogers, *Diffusion of innovation*. New York: Free Press, 1995.
- [27] Md. K. Amin and J. Li, "Applying Farmer Technology Acceptance Model to Understand Farmer's Behavior Intention to use ICT Based Microfinance Platform: A Comparative analysis between Bangladesh and China," *WHICEB 2014 Proceedings*, vol. 31, 2014. [Online]. Available: <https://aisel.aisnet.org/whiceb2014/31>
- [28] W. M. Al-Rahmi et al., "Integrating technology acceptance model with innovation diffusion theory: An empirical investigation on students' intention to use E-learning systems," *IEEE Access*, vol. 7, pp. 26797-809, Feb. 2019.
- [29] S. Chaveesuk and S. Horkondee, "An integrated model of business intelligence adoption in Thailand logistics service firms," in **2015 7th International Conference on Information Technology and Electrical Engineering (ICITEE)**, 2015.
- [30] A. Calabrò et al., "Innovation in family firms: A systematic literature review and guidance for future research," *Int. J. Manag. Rev.*, vol. 21, no. 3, pp. 317-355, 2019.
- [31] I. Ajzen and M. Fishbein, "A Bayesian analysis of attribution processes," *Psychol. Bull.*, vol. 82, no. 2, pp. 261, Mar. 1975.
- [32] M. Savolainen, "Tough Crowd: Consumer Acceptance of Equity Crowdfunding Platforms," Ph.D. dissertation, Univ. of Jycaskyla, 2016.
- [33] D. J. O'keefe, "Persuasion," in *The Handbook of Communication Skills*, Jul. 2018, pp. 319-335. Routledge.
- [34] M. Harjuma and H. Oinas-Kukkonen, "Persuasion theories and IT design," in *Persuasive Technology: Second Int. Conf. on Persuasive Technology, PERSUASIVE 2007*, Palo Alto, CA, USA, Apr. 26-27, 2007, Revised Selected Papers 2, 2007, pp. 311-314. Springer Berlin Heidelberg.
- [35] M. Al-Okaily, A. Lutfi, A. Alsaad, A. Taamneh, and A. Alsyouf, "The Determinants of Digital Payment Systems' Acceptance under Cultural Orientation Differences: The Case of Uncertainty Avoidance," *Technology in Society*, vol. 63, no. C, 2020, Elsevier.
- [36] G. Burtch, A. Ghose, and S. Wattal, "An Empirical Examination of the Antecedents and Consequences of Contribution Patterns in Crowd-Funded Markets," *Inf. Syst. Res.*, vol. 24, no. 3, pp. 499-519, 2013. [Online]. Available: <http://www.jstor.org/stable/42004279>
- [37] D. Abdul Razak et al., "Determinant factors of equity-based crowdfunding in Malaysia," *Labuan Bulletin Int. Bus. Fin.*, vol. 19, no. 1, pp. 33-48, 2021. [Online]. Available: <https://doi.org/10.51200/lbif.v19i1.2859>
- [38] A. Schwienbacher and B. Larralde, "Alternative types of entrepreneurial finance," 2012.
- [39] V. Kuppaswamy and B. L. Bayus, *Crowdfunding creative ideas: The dynamics of project backers*. Springer International Publishing, 2018.
- [40] A. Lukkarinen et al., "Success drivers of online equity crowdfunding campaigns," *Decis. Support Syst.*, vol. 87, pp. 26-38, 2016.
- [41] C. W. Okonkwo et al., "Mobile wallets in cash-based economies during COVID-19," *Ind. Manag. Data Syst.*, vol. 123, no. 2, pp. 653-71, Aug. 2022.
- [42] K. Y. Lin, Y. T. Wang, and T. K. Huang, "Exploring the antecedents of mobile payment service usage: Perspectives based on cost-benefit theory, perceived value, and social influences," *Online Inf. Rev.*, vol. 44, no. 1, pp. 299-318, Jan. 2022.
- [43] N. Bureshaid, J. Lu, and A. Sarea, "Investigation of Fintech Services Adoption in the Banking Industry," in *Proc. Ind. Revol. Bus. Manag.: 11th Annu. PwR Doctoral Symp. (PWRDS) 2020*. [Online]. Available: <http://dx.doi.org/10.2139/ssrn.3659074>, 2020.
- [44] S. I. Wahjono et al., "Promoting creators intentions: Measurement of crowdfunding performance," *Int. J. Bus. Soc.*, vol. 22, no. 3, pp. 1084-101, Dec. 2021.
- [45] S. Karim et al., "Is FinTech providing effective solutions to Small and Medium Enterprises (SMEs) in ASEAN countries?," *Econ. Anal. Policy*, vol. 75, pp. 335-44, Sep. 2022.
- [46] M. E. Hughes, "Entrepreneurship in a Web 2.0 World: Factors influencing Intentions to Adopt Web 2.0 Social Media in US Entrepreneurial Activities," State Univ. of New York at Albany, 2016.
- [47] A. M. Mutahar, N. M. Daud, T. Ramayah, L. Putit, and O. Isaac, "Examining the effect of subjective norms & compatibility as external variables on TAM," *Science International*, vol. 29, no. 4, pp. 769-776, 2017.
- [48] Y. Hong, Y. Hu, and G. Burtch, "Embeddedness, pro-sociality, and social influence: Evidence from online crowdfunding," *MIS Quarterly*, Forthcoming, Feb. 2018. [Online]. Available: <https://ssrn.com/abstract=3125936>
- [49] D. I. Prastiawan, S. Aisjah, and R. Rofiaty, "The effect of perceived usefulness, perceived ease of use, and social influence on the use of mobile banking through the mediation of attitude toward use," *APMBA (Asia Pacific Management and Business Application)*, vol. 9, no. 3, pp. 243-60, Apr. 2021.
- [50] R. Kandifar and A. Retnowardhani, "Factors that increase interest in using mutual fund application with user acceptance approaches," *Journal of Theoretical and Applied Information Technology*, vol. 101, no. 7, pp. 2698-2711, Apr. 2023.
- [51] M. A. Mohd Thas Thaker, H. Mohd Thas Thaker, and A. Allah Pitchay, "Modeling crowd funders' behavioral intention to adopt the crowdfunding-waqf model (CWM) in Malaysia," *International Journal of Islamic and Middle Eastern Finance and Management*, vol. 11, no. 2, pp. 231-249, 2018. [Online]. Available: <https://doi.org/10.1108/imefm-06-2017-0157>
- [52] M. Salim, S. Kassim, and M. A. Thaker, "Factors influencing the acceptance of Islamic crowdfunding in Malaysia: A study of youth entrepreneurs," *Pakistan Journal of Commerce and Social Sciences (PJCSS)*, vol. 15, no. 3, pp. 443-75, 2021.
- [53] C. E. Guirado, C. M. de Ibarreta Zorita, and C. G. Castro, "Beyond signed t-shirts: A socio-technological model of equity crowdfunding adoption," *Journal of Innovation Economics Management*, no. 2, pp. 137-172, 2018.
- [54] A. W. Perwitasari, "The effect of perceived usefulness and perceived easiness towards behavioral intention to use fintech by Indonesian msms," *The Winners*, vol. 23, no. 1, pp. 1-9, 2022. [Online]. Available: <https://doi.org/10.21512/tw.v23i1.7078>
- [55] S. Singh, M. M. Sahni, and R. K. Kovid, "What drives FinTech adoption? A multi-method evaluation using an adapted technology acceptance model," *Management Decision*, vol. 58, no. 8, pp. 1675-1697, 2020. [Online]. Available: <https://doi.org/10.1108/MD-09-2019-1318>
- [56] M. F. Hamzah, T. M. Razak, C. K. Yahaya, Z. Shamsuddin, and S. N. Zahrin, "Adoption Factors of FinTech Products & Services in Islamic Banking Industry in Malaysia: A Literature Review," *Journal of Positive School Psychology*, vol. 6, no. 3, pp. 8883-93, May 2022.
- [57] I. R. Alnsour, "Impact of fintech over consumer experience and loyalty intentions: An empirical study on Jordanian Islamic Banks," *Cogent Business & Management*, vol. 9, no. 1, pp. 1-17, 2022. [Online]. Available: [doi:10.1080/23311975.2022.2141098](https://doi.org/10.1080/23311975.2022.2141098)

Delivering Delight: Analyzing Luxury Consumer Satisfaction with Home-Delivered Premium Ingredients for Exquisite Home Cooking in Bangkok

Phatcharaphon Prommin
 KMITL Business School,
 King Mongkut's Institute of Technology
 Ladkrabang
 Faculty of Business Administration,
 Ramkhamhaeng University
 Bangkok, Thailand
 phatcharaphonprom@gmail.com

Manoj Chatpibal
 KMITL Business School
 King Mongkut's Institute of Technology
 Ladkrabang
 Bangkok, Thailand
 mchatpibal@gmail.com

Korakit Piyamongkol
 KMITL Business School
 King Mongkut's Institute of Technology
 Ladkrabang
 Bangkok, Thailand
 korakitp@hotmail.com

Burin Sukphisal
 KMITL Business School
 King Mongkut's Institute of Technology
 Ladkrabang
 Bangkok, Thailand
 burin.su@kmitl.ac.th

Abstract— There was an increase in demand for high-quality ingredients delivered for home cooking in response to the COVID-19 pandemic. Even after the pan-demic, this shift in customer demand is ongoing. The purpose of this study was to develop a conceptual framework to identify the factors influencing luxury consumer satisfaction with the consumption of premium home cooking ingredients during and after the Covid-19 pandemic, with a focus on the Bangkok metropolitan area. The American Customer Satisfaction Index (ACSI) model was used to define factors influencing customer satisfaction when purchasing fresh premium ingredients. This study highlights five antecedent factors of customer satisfaction: customer expectation, perceived quality of food, perceived quality of services, perceived value with an emphasis on luxury, and various relevant indicators. Nine key hypotheses were identified while developing the framework model, creating the possibilities for relationship verification. Indicators were then developed to measure consumer expectations of home delivery premium ingredients in terms of quality, value, and satisfaction.

Keywords— *home delivery, food ingredients, customer satisfaction, SERVQUAL*

I. INTRODUCTION

In January 2020, Chinese media reported the first case of death in China from the Coronavirus disease, which was also known as "Covid-19." Following that, on January 13, 2020, the World Health Organization (WHO) officially confirmed the first pandemic case in Thailand. According to records, there have been more than 1.25 million Covid-19 cases and a total of 12,374 deaths reported in Thailand, and in September 21, the numbers appeared to be rapidly rising [1]. As a result, the Thai government and the Epidemic Administrative Center in Thailand implemented several leveraged measures, such as social distancing, transit restrictions, and city lockdowns in

several regions, in an attempt to rapidly control the Covid-19 pandemic [2]. Department stores and convenience stores across Thailand had limited hours of operation, and dining in restaurants was strictly prohibited. The deterioration of Covid-19 situation as well as the measures implemented by Thailand's Epidemic Administrative Center caused changes and shifts in Thai lifestyles and consumer behavior, and this was apparent in the areas of dining and food consumption. MGR Online (2021) [3] reported that, as a result of the Covid-19 pandemic in Thailand, changes to the Thai consumer lifestyles and behavior included the prioritization of convenient and fast food take-aways, and an increase in home-cooking, both of which became part of the so-called 'New Normal.

The Suan Dusit Poll (2021) [4] survey, which was concerned with changes and shifts in dining and food consumption behavior, revealed two helpful pieces of information. First, prior to the Covid-19 pandemic in Thailand, 70.94 percent of the surveyed population expressed concern about dining and food consumption that would not carry Covid-19 infections from others such as Food Delivery Service or Restaurants. Second, during the Covid-19 pandemic, dining behavior leveraged a 75.81 percent incremental for in-home cooking and dining, a 71.70 percent incremental for being mindful of the cleanliness of food that they consumed, and a 59.99 percent incremental for choosing health-conscious ingredients.

From the above information, it can be seen that dietary and food consumption requirements continuously evolve in response to social, economic, and predicament contexts and circumstances, and as a result, the segment of consumers who express additional concerns about cooking at home has grown significantly. It seems that people have become fearful of the

possibility of catching Covid-19 in a variety of ways when dining out [5, 6]. Fine dining restaurants serving high-quality ingredients were among those most impacted by waves of lockdowns, government measures, and customer behavioral shifts as their customers avoided dining out. Their menu selections for delivery services served only to whet customer appetites for high-quality food. Instead of looking for more delivery services, consumers looked for raw materials and high-quality ingredients for home cooking.

Numerous studies [7, 8, 9] have investigated the transition from traditional sit-down dining to food delivery services, including premium and fine dining experiences. However, there is a notable absence of research in the context of delivery of ingredients for home cooking, especially premium and high-quality ingredients. Therefore, our study aims to address this research gap as we delve into this unexplored territory.

In this study, we focus on customer expectations of the delivery of high-quality ingredients for home cooking. We use a special handling protocol, which is currently limited in use. It can be seen that due to the above mentioned circumstances, the delivery of high-quality cooking ingredients to consumer homes has become a significant issue, particularly with regard to premium or luxury ingredients [10, 11]. In order to ensure that the customer demand for premium ingredient home deliveries is met, a better understanding of the factors influencing the situation is required. We therefore developed a conceptual framework to identify factors influencing luxury consumer satisfaction with premium home cooking ingredient consumption during and after the COVID-19 pandemic, with a focus on Bangkok. As its urban environment presents unique challenges and opportunities for premium ingredient delivery, given its dense population and traffic conditions [12], having Bangkok as a focal of our study aims to provide valuable insights that can be applied to address similar challenges in other urban centers worldwide. Additionally, the COVID-19 pandemic has significantly impacted consumer behavior and preferences, making it crucial to investigate how these changes affect luxury consumer satisfaction in a dynamic city like Bangkok as well as future studies on other urban centers worldwide.

II. THEORY AND LITERATURE REVIEW

A. ACSI Model

The American Customer Satisfaction Index, abbreviated as ACSI, is a customer-based strategic economic indicator used to assess the quality of goods and services. Derived from an original Swedish model, the ACSI model was adopted on a smaller scale in New Zealand, Taiwan [13], and Austria [14], and serves as the foundation for models used in Norway and the European Union. Customer satisfaction (ACSI) as depicted in Figure 1, has three antecedents: perceived quality, perceived value, and customer expectation. The evaluation of recent purchases or consumption experience represents the perceived quality or performance. It is intended to have a direct and positive impact on customer satisfaction the focal point of this chain of relationships in order to ensure that the customer's demand is met.

Perceived value, as a second determinant of customer satisfaction, indicates the perceived level of product quality in relation to the price paid. The third determinant, customer

expectation, reflects both non-experiential information available (pre-purchase) and a forecast of a firm's future ability to deliver quality [15]. As a result, the ACSI model depicts voice and loyalty. Customers who are dissatisfied have the option of leaving or filing a complaint. Voice can refer to both management and personnel complaints. Increased satisfaction not only reduces complaints, but it should also increase customer loyalty. Customer loyalty was identified as a firm's ultimate profitability and is a dependent variable in the ACSI model [16].

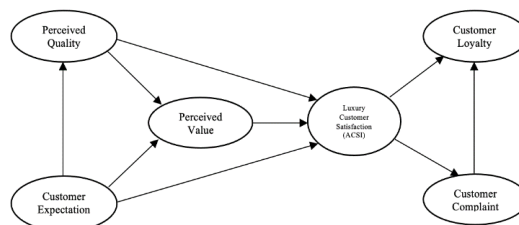


Fig. 1. The American Customer Satisfaction (ACSI) Model by ACSI, 1999

The American Customer Satisfaction Index has been utilized in several study areas including the fields of online and offline purchases from restaurants and the fast-food industry [17, 18, 19, 20, 21], and thus has been adopted for the study of the factors influencing customer satisfaction with premium ingredient home delivery. This study excludes the consequence factors (customer complaints and customer loyalty) in order to focus on the antecedents of customer satisfaction. Furthermore, perceived quality was divided into two dimensions (food quality and service quality) to reflect how each factor influences perceived value and customer satisfaction. Customer satisfaction factors were then classified into three dimensions: fulfillment of expectation, esteem of expectation, and overall satisfaction.

B. Customer Expectation

The literature focuses on the factors that influence food quality, service quality, luxury value, and customer satisfaction. Customer expectation is the benchmark against which a customer measures the performance of a product or service [22]. The process of a consumer's product or service can meet the actual needs and expectations of customers [23]. Furthermore, theories of hypothetical infrastructure inundating those products or services are known to be customer expectations [24]. One of the key factors explaining the model is customer expectation. Specifically, customer expectation of premium fresh ingredients for home cooking is a focal point, and this begins with the contributions to food quality of premium fresh ingredients. The impact of customer expectations on the quality of service on the delivery of premium fresh ingredients to the customer was conducted and customer expectations influenced the perceived value of luxury and customer satisfaction [24].

According to a previous study, product-related features and in-store quality are the most important dimensions of customer expectation in fresh food retailing [25]. Structural model evaluation revealed a significant impact on customer satisfaction. A study of customer emotional experience awareness and co-creation behavior in luxury

hotels highlighted prominent emotions that customers experience as well as various important emotional triggers and constructors [26]. Other researchers concluded that expectation as an attribute has a significant impact on perceived service quality, with desired expectation being the most influential factor on customer satisfaction. The outcome in terms of customer expectation and perceived quality; quality and environmental factors are primarily influenced by perceived value, quality, and service; and environmental factors influence customer satisfaction in a Bangkok themed restaurant [27, 28].

In this study, we look into the influences of consumer expectations on perceived quality, perceived value, and customer satisfaction. According to previous research, customers will evaluate each factor based on the following criteria: freshness, quality, on-time delivery, precision, short delivery lead time, ease of use, dependability, and personalization. As shown below, the focal point is used to determine the contribution of the customer expectation dimension to the hypothesis development.

H1: The customer expectation dimension contributes to food quality of premium fresh ingredients.

H2: The customer expectation dimension contributes to service quality of premium fresh ingredients.

H3: The customer expectation dimension contributes to luxury value of premium fresh ingredients.

H4: The customer expectation dimension contributes to luxury customer satisfaction with premium fresh ingredients.

C. Food Quality and Service Quality

The concept of "Perceived Quality" is a reconciliation of consumer preferences and product attributes [29]. The concept emphasizes the distinction between expected quality and quality as perceived by consumers, and numerous studies focused on various foods were performed. Perceived service quality, perceived product quality, and perceived price fairness were shown to have a decisive and critical influence on customer satisfaction at Indonesian fast-food restaurants [30]. Previous researchers found that service and food quality had an impact on customer satisfaction and willingness to repurchase [31]. The study also empirically investigated the relationship between and mutual dependence of perceived quality (service quality and food quality) and satisfaction/loyalty in the moderating role of surroundings in a restaurant origin sector [32]. As a result, two distinct quality elements: food quality and service quality, as shown below.

1) Food quality.

In terms of customer satisfaction, Peri [33] defined "quality" as "fitness for use" or "fitness for consumption" in the food context. Food quality is required to meet the needs and expectations of consumers [33]. According to an analysis of the linkages of factors affecting customer satisfaction, "food quality" and "variety of foods being offered" are critical components of customer satisfaction [34]. "Cleanness," "freshness," "variety of foods," and "healthiness" are among the indicators that specify "food

quality" in terms of fast-food restaurant "ingredients" and "foods." Other factors considered important in measuring customer satisfaction are "product quality" and "price" [35]. According to Johns and Howard [36], food quality is a construct of customer satisfaction.

In this paper, the food quality construct specifies the following dimensions: freshness, taste, price, value, rightness and reliability, tailor-making, and appropriateness of packaging. The following hypotheses were then defined:

H5: The dimension of food quality contributes to luxury value of premium fresh ingredients.

H6: The dimension of food quality contributes to luxury customer satisfaction of premium fresh ingredients.

2) Service quality.

The Service Quality (SERVQUAL) model, introduced by Parasuraman et al. [37], has been recognized globally as an assessment tool for the consistency of service level of a corporation, and can indicate the level of customer satisfaction over time. The American and European Customer Satisfaction Index [13] advocates that satisfaction be measured by "service quality." The service quality of the product or service can be evaluated, resulting in an emotive satisfaction assessment that drives behavioral intentions [38]. It was also discovered that service quality influences customer loyalty positively through customer satisfaction [39].

"Service quality perceptions lead to customer satisfaction," was stated by a number of researchers, even though there was no agreement on the formal consequences of these two constructs in any literature [40]. The SERVQUAL instrument was developed as a result of this popular concept [41, 42, 43, 44, 45, 46]. Previously, SERVQUAL was used as a measurement tool by a number of service businesses. Tangibility, reliability, responsiveness, assurance, and empathy are the five dimensions of the SERVQUAL instrument. Based on the information presented above, it can be assumed that "service quality" is a prerequisite for "customer satisfaction." As a result, the following hypotheses were developed.

H7: The dimension of service quality contributes to luxury value of premium fresh ingredients.

H8: The dimension of service quality contributes to luxury customer satisfaction of premium fresh ingredients.

D. Luxury Value of Premium Fresh Ingredients

Perceived value is defined as a consumer's overall assessment of the utility of a product based on perceptions of what is received and what is given. It is the relationship between the benefits received by consumers and the costs that such consumers must bear [42]. In conjunction with the investigation of luxury food, luxury consumption can be measured for both old and new motives [47]. Financial value, functional value, individual value, social value, and new luxury value are critical essential factors that define luxury value, with practical and luxury aspects of each individual having the greatest impact consequences. Previous research has shown that perceived value is an important precursor to "overall satisfaction" [48]. Luxury food is defined as food delicacies that are in high demand [49]. In coherence, the social component of luxury food was revealed as being a

means of building and bridging social relations. As a result, by conditional, price, and social value, epistemic value is the primary driver of purchase intentions toward food-delivery application [50]. From the above research related to luxury value, nine value elements were identified: prestige value, usability value, hedonistic value, self-identify value, materialistic value, uniqueness value, price value, authenticity value, and sustainability value, all of which are involved in the codification of the following hypothesis.

H9: Luxury value is an additional significant dimension that contributes to the luxury value of premium fresh ingredients.

III. CONCEPTUAL FRAMEWORK AND INDICATORS DEVELOPMENT

A. Conceptual Framework

This research framework was adapted from the ACSI model in order to identify the factors that have a significant impact on customer satisfaction with home delivery of premium fresh ingredients in Bangkok during and after the COVID-19 pandemic. Based on the preceding discussion, a conceptual framework for investigating the factors influencing customer satisfaction was proposed. This model is made up of five interconnected factors: customer expectation, food quality, service quality, luxury value, and customer satisfaction. Figure 2 depicts the conceptual framework and the hypotheses that were proposed.

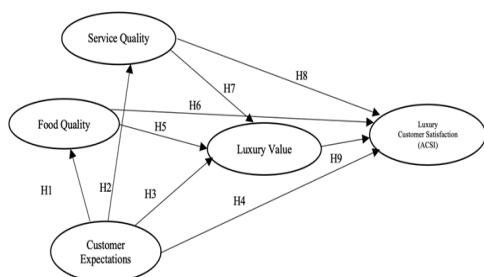


Fig. 2. Conceptual framework model and hypotheses. The modified American Customer Satisfaction Index Model.

B. Variables and Indicators

The variable dimensions were described in the literature. These dimensions, which are customer expectation, service quality, food quality, luxury value, and luxury customer satisfaction, were modified based on luxury customer satisfaction. All variable operational definitions are provided below.

1) Customer expectation is defined as a set of thoughts, desires, and expectations that a customer may have before, during, and after purchasing a product or service from a business. In this study, customer expectations included freshness, ingredient quality, on-time delivery, precision, short delivery lead time, simple usage, reliability, and personalization. Taste, freshness, ease of use, time delivery, time savings, and personalization are definitions that were used for measuring customer expectations to do with online food delivery services [51, 52]. Customer expectations for online and offline purchases are included in reliability [18].

2) Food quality, defined as fresh ingredients, great taste, and a reasonable price point for quality, is the most important

factor in online retailing strategies, particularly for those catering to fast food [52]. Value for money, right and reliable ingredients, tailored ingredients, and appropriate packaging are frequently used as significant attributes in rating satisfaction [18].

3) Service quality is a measure of how well an organization delivers its products and services in comparison to the expectations of its customers. It has been defined in terms of punctuality, correct delivery procedure, helpful and knowledgeable staff, precise order delivered, easy of ordering, prompt correction of errors, accurate and trustworthy payment, traceable delivery, right servicing mind and manner, and protection of customer privacy. These attributes were modified to fit the study and were the antecedents and consequences of customer satisfaction [18, 43, 53]

4) The highest level of prestigious products and services encompassing physical and psychological values is defined as luxury value. This study includes indicators that associate high price with particularly high quality, luxurious feeling, pleasant feeling, uniqueness, exclusivity, match to lifestyle, making of a good impression on others, environmental friendliness, and production of products with fairness to humans and animals. The importance of the definitional dimension of luxury food was determined by price value, quality value, uniqueness value, hedonistic value, prestige value, and sustainability value [47]. The primary driver of purchase intentions toward food-delivery applications is epistemic value, followed by conditional, price, and social value. Concerns about food safety and health consciousness had no statistically significant relationship with purchase intentions for food-delivery applications [50]. Satisfaction with customization was influenced by hedonic, utilitarian, creative achievement, and social value, which in turn influenced brand loyalty. These findings have practical implications for developing effective luxury brand customization programs in the online retail industry [53]. Modifications to utilitarian value, hedonic value, economic value, and purchase intention were made to fit the study of luxury value perception and purchase intention [54].

5) Luxury customer satisfaction is an indicator that shows how well a company's premium fresh ingredients meet or exceed customer expectations. In this study, luxury customer satisfaction was measured by the fulfillment of expectations, the esteem of expectations, and overall satisfaction [18]. The overall quality of the purchase experience and customer expectations were found to be stronger drivers of customer satisfaction.

The conceptual framework in this study was developed by reviewing a variety of literature. The goal was to understand how different factors related to "Luxury/Premium" are connected. Specifically, the focus was on the satisfaction that comes from choosing high-quality fresh ingredients, as shown in Table I.

The study suggests that customer expectations are important in determining what they want from a product or service. When these expectations are met through good service quality and food quality, customers feel satisfied. The idea of luxury value is also significant because it provides

extra benefits to customers. Ultimately, customer satisfaction is achieved by offering a luxurious experience.

TABLE I. IDENTIFY VARIABLES AND INDICATORS OF CUSTOMER SATISFACTION IN HOME DELIVERY OF PREMIUM FRESH INGREDIENTS.

| Variables | Indicators |
|--|---|
| Customer Expectation [18, 52, 55] | Freshness; Quality of ingredients; On-time delivery; Preciseness; Short delivery lead time; Simple usage; Reliability; and Personalization |
| Food Quality [18, 52] | Fresh ingredients; Great taste; Price point for quality; Value for money; Right and reliable ingredients; Tailored ingredients; and Appropriated packaging |
| Service Quality [18, 42, 55] | Punctuality; Correct procedure of delivery staff; Helpful and knowledgeable staff; Precise order delivery; Easy to make order; Prompt correction of errors; Accurate and trustworthy payment; Traceable delivery; Right servicing mind and manner; and Customer privacy |
| Luxury Value [47, 50, 53, 54] | Association of high price with particularly high quality; Luxurious feel; Pleasant feel; Uniqueness; Exclusivity; Match with lifestyle; Creation of a good impression on others; Environmental friendliness; and Humans and animals fair trade production |
| Luxury Customer Satisfaction (ACSI) [18] | Fulfilment of expectations; Esteem of expectations; and Overall satisfaction |

In summary, this conceptual framework brings together ideas from various literature sources to understand the relationship between luxury/premium factors, customer expectations, satisfaction, and the role of service quality, food quality, and luxury value in shaping customer experiences. It is important to note that the framework developed in this study is theoretical and serves as a guide for future empirical research. By building upon existing knowledge and theories, this conceptual framework provides a foundation for further investigation and hypothesis testing in the field of luxury/premium products and customer satisfaction.

IV. CONCLUSION AND FUTURE STUDY

A range of relevant literature was reviewed and studied in order to identify the variables that influence customer satisfaction when ordering and purchasing premium ingredients for home cooking, particularly in the context of the Covid-19 pandemic. This study was focused on premium food ingredients delivered for home cooking; for a more general application, an additional review may be required before composing the completed interpretation of the conceptual framework. This research paper framework was created using the ACSI model. According to previous studies, the perceived quality facet is associated with "Food Quality" and "Service Quality." As a result, the variables in

this research framework were as follows: "Customer Expectation," "Food Quality," "Service Quality," "Luxury Value," and "Customer Satisfaction." While the "SERVQUAL" model was focused on "Service Quality," the Luxury Value Theory was also applied to "Perceived Value" in relation to "Premium Ingredients." When developing the framework model, nine hypotheses were identified based on the possibilities of relationship verifications. Indicators were then established to measure consumer expectations based on quality, value, and the satisfaction aspects of premium ingredients home delivery. Validation and reliability tests on variables and indicators will be performed in the future to confirm all defined hypotheses using the Structural Equation Model (SEM). Although excluded from this paper, further study should be conducted to cover the ACSI model's consequences, customer complaints, and customer loyalty. Kulchitaphong [56] addressed the need for loyalty as a final stage to customer satisfaction in order to achieve a sustainable assumption.

REFERENCES

- [1] World Health Organization (WHO), Archived: WHO Timeline-COVID-19, (2020). Retrieved August 20, 2021, from <https://www.who.int/news/item/27-04-2020-who-timeline-covid-19>.
- [2] Tourism Authority of Thailand Newsroom, Bangkok extends COVID-19 control measures until 31 August 2021, (2021). Retrieved Sep 2, 2021, from <https://www.tatnews.org>.
- [3] MGR ONLINE, ผู้คิดค้น เชาวเทรนส์อุตสาหกรรมอาหาร ลอบใจ New Normal., (2021). Retrieved August 27, 2021, from <https://mgronline.com>.
- [4] Suan Dusit Poll, "อาหารไทย" ในยุคโควิด 19., (2021). Retrieved August 27, 2021, from <https://suandusitpoll.dusit.ac.th>.
- [5] Bangkok Post, Thais cook at home more during Covid outbreak: Poll, (2021). Retrieved August 27, 2021, from <https://www.bangkokpost.com>.
- [6] Bank of Thailand Magazine, New normal ของธุรกิจร้านอาหารในยุคโควิด 19., (2020). Retrieved August 27, 2021, from <https://www.bot.or.th>.
- [7] T. S. P. de Souza, R. F. Miyahira, J. R. V. Matheus, T. B. de B. Nogueira, C. Maragani-Santos, F. F. C. Barros, A. E. C. Antunes, and A. E. C. Fai, "Food service in time of uncertainty: Remodeling operations, changing trends, and looking into perspectives after the Covid-19 pandemic", *Trends in food Sci & Tech J*, vol.120, pp.301-307, 2022.
- [8] R. J. Zwanka and C. Buff, "COVID-19 Generation: A Conceptual Framework of the Consumer Behavioral Shifts to Be Caused by the COVID-19 Pandemic", *J. of Int Con Mark*, vol.33,no. 1, pp.58-67, 2020.
- [9] K. T. John and R. Gopalakrishnan, "Disrupted dining: decline of the premium food service segment in India dua to the COVID-19 pandemic", *Hosp Mang*, vol.12, no. 2, pp.191-207, 2022.
- [10] Thai Institute of Directors, AGILITY AMIDST ABNORMALITY: องค์การปรับตัวอย่างไรในยุค COVID?., (2020). Retrieved September 2, 2021, from <https://www.thai-iod.com/th/publications-detail.asp?id=635>.
- [11] Bangkok Biz News, สื่อ "ร้านอาหาร" ทรูถูกดีสรับจนต้องปรับตัวจะตลาด "เดลิเวอรี่", (2021). Retrieved September 2, 2021, from <https://www.bangkokbiznews.com/lifestyle/876516>.
- [12] The standard, เปิดสถิติประชากรไทยขึ้นปี 2565 กทม. ครองแชมป์สูงสุดกว่า 3 ล้านคน, (2023). Retrieved September 17, 2023, from <https://thestandard.co/thailand-demographics-2565/>
- [13] C. Fornell, M. D. Johnson, E. W. Anderson, J. Cha, and B. Everitt Bryant, "The American customer satisfaction index: nature, purpose and findings", *J. Mark*, vol. 60, no. 4, pp.7-18, October 1996.
- [14] P. Hackl, D. Scharitzer, and R. Zuba, "The Austrian customer satisfaction barometer (ACSB): a pilot study", *der markt*. vol. 35, no. 2, June 1996.

- [15] E. W. Anderson, and C. Fornell, "Foundation of the American customer satisfaction index", *Total Qual. Manag.*, vol.11, no.7, pp.869-882, 2000.
- [16] F. F. Reichheld and W. E. Sasser, "Zero defections: quality comes to services", *Harv. Bus. Rev.*, vol.68, no.5, pp.105-111, September-October 1990.
- [17] P. Sombat, W. Chaiyasoonthorn, and S. Chaveesuk, "The acceptance model of hospital information systems in Thailand: A conceptual framework extending TAM", *IEEE*, In Proceedings of the IEEE 5th International Conference on Industrial Engineering and Applications (ICIEA'18), pp.89-94, 2018.
- [18] G. Tomas M. Hult, P. N. Sharma, F. V. Mogeson and Y. Zhang, "Antecedents and consequences of customer satisfaction: Do they differ across online and offline purchases?", *J. Retail.* 95, vol.1, pp.10-23, March 2019.
- [19] M. Mao and P. James, "Evaluating customer satisfaction using the ACSI model in a themed restaurant in Bangkok", *Bus. Manag. Strategy*, vol.11, no.1. pp. 55-71, February 2020.
- [20] S. Chaveesuk, B. Khalid, and W. Chaiyasoonthorn, "Emergence of new business environment with big data and artificial intelligence", In Proceedings of the 9th International Conference on Information Communication and Management (ICICM'19), pp.181-185, August 2019,
- [21] C. Nquyen, D. Nquyen and T. Do, "The determinants of customer satisfaction in fast food industry: the case study of KFC Vietnam", *Humanit. Soc. Sci. Science Res*, vol.2, no.2 pp.1-8, April 2019.
- [22] M. A. Machado, A. Ribeiro, and M. Basto, "An empirical assessment of customer satisfaction and quality of service: Comparing SERVQUAL and SERVPERE", *Universidade Tecnológica Federal do Paraná - UTFPR Campus Ponta Grossa - Paraná – Brasil*, vol.10, no.2, pp.264-283, 2014.
- [23] S. Almsalam, "The effects of customer expectation and perceived service quality on customer satisfaction", *Int. J. Bus. Manag. Invent*, vol.3, no.8, pp.79-84, August 2014.
- [24] J. C. Olson and P. A. Dover, "Disconfirmation of consumer expectation through product trial", *J. Appl. Psychol.*, vol.64, pp.179-189, 1979.
- [25] R. Antony, V. B. Khanapuri, and K. Jain, "Customer expectations and moderating role of demographics in fresh food retail: A study among Indian consumers", *Int. J. Retail. Distrib. Manag.*, vol.46, pp.870-890, July 2018.
- [26] S.H. Wu and Y. Gao, "Understanding emotional customer experience and co-creation behaviors in luxury hotels", *Int. J. Contemp. Hosp. Manag.* Vol.31, no.11, pp.4247-4275, November 2019.
- [27] X. Xu and Y. Huang, "Restaurant information cues, diners' expectation, and need for cognition: Experimental studies of online-to-offline mobile food ordering", *J. Retail. Consum. Serv.* Vol.51, pp.231-241, November 2019.
- [28] M. Mao and P. James, "Evaluating customer satisfaction using the ACSI model in a themed restaurant in Bangkok. Bus", *Manag. Strategy*. Vol.11, no.1, pp. 55-7, June 2020.
- [29] J.-B. E. M. Steenkamp, "Product quality: an investigation into the concept and how it is perceived by consumers", PhD Thesis, Wageningen University and Research, 1989.
- [30] A. Hidayat, A. P. Adanti, A. Darmawan and A. N. A. Setyaning, "Factor influencing Indonesian customer satisfaction and customer loyalty in local fast-food restaurant", *Int. J. Mark. Stud* vol.11, no.3, pp.131-139, August 2019.
- [31] S. N. F. B. A. Shariff, M. B. Omar, S. N. B. Sulong, H. A. B. M. A. Majid, H. B. M. Ibrahim, Z. B. Jaafar, and M. S. K. B. Ideris, "The influence of service quality and food quality towards customer fulfillment and revisit intention" *Can. Soc. Sci.*, vol.11, no.8, pp.110-116, November 2015.
- [32] J. Ha and S. S. Jang, "Effects of service quality and food quality: The moderating role of atmospherics in an ethnic restaurant segment", *Int. J. Hosp.*, vol.29, no.3, pp.520-529, September 2010.
- [33] C. Peri, "The universe of food quality", *Food Qual. Prefer.*, vol.17, pp.3-8, 2006.
- [34] A. K. Y. Law, Y. V. Hui, and X. Zhao, "Modeling repurchase frequency and customer satisfaction for fast food outlets", *Int. J. Qual. Reliab. Manag.*, vol.21, no.5, pp.545-563, June 2004.
- [35] V. A. Zeithaml and M. J. Bitner, "Service Marketing", McGraw-Hill, New York, NY, 1996.
- [36] N. Johns and A. Howard, "Customer expectations versus perceptions of service performance in the food service industry", *Int. J. Serv. Ind. Manag.*, vol.9, no.3, pp.248-256, August 1998.
- [37] A. Parasuraman, V. A. Zeithaml, and L. L. Berry, "A conceptual model of service quality and its implications for future research", *J. Mark.*, vol.49, no.4, pp.41-50, September 1985.
- [38] R. P. Bagozzi, "The self-regulation of attitudes, intentions, and behavior", *Soc. Psychol. Q.*, vol.55, pp.178-204, 1992.
- [39] W.K. Liu, Y.S. Lee, and L.M. Hung, "The interrelationships among service quality, customer satisfaction, and customer loyalty: Examination of the fast-food industry", *J. Foodserv. Bus. Res.*, vol.20, no.2, 2017.
- [40] J. Cronin, Jr., M. K. Brady, and G. T. M. Hult, "Assessing the effects of quality, value, and customer satisfaction on consumer behavioral intentions in service environments", *J. Retail.*, vol.76, no.2, pp.193-218, 2000.
- [41] A. Parasuraman, V. A. Zeithaml, and L. L. Berry, "SERVQUAL: A multiple-item scale for measuring consumer perceptions of service quality", *J. Retail.*, vol.64, no.1, pp.12-40, 1988.
- [42] S. Banerjee, D. Jain, and R. Nayyar, "Measuring service quality of food delivery services: A study of generation Z", *Afr. J. Hosp. Tour. Leis.* Vol.8, no.1, pp.1-12, 2019.
- [43] Yusra and A. Agus, "The influence of online food delivery service quality on customer satisfaction and customer loyalty: The role of personal innovativeness", *J. Environ. Treat. Tech.*, vol.8, no.1, pp.6-12, 2020.
- [44] A. Namin, "Revisiting customers' perception of service quality in fast food restaurants", *J. Retail. Consum. Serv.*, vol.34, no.C, pp.70-81, 2017.
- [45] S. Junsawang, W. Chaiyasoonthorn, and S. Chaveesuk, "Willingness to use self-service technologies innovation on omnichannel". In Proceedings of the IEEE 8th International Conference on Industrial Engineering and Applications (ICIEA'21), pp.575-582, 2021.
- [46] S Chaveesuk, P Wutthirong, and W Chaiyasoonthorn, "Cloud computing classroom acceptance model in Thailand higher education's institutes", In Proceedings of the 10th International Conference on Information Management and Engineering (ICIME'18), pp.141-145, 2018.
- [47] L. H. Hartmann, S. Nitzko, and A. Spiller, "The significance of definitional dimensions of luxury food", *Br. Food J.*, vol.118.
- [48] J.S. Chiou, "The antecedents of consumers' loyalty toward internet service providers", *Inf. Manag.*, vol.41, no.6, pp.685-695, July 2004.
- [49] M. v. d. Veen, "When is food a luxury?", *World Archaeol.*, vol.34, no.3, pp.405-427, February 2003.
- [50] P.Kaur, A. Dhir, S. Talwar, and K. Ghuman, "The value proposition of food delivery apps from the perspective of theory of consumption value", *Int. J. Contemp. Hosp. Manag.*, vol.33, no.4, pp.1129-1159, 2021.
- [51] R. Katochand and A. Sidhu. 2021. Online food delivery industry in India: A case of customer satisfaction dynamics. *Adv. Math.: Sci. J.* 10, 1, 507-516.
- [52] Deepayan Ghosh. 2020. Customer satisfaction towards fast food through online food delivery (OFD) services: An exploratory study. *Int. J. Manag.* 11, 10 (October 2020), 645-658. <https://doi.org/10.34218/IJM.11.10.2020.061>
- [53] Jungmin Yoo and Minjung Park. 2016. The effects of e-mass customization on consumer perceived value, satisfaction, and loyalty toward luxury brands. *J. Bus. Res.* 1-10. <https://doi.org/10.1016/j.jbusres.2016.04.174>
- [54] K. Vijaranakorn and R. Shannon, "The influence of country image on luxury value perception and purchase intention", *J. Asia Bus. Stud.*, vol.11, 2017.
- [55] V. Siagian, "Customer expectation and customer satisfaction: Reviewing service quality of Uber", *Journal Honsep Bisnis Dan Manajemen*, vol.6, no.2, pp.209-217, May 2020.
- [56] I. Kulchitaphong, W. Chaiyasoonthorn, and S. Chaveesuk, "Management of innovation and sustainable development of FMCG across OMNI-channels", *Pol. J. Manag. Stud.*, vol.23, no.1, pp.227, 2021.

Interview Guide Development for Qualitative Research on Exploring Acceptance of Autonomous Vehicles in Thailand

Thana Sithanant
 KMITL Business School
 King Mongkut's Institute of Technology
 Ladkrabang,
 Bangkok, Thailand
 +66818252718
 63611005@kmitl.ac.th

Wornchanok Chaiyasoonthorn
 KMITL Business School
 King Mongkut's Institute of Technology
 Ladkrabang,
 Bangkok, Thailand
 +66891533845
 wornchanok.ch@kmitl.ac.th

Singha Chaveesuk
 KMITL Business School King
 Mongkut's Institute of Technology
 Ladkrabang
 Bangkok, Thailand
 +66868925424
 singha@it.kmitl.ac.th

Abstract— The aim of this article is to create a semi-structured interview guide for a qualitative research project centered on the exploring acceptance of autonomous vehicles (AVs) in Thailand. The widespread acceptance of AVs holds significant potential for enhancing the quality of life. While existing studies have predominantly focused on the acceptance of AVs through quantitative research and technology acceptance theories, this paper seeks to address this gap by proposing an innovative approach. This approach involves qualitative research rooted in the use of grounded theory methodology, employing semi-structured interviews to generate a novel theoretical framework. The collection of qualitative data will be facilitated through the adoption of semi-structured interviews, with the interview guide serving as the principal tool for data collection. The article will commence with a concise overview of AVs, pertinent technology acceptance theories, past research on AV acceptance, and the adoption of conventional car studies. Following that, a synthesis of knowledge and identification of gaps will be presented. Subsequently, a new research approach will be introduced, and a systematic procedure for crafting the semi-structured interview guide will be detailed and summarized.

Keywords— *interview guide, qualitative research, acceptance, autonomous vehicle*

I. INTRODUCTION

Numerous studies have highlighted the manifold positive impacts of AVs on society. These benefits encompass a reduction in accident rates [1 - 3], heightened energy efficiency [4, 5], alleviation of urban congestion [5, 6], diminished demand for parking spaces [3], mitigation of pollution [6, 8], enhanced utilization of passengers' time [9], and overall environmental advantages [6 - 8].

Autonomous vehicles, or AVs, are self-operating vehicles that perform tasks like steering, acceleration, and braking without direct driver input. AVs are classified into six tiers, with "full automation" being the highest level, where the vehicle handles all driving tasks [10]. The emergence of AVs is a rapidly evolving and controversial technology [11, 12]. While existing studies often use quantitative approaches based on Technology Acceptance Theories, this article proposes an innovative approach. It employs qualitative research, Grounded Theory methodology, and semi-structured interviews to create a novel framework and bridge gaps.

In the context of Thailand, the adoption of this technological transition holds the potential not only to decrease road fatalities and enhance the overall quality of life, but also to yield positive outcomes for domestic automobile manufacturers and associated downstream sectors, including car part producers, automotive service providers, and electronics industries. Consequently, Thailand has the opportunity to assume a pioneering role in advancing the acceptance and utilization of autonomous vehicles in the region.

The primary objective of this article is to outline the procedure for creating a semi-structured interview guide aimed at exploring the acceptance of autonomous vehicles in Thailand. The primary focus of these interviews is to gather insights addressing the subsequent research questions:

- What are the most influential factors for the Thai consumer's intent to buy AVs?
- What are the primary barriers preventing Thais from intention to owning AVs?
- How will sociodemographic factors influence the intention to adopt AVs in Thailand?

The article commences by conducting a thorough review of pertinent theories and prior research, subsequently introducing a systematic approach to constructing the interview guide. A succinct overview of the interview questions follows, and the final section concludes with a discussion.

II. LITERATURE REVIEW

A. Technology of Autonomous Vehicles

Since the mid-1980s, numerous entities, including academic institutions, research organizations, and automotive manufacturers, have engaged in autonomous vehicle research. A pivotal moment occurred in 2007 with DARPA's Grand Urban Challenge, showcasing notable progress in driverless car development despite simpler obstacles [13, 14].

The Society of Automotive Engineers (SAE) International introduced a classification system to gauge autonomous vehicle autonomy. This spectrum ranges from level 0, where the vehicle offers alerts and brief assistance without continuous control, to level 5, where the vehicle operates entirely autonomously without human involvement

in any situation [15]. Autonomous vehicle architecture rests on two pillars: the perception system and decision-making system. The perception system manages functions like localization, obstacle mapping, obstacle tracking, and traffic signal recognition. Decision-making covers route planning, behavior selection, motion planning, obstacle avoidance, and vehicle control [16]. The perception system processes data from sensors like LIDAR, RADAR, cameras, GPS, IMU, and odometer. Coupled with prior sensor data, road info, and rules, it assesses the vehicle's state and surroundings. The Decision-Making system factors in status, surroundings, rules, safety, and comfort, guiding the vehicle to its destination [16].

B. Previous research on Acceptance on Autonomous vehicles

Autonomous vehicles are a rapidly emerging technology that has generated controversy. This section will give a brief overview of previous articles of the user's acceptance for autonomous vehicles. The definition of acceptance is when individuals possess a positive attitude, intention, and/or willingness to use innovation in the future [17].

The review of 41 studies identifies three dominant theories—TAM, UTAUT, and TPB—as foundational frameworks for studying autonomous vehicle acceptance.

The Technology Acceptance Model (TAM) explains technology adoption mechanisms and predicts successful application. It emphasizes assessing benefits versus effort, with perceived usefulness and ease of use as key factors [18, 19]. TAM addresses complexity barriers hindering innovation diffusion [20]. It integrates behavior predictors like ease of use, usefulness, and intention to behave [18, 19, 21].

The Unified Theory of Acceptance and Usage of Technology (UTAUT) unifies eight theories to predict new technology adoption [22]. It focuses on factors like performance expectancy, effort expectancy, social impact, and facilitating conditions [22]. UTAUT incorporates diverse fields like psychology and IT [22].

The Theory of Planned Behavior (TPB) predicts consumer acceptance of new technologies. It considers factors like Attitude, Subjective Norms, Perceived Behavioral Control, Intention, and Behavior [23]. Personal control over internal and external factors influences behavior [23]. Attitudes, normative beliefs, and belief in control shape behavioral inclination [23].

Among them, 21 studies employed TAM or its extension to gauge AV adoption intentions. In TAM-based research, perceived usefulness consistently predicted AV usage intentions, except for [25]. Nonetheless, all studies found perceived ease of use significantly influenced AV usage intentions. Six studies [26 – 31] examined the UTAUT and its extension. Meanwhile, four studies [31 - 34] applied the TPB.

Additional Other featured models include MPAM [35], Grey-DEMATEL [36], DOI-TAM-Trust combination [37], CAT [38], novel agent-based model [39], ICLV [40], and ISA [41]. [42] examined attitudes of blind individuals. [26] stressed attitude, [31] found strong attitudes in France and Sweden, [37, 43, 44] found trust consistent, [44] highlighted ethical standards. Innovativeness mattered in [41, 45],

but not [30]. [30] revealed subsidy's mediating role. Social influence, price reduction, WOM, and media impact mattered [35, 39]. Perceived risk varied [43, 38, 41]. Hedonic motivation was key [27, 28, 32, 38], and sensation seeking in [41].

C. Past research on Acceptance on conventional vehicles

Autonomous vehicle acceptance research often employs technology acceptance models, while conventional vehicle studies typically focus on individual or car-related factors. For example, [46] used linear regression to assess factors impacting conventional car purchase in Pakistan. [47] tested internet and social media influence in India using chi-square. Demographic and economic variables in Nigeria were studied through multiple regressions in [48]. [49] examined Brand identity and marketing effects in Ghana using ANOVA. Color brightness's role in car purchase decisions was explored via chi-square in [50]. Brand loyalty and purchase intention were investigated in Pakistan using regression analysis in [51]. SEM was utilized in [52] to explore brand equity's impact on purchase intention in Vietnam. Nostalgic advertisement and Brand Heritage effects in Egypt were assessed through SEM in [53]. Values affecting loyalty in Turkey were identified using regression analysis in [54], with [55] using t-test to quantify social norms and socio-demographic factors on car buying intention among US students.

III. SYNTHESIS KNOWLEDGE AND THE NEW APPROACH

The researcher emphasizes a notable difference in critical factors between conventional cars and AVs, underscored by AVs being a subset of durable goods within traditional vehicles. This highlights the significant challenge in understanding AV adoption factors, prompting the need for further exploration. These reviews reveal limitations in their application to Thailand, attributed to various factors:

- Previous research relies on established IT or computer adoption models (TAM, UTAUT and TPB) due to the absence of a dedicated AV model.
- Limited studies contextualized in Thailand overlook crucial factors tied to local behavior, culture, and lifestyle.
- Variability in results across studies makes identifying a common framework challenging due to differing focuses, regions, and cultures.
- Few studies consider AVs as a subset of conventional vehicles, overlooking relevant factors from car purchasing studies.
- Quantitative research predominates, while qualitative approaches are untapped, which could yield valuable insights.

In conclusion, while previous studies have examined AV adoption intentions in Thailand and their correlations, they may not fully capture current dynamics. To address this, conducting tailored qualitative research with grounded theory is essential for achieving the research objectives.

A. Qualitative research with Grounded Theory

Qualitative research offers a unique pathway, exploring the intricate social realities of individuals by analyzing descriptive, non-numeric data to uncover their attitudes,

beliefs, and motivations. In the realm of research, data is the cornerstone, providing the means to address questions and fulfill objectives [56]. For research outcomes of the highest caliber, robust data collection tools are indispensable. Among the array of qualitative methods, such as interviews, observation, and document review, interviewing emerges as a pivotal tool. [57] emphasizes its elemental role as "one of the most basic forms of data gathering", anchoring various qualitative strategies [58].

The inception of grounded theory by [59] introduced a systematic approach to qualitative research, dedicated to the formulation of theories. In contrast to quantitative methods, grounded theory takes root in empirical observations, nurturing theory organically from the data itself [59]. This iterative process involves the interplay of data collection, analysis, and the blossoming of theory [60, 61]. The interview reverberates through qualitative data collection, accentuating the significance of proficient tools [61]. With interviews taking center stage, this paper's focus is the construction of interview tools to cultivate high-quality data within qualitative research. The interview process entails recording, transcription, cleaning, and analysis, progressing through coding, category formation, and thematic design. This cycle persists with participants until saturation, and the potential for further recruitment remains to solidify confirmation [61].

B. Semi-Structure Interview Development Guide

Conducting comprehensive one-on-one interviews will involve both in-person and virtual formats based on participants' preferences. These interviews will be guided by an interview guide, consisting of questions and topics for discussion [62]. Data collection and analysis will occur simultaneously, primarily through in-person interviews, while virtual interviews will also be offered for convenience. The development of the interview guide follows Jountrakul's methodology [56], encompassing seven sequential steps: (1) Specify research questions. (2) Define research objectives. (3) Summarize the literature review. (4) Identify expected participant information. (5) Formulate targeted questions. (6) Select pertinent questions for the interview guide draft. (7) Explain the rationale behind the selected questions for obtaining necessary information.

Following the completion of the table as presented in Table 1, fourteen selected interview questions can be summarized in column 6. These questions will provide interviewers with a structured framework to effectively guide their interactions with interviewees.

IV. CONCLUSION

Considering the absence of a dedicated AV model, predominant quantitative focus, and outdated Thai research data, the researcher introduces an innovative qualitative approach using grounded methodology. High-quality data collection tools are crucial for optimal outcomes, and a well-structured semi-structured interview guide is proposed. Insights from this guide are synthesized, providing interviewers with an efficient framework for interactions. Skillfully combined with an interviewer's expertise, this guide consistently yields superior results, enabling effective model formulation. Ethical considerations remain vital, ensuring participant understanding, voluntary participation, and withdrawal options. Upholding ethical standards is essential

for a robust theoretical model grounded in sound research findings.

REFERENCES

- [1] C. Xu, Z. Ding, C. Wang, and Z. Li, "Statistical analysis of the patterns and characteristics of connected and autonomous vehicle involved crashes," *Journal of Safety Research*, 71, 2019, pp. 41-47. doi:10.1016/j.jsr.2019.09.001
- [2] L. Wang, H. Zhong, W. Ma, M. Abdel-Aty, and J. Park, "How many crashes can connected vehicle and automated vehicle technologies prevent: A meta-analysis," *Accident Analysis & Prevention*, vol. 136, 105299., 2020,
- [3] J. Mueller, B. Cicchino, and D. S. Zuby, "What humanlike errors do autonomous vehicles need to avoid to maximize safety?," *Journal of Safety Research*, vol. 75, 2020, pp.310-318.
- [4] L. Tate, S. Hochgreb, J. Hall, and M. Bassett, "Energy efficiency of autonomous car powertrain," *SAE Technical Paper Series*, 2018.
- [5] F. Liu, F. Zhao, Z. Liu, and H. Hao, "The impact of purchase restriction policy on car ownership in China's four major cities," *Journal of Advanced Transportation*, 2020, pp. 1-14.
- [6] R. Neufville, H. Abdalla, and A. Abbas, "Potential of connected fully autonomous vehicles in reducing congestion and associated carbon emissions," *Sustainability*, vol. 14(11), 2022.
- [7] I. Gokasar, A. Timurogullari, M. Deveci, and H. Garg,"SWSCAV: Real-time traffic management using connected autonomous vehicles," *ISA Transactions*, vol. 132, 2023, pp. 24-38.
- [8] K. Akimoto, F. Sano, and J. Oda, "Impacts of ride and car-sharing associated with fully autonomous cars on global energy consumptions and carbon dioxide emissions," *Technological Forecasting and Social Change*, vol. 174, 2021,
- [9] C. McCarroll, and F. Cugurullo, "Social implications of autonomous vehicles: A focus on time," *AI and SOCIETY*, vol. 37(2), 2022, pp. 791-800.
- [10] J. Fleetwood, "Public health, ethics, and autonomous vehicles," *American Journal of Public Health*, vol. 107(4), 2017, pp. 532-537.
- [11] O. Tengilimoglu, O. Carsten, and Z. Wadud, "Implications of automated vehicles for physical road environment: A comprehensive review," *Transportation research part E: logistics and transportation review*, vol. 169, 2023.
- [12] F. Liu, F. Zhao, Z. Liu, and H. Hao, "Can autonomous vehicle reduce greenhouse gas emissions? A country-level evaluationm," *Energy Policy*, vol. 132, 2019, pp. 462-473.
- [13] B. Claudine, G. Ränik, V. C. Raphael, A. Pedro, B. C. Vinicius, F. Avelino F. and Alberto, "Self-driving cars: A survey," *Expert Systems With Applications*, vol. 165, 2021.
- [14] M. Buehler, K. Iagnemma, S. Singh (eds), "The DARPA urban challenge: autonomous vehicles in city traffic," Springer A.S., vol. 56 , 2009.
- [15] D. Parekh, N. Poddar, A. Rajpurkar, M. Chahal, N. Kumar, G. P. Joshi, G. P., and W. Cho, "A review on autonomous vehicles: Progress, methods and challenges," *Electronics*, vol. 11(14), 2016,
- [16] B. Paden, M. Cap, S. Z. Yong, D. Yershov, and E. Frazzoli, "A survey of motion planning and control techniques for self-driving urban vehicles," *IEEE Transactions on Intelligent Vehicles*, vol. 1(1), 2016, pp. 33-55.
- [17] H. Taherdoost "A review of technology acceptance and adoption models and theories," *Procedia manufacturing*, vol. 22, 2018, pp. 960-967.
- [18] F. D., Davis "Perceived Usefulness, Perceived Ease of Use, and End User Acceptance of Information Technology," *MIS Quarterly*, vol. 13, 2013, pp. 318-339.
- [19] F. D. Davis, R. P. Bagozzi, and P. R. Warshaw, "User Acceptance of Computer Technology: A Comparison of Two Theoretical Models," *Management Science*, vol. 35, 1898, pp. 982-1003.
- [20] V. Mahajan, *Innovation diffusion*. Wiley International Encyclopedia of Marketing, 2010.
- [21] F. D. Davis, "User acceptance of information technology: System characteristics, user perceptions and behavioral impacts," *International Journal of Man-Machine Studies*, vol. 38, no. 3, 1993, pp. 475-487.

TABLE I INTERVIEW DEVELOPMENT GUIDE ON EXPLORING ACCEPTANCE FOR AUTONOMOUS VEHICLES IN THAILAND

| Research question | Research Objective | Literature Review | Expected Answer | Interview questions as guided by Patton (1990) | Selected interview questions | Reason to select the question |
|---|--|--|--|---|---|---|
| 1) What are the most influential factors for the Thai consumer's intent to buy AVs? | 1) To investigate the important factors that influence the use of AVs in Thailand. | -Review of Technology used for AVs | Factors that drive the Thai users to adopt AVs | 1) Have you ever heard about AVs? If so, please explain. | 1) Have you ever heard about AVs? If so, please explain. | To share a common understanding of what AVs are. |
| | | -Review of previous research on factors to AV adoption | | 2) What are the key factors that you will buy AV to use? | 2) What are the key factors that you will buy AV to use? | To comprehend the primary factors that motivate Thai consumers to purchase AVs. |
| | | | | 3) Do you agree AV can reduce accidents dramatically? | | |
| | | | | 4) Do you think you will enjoy driving AVs like driving normal cars? | | |
| | | -Review of past research on factors to conventional car adoption | | 5) Is it important for AVs to match the performance of traditional cars, and if so, what is the reasoning behind this perspective? | 3) Is it important for AVs to match the performance of traditional cars, and if so, what is the reasoning behind this perspective? | To gain a deeper understanding of the performance comparison between autonomous vehicles (AVs) and conventional cars. |
| | | -Review of past research on factors to conventional car adoption | | 6) Is safety, in your opinion, equally significant for AVs as it is for traditional cars? If so, could you please elaborate on your reasoning? | 4) Is safety, in your opinion, equally significant for AVs as it is for traditional cars? If so, could you please elaborate on your reasoning? | To comprehend whether safety is a determining factor for individuals. |
| | | -Review of previous research on factors to AV adoption | | 7) Do you think AV is too expensive? | 5) Do you think AV is too expensive? | To make sure that different in price will not be the main impact. |
| | | -Review of past research on factors to conventional car adoption | | 8) What's your take on AV brands? Would a strong presence of Japanese brands like Toyota sway you towards AVs? | 6) What's your take on AV brands? Would a strong presence of Japanese brands like Toyota sway you towards AVs? | To investigate whether the brand of autonomous cars plays a role. |
| | | -Review of previous research on factors to AV adoption | | 9) Do you hold the belief that the environment would benefit from the use of AVs? If so, could you elaborate on your reasoning behind this perspective? | 7) Do you hold the belief that the environment would benefit from the use of AVs? If so, could you elaborate on your reasoning behind this perspective? | To evaluate whether individuals perceive AVs as potential solutions to pollution issues. |
| | | -Review of previous research on factors to AV adoption | | 10) Would the widespread adoption of AVs among the people around you influence your own consideration of using them? | 8) Would the widespread adoption of AVs among the people around you influence your own consideration of using them? | To explore the impact of the external influence from the other people. |

| | | | | | | |
|--|---|---|--|--|---|--|
| | | | | 11) What do you know about government policy toward AV? | | |
| 2) What are the primary barriers preventing Thais from intention to owning AVs? | To identify the most significant obstacles that users may avoid to AVs in Thailand. | - Review of Technology used for AVs | The disadvantages of using AVs in Thailand | 1) Have you ever had any experience using AVs? If so, please provide details and explanations. | 9) Have you ever had any experience using AVs? If so, please provide details and explanations. | To determine if participants have prior experience with driving AVs or have encountered any negative experiences. |
| | | - Review of past research on factors to conventional car adoption | | 2) What is the major advantage and disadvantage of AVs you have known of? | 10) What is the major advantage and disadvantage of AVs you have known of? | To gather insights from participants' perspectives on the significant advantages and disadvantages of AVs, whether they are already aware of them or not. |
| | | - Review of previous research on AV adoption | | 3) What are the key obstacles to you not buying the AVs | 11) What are the key obstacles to you not buying the AVs? | To understand what are the major obstacles that Thai consumer will not buy AVs. |
| | | | | 4) Would your friend's negative opinion about AVs influence your consideration? | | |
| | | | | 5) What are your thoughts if the price of AVs is relatively high? | | |
| 3) How will sociodemographic factors influence the intention to adopt AVs in Thailand? | To examine the effects of these factors among multiple elements, such as age, gender, living location, household factor toward users' intention to use AVs in Thailand. | - Review of previous research on AV adoption | Sociodemographic that impact the decision to adopt AVs | 1) If this is OK, please let me know your age, gender, status, or living location. | 12) If this is OK, please let me know your age, gender, status, or living location. | To request participants' permission for recording personal information. |
| | | | | 2) Do you currently own a conventional car? | | |
| | | - Review of previous research on AV adoption | | 3) Do you have any plans to use or purchase AVs? If yes, could you please elaborate on your reasons for that decision? | 13) Do you have any plans to use or purchase AVs? If yes, could you please elaborate on your reasons for that decision? | Responses to question 1 could potentially reveal a notable inclination among participants towards AVs. |
| | | - Review of previous research on AV adoption | | 4) Do you believe that your age, gender, status, or living location influences your decision regarding the previous question? If so, could you please explain why you think these factors play a role? | 14) Do you believe that your age, gender, status, or living location influences your decision regarding the previous question? If so, could you please explain why you think these factors play a role? | To comprehensively grasp the implications of these factors across various variables, including age, gender, residential location, and household dynamics, on users' intent to adopt AVs in Thailand. |

- [22] V. Venkatesh, M. G. Morris, G. B. Davis, and F. B. Davis, "User Acceptance of Information Technology: Toward a Unified View," *MIS Quarterly*, vol. 27, no. 3, 2003.
- [23] I. Ajzen, "The theory of planned behaviour: Reactions and reflections," *Psychology and health*, vol. 26(9), 2011, pp. 1113-1127.
- [24] V. Venkatesh, A. Susan, A. Brown, and B. Hillol "Bridging the qualitative-quantitative divide: Guidelines for conducting mixed methods research in information systems," *MIS quarterly* (2013), 2013, pp. 21-54.
- [25] P. Sakuljao, W. Satiennam, T. Satiennam, N. Kronprasert, and S. Jaensirisak, "Understanding intention to use conditionally automated vehicles in Thailand, based on an extended technology acceptance model," *Sustainability*, vol. 15(3), 2023.
- [26] K. Ljubi, and A. Groznik, "Role played by social factors and privacy concerns in autonomous vehicle adoption," *Transport Policy*, vol.132, 2023, pp. 1-15.
- [27] S. Nordhoff, J. Stapel, B. van Arem, and R. Happee, "Passenger opinions of the perceived safety and interaction with automated shuttles: A test ride study with 'hidden' safety steward," *Transportation research part A: policy and practice*, vol. 138, 2020, pp. 508-524.
- [28] T. Keszey, "Behavioural intention to use autonomous vehicles: Systematic review and empirical extension," *Transportation research part C: emerging technologies*, vol. 119, 2020.
- [29] A. Manfreda, K. Ljubi, and A. Groznik, "Autonomous vehicles in the smart city era: An empirical study of adoption factors important for millennials," *International Journal of Information Management*, vol. 58, 2021.
- [30] S. Chaveesuk, W. Chaiyasoonthorn, N. Kamales, Z. Dacko-Pikiewicz, W. Liszewski, and B. Khalid, "Evaluating the determinants of consumer adoption of autonomous vehicles in Thailand—An extended UTAUT model," *Energies*, vol. 16(2), 2023, pp. 855.
- [31] S. A. Kaye, I. Lewis, S. Forward and P. Delhomme, "A priori acceptance of highly automated cars in Australia, France, and Sweden: A theoretically-informed investigation guided by the TPB and UTAUT," *Accident Analysis and Prevention*, vol. 137, 2020.
- [32] K. Weigl, M. A. Nees, D. Eisele and A. Rieger, "Acceptance of automated vehicles: Gender effects, but lack of meaningful association with desire for control in Germany and in the US," *Transportation research interdisciplinary perspectives*, vol.13, 2022.
- [33] R. A. Acheampong and F. Cugurullo, "Capturing the behavioural determinants behind the adoption of autonomous vehicles: Conceptual frameworks and measurement models to predict public transport, sharing and ownership trends of self-driving cars," *Transportation research part F: traffic psychology and behaviour*, vol. 62, 2019, pp. 349-375.
- [34] M. M. Rahman, S. Deb, L. Strawderman, R. Burch, and B. Smith, "How the older population perceives self-driving vehicles," *Transportation research part F: traffic psychology and behaviour*, vol.65, 2019, pp. 242-257.
- [35] G. Zhu, Y. Chen, and J. Zheng, "Modelling the acceptance of fully autonomous vehicles: a media-based perception and adoption model," *Transportation research part F: traffic psychology and behaviour*, vol. 73, 2020, pp. 80-91.
- [36] A. Raj, J. A. Kumar, and P. Bansal, "A multicriteria decision making approach to study barriers to the adoption of autonomous vehicles," *Transportation research part A: policy and practice*, vol. 133, 2020, pp. 122-137.
- [37] K. F. Yuen, L. Cai, G. Qi, and X. Wang, "Factors influencing autonomous vehicle adoption: An application of the technology acceptance model and innovation diffusion theory," *Technology Analysis and Strategic Management*, vol. 33(5), 2021, pp. 505-519.
- [38] M. A. Ribeiro, D. Gursoy, and O. H. Chi, "Customer acceptance of autonomous vehicles in travel and tourism," *Journal of Travel Research*, vol. 61(3), 2022, pp. 620-636.
- [39] S. Dubey, I. Sharma, S. Mishra, O. Cats, and P. Bansal, "A general framework to forecast the adoption of novel products: A case of autonomous vehicles," *Transportation research part B: methodological*, vol. 165, 2022, pp. 63-95.
- [40] P. Jabbari, J. Auld, and D. MacKenzie, "How do perceptions of safety and car ownership importance affect autonomous vehicle adoption?," *Travel behaviour and society*, vol. 28, 2022, pp. 128-140.
- [41] A. Z. Benleulmi, and B. Ramdani, "Behavioural intention to use fully autonomous vehicles: Instrumental, symbolic, and affective motives," *Transportation research part F: traffic psychology and behaviour*, vol. 86, 2022, pp. 226-237.
- [42] R. Bennett, R. Vijaygopal, R. and Kottasz, "Willingness of people who are blind to accept autonomous vehicles: An empirical investigation," *Transportation research part F: traffic psychology and behaviour*, vol 69, 2020, pp. 13-27.
- [43] W. Ackaah, V. L. Leslie, and K. K. Osei, "The adoption of self-driving vehicles in Africa: Insight from Ghana. *Urban, Planning and Transport Research*, vol 10(1), 2022. Pp. 333-357.
- [44] S. Ramjan, and P. Sangkaew, "Understanding the adoption of autonomous vehicles in Thailand: An extended TAM approach," *Engineering Management in Production and Services*, vol 14(1), 2022.
- [45] I. Nastjuk, B. Herrenkind, M. Marrone, A. B. Brendel, and L. M. Kolbe, "What drives the acceptance of autonomous driving? An investigation of acceptance factors from an end-user's perspective," *Technological Forecasting and Social Change*, vol 161, 2020.
- [46] M. Naeem, and A Sami, "Product brand loyalty and purchase decision: a comparative study of automobile industry of Pakistan," *International Journal of Entrepreneurial Research*, vol 3(3), 2020, pp. 76-87.
- [47] B. M. Darshan, "Influence of social media on vehicle purchasing decisions: An empirical study on automobile industry," *International Journal of Mechanical Engineering and Technology*. Vol 9, 2018, pp. 974-981.
- [48] H. D. Koce, M. Z. Ndaba, and E. G. Gata, (2021). Economic and demographic determinants and its effect on consumer purchasing decision in the Nigerian automobile industry," *International Journal of Research -GRANTHAALAYAH*, 2021.
- [49] S. I. Nnindini, and J. B. Dankwah, "Consumer Loyalty and Brand Marketing Programs in an Emerging Economy: Evidence from the Automobile Industry," *Information Management and Business Review*, vol 13(4 (I)), 2021, pp. 23-38.
- [50] T. Kato, "Perceived color quality: The effect of light reflection brightness of a car's exterior design on consumers' purchase intentions," *International Journal of Engineering Business Management*, vol 14, 2022.
- [51] D. R. Q. Danish, D. M. K. Khan, D. M. M. Ghafoor, D. I. Ahmad, D. A. A. Humayon, and S. Aslam, "Impact of brand loyalty in assessing purchase intentions of a customer: A study of automobile industry in South Asian perspective," *South Asian Studies*, vol 33(2), 2020.
- [52] N. T. H. Phan, T. Q. Nguyen, and D. Truong, "The effect of brand equity components on automobile purchase intention of consumers in Ho Chi Minh city, Vietnam," *The Journal of Asian Finance, Economics and Business (JAFEB)*, vol 6(2), 2019, pp. 135-145.
- [53] H. Ahemd Nabih El-Sayed Nassef, and G. Sayed Abd El-Aziz, "Investigating the relationship between nostalgic advertisement, brand heritage, and automobile purchase intention (Applying on Mercedes – Benz Egypt)," *The Academic Journal of Contemporary Commercial Research*, vol 2(1), 2022, pp. 16-34.
- [54] Ö. Ü. O. ÖZDEMİR, "The relationship between consumer perceived value and purchase intention: an empirical study of automobile sector in turkey," *Journal of Academic Value Studies*, vol 5, issue 3, 2019, pp. 324-332.
- [55] P. F. Belgiawan, J. D. Schmöcker, M. Abou-Zeid, J. Walker, and S. Fujii, "Modelling social norms: Case study of students' car purchase intentions," *Travel Behaviour and Society*, vol 7, 2017, pp. 12-25.
- [56] J. Joungtrakul, B. Sheehan, and S. Aticomswan, "Qualitative Data Collection Tool: A New Approach to Developing an Interview Guide," *AFBE* 6, vol 2, 2013, pp. 140-154.
- [57] B. A. Chadwick, H. M. Bahr, and S. L. Albrecht, "Qualitative research. Social science research methods," 1984, pp 205-237.
- [58] J. W. Creswell, *Qualitative Inquiry and Research Design*. (3rd ed.), Sage Publications, Thousand Oaks, CA, 2013.

- [59] B. G. Glaser, and A. L. Strauss, *The Discovery of Grounded Theory: Strategies for Qualitative Research*. Chicago, IL: Aldine Altherton. ISBN:0-202-30260-1., 1967.
- [60] J. Corbin, and A. Strauss, *Basics of Qualitative Research: Techniques and Procedures for Developing Grounded Theory*. Fourth edition. Sage, Thousand Oaks, Ca., 2015.
- [61] T. M. Giles, S. de Lacey, and E. Muir-Cochrane, "Coding, Constant Comparisons, and Core Categories: A Worked Example for Novice Constructivist Grounded Theorists," *ANS* 39, vol 1, 2016, pp. E29-E44.
- [62] M. Q. Patton, *Qualitative evaluation and research methods*. SAGE Publications, inc., 1990.

Factors Effecting Employees Motivation: A Study of the Ministry of Foreign Affairs in Myanmar

Htet Aung Kyaw
KMITL Business School
King Mongkut's Institute of Technology Ladkrabang
Bangkok, Thailand
63611142@kmitl.ac.th

Vasu Keerativutisest
KMITL Business School
King Mongkut's Institute of Technology Ladkrabang
Bangkok, Thailand
vasu.ke@kmitl.ac.th

Abstract—The study aimed to determine the organizational factors that influence employee motivation in the Ministry of Foreign Affairs in Myanmar. Organizational factors as the independent variable were hypothesized to influence the dependent variable. Organizational factors are organization policies, salary, compensation and bonus, working conditions, job security, interpersonal relationships, psychological conditions, and emotional intelligence directly affect employee motivation. This research employed a mixed method that collects the qualitative data first and the results from the qualitative data analysis use the questionnaires for the quantitative data collection. Descriptive statistics of dependent and independent variables are obtained to interpret the responses of participants and draw comparisons of how the responses are distributed. Multiple regression and Pearson correlation coefficient were applied to test hypotheses. Organizational commitment as a moderating variable can strengthen the relationship between organizational factors and employees' motivation. Testing of the hypothesis found that organization factors significantly influence employees' motivation and organizational commitment can modify the relationship between organization factors and employees' motivation

Keywords—Employee motivation, Organizational factors, Organizational Commitment

I. INTRODUCTION

Employee motivation is a workplace approach resulting in the right conditions for all members of an organization to give their best each day, be committed to their organization's goals and values, motivated to contribute to the organizational success, with an enhanced sense of their own well-being. Even more significantly, there is evidence that improving motivation correlates with improving performance [1]. Motivation also emphasizes an emotional connection with the organization, a passion for work, and feelings of hope about the future within the organization. Employee motivation is also derived in the form of satisfaction from the success of the organization [2]. Myanmar governments face fundamental challenges such as determining the right individuals to select for public sector jobs, recruiting these candidates effectively, and motivating them to perform well [3]. Based on the significant findings of the employee motivation study, this research aims at the organizational factors that influence employee motivation at selected

Government Organizations in Myanmar. This study's main concepts were employee motivation as the dependent variable, organizational factors as independent variables and organizational commitments as moderating variables.

II. LITERATURE REVIEW AND CONCEPTUAL FRAMEWORK

A. Employee Motivation

Employee motivation is the dependent variable in this study. Employees' motivation is one of the important parts of people's lives. Organizations or companies can be very dangerous without a motivating workplace. Motivation plays an important role in identifying how individuals act the way they do at the workplace. Employee motivation means that ,one of the strategies of organizations to enhance its performance through its workers by providing a conducive, motivated environment in the organization [4]. Employee motivation is important at the organizational and individual level. The organization level and work motivation are related to employee performance, productivity, organizational commitment, absenteeism, and turnover intention [5].

B. Organization Factors Influence on Employees Motivation

Organizational factors as the independent variable (IV) were hypothesized to influence the dependent variable (DV). Organizational factors such as organization policies, salary, compensation and bonus, working conditions, job security, interpersonal relationships, psychological conditions, and emotional intelligence directly affect employee motivation.

Organization policies: Myanmar governments face fundamental challenges such as determining the right individuals to select for public sector jobs, recruiting these candidates effectively, and motivating them to perform well. Promoting and protecting the rights of persons belonging to minorities has been an integral responsibility and significant priority of the High Commissioner and OHCHR [6].

Salary, Compensation, and Bonus: In Myanmar, the salary in the public sector is lower than the salary in the private sector. To facilitate motivation and incentives in

civil service, it is important to take a step forward to improve transparency in pay and compensation [7]. The World Bank has indicated their possible assistance for pay, compensation, and human resource management, following findings and recommendations from their reviews undertaken recently.

Working Conditions: Working conditions form the basic core of paid work and labor relations. Poor working conditions create an atmosphere that affects employee productivity. Unproductive employees tend to be lethargic and demotivating, which slows down the progress of the organization [8].

Psychological Conditions: The psychology of motivation is the study of how biological, psychological, and environmental variables contribute to motivation. That is, what the body and brain contribute to motivation; what mental processes contribute to; and finally, how material incentives, goals, and their mental representations motivate individuals [9].

Emotional Intelligence: Emotional intelligence can be learned but a significant improvement probably requires intensive individual coaching, relevant feedback, and a strong desire for significant personal development [10].

Job securities: Job security is the assurance an employee has that they can continue working their current job for the foreseeable future. An employee who feels safe at work might be more loyal to their organization. This means they trust the relationship and that they commit to performing well and staying with the organization [11].

Interpersonal relationship: (Prachi, 2018), opined that interpersonal relationship refers to a strong association between individuals working together in the same organization. Employees working together should share a special bond for them to achieve the best possible level [12].

The hypothesis test is as follows-

H10: There is no significant relationship between organization policies on employee motivation.

H1A: There is a significant relationship between organization policies on employee motivation.

H20: There is no significant relationship between salary, compensation, and bonuses on employee motivation.

H2A: There is a significant relationship between salary, compensation and bonuses on employee motivation.

H30: There is no significant relationship between working conditions on employee motivation.

H3A: There is a significant relationship between working conditions on employee motivation.

H40: There is no significant relationship between psychological conditions on employee motivation.

H4A: There is a significant relationship between psychological conditions on employee motivation.

H50: There is no significant relationship between emotional intelligence on employee motivation.

H5A: There is a significant relationship between emotional intelligence on employee motivation.

H60: There is no significant relationship between job securities on employee motivation.

H6A: There is a significant relationship between job securities on employee motivation.

H70: There is no significant relationship between interpersonal relationships on employee motivation.

H7A: There is a significant relationship between interpersonal relationships on employee motivation.

H80: Organization policies, salary, compensation and bonus, working conditions, psychological conditions, emotional intelligence, job security, and interpersonal relationships do not statistically significantly predict employee motivation.

H8A: Organization policies, salary, compensation and bonus, working conditions, psychological conditions, emotional intelligence, job security, and interpersonal relationships do statistically significantly predict employee motivation.

C. Moderating Variable Modify for Relationship between Organization Factors and Employees Motivation

In this study organization commitment as a moderating variable can strengthen the relationship between organizational factors and employees' motivation. Organizational commitment helps organizations perform better and achieve their goals because their employees feel connected to the organization and are more productive and dedicated to their work [13]. Organizational commitment as moderating variables (Mod) was measured in terms of recognition, achievement, responsibility, and training.

Recognition: recognizing employees in front of friends and colleagues is the greatest motivation one can get to do better anytime. Great Place to Work analyzed 1.7 million employee survey responses gathered between 2018 and 2020 across small, mid-sized and large companies. Recognition makes employees feel promotions are fair, spurs innovation and extra effort [14].

Achievement: Employee motivation and achievement have a statistically significant, positive linear relationship. While it may be a weak relationship based on the Pearson correlation coefficient, the relationship is statistically significant [15].

Responsibility: People are motivated when their responsibilities are meaningful and engage their abilities and values. Management is required to impose systematically the responsibility for work-community decisions on the employees [16].

Training: Training is an indicator of the importance given to the employees and constitutes an important wing of the investments made by people. In terms of employees, participation in training programs, of which expenses are covered by companies, can enable them to feel privileged and to increase their knowledge and skills. In this way, they can perform their tasks more motivated without feeling lacking [17].

Then, the hypothesis can be proposed:

Hypothesis: The moderating variable significantly moderates the relationship between organizational factors and employees' motivation.

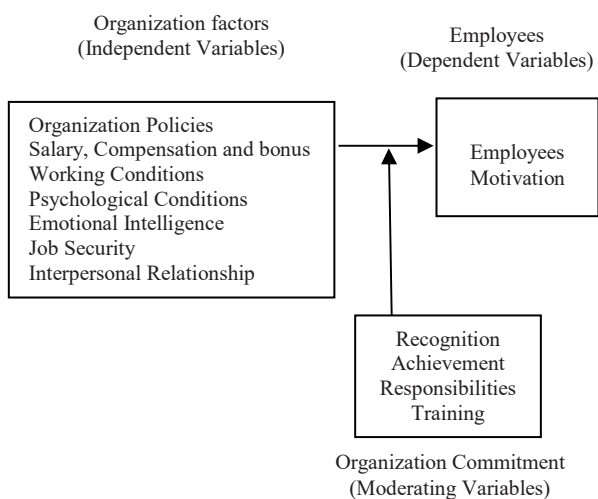


Fig. 1 Conceptual Framework of Employee Motivation

The main purpose of conceptual framework was to clarify concepts and purpose relationships among the variables in the study, provide a context for interpreting the study findings and explain observations. It illustrated the relationship between organizational factors, organization commitments and employee motivation. In this study, the main concepts were employee motivation as the dependent variables, organizational factors as independent variables and organizational commitments as moderating variables.

III. RESEARCH METHOD

The researcher applied the mixed method that combines and integrates qualitative and quantitative. The data are collected by different means to interpret the findings. This offers a stronger understanding of the research method alone because it can exploit the strength of both methods and minimize limitations [18].

A. Qualitative Research

Qualitative research is a major branch of analyzing respondent patterns toward significant findings and successful implementation. Qualitative research involves the collection and analysis of written or spoken word and textual data. It can also focus on body language or visuals to help create a detailed description of the researchers' observations. In this study collects the qualitative data first and the result from the qualitative data analysis uses questionnaires for the quantitative data collection. Qualitative data obtained from interviews typically are unstructured textual materials and not straightforward to analyze [19]. The researcher used convenience sampling to determine the sample for qualitative research. Convenience sampling is a type of non-probability sampling where the sample is taken by the people who are easy to reach. The qualitative approach collected data through 9 semi-structured interviews with 8 representing persons from all position levels in the Ministry of Foreign Affairs to analyze the factors of motivation. Semi-structured interviews are often open-ended, allowing for flexibility. Asking set questions in a set order allows for easy comparison between respondents, but it can be limiting. Having less structure can help you see patterns,

while still allowing for comparisons between respondents [20].

B. Quantitative Research

In this study, quantitative analysis is used as the main method. The quantitative research allows for testing the relationship between factors and employee motivation in the Ministry of Foreign Affairs in Myanmar. Using the self-administered questionnaire will fulfill the purpose because it has many advantages such as being inexpensive and rapid to administer. Moreover, the method is convenient for respondents and has no interviewer's impact on subjects or interviewer variability [21]. A questionnaire is used as an instrument to collect quantitative data. The questionnaire intends to measure the factor of employee motivation in the Ministry of Foreign Affairs in Myanmar. The composition of motivation factors will be measured with a 5-point Likert scale (1= Strongly disagree to 5= Strongly agree). The sampling frame for the quantitative study consisted of 811 employees from 7 departments of the Ministry of Foreign Affairs. The stratified random sampling technique was used in the selection of sample elements from the sampling frame.

The required sample size is calculated using the formula of Yamane (1967) as follows [22].

$$n = 811 / (1 + 811(0.05)^2)$$

n = sample size required

N = number of people in the population = 811

e = allowable error (%) = 0.05 (5%)

$n = 267.87$

IV. ANALYSIS

A. Qualitative analysis

The focus is on analyzing the findings of the 9-semi structured question as it was used to support the two main theoretical frameworks of the study which are Maslow's Hierarchy of Needs and Herzberg's Two-Factor Theory [23].

Following Maslow's theory, Employees respond to the same types of needs, and it goes from the basic things they need for survival to a sense of fulfilling their potential and finding their purpose in life. This is a fundamental need at the bottom of the pyramid model. The key points from employees' responses are mental and physical, security, social, esteem, and self-actualization needs.

Following Herzberg's theory, employees respond to the needs of hygiene factors such as interpersonal relations, policies, salary, working conditions, psychological conditions, emotional intelligence, and job security. Hygiene factors are essential for helping individuals achieve motivation at work, but no matter how strong these factors are, they will never lead an employee to become highly motivated at work. According to Maslow's theory, these factors are basic factors motivating employees to move to higher levels of needs

only when the previous lower levels are successfully achieved, or at least, to be motivated.

The employees also respond to the needs of motivator factors such as recognition, achievement, responsibility, and training. According to Herzberg's theory, motivating factors will not help motivation when hygiene factors are not present. But, once hygiene has been established, the motivating factors are essential for creating highly motivated employees.

B. Quantitative analysis

To test the hypothesis was conducted by using regression analysis. The reliability of each construct was assessed by using Cronbach's Alpha.

TABLE I Findings of Reliability Analysis motivation factors influence employee motivation

| No | Variables | Number of items | Cronbach's Alpha |
|----|-----------------------|-----------------|------------------|
| 1 | Independent Variables | 27 | 0.92 |
| 2 | Moderating Variables | 17 | 0.93 |
| 3 | Dependent Variables | 5 | 0.76 |
| | All items | 49 | 0.93 |

It can be observed that Cronbach's alpha values of motivation factors that influence on employees' motivation are 0.92, 0.93, and 0.76 indicating that these items are highly internal consistency. Also, it is reliable to analyze the motivation factors on employees' motivation in MOFA.

TABLE II Correlation of Motivation Factors and Employees' Motivation

| | Independent Variables | Moderating Variables | Dependent Variables |
|-----------------------|-----------------------|----------------------|---------------------|
| Independent Variables | 1 | | |
| Moderating Variables | .828** | 1 | |
| Dependent Variables | .444** | .430** | 1 |

The table shows that there exists a correlation between the independent variable factors and employees' motivation. This research is also aimed to examine the impact of moderating variables between independent variables and dependent variables. It is purposed to assess the interaction effect of moderating variables.

TABLE III Multiple Regression Model Summaries

| Model | R | R Square | Adjusted R Square | Std. Error of the Estimate |
|-------|-------------------|----------|-------------------|----------------------------|
| 1 | .730 ^a | .532 | .520 | .26995 |

The R-value represents the correlation between the dependent and independent variables. The R-value must be greater than 0.4 for further analysis. As a result, the value is 0.730 which is greater than 0.4. So, it indicates a good level of prediction.

R-square shows the total variation for the dependent variable that could be explained by the independent variables. The R-square value should be greater than 0.5

shows that effective enough to determine the relationship. In this result, the R-square is at 0.532 or 53.2% so is effective enough to determine the relation.

TABLE IV Regression Analysis Test for Organization Factors Influence on Employees' Motivation

| Model | Unstandardized Coefficients | | Standardized Coefficients | t | Sig. |
|----------------------------|-----------------------------|------------|---------------------------|-------|-------|
| | B | Std. Error | Beta | | |
| (Constant) | 3.28 | .183 | | 17.99 | <.001 |
| Policies | .23 | .041 | .473 | 5.76 | <.001 |
| Salary | -.04 | .028 | -.102 | -1.73 | .085 |
| Working Conditions | .12 | .062 | .143 | 1.99 | .048 |
| Psychological | .03 | .030 | .052 | 1.05 | .293 |
| Emotional Intelligence | -.51 | .063 | -.660 | -8.17 | <.001 |
| Job Security | .55 | .043 | .826 | 12.91 | <.001 |
| Interpersonal Relationship | -.11 | .046 | -.161 | -2.47 | .014 |

TABLE V Regression Analysis of Moderating Variable Moderates Relationship between Independent Variable and Dependent Variable

| Model | Unstandardized Coefficients | | Standardized Coefficients | t | Sig. |
|----------------------|-----------------------------|------------|---------------------------|-------|-------|
| | B | Std. Error | Beta | | |
| (Constant) | 8.01 | .733 | | 10.94 | <.001 |
| Independent | -1.20 | .214 | -1.479 | -5.60 | <.001 |
| Moderating Variables | -1.28 | .210 | -1.844 | -6.11 | <.001 |
| Integration | .39 | .055 | 3.652 | 7.09 | <.001 |

The moderating variable significantly predicted the relationship between the independent variable and dependent variable $p < 0.001$ which indicates that modified between organizational factors and employees' motivation.

V. RESULTS AND FINDINGS

A. Qualitative Findings

According to the interview results, most of the employees feel motivated when they have a good relationship with colleagues and supervisors, opportunities for career development, good working conditions, good organization policies, equal opportunity and serving at abroad as diplomats. And, employees also want to know feedback on their work. During the interview, the employees who serve in Naypyitaw responded they want to work near their family and they feel homesick. The factors demotivating employees are no recognition, working with bad supervisors, no equal opportunity, without job training and no teamwork.

B. Quantitative Findings

The result from the qualitative data analysis uses questionnaires for the quantitative data collection. In this study quantitative analysis is used as the main method. There are 268 questionnaires distributed in the ministry. And, there were 267 questionnaires were returned.

TABLE VI Descriptive Rating

| Organization factor | Descriptive rating |
|--------------------------------|--------------------|
| Organization policies | Uncertain |
| Salary, Compensation and Bonus | Uncertain |
| Working Conditions | Agree |
| Psychological conditions | Uncertain |
| Emotional Intelligence | Agree |
| Job Security | Agree |
| Interpersonal Relationship | Agree |
| Employee motivation | Strongly Agree |

According to the descriptive rating, working conditions, emotional intelligence, job security, and interpersonal relationship factors are that the employees agree on the factors. The employees are uncertain about organization policies, salary, compensation bonuses, and psychological conditions factors.

After questionnaires about the factors that influence employee motivation, the survey moved to examine how employee motivation is effective in their job, organization, and daily. Respondents strongly agree that motivation is important for organizational success and improvement in daily life. As for the civil servant, motivation can deliver better service to the public.

Testing of the hypothesis found that organizational factor significantly influences employee motivation. And, the researcher also tested each factor of independent variable relationship between the employees' motivation. It can be known, which factors are significant and which are not significant in detail tested by regression analysis.

The result of hypothesis testing followed by table IV is as follows-

H1: There is a significant relationship between organization policies on employees' motivation because there was $p < 0.001$ which is less than 0.05.

H2: There is no significant relationship between salary, compensation, and bonus on employees' motivation because there was $p = 0.085$ which is greater than 0.05

H3: There is a significant relationship between working conditions on employees' motivation because there was $p = 0.048$ which is less than 0.05.

H4: There is no significant relationship between psychological conditions on employees' motivation because there was $p = 0.293$ which is greater than 0.05.

H5: There is a significant relationship between emotional intelligence on employees' motivation because there was $p < 0.001$ which is less than 0.05.

H6: There is a significant relationship between job securities on employees' motivation because there was $p < 0.001$ which is less than 0.05.

H7: There is a significant relationship between interpersonal relationships on employees' motivation because there was $p = 0.014$ which is less than 0.05.

H8: Organization policies, salary compensation, and bonuses, working conditions, psychological conditions, emotional intelligence, job security, and interpersonal relationships statistically significantly predict employees' motivation there was $p < 0.001$ which is less than 0.05.

The result of the testing hypothesis supported the role of moderating variables that can modify the relationship between organizational factors and employees' motivation. According to the findings, the employees' motivation is supported by the moderating variable i.e. recognition, achievement, responsibility, and training.

VI. CONCLUSION

According to the interview results, most of the employees feel motivated when they have a good relationship with colleagues and supervisors, opportunities for career development, good working conditions, good organization policies, equal opportunity, and serving abroad as diplomats. And, employees also want to know feedback on their work. During the interview, the employees who serve in Naypyitaw responded they want to work near their families and they feel homesick. The factors demotivating employees are no recognition, working with bad supervisors, no equal opportunity, job training, and no teamwork.

The questionnaires for the quantitative were conducted to the results of the interview qualitative data. In this paper, the quantitative data was used random sampling method and focused on 267 employees of the Ministry of Foreign Affairs and collected survey questionnaires. Testing of the hypothesis found that organizational factor significantly influences employee motivation. And, the researcher also tested each factor of the independent variable relationship between the employees' motivation.

VII. RECOMMENDATION

Organizations must practice the policy and also need to provide good administration to all employees. It would especially like to recommend practicing equal gender equality and equal opportunity. Organizations need to determine the right individuals to select for public sector jobs and motivate them to perform well. It is suggested that creating a good working environment for employees can impact employees' motivation. It is needed to allow employees to openly discuss the job problem. The employees working at Naypyitaw replied inconvenient for them because of being away from family. So, organizations should practice rotating the place for them and giving them leave as the organization's policy.

Furthermore, working under pressure is demotivating and lacks enthusiasm. Thus, it is recommended for organizations to implement job rotation in order to keep the employees' interest and satisfaction with

work. Support for employee well-being can contribute to a sense of job security. Discuss the prospect of contract work with employees. This gives employees some hope of continued employment. Create opportunities for teams to bond each employee shares one thing about a team member they appreciate so that employees don't feel alone and are able to connect with their colleagues.

It suggests that the motivation of employees can be achieved through the empowerment of employees. It indicates that the employees would like to be involved in the freedom to use their own judgment and the existence of a mutual connection between the employees and the organization. Therefore, engaging in meetings and discussions and letting them know that their ideas and contributions are listened to and appreciated, gives them space and opportunities for their idea. Sufficient training programs and feedback systems are necessary to be included not only to provide employees with adequate knowledge and skills to do the work but also to improve working environments, techniques, quality, and career development. Prefer recognition of well-done work and opportunities to grow and become promoted are effective for motivation. Practicing fair organization is one of the factors that support motivation.

Finally, the motivation of employees can be influenced by many factors. Employees' motivation is important in the government sector. An organization with motivated employees contributes to success and development. In the government sector, motivated civil service personnel can deliver better service to the public.

VIII. FUTURE RESEARCH RECOMMENDATION

This study employed a mixed-method approach to study the motivation of government employees in MOFA. The impact of employee motivation from the factors explored in this study offers much room for further research, particularly in the public sector. This thesis included employee data only from the Head office and Yangon branch of MOFA. The study also looked at the data from head office and Yangon branch surveys. Future studies should be conducted on the employees from other ministries. Results can then be compared with this study, which enhances the knowledge and understanding of the public sector of employees' motivation.

REFERENCES

- [1] MacLeod, D. and Clarke, N. (2010). Leadership and employee engagement: passing fad or a new way of doing business? *International journal of leadership in public services*, 26-30.
- [2] Macey, W. H., & Schneider, B. (2008). The meaning of employee engagement. *Industrial and organizational Psychology*, 1(1), 3-30.
- [3] Thiha. (2017). Myanmar Labour issues from perspective of enterprise. Retrieved from International Labour Organization: <https://consult-myanmar.com/tag/myanmar-labour-issues-from-the-perspective-of-enterprises/>
- [4] T. (2013). *Job Performance: Mediate Mechanism of Work*.
- [5] Owusu, T. (2012). Effects of motivation on employee performance.
- [6] UN. (2022, September 1). United Nations Department of Economic and Social Affairs. Retrieved from <https://www.un.org/development/desa/dpad/publication/world-economic-situation-and-prospects-september-2022-briefing-no-164/#:~:text=The%20g>
- [7] Agency, J. I. (2017). Data Collection Survey on Civil Service System in Myanmar. *International Development Center of Japan*.
- [8] Bank, W. (2021). COVID-19 to Add as Many as 150 Million Extreme Poor by 2021. World Bank Group.
- [9] Souders, B. (2019, November 5). 20 Most Popular Theories of Motivation in Psychology. Retrieved from [positivepsychology.com: https://positivepsychology.com/motivation-theories-psychology/](https://positivepsychology.com/motivation-theories-psychology/)
- [10] Yukl, G. (2013). *Leadership in Organizations*. New York: Pearson .
- [11] Herrity, J. (2023, May 30). Indeed. Retrieved from The Importance of Job Security in the Workplace (With Tips): <https://www.indeed.com/career-advice/career-development/job-security>
- [12] Prachi. (2018). Effective Communication. Course Hero.
- [13] Hastwell, C. (2021, September 9). Creating a Culture of Recognition. Retrieved from Great Place to Work: <https://www.greatplacetowork.com/resources/blog/creating-a-culture-of-recognition>
- [14] Metz, J. D. (2018). The impact of achievement motivation, job satisfaction and work-life balance among retail manager. Pepperdine.
- [15] Satyendra. (2018, December 26). Ispatguru. Retrieved from [www.ispatguru.com: https://www.ispatguru.com/employees-and-organizational-responsibility/#:~:text=They%20are%20responsible%20for%20thinking,processes%2C%20and%20their%20own%20skills](https://www.ispatguru.com/employees-and-organizational-responsibility/#:~:text=They%20are%20responsible%20for%20thinking,processes%2C%20and%20their%20own%20skills)
- [16] Ozjeser, B. (2019). Impact of Training on Employee Motivation in Human Resources Management. *Procedia*.
- [17] Jay, S. (2022). Organizational Commitment: 7 Ways HR Can Contribute. Academy to innovate HR.
- [18] John W. Creswell and J. David Creswell. (2018). Research design: qualitative, quantitative, and mixed methods approaches. Lao Angeles: SAGE
- [19] Bryman. (2016). Social research method. Oxford University Press.
- [20] George, T. (2022, January 27). Scribbr. Retrieved from <https://www.scribbr.com/>
- [21] Bryman. (2016). Social research method. Oxford University Press.
- [22] Yamane. (1967). *Uniprojectmaterial*. Retrieved from How to calculate a reliable sample size using Trao Yamane method.: <https://uniprojectmaterials.com/view-blog/how-to-calculate-a-reliable-sample-size-using-taro-yamane-method>
- [23] Gawel, J. (1997). Herzberg's Theory of Motivation and Maslow's Hierarchy of Needs. *ERIC Digests*.

Augmented Imagination: Exploring Generative AI from the Perspectives of Young Learners

Tat Putjorn
Samakki Witthayakhom School
Chiang Rai, Thailand
stu43571@samakki.ac.th

Pruet Putjorn
Center of Excellence in AI and
Emerging Technologies,
School of Information Technology,
Mae Fah Luang University.
pruet@mfu.ac.th

Abstract— *Acquiring AI literacy is crucial for empowering individuals to engage intelligently and responsibly with generative AI, a technology that is increasingly pervasive in creative domains and daily life. This innovative tool can create images and content based on natural language descriptions, unlocking a world of creative possibilities. Recognizing the significance of young learners' interaction with generative AI in today's tech-driven world, this study explores how it shapes their creativity, problem-solving, and critical thinking skills. The study involved a user workshop with 15 high school students from Northern Thailand, utilizing both quantitative and qualitative analyses to assess their experience with generative AI in creating creative content. The workshop was conducted online, providing young learners with basic knowledge of AI and generative AI. Participants were introduced to three free-to-use applications - Canva for graphic design, ChatGPT as an AI chatbot, and Leonardo.AI for generating production-quality assets for creative projects. The findings from the workshop highlighted positive perceptions and high usability among young learners interacting with generative AI. The insights gained from the study emphasized five key aspects, namely providing inspiration and encouraging creative thinking, enabling iteration and experimentation, promoting accessibility, fostering collaboration, and facilitating skill development. Understanding generative AI and its responsible use is becoming increasingly important in today's world. By embracing generative AI, young learners can explore new avenues of art creation, content generation, and idea expression, thus fostering digital literacy and equipping them with essential skills to navigate an AI-driven future. This research contributes valuable insights into the significance of generative AI literacy among young learners, emphasizing the need to integrate AI education into curricula to prepare students for an AI-dominated world.*

Keywords—Generative AI, AI literacy, HCI, Child AI Interaction

I. INTRODUCTION

The rapid advancements in computing power, abundant data availability, and enhanced machine learning algorithms have driven significant progress in Artificial Intelligence (AI) [1]. As AI technologies become increasingly integrated into our daily lives, including virtual assistants and real-time search systems, there is a growing interest in educating the public about AI [2]. Recognizing the concerns and misconceptions surrounding AI, it is crucial to incorporate AI education into educational curricula [3,4]. This approach will provide individuals with a holistic understanding of AI's

capabilities, limitations, and societal implications, enabling them to navigate the AI-driven world responsibly, make informed decisions, and actively contribute to the future development and utilization of AI [5].

The recent rise of generative AI tools, like Dall.E, Stable Diffusion, and ChatGPT, has opened up new possibilities for individuals to create imaginative stories, images, videos, and animations. These AI systems, such as Stable Diffusion, Dall.E 2, and Midjourney, allow people to utilize the power of AI in their creative endeavors [6]. In the creative sector, the adoption of AI has been hindered by concerns about replicating human creativity and technological limitations. However, a recent survey by Adobe reveals that artists are increasingly open to using AI as assistants, particularly for tasks like image search and editing [7]. According to an Adobe survey across 14 countries, consumers believe generative AI will enhance personal creativity (57%), improve customer experiences (72%), and expect responsible usage. Marketing professionals see it as a tool to boost efficiency, personalize experiences, and generate content faster. The findings highlight a promising future for generative AI, emphasizing the importance of brands utilizing it responsibly to meet customer expectations [8]. This acceptance highlights the growing recognition of AI as a tool that supports and augments human creativity in specific domains rather than replacing it entirely.

The future creative economy will require youth to have a variety of skills and knowledge that can help them adapt to the changing digital landscape. To achieve this, youth need to constantly learn about the latest digital innovations and how they can use them effectively. This involves acquiring both hard skills and soft skills that are relevant for the digital age [3]. Hard skills are the technical skills that enable youth to interact with digital technologies, such as digital literacy and AI literacy. Digital literacy is the ability to access, evaluate, create, and communicate information using digital devices and platforms. AI literacy is the ability to understand, use, and critically evaluate artificial intelligence applications and systems. Soft skills are the interpersonal and cognitive skills that enable youth to collaborate, communicate, think critically, and solve problems in complex and uncertain situations [3,6,9].

The objective of this study is to investigate how young learners utilize and perceive generative AI, as well as to determine the ways in which generative AI can facilitate their exploration of creativity.

These are the research questions that will be addressed.

- How do young learners use and think about generative AI?
- How can generative AI help learners explore their creativity?

II. LITERATURE REVIEW

A. An overview of AI and Generative AI

Artificial Intelligence (AI) uses various data sources to make decisions, recognize patterns, and learn statistics. It was first introduced by John McCarthy in 1956 and has since become a major force in many mainstream technologies [10]. AI has been successful in speech recognition, medical diagnosis, autonomous vehicles, and voice-activated assistants like Alexa, Siri, and Google Assistant. Additionally, AI has been invaluable in industrial process monitoring, fault detection, forecasting, and improving healthcare treatments [11]. AI has shown its ability to analyze human behavior and social interactions at advanced levels by closely observing conversations and actions. It has also been effectively applied to address socially significant issues such as homelessness and has shown promise in predicting natural events. Governments worldwide have recognized the potential of AI as a crucial catalyst for driving economic growth and fostering social progress. The transformative impact of AI on various sectors underscores its importance as a powerful tool for shaping a better future [12].

Generative AI is a subset of AI that creates new content based on learned patterns from its training data. It employs machine learning algorithms, such as Generative Adversarial Networks (GANs) and Variational Autoencoders (VAEs), to generate original and realistic content, such as images, text, and music, resembling examples it was trained on [13]. Diffusion models are a type of generative AI that use Gaussian noise to train a neural network to recover the original data. This results in the synthesis of high-quality images and surpasses GANs in terms of image fidelity. DALL-E 2 and Midjourney are platforms that predominantly use text-to-image generation as the main means of user interaction with diffusion models [14,15]. Unlike traditional AI, which is designed for specific tasks, generative AI is capable of producing novel and creative outputs. [16]. Ongoing research is being conducted to find solutions for these challenges and promote responsible development.

B. Image Generative AI Platforms

Leonardo.AI [17] offers a superior AI image generation experience with its user-friendly interface, diverse range of features, and cost-effective free forever option. Accessible through its own web app, Leonardo.AI eliminates the need for third-party platforms like Discord, making it easily accessible to users. The platform's intuitive design allows for quick customization of 3D creations, transforming them into stunning visuals effortlessly. With features like AI Canvas, Texture Generation, and the ability to upload custom images for personalized models, Leonardo.AI empowers users to

unleash their creativity. Its faster image generation, additional tools like background removal, and prompt generation further enhance its appeal, making Leonardo.AI a top choice for professionals and enthusiasts alike.

In the comparison between MidJourney [18] and Leonardo.AI, both AI-driven tools excel in generating stunning images for digital art and design. MidJourney is known for its colorful and intricate designs, while Leonardo.AI stands out with its sleek and modern aesthetic. Both platforms offer similar features for businesses, but Leonardo.AI gains an edge with its automatic email replies and comprehensive analytics. Additionally, Leonardo.AI provides a free forever option, making it more accessible than MidJourney, which has discontinued its free plan [19,20,21]. Furthermore, Leonardo.AI's user-friendly design and a comprehensive range of features, including AI Canvas and Texture Generation, set it apart from MidJourney [22]. As a result, Leonardo.AI emerges as the preferred choice, offering superior value, accessibility, and overall user experience for AI image generation.

C. AI Literacy

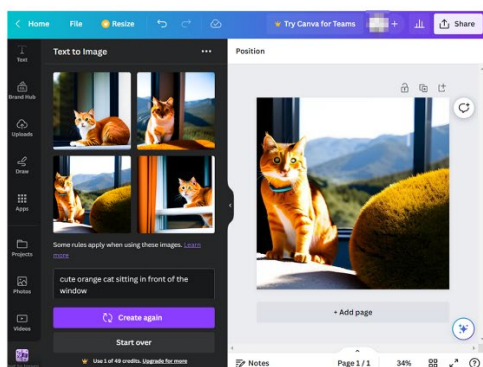
AI literacy for youth is a crucial skill that can help them thrive in the digital age. AI is becoming more ubiquitous and impactful in various domains of life, such as education, health, entertainment, and social media. Therefore, young people need to be able to understand, use, and critically evaluate artificial intelligence applications and systems [6,9]. Acquiring AI literacy entails understanding both the technical and ethical dimensions of AI. It involves comprehending how AI operates, recognizing its limitations, and understanding its potential benefits and risks. Moreover, AI literacy equips individuals with the knowledge to make informed and ethical decisions when using or creating AI. It fosters creativity and innovation by harnessing AI as a valuable tool [6]. Additionally, AI literacy empowers youth to actively engage in democratic processes and discussions concerning AI's impact on society. Through AI literacy, young individuals can enhance their personal growth and contribute meaningfully to the progress of society as a whole [23].

AI literacy is the ability to comprehend and interact with AI. It has three main elements that help individuals learn about AI. The first element is to know the basics of AI, such as what it is, how it works, and what techniques it uses. The second element is to be aware of how AI affects our daily lives and society. The third element is to go beyond just using AI tools in education and to have a wider perspective on AI's consequences [3]. AI literacy enables individuals to develop the skills to critically assess AI technology, communicate effectively with AI systems, and recognize AI applications. This knowledge prepares individuals to cope with the AI-driven world and make informed choices about AI's benefits and challenges [3,23].

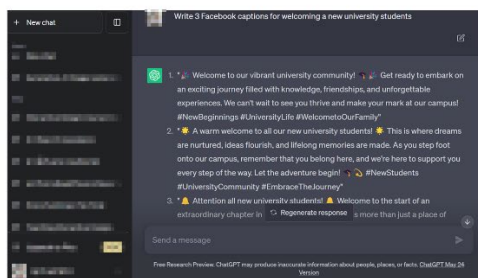
III. METHODS

To collect feedback from young learners using generative AI, the generative AI workshop was conducted online via the

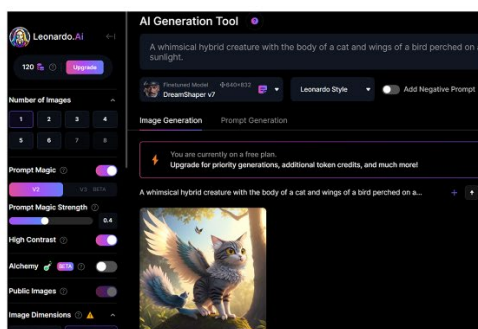
Zoom Meeting application and lasted for three hours. The workshop aimed to provide basic knowledge of AI and generative AI. Generative AI can synthesize new data such as images, text, or music. The workshop covered applications that can be used for generating artwork, designing new products, and creating virtual characters. The workshop introduced three free-to-use applications including Canva, ChatGPT, and Leonardo.AI (Fig.1). Canva is a free graphic design tool that lets you create visual materials like flyers, posters, presentations, and videos using templates, images, and a drag-and-drop interface. ChatGPT is an AI chatbot that uses machine learning algorithms to analyze and understand written or spoken language and then generate responses based on that input. Leonardo.AI is a platform based on the Stable Diffusion Model that allows users to generate production quality assets for their creative projects with AI-generated speed and style-consistency. Users can create visual assets like items, environments, helmets, buildings, and concept art using pre-trained AI models or train their own.



a



b



c

After the workshop, a quantitative survey was conducted using a questionnaire distributed through a Google Form to collect data from the participants. The survey was conducted using an online questionnaire, which included a combination of questions with predefined answer choices as well as questions that allowed respondents to provide open-ended responses. Before participating in the survey, respondents were provided with an informed consent form that outlined the purpose and procedures of the survey. The survey consisted of demographic questions along with five research-related inquiries specifically aimed at gathering reflections on the utilization of generative AI. Additionally, qualitative study was conducted with a focus group online session to gather their reflections and perceptions regarding the use of AI generative applications. The purpose of this session was to obtain valuable insights into how users perceive and interact with these applications.

IV. RESULTS AND DISCUSSION

A. Exploring Young Learners' Perceptions and Skills in Using Generative AI

Fifteen young participants, consisting of 13 boys (86.7%) and 2 girls (13.3%) aged 16 to 18 years, voluntarily enrolled in our workshops and completed the questionnaire. These students attended various schools in Chiang Rai province. The quantitative analysis revealed that most learners had a high level of computer experience, with an average score of 3.60 (SD = .83). Notably, their knowledge and skills significantly improved after participating in the workshop ($t(14) = 4.836, p < .001$), as reflected in a post-workshop mean of 4.27 (SD = .59), compared to the pre-workshop mean of 2.87 (SD = 1.30).

In terms of perception, the young learners displayed a positive outlook towards generative AI. They believed that AI had the capability to generate creative content and images while assisting creators ($M = 4.53, SD = .64$). Furthermore, they acknowledged the importance of AI literacy and possessing knowledge about generative AI ($M = 4.60, SD = .63$). However, concerns regarding potential negative impacts of AI were also evident, particularly in relation to job displacement for creators ($M = 3.53, SD = 1.302$) and potential harm to humans in the future ($M = 3.27, SD = 1.28$).

The learners' usability of the web-based generative AI platform (Leonardo.AI) for image creation using prompts was evaluated based on five components of usability. The survey findings revealed that learners expressed a high level of satisfaction with the platform ($M = 3.53, SD = 1.302$) and demonstrated the ability to successfully complete basic tasks during their initial use ($M = 4.07, SD = .799$). Additionally, they exhibited proficiency in reestablishing their skills upon returning to the platform after a period of non-use ($M = 4.20, SD = .775$), and they quickly learned how to perform tasks ($M = 4.07, SD = .799$). However, some learners encountered errors while using the platform or experienced difficulty in recovering from those errors ($M = 3.00, SD = 1.414$).

Fig. 1. Interface of AI generative platforms: Canva (a) ChatGPT (b) and Leonardo.AI (c)

B. Reflections on the use of generative AI: How can generative AI help learners explore their creativity?

To explore how learners engage with generative AI platforms, an interview and card sorting session were conducted. The card sorting technique [24,25,26], commonly used in user experience design, helped categorize and gather information from the interviews. This approach allowed for a comprehensive overview of reflections specifically related to the use of generative AI platforms in generating creative content and images. The five findings from this study (Fig.2) will provide valuable insights to deepen our understanding of the subject and contribute to its overall comprehension.

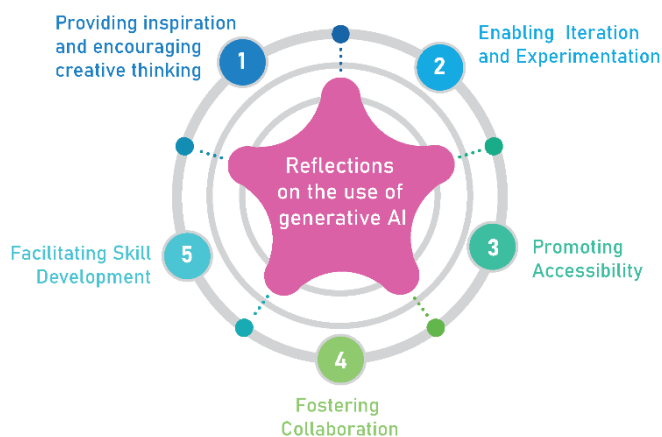


Fig. 2. Five reflections on the use of generative AI

1) Providing inspiration and encouraging creative thinking.

Generative AI tools can help learners generate fresh ideas and ignite creativity across various domains. By establishing connections between different ideas and producing entirely new concepts, these tools can help learners input diverse inputs or prompts, and the AI algorithms will use sophisticated techniques to explore the possibilities and generate novel outputs. These outputs can encompass a wide range of creative outputs, such as images, text, or even business ideas. The process of connecting different ideas is a fundamental aspect of generative AI. By combining unrelated concepts, the AI algorithms can discover associations and resemblances that humans may not have initially considered. Participant 2 stated *"This AI-generated image is like nothing I've seen before! It's out of this world...Even though I'm not an artist, I can create stunning images and make my own artworks with this AI tool. It's like having a whole new world of creativity at my fingertips!"* This capability allows for the exploration of uncharted territories, enabling learners to break free from conventional thinking patterns and embrace innovative approaches. Moreover, generative AI tools offer a fresh perspective by presenting learners with outputs that are often unexpected or unconventional. These outputs can challenge preconceived notions and provide alternative viewpoints, inspiring individuals to think outside the box and approach problems from different angles. Participant 5 expressed *"I was given some key words to mix up a bird and a cat, and what I ended up seeing was this totally new creature I never even dreamed of! It was way beyond anything I could've imagined, and it just got me all excited*

and creative. Like, who would've thought generative AI could do something like that, right?" This potential expands creative possibilities, providing learners with new sources of inspiration.

2) Enabling Iteration and Experimentation

Learners can quickly and easily explore a variety of options and styles. These tools provide the ability to generate multiple variations of outputs based on different inputs or prompts. This rapid exploration allows learners to experiment with different creative choices, such as colors, shapes, or compositions, and observe how they impact the final result. Participant 10 said *"You won't believe what this AI tool can do for my iPhone case designs! It's like magic – I can regenerate different styles and patterns for my mockups in no time...I can now create endless possibilities for my iPhone case designs effortlessly!"* By offering a wide range of possibilities, generative AI tools empower users to iterate and refine their creative work. Learners can try out different styles, explore various combinations, and make adjustments until they achieve the desired outcome. This flexibility and ease of experimentation enable artists and creators to push the boundaries of their work, discover new artistic directions, and refine their artistic vision.

3) Promoting Accessibility

Generative AI involves developing user-friendly tools that cater to learners with diverse backgrounds. Participant 12 said *"I'm not a gamer or a computer geek at all, and I had zero knowledge about AI. But guess what? These AI tools were so user-friendly that I got the hang of it in no time! The interface was a breeze to navigate, and I quickly learned how to create my first image just by using some simple keywords. It was like magic!"* These tools are designed to be intuitive and require minimal technical expertise, making them accessible to a wide range of users. By prioritizing accessibility, generative AI provides an inclusive platform for artists who may not have access to traditional art supplies or resources. Generative AI tools offer a welcoming space for individuals to explore their creativity, regardless of their artistic background. With simplified interfaces and intuitive controls, these tools ensure that learners can easily navigate and utilize the full potential of generative AI technology. By making art creation more accessible, generative AI empowers artists to unleash their imagination and express their ideas. It eliminates barriers that may hinder learners' expression, fostering a more inclusive arts community. Participant 7 also shared *"I'm hooked. I can't wait to keep generating these amazing images every single day. AI has opened up a whole new world of creativity for me."* The accessibility of generative AI democratizes creativity by offering opportunities to learners from various socio-economic backgrounds. Young learners who lack access to expensive art supplies or specialized training can now explore their artistic potential through generative AI tools, expanding their artistic horizons. Participant 5 implied *"You know, AI has been a game-changer for me. Even though my family couldn't afford art supplies due to our humble background, I can now express my creativity for free! It feels like a dream come true!"*

4) Fostering Collaboration

Generative AI tools encourage young learners to collaborate with AI systems to enhance their creativity. By providing a platform for collaboration and experimentation, generative AI tools can help young learners develop their creative skills and explore new ideas. Collaborating with AI systems can benefit young learners by giving them opportunities to deepen their understanding of the creative process. Participant 11 stated *"After diving into AI and understanding how prompts work, I feel like I've got a better grasp of how it all comes together. It's fascinating how it can give me answers or spark new ideas"*. They can learn how to effectively work with AI tools to achieve their artistic goals, leveraging the capabilities of AI systems to enhance their creative outputs. Through collaboration, young learners can also acquire new skills and techniques. Participant 3 also stated *"I'm discovering so many things about shaping the answers or getting specific creative images from the AI system. It's not always easy to get exactly what you want, but I'm learning to prompt it more effectively and concisely. It's a learning process, but it's exciting!"*. Working alongside AI systems allows them to explore different approaches, experiment with various parameters, and learn from the outputs generated by the AI.

5) Facilitating Skill Development

Generative AI serves as a supportive tool for skill development in multiple areas. When using AI models, learners can improve their language proficiency through the prompts and conversations. By actively engaging with the AI, they can expand their vocabulary, strengthen their understanding of sentence structures, and develop their ability to articulate ideas effectively. Additionally, by observing and analyzing the outputs generated by generative AI, learners can gain valuable insights into artistic techniques, styles, and approaches. Participant 6 revealed *"Since I started using AI, my English has improved so much! I've learned a bunch of new vocabulary that helps me create better prompts to get the right answers and amazing image outputs. It's like a double win - improving my language skills and unleashing my creativity with AI!"*. This exposure to AI-generated artwork or content can broaden their artistic horizons, inspire new ideas, and assist in refining their own artistic abilities. Overall, generative AI offers a dual opportunity for skill development - enhancing language skills through interaction with AI models and refining artistic abilities by learning from AI-generated outputs. This combination of language and artistic development creates a rich learning experience for young learners, enabling them to grow and excel in both areas.

All five key findings that offer valuable insights into how generative AI platforms can assist learners in exploring their creativity and developing essential skills are presented in Table 1.

TABLE I: KEY INSIGHTS INTO THE IMPACT OF GENERATIVE AI ON LEARNERS

| Key Findings | Description |
|----------------------------------|---|
| 1) Inspiration and Creativity | Generative AI sparks creativity by connecting diverse ideas and producing novel outputs, encouraging innovative thinking. |
| 2) Iteration and Experimentation | Learners can quickly explore various creative options, empowering them to experiment, refine, and push the boundaries of their work. |
| 3) Accessibility | Generative AI tools are user-friendly and inclusive, democratizing creativity for individuals from diverse backgrounds. |
| 4) Collaboration | Collaboration with AI systems enhances learners' creative understanding and skills, enabling effective interaction with AI. |
| 5) Skill Development | Generative AI supports language proficiency and exposes learners to artistic techniques, fostering growth in language and art skills. |

V. CONCLUSION AND FUTURE STUDY

The study emphasizes the significance of AI literacy in empowering individuals to engage intelligently with generative AI. As this technology becomes increasingly pervasive in creative domains and daily life, it unlocks a world of creative possibilities, generating content based on natural language descriptions. The research focuses on young learners' interaction with generative AI and its impact on creativity, problem-solving, and critical thinking. Findings from the workshop with high school students in Northern Thailand reveal positive perceptions and high usability of generative AI. The study highlights five key aspects: inspiring creative thinking, enabling iteration, promoting accessibility, fostering collaboration, and facilitating skill development. Young learners can expand their horizons in art creation, content generation, and idea expression by embracing generative AI, fostering digital literacy, and equipping them with essential skills to navigate an AI-driven future. This research offers valuable insights into the importance of generative AI literacy among young learners, underlining the need to integrate AI education into curricula.

Future research study could explore the long-term impact of generative AI literacy on students' artistic development. A longitudinal study could track participants' creative progress over time, while a comparative study might assess differences between traditional and AI-augmented artistic outcomes. Investigating the ethical implications of AI usage and developing responsible AI guidelines could enhance AI-focused curricula. Additionally, understanding educators' role in facilitating generative AI education and exploring AI's potential in other creative disciplines could further enrich the field. These studies aim to equip students with essential skills for thriving in an AI-driven society and contribute to evidence-based strategies for fostering creativity and innovation.

ACKNOWLEDGMENT

We are extremely grateful to the pupils of Samakkhi Witthayakhom School in the province of Chiang Rai for their invaluable contribution to our research. In addition, we would like to thank the Center of Excellence in AI and Emerging Technologies and the dedicated research team at Mae Fah Luang University in Chiang Rai, Thailand for their unwavering support.

REFERENCES

- [1] Lim, W. M., Gunasekara, A., Pallant, J. L., Pallant, J. I., & Pechenkina, E. (2023). Generative AI and the future of education: Ragnarök or reformation? A paradoxical perspective from management educators. *The International Journal of Management Education*, 21(2), 100790.
- [2] Giannini, S. (2023). Reflections on generative AI and the future of education. UNESCO. <https://unesdoc.unesco.org/ark:/48223/pf0000385877>
- [3] Casal-Otero, L., Catala, A., Fernández-Morante, C., Taboada, M., Cebreiro, B., & Barro, S. (2023). AI literacy in K-12: a systematic literature review. *International Journal of STEM Education*, 10(1), 29.
- [4] Seo, K., Tang, J., Roll, I., Fels, S., & Yoon, D. (2021). The impact of artificial intelligence on learner–instructor interaction in online learning. *International journal of educational technology in higher education*, 18(1), 1-23.
- [5] Chan, C. K. Y., & Hu, W. (2023). Students' Voices on Generative AI: Perceptions, Benefits, and Challenges in Higher Education. *arXiv preprint arXiv:2305.00290*.
- [6] Han, A. (2023, June). AI virtuous circle: preparing youth for the future of creative economy. In *Proceedings of the 22nd Annual ACM Interaction Design and Children Conference* (pp. 748-751).
- [7] Anantrasrichai, N., & Bull, D. (2022). Artificial intelligence in the creative industries: a review. *Artificial Intelligence Review*, 55(1), 589-656.
- [8] Adobe. (2023, March 21). Research: Generative AI will play starring role in customer experiences. Adobe Blog. <https://blog.adobe.com/en/publish/2023/03/21/research-generative-ai-will-play-starring-role-in-customer-experiences.html>
- [9] Faruqe, F., Watkins, R., & Medsker, L. (2021). Competency model approach to AI literacy: Research-based path from initial framework to model. *arXiv preprint arXiv:2108.05809*.
- [10] McCarthy, J., Minsky, M. L., Rochester, N., & Shannon, C. E. (2006). A proposal for the dartmouth summer research project on artificial intelligence, august 31, 1955. *AI magazine*, 27(4), 12-12.
- [11] Bhatti, A., & Hussain, M. (2021). A review of artificial intelligence in healthcare: Challenges and opportunities. *Journal of Healthcare Engineering*, 2021. <https://doi.org/10.1155/2021/6679739>
- [12] Anantrasrichai, N., & Bull, D. (2022). Artificial intelligence in the creative industries: a review. *Artificial intelligence review*, 1-68.
- [13] Bond-Taylor, S., Leach, A., Long, Y., & Willcocks, C. G. (2021). Deep generative modelling: A comparative review of vaes, gans, normalizing flows, energy-based and autoregressive models. *IEEE transactions on pattern analysis and machine intelligence*.
- [14] Rafner, J., Zana, B., Dalsgaard, P., Biskjaer, M. M., & Sherson, J. (2023, June). Picture This: AI-Assisted Image Generation as a Resource for Problem Construction in Creative Problem-Solving. In *Proceedings of the 15th Conference on Creativity and Cognition* (pp. 262-268).
- [15] Jaruga-Rozdolska, A. (2022). Artificial intelligence as part of future practices in the architect's work: MidJourney generative tool as part of a process of creating an architectural form. *Architectus*, 3 (71).
- [16] Generative AI: Advantages, Disadvantages, Limitations, and Challenges. (2023). Fact.technology. <https://fact.technology/learn/generative-ai-advantages-limitations-and-challenges/>
- [17] Leonardo.ai. (n.d.). Home. <https://leonardo.ai/>
- [18] Midjourney. (n.d.). Home. <https://www.midjourney.com/>
- [19] Openaimaster.com. (2022). Leonardo AI vs Midjourney. <https://openaimaster.com/leonardo-ai-vs-midjourney/>
- [20] Conway, S. (2022, June 10). Leonardo AI vs Midjourney: A Comparative Review of AI-Driven Image Creation Platforms. LinkedIn. <https://www.linkedin.com/pulse/leonardoai-vs-midjourney-comparative-review-ai-driven-sean-conway/>
- [21] Openaitrend.com. (2022). Midjourney vs Leonardo AI. <https://openaitrend.com/midjourney-vs-leonardo-ai/>
- [22] Digialps.com. (2022). Midjourney AI vs Leonardo AI: Same Prompts, Different Results. <https://digialps.com/midjourney-ai-vs-leonardo-ai-same-prompts-different-results/>
- [23] Long, D., & Magerko, B. (2020, April). What is AI literacy? Competencies and design considerations. In *Proceedings of the 2020 CHI conference on human factors in computing systems* (pp. 1-16).
- [24] Pampoukidou, S., & Katsanos, C. (2021, May). Test-retest reliability of the open card sorting method. In *Extended Abstracts of the 2021 CHI Conference on Human Factors in Computing Systems* (pp. 1-7).
- [25] Macías, J. A., & Culén, A. L. (2021). Enhancing decision-making in user-centered web development: a methodology for card-sorting analysis. *World Wide Web*, 24(6), 2099-2137.
- [26] Interaction Design Foundation. (n.d.). Card Sorting. The Encyclopedia of Human-Computer Interaction, 2nd Ed. <https://www.interaction-design.org/literature/book/the-encyclopedia-of-human-computer-interaction-2nd-ed/card-sorting>

Performance Evaluation of the M-QAM Enhanced Subcarrier Index Modulation in the Multipath Fading Channel with the Non-linear Amplifier

Si Sar Mi
School of Engineering
King Mongkut's Institute
of Technology Ladkrabang
Bangkok, Thailand
63601235@kmitl.ac.th

Aphitchaya Siriwanitpong
School of Engineering
King Mongkut's Institute
of Technology Ladkrabang
Bangkok, Thailand
64601167@kmitl.ac.th

Pornpawit Boonsrimuang
Faculty of Industrial
Technology
Suan Sunandha Rajabhat
University
Bangkok, Thailand
pornpawit.bo@ssru.ac.th

Pisit Boonsrimuang
School of Engineering
King Mongkut's Institute
of Technology Ladkrabang
Bangkok, Thailand
*Corresponding author's
pisit.bo@kmitl.ac.th

Abstract—One of the specifications of the next-generation mobile communication is to reduce the power consumption to transmit the signal. Enhanced subcarrier index modulation (eSIM-OFDM) is a novel multicarrier modulation scheme. However, the eSIM-OFDM scheme degraded a little frequency utilization than the conventional orthogonal frequency division multiplexing (C-OFDM) scheme at the higher M-QAM modulation techniques. It has a special feature to transmit the signal when compared with the C-OFDM scheme. Its special feature increased the power efficiency and improved the bit error rate (BER) performance than the C-OFDM scheme. In the literature, the BER performance of the eSIM-OFDM scheme is analyzed in the additive white Gaussian noise (AWGN) channel and compared BER performance of the C-OFDM scheme. But in the literature, the BER performance of the eSIM-OFDM scheme and C-OFDM scheme were not evaluated in the multipath fading channel. Because eSIM-OFDM includes a special feature called inactive and active subcarriers. In this paper, we will evaluate the BER performance of higher order modulated eSIM-OFDM signal in the multipath Rician fading channel by using the Zadoff-Chu sequence pilot in the non-linear mobile communication system and will compare the BER performance with the C-OFDM scheme. From the simulation results, we can see that the BER performance of the eSIM-OFDM scheme is much better than the C-OFDM scheme in the multipath Rician fading non-linear channel. In this paper, computer simulation will evaluate the BER performance of the higher order modulated eSIM-OFDM scheme in the multipath Rician fading non-linear channel.

Keywords— *channel estimation, higher order index modulation, OFDM, Zadoff-Chu sequence, non-linear multipath fading channel*

I. INTRODUCTION

As mobile wireless communication evolves today, the continuous demand for high transmission data rates, high spectral efficiency, and energy efficiency [1-5]. The spatial modulation (SM) technique [6] was developed to fulfill the demand for high transmission data rates, which transmitted additional information bits using the indices of antennas.

Subcarrier index modulation (SIM-OFDM) [7] is an extension new multicarrier modulation technique where

instead of using indices of antennas, which includes an additional dimension called the index of the subcarriers that transmitted additional information bits. In the SIM-OFDM scheme, spectral efficiency (SE) performance improvement depends on the average number of majority bit values. Still, the SIM-OFDM scheme improved power efficiency over the C-OFDM scheme by switching off some subcarriers. In the SIM-OFDM scheme, BER performance is analyzed by two conditions power reallocation policy (PRP) and power saving policy (PSP). The BER performance of the SIM-OFDM scheme using PRP improved than the PSP when compared with the C-OFDM scheme. Therefore, there is a trade-off between the power efficiency and the BER performance of the SIM-OFDM scheme. The BER performance of the SIM-OFDM scheme is analyzed and simulated by transmitting the excess subcarriers used to convey the control information for correctly detecting the type of majority bit-value at the receiver side. This BER performance improvement will degrade if the kind of majority bit-value is detected incorrectly at the receiver side.

To improve the spectral efficiency performance of the subcarrier index modulation (SIM-OFDM) scheme, researchers split m information bits into many subblocks and created different look-up tables to map the pattern of the subcarriers in the subblocks. The performance of many advanced subcarrier index modulation techniques can be seen in the literature review [8-10]. Although many advanced subcarrier index modulation (SIM-OFDM) improved SE performance, its BER performance will degrade if the receiver side incorrectly detects the state of the received subcarrier patterns. The BER performance of the SIM-OFDM scheme was improved by using enhanced subcarrier index modulation (eSIM-OFDM) scheme [11]. In the eSIM-OFDM scheme, one on-off keying bit changed two states of subcarriers in a subcarrier pair. Therefore, eSIM-OFDM scheme improved BER performance more than the conventional SIM-OFDM scheme without losing the special feature of transmitting additional information bits using the index of subcarriers. Although the eSIM-OFDM scheme degrades SE performance a little more than the C-OFDM scheme at the higher M-QAM modulation techniques, it increases power efficiency and BER performance more than the C-OFDM scheme. In the literature review, the BER performance of the eSIM-OFDM scheme is analyzed and compared with the C-OFDM in the AWGN channel. But in the literature review, the compared BER

This research was supported by King Mongkut's Institute of Technology Ladkrabang.

performance of the eSIM-OFDM scheme and C-OFDM scheme were not evaluated in the multipath fading non-linear channel. We will evaluate the BER performance of the higher order modulated eSIM-OFDM signal and C-OFDM signal in the multipath Rician fading channel using the Zadoff-Chu sequence in the non-linear mobile communication system.

The rest of this paper is divided into three parts. Section II describes the channel estimation of the higher-order modulated eSIM-OFDM using the Zadoff-Chu sequence pilot. Section III shows the results and discussion of channel estimation for higher order modulated eSIM-OFDM scheme. Finally, section IV concludes the paper.

II. ESIM-OFDM CHANNEL ESTIMATION SYSTEM MODEL

A. Zadoff-Chu Sequence Pilot Generations

The Zadoff-Chu sequences are used in 3GPP preamble sequence generation. The random access preambles are generated from Zadoff-Chu sequences with zero correlation zone, generated from one or several root Zadoff-Chu sequences by increasing the order of cyclic shift, which is defined in 3GPP [12]. The u^{th} root Zadoff-Chu sequence is defined as in [12].

$$x_u(n) = e^{-j\frac{\pi un(n+1)}{N_{ZC}}}, 0 \leq n \leq N_{ZC} \quad (1)$$

where N_{ZC} is the length of the Zadoff-Chu sequence. We generate the lowest peak-to-average power ratio (PAPR) of the Zadoff-Chu sequence with a length of 128 for the pilot data information.

B. eSIM-OFDM modulator

Fig. 1 shows the traditional higher-order modulated eSIM modulation technique. Here eSIM modulation technique will be described briefly. Unlike the conventional modulator, the eSIM modulation technique includes an enhanced subcarrier index modulator (eSIM). In the eSIM modulator, the incoming information bits are partitioned into two parts of information bits. The first part of bits is called on-off keying B_{OOK} bits, and

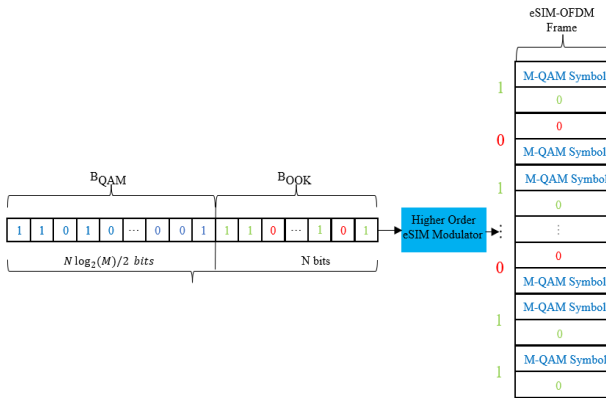


Fig. 1. Traditional higher-order enhanced subcarrier index modulation eSIM-OFDM scheme (M-QAM)

the remaining part of bits is called B_{QAM} bits. The eSIM modulator will change the transmitted subcarrier patterns, which depend on the incoming B_{OOK} bits. In the eSIM modulator, if B_{OOK} 1 bit comes, the first transmitted subcarrier will be activated, and the second transmitted subcarrier will be inactivated in a subcarrier pair. Another way is if B_{OOK} 0 bit comes, the first transmitted subcarrier will be inactivated, and

the second transmitted subcarrier will be activated in a subcarrier pair. Although inactivated subcarriers will not be used to convey the B_{QAM} bits, the eSIM modulator is transmitting additional information B_{OOK} bits using the indices of subcarriers, and the remaining B_{QAM} bits are conveyed by the activated subcarriers.

C. Channel Estimation of Higher Order Modulated eSIM-OFDM Scheme

The block diagram of the higher-order modulated (16-QAM) eSIM-OFDM channel estimation scheme is shown in Fig. 2. Here, the channel characteristics of the higher-order modulated (16-QAM) eSIM-OFDM will be estimated using the Zadoff-Chu sequence pilot in the multipath Rician fading channel. The BER performance of the higher order modulated (16-QAM) eSIM-OFDM scheme will be evaluated and compared with the higher order modulated (16-QAM) C-OFDM scheme in the next section III.

Firstly, the serial arbitrary transmitting information bits are converted into parallel sequences. Then, the parallel bits sequences are modulated by the eSIM modulator. The higher-order modulation technique (16-QAM) is used in the eSIM modulator. Then the modulator outputs the higher order eSIM modulated symbols. Let X_m be the higher order eSIM modulated symbols. Then, pilot symbol insertion is done on the frequency domain modulated symbols in the eSIM-OFDM scheme. The structure of transmitted frame formats for channel estimation higher order modulated (16-QAM) eSIM-OFDM and C-OFDM with Zadoff-Chu Sequence pilot data information are shown in Fig. 3. Then, Inverse Fast Fourier Transforms (IFFT) were applied to convert the time-domain eSIM-OFDM symbols. The time-domain eSIM-OFDM symbols can be represented by the following equations.

$$x_n = \sum_{m=0}^{N-1} X_m e^{(j2\pi nm/N)}, 0 \leq n \leq N-1 \quad (2)$$

where N is the number of the IFFT points. The output of IFFT signals is converted from parallel to serial. The time domain higher order modulated eSIM-OFDM symbols are inserted with the cyclic prefix called the guard interval (GI) to avoid the inter-symbol interference (ISI) from the multipath fading channel. In this paper, we would like to do the channel estimation of the higher order modulated (16-QAM) eSIM-OFDM signal and compare it with the C-OFDM signal in the multipath Rician fading non-linear channel. The time-domain

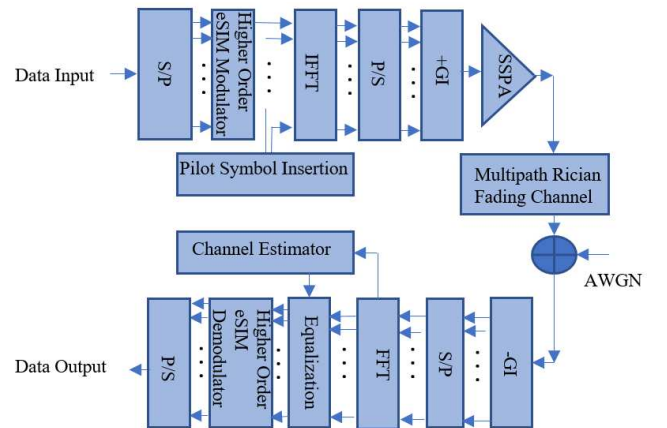


Fig. 2. The block diagram of the higher order modulated (16-QAM) eSIM-OFDM channel estimation scheme

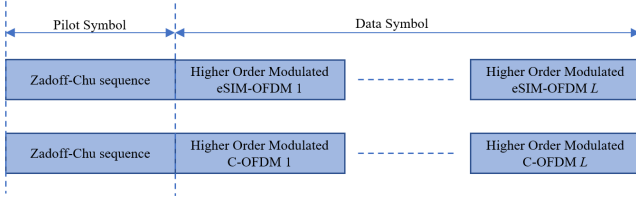


Fig. 3. Structure of transmitted frame formats for channel estimation higher order modulated (16-QAM) eSIM-OFDM and C-OFDM with Zadoff-Chu pilot data information

serial transmitted eSIM-OFDM signal passes through the solid-state power amplifier (SSPA). The SSPA power amplifier is a well-known power amplifier to evaluate the performance of the non-linear channel, which can be seen from the literature review [13].

The output of the SSPA power amplifier can be represented by the following equation, as in [13].

$$u(t) = s(t) \cdot G[s(t)] \quad (3)$$

$$G[s(t)] = \frac{A[s(t)] \cdot e^{j\Phi[s(t)]}}{|s(t)|} \quad (4)$$

and the related non-linear transformation:

$$A[s(t)] = \frac{K_1 |s(t)|}{\left[1 + \left(\frac{K_1 |s(t)|}{A_0}\right)^{2r}\right]^{\frac{1}{2r}}} \quad (5)$$

$$\Phi[s(t)] = \alpha_\phi \cdot \left(\frac{K_1 |s(t)|}{A_0}\right)^4 \quad (6)$$

where $u(t)$ is the amplified signal, $G[\]$ is the amplifier gain, A_0 is the saturating amplitude, K_1 is the small-signal gain, $s(t)$ is the complex envelope of the SSPA input signal, r is a parameter that controls the smoothness of the transition from the linear region to the saturation region, α_ϕ is typically set to zero, meaning SSPA adds no phase distortion [13].

The output signal of the SSPA power amplifier is filtered with the multipath Rician fading channel. The components of the sample rate channel model are $1 \cdot 10^6$, path delays are $[0 \ 0.5 \ 1.2] \cdot 10^{-6}$, average path gains are $[0.1 \ 0.5 \ 0.2]$, K-factor is 2.8, direct path Doppler shift is 5, direct path initial phase is 0.5 and maximum Doppler shift is 50. The channel-filtered signal is added with the additive white Gaussian noise (AWGN).

The received time-domain higher order modulated (16-QAM) eSIM-OFDM signal can be represented by using equation (7).

$$y_n = \sum_{l=0}^{L-1} h_n u_{n-l} + w_n \quad (7)$$

where L is the number of multipath, h_n is the time-domain channel impulse response, and w_n represents noise. Then GI is removed from the received time-domain higher order

modulated (16-QAM) eSIM-OFDM signal and convert it from serial to parallel. After that, the Fast Fourier Transform (FFT) is applied to the received time-domain eSIM-OFDM symbols. The frequency-domain eSIM-OFDM symbols can be represented by the following equation (8).

$$Y_m = \sum_{k=0}^{N-1} \sum_{l=0}^{L-1} X_k H_l^{(m-k)} e^{-j2\pi k l / N} + w_m \quad (8)$$

Before demodulation, the channel effects can be estimated by using the Least-Square (LS) channel estimation method. The LS method [14], [15] divides the received frequency domain pilot data information by the known pattern pilot data information at the receiver side. Then the preamble symbol is removed from the received eSIM-OFDM symbols. Then the data channel is compensated by the channel effects using the equalization method. Finally, the equalized signal can be represented by the following equation, as in [15].

$$X_{eq} = H^{-1} Y \quad (9)$$

After equalization, the equalized frequency domain eSIM modulated symbols are demodulated by the eSIM demodulator using a higher-order demodulation technique and converted from parallel to serial. Finally, the serial data output is reconstructed.

III. RESULTS AND DISCUSSION OF CHANNEL ESTIMATION FOR HIGHER ORDER MODULATED ESIM-OFDM

Computer simulations have been done to evaluate the BER performance of the higher order modulated (16-QAM) eSIM-OFDM and C-OFDM schemes in the same multipath Rician fading non-linear channel. The simulation parameters are shown in table I. In order to fairly compare eSIM-OFDM with C-OFDM on a power-per-bit basis, each active subcarrier should receive the energy of its M-QAM symbol and additional energy to account for the bit encoded in the carrier states. Fig. 5. Shows the comparisons between BER versus SNR of channel estimation 16-QAM, eSIM-OFDM and 16-QAM, C-OFDM using Zadoff-Chu sequence pilot at different non-linear operating points input back off (IBO) is 0dB, -2dB, -4 dB and -6dB.

Fig. 5 shows the BER performance of channel estimation higher order modulated 16-QAM, eSIM-OFDM and 16-QAM, C-OFDM simulation results of ideal equalization (Ideal-Eq) and the zero forcing equalization (ZF-Eq) results. From the simulation results, the BER performance of C-OFDM is worse than eSIM-OFDM when the SNR is reached in the SNR higher region. From Fig. 5, we can observe that

TABLE I. SIMULATION PARAMETERS

| Information | eSIM-OFDM | C-OFDM |
|--|-------------------|--------|
| Pilot Sequence | Zadoff-Chu, OFDM | |
| Modulation technique | 16-QAM | |
| Frame length (L -symbol) | 20 | |
| Number of IFFT points (N_{fft}) | 128 | |
| Number of subcarriers (N) | 128 | |
| Number of the guard interval (N_g) | 16 | |
| Input back off, IBO (dB) | 0, -2, -4, and -6 | |
| SSPA, r | 2 | |

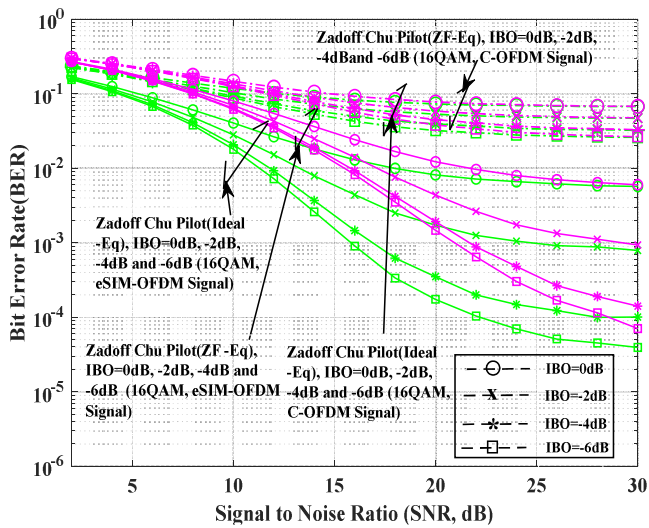


Fig. 5. Comparisons between BER vs. SNR of 16-QAM, eSIM-OFDM, and 16-QAM, C-OFDM using Zadoff-Chu sequence pilot IBO=0dB, -2dB, -4dB, and -6dB

the BER performance of channel estimation 16-QAM, eSIM-OFDM scheme is better than the 16-QAM, C-OFDM in all non-linear operating points (IBO) is 0dB, -2dB, -4dB, and -6dB. The BER performance of the channel estimation 16-QAM, eSIM-OFDM scheme is a better improvement than the C-OFDM scheme when decreasing IBO values 0dB, -2dB, -4dB, and -6dB.

There are two main reasons about the BER performance of higher order modulated eSIM-OFDM is better than the C-OFDM scheme in the same multipath Rician fading channel conditions. The first one is we generate the lowest PAPR of the Zadoff-Chu pilot data information, which avoids the intermodulation noise of the non-linear power amplifier. This will improve the estimation of channel frequency response (CFR) accuracy. The second one is eSIM-OFDM has a special feature that switches off some subcarriers in the transmitted subcarriers which will improve the power efficiency. The BER performance of channel estimation higher order modulated (16-QAM), eSIM-OFDM is better than the BER performance of channel estimation higher order modulated (16-QAM), C-OFDM in all different non-linear operating points IBO=0dB, -2dB, -4dB and -6dB.

IV. CONCLUSION

This paper uses conditions to show the high-QAM modulated signal performances in the multipath fading channel with a non-linear amplifier between the eSIM-OFDM and C-OFDM systems. The Zadoff-Chu sequence pilot was employed in both systems by varying the different non-linear operating points of the power amplifier. From the simulation results, we can observe that the BER performance of the eSIM-OFDM system is better than the BER performance of the C-OFDM system at all different non-linear operating points IBO=0dB, -2dB, -4dB, and -6dB. Because of the high QAM usually has small robustness for the multipath fading and the intermodulation noise in the non-linear amplifiers. However, the eSIM-OFDM systems have a better power efficiency than the C-OFDM systems, which conduct an improved tolerance for multipath fading and intermodulation noise. These simulation results clearly show the power efficiency of the 16-QAM of eSIM-OFDM systems brings the

BER performance better than the 16-QAM of C-OFDM systems for all the operating points of the non-linear amplifier.

ACKNOWLEDGMENT

The authors would like to thank King Mongkut's Institute of Technology Ladkraband (KMITL) for supporting this research.

REFERENCES

- [1] Md. Noor-A-Rahim *et al.*, "6G for Vehicle-to-Everything (V2X) Communications: Enabling Technologies, Challenges, and Opportunities," *Proceedings of the IEEE*, vol. 110, no. 6, pp. 712–734, May 2022, doi: 10.1109/jproc.2022.3173031.
- [2] F. Tariq, M. R. A. Khandaker, K. K. Wong, M. A. Imran, M. Bennis, and M. Debbah, "A Speculative Study on 6G," *IEEE Wirel Commun*, vol. 27, no. 4, pp. 118–125, Aug. 2020, doi: 10.1109/MWC.001.1900488.
- [3] S. Nayak and R. Patgiri, "6G Communications: A Vision on the Potential Applications," Apr. 2020, doi: 10.1007/978-981-19-0019-8_16.
- [4] I. F. Akyildiz, A. Kak, and S. Nie, "6G and Beyond: The Future of Wireless Communications Systems," *IEEE Access*, vol. 8, pp. 133995–134030, 2020, doi: 10.1109/ACCESS.2020.3010896.
- [5] S. Parkvall, E. Dahlman, A. Furuskar, and M. Frenne, "NR: The new 5G radio access technology," *IEEE Communications Standards Magazine*, vol. 1, no. 4, pp. 24–30, Dec. 2017, doi: 10.1109/MCOMSTD.2017.1700042.
- [6] R. Y. Mesleh, H. Haas, S. Sinanović, C. W. Ahn, and S. Yun, "Spatial Modulation Index Terms-Interchannel interference (ICI), multiple-input-multiple-output (MIMO), orthogonal frequency division multiplexing (OFDM), receiver complexity, space-time coding (STC) coded modulation, spatial modulation (SM), vertical Bell Labs layered space-time (V-BLAST)," *IEEE Trans Veh Technol*, vol. 57, no. 4, 2008, doi: 10.1109/TVT.2008.912136.
- [7] R. Abu-alhiga and H. Haas, "Subcarrier-index modulation OFDM," in *IEEE International Symposium on Personal, Indoor and Mobile Radio Communications, PIMRC*, 2009, pp. 177–181. doi: 10.1109/PIMRC.2009.5449882.
- [8] Z. Chen, Y. Lu, and S. G. Kang, "High-Dimensional OFDM with In-Phase/Quadrature Index Modulation," *IEEE Access*, vol. 9, pp. 44198–44206, 2021, doi: 10.1109/ACCESS.2021.3066852.
- [9] S. El-Khany, H. M. Elragal, and R. A. Polus, "Index Modulation Multiple-Access (IMMA): Efficient Techniques for Downlink Millimeter Waves Outdoor Channel," *IEEE Open Journal of Vehicular Technology*, vol. 2, pp. 403–411, 2021, doi: 10.1109/OJVT.2021.3112942.
- [10] M. Salah, O. A. Omer, and U. S. Mohammed, "Spectral Efficiency Enhancement Based on Sparsely Indexed Modulation for Green Radio Communication," *IEEE Access*, vol. 7, pp. 31913–31925, 2019, doi: 10.1109/ACCESS.2019.2903391.
- [11] D. Tsonev, S. Sinanovic, and H. Haas, "Enhanced subcarrier index modulation (SIM) OFDM," in *2011 IEEE GLOBECOM Workshops, GC Wkshps 2011*, 2011, pp. 728–732. doi: 10.1109/GLOCOMW.2011.6162549.
- [12] TSGR, "TS 136 211 - V11.0.0 - LTE; Evolved Universal Terrestrial Radio Access (E-UTRA); Physical channels and modulation (3GPP TS 36.211 version 11.0.0 Release 11)," 2012. [Online]. Available: http://portal.etsi.org/chaircor/ETSI_support.asp.
- [13] C. Dudak, A. Tuncay Koc, and S. Koc, "Solid State Power Amplifier (SSPA) Nonlinearity Effects on Quadri-Phase Shift Keying Modulation," 2004.
- [14] J. . -J. van de Beek, O. Edfors, M. Sandell, S. K. Wilson and P. O. Borjesson, "On channel estimation in OFDM systems," 1995 IEEE 45th Vehicular Technology Conference. Countdown to the Wireless Twenty-First Century, Chicago, IL, USA, 1995, pp. 815–819 vol.2, doi: 10.1109/VETEC.1995.504981.
- [15] S. Colieri, M. Ergen, A. Puri and Bahai A, "A study of channel estimation in OFDM systems," Proceedings IEEE 56th Vehicular Technology Conference, Vancouver, BC, Canada, 2002, pp. 894–898 vol.2, doi: 10.1109/VETECF.2002.1040729.

Bragg Peak Detection Using Compatible Mother Wavelet on Oceanographic HF Radar Signals

Iswandi

Department of Electrical Engineering
and Information Technology
Faculty of Engineering,
Universitas Gadjah Mada
Yogyakarta, Indonesia, 55281
iswandi@ugm.ac.id
Orcid ID. 0000-0003-4685-3474

Risanuri Hidayat

Department of Electrical Engineering
and Information Technology
Faculty of Engineering,
Universitas Gadjah Mada
Yogyakarta, Indonesia, 55281
risanuri@ugm.ac.id
Orcid ID. 0000-0002-7381-4633

Sigit Basuki Wibowo

Department of Electrical Engineering
and Information Technology
Faculty of Engineering,
Universitas Gadjah Mada
Yogyakarta, Indonesia, 55281
sigitbw@ugm.ac.id

Abstract— High-frequency surface wave radar (HFSWR) has been proven as a long-range sensor for estimating the sea state. The coupling between radar wave and dynamic sea surface produces the Bragg components in the Doppler space of received signals. These components contain the sea-state information, which can be extracted by using an inversion algorithm. However, the dense traffic and any natural phenomena on the HF spectrum cause the received signal to be mixed up with clutters and interference, sometimes overlap in time, frequency, and Doppler domain. This research considered the discrete wavelet transformation (DWT) to decompose the radar signal and highlight the Bragg peaks. The choice of mother wavelet highly influences the wavelet. Thus, the scrutiny was initialized by selecting the mother wavelet as reported in this paper. The results show the 6-order Daubechies (db6) and 3-5 pairs of biorthogonal (bior3.5) functions at level 3 of DWT can detect the proper position of Bragg peaks.

Keywords— Discrete wavelet transform, peak detection, HF radar, Doppler spectra, mother wavelet selection.

I. INTRODUCTION

High-frequency surface wave radar (HFSWR) is a long-range, low-cost, multi-purpose sensor for sea monitoring and surveillance. It can continuously estimate the sea state and detect objects on the sea surface, such as ships, low-altitude aircraft, icebergs, etc. [1].

The unique propagation phenomenon in the HF band is the coupling between the radar signal and the sea surface. The interaction between radar and sea waves generates a constructive back-scattering to the receiver. The dynamic motions of the sea surface construct the Bragg components in the Doppler map of the radar receiver [2]. These components have frequency and amplitude influenced by the sea state, such as wind, surface current, wave height, etc. Therefore, the sea state can be estimated from the Bragg characteristics by using inversion algorithm [3].

However, the radar receiving signal does not merely contain the sea scattering. It is also contaminated by scattering signals from other objects on the sea. In addition, it is also contaminated by ionospheric clutter and radio frequency interference [4]. This first term is caused by the natural characteristic of the HF signal to be reflected by the ionosphere layer. The second one is generated by a man-made long-range communication system [5]. Therefore, the

radar signal processing has to distinguish the Bragg components among the clutter and interferences.

Taking advantage of extended range coverage, the HFSWR is also developed to detect and track ships [6]. In this case, the Bragg components become the clutter in the detection process and are called sea clutter. Again, the signal processing has to separate the ship signal from the sea clutter and other interferences.

The radar signal processing for sea state estimation and ship detection deals with the mixed signal. The wanted signals must be extracted from the composite signals, so that the signal decomposition may be essential in the HFSWR signal processing.

The wavelet transform is a powerful mean for signal decomposition especially for the non-stationary signals. It has been applied in various fields, such as for denoising and peak detection [7]. Jangal *et al.* introduced the wavelet transform into the signal processing of HFSWR [8]. He applied DWT and concluded that the ship scattering signal can be distinguished from the sea clutter. After signal decomposition by wavelet, it continues with automatic ship detection such as fuzzy algorithm [9], principle component analysis (PCA) [10], etc. The wavelet transformation is also employed to mitigate the ionospheric clutter by combining it with an oblique projection filter [11].

Although the wavelet transformation is widely used for ship detection on HFSWR, it has less attention in the signal processing for estimating oceanic parameters. Wang *et al.* have tried to utilize the wavelet transform to detect the position of the Bragg peak in the presence of high and close interference [12]. In his work, the mother wavelet daubechies order 4 (db4) was chosen to work on 4 levels of DWT decomposition. After the decomposition process, the first order Bragg peak was localized in the level detail component and detected by the independent component analysis (ICA) method. The proposed technique has been implemented in selected empirical HF radar data and gave a good result. However, there is no further investigation for this kind of method.

Motivated by the promising result of Wang's method, further research on the implementing of wavelet transform for estimating the sea state is reinvestigated in our study. The empirical data in previous work is changed to the analytical data, which reduce uncertainty and unknown

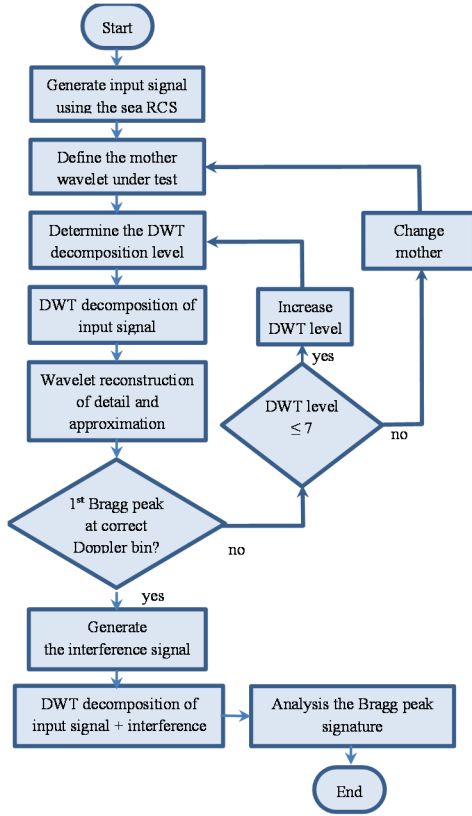


Fig. 1. Procedure for selecting a proper mother wavelet for Bragg peak detection.

component in the measured data. The Bragg components are generated by the mathematical formulation of sea radar cross-section (RCS) [13], and the interference is modeled as the ship reflection [14]. The use of analytical data can reduce the data uncertainty, control any considered signal components, and provide reproducible data.

This paper proposes selecting the appropriate mother wavelet and decomposition level to highlight the Bragg peak components on the analytical data of Doppler spectra for the HFSWR signal. The accuracy detection of first-order Bragg peak is evaluated with interference close to the peak location. For this purpose, a proper mother wavelet function is proposed as a novel contribution to current works.

II. RESEARCH METHODOLOGY

The main task of oceanographic radar is detecting the Bragg peaks to be used for estimating the sea state. Since the radar signal is a mixture of various components, signal decomposition is required to localize the Bragg and ease the detection process. This research aims to achieve this purpose by employing the wavelet transform. An appropriate mother wavelet must be chosen to localize the wanted signal.

Fig. 1 shows the research procedures. It is initiated by generating the input signal using the sea radar RCS model and the interference signal from the ship, continuing by decomposing the radar signal without interference. Various types of mother wavelet are tested to select the appropriate

TABLE I. RADAR SPECIFICATION IN THE SIMULATION.

| Radar Parameters | Descriptions |
|-------------------------------------|--------------|
| Center frequency (fc) | 25 MHz |
| Waveform | FMCW |
| Chirp repetition frequency (fr) | 2 Hz |
| Bandwidth (B) | 100 kHz |
| Range resolution ($\Delta\rho_s$) | 1.5 km |
| Coherent integration time | 512 s |

one. It is worth noticing that the indicator for selection is specific in this case. Instead of getting the lowest reconstruction error or the highest entropy, the properness of the mother wavelet is the existence of a reconstructed signal that contains the first Bragg peak in the proper location. Since the input signal is theoretical data, the exact position of the Bragg peak is obviously known.

After a proper mother wavelet is obtained, the process is continued by decomposition of the mixture between the Bragg peak and interference.

This work considers the HFSWR with the specification as listed in Table 1. In this case, the analysis is applied on a single radar patch. Thus, only the required parameters are described in the table.

III. MATHEMATICAL MODELING

This section describes the mathematical model of signals and briefly explains the wavelet transform. The signal consists of the sea scattering signal generated by sea RCS and the interference by using the ship scattering signal.

A. Sea radar cross-section

The interaction between radar signal and dynamic sea surface produces the Bragg components with a unique pattern in the Doppler spectrum. It is generally expressed by the sea radar cross-section (RCS) σ .

$$\sigma = \sigma_1 + \sigma_2, \quad (1)$$

where σ_1 and σ_2 are first and second-order Bragg components, respectively. This work considers the RCS model for HF radars with a frequency-modulated continuous wave (FMCW) waveform [13]. The first-order Bragg components are generated by a single scattering of radar signal by the dynamic sea surface. The first order RCS is expressed in the Doppler domain ω_d as follows

$$\sigma_1(\omega_d) = 16\pi k_0^2 \Delta\rho_s \sum_{m=\pm 1} S_1(m\mathbf{K}) \frac{K^{2.5}}{\sqrt{g}} S_a \left[\frac{\Delta\rho_s}{2} (K - 2k_0) \right], \quad (2)$$

where k_0 is the wave number of the radar signal, $\Delta\rho_s$ is the radial-range resolution of radar, and g is earth gravity. $S_1(m\mathbf{K})$ is the Pierson-Moskowitz model of the ocean wave with \mathbf{K} is the directional wave number of sea wave and K is the non-directional wave number in the inward direction to the radar position. Lastly, the $S_a[\]$ is the sinc function.

The second-order RCS is caused by the double scattering of radar by the dynamic rough sea surface. It can be expressed as follows [13]

$$\sigma_2(\omega_d) = 4\pi k_0^2 \Delta\rho_s \sum_{m_1=\pm 1} \sum_{m_2=\pm 1} \int_0^\infty \int_{-\pi}^\pi \int_0^\infty |H\Gamma|^2 S_1(m_1 \mathbf{K}_1) S_1(m_2 \mathbf{K}_2) K^2 S a^2 \left[\frac{\Delta\rho_s}{2} (K - 2k_0) \right] \delta(\omega_d + m_1 \sqrt{gK_1} + m_2 \sqrt{gK_2}) K_1 dK_1 d\theta_{K_1} dK, \quad (3)$$

where \mathbf{K}_1 and \mathbf{K}_2 are the directional wave number of the first and second scatterer.

B. Interference signal

The sailing ship in the radar scene can scatter the radar signal, which acts as interference. In this case, the radar waveform is frequency modulated continuous wave (FMCW), thus the scattering signal is in time domain defined as a delayed and attenuated copy version of the transmitting signal. If the radar has the center frequency f_c , bandwidth B , transmit power P_t , chirp repetition frequency f_r , the ship scattering signal is expressed as follows.

$$S_R(t) = A_s \sqrt{2P_t} \cos \left[2\pi \left(f_c - \frac{B}{2} \right) (t - \tau_s) \pm \frac{Bf_r}{2} (t - \tau_s)^2 \right] \quad (5)$$

where the τ_s and A_s are the delay time and attenuation of the received signal. The delay time is calculated from the distance between transmitter to ship, distance ship to receiver, and the reflector radial velocity.

$$\tau_s = \frac{r_T + r_R + 2v_r t}{c} \quad (6)$$

where $c = 3 \cdot 10^8$ m/s is the speed of radio wave propagation in free space. The attenuation is also influenced by the propagation distance with following relation.

$$A_s = 0.5 \left[\frac{G_T G_R \sigma_s}{4\pi(r_T + r_R)^2} \right]^{1/2} \quad (7)$$

The parameters G_T and G_R are the gain of array element on transmitter and receiver.

The wavelet transform in this research works on the Doppler domain. A series of signal processing is applied to transform the ship scattering signal into Doppler domain i.e demodulation, and double fast Fourier transform [15].

C. Discrete wavelet transforms

The wavelet transform is a tool to observe the time and frequency information of any signal, simultaneously. Mathematically, the information is revealed by inner product of signal with a function called mother wavelet. There are various kind of mother wavelets, and they can be chosen based on the signal characteristics.

There are two types of wavelet transform: continuous and discrete wavelets. The continuous wavelet transform (CWT) compares the signal $f(t)$ with the mother wavelet $\psi(t)$ at different scale and position.

$$C(a, b; f(t), \psi(t)) = \int_{-\infty}^{\infty} f(t) \frac{1}{\sqrt{a}} \psi\left(\frac{t-b}{a}\right) dt \quad (8)$$

where a and b is the scaling and translation factors.

The discrete wavelet transform (DWT) discretizes the CWT by replacing the a and b by integer power of $2^{\frac{m}{2}}$.

$$D(m, n) = 2^{\frac{m}{2}} \sum_k f(k) \psi(2^m, k - n) \quad (9)$$

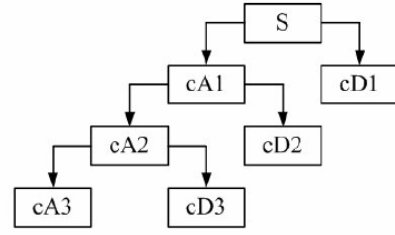


Fig. 2. DWT signal decomposition with wavelet model.

where m is the grid scale, n is the time scale, and k is the $k=0$ to $n-1$.

For the signal decomposition, the DWT is commonly used, because it has lower computation cost. The input signal is decomposed into two parts: detail and approximation. The detail contains the higher frequency component while the approximation has lower components. A multi level DWT is applied to look forward more detail decomposition. There are model in the decomposition that are wavelet packet model and wavelet model. The wavelet packet model decomposes both approximation and detail part, while the wavelet model only the detail part is decomposed in the next decomposition. Fig. 2 shows the block diagram of the decomposition process by using DWT with the wavelet model.

IV. RESULTS AND DISCUSSIONS

This section delivers the ability of wavelet transform to decompose the HFSWR signal and detect the peak position of the first-order Bragg peak. The signal modeling results are presented, followed by the implementation of DWT.

A. Sea Radar Cross Section

The simulation result of sea radar cross section computed from Eq. (1), Eq. (2), and Eq. (3) is shown in Fig. 2. It is calculated with the radar setup listed in Table 1. The Pierson-Moskowitz spectra is calculated with the wind speed 15 m/s and directed 60° from the radar look direction. The first Bragg components are recognized by two peaks at the Doppler frequency

$$\omega_B = \pm \sqrt{2gk_0}. \quad (4)$$

The theoretical first Bragg peak frequencies are indicated by the red dashed lines in the Fig. 3. The effect of wind to the magnitude of Bragg peaks is also simulated in our previous publication. Additionally, the first Bragg peaks location is shifted when the sea surface current is existed, but it is assumed to be zero. The second Bragg components are appeared as the continuum near the first order Bragg peaks.

The magnitude and Doppler frequency of Bragg components are influenced by the sea states such as wind, surface current, and wave height. Therefore, they can be utilized to estimate the sea state by the inversion algorithms.

Next, the Doppler map is constructed from the spectra of sea scattering along the radial direction from the radar station. In this case, the sea state is assumed to be constant

along the observation path. The attenuation is calculated by the free space path-loss model. The result is shown in Fig. 4.

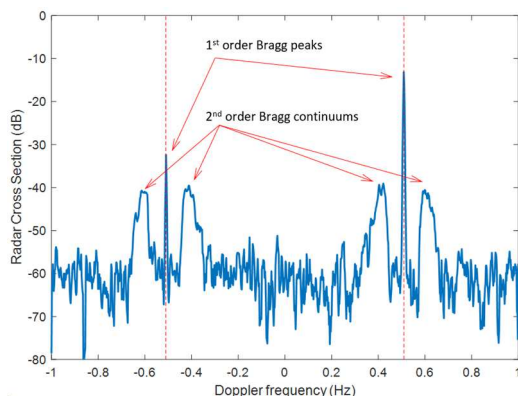


Fig. 6. The simulated sea RCS with the radar frequency 25 MHz and the wind with the speed 15 ms^{-1} and direction 60° from the radar look.

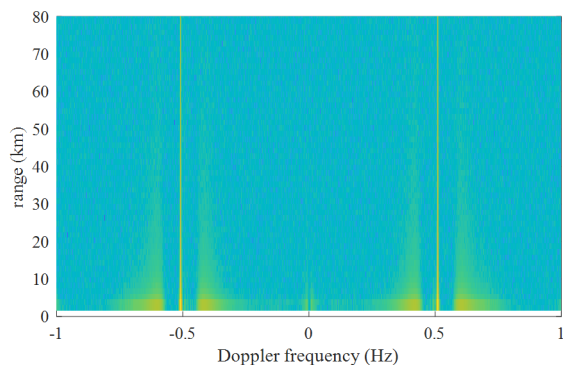


Fig. 7. The doppler map of simulated radar signal.

B. Interference Signals

The radar is considered as the oceanographic radar, so the incoming signal due to ship reflection becomes one of the interference. Fig. 5 shows the result simulation based on on the Eq. 5.6, and 7. There are five vessels assumed in the radar scene, with their position and speed are adjusted to produce the Doppler component around the Bragg peaks.

The mix of sea scattering and the interference signal is simultaneously arrived in the radar receiving antenna, as shown in Fig. 6. The figure shows that the interference signal is very close to the first-order Bragg peak in some ranges. Thus, it probably causes a misdetection of the Bragg peak.

C. Wavelet decomposition and Bragg peak detection

The choice of the mother wavelet highly influences the ability of DWT to decompose signals. Some available wavelet functions in the Haar, Daubechies, Symlet, Biorthogonal functions, and their derivations are tested in some decomposition levels. Then, the existence of local maxima in all decomposition components is analyzed. The proper mother wavelet is indicated by the similar position of local maxima with the Bragg peaks.

Initially, the interference free signal is observed and found that there are two mother wavelet with proper results,

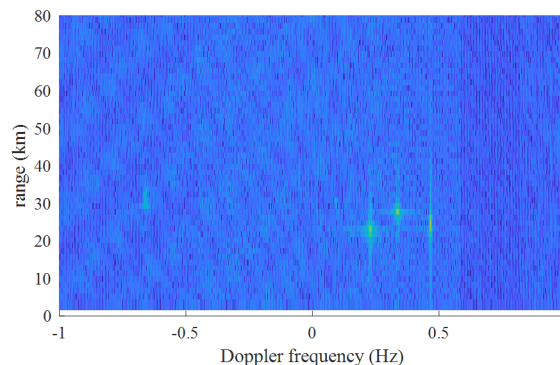


Fig. 3. The doppler map of simulated radar signal.

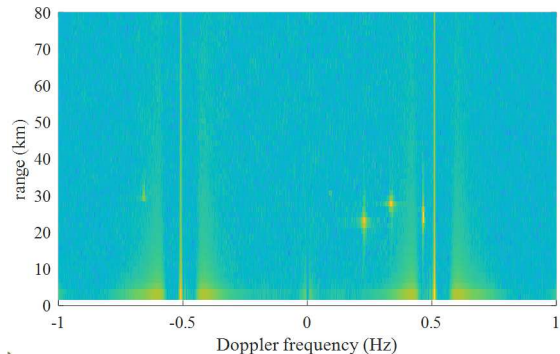


Fig. 4. The doppler map of mixed sea scattering and interferences.

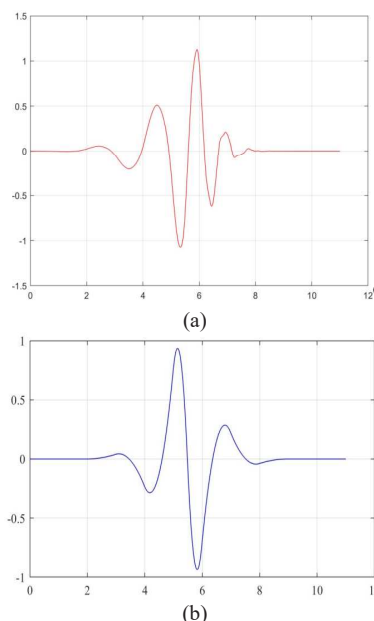


Fig. 5. The mother wavelet in the analysis (a) db6 (b) bior3.5.

i.e., Daubechies 6 (db6) and Biorthogonal 3.5 (bior3.5). Fig. 7 shows those two wavelet functions.

The implementation of DWT with Daubechies 6 in level 3 decomposes the signal into detail and approximation, as depicted in Fig. 8. Then, each element's signal reconstruction is applied to find the peak in the theoretical position of first-order Bragg peaks. Fig. 8 shows the magnification of the reconstruction signal. The reconstructed signal observation shows that the appropriate peak is detected in the level 3 detail reconstruction, concluding the wavelet function's properness for the determined purpose. Similar results were also found for the

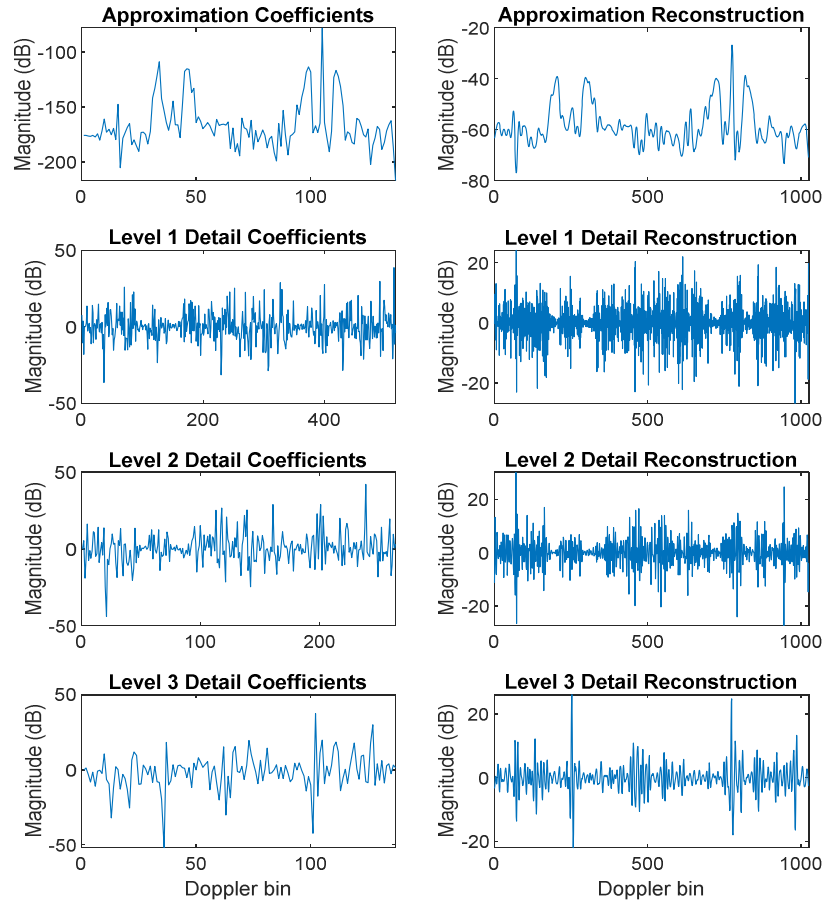


Fig. 9. Signal decomposition with mother Wavelet db6 in DWT level 3.

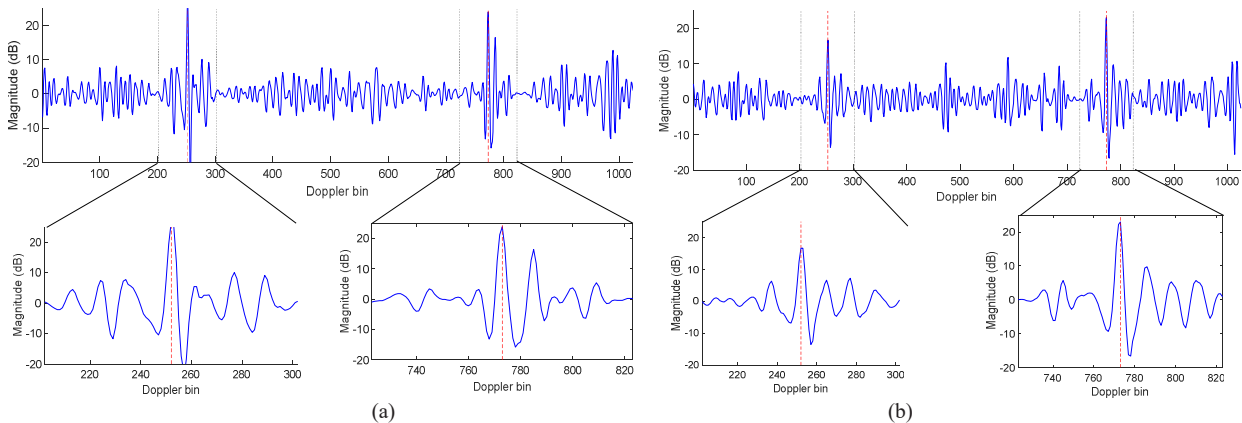


Fig. 8. Peak detection of first order Bragg peak with mother wavelet (a) Daubechies-6 (b) Biorthogonal 3.5.

mother wavelet Biorthogonal 3.5, although it is not shown here due to paper length limitation.

The appropriateness of the mother wavelet function is applied in the radar signal which contains interference close to the Bragg peak position. The example of analyzed signal is shown in Fig. 9. The use of simulated data brings an advantage of easy adjustment of amplitude and position of interference in the Doppler spectra. The analyzed interference in Fig. 9 is set to lie in the closely position to Bragg peaks with higher amplitude.

Following the previous decomposition process and first-order Bragg peak detection is applied on the signal with interference. The information of first-order Bragg peak is contained in level 3 detail components. The results are shown in Fig. 10.

V. CONCLUSIONS

This paper proposed the discrete wavelet transform to detect the first-order Bragg peak on the Doppler spectra of the HFSWR signal. The results show that the Daubechies 6 and Biorthogonal 3.5 are suitable mother wavelet functions

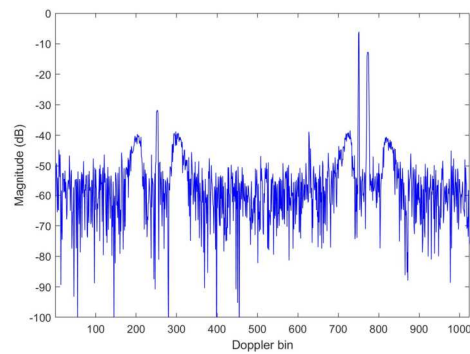


Fig. 11. The doppler spectra of radar HF with interference near the first-order Bragg peak.

for this purpose. The appropriateness is also evaluated in the existence of an interference signal near the Bragg peak component in the Doppler spectra of the radar receiving signal. This proposed method can avoid the misdetection of Bragg peaks position, which can cause the error estimation on the HFSWR as oceanographic radar.

ACKNOWLEDGMENT

This paper publication is financially supported by RTA Grant from Universitas Gadjah Mada awarded to Dr. Risanuri Hidayat with contract number 5075/UN1.P.II/Dit-Lit/PT.01.01/2023.

REFERENCES

- [1] S. Fujii *et al.*, "An overview of developments and applications of oceanographic radar networks in Asia and Oceania countries," *Ocean Science Journal*, vol. 48, no. 1, pp. 69–97, 2013, doi: 10.1007/s12601-013-0007-0.
- [2] S. Grosdidier, P. Forget, Y. Barbin, and C. A. Guérin, "HF bistatic ocean doppler spectra: Simulation versus experimentation," *IEEE Transactions on Geoscience and Remote Sensing*, vol. 52, no. 4, pp. 2138–2148, 2014, doi: 10.1109/TGRS.2013.2258352.
- [3] R. L. Hardman, L. R. Wyatt, and C. C. Engleback, "Measuring the directional ocean spectrum from simulated bistatic HF radar data," *Remote Sensing*, vol. 12, no. 2, pp. 1–28, 2020, doi: 10.3390/rs12020313.
- [4] J. Walsh, W. Huang, and E. W. Gill, "An analytical model for HF radar ionospheric clutter," *IEEE Antennas and Propagation Society, AP-S International Symposium (Digest)*, vol. 1, no. 4, pp. 1974–1975, 2013, doi: 10.1109/APS.2013.6711645.
- [5] Z. Chen, F. Xie, C. Zhao, and C. He, "Radio Frequency Interference Mitigation in High-Frequency Surface Wave Radar Based on CEMD," *IEEE Geoscience and Remote Sensing Letters*, vol. 15, no. 7, pp. 764–768, 2017, doi: 10.1109/LGRS.2018.2828990.
- [6] K. E. Laws, J. F. Vesecky, M. N. Lovellette, and J. D. Paduan, "Ship tracking by HF radar in coastal waters," *OCEANS 2016 MTS/IEEE Monterey, OCE 2016*, 2016, doi: 10.1109/OCEANS.2016.7761012.
- [7] G. Ramesh, D. Satyanarayana, and M. Sailaja, "ECG signal enhancement through subband adaptive soft thresholding and EMD for efficient Cardiac Arrhythmia Analysis," *International Journal of Intelligent Engineering and Systems*, vol. 11, no. 5, pp. 36–47, 2018, doi: 10.22266/IJIES2018.1031.04.

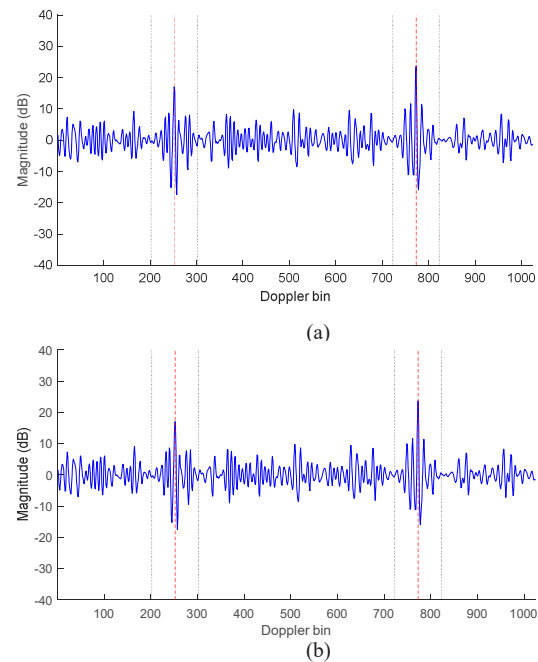


Fig. 10. The peak detection on the existing of interference near the Bragg-peak position with wavelet (a) db-6 (b) bior 3.5.

- [8] F. Jangal, S. Saillant, and M. Hélier, "Wavelet contribution to remote sensing of the sea and target detection for a high-frequency surface wave radar," *IEEE Geoscience and Remote Sensing Letters*, vol. 5, no. 3, pp. 552–556, 2008, doi: 10.1109/LGRS.2008.923211.
- [9] Q. Li, W. Zhang, M. Li, J. Niu, and Q. M. J. Wu, "Automatic Detection of Ship Targets Based on Wavelet Transform for HF Surface Wavelet Radar," *IEEE Geoscience and Remote Sensing Letters*, vol. 14, no. 5, pp. 714–718, 2017, doi: 10.1109/LGRS.2017.2673806.
- [10] B. Lu, B. Wen, Y. Tian, and R. Wang, "A Vessel Detection Method Using Compact-Array HF Radar," *IEEE Geoscience and Remote Sensing Letters*, vol. 14, no. 11, pp. 2017–2021, 2017, doi: 10.1109/LGRS.2017.2748142.
- [11] Y. Su, Y. Wei, R. Xu, and Y. Liu, "Ionospheric clutter suppression using Wavelet Oblique Projecting Filter," in *IEEE Radar Conference 2017 (RadarConf)*, 2017, pp. 1552–1556. doi: 10.1109/RADAR.2017.7944454.
- [12] L. R. Wyatt and Wei Wang, "Wavelet and independent component analysis of Doppler spectrum for higher validity of sea sensing by HF radar," in *IET International Conference on Radar Systems (Radar 2012)*, 2012, vol. 1, pp. 45–45. doi: 10.1049/cp.2012.1727.
- [13] J. Walsh, J. Zhang, and E. W. Gill, "High-frequency radar cross section of the ocean surface for an FMCW waveform," *IEEE Journal of Oceanic Engineering*, vol. 36, no. 4, pp. 615–626, 2011, doi: 10.1109/JOE.2011.2161706.
- [14] Iswandi, R. Hidayat, and S. B. Wibowo, "Simulation of Signal Processing for Ship Detection on Two Overlapping HF Radars with FMCW Waveforms," *ICITEE 2020 - Proceedings of the 12th International Conference on Information Technology and Electrical Engineering*, pp. 39–44, 2020, doi: 10.1109/ICITEE49829.2020.9271698.

Non-Uniform Metasurface-Based Omnidirectional Patch Antenna Using Characteristic Mode Analysis

Nathapat Supreeyatitikul¹

Aeronautical Engineering Division
Civil Aviation Training Center
Bangkok 10900, Thailand
nathapat@catc.or.th

Nonchanutt Chudpoo²

Department of Industrial Physics and
Medical Instrumentation,
Faculty of Applied Science,
King Mongkut's University of
Technology North Bangkok, Bangkok
10800, Thailand
nonchanutt.c@sci.kmutnb.ac.th

Chuwong Phongcharoenpanich³

School of Engineering
King Mongkut's Institute of
Technology Ladkrabang
Bangkok 10520, Thailand
chuwong.ph@kmitl.ac.th

Abstract— This paper proposes a non-uniform metasurface (MTS) omnidirectional patch antenna for WLAN applications. The antenna configuration is characterized by using characteristic mode analysis (CMA). The proposed non-uniform MTS-based patch antenna comprised a single-layer FR-4 substrate. Non-uniform square-shaped MTS unit cells were present in the upper-substrate layer. The lower-substrate layer is a circular-shaped ground plane. Besides, the excitation method of the proposed non-uniform MTS-based antenna is a single-probe-fed method. The use of a non-uniform square-shaped MTS structure achieved wide frequency resonance, resulting in wide impedance bandwidth. In addition, the circularly rotated direction of current distributions and magnetic fields on the non-uniform MTS structure can generate omnidirectional radiation by Mode 1 at 2.4 GHz (center frequency). The simulated IBW at 2.4 GHz is 26.67% (2.26 – 2.9 GHz). The optimum gain is 4.13 dBic at 2.8 GHz. The proposed antenna exhibits omni-directional radiation characteristics, making it well-suited for wireless communication applications.

Keywords—characteristic mode analysis, ground plane, metasurface, omnidirectional radiation, surface current distribution.

I. INTRODUCTION

In wireless communication systems, omnidirectional antennas are widely employed to ensure uniform signal coverage in all directions [1]. They are particularly useful in scenarios where the location or direction of the transmitter or receiver is not fixed or known in advance. The design of an omnidirectional antenna is based on achieving a symmetric radiation pattern that has consistent signal strength in all directions. Various antenna configurations can be used to achieve omnidirectional coverage, such as the monopole antenna, dipole antenna, and metasurface-based antenna.

Metasurface (MTS)-based antenna refers to an antenna design that incorporates a metasurface as an element [2]. A metasurface is a two-dimensional array of subwavelength-scale structures, typically arranged in a periodic pattern. These structures can manipulate the behavior of electromagnetic waves in a precise and controlled manner. By manipulating the properties of the metasurface elements, such as their shape, size, and orientation, the antenna performance can be tailored to specific requirements.

In [3], a patch antenna designed for C-band applications utilizes a 4×4 S-shaped MTS-based structure. This antenna achieves an impedance bandwidth (IBW) of 43.22% from 4.05 GHz to 6.6 GHz and an axial ratio bandwidth (ARBW) of 22% from 5.3 GHz to 6.6 GHz. In [4], an antenna array

consisting of four clusters with sequentially rotated MTS-based elements is developed for C-band satellite communications. This antenna achieves an IBW of 84.74% from 4 GHz to 9 GHz and an ARBW of 57.6% from 4.2 GHz to 7.6 GHz. In [5], a resonant cavity antenna for satellite communication is designed using a 9×9 Z-shaped MTS-based structure. It achieves an IBW of 64% from 4.4 GHz to 7.6 GHz and an ARBW of 18% from 4.4 GHz to 5.3 GHz.

Characteristic mode analysis (CMA) is a technique used in electromagnetic field analysis to study the resonant behavior and radiation characteristics of complex structures (i.e., antennas) [6]. The concept is based on the idea that any perfect electric conductor (PEC) structure can be expressed as a composite of its characteristic modes, which correspond to its fundamental resonant modes [7]. By determining the characteristic modes and their associated frequencies, current distributions, electric fields, and radiation field, CMA provides insights into the resonant behavior and radiation properties of the antenna structure [8].

In [9], an octagonal-ring slot antenna array designed for S-band applications utilizes a CMA-based four-element broadband CP configuration. This antenna achieves an IBW of 91.6% from 1.8 GHz to 4 GHz and ARBW of 84.5% from 1.97 GHz to 4 GHz. On the other hand, a stacked-patch antenna array for 5G wireless systems is described, which employs a CMA-based four-cluster leaf-shaped MTS-based structure. This antenna array achieves an IBW of 62.5% from 3.4 GHz to 5.9 GHz and an ARBW of 21% from 3.8 GHz to 4.54 GHz, as reported in [10]. However, those CMA-based antennas have not been made for omnidirectional radiation.

This research proposes non-uniform MTS omnidirectional patch antenna for Wi-Fi applications. The design process of this antenna involves the utilization of CMA to optimize the non-uniform MTS structure. The proposed non-uniform MTS omnidirectional patch antenna included circular-shaped substrate: upper layer and lower layer. The upper substrate is comprised of uniformly square-shaped MTS unit cells, while the lower substrate serves as a circular-shaped ground plane. The CST Microwave Studio Suite is utilized to conduct simulations, focusing on key antenna performance parameters such as IBW, realized gain, and radiation pattern.

II. ANTENNA DESIGN

A. Characteristic mode analysis

Characteristic mode analysis (CMA) is employed to define the antennas development [11]. CMA involves the use of surface current distributions and far-field radiation patterns to

accurately describe the properties of the antenna, including its PEC structures and radiation characteristics. Additionally, the external source determines the current and radiation associated with the electric field [12]. The modal significance modes (MS) play a crucial role in the frequency resonances.

To achieve frequency resonance and omnidirectional radiation, the modal significance (MS) to greater than a value of 0.707 ($MS \geq 0.707$). The MS values of the modes can be calculated using equation (1) [13]. Besides, the surface current distribution and modal magnetic field must be traveled circularly rotated direction on the surface of the antenna [14].

$$MS = \left| \frac{1}{1 + j\lambda_n} \right| \quad (1)$$

where λ_n is the eigen values, given $\lambda_n = 0$ (resonant stage) and n^{th} is mode numbers.

B. CMA-based non-uniform MTS structure

Fig. 1(a) shows geometry of the MTS-FIRST structure. The substrate is lossless FR-4 type with 4.8 mm in thickness and 140 mm in diameter. The upper-substrate layer consisted of 2×2 MTS unit cells ($26 \text{ mm} \times 26 \text{ mm}$). In Fig. 1(b), the MS results ($MS \geq 0.707$) of Modes 1 – 6 are 1 at 2.38 GHz, 2.1 GHz, 2.1 GHz, 2.5 GHz, 2.53 GHz, and 2.45 GHz. Therefore, the MTS-FIRST structure achieved frequency resonance between 2.1 – 2.53 GHz. Fig. 2(a) shows the geometry of the MTS-SECOND structure. The MTS-SECOND structure comprised of 12 MTS unit cells ($20 \text{ mm} \times 20 \text{ mm}$). In Fig. 2(b), the MS results ($MS \geq 0.707$) of Modes 1 – 6 are 1 at 3 GHz, 2.99 GHz, 3 GHz, 2.9 GHz, 2.9 GHz, and 2.97 GHz. Thus, the MTS-SECOND structure achieved frequency resonance between 2.97 – 3 GHz. Fig. 3(a) shows the configuration of the proposed non-uniform square-shaped MTS structure. The non-uniform MTS structure consisted of MTS-FIRST structure and MTS-SECOND structure. In Fig. 3(b), the MS results ($MS \geq 0.707$) of the proposed non-uniform MTS structure of Mode 1 – 6 are 1 at 2.4 GHz, 2.44 GHz, 2.41 GHz, 2.33 GHz, 2.78 GHz, and 2.78 GHz. As a result, the proposed non-uniform MTS structure achieved wide frequency resonance between 2.33 – 2.78 GHz.

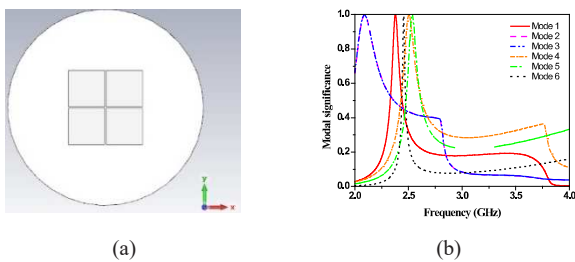


Fig. 1. MTS-FIRST structure: (a) geometry, (b) MS result.

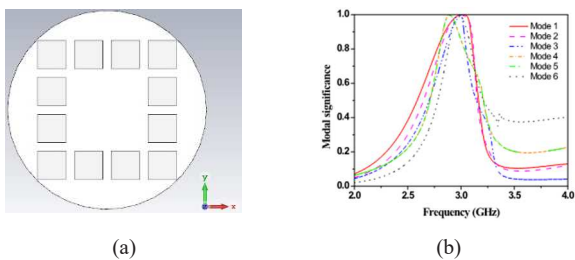


Fig. 2. MTS-SECOND structure: (a) geometry, (b) MS result.

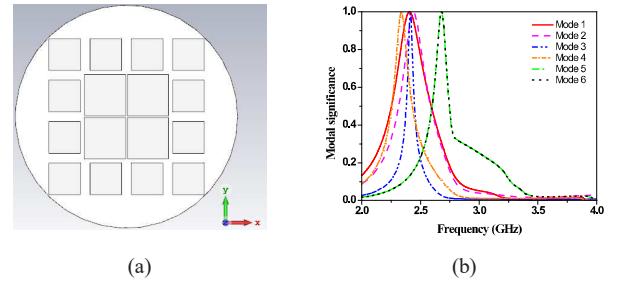
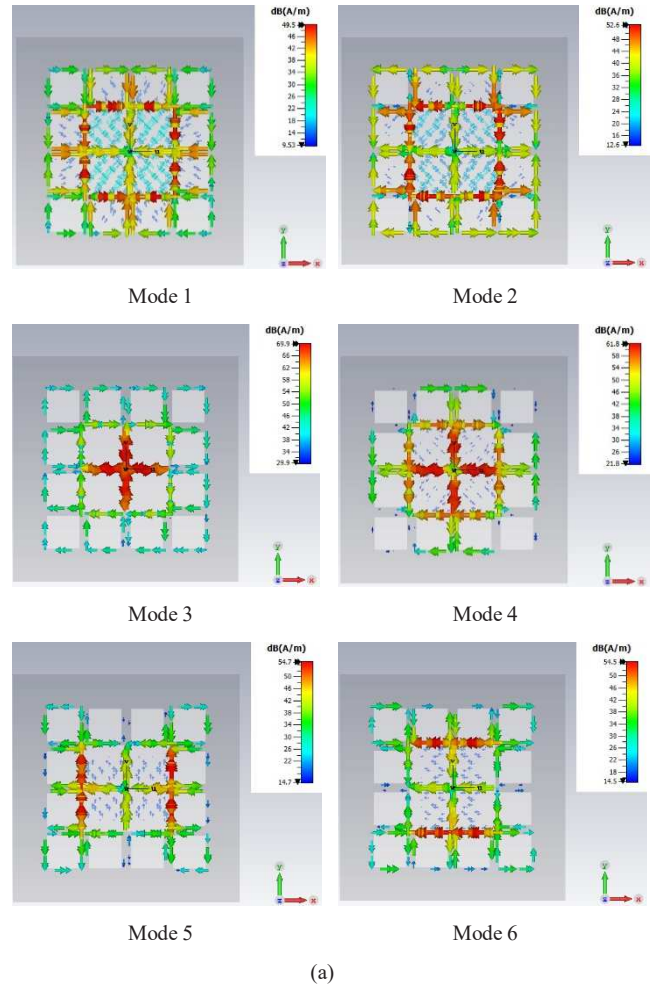


Fig. 3. Non-uniform MTS structure: (a) geometry, (b) MS result.

The surface current distribution, far-field radiation pattern, and modal magnetic field at 2.4 GHz of the proposed non-uniform MTS structure are used to characterize omnidirectional patterns. In Fig. 4(a), the surface current distributions of Modes 1 and 2 are concentrated at the center of MTS unit cells. Meanwhile, current distribution (Mode 3 – 6) traveled along the edge of the MTS unit cells. Thus, Modes 1 and 2 could be omnidirectional patterns. In Fig. 4(b), the far-field radiation patterns of Mode 1 and 3 are symmetry-lobe radiation, which is most likely an omnidirectional pattern. Moreover, the modal magnetic field is further verified to characterize the omnidirectional pattern. In Fig. 4(c), the modal magnetic field of Mode 1 traveled in a circularly rotated direction at the center of MTS unit cells. As a result, the non-uniform MTS structure can be achieved by an omnidirectional pattern by Mode 1 at the center frequency (2.4 GHz).



(a)

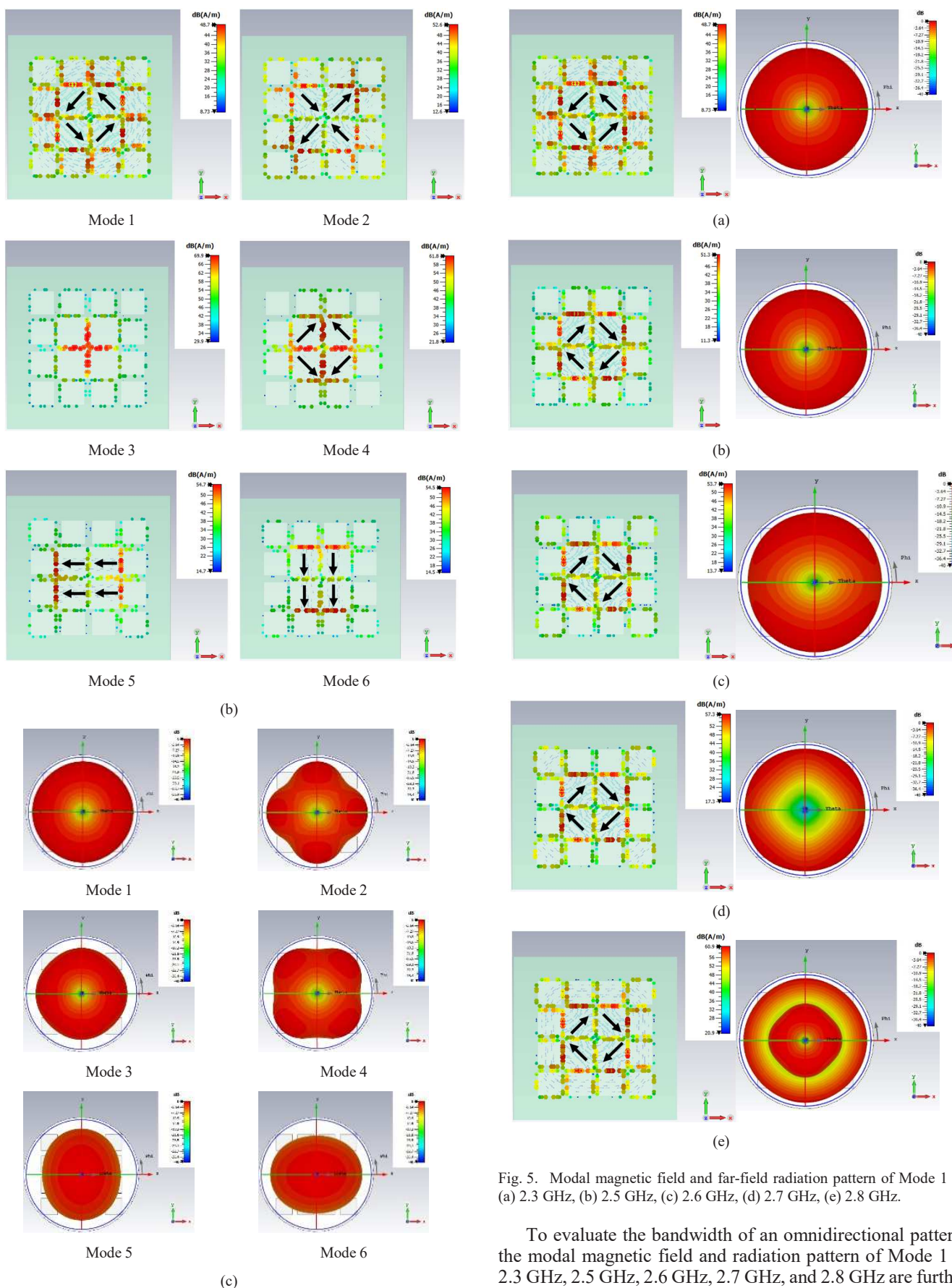


Fig. 4. Simulated results of non-uniform MTS structure at 2.4 GHz: (a) surface current distribution, (b) modal magnetic field, (c) far-field radiation pattern.

Fig. 5. Modal magnetic field and far-field radiation pattern of Mode 1 at: (a) 2.3 GHz, (b) 2.5 GHz, (c) 2.6 GHz, (d) 2.7 GHz, (e) 2.8 GHz.

To evaluate the bandwidth of an omnidirectional pattern, the modal magnetic field and radiation pattern of Mode 1 at 2.3 GHz, 2.5 GHz, 2.6 GHz, 2.7 GHz, and 2.8 GHz are further investigated. Fig. 5(a-e), the magnetic fields are the circularly rotated direction at the center of MTS unit cells. The far-field radiation pattern is likely an omnidirectional pattern.

To excite the non-uniform MTS structure, a single-probe feed is linked to the circular-shaped ground plane, positioned beneath the center of the MTS structure. The configuration of the CMA-based non-uniform MTS-based omnidirectional patch antenna is depicted in Figure 6(a)-(b).

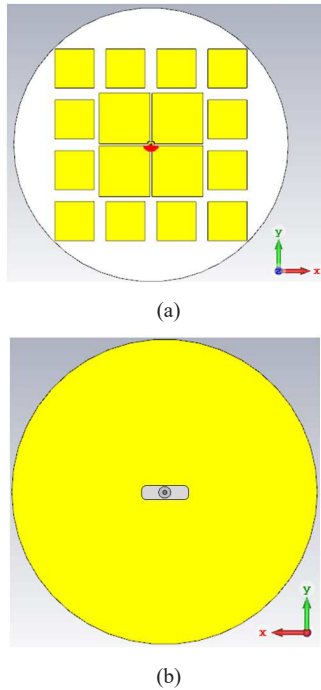


Fig. 6. Configuration of the proposed the proposed non-uniform MTS-based omnidirectional patch antenna: (a) front view, (b) rear view.

III. RESULTS AND DISCUSSION

The antenna performance is analyzed through simulations conducted by the CST Microwave Studio Suite. The essential parameters used to analyze the antenna performance include IBW ($|S_{11}|$), realized gain, and radiation pattern. Fig. 7 shows simulated IBW ($|S_{11}| \leq -10$ dB) of the proposed non-uniform square-shaped MTS omnidirectional patch antenna and realized gain. The simulated IBW is 26.67% between 2.26 – 2.9 GHz, and the optimum gain is 4.13 dBic at 2.8 GHz. Fig. 8(a)-(f) respectively show the normalized radiation patterns of the proposed non-uniform square-shaped MTS omnidirectional patch antenna at 2.3 GHz, 2.4 GHz, 2.5 GHz, 2.6 GHz, 2.7 GHz, and 2.8 GHz.

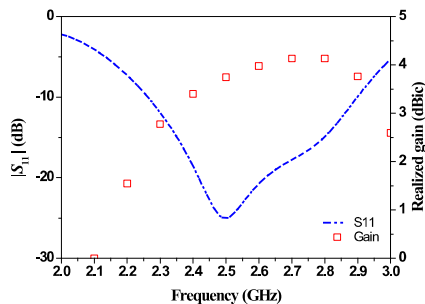


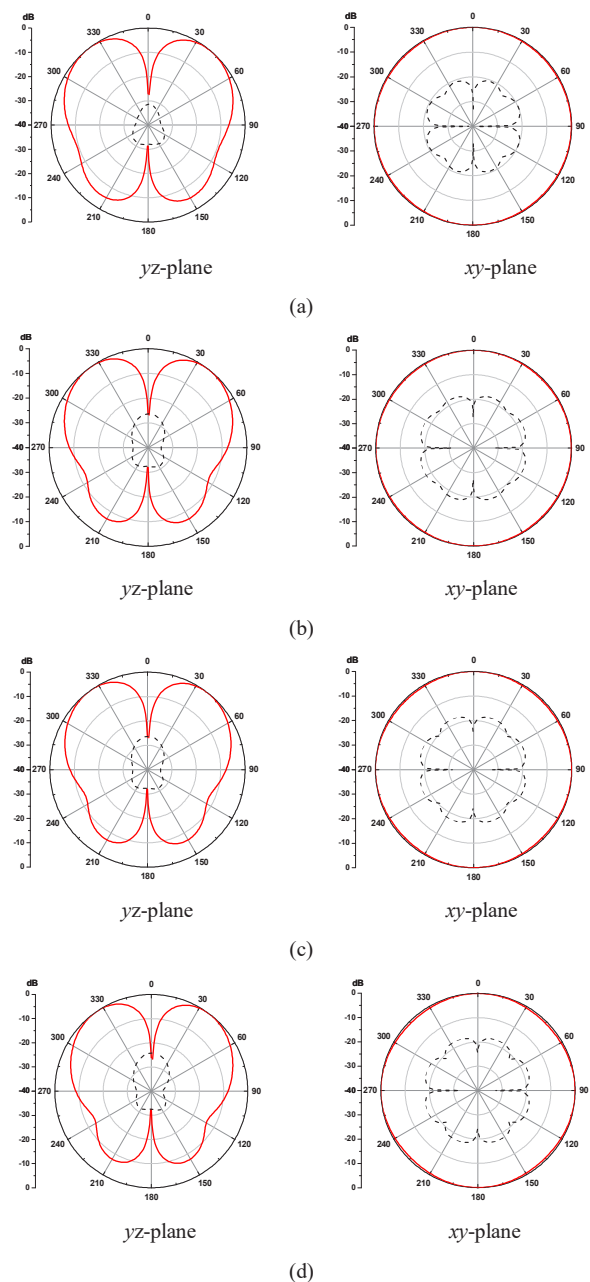
Fig. 7. Simulated IBW and realized gain results.

The radiation patterns demonstrate that the proposed non-uniform MTS patch antenna is omnidirectional radiation between 2.3 – 2.8 GHz for wireless applications. Table I

composes the simulation results comparison between the related omnidirectional patch antenna and the proposed non-uniform square-shaped MTS omnidirectional patch antenna.

TABLE I. COMPARISON BETWEEN THE RELATED OMNIDIRECTIONAL PATCH ANTENNA AND THE PROPOSED NON-UNIFORM MTS OMNIDIRECTIONAL PATCH ANTENNA

| Reference | f_c (GHz) | IBW (%) | Optimum gain (dBic) | dimension (λ_0) |
|------------------|-------------|--------------|---------------------|--|
| [15] | 4.5 | 8.9 | 6 | Diameter = 1.48 thickness = 0.030 |
| [16] | 5.2 | 16.6 | 1.8 | Diameter = 1.13 thickness = 0.060 |
| [17] | 0.915 | 5.46 | 0.65 | Diameter = 1.13 thickness = 0.078 |
| [18] | 4.1 | 21.4 | 7.8 | Diameter = 1.09 thickness = 0.027 |
| This work | 2.4 | 26.67 | 4.13 | Diameter = 1.12 thickness = 0.038 |



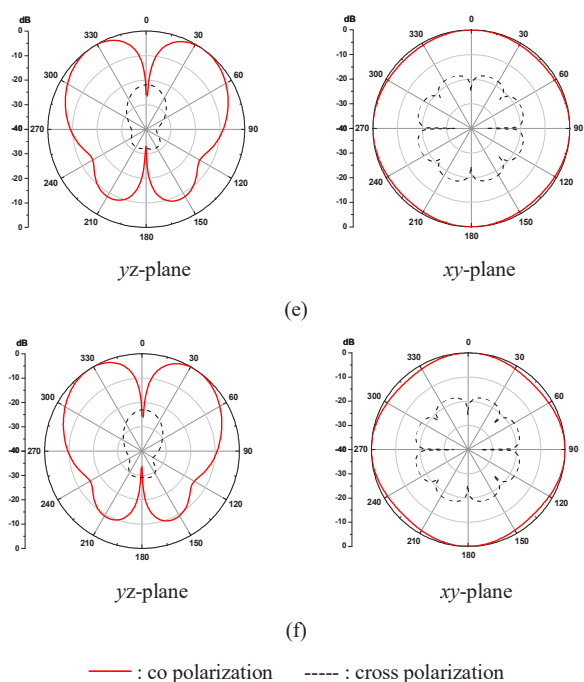


Fig. 8. Radiation pattern at: (a) 2.3 GHz, (b) 2.4 GHz, (c) 2.5 GHz, (d) 2.6 GHz, (e) 2.7 GHz, (f) 2.8 GHz.

IV. CONCLUSION

This paper proposes a non-uniform MTS-based omnidirectional patch antenna for WLAN applications. The CMA is applied to realize the antenna configuration and achieve omnidirectional radiation in the proposed non-uniform MTS patch antenna. The proposed MTS-based patch omnidirectional antenna consisted of 16 non-uniform MTS unit cells and circular-shaped ground plane. In CMA results, Mode 1 of the non-uniform square-shaped MTS structure can be achieved the omnidirectional radiation between 2.3 – 2.8 GHz. Furthermore, the surface current distribution and modal magnetic field on the surface of non-uniform MTS are used to verify the omnidirectional radiation. The simulated IBW achieved 26.67% between 2.26 – 2.9 GHz. The optimum gain is 4.13 dBic at 2.8 GHz. The radiation pattern of the proposed non-uniform MTS-based omnidirectional patch antenna is omnidirectional characteristic, which is functional for wireless communications.

V. ACKNOWLEDGMENT

This research was funded by National Science, Research and Innovation Fund (NSRF), and King Mongkut's University of Technology North Bangkok with Contract no. KMUTNB-FF-67-B-16.

REFERENCES

- [1] S. Liu, D. Yang, Y. Chen, X. Zhang and Y. Xiang, "Compatible Integration of Circularly Polarized Omnidirectional Metasurface Antenna With Solar Cells," *IEEE Transactions on Antennas and Propagation*, vol. 68, no. 5, pp. 4155-4160, May 2020.
- [2] K. Iqbal and Q. U. Khan, "Review of Metasurfaces Through Unit Cell Design and Numerical Extraction of Parameters and Their Applications in Antennas," *IEEE Access*, vol. 10, pp. 112368-112391, 2022.
- [3] N. Supreeyattikul, T. Lertwiriayaprapa and C. Phongcharoenpanich, "S-Shaped Metasurface-Based Wideband Circularly Polarized Patch Antenna for C-Band Applications," *IEEE Access*, vol. 9, pp. 23944-23955, 2021.
- [4] N. Supreeyattikul, D. Torrungrueng and C. Phongcharoenpanich, "Quadri-Cluster Broadband Circularly-Polarized Sequentially-Rotated Metasurface-Based Antenna Array for C-Band Satellite Communications," *IEEE Access*, vol. 9, pp. 67015-67027, Apr. 2021.
- [5] N. Supreeyattikul, A. Boonpoonga and C. Phongcharoenpanich, "Z-Shaped Metasurface-Based Wideband Circularly Polarized Fabry-Pérot Antenna for C-Band Satellite Technology," *IEEE Access*, vol. 10, pp. 59428-59441, 2022.
- [6] J. J. Adams, S. Genovesi, B. Yang and E. Antonino-Daviu, "Antenna Element Design Using Characteristic Mode Analysis: Insights and research directions," *IEEE Antennas and Propagation Magazine*, vol. 64, no. 2, pp. 32-40, April 2022.
- [7] B. B. Q. Elias, P. J. Soh, A. A. Al-Hadi, P. Akkaraekthalin and G. A. E. Vandenbosch, "A Review of Antenna Analysis Using Characteristic Modes," *IEEE Access*, vol. 9, pp. 98833-98862, 2021.
- [8] X. Gao, G. Tian, Z. Shou and S. Li, "A Low-Profile Broadband Circularly Polarized Patch Antenna Based on Characteristic Mode Analysis," *IEEE Antennas and Wireless Propagation Letters*, vol. 20, no. 2, pp. 214-218, Feb. 2021.
- [9] N. Supreeyattikul, P. Janpangngern, T. Lertwiriayaprapa, M. Krairiksh and C. Phongcharoenpanich, "CMA-Based Quadruple-Cluster Leaf-Shaped Metasurface-Based Wideband Circularly-Polarized Stacked-Patch Antenna Array for Sub-6 GHz 5G Applications," *IEEE Access*, vol. 11, pp. 14511-14523, 2023.
- [10] N. Supreeyattikul, T. Lertwiriayaprapa, M. Krairiksh and C. Phongcharoenpanich, "CMA-Based Four-Element Broadband Circularly Polarized Octagonal-Ring Slot Antenna Array for S-Band Satellite Applications," *IEEE Access*, vol. 10, pp. 130825-130838, 2022.
- [11] S. Liu, D. Yang and J. Pan, "A Low-Profile Broadband Dual-Circularly-Polarized Metasurface Antenna," *IEEE Antennas and Wireless Propagation Letters*, vol. 18, no. 7, pp. 1395-1399, July 2019.
- [12] A. El Yousfi, A. Lamkaddem, K. A. Abdalmalak and D. Segovia-Vargas, "A Broadband Circularly Polarized Single-Layer Metasurface Antenna Using Characteristic-Mode Analysis," *IEEE Transactions on Antennas and Propagation*, vol. 71, no. 4, pp. 3114-3122, April 2023.
- [13] S. Genovesi and F. A. Dicandia, "Characteristic Modes Analysis of a Near-Field Polarization-Conversion Metasurface for the Design of a Wideband Circularly Polarized X-Band Antenna," *IEEE Access*, vol. 10, pp. 88932-88940, 2022.
- [14] T. Li and Z. N. Chen, "A Dual-Band Metasurface Antenna Using Characteristic Mode Analysis," *IEEE Transactions on Antennas and Propagation*, vol. 66, no. 10, pp. 5620-5624, Oct. 2018.
- [15] T. L. Wu, Y. M. Pan, P. F. Hu and S. Y. Zheng, "Design of a Low Profile and Compact Omnidirectional Filtering Patch Antenna," *IEEE Access*, vol. 5, pp. 1083-1089, 2017.
- [16] X. Yang, Y. Liu and S. -X. Gong, "Design of a Wideband Omnidirectional Antenna With Characteristic Mode Analysis," *IEEE Antennas and Wireless Propagation Letters*, vol. 17, no. 6, pp. 993-997, June 2018.
- [17] J. E. Diener and A. Z. Elsherbeni, "Miniaturized Omnidirectional UHF RFID Antennas," *2019 International Applied Computational Electromagnetics Society Symposium (ACES)*, Miami, FL, USA, 2019, pp. 1-2.
- [18] T. L. Wu, Y. M. Pan and P. F. Hu, "Wideband Omnidirectional Slotted Patch Antenna With Filtering Response," *IEEE Access*, vol. 5, pp. 26015-26021, 2017.

Compact Broadband Circularly Polarized Metasurface Antenna with Split-Annular Slot Ground Structure

Nathapat Supreeyatitikul¹
Aeronautical Engineering Division
Civil Aviation Training Center
Bangkok 10900, Thailand
nathapat@catc.or.th

Nonchanutt Chudpoo²
Department of Industrial Physics and
Medical Instrumentation,
Faculty of Applied Science,
King Mongkut's University of
Technology North Bangkok, Bangkok
10800, Thailand
nonchanutt.c@sci.kmutnb.ac.th

Chuwong Phongcharoenpanich³
School of Engineering
King Mongkut's Institute of
Technology Ladkrabang
Bangkok 10520, Thailand
chuwong.ph@kmitl.ac.th

Abstract— This paper presents a broadband CP MTS-inspired antenna with split-annular slot ground structure. The CP radiation and antenna configuration are deployed characteristic mode analysis (CMA). The proposed CP MTS-inspired antenna with split-annular slot ground structure comprised of upper substrate and lower substrate. The upper substrate consisted of 5×5 uniformly MTS unit cells, and the split-annular slot ground plane and microstrip feed line are included on the lower substrate. In CMA results, the 5×5 MTS-inspired unit cells generated CP radiation by Modes 1 and 2. Besides, the split-annular slot ground structure can be produced two orthogonal electric fields at the center frequency of 5 GHz by Modes 3 and 5 for excitation source. This proposed antenna achieved simulated IBW of 59.4% (3.57 – 6.55 GHz), and simulated ARBW of 24.22% (4.43 – 5.64 GHz). The maximum gain at 4.7 GHz is 5.72 dBic, which has RHCP characteristic radiation. The proposed antenna is appropriate functionally for C-band wireless applications.

Keywords— Characteristic mode analysis, circular polarization, MTS-inspired antenna, RHCP, split-annular slot.

I. INTRODUCTION

Circularly polarized (CP) antennas have garnered essential attention due to their potentiality to mitigate multipath fading, enhance signal robustness, and support polarization diversity in wireless communication systems [1]. The CP radiation aims to provide an in-depth understanding of circularly polarized antennas and their impact on modern communication technologies. CP antennas have emerged as a promising solution to overcome limitations associated with linearly polarized antennas. By generating rotating electric fields, circularly polarized antennas offer numerous benefits, including improved signal propagation, enhanced link stability, and compatibility with diverse applications [2]. For examples include satellite communication systems, wireless sensor networks, radio frequency identification (RFID) systems, global navigation satellite systems (GNSS), and unmanned aerial vehicles (UAVs) [3].

Several antenna types aim to develop a CP antenna with wide CP bandwidth (i.e., axial ratio bandwidth or ARBW) such as helix antenna [4], dipole antenna [5], dielectric resonator antenna [6], spiral antenna [7], and patch antenna [8]. Due to the complex antenna structure in [3]–[6], the patch antenna type is a good candidate for a wideband CP antenna because of its compact size and ease of design. On the other hand, the disadvantages of the patch antenna are suffered from low gain and narrow bandwidth (i.e., impedance bandwidth or IBW). Accordingly, a metasurface (MTS) structure is adopted to compose in front of a patch antenna to function as

bandwidth and gain enhancement. The MTS structure is a two-dimensional arrangement of subwavelength-scale structures or elements that manipulate the propagation of electromagnetic waves [9]. Furthermore, the MTS structure can be used to control the phase, polarization, and amplitude of incident electromagnetic waves as a circular polarizer [10].

To develop a broadband CP MTS-inspired antenna, the characteristic mode analysis (CMA) is effectively deployed to characterize the CP radiation. The CMA method is a technique used in electromagnetic field theory and antenna engineering to analyze and understand the behavior of complex structures [11]. The CMA can assist in various aspects of antenna, such as reducing interference, optimizing radiation efficiency, improving bandwidth, and understanding the effects of surrounding structures. This technique is a powerful tool for predicting and understanding the behavior of complex electromagnetic systems and has found applications in fields like wireless communication, radar systems, satellite technology [12].

In this research, CMA-based broadband CP MTS-inspired antenna with split-annular slot ground structure is proposed for C-band wireless communication systems and described the use of the CMA concept to develop the proposed antenna. The proposed antenna comprised of double-layer FR-4 substrates. The upper substrate included 5×5 uniformly square-shaped MTS unit cells. The lower substrate is composed of a split-annular slot ground plane and a microstrip feed line. In mechanism operation, the split-annular slot ground structure generated the 90° phase difference between two modes at center frequency (5 GHz). Those modes excited the symmetric-lobe radiation of the 5×5 MTS unit cells, resulting in CP radiation.

II. ANTENNA DESIGN

The procedure design of the CMA-based CP MTS-inspired antenna with split-annular slot ground structure consisted of two stages: (i) MTS-inspired model and (ii) split-annular slot ground plane (feed structure). Furthermore, those design processes used the CMA to characterize the antenna structures. The first stage, the 5×5 uniformly square-shaped MTS unit cells are located on the lossless FR-4 upper substrate. The square-shaped MTS unit cells are $7.5 \text{ mm} \times 7.5 \text{ mm}$ in dimension with 0.5 mm in voids. The FR-4 substrate is $40 \text{ mm} \times 40 \text{ mm}$ in dimension, and 3.2 mm in thickness. The second stage, the split-annular slot sits on lower substrate, functioning as a ground plane. The microstrip line functioned as a feed network. The thickness of the lower substrate is 0.8 mm .

In CMA theory, the resonance frequency of the PEC structure could be generated when the modal significance (MS) must be 0.707. In other words, the MS could refer to how much each characteristic mode contributes to the overall behavior of the antenna. To realize CP radiation, the MS results at the center frequency of the two modes must be identical. Meanwhile, the symmetric lobe of the 3D radiation pattern between the two modes must be orthogonal. Furthermore, the intensive modal magnetic field of the MTS-inspired model should be verified for determining feed position. To further investigate the CP radiation, the characteristic angle ($CA = \pm 90^\circ$) between the identical MS mode of the two orthogonal modes. CA refers to an angle associated with the radiation pattern of an antenna structure characteristic modes. This is used to describe the orientation or directionality of the radiation pattern corresponding to identical two modes.

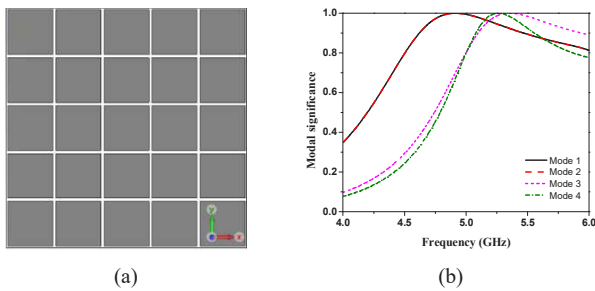


Fig. 1. The MTS model: (a) Structure, (b) MS result.

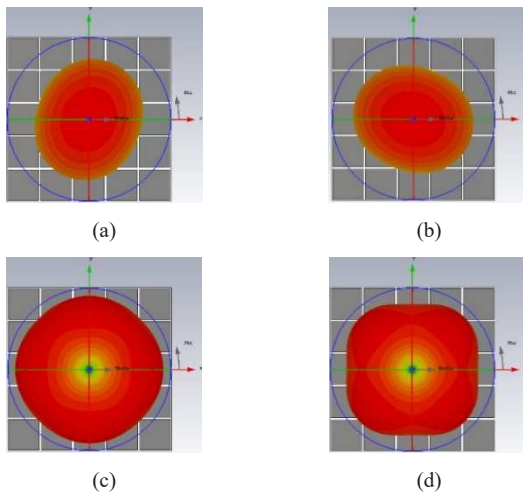


Fig. 2. 3D radiation pattern: (a) Mode 1, (b) Mode 2, (c) Mode 3, (d) Mode 4.

Fig. 1(a)-(b) show the configuration and MS results of the MTS model. In Fig. 1(b), the MS results ($MS \geq 0.707$) of Mode 1 – 4 are 1 at 5 GHz, 5 GHz, 5.25 GHz, 5.35 GHz, respectively. Thus, the proposed MTS model achieved the resonance frequency between 5 – 5.35 GHz. Fig. 2(a)-(d) show the 3D radiation pattern at 5 GHz (center frequency) of Modes 1 – 4. The radiation pattern between Mode 1 and 2 are orthogonal while the center of the main-lobe radiation of Modes 3 and 4 are null. As a result, Modes 1 and 2 of the proposed MTS model can radiate from the CP radiation.

Fig. 3(a)-(d) respectively show the modal magnetic field at 5 GHz of Modes 1 – 4. In Fig. 3(a)-(b), the magnetic field of Modes 1 and 2 are concentrated at the center of the proposed MTS model. Fig. 3(c)-(d), the magnetic fields of Modes 3 and 4 are collected at the lateral MTS model. Consequently, the feed position must be underneath the center of the proposed MTS model for exciting the CP radiation (Modes 1 and 2).

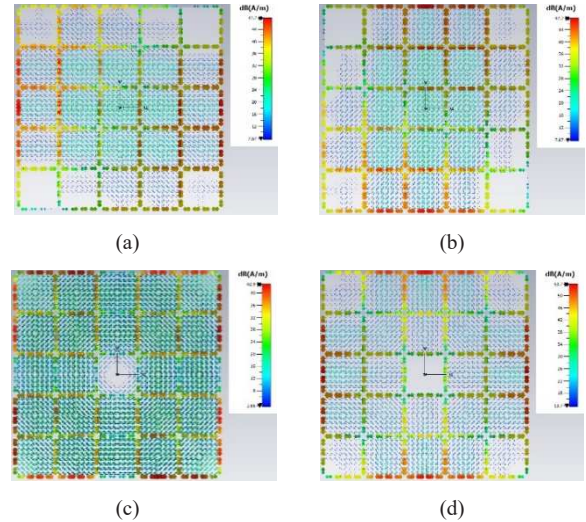


Fig. 3. Modal magnetic field: (a) Mode 1, (b) Mode 2, (c) Mode 3, (d) Mode 4.

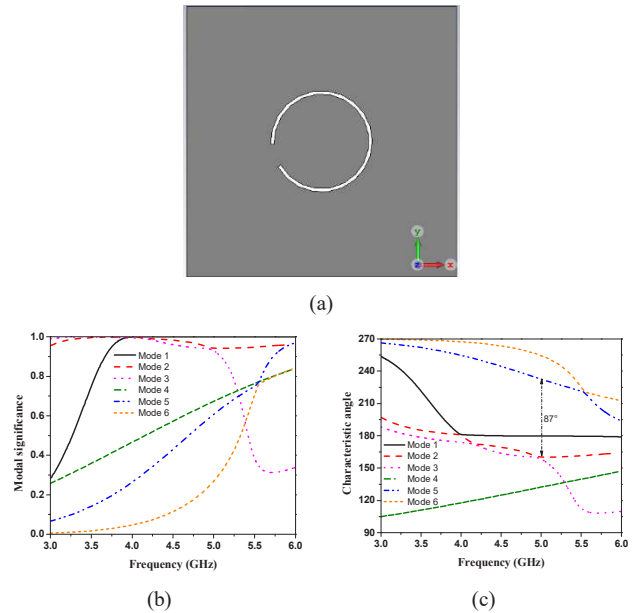


Fig. 4. Split-annular slot ground structure: (a) configuration, (b) MS results, (c) CA results.

Fig. 4(a)-(c) show the configuration, MS results, and CA results of the split-annular slot ground structure. The proposed split-annular slot ground plane on the lower substrate represented as a feed technique method (outer radius = 7.5 mm and inner radius = 7 mm). In Fig. 4(b), the MS results at 5.3 GHz of Modes 3 and 5 are identical (0.7). The CA ($CA = \pm 90^\circ$) of the proposed split-annular slot ground structure is further verified for generating the two orthogonal electric fields. In

Fig. 4(c), the CA results at 5.3 GHz of Modes 3 and 5 are 87° . As a result, Modes 3 and 5 can generate the two-orthogonal electric fields. In CMA results, the proposed split-annular slot must be positioned beneath the center of the proposed MTS-inspired model for wave excitation.

Fig. 5(a)-(b) show the geometry of the proposed CMA-based CP MTS-inspired antenna with split-annular slot ground plane. The upper layer included 5×5 square-shaped MTS unit cells. The lower substrate is composed of split-annular slot ground plane and microstrip feed line. The upper and lower substrates are assembled as a stacked patch antenna.

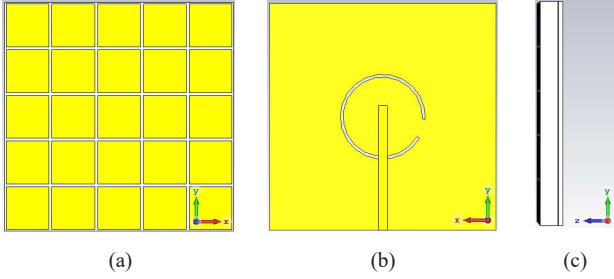


Fig. 5. The proposed antenna: (a) front view, (b) rear view, (c) side view.

III. RESULTS AND DISCUSSION

CST Microwave Studio Suite is utilized to carry out the simulation. The primary factors used to evaluate the performance of the antenna in terms of the following metrics: IBW ($|S_{11}|$), ARBW, realized gain, and radiation pattern. The wide IBW ($|S_{11}| \leq -10$ dB) indicates that the antenna can operate effectively over a broader range of frequencies without significant impedance mismatch or reflection issues. The ARBW (AR ≤ 3 dB) of an antenna refers to the range of frequencies over which the AR remains within a specified limit. This means that the circular polarization of the antenna remains close to being perfect (AR = 0 dB) within this frequency range. The realized gain of an antenna is a measure of its effectiveness in converting input power into radiated energy in a particular direction. The radiation pattern of an antenna is a 2D representation of how the radiated energy is distributed in space as the antenna is rotated or as electromagnetic waves are incident upon it. It shows the relative strength of the radiated field in different directions.

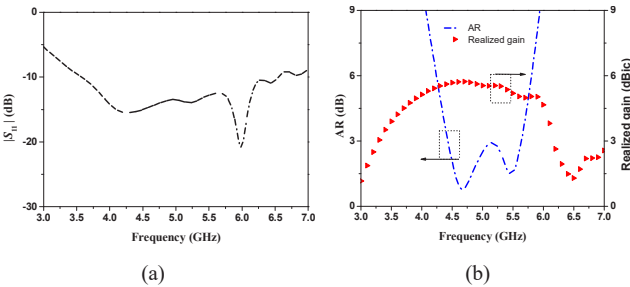


Fig. 6. Simulated results: (a) IBW (b) ARBW and realized gain.

Fig. 6(a)-(b) depicts simulated IBW, ARBW, and realized gain of the proposed CMA-based CP MTS-inspired antenna with split-annular slot ground structure. In Fig. 6(a), the

simulated IBW of the proposed CP MTS-inspired antenna with split-annular slot ground structure at 5 GHz (center frequency) is 59.4% between 3.57 – 6.55 GHz. In Fig. 6(b), the simulated ARBW and peak gain are 24.22% between 4.43 – 5.64 GHz, and 5.72 dBic at 4.7 GHz. Fig. 7(a)-(c) illustrates simulated radiation patterns at 4.5 GHz, 5 GHz, 5.5 GHz of the proposed CP MTS-inspired antenna with split-annular slot ground structure. The characteristic of radiation is unidirectional with RHCP.

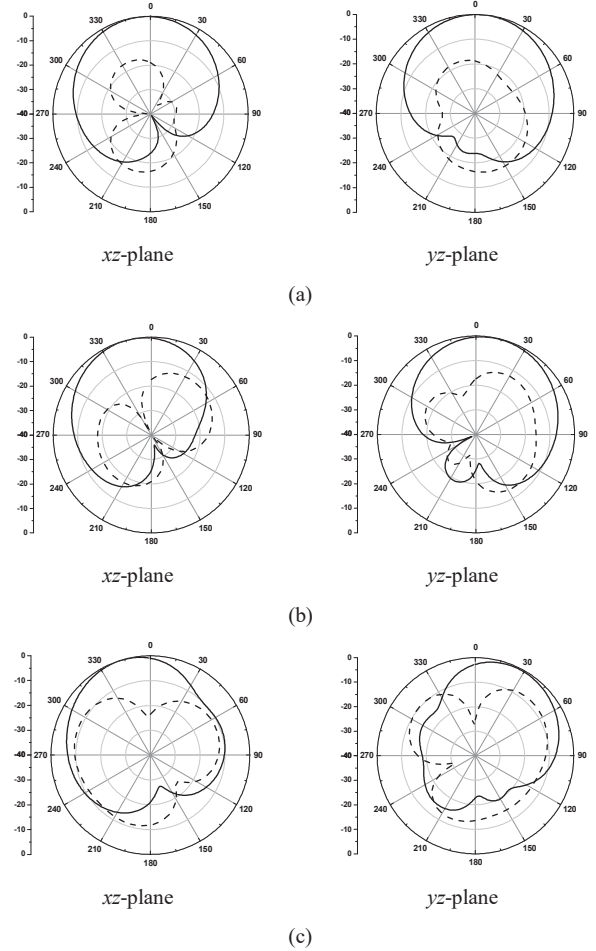


Fig. 7. Radiation pattern (— : RHCP and ---- : LHCP) of the proposed CP MTS-inspired antenna with split-annular slot ground structure at: (a) 4.5 GHz, (b) 5 GHz, (c) 5.5 GHz.

Table I presents the simulation results comparison among the recently related CP MTS antenna and the proposed CMA-based CP MTS antenna with split-annular slot ground structure. Those antennas compared antenna performance, including IBW, ARBW, peak gain, and electrical dimensions. Besides, the CP radiation techniques of each antenna are compared to attain a wide IBW and ARBW for the C-band spectrum (4 – 8 GHz).

In [13], a CP patch antenna with 4×4 MTS unit cells structure achieved 44.16% (3.9 – 6.11 GHz) of IBW and 20.35% (4.81 – 5.9 GHz) of ARBW. This antenna used the irregular-shaped MTS structure to realize the CP radiation. In [14], a high-gain CP antenna with a nut-shaped MTS structure achieved IBW (29.66%, 5.2 – 6.9 GHz) and ARBW (21.42%,

5.6 – 6.9 GHz). This antenna utilized the driven patch to cooperate with a parasitic element for bandwidth improvement.

In [15], a CP antenna with a gamma-shaped MTS structure is characterized by the CMA technique. The gamma-shaped MTS CP antenna achieved IBW of 30% (5.1 – 6.9) and ARBW of 17.3% (5.8 – 6.9 GHz). In [16], a low-profile CP patch antenna with 3×3 parallelogram-shaped MTS structure achieved 31.8% (5.2 – 7.13 GHz) of IBW and 18.8% (6 – 7.1 GHz) of ARBW. The CMA technique is used to realize the CP radiation for parallelogram-shaped MTS structures. In comparison, the proposed CMA-based CP MTS-inspired antenna with split-annular slot ground structure for the C-band frequency band achieved broadband IBW and ARBW.

TABLE I. SIMULATION RESULTS COMPARISON AMONG THE RECENTLY RELATED CP MTS-INSPIRED ANTENNA AND THE PROPOSED CMA-BASED CP MTS-INSPIRED ANTENNA WITH SPLIT-ANNULAR SLOT GROUND STRUCTURE

| Ref. | f_c (GHz) | IBW (%) | ARBW (%) | Peak gain (dBic) | dimension (λ_z) |
|------------------|-------------|-------------|--------------|------------------|---------------------------|
| [13] | 5 | 44.16 | 20.35 | 6 | 0.60×0.60×0.070 |
| [14] | 5.8 | 29.66 | 21.42 | 9.35 | 0.62×0.62×0.134 |
| [15] | 6.2 | 30 | 17.3 | 7.8 | 0.72×0.72×0.080 |
| [16] | 6 | 31.8 | 18.8 | 7.55 | 0.45×0.45×0.065 |
| This work | 5 | 59.4 | 24.22 | 5.72 | 0.67×0.67×0.060 |

IV. CONCLUSION

This paper proposes a broadband CP MTS-inspired antenna with split-annular slot ground structure for C-band wireless systems. CMA is used to realize the antenna configuration and CP radiation. The proposed CMA-based CP MTS-inspired antenna with split-annular slot ground structure is composed of upper and lower substrates. The upper substrate consisted of 5×5 MTS unit cells. The lower substrate comprised of split-annular slot ground plane and microstrip feed line. In CMA study, the proposed MTS-inspired model is realized the CP radiation by Modes 1 and 2. Moreover, the split-annular slot ground structure is characterized by Modes 3 and 5 for excitation source. The simulated IBW and ARBW at the center frequency of 5 GHz are 59.4% (3.57 – 6.55 GHz), 24.22% (4.43 – 5.64 GHz), and the peak gain is 5.72 dBic at 4.7 GHz. Further research will involve fabricating an antenna prototype and conducting experiments. In future works, a comparison and detailed explanation of the simulation and measurement results will be provided.

V. ACKNOWLEDGMENT

This research was funded by National Science, Research and Innovation Fund (NSRF), and King Mongkut's University of Technology North Bangkok with Contract no. KMUTNB-FF-67-B-16.

REFERENCES

- [1] N. Nasimuddin, Z. N. Chen and X. Qing, "Bandwidth Enhancement of a Single-Feed Circularly Polarized Antenna with a Metasurface: Metamaterial-inspired wideband CP rectangular microstrip antenna," *IEEE Antennas and Propagation Magazine*, vol. 58, no. 2, pp. 39-46, April 2016.
- [2] S. Gao, Q. Luo, F. Zhu, *Circularly Polarized Antennas*. Hoboken, NJ, USA: Wiley, 2014
- [3] N. Supreeyattitukul, N. Teerasuttakorn, P. Boontamchaay and M. Rattanasuttikan, "A Compact Printed Wideband Circularly Polarized Slot Antenna for Universal UHF RFID Reader," *2020 14th European Conference on Antennas and Propagation (EuCAP)*, Copenhagen, Denmark, 2020, pp. 1-5.
- [4] X. Bai, J. Tang, X. Liang, J. Geng and R. Jin, "Compact Design of Triple-Band Circularly Polarized Quadrifilar Helix Antennas," *IEEE Antennas and Wireless Propagation Letters*, vol. 13, pp. 380-383, 2014.
- [5] Y. Sun, Y. He, W. He, L. Zhang and S. -W. Wong, "A Wideband Circularly Polarized Cross-Dipole Antenna With L-shape Slots," *2020 IEEE International Symposium on Antennas and Propagation and North American Radio Science Meeting*, Montreal, QC, Canada, 2020, pp. 673-674.
- [6] L. Lu, Y. -C. Jiao, H. Zhang, R. Wang and T. Li, "Wideband Circularly Polarized Antenna With Stair-Shaped Dielectric Resonator and Open-Ended Slot Ground," *IEEE Antennas and Wireless Propagation Letters*, vol. 15, pp. 1755-1758, 2016.
- [7] Y. -W. Zhong, G. -M. Yang, J. -Y. Mo and L. -R. Zheng, "Compact Circularly Polarized Archimedean Spiral Antenna for Ultrawideband Communication Applications," *IEEE Antennas and Wireless Propagation Letters*, vol. 16, pp. 129-132, 2017.
- [8] Q. W. Lin, H. Wong, X. Y. Zhang and H. W. Lai, "Printed Meandering Probe-Fed Circularly Polarized Patch Antenna With Wide Bandwidth," *IEEE Antennas and Wireless Propagation Letters*, vol. 13, pp. 654-657, 2014.
- [9] S. X. Ta and I. Park, "Low-Profile Broadband Circularly Polarized Patch Antenna Using Metasurface," *IEEE Transactions on Antennas and Propagation*, vol. 63, no. 12, pp. 5929-5934, Dec. 2015.
- [10] N. Supreeyattitukul, T. Lertwiriyaprapa and C. Phongcharoenpanich, "S-Shaped Metasurface-Based Wideband Circularly Polarized Patch Antenna for C-Band Applications," *IEEE Access*, vol. 9, pp. 23944-23955, 2021.
- [11] M. Cabedo-Fabres, E. Antonino-Daviu, A. Valero-Nogueira and M. F. Bataller, "The Theory of Characteristic Modes Revisited: A Contribution to the Design of Antennas for Modern Applications," *IEEE Antennas and Propagation Magazine*, vol. 49, no. 5, pp. 52-68, Oct. 2007.
- [12] J. Zeng, X. Liang, L. He, F. Guan, F. H. Lin and J. Zi, "Single-Fed Triple-Mode Wideband Circularly Polarized Microstrip Antennas Using Characteristic Mode Analysis," *IEEE Transactions on Antennas and Propagation*, vol. 70, no. 2, pp. 846-855, Feb. 2022.
- [13] J. Zhang, Z. Xing and J. Li, "Study of Low-Profile Broadband Circularly Polarized Patch Antenna-Based on Metasurface Structure," *2021 IEEE International Symposium on Antennas and Propagation and USNC-URSI Radio Science Meeting (APS/URSI)*, Singapore, Singapore, 2021, pp. 1315-1316.
- [14] K. D. Chinh, P. Van Lam and T. T. Lan, "A Wideband High Gain Circularly Polarized Antenna Based on Nut-Shape Metasurface," *2022 International Conference on Advanced Technologies for Communications (ATC)*, Ha Noi, Vietnam, 2022, pp. 214-218.
- [15] C. Ding, J. Dong, M. Wang and J. Mo, "Design of a Circularly Polarized Metasurface Antenna with Characteristic Mode Theory," *2020 IEEE MTT-S International Conference on Numerical Electromagnetic and Multiphysics Modeling and Optimization (NEMO)*, Hangzhou, China, 2020, pp. 1-3.
- [16] Q. Xia and G. S. Cheng, "A Low-Profile Broadband Circularly Polarized Metasurface Antenna Using CMA," *2022 IEEE 5th International Conference on Electronic Information and Communication Technology (ICEICT)*, Hefei, China, 2022, pp. 295-298.

Machine Learning-based Multi-room Indoor Localization using Fingerprint Technique

Farid Yuli Martin Adiyatma
School of Engineering
King Mongkut's Institute of Technology
Ladkrabang
 Bangkok 10520, Thailand
 65016002@kmitl.ac.th

Dwi Joko Suroso
Department of Nuclear Engineering
and Engineering Physics
Universitas Gadjah Mada
 Yogyakarta 55281, Indonesia
 dwi.jokosuroso@ugm.ac.id

Panarat Chertnanomwong
School of Engineering
King Mongkut's Institute of Technology
Ladkrabang
 Bangkok 10520, Thailand
 panarat.ch@kmitl.ac.th

Abstract— Nowadays, developing Wi-Fi-based indoor localization systems has become an attractive research topic due to the growing need for pervasive location determination. The fingerprint technique offers higher positioning accuracy in indoor localization than the distance-based technique. Fingerprint-based techniques via machine learning have been proposed for many years to provide high-accuracy indoor localization services. These works attempt to establish the optimal correlation between the user fingerprint and a pre-defined set of grid points on a radio map. In this paper, a comparative analysis of selected machine learning algorithms is conducted within the context of online phase fingerprint techniques for localization, focusing on implementation in a multi-room case. The experiment involves measurements using a Wi-Fi module in a laboratory, an aisle, a lobby, and a typical classroom, resulting in a small-sized fingerprint database covering a total area of 573.71 m². The results reveal that Naïve Bayes (NB) obtains the highest localization accuracy in the laboratory and classroom. Meanwhile, Support Vector Machine (SVM) outperforms other algorithms in the aisle, while K-Nearest Neighbor (KNN) delivers the best accuracy in the lobby. In summary, NB, KNN, and SVM are suitable pattern-matching algorithms for multi-room indoor localization and relatively small fingerprint databases.

Keywords—component, formatting, style, styling, insert (key words)

I. INTRODUCTION

Nowadays, the increase in adoption of internet-enabled wireless devices such as smartphones is inextricably linked to the advantages of utilizing location-based services (LBS). As an essential part of the LBS, localization has become the primary assistive technology for wayfinding and advertising based on location [1]. In the outdoor environment, satellite-based positioning, e.g., Global Positioning System (GPS), remains well-established for localization, benefiting from unblocked communication between satellites and receivers or users [2]. However, due to signal obstruction by the wall and interior, GPS cannot be considered a dependable solution for indoor localization, leading to various inaccuracies and failures in achieving high-accuracy localization [3]. This challenge has prompted the development of localization systems that can deliver high-performance results in indoor environments. Several alternative technologies have been put out to construct indoor localization systems, with an emphasis on radio frequency-based methods such as wireless fidelity

(Wi-Fi), radio frequency identification (RFID), ultra-wideband (UWB), ZigBee, and Bluetooth Low Energy (BLE) [4]. Wi-Fi has become the preferred alternative for indoor environments among these technologies due to its widespread infrastructure within buildings.

Initially, Wi-Fi technology is used for delivering widespread wireless communication and internet connectivity [5]. However, in recent years, the utilization of Wi-Fi technology has enhanced to include sensing capability [6]. This enhancement enables Wi-Fi signals to be harnessed for sensing and detecting changes in the surrounding environment. Hence, Wi-Fi has become a prominent solution for various applications, including daily human activity detection and recognition, object sensing, and localization [7]. For localization purposes, Wi-Fi empowers various parameters, such as Received Signal Strength Indicator (RSSI), Angle of Arrival (AoA), Time of Arrival (ToA), and Channel State Information (CSI) [4]. Compared to others, RSSI stands out with its primary advantage of straightforward extraction, requiring simple procedures and not necessitating additional hardware installation.

Regarding indoor localization based on RSSI, two techniques are commonly used: distance-based and distance-free. Distance-based techniques, such as trilateration, utilize RSSI-to-distance translation for direct localization without requiring a site survey. However, these techniques may produce less accurate results due to the poor correlation between RSSI and distance caused by multipath fading. On the other hand, distance-free techniques, particularly the fingerprint technique, are more robust against multipath fading, resulting in higher accuracy localization, and thus are often preferred. The fingerprint technique involves two phases: the offline phase entails conducting a site survey to build the fingerprint database. In contrast, the online phase utilizes a pattern-matching algorithm to compare the RSSI measurements from the target with those stored in the fingerprint database.

In fingerprint-based indoor localization, machine learning (ML) algorithms are widely employed as reliable pattern matching techniques to determine the target location. The methods for pattern matching can be categorized as classification. Several ML techniques are provided for the classification task. This paper attempted to find the most accurate classification algorithm for RSSI-based indoor localization, especially in multi-room cases. We conducted a

comparison of six different ML algorithms: K-Nearest Neighbors (KNN), Naïve Bayes (NB), Logistic Regression (LogR), Support Vector Machine (SVM), Decision Tree (DT), and Random Forest (RF). The primary contribution of this research lies in gaining valuable insights into the classification task for multi-room indoor localization, focusing on achieving highly accurate positioning using ML algorithms.

This paper is organized as follows. Section II discusses the related work. Section III introduces the RSSI-based fingerprint technique, and Section IV describes the machine learning algorithms. In Section V, we delve into the measurement campaign, while data description and evaluation are presented in Section VI. Results and discussion will then be presented in Section VII. Finally, we will conclude our inferences and discuss the outcome results and the plan for our future works in Section VIII.

II. RELATED WORK

Many studies have tried to utilize various ML algorithms in the online phase to determine the target's location using RSSI accurately. Some research studies have used publicly available datasets to assess the performance of ML classification algorithms in the online phase of indoor localization. The authors in [8] conducted the comparison of machine learning algorithms for Wi-Fi-based indoor localization. The dataset used in their study consisted of RSSI data, which was publicly available. The target's location indoors was determined using classification algorithms, including Artificial Neural Networks (ANN), KNN, DT, NB, Extreme Learning Machine (ELM), and SVM. They also performed normalization on the dataset for further analysis. The results indicated that the KNN algorithm showed the most promising performance. In [9], the focus was on utilizing ML algorithms to identify the optimal classifier for indoor positioning. The study employed the UJIIndoorLoc dataset for evaluation. Various classification algorithms were assessed in the research, including DT (J48), NB, Bayesian Network, KNN, Sequential Minimal Optimization (SMO), AdaBoost, and Bagging. After thorough analysis, the authors concluded that KNN outperformed all other methods for accurately estimating the position in indoor environments.

The assessment of machine learning classification in indoor localization is done through experiments and simulations using radio frequency (RF)-based technology. In [10], supervised learning algorithms are utilized to assess the use of Principal Component Analysis (PCA) for Wi-Fi-based indoor localization. The authors conducted the study in a real indoor environment in static and dynamic modes. The comparison shows that the computation time was reduced by 70% when using the Random Forest classifier in the static mode and by 33% when using KNN in the dynamic mode. Authors in [11] employed machine learning algorithms in a proposed system that utilized BLE RSSI fingerprints. The system was deployed in a narrow corridor with $44 \text{ m} \times 1.8 \text{ m}$ dimensions. By comparing KNN, SVM, Random Forest (RF), and Multi-Layer Perceptron (MLP) in both one-dimensional and two-dimensional environments, the findings indicated that RF outperformed the other algorithms, achieving an accuracy of over 99%. In [12], a different study utilized five distinct classifier algorithms: RF, XGBoost, DT, KNN, and SVM, to evaluate various localization metrics. The indoor localization systems were deployed in a layout of $3.048 \text{ m} \times$

3.048 m using four BLE APs. Among the classifiers examined, RF demonstrated the highest accuracy, achieving a 96% accuracy rate.

The previous comparisons of machine learning algorithms for RSSI-based indoor localization were conducted within a single room or using a public dataset. The author has identified a need for comprehensive comparisons of the algorithms, particularly in diverse room environments. Thus, this paper focuses on implementing ML classifiers in an RSSI-based indoor localization system and emphasizes evaluating their performance in different room environments.

III. RSSI-BASED FINGERPRINT TECHNIQUE

The ‘‘Fingerprint technique,’’ as its name implies, emulates the human biological fingerprint to identify and locate objects or devices by employing a process of pattern matching. This process involves comparing the fingerprint database with new data. The implementation of the fingerprint technique in indoor localization can be divided into two phases: the offline and the online phases. The general fingerprint technique procedure is depicted in Fig. 1.

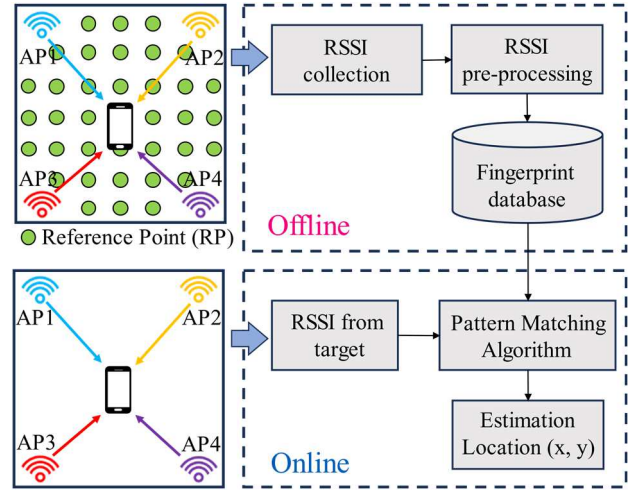


Fig. 1. General Scheme of Fingerprint Technique

During the offline phase, a site survey is conducted to collect RSSI measurements at multiple reference points (RPs). The RSSI values collected during a short period are then stored as unique information in the fingerprint database. Suppose we have m RPs and n APs. Let \overline{RP} are the coordinates of the RPs:

$$\overline{RP} = [(x_1; y_1), (x_2; y_2), \dots, (x_m; y_m)]^T. \quad (1)$$

In this formula, x and y represent the physical latitude and longitude in Cartesian coordinate of each RP. The RSSI values collected from all APs in all RPs are organized into a set:

$$R = \begin{bmatrix} RSSI_{1,1} & RSSI_{1,2} & \dots & RSSI_{1,j} \\ RSSI_{2,1} & RSSI_{2,2} & \dots & RSSI_{2,j} \\ \vdots & \vdots & & \vdots \\ RSSI_{i-1,1} & RSSI_{i-1,2} & \dots & RSSI_{i-1,j} \\ RSSI_{i,1} & RSSI_{i,2} & \dots & RSSI_{i,j} \end{bmatrix}. \quad (2)$$

$RSSI_{i,j}$ denotes the RSSI collected from the j -th AP at the i -th RP. Finally, the fingerprint database is constructed as follows:

$$FP_database = [\overline{RP}, R]. \quad (3)$$

In the online phase, the constructed fingerprint database's RSSI values are compared to the new RSSI values obtained from the target using a pattern matching algorithm. The chosen RP is then used to determine the target's location. The ML-based fingerprint technique for indoor localization utilizes the RSSI values from n APs as features, with the RPs serving as the target labels. The following section describes ML algorithms that commonly used as pattern matching.

IV. MACHINE LEARNING ALGORITHMS

This section provides a brief overview of the classification algorithms employed in this research for indoor localization utilizing RSSI data. These algorithms encompass six ML methods, namely KNN, DT, LogR, NB, SVM, and RF.

A. *K-Nearest Neighbors (KNN)*

The fundamental K-Nearest Neighbors (KNN) classifier algorithm for indoor localization, as explained in [13], entails calculating the distance between the RSSI values collected from APs at an unidentified location with the RSSI values stored in the database. This comparison is done by computing the distance using the Euclidean Distance formula as follows:

$$ED = \sqrt{\sum_{j=1}^n (RSSI_{FD_{i,j}} - RSSI_{new_j})^2}, \quad (4)$$

where ED denotes Euclidean distance. $RSSI_{FD_{i,j}}$ represents the RSSI value retrieved from the j -th AP at the i -th RP and $RSSI_{new_j}$ is the new RSSI value from the target that was collected from n APs. The distances are computed for each location, then arranged in ascending order from the shortest to the longest. Subsequently, the K shortest distances are chosen, where K is a parameter set. In the KNN algorithm, these K distances "vote" for the most prevalent class, which is assigned as the target location.

B. *Naïve Bayes (NB)*

The Naïve Bayes (NB) classifier is a straightforward probabilistic machine learning model for classification tasks. It determines the receiver's position by calculating probabilities associated with the stored RSSI values to find the location with the highest likelihood of occurrence. During the classification phase, it is assumed that features are not probability-connected. This assumption is termed class conditional independence [9]. The NB classifier conducts classification based on the principles of Bayes' theorem:

$$P(m|RSSI_1, RSSI_2, \dots, RSSI_n) = \frac{P(RSSI_1, RSSI_2, \dots, RSSI_n|m) \cdot P(m)}{P(RSSI_1, RSSI_2, \dots, RSSI_n)}. \quad (5)$$

In the (5), $P(m|RSSI_1, RSSI_2, \dots, RSSI_n)$ represents the likelihood of class m given knowledge of the features $RSSI_1, RSSI_2, \dots, RSSI_n$. This likelihood can be calculated by determining the probability of observing the features $RSSI_1, RSSI_2, \dots, RSSI_n$, when target m is the true class and then multiplying it by the probability of target m . The result is then divided by the probability of observing the features $RSSI_1, RSSI_2, \dots, RSSI_n$.

C. *Logistic Regression (LogR)*

Logistic Regression (LogR) is a classification algorithm originally developed for binary classification. Despite its name containing "regression," LogR is actually employed for classification tasks. This algorithm was designed by addressing the issue of linear regression sensitivity to outliers using the sigmoid function. The formula for linear regression using RSSI values from multiple APs is as:

$$y(RSSI) = \alpha + \sum_{j=1}^n \beta_j \cdot RSSI_j, \quad (6)$$

where α represents the intercept, and β is the slope. The sigmoid function is employed to constrain the output of linear regression within the range of 0 and 1. The mathematical representation of the sigmoid function in relation to linear regression is as follows:

$$f_{\text{sig}}(y(RSSI)) = \frac{1}{1 + e^{-(y(RSSI))}}. \quad (7)$$

In a general implementation, LogR can also be extended to handle multiclass classification. In multiclass scenarios, a common strategy used during the prediction step is called "one vs rest (OvR)." The OvR strategy breaks down the problem into multiple binary classification subproblems. For each class, it sets up a binary classification problem where that class is treated as the positive class, and all other classes are grouped together as the negative class.

D. *Support Vector Machine (SVM)*

Support Vector Machine (SVM) classifies data based on class labels by creating a hyperplane in a multi-dimensional space, effectively separating distinct classes. This hyperplane is designed to optimize the margin on either side through multiple training iterations of support vectors. The hyperplane h is given by the general formula of a straight line:

$$h(RSSI) = \beta^T \cdot RSSI + \alpha, \quad (8)$$

where w represents the slope, and b is the intercept. In order to make a prediction, the decision rule is established when $h = 0$. Thus, the hyperplane function h can be defined as:

$$h(RSSI) = \begin{cases} +1, & \beta^T \cdot RSSI + \alpha \geq 0, \\ -1, & \beta^T \cdot RSSI + \alpha < 0. \end{cases} \quad (9)$$

Points above or on the hyperplane will be classified as class +1, while those below the hyperplane will be designated class -1. When a hyperplane cannot linearly separate the data, it is transformed into a higher-dimensional space until it becomes linearly separable. This conversion is achieved effectively through various kernel functions, such as linear, polynomial, RBF, and sigmoid.

E. *Decision Tree (DT)*

The Decision Tree (DT) algorithm employs a hierarchical arrangement of nodes, resembling a tree structure, for making decisions based on input data. This tree structure encompasses root, branch, and leaf nodes [10]. The primary objective of the decision tree algorithm is to construct a hierarchy of choices that can effectively differentiate various classes within the dataset. Purity offers a quantitative measure of how effectively a subset of data uniformly comprises instances from a single

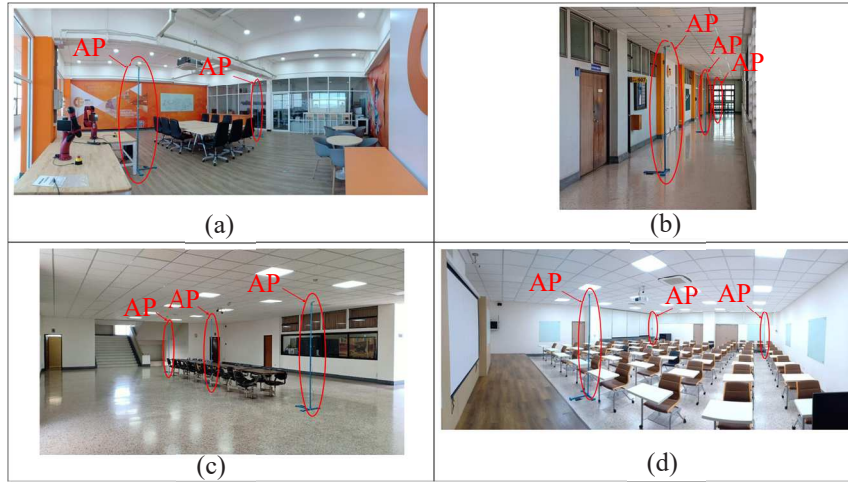


Fig. 2. Actual measurement layout: (a) Laboratory (b) Aisle (c) Lobby (d) Classroom

class. To assess purity, the Gini impurity can be calculated using the subsequent formula:

$$\text{Gini}(P) = 1 - \sum_{i=1}^n P_i^2, \quad (10)$$

where n represents the total number of classes and the is P_i the probability of data points belonging to feature i in the given node. The Gini impurity ranges between 0 and 1, where 0 indicates perfect purity, and 1 indicates maximum impurity (data points are equally distributed across all classes). In creating a hierarchical tree structure, Gini Gain is computed by deducting the combined impurities of the branches from the initial impurity. The Gini Gain enables the formation of a tree with optimal branch organization, selecting the feature that offers the most effective classification. The selection of the finest division is based on the principle of maximizing Gini Gain.

F. Random Forest (RF)

Random Forest (RF) is a classifier that combines multiple DTs. The primary aim of leveraging RF is to reduce the overfitting that occurs in the DT. Each tree is constructed using a subset of the training data. This subset of data is randomly sampled with replacement from the original training dataset. This process is called "bootstrapping." For each DT, a random subset of features is considered for each split. The splitting introduces variability among the trees, mitigating the risk of overfitting. Each DT within an RF is constructed autonomously without awareness of the behavior or structure of other trees. In the context of classification, the final output of the RF classifier is determined by identifying the most frequently appearing class number.

V. MEASUREMENT CAMPAIGN

A. Testbed

The experiment was conducted in four rooms in our campus. These rooms include the laboratory, aisle, lobby, and classroom, as depicted in Fig. 2. In the laboratory, the environment consists of various furniture items, such as chairs, tables, robotic arms, and an air compressor. The room's dimensions are $10.17 \text{ m} \times 9.12 \text{ m}$, containing two APs. The aisle represents a one-dimensional environment without any furniture due to its shape. It is $35.04 \text{ m} \times 3.03 \text{ m}$, and three

APs were deployed along the aisle. The lobby is the largest room in the experiment, covering an area of 247.69 m^2 . It has only a few tables and chairs in the middle, while three APs were positioned in this room. The last room is a typical classroom, measuring $10.16 \text{ m} \times 12.51 \text{ m}$, with three APs strategically placed and many tables and chairs.

B. Data Collection

To build an indoor localization, we employed the ESPino32 module depicted in Fig. 3. This module can be configured to function as a Wi-Fi and BLE device. In this work, the ESPino32 was utilized as Wi-Fi APs and receiver for RSSI data collection. We positioned 11 available APs at a height of 2.5 m, strategically distributed across four rooms.

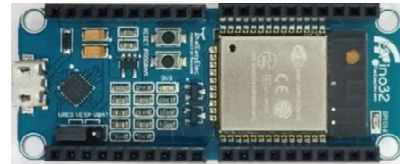


Fig. 3. ESPino32 Wi-Fi and BLE module

To establish a star topology, we designated the sink nodes as targets and positioned them at a 1 m elevation within the area of interest. The APs transmitted signals, receiving and storing the RSSI values in a cloud database. In the experiment, there were instances of 0 values representing RSSI values that were not received from the APs. Given that RSSI values are indicated as negative numbers, 0 is interpreted as being above the factual RSSI value. To ensure accurate calculations, we replace the 0 dBm values with -95 dBm, representing a very low signal strength in the preprocessing data step.

To construct the fingerprint database, RSSI values were collected at 73 RPs as depicted in Fig. 4. The grid size for RPs was set to $2 \text{ m} \times 2 \text{ m}$ in the CIE Lab, aisle, and classroom 904. However, due to the larger size of the lobby, we set the grid size to $2 \text{ m} \times 4 \text{ m}$ for the x and y -axis, respectively, to ensure adequate coverage. To assess the performance of the ML classifier algorithms, we conducted a simulation where the target was simulated to move from the laboratory to classroom. During this movement, we collected RSSI values from the target at 79 sequential points, as illustrated in Fig. 5. The constructed fingerprint database serves as the training

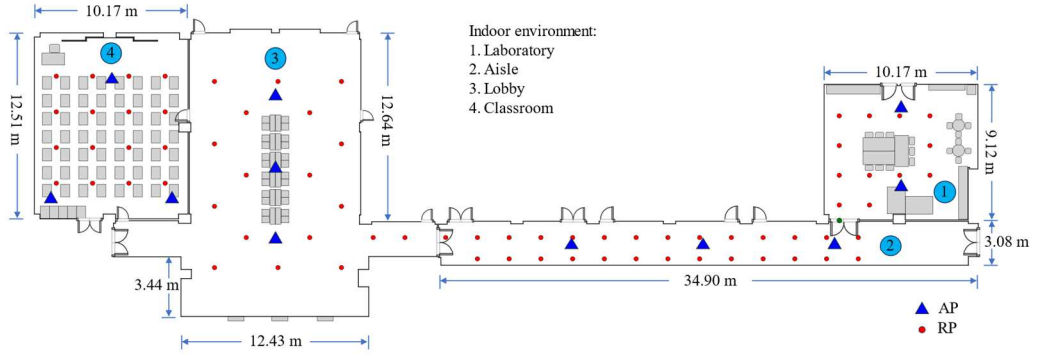


Fig. 4. Fingerprint Database Construction Map Layout

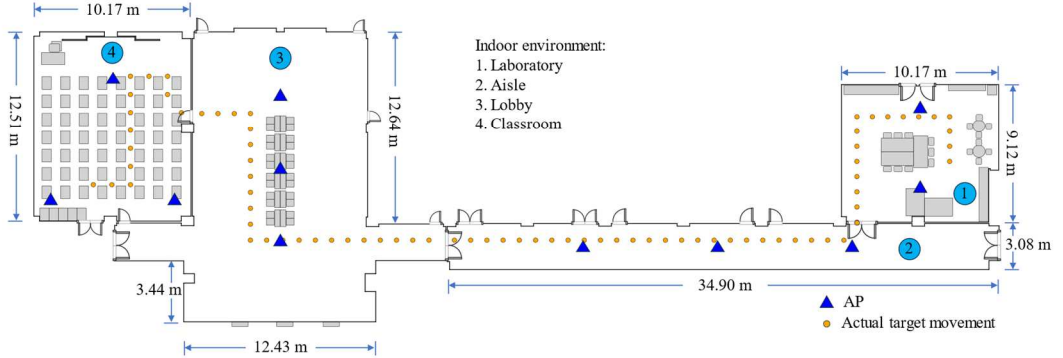


Fig. 5. Target Movement Layout

dataset for the machine learning classifier. The target data will be classified using this trained model in the testing phase. The dataset's structure, which encompasses the fingerprint database and the target data, will be described in the following section.

VI. DATA DESCRIPTION AND EVALUATION

In this section, we will delve into the dataset used in our study and the evaluation process, which includes a concise overview of the evaluation metrics.

A. Dataset Description

In indoor localization, the fingerprint database serves as the training dataset. Our training dataset comprises 73 distinct classes, each corresponding to an RP. The fingerprint database contains a total of 824 sequential rows of raw Wi-Fi output. Within the fingerprint database, there are 14 columns, which include the RSSI readings from 11 APs, the coordinates of the RP, and the timestamp. At each RP, we have collected 10 to 13 RSSI data points within a short recording time. Meanwhile, the testing data consists of 158 rows collected from the target point.

B. Evaluation Procedure

The evaluation process involved running the program in Python 3.11, utilizing the sklearn library for implementing machine learning algorithms. We relied on the pandas and numpy libraries for dataset management and numerical operations. In the training phase, we divided the dataset into training and validation sets, with proportions of 80% and 20%, respectively. Each algorithm has its own set of hyperparameters that can significantly impact the classification performance. To find the best hyperparameter settings, we employed GridSearchCV, which systematically

explores all possible combinations of hyperparameter values. The model's performance was evaluated using cross-validation for each combination to ensure an unbiased assessment. Based on the specified evaluation metric, the model with the highest performance was then chosen as the final model with the optimized hyperparameters. The final model will be used to estimate the location.

After obtaining the estimated location using several ML classification algorithms, we evaluate the accuracy of the localization results by measuring the mean localization error (MLE). Considering there are recorded target locations, we employ the MLE to calculate the distance between the actual position (x_{act}, y_{act}) and the estimated position (x_{est}, y_{est}) as the error for each target $n = 1, 2, 3, \dots, N$. The MLE can be represented as (11),

$$MLE = \frac{1}{N} \sum_{n=1}^N \sqrt{(x_{act,n} - x_{est,n})^2 + (y_{act,n} - y_{est,n})^2}. \quad (11)$$

VII. RESULTS AND DISCUSSION

In this section, we present the results of our experiment, followed by a comprehensive discussion. In the laboratory; five algorithms exhibit MLE values below 2 m. NB demonstrated the lowest error at 1.77 m. The next algorithms were SVM, KNN, RF, and LogR with overall errors of 1.79 m, 1.86 m, 1.94 m, and 1.99m, respectively. With a grid dimension of 2 m \times 2 m, these algorithms provide reasonable accuracy in the laboratory. DT is the only one generating errors exceeding 3 m, making it the least accurate in the laboratory environment. This low accuracy may be caused by the difficulties of DT in selecting the optimal decision during

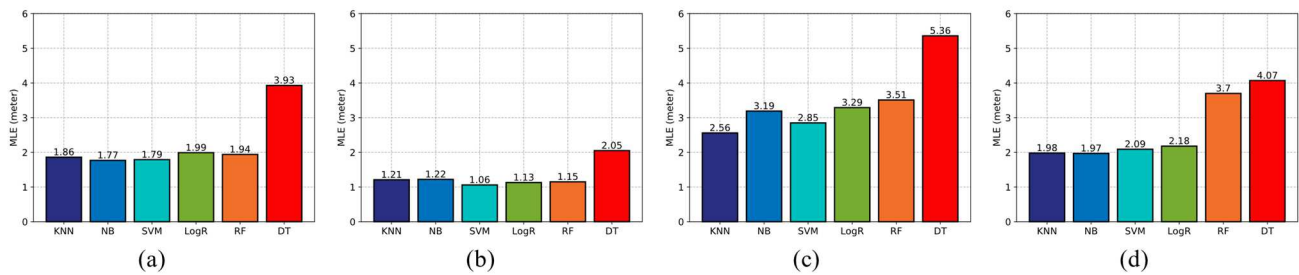


Fig. 6. MLE results in: (a) Laboratory (b) Aisle (c) Lobby (d) Classroom

branch development, which eventually results in less accurate final judgments.

In the aisle, five of the algorithms used exhibit MLE values below 1.25 m where SVM emerges as the best-performing algorithm in terms of accuracy, achieving an MLE of 1.06 m. In sequence, the algorithms producing MLEs below 1.5 m, ranging from the second lowest to the highest, are LogR, RF, KNN, and NB, respectively. Lastly, the algorithms with the highest errors are DT, which exhibits an error of approximately 2 m. Generally, the localization accuracy in the aisle surpasses that of the laboratory and classroom, despite these rooms having the same grid dimensions. This result could be associated with the less complex interior in the aisle compared to the other rooms with the same grid layout.

Within the lobby, the errors in KNN and SVM algorithms remain below 3 m. On the other hand, DT exhibits the poorest performance, with an MLE surpassing 5 m. Meanwhile, the remaining algorithms, including NB, LogR, and RF, yield errors of 3.19 m, 3.25 m, and 3.51, respectively. Both KNN and SVM show reasonably high accuracy when compared to the grid size utilized in the lobby (2 m × 4 m).

Classroom has many tables and chairs, contributing to a setting with complex multipath fading. Within this environment, both NB and KNN achieved errors below 2 m. SVM and LogR exhibited an error of approximately 2 m, slightly surpassing NB and KNN. In contrast to other classification algorithms, DT emerged as the least accurate, with an error of 4.07 m. Finally, RF demonstrated marginally better accuracy than DT, with errors falling below 4 m.

VIII. CONCLUSION

In this research, a fingerprint-based indoor localization system was developed using Wi-Fi technology. During the online phase, six distinct machine learning algorithms, i.e., KNN, DT, NB, LogR, SVM, and RF, were employed as pattern matching algorithms. These algorithms were assessed for their accuracy in localizing a target within four distinct rooms, utilizing RSSI data from 11 Wi-Fi APs. The results highlighted that KNN, SVM, and NB exhibited the highest accuracy, making them suitable pattern matching algorithm for multi-room indoor localization. Additionally, LogR demonstrated competitive and reasonable localization accuracy. Conversely, DT consistently exhibited the poorest performance across all rooms. This result could be due to numerous decision nodes and leaves, resulting in a convoluted structure that fits the training data well. While not excelling compared to other ML algorithms due to its reliance on multiple DTs, RF exhibited better accuracy than a single DT.

ACKNOWLEDGMENT

This work was financially supported by King Mongkut's Institute of Technology Ladkrabang [2566-02-01-011].

REFERENCES

- [1] H. Liu, H. Darabi, P. Banerjee, and J. Liu, "Survey of wireless indoor positioning techniques and systems," *IEEE Trans. Syst. Man Cybern. Part C Appl. Rev.*, vol. 37, no. 6, pp. 1067–1080, 2007, doi: 10.1109/TSMCC.2007.905750.
- [2] V. Moghtadaiee, S. A. Ghorashi, and M. Ghavami, "New Reconstructed Database for Cost Reduction in Indoor Fingerprinting Localization," *IEEE Access*, vol. 7, pp. 104462–104477, 2019, doi: 10.1109/ACCESS.2019.2932024.
- [3] P. S. Farahsari, A. Farahzadi, J. Rezaadeh, and A. Bagheri, "A Survey on Indoor Positioning Systems for IoT-Based Applications," *IEEE Internet Things J.*, vol. 9, no. 10, pp. 7680–7699, 2022, doi: 10.1109/IJOT.2022.3149048.
- [4] A. Nessa, B. Adhikari, F. Hussain, and X. N. Fernando, "A Survey of Machine Learning for Indoor Positioning," *IEEE Access*, vol. 8, pp. 214945–214965, 2020, doi: 10.1109/ACCESS.2020.3039271.
- [5] K. Pahlavan and P. Krishnamurthy, "Evolution and Impact of Wi-Fi Technology and Applications: A Historical Perspective," *Int. J. Wirel. Inf. Networks*, vol. 28, no. 1, pp. 3–19, 2021, doi: 10.1007/s10776-020-00501-8.
- [6] Y. Ma, G. Zhou, and S. Wang, "WiFi sensing with channel state information: A survey," *ACM Comput. Surv.*, vol. 52, no. 3, 2019, doi: 10.1145/3310194.
- [7] C. Wang, S. Chen, Y. Yang, F. Hu, F. Liu, and J. Wu, "Literature review on wireless sensing-Wi-Fi signal-based recognition of human activities," *Tsinghua Sci. Technol.*, vol. 23, no. 2, pp. 203–222, 2018, doi: 10.23919/TST.2018.8329114.
- [8] K. Sabanci, E. Yigit, D. Ustun, A. Toktas, and M. F. Aslan, "Wi-Fi Based Indoor Localization: Application and Comparison of Machine Learning Algorithms," *Proc. Int. Semin. Direct Inverse Probl. Electromagn. Acoust. Wave Theory, DIPED*, vol. 2018-Septe, pp. 246–251, 2018, doi: 10.1109/DIPED.2018.8543125.
- [9] S. Bozkurt, G. Elibol, S. Gunal, and U. Yayan, "A comparative study on machine learning algorithms for indoor positioning," *INISTA 2015 - 2015 Int. Symp. Innov. Intell. Syst. Appl. Proc.*, 2015, doi: 10.1109/INISTA.2015.7276725.
- [10] A. H. Salamah, M. Tamazin, M. A. Sharkas, and M. Khedr, "An enhanced WiFi indoor localization System based on machine learning," *2016 Int. Conf. Indoor Position. Indoor Navig. IPIN 2016*, no. October, pp. 4–7, 2016, doi: 10.1109/IPIN.2016.7743586.
- [11] A. P. Ladislav Polak, Stanislav Rozum, Martin Slanina, Tomas Bravenec, Tomas Fryza, "Received Signal Strength Fingerprinting-Based Indoor Location Estimation Employing Machine Learning," *mdpi sensors*, pp. 1–25, 2021.
- [12] C. Jain, G. V. S. Sashank, N. Venkateswaran, and S. Markkandan, "Low-cost BLE based Indoor Localization using RSSI Fingerprinting and Machine Learning," *2021 Int. Conf. Wirel. Commun. Signal Process. Networking, WiSPNET 2021*, pp. 363–367, 2021, doi: 10.1109/WiSPNET51692.2021.9419388.
- [13] S. Sadowski, S. Member, P. Spachos, and S. Member, "Memoryless Techniques and Wireless Technologies for Indoor Localization with the Internet of Things," no. May, 2020.

Steganalysis on dual-layer security of messages using steganography and cryptography

Zeba Shamsi¹, Anish Kumar Saha¹, Ripon Patgiri¹, Khoirom Motilal Singh², Laiphrakpam Dolendro Singh^{1*}

Dept. of Computer Science and Engineering,

¹National Institute of Technology Silchar, Assam-788010, India

²Indian Institute of Information Technology Senapati, Manipur 795002, India

ldsingh.cse@gmail.com*, ldsingh@cse.nits.ac.in*

Abstract—Recently, Bansal *et al.* proposed a dual-layer message security technique using steganography and cryptography. An index table maps each text data to an index point and an elliptic curve point. The text data are encrypted using elliptic curve cryptography, and the corresponding index values are embedded in a cover image using the Least Significant Bit Inversion technique. The proposed paper breaks the security of the key exchange technique in the Bansal *et al.* method and the secret text is extracted.

Index Terms—steganalysis, cryptanalysis, steganography, elliptic curve cryptography.

I. INTRODUCTION

Information security refers to the safeguarding of data while it's being stored, processed, and sent. Data transmission was completely transformed by 4G/5G cellular technology and optical fiber connectivity due to their vastly improved bandwidth and data rates. The internet has enabled the widespread transfer of information in the forms of text, photos, audio, and video [1]. Governments, law enforcement, and medical facilities are all using multimedia data interchange for telemedicine and other purposes. There was an increase in internet traffic during the COVID-19 international lockdown. While there are many benefits to using the internet, there are also risks associated with sharing personal information online [2]. Hackers now have access to a wider variety of tools, making it easier for them to steal, modify, or otherwise corrupt data. This has made data security an extremely difficult but crucial task for academics [3]. Data security challenges have been approached from a number of different angles, with proposals including cryptography and data masking techniques. Cryptography and data masking are two of the most common methods used to improve the security of confidential messages transmitted over the Internet. Using cryptography, sensitive information is transformed into an unintelligible format that cannot be read by an outsider [4]. Both traditional encryption methods and Chaos-based approaches are viable options for performing cryptography [5]. Additionally, there are many standard techniques for encryption, like Data Encryption Standard, Advanced Encryption Standard, Rivest Shamir Adleman algorithm, and so on. In such approaches, the secret key is first utilized to encrypt the vital information before embedding [6]. Laiphrakpam *et al.* [7] proposed a multiple-image encryption scheme using an amplified chaotic map. In their method, the input images are gray images combined into three groups and act as each plane of an

RGB image. Pixel shuffling along the horizontal and vertical was performed using the amplified sine map. Chaos-based encryption methods are effective in overcoming standard encryption techniques' limitations. Initial encryption keys in the chaos encryption method are change-sensitive. Thus, techniques based on chaos offer a more robust cryptography tool for protecting sensitive information [8]. By encrypting data and thereby altering its appearance, cryptography is able to give a high level of protection for the data it handles. However, the encrypted form of data still leaves it vulnerable to modification or hacking, therefore cryptography cannot stand alone as a security measure. The encrypted form may catch the attention of an eavesdropper, making this an unsatisfactory technique of data security. Therefore, data concealing has been frequently employed by researchers as a means of hiding a message inside another message so that only the intended receiver can read it and get the original message [10]. Thus, the current trend is towards crypto-stego mechanisms, which combine steganography and cryptography to give data a double layer of security, as shown in Fig. 1.

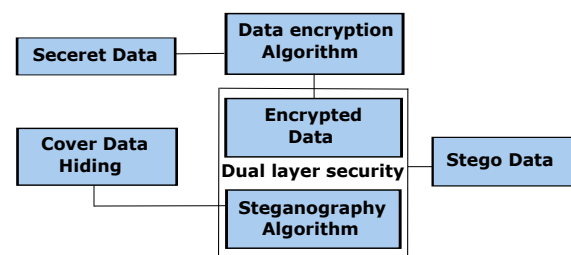


Fig. 1: Block diagram of dual layer security

Dual security proposes a unified system that combines the strengths of steganography and cryptography. In the dual layer security approach, [14], the intended secret data is first encrypted with the aid of an encryption algorithm. Then, the encrypted data is concealed within a cover file utilizing a number of steganographic techniques. Afterward, they assembled the cover file that would be transmitted. If a hacker has any worries about the data in the cover file, he can still extract the cover file, which is encrypted text, and use an appropriate decryption technique to read the encrypted message. Therefore, employing both encryption

and steganography together offers superior security to either method alone.

Most importantly, many people are drawn to this area because the combination of cryptography and steganography increases the security of secret communication. Sharma *et al.* [11] proposed employing both cryptography and steganography as a double layer of protection. They used a key image to encrypt a target image, and then they used steganography to put the encrypted target image. They employed images as a cover medium in steganography. To facilitate data extraction on the receiving end, they transmitted both the stego-image and the key image. Using an additional image as a key always results in more bandwidth usage and a higher probability of interception. Sriram *et al.* [12] using encryption and steganography to create a double layer of security, which would allow for uncompromised data transmission even in the event of a communication channel interruption. Rotor cipher was employed to encrypt sensitive information, and 2-bit Least Significant Bit (LSB) substitution was utilized to embed the encrypted data. Karthikeyan *et al.* [13] used LSB substitution to conceal a secret message in an image. In order to increase stability, the buried pixels were picked in a spiral pattern. The encryption method used in this case is based on the widely used Data Encryption Standard (DES) algorithm. However, the cryptographic key handling mechanism is not highlighted in this approach. Shanthakumari *et al.* [15] predicted the Least Significant Bit Inversion (LSBI) computation is a good approach for steganography in information correspondence, with a higher implanting limit and very low mutilation between the original and stego-image. Concerning privileged Intel implanting by dark code standard, satisfactory security was achieved by constructing an assurance layer of the cover image and concealing data that is not visible to the naked eye. This illustrates that whichever way of compelling executes information inserting strategies, some trouble, such as implanting limit, security, and distortion of the first picture, etc., is visible at the end-product.

II. PRELIMINARIES

To better understand the operations performed in the Bansal *et al.* technique, some of the preliminaries are elaborated.

A. Mathematical operation of elliptic curve cryptography

Let $E_p : y^2 \equiv x^3 + ax + b \pmod{p}$ be an elliptic curve and point $P_1 = (x_1, y_1)$ and $P_2 = (x_2, y_2) \in E_p$. $P_1 + P_2 = P_3(x_3, y_3)$ is computed as:

- (i) If the x -coordinate of P_1 and P_2 are different

$$m = [(y_2 - y_1)/(x_2 - x_1)] \pmod{p} \quad (1)$$

x_3 and y_3 of P_3 is computed as $x_3 = m^2 - x_1 - x_2 \pmod{p}$ and $y_3 = m(x_1 - x_3) - y_1 \pmod{p}$

- (ii) If the x -coordinate of P_1 and P_2 are the same but the y -coordinate of P_1 and P_2 are different, then $P_1 + P_2$ is given by an identity element known as the point at infinity denoted as $P_1 + P_2 = \infty$.

- (iii) If the x and y coordinate of P_1 and P_2 are same and the y coordinate is not equal to zero, then

$$m = (3x_1^2 + a)/2y_1 \quad (2)$$

$x_3 = m^2 - 2x_1$ and $y_3 = m(x_1 - x_3) - y_1$

- (iv) If the x and y coordinate of P_1 and P_2 are same and the y coordinate is equal to zero, then $P_1 + P_2$ is given by point at infinity denoted as $P_1 + P_2 = \infty$.

III. BANSAL *et al.* MESSAGE SECURITY TECHNIQUE USING STEGANOGRAPHY AND CRYPTOGRAPHY

Bansal *et al.* [14] proposed a message-securing technique using steganography and cryptography. The confidential text message is encrypted using elliptic curve cryptography as elliptic curve coordinates. Each coordinate is assigned an index value. The index table used by Bansal *et al.* is given in Table I. It is obtained when the elliptic curve equation is given by $E_{131} : y^2 \equiv x^3 + x + 1 \pmod{131}$, where $a = 1$ (coefficient of x), $b = 1$ and $p = 131$.

Bansal *et al.* technique requires sharing of a secret random number K which is computed using the concept of elliptic curve Diffie Hellman technique. All the possible symbols of input data with corresponding elliptic curve coordinates along with index value are given in Table I. The input data is enciphered using elliptic curve cryptography, where the cipher text CT_i is given by:

$$CT_i = \{ID_i + K.PUB_R\} \quad (3)$$

where,

ID_i : denotes the elliptic curve coordinate for input symbol i represented in Table I.

K : secretly shared random number using elliptic curve Diffie Hellman technique.

PUB_R : Public key of the receiver.

After obtaining the cipher text CT_i for each input symbol, the corresponding index value (IV_i) of CT_i is embedded in the cover image. The steps involved in Bansal *et al.* embedding technique are as follows:

- 1) Import a cover image (CI).
- 2) Divide the cover image into four equal blocks as CI_{11} , CI_{12} , CI_{21} and CI_{22} .
- 3) The index values (IV_i) corresponding to cipher text CT_i are converted to seven bit binary.
- 4) If the length of binary bits in the above step is odd, then an extra 0 is padded and divided into two bits (BB_j) each. The possible pattern is $\{00, 01, 10, 11\}$.
- 5) Binarize the pixel values of CI_{11} , CI_{12} , CI_{21} and CI_{22} and store as PV_{11} , PV_{12} , PV_{11} and PV_{22} respectively.
- 6) For each binary bit pattern in (BB_j), if the two binary bit pattern matches the 6th and 7th binary bit in PV_k , $k \in (11, 12, 21, 22)$ and the LSB of matching $PV_k = 0$ then, the remaining LSB of other PV_k are set as 1. If the LSB of matching $PV_k = 1$ then, the remaining LSB of other PV_k are set as 0.

TABLE I: Index table

| Index | Message | Elliptic curve | Index | Message | Elliptic curve | Index | Message | Elliptic curve |
|-------|---------|----------------|-------|---------|----------------|-------|---------|----------------|
| Value | | Co-ordinate | Value | | Co-ordinate | Value | | Co-ordinate |
| 1 | a | (0, 1) | 33 | F | (67, 29) | 65 | @ | (2, 81) |
| 2 | b | (1, 38) | 34 | G | (68, 25) | 66 | # | (7, 73) |
| 3 | c | (2, 50) | 35 | H | (70, 47) | 67 | | (9, 79) |
| 4 | d | (7, 58) | 36 | I | (71, 22) | 68 | % | (10, 116) |
| 5 | e | (9, 52) | 37 | J | (72, 44) | 69 | ^ | (11, 66) |
| 6 | f | (10, 15) | 38 | K | (73, 26) | 70 | & | (12, 118) |
| 7 | g | (11, 65) | 39 | L | (79, 64) | 71 | * | (16, 107) |
| 8 | h | (12, 13) | 40 | M | (86, 20) | 72 | (| (17, 79) |
| 9 | i | (16, 24) | 41 | N | (88, 19) | 73 |) | (21, 84) |
| 10 | j | (17, 52) | 42 | O | (91, 46) | 74 | - | (22, 86) |
| 11 | k | (21, 47) | 43 | P | (92, 36) | 75 | _ | (24, 116) |
| 12 | l | (22, 45) | 44 | Q | (96, 37) | 76 | + | (25, 113) |
| 13 | m | (24, 15) | 45 | R | (97, 15) | 77 | - | (26, 124) |
| 14 | n | (25, 18) | 46 | S | (102, 39) | 78 | = | (27, 89) |
| 15 | o | (26, 7) | 47 | T | (105, 52) | 79 | [| (29, 70) |
| 16 | p | (27, 42) | 48 | U | (107, 63) | 80 |] | (0, 69) |
| 17 | q | (29, 61) | 49 | V | (108, 16) | 81 | { | (33, 83) |
| 18 | r | (30, 62) | 50 | W | (110, 46) | 82 | } | (34, 68) |
| 19 | s | (33, 48) | 51 | X | (113, 35) | 83 | ; | (35, 104) |
| 20 | t | (34, 63) | 52 | Y | (114, 7) | 84 | ' | (37, 115) |
| 21 | u | (35, 27) | 53 | Z | (115, 9) | 85 | : | (39, 127) |
| 22 | v | (37, 16) | 54 | 1 | (117, 16) | 86 | " | (40, 84) |
| 23 | w | (39, 4) | 55 | 2 | (120, 10) | 87 | , | (43, 77) |
| 24 | x | (40, 47) | 56 | 3 | (121, 63) | 88 | . | (48, 83) |
| 25 | y | (43, 54) | 57 | 4 | (122, 7) | 89 | < | (49, 89) |
| 26 | z | (48, 48) | 58 | 5 | (123, 23) | 90 | > | (50, 83) |
| 27 | A | (49, 42) | 59 | 6 | (124, 31) | 91 | / | (55, 89) |
| 28 | B | (50, 48) | 60 | 7 | (125, 33) | 92 | ? | (58, 80) |
| 29 | C | (55, 42) | 61 | 8 | (127, 44) | 93 | | (61, 85) |
| 30 | D | (58, 51) | 62 | 9 | (128, 44) | 94 | | (62, 87) |
| 31 | E | (61, 46) | 63 | 0 | (0, 130) | 95 | - | (63, 89) |
| 32 | F | (62, 44) | 64 | ! | (1, 93) | 96 | _ | (64, 91) |

IV. STEGANALYSIS OF BANSAL *et al.* MESSAGE SECURITY TECHNIQUE

Kerckhoff's principle states that the security of an algorithm lies in the key, not in the algorithm. An algorithm is known to all. Bansal *et al.* technique proposed to provide dual security of text data by using the concept of ECC to generate cipher data and further hide the information in a cover image using the LSBI method. The elliptic curve parameter used by Bansal *et al.* technique is not large enough to provide adequate security. The secret key K shared between the sender and the receiver, the private key of the sender PRI_S and the private key of the receiver PRI_R can all be compromised using naive attack or BSGS attack or PR attack.

A. Extraction of embedded message from cover image embedded using Bansal *et al.* message security technique

The index value (IV_i) corresponding to the cipher text data can be extracted from the stego-image as no separate security algorithm is deployed for embedding in the Bansal *et al.* technique. To extract the index value (IV_i) from the stego-image, the following steps are to be performed.

- 1) Divide the stego-image into four equal blocks $SI_{11}, SI_{12}, SI_{21}$ and SI_{22} .

- 2) Extract and store the LSB of $SI_{11}, SI_{12}, SI_{21}$ and SI_{22} as $LSB_{11}, LSB_{12}, LSB_{21}$ and LSB_{22} respectively.
- 3) Identify the odd LBS_j where $j \in \{11, 12, 21, 22\}$ and extract the sixth and seventh binary bits from corresponding SI_j .
- 4) Once all the sixth and seventh binary bits are extracted from the relevant SI_j , the binary bits are converted to a single list and divided into blocks, each containing seven bits. Every seven bits are converted to decimal digits forming the retrieved index value (IV_i).

Using Table I, each (IV_i) is mapped to corresponding ciphertext CT_i .

B. Cryptanalysis of Bansal *et al.* technique

The security of elliptic curve cryptography is maintained by the difficulty of solving the elliptic curve discrete logarithmic problem (ECDLP). Let p, a, b, G be the elliptic curve parameter for the elliptic curve equation $E_p: y^2 = x^3 + ax + b \pmod p$ and G denotes the generator with cyclic order n . Let the public key of the sender and the receiver be PUB_S and PUB_R computed as $PRI_S.G$ and $PRI_R.G$ respectively where PRI_S and PRI_R are the private keys of the sender and receiver respectively and $.$ denoted elliptic curve point multiplication operation. $PRI_S.G$ is computed as PRI_S

times point addition of G and $PRI_R.G$ is computed as PRI_R times point addition of G . Solving the private key PRI_S and PRI_R given the public keys (PUB_R, PUB_R), G and the elliptic curve parameters p, a, b, G, n is known as cryptanalysis on ECDLP. If the cyclic order (n) of a given elliptic curve equation E_p is small, then a naive attack (NA) can be performed. Other cryptanalysis techniques on ECDLP are Baby-step, Giant-step attack (BSGS), and Pollard's rho (PR) attack which required \sqrt{n} steps. The algorithms for performing NA, BSGS, and PR are given below:

1) *Naive attack on elliptic curve discrete logarithmic problem*: A naive attack is a brute force attack where an exhaustive search of keys is performed. It is computationally expensive and feasible only if cyclic over n of the elliptic curve equation E_p is small.

Algorithm 1: Naive attack on ECDLP

Input: PUB_R, G, p, a, b, n
Output: PRI_R

```

1 i=1; while (i ≠ n) do
2   if (iG ≠ PUBR) then
3     | i = i + 1
4   end if
5   else
6     | PRIR = i
7     | break
8   end if
9 end while

```

2) *BSGS attack on ECDLP*: The BSGS attack is a deterministic type of attack on ECDLP that requires \sqrt{n} steps and space for computation. It is feasible for a moderate size of cyclic over n of the elliptic curve equation E_p .

Algorithm 2: BSGS attack on ECDLP

Input: PUB_R, G, p, a, b, n
Output: PRI_R

```

1 Compute an integer  $m \geq \sqrt{n}$  and solve  $mG$ , where  $mG$ :
  point addition of  $m$  times  $G$ ;
2 for (i=0 to m) do
3   | Computer and store iG
4 end for
5 j=0;
6 while (j < m - 1) do
7   if ( $PUB_R - j.m.G \in iG$ ) then
8     | Break
9   end if
10  else
11   | j=j+1
12  end if
13 end while
14  $PRI_R \equiv i + j \times m \pmod{n}$ .

```

3) *Pollard's rho attack on ECDLP*: Pollard's rho attack is a probabilistic type of attack on ECDLP that requires \sqrt{n} steps. It is feasible for a moderate size of cyclic over n of the elliptic curve equation E_p .

Using the elliptic curve parameter given in Bansal *et al.*, cryptanalysis is done on randomly selected public keys using naive attack, BSGS attack, and PR attack and the execution time is recorded in Table II. Once the private keys are

Algorithm 3: Pollard's rho attack on ECDLP

Input: PUB_R, G, p, a, b, n
Output: PRI_R

```

1 Compute  $P_0 = a_0.G + b_0.PUB_R$ , where  $a_0$  and  $b_0$  are
  random integers.
2 Define a set of  $M_i = a_i.G + b_i.PUB_R$ , generally  $i$  is
  around 20 and  $a_i$  and  $b_i$  are random integers.
3  $P_{j+1} = P_j + M_i$ , where  $M_i$  is chosen by taking modulo
  ( $N$ ) on  $x$ -coordinate of  $P_j$ , where  $N$  is the number of
   $M_i$ 's.
4 Let  $P_j = u_j.G + v_j.PUB_R$  and  $P_{j+1} = P_j + M_i$ , then
   $P_{j+1}$  can be expressed as
   $P_{j+1} = (u_j + a_i).G + (v_j + b_i).PUB_R$ .
5 if ( $P_{j_0} == P_{i_0}$ ) then
6   |  $u_{j_0}.G + v_{j_0}.PUB_R = u_{i_0}.G + v_{i_0}.PUB_R$ 
7   |  $(u_{j_0} - u_{i_0}).G = (v_{j_0} - v_{i_0}).PUB_R$ 
8 end if
9 Compute  $d = GCD(v_{j_0} - v_{i_0}, n)$ 
10  $PRI_R \equiv [(v_{j_0} - v_{i_0})^{-1} \times (u_{j_0} - u_{i_0})] \pmod{n/d}$ 

```

compromised, the secretly shared key K can be computed and ciphertext CT_i can be deciphered

TABLE II: Execution time to crypt-analyze on random key.

| Attacks | Time taken to retrieve the private key |
|---------|--|
| Naive | 0.0156250 Sec. |
| BSGS | 0.0015001 Sec. |
| PR | 0.0016316 Sec. |

C. Deciphering of Bansal *et al.* ciphertext data

Once the secretly shared key K is compromised, the cipher-text extracted in Section IV-A can be deciphered. The equation for deciphering is as follows:

$$D_i = CT_i - K.PUB_R \quad (4)$$

where, D_i : deciphered elliptic curve coordinate. Using Table I, the D_i are mapped to corresponding symbols, and the secret message is revealed.

V. SIMULATION

The simulation of the proposed steganalysis is performed using Wolfram Mathematica on an 11th-generation Intel core i7 @ 2.8GHz laptop with 16GB RAM. The cover image used in the steganalysis is obtained from the USC SIPI image database [17]. Some of the sample standard images are shown in Fig. 2. The elliptic curve parameter given in Bansal *et al.* is also used for the proposed steganalysis. The cover image, the plain message, its corresponding encrypted plain message using ECC, and the index value corresponding to the encrypted ECC points are shown in Table IV. Further, the stego image, extracted index, the deciphered elliptic curve data, and the corresponding plain messages are also shown in Table V. To determine the changes between the cover image and the stego image, PSNR is computed for the sample images used in the simulation and is obtained as 86.99 dB, 87.06 dB, 86.69 dB, and 88.62 dB respectively.

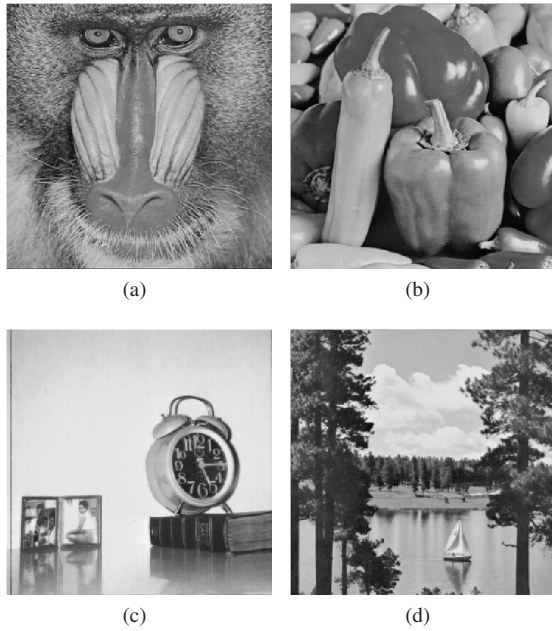


Fig. 2: Sample images from SIPI database: (a) Baboon (b) Peppers (c) Clock (d) Sailboat on lake.

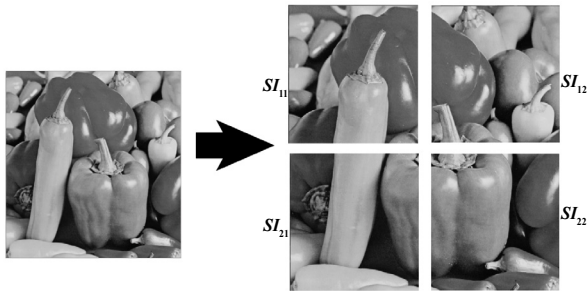


Fig. 3: Decomposition of pepper image in four equal parts.

1) *Extraction of cipher index*: The stego-image is divided into four equal blocks ($SI_{11}, SI_{12}, SI_{21}, SI_{22}$) as shown in Fig. 3. Then, the embedded index values are extracted by following the procedures as in Section IV-A. The pixel values in each block ($SI_{11}, SI_{12}, SI_{21}, SI_{22}$) are binarized to a length of eight bits with 0's padding if necessary. Some sample possible cases for extraction of the bits at the sixth and the seventh binary bits based on odd LSBs are given in Table III.

The extracted binary bits are divided into blocks of seven bits each (**0010011**, **1010001**, ...). Each block is converted to an integer which represents the index in Table I.

2) *Deciphering the embedded message*: The embedded cipher index values are then mapped to their corresponding elliptic curve coordinate points using the index Table I. For eg, $0010011_2 \rightarrow 19$, the elliptic curve coordinates (33, 48) will be selected. The secret private keys are also extracted using any of the Algorithm 1, 2, or 3. Further, elliptic curve point subtraction is performed to obtain the input elliptic curve points. Finally, the elliptic curve points are mapped

TABLE III: Sample Bits information extraction. (Underlined bits indicate the odd LSB bits. The bold bits are the extracted sixth and seventh bits.)

| SI_{11} | SI_{12} | SI_{21} | SI_{22} | Extracted bits |
|-------------------|-------------------|-------------------|-------------------|----------------|
| 10101011 | 1101 <u>000</u> 0 | 11011001 | 11101101 | 00 |
| 10100111 | 11010000 | 11001011 | 11001110 | No odd LSB |
| 10111010 | 11010000 | 11101000 | 10110110 | No odd LSB |
| 10111001 | 11010011 | 11100 <u>10</u> 0 | 10110111 | 10 |
| 10111111 | 11001111 | 1110010 <u>1</u> | 1011 <u>10</u> 10 | 01 |
| 10111 <u>11</u> 0 | 11010001 | 11100101 | 11001111 | 11 |
| 11000000 | 11010000 | 11100110 | 0101 <u>10</u> 11 | 01 |
| 11000110 | 11001100 | 00101 <u>00</u> 1 | 11100110 | 00 |
| 11100110 | 1000 <u>10</u> 11 | 11001100 | 11000110 | 01 |

to their corresponding characters using the index table.

TABLE IV: Cover Image, Plain message, Encrypted plain message using ECC and Index value.

| Cover Image | Plain Message | Encrypted ECC points | Index Value |
|-------------|---------------|---|-------------------|
| | NITS | {(115, 9), (124, 31), (10, 15), (33, 48)} | {53, 59, 6, 19} |
| | 0976 | {(72, 87), (17, 52), (39, 4), (26, 124)} | {101, 10, 23, 77} |
| | @% * + | {(96, 37), (115, 122), (7, 58), (70, 47)} | {44, 118, 4, 35} |
| | Kl@9 | {(128, 87), (9, 52), (96, 37), (17, 52)} | {127, 5, 44, 10} |

TABLE V: Stego Image, Extracted index, Deciphered elliptic curve data, Corresponding plain message.

| Stego Image | Extracted index | Deciphered elliptic curve point | Secret text |
|-------------|-------------------|---|-------------|
| | {53, 59, 6, 19} | {(86, 20), (70, 47), (102, 39), (97, 15)} | NITS |
| | {101, 10, 23, 77} | {(72, 87), (17, 52), (39, 4), (26, 124)} | 0976 |
| | {44, 118, 4, 35} | {(1, 93), (9, 79), (12, 118), (24, 116)} | @% * + |
| | {127, 5, 44, 10} | {(72, 44), (115, 9), (1, 93), (127, 8)} | Kl@9 |

VI. DISCUSSION

From the simulation results, it is shown that the proposed steganalysis can successfully retrieve the secret data by an adversary from the cover image.

Issues in Bansal *et al.* technique.

- 1) The elliptic curve parameter chosen is not a standard parameter and has got a small cyclic order. So, a cryptanalysis is possible for the elliptic curve parameter chosen by Bansal *et al.*
- 2) Many of the elliptic curve points are not invertible. Bansal *et al.* algorithm will not work when the inverse cannot be computed.
- 3) The number of points given in Table I that are assigned with an index value is less than the actual number of points. When an encrypted point falls to an elliptic curve not in Table I, an issue arises as the missing index value must be embedded in the cover image.
- 4) The algorithm given in Bansal *et al.* embedding technique needs to consider the case of false positives during extraction. For instance, the possibility arises that LSB patterns from the four blocks can be {0001 or 0010 or 0100 or 1000 or 0111 or 1011 or 1101 or 1110} with secret data pattern {00 or 01 or 10 or 11} not matching any of the four divided blocks. In such cases, false positive extraction of the 6th and 7th bit pattern occurs resulting in incorrect encrypted data extraction.

VII. CONCLUSION

The encryption technique adopted by Bansal *et al.* is based on the concepts of ECC. The security of elliptic curve-based cryptographic schemes relies on the presumed computational infeasibility of solving the ECDLP. However, the elliptic curve parameters adopted in the Bansal *et al.* method were too small to withstand certain general discrete log attacks. Some of the issues related to the Bansal *et al.* method such as invertible issues, missing index values, and false positive extraction are highlighted. Cryptanalysis and Steganalysis were successfully performed and the secret text was recovered from the dual-layer security. A possible solution will be to use standard elliptic curve parameters suggested by standard organizations like NIST [18] or Brainpool [19] that can resist naive, BSGS, or Pollard's rho attack. Using the standard elliptic curve parameters will increase security and prevent the attacks but future research can be carried out by considering the issue of embedding numerically large elliptic curve points in the cover data. Moreover, improvement can be made by removing the concept of the static index table and embedding data at random coordinates of the cover image using a random coordinate generator.

REFERENCES

- [1] A. Jan, S. A. Parah, B. A. Malik, and M. Rashid, "Secure data transmission in IoTs based on CLoG edge detection," *Future Generation Computer Systems*, vol. 121, pp. 59–73, Aug. 2021, doi: <https://doi.org/10.1016/j.future.2021.03.005>.
- [2] W. Z. Khan, M. Y. Aalsalem, M. K. Khan, and Q. Arshad, "Data and Privacy: Getting Consumers to Trust Products Enabled by the Internet of Things," *IEEE Consumer Electronics Magazine*, vol. 8, no. 2, pp. 35–38, Mar. 2019, doi: <https://doi.org/10.1109/MCE.2018.2880807>.
- [3] A. K. Singh, B. Kumar, S. K. Singh, S. P. Ghrera, and A. Mohan, "Multiple watermarking technique for securing online social network contents using Back Propagation Neural Network," *Future Generation Computer Systems*, vol. 86, pp. 926–939, Sep. 2018, doi: <https://doi.org/10.1016/j.future.2016.11.023>.
- [4] B. O. Al-Roithy and A. Gutub, "Remodeling randomness prioritization to boost-up security of RGB image encryption," *Multimedia Tools and Applications*, vol. 80, no. 18, pp. 28521–28581, Jun. 2021, doi: <https://doi.org/10.1007/s11042-021-11051-3>.
- [5] A. Jan, S. A. Parah, and Bilal Haider Malik, "A Novel Laplacian of Gaussian (LoG) and Chaotic Encryption Based Image Steganography Technique," Jun. 2020, doi: <https://doi.org/10.1109/incet49848.2020.9154173>.
- [6] A. Jan, S. A. Parah, and Bilal Haider Malik, "Logistic Map-Based Image Steganography Using Edge Detection," pp. 447–454, Jan. 2021, doi: https://doi.org/10.1007/978-981-15-6067-5_50.
- [7] D. S. Laiphrakpam, R. Thingbaijam, K. M. Singh and M. Al Awida, "Encrypting Multiple Images With an Enhanced Chaotic Map," in *IEEE Access*, vol. 10, pp. 87844–87859, 2022, doi: [10.1109/ACCESS.2022.3199738](https://doi.org/10.1109/ACCESS.2022.3199738).
- [8] C. Li, B. Feng, S. Li, Jürgen Kurths, and G. Chen, "Dynamic Analysis of Digital Chaotic Maps via State-Mapping Networks," vol. 66, no. 6, pp. 2322–2335, Oct. 2014, doi: <https://doi.org/10.1109/tcsi.2018.2888688>.
- [9] Z. Hua, F. Jin, B. Xu, and H. Huang, "2D Logistic-Sine-coupling map for image encryption," *Signal Processing*, vol. 149, pp. 148–161, Aug. 2018, doi: <https://doi.org/10.1016/j.sigpro.2018.03.010>.
- [10] C. Kim, C.-N. Yang, and L. Leng, "High-Capacity Data Hiding for ABTC-EQ Based Compressed Image," vol. 9, no. 4, pp. 644–644, Apr. 2020, doi: <https://doi.org/10.3390/electronics9040644>.
- [11] V. Sharma and Madhusudan, "Two new approaches for image steganography using cryptography," Dec. 2015, doi: <https://doi.org/10.1109/iciip.2015.7414766>.
- [12] S. Sriram, B. Karthikeyan, V. Vaithyanathan, and A. Raj, "An approach of cryptography and steganography using rotor cipher for secure transmission," Dec. 2015, doi: <https://doi.org/10.1109/iccic.2015.7435669>.
- [13] B. Karthikeyan, Adarsh Deepak, K.S. Subalakshmi, A. Raj, and V. Vaithyanathan, "A combined approach of steganography with LSB encoding technique and DES algorithm," Feb. 2017, doi: <https://doi.org/10.1109/aceicb.2017.7972388>.
- [14] R. Bansal and N. Badal, "A novel approach for dual layer security of message using Steganography and Cryptography," *Multimedia Tools and Applications*, vol. 81, no. 15, pp. 20669–20684, Mar. 2022, doi: <https://doi.org/10.1007/s11042-022-12084-y>.
- [15] Shanthakumari, R., S. Malliga, and S. Dheepika. "Data hiding scheme in spatial domain." *International Journal of Science, Engineering and Computer Technology* 4.12 (2014): 400.
- [16] B. Sharmila, "Efficient Adaptive Steganography For Color Images Based On LSBMR Algorithm," Feb. 2012. doi: [10.21917/ijivp.2012.0055](https://doi.org/10.21917/ijivp.2012.0055)
- [17] The USC-SIPI Image Database. <http://sipi.usc.edu/database/> accessed 19 May 2020.
- [18] NIST Elliptic curve parameter, <https://nvlpubs.nist.gov/nistpubs/SpecialPublications/NIST.SP.800-186-draft.pdf>, accessed 13 June 2023.
- [19] Brainpool Elliptic curve parameter, http://www.ecc-brainpool.org/download/Domain_parameters.pdf, accessed 19 May 2016

Incomplete Adventure: An educational game for the TOEIC exam

Surawee Tedsakorn*

Nattapong Aksaraliksanti †

Sirion Vittayakorn‡

School of Information Technology

King Mongkut's Institute of Technology Ladkrabang

Bangkok, Thailand, 10520

Email: {61070252*, 61070056†, sirion.vi‡}@kmitl.ac.th

Abstract—These days, the Test of English for International Communication (TOEIC) plays an essential role in both the work environment and everyday life. In daily life, fluency in English offers tremendous benefits including exposure to new experiences, opportunities, cultures, and friends. In the work environment, it is a crucial factor in client relationships, profitability, team effectiveness, and employee engagement. Although TOEIC preparation sources can be seen everywhere, most of them aren't very attractive or motivating. As a result, it is very hard for test takers to fully focus on exam practice for a long period of time. Unfortunately, the lack of attractive and interesting of the traditional methods e.g, book or web-based exam, negatively effect the test takers' learning performance. To mitigate this problem, we propose a game-based application for TOEIC preparation called *Incomplete Adventure*. In game-play, player needs to answer a series of TOEIC questions to defeat the enemy without dying. Even though the experimental results demonstrate that *Incomplete Adventure* is comparable with traditional learning methods in improving English skill, the game receives a better degree of satisfaction than the web-based exam by 7.6%. Moreover, the overall performance score of our game also outperforms other TOEIC games by 2.68%. We posit that the enjoyment from *Incomplete Adventure* will enhance the motivation of learning among students and finally effect the students' perception of learning in the end.

I. INTRODUCTION

Now more than ever, English proficiency is a necessity in our life including education or work environments. English communication is one of the most required skills in many organizations. Nowadays, many job opportunities not only require the potential employees to have a strong technical skills but also proficient communication skills, especially in English [1], [2]. Since English is the most widely spoken and written language in the world, it allows the organization to be able to conduct their business internationally as well as recruit prospective employees worldwide [3]. Moreover, quality communication among co-workers and with clients can eliminate unnecessary problems and promote better performance.

The Test of English for International Communication (TOEIC) has been one of the global standards for assessing English-language communication skills needed in the workplace and everyday life for more than 40 years. Although there are several practice resources for TOEIC including websites, books, or English language institutes [4], these traditional ways fail in many cases. The report reveals that 80% of test takers had spent more than 6 years studying English and 37% of test takers indicated that they had previously taken the TOEIC test

three or more times [5]. Several possibilities for these failures are 1) choosing inappropriate materials or learning methods [6] and 2) practicing in a different setting from the actual test (e.g., taking a break during the test, listening to background music, snacking or not timing the practice) [7].

To mitigate this problem, we propose a game-based learning approach for preparing for the TOEIC exam called "*Incomplete Adventure*". In our game, players have to answer series of TOEIC questions from five categories to complete the mission in a limited time. The game aims to offer an exam-like setting including timing and scoring and also provides the enjoyment of play which would enhance the student's attention and motivation to learn. The expected outcomes of *Incomplete Adventure* are the following: 1) students will acquire TOEIC-level English knowledge which can also be used in the TOEIC exam and 2) students will experience amusement and motivation to learn.

II. RELATED WORK

This section reviews relevant previous works on 1) Test of English for International Communication (TOEIC) and 2) Game-based learning.

A. Test of English for International Communication (TOEIC)

TOEIC is a international standardized test of English language for non-native speakers [8]. The test is based on real life work situations including email, telephoning, meetings and other conversations in everyday life. The test includes 2 parts; Listening and Reading. The total time for the test is 150 minutes with 45 minutes for the listening section, 75 minutes for the reading section and approximately 30 minutes to answer biographical questions. The listening section has 4 parts including Photographs, Question-Response, Conversation and Short Talk, while the Reading section includes Incomplete Sentences, Text Completion and Reading Comprehension. The report on test takers shows that the average score of the reading part is always lower than the listen part [9]. Meaning that test takers are struggle with reading more than listening skills. Thus, in this work, we propose a game that focus on improving the reading skills of the players.

B. Game-based learning

Game-based learning is an active learning technique where games are used to enhance student learning. The learning

TABLE I: Examples of questions from the dataset.

| Topic | Example questions |
|----------------|--|
| Part of speech | - We promise to send ____ proposed contract to them by Wednesday morning. |
| Vocabulary | - Could you please ____ the next candidate to come in? |
| Preposition | - They have been asked to contribute ____ a scholarship program. |
| Conjunction | - The company has shown a profit ____ the last 12 years. |
| Tense | - A special sale on stationery ____ on the Write Things Web site yesterday |

comes from playing the game and promotes student engagement and motivation to learn [10]. Modern education has changed from memorization and recitation to be more interactive and engaging, for which game-based learning is one of the most effective modern teaching methods [11]. Several scholarly works demonstrate that game-based learning is effective and beneficial for students in many ways including 1) increasing motivation for learning, 2) improving problem solving skills and 3) improving student perception of learning [12]–[14].

1) *Game-based language learning*: Due to the advantages of game-based learning approach, several works have been integrated game with language learning to provide learners with methods to maintain their interest in the learning process in many platforms e.g, board games [15], computer games [16], [17], virtual reality games [18], game-based websites [19] or mobile applications [20], [21]. And they have demonstrated that integrating a game-like environment into the language learning process, especially vocabulary learning, can be a successful strategy by offer an opportunity to practice the language repeatedly as players progress through the game. Unlike the previous works, we design a game specially for TOEIC exam preparation where we aim to mimic the TOEIC exam environment and reading content as closely as possible as well as provide the amusement during the game-play.

III. DATASET

To replicate the TOEIC reading exam, we created a novel dataset called "*Incomplete adventure quiz dataset*". The dataset consists of about 500 questions from reading part of TOEIC used during 2019 - 2020 under five topics: 1) Part of speech, 2) Vocabulary, 3) Prepositions, 4) Conjunctions and 5) Tense. The questions are collected from two resources: 1) *opendurian.com* which is an online education platform that specialize in tutoring several exams [22] e.g., TOEIC, IELTS, Thai University Central Admission System (TCAS), etc. 2) *TOEIC24.com* which is a website for testing TOEIC specifically [23]. Some example questions are shown in Table I. Player is required to answers these questions correctly in the limited time in order to complete the game-play.

IV. SYSTEM SCENARIO

Incomplete Adventure integrates the TOEIC practice tests with a game-based learning approach to provide enjoyment and an alternative exam-like setting resource for the player. The game pipeline is shown in Fig. 1. When player enters the game, the main menu is displayed (Fig. 1a). Player can choose among 5 different options as follows:

- 1) **New game**: Player is able to choose one among five missions where each mission corresponds to particular topic in the exam or map (Fig. 1b). Then the new game starts.
- 2) **Continue**: Player can continue their own progress from their previous games (Fig. 1a).
- 3) **Tutorial**: Player will be guided step by step about game-play and completed sample questions (Fig. 1i).
- 4) **Setting**: Player can customize the screen resolution and background music volume.
- 5) **Exit**: The program will be terminated.

V. INCOMPLETE ADVENTURE

In this section, we describe system requirements and fully explain the Incomplete Adventure game in both Tutorial mode and Game-play mode.

A. System Requirement

Incomplete Adventure requires a personal computer with the minimum specifications of Intel i7-6700 with NVIDIA GTX 960, 16 GB of RAM and Windows 10.

B. Tutorial

In this mode, player can learn how to play the game. When player enters the tutorial, the game instructions are shown to the player (Fig. 1i). Then, the player is guided, step-by-step, to perform two different actions – attacking or healing – and answer six sample questions to complete the mission.

C. Game-play

During a game, player needs to defeat the enemy without themselves dying. To do so, player is required to answer set of questions and answers correctly and quickly: comparable to an exam-like setting. In each turn, player has to answer series of question sets where each question set contains 3 questions randomly taken from the dataset (Fig. 1d). In order to gain the maximum attacking or healing power, player needs to answer *ALL* 3 questions correctly within 2 minutes. The number of questions in each game is around 30 - 45 questions. Thus, the average time for each round is 20 - 30 minutes.

The immediate feedback will be provided after each question in order to enhance players' memory (Fig. 1e). After one player's turn, it is the enemy's turn to attack the player. If the time runs out before player can complete the questions, the enemy's damage will be empowered.

1) *Questions and answers*: There are 5 topics of TOEIC questions in Incomplete Adventure. Since we want to ensure the diversity of the questions in the game-play, the questions that have already been answered will be excluded from future game-play. These questions will not be repeated unless player has completed the whole dataset.

2) *Maps*: The game consists of 6 maps where first 5 maps correspond to the 5 question topics: 1) Parts of speech, 2) Vocabulary, 3) Prepositions, 4) Conjunctions and 5) Tense, as shown in Fig. 1b. The last map called "*TEST*" includes questions from *ALL* topics. The player has to complete all 5 maps at least once in order to play the last map. To keep track

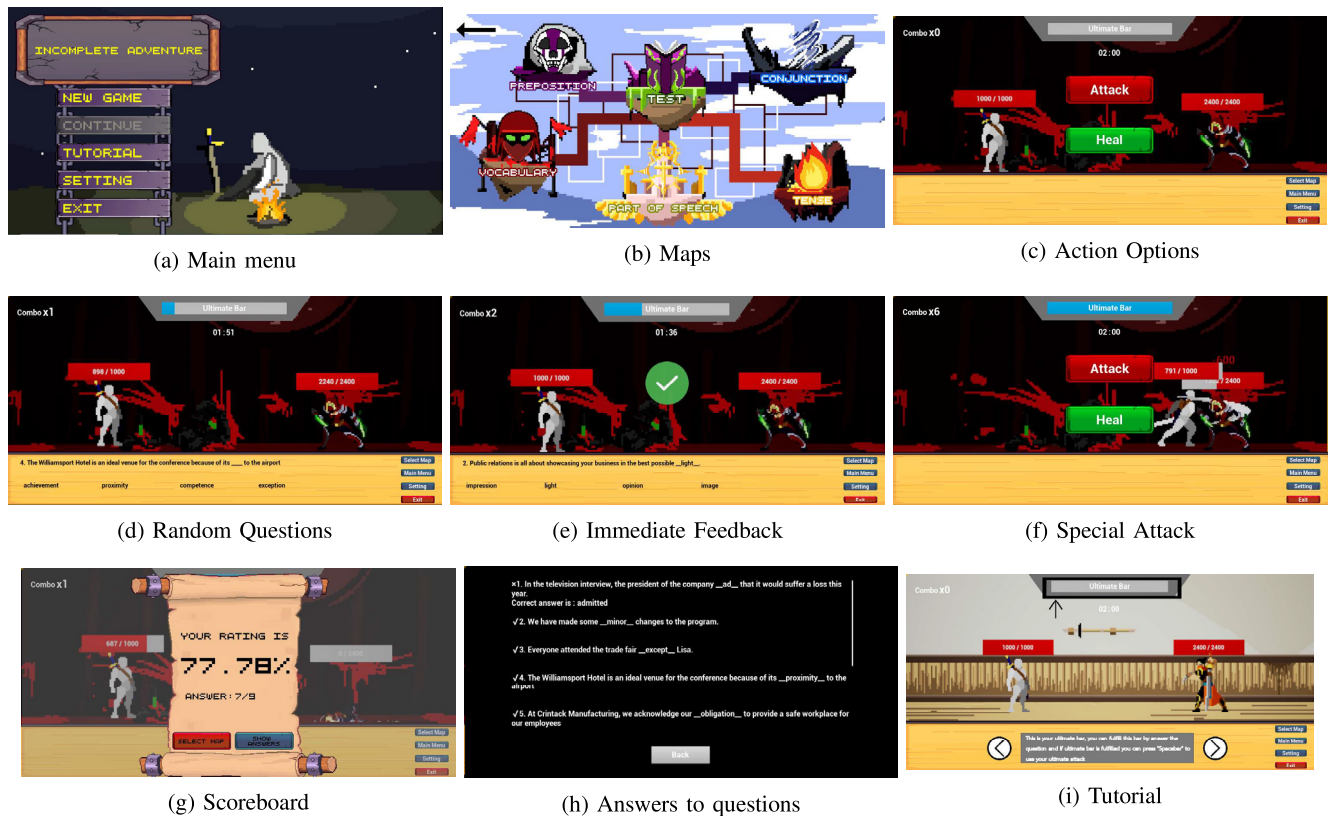


Fig. 1: Incomplete Adventure Pipeline

of the performance of the player in each topic, the game also provide several statistics for the player including:

- **Best rate:** The best accuracy (percentage) that the player has achieved from that topic.
- **Average rate:** The average accuracy (percentage) that the player achieved from that topic.
- **Number of questions:** The total number of unique questions in that topic that the player has finished.

We believe that these numbers could help player to track their own performance and encourage them to do better in their weaker topics.

3) **Attacking or Healing mode:** To enhance the amusement of the game-play, in each turn, player has two options: "attacking the enemy" or "healing themselves" as shown in Fig. 1c. While attacking mode decreases the enemy's hit points (HP), a numerical attribute representing the health of a character, healing mode increase the player's HP. During the game-play, the player needs to plan their moves carefully to defeat the enemy without dying.

4) **Ultimate skill:** To encourage the player to focus on continuously answering the questions correctly, we introduce the "Ultimate skill". With every correct answer, the ultimate bar will be fulfilled. In addition, player also gains a combo for consecutive correct answers, which helps speed up the ultimate bar. Once the ultimate bar is full, player can press

the keyboard space-bar to perform a special attack, dealing significant damage to the enemy (Fig. 1f).

After the game ends, the scoreboard will be displayed (Fig. 1g). The scoreboard includes the players' performance in the lasted round. If the player clicks "Show answers", the correct answers of their latest questions will be displayed such that player can review their answers as shown in Fig. 1h.

VI. EXPERIMENTAL RESULTS

In this section, we evaluate our game in two aspects: 1) as an effective alternative learning approach compares with the traditional method: web-based exam and 2) as an enjoyable game compares with another vocabulary mobile game. Thus, we conduct several experiments to answer two important questions: 1) Is Incomplete Adventure an effective learning tool for the TOEIC exam? and 2) Is Incomplete Adventure a entertaining educational game?

A. Is Incomplete Adventure an effective learning tool for TOEIC exam?

To answer the first question, we conduct an experiment to compare our game with the web-based exam baselines. This experiment includes 10 participants (8 males and 2 females) whose average age is 21.

TABLE II: The average scores of the pre-test and post-test exam of two groups.

| | Pre-test(%) | Post-test(%) |
|------------|-------------|--------------|
| Web-based | 52 ± 3.61 | 58 ± 2.65 |
| Game-based | 46.0 ± 3.25 | 53.0 ± 3.26 |

TABLE III: The average degree of satisfaction of Incomplete Adventure compared to the web-based baseline.

| | Web-based exams | Incomplete Adventure |
|-------------------|-----------------|----------------------|
| Attractive | 3.2 ± 0.79 | 4.1 ± 0.32 |
| Enjoyment | 2.6 ± 1.26 | 4.0 ± 0.67 |
| Smoothness of use | 3.6 ± 0.84 | 3.8 ± 0.63 |
| Ease of use | 3.7 ± 0.82 | 3.4 ± 0.70 |
| Informative | 4.1 ± 0.74 | 3.8 ± 0.42 |
| Average score | 3.44 ± 0.57 | 3.82 ± 0.27 |

1) *Examination evaluation*: First, all participants are required to complete the pre-test TOEIC exam and their scores are recorded. Then, we split the participants into 2 groups to study the same topics in 2 different methods for a week as follows:

- **Web-based group**: Which consists of 5 people who practice the TOEIC exam at least 3 times, each time for at least 1 hour for a week from one of the following websites:
 - **Opendurian**: The website offers various resources for exam preparation including sample TOEIC exams with detailed solutions and additional TOEIC exams from other sources [22].
 - **Toeic24**: The website provides free TOEIC online practice tests to help students prepare for the TOEIC exam. There are about 10 practice tests and 10 mini listening and reading tests available on their website [23].

Although there are several websites that offer practice exams for TOEIC, most of them are almost identical where test takers have to complete hundreds of multiple-choice questions in a limited time.

- **Game-based group**: Which consists of 5 people who have to play Incomplete Adventure at least 3 times, each time for at least 1 hour for 1 week.

After a week, both groups have to take the post-test TOEIC exam. Their scores from Table II reveals that reviewing the topics either way (website or game) improves the participants' performance. Incomplete Adventure increases the participants' scores by 7% while reviewing the topic via the website helps enhance the participants performance only 6%. The result demonstrates that Incomplete Adventure is an effective learning tool because 1) the game improves the English skill of the players by 7% and 2) its performance is comparable with the traditional learning approach (website), meaning that it could be widely used as alternative learning tool in the future.

2) *Degree of satisfaction*: Moreover, we also examine the degree of satisfaction of all participants with both learning methods. After completing the post-test exam, all 10 participants tried both learning methods, then they were asked to

measure their attitudes toward both learning methods by rating each criteria on a scale from 1-5 where 1 means 'Hate it' and 5 means 'Love it'. The average satisfaction scores of several criteria are shown in Table III. All criteria and the corresponding degree of satisfaction are further explained as follows:

- **Attractive**: Most participants think that Incomplete Adventure provides more excitement and attraction than the web-based exam since the web-based exams usually contains only text. Therefore, Incomplete Adventure has a higher average score than the web-based exam by 18%.
- **Enjoyment**: Participants enjoy playing Incomplete Adventure since it provides more interaction than the website. The pleasure from the game-play motivates participants to learn and play more. Thus, Incomplete Adventure achieves an average score of 4 ± 0.67 which outperforms the web-based method by 28%.
- **Smoothness of use**: The participants are familiar with the web-based exam setting, thus they have no major difficulties during practice the exam via the websites. However, most of them prefer the continuity of Incomplete Adventure game-play. During the game, player has to answer 30-45 questions continuously. Player cannot take a break during the game, same situation with the real exam. Some of them think that this scenario helps them be more focus on the learning process. As a result, the Incomplete Adventure outperforms web-based exam by 4%.
- **Ease of use**: The web-based approach outperformed Incomplete Adventure in this criteria about 6% mainly for 2 reasons: 1) the web-based exam is accessible on several platforms including PC, tablet or mobile while Incomplete Adventure only available on PC, and 2) everyone is familiar with multiple-choice exams while no one had played Incomplete Adventure before. Although the game-play is simple, the web-based is effortless.
- **Informative**: Some participants think that learning process via web-based exams is slightly more informative than Incomplete Adventure. Because several websites provide instant feedback to the test takers right after they make a mistake, and they can spend time study the incorrect answer as long as they need. Although Incomplete Adventure also provides the instant feedback to player as well, but the feedback will be showed in only a short period of time due to the continuity of the game-play. Even though player can review all the feedback again after the game ends (as long as the player need), some participants prefer the web-based setting. Thus, the web-based approach slightly outperforms Incomplete Adventure by 6%.

The average score confirm that participants prefer Incomplete Adventure to web-based exams with a higher average score of 3.82 ± 0.27 which is more than the web-based exam's score of about 7.6%.

3) *Qualitative results*: Furthermore, we gathered feedback from both groups on their experiences from preparing for the

TABLE IV: The average degree of satisfaction of Incomplete Adventure compared to the game-based learning baseline.

| | Incomplete Adventure | TOEIC Zombie |
|-------------------|----------------------|--------------|
| Attractive | 4.1 ± 0.32 | 3.7 ± 0.7 |
| Enjoyment | 4.0 ± 0.67 | 3.8 ± 0.97 |
| Smoothness of use | 3.8 ± 0.63 | 4.1 ± 0.88 |
| Ease of use | 3.4 ± 0.70 | 3.5 ± 0.97 |
| Informative | 3.8 ± 0.42 | 3.4 ± 1.14 |
| Average score | 3.82 ± 0.27 | 3.69 ± 0.29 |

test via their assigned resource. Some of their comments are shown as follows:

- "Even though the web-based exam provides a better experience in terms of an exam-like setting, practicing for the exam could be very boring. Incomplete Adventure cracked this problem very well even if the web-based exam is more practical. I really enjoy the game."
- "Practicing for the exam via the game is more entertaining and exciting than the web-based exam."
- "The idea that I have to defeat the enemy without dying in a limited time, encouraged me to stay active at all times."

Although the traditional web-based exam provides a realistic exam-like environment, this has both advantages and disadvantages. While the exam-like setting helps test takers to be familiar with the real exam, it decreases the learning motivation of test takers.

Finally, the results confirm that Incomplete Adventure, a game-based approach, increases the student's motivation for learning. They enjoy the alternative learning approach that provides both enjoyment and knowledge better than the traditional method.

B. Is Incomplete Adventure an entertaining educational game?

To answer the second question, we conducted an experiment with 10 participants (8 males and 2 females) whose average age is 21. We compare our game with *TOEIC Zombie* [21].

TOEIC Zombie: A free mobile application that integrates a simple shooting game-play with TOEIC vocabulary. The game achieves 4.3 of 5 rating scores from the users [21]. In this game, player needs to answer the correct meaning of the given vocabulary from two choices (Fig. 2b) or they will be killed by zombies. There are 3 vocabulary levels: easy, medium and hard. If the player gets the correct answer, the zombie will be killed, otherwise the player will be dead and the game is over. Special items could be purchased to slow down the zombie's speed, or to increase the time to complete a question. After the game, player can review their latest questions and scoreboard which includes both their latest score (number of correct answers) and their best score (Fig. 2c).

1) *Degree of satisfaction:* We ask all the participants to play both games at least an hour and then collect the degree of satisfaction toward both games. The participants are asked to measure their attitudes toward games by rating each criteria on a scale from 1-5 where 1 means 'Hate it' and 5 means

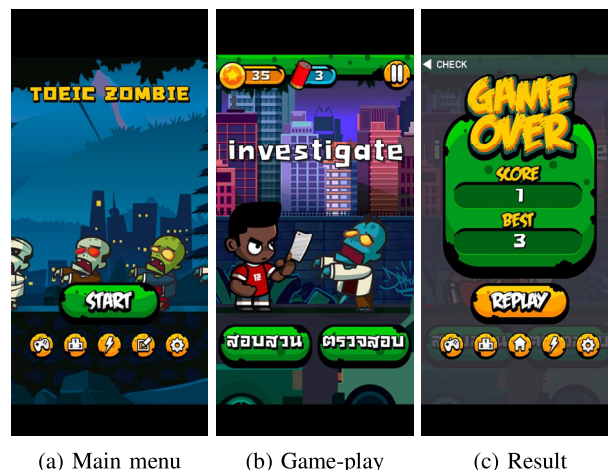


Fig. 2: Example screenshots from TOEIC Zombie game.

'Love it'. The average satisfaction scores of several criteria are shown in Table IV. All criteria and the corresponding degree of satisfaction are further explained as follows:

- **Attractive:** Most participants like Incomplete Adventure more than TOEIC Zombie because in Incomplete Adventure, player needs to type their selected answer correctly in a limited time, which is more challenging than TOEIC Zombie where they just click the button. Therefore, Incomplete Adventure has a higher average score than TOEIC Zombie by 8.63%.
- **Enjoyment:** Since Incomplete Adventure's game-play is more complicated than TOEIC Zombie's, the participants feel that it provides more enjoyment for them. In TOEIC Zombie, the game-play is simple: when the player answers the question correctly in limited time, the zombie is killed, otherwise they are killed. In Incomplete Adventure, player has to carefully plan their strategy in each round, where they could either attack the enemy or heal themselves, as well as work on their ultimate skill. More challenging game-play yields more amusement for the player. Thus, we outperform TOEIC Zombie by about 4.21%.
- **Smoothness of use:** Although more complicated game-play offers better entertainment, it decreases the smoothness of use score. Some participants feel that the more complicated game-play sometimes causes them difficulties. Therefore, Incomplete Adventure has an average score lower than TOEIC Zombie by 6.33%.
- **Ease of use:** There are similar reasons for the ease of use. Some participants prefer TOEIC Zombie's game-play – simple and straightforward. Therefore, the baseline slightly outperforms our game by 1.94%.
- **Informative:** Participants agree that Incomplete Adventure is better since it includes more diverse topics (five topics) while TOEIC Zombie only focuses on vocabulary. Thus, our game outperforms TOEIC Zombie by 8.84%.

In conclusion, the average score demonstrates that *Incomplete Adventure* is an entertaining educational game which slightly outperforms the baseline by 2.68%.

2) *Qualitative results*: In addition, we gathered feedback from the participants on their experiences from both games. Some of their comments are shown as follows:

- "There are several TOEIC topics in *Incomplete Adventure* while *TOEIC Zombie* only has vocabulary part. However, I think the UI of *TOEIC Zombie* is more attractive."
- "*Incomplete Adventure* is more challenging and informative."
- "The game-play of *TOEIC Zombie* is very short. The game is over when the answer is incorrect. This is annoying more than entertaining for me. In my opinion, I prefer *Incomplete Adventure* game-play, the combat system, attacking or healing, is challenging and the UI is more readable."
- "There is only vocabulary part in *TOEIC Zombie* while *Incomplete Adventure* covers more topics and provide more exam-like setting. The diversity of the combat system enhances the interest of the game. The timing system provides the exam-like environment as well as amplify the concentration of learning process. Moreover, it's an entertaining game."

Although *Incomplete Adventure*'s scores for smoothness of use and ease of use are slightly lower than *TOEIC Zombie* due to the complication of the game-play, most participants prefer our game-play that *TOEIC zombie* as shown in the above comments. The participants think that our game is more challenging and informative than *TOEIC Zombie*.

VII. CONCLUSION

In this work, we propose *Incomplete Adventure* as an alternative tool for preparing for the TOEIC. *Incomplete Adventure* is a game-based learning application which aims to improve the student's attention and motivation to prepare for TOEIC as well as improving their English skills. In our game, we provide an exam-like situation for player to prepare for the actual exam. During the game-play, player has to answer TOEIC questions in a limited time, and both the correctness and the time-used impact their effectiveness to defeat the enemy. We also gathered a novel dataset, "*Incomplete Adventure quiz dataset*", to ensure a diversity of questions.

The experimental results demonstrate that *Incomplete Adventure* is an effective alternative learning tool where it can 1) increase motivation for learning and 2) improve student perception of learning. The quantitative results demonstrate that *Incomplete Adventure* improves the participants' scores by about 7%. Moreover, the game receives more positive comments than the web-based exam. In addition, the participants confirm that they enjoy playing *Incomplete Adventure* and it does enhance their motivation for learning, where our game outperforms the web-based exams 7.6%. We posit that the pleasure from playing the game will encourage player to play it repetitively which will improve the players' retention. Beside, *Incomplete Adventure* is also successful as an educational game where it outperforms *TOEIC Zombie* by 3.68%.

REFERENCES

- [1] D. Pandey and P. Pandey, "Better english for better employment opportunities," *International Journal of Multidisciplinary Approaches and Studies*, vol. Volume 1, pp. 96–103, 08 2014.
- [2] Jyothi. (2012) Importance of english in employment. [Online]. Available: <https://www.deccanherald.com/content/249714/importance-english-employment.html>
- [3] K. Knight. (2015) Benefits of using english in the workplace. [Online]. Available: <https://www.regent.org.uk/blog/post/6016/benefits-of-using-english-in-the-workplace>
- [4] GlobalExam. What are the best resources to study toEIC? [Online]. Available: <https://global-exam.com/blog/en/best-resources-to-study-toEIC/>
- [5] ETS. ToEIC 2020 report on test takers worldwide. [Online]. Available: <https://www.ets.org/s/toEIC/pdf/2020-report-on-test-takers-worldwide.pdf>
- [6] TOEIC-Testpro. 6 common mistakes of self-study toEIC learners. [Online]. Available: <https://toEIC-testpro.com/blog/6-common-mistakes-of-self-study-toEIC-learners/>
- [7] A. Case. ToEIC exam problems and solutions. [Online]. Available: <https://www.usingenglish.com/articles/toEIC-exam-problems-solutions.html>
- [8] P. E. Woodford, "The test of english for international communication (toEIC)." 1980.
- [9] E. T. Service. (2020) ToEIC 2020 report on test takers worldwide. [Online]. Available: <https://www.ets.org/s/toEIC/pdf/2020-report-on-test-takers-worldwide.pdf>
- [10] M. Qian and K. R. Clark, "Game-based learning and 21st century skills: A review of recent research," *Computers in Human Behavior*, 2016.
- [11] S. Mehta, "Modern teaching methods—it's time for the change," *Edu-voice India*, vol. 1, no. 1, pp. 3–11, 2020.
- [12] A. Ghazy, M. Wajdi, C. Sada, and I. Ikhsanudin, "The use of game-based learning in english class," *Journal of Applied Studies in Language*, vol. 5, pp. 67–78, 06 2021.
- [13] S. Tang, M. Hanneghan, and A. El Rhalibi, "Introduction to games-based learning," *Games-Based Learning Advancements for Multi-Sensory Human Computer Interfaces: Techniques and Effective Practices*, pp. 1–17, 01 2009.
- [14] Z. Eslami and M. Chowdhury, *Digital Game-based Learning*, 01 2021, pp. 621–625.
- [15] J. York, *Promoting Spoken Interaction and Student Engagement With Board Games in a Language Teaching Context*, 01 2020, pp. 1–26.
- [16] A. Berns, A. Gonzalez-Pardo, and D. Camacho, "Game-like language learning in 3-d virtual environments," *Computers Education*, vol. 60, no. 1, pp. 210–220, 2013.
- [17] Q.-F. Yang, S.-C. Chang, G.-J. Hwang, and D. Zou, "Balancing cognitive complexity and gaming level: Effects of a cognitive complexity-based competition game on eFL students' english vocabulary learning performance, anxiety and behaviors," *Computers Education*, vol. 148, p. 103808, 2020.
- [18] Y.-L. Chen and C.-C. Hsu, "Self-regulated mobile game-based english learning in a virtual reality environment," *Computers Education*, vol. 154, p. 103910, 2020.
- [19] C.-C. Cheng, "Game-based learning and toEIC vocabulary building: nnes students' learning attitudes and motivations," *Journal of Applied Linguistics and Language Research*, vol. 7, no. 1, pp. 135–143, 2020.
- [20] T.-I. Lu and K. T.-C. Chen, "The effects of mobile game based application on high school students' toEIC vocabulary learning," *Mihaela Cvek, Mateja Pšunder*, p. 108.
- [21] W. Chatwaranon. ToEIC zombie. [Online]. Available: <https://apple.co/36C6q4C>
- [22] "ToEIC reading test." [Online]. Available: https://www.opendurian.com/news/toEIC_rcpractice/
- [23] "ToEIC online test." [Online]. Available: <https://toEIC24.com/toEIC-online-test>

Naval Wargame Prototyping: Multiplayer Real-Time Strategy Game Simulation using Unreal Engine

Nattawat Chavanit
62070066@it.kmitl.ac.th

Sukawit Bualoy
62070203@it.kmitl.ac.th

Samart Moodleah
samart@it.kmitl.ac.th

*School of Information Technology
King Mongkut's Institute of Technology Ladkrabang
Bangkok, Thailand*

Abstract—We propose an integration framework for a wargame prototype using the modern game engine - Unreal Engine. This wargame functions as a simulation tool for strategy training, strategy testing, and simulating enemy forces like warships, aircraft, and weapons. Existing wargames come in proprietary and free versions. The former is often expensive and exclusive due to security reasons, while developing a functional wargame is complex, requiring various technological components such as a physics system and artificial intelligence (AI). To overcome these challenges, we propose a rapid prototype using Unreal Engine. This approach leverages advanced technology and ensures the prototype is ready for future upgrades when new versions of the game engine are released. We evaluate the prototype's system capabilities and expert assessments.

Index Terms—Wargame, Game prototyping, Unreal Engine, Real-Time Strategy (RTS)

I. INTRODUCTION

For national security, especially in the military, war strategies are periodically refined for thorough officer preparation. Training occurs physically and virtually. Physical training offers realism but demands significant preparation and expenses. Virtual training excels in generating secure dynamic scenarios, serving as preparation before physical exercises. The Royal Thai Navy uses the Naval Wargame Simulator 980 (NWS 980) for virtual training, originating from the now-discontinued open-source platform Global Conflict Blue 2 (GCB2). This poses challenges for future core wargame improvements.

Creating a robust combat simulation system is a formidable challenge. It involves intricate convergence of detailed weapon models, dynamic cartography, strategic formulations, and cutting-edge artificial intelligence. Adding online multiplayer capabilities adds complexity. Fortunately, a modern game engine like Unreal Engine offers advanced simulation tech, high-quality graphics, robust networking, and state-of-the-art AI. This makes it perfect for crafting real-time naval warfare strategy

games. Using a modern game engine accelerates development, as demonstrated in [1]–[5].

In this paper, we present a wargame prototype utilizing Unreal Engine for naval warfare simulation, encompassing all essential elements. This is based on interviews conducted with a group of senior navy officers who are experts in wargame simulation. We leverage public data from the Royal Thai Navy, including ships, missiles, and weapons, as the foundation for developing 3D game assets. Note that we do not cover army and air battles in this research. Our focus is prototyping the navy wargame (NWS 980) using a modern game engine. However, the prototype can extend to other warfare fields with more assets and configurations.

The paper is organized as follows: Section II explains existing wargames and related tools, while Section III elaborates on the design and development process. The following Section IV details the experiments and results. Lastly, Section V provides a summary of the conclusion and future work.

II. RELATED WORKS

In this section, we provide details about the real-time strategy (RTS) game genre to which the wargame belongs, along with specifics about the wargame simulator. Finally, we discuss existing notable wargames.

A. Real-time Strategy Game (RTS)

A Real-Time Strategy Game (RTS) is a subgenre of strategy games where players make decisions and control units in real time [6], [7]. The goal is to strategize, manage units, and engage in battles against opponents. Players construct units, gather resources, and use tactics to defeat enemies. RTS games often feature multiplayer modes where players interact, cooperate, or compete, fostering social communication and engagement. This genre is known for its dynamic gameplay and requires quick thinking and resource management for success.

B. War Game Simulator

Simulation involves imitating real-world processes or scenarios to replicate key features, behaviors, or appearances. In the context of strategy and training, a Wargame Simulator serves as a valuable tool for planning battles, testing strategies, and simulating enemy forces such as warships, aircraft, and weapons. This simulation enables factions to execute real-like strategies and employ virtual weapons to engage opponents. On a more professional level, Professional War Games, or Professional Wargaming, provide realistic war simulations used by military organizations to train officers in strategic decision-making, develop new tactics, and anticipate future warfare trends [8], [9]. These simulations contrast with recreational war games played for entertainment, emphasizing practical training and accurate battlefield insights [10]–[12].

C. Existing War Simulation Games

Virtual Battlespace 4 (VBS4) takes the lead as a prime selection for professional military training [13]. Its exceptional realism and customization capabilities make it an invaluable tool for honing skills. Built to accurately replicate real-world scenarios, VBS4 plays a vital role in tactical and strategic exercises. However, its robust features come with a higher cost, attributed to licensing and customization fees. This expenditure is often justified by the platform's ability to create immersive training environments that closely mirror actual operational settings.

Alternatively, open-source and freemium alternatives present themselves. The World Digital Combat Simulator (DCS) is one of the most realistic air combat simulators to date and is available for free on STEAM (a popular gaming platform) [14]. The DCS adopts a unique model, combining free base content with purchasable modules. It's an ideal choice for aviation enthusiasts and gamers looking for a realistic experience across various combat scenarios.

Global Conflict Blue 2 (GCB2), an open-source platform, is tailored for naval and underwater combat simulation. Particularly advantageous for enthusiasts, schools, and smaller organizations, GCB2 encourages community-driven customization. It's important to note that GCB2 also serves as a foundational component of the Naval Wargame Simulator 980 (NWS 980), developed by the Royal Thai Navy for internal training purposes. Regrettably, it's worth noting that GCB2 has been discontinued. Its infrastructure struggles to keep pace with modern technology demands, hindering improvements and updates. This limitation underscores the dynamic nature of simulation software development, as platforms must continually evolve to remain relevant and effective.

We build our prototype upon the features of NWS 980, GCB2, and DCS. The development of the prototype takes place using Unreal Engine 4, incorporating relevant sub-technologies to achieve the necessary features.

III. METHODS: GAME DESIGN AND DEVELOPMENT

This section presents the game design and development methodology. The design process begins with user inquiries gathered from various public data resources, the NWS 980 system, and interviews with navy officers. Subsequently, game design elements are adopted to finalize the game concept. The development path outlines the wargame system's structure as well as its technological components.

A. Game Requirements and Design

We gather game data from various sources, including public data, existing games like DCS and NWS 980, and interviews with senior navy officers from the Royal Thai Navy. The data requirements are substantial, and after careful consideration, we narrow our focus to creating a proof of concept prototype centered around ship deployment. This prototype will enable trainees to strategize with their teams to achieve victory in the wargame. Details are provided below.

- **Diverse Boat Types with Unique Attributes:** Exploring warships, cargo ships, fishing boats, armed fishing boats, and Dana Boats, each offering distinct strategic attributes.
- **Standardized Ship Symbols for Visual Clarity:** Game employs standardized ship symbols aligned with Naval Tactical Data System (NTDS) standards [15], enhancing understanding of ship ownership, enemy presence, neutrality, and unidentified status.
- **Balanced Strategy and Action:** Players manage ship features, utilizing sensors and weapons to engage diverse targets, enhancing tactical depth by combining theory and practice for realistic strategic thinking. Additionally, the battle scenario can be divided into three possible factions: alliance, hostile, and neutral. Each ship can be assigned to one of these factions. The game allows users to deploy ships based on their assignments.
- **Game Objective:** The goal of the wargame is to achieve victory in battle by employing team strategies within dynamic scenarios. For instance, the battles encompass activities such as attacking the hostiles, which includes details such as hostile validation, deploying guided missiles and guns, utilizing sensors such as sonar, and enabling an automatic defense system based on AI, etc.
- **Game Balance:** We assess game balance using Jesse Schell's framework [16], focusing on dimensions like fairness, meaningful choices, skill versus

chance, and competition versus cooperation. The game emphasizes strategic thinking over physical skills, offers both simple and complex gameplay, and incorporates unique ship abilities for depth. Our study explores how these aspects interact to shape the gaming experience.

- **Game Procedure:** The host creates a session (room), and the client joins it. Once both are in the room, the simulation begins. Here's a brief summary of the user-host relationship:
 - **Room Owners:** They shape the gaming experience by starting rooms and gameplay sessions. They control in-game time and can end sessions.
 - **Users:** They seamlessly join rooms, choose factions, control troop movement, and launch attacks. They strategically position troops, access unit details, change camera views, and leave rooms.

By organizing these functions in these pathways, we ensure a unified and exciting gameplay experience known for its strategic depth and immersive interaction.

B. Game Assets and Map

For realism, we have collected a range of ship and weapon data from the Royal Thai Navy's public data, covering 8 ship categories, 4 missile types, and 12 naval gun variants. Our detailed 3D modeling process ensures authenticity through precise prototypes and textures, enhancing war simulations with variety.

The process of developing a 3D model begins by selecting a real object (data), such as a ship, from the available data. We thoroughly examine the ship's specifications, including dimensions and capabilities. Next, the model is created using software like Maya, which involves the UV spreading step (projecting the 3D model's surface onto a 2D image for texture mapping), before sending the texture to Substance Painter. Ultimately, the model is seamlessly integrated into Unreal Engine as a 3D asset. Fig. 1 and Fig. 2 illustrate the 3D modeling development process of a ship and a weapon, respectively. To shape the 3D landscapes, we employ tools like World Creator, drawing inspiration from the Java Sea (refer to Fig. 3). These maps are smoothly integrated into Unreal Engine and enhanced with refined materials to achieve a sense of realism. As a result, we have created 3D models of 17 ships and 22 weapons available for use in simulations. Ship, missile, and naval gun types are detailed in Tables I, II, and III, respectively. Note that units are mixed based on data nature, e.g., using both miles and kilometers in these tables.

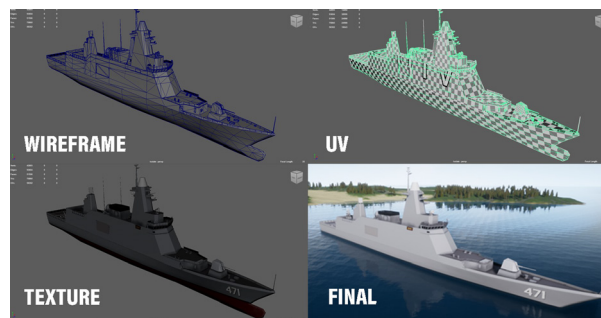


Fig. 1: Example: HTMS Bhumibol Adulyadej Frigate-Class Ship 3D Model Development

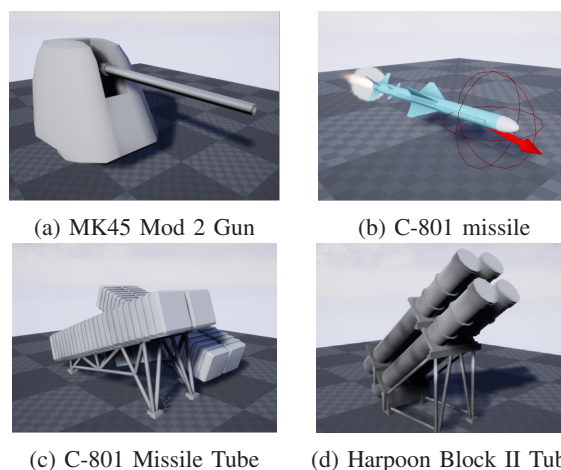


Fig. 2: Example: Missile and Gun 3D Model Development

C. Game Development

1) **System Architecture:** In our simulated game setup, the functionality is divided between two essential components: the server and the client. These two entities work in tandem to create a seamless and engaging gaming experience. Each component has specific roles that contribute to the overall operation of the game.

- **Server Role:** The server assumes the role of managing game sessions. It acts as the central hub of control, orchestrating various aspects of the gameplay. This includes initiating game sessions, maintaining game rules, and overseeing the passage of in-game time. By holding the authoritative position in the game, the server ensures that the rules are upheld consistently across all players and sessions. This is crucial for creating a fair and balanced environment that offers players an equal opportunity to engage in the game.
- **Client Role:** On the other hand, the client plays a pivotal role in providing players with access to the game. Players effortlessly join the game sessions

TABLE I: Summary of Ship Types and Key Features

| No. | Ship Type | Displacement | Dimensions | Speed | Operational Range |
|-----|--|--------------------|-----------------------------|----------------|-------------------|
| 1 | HTMS Tapee Frigates | 1,079 - 1,125 tons | L 82.5m, W 9.9m, D 4.2m | Max 20 knots | Max 2,400 miles |
| 2 | HTMS Chao Phraya Frigates | 1,676 - 1,924 tons | L 102.87m, W 11.36m, D 3.1m | Max 30 knots | Max 3,500 miles |
| 3 | HTMS Bhumibol Adulyadej Frigates | 3,700 tons | L 124.10m, W 14.40m, D 8m | Max 33.3 knots | Max 4,000 miles |
| 4 | HTMS Naresuan Frigates | 2,985 tons | L 120.50m, W 13.70m, D 6m | Max 32 knots | Max 4,000 miles |
| 5 | Corvettes of Rattanakosin | 840 - 960 tons | L 76.8m, W 9.6m, D 4.5m | Max 24 knots | Max 3,568 miles |
| 6 | Anti-submarine patrol boats of HTMS Khamrongsindhu | 475 tons | L 62m, W 8.22m, D 4.5m | Max 25 knots | Max 2,850 miles |
| 7 | Offshore patrol boats of HTMS Pattani | 1,635 tons | L 94.5m, W 11.8m, D 3.3m | Max 25 knots | Max 3,500 miles |
| 8 | Medium range patrol boats of HTMS Sattahip | 260 - 300 tons | L 50.14m, W 7.28m, D 2.8m | Max 22 knots | Max 2,500 miles |

TABLE II: Summary of Guided Missile Types

| No. | Guided Missile | Description | Operating Range |
|-----|----------------|---|-----------------|
| 1 | AGM-84 Harpoon | Surface-to-surface and air-to-ground missile, active homing, targets surface warships, multiple launch platforms. | 124 km |
| 2 | C-801 | Subsonic anti-ship missile, low altitude flight, mounted on ships and subs. | 42 km |
| 3 | C-802A | Subsonic anti-ship missile, low altitude flight, turbojet engine, various platforms. | 120 km |
| 4 | RIM-162 ESSM | Medium-range surface-to-air missile, ship protection, vertical launch systems VLS installation. | 92 km |

TABLE III: Summary of Navy Guns and Key Features

| No. | Gun Name | Details | Range | Rate of Fire |
|-----|-----------------------------|--|--------|------------------------|
| 1 | Type 79 100mm | 100mm barrel, twin barrel | 22 km | 60 rounds/min |
| 2 | Navy gun H/PJ33 100mm | New turret design, stealth feature | 22 km | 60 rounds/min |
| 3 | Type 76 37mm | First anti-aircraft turret, 37mm muzzle | 8 km | 180 rounds/min |
| 4 | Type 76A 37mm | Twin-barreled gun | 8 km | 240 rounds/min |
| 5 | OTO Melara 76mm | Single-barreled | 16 km | 120 rounds/min |
| 6 | OTO Melara 40L70 | Twin-barreled | 12 km | 600 rounds/min |
| 7 | OTO Melara 40L70 | Single-barreled, similar to Dual Platform | 12 km | 300 rounds/min |
| 8 | OTO Melara 76mm Super Rapid | Based on OTO Melara 70/62C | 16 km | 120 rounds/min |
| 9 | Mk-15 Phalanx Block 1B CIWS | Close-range defense | 4 km | 3000 – 4500 rounds/min |
| 10 | DS30M Mk2 | 30mm caliber, close-range naval defense, automatic turret | 5.1 km | 200 rounds/min |
| 11 | Mk 45 Mod 2 5-inch | Fires a 5-inch barrel, surface warships, aircraft, coastal targets | 27 km | 20 rounds/min |
| 12 | Breda-Mausier 30mm | Defends against surface and air targets | 2.5 km | 800 rounds/min |

set up by the server. Once they are part of a session, they become participants in the immersive world of the game. While the server handles the mechanics and rules of the game, the client side is responsible for delivering an interactive and visually rich experience to the players. This includes rendering graphical elements, facilitating user interactions, and displaying the results of their actions.

Fig. 4 visually represents the dynamic relationship between these two components. The server's role in managing sessions and maintaining game integrity is demonstrated, while the clients' role in delivering the game experience to individual players is also highlighted.

Note that while the server manages game rules, ensur-

ing a consistent and authoritative game environment, the client's responsibility lies in providing players with the means to interact with the game world and experience its visual and interactive elements. This division of roles between the server and the client is crucial for creating a cohesive and enjoyable gameplay experience that combines rule-based mechanics with immersive interactivity.

2) *Game Elements*: The major game elements in this prototype are the gameplay framework, ship deployment, missile and weapon configuration, radar system, and artificial intelligence aid for battle strategy. We utilize Unreal Engine 4.27 features for this rapid prototype. Programming in Unreal Engine can be approached in two different ways: Visual Scripting, known as Blueprint, or



Fig. 3: Example: Map Integration in Unreal Engine

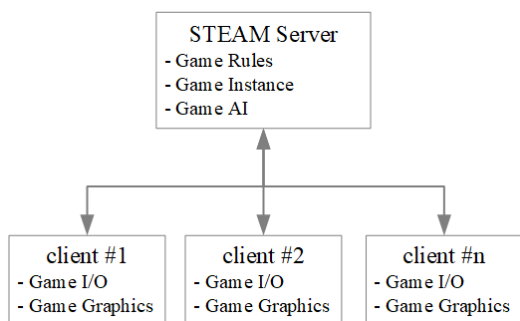


Fig. 4: Game System Architecture: Server and Client Model

traditional coding in C++. We adopt Blueprint scripting because it's suitable for prototyping games and avoids non-optimized outcomes due to a lack of skill in C++ programming. It's important to note that performance-wise, both programming techniques are comparable across most of the game engine's features. Further details are provided below.

- **Gameplay Framework:** This element manages all input/output interactions, game sessions, game rules, and related functional game features.
- **Ship Deployment:** It handles the allocation of ships, assigning them to alliances, hostiles, or neutrals. In a real scenario, open seas have different types of ships, enabling the wargame to create dynamic scenarios where ships can belong to various factions, requiring the right strategies to achieve training objectives. This also covers general configurations like ship type, position, movement direction, speed, etc.
- **Missile and Weapon Configuration:** This part manages how guided missiles and weapons installed on each type of ship are utilized.
- **Radar System:** Both naval bases and ships have defense radar systems that can be configured, including aspects like radius and secret frequency or code for faction validation.

- **Artificial Intelligence Aid for Battle Strategy:** This feature lets players utilize automatic tasks that align with their battle strategy. For instance, it can automatically control defense systems, missile systems, or targeting systems. Once the system is fully set up, the AI takes control of all simulated objects accordingly. Additionally, to validate strategies, the host can accelerate the simulation up to 7 times to expedite battle results.

To make the game realistic, we develop these elements by utilizing available sub-systems in Unreal Engine, such as the Physics engine to simulate the laws of physics or Level of Detail (LOD) to optimize graphics' realism. Structuring our code as described above allows us to improve any part of the system freely. For example, to enhance missile projectile calculation, we can focus on the physics engine part only. Additionally, in case of the game engine releasing a new version, we can effectively integrate the up-to-date version into our existing prototype.

IV. EXPERIMENT AND RESULT

We conducted two experiments: system testing and expert assessments. The first experiment aimed to evaluate the system's overall performance and capabilities in a scenario involving 15 players. This was achieved by using an Ethernet network system to engage with over 50 warships simultaneously, as shown in Fig.5. It's important to note that each player can deploy as many ships as they want. Notably, the results revealed no issues related to simulation performance or client control during the simulation. Fig.6 illustrates the network performance during a test involving 15 users and approximately 80 ships. Outgoing bandwidth increases as more ships are added, without network disruptions. After 6,000 frames, average outgoing bandwidth reaches 12.7 KB/s, with a peak of approximately 30 KB/s.

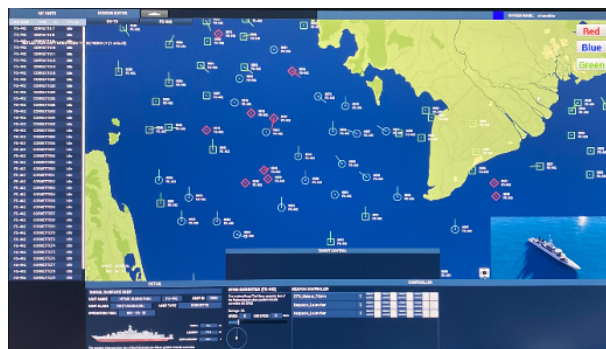


Fig. 5: Experiment Setup: 15 Players and Over 50 Ship Deployments

The latter aims to gather the opinions of three senior navy officers with specialized knowledge in naval

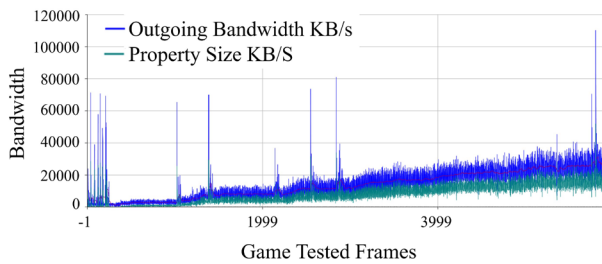


Fig. 6: Experiment Network Profile

wargames. This is accomplished by examining our research prototype's features in accordance with user requirements and the existing simulation system. The following are the expert opinions:

- Overall: The prototype system meets expectations and presents avenues for advancement. It replicates complex gameplay dynamics, including team synergies, precise ship positioning, and strategic weapon use. Ship and weapon models' accuracy enriches the experience, and the system handles dynamic combat scenarios, adapting autonomously.
- Game Highlights: The game seamlessly bridges legacy and contemporary systems, facilitating navigation for existing users. Toggling between 3D and 2D offers a view to track strategy progress. Additionally, high-quality graphical 3D enhances immersion, raising gameplay realism.
- Immersive 3D Realism: 3D elements achieve heightened realism, capturing ship and weapon details, and dynamic weapon motions mirror reality, adding authenticity.
- Enhanced User Interface: The user interface design is intuitive, drawing inspiration from established interfaces like the NWS980 program, ensuring user-friendly interaction.
- Multiplayer Seamlessness: Integrated through Steam, multiplayer mode facilitates effortless collaboration, simplifying connectivity for immersive experiences.

V. CONCLUSION AND FUTURE WORK

We've developed a prototype for an advanced online multiplayer naval combat strategy game, with a primary focus on simulating sea battles featuring Thai Navy ships. We've enhanced the AI system, refined multiplayer dynamics, and improved user interfaces through extensive testing and user feedback. Constructed on a modern game engine, this prototype enables rapid development and future expansion, enhancing interactive simulation experiences in dynamic battle scenarios.

Future improvements include incorporating diverse map elements, refining sea water physics, expanding unit types and weaponry, enhancing multiplayer stability,

creating an intuitive AI system, and optimizing network connectivity. These enhancements aim to enhance the practicality of virtual battle strategy training.

VI. ACKNOWLEDGEMENT

We express our gratitude to the Naval Strategic Studies Center, Naval Education Department, Royal Thai Navy for providing valuable information and conducting a detailed assessment of our prototype.

REFERENCES

- [1] J. Manjón Prado, "Using unreal engine as an engineering tool for traffic simulation and analysis," Master's thesis, Universitat Politècnica de Catalunya, 2020.
- [2] P. Young, S. Kysar, and J. P. Bos, "Unreal as a simulation environment for off-road autonomy," in *Autonomous Systems: Sensors, Processing, and Security for Vehicles and Infrastructure 2020*, vol. 11415. SPIE, 2020, pp. 113–120.
- [3] D. Michalík, M. Jirgl, J. Arm, and P. Fiedler, "Developing an unreal engine 4-based vehicle driving simulator applicable in driver behavior analysis—a technical perspective," *Safety*, vol. 7, no. 2, p. 25, 2021.
- [4] J. V. Sørensen, Z. Ma, and B. N. Jørgensen, "Potentials of game engines for wind power digital twin development: an investigation of the unreal engine," *Energy Informatics*, vol. 5, no. 4, pp. 1–30, 2022.
- [5] X. Zhang, Y. Fan, H. Liu, Y. Zhang, and Q. Sha, "Design and implementation of autonomous underwater vehicle simulation system based on moos and unreal engine," *Electronics*, vol. 12, no. 14, p. 3107, 2023.
- [6] P. Sweetser, D. Johnson, P. Wyeth, A. Anwar, Y. Meng, and A. Ozdowska, "Gameflow in different game genres and platforms," *Computers in Entertainment (CIE)*, vol. 15, no. 3, pp. 1–24, 2017.
- [7] A. J. Toth, E. Conroy, and M. J. Campbell, "Beyond action video games: Differences in gameplay and ability preferences among gaming genres," *Entertainment Computing*, vol. 38, p. 100408, 2021.
- [8] N. Robinson, "Military videogames: More than a game," *The RUSI Journal*, vol. 164, no. 4, pp. 10–21, 2019.
- [9] C. Turnitsa, C. Blais, and A. Tolc, *Simulation and wargaming*. Wiley Online Library, 2022.
- [10] P.-I. Evensen, S. E. Martinussen, M. Halsør, and D. H. Bentsen, "Wargaming evolved: Methodology and best practices for simulation-supported wargaming," in *The Interservice/Industry Training, Simulation & Education Conference (IITSEC), Volume 2019*, 2019.
- [11] K. Brathen, R. A. Seehuus, and O. M. Mevassvik, "Simulation support to wargaming for tactical operations planning," *Simulation and Wargaming*, pp. 223–247, 2021.
- [12] J. Langreck, H. Wong, A. Hernandez, S. Upton, M. McDonald, A. Pollman, and W. Hatch, "Modeling and simulation of future capabilities with an automated computer-aided wargame," *The Journal of Defense Modeling and Simulation*, vol. 18, no. 4, pp. 407–416, 2021.
- [13] A. W. Dorn and P. F. Dawson, "Simulating peace operations: New digital possibilities for training and public education," *Simulation & Gaming*, vol. 52, no. 2, pp. 226–242, 2021.
- [14] J. Yoo, D. Kim, and D. H. Shim, "Deep reinforcement learning based autonomous air-to-air combat using target trajectory prediction," in *2021 21st International Conference on Control, Automation and Systems (ICCAS)*. IEEE, 2021, pp. 2172–2176.
- [15] S. M. McFadden, J. Jeon, A. Li, and A. Minniti, "Evaluation of symbol sets for naval tactical displays," DRDC-TORONTO-TR-2007-046. Waterloo ONT (CAN): Defense R&D Canada-Toronto . . . , Tech. Rep., 2008.
- [16] J. Schell, *The Art of Game Design: A book of lenses*. CRC press, 2008.

Decentralized Trusted Database Approach to Online Product Reviews

Yuwana Rosoon
Division of Computational Science,
Faculty of Science
Prince of Songkla University
Songkhla, Thailand
6410220015@email.psu.ac.th

Chidchanok Choksuchat
Division of Computational Science,
Faculty of Science
Prince of Songkla University
Songkhla, Thailand
chidchanok.ch@psu.ac.th

Pattara Aiyarak*
Division of Computational Science,
Faculty of Science
Prince of Songkla University
Songkhla, Thailand
pattara.a@psu.ac.th
* Corresponding author

Abstract— Nowadays, Blockchain technology can address risks by providing a decentralized database that ensures data integrity and prevents unauthorized alterations. Traditional centralized database systems are the preferred choice for organizing large collections of data due to their rapid and systematic data accessibility. However, the concentration of access authority in the hands of administrators or individuals with power introduces potential risks to data integrity. This research proposes a decentralized approach to online product reviews that integrates a centralized database with Blockchain technology. By integrating these two systems, users can access and review content data with the assurance that the information remains unaltered. The research proposes a method to verify the integrity of data stored in the centralized database and a strategy to optimize the balance between trust and gas fees when storing data on the Blockchain. The proposed approach has the potential to improve the trustworthiness and security of online product reviews. It can also help to reduce the risks of data manipulation and fraud. Our method serves to enhance the credibility of the database.

Keywords— *Blockchain, Smart Contract, Data Integrity, Decentralized Trusted Database.*

I. INTRODUCTION

In the present day, many systems rely on Centralized Databases. This approach enables organized data storage, reducing duplicate entries and facilitating efficient data retrieval through Query Language. Furthermore, developers are well-versed in centralized database systems [1], allowing for further information development, data analysis from various perspectives, and the creation of new applications.

Some research studies the application of blockchain technology to address trust and data integrity concerns in online transactions. With the current centralized database storage, administrators may access and modify data, leading to user mistrust, as seen in instances like TripAdvisor's removal of negative reviews [2]. However, not all administrators could modify databases. Blockchain technology offers a solution by employing hash-linked blocks, ensuring any changes to data within a block impact subsequent linked block. The added decentralization enhances security, as nodes within the Blockchain network share the same data through mutual agreement. Moreover, transparency in transaction data allows members of the Blockchain network to access the same dataset from any node. The tampering of data at any node is time consuming, making data falsification on a specific node an arduous process [3].

The Ethereum Blockchain is widely regarded as one of the most decentralized and secure blockchains [4]. With 8,658 nodes and an average of 1.005 million transactions daily [5], data tampering on this platform is considered practically impossible. Data storage on the Ethereum Blockchain is facilitated through Smart Contracts [6], which allow developers to create self-executing programs. When data is written via Smart Contracts, it follows the predefined conditions set in the program. This information is accessible to anyone on the network.

Indeed, while utilizing Smart Contracts for data storage on the Ethereum Blockchain offers security and decentralization benefits, it comes with the requirement of a transaction fee or gas fee each time data is written. Complex tasks and large data storage can lead to high gas fees, posing a challenge for efficient data management.

To tackle this issue, researchers [7] have proposed Smart Contract designs focused on reducing gas costs. Their approach involves minimizing the use of over-public variables, redundant initial values, loose packing, non-base unit types, and non-constant variables. By optimizing the Smart Contract code and avoiding unnecessary operations, gas consumption can be significantly reduced. Additionally, they suggest arranging variables in groups of not more than 32 bytes to maximize gas efficiency when handling data. These efforts aim to make data storage on the Ethereum Blockchain more cost-effective.

The research [8] suggests a method to store hash data on the Blockchain through Smart Contracts, including the corresponding IDs. Adding credibility to a centralized database system can be achieved by hashing transaction data in the database and then storing it on the Blockchain through Smart Contracts, the integrity and immutability of the data can be ensured. This approach provides an added layer of trust and security, as data stored on the Blockchain cannot be altered or tampered with, enhancing the credibility and reliability of the centralized database system. This approach can increase the integrity of the database system as data stored in the Blockchain cannot be altered. However, it notes that storing data in a dynamic array format can lead to high gas costs, which can be a concern in terms of cost efficiency.

On the other hand, in another study [9], data is stored in two locations: the centralized database and the Blockchain. The Hyperledger Fabric is utilized for the Blockchain implementation. Hyperledger Fabric is a private and

permissioned blockchain framework that restricts access to authorized participants. It enables specific user roles and permissions, allowing controlled read and write access to the blockchain. The network is tailored for business and enterprise use cases, prioritizing data privacy and confidentiality. Only known members of a consortium or organization can participate in the consensus process and create new blocks with transactions. Hyperledger Fabric's design provides a higher level of privacy compared to public blockchains. Its selective participation makes it suitable for various applications requiring restricted access and secure data management. However, the research [9] identifies that the design for checking data integrity between the database and the Blockchain is carried out row-by-row. When dealing with a large volume of data to be audited, the time required for integrity checks depends on the amount of data being reviewed. This may pose scalability challenges when auditing substantial datasets.

In our research, the focus is on an online product review system as a case study. To enhance trust and credibility, the system employs a combination of a Centralized Database and Blockchain technology. This approach allows users to access review content information with confidence, as the data remains unaltered and secure on the Blockchain. Additionally, the research proposes a method to verify the data integrity on the centralized database side. This research aims to create a robust and reliable online product review system that leverages the benefits of both centralized and decentralized technologies, ultimately enhancing user trust and confidence in the review content.

II. METHODOLOGY

A. System Architecture

In the digital age, online product reviews play a critical role in shaping consumer decisions. However, the trustworthiness of such reviews can often be compromised due to data tampering and manipulation. To address this challenge, we propose an architecture that combines the strengths of a Centralized Database, Ethereum Blockchain, and Smart Contracts as described in Fig. 1. Our system records only the hash of online product review data on the Blockchain, which not only verifies the integrity of both the Database and the Blockchain but also reduces operational costs by minimizing gas fees. This paper presents the design and implementation of our system, which offers a platform for managing online product reviews while ensuring data reliability and user confidence.

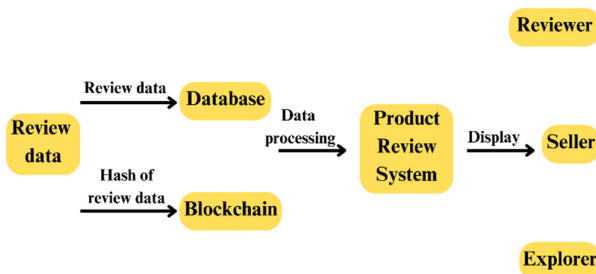


Fig. 1 System Architecture

The trustworthiness of these reviews can be compromised due to data tampering and manipulation. To address this issue, we present an integrated system that combines a Centralized Database with the Ethereum Blockchain. The Database stores essential transactional data, including shops, products, users, and reviews, while the Blockchain stores only the hash information of the review table. By utilizing Smart Contracts, the system ensures the integrity of review content in the Database through Blockchain-backed data validation.

B. Database Section

The Database section comprises four tables - shops, products, users, and reviews, as illustrated in Fig. 2. These tables store crucial transaction information, enabling the Web Application to display relevant details to users. Reviews, being a vital part of the validation process, are subject to Blockchain hashing. The hash values of the review table entries are generated and utilized for ensuring data integrity.

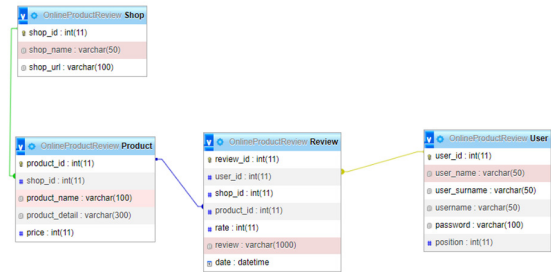


Fig. 2 Designing Entities' Relationship in Database

C. Blockchain Section

In the Blockchain section, the Ethereum Blockchain plays a pivotal role in data verification. However, instead of storing complete review data, our system records only the hash information originating from the review table. By doing so, we create a secure and immutable ledger of review content. This approach allows for easy validation of review data integrity without the need to store extensive information on Blockchain.

D. Smart Contract Design

Smart Contracts are stored and executed on the blockchain. When a Smart Contract is deployed, its code is added to the blockchain, and its address is generated. Users interact with Smart Contracts by sending transactions to their addresses. These transactions trigger the execution of the Smart Contract's code. The algorithm has been designed.

Algorithm 1: Address Default Setting for System.

Algorithm 1 is a process that outlines the steps to configure default settings for the components of a system. The input to this algorithm includes the initial parameters and configurations of the system, while the output is the establishment of default settings for its components as described in TABLE I.

TABLE I. Address Default Settings for System

| Algorithm 1: Initializes address for System/Admin | |
|---|---|
| Input: | Declaration of address for System/Admin |
| Output: | Address for System/Admin |

Algorithm 2: Smart Contract-Based Review Data Storage Authorization.

The proposed algorithm establishes a Smart Contract with access control parameters, granting only authorized entities (system or administrator) the right to store review data on the Blockchain. The process involves verifying the requester's identity using digital signatures and authentication. Upon successful verification, authorized entities can append review data securely to Blockchain, ensuring data integrity and creating an auditable record of review submissions. This approach enhances trust and transparency in online review systems as described in TABLE II.

TABLE II. Modifier for System/Admin

| Algorithm 2: Modifier for System/Admin | |
|--|---|
| Input: | The address of system/admin |
| Output: | Allow only the address of the system/admin to write data into Blockchain. |
| 1 OnlyAdmin: | Access restricted |

Algorithm 3: Smart Contract-Based Hash Data Recording.

This algorithm facilitates hash data recording on the Smart Contract. Before saving the hash, the system verifies the authorization for the record. If authorized, the system accepts the input hash and securely stores the data on the Blockchain. If unauthorized, the system prevents the hash from being saved, ensuring only permitted parties can record hash data as described in TABLE III.

TABLE III. Adding Hash

| Algorithm 3: Adding hash. | |
|---------------------------|-------------------------|
| Input: | Hash of review data |
| Output: | Current hash |
| 1 | If Admin == True: |
| 2 | Input hash |
| 3 | Broadcast current hash. |
| 4 | Else: |
| 5 | Access denied. |

Algorithm 4: Broadcasting Hash Data Storage on Blockchain to All Users for Visibility and Verification.

This algorithm describes a process for broadcasting a hash value related to review data. This is a hash value that has been generated from the review data using a hash function. Everyone can view hash suggests that the hash value is made available for everyone to see. They are useful for verifying data integrity. If even a tiny bit of the input data changes, the resulting hash will be drastically different. In summary, the "Broadcast Hash" algorithm is a way to share a hash value derived from review data with others, allowing them to verify the integrity of the data as described in TABLE IV.

TABLE IV. Broadcast Hash

| Algorithm 4: Broadcast hash. | |
|------------------------------|------------------------|
| Input: | Hash of review data |
| Output: | Everyone can view hash |

1 Broadcast hash

E. Hashing Design

TABLE V shows the first hit obtained from all data across each row in the review table. Subsequent hashes are generated from all data in each row, including the columns and the previous row hash. This process ensures the quick verification of information integrity for every transaction, requiring only one comparison with the latest hash.

TABLE V. Hashing Design

| Columns | Hash |
|---------|--------------------|
| R1 | H1 = hash (R1) |
| R2 | H2 = hash (H1, R2) |
| R3 | H3 = hash (H2, R3) |

F. Design Data Integrity Validation

Before performing any data, reading, or writing operations, it is essential to ensure the integrity of the information. This can be achieved by cross-referencing the latest hash from both the Database and the Blockchain. If the hashes match, it signifies that the data is complete and has not been altered. However, if there is a discrepancy between the hashes, it indicates that the Database side has been modified, as depicted in Fig. 3. This approach combines the efficiency of the Database with the tamper-proof nature of Blockchain, creating a robust data integrity validation mechanism.

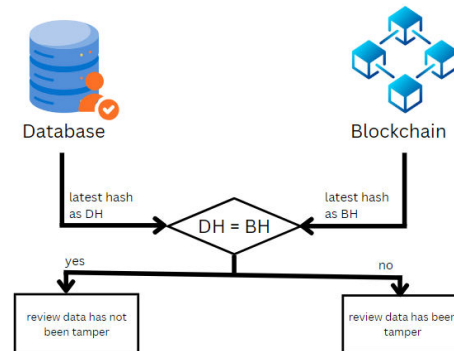


Fig. 3 Design Data Integrity Validation

G. Latest Hash on the Database

The provided SQL command retrieves a hash value from the 'Review' table while ordering the results based on the 'review_id' in descending order. The alias 'prevhash' is assigned to this hash value. The 'LIMIT 1' clause ensures that only one record is retrieved from the query result. This command essentially fetches the most recent hash value from the 'Review' table as described in Fig. 4.

```
app.get("/latest_hash",(req, res) => {
    let query = "SELECT hash over (ORDER BY review_id DESC) as prevhash FROM 'Review' LIMIT 1";
```

Fig. 4 Latest Hash on Database

H. Latest hash on the Blockchain

This code fetches past events of the 'Log' type from the hashContract using the getPastEvents function. The retrieved data is then used to update the showLog state variable. The function is anticipated to return an array named showLog, which contains event data related to the 'Log' type. This array

would contain information about events that have occurred in the past, adhering to the specified event type as described in Fig. 5.

```
const logHandler = async () => {
  try{
    const showLog = await hashContract.getPastEvents(
      'Log',
      {
        fromBlock: '0'
      }
    )
  }
}
```

Fig. 5 Latest Hash on the Blockchain

III. RESULT AND DISCUSSION

The case study focuses on Online Product Review, utilizing a combination of Centralized Database, Ethereum Blockchain, Smart Contract, Web3.js, and React.js. The study proposes an innovative method to store data on Blockchain, striking a balance between trustworthiness and gas fees. By leveraging a Centralized Database and Ethereum Blockchain, the system ensures data integrity and immutability. Smart Contracts facilitate secure interactions, while Web3.js and React.js enhance the user experience. The optimization approach aims to provide reliable data storage on the Blockchain while minimizing transaction costs. This integrated solution presents a comprehensive framework for building a robust and cost-effective Online Product Review system.

A. User Interface

The User Interface (UI) allows users to write product reviews through a form where they input shop name, product name, rating, and review content. The UI displays the previous hash from both the Database and Blockchain sides, enabling users to validate the database review's integrity before submission. This verification can be done by cross-referencing the Blockchain. Additionally, the UI shows the database integrity status. The "New Hash" section dynamically calculates the new hash based on the previous hash and the entered information. Upon submitting the review form, the user's input is stored in the database, and the corresponding hash is recorded in the Blockchain, ensuring secure and trusted data storage. The UI provides an intuitive way for users to interact with the system while maintaining data integrity and Blockchain-based verification for review submissions as described in Fig.6.

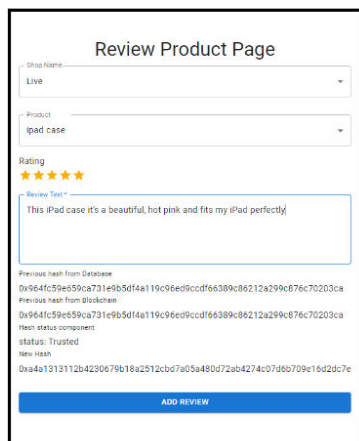


Fig. 6 Review Product Page

B. Connecting to the Ethereum Blockchain

The system connects to the Ethereum Blockchain using Web3.js, a JavaScript library designed for blockchain technology. Web3.js serves as the intermediary to establish communication with the blockchain network through API. It enables the system to interact with smart contracts, execute their functions, read variable values, and perform operations. To connect and interact with a specific smart contract on the blockchain, the system uses the contract method, which requires specifying the Application Binary Interface (ABI) of the smart contract and its address on the network. For this system, the address of the Smart Contract to be connected is 0x70B825345Fb7e8B3A2816D0c78C5B6752F098037. This integration enables seamless communication with the Ethereum Blockchain, facilitating secure and reliable data storage and retrieval for the Online Product Review system as described in Fig. 7.

```
1 /**
2  *Submitted for verification at Etherscan.io on 2023-09-24
3  */
4
5  // SPDX-License-Identifier: MIT
6  pragma solidity ^0.8.11;
7  contract storeHash {
8    address public admin;
9    constructor(){
10     admin = msg.sender;
11   }
12   modifier onlyAdmin{
13     require(msg.sender == admin, "only the admin.");
14   }
15   event Log( bytes32 _hash);
16
17   function setReviewData( bytes32 _hash ) onlyAdmin public {
18     emit Log(_hash);
19   }
20 }
21 }
```

Fig. 7 Smart Contract

Once the connection to the Smart Contract is established, users can interact with it by calling functions. To save the hash to the Blockchain, users execute the "setReviewData" function in the Smart Contract. This input can be received from the User Interface page via the ".send" method, provided by the web3.js library. The ".send" method facilitates sending transactions to the smart contract on the Ethereum network. As the system is designed to store only the hash on the Blockchain, the gas cost is relatively low, estimated at 0.000093 GoerliETH. The gas cost is determined based on the length and complexity of the data to be stored, and in this case, it remains minimal due to the optimized approach for data storage, ensuring cost-effectiveness and efficiency for the Online Product Review system on the Ethereum Blockchain as described in Fig. 8 and 9.

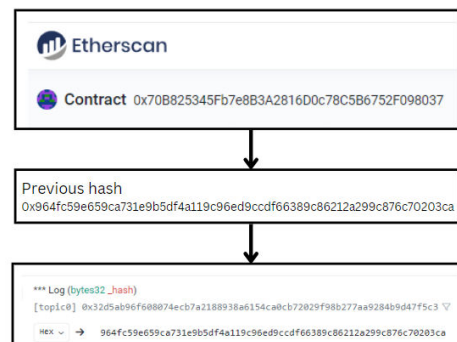


Fig. 8 Storing Hash in Blockchain

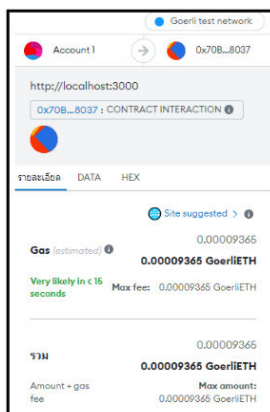


Fig. 9 Gas Fee

IV. CONCLUSION

This research introduces a methodology to enhance the reliability of a database system through the integration of Blockchain technology for the storage of transaction hashes. This is due to Blockchain's inherent capacity to mitigate data manipulation, attributed to its transparent nature. Transactions are openly accessible, fostering a sense of transparency within the Blockchain network. This transparency enables network participants to access identical data sets from any node, rendering the fabrication of data at a single node a challenging endeavor. Whenever data is written to the Ethereum Blockchain via a Smart Contract, it necessitates a transaction fee, commonly referred to as a gas fee. Engaging in the intricate task of amassing substantial volumes of data entails significant complexities, further compounded by the necessity to cover elevated gas expenses. This paper presents an approach to alleviate gas expenditure through the implementation of hybridization between centralized and decentralized database. This is achieved by capitalizing on the inherent characteristics of cryptographic hashing, which ensures a fixed length for hash outputs. Our method serves to enhance the credibility of the database. Additionally, the paper introduces a mechanism for singular integrity verification. By inspecting the most recent hash, this method can authenticate every transaction, as the hash outcome is generated from the latest data and the preceding hash value. We delineate the directions for future work, with a specific emphasis on the

pursuit of optimal equilibrium between gas fees and reliability. It is imperative to accord paramount importance to gas costs, as data storage on the Ethereum blockchain entails a significantly elevated expenditure. In forthcoming endeavors, the subject of gas optimization should be prominently elevated.

ACKNOWLEDGMENT

This work was partially supported by Digital Research and Innovation Institute (DRii), Research and Development Office, Prince of Songkla University.

REFERENCES

- [1] M. J. M. Chowdhury, A. Colman, M. A. Kabir, J. Han and P. Sarda, "Blockchain Versus Database: A Critical Analysis," in 2018 17th IEEE International Conference On Trust, Security And Privacy In Computing And Communications/ 12th IEEE International Conference On Big Data Science And Engineering (TrustCom/BigDataSE), New York, NY, USA, 2018.
- [2] K. Salah, A. Alfalasi and M. Alfalasi, "A Blockchain-based System for Online Consumer Reviews," in IEEE INFOCOM 2019 - IEEE Conference on Computer Communications Workshops (INFOCOM WKSHPS), Paris, France, 2019.
- [3] N. Six, N. Herbaut and C. Salinesi, "Blockchain software patterns for the design of decentralized applications: A systematic literature review, Blockchain: Research and Applications," Blockchain: Research and Applications, vol. 3, no. 2, 2022.
- [4] M. E. a. H. T. J. S. H. Maeng, "Analysis of Ethereum Network Properties and Behavior of Influential Nodes," in Asia-Pacific Network Operations and Management Symposium (APNOMS), Korea (South), 2020.
- [5] "Ethereum," Ethereum, [Online]. Available: <https://ethereum.org/en/>. [Accessed 15 June 2023].
- [6] A. A. a. C. C. Tan, "Smart Contract Designs on Blockchain Applications," in 2020 IEEE Symposium on Computers and Communications (ISCC), Rennes, France, 2020.
- [7] Park, J. & Lee, D. & In and Hoh, "Saving Deployment Costs of Smart Contracts by Eliminating Gas-wasteful Patterns," International Journal of Grid and Distributed Computing, vol. 10, pp. 53-64, 2017.
- [8] Kalis, R. a. Belloum and Adam, "Validating Data Integrity with Blockchain," in 2018 IEEE International Conference on Cloud Computing Technology and Science (CloudCom), Nicosia, Cyprus, 2018.
- [9] X. a. L. M. a. Y. Yang, H. a. Wang, M. a. Xu, D. a. Sun and Chuanheng, "A Trusted Blockchain-Based Traceability System for Fruit and Vegetable Agricultural Products," IEEE Access, vol. 9, pp. 36282-36293, 2021.

Generating Use Case Specification From SALT GUI

Halim Wildan Awalurahman
*Information Systems, Faculty of
 Science and Technology Universitas
 Airlangga Surabaya, Indonesia*
 halim.wildan.awalurahman-
 2019@fst.unair.ac.id

Indra Kharisma Raharjana
*Information Systems, Faculty of
 Science and Technology
 Universitas Airlangga, Surabaya,
 Indonesia*
 indra.kharisma@fst.unair.ac.id

Rifqi Hanief
*Information Systems, Faculty of
 Science and Technology
 Universitas Airlangga, Surabaya,
 Indonesia*
 rifqi.hanief-2019@fst.unair.ac.id

Syahrul Akbar Rohmani
*Information Systems, Faculty of
 Science and Technology
 Universitas Airlangga, Surabaya,
 Indonesia*
 syahrul.akbar.rohmani-
 2019@fst.unair.ac.id

Rikza Biknada Korompis
*Information Systems, Faculty of
 Science and Technology
 Universitas Airlangga, Surabaya,
 Indonesia*
 rikza.biknada.korompis-
 2019@fst.unair.ac.id

Mahardika Riesma Oktavian
*Information Systems, Faculty of
 Science and Technology
 Universitas Airlangga, Surabaya,
 Indonesia*
 mahardika.riesma.oktavian-
 2019@fst.unair.ac.id

Muhammad Wildan Azky Hamdani
*Information Systems, Faculty of
 Science and Technology
 Universitas Airlangga, Surabaya,
 Indonesia*
 muhammad.wildan.azky.hamdani-
 2019@fst.unair.ac.id

Badrus Zaman
*Information Systems, Faculty of
 Science and Technology
 Universitas Airlangga, Surabaya,
 Indonesia*
 badrus.zaman@fst.unair.ac.id

Kartono
*Information Systems, Faculty of
 Science and Technology
 Universitas Airlangga, Surabaya,
 Indonesia*
 kartono@fst.unair.ac.id

Abstract— Requirement engineering plays a crucial role in the initial phase of software development. Among the commonly utilized artifacts for requirements is the Use Case Specification, which aids in identifying scenarios and resolving inconsistencies, ambiguities, and incompleteness in the requirements document. This process of scenario identification is also applicable in human-computer interaction, particularly in user interfaces where the graphical user interface (GUI) serves as the closest interface for user interaction and feedback. Recognizing this connection, using GUIs to generate a Use Case Specification emerged. This research proposes an approach for generating a Use Case Specification from the SALT GUI. The primary method employed in this study involves the use of Regular Expressions. A SALT GUI format was also formulated and integrated into an activity diagram to achieve the desired output. Consequently, the proposed approach successfully predicts tasks from SALT GUI to generate a Use Case Specification, yielding a precision score of 0.875, a recall of 0.625, and an f-score of 0.833. These results substantiate the feasibility of generating a Use Case Specification from SALT GUI.

Keywords— *Use Case Specification, SALT GUI, Requirements Engineering, Regular Expressions, Process Innovation*

I. INTRODUCTION

Requirements engineering initiates the software life cycle as its earliest phase. In this phase, the requirements should be translated from the customer's language to the software engineer's terminology [1]. The requirement specification can be in the form of a textual written document and used to describe the system functionalities, which can be converted to a use case that shows the user and system interaction, known as use case analysis [2]. Use case analysis helps identify scenarios, removing inconsistencies, ambiguities, and incompleteness in the requirement specification document [3].

Generating UML use case diagrams as part of software analysis is essential in software's life-cycle phases [4].

Developing UML use cases needs procedures to take. The methods of gathering interviewing requirements, questionnaires, and other methods, but we need time and effort to complete, correct, and accurate requirements [5]. Current research has focused on automating the extraction of information from the natural language text by using Natural Language Processing (NLP), a field in computer science and linguistics related to artificial intelligence (AI) and computer linguistics [6], [7].

The interaction interface or the UI of mobile applications is one of the most critical factors determining the application's usability [8]. Interaction between the user and the system, as pictured by the use case specification, naturally comes when the user interacts with the graphical user interface (GUI). GUIs are the closest interface users can interact with and get feedback or output from their interaction. It can draw a relationship between interface and interaction that, somehow, the user interface can produce interaction. In other words, the user interface can be used to picture case specifications.

Previous studies, including [2], [9]–[12] have discussed using NLP to satisfy or to get the requirements specification, such as use case diagrams, use case scenarios, and activity diagrams from textual documents and other requirements artifacts such as user stories. In [9], the research discussed how to textually represent data entity, attribute, data type, data entity constraint, and attribute constraint from textual documents. In [2], [10] explicitly discussed identifying use case scenarios and elements from the textual specification. While [11], [12] discussed mechanisms to generate use cases from different sources. These studies have proven that use case specification is available in textual documents. However, most of the studies use natural language processing and documents that are written in natural language. None of the previous studies have explored the possibility of using SALT GUI to get use case specifications.

This study proposes a new approach to generate the UML Use Case Specification (UCS) from SALT GUI. The web-

based application can convert SALT input to use case specification. This study contributes towards a more practical approach to generating requirements specification, specifically by using other languages rather than natural ones.

II. RELATED WORKS

Topics about requirements engineering have been studied in recent years, especially in requirements elicitation. Few studies expressed mechanisms to generate software requirements using machine learning and natural language processing. These mechanisms are essential in our case to establish the baseline model for extracting information from SALT GUI and generating use case specifications. Following are some studies that relate to our topic.

Use cases are a popular means of capturing a software system's functional requirements, and many NL issues have been introduced in the use case specification [10]. Regarding raising NL to use case generation, [10] uses a natural language parser to identify a part of speech (POS) tags, type dependencies, and semantic roles to generate use case elements from input text specification. This study is similar to ours, except that they dealt with textual input data that are not syntax. The method that they are using is considered in our study.

To further their study, [2] presents an initial approach for the automated identification of use case names and actor names from the textual requirements specification using machine learning techniques. Specifically, they use named entity recognition (NER) in the context of textual information to extract the use case names and actors. They also use machine learning such as multinomial naive Bayes, perceptron, linear classifier, and passive-aggressive classifier to build the prediction model. The most important part of this

study was that extracting basic/alternative/exceptional flow of events requires formulation and analysis of sentence structure and cannot be possible with the current approach.

Maatuk and Abdelnabi [11] propose an approach to facilitate the NL requirements analysis process and UML diagrams extraction from NL textual requirements using natural language processing techniques and heuristic rules. In [11], NLP techniques such as tokenization, POS tagging, and type dependency are used to automate generating the UML elements. This study is another one that is quite in line with the one we did. They created UML diagrams from textual requirements, the same as [10] but with different outputs and methods. The output from this study seems closer to our goal. However, the method might not be fully applicable due to the different syntax and textual requirements contexts. The idea to create the output has been laid out in this study.

Regular expressions (Regex) are a unique series or set of characters that can be used to find other strings. Regular expressions have been used for clinical purposes on a few occasions. Veena et al. [13] used regular expressions by filtering any string that contains "symptoms of," which will be further utilized following other NLP techniques such as POS tagging and labeling. Using regular expressions to filter a set of characters from this study is similar to our goals. The differences are that we used regular expressions to filter some set of characters in the syntax and extract those characters in another form in this study.

Gilson et al. [12] propose a technique to automatically transform textual user stories into visual use case scenarios in the form of robustness diagrams. The same topic but a different outcome from [2], [10], [11]. This study emphasizes how to contextualize the user stories in graphical form. In this case, Gilson et al. had to deal with four elements of the

```

@startuml
title ***write your use case name here***

!unquoted procedure SALT($x)
"{{
salt
%invoke_procedure("_"+$x)
}}" as $x
!endprocedure

!procedure _form()
{+
***write your code (GUI) here***
}
!endprocedure

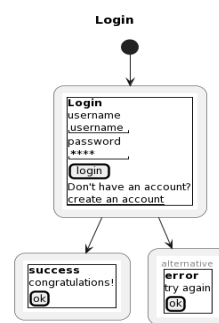
!procedure _success()
{+
***write your code (main scenario) here***
}
!endprocedure

!procedure _error()
{+
***write your code (alternative scenario) here***
}
!endprocedure

(*) --> SALT(form)
form --> SALT(success)
form --> SALT(error)

@enduml
    
```

(a)



(b)

| | |
|----------------------------|---|
| Nama Usecase | Login |
| Deskripsi | Pengguna akhir melakukan login untuk masuk ke dalam aplikasi terkait |
| Aktor | Pengguna akhir |
| Kondisi Awal | Pengguna akhir belum masuk ke dalam aplikasi |
| Kondisi Akhir | Pengguna akhir telah masuk ke dalam aplikasi |
| Skenario Utama | <ol style="list-style-type: none"> 1. Pengguna akhir memasukkan data username yang dimilikinya 2. Pengguna akhir memasukkan data password yang dimilikinya 3. Pengguna akhir menekan tombol "Login" 4. Jika akun valid, maka sistem menampilkan pesan login berhasil |
| Skenario Alternatif | <ol style="list-style-type: none"> 1. Pengguna akhir memasukkan data username yang dimilikinya 2. Pengguna akhir memasukkan data password yang dimilikinya 3. Pengguna akhir menekan tombol "Login" 4. Jika akun tidak valid, maka sistem menampilkan pesan login gagal |

(c)

Fig. 1. The input and the output of the proposed system. The input will be (a) source code for SALT GUI. (b) Preview represents the result of the SALT GUI generated from the code. The main output is (c) Use Case Specification

robustness diagram: actor, boundary, control, and entity. Their method showed that the critical part of generating a UML diagram, in general, is how to map the output into some variables that need to be fulfilled.

III. METHOD

This study applied the Scrum method to build the application. Scrum is a software engineering method using the principles of an agile approach that is easy to control, flexible, and contains a comprehensive development strategy where the entire team works as a unit to achieve the same goal [14]. During the development stage, with the help of Notion, we were able to lay out our project into six sprints and produce necessary artifacts, including product backlog, sprint planning, sprint meetings, and project overview. Before the project starts, we define our application requirements which will be described in the process design section. By defining application requirements, we decided to build a web application with Django and use Regular Expression to help generate targeted output.

A. Formulation

The system requires SALT input to generate targeted use case specification output. To create a sense of what variables to input, we tested SALT GUI to find the suitable formulation to extract the information needed for use case specification. To formulate the correct method, we compared the output and the input to understand the variables that must be fulfilled.

Use case specifications typically have seven variables: use case name, actor, description, initial condition, end condition, main scenario, and alternative scenario, as pictured in Fig. 1c. SALT GUI, on the other hand, typically has only been used to create one view. This could be challenging because use case specifications have two scenarios. However, SALT, in their documentation, mentioned that there is a way to include SALT inside an activity diagram.

With an activity diagram, we can draw the flow of the GUI produced by SALT, as pictured in Fig. 1b. Regarding having to include SALT in an activity diagram. The plantUML documented that two ways could be implemented: with or without macro. We tested both, and our preferences lean into using the macro as it simplifies the code and practically does not change much. Macro allows us to create functions directly to represent the main and alternative scenarios, as pictured in Fig. 1a. This is a massive advantage because it will make it easier to process and present to the user. Users will only have to change what is inside the macro function without worrying about writing the wrong thing.

After finding out the best scenario to implement SALT, including the SALT in an activity diagram, we identify what variables can be extracted from the proposed input. We breakdown the SALT code in Fig. 2. We decided to use four indicators to find the UCS aspects. The four indicators are 'title' to extract title of the UCS, '!procedure _form()' to extract the form or GUI, '!procedure _succes()' to extract main scenario, and '!procedure _error()' to extract alternative scenario. Inside the '!procedure _form()', there will be code that represents input fields. We used the general documentation from SALT to translate the field into actions before achieving main scenario and end scenario. In Fig. 2, as an example, if we write quote ("...") after a colon, that would automatically be translated as input field, thus translated into

action as 'fill the input field' in UCS using Regular Expression. So, we use Regular Expression to capture these indicators, read the content following them, and translates them to relevant sentences that can be used in UCS.

```
@startuml
title Login → act as the title of the use case scenario

!unquoted procedure SALT($x)
"{{
salt
%invoke_procedure("_"+$x)
}}" as $x
!endprocedure

!procedure _form() → act as the form or GUI
{+
<b>Login
username:
"username" → colon followed by " " represent input field
password:
"*****"
[login] → [ ] represent button
Don't have an account?
_create an account__
}
!endprocedure

!procedure _success() → act as the main scenario
{+
<b>success
congratulations!
[ok]
}
!endprocedure

!procedure _error() → act as the alternative scenario
{+
<b>error
try again
[ok]
}
!endprocedure

(*) --> SALT(form)
form --> SALT(success)
form --> SALT(error)

@enduml
```

Fig. 2. Breakdown of SALT GUI to be converted to UCS

Having analyzed the SALT code, we found that three variables can be extracted: use case name, main scenario, and alternative scenario. We eliminated these three variables from the target output, leaving four variables to fulfill. Besides, SALT could never tell what the description is, who the actor is, and what the condition was and will be before and after implementing the use case solely from their code. We then decided to use input fields to make it simple for the user, and more importantly, it is impossible to put the four variables left in SALT because of the different contexts they both offer.

After the formulation, we employ regular expressions to handle the process. This decision was made because regular expressions are sufficient for the problem, for we only need to convert a specific part of the code, some words, to another language, as in a sentence. We developed the application in Django with Javascript Regular Expression. Our formulation is finished, and the procedure and system flow are represented in the next section.

B. System Procedure

The system procedure includes three main phases: input, process, and output. In this study, after we perform formulation. we use five system inputs: actor, description, initial condition, end condition, and SALT. Only SALT is processed; the rest are used directly as output variables. SALT is processed with Regular Expressions to produce three variables: use case name, main scenario, and alternative scenario.

We provide a dataset of 10 SALT GUIs we created for the evaluation that followed our formulation. In order to create the dataset, we propose ten possible use cases and manually coded them using SALT GUI. Our dataset is available in Github [15]. The data is in form of SALT GUI similar to what is displayed in Fig. 1a with 10 different use case specifications as shown in Table 1. We will evaluate by a manual generation of use case specification and then compare the result to our system-generated use case specification. We will then calculate the precision, recall, and f-score. To calculate the mentioned indicators, we use the following formula:

$$Precision = \frac{Tp}{Tp+Fp} \tag{1}$$

$$Recall = \frac{Tp}{Tp+Fn} \tag{2}$$

$$F - Score = \frac{2Tp}{2Tp+Fp+Fn} \tag{3}$$

Precision describes the accuracy between the results of manual conversion by the expert and the results provided by the web application model, recall describes the success of the

web application model in rediscovering information, and F-measure represents the accuracy of the web application model [16].

IV. RESULT

Figure 3 shows the result of our application. It can be seen that the application successfully identifies all the manual input by the user (actor, description, pre-condition, and post-condition), and it also successfully identifies SALT GUI attributes used for the UCS output (title, main scenario, and alternative scenario). Our application is still using Bahasa Indonesia as its primary language for output.

As the base of our application, we created a web page that consists of input fields. We separated input fields into three sections: Use Case Specification Variables, SALT Syntax, and Result. As mentioned before, to use the application, there are three main steps which are to input the variables related to the use case specification, as shown in Fig. 3a. and to input the SALT GUI code, as shown in Fig. 3b, and get the result in the form of preview and use case specification as shown in Fig.

1. Use Case Specification Variables

(a)

2. SALT Syntax

```

Salt PlantUML Syntax
Salt
[+
->-error
There seems to be an error to the adding product process.
Please try again later.
[ok]
]
!endprocedure

(*) --> SALT(form)
form --> SALT(success)
form --> SALT(error)

@enduml
    
```

(b)

3. Result

| # | Value |
|---------------------|--|
| Nama Use Case | Add Product |
| Deskripsi | Adding product |
| Aktor | Rifqi |
| Kondisi Awal | The product hasn't been added |
| Kondisi Akhir | Product added |
| Skenario Utama | 1. Mengisi input Product name 2. Mengisi input Product cost 3. Mengisi input Stock 4. Menekan tombol Add 5. Muncul pesan "Product added successfully" |
| Skenario Alternatif | 1. Mengisi input Product name 2. Mengisi input Product cost 3. Mengisi input Stock 4. Menekan tombol Add 5. Muncul pesan "There seems to be an error to the adding product process. Please try again later." |

(c)

Fig. 3. The result of the system. The first step is to (a) fill in variables, then (b) SALT, and (c) the result consists of preview and use case specification

3c. We also added a feature: the download button for the SALT wireframe preview and Use Case Specification.

After finishing our development, we continue to evaluate our application. For the evaluation, we asked one expert to create use case specifications based on the SALT GUI dataset we provided. A total of ten SALT GUIs are available, indicating that the expert will create ten corresponding use case specifications. Subsequently, we employ our application to obtain the generated use case specification from the dataset. We documented both results and then started comparing the expert-generated UCS and system-generated UCS.

During the comparison, we looked at both results thoroughly and compared them for each task they were generated. For example, the expert wrote "User memasukkan nomor tujuan transfer" which translates to "User insert transfer destination number" and our system wrote "mengisi input Card Number" which translates to "input card number". In this case, even though they are not identical in words, after reviewing them, we got the same meaning. So, in our case, comparing these results have to be done manually to ensure that each task has the same meaning. However, there are exceptional cases where we also had to confirm to the expert what they meant. For example, the expert only wrote "User konfirmasi transfer" which does not specify what kind of action it takes to confirm the transfer, whether by pressing a button or anything else. So we had to double-check with the expert for these special cases. Overall, our evaluation can be summarised as shown in Table 1.

Our application can identify the main scenario and alternative scenario. Our evaluation in Table 1 shows only one different outcome in Send a question message UCS. Our system comfortably handled all the other UCS and matched the task generated by the expert.

After calculating the precision, recall, and f-score, we got 87.5% for precision, 62.5% for recall, and 83.3% for f-score. We could generate almost the same amount of tasks as the expert. We only failed to identify one particular task: the one with the text area. However, all the other types of SALT GUI code could be generated using our system. Our findings prove that generating UCS from SALT GUI is possible using Regular Expressions.

V. DISCUSSION

Based on our research, we found a few interesting findings. Our findings mainly related to the process's limitations and constraints that follow the conversion of SALT GUI to Use Case Specification.

First, the SALT GUI can only represent a single use case. This is because SALT GUI cannot handle more than one wireframe. The best approach to address this problem is to use an activity diagram. However, due to the unique characteristics of the activity diagram, it would still be problematic to implement. In this research, we decided to only use or represent a single-use case.

The SALT GUI is an activity consisting of at least one main scenario. This problem arises for the same reason as the previous one. SALT GUI is made to represent one scene which means one scenario. In order to extend that, we use an activity diagram defining the main and alternative scenarios. Still related to the activity diagram is the third finding that the SALT GUI must implement the usage of the macro. The reason for using a macro is to make defining the main and alternative scenarios more identifiable. Also, the macro is shorter to write than the regular way of implementing SALT GUI inside an activity diagram.

Other findings related to the constraint are that: The SALT GUI must contain a title since it will be used as the use case title. The SALT GUI must contain `!procedure_form()`, since it will be used as the part representing the GUI being used. The SALT GUI must contain `!procedure_success()`, since it will be used as the part representing the main scenario. The description ought to encompass the visual representation of the expected output. The SALT GUI must contain `!procedure_error()`, since it will be used as the part that represents an alternative scenario. It should contain what the alternative output looks like. And finally The SALT GUI must not contain header attributes in the `"!procedure_success()"` and `"!procedure_error()"`, since it will break the specification output.

Additionally, we found another constraint related to the writings of SALT GUI which are: The SALT GUI must contain ":" before an input field since it will be used as the part that represents the input field, The SALT GUI must only have one button in each interface since it will be used as the part that represents the button. The system can't handle two different buttons and can only decide the action for main scenario or alternative scenario by using one button, or in other word, button supposed to be the marker for the end of a form, And finally The application cannot handle the textarea type from SALT GUI. This happens because the syntax used for textarea type is similar to the syntax used to create a single Wireframe; hence, the application cannot read the textarea type as an input field.

Previous studies, including [2], [10]–[12] have discussed how to use NLP to get the requirements specification, such as

TABLE 1. RESULT OF GENERATED USE CASE SPECIFICATION FROM THE EXPERT AND SYSTEM

| Use Case Specification | Expert | | Proposed System | |
|-------------------------|-----------------------|------------------------------------|-----------------------|------------------------------------|
| | Main Scenario (Tasks) | Alternative Scenario (Conditional) | Main Scenario (Tasks) | Alternative Scenario (Conditional) |
| Transfer | 4 | 4 | 4 | 4 |
| Add product | 5 | 5 | 5 | 5 |
| Send Message | 3 | 3 | 3 | 3 |
| Rating | 4 | 4 | 4 | 4 |
| Send a question message | 6 | 6 | 5 | 5 |
| Verification account | 3 | 3 | 3 | 3 |
| Select item to buy | 3 | 3 | 3 | 3 |
| Register | 6 | 6 | 6 | 6 |
| Reset password request | 3 | 3 | 3 | 3 |
| Attacking | 3 | 3 | 3 | 3 |

use case diagrams, use case scenarios, and activity diagrams from textual documents and other requirements artifacts. In [2], [10] the idea of identifying use case scenarios and elements from textual specification is presented. While [11], [12] discussed mechanisms to generate use cases from different sources. The closest research to ours is [2] [10] which have proved that use case specification can be extracted from textual documents. However, they have not explored the possibility of using SALT GUI to get use case specifications. Therefore, this study can be considered as the first one to prove that use case specification can be extracted from SALT GUI syntax.

Further research opportunities for the study include improving automation techniques, exploring different input modalities, gathering user feedback for usability assessment, and investigating how the generated use case specifications integrate with requirements management systems. These research directions aim to enhance the efficiency and effectiveness of automating requirements engineering in software development [17].

VI. CONCLUSION

To generate UCS from SALT GUI, the first approach that we did was to formulate the output. It means we have to define the output to decide how to process the input. In general, use case specifications must at least have the main scenario and alternative scenario. So we decided to include the SALT GUI in an activity diagram to create a clear distinction between the main and alternative scenarios. Then, we identified three UCS variables that can be extracted from the SALT GUI, which are: main scenario, alternative scenario, and title. The rest of the UCS variables were defined by using manual input.

From the result, our research have proved that it is possible to get Use Case Specification from SALT GUI by using Regular Expressions in Javascript. Our application can generate UCS as desired. We were able to identify tasks based on the input generated by SALT GUI. In this research, we were able to generate the main scenario and alternative scenario. After the evaluation, we reach 87.5% precision, 62.5% recall, and 83.3% f-score. Both the main scenario and alternative scenario reach the same number. Thus, we use these numbers to represent both the main and alternative scenarios' evaluations. This result proves the possibility of generating UCS from SALT GUI.

In this research, we were only using Regular Expressions. However, to improve the UCS output significantly, machine learning can be used in accordance with regular expressions usage. A more advanced Natural Language Processing approach is encouraged for future research. Also, future research can consider adding exceptional scenarios to the UCS output. This research is the first approach to generating UCS from SALT GUI; hence the application still uses Bahasa Indonesia as its primary language.

ACKNOWLEDGMENT

This work was supported by Direktorat Riset, Teknologi, dan Pengabdian Kepada Masyarakat Kementerian Pendidikan, Kebudayaan, Riset, dan Teknologi Republik Indonesia through Penelitian Fundamental Reguler (PFR) under Grant 0536/E5/PG.02.00/2023.

REFERENCES

- [1] Z. A. Hamza and M. Hammad, "Generating UML use case models from software requirements using natural language processing," in *2019 8th International Conference on Modeling Simulation and Applied Optimization, ICMSAO 2019*, IEEE, 2019, pp. 1–6. doi: 10.1109/ICMSAO.2019.8880431.
- [2] S. Tiwari, S. S. Rathore, S. Sagar, and Y. Mirani, "Identifying Use Case Elements from Textual Specification: A Preliminary Study," in *Proceedings of the IEEE International Conference on Requirements Engineering*, 2020, pp. 410–411. doi: 10.1109/RE48521.2020.00059.
- [3] A. Fantechi, S. Gnesi, G. Lami, and A. Maccari, "Applications of linguistic techniques for use case analysis," *Requir Eng*, vol. 8, no. 3, pp. 161–170, 2003, doi: 10.1007/s00766-003-0174-0.
- [4] R. G. Tiwari, A. Pratap Srivastava, G. Bhardwaj, and V. Kumar, "Exploiting UML Diagrams for Test Case Generation: A Review," in *Proceedings of 2021 2nd International Conference on Intelligent Engineering and Management, ICIEEM 2021*, 2021, pp. 457–460. doi: 10.1109/ICIEEM51511.2021.9445383.
- [5] D. Siahaan, I. K. Raharjana, and C. Fatichah, "User story extraction from natural language for requirements elicitation: Identify software-related information from online news," *Inf Softw Technol*, vol. 158, no. June 2023, p. 107195, Jun. 2023, doi: 10.1016/j.infsof.2023.107195.
- [6] M. S. Osman, N. Z. Alabwaini, T. B. Jaber, and T. Alrawashdkeh, "Generate use case from the requirements written in a natural language using machine learning," *2019 IEEE Jordan International Joint Conference on Electrical Engineering and Information Technology, JEEIT 2019 - Proceedings*, pp. 748–751, 2019, doi: 10.1109/JEEIT.2019.8717428.
- [7] I. K. Raharjana, D. Siahaan, and C. Fatichah, "User Stories and Natural Language Processing: A Systematic Literature Review," *IEEE Access*, vol. 9, pp. 53811–53826, 2021, doi: 10.1109/ACCESS.2021.3070606.
- [8] N. Arambepola and L. Munasinghe, "Empirical analysis of user factors that affect the user interface design in mobile applications," in *20th International Conference on Advances in ICT for Emerging Regions, ICTer 2020 - Proceedings*, 2020, pp. 166–171. doi: 10.1109/ICTer51097.2020.9325452.
- [9] A. R. da Silva and D. Savić, "Linguistic patterns and linguistic styles for requirements specification: Focus on data entities," *Applied Sciences (Switzerland)*, vol. 11, no. 9, 2021, doi: 10.3390/app11094119.
- [10] S. Tiwari, D. Ameta, and A. Banerjee, "An approach to identify use case scenarios from textual requirements specification," *ACM International Conference Proceeding Series*, 2019, doi: 10.1145/3299771.3299774.
- [11] A. M. Maatuk and E. A. Abdelnabi, "Generating UML use case and activity diagrams using NLP techniques and heuristics rules," in *ACM International Conference Proceeding Series*, 2021, pp. 271–277. doi: 10.1145/3460620.3460768.
- [12] F. Gilson, M. Galster, and F. Georis, "Generating use case scenarios from user stories," *Proceedings - 2020 IEEE/ACM International Conference on Software and System Processes, ICSSP 2020*, pp. 31–40, 2020, doi: 10.1145/3379177.3388895.
- [13] G. Veena, R. Hemanth, and J. Hareesh, "Relation Extraction in Clinical Text using NLP Based Regular Expressions," in *2019 2nd International Conference on Intelligent Computing, Instrumentation and Control Technologies, ICICICT 2019*, 2019, pp. 1278–1282. doi: 10.1109/ICICICT46008.2019.8993274.
- [14] A. Hermawan and L. P. Manik, "The Effect of DevOps Implementation on Teamwork Quality in Software Development," *Journal of Information Systems Engineering and Business Intelligence*, vol. 7, no. 1, p. 84, 2021, doi: 10.20473/jisebi.7.1.84-90.
- [15] "AgileRE-2022/SaltySpec: Generating User Specification from Salt (PlantUML) Syntax." <https://github.com/AgileRE-2022/SaltySpec> (accessed Aug. 09, 2023).
- [16] I. N. Fatimah *et al.*, "USESPEC to BPMN: Web generator program for use case specification to BPMN," in *AIP Conference Proceedings*, 2023, p. 040008. doi: 10.1063/5.0103694.
- [17] H. W. Awalurahman, I. H. Witsqa, I. K. Raharjana, and A. H. Basori, "Security Aspect in Software Testing Perspective: A Systematic Literature Review," *J. Inf. Syst. Eng. Bus. Intell.*, vol. 9, no. 1, pp. 95–107, 2023, doi: 10.20473/jisebi.9.1.95-107.

Influence of Human Skills on Scrum Teams: A Case Study of Junior Team Software Development

Nuttaporn Phakdee
Department of Software Engineering,
Faculty of Informatics,
Burapha University,
Chonburi, Thailand.
nuttaporn@go.buu.ac.th
ORCID: 0000-0002-0841-8343

Apisit Saengsai
Department of Software Engineering,
Faculty of Informatics,
Burapha University,
Chonburi, Thailand
apisit.sa@buu.ac.th
ORCID: 0009-0008-7850-650X

Abstract—Agile software development methodologies, including Scrum, have become popular for their flexibility and collaborative approach. However, the success of Scrum teams heavily depends on the dynamics among team members. This study explores the challenges related to Agile software development, specifically focusing on the influence of human skills on the Scrum team. While Scrum encompasses various well-defined aspects, it does not explicitly address personality traits. Consequently, this study seeks to explore how teams' performance is influenced by the human skills possessed by their members during the implementation of Agile methodologies. This study investigated eight teams of software engineering students engaged in software development projects by observing impacted team processes in each iteration. The results show that soft skills and J/P significantly influence team processes. However, their impact on the team's product varies across cycles. Additionally, soft skills interact with the Feeling (F)/Thinking (T) and Judging (J)/Perceiving (P), affecting team processes and products.

Keywords—Agile software development, human skill, personality traits, soft skills, team performance, MBTI, Scrum

I. INTRODUCTION (HEADING 1)

Consumer demand for technology is increasing, leading to the expansion of software development projects that are becoming larger, more complex, and characterized by uncertain needs. Therefore, traditional software development approaches are being replaced by Agile methodologies, which prioritize the swift delivery of products to users [1]. The success of software development projects, ensuring timely and high-quality deliveries to clients, hinges on the skills of the software development team members. While technical expertise and good software engineering are vital, more is needed. It is becoming increasingly indispensable to work effectively in teams, collaborate across disciplines, engage with various stakeholders, and address diverse concerns and impacts by human skills, including social, emotional, and ethical intelligence [2]. The success of software development projects is ensured by these human skills, which serve as a crucial element [3][4].

Personality, professional knowledge, formal education, leadership style, and work experience were identified as significant factors affecting team performance by Ma et al. [5].

The higher performance levels were found to be achieved by teams when technical leaders have a central role in communication networks, as reported by Garcia et al. [6]. Monsalves et al. [7] emphasized the importance of selecting the right individuals for Agile teams to ensure successful implementation. [8][9] studies highlight the significance of soft skills in IT operations and software development success, such as communication, team building, leadership, emotional intelligence, critical thinking, and collaboration. Despite this, Agile needs a framework for considering team members' skills that may impact software development success.

Moreover, Poonam and Yasser [10] investigated personality traits that affect the efficiency of pair programming. Barroso et al. [11] examined the influence of human personality, measured by the MBTI model, on the quality of software products among students. The results showed no significant relationship between MBTI types and software product quality, requiring further research. Iqbal et al. [12] presented an MBTI personality profile for software developers that aligns with their positions and roles, optimizing job allocation throughout the software development life cycle. Zähl et al. [13] demonstrated the significant impact of personality on team performance and satisfaction levels.

While numerous studies have studied soft skills and MBTI personality traits, this study has yet to focus on junior software developers in Thailand. This research aims to fill this gap by providing valuable insights tailored to junior software developers. These insights can guide their personal development in terms of soft skills and understanding of personality traits. Moreover, stakeholders in software organizations, including management, team leaders, and developers, provide valuable insights into the significance of human skills for use in adapting and developing themselves and teams to achieve team performance.

II. VARIABLE DESIGN

In this section, the scope of our study is explained, encompassing team performance, human skills, and the Agile software development process.

A. Team Performance

The term "team performance" in this study refers to the overall outcomes of the team's actions, including the team's collaborative efforts, known as team processes and the team product of the software development team. By considering both aspects, we aim to understand team performance comprehensively. Previous research [14][15] has yet to consider that both team processes and product outcomes may lead to potential confusion and biased reasoning in team performance assessments.

B. Human Skills

In this research, human skills encompass both soft skills and personality traits.

- Soft skills are interpersonal skills that showcase an individual's ability to communicate effectively and build positive relationships while interacting with others. In this research, we evaluate team members' soft skills through an observational form. This form has been created by our researchers. It utilizes a 5-point rating scale to measure behaviors, including communication, emotional management, collaboration, patience, analysis and problem-solving, and time management. These skills are essential for software development teams [16][17].
- The Myers-Briggs Type Indicator (MBTI) is used as a personality assessment model that has seen significant success in the software engineering field over the past few decades. It has been employed to determine the most suitable job roles for individuals throughout the software development lifecycle [18]. The MBTI personality model classifies into four opposite traits: Extrovert (E) and Introvert (I), Sensing (S) and Intuition (N), Thinking (T) and Feeling (F), and Judging (J) and Perceiving (P). This assessment allows a better understanding of individuals' personality preferences and how they may best align with specific software development tasks

C. Agile Software Development Process

Agile Software Development [19] is an adaptable, collaborative, and repetitive approach that values individuals, working software, customer collaboration, and responsiveness to change. It aims to deliver software quickly while adapting to evolving requirements and customer feedback. Scrum, a popular Agile framework [19], follows transparency, inspection, and adaptation principles. It involves small, cross-functional teams led by a Scrum master. Sprints, lasting 1-4 weeks, drive the team to deliver a potentially shippable product increment. Scrum ceremonies, like daily stand-ups and sprint reviews, aid team coordination and improvement, empowering them to make decisions and achieve project success. This paper explores the challenges associated with Agile software development, specifically focusing on the influence of individual personalities within a Scrum team.

III. RESEARCH APPROACH

This section contains essential information for conducting studies to answer the research question.

A. Subject Selection

In 2022, Our experiment was carried out at Burapha University in Thailand, involving third-year students pursuing

a Bachelor of Science in software engineering. The study comprised 67 participants, consisting of 43 male and 24 female students, who were enrolled in the "Team Software Development Process (TSDP)" course. In the TSDP course, students engaged in a software development team simulation, where they were tasked with creating a year-long software project. The simulation followed the Agile software development process, specifically Scrum methodologies. The deliberate choice to experiment within an academic setting was purposeful, as proof of concept and aligning with the study's defined objectives. [20][21].

B. Team Formation

Teams were formed by combining students with varying programming skill levels. The clusters were designed based on the previous year's academic performance and assessments. These clusters were categorized as follows:

- Cluster 1 (emerging): Students with an initial understanding of the relevant concepts and competencies.
- Cluster 2 (developing): Students with a partial understanding of the relevant concepts and competencies.
- Cluster 3 (proficient): Students with a competent understanding of the relevant concepts and competencies.
- Cluster 4 (extending): Students with a sophisticated understanding of the relevant concepts and competencies.

Two members are selected from each cluster to compose a team, resulting in a team encompassing a spectrum of skill levels. Each team is comprised of 8-9 members. This selection process serves the dual purpose of balancing and controlling the influence of programming skill levels on the research outcomes. The researcher conducted hypothesis testing to validate the grouping of programming abilities across teams, affirming the efficacy of this balanced grouping through statistical analysis. The results indicated that all teams exhibited similar skill levels at a significance level of 0.05.

C. Identification of Personality Traits Based on MBTI

The MBTI personality assessment employed in this study comprises 60 items, assessed on a scale ranging from 'strongly agree' to 'strongly disagree.' Participants completed the assessment online. Each item corresponds to a specific dimension or trait. The assessment categorizes individuals based on four traits: E/I, S/N, T/F, and J/P. Upon completing the assessment, participants recorded their personality trait dimensions using a provided data recording form based on the assessment results.

D. Soft Skills Assessment

In this study, team members' soft skills are assessed by their project managers, evaluated by their teammates, and self-assessed. These soft skills include communication, emotional management, collaboration, patience, analysis and problem-solving, and time management. The assessment uses a 5-point rating scale where: 5 stands for excellent, 4 for impressive, 3 for neutral, 2 for improvement needed, and 1 for very dissatisfied.

E. Team Performance Assessment

This research incorporated two parts for evaluating team performance, such as team process and team software products. The assessment details are as follows:

1) *Team process*: Team indicators for assessment were designed by a team of 5 experts and professors in software engineering, incorporating elements from the Capability Maturity Model Integration (CMMI) standard and AUN-QA [22][23], including team goals, plans and progress, meetings, requirements documents, software design and engagement, coding standards, software testing, and software configuration and reuse. Each indicator is assessed with a five-score rating according to the scoring rubric, as shown in Table I.

TABLE I. THE DESCRIPTION OF SCORE OF ASSESSMENT FOR EACH METRIC IN THE TEAM PROCESS

| Score | Description |
|-------|---|
| 5 | Processes undergo continuous improvement through a quantitative analysis of typical variations encountered in the processes. |
| 4 | Specific subprocesses that make a significant contribution to the overall process performance are chosen. These selected subprocesses are then managed and monitored using statistical and other quantitative methods. |
| 3 | Processes are thoroughly defined and comprehended, and their details are outlined in standards, procedures, tools, and methodologies. |
| 2 | The team's project ensures effective management of requirements and meticulous planning, execution, measurement, and control of processes. |
| 1 | Processes are often disorganized and lack stability, leading to an ad hoc and chaotic environment. Success primarily relies on the competence and extraordinary efforts of individual team members rather than the implementation of established and processes. |

2) *Team software product*: The assessment details for the team product are as follows: six criteria were employed, including functionality, reliability, usability, efficiency, maintainability, and portability [24]. Each criterion was assessed by a 5-point rating scale, ranging from 5 ("Very Satisfied") to 1 ("Very Dissatisfied").

F. "Team Software Development Process" Course Design

The "Team Software Development Process" The course adopts active learning techniques related to Software Development Lifecycle (SDLC) topics, such as requirements elicitation, user story creation, software testing, and quality management, inspired by project-based learning approaches. The course is structured into four cycles of assessment, each comprising around eight to nine sprints. These sprints follow the SDLC. Each sprint is designed to last approximately one week, and it begins with a sprint planning meeting held during class time. To simulate real-world software teams, the teams are responsible for self-directing the final product based on changing requirements throughout the semester. They receive requirements from both the instructor and software firm specialists. The students experience a more dynamic and Agile approach to software development. Additionally, the course involves experts and project managers who are required to possess proficiency and experience in CMMI standards. Specifically, project managers must demonstrate a minimum of two years of experience leading Scrum software development teams.

G. Hypotheses

In this research, our objective is to investigate the impact of human skills represented by soft skills, including E/I, S/N, T/F, J/P, and soft skills levels categorized as high, medium, and low. Specifically, it aims to answer the question, "What do the human skill factors of team members affect team performance?". We employed a multiple-way analysis of variance (ANOVA) technique to find an answer to this question, which covered the main effects and all possible interactions effect between them for team process and team product aspects [25]. The aim was to gain insights into what personality traits and soft skills levels contribute to team performance. All hypotheses for this research are as follows:

Hypothesis main effect of process score (HM_Pc): The team process is influenced by each independent variable (E/I, S/N, T/F, J/P, and soft skills).

Hypothesis main effect of product score (HM_Pr): The team product is influenced by each independent variable (E/I, S/N, T/F, J/P, and soft skills).

Hypothesis interaction effect of process score (HI_Pc): At least one interaction between the independent variables (E/I, S/N, T/F, J/P, and soft skills) affects the team process.

Hypothesis interaction effect of product score (HI_Pr): At least one interaction between the independent variables (E/I, S/N, T/F, J/P, and soft skills) affects the team product.

IV. DATA COLLECTION

The data collection process consists of six steps involving the collection of variables for data analysis, including team process scores, team product scores, MBTI personality assessment results, and soft skills assessment results. The data collection steps are as follows:

1) *Step 1*: Researchers and professors formed Scrum software development teams based on specific criteria and guidelines to ensure alignment with the research objectives.

2) *Step 2*: A collaborative meeting was conducted involving professors, researchers, and project managers with the aim of deepening everyone's understanding of the research objectives, processes, and assessment criteria. This meeting facilitated the exchange of insights, clarification of expectations, and alignment of perspectives to ensure a cohesive and effective research effort.

3) *Step 3*: Each team was assigned to develop a year-long software project, delivered in 4 cycles, with each cycle consisting of 8-9 sprints. Work was allocated to each team according to the software requirements from the project manager to ensure a distributed workload and comparable challenges for each team member. Time requirements were established, and at the end of each cycle, teamwork was assessed, covering both team process and team product results.

4) *Step 4*: Each cycle's assessment was evaluated by experts and professors, focusing on both team process and team product aspects. The team process evaluation comprised eight criteria, each rated on a scale of 1 to 5, as outlined in Table II. The product evaluation included six criteria rated on a scale of 1 to 5. All scores were recorded for analysis in the final step.

5) *Step 5*: After the conclusion of the four cycles, the researcher collected data on students' personalities and

individual skills using a soft skills observational form. This form included self-ratings, teammate ratings, and project manager assessments.

6) *Step 6*: The researcher collected all scores, including team process scores, team product scores, personality traits types, and personal skills scores, to ensure data accuracy and to find results for the research questions. These insights into the team's performance outcome and software quality developed throughout the project were also examined.

TABLE II. THE DESCRIPTION OF SCORE OF ASSESSMENT FOR EACH METRIC IN THE TEAM PROCESS

| # | Criteria and Evidence |
|---|---|
| 1 | Team Goals (The goals and indicators of goals include team goals, role goals, and personal goals.) |
| 2 | Plans and Progress (Software plans and progress encompass strategic planning and monitoring of software development activities. Example work products include project plans, progress reports, timelines, milestones, and Gantt charts, facilitating effective project management and visual representation of project schedules.) |
| 3 | Meetings (Meeting documents include meeting invitation letters, meeting agendas, and meeting summary reports.) |
| 4 | Software Requirements Document (A comprehensive specification outlining functional and non-functional requirements, use cases, user stories, acceptance criteria, and a traceability matrix, among others.) |
| 5 | Software Design and Engagement (Specify the use of UML diagrams for designing the software's functionality, such as activity diagram, class diagram, entity-relationship diagram, and employ UX/UI tools for designing the system's user interface.) |
| 6 | Coding Standards (Guidelines and rules that dictate how software code should be written, formatted, and organized, ensuring consistency and best practices. Example work products for coding standards include comprehensive documentation outlining guidelines for file structure, naming conventions, coding style, documentation practices, and error handling techniques.) |
| 7 | Software Testing (The degree to which software meets specific requirements and satisfies user expectations, focusing on factors such as functionality, reliability, usability, performance, and maintainability. Example work products for software quality include test plans, test cases, code reviews, bug reports, quality assurance processes, and metrics tracking.) |
| 8 | Software Configuration & Reuse (Software configuration and reuse involves managing and leveraging software assets for efficient development. Example work products include version control systems, configuration management plans, and reusable components, promoting consistency, productivity, and maintenance in software projects.) |

V. RESULT AND DISSEMINATION

This section presents the outcomes obtained from gathering data and analysis on human skills and team performance in each team based on data characteristics.

A. Human Skills

The analysis of the Scrum development team's personality characteristics revealed that the majority of participants were Introverts (72%), with a preference for Intuition (52%), Feelings (81%), and Perception (55%) in their personality traits. When delving into the specifics of each team's dimensions, it was observed that in the E/I dimension, all teams had more members leaning toward Introverts than Extroverts. In the S/N dimension, each team had a balance between Sensing and Intuition preferences. Regarding the F/T dimension, there were consistently over twice as many members favoring Feeling over Thinking. Lastly, in the J/P dimension, it varied among teams, with some having a greater

number of Judging types than Perceiving types, while in other teams, it was the opposite.

The evaluation of soft skills results indicated that a substantial number of participants exhibited high levels of soft skills (54.55%), followed by those with intermediate levels (40.26%), and a smaller proportion demonstrated low levels of soft skills (5.19%). In examining each team based on the three-level categorization of soft skills, it was observed that almost all teams had medium to high levels, with over 80% of their members falling into this range. However, Teams 5 and 6 were exceptions, with values lower than 65%.

B. Team Performance: Process

Fig. 1 is the data analysis for each team's results. In cycle 1, all the teams had relatively similar performances. However, in cycle 2, there was an improvement in team performances, but the rates varied across teams. Some teams showed rapid progress, while others made moderate advancements. Moving to cycle 3, the range of team performance became more diverse compared to cycle 1. Most teams showed significant improvements except Team 6. Finally, in cycle 4, Team 1 maintained its exceptional performance, and Team 6, which previously had the lowest performance, experienced rapid development in the last cycle. Notably, all teams demonstrated considerable improvement compared to their performance in the first cycle.

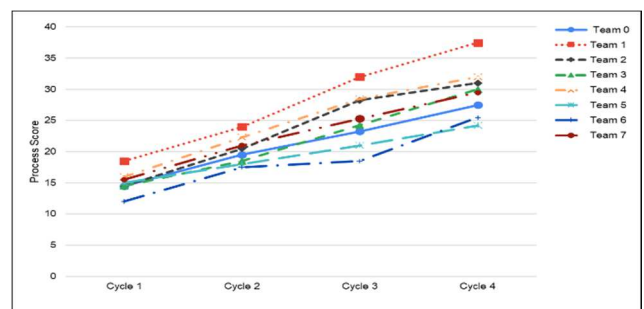


Fig. 1. Team process score categorized by team

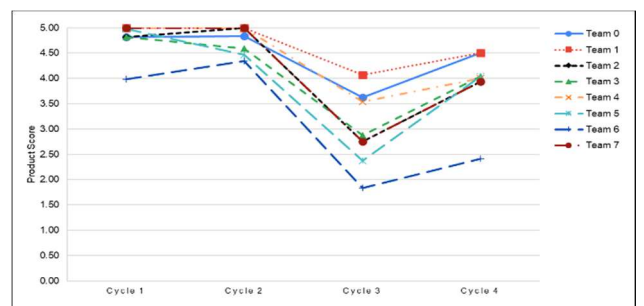


Fig. 2. Team product score categorized by team

C. Team Performance: Product

The team product results are in Fig. 2. In cycle 1, most teams achieved high product scores, except for Team 6, which scored significantly lower than the others. Moving to cycle 2, Team 6 showed improvement and reached a level of performance similar to other teams. During this cycle, the product scores of most teams were closely aligned. However, in cycle 3, there was a dramatic decline in team product scores, which was attributed to the complexity of the requirements. The majority of teams experienced a drop in their product scores. Finally, in cycle 4, every team made efforts to enhance their product scores compared to cycle 3. However, Team 6

continued to achieve a significantly lower score compared to the other teams, while Team 1 attained the highest product score in all cycles.

D. Hypothesis Testing

The hypotheses in this study were validated through the implementation of a multiple-way ANOVA at each cycle. The ANOVA tested the main effects and interaction effects of all independent variables on both team processes and team products. A significance level of p-value (0.05) was used to determine the rejection or acceptance of the null hypothesis. If the p-value was greater than 0.05, there was insufficient evidence to reject the null hypothesis, while p-values less than or equal to 0.05 provided evidence for rejecting the null hypothesis. These analytical procedures allowed us to thoroughly assess the impact of all variables on team performance and draw meaningful conclusions from the collected data.

Table III presents the results of the main effect hypothesis testing for the team process. The hypotheses tested (HM_{Pc}) were the main effects of E/I, S/N, T/F, J/P, and soft skills on the team process. The test results for each hypothesis found that the p-values for the main effects of J/P and soft skills in all cycles were less than 0.05. These results indicate that both J/P and soft skills significantly impact the team process. However, the p-values were higher than 0.05 for the other, suggesting that they do not significantly influence the team process in all cycles.

TABLE III. THE P-VALUE OF MUTIWAY ANOVA RESULTS FOR THE MAIN EFFECT OF THE TEAM PROCESS

| Independent | Sig.(p-value) | | | |
|-------------|---------------|---------------|---------------|---------------|
| | Cycle 1 | Cycle 2 | Cycle 3 | Cycle 4 |
| E/I | 0.6773 | 0.5296 | 0.3383 | 0.7749 |
| S/N | 0.8506 | 0.7987 | 0.7122 | 0.8485 |
| F/T | 0.7848 | 0.3680 | 0.4889 | 0.1214 |
| J/P | 0.0197 | 0.0099 | 0.0206 | 0.0213 |
| Soft skills | 0.0011 | 0.0001 | 0.0003 | 0.0001 |

TABLE IV. THE P-VALUE OF MUTIWAY ANOVA RESULTS FOR THE MAIN EFFECT OF THE TEAM PRODUCT

| Independent | Sig.(p-value) | | | |
|-------------|---------------|---------------|---------------|---------------|
| | Cycle 1 | Cycle 2 | Cycle 3 | Cycle 4 |
| E/I | 0.3853 | 0.0965 | 0.6643 | 0.8345 |
| S/N | 0.3007 | 0.8894 | 0.8764 | 0.5015 |
| F/T | 0.1046 | 0.9723 | 0.5136 | 0.2482 |
| J/P | 0.1781 | 0.0485 | 0.0019 | 0.0285 |
| Soft skills | 0.0523 | 0.0008 | 0.0117 | 0.0890 |

The main effects test to answer hypothesis HM_{Pr} in Table IV found that in cycle 1, the p-values for the main effects of all human skills do not affect the team product for those variables (p-values > 0.05), indicating that human skills have no significant influence on team product. In cycle 2 and cycle 3, the p-values for the main effects of J/P and soft skills are less than 0.05. These results indicate that J/P and soft skills affect the team product in cycle 2 and 3. However, the other human skills do not affect the team product for those variables. In cycle 4, the J/P has p-values for the main effects is 0.0285 (<0.05). These results indicate that J/P affects the team product. However, the other human skills do not affect the team product for those variables (p-values > 0.05).

The hypothesis test for HI_{Pc} resulted that in cycles 1, 2, 3, and 4, p-values greater than 0.05 were obtained, suggesting no significant co-interactions between individual variables during these cycles. In other words, the interactions between these variables did not have a notable impact on the team process, except for F/T and soft skills in cycles 1 and 2, and F/T, J/P, and soft skills in cycle 2 found that p-values were less than 0.05. These results indicate their significant influence on the team process, as shown in Table V.

TABLE V. THE P-VALUE OF MUTIWAY ANOVA RESULTS FOR THE INTERACTION EFFECT OF THE TEAM PROCESS

| Independent | Sig.(p-value) | | | |
|--------------------------------|----------------|---------------|---------|---------|
| | Cycle 1 | Cycle 2 | Cycle 3 | Cycle 4 |
| E/I : S/N | 0.75440 | 0.7758 | 0.9097 | 0.9473 |
| E/I : F/T | 0.46217 | 0.0933 | 0.1891 | 0.0938 |
| E/I : J/P | 0.73700 | 0.6569 | 0.5456 | 0.4251 |
| E/I : Soft skills | 0.29486 | 0.4420 | 0.6070 | 0.7014 |
| S/N : F/T | 0.89401 | 0.3314 | 0.3467 | 0.2678 |
| S/N : J/P | 0.76296 | 0.6184 | 0.4308 | 0.6238 |
| S/N : Soft skills | 0.20897 | 0.1607 | 0.3144 | 0.2418 |
| F/T : J/P | 0.44650 | 0.4363 | 0.8575 | 0.7586 |
| F/T : Soft skills | 0.04278 | 0.0343 | 0.2129 | 0.2479 |
| J/P : Soft skills | 0.57773 | 0.8934 | 0.9112 | 0.4954 |
| E/I : S/N : F/T | 0.45347 | 0.7568 | 0.4187 | 0.9376 |
| E/I : S/N : J/P | 0.40721 | 0.6007 | 0.4507 | 0.2977 |
| E/I : F/T : J/P | 0.75432 | 0.1314 | 0.3396 | 0.2381 |
| E/I : S/N : Soft skills | 0.32591 | 0.0527 | 0.3940 | 0.7105 |
| E/I : J/P : Soft skills | 0.99360 | 0.5090 | 0.7163 | 0.8565 |
| S/N : J/P : Soft skills | 0.85337 | 0.6631 | 0.9260 | 0.7052 |
| F/T : J/P : Soft skills | 0.33503 | 0.0214 | 0.1014 | 0.0834 |
| F/T:S/N:J/P:Soft skills | 0.72468 | 0.7454 | 0.8757 | 0.7833 |

TABLE VI. THE P-VALUE OF MUTIWAY ANOVA RESULTS FOR THE INTERACTION EFFECT OF THE TEAM PRODUCT

| Independent | Sig.(p-value) | | | |
|--------------------------------|---------------|---------------|---------|---------|
| | Cycle 1 | Cycle 2 | Cycle 3 | Cycle 4 |
| E/I : S/N | 0.7211 | 0.7682 | 0.3749 | 0.5656 |
| E/I : F/T | 0.8459 | 0.0594 | 0.2126 | 0.6314 |
| E/I : J/P | 0.8818 | 0.8174 | 0.9662 | 0.9357 |
| E/I : Soft skills | 0.5469 | 0.6880 | 0.7270 | 0.5998 |
| S/N : F/T | 0.7773 | 0.3870 | 0.7688 | 0.6948 |
| S/N : J/P | 0.4250 | 0.3587 | 0.5212 | 0.9678 |
| S/N : Soft skills | 0.4127 | 0.5374 | 0.6103 | 0.6576 |
| F/T : J/P | 0.5878 | 0.9718 | 0.4191 | 0.8343 |
| F/T : Soft skills | 0.1274 | 0.1115 | 0.6039 | 0.6028 |
| J/P : Soft skills | 0.1281 | 0.9631 | 0.9785 | 0.4043 |
| E/I : S/N : F/T | 0.2913 | 0.8351 | 0.7011 | 0.3759 |
| E/I : S/N : J/P | 0.3408 | 0.8495 | 0.2597 | 0.4591 |
| E/I : F/T : J/P | 0.6709 | 0.2256 | 0.9506 | 0.3130 |
| E/I : S/N : Soft skills | 0.4242 | 0.0196 | 0.2500 | 0.6000 |
| E/I : J/P : Soft skills | 0.9551 | 0.5481 | 0.9351 | 0.6661 |
| S/N : J/P : Soft skills | 0.8038 | 0.4843 | 0.8790 | 0.6339 |
| F/T : J/P : Soft skills | 0.6366 | 0.0077 | 0.0733 | 0.4944 |
| F/T:S/N:J/P:Soft skills | 0.5105 | 0.7115 | 0.9486 | 0.9275 |

For the hypotheses testing (HI_{Pr}) shown in Table VI, the test results for cycles 1, 3, and 4 showed p-values greater than 0.05, suggesting that there were no significant co-interactions between personal variables during these cycles. Consequently, the interactions between the personal variables had no notable

impact on the team product in these cases. However, in cycle 2, we observed significant co-interactions between the E/I, S/N, and soft skills and the F/T, J/P, and soft skills. The p-values for these co-interactions were less than 0.05, respectively, indicating that they had a significant influence on the team product during cycle 2.

VI. CONCLUSION

This research investigates the influence of human skills within junior software development teams, encompassing process and product dimensions. The evaluation process follows a cyclical approach. The findings reveal that personality traits, precisely the J/P dimension, and soft skills, significantly impact team processes and products. Additionally, there are notable interaction effects with F/T, E/I, and S/N during specific cycles.

The results emphasize the importance of soft skills in Scrum team collaboration, particularly in the context of the J/P dimension. Prospective personality types are associated with adaptability, responsiveness to change, and creativity. Scrum's emphasis on flexibility and responsiveness aligns with the strengths of Prospective personality types, making them potential in this environment.

The insights from this research can provide valuable guidance to managers, team leaders, and team members when forming teams and devising strategies to enhance team performance. Soft skills and personality traits should be considered essential criteria during team composition, contributing to more effective teams. Moreover, recognizing the impact of soft skills on performance enables their deliberate utilization to foster individual and team achievements.

ACKNOWLEDGMENT

The authors would like to extend their gratitude to the Faculty of Informatics at Burapha University for their financial support. This support was allocated to research identified by reference ID 08/2565 and approved by the Institutional Review Board (IRB) under the number HS080/2565(C1).

REFERENCES

- [1] S. Alsaqqa, S. Sawalha, and H. Abdel-Nabi, "Agile Software Development: Methodologies and Trends," *Int. J. Interact. Mob. Technol.*, vol. 14, no. 11, pp. 246-270, Jul. 2020.
- [2] F. Geraldine, "Software engineering is more than code - human skills are essential," in *Evaluation and Assessment of Software Engineering EASE2021*, Trondheim, Norway, EU. [Online]. Available: <http://hdl.handle.net/20.500.12708/87294>.
- [3] B. M. Ephraim and M. Carl, "Critical success factors in software development projects," *South African Computer Journal*, vol. 34, no. 1, pp. 1-34, <https://dx.doi.org/10.18489/sacj.v34i1.820>.
- [4] J. Koch, I. Drazic, and C. C. Schermuly, "The affective, behavioural and cognitive outcomes of Agile project management: a preliminary meta-analysis," *Journal of Occupational and Organizational Psychology*, pp. 1-29, <https://doi.org/10.1111/joop.12429>.
- [5] Y. Ma and V. Dochibhotla, "Influence of individual human factors on team performance in Agile software development," *Dissertation*, Faculty of Computing, Blekinge Institute of Technology, Sheffield, Sweden, 2022.
- [6] J. Garcia, F. Trentino, J. A. Oliveira, C. Nobre, V. Cunha, N. Hirata, E. Nunes, and C. Maciel, "Communication in software development teams," *International Journal of Business Information Systems*, 2022, pp. 327-356.
- [7] D. Monsalves, H. Cornide-Reyes, and F. Riquelme, "Relationships Between Social Interactions and Belbin Role Types in Collaborative Agile Teams," *IEEE Access*, vol. 11, pp. 17002-17020, 2023, doi: 10.1109/ACCESS.2023.3245325.
- [8] S. Burbekova, "Soft Skills as the Most In-Demand Skills of Future IT Specialists," in *2021 IEEE International Conference on Smart Information Systems and Technologies (SIST)*, Nur-Sultan, Kazakhstan, 2021, pp. 1-5, doi: 10.1109/SIST50301.2021.9465935.
- [9] K. Borrageiro and N. Mennega, "Essential Skills Needed in the Fourth Industrial Revolution (4IR): A Systematic Literature Review," in *2023 IST-Africa Conference (IST-Africa)*, Tshwane, South Africa, 2023, pp. 1-13, doi: 10.23919/IST-Africa60249.2023.10187815.
- [10] R. Poonam and C. M. Yasser, "An Experimental Study to Investigate Personality Traits on Pair Programming Efficiency in Extreme Programming," in *Proc. Int. Conf. on Industrial Eng. and Applications*, 2018, pp. 96-99.
- [11] A. S. Barroso, K. H. J. Prado, M. S. Soares, and R. P. C. Nascimento, "How personality traits influence the quality of software developed by students." In *Proc. of the XV Brazilian Symp. on Info. Syst., Assoc. for Comp. Machinery*, pp. 1-8, 2019.
- [12] M. A. Iqbal, F. A. Ammar, A. R. Aldaihani, T. K. U. Khan, and A. Shah, "Predicting Most Effective Software Development Teams by Mapping MBTI Personality Traits with Software Lifecycle Activities," in *2019 IEEE 6th International Conference on Engineering Technologies and Applied Sciences (ICETAS)*, Kuala Lumpur, Malaysia, 2019, pp. 1-5, doi: 10.1109/ICETAS48360.2019.9117370.
- [13] P. M. Zähl, S. Theis, M. R. Wolf, and K. Köhler, "Teamwork in Software Development and What Personality Has to Do with It - An Overview," in *Virtual, Augmented and Mixed Reality. HCII 2023. Lecture Notes in Computer Science*, vol. 14027, J. Y. C. Chen and G. Fragomeni, Eds., Springer, Cham, 2023, pp. 1-10. https://doi.org/10.1007/978-3-031-35634-6_10.
- [14] T. Dingsøyr, T. E. Fægri, T. Dybå, B. Haugset, and Y. Lindsjörn, "Team Performance in Software Development: Research Results versus Agile Principles," in *IEEE Software*, vol. 33, no. 4, pp. 106-110, July-Aug. 2016, doi: 10.1109/MS.2016.100.
- [15] D. E. Strode, T. Dingsøyr, and Y. Lindsjörn, "A teamwork effectiveness model for Agile software development," *Empirical Software Engineering*, vol. 27, pp. 1-50, 2022.
- [16] I. Avença, L. Domingues, and H. Carvalho, "Project Managers soft skills influence in knowledge sharing," *Procedia Computer Science*, vol. 219, pp. 1705-1712, 2023, ISSN 1877-0509, <https://doi.org/10.1016/j.procs.2023.01.464>.
- [17] M. Castro, A. Barcaui, B. Bahli, and R. Figueiredo, "Do the Project Manager's Soft Skills Matter? Impacts of the Project Manager's Emotional Intelligence, Trustworthiness, and Job Satisfaction on Project Success," *Adm. Sci.*, vol. 12, p. 141, 2022. <https://doi.org/10.3390/admsci12040141>.
- [18] I. B. Myers, M. H. McCaulley, N. L. Quenk, and A. L. Hammer, "MBTI manual: A guide to the development and use of the Myers-Briggs Type Indicator," *Consulting Psychologists Press*, Palo Alto, CA, 1998.
- [19] B. Boehm, "Get ready for Agile methods, with care," *Computer*, vol. 35, no. 1, pp. 64-69, Jan. 2002, doi: 10.1109/2.976920.
- [20] D. Falessi, N. Juristo, C. Wohlin, B. Turhan, J. Münch, A. Jedlitschka, et al., "Empirical software engineering experts on the use of students
- [21] S. L. Pfleeger, "Experimental design and analysis in software engineering," in *Ann. Softw. Eng.*, vol. 1, no. 1, 1995, pp. 219-253.
- [22] M. Chrissis, M. Konrad, and S. Shrum, "CMMI: Guidelines for Process Integration and Product Improvement," 3rd ed., Addison-Wesley, 2003.
- [23] O. C. B. Johnson, "The Impact of ASEAN University Network-Quality Assurance (AUN-QA) Assessment on the Quality of Educational Programmes," in *Theory and Practice of Quality and Reliability Engineering in Asia Industry*, Springer, Singapore, 2017, pp. 87-97.
- [24] T. Punter, R. van Solingen, and J. Trienekens, "Software product evaluation current status and future needs for customers and industry," in *Proceedings of 4th European Conference on Evaluation of Information Technology*, 1997, pp. 57-66.
- [25] A. O. J. Cramer, D. van Ravenzwaaij, D. Matzke, et al., "Hidden multiplicity in exploratory multiway ANOVA: Prevalence and remedies," in *Psychon Bull Rev*, vol. 23, 2016, pp. 640-647. doi: 10.3758/s13423-015-0913-

PWM Rectifier Impedance Modeling for the UGM-INKA Hybrid Train

Musyaffa' Ahmad, Eka Firmansyah*, Yohan Fajar Sidik, F. Danang Wijaya, Mudarris, and Sigit Doni R.

Department of Electrical Engineering and Information Technology,

Faculty of Engineering, Gadjah Mada University

Yogyakarta 55281, Indonesia

musyaffaahmad1998@mail.ugm.ac.id, eka.firmansyah@ugm.ac.id*, yohanfajarsidik@ugm.ac.id, danangwijaya@ugm.ac.id,

mudarris@mail.ugm.ac.id, sigitdoniramdan@mail.ugm.ac.id

Abstract—The hybrid train developed through the collaboration between UGM and INKA, utilizes the dc bus voltage to incorporate multiple energy sources, such as fuel cells, generators, and batteries. The hybrid train's dc voltage regulation requires a PWM rectifier to connect the generator to the dc bus and ensure voltage stability. The PWM rectifier needs an inductor on the input side as a filter, and a capacitor on the output side as a buffer to operate efficiently. In its practical application, the impedance value supplied by the generator may not satisfy or surpass the demands, causing the system to become unstable. This paper presents a model to determine the required inductance and capacitance values for the PWM rectifier. A 380 V three-phase ac generator with a power specification of 180 kW maintains the rectifier's dc output voltage at a constant 600 V. The inductance values were tested under various values and conditions. Based on the simulation results, the voltage-current ripple and drop increased with larger inductor values and decreased with smaller values. At 100% load, the voltage drop is 20.54% with the maximum limit inductor and 13.96% with the minimum limit inductor. The voltage ripple reached 2.65% at its upper limit and 0.47% at its lower limit. Meanwhile, the current ripple on the upper limit inductor measures 2.68%, and 0.54% on the lower limit. These results indicate that the proposed impedance model is suitable for implementation in a 180 kW PWM rectifier and ensures dc voltage stability.

Index Terms—PWM rectifier, hybrid train, impedance model.

I. INTRODUCTION

The electrical architecture of the hybrid train must be well-designed to ensure the proper functioning of the PWM rectifier in both ideal and non-ideal conditions [1] [2]. Non-ideal conditions may result from generator output voltage tolerance, loading variations, or the selection of inappropriate component specifications. These conditions directly affect the system's stability and harmonics. The stability of the dc bus voltage is crucial and should be kept consistent. A PWM rectifier is used as a connector between the generator and the bus. A PWM rectifier requires an inductor as a filter on the input side and a capacitor as a buffer on the output side to function properly.

Based on phasor diagram principles, the voltage of the direct current, alternating current, and impedance are interconnected [3]. In the PWM rectifier, the generator ac and dc voltage value are constant. Thus, the stability of the output voltage is dependent on the impedance voltage. The impedance value

parameter influences the impedance voltage. However, in the practical application, the impedance value supplied by the generator may not satisfy or surpass the demands, causing the system to become unstable. In addition, the inductor component has a tolerance value, which makes the installed impedance value inaccurate. Therefore, it is essential to model the impedance value of the PWM rectifier to enhance system stability and performance.

Several studies have investigated PWM rectifiers and analyzed their impedance. In [4], the stability of power systems was analyzed and evaluated using impedance-based methods. Researchers in [5] modeled the impedance and admittance of the PWM rectifier based on its output characteristics and then analyzed their performance through circuit testing. In [6], researchers employed the small signal method in the dq frame to model the impedance of the PWM rectifier.

This research aimed to model the impedance value of the PWM rectifier on a hybrid train designed by UGM and INKA. In contrast to earlier studies, our model provides a detailed calculation of both the upper and lower limits of impedance in abc frames, along with the actual value in steady-state conditions. This paper also modeled the value of dc capacitors. The upper and lower limits are calculated to represent the tolerance of the inductor value in the market and the tolerance of the voltage generated at the output. The obtained impedance model was then validated using the PWM rectifier model in PLECS simulation. The simulation specifications were adjusted to fit with the parameters of the UGM-INKA hybrid train system, which generates 180 kW of power and maintains a constant output voltage of 600 V. To adjust for component availability in the marketplace, simulations were also performed using impedance values in the marketplace that were close to the calculated values. Tests were conducted under various conditions to illustrate the response and performance of the PWM rectifier system.

II. PWM RECTIFIER ON THE HYBRID TRAIN

The electrical system of a hybrid train consists of several integrated power components. Fig. 1 shows the structure of the electrical system of PT INKA's Commuter Class Hybrid Rail Train (KRHKC). The hybrid train is connected to two sources: A 3-phase generator on the input side and a battery

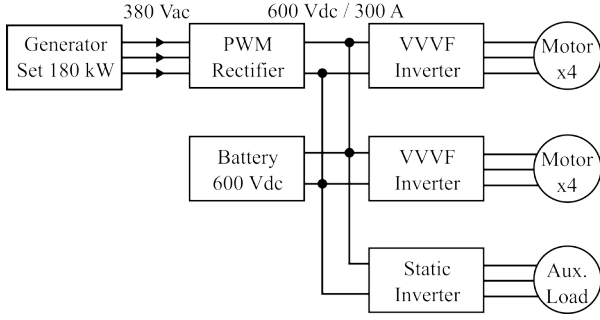


Fig. 1. Hybrid train electrical construction.

connected directly to the 600 V_{dc} . The generator is connected to a PWM rectifier converter which converts the ac voltage to dc voltage. Through the PWM rectifier, the voltage at the generator can be integrated into the 600V dc bus to supply the load. The VVVF (Variable Voltage Variable Frequency) inverter functions to convert the dc voltage on the dc bus to ac voltage to supply the load. The load included in the KRHKC system is divided into two types: motor load, and auxiliary load.

In the PWM rectifier, the estimated value of the power delivered from the source to the load side was calculated using Eq. 1. This calculation assumes that the system is in an ideal state without considering the value of losses,

$$P = \frac{3}{2}E_m I_m \cos\phi \quad \text{and} \quad Q = \frac{3}{2}E_m I_m \sin\phi. \quad (1)$$

In Equation 1, P is the active power of the generator in watts, Q is the reactive power of the generator in VAR, and E_m is the peak voltage of the generator. Then I_m is the peak ac current and ϕ is the phase difference between E_m and I_m . The ϕ value must be set to zero or a state of unity power factor for the PWM rectifier to operate properly. Thus, the new power transfer equation for the PWM rectifier system in the hybrid train is obtained as shown below,

$$P = \frac{3}{2}E_m I_m \quad \text{and} \quad Q = 0. \quad (2)$$

The circuit of a 3-phase, 2-level PWM rectifier is shown in Fig. 2, which consists of several main components, such as semiconductor switches, capacitors and inductors [6] [7].

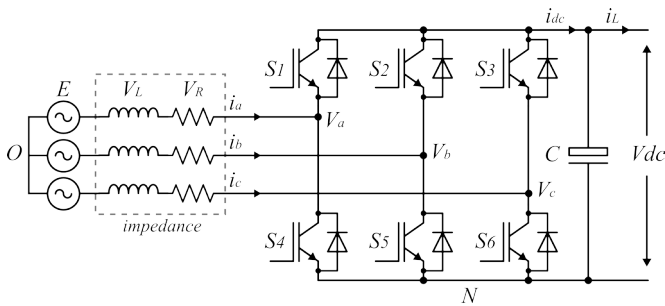


Fig. 2. PWM rectifier model in hybrid train.

The PWM rectifier was connected to the 3-phase source on the input side through the inductor component. In Fig. 2, E_a , E_b and E_c are the ac input side voltages, with O as the neutral point of the source. The PWM rectifier operates with six semiconductor switches (Q_{1-6}) with N as the neutral of the converter. Then i_a , i_b and i_c are the input currents of the source for phases a, b and c. The components i_{dc} and i_L are the output current on the dc side and the current at the load, respectively. Then there is a capacitor C on the output side, which is the capacitor on the dc bus. Meanwhile, V_{dc} is the dc voltage resulting from the PWM rectifier used to supply the load.

III. INDUCTANCE MODEL FOR PWM RECTIFIERS

The inductor component in the PWM rectifier system plays an important role in the converter operation process. The inductor value determines the amount of power delivered from the generator to the load and affects the performance of the PWM rectifier. Therefore, the inductor value must be modeled in such a way that the current variation can be close to zero [7]. Based on the PWM rectifier model in Fig. 2, the input voltage value in the three-phase system can be modeled using Kirchoff's law [8] [9].

$$\begin{bmatrix} E_a \\ E_b \\ E_c \end{bmatrix} = R \begin{bmatrix} i_a \\ i_b \\ i_c \end{bmatrix} + L \frac{d}{dt} \begin{bmatrix} i_a \\ i_b \\ i_c \end{bmatrix} + \begin{bmatrix} V_{aN} \\ V_{bN} \\ V_{cN} \end{bmatrix} + \begin{bmatrix} V_{aO} \\ V_{bO} \\ V_{cO} \end{bmatrix}. \quad (3)$$

Equation 3 explained that the voltage value at the PWM rectifier input side is the sum of the voltage at the impedance RL and the voltage at the converter phase node. V_{aN} , V_{bN} , and V_{cN} are the voltages between nodes abc and point N. Meanwhile, V_{aO} , V_{bO} , and V_{cO} are the voltages between nodes a-b-c and point O. Thus, from the point of view of the impedance voltage, Eq. 3 can be written as shown below,

$$\begin{bmatrix} V_{Ra} \\ V_{Rb} \\ V_{Rc} \end{bmatrix} + \begin{bmatrix} V_{La} \\ V_{Lb} \\ V_{Lc} \end{bmatrix} = \begin{bmatrix} E_a \\ E_b \\ E_c \end{bmatrix} - \left(\begin{bmatrix} V_{aN} \\ V_{bN} \\ V_{cN} \end{bmatrix} + \begin{bmatrix} V_{aO} \\ V_{bO} \\ V_{cO} \end{bmatrix} \right). \quad (4)$$

The variables V_{Ra} , V_{Rb} , and V_{Rc} are the voltage at impedance R for the three phase poles (a, b, and c). Meanwhile, V_{La} , V_{Lb} , and V_{Lc} are the voltage at impedance L for the three poles of the PWM rectifier phase.

A. Upper Limit Inductance Model for the PWM Rectifier

The upper limit of the inductance in the PWM rectifier is reached when the sinusoidal voltage approaches zero, as shown in Fig. 3 with the blue line. T_1 and T_2 are the switching periods when $S_a=0$ and $S_a=1$, respectively. ΔI_1 is the change in current when $S_a=0$ and ΔI_2 is the change in current when $S_a=1$. The current value tracked by the control system is represented by i^* . With the initial assumption that the 3-phase system used is a balanced system, inductance modeling can be done by phasor analysis using the PWM rectifier equivalent circuit shown in Fig. 4.

Based on the PWM rectifier equivalent model in Fig. 4, E is the ac input voltage, V_L is the voltage across inductor L , and

V_R is the switching output voltage. Then, with reference to the model, phasor analysis was performed for the matrix model in Eq. 4. The selected phase pole was phase a . Therefore, the following impedance voltage equation for phase a is shown below,

$$V_L + V_R = E_a - (V_{aN} - V_{NO}). \quad (5)$$

From Equation 5, V_{aN} and V_{NO} are the voltage from point a to neutral and the voltage from neutral to point O , respectively. Since the impedance value of R is very small and does not significantly affect the performance of the converter, the voltage value across the resistor is ignored. Equation 5 is then rewritten to the equation below.

$$L \frac{di_a}{dt} = E_a - (V_{aN} - V_{NO}), \quad (6)$$

the component $\frac{di_a}{dt}$ is the change in current value with time in phase a .

In the 2-level PWM rectifier, the PWM signal modulation was used as a logic input to control the firing of six semiconductor switches. The logic input sent to the gate side of the switch was a digital signal of configuration [7] [10],

$$S_k = \begin{cases} 1 & \text{upper switch ON, lower switch OFF} \\ 0 & \text{upper switch OFF, lower switch ON} \end{cases} \quad (7)$$

In Equation 7, k indicates the pole of one of the phases (a , b , c). Based on this rule, when the upper bridge of a leg is turned on, the lower bridge is automatically turned off, and vice versa. Substituting Eq. 7 into Eq. 6 gives the following inductor voltage model:

$$L \frac{\Delta I_1}{T_1} \approx E_a + \frac{V_{dc}}{3} (S_b + S_c). \quad (8)$$

$$L \frac{\Delta I_2}{T_2} \approx E_a + \frac{V_{dc}}{3} (-2 + S_b + S_c). \quad (9)$$

Equation 8 and 9 show the inductor voltage model when the switch is in the off state ($S_a=0$) and the on state ($S_a=1$). ΔI_1 is the change in current value when $S_a=0$, while ΔI_2 is the change in current value when $S_a=1$. V_{dc} is the dc voltage at the output side of the PWM rectifier. T_1 and T_1 are the rise

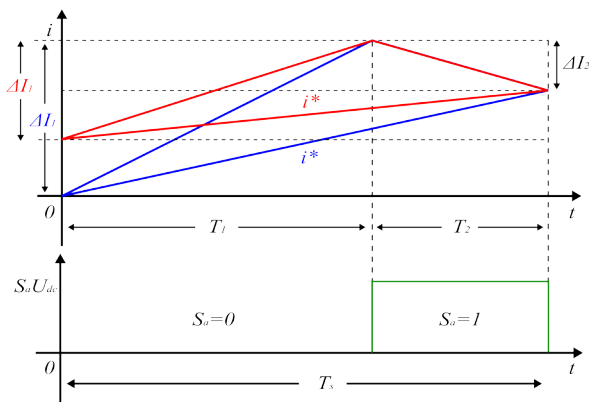


Fig. 3. Current near zero (blue) and peak (red) point condition [7].

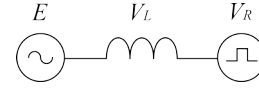


Fig. 4. PWM rectifier equivalent model.

time ($S_a=0$) and fall time ($S_a=1$), respectively. Based on the switching graphs in Fig. 3, the following equation is obtained:

$$T_2 = T_s - T_1. \quad (10)$$

Then, to facilitate the tracking of the current value, the PWM rectifier system must satisfy the following equation,

$$\frac{\Delta I_1 + \Delta I_2}{T_s} \approx E_a + \frac{V_{dc}}{3} (-2 + S_b + S_c). \quad (11)$$

To obtain the inductance model at the upper limit, Equations 8 and 9 were substituted into Eq. 11, to obtain the following equation:

$$L \leq \frac{E_m T_s}{2I_m} * \frac{V_{dc}}{3I_m \omega} * \frac{T_1(S_b + S_c) + T_2(-2 + S_b + S_c)}{T_s}. \quad (12)$$

B. Lower Limit Inductance Model for the PWM Rectifier

Contrary to the zero-point condition, when the sinusoidal voltage is at its highest point (near the peak), the current in the PWM rectifier will reach its maximum value. In this condition, the difference between the current and voltage reaches the optimum value. Thus, the energy conversion process from ac to dc is at the highest efficiency value. This state is shown in Fig. 3 with the red line. Under steady state conditions, the rise of the current and voltage can be written by the following equation [7],

$$E_m + \frac{V_{dc}}{3} (S_b + S_c) \approx \frac{L \Delta I_1}{T_1}. \quad (13)$$

Under the condition that the switching cycle approaches the peak current, the following condition is obtained:

$$|\Delta I_1| = |\Delta I_2|. \quad (14)$$

To obtain the lower limit inductance equation, Eq. 14 was substituted into Eq. 13:

$$L \leq \frac{(2V_{dc} - 3E_m) E_m T_s}{2V_{dc} \cdot 0.2I_m}, \quad (15)$$

The calculated inductance value can be used in the simulation of the PWM controller to evaluate the functionality of the proposed system model.

IV. PWM RECTIFIER IMPEDANCE CALCULATION

The inductance and capacitance parameters of the PWM rectifier were calculated using the impedance model obtained earlier. The calculation used the specifications of the 180 kW PWM rectifier listed in Table I.

TABLE I
PWM RECTIFIER SPECIFICATION

| Parameter | Value |
|---------------------|--------------|
| Input power | 180 kW |
| Input voltage | 380 V_{LL} |
| Output voltage | 600 V_{dc} |
| Ripple V & I | 1% |
| Switching frequency | 10 kHz |

A. Upper and Lower Limit Inductance Calculation

Inductor values available on the market have tolerance values. Thus, it is necessary to calculate the appropriate upper and lower tolerance limits. Furthermore, the tolerance of the generator output voltage significantly affects the selection of component specifications. The upper and lower limits of the inductor can be calculated using Eq. 12 and 15, based on the obtained parameters,

$$0.179 \text{ mH} < L < 1.5 \text{ mH}. \quad (16)$$

B. Inductance Calculation Under Steady-state Conditions

The steady-state calculation uses a phasor scheme using the equivalent circuit shown in Fig. 4, where the input voltage value E is the rms input voltage calculated by the following formula:

$$E = V_{LN,rms} = V_{LN}\sqrt{2} = 220 \cdot \sqrt{2} = 311 \text{ V}. \quad (17)$$

Meanwhile, the V_R voltage was calculated as shown below:

$$V_R = V_{dc,1\phi} = V_{dc}/\sqrt{3} = 600/\sqrt{3} = 346 \text{ V}. \quad (18)$$

The constant value of $\sqrt{3}$ was obtained when the Space Vector Modulation (SVM) method was used to control the PWM rectifier. Then, the equivalent circuit in Fig. 4 is remodeled into a vector diagram as shown in Fig. 5 [11].

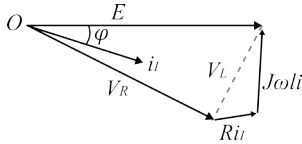


Fig. 5. The vector diagram for PWM rectifier.

In the phasor diagram of Figure 8, two vectors represent impedance values: the Ri_I vector for resistance and $j\omega Li$ for inductance. Since the R value is very small and does not really affect the system, the resistance value was ignored.

Based on the vector diagram in Figure 5, the three voltage components E , V_R and V_L interact. Since the values of E and V_R are set at the beginning, the variable that can be modeled is V_L , which is the voltage across the inductor. The inductance voltage can be calculated using the Pythagorean formula,

$$V_L = \sqrt{V_R^2 - E^2} = \sqrt{346^2 - 311^2} = 151.6 \text{ V}. \quad (19)$$

The value of the current flowing in the system can be calculated using the Eq. 20,

$$I = \frac{1}{\sqrt{3}} \cdot \frac{P}{E} = \frac{1}{\sqrt{3}} \cdot \frac{180k}{311} = 334.16 \text{ A}. \quad (20)$$

Thus, the steady-state inductor value was obtained, as shown below:

$$L = \frac{V_L}{2\pi f \cdot I} = \frac{151.6}{2\pi \cdot 50 \cdot 334.16} = 1.44 \text{ mH}. \quad (21)$$

C. Dc-link Capacitor Calculation

PWM rectifiers utilize dc-link capacitors to smoothen the output current and voltage, which reduces voltage ripple and ensures output stability. According to research [12], the minimum capacitance value in the PWM rectifier can be calculated by considering changes in the output power value,

$$C_{\min} = \frac{(P_2 - P_1) \cdot T_{\min} - 3 \cdot (A)^2}{V_{dc} \cdot \Delta V - \frac{1}{2} \cdot \Delta V^2}, \quad (22)$$

$$A = K_{p-\max} \cdot \Delta V \cdot \frac{T_{\min}}{2} + K_i \cdot f_{\text{samp}} \cdot \Delta V \cdot \frac{T_{\min}}{3}. \quad (23)$$

The rectifier output power changes are denoted as P_1 and P_2 . T_{\min} represents the minimum duration of the current change, $K_{p-\max}$ is the maximum proportional gain (A/V), and K_I is the integral gain (A/(V.sec)). ΔV and f_{samp} represents the variation of dc-link voltage value and sampling frequency of the dc bus controller, respectively.

The power change value is set to 40% and the ΔV to 1%. Therefore, the capacitor's minimum value based on Eq. 22 is 1.23 mF.

V. RESULTS AND DISCUSSION

A. PWM Rectifier Model

To validate the impedance calculation results, the PWM rectifier system was tested using the PLECS software with the specifications shown in Table I. Then, the SVPWM control method was used to test the PWM rectifier circuit as shown in Fig. 6. PWM rectifier testing involves providing load condition variations every 0.2 seconds, including no-load, 10%, 30%, 60%, and full load conditions. These conditions enable a thorough evaluation of the rectifier's performance.

B. Simulation Results using the Obtained Impedance Model

The experiment used three versions of inductor models and a capacitor, as shown in Table II.

TABLE II
IMPEDANCE MODEL SPECIFICATION

| Impedance | L_{\max} | L_{std} | L_{\min} | C |
|-----------|------------|------------------|------------|---------|
| Value | 1.5 mH | 1.44 mH | 0.179 mH | 1.23 mF |

Test results were obtained by varying the impedance and load as four different loading variations at 0.2 seconds intervals, namely 10%, 30%, 60%, and 100%. As exhibited in Fig. 7, the voltage drop at each loading is directly proportional to the applied load. Figure 2 shows that at 10% loading, the voltage drop reaches 7.49%, 7.48%, and 8.425% for L_{\max} , L_{std} , and L_{\min} , respectively. Fig. 8 demonstrates that at 100% loading, the voltage drop is 20.54%, 20.07%, and 13.96% for L_{\max} , L_{std} , and L_{\min} , respectively.

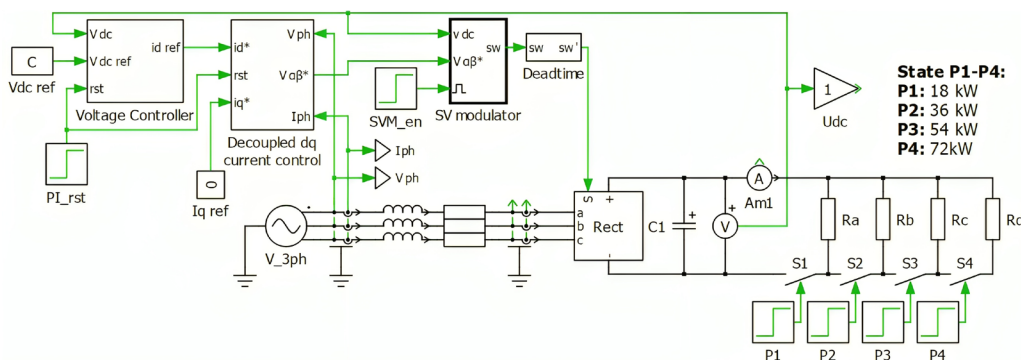


Fig. 6. PWM rectifier schematic.

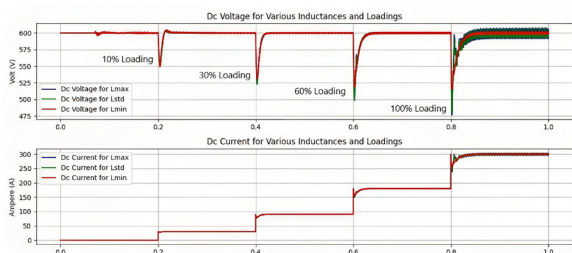


Fig. 7. System test using various impedances and loadings.

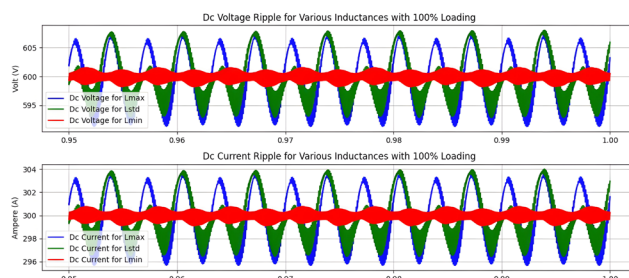


Fig. 9. Dc Voltage Ripple using various impedances at 100% load.

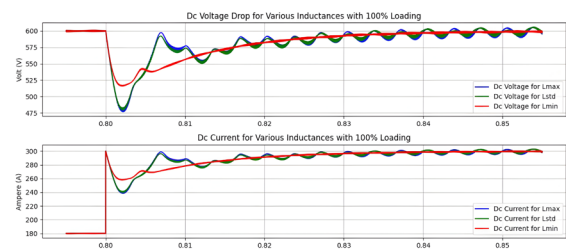


Fig. 8. System test using various impedances at 100% load.

Based on the results presented in Fig. 8, a lower inductance value results in a higher percentage of voltage drop at low loads. However, as the load increases, the percentage of voltage drop at the L_{min} is lower compared to both L_{max} and L_{std} . Technical term abbreviations are explained when first used for clear comprehension.

The current and voltage ripples at full load are displayed in Fig. 9. The three inductance models generate 2.65%, 2.46%, and 0.477% voltage ripple at 100% loading for L_{max} , L_{std} , and L_{min} respectively. Similarly, the current ripples at that point is 2.68%, 2.49%, and 0.54% for the same inductance models.

A constant dc output voltage with minimal ripple can be maintained by employing these models. The voltage drop lasts for only around 55 milliseconds and returns to the 600V setpoint value. This is particularly true at low voltage drop values and for very small voltage ripples. The proposed impedance model can be implemented in the 180 kW PWM rectifier circuit, as the inductance value L_{min} yields a superior

response compared to the other two models. Therefore, it is indicated by the test results that the proposed model is appropriate for implementation.

C. Simulation Results Using Market Impedance

For the practical application of the impedance model, we implemented the commercially available impedance values for the 180 kW PWM rectifier. Impedance data is presented in Table III.

 TABLE III
SYSTEM TEST USING MARKET IMPEDANCE

| Impedance | V Rating | I Rating | Tolerance | Value |
|-----------|----------|----------|-----------|----------|
| Inductor | - | 530 A | 20% | 0.231 mH |
| Capacitor | 1.1 kV | - | - | 1.2 mF |

The inductor value available in the market was chosen by considering a 20% tolerance value. The inductor's current rating was selected by considering a safety factor value of 70% of the maximum current of 300 A. For the capacitor, a safety factor is given for a voltage of 70% of the 600 V voltage. The impedance value's test results can be seen in Fig. 10 under the same test conditions applied in the previous model.

The voltage drop value of L_{mkt} is 8.38% at 10% load and 14.37% at full load, as indicated in Fig. 11. At low load, L_{mkt} 's voltage drop is lower than L_{min} 's, but the opposite is true at full load. The voltage drop value is dependent on the load given.

At full load, there is a 0.5% ripple in dc voltage and a 0.56% ripple in dc current, as shown in Fig. 12. The dc voltage ripple

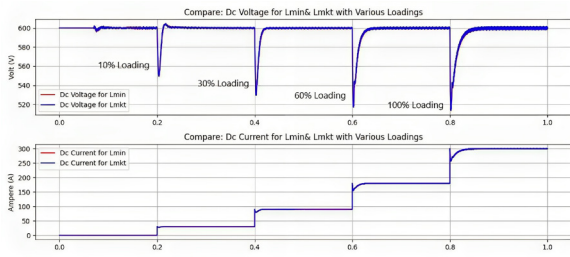


Fig. 10. System test using L_{mkt} vs L_{min} at various loadings.

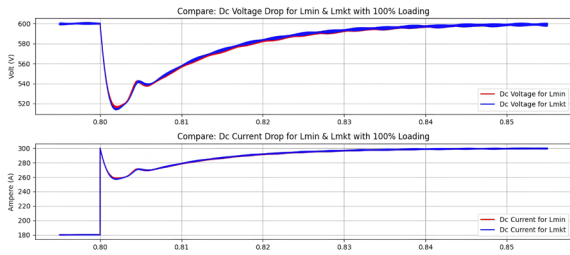


Fig. 11. System test using L_{mkt} vs L_{min} at 100% loading.

for L_{min} is just 0.47%, while the dc current ripple is 0.54%. In comparison, L_{mkt} produces higher current and voltage ripple values.

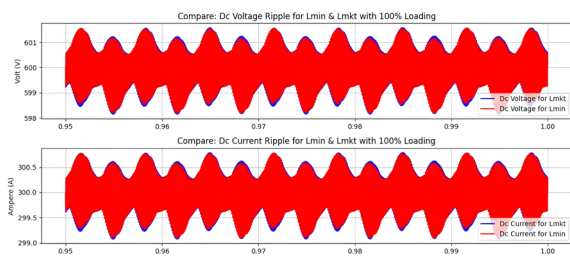


Fig. 12. Dc Voltage Ripple using L_{mkt} vs L_{min} at 100% load.

Based on the market impedance test results, the suggested L_{mkt} for PWM rectifier can be used, resulting in favorable system response. The direct current voltage can be maintained at a stable 600V. The ripple of the direct current voltage and current is negligible, and the voltage drop is lower in comparison to L_{max} and L_{std} .

VI. CONCLUSION

In this paper, the PWM rectifier impedance was modeled and tested using four loading levels: 10%, 30%, 60%, and 100% of load. The inductance was classified into four categories: upper limit L_{max} (1.5 mH), steady-state L_{std} (1.44 mH), commercially available L_{mkt} (0.231 mH), and lower limit inductor L_{min} (0.179 mH). The dc capacitor value was determined through the 40% power change method, thus requiring a 1.23 mF capacitor. The simulation results demonstrate that the current and voltage response varies with the value of each inductor. At 100% loading, the voltage experiences a drop of 20.54%, 20.07%, 14.37%, and 13.96%

at L_{max} , L_{std} , L_{mkt} , and L_{min} , respectively. For L_{max} , the voltage ripple at 100% load was 2.65%, 2.46% for L_{std} , 0.5% for L_{mkt} , and 0.47% for L_{min} . The current ripple was also present at L_{max} load at 2.68%, L_{std} load at 2.49%, L_{mkt} load at 0.56%, and L_{min} load at 0.54%. Based on the resulting pattern, it can be inferred that the inductor value is directly proportional to the current-voltage ripple and the accompanying voltage drop. The system can return to its steady-state value within ± 0.045 seconds with a relatively low ripple and voltage drop. Overall, the proposed impedance model is effective at the 180 kW power level, thereby ensuring the stability of the dc voltage value.

VII. ACKNOWLEDGEMENT

This paper was funded by the Research Directorate of Universitas Gadjah Mada through the Final Project Recognition Program (RTA) in 2023. The investigation also incorporates hybrid train specification data from the cooperation of UGM and PT INKA. The author bears full responsibility for its content.

REFERENCES

- [1] Y. Zhang, J. Jiao, and J. Liu, "Direct power control of pwm rectifiers with online inductance identification under unbalanced and distorted network conditions," *IEEE Transactions on Power Electronics*, vol. 34, no. 12, pp. 12 524–12 537, 2019.
- [2] H. Yang, Y. Zhang, J. Liang, J. Liu, N. Zhang, and P. D. Walker, "Robust deadbeat predictive power control with a discrete-time disturbance observer for pwm rectifiers under unbalanced grid conditions," *IEEE Transactions on Power Electronics*, vol. 34, no. 1, pp. 287–300, 2018.
- [3] W. Stevenson Jr and J. Grainger, *Power system analysis*. McGraw-Hill Education, 1994.
- [4] X. Zhang, X. Ruan, and K. T. Chi, "Impedance-based local stability criterion for dc distributed power systems," *IEEE Transactions on Circuits and Systems I: Regular Papers*, vol. 62, no. 3, pp. 916–925, 2015.
- [5] F. Liu, J. Liu, H. Zhang, D. Xue, and Q. Dou, "Comprehensive study about stability issues of multi-module distributed system," in *2014 International Power Electronics Conference (IPEC-Hiroshima 2014-ECCE ASIA)*. IEEE, 2014, pp. 3604–3610.
- [6] Y. Bie, Y. Li, G. He, and X. Zhang, "Pwm rectifier impedance modelling and analysis," in *IOP Conference Series: Earth and Environmental Science*, vol. 675, no. 1. IOP Publishing, 2021, p. 012064.
- [7] W. Xinbo, B. Baodong, Y. Jianghua, and C. Dezhi, "Parameter analysis and calculation of inductor for pwm rectifier," in *Proceedings 2013 International Conference on Mechatronic Sciences, Electric Engineering and Computer (MEC)*. IEEE, 2013, pp. 3822–3826.
- [8] S. Kakkar, T. Maity, R. K. Ahuja, P. Walde, R. Saket, B. Khan, and S. Padmanaban, "Design and control of grid-connected pwm rectifiers by optimizing fractional order pi controller using water cycle algorithm," *IEEE Access*, vol. 9, pp. 125 941–125 954, 2021.
- [9] W. Qiang, L. Yong-bao, H. Xing, and L. Qian-chao, "Simulation study of three-phase pwm rectifier with square of the voltage double closed loop control," in *IOP Conference Series: Materials Science and Engineering*, vol. 199, no. 1. IOP Publishing, 2017, p. 012148.
- [10] Y. Wang, D. Wang, and Z. Peng, "Model predictive direct power control for pwm rectifiers based on online parameter identification," in *2021 11th International Conference on Intelligent Control and Information Processing (ICICIP)*. IEEE, 2021, pp. 272–277.
- [11] W. Yan, H. Du, and S. Yan, "A current control method with impedance estimator for single-phase pwm rectifier," in *2012 Third International Conference on Intelligent Control and Information Processing*. IEEE, 2012, pp. 450–453.
- [12] J. Xu and Y. Sato, "An investigation of minimum dc-link capacitance in pwm rectifier-inverter systems considering control methods," in *2012 IEEE Energy Conversion Congress and Exposition (ECCE)*. IEEE, 2012, pp. 1071–1077.

Hybrid PV-WT Microgrid Stability Control Using Synchronverter Algorithm

1st Mohd. Brado Frasetyo
Faculty of Engineering
Universitas Gadjah Mada
Yogyakarta, Indonesia
mohd.brado41@mail.ugm.ac.id

2nd Fransisco Danang Wijaya
Faculty of Engineering
Universitas Gadjah Mada
Yogyakarta, Indonesia
danangwijaya@ugm.ac.id

3rd Husni Rois Ali
Faculty of Engineering
Universitas Gadjah Mada
Yogyakarta, Indonesia
husni.rois.ali@ugm.ac.id

Abstract—The use of renewable energy in the microgrid has been increasing in recent years. The renewable integration causes several negative impacts on the stability of power grid such as power fluctuations and frequency instability. To overcome the aforementioned problems, adding additional inertia virtually is one solution to stabilize microgrid, virtual inertia is obtained by utilizing energy storage system (ESS) and power electronics along with reliable control mechanisms. One of the control concepts that can produce the ability to stabilize the microgrid is known as synchronverter. The synchronverter is a model that delivers the conventional synchronous generator model directly into the control algorithm. However, to the best of our knowledge, there are no research that uses synchronverter on microgrid connected to several renewable energy resources. In this research, the microgrid stability control will be carried out on a microgrid using the synchronverter method that consists of several components, namely photovoltaic (PV) and wind turbine (WT), local loads, and ESS. Furthermore, to study the robustness synchronverter algorithm is tested using a scenario namely parallel synchronverter with wind turbine. Therefore, the use of a synchronverter in different microgrid scenarios can clarify that the control algorithm can maintain the system stability. The results of this research indicate that the synchronverter algorithm can work properly in controlling the stability of the hybrid PV-WT microgrid system.

Index Terms—Microgrid, Virtual Synchronous Generator, Synchronverter, Stability, Inverter, Wind Turbine, Photovoltaic

I. INTRODUCTION

Microgrid is a small-scale electric power system consisting of several local loads integrated with an energy storage system (ESS) and several distributed energy sources (DER) [1]. The installation of DER that uses renewable energy in microgrids is growing rapidly. For example, Indonesia targets the installation of renewable energy as much as 23 percents of total generation by 2025, and Japan targets 53 GW of solar energy (PV) to be connected to the electricity grid by 2030 [2] [3].

The increasing of renewable energy installation in microgrid brings several negative impacts on power stability such as power fluctuations due to the renewable energy intermittent characteristics and a decrease in the frequency stability of the grid, especially when the microgrid is in islanded mode [4] [5]. Some of these negative impacts are

caused by renewable energy sources, which have small inertia when compared to conventional energy sources. In contrast, inertia has an essential role in maintaining network stability. One solution that can solve the problem is using synchronverter algorithm.

Synchronverter is a model that derives the conventional synchronous generator model directly into the control algorithm. Thus, the synchronverter model has the exact dynamics as a traditional synchronous generator [6]. The advantage of the synchronverter is that the parameter values used can be adjusted flexibly according to network needs. The parameter values can be changed even though the system is still operating.

Research on voltage and frequency stability on microgrids using synchronverter has been carried out by several previous studies. In [6] [7], synchronverter is used as a power electronics-based generator control (inverter). This study describes the model, dynamics, implementation, and operation of the synchronverter. Furthermore, this research shows that the active power and reactive power in the synchronverter can be automatically injected based on the load requirements using a droop frequency and voltage mechanism. However, this study uses a single generator scenario. So that further research is needed to assess the performance of the synchronverter on a microgrid with several generators, especially plants based on renewable energy sources.

In some research, synchronverters are used in microgrid systems with a single renewable energy source [8] [9] [10] [11] [12] [13] [14]. Microgrid operations have several varied renewable energy sources such as solar power plants, wind power plants, micro hydro, and other renewable energy plants. Thus, the next project should carry out research on the application of synchronverters on microgrids with several renewable energy sources.

In [15] present a sensitivity analysis for fifth order synchronverter model connected to an infinite bus, with respect to voltage and current measurement errors. They have shown that the sensitivity of the grid currents to voltage measurement errors is too large to be acceptable, leading to distorted grid currents (as observed in experiments). However, from the some synchronverter model, the measurement errors are ignored. Therefore, to minimize

some measurement error, this paper adopted their strategy. An additional filter are used to increase the ability of developed synchronverter model.

With regards to the above mentioned problems, this paper analyses microgrid stability control using synchronverter method. The contribution of this paper are the microgrid testing scenario and synchronverter model development. The application of synchronverters on microgrids with several renewable energy sources should be investigated. Therefore, in this paper, the microgrid test system consists of parallel synchronverter which means hybrid PV-WT test system. In addition, we develop an advanced synchronverter model compared with the original synchronverter.

II. SYNCHRONVERTER

In this research, the synchronverter model is used as a reference for the mathematical model that used to control power electronics. This chapter will explain about the two main parts of a synchronverter, namely the electrical and mechanical parts. Furthermore, the synchronous generator model was adapted to the synchronverter model which is assumed to be ideal with some neglected physical parts such as magnetic saturation effect, iron core losses and eddy currents. This synchronous generator model uses reference from [6] and [16].

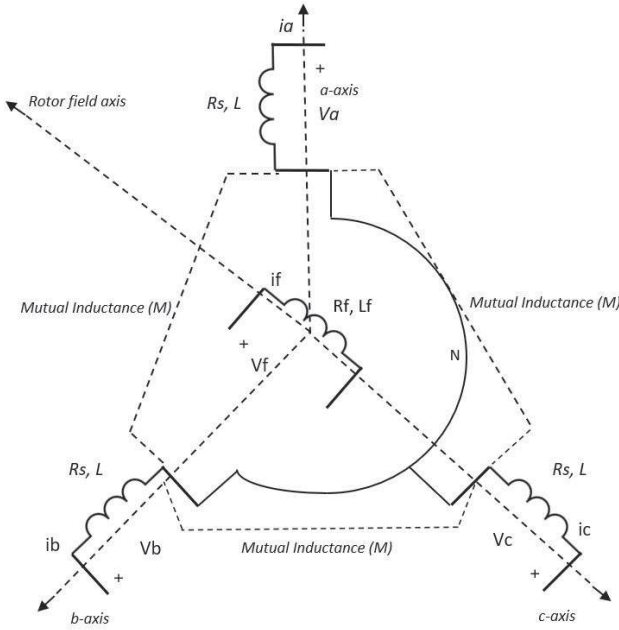


Fig. 1. Ideal three-phase synchronous generator.

A. Electrical Part

The structure of an ideal three-phase generator can be seen in Figure 1. The current in the stator winding is denoted as i_a , i_b and i_c , while the three-phase voltage denoted as v_a , v_b and v_c . The current and voltage in the rotor windings are i_f and v_f , respectively. The stator

winding can be regarded as a coil having an inductance L , mutual inductance $-M$ and resistance R_s . Furthermore, define $L_s = M + L$. Then the winding on the rotor is also considered as a coil that has an inductance L_f and resistance R_f . M_f is the mutual inductance amplitude between the rotor and each stator winding. The rotor angle is denoted as θ .

It is assumed that there is no neutral line, so:

$$i_a + i_b + i_c = 0. \quad (1)$$

The flux in the stator is denoted as Φ_a , Φ_b and Φ_c . Then it is defined into the following vector.

$$i = \begin{bmatrix} i_a \\ i_b \\ i_c \end{bmatrix}, \Phi = \begin{bmatrix} \Phi_a \\ \Phi_b \\ \Phi_c \end{bmatrix}, v = \begin{bmatrix} v_a \\ v_b \\ v_c \end{bmatrix} \quad (2)$$

The flux linkage in the stator is:

$$\Phi = L_s i + M_s i_f \cos \theta \quad (3)$$

The flux linkage in the rotor is:

$$\Phi_f = L_f i_f + M_f \langle i, \cos \theta \rangle \quad (4)$$

The terminal voltage is modeled in vector v as follow:

$$v = e - R_s i - L_s \frac{di}{dt} \quad (5)$$

With $e = [e_a e_b e_c]^T$ is the EMF caused by the movement of the rotor which has the following formula:

$$e = M_f i_f \omega \sin \theta - M_f \frac{di_f}{dt} \cos \theta \quad (6)$$

While $\omega = \dot{\theta}$ is the angular speed of the rotor. e is also called synchronous internal voltage. Furthermore, the field terminal voltage is:

$$V_f = -R_f i_f - \frac{d\Phi_f}{dt} \quad (7)$$

B. Mechanical Part

The machine's magnetic field energy is:

$$E_{mag} = \frac{1}{2} \langle i, L_s i \rangle + M_f i_f \langle i, \cos \theta \rangle + \frac{1}{2} L_f i_f^2 \quad (8)$$

Electromagnetic torque can be calculated by the equation below; the equation uses the relationship of $\theta = p\theta_m$, θ_m is the mechanical rotor angle and $p = 1$.

$$T_e = \sqrt{\frac{3}{2}} M_f i_f i_q = -m i_f i_q \quad (9)$$

The mechanical torque is produced by prime mover. In this model, the prime mover's dynamics are neglected, and it is assumed that the mechanical torque T_m (plus active power droop) acts on the rotor. If it is assumed that there is no cogging torque, that is, the torque caused by the interaction of the permanent magnet or electromagnet of the rotor and stator, then the mechanical model of the machine is:

$$J\dot{\omega} = T_m - T_e - D_p \omega \quad (10)$$

J , D_p , and ω are moment of inertia of all rotating parts, damping factor, and the rotational frequency, respectively. While $\dot{\omega}$ is the first derivative of the rotor angle. The term $-D_p\omega$ is generated by friction, which is mainly generated by the droop control of the prime mover, then adjusted according to ω .

It should be noted that if no significant friction occurs, then the rotor's virtual torque is $T_m - D_p\omega$. So, the equation depends on ω which is feedback or called frequency droop. As explained in the previous chapter, torque T_m considered constant or a value that changes depending on user requirements. The synchronverter frequency will follow the network frequency, the synchronverter will change the power output if the frequency is more than or less than the nominal frequency. If the synchronverter frequency exceeds the frequency set-point, then the power output will be reduced. Otherwise, if the synchronverter frequency is less, then the power output will be increased. Furthermore, the droop coefficient value D_p is the coefficient value commonly used in conventional synchronous generators. For example, the European generators standard uses 3 percents change in frequency causes the 100 percent nominal power.

Another critical parameter is inertia J . J must have the same value as the original synchronous generator. For synchronverter, the value of J is better to have a small value because the inertia will affect the system's speed in responding to changes. Furthermore, if H is the synchronous generator time constant, it is denoted as $H = \frac{1}{2}J\omega^2/P_n$. Noted that: $2s \leq H \leq 12s$. The time constant causes the value of $J \geq 4P_n/\omega_n^2$ and $D_p = P_n/(\text{drooprate} * \omega_n^2)$, where the droop rate is a proportion ω_n that results in T_m as much as 100 percents (Commonly around 0.03).

III. SYNCHRONVERTER

Synchronverter is power electronics system that has a unique control algorithm. The model used is the same as the synchronous machine, as shown in Figure 1. The synchronverter model will use equations 5, 6, 7, 9 and 10 from the previous chapter. Next, the formula will add the assumption of constant rotor current to simplify the calculation. The assumption is not a good approach but is needed to streamline controller design. If the synchronverter is considered a small capacity inverter in a large system, the main network will be considered an infinite bus. The synchronverter equation is as follows:

$$v = -R_s i - L_s \frac{di}{dt} + e \quad (11)$$

$$e = \omega M_f i_f \sin\theta \quad (12)$$

$$T_e = M_f i_f (i, \sin\theta) \quad (13)$$

$$J\dot{\omega} = T_m - T_e - D_p\omega, \text{ with } \dot{\omega} = \dot{\theta} \quad (14)$$

Active and reactive power are defined by $P = \langle i, e \rangle$ and $Q = \langle i, e_{quad} \rangle$, with $e_{quad} = -\omega M_f i_f \cos\theta$. Active

and reactive power can be calculated using the following equation:

$$P = \omega M_f i_f \langle i, \sin\theta \rangle \quad (15)$$

$$Q = -\omega M_f i_f \langle i, \cos\theta \rangle \quad (16)$$

These equation can be implemented into the synchronverter block diagram in figure 2

IV. SIMULATION SCENARIO

This research uses simulink to simulate microgrid with synchronverter control. The microgrid consists of two renewable energy sources: photovoltaic (PV) and wind turbine (WT). With PV connected to a battery to store the power that has been generated.

Synchronverter algorithm is used to control the PV inverter output. In the simulation, PV is considered a unit with the battery and is a constant DC source. Furthermore, WT will be given a different wind speed input value to test the synchronverter control performance against changes in power. The diagram for a microgrid system with synchronverter control can be seen in Figure 3. In addition, the parameter values for the microgrid system can be seen in Table I.

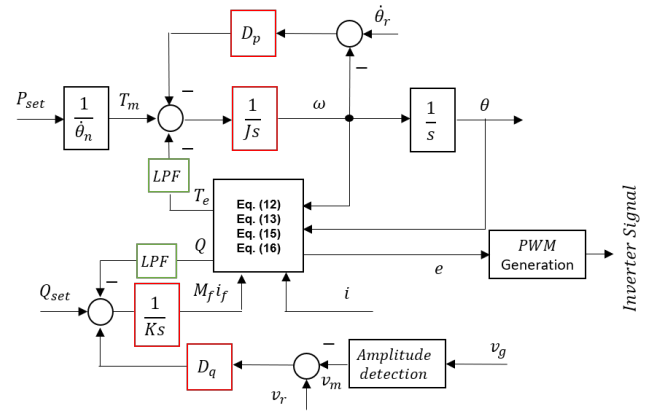


Fig. 2. Synchronverter block diagram

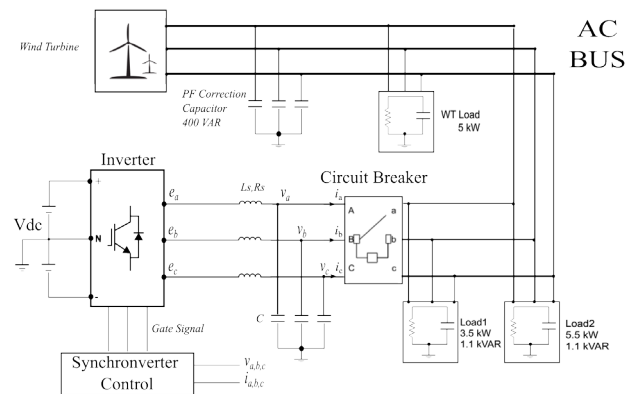


Fig. 3. PV-WT diagram

TABLE I
MICROGRID PARAMETER VALUE.

| Parameters | Value |
|-----------------------------|--------------------|
| J | 0.2 km^2 |
| D_p | 1.7 |
| D_q | 120 |
| R_s | 0.152Ω |
| L_s | 15 mH |
| C | $10 \mu\text{F}$ |
| L_g | 15 mH |
| Sample Time | $0.1 \mu\text{s}$ |
| v_n | 220 V |
| M_{ff} initial condition | 0 |
| Inverter Power | 20 kW |
| Inverter Current | 0 – 80 A |
| P_n | 3.5 kW |
| Q_n | 0 VAR |
| Wind Turbine Power Capacity | 5.2 kVA |
| Load 1 | 3.5 kW, 1.1 kVAR |
| Load 2 | 5.5 kW, 1.1 kVAR |
| Wind Turbine Load | 5 kW |
| Capacitor Bank | 400 VAR |
| V_{dc} | 700 V |

In analyzing whether the synchronverter algorithm can maintain the frequency and voltage values at their nominal values, this research has simulation scenario namely simulation of a synchronverter connected in parallel with a wind turbine.

Several measurable variables will be seen from these scenarios, namely voltage, frequency, inverter power, WT power and load. Furthermore, to test the the control algorithm's ability to deal with changes, a simulation will be carried out with the following changes in conditions.

- Condition 1: Change in load (Up/Down).
- Condition 2: Microgrid connected to utility grid.
- Condition 3: Changes in WT wind speed.

Furthermore, by changing the conditions above, it can be analyzed whether the synchronverter algorithm can maintain the frequency and voltage values at their nominal values.

V. RESULT AND DISCUSSION

The scenario of the synchronverter control algorithm testing is the synchronverter test connected in parallel with the wind turbine. This test is done by checking the inverter's response to load, and wind turbines speed changes.

In this experiment, the simulation was carried out for 10 seconds with the following test scheme:

- At 0 seconds, the wind turbine is connected to the inverter.
- At 0 to 2nd second, load 1 (3.5 kW and 1.1 kVAR) and the internal wind turbine load (5 kW) are connected.
- At 2nd to 4th second, load 2 (5.5 kW and 1.1 kVAR) is connected to the system and then disconnected.
- At 5th to 6th second, the wind speed increased from 9 m/s to 11 m/s.
- At 6th to 7th second, the wind speed drops from 11 m/s to 8 m/s.

- At 7th to 10th second, wind speed is constant at 8 m/s, then load 1 and internal load WT are connected.

This simulation aims to test whether the inverter can maintain the frequency and voltage values of the system when the microgrid is connected to the wind turbine. In this experiment, two parameters will be changed, namely the increase/decrease in load and changes in wind speed. Furthermore, the frequency and voltage values of the system can be seen in Figure 4 and 5, while the values for the active power and reactive power of the synchronverter and wind turbine can be seen in Figures 6, 7, 8 and 9, respectively.

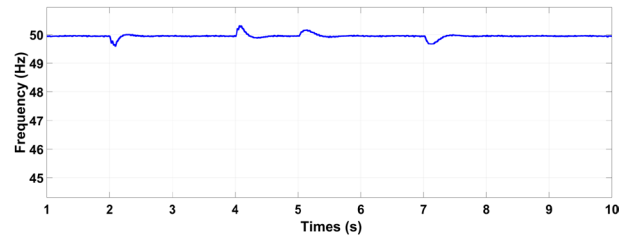


Fig. 4. Microgrid Frequency

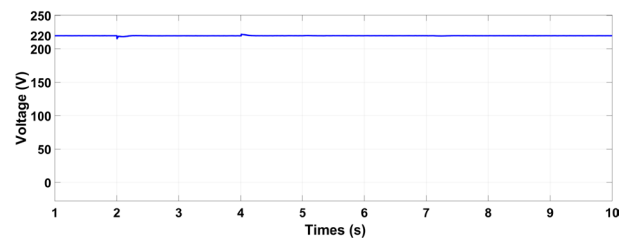


Fig. 5. Microgrid Voltage

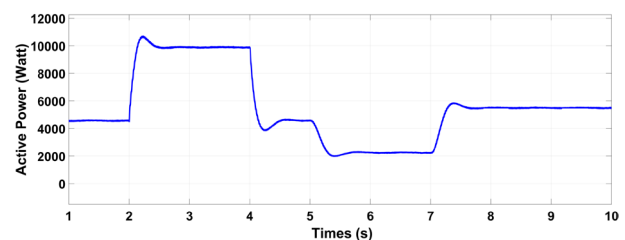


Fig. 6. Synchronverter Active Power

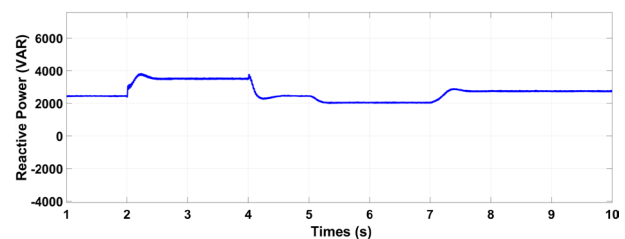


Fig. 7. Synchronverter Reactive Power

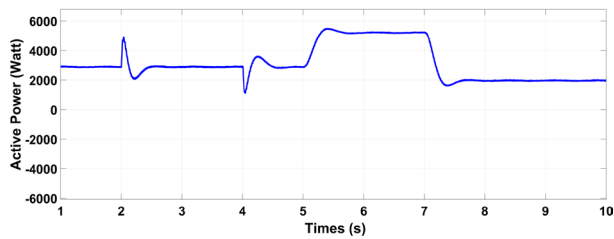


Fig. 8. Wind Turbine Active Power

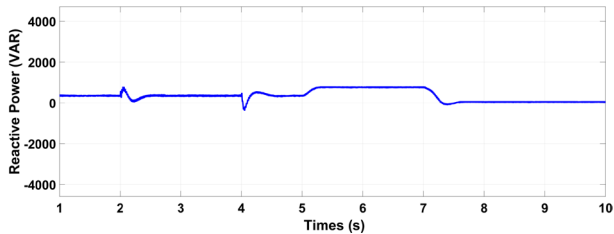


Fig. 9. Wind Turbine Reactive Power

From the experimental results, the microgrid's frequency and voltage are always at their nominal values. Furthermore, the synchronverter algorithm is very effective in maintaining stability. The inverter can inject power according to the system's load demand. For example, when the wind speed increases, the inverter reduces the power supplied. On the other hand, when the wind speed decreases, the inverter increases the power. With this condition, the system will always be stable at its nominal value. Another example is when load change occurs. Since the power from the wind turbine depends on the wind speed, the inverter must help supply the power required by the load. So that the stability of the microgrid system that uses a synchronverter can be said to be good.

VI. CONCLUSION

Synchronverter is a special control algorithm that mimics the operation of a synchronous generator. In this study, the synchronverter algorithm is used as a power electronics controller that maintains frequency and voltage stability on the microgrid under different conditions such as changes in load and wind turbines generator power output changes. The results of these scenarios are that the synchronverter can inject power according to the system's load demand. In the wind turbine generator power output changes test, inverter reduces the power supplied when the wind speed increases. On the other hand, when the wind speed decreases, the inverter increases the power. Furthermore, since the power from the wind turbine depends on the wind speed, the inverter must help supply the power required by the load. Based on the result above, the robustness of synchronverter algorithm in maintain the microgrid stability are achieved.

ACKNOWLEDGMENT

The authors would like to thank to Lembaga Pengelola Dana Pendidikan (LPDP) Indonesia for supporting this project

REFERENCES

- [1] Fang, Zongjie, Mingche Li, Rui Zhang, and Lihui Qiao., "Review of Research-Based on Control and Stability Analysis of DC Microgrids," 3rd International Conference on Advanced Electrical and Energy Systems (AEES), pp. 139-144, 2022.
- [2] PT. Perusahaan Listrik Negara, "Rencana usaha penyediaan tenaga listrik.: Rencana Usaha Penyediaan Tenaga Listrik," 2019.
- [3] Badreddien, Mahmoud M., and Brian K. Johnson. "Virtual Synchronous Generator Controller for Solar Photovoltaic System.," IEEE Electrical Power and Energy Conference (EPEC), pp. 480-485, 2021.
- [4] Bevrani H, Raisch J., "On virtual inertia application in power grid frequency control," Energy Procedia, 2017.
- [5] Frassetto Mohammad Brado, and Jaesung Jung, "Comparison of Distributed Generation Control Strategy to Realize a Microgrid." Korean Institute of Electrical Engineering, 2019.
- [6] Vasudevan, Krishnakumar R., Vigna K. Ramachandaramurthy, Thanikanti Sudhakar Babu, and Aref Pouryekt, "Synchronverter: A comprehensive review of modifications, stability assessment, applications and future perspectives," IEEE Access, 2020.
- [7] Shekhar, KS Raja, and M. A. Chaudhari., "Operation and control of Synchronverter technique in grid connected and intentional islanding modes for AC micro grids." In 2020 First International Conference on Power, Control and Computing Technologies (ICPC2T), pp. 426-431. IEEE, 2020.
- [8] Vasudevan KR, Ramachandaramurthy VK, Babu TS, Pouryekt A., "Synchronverter: A comprehensive review of modifications, stability assessment, applications and future perspectives," IEEE Access, 2020.
- [9] Rosso R, Engelken S, Liserre M., "Robust stability analysis of synchronverters operating in parallel," IEEE Transactions on Power Electronics, 2019.
- [10] Nair NR, Kanakasabapathy P., "A three phase grid connected SPV system using synchronverter," 8th IEEE India International Conference on Power Electronics (IICPE), pp.1-6, 2018.
- [11] Sonawane AJ, Umarikar AC., "Three-phase single-stage photovoltaic system with synchronverter control: Power system simulation studies," IEEE Access, 2022.
- [12] Hansen, J.B., Østerfelt, S.T. and Randewijk, P.J., "The use of synchronverters for fast frequency response and automatic voltage regulation in low inertia islanded power networks," 56th International Universities Power Engineering Conference (UPEC), pp. 1-6, 2021.
- [13] Pawar, Rahul Rajendra, and Trapti Jain, "Controller Hardware-In-Loop Validation of Synchronverter in Islanded Microgrid." 22nd National Power Systems Conference (NPSC), pp. 260-265. IEEE, 2022.
- [14] Hirase Y, Abe K, Sugimoto K, Sakimoto K, Bevrani H, Ise T., "A novel control approach for virtual synchronous generators to suppress frequency and voltage fluctuations in microgrids," Applied Energy, 2018.
- [15] Kustanovich Z, Reissner F, Shivratri S, Weiss G., "The sensitivity of grid-connected synchronverters with respect to measurement errors," IEEE Access, 2021.
- [16] J. J. Grainger and W.D. Stevenson, Power System Analysis. McGraw-Hill, New York, 1994.

Adaptive model predictive control of current interharmonics in PV system

Fuping Ma
School of Electrical Engineering
Chongqing University
Chongqing, China
fupingma@stu.cqu.edu.cn

Mingxuan Mao
School of Electrical Engineering
Chongqing University
Chongqing, China
mingxuanmao@gmail.com

Liuqing Zhao
School of Electrical Engineering
Chongqing University
Chongqing, China
zqliuqing@stu.cqu.edu.cn

Abstract—This paper proposes a novel adaptive model predictive control (MPC) for current interharmonics in photovoltaic (PV) system. In this method, a two-step prediction model for the output current and interharmonic currents of PV system is firstly derived. Then, MPC is used to realize the inverter control and interharmonic suppression at the same time. In addition, enhanced suppression of interharmonics at specific frequencies is realized by introducing a key parameter adaptive adjustment mechanism. Simulation results show that the proposed interharmonic suppression strategy can effectively reduce the interharmonic amplitude with a suppression ratio of up to 75%. And adaptive parameter adjustment can significantly improve the suppression effect of specific interharmonics by more than 26%.

Keywords—PV system, Adaptive model predictive control, Interharmonic suppression, Adaptive parameter adjustment

I. INTRODUCTION

The volatility of PV output and the implementation of the maximum power point tracking (MPPT) algorithm significantly degraded the power quality of the power system as it introduced complex harmonic and interharmonic difficulties to the power grid [1]. The component whose frequency is non-integral multiple of the fundamental frequency is referred to as interharmonic.

Interharmonics are more dispersed and difficult to evaluate than harmonics, which not only lower power factor and the quality of grid-connected power but also create a host of additional issues. For instance, waveform distortion caused by interharmonics will hinder the effective operation of relay protection devices and may even result in malfunctions [2]. The flicker phenomenon, which is the visual response of the human eye to incandescent lamps, can also be caused by low-frequency interharmonics with larger amplitude [3]. When the interharmonic frequency is in the sub-synchronous region, it will interact with the mechanical oscillation of the adjacent generator shaft system and cause sub-synchronous oscillation of the system, which will have a significant negative effect on the stable functioning of the power system [4].

The interharmonic generation mechanism and mathematical modeling of photovoltaic grid-connected system had both been explored by several academics. Experimental data in [5] demonstrated that the MPPT algorithm was the primary contributor to the interharmonic current of grid-connected PV system. Sangwongwanich et al. [6] explained the precise process of interharmonics creation in PV grid-connected system due to MPPT perturbations.

The suppression of interharmonics can probably be achieved by optimizing the MPPT algorithm, optimizing the grid-connection control algorithm and optimizing the

topology. Based on the optimization of the MPPT method, Hou et al. [7] suggested a zero-disturbance MPPT algorithm. The DC voltage perturbation at steady state is eliminated, thus suppressing the interharmonics, but it also leads to a decrease in the sensitivity of the MPPT algorithm. In addition, randomizing the perturbation frequency of the MPPT algorithm [8] can also reduce the overall level of the interharmonic current amplitude, but more frequencies of interharmonic components result from it. By improving the grid-connected control technique, a nonlinear current control strategy was suggested in [9]. The injection of a continuous term produced by the reliable, exact high-order sliding-mode differentiator precisely compensated for the disturbance.

The interharmonics suppression objective can also be achieved via the optimization topology. The interharmonic filter [10] and the phase-shifting MPPT method based on cascaded inverters [11] were sequentially proposed by Sangwongwanich et al. The former introduced an additional set of switching tubes as the interharmonic filter to suppress interharmonics. The latter suppresses interharmonics by removing DC voltage disturbances through phase shift control of the cascaded inverter.

However, optimizing the MPPT algorithm sacrifices the MPPT tracking effectiveness and optimizing the topology increases the system cost, both of which can burden the system. Optimized grid-connected control strategies do not have these problems, except that the implementation of existing control techniques is difficult. To address these issues, this paper proposes an interharmonic suppression strategy that is less difficult to implement based on model predictive control.

This paper focuses on the implementation of interharmonic current suppression strategies in PV system. The second part analyzes the interharmonic current characteristics of PV system based on MPPT perturbation. In the third part, the proposed adaptive model predictive control method with interharmonic suppression (ISMPC) is established, and the parameter adaptive adjustment is used to regulate the suppression capability. Finally, the fourth part verifies the effectiveness of the proposed strategy through simulations.

II. INTERHARMONIC CHARACTERIZATION OF PV SYSTEM BASED ON MPPT PERTURBATION

The topological structure of the PV system is depicted in Fig. 1. The MPPT algorithm is used to track the maximum power point in order to maximize the output power of the PV arrays. The perturbed MPPT algorithm, which is widely used in industry, presents a three-point oscillation in its DC voltage at steady state as shown in Fig. 2.

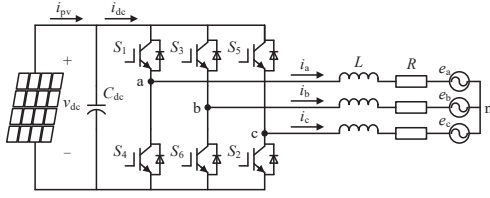


Fig. 1. Topology diagram of PV system (v_{dc} -- DC voltage; i_{pv} -- output current of PV array; i_{dc} -- DC current; i_a, i_b, i_c -- grid-connected currents; e_a, e_b, e_c -- power grid voltage; S_1 - S_6 -- switching tubes; C_{dc} -- DC capacitance; L -- filter inductance; R -- parasitic resistance).

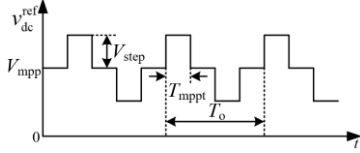


Fig. 2. Diagram of the DC-link voltage command three-point oscillation output by perturbation MPPT algorithm.

The DC voltage command v_{dc}^{ref} generates a jump of magnitude V_{step} at each perturbation cycle T_{mpppt} , which rapidly generates a voltage error in the control link. This error in the action of the controller causes the output current of the inverter to carry interharmonic components [12]. The three-point oscillating DC voltage command with frequency $\omega_o = 2\pi/T_o$ can be realized by Fourier expansion:

$$\begin{aligned} v_{dc}^{ref} &= V_{mpp} + \sum_{n=1,3,5,\dots} v_n \cos(n\omega_o t + \theta_n) \\ &= V_{mpp} + \frac{2V_{step}}{\pi} \sum_{n=1,3,5,\dots} \frac{1}{n} \left[\cos\left(\frac{n\pi}{4}\right) - \cos\left(\frac{3n\pi}{4}\right) \right] \cos(n\omega_o t + \theta_n) \end{aligned} \quad (1)$$

Where: v_n and θ_n are the amplitude and phase angle.

According to the frequency response characteristics of the linear system, the component of d-axis in inverter current will contain the AC component of the corresponding frequency under the action of the AC component in the DC voltage command, which are:

$$i_d(t) = i_{d0} + \sum_{n=1,3,5,\dots} i_{dn} \cos(n\omega_o t + \theta_{dn}) \quad (2)$$

Where: i_{d0} is the DC component of the d-axis component in output current; i_{dn} , θ_{dn} are respectively the amplitude and phase angle of each AC component frequency.

The q-axis component of the output current can be approximated as 0 when the power factor is 1. The three-phase output current of the inverter is:

$$\begin{aligned} i_{a/b/c} &= i_{d0} \cos(\omega_g t + \theta_g + m \frac{2\pi}{3}) + \\ &\frac{1}{2} \sum_{n=1,3,5,\dots} i_{dn} \cos[(\omega_g + n\omega_o)t + \theta_{dn} + \theta_g + m \frac{2\pi}{3}] + \quad (m=0,-1,1) \\ &\frac{1}{2} \sum_{n=1,3,5,\dots} i_{dn} \cos[(\omega_g - n\omega_o)t - \theta_{dn} + \theta_g + m \frac{2\pi}{3}] \end{aligned} \quad (3)$$

The output current of the PV system will contain interharmonics at angular frequencies $\omega_g - n\omega_o$ and $\omega_g + n\omega_o$ ($n=1, 3, 5, \dots$) when the DC voltage command exhibits three-point oscillation feature with angular frequency ω_o , as can be seen from equations (1)–(3).

III. PREDICTIVE CONTROL OF CURRENT INTERHARMONICS IN PV SYSTEMS

A. Model predictive control method with interharmonic suppression function

To achieve the two objectives of inverter control and

interharmonic suppression simultaneously, this work uses model predictive control [13], which has good multi-objective processing capability and is simple to implement. It can use a nonlinear model of the system as a predictive model to predict the behavior of the system over time and calculate the optimal control input sequence in combination with optimization algorithms and real-time measurement data.

The current discrete prediction model [14] for the topology used in this paper in the $\alpha\beta$ two-phase stationary coordinate system is given by:

$$\begin{cases} i_{\alpha}^*(k+1) = \left(1 - \frac{RT_s}{L}\right) i_{\alpha}(k) + \frac{T_s}{L} [v_{\alpha}(k) - e_{\alpha}(k)] \\ i_{\beta}^*(k+1) = \left(1 - \frac{RT_s}{L}\right) i_{\beta}(k) + \frac{T_s}{L} [v_{\beta}(k) - e_{\beta}(k)] \end{cases} \quad (4)$$

Where: $i_{\alpha}^*(k+1)$ and $i_{\beta}^*(k+1)$ are anticipated values of the output current for the α -axis and β -axis, respectively; $i_{\alpha}(k)$ and $i_{\beta}(k)$ are actual values of the output current, respectively. The α -axis and β -axis components of the grid voltage, respectively, are represented by $e_{\alpha}(k)$ and $e_{\beta}(k)$. The α -axis and β -axis components of the output voltage vector are $v_{\alpha}(k)$ and $v_{\beta}(k)$, respectively.

Actual digital control requires a certain amount of time for sampling and computation. The optimal switching state selected based on the system information at moment k cannot be executed immediately during this control cycle, which will lead to a delay in the MPC and make the control fail. Therefore, a second step of model prediction is necessary:

$$\begin{cases} i_{\alpha}^*(k+2) = \left(1 - \frac{RT_s}{L}\right) i_{\alpha}^*(k+1) + \frac{T_s}{L} [v_{\alpha}(k+1) - e_{\alpha}(k+1)] \\ i_{\beta}^*(k+2) = \left(1 - \frac{RT_s}{L}\right) i_{\beta}^*(k+1) + \frac{T_s}{L} [v_{\beta}(k+1) - e_{\beta}(k+1)] \end{cases} \quad (5)$$

The first step is predicted based on the information of system at time k , and the expected value of the output current at time $k+1$ is determined. The second stage of prediction is then performed to determine the predicted value of the current at $k+2$ time with the help of the predicted value at $k+1$ time. The current cost function is used to realize the grid-connected control in the following form:

$$g_c = |i_{\alpha}^{ref} - i_{\alpha}^*(k+2)| + |i_{\beta}^{ref} - i_{\beta}^*(k+2)| \quad (6)$$

Where: the current instruction from the voltage ring has two components, i_{α}^{ref} and i_{β}^{ref} , which are components of α -axis and β -axis, respectively.

Taking the frequency resolution and period as f_i and T_r , respectively, and the sampling period as T_s . The amplitude of the sinusoidal component about the interharmonic current in α -axis at time k and frequency f_i can be calculated through discrete integration:

$$I_{afis} = 2f_i T_s \sum_{l=kT_s-T_r}^{kT_s} i_{\alpha}(l) \sin 2\pi f_i l \quad (7)$$

The predicted value of amplitude at $k+2$ time can be obtained as follows after eliminating the first two terms in the discrete integral and adding the prediction terms of $k+1$ time and $k+2$ time obtained by the prediction model:

$$\begin{aligned} I_{afis}^*(k+2) &= 2f_i T_s \left[\sum_{l=(k+2)T_s-T_r}^{kT_s} i_{\alpha}(l) \sin 2\pi f_i l + \right. \\ &\left. i_{\alpha}^*(k+1) \sin 2\pi f_i (k+1) T_s + i_{\alpha}^*(k+2) \sin 2\pi f_i (k+2) T_s \right] \end{aligned} \quad (8)$$

Similar prediction models may be obtained for the sine components $I_{\beta f_{is}}^*(k+2)$ and the cosine components $I_{\beta f_{ic}}^*(k+2)$ of the interharmonic current at β -axis, and cosine component $I_{\alpha f_{ic}}^*(k+2)$ of the interharmonic current at α -axis. The prediction model of interharmonic current for time $k+2$ in the $\alpha\beta$ coordinate system is then as follows:

$$\begin{aligned} i_{\alpha f_i}^*(k+2) &= I_{\alpha f_{is}}^*(k+2) \sin[2\pi f_i(k+2)T_s] + I_{\alpha f_{ic}}^*(k+2) \cos[2\pi f_i(k+2)T_s] \quad (9) \\ i_{\beta f_i}^*(k+2) &= I_{\beta f_{is}}^*(k+2) \sin[2\pi f_i(k+2)T_s] + I_{\beta f_{ic}}^*(k+2) \cos[2\pi f_i(k+2)T_s] \end{aligned}$$

The interharmonic cost function is constructed in the form of a weighted sum of the absolute values of the interharmonic currents at each frequency:

$$g_{\text{inter}} = \sum_{f_i} \lambda_{f_i} \left[|i_{\alpha f_i}^*(k+2)| + |i_{\beta f_i}^*(k+2)| \right] \quad (10)$$

Where: λ_{f_i} is the secondary interharmonic coefficients, which corresponds to the interharmonic current with frequency f_i .

The following accuracy of the output current and the impact of interharmonic suppression can be traded off by varying the weighting factor λ_{inter} . The whole cost function is:

$$g_1 = g_c + \lambda_{\text{inter}} g_{\text{inter}} \quad (11)$$

B. Adaptive parameter adjustment mechanism

The secondary interharmonic coefficients λ_{f_i} must be set suitably to allocate the suppression capability more to the interharmonic components with larger amplitude in order to make the most effective use of the interharmonic suppression capability. However, obtaining the ideal weighting coefficients necessitates carrying out numerous tests, which is a difficult procedure. In order to give system the ability to automatically change and attain the ideal parameter settings, the adaptive parameter adjustment method is introduced in this section.

If the amplitude of a certain interharmonic frequency is I_{f_i} , it is obvious that the larger its corresponding secondary interharmonic coefficients λ_{f_i} is within a certain range, the stronger the suppression effect it obtains, which in turn reduces its amplitude I_{f_i} . The gradient descent method can be used to arrive at the following result, assuming that the gradient value of the change of both variables is p :

$$\frac{d\lambda_{f_i}}{d\lambda_{f_i}} = -p \quad (p > 0) \quad (12)$$

The gradient p is substituted by the nominal value P since the functional link between the amplitude of the interharmonics and the weighting coefficients is unclear. The discretization of the above equation can be processed to obtain the weighting coefficient adjustment step as follows:

$$\Delta\lambda_{f_i} = -\frac{1}{P} \Delta I_{f_i} \quad (P > 0) \quad (13)$$

The error between the fixed P-value and the actual gradient may cause the system to oscillate around the optimal parameters and fail to converge. Therefore, it is also required to include a convergence factor in the adjustment step in order to guarantee the convergence of parameters. The convergence factor is high at the beginning stage, ensuring that the optimal value is soon approached with a sizable adjustment step. The convergence factor swiftly converges to 0 over time, and the step size of the parameter change is similarly reduced, which means the weighting coefficients tend to stabilize. The final adjustment step size is as follows:

$$\Delta\lambda_{f_i} = -\frac{1}{P} \Delta I_{f_i} e^{-qt} \quad (P > 0, q > 0) \quad (14)$$

Where q is the convergence constant.

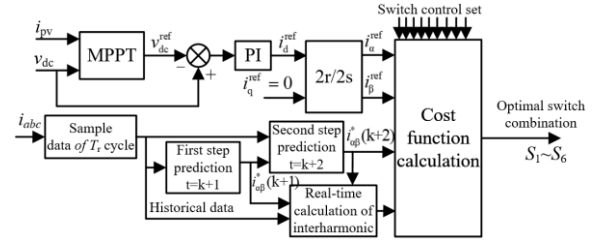


Fig. 3. Block diagram of ISMPC control.

The block diagram of ISMPC control is illustrated in Fig. 3, and its flowchart is given in Fig. 4. By sampling the DC voltage v_{dc} and output current i_{pv} of PV arrays, MPPT algorithm outputs the DC voltage command v_{dc}^{ref} . The voltage loop outputs the d-axis current command i_d^{ref} and enables the DC voltage to follow the instructions through the PI controller. Current instructions of $\alpha\beta$ -axis i_{α}^{ref} and i_{β}^{ref} are obtained after the coordinate transformation. On the other hand, the actual output currents i_{α} and i_{β} of the $\alpha\beta$ -axis are obtained from the output currents i_{abc} of the inverter by coordinate transformation. The optimal switching state is then found by calculating the value of the cost function and is applied to the switching tube at the next moment through the drive circuit to complete the control of the inverter and the suppression of interharmonics.

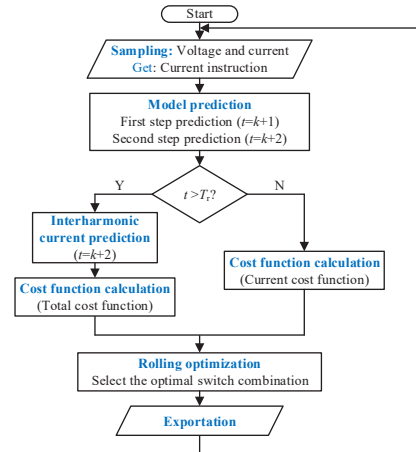


Fig. 4. The Flowchart of ISMPC control.

IV. SIMULATION RESULTS AND ANALYSIS

In order to validate the effectiveness of the proposed ISMPC control approach, a PV system with the function of interharmonic suppression is simulated. Settings of MPPT are configured as follows: disturbance period $T_{\text{mppi}} = 0.05\text{s}$, disturbance step size $V_{\text{step}} = 5\text{V}$.

Fig. 5 illustrates the simulated waveform employing classic model predictive control (MPC). The fundamental amplitude of inverter output current is 13.91 A and the THD is 3.31%. The A-phase current spectrum shows that the interharmonics with large amplitude are distributed at $5m$ Hz ($m = 1, 3, 5, \dots, 19$), which will be the next target for suppression. λ_{inter} is set to 1000, and the secondary interharmonic coefficients are all 1. Simulation waveform of the suggested ISMPC control with interharmonic suppression function is illustrated in Fig. 6. The fundamental amplitude of

inverter output current is 13.95 A and the THD is 3.19%. From the spectrum of current, it can be seen that the amplitude of interharmonic current at each frequency decreases to some extent compared to that with MPC control.

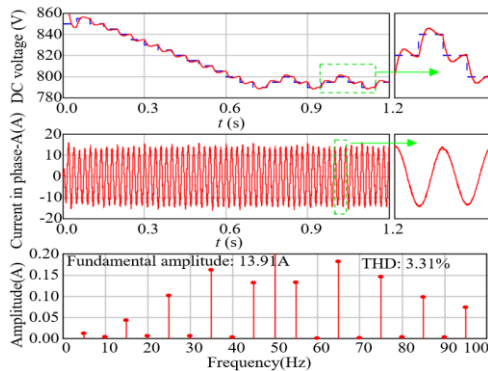


Fig. 5. Simulation waveform of PV system with MPC control.

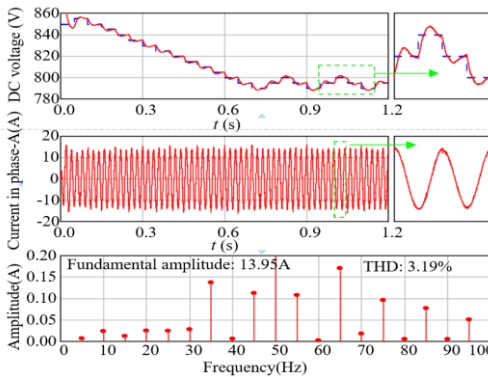


Fig. 6. Simulation waveform of PV system with ISMPC control.

TABLE I. INTERHARMONIC CURRENT AMPLITUDE USING MPC CONTROL AND ISMPC CONTROL

| Frequency (Hz) | Amplitude(A) MPC | Amplitude(A) ISMPC | Suppression ratio (%) | Frequency (Hz) | Amplitude(A) MPC | Amplitude(A) ISMPC | Suppression ratio (%) |
|----------------|------------------|--------------------|-----------------------|----------------|------------------|--------------------|-----------------------|
| 5 | 0.012 | 0.007 | 40.865 | 55 | 0.133 | 0.108 | 18.825 |
| 15 | 0.043 | 0.013 | 70.582 | 65 | 0.186 | 0.171 | 7.937 |
| 25 | 0.102 | 0.025 | 75.504 | 75 | 0.146 | 0.096 | 34.200 |
| 35 | 0.170 | 0.147 | 13.529 | 85 | 0.098 | 0.077 | 21.163 |
| 45 | 0.132 | 0.113 | 14.514 | 95 | 0.074 | 0.051 | 30.755 |

Table. 1 lists the interharmonic amplitudes before and after suppression. When ISMPC control is applied, the amplitude of the interharmonic current at each frequency is suppressed to a considerable level compared with MPC control. Among them, the best suppression effect is 25 Hz interharmonic whose suppression ratio reaches 75.504%, and its amplitude decreases from the original 0.102 A to 0.025 A. Those also have a good suppression impact at 5 Hz, 15 Hz, 75 Hz, and 95 Hz, and the suppression ratio all exceed 30%. However, the suppression effect of the interharmonic current at 65 Hz is weak, and the suppression ratio is only 7.937%. In addition, some of the interharmonic currents are suppressed and still have large values such as 35 Hz and 65 Hz.

In order to strengthen the suppression effect of specific interharmonics, the secondary interharmonic coefficients at 35 Hz and 65 Hz are adjusted using the parameter adaptive adjustment. The real-time calculation of interharmonic amplitude and the parameter adjustment process are shown in Fig. 7 and Fig. 8, respectively. Conventional MPC control is used between 0-1s with no suppression effect. The

interharmonics at 35Hz and 65Hz are reduced by using an initialization factor of 1 during 1-2s, but the suppression effect is not significant. The adaptive adjustment of the parameters starts at 2s and ends at about 3.1s. The stabilized interharmonic rejection ratios at 35 Hz and 65 Hz are increased to 31.213 % and 34.367 %, respectively, which is an increase of up to 26 %.

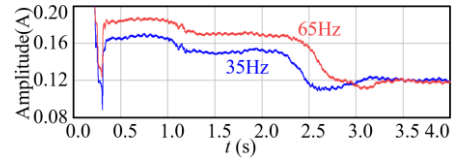


Fig. 7. The real-time calculation of interharmonic amplitude.

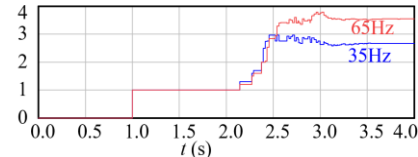


Fig. 8. The process of adaptive adjustment of parameters.

Fig. 9 demonstrates the comparison of the suppression effect with ISRS strategy (Interharmonic Suppression based on Random Sampling-rate MPPT) and ISMPC strategy for the same operating conditions. At certain frequencies, the ISRS control provides better rejection such as 25Hz, 35Hz, 75Hz and 85Hz. However, it also introduces interharmonics at frequencies of multiples of 10, which are almost nonexistent before, and the total interharmonic content is rather than increased. In contrast, the proposed ISMPC control strategy does not introduce new interharmonic frequencies and demonstrates reliable suppression of existing interharmonics.

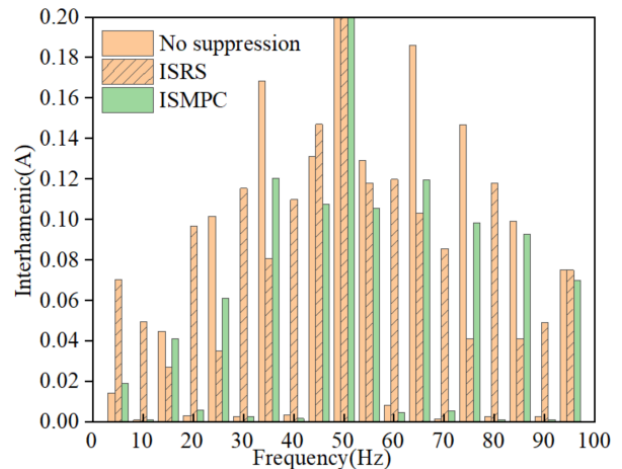


Fig. 9. Comparison of the suppression effect with ISRS strategy and ISMPC strategy.

V. CONCLUSION

In this paper, the interharmonic current characteristics of PV system based on MPPT perturbation are analyzed and an adaptive model predictive control strategy with interharmonic suppression is established. On this basis, automatic parameter optimization is achieved through the parameter adaptive adjustment to better achieve the interharmonic suppression effect. Simulation results show that the proposed method can effectively reduce the interharmonic amplitude, and the parameter adaptive adjustment ensures the enhanced suppression of specific interharmonics.

REFERENCES

- [1] V. Ravindran, S. Sakar, S. Rönnerberg, and M. H. J. Bollen, "Characterization of the impact of PV and EV induced voltage variations on LED lamps in a low voltage installation," *Electr. Power Syst. Res.*, vol. 185, no. November 2019, p. 106352, 2020.
- [2] W. T. El-Sayed, E. F. El-Saadany, and H. H. Zeineldin, "Interharmonic Differential Relay with a Soft Current Limiter for the Protection of Inverter-Based Islanded Microgrids," *IEEE Trans. Power Deliv.*, vol. 36, no. 3, pp. 1349–1359, 2021.
- [3] T. Busatto, F. Abid, A. Larsson, M. H. J. Bollen, and G. Singh, "Interaction between grid-connected PV systems and LED lamps: Directions for further research on harmonics and supraharmonics," *Proc. Int. Conf. Harmon. Qual. Power, ICHQP*, vol. 2016-December, pp. 193–197, 2016.
- [4] W. Chen, X. Yu, X. Han, Y. Jia, X. Chang, and X. Guo, "Analysis of Forced SSOs Excited by Subsynchronous Interharmonics from DPMSG-Based Wind Farms," *IEEE Trans. Sustain. Energy*, vol. 12, no. 2, pp. 978–989, 2021.
- [5] P. Pakonen, A. Hilden, T. Suntio, and P. Verho, "Grid-Connected PV Power Plant Induced Power Quality Problems – Experimental Evidence," *18th Eur. Conf. Power Electron. Appl.*, pp. 1–10, 2016.
- [6] A. Sangwongwanich, Y. Yang, D. Sera, H. Soltani, and F. Blaabjerg, "Analysis and Modeling of Interharmonics from Grid-Connected Photovoltaic Systems," *IEEE Trans. Power Electron.*, vol. 33, no. 10, pp. 8353–8364, 2018.
- [7] J. Hou, G. Ding, J. Shang, C. Wu, Z. Pan, and J. Wang, "An Interharmonics Suppression Control Scheme for PV System with Modified MPPT Algorithm," *Proc. Energy Convers. Congr. Expo. - Asia, ECCE Asia 2021*, vol. 0, pp. 238–242, 2021.
- [8] A. Sangwongwanich and F. Blaabjerg, "Mitigation of Interharmonics in PV Systems with Maximum Power Point Tracking Modification," *IEEE Trans. Power Electron.*, vol. 34, no. 9, pp. 8279–8282, 2019.
- [9] N. M. Dehkordi, N. Sadati, and M. Hamzeh, "A Robust Backstepping High-Order Sliding Mode Control Strategy for Grid-Connected DG Units With Harmonic/Interharmonic Current Compensation Capability," *IEEE Trans. Sustain. Energy*, vol. 8, no. 2, pp. 561–572, 2017.
- [10] Y. Pan, A. Sangwongwanich, Y. Yang, and F. Blaabjerg, "A Series Interharmonic Filter for Cascaded H-bridge PV Inverters," *ECCE 2020 - IEEE Energy Convers. Congr. Expo.*, pp. 341–346, 2020.
- [11] Y. Pan, A. Sangwongwanich, Y. Yang, and F. Blaabjerg, "A Phase-Shifting MPPT to Mitigate Interharmonics from Cascaded H-Bridge PV Inverters," *IEEE Trans. Ind. Appl.*, vol. 57, no. 3, pp. 3052–3063, 2021.
- [12] Q. Zhong, Q. Shi, G. Wang, and H. Li, "Interharmonic Analysis Model of Photovoltaic Grid-connected System Based on Perturbed MPPT Control," *Proceedings of the CSEE*, vol. 38, no. 22, pp. 6533–6542, 2018.
- [13] A. Mora, R. Cárdenas-Dobson, R. P. Aguilera, A. Angulo, F. Donoso, and J. Rodríguez, "Computationally Efficient Cascaded Optimal Switching Sequence MPC for Grid-Connected Three-Level NPC Converters," *IEEE Trans. Power Electron.*, vol. 34, no. 12, pp. 12464–12475, 2019.
- [14] N. Jin, M. Chen, L. Guo, Y. Li, and Y. Chen, "Double-Vector Model-Free Predictive Control Method for Voltage Source Inverter With Visualization Analysis," *IEEE Trans. Ind. Electron.*, vol. 69, no. 10, pp. 10066–10078, 2022.

Optimal Allocation of Vanadium Redox Flow Battery Storage Systems With Integrated Variable Renewable Energy

Chico Hermanu Brillianto Apribowo
*Department of Electrical and
 Information Engineering
 Universitas Gadjah Mada
 Yogyakarta, Indonesia*
 chico.hermanu1688@mail.ugm.ac.id
*Department of Electrical Engineering
 Universitas Sebelas Maret
 Surakarta, Indonesia*
 chico@staff.uns.ac.id

Sarjiya*
*Department of Electrical and
 Information Engineering
 Universitas Gadjah Mada
 Yogyakarta, Indonesia*
 sarjiya@ugm.ac.id

Sasongko Pramono Hadi
*Department of Electrical and
 Information Engineering
 Universitas Gadjah Mada
 Yogyakarta, Indonesia*
 sasongko@ugm.ac.id

F. Danang Wijaya
*Department of Electrical and
 Information Engineering
 Universitas Gadjah Mada
 Yogyakarta, Indonesia*
 danangwijaya@ugm.ac.id

Mokhammad Isnaeni Bambang
 Setyonegoro
*Department of Electrical and
 Information Engineering
 Universitas Gadjah Mada
 Yogyakarta, Indonesia*
 isnaeni@ugm.ac.id

Abstract: In recent years, the integration of variable renewable energy (VRE) into power grid systems has substantially increased. Nevertheless, the intermittent and uncertain nature of VRE presents fresh challenges to the power system's operation. To address these challenges, battery energy storage systems (BESS) emerge as a promising solution. Among various BESS technologies, the vanadium redox flow battery (VRFB) proves to be particularly effective in stabilizing the intermittent output power from renewable sources. The VRFB's extended lifespan ensures consistent battery performance over the long term. This study aims to tackle these challenges by optimizing the allocation and size of BESS with VRFB on a grid scale. Leveraging the general algebraic modeling system (GAMS) and the IEEE 39-bus system, the optimization process identifies the most optimal BESS allocation at buses 4 and 21, with a total power rating of 828.18 MW and an energy rating of 6363.84 MWh. Based on the comparison, VRFB-ESS exhibits approximately 7% lower daily operational costs than Li-ion BESS. The deployment of BESS enables efficient management of energy demand and generation fluctuations, reducing overall operational costs. Moreover, BESS plays a significant role in establishing a reliable, efficient, and sustainable energy system amidst the growing integration of renewable energy sources.

Keywords: Vanadium redox flow battery, battery energy storage systems, variable renewable energy, energy storage systems, optimal sizing, siting.

I. INTRODUCTION

Over the past few years, the integration of variable renewable energy (VRE) sources into power grid systems has seen a remarkable surge. Solar photovoltaic (PV) and wind turbine generators have become indispensable in meeting the rising energy needs while striving to lower greenhouse gas emissions [1]. Nevertheless, these sources intermittent and uncertain nature introduces novel challenges to power system operations.

The variability and unpredictability of photovoltaic and wind generators can result in energy supply instability and fluctuations. As an illustration, power flow in divergent directions during peak generation periods may lead to voltage surges within the network [2]. Furthermore, the mismatch between energy demand and generator output can increase the peak-to-average demand ratio, which impacts overall energy costs [3], [4].

Battery energy storage systems (BESS) have emerged as a comprehensive and promising solution to effectively address sudden power generation variations and intermittent fluctuations in VRE sources [5]. BESS offers a wide range of benefits that can significantly enhance power system performance. These advantages include the provision of additional services, load cutting during off-peak periods, load shifting, backup power support, demand response capabilities, microgrid utilization, seamless integration of renewable energy sources, frequency regulation, voltage control, load balancing, long-term energy storage, and even seasonal storage options [6], [7].

Among various battery technologies in BESS, large-scale electrochemical batteries such as lithium-ion (Li-Ion) and flow batteries have garnered significant attention in power systems due to their remarkable attributes of high energy density, flexibility, and scalability. The power system landscape has witnessed the suitability of various battery technologies, including Li-Ion, lead-acid, redox flow batteries, sodium-sulfur batteries, and more, catering to diverse applications [8]. Due to its capability for long-term, large-scale energy storage systems (ESS), the vanadium redox flow battery (VRFB) stands out as an extraordinary solution to stabilize fluctuating output power from VRE sources and ensure the dependability of power grids. VRFBs are a tempting option for developing strong and sustainable power systems with the seamless integration of renewable energy because of their versatility and efficiency [9]. VRFB holds

promise for stationary applications and renewable energy support. It boasts several advantages, including room temperature operation, a lengthy cycle life, and the ability to independently adjust power and capacity. With a projected lifespan exceeding 13,000 cycles, VRFB reliably performs for 10 to 20 years [10].

To achieve maximum efficiency, it is crucial to identify the optimal daily operational allocation of BESS integrated with VRE. Previous research has explored the use of BESS for peak load leveling, minimizing power losses in microgrids [11]. Optimizing BESS size and scheduling based on various battery technologies [12]. And supporting uncertainties in wind generation at the grid scale [13]. However, previous studies have not fully considered BESS allocation and optimization in grid-scale applications.

This paper focuses on a case study to determine the appropriate allocation and size of vanadium redox flow battery energy storage system (VRFB-ESS) at the grid scale to fill this research gap. The following are the primary contributions of this research:

1. Evaluating the impact of VRFB-ESS on the appropriate grid allocation and sizing to reduce curtailment of integrated VRE. The findings of this study will provide insights into how the adoption of VRFB-ESS affects the effectiveness and reliability of the power system at the integrated VRE grid level.
2. A mixed-integer linear programming (MILP) model is presented that may be applied to the IEEE 39-bus system integrated VRE with VRFB-ESS to identify optimal allocation and sizing solutions. This model can help practitioners and researchers plan and execute BESS in power systems.

The paper is organized as follows. Section 2 offers the mathematical formulation of the objective function and the constrained VRFB-ESS. Section 3 outlines the case study that was used. Section 4 contains the quantitative research findings. Section 5 reviews and discusses optimization performance. Finally, Section 6 discusses the conclusions and future work.

II. PROBLEM FORMULATION

The main objective of enhancing BESS operation is to lower power system operating expenses by using BESS allocation and sizing best. This is accomplished by maximizing the utilization of available BESS resources. In addition, acquiring accurate ideal findings from the ESS can improve network performance by lowering total losses and expenses and raising both the network's reliability and resilience[14].

A. Main Objective Function

The main objective function is developed using (1) to reduce daily operating costs, taking into account the generator operating cost, μ^G using (2), the VRE curtail cost, μ^{VREC} using (3), the cost of electricity not being supplied, μ^{VOLL} using (4), and the dan BESS cost, μ^{BESS} using (5). The following is the daily operating cost function:

$$\text{Min } C^{Operation} = \mu^G + \mu^{VREC} + \mu^{VOLL} + \mu^{BESS} \quad (1)$$

$$\mu^G = \sum_{i,t,g} (c_g^0 (p_{g,t}^{Gen})^2 + c_g^1 (p_{g,t}^{Gen}) + c_g^2) \quad (2)$$

$$\mu^{VREC} = \sum_{i,t} \mu_i^{VREC} p_{i,t}^{VREC} \quad (3)$$

$$\mu^{VOLL} = \sum_{i,t} c_i^{VOLL} p_{i,t}^{LS} \quad (4)$$

$$\mu^{BESS} = \frac{\sum_{b,i} P_{b,i}^{BESS} (\varepsilon_b^p + \varepsilon_b^{om}) + E_{b,i}^{BESS} (\varepsilon_b^e + \varepsilon_b^{ins})}{365 Tself} \quad (5)$$

Where g represents the generator unit index, i, j represents the time the bus unit index, t indicates the hours index, and b indicates the type of battery technology index. c_g^0, c_g^1, c_g^2 indicates the fuel cost coefficient generators, $p_{g,t}^{Gen}$ generator output power in MW, μ_i^{VREC} represents the value from VRE curtailment penalty, $p_{i,t}^{VREC}$ Represents VRE curtailment power in MW. c_i^{VOLL} represents the value from loss of load penalty, $p_{i,t}^{LS}$ Load shedding power in MW. The capital cost for the BESS rated power, the costs of operating and repairing the BESS, the installation fee for the BESS, and the investment cost for the energy rating of the BESS are represented by $\varepsilon_b^p, \varepsilon_b^{om}, \varepsilon_b^e, \varepsilon_b^{ins}$. The end-of-life battery in the year represented by $Tself$. $E_{b,i}^{BESS}$ represents BESS energy installed in MWh, and $P_{b,i}^{BESS}$ represents Installed BESS power in MW.

B. Operational constraint

To prevent overcharging and overcharging of the BESS and overcharging, it is required to restrict it using the number (6), (7). Equations (8) and (9) reflect the constraints that must be followed in order to maintain the balance of the BESS energy capacity. These equations ensure that the quantity of energy stored in the BESS at each interval is the same as the amount of energy stored in the previous interval and the energy consumed to charge or discharge the battery. Furthermore, these equations ensure that the amount of energy consumed to charge or discharge the battery is taken into account.

$$0 \leq p_{b,i,t}^{dch} \leq P_{b,i}^{BESS} \quad (6)$$

$$-P_{b,i}^{BESS} \leq p_{b,i,t}^{ch} \leq 0 \quad (7)$$

$$E_{b,i,t}^{BESS} = (1 - k_b^{sd}) E_{b,i,(t-1)}^{BESS} + \left(\eta_b^{ch} P_{b,i,t}^{ch} + \frac{p_{b,i,t}^{dch}}{\eta_b^{dch}} \right) \quad (8)$$

$$0 \leq E_{b,i,t}^{BESS} \leq E_{b,i}^{BESS} \quad (9)$$

Where $E_{b,i,t}^{BESS}$ represents state-of-charge or energy continuity BESS, k_b^{sd} represents battery self-discharge. $\eta_b^{ch}, \eta_b^{dch}$ represents efficient charging and discharge of the battery.

For limit the output of conventional generator, the outgoing power must be constrained with the generator operation constraint (10), the ramping-up constraint (11), and the decrease constraint (12) as follows:

$$p_{g,t}^{Gen,min} \leq p_{g,t}^{Gen} \leq p_{g,t}^{Gen,max} \quad (10)$$

$$p_{g,t}^{Gen} - p_{g,(t-1)}^{Gen} \leq RU_g \quad (11)$$

$$p_{g,(t-1)}^{Gen} - p_{g,t}^{Gen} \leq RD_g \quad (12)$$

Where the minimum and maximum limit of the conventional generator represented by $p_{g,t}^{Gen,min}$, $p_{g,t}^{Gen,max}$. Meanwhile, RU_g, RD_g represents ramp-up and ramp-down generators.

The available power supply places constraints on PV and wind, which can be represented by (13) and (14). The VRE curtailment in the system must be calculated; therefore, (15-17) represents the VRE curtailment electricity generated by subtracting the active photovoltaic output from the available power.

$$0 \leq p_{i,t}^{pv} \leq ppv_{i,t} \rho_i^{pv} \quad (13)$$

$$0 \leq p_{i,t}^w \leq pw_{i,t} \rho_i^w \quad (14)$$

$$p_{i,t}^{pvc} = ppv_{i,t} \rho_i^{pv} - p_{i,t}^{pv} \quad (15)$$

$$p_{i,t}^{pwc} = pw_{i,t} \rho_i^w - p_{i,t}^w \quad (16)$$

$$P_{i,t}^{VREc} = p_{i,t}^{pvc} + P_{i,t}^{pwc} \quad (17)$$

Where $ppv_{i,t}, pw_{i,t}$ represents Bus-Connected PV and Wind Availability. ρ_i^{pv}, ρ_i^w represents availability PV and wind power is connected to the bus in MW.

To maximize the BESS daily allocation and operational capacity while lowering daily operating costs, several operational constraints need to be considered to ensure grid balance. The following are the constraints to achieve grid balance using (18).

$$\sum_{g,t} p_{g,t}^{Gen} + \sum_{b,t} (-p_{b,t}^{ch} + p_{b,t}^{dch}) + p_{i,t}^{pv} + p_{i,t}^w + p_{i,t}^{LS} - p_{i,t}^{LD} = p_{i,j,t} \quad (18)$$

$$p_{i,j,t} = \frac{\theta_{i,t} - \theta_{j,t}}{X_{i,j}} \quad (19)$$

$$-p_{i,j,t}^{max} \leq p_{i,j,t} \leq p_{i,j,t}^{max} \quad (20)$$

$$0 \leq p_{i,t}^{LS} \leq (p_{i,t}^{LD}) \quad (21)$$

Equations (19), (20), and (21) indicate the active power flow from the branch and the limit of demand power, respectively. Where the charging of BESS represented by $p_{b,t}^{ch}$, and BESS was discharging power in MW which was represented by $p_{b,t}^{dch}$. The active power output from PV and the wind, and active power of the load were represented by $p_{i,t}^{pv}, p_{i,t}^w, p_{i,t}^{LD}$ respectively. $p_{i,j,t}$ represents the active flow of power coming from the branch that is linked to the bus. The voltage angle between the buses, as well as the bus's reactance, have a direct impact on the quantity of power transferred. The voltage angle of bus I, indicated by, and the branch's reactance are shown $\theta_{i,t}$, and $X_{i,j}$. The maximum amount of power that can pass through the branch-connected bus, represented by $p_{i,j,t}^{max}$.

III. PROPOSED METHODOLOGY

The main purpose of the research is to establish the optimum size and distribution of BESS on a grid-scale, considering the demand reduction and peak shaving that VRE

can achieve. A few factors, including the power rating variable, determine the ideal outcomes of the BESS system, $P_{b,i}^{BESS}$, the energy rating, $E_{b,i}^{BESS}$, and the allocation of BESS buses. The method employed is MILP, and the system model applied is DC optimal power flow (OPF). The objective of the DC OPF is to optimize the power output generated by the generators and the power flow through the power network by minimizing costs, as formulated in the objective function (1). Generally, the MILP algorithm uses the branch-and-bound approach, as illustrated in Fig. 1. The bounding process offers solutions to relaxed issues, which can act as lower bounds for problems involving minimization or as upper bounds for problems involving maximization. On the other hand, the branching process entails breaking down the primary problem into several more manageable pieces [15].

IV. CASE STUDY

For the purposes of this study, a modified of the IEEE 39-bus system was utilized [16] in order to do an analysis of the best sizing and allocation of BESS on a grid scale integrated with VRE. The National Renewable Energy Laboratory (NREL) is the source for the VRE data curves in position (48.94W°, -123.054N°) [17]. Both bus 21 and bus 26 have photovoltaic capacity installed, with bus 21 having 2700 MW and bus 26 having 100 MW. As can be seen in Fig. 2, the installed wind turbines have capacity of 500 MW at bus 4 and 250 MW at bus 8. Fig. 3 illustrates the demand curve that will be utilized in this analysis. The generation curves for photovoltaic and wind energy are shown in Fig. 4, respectively. In this study, the cost loss of load (VOLL) is \$50,000/MWh, and the cost of VRE reduction is \$50/MWh. The BESS characteristic data in Table 1 is based on VRFB. All optimization models were implemented using GAMS 39.2.1. The computational study was carried out using the MILP solver that was provided by CONOPT. This was accomplished using an AMD Ryzen 5 3550h processor with 16 GB of RAM at a clock speed of 3.6 GHz.

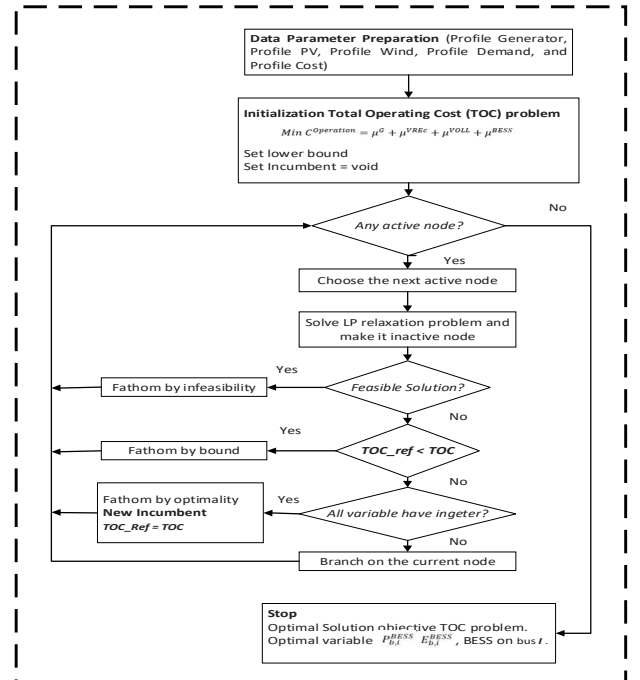


Fig. 1. Flowchart allocation and sizing VRFB-ESS

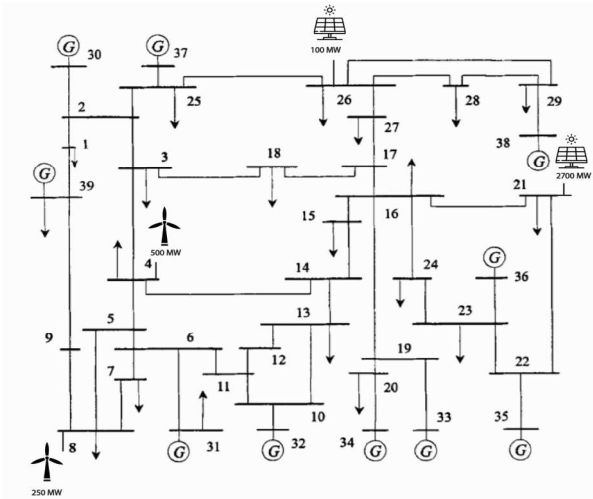


Fig. 2. Modified IEEE 39-bus system [16]

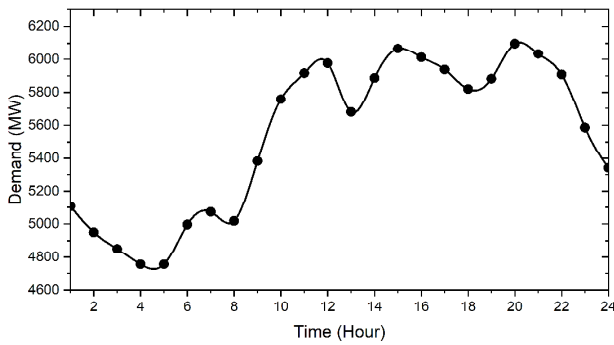


Fig. 3. Hourly load demand data for the modified IEEE 39-bus system

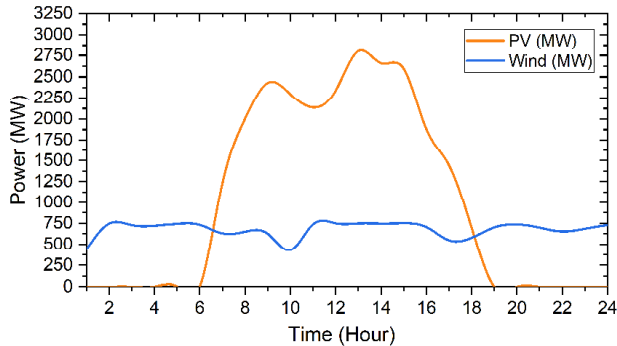


Fig. 4. PV and wind power generation

TABLE I. DATA PARAMETER BATTERY [9], [14], [18]

| Parameter | VRFB | Li-Ion |
|-----------------------------|-----------|----------|
| Efficiency Round-Trip (%) | 90 | 90 |
| Self Discharge on Daily (%) | 0.2 | 0.2 |
| End-of-life Battery (year) | 20 | 10 |
| Power Rate Cost (\$/kW) | 2300 | 320 |
| Energy Rate Cost (\$/kWh) | 58.4 | 360 |
| Installation Cost | \$ 250000 | 15 \$/kW |
| Maintenance Cost (\$/kW/yr) | 300 | 5 |

V. NUMERICAL RESULT

This study aimed to analyze the impact of VRFB-ESS on the optimal allocation and sizing at the grid scale to reduce curtailment of unused VRE. Three cases were considered:

- Case 1 focused on minimizing daily operation costs in the IEEE 39-bus system without VRE and VRFB-ESS.
- Case 2 involved the inclusion of VRE in the system, with PV capacity of 2800 MW and wind capacity of 750 MW.
- Case 3 incorporated VRFB-ESS with integrated VRE in the system.
- Case 4 incorporated Li-ion BESS with integrated VRE in the system.

Using the GAMS program and predefined case parameters, the optimal allocation and size of VRFB-ESS were determined. To determine the allocation and size of VRFB-ESS, the variables $P_{b,i}^{BESS}$ and $E_{b,i}^{BESS}$ were utilized according to equation (5). A comparison of the production of the conventional generator unit is illustrated in Fig. 5. From the comparison figure, it can be observed that in the all case, there are changes in the production of generator capacities compared to the first and second cases. VRE and VRFB-ESS use. In the first case, the production of generators g1 to g10 solely depends on the power allocation of the demand for generators and the load at specific times. In the second case, the integrated VRE causes some generators, such as g5 and g6, to experience power curtailment, as the power generated from renewable sources partially meets the load demand.

In contrast, in case 3 and 4, the VRFB-ESS helps store excess energy from VRE when the generated power exceeds the load demand and discharges energy when VRE cannot meet the load demand. As a result, some generators involved in Case 2, such as g5 and g6, experience an increase in power production as the VRFB-ESS optimizes production and minimizes VRE curtailment. The optimization results demonstrate that the generators collectively contribute to a total capacity ranging from 2958.89 MW to 4532.64 MW. The presence of VRFB-ESS allows the system to be more efficient in dealing with VRE fluctuations.

The optimization results shown in Fig. 6 indicate that the VRFB-ESS system is efficiently managed to optimize the utilization of energy sources and meet fluctuating energy demands. The power output of PV and wind varies from one time interval to another, highlighting the uncertainty in renewable energy generation. In order to prevent energy waste, photovoltaic generation is restricted from intervals t6 to t17 when the energy demand is less than the production of solar energy. Consequently, the VRFB-ESS during intervals t7 to t16 to charge and provide power when the energy demand exceeds generation during t17 to t24. As shown in Fig. 7, during the intervals t7 to t16, the BESS charges for storing excess energy from PV and wind generation. And discharges to balance energy demand and generation in intervals t17 to t24.

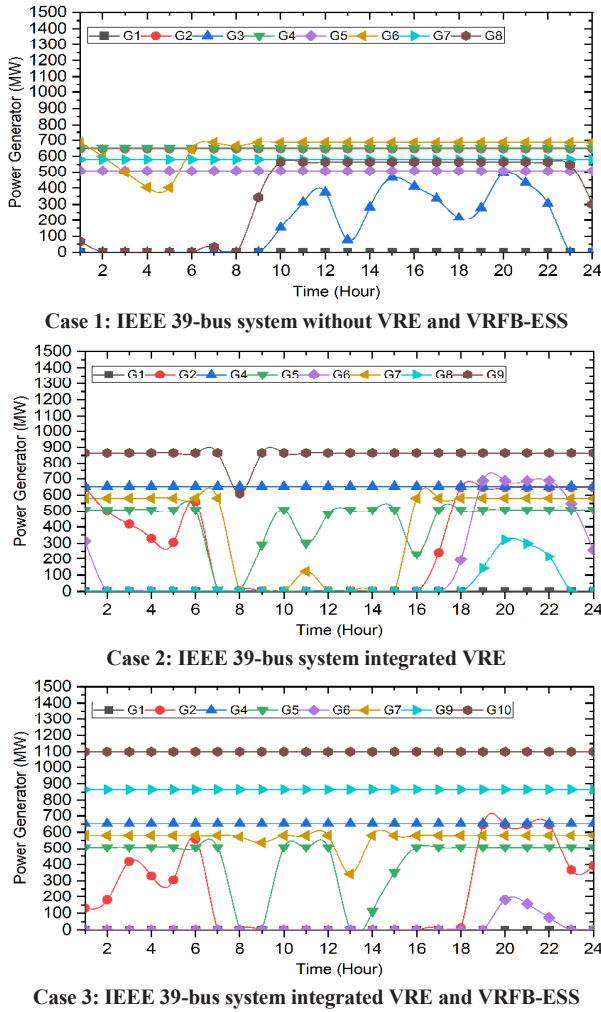


Fig. 5. A comparison of the production of conventional generators unit in varying case

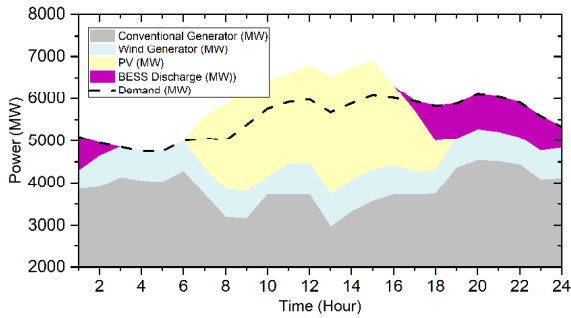


Fig. 6. Daily energy dispatch in VRE and VRFB-ESS integrated

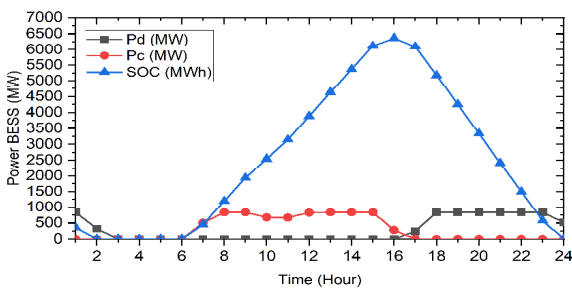


Fig. 7. Daily energy dispatch VRFB-ESS

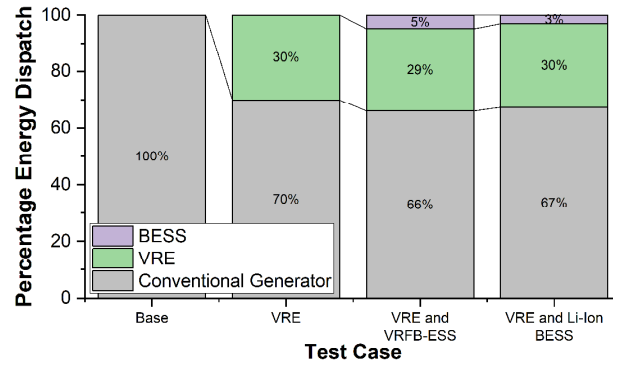


Fig. 8. Percentage energy dispatch in varying case

TABLE II. NUMERICAL SIMULATION RESULTS OF THE OPTIMIZATION

| Variable | Case 1 | Case 2 | Case 3 | Case 4 |
|---------------------------|-------------------|-------------------|-------------------|-------------------|
| Technology BESS | - | - | VRFB | Li-ion |
| Lifetime BESS (year) | - | - | 20 | 10 |
| Generator cost (\$) | 6746872.26 | 2498746.30 | 1730913.74 | 1978598.57 |
| Loss of load cost (\$) | - | - | - | - |
| VRE curtail cost(\$) | - | 35788.18 | - | - |
| BESS cost(\$) | - | - | 530422.75 | 452587.65 |
| Daily operation cost (\$) | 6746872.26 | 2534534.48 | 2261336.49 | 2431186.23 |
| Power Rate (MW) | - | - | 828.18 | 619.57 |
| Energy Rate (MWh) | - | - | 6363.84 | 3868.23 |
| Bus Location for BESS | - | - | 4, 21 | 21 |

Fig. 8 shows that in Case 2, VRE contributes 30% of the energy, while the remaining 70% of the total energy production is obtained from generators. On the contrary, in Case 3, the conventional generator energy production decreases to 66% of the total production, with VRE still contributing 29% and VRFB-ESS contributing 5%. In Case 4, the generator energy production decreases to 67%, with VRE contributing 30% and VRFB-ESS contributing 3%. This indicates that the utilization of VRE and BESS has the potential to reduce dependence on conventional generators to meet energy demands.

The cost comparison results of the optimization are shown in Table 2. From the table, it can be concluded that the use of VRE and VRFB-ESS in Cases 3 leads to increased efficiency and reduced operational costs of the power system. In these cases, the conventional generator costs experience a significant decrease, resulting in a lower daily operating cost. The daily operation cost in case 3 is \$2,261,336.49, with the optimal allocation and size of VRFB-ESS determined at bus 4 with a rating of 9.18 MW and 61.21 MWh, and on bus 21 with a rating of 819.00 MW and 6302.63 MWh. This suggests that the system model ultimately decides on the optimal allocation of VRFB-ESS in the location with the highest PV capacity (2700 MW) in bus 21 to reduce curtailment and at bus 4 to provide backup power at the load of the IEEE 39-bus system.

Based on the comparison, VRFB-ESS exhibits approximately 7% lower daily operational costs than Li-Ion BESS despite the higher initial cost of VRFB. This cost

advantage can be attributed to the longer end-of-life duration of VRFB-ESS compared to that of Li-ion BESS. Consequently, in the simulation results, the percentage of energy dispatch allocated to VRFB-ESS is higher by 5%, resulting in reduced conventional generator costs as well.

Overall, the integration of VRE and VRFB-ESS in the power system can bring benefits in terms of efficiency, reduced operational costs, and reduction in the reduction of renewable energy sources, making the power system more sustainable and environmentally friendly.

VI. CONCLUSION AND FUTURE WORK

BESS has been considered a promising solution to mitigate sudden variations in power generation and intermittent fluctuations in VRE. Among various battery technologies in BESS, VRFB is considered an excellent solution to stabilize VREs fluctuating output power and assure the dependability of power grids through its capacity for long-term and large-scale energy storage.

This study aims to optimize the allocation and sizing of VRFB-ESS on a grid-scale to cope with the increasing penetration and reduce curtailment of VRE in the distribution system. This will help address the difficulties that have been presented. Incorporating both the GAMS and IEEE 39-bus system.

The optimization results reveal the optimal allocation of VRFB-ESS to buses 4 and 21, with a total power rating of 828.18 MW and an energy rating of 6363.84 MWh. With VRFB-ESS, the reduction of VRE from sources such as photovoltaic and wind generators is effectively managed, avoiding energy waste and maintaining a balance between energy demand and generation. The optimized operational cost of the power system is \$2,261,336.49, covering generator costs, PV curtailment costs, and VRFB-ESS costs. VRFB-ESS has a 7% lower daily operational cost than Li-Ion BESS despite VRFB having a higher initial cost. This is because VRFB-ESS has a longer end-of-life duration. The simulation results also show a 5% increase in energy dispatch to VRFB-ESS, leading to lower conventional generator costs.

Due to the limitations of this study, unit commitment and battery degradation were not considered. In future research, the focus should be on BESS with a focus on long-term planning, considering the unit commitment of generators and battery degradation to assess their potential impact on power system planning.

ACKNOWLEDGMENT

We gratefully acknowledge the funding from the Center for Higher Education Funding – Ministry of Education, Culture, Research, and Technology Republic of Indonesia (BPPT – Kemendikbudristek RI), the Indonesia Endowment Fund for Education – Ministry of Finance Republic of Indonesia (LPDP – Kemenkeu RI).

REFERENCES

- [1] Y. Zheng, Y. Song, A. Huang, and D. J. Hill, "Hierarchical Optimal Allocation of Battery Energy Storage Systems for Multiple Services in Distribution Systems," *IEEE Trans Sustain Energy*, vol. 11, no. 3, pp. 1911–1921, 2020, doi: 10.1109/TSTE.2019.2946371.
- [2] H. Hao, D. Wu, J. Lian, and T. Yang, "Optimal Coordination of Building Loads and Energy Storage for Power Grid and End User Services," *IEEE Trans Smart Grid*, vol. 9, no. 5, pp. 4335–4345, Sep. 2018, doi: 10.1109/TSG.2017.2655083.
- [3] X. Wang, F. Li, Q. Zhang, Q. Shi, and J. Wang, "Profit-Oriented BESS Siting and Sizing in Deregulated Distribution Systems," *IEEE Trans Smart Grid*, vol. 14, no. 2, pp. 1528–1540, 2023, doi: 10.1109/TSG.2022.3150768.
- [4] F. X. N. Soelami *et al.*, "Energy Management Modeling for Microgrid System in a Smart Build," *Jurnal Nasional Teknik Elektro dan Teknologi Informasi*, vol. 9, no. 4 SE-Articles, Dec. 2020, doi: 10.22146/jnteti.v9i4.488.
- [5] C. H. B. Apriowo, S. Sarjiya, S. P. Hadi, and F. D. Wijaya, "Optimal Planning of Battery Energy Storage Systems by Considering Battery Degradation due to Ambient Temperature: A Review, Challenges, and New Perspective," *Batteries*, vol. 8, no. 12, 2022, doi: 10.3390/batteries8120290.
- [6] M. Stecca, L. R. Elizondo, T. B. Soeiro, P. Bauer, and P. Palensky, "A comprehensive review of the integration of battery energy storage systems into distribution networks," *IEEE Open Journal of the Industrial Electronics Society*, vol. 1, no. 1, pp. 46–65, 2020, doi: 10.1109/OJIES.2020.2981832.
- [7] C. H. B. Apriowo, Sarjiya, S. P. Hadi, and F. D. Wijaya, "Integration of Battery Energy Storage System to Increase Flexibility and Penetration Renewable Energy in Indonesia: A Brief Review," *2022 5th International Conference on Power Engineering and Renewable Energy (ICPERE)*, 2022, doi: 10.1109/ICPERE56870.2022.10037530.
- [8] C. H. B. Apriowo, Sarjiya, S. P. Hadi, and F. Danang Wijaya, "Optimal Sizing and Siting of Battery Energy Storage Systems with Retired Battery," *2022 International Conference on Technology and Policy in Energy and Electric Power (ICT-PEP)*, pp. 327–332, 2022, doi: 10.1109/ICT-PEP57242.2022.9988958.
- [9] T. A. Nguyen, M. L. Crow, and A. C. Elmore, "Optimal sizing of a vanadium redox battery system for microgrid systems," *IEEE Trans Sustain Energy*, vol. 6, no. 3, pp. 729–737, Jul. 2015, doi: 10.1109/TSTE.2015.2404780.
- [10] D. Cremoncini, G. F. Frate, A. Bischi, and L. Ferrari, "Mixed Integer Linear Program model for optimized scheduling of a vanadium redox flow battery with variable efficiencies, capacity fade, and electrolyte maintenance," *J Energy Storage*, vol. 59, no. August 2022, 2023, doi: 10.1016/j.est.2022.106500.
- [11] A. Pena-Bello, E. Barbour, M. C. Gonzalez, M. K. Patel, and D. Parra, "Optimized PV-coupled battery systems for combining applications: Impact of battery technology and geography," *Renewable and Sustainable Energy Reviews*, vol. 112, no. February, pp. 978–990, 2019, doi: 10.1016/j.rser.2019.06.003.
- [12] I. Alsaïdan, A. Khodaei, and W. Gao, "A Comprehensive Battery Energy Storage Optimal Sizing Model for Microgrid Applications," *IEEE Transactions on Power Systems*, vol. 33, no. 4, pp. 3968–3980, 2018, doi: 10.1109/TPWRS.2017.2769639.
- [13] Y. Zhang, Y. Su, Z. Wang, F. Liu, and C. Li, "Cycle-Life-Aware Optimal Sizing of Grid-Side Battery Energy Storage," *IEEE Access*, vol. 9, pp. 20179–20190, 2021, doi: 10.1109/ACCESS.2021.3054860.
- [14] M. Amini, A. Khorsandi, B. Vahidi, S. H. Hosseinian, and A. Malakmahmoudi, "Optimal sizing of battery energy storage in a microgrid considering capacity degradation and replacement year," *Electric Power Systems Research*, vol. 195, Jun. 2021, doi: 10.1016/j.epsr.2021.107170.
- [15] I. Alsaïdan, A. Khodaei, and W. Gao, "A Comprehensive Battery Energy Storage Optimal Sizing Model for Microgrid Applications," *IEEE Transactions on Power Systems*, vol. 33, no. 4, pp. 3968–3980, Jul. 2018, doi: 10.1109/TPWRS.2017.2769639.
- [16] T. Athay, R. Podmore, and S. Virmani, "A practical method for the direct analysis of transient stability," *IEEE Transactions on Power Apparatus and Systems*, vol. PAS-98, no. 2, pp. 573–584, 1979, doi: 10.1109/TPAS.1979.319407.
- [17] NREL, "Solar Power Data for Integration Studies | Grid Modernization."
- [18] A. A. Kebede, T. Kalogiannis, J. Van Mierlo, and M. Berecibar, "A comprehensive review of stationary energy storage devices for large scale renewable energy sources grid integration," *Renewable and Sustainable Energy Reviews*, vol. 159, p. 112213, May 2022, doi: 10.1016/J.RSER.2022.112213.

AUTHOR INDEX

| Author | Session | Start page |
|--|----------|---------------------|
| Action, Anish Kumar Saha | CNT-2.6 | 348 |
| Adiyatma, Farid Yuli | CNT-2.5 | 342 |
| Ageng, Gregorio | AIML-1.6 | 55 |
| Ahmad, Musyaffa' | PS-2.1 | 383 |
| Aiyarak, Pattara | IT-1.3 | 366 |
| Aji, Alharisy | AIML-1.6 | 55 |
| Aji, Hilal Bayu | AIML-1.6 | 55 |
| Aksaraliksanti, Nattapong | IT-1.1 | 354 |
| Alfarozi, Syukron Abu Ishaq | AIML-3.7 | 121 |
| Ali, Husni Rois | PS-1.1 | 196 |
| | PS-2.2 | 389 |
| Angkurawaranon, Salita | AIML-5.1 | 263 |
| Anusas-amornkul, Tanapat | AIML-4.4 | 247 |
| Apibowo, Chico Hermanu Brillianto | PS-2.4 | 399 |
| Arfakhsyad, Azfar | CNT-1.6 | 155 |
| Arfiantino, Dimas | AIML-1.6 | 55 |
| Arshella, Ika | AIML-3.1 | 87 |
| | AIML-1.4 | 43 |
| | AIML-1.5 | 49 |
| | AIML-1.6 | 55 |
| Ataka, Ahmad | CNT-1.6 | 155 |
| | | |
| Auephanwiriyaikul, Sansanee | AIML-5.4 | 281 |
| Awalurahman, Halim | IT-1.4 | 371 |
| Bambang Setyonegoro, Mokhammad Isnaeni | PS-2.4 | 399 |
| Barr, Abdul | AIML-1.6 | 55 |
| Boondamnoen, Mongkol | JSCI.5 | 186 |
| Boonkorkoer, Chukiat | JSCI.1 | 162 |
| Boonsang, Siridech | AIML-1.2 | 31 |
| | AIML-5.5 | 287 |
| Boonsrimuang, Pisit | CNT-2.1 | 323 |
| Boonsrimuang, Pornpawit | CNT-2.1 | 323 |
| Bualoy, Sukawit | IT-1.2 | 360 |
| Bunjongsat, Sarun | JSCI.2 | 168 |

| Author | Session | Start page |
|-----------------------------|----------|---------------------|
| Bussabong, Naphat | AIML-4.4 | 247 |
| Cahyadi, Adha | AIML-1.5 | 49 |
| Cahyadi, Adha Imam | PS-1.3 | 208 |
| Cahyeni, Nadia | PS-1.2 | 202 |
| Candra, Rizky | AIML-1.6 | 55 |
| Chaiyasoonthorn, Wornchanok | BMI.3 | 304 |
| Chalongvorachai, Thasorn | AIML-1.3 | 37 |
| Chatpibal, Manoj | BMI.2 | 298 |
| Chavanit, Nattawat | IT-1.2 | 360 |
| Chaveesuk, Singha | BMI.3 | 304 |
| Cherntanomwong, Panarat | CNT-2.5 | 342 |
| Chidchuea, Kemmathad | CNT-1.2 | 131 |
| Choksuchat, Chainarong | AIML-5.2 | 269 |
| Choksuchat, Chidchanok | IT-1.3 | 366 |
| Chudpooti, Nonchanutt | CNT-2.3 | 333 |
| | CNT-2.4 | 338 |
| Chuwongin, Santhad | AIML-1.2 | 31 |
| | AIML-5.5 | 287 |
| Deebhijarn, Samart | BMI.1 | 293 |
| Dilokthanakul, Nat | AIML-3.2 | 93 |
| | AIML-3.3 | 99 |
| Farda, Irfan | AIML-2.1 | 61 |
| Farel, Daud | PS-1.5 | 220 |
| Fazekas, Szilard | AIML-1.1 | 25 |
| Firmansyah, Eka | PS-1.2 | 202 |
| | PS-2.1 | 383 |
| Frasetyo, Mohd. Brado | PS-1.3 | 208 |
| | PS-2.2 | 389 |
| Fu, Xiao Da Terrence | AIML-3.4 | 104 |
| Hadi, Sasongko | PS-2.4 | 399 |
| Hakim, Alfin Luqmanul | AIML-1.6 | 55 |
| Hakim, Iqbal Burhanul | CNT-1.5 | 149 |
| Hamdani, Muhammad | IT-1.4 | 371 |
| Hanief, Rifqi | IT-1.4 | 371 |

| Author | Session | Start page |
|-----------------------------|----------|---------------------|
| Hanun, Amira | PS-1.4 | 214 |
| | PS-1.5 | 220 |
| | PS-1.6 | 226 |
| Hartanto, Rudy | AIML-3.1 | 87 |
| Hidayat, Risanuri | CNT-2.2 | 327 |
| Homwiseswongsa, Akarasate | AIML-2.3 | 71 |
| Inkeaw, Papangkorn | AIML-5.1 | 263 |
| Irnawan, Roni | PS-1.3 | 208 |
| Isawa, Sho | AIML-1.1 | 25 |
| Ishmatuka, Cendikia | AIML-1.4 | 43 |
| | AIML-1.6 | 55 |
| Iswandi, Iswandi | CNT-2.2 | 327 |
| Jaksukam, Komgrit | AIML-5.5 | 287 |
| Jaruenpunyasak, Jermphiphut | AIML-5.2 | 269 |
| Jitkongchuen, Duangjai | AIML-2.2 | 66 |
| | AIML-4.2 | 237 |
| Jitpattanakul, Anuchit | AIML-4.5 | 253 |
| Jomtarak, Rangsan | AIML-5.5 | 287 |
| Kaewkiriya, Thongchai | JSCI.3 | 174 |
| Kantawong, Krittika | AIML-2.2 | 66 |
| Kanungsukkasem, Nont | AIML-5.3 | 275 |
| Kartono, Kartono | IT-1.4 | 371 |
| Keerativutisest, Vasu | BMI.4 | 311 |
| Khoirom, Motilal | CNT-2.6 | 348 |
| Khoirunnisaa, Kunti | AIML-3.1 | 87 |
| Kinanti, Larasati | CNT-1.6 | 155 |
| Kisna, Kurnia | PS-1.4 | 214 |
| | PS-1.6 | 226 |
| Kitchat, Kotcharat | AIML-4.6 | 258 |
| Kittichai, Veerayuth | AIML-5.5 | 287 |
| Korompis, Rikza | IT-1.4 | 371 |
| Kumkhet, Boonyarit | CNT-1.3 | 137 |
| Kundu, Sukanya | AIML-2.5 | 81 |
| Kusumawardani, Sri Suning | AIML-3.7 | 121 |
| Kyaw, Htet | BMI.4 | 311 |
| Lalitrojwong, Pattarachai | AIML-1.2 | 31 |

| Author | Session | Start page |
|--------------------------|----------|---------------------|
| Lavangnananda, Kittichai | AIML-3.6 | 115 |
| Leelanupab, Teerapong | AIML-5.3 | 275 |
| Leprevost, Franck | AIML-3.6 | 115 |
| Li, Feifan | JSCI.4 | 180 |
| Liu, Zongying | JSCI.4 | 180 |
| Longpradit, Panchit | AIML-2.2 | 66 |
| Loo, Chu Kiong | AIML-3.2 | 93 |
| Ma, Fuping | PS-2.3 | 394 |
| Madla, Chakri | AIML-5.1 | 263 |
| Maitra, Sarit | AIML-2.5 | 81 |
| Maliyaem, Maleerat | JSCI.1 | 162 |
| Mancellari, Enea | AIML-3.6 | 115 |
| Maneelert, Prawai | AIML-5.2 | 269 |
| Mao, Mingxuan | PS-2.3 | 394 |
| Maulana, Rifqi | PS-1.1 | 196 |
| Meesad, Phayung | JSCI.1 | 162 |
| Mekruksavanich, Sakorn | AIML-4.5 | 253 |
| Mi, Si Sar | CNT-2.1 | 323 |
| Mishra, Vivek | AIML-2.5 | 81 |
| Moodleah, Samart | IT-1.2 | 360 |
| Mudarris, Mudarris | PS-2.1 | 383 |
| Muhammad, Hannan | CNT-1.6 | 155 |
| Mukti, Aldo Arya Saka | AIML-3.7 | 121 |
| Murnani, Suatmi | CNT-1.5 | 149 |
| Mustika, I Wayan | AIML-3.1 | 87 |
| | CNT-1.1 | 127 |
| Muthahhari, Ahmad | PS-1.6 | 226 |
| Namkhun, Songphon | AIML-4.1 | 232 |
| Nanda, Aan Aria | AIML-1.6 | 55 |
| Nawae, Marwan | AIML-5.2 | 269 |
| Ng, Qi Ding | AIML-3.2 | 93 |
| Ngamkham, Woramat | JSCI.6 | 192 |
| Nugraha, Ghanis Kauchya | AIML-1.6 | 55 |
| Obrochta, Stephen | AIML-1.1 | 25 |
| Oktavian, Mahardika | IT-1.4 | 371 |

| Author | Session | Start page |
|------------------------------------|----------|---------------------|
| Pan, Mingyang | JSCI.4 | 180 |
| Panitkulpong, Kaimuk | BMI.1 | 293 |
| Pasupa, Kitsuchart | AIML-3.2 | 93 |
| Patgiri, Ripon | CNT-2.6 | 348 |
| Pavarangkoon, Praphan | AIML-3.3 | 99 |
| Pechrkool, Tanaporn | CNT-1.3 | 137 |
| Pengchata, Rattasak | AIML-2.2 | 66 |
| Phairatana, Tonghathai | AIML-5.2 | 269 |
| Phakdee, Nuttaporn | IT-1.5 | 377 |
| Phettom, Rattanathon | AIML-5.4 | 281 |
| Phongcharoenpanich, Chuwong | CNT-2.3 | 333 |
| | CNT-2.4 | 338 |
| Phu-ang, Ajchara | AIML-2.4 | 77 |
| Pimsen, Taiwit | CNT-1.2 | 131 |
| Pinetsuksai, Natchapon | AIML-5.5 | 287 |
| Pirajnanchai, Virote | CNT-1.3 | 137 |
| Piyamongkol, Korakit | BMI.2 | 298 |
| Polsena, Tatshakon | AIML-4.2 | 237 |
| Praking, Phornnatee | AIML-4.6 | 258 |
| Pratama, Azkario Rizky | AIML-4.3 | 241 |
| Pravesjit, Sakkayaphop | AIML-2.2 | 66 |
| Prommin, Phatcharaphon | BMI.2 | 298 |
| Promsuk, Natthanan | CNT-1.4 | 143 |
| Pruthipanyasakul, Nareeekarn | AIML-5.3 | 275 |
| Pukrongta, Nisit | CNT-1.3 | 137 |
| Putjorn, Pruet | BMI.5 | 317 |
| Putjorn, Tat | BMI.5 | 317 |
| Putra, Bagus Rakadyanto Oktavianto | AIML-4.3 | 241 |
| Putra, Muhammad Ichsan Ramadani | CNT-1.5 | 149 |
| Putranto, Lesnanto Multa | PS-1.4 | 214 |
| | PS-1.5 | 220 |
| | PS-1.6 | 226 |
| Raharjana, Indra | IT-1.4 | 371 |
| Rahman, Aufa | CNT-1.6 | 155 |
| Ramdan, Sigit | PS-2.1 | 383 |

| Author | Session | Start page |
|-----------------------------|----------|---------------------|
| Ratanavilisagul, Chiabwoot | AIML-2.3 | 71 |
| Rohmani, Syahrul | IT-1.4 | 371 |
| Rosoon, Yuwana | IT-1.3 | 366 |
| Saengnoree, Amnuay | BMI.1 | 293 |
| Saengsai, Apisit | IT-1.5 | 377 |
| Sahabantoegnsin, Thanapat | JSCI.5 | 186 |
| Sangmahamad, Pubet | CNT-1.3 | 137 |
| Sarapugdi, Wanaporn | AIML-4.1 | 232 |
| Sarjiya, Sarjiya | PS-1.5 | 220 |
| | PS-1.6 | 226 |
| | PS-2.4 | 399 |
| Sasisaowapak, Thanyathep | AIML-1.2 | 31 |
| Savitri, Ira | PS-1.5 | 220 |
| Setiadilaga, Ocklen | AIML-1.5 | 49 |
| Setiawan, Hendra | CNT-1.5 | 149 |
| Setya Budi, Rizki | PS-1.6 | 226 |
| Setyadi, Ahmad Didik | AIML-1.6 | 55 |
| Shamsi, Zeba | CNT-2.6 | 348 |
| Sidik, Yohan | PS-1.1 | 196 |
| | PS-1.2 | 202 |
| | PS-1.3 | 208 |
| | PS-2.1 | 383 |
| Singh, Laiphrakpam Dolendro | CNT-2.6 | 348 |
| Siriwanitpong, Aphitchaya | CNT-2.1 | 323 |
| Sithanant, Thana | BMI.3 | 304 |
| Soesanti, Indah | AIML-1.4 | 43 |
| Soon, Xiao Xi Natasha | AIML-3.5 | 109 |
| Srigrarom, Sutthiphong | AIML-3.4 | 104 |
| | AIML-3.5 | 109 |
| Suetrong, Nopparuj | CNT-1.4 | 143 |
| Sukphisal, Burin | BMI.2 | 298 |
| Supreeyatitikul, Nathapat | CNT-2.3 | 333 |
| | CNT-2.4 | 338 |
| Surasak, Thattapon | AIML-4.6 | 258 |
| Suroso, Dwi | CNT-2.5 | 342 |

| Author | Session | Start page |
|-------------------------------|----------|---------------------|
| Taparugssanagorn, Attaphongse | CNT-1.4 | 143 |
| Tedsakorn, Surawee | IT-1.1 | 354 |
| Teerarattanyu, Thanapat | AIML-3.3 | 99 |
| Teerawatananond, Thapong | BMI.1 | 293 |
| Thabarsa, Phattanun | AIML-5.1 | 263 |
| Thaenthong, Jirawat | CNT-1.2 | 131 |
| Thammano, Arit | AIML-2.1 | 61 |
| | AIML-2.2 | 66 |
| | AIML-2.4 | 77 |
| Theera-Umpon, Nipon | AIML-5.4 | 281 |
| Thiamsinsangwon, Puttiporn | CNT-1.3 | 137 |
| Thongsri, Kamolwich | JSCI.5 | 186 |
| Thusaranon, Panita | AIML-4.2 | 237 |
| Tongloy, Teerawat | AIML-1.2 | 31 |
| | AIML-5.5 | 287 |
| Topal, Ali Osman | AIML-3.6 | 115 |
| Triyanto, Dedi | CNT-1.1 | 127 |
| Tumiran, Tumiran | PS-1.5 | 220 |
| | PS-1.6 | 226 |
| Unsrison, Kittisak | AIML-5.1 | 263 |
| Urruty, Thierry | AIML-5.3 | 275 |
| Vittayakorn, Sirion | JSCI.2 | 168 |
| | IT-1.1 | 354 |
| Vuthiwong, Withawat | AIML-5.1 | 263 |
| Wibowo, Sigit | CNT-2.2 | 327 |
| Widiastuti, Avrin | PS-1.4 | 214 |
| Widyawan, Widy | CNT-1.1 | 127 |
| | PS-1.3 | 208 |
| | PS-2.1 | 383 |
| | PS-2.2 | 389 |
| Wijaya, Fransisco | PS-2.2 | 389 |
| | PS-2.4 | 399 |
| Wisudawan, Hasbi Nur Prasetyo | CNT-1.5 | 149 |
| Wongchai, Tunlaton | AIML-3.3 | 99 |

| Author | Session | Start page |
|------------------------|----------|---------------------|
| Woraratpanya, Kuntpong | AIML-1.3 | 37 |
| | AIML-3.1 | 87 |
| | JSCI.3 | 174 |
| | JSCI.5 | 186 |
| | JSCI.6 | 192 |
| Zaman, Badrus | IT-1.4 | 371 |
| Zhang, Jie | AIML-3.2 | 93 |
| Zhang, Wenru | JSCI.4 | 180 |
| Zhao, Liuqing | PS-2.3 | 394 |



<https://icitee2023.it.kmitl.ac.th>